



SAKARYA
ÜNİVERSİTESİ

Sakarya University Journal of Science



e-issn: 2147-835X

Volume 22 Issue 6

<http://www.saujs.sakarya.edu.tr/issue/31266>



Sakarya Üniversitesi Fen Bilimleri Enstitüsü Dergisi
Sakarya University Journal of Science

Editör Listesi

Editorial Board

Cilt 22 Sayı 6

Volume 22 Issue 6

Baş Editör
Executive Editor

Emrah Doğan Sakarya Uni.

Genel Yayın Yönetmeni
General Publication Director

Naci Çağlar Sakarya Uni.

Editörler

Editors

Ahmet Çağatay Çilingir	Sakarya Uni.	Mehmet Nebioğlu	Sakarya Uni.
Alparslan Demir	Sakarya Uni.	Sadık Bağcı	Sakarya Uni.
Beytullah Eren	Sakarya Uni.	Serkan Zeren	Kocaeli Uni.
Cüneyt Bayılmış	Sakarya Uni.	Şevket Gür	Sakarya Uni.
Ertan Bol	Sakarya Uni.	Zafer Barlas	Sakarya Uni.
Kerem Küçük	Kocaeli Uni.		

Bölüm Editörleri

Section Editors

Ahmet Aygün	Bursa Teknik Uni.	Maryna Van De Venter	Nelson Mandela M. Uni
Ali Çoruh	Sakarya Uni.	M. İskender Özsoy	Sakarya Uni.
Ali Pınar	Boğaziçi Uni.	Mehmet Ozen	Sakarya Uni.
Ali Sarıbiyık	Sakarya Uni.	Murat Tuna	Sakarya Uni.
Aliye Suna Erses Yay	Sakarya Uni.	Murat Utkucu	Sakarya Uni.
Arif Özkan	Düzce Uni.	Mustafa Alkan	Akdeniz Uni.
Barış Boru	Sakarya Uni.	Mustafa Bozkurt	Sakarya Uni.
Bengü Bayram	Balıkesir Uni.	Mustafa Kurt	Ahi Evran Uni.
Çidem Gündüz	Kocaeli Uni.	Nazan Deniz Yön	Sakarya Uni.
Devrim Akgün	Sakarya Uni.	Nesrin Güler	Sakarya Uni.
Dilek Angın	Sakarya Uni.	Nevra Akbilek	Sakarya Uni.
Emre Tabar	Sakarya Uni.	Nilgün Balkaya	İstanbul Uni.
Faruk Yalçın	Sakarya Uni.	Osman Kırtel	Sakarya Uni.
Fatih Çalışkan	Sakarya Uni.	Özer Uygun	Sakarya Uni.
Halil Yiğit	Kocaeli Uni.	Özgül Keleş	İstanbul Teknik Uni
Hüseyin Aksoy	Sakarya Uni.	Peter Claisse	Coventry Uni.
Hüseyin Pehlivan	Sakarya Uni.	Ramazan Meral	Bingöl Uni.
İdris Cesur	Sakarya Uni.	Sema Salur	Rochester Uni.
İhsan Pehlivan	Sakarya Uni.	Sezgin Kaçar	Sakarya Uni.
İlkay Şişman	Sakarya Uni.	Tahsin Turgay	Sakarya Uni.
İnan Keskin	Karabük Uni.	Tijen Talas Oğraş	TÜBİTAK
Jamal Khatib	Wolverhampton Uni.	Vezir Ayhan	Sakarya Uni.
Mahmut Özacar	Sakarya Uni.	Yılmaz Uyaroğlu	Sakarya Uni.

Ahmet Demir		
Channel length modulation in organic field effect transistor with a polystyrene insulator using a pe...	1493	1499
Ayça Kıyak Yıldırım, Barış Altıokka		
Structural and physical properties of the pbs films obtained by chemical bath deposition at different deposition temperature...	1500	1507
Sema Bilgin, Yakup Ulusu, Hülya Kuduğ, İsa Gökçe		
Cloning, expression and characterization of xylanase (xyn-akky1) from bacillus subtilis in escherichia coli...	1508	1517
Gülten Onay, Ramazan Şahin		
Optical properties of the electron and gamma-ray irradiated soda-lime glass samples...	1518	1523
Mehmet Çitil, Feride Tuğrul		
Some new equalities on the intuitionistic fuzzy modal operators...	1524	1531
Gülden Altay Suroğlu		
Some characterizations of surfaces generated by two curves in heis3...	1532	1537
Nursel Can, Birsal Can Ömür, Ahmet Altındal		
Meyer-neldel rule in ac conductivity of cu doped zno thin films...	1538	1543
Hülya Kodal Sevindir, Cüneyt Yazıcı, Süleyman Çetinkaya		
Asymptotic analysis of shearlet transform for inpainting...	1544	1551
Ezman Karabulut		
The effect of the rotation energies of h ₂ ⁺ molecule on the ne + h ₂ ⁺ --> neh ⁺ + h reaction...	1552	1558
Yasemin Kemer, Erhan Ata		
Conjugate tangent vectors, asymptotic directions, euler theorem and dupin indicatrix for k-kinematic surfaces...	1559	1566
Ali Nafiz Ekiz		
Comparison of leaf beetle (coleoptera: chrysomelidae) diversity of turkey and neighboring countries with respect to species numbers and ende...	1567	1570
Sezen Sivrikaya, Sefa Durmuş, Aslıhan Dalmaz		
Preparation of nano polymeric thiophenes and characterization of the structures...	1571	1575
Özlem Ersoy Hepson		
Numerical solutions of the gardner equation via trigonometric quintic b-spline collocation method...	1576	1584
Gamze Akbulut, Ebru Akkemik		
An investigation of inhibition effects of honey, pollen, propolis and royal jelly extracts on thioredoxin reductase enzyme activity...	1585	1590

Meryem Evecen		
Structural, conformational and spectroscopic properties of c16h16brno3 schiff-base molecule: a theoretical investigation...	1591	1600
Sertan Alkan, Aydın Seçer		
A collocation method for solving boundary value problems of fractional order...	1601	1608
Hayrinisa Demirci Biçer, Cenker Biçer		
Effects of different parameter estimators to error rate in discriminant analysis...	1609	1616
Sibel Alagöz Ergüden, Ayhan Altun, Deniz Ergüden		
Length-weight relationship and condition of arnoglossus kessleri schmidt, 1915 in iskenderun bay (eastern mediterranean, turkey)...	1617	1622
Vakkas Bozkurt, Sefa Ertürk		
The first indoor radon gas measurement at historical places in cappadocia, nigde, turkey...	1623	1627
Veysel Fuat Hatipoğlu		
A lyapunov function for generalized logistic equation on time scales...	1628	1630
Selma Toker, Nimet Özbay		
Evaluation of two stage modified ridge estimator and its performance...	1631	1637
Serpil Eryılmaz		
The theoretical investigation of global reactivity descriptors, nlo behaviours and bioactivity scores of some norbornadiene derivatives...	1638	1647
Zeynep Sümeyye Çelik, Şevket Gür		
Continuous dependence for benjamin-bona-mahony-burger equation...	1648	1650
Pembe Ipek Al		
Description of maximally dissipative quasi-differential operators for first order...	1651	1658
Sevin Gümgüm, Nurcan Baykuş Savaşaneril, Ömür Kıvanç Kürkçü, Mehmet Sezer		
A numerical technique based on lucas polynomials together with standard and chebyshev-lobatto collocation points for solving functional inte...	1659	1668
Ümit Kumbıçak		
Cytogenetic analysis of tegeraria elysii (araneae: agelenidae)...	1669	1673
Fatma Özdemir, Seza Arslan		
Biofilm production and antimicrobial susceptibility profiles of bacillus spp. from meats...	1674	1682
Fethi Turgut		
Contributions to culicoides latreille, 1809 (diptera: ceratopogonidae) fauna of sinop province...	1683	1693

Aynur Manzak	1694	1698
Extraction of propionic acid by emulsion liquid membrane using trioctylamine in toluene...		
Hüseyin Karaca	1699	1703
Catalytic oxidation of 2-mercaptoethanol by cobalt(ii)phthalocyanines bearing chalcone with furan and thiophene...		
Fatma Özütok, Emin Yakar	1704	1710
Annealing time effect on the optical properties of zn(o,oh,s) films onto zno seed layer under unvacuum ambient...		
Murat Olgun, Okan Sezer, Metin Turan, Zekiye Budak Başçiftçi, Nazife Gözde Ayter Arpacioğlu, Murat Ardiç, Onur Koyuncu	1711	1719
Determination of the effects of mineral on seed yield by different statistic methods in bread wheat (triticum aestivum l.) under drought con...		
Keziban Atacan, Nuray Güy, Soner Çakar	1720	1726
Preparation and antibacterial activity of solvothermal synthesized znfe ₂ o ₄ /ag-tio ₂ nanocomposite...		
Nuray Güy, Soner Çakar, Keziban Atacan	1727	1735
Role of ag and tannin modification on photocatalytic and antibacterial properties of zno nanoplates...		
Soner Cakar	1736	1742
Fe/zno nanorod photoanode and pyrocatechol violet sensitizer based dye sensitized solar cells...		
Sevda Yıldız	1743	1751
Korovkin theorem via statistical e-modular convergence of double sequences...		
Nilgün Özgül, Esra Polat	1752	1759
Burnout levels of academic staff: an investigation at a public university in turkey...		
Muhammed Talat Sarıaydın	1760	1764
Bisector surfaces through a common line of curvatures and its classifications...		
Kadri Arslan, Betül Bulca	1765	1769
On total shear curvature of surfaces in $e^{\{n+2\}}$...		
Mustafa Yeneroğlu	1770	1773
On inextensible flows developable surfaces associated focal curve according to ribbon frame...		
Nazmiye Gönül Bilgin, Merve Çetinkaya	1774	1786
Approximation by three-dimensional q-bernstein-chlodowsky polynomials...		
Vahide Bulut	1787	1792
Geometric kinematic approach to rigid objects with point contact based on a local-surface frame...		

Hacer Pir	1793	1798
Theoretical calculations of laso molecule by using dft/b3lyp and dft/hseh1pbe levels...		
Adnan Tercan, Ramazan Yaşar	1799	1803
Extending property on ec-fully submodules...		
Dilsat Nigar Colak, Kadriye Inan Bektas, Muslum Tokgoz, Sabriye Canakcı, Ali Osman Belduz	1804	1811
Screening of xylanase and glucose isomerase producing bacteria isolated from hot springs in turkey...		
Esra Altıntığ, Ömer Faruk Soydan	1812	1819
Methylene blue adsorption and preparation silver bound to activated carbon with sol-gel method...		
Handan Tanyildizi, İffet Çavdar, Mustafa Demir	1820	1827
A clinical trial of the evaluation of environmental exposure in yttrium 90 radioembolization...		
Tuğba Şaşmaz Kuru, Volkan Eyüpoğlu	1828	1835
Co-mg ferrite nanocomposite as a humidity sensor device prepared by co-precipitation method...		
Mine Menekşe Yılmaz	1836	1841
A note on convergence of nonlinear general type two dimensional singular integral operators...		
Sadık Bağcı	1842	1847
The explanation of metallic nature of bbi(110) surface...		
Urkiye Akar Tarım, Orhan Gürler	1848	1852
Application of monte carlo method for gamma ray attenuation properties of lead zinc borate glasses...		
Engin Özkan, Ali Aydoğdu, Aykut Göçer	1853	1856
A sequence bounded above by the lucas numbers...		
Nimet P. Akın, Erdiñç Dundar, Uğur Ulusu	1857	1862
Asymptotically lacunary i-invariant statistical equivalence of sequences of sets defined by a modulus function...		
İlim Kişi	1863	1867
Aw(k)-type salkowski curves in euclidean 3-space ie^3 ...		
Melek Masal	1868	1873
Curves according to the successor frame in euclidean 3-space...		
Nuray Eroğlu	1874	1877
Rings and modules whose socles are relative ejective...		
Nimet Özbay, Selma Toker	1878	1885
Determining the effect of some biasing parameter selection methods for the two stage ridge regression estimator...		

Emine Babur Şaş, Mustafa Kurt	1886	1892
Characterization of 3 fluoro-4-formylphenylboronic acid molecule with density functional teory...		
Merve İlkhan, Emrah Evren Kara	1893	1900
Some remarks on completeness and compactness in g-metric spaces...		
Mehmet Gökhan Şensoy, Mehmet Batı	1901	1906
Investigation of magnetic properties of spin 5/2 ising chain by using tranfer matrix method...		
Erdem Seven, Cihan Yıldız	1907	1916
On the Butterflies of Savur district (Mardin Province, Southeastern Turkey) ...		
Sinan Karakaya, Halim Özdemir, Tuğba Petik	1917	1922
3x3 Dimensional Special Matrices Associated with Fibonacci and Lucas Numbers...		
G. Canan Hazar Güleç	1923	1926
Summability factors between the absolute Cesàro methods...		
Bahadır Saygı	1927	1930
Pseudo-mirror nuclei in the mass regions $A \sim 170$ and $A \sim 200$...		
Kadriye Şimşek Alan	1931	1938
Normal Stress Analysis In an Infinite Elastic Body With A Locally Curved Carbon Nanotube...		
Sezgin Büyükkütük	1939	1946
Timelike Factorable Surfaces in Minkowski Space-Time...		
Erhan Budak	1947	1950
Incorporation of Cadmium into Hexagonal Boron Nitride by Solid State Reaction...		

	SAKARYA UNIVERSITY JOURNAL OF SCIENCE		 SAKARYA UNIVERSITY
	e-ISSN: 2147-835X http://www.saujs.sakarya.edu.tr		
	<u>Received</u> 13-10-2017 <u>Accepted</u> 16-11-2017	<u>Doi</u> 10.16984/saufenbilder.343272	

Channel Length Modulation in a Polystyrene Insulated Organic Field Effect Transistor Using PEDOT: PSS Composite Electrode

Ahmet DEMİR^{*1}

ABSTRACT

Channel length-modulated Organic Field Effect Transistor (OFET) was fabricated on a prepatterned source-drain Indium Tin Oxide (ITO) substrate by spin coating method using a Poly (3-hexylthiophene-2,5-diyl) (P3HT) semiconductor and Polystyrene (PS) insulator. Poly (3,4-ethylenedioxythiophene)-poly (styrenesulfonate) (PEDOT:PSS) was used as the gate electrode. Thus, the structure of the OFET device was obtained as ITO/P3HT/PS/PEDOT:PSS. ITO/PS/PEDOT:PSS structure was prepared using the same method for measuring the capacitance of the polymer insulator. Output and transfer current-voltage (I - V) characteristics of the electrical characterization of the obtained OFET devices were obtained in full darkness and in the air environment. Basic parameters of OFET devices; voltage threshold (V_{Th}), field effect mobility (μ_{FET}) and the current on/off ratio ($I_{on/off}$) are extracted from the capacitance-frequency (C - f) graph of the ITO/PS/PEDOT:PSS structure. Produced PS-OFETs have been found to exhibit good device performance, such as low V_{Th} , acceptable mobility and $I_{on/off}$ values.

Keywords: Polymer gate electrode, Transparent OFETs, Insulators, PEDOT:PSS, Polystyrene, P3HT

1. INTRODUCTION

Organic field effect transistors (OFETs) have received great interest due to their potential to implement low-cost, flexible and wide-area thin-film devices for the fabrication of next-generation universal electronic systems [1-4]. Recently, research efforts have been increased to develop transparent OFETs that are one of the driver components of the pixel multiplier for transparent active matrix displays. In this context, transparent organic field effect transistors (OFET) have received increasing attention as an important building block in transparent electronic systems, and their outstanding properties and the extent of application of modern electrons are expected to expand greatly [5-7]. Transparency, which is

needed for some of these applications and brings additional quality and value, is a feature that leads to new possibilities in device design [8]. In this way, numerous transparent conductive films such as indium tin oxide (ITO), carbon nanotube, graphene for transparent OFETs [9-11]. However, the OFETs produced in this way have low work function, high substrate temperature, low permeability and high plate resistance; resulting in increased contact resistance, irregular organic semiconductor film and reduced device permeability [12-15].

The first studies have shown that organic semiconductors are not the only component to produce high quality OFET. At the same time a suitable gate insulator is required as well. OFET gate insulators should meet the standard demands

^{*} Ahmet DEMİR

¹Department of Physics, Faculty of Sciences, Düzce University, 81620, Düzce, Turkey, ahmetdemir@duzce.edu.tr

of organic electrons in the context of low cost production of organic circuits.

It has been shown that the OFET gate insulators must ideally conform to the flexible surfaces during the coating and be insoluble in the solvent used for organic semiconductors [16-22]. Polystyrene, which is a kind of gate insulator, has good dielectric properties [23]. Polystyrene (PS) is a versatile polymer in terms of chemical and structural properties and can be easily synthesized by various polymerization mechanisms with various orientations and chain lengths [24]. High reactive Polystyrene has become the most frequently used raw material polymer in packaging, insulation and filtration applications for the production of chemically diverse materials including high resistivity and low dielectric loss transparent, solid materials [25]. Thus, PSs as dielectric materials have interesting applications in areas such as electronics and composite materials [26, 27]. PS is a non-polar organic polymer and can be expected to form low energy interfaces with other non-polar materials.

As an alternative to inorganic contacts, the PEDOT:PSS conductive polymer blend has previously been used in solid electrolyte capacitors, organic electronic devices (OECs), and touch screens [28]. PEDOT:PSS, in particular, is a superior material whose conductivity can be adjusted and very good in terms of transparency and film-forming properties [29]. At the same time, PEDOT:PSS is transparent, such as indium tin oxide (ITO), a transparent conductor that is often used in organic electronic devices, and has a higher mechanical flexibility [30].

In this study, it is aimed to fabricate an OFET device using Polystyrene organic dielectric material. The focus of this study is to minimize the interface conditions between the gate insulator and the gate electrode. In this context, first, an organic top gate bottom contact field-effect transistor (TGBC) was fabricated using a transparent electrode PEDOT:PSS with high conductivity as a gate electrode on the prepatterned OFET substrate and this transistor was electrically characterized. It has also been shown that an amorphous Polystyrene polymer that changes the transfer characteristic of OFET devices can be manipulated in the transistor performance. In the study, it has been verified that this OFET device with polymer gate electrode exhibits good current saturation regime and acceptable mobility.

2. EXPERIMENTAL PROCEDURE

2.1. The Preparation of PEDOT:PSS Composite Formulation

PEDOT:PSS PH 1000 and PEDOT:PSS CPP 105D Conductor formulations were procured from Heraeus Clevis. Dimethyl Sulfoxide (DMSO) was added to the PH-1000 solution (1:19 by volume) and mixed in the hot plate overnight at 300 rpm at room temperature to provide conductivity enhancement. The resulting mixture CPP-PEDOT was added to control the surface wettability (1:1 by volume) and the resulting mixture was prepared. As a result, a conductive PEDOT:PSS composite formulation was obtained.

2.2. Fabrication of OFET Devices with Polystyrene Polymer Insulator

In this experimental study, prepatterned ITO substrates for OFETs were used as source-drain contacts and PEDOT:PSS composite formulation has been used as gate contact to obtain Polystyrene polymer insulated OFET devices. Prior to the fabrication process, the prepatterned substrates were dipped in acetone and ethanol, respectively, with 15 minutes sonic shaking. Then all the surfaces have been washed with 2-propanol and dried with a nitrogen gun. P3HT dissolved in chlorobenzene at 8 mg/mL in an unconjugated environment was purchased from Sigma-Aldrich Chemical Company and plated on prepatterned substrate by spin casting at 3000 rotation per minutes during 60 second. Annealing was carried out by placing the substrate on a hot plate for 60 seconds at 150°C, then taking it from the plate and slowly cooling it at room temperature. As an insulator layer, 15 mg PS polymer was dissolved in 1 mL dichloromethane and coated on the active layer at 1500 rpm for 60 seconds. This film was also placed on a hot plate and heated at 150° C for 60 seconds. All tempering operations were carried out to remove solvents from the films. Finally, the PEDOT:PSS composite formulation was coated on the insulating layer as a gate electrode, at 1000 rpm for 30 seconds. With this last step, the production of PS-OFET devices has been completed. As a result, PS-OFET devices designed as in Fig. 1 have been manufactured.

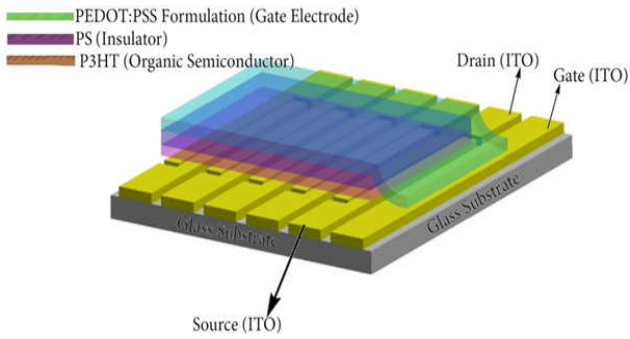


Figure 1. OFET's ITO/PS/PEDOT:PSS based schematic structure.

2.3. The Electrical Characterization of TGBC PS-OFET devices

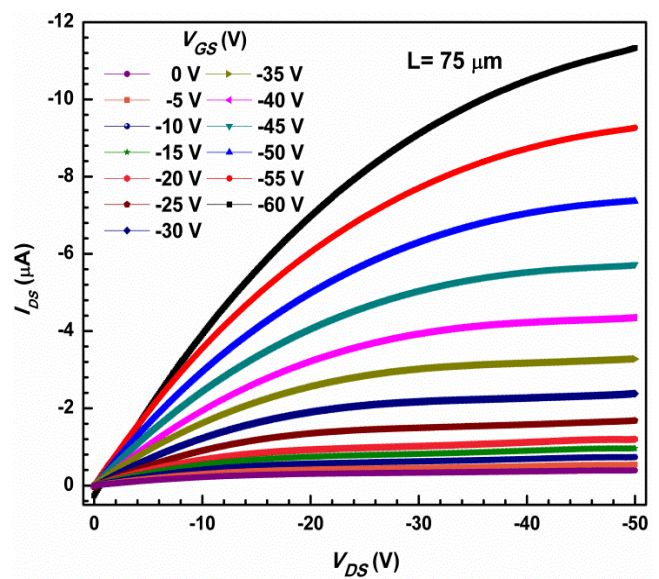
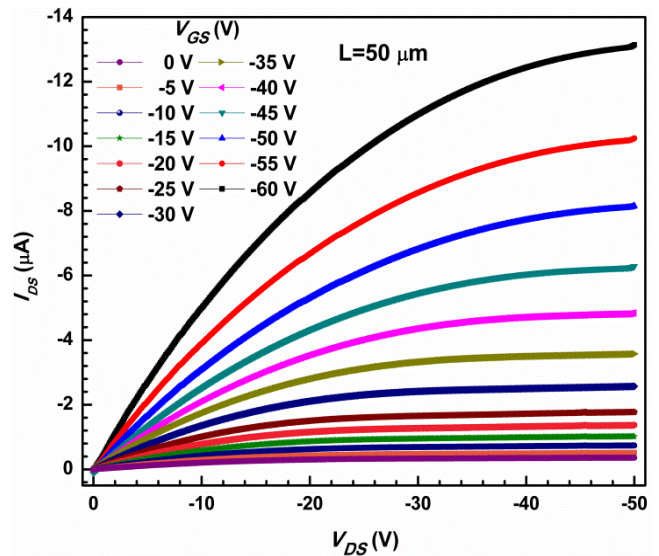
The OFET devices made with PEDOT:PSS composite formulation were placed in a vacuum environment to move away DMSO from the mixture. After the vacuum process, the OFET devices are ready for measurement. Electrical output (I - V) measurements of the obtained PS-OFET devices were examined using an OFET test card using a Keithley 2612B SMU device and measurements progressed with 5 V steps gate-source voltage (V_{GS}) between 0 to -60 V and the source-drain voltage (V_{DS}) scan is performed to calculate the gate-source voltage (V_{GS}) and at least 100 data between 0 and -50 V. Besides that the C - f measurement for the ITO/PS/PEDOT:PSS structure was performed with the Nova-control Alpha-A Impedance Analyzer Instrument. All characteristic measurement operations are carried out in the dark at room temperature

3. RESULT AND DISCUSSION

The output characteristics of the PS-OFET devices were measured at room temperature and the results are given in Figure 2. The results show that the PS gate insulator exhibits a remarkable output characteristic at -50 V value. The reason for this is that the PS polymer in the gate insulator can increase the flat-lying orientation density of the molecules responsible for enhancing hole mobility [31,32].

A higher channel length may cause lower channel conductivity due to trapped loads. For this reason, the maximum level of current between the source

and the drain decreased as the channel length increased [33]. The performance parameters of the OFETs can be modulated by changing the channel length [33,34]. For compatibility between the gate insulator and the composite polymer gate electrode, the charge transfer in the PEDOT:PSS/PS interface was optimized [31,35]. The channel lengths between the contacts were changed between 50 μm to 100 μm .



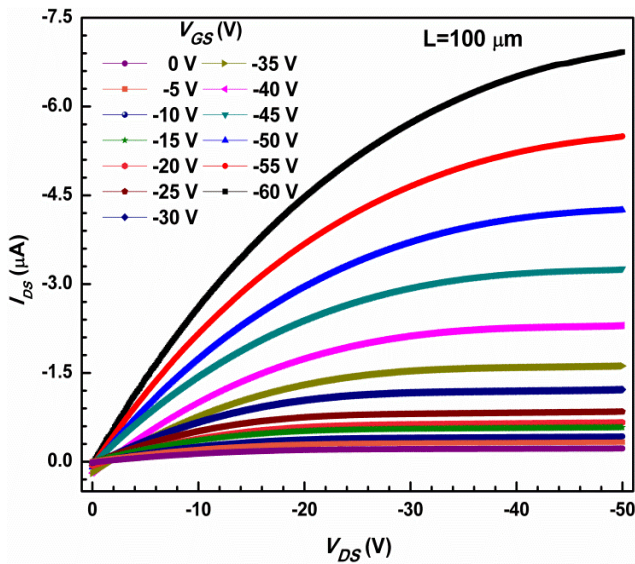


Figure 2. Variation of output characteristics of PS-OFET device according to channel length.

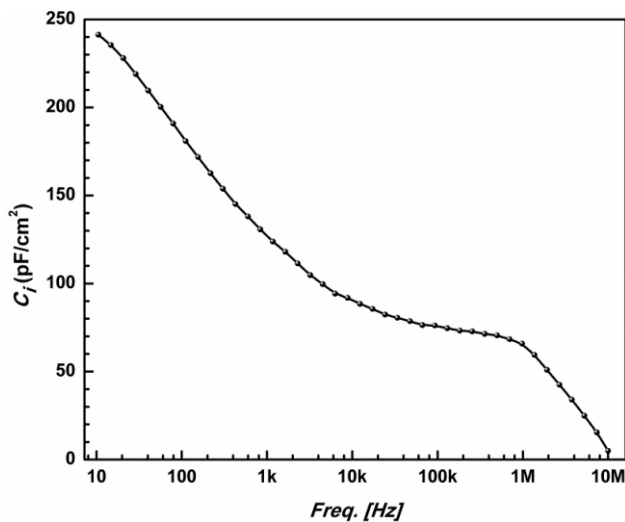


Figure 3. Graph of the effective capacitance of the PS gate insulator according to frequency

The capacitance of the PS gate insulator was obtained from 10 Hz to 10 MHz to calculate the mobility of the devices. The effect of the frequency on the capacitance of the PS gate insulator is exhibited in Figure 3. As obviously seen, the capacity per unit area of the PS gate dielectric is measured to be 220 pF/cm². Transistor can operate at high efficiency and shows good performance in terms of high $I_{on/off}$ device [36-39]. Field effect mobility (μ_{FET}) of the OFET can be calculated using the following equation (1) [39-41].

Maximum drain current (I_{DS}) is obtained following formula:

$$I_{DS} = \left[\mu_{FET} \left(\frac{WC_i}{2L} \right) \right] (V_{GS} - V_{Th})^2 \quad (1)$$

Here, W , L , and C_i denote the channel width, the channel length, and the effective capacitance of the insulating layer, respectively.

The semi-logarithmic plot of I_{DS} and V_{GS} at $V_{DS} = -50$ V for PS gate insulated OFET devices with different channel lengths is shown in Figure 4. It is believed that the reduction in the on/off ratio is due to the channel length effect. As a result, it can be said that in the presence of morphological disorders, the dependence of the $I_{on/off}$ ratio of PS insulated OFET devices on the channel length decreases. These disorders are caused by traps increased with channel width, impurity concentrations, and interface state density.

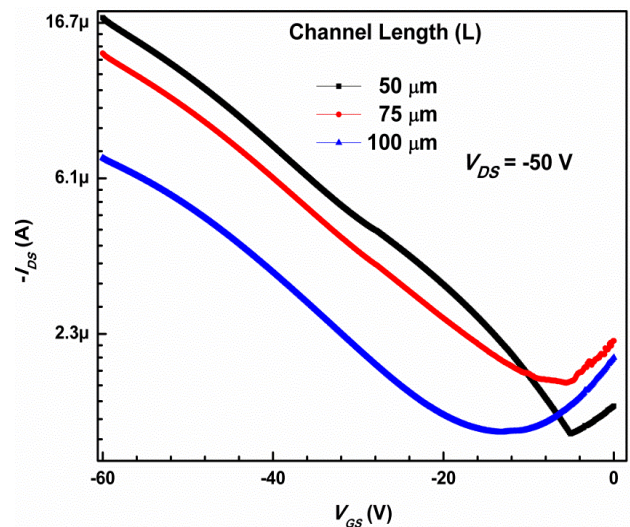


Figure 4. The drain current change of the OFET devices with PS-EDOT gate dielectrics according to the channel length modulation (Semi-logarithmic $I_{DS}-V_{GS}$)

For devices manufactured with PS gate insulation of various channel lengths, $(I_{DS})^{1/2}$ graphs versus V_{GS} at $V_{DS} = -50$ V can be seen in Figure 5. The main parameters of PS-OFETs at different channel lengths were obtained using graphical data of the $(I_{DS})^{1/2}-V_{GS}$ transfer characteristic in the saturation regime. For each channel, the threshold voltages (V_{Th}) of the PS gate dielectrical OFETs can be obtained by the point at which the x-axis of the graph's best linear slope is cut (Figure 5). Mobility is calculated in the linear regime of the drawn transfer characteristics in the saturation regime of the output characteristics (Figure 5).

Field effect mobility can be obtained from the formula below.

$$\alpha = \left(\frac{WC_i}{2L} \right)^{1/2} \quad (2)$$

Here, α is the best linear slope in Figure 5.

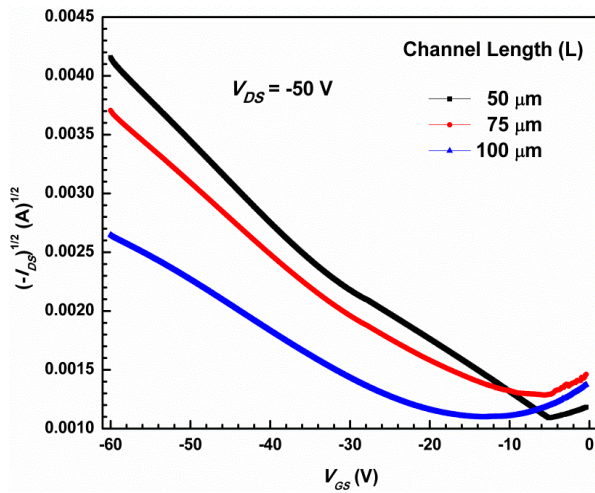


Figure 5. The variation on channel length of the $(I_{DS})^{1/2}$ - V_{GS} transfer curves of PS-EDOT gate dielectric-based OFET devices.

3.1. Figures and Tables

The ratio of the $I_{on/off}$ current, which is the ratio of the maximum I_{DS} value to the minimum I_{DS} value, is obtained from the transfer characteristics for each channel length.

Table 1. Performance parameters of the fabricated OFETs.

Channel Length (L)	Threshold Voltage (V_{Th})	Mobility (μ_{FET})	$I_{on/off}$
50 μm	0.38 V	0.569 $\text{cm}^2/\text{V.s}$	1.21x10 ¹
75 μm	0.8 V	0.487 $\text{cm}^2/\text{V.s}$	0.63x10 ¹
100 μm	1.19 V	0.381 $\text{cm}^2/\text{V.s}$	0.36x10 ¹

It has been determined that the parameters of “on state and off state of device current ratio ($I_{on/off}$) threshold voltages (V_{Th}) and field effect mobility (μ_{FET}) of PS-OFET exhibiting proportional dependence are dependent on the channel length, and in the on state (accumulation layer formed) it is obtained from I_{DS} - V_{GS} characteristic ($V_{DS} = -50$ V) and given in Table 1. As can be clearly seen from Table 1, as the channel length increases, the $I_{on/off}$ values decreased as the number of electrical charges trapped between the source-drain electrodes and the other impurities of the PS at the PS/PEDOT:PSS interface increased.

The mobility and threshold voltage values due to the channel length of the PEDOT:PSS formulated gate electrode PS-OFET can be obtained from the equation. As channel length increases, it is clear that field effect mobility (μ_{FET}) decreases from 0.569 to 0.381 $\text{cm}^2/\text{V.s}$. Similarly, the threshold voltage (V_{Th}) increased from 0.38 to 1.19 V. The change in these two parameters revealed the presence of ionic impurities in the channel

between the source and the drain and the charges that were caught in the traps [41]. If simple electrostatic laws are considered, it can be said that the carriers in the longer channel are more localized at the interface due to the larger attractive electrostatic force. In Figure 5, it can be seen that this thinking is correct when considering transfer curves that are exponentially consistent with field effect charges.

CONCLUSION

In this study, produced PS-OFET devices exhibited remarkably good characteristics due to the fact that the PS polymer of the gate insulator can increase the density of flat-lying molecules between the PEDOT:PSS composite electrode and the PS polymer gate insulator. The results obtained are very promising in terms of the $I_{on/off}$, μ_{FET} and V_{Th} values of PS-OFETs. The $I_{on/off}$ values of PS-OFETs vary from 1.21x10¹ to 0.36x10¹ depending on the channel length, while the μ_{FET} values range from 0.569 to 0.381 $\text{cm}^2/\text{V.s}$ with decreasing channel length. These characteristic behaviors may be due to the molecular compatibility and dipole interaction of PS. For this reason, it can be said that PS-OFETs with high conductive polymer composite electrodes show a good interaction between the gate insulator and the gate electrode. In addition, these devices have shown promising performance improvement in some parameters, such as field-effective mobility, threshold voltage, current on/off ratio, and significant response to channel length variations. This study aims to clarify the properties of transparent polymer composite electrode OFETs and to demonstrate the potential use of functional Polystyrene polymer in OFET. From the results obtained so far, further studies on this new study are thought to provide additional opportunities.

REFERENCES

- [1] E. Scavetta, A.G. Solito, M. Demelas, P. Cosseddu, A. Bonfiglio, “Electrochemical characterization of self assembled monolayers on flexible electrodes”, *Electrochim. Acta*, vol.65 pp. 159-164, 2012.
- [2] H.T. Nguyen, B.C. Dong, N.H. Nguyen, “A novel conducting amphiphilic diblock copolymer containing regioregular poly(3-hexylthiophene)”, *Macromol. Res.*, vol.22 pp. 85-91, 2014.

- [3] P. Dataa, P. Pander, M. Lapkowski, A. Swist, J. Soloduchoc, R.R. Reghud, J.V. Grazulevicius, "Unusual properties of electropolymerized 2,7- and 3,6- carbazole derivatives", *Electrochim. Acta*, vol. 128 pp. 430-438, 2014.
- [4] C. Solis, E. Baigorria, M.E. Milanesio, G. Morales, E.N. Durantini, L. Otero, M. Gervaldo, "Electrochemical polymerization of EDOT modified Phthalocyanines and their applications as electrochromic materials with green coloration, and strong absorption in the Near-IR", *Electrochim. Acta*, vol. 213 pp. 594-605, 2016.
- [5] J. Sun, B. Zhang, H.E. Katz, Materials for Printable, "Transparent, and Low-Voltage Transistors", *Adv. Funct. Mater.*, vol. 21 pp. 29-45, 2011.
- [6] R.A. Street, "Thin-Film Transistors", *Adv. Mater.*, vol. 21 pp. 2007-2022, 2009.
- [7] J.Y. Kwon, D.J. Lee, K.B. Kim, "Review paper: "Transparent amorphous oxide semiconductor thin film transistor", *Electron. Mater. Lett.*, vol. 7 pp. 1-11, 2011.
- [8] S. Ju, L. Li, J. Liu, P.C Chen, Y.G Ha, F. Ishikawa, H. Chang, C. Zhou, A. Facchetti, D.B. Janes, T.J. Marks, "Transparent Active Matrix Organic Light-Emitting Diode Displays Driven by Nanowire Transistor Circuitry", *Nano Lett.*, vol. 8 pp. 997-1270, 2008.
- [9] Q. Cao, Z.T Zhu, M.G Lemaitre, M.G. Xia, M. Shim, J.A. Rogers, "Transparent flexible organic thin-film transistors that use printed single-walled carbon nanotube electrodes", *Appl. Phys. Lett.*, vol. 88 pp. 113511-1-113511-3, 2006.
- [10] W.H. Lee, J. Park, S.H Sim, S.B. Jo, K.S. Kim, B.H Hong, K. Cho, "Transparent Flexible Organic Transistors Based on Monolayer Graphene Electrodes on Plastic", *Adv. Mater.*, vol. 23 pp. 1752-1756, 2011.
- [11] Y. Yu, H. Wada, J.I. Inoue, S. Imaizumi, Y. Kounosu, K. Tsuboi, H. Matsumoto, M. Ashizawa, T. Mori, M. Minagawa, A. Tanioka, "Inkjet Printing of Graphene Nanoribbons for Organic Field-Effect Transistors", *Appl. Phys. Express*, vol. 4 pp. 115101-1-115101-3, 2011.
- [12] H. Ohta, T. Kambayashi, K. Nomura, M. Hirano, K. Ishikawa, H. Takezoe, H. Hosono, Channel, "Transparent Organic Thin-Film Transistor with a Laterally Grown Non-Planar Phthalocyanine Channel", *Adv. Mater.*, vol. 16 pp. 312-316 2004.
- [13] D.J. Yun, S.W. Rhee, "Deposition of Al-doped ZnO thin-films with radio frequency magnetron sputtering for a source/drain electrode for pentacene thin-film transistor", *Thin Solid Films*, vol. 517 pp. 4644-4649, 2009.
- [14] J.M. Choi, D.K. Hwang, J.H. Kim, S. Im, "Transparent thin-film transistors with pentacene channel, AlOxAlOx gate, and NiOxNiOx electrodes", *Appl. Phys. Lett.*, vol. 86 pp. 123505-1-123505-3, 2005.
- [15] S. Cho, K. Lee, J. Yuen, G. Wang, D. Moses, A.J. Heeger, M. Surin, R. Lazzaroni, "Thermal annealing-induced enhancement of the field-effect mobility of regioregular poly(3-hexylthiophene) films", *J. Appl. Phys.*, vol. 100 pp. 114503-1-114503-6, 2006.
- [16] L.A. Majewski, M. Grell, S.D. Ogier, J. Veres, "A novel gate insulator for flexible electronics", *Org. Electron.*, vol. 4 pp. 27-32, 2003.
- [17] Z. Bao, Y. Feng, A. Dodabalapur, V.R. Raju, A.J. "Lovinger, High-Performance Plastic Transistors Fabricated by Printing Techniques", *Chem. Mater.*, pp. 9 pp. 1299-1301, 1997.
- [18] V. Dyakonov, I. Riedel, C. Deibel, J. Parisi, C.J. Brabec, N.S. Sariciftci, J.C. Hummelen, "Electronic Properties of Polymer-Fullerene Solar Cells", *Mat. Res. Soc. Symp. Proc.* Vol. 665 pp. C7.1.1-C7.1.12, 2001.
- [19] W. Fix, A. Ullmann, J. Ficker, W. Clemens, "Fast polymer integrated circuits", *Appl. Phys. Lett.* vol. 81 pp. 1735, 2002.
- [20] J. Ficker, A. Ullmann, W. Fix, H. Rost, W. Clemens, "Stability of polythiophene-based transistors and circuits" *J. Appl. Phys.*" Vol. 94 pp. 2638-2641, 2003.
- [21] Y. Jang, D.H. Kim, Y.D. Park, J.H. Cho, M. Hwang, K. Cho, "Influence of the dielectric constant of a polyvinyl phenol insulator on the field-effect mobility of a pentacene-based thin-film transistor", *Appl. Phys. Lett.*, vol. 87 pp. 152105, 2005.
- [22] S. Han, X. Zhuang, W. Shi, X. Yang, L. Li, J. Yu, "Poly(3-hexylthiophene)/polystyrene (P3HT/PS) blends based organic field-effect transistor ammonia gas sensor", *Sens. Actuators B*, vol. 225 pp. 10-15, 2016.
- [23] R.K. Goyal, P.A. Jagadale, U.P. Mulik, "Thermal, mechanical, and dielectric

- properties of polystyrene/expanded graphite nanocomposites”, *J. Appl. Polym. Sci.*, vol. 111 pp. 2071-2077, 2009.
- [24] K. Chen, K. Harris, S. Vyazovkin, “Tacticity as a Factor Contributing to the Thermal Stability of Polystyrene”, *Macromol. Chem. Phys.*, vol. 208 pp. 2525-2532, 2007.
- [25] C. Shin, “Filtration application from recycled expanded polystyrene”. *J. Colloid Interface Sci.*, vol. 302 pp. 267-271, 2006.
- [26] D. Aussawasathien, S. Sahasithiwat, L. Menbangpung, “Electrospun camphorsulfonic acid doped poly(o-toluidine)-polystyrene composite fibers: Chemical vapor sensing”, *Synth. Met.*, vol. 158 pp. 259-263, 2008.
- [27] J.Y. Lee, V. Kumar, X.W. Tang, D.J. Lee, “Mechanical and electrical behavior of rubber nanocomposites under static and cyclic strain”, *Compos. Sci. Technol.*, vol. 142 pp. 1-9, 2017.
- [28] G. Albrecht, S. Heuser, C. Keil, D. Schlettwein, “Strategy for preparation of transparent organic thin film transistors with PEDOT:PSS electrodes and a polymeric gate dielectric”, *Mater. Sci. Semicond. Process.*, vol. 40 pp. 772-776, 2015.
- [29] J.G. Tait, B.J. Worfolk, S.A. Maloney, T.C. Hauger, A.L. Elias, J.M. Buriak, K.D. Harris, “Spray coated high-conductivity PEDOT:PSS transparent electrodes for stretchable and mechanically-robust organic solar cells”, *Sol. Energy Mater. Sol. Cells*, vol. 110 pp. 98-106, 2013.
- [30] Z. Chen, B. Cotterell, W. Wang, E. Guenther, S.J. Chua, “A mechanical assessment of flexible optoelectronic devices”, *Thin Solid Films.*, vol. 394 pp. 201-205, 2001.
- [31] J. Veres, S. Ogier, G. Lloyd, “Gate Insulators in Organic Field-Effect Transistors”, *Chem. Mater.*, vol. 16 pp. 4543-4555, 2004.
- [32] T.W. Kelley, L.D. Boardman, T.D. Dunbar, D.V. Muires, M.J. Pellerite, T.P. Smith, “High-Performance OTFTs Using Surface-Modified Alumina Dielectrics”, *J. Phys. Chem. B*, vol. 107 pp. 5877-5881, 2003.
- [33] P. Mittal, B. Kumar, Y.S. Negi, B.K. Kaushik, R.K. Singh, “Channel length variation effect on performance parameters of organic field effect transistors”, *Microelectron. J.*, vol. 43 pp. 985-994, 2012.
- [34] Y. Yan, L.B. Huang, Y. Zhou, S.T. Han, L. Zhou, J. Zhuang, Z.X. Xu, V.A.L. Roy, “Self-aligned, full solution process polymer field-effect transistor on flexible substrates”, *Sci. Rep.*, vol. 5 pp. 15770-115770-8, 2015.
- [35] A. Demir, O. Köysal, “Investigation of photo-induced change of electro-optical performance in a liquid crystal-organic field effect transistor (LC-OFET)”, *Philos. Mag.*, vol. 96 pp. 2362-2371, 2016.
- [36] A. Demir, A. Atahan, S. Bağcı, M. Aslan, M.S. Islam, “Organic/inorganic interfaced field-effect transistor properties with a novel organic semiconducting material”, *Philos. Mag.*, vol. 96 pp. 274-285, 2016.
- [37] L. Herlogsson, X. Crispin, N.D. Robinson, M. Sandberg, O.J. Hagel, G. Gustafsson, M. Berggren, “Low-Voltage Polymer Field-Effect Transistors Gated via a Proton Conductor”, *Adv. Mater.*, vol. 19 pp. 97-101, 2007.
- [38] F. Bordi, C. Cametti, R.H. Colby, “Dielectric spectroscopy and conductivity of polyelectrolyte solutions”, *J. Phys.: Condens. Matter*, vol. 16 pp. R1423-R1463, 2004.
- [39] Y. Sun, Y. Liu, D. Zhu, “Advances in organic field-effect transistors”, *J. Mater. Chem.*, vol. 15 pp. 53-65, 2005.
- [40] B.C. Shekar, J. Lee, S.W. Rhee, “Organic thin film transistors: Materials, processes and devices”, *Korean J. Chem. Eng.*, vol. 21 pp. 267-285, 2004.
- [41] A. Demir, S. Bağcı, S.E. San, Z. Doğruyol, “Pentacene-Based Organic Thin Film Transistor With SiO₂ Gate Dielectric”, *Surf. Rev. Lett.*, vol. 22 pp. 1550038-1-1550038-6, 2015.

	SAKARYA UNIVERSITY JOURNAL OF SCIENCE		 SAKARYA UNIVERSITY
	e-ISSN: 2147-835X http://www.saujs.sakarya.edu.tr		
	<u>Received</u> 25-03-2018 <u>Accepted</u> 02-05-2018	<u>Doi</u> 10.16984/saufenbilder.409328	

Structural and Physical Properties of the PbS Films Obtained by Chemical Bath Deposition at Different Deposition Temperature

Ayça Kıyak Yıldırım^{*1} Barış Altıokka²

Abstract

In the present study, structural and physical properties of the PbS thin films produced using chemical bath deposition method were investigated. Deposition temperature was varied between 25 °C and 50 °C throughout the deposition period. The pH value of electrolyte solution and the deposition time of the films were 10.5 and 25 min, respectively. Characterizations of the PbS thin films were performed using scanning electron microscopy (SEM) and X-ray diffraction (XRD) methods. XRD results showed that all PbS thin films had a cubic structure irrespective of deposition temperature. Morphological characterizations of the films indicated that not only the number but also the size of pinholes, formed on the film surfaces, were significantly affected by the deposition temperature. Consequently, the film obtained at 25 °C exhibited a surface morphology with less and smaller pinholes, compared to others deposited at higher deposition temperatures.

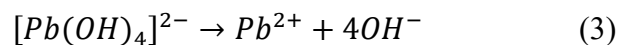
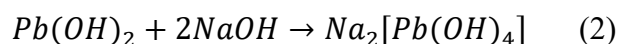
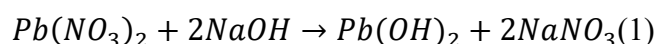
Keywords: Chemical bath deposition, Thin film, Lead nitrate, Thiourea, Pinhole

1. INTRODUCTION

Recently, interest in nanoscale lead sulphide (PbS) has increased in solar photovoltaics due to their extraordinary exciting physical properties and potential applications [1]. PbS is an important dual IV-VI semiconductor material [2] with a direct narrow optical energy gap (0,41 eV at 300 K) and a relatively large excitation Bohr radius (18 nm). Thus, by controlling the crystallite size, it provides strong quantum and electron confinement that varying the band gap value. PbS thin films have become a comprehensive research topic due to their wide applications such as gas sensors, infrared radiation detectors, optoelectronics, solar cells, diode lasers, etc. [3]. There is dry and wet method to produce PbS. Vacuum evaporation; hot wall epitaxy and molecular beam epitaxy are among the most successful "dry" methods for PbS synthesis. Frequently used "wet" methods, spray

pyrolysis, electrochemical deposition and chemical bath deposition [4]. Among these methods, CBD is relatively less expensive, easy to use and can cover large surfaces. Some metal dopings to PbS films were investigated to varied in the electrical properties of the film materials. The doping to the PbS thin film precipitate is intended to increase the electrical conductivity or resistivity [5].

The reactions for the formation of PbS are given by [6] as follows:



*Corresponding Author/Ayça Kıyak Yıldırım

^{1*} Ayça Kıyak Yıldırım, Bilecik Şeyh Edebali Üniversitesi, Meslek Yüksek Okulu, Motorlu Araçlar ve Ulaştırma Teknolojisi Bölümü, Otomotiv Teknolojisi Programı, Bilecik-ayca.kiyak@bilecik.edu.tr

² Barış Altıokka, Bilecik Şeyh Edebali Üniversitesi, Meslek Yüksek Okulu, Elektrik ve Enerji Bölümü Elektrik Enerjisi Üretim, İletim ve Dağıtım Programı, Bilecik-baris.altiokka@bilecik.edu.tr



2. MATERIALS AND METHODS

PbS thin films were deposited on the chemically cleaned substrate. Glass substrates were cleaned using nitric acid and isopropyl alcohol. After this process, the glass substrates were washed with distilled water. To prepare the PbS thin films, aqueous solutions of 0.0090 M Pb(NO₃)₂ (lead nitrate) and 0.051 M CS(NH₂)₂ (thiourea) were mixed together by rotating at 600 rpm. The pH value of the prepared bath solution was adjusted to 10.5 by adding dropwise of NH₃. The volumes of bath solutions were chosen as to be 90 mL. The glass substrates are immersed vertically in the bath solution. The bath temperatures were varied between 25 °C and 50 °C. Deposition duration was chosen as to be 25 minutes. Deposition parameters are shown in Table 1. After the deposition, the glass is covered with PbS on both sides of the substrates. After the deposition, the substrates were washed with distilled water and dried in the air. However, the other side of surface was cleaned with 10% dilute hydrochloric acid.

PANalytical Empyrean XRD (X-ray diffractometer) was used to analyze the structural properties of the produced PbS thin films. Thicknesses of PbS thin films were calculated by gravimetric method. Zeiss SUPRA 40VP SEM (scanning electron microscope) was used to analyze the surface morphology of the PbS thin films.

Table 1. Deposition parameters

Experiments	Pb(NO ₃) ₂ (M)	CS(NH ₂) ₂ (M)	Deposition Time (min)	Solution Volume (mL)	Deposition Temperature (°C)	pH
D1	0,0090	0,051	25	90	25	10,5
D2	0,0090	0,051	25	90	30	10,5
D3	0,0090	0,051	25	90	35	10,5
D4	0,0090	0,051	25	90	40	10,5
D5	0,0090	0,051	25	90	45	10,5
D6	0,0090	0,051	25	90	50	10,5

2.1. The X-ray Analysis of the PbS films

The properties of the films examined by XRD technique such as crystal structure, crystalite size, preferential orientation, strain and stress acting on the unit surface have been determined.

XRD analyzes of PbS thin films produced in D1, D2, D3, D4, D5 and D6 are given in Figure 2.1. The peaks of 25.9 °; 30 °; 43 °; 50.9 °; 53.4 °; 62.5 ° and 68.9 ° belong to the (111), (002), (022), (113), (222) and (133) planes of PbS respectively. These peaks were examined and found to be in conformity with the ASTM number (98-060-0243). In XRD analyzes, it was determined that all films were in cubic structure. In addition, the film obtained in D6 has a higher XRD peak intensity than the others. The calculated film thicknesses for the produced PbS thin films were measured using gravimetric analysis and tabulated.

The TC (Texture coefficient) is used to determine the preferential orientation of the PbS thin films. It is not mentioned that if there are two or more TC bigger than 1 [7-10]. The value of the texture coefficient of the films obtained in this study is calculated using equation (7) for any (hkl) reflection plane and they are given in Table 2.

$$TC = \frac{I_{(hkl)}/I_{0(hkl)}}{\frac{1}{N} \sum_N \left(\frac{I_{(hkl)}}{I_{0(hkl)}} \right)} \quad (7)$$

The crystalite sizes of the films obtained in this study were calculated by the Scherrer formula which is given in Eq. (8) and the crystallite sizes are also given in Table 3.

$$D = \frac{0,9\lambda}{B(\text{radyan})\cos(\theta_B)} \quad (8)$$

Where D is the crytallite size, λ the wavelength of the x-ray used in the diffraction, the width at half maxima of the considered peak B, and θ_B the peak angle Bragg reflection angle [11]. The lattice constant for the cubic rock salt structure is calculated by using the Equation (9).

$$a = d\sqrt{(h^2 + k^2 + l^2)} \quad (9)$$

where h, k and l are Miller indices, and d is the distance between planes [12].

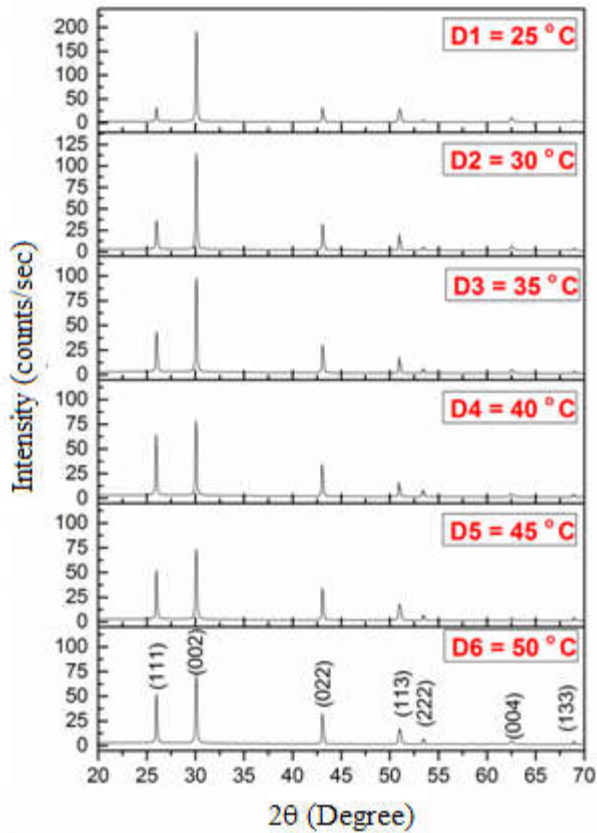


Figure 2. XRD analysis of PbS thin films produced in D1, D2, D3, D4, D5 and D6

Furthermore, average stress and micro strain for all planes were calculated using Equation (10) and Equation (11), respectively, and they are given in Table 3.

$$S = \varepsilon Y / (2\sigma) \tag{10}$$

$$\varepsilon = (a_0 - a) / a_0 \tag{11}$$

where, a_0 the lattice parameter of the bulk sample a is the corrected value of the lattice parameter of a thin film samples, σ is the poisson ratio of bulk crystal and Y is Young's modulus. The value of Y for PbS is 70.2GPa and σ value is taken as 0.28. Using Nelson-Riley graphs, the corrected values were calculated and it is given in Figure 2.2

Table 2. XRD intensities of the obtained PbS thin films, calculated constructions coefficient values of the obtained PbS thin films and calculated film thicknesses of the obtained PbS thin films using gravimetric analysis

EXPERIMENT	INTENSITY (COUNT/SECONDS)		I/I_0	TC	(hkl)	FILM THICKNESS (nm)		
	2θ							
D1	25,908	52567,3	73,5	1,88	(111)	510		
	30,062	71462,9			(002)			
	43,053	32439,9	53,96	1,38	(022)			
	50,997	16389,3			(113)			
	53,430	7088,88	25,08	0,64	(222)			
	62,511	4914,72	9,91	0,25	(004)			
	68,901	4306,28	5,17	0,13	(133)			
	1	5,88	0,15					
	5	52318,5			(111)			
	25,977	5	70,91	1,83	(002)			
30,058	6	100	2,57	(022)				
D2	43,048	34572,5	54,32	1,40	(022)	568		
	50,991	17232,6			(113)			
	53,427	7579,82	10,53	0,27	(222)			
	62,505	4363,98	5,53	0,14	(004)			
	68,895	4235,38	5,82	0,15	(133)			
	6	59329,3			(111)			
	25,969	6	78,39	2,02	(002)			
	30,061	6	100	2,58	(022)			
	43,043	34592,3	47,86	1,24	(022)			
	50,961	16235,0			(113)			
D3	53,412	7263,76	11,07	0,29	(222)	620		
	62,515	5107,37	5,21	0,13	(004)			
	68,884	3006,55	4,99	0,13	(133)			
	6	42867,7			(111)			
	25,994	6	38,47	1,32	(002)			
	30,075	97401,3	100	3,42	(022)			
	43,067	30476,2			(022)			
	50,973	18028,7	20,46	0,70	(113)			
	D4	53,432	6318,23	5,69	0,19		(222)	692
		62,510	5569,29	4,47	0,15		(004)	

	68,900	3841,97	3,19	0,11	(133)	
		36445,5			(111)	
	25,989	6	27,04	1,00	()	
		114354,			(002)	
	30,073	1	100	3,71	()	
		32737,4			(022)	
D5	43,068	7	29,8	1,11	()	
		20435,3			(113)	755
	50,973	7	20,08	0,75	()	
					(222)	
	53,441	5643,00	4,03	0,15	()	
					(004)	
	62,514	6922,47	4,81	0,18	()	
					(133)	
	68,913	4062,92	2,76	0,10	()	
		32453,6			(111)	
	25,987	5	14,54	0,66	()	
		190282,			(002)	864
	30,075	6	100	4,51	()	
		31844,1			(022)	
	43,062	1	17,36	0,78	()	
		26374,8			(113)	
D6	51,005	3	14,47	0,65	()	
					(222)	
	53,430	5551,34	2,35	0,11	()	
		10681,2			(004)	
	62,515	7	4,86	0,22	()	
					(133)	
	68,907	4035,55	1,64	0,07	()	

The calculated lattice parameters of the produced films are plotted versus $F(\theta)$ and given in Equation (12)

$$F(\theta) = (\cos^2 \theta / 2) * (\frac{1}{\sin^2 \theta} + \frac{1}{\theta}) \quad (12)$$

$$(\cos^2 \theta / 2) * (\frac{1}{\sin^2 \theta} + \frac{1}{\theta}) = 0 \quad (13)$$

Equation (13) which is the linear line cut off point, provides the presence of the corrected lattice constant and is given in Table 3 [13]. The dislocation density of the produced films can be derived from the crystallite size as given in Equation (14) and is given in Table 3 [3].

$$\delta = \frac{1}{(D)^2} \quad (14)$$

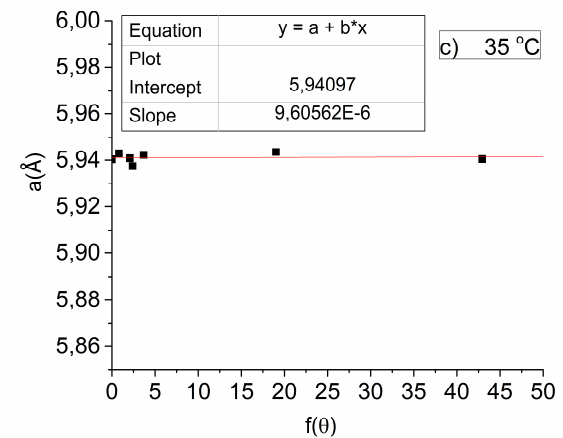
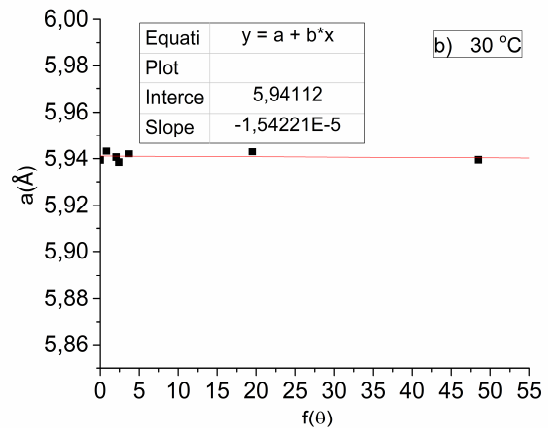
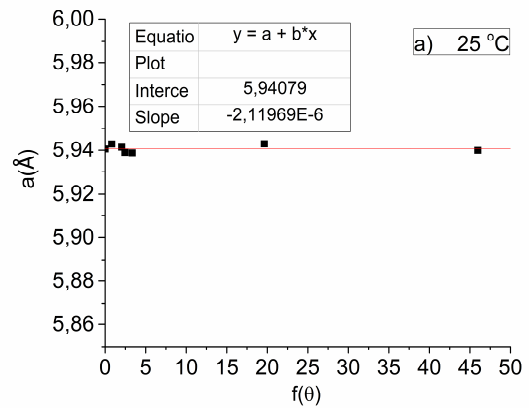


Figure 2.2 Nelson-Riley graphs of PbS thinfilms a) D1, b) D2 and c) D3

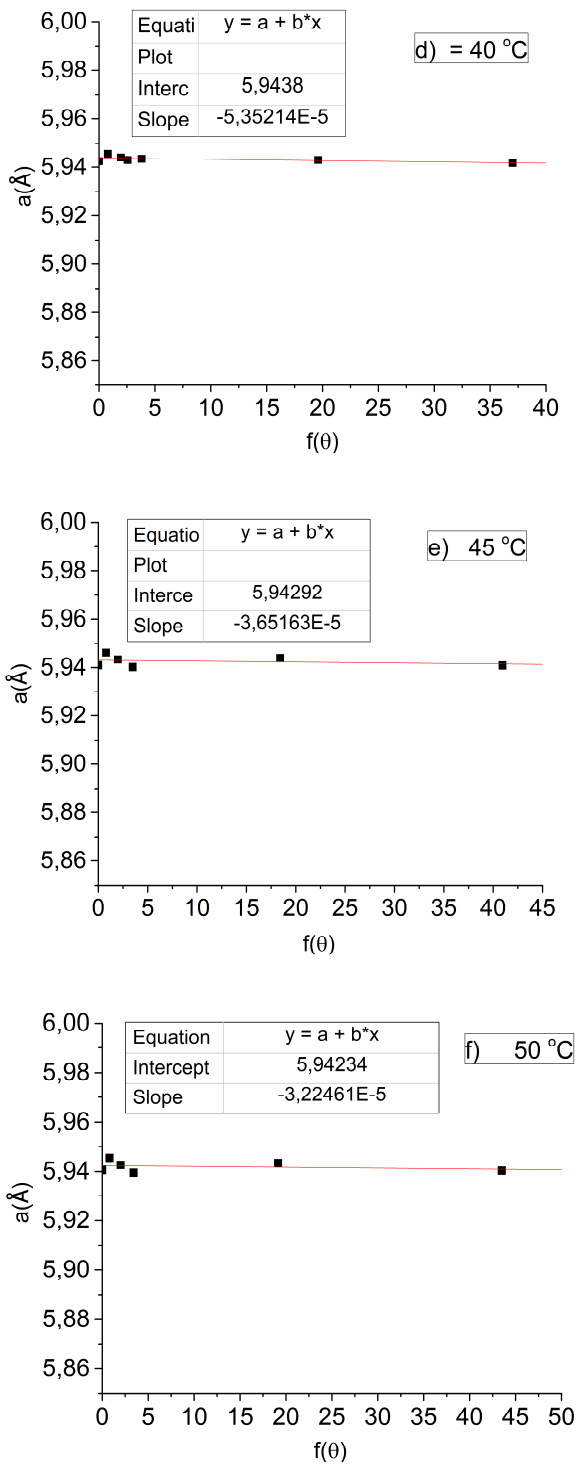


Figure 2.2 Nelson-Riley graphs of PbS thin films d) D4, e) D5 and f) D6

Table 3. The particle sizes, dislocation densities, confirmed weave parameters, micro tensile values and average stress values of the produced PbS thin films obtained from D1, D2 to D3, D4 and D5

EXPERIMENT	CRYSTALITE SIZE (nm)	LATICE PARAMETER ^a (VERIFIED) (Å)	MIKRO STRAIN *10 ⁻⁴	DISLOCATION DENSITY (lines/m ²)*10 ¹⁴	AVERAGE STRESS (10 ⁷ N/m ²)	
D1	25,908	63,0 ₀	5,94038	7,38	2,52	9,25
	30,062	52,9 ₇	5,94538	15,80	3,56	19,8
	43,053	66,0 ₀	5,94261	11,14	2,30	14,0
	50,997	42,5 ₀	5,93954	5,97	5,54	7,48
	53,430	68,7 ₄	5,94055	7,67	2,12	9,62
	62,511	29,9 ₂	5,94336	12,40	11,2	15,5
D2	68,901	93,0 ₉	5,94035	7,33	1,15	9,19
	25,977	63,0 ₁	5,9410	8,49	2,52	10,6
	30,058	52,9 ₇	5,9461	17,01	2,47	21,3
	43,048	66,0 ₀	5,9432	12,18	1,47	15,3
	50,991	42,5 ₀	5,9402	7,03	5,53	8,82
	53,427	85,9 ₄	5,9409	8,25	1,35	10,3
D3	62,505	89,7 ₉	5,9439	13,27	4,96	16,6
	68,895	93,0 ₉	5,9408	8,14	1,15	10,2
	25,969	63,0 ₁	5,9429	11,67	2,52	14,6
	30,061	63,5 ₇	5,9455	16,11	2,47	20,2
	43,043	66,0 ₀	5,9439	13,47	2,30	16,9
	50,961	85,0 ₄	5,9434	12,56	1,38	15,7
D4	53,412	85,9 ₃	5,9424	10,88	1,35	13,6
	62,515	44,8 ₈	5,943	11,79	4,97	14,8
	68,884	93,0 ₈	5,9417	9,606	1,15	12,0
	25,994	52,5 ₀	5,9374	2,36	3,63	2,96
	30,075	63,5 ₈	5,9429	11,56	2,47	14,5
	43,067	66,0 ₁	5,9408	8,04	2,30	10,1
D5	50,973	85,0 ₄	5,9422	10,44	1,38	13,1
	53,432	85,9 ₄	5,9403	7,32	1,35	9,18
	62,510	44,8 ₈	5,9434	12,53	4,97	15,7

	68,900	93,0 9	5,9404	7,48	1,15	9,37
	25,989	52,5 0	5,938	4,19	3,63	5,26
	30,073	63,5 8	5,943	12,3	2,47	15,4
	43,068	66,0 1	5,941	7,85	2,30	9,84
D5	50,973	85,0 4	5,942	10,4	1,38	13,1
	53,441	68,7 4	5,939	5,75	2,12	7,20
	62,514	35,9 1	5,943	11,93	7,75	15,0
	68,913	74,4 6	5,939	5,86	1,80	7,35
	25,987	63,0 1	5,9389	4,90	2,52	6,14
	30,075	63,5 8	5,9428	11,6	2,47	14,5
	43,062	66,0 1	5,9413	9,09	2,30	11,4
D6	51,005	42,5 0	5,9387	4,57	5,54	5,73
	53,430	85,9 4	5,9405	7,67	1,35	9,62
	62,515	35,9 1	5,943	11,8	7,75	14,8
	68,907	74,4 6	5,9399	6,60	1,80	8,27

2.2. SEM Analysis of the PbS Thin Films

The surface morphologies of the obtained PbS thin films were examined by using JEOL SM-5600LV electron microscope. The SEM images of the PbS thin films with 100 and 30.000 magnifications are shown in Figure 2.3. As clearly seen from Fig. 2.3, there are pinholes on the surfaces of the films regardless of deposition temperature. Furthermore, the deposition temperature significantly influenced the number and the size of pinholes observed on the film surfaces. As the deposition temperature increased, the pinholes in the SEM images were observed to be larger and larger. Furthermore, the number of pinholes also increased with increasing deposition temperature.

As seen from Figure 2.3a, the granules were observed to be polymorphic form.

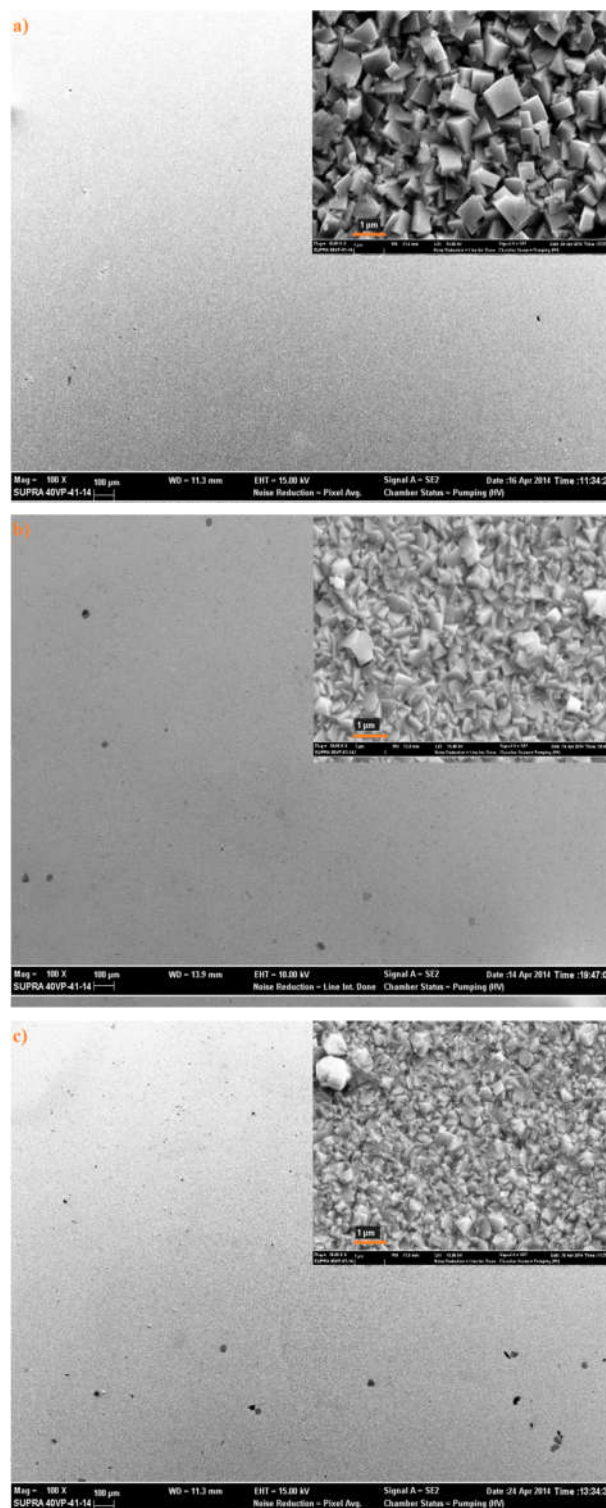


Figure 2.3. 100 times and 30000 times magnified SEM images of PbS thin films obtained from a)D1 b) D2 c)D3

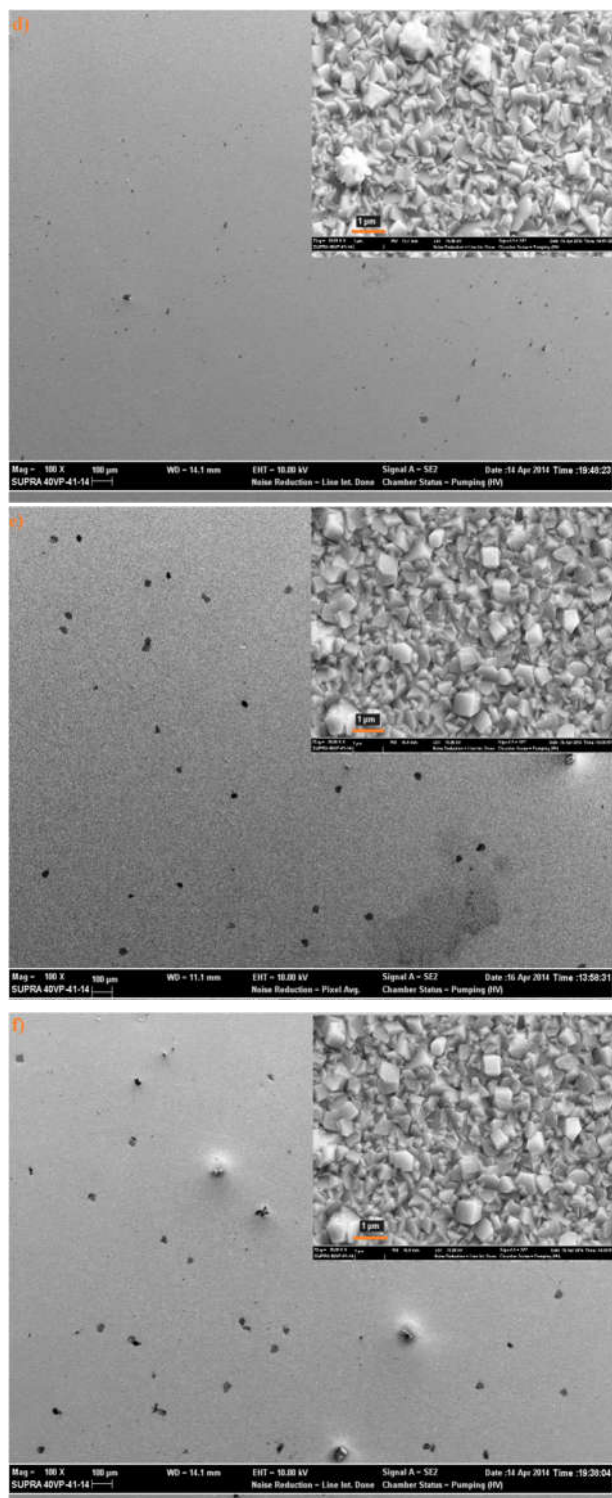


Figure 2.3. 100 times and 30000 times magnified SEM images of PbS thin films obtained from **d)D4 e) D5f) D6**

3. CONCLUSION

In this study, PbS thin films were produced on glass substrates by chemical bath deposition technique. $Pb(NO_3)_2$ and $CS(NH_2)_2$ aqueous solutions were used to produce the films. The amount of $CS(NH_2)_2$ and the amount of $Pb(NO_3)_2$ were kept constant. The structural properties of all the PbS films were determined by XRD analysis.

According to XRD results, it is understood that all films formed in cubic PbS structure. It has been found that the PbS thin films have three texture coefficient values larger than 1 belonging to different planes. However, it is understood that the film produced in D6 has a preferential orientation of (002) plane. In addition to that, this film has higher peak intensities compared to other films. It is thought that the preferred orientation for other films is random.

The dislocation densities, the microstrain, and mean stress values were also estimated from the XRD analyses. According to findings, it is found that the dislocation density of the film obtained in D1 is greater than that of the other films. The SEM analyses suggest that not only the number but also the size of pinholes formed on the film surfaces increase with increasing deposition temperature. This study showed that when bath temperature was kept at 25°C, the XRD peak intensity was measured high although film thickness of this film was measured low. Furthermore, there are no voids, cracks and pinhole on the surface of this film.

REFERENCES

- [1] Naresh B. Kotadiya, Anjana J. Kothari, Devendra Tiwari, and Tapas K. Chaudhuri, "Photoconducting nanocrystalline lead sulphide thin films obtained by chemical bath deposition," *Applied Physics A Materials Science & Processing*, vol. 108, pp. 819–824, 2000.
- [2] A.S. Obaid, M.A. Mahdi, Z. Hassan, and M. Bououdina, "PbS nanocrystal solar cells fabricated using microwave-assisted chemical bath deposition," *International Journal of Hydrogen Energy*", vol. 38, pp. 807–815, 2013.
- [3] A. N. Fouda, M. Marzook, H. M. Abd El-Khalek, S. Ahmed, E. A. Eid, and A. B. El Basaty, "Structural and Optical Characterization of Chemically Deposited PbS Thin Films," *Springer Science+Business Media Dordrecht Silicon* vol. 9, pp. 809-816, 2017.
- [4] Alex P. Gaiduk, Peter I. Gaiduk, and Arne Nylandsted Larsen, "Chemical bath deposition of PbS nanocrystals: Effect of substrate," *Thin Solid Films*, vol. 516 pp. 3791–3795, 2008.

- [5] H. Soetedjo, B. Siswanto, I. Azizand S. Sudjatmoko, "Low Resistivity Of Cu And Fe Doped Pbs Thin Films Prepared Using DC Sputtering Techniqueh," *Journal of Non-Oxide Glasses*, vol. 9, No 2, p. 55 – 63, 2017.
- [6] E. Pentia, L. Pintilie, T. Botila, I. Pintilie, A. Chaparro, and C. Maffiotte, "Bi influence on growth and physical properties of chemical deposited PbS films," *Thin Solid Films*, vol. 434, pp. 162–170, 2003.
- [7] J. P., Nair, R., Jayakrishnan, C. B. Nandu, and R. KPandley, "'In situ Sb-doped CdTe Films," *Semicond. Science and Technology*, vol. 13, no. 3, pp. 340, 1998.
- [8] S. B., Park, S. W., Moon, and I. S. Woo, "Preparation and characterization of lead zirconate titanate thin flims," *Thin Solid Films*, vol.339, pp. 77, 81,2000.
- [9] P. K., Manoj, , K. G., Gopchandran, P., Koshy, V. K., Vaidyan, and Josephc, B., "Growth and characterization of indium oxide thin films prepared by spray pyrolysis," *Optical Materials*, Vol. 28, No. 12, pp. 1405-1411.
- [10] M., Saleem, Fang, L., Liang,A., Wakeel, M., Rashad, ve C. Y. Kong, "Simple preparation and characterization of nanocrystalline zinc oxide thin films by sol-gel method on glass substrate," *World Journal of Condensed Matter Physics*, No. 2, pp.10-15, 2012.
- [11] Cullity B.D., "X-Işınlarnın Difaksiyonu", Çeviren; Sümer A., İTÜ Fizik Profesörü, *İstanbul Teknik Üniversite Matbaası Gümüşsuyu*, 1966.
- [12] A. Hussain, A.Begum, and A. Rahman "Characterization of Nanocrystalline Lead Sulphide Thin Films Prepared by Chemical Bath Deposition Technique', *Arabian Journal for Science and Engineering*, Vol. 38 No. 1, pp.169–174, 2013.
- [13] S. Rajathi, K. Kirubavathi, and K Selvaraju "Structural, morphological, optical, and photoluminescence properties of nanocrystalline PbS thin films grown bychemical bath deposition', *Arabian Journal of Chemistry*, 2015

	SAKARYA UNIVERSITY JOURNAL OF SCIENCE		 SAKARYA UNIVERSITY
	e-ISSN: 2147-835X http://www.saujs.sakarya.edu.tr		
	<u>Received</u> 07-07-2017 <u>Accepted</u> 28-11-2017	<u>Doi</u> 10.16984/saufenbilder.327153	

Cloning, Expression and Characterization of Xylanase (*xyn-akky1*) from *Bacillus subtilis* in *Escherichia coli*

Sema BİLGİN^{*1}, Yakup ULUSU², Hülya KUDUĞ³, İsa GÖKÇE³

ABSTRACT

In this study, *Bacillus subtilis* akky1 strain was isolated from the soil of beech forest in Akkuş City, Ordu Province, Turkey. akky1 strain was identified by 16S rRNA analysis. The full-length 16S rRNA sequence of akky1 strain showed the 100% similarity with *Bacillus subtilis* strain B7 (KC310823.1). A 642 bp DNA fragment was obtained from genomic DNA using primers designed based on the gene sequence of *Bacillus subtilis* xylanase given in GenBank. The gene encoding xylanase was cloned into pET28b (+) plasmid vector, sequenced and expressed in *Escherichia coli* BL21 (DE3). The hexahistidine (6xHis) tagged fusion protein was purified using nickel affinity chromatography and the xylanase activity was measured. The molecular mass of the purified xylanase was approximately 26 kDa as estimated by SDS-PAGE. The xylanase had optimal activity at pH 6.0 and 60°C. The K_m values of the recombinant enzyme towards beechwood was 3.33 mg/ml.

Keywords: *Bacillus subtilis*, Xylanase, Recombinant Protein, Industrial Enzymes, *Escherichia coli*

* Corresponding Author

¹Gaziosmanpaşa Üniversitesi, Fen Edebiyat Fakültesi, Kimya Bölümü, Tokat sema.bilgin@gop.edu.tr

²Karamanoğlu Mehmetbey Üniversitesi, Mühendislik Fakültesi, Biyomühendislik Bölümü, Karaman yakupulusu@yahoo.com

³Gaziosmanpaşa Üniversitesi, Mühendislik ve Doğa Bilimleri Fakültesi, Biyomühendislik Bölümü, Tokat, hlykudug@gmail.com, isa_gokce@yahoo.co.uk

1. INTRODUCTION

Hemicellulose is a heterogeneous polymer composed of pentose (such as xylose, arabinose) and hexose sugars (such as mannose, glucose, galactose) and sugar acids. Hemicelluloses collectively are classified into three groups as xylan, glucomannan, arabinogalactan (1). An essential component of the xylan is 5-carbon sugar, D-xylose, which can be converted into chemical fuel by microbial cells (3). Complete degradation of plant xylenes requires the collaboration of several hydrolytic enzymes because of the complex chemical structure and heterogeneity of the xylan. Therefore, it is not surprising that producing a multitude number of polymer disintegrate enzymes by the xylan digesting microbial cells. The xylanolytic enzyme system which is performed xylan hydrolysis usually consists of several hydrolytic enzymes: β -1,4-endoxylanase, β -xylosidase, α -L-arabinofuranosidase, α -glucuronidase, acetyl xylan esterase and phenolic acid esterase (ferulic acid and p-coumaric acid). Among them, endo-1,4- β -xylanase (1,4- β -D-xylan-xylan hydrolase E.C. 3.2.1.8) is the key enzyme. This enzyme breaks down the glycosidic bonds in xylan structure. Initially, the product of hydrolysis is β -D-xylopyranosyl oligomers and at the later stages small molecules such as mono-, di- and trisaccharides of β -D-xylopyranosyl (16). Endo-1,4- β -xylanase is produced by various microorganisms such as fungi (3; 2), actinomycetes (6) and bacteria (4).

Xylanases derived from microorganisms caught major attention due to their expended industrial applications including textile industry (5), production of xylo-oligosaccharides (14), clarification of juices (3), waste-water treatment (17), bioconversion of lignocellulosic wastes into useful economical products (ethanol, sugar

syrops, gaseous fuels etc.) (5), biobleaching of pulp (11, 18).

In this study, xylanase-producing *Bacillus subtilis* strain akky1 was isolated from the soil of beech forest in Akkuş City, Ordu Province, Turkey. The identification of the strain akky1 was performed with PCR amplification of 16S rRNA. Xylanase gene was amplified from the genomic DNA of akky1 strain by polymerase chain reaction using two oligonucleotides. After *Xyn-akky1* gene had been sequenced, it was cloned into the pET28b vector and expressed in *Escherichia coli*. The recombinant xylanase was characterized by biochemical methods.

2. MATERIALS AND METHODS

2.1. Microorganism Isolation and Screening Xylanase Activity

The soil of beech forest was collected from Akkuş City, Ordu Province, Turkey. The growth medium contained 0.25% yeast extract, 0.5% peptone, 0.1% glucose and adjusted to pH 4.8 using HCl. Culter was incubated at 37°C and 250 rpm for 30 h. The diluted cultures were spread on agar plates containing 0.5% peptone, 0.25% yeast extract, 1.0% beechwood xylan and 2.0% agar (pH 4.8). Congo red method has been used to screen xylanase-producing strains (1) The strains identified as xylanase producers were inoculated into 5 ml of PCA medium pH 5.5 and incubated overnight at 37°C at 250 rpm agitation. The isolation of genomic DNA from overnight culture after incubation was carried out in accordance with the manufacturer's recommendation using the kit 'Fermantes. The isolated genomic DNA and two oligonucleotides were utilized in order to amplify the 16S rRNA (Table 1). Sequence analysis was performed by Refgen Company. So that choosen xylanase-producing strains was identified by 16S rRNA analysis.

Table 1. Two oligonucleotides were utilized in order to amplify the 16S rRNA

Primer	Sequence (5'→3')	Accession Number
Unv-Bac-27F	agagtttgatcmtggctcag	AB579660-765
Unv-Bac-1525R	aaggaggtgwtccarcc	

2.2. Cloning and Expression of the xylanase Gene in Escherichia coli

Two different oligonucleotides were used to amplify DNA fragment encoding the

Table 2. Two oligonucleotides were utilized in order to amplify the xylanase gene

Primer	Sequence (5'→3')
xyn1	tttgatccgatgttaagttaaaaag
xyn2	tttctcgagtaccacactgttagctt

xylanase gene for *Bacillus subtilis* akky1 (Table 2).

Genomic DNA used as template DNA for PCR, isolated from *Bacillus subtilis* akky1 using Fermentes genomic DNA purification kit. xylanase gene was cloned to construct the pET28b-xyn recombinant vector DNA using *XhoI* and *BamHI* restriction enzymes (Figure 1). The positive clones for recombinant xylanase were identified using the Congo Red.

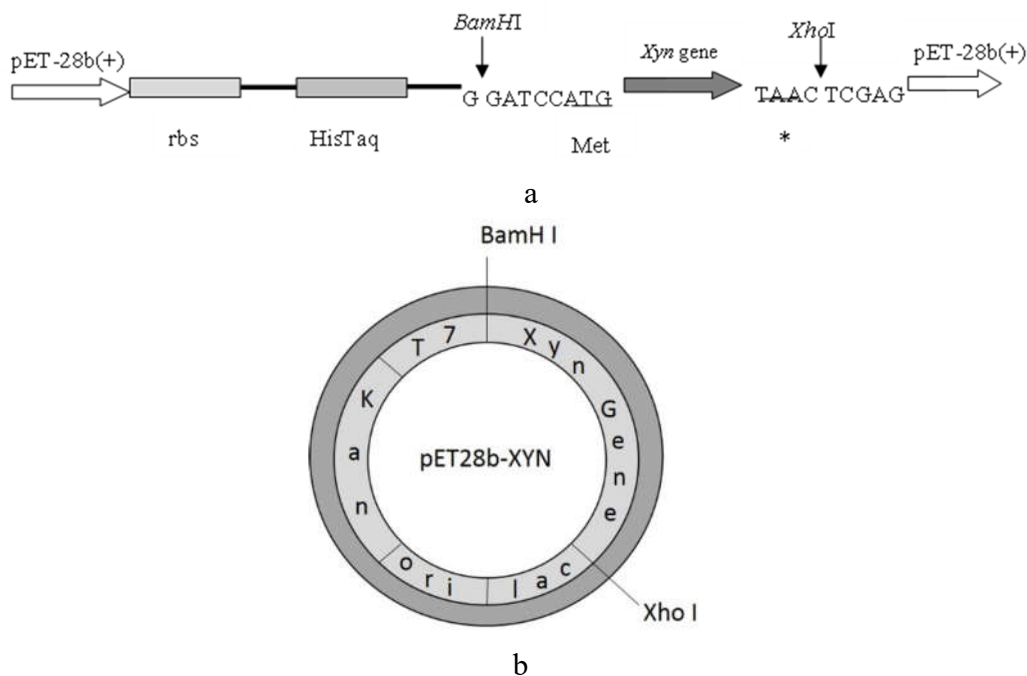


Figure 1. a. Schematic diagram of the gene region where the Xyn DNA sequence transferred to pET-28b (+) vector. b. Circular the pET28b-xyn map of construct which used to produce *Bacillus subtilis* xyn-akky1 xylanase.

2.3. Purification of Recombinant Xylanase

The *E. coli* BL21 (DE3) was transformed with the pET28b-xyn construct and growth on Luria Bertani agar containing kanamycin

(50 mg/ml). Briefly, the transformant was inoculated into 3 ml culture tube containing LB broth and incubated overnight at 37 °C and 200 rpm. Then this culture was inoculated into 500 ml of LB containing kanamycin and grown at 37 °C with shaking at 200 rpm. The

culture was induced for 3 hours with a final concentration 1mM IPTG when the OD₆₀₀ reached 0.6-0.7.

Next, the cells were harvested by using centrifugation (at +4°C, 8000 rpm 5 min), followed by re-suspended the pellet using RNase (20 µg/ml) and DNase (20 µg/ml) with 20 mM phosphate buffer (pH 8.0) and protease inhibitors (0.5 mM Phenyl methyl sulfonyl fluoride (PMSF) and 2 mM Benzamidine). Cells were first lysed using a sonicator (Sonics VCX 130), then high-speed (30,000 rpm) centrifugation was performed for 1 hour. Qiagen Ni-NTA affinity column was used to purification of soluble recombinant protein carrying N-terminal 6x histidine. The column was washed first with 50 mM phosphate buffer (pH 8.0) and then 50 mM phosphate buffer (pH 8.0) containing 30 mM imidazole. The protein was eluted from column with 300 mM imidazole in 50 mM phosphate buffer (pH 8.0). Purity of this isolated protein was checked by SDS-PAGE. Concentration of protein was determined by UV absorption at 280 nm (19).

2.4. Plate Assay

E. coli strain BL21 (DE3) containing the recombinant plasmid pET28b-xyn was inoculated on LB agar plate containing 1% beechwood xylan, 50 mg/ml kanamycin and 100 mg/ml IPTG. Following overnight incubation at 37°C, staining of the plates done using 1% Congo-red solution and destained by three washes using 1 M NaCl followed by 0.1 N NaOH. The enzyme activity was examined by a clear zone formation around the colony (Wood et al., 1998).

2.5. Biochemical Characterization

3,5-dinitrosalicylic acid (DNS) method was used to determine the recombinant xylanase activity (10). The optimal pH for purified 6x

His tagged enzyme was determined at 37°C. Beechwood xylan was used as a substrate in wide pH which ranging from 4.0 to 10.0. pH range of substrate was adjusted by McIlvaine buffer for pH 4-7, Tris-HCl buffer for pH 8, and glycine-NaOH buffer for pH 9-10. To determine the optimal temperature for enzymatic activities the enzyme was incubated between 30°C to 70°C in presence of McIlvaine buffer (pH 6.0). The thermostability of the xylanase was tested by pre incubating the enzyme in McIlvaine buffer (pH 6.0) at 50°C, 55°C, 60°C without substrate. Km and V_{max} values for purified enzyme were calculated in McIlvaine buffer (pH 6.0 at 60°C using 1-10 mg/ml beechwood xylan as a substrate). The data were plotted by Lineweaver-Burk method (13).

2.7. Nucleotide sequence accession numbers

Bacillus subtilis strain akky1 16S rRNA nucleotide sequences and xylanase gene were deposited in the GenBank (accession numbers KJ540929.1 and KJ540928.1).

3. RESULTS AND DISCUSSION

3.1. Microorganism Identification Using PCR

Six strains isolated from soil samples collected from Ordu province, Turkey demonstrated xylanolytic activity. New strains were identified using 16S rRNA sequences. The xylanase activity was revealed by strain akky1 which produce highest zone clearance on agar plate containing xylan (Figure 2a,b).

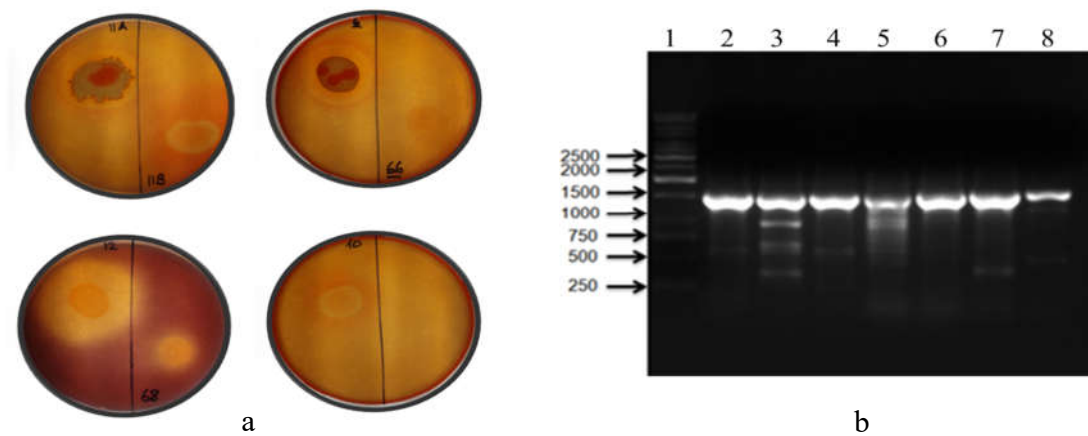


Figure 2. a. Hydrolysis zones of the xylanase-producing microorganisms. b. The result of agarose gel (%1) electrophoresis shows PCR products for the 16S rRNA of the xylanase-producing microorganisms. 1. λ -EcoR I /Hind III DNA marker, 2-8 16S rRNA PCR product of xylanase-producing microorganisms.

The species that have a similarity of 16S rRNA sequences was analysed by BLAST server at the NCBI public database. A taxonomy report was established by using the Taxonomy Report tool within BLAST.

According to taxonomy report, 16S rRNA sequence of *Bacillus subtilis* strain akky1 (KJ540929) exhibited 100% nucleotide identity with *Bacillus subtilis* strain therefore new species were classified under the genus *Bacillus subtilis* (Figure 3).



Figure 3. Taxonomy BLAST report of Bacillus subtilis strain akky1 16S ribosomal RNA gene, partial sequence (KJ540929)

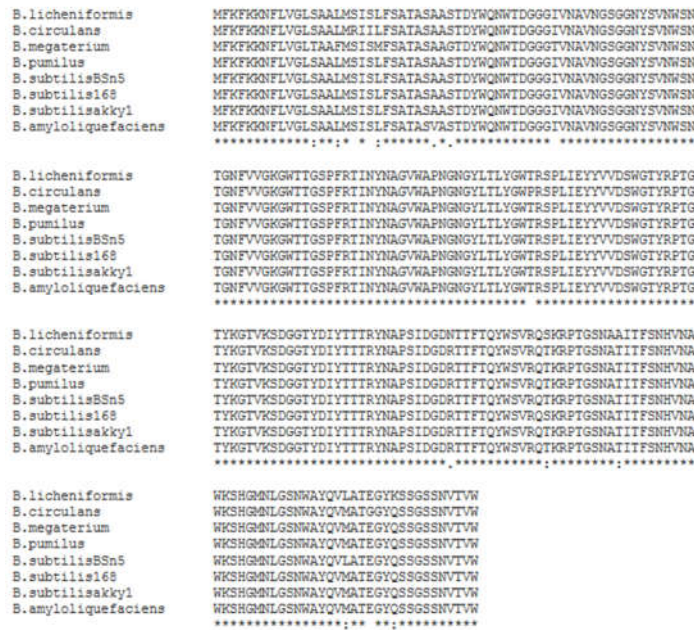


Figure 4. The multiple alignment of amino acid sequence of the xylanase enzymes of different species of *Bacillus* with the amino acid sequence isolated from *Bacillus* and used for cloning and expression studies of xylanase enzyme, by using ClustalW2 program. The accession numbers are: *B. subtilis* strain akky1, KJ540928.1; *Bacillus pumilus*, AAZ17390.1; *Bacillus subtilis* subsp. *subtilis* str. 168, NP_389765.1; *Bacillus subtilis* BSn5, YP_004203820.1; *Bacillus amyloliquefaciens*, AAZ17388.1; *Bacillus megaterium*, ACT21830.1; *Bacillus licheniformis*, AAZ17387.1; *Bacillus circulans*, AAM08360.1

3.2. Cloning of the Xylanase gene in *Escherichia coli*

DNA fragment encoding-xylanase from *Bacillus subtilis* strain akky1 xylanase was amplified and this fragment was cloned to pET 28b (+) vector using *XhoI* and *BamHI* restriction enzymes. Final plasmid was named as a pET28b-xyn. The results obtained from colony PCR (template: the *E.coli* DH5α strains harboring pET28b-xyn; primers: xyn1-xyn2) (Figure 5 a), restriction

fragment analysis (Figure 5 b), confirm the success of cloning. Furthermore DNA sequencing was done to verify correct insertion of xylanase-encoding DNA fragment. *E. coli* DH5α cells transformed by constructed pET28b-xyn were selected with kanamycin selection. Consecutive plasmid preparation method was utilized for sequencing DNA samples and transformation of competent *E. coli* BL21 (DE3) cells. Figure 1b. demonstrates the circular plasmid map of the construct.

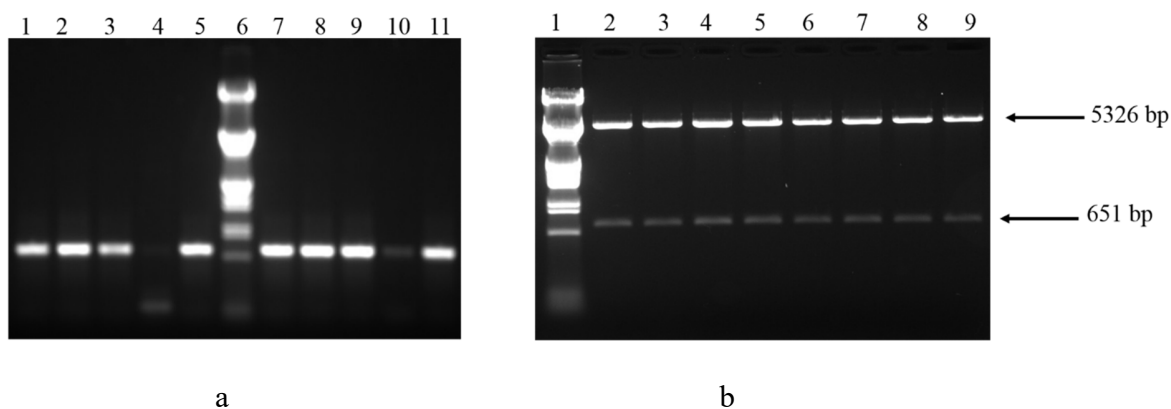


Figure 5. a. Agarose gel (1%) electrophoresis result showing PCR verification of recombinant plasmid pET28b-xyn after the cloning. Columns 1-5 and 7-11 indicates PCR products from the colonies and column 6 indicate, λ -EcoR I /Hind III DNA marker. b. 1% Agarose gel demonstrating digesting of recombinant plasmid pET28b-xyn with *NcoI* restriction enzyme after the cloning. 1, λ -EcoR I /Hind III DNA marker 2-9, DNA fragments obtained after the digestion.

3.3. Qualitative Analysis of the Purified Protein

The 6xHis tagged recombinant xylanase was purified from *E. coli* cell lysate by Ni-NTA chromatography as described above. Eluted samples were analysed on SDS-PAGE and the purified enzyme migrated on the gel as a

single band with a molecular mass of around 26.0 kDa (Figure 6 a). The calculated molecular mass of protein using the “ExPASy ProtParam Tool” was 26970.6 Da which is very close to the experimental molecular mass.

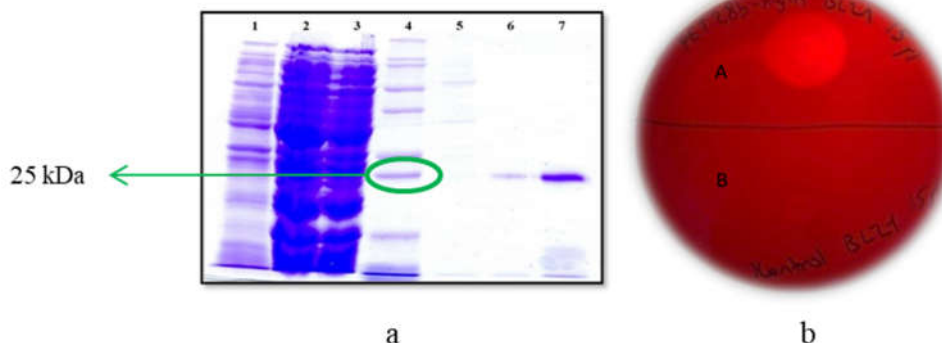


Figure 6.a. Purification of xylanase enzyme was confirmed with SDS-PAGE (%12). Samples from induced *E. coli* BL21 pLysE cell lysate carrying pET28b plasmid (1). Samples from induced *E. coli* BL21 pLysE cell lysate carrying pET28b-xyn plasmid (2). Collected supernatant after centrifugation of the lysate (3). BioRad dual colour precision plus protein marker (4). The eluate collected from Ni-NTA agarose affinity column (imidazole concentrations are respectively 10, 25, 300 mM) (5-7). b. The image of zone formation at the periphery of the recombinant colony by Congo-red plate containing beechwood xylan. A. Recombinant colony B. *E. coli* BL21 without plasmid

3.4. Biochemical Characterization

Activity of recombinant xylanase was observed for various pH values. The optimum condition for activity of recombinant xylanase predicted as follows:

pH 6.0 (Figure 7a) and at 60°C (Figure 7b). 35% of the enzyme activity was able to maintain stability for 200 minutes at 55°C (Figure 7c). Km value for xylanase was 3.33 mg/ml when beechwood xylan was used as substrate (Figure 8).

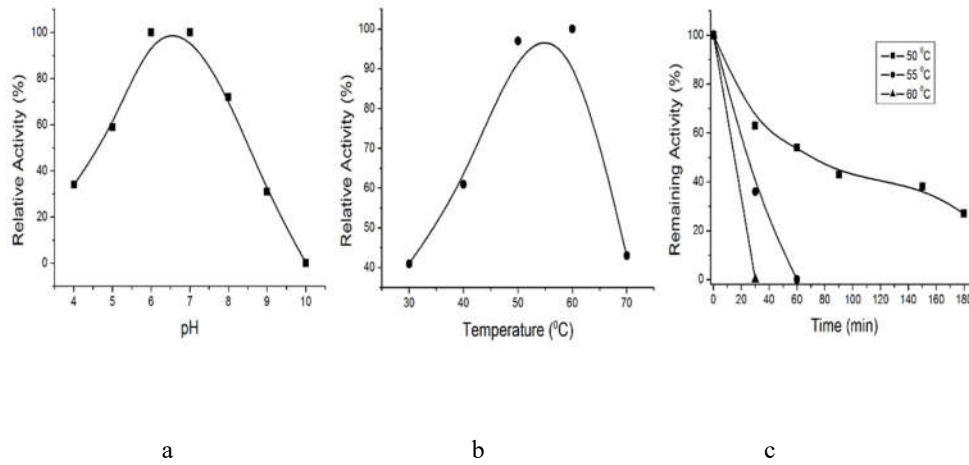


Figure 7. Characterization of recombinant xylanase. a. Effect of pH. b. Effect of temperature. c. Thermostability of recombinant xylanase

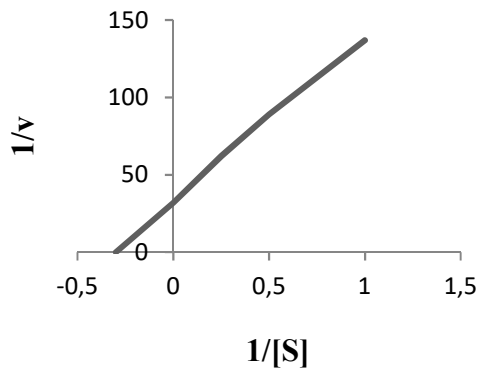


Figure 8. Lineweaver-Burk curve for the purified xylanase enzyme

Several xylanases from microorganisms, such as fungi, bacteria and yeast, were isolated, cloned and expressed in *E. coli* (9, 10, 21, 22). In this study, xylanolytic *Bacillus subtilis* strain akky1 was isolated from the soil of beech forest in Akkuş City, Ordu Province, Turkey. *Bacillus* species are soil bacteria with gram-positive cell membrane. These species can utilize complex carbohydrates in their native environment by expressing and secreting a variety hydrolytic enzymes (9).

In the current study, we first identified the xylanase gene sequence of xylanase from public database (NCBI/GenBank accession no NC000964) and further designed the primers to amplify of 642-bp DNA fragment by PCR using genomic DNA as a template. DNA sequence of xylanase gene from akky1 and the xylanase gene (accession no NC000964) showed 99.7% similarity with only two bases differences (in positions 484 and 498). These two bases cause mutation of serine at position 160, becomes threonine (S160T) (Figure 4). The observed phenomenon could be due to similarity in the some species caused by high conservation of xylanase gene sequence in the microorganism.

Xyn-akky1 derivatives exhibit substantial thermal and pH stability which make possible for their use in industries. Xyn-akky1 retains its activity at pH 6 to 8 range therefore it can be useful in the paper industry (8).

Xyn-akky1 enzyme is more useful for pulp bleaching than non-enzymatic multistage process because of its cost effectiveness and eco-friendly characteristics. Additionally, the combination of our xylanase with other xylan-degrading enzymes

may be applicable in processing food products, manufacturing vegetable and juice products and optimization of animal feedstock digestibility.

ACKNOWLEDGEMENTS

This study was supported by Gaziosmanpasa University Research Council (Project Number: 2012/60). Sema BİLGİN, one of the researchers of this study, was financially supported by TUBITAK-BİDEB 2211 National Scholarship Programme for PhD Students. We wish to thank Assoc. Prof. Dr. Bilge Hilal CADIRCI for her contribution during isolation of microorganisms.

CONFLICT OF INTEREST

The authors declare that they have no conflict of interests.

REFERENCES

- [1] Beg Q K, Kapoor M, Mahajan L, Hoonda G S "Microbial xylanases and their industrial applications: a review," *Appl Microbiol Biotechnol* 56: 326–338, 2001
- [2] Belancic A, Scarpa J, Peirano A, Diaz R, Steiner J "Eyzayuirre J. *Penicillium purpurogenum* produces several xylanases: purification and properties of two of the enzymes," *Biotechnol* 41: 71–79, 1995.
- [3] Biely P, "Microbial xylanolytic systems," *Trends Biotechnol* 3:286–290, 1985.
- [4] Dey D, Hinge J, Shendye A, Rao M "Purification and properties of extracellular endo-xylanases from alkalophilic thermophilic *Bacillus* sp." *Can J Microbiol* 38: 436–442, 1992.
- [5] Dhiman SS, Sharma J, Battan B, "Industrial applications and future prospects of microbial xylanases: a review," *BioResources* 3(4):1377–1402, 2008.
- [6] Elegir G, Sykes M, Jeffries TW, "Differential and synergistic action of *Streptomyces* endoxylanases in prebleaching of kraftpulp," *Enzyme Microb Technol* 17: 954–959, 1995.
- [7] Fernandez-No I C, Böhme K, Díaz-Bao M, Cepeda A, Barros-Velázquez J, "Characterisation and profiling of *Bacillus subtilis*, *Bacillus cereus* and *Bacillus licheniformis* by maldi-tof mass fingerprinting," *Food Microbiol*, 33: 235–242, 2013.

- [8] Georis J, Giannotta F, de Buyl E, Granier B, Fre`re J M, "Purification and properties of three endo-b-1,4-xylanases produced by *Streptomyces* sp. strain S38 which diver in their ability to enhance the bleaching of kraft pulps," *Enzyme Microb Technol*, 26:178–186, 2000.
- [9] Huang J, Wang G, Xiao L, "Clonning, Sequencing and Expression of the xylanase gene from a *Bacillus subtilis* strain B10 in *Escherichia coli*," *Bioresource Technol*, 97: 802-808, 2006.
- [10] Jalal A, Rashid N, Rasool N, Akhtar, M, "Gene Cloning and Characterization of a xylanase from a newly isolated *Bacillus subtilis* strain R5," *J Biosci Bioeng*, 107: 360-365, 2008.
- [11] Kiddinamoorthy J, Alfredo J, Gulelat DH, Rakshit SKV, "Production, purification and characterization of *Bacillus* sp. GRE7 xylanase and its application in eucalyptus Kraft pulp biobleaching," *World J Microbiol Biotechnol* 24:605–612, 2008
- [12] Kulkarni N., Shendye A., Rao M, "Molecular and biotechnological aspects of xylanases," *Fems Microbiol Rev* 23: 411-456, 1999.
- [13] Lineweaver H, Burk D, "The determination of enzyme dissociation constants" *J Am Chem Soc*, 56: 658-666, 1934.
- [14] Maalej-Achouri I, Guerfali M, Gargouri A, Belghith H, "Production of xylo-oligosaccharides from agro-industrial residues using immobilized *Talaromyces thermophiles* xylanase," *J Mol Cata B Enzymatic* 59:145–152, 2009
- [15] Miller G L, "Use of dinitrosalicylic acid reagent for determination of reducing sugar," *Anal Chem*, 31: 426-428, 1959.
- [16] Polizeli M L, Rizzatti A C, Monti R, Terenzi H F, Jorge J A, Amorim D S, "Xylanases from fungi: properties and industrial applications," *Appl Microbiol Biotechnol* 67: 577–591, 2005.
- [17] Rani S, Nand, K, "Development of cellulase-free xylanase-producing anaerobic consortia for the use of lignocellulosic wastes," *Enzyme Microb Technol* 18:23–28, 1996
- [18] Sanghi A, Garg N, Kuhar K, Kuhad RC, Gupta VK, "Enhanced production of cellulase-free xylanase by alkalophilic *Bacillus subtilis* ASH and its application in biobleaching of kraft pulp," *BioResources* 4(3):1109–1129, 2009.
- [19] Uluşu Y, Bilgin Ş S, Kuduđ H, Gökçe İ, "Expression, purification, and characterization of bovine chymosin enzyme using an inducible pTOL system," *PREP Biochem Biotech*. DOI: 10.1080/ 10826068. 2015.1085399, 2016.
- [20] Wood P J, Erfle J D, Teather R M, "Use of complex formation between Congo Red and polysaccharides in detection and assay of polysaccharide hydrolases," *Method Enzymol*, 160:59-7, 1998.
- [21] Gallardo, O., Diaz, Pastor, P., F.I. J., "Cloning and Characterization of Xylanase A from the Strain *Bacillus* sp. BP 7: Comparison with Alkaline pI-Low Molecular Weight Xylanases of Family 11," *Current Microbiology* Vol. 48, 276–279, 2004.
- [22] Yoon, K-H., "Cloning of the *Bacillus subtilis* AMX-4 Xylanase Gene and Characterization of the Gene Product," *J. Microbiol. Biotechnol.*, 19(12), 1514–1519, 2009.

	SAKARYA UNIVERSITY JOURNAL OF SCIENCE		 SAKARYA UNIVERSITY
	e-ISSN: 2147-835X http://www.saujs.sakarya.edu.tr		
	<u>Received</u> 21-07-2017 <u>Accepted</u> 28-11-2017	<u>Doi</u> 10.16984/saufenbilder.330029	

Optical properties of the electron and gamma-ray irradiated soda-lime glass samples

Gulten Onay¹, Ramazan Sahin*¹

ABSTRACT

Optical transmission and absorption spectra of Soda-lime glass samples were studied after irradiation by 8 MeV electron and γ -ray beams. We used modified clinical LINAC for production of electron beam whereas ^{60}Co was used as a γ -ray source. Optical properties of glass samples were analyzed for different doses and radiation types. Irradiation induced color centers in the glass samples were observed in both cases. Moreover, time-dependent optical properties were also acquired after irradiation source was turned off and we observed that these colour centers disappear slowly even at room temperature. Optical transmission spectra of 8 MeV electron and γ -ray beam irradiated samples show spectacular absorption band in the visible region. On the other hand, these absorption bands nearly recover themselves when the irradiated samples are baked for a short time above 100 °C.

Keywords: irradiation, soda-lime glass, gamma, electron beam, LINAC and ^{60}Co

1. INTRODUCTION

Interaction of high energy photons and accelerated charged particles with target materials has gathered an increasingly attention. γ -ray, photo-neutron (photo- n^0) and high energy electron beams (e^- -beam) are widely used types of radiation. These ionizing beams can excite the electrons in target materials leaving the hole centers [1]. Transition of electrons between the states causes irradiation induced color centers in glassy materials [2]-[6]. Therefore, their contents define the interaction mechanism [7]-[14]. The response of glass samples to different radiation sources make them a better candidate for radiation protection [15]-[17] and sensing [18] applications. Moreover, glasses are used as substrates for thin film deposition. Therefore, when these thin films are exposed to radiation, the glass substrates are also affected by the radiation [19]. The effects of different kind of radiations on glass materials

require more attention during and after irradiation with no dependence on field of use. Even though the majority of previous works focus the effects of radiation on the target glass samples, time-dependent analysis about irradiation induced colour centers are missing. So, in this work, we systematically applied different types of radiations to widely used soda-lime glass samples and characterized them at certain time intervals even after the radiation source was turned off. Moreover, bleaching of the irradiated glass samples is applied to quicken the recovery process.

2. EXPERIMENTS

In our experiments, soda-lime glass samples were employed from Sisecam Co., Turkey. The size of the samples were 1x1 *inch* and of 1 mm thickness. Before irradiation process, all glass samples were cleaned with acetone, isopropanol and pure water respectively by using an ultrasonic cleaner. After cleaning, glass samples were handled with dust-

* Corresponding Author

¹ Akdeniz University, Faculty of Science, Department of Physics, ramazansahin@akdeniz.edu.tr

free gloves throughout the experiments. One sample was used for each measurement and radiation type. We used ^{60}Co radioisotope as a natural source of γ -rays in the first part of our experiments. As a comparison a modified clinical LINAC (cLINAC) for research activities from Elekta was used as a source of e^- beam. In cLINAC, a 50 keV potential difference was applied to an electron gun. Then, emitted electrons were accelerated by ~ 3 GHz radio-frequency and were collimated by magnets and electrostatic components. γ -rays obtained from ^{60}Co with average energy of 1.25 MeV and 8 MeV energy of e^- -beam obtained from cLINAC were directly sent to the glass samples. The beam on the sample side is very stable and homogenous. The details about the cLINAC can be found at [20]. For each type of radiation, consequent γ -ray and e^- -beams were almost uniform on the sample. The dose rates are kept constant at 200 Gy/min and 7.5 Gy/min for γ -ray and e^- -beams, respectively.

For each radiation type, we applied the following procedures. The glass samples were positioned perpendicular to incoming direction of the radiation beam. All experiments were conducted on at room temperature and in ambient conditions. First, the glass samples were irradiated by radiation source. Then, we measure transmission spectra of irradiated samples in the spectral range of 300-1000 nm by using a fiber coupled spectrometer (CCS200- Thorlabs).

Both total irradiation dose and its time-dependent behavior after the radiation source was turned off were observed through optical transmission measurement. From these results, we also calculated the change in absorption coefficient of the irradiated glass samples. In order to compare observed irradiation induced changes in optical properties, we used Abbe refractometer to measure refractive index of the glass samples before and after the irradiation at a certain irradiation dose.

We also baked the irradiated glass samples between 100-150 °C to see whether there was a recovery of irradiation induced effects in optical properties of glass samples. Therefore, we measured transmission spectra of irradiated samples after they were baked at 100 °C, 125 °C, 150 °C for an hour. Since we are interested in physical properties of irradiation induced effects on the chemical composition of target materials.

3. RESULTS AND DISCUSSION

We started irradiation experiments with ^{60}Co γ -ray source and the glass samples were irradiated for 30 min. then, by using cLINAC 8 MeV energy of e^- beam was used to irradiate the other glass samples for 30 min. Regardless of radiation type, all irradiated samples became brown. In order to observe the effect of the total dose in optical properties of glass samples, we gradually increased the radiation exposure time with 30 min intervals up to 120 min for each radiation type and different glass samples. Fig. 1 shows measured transmission spectra from irradiated samples at different doses. As it can be seen from the Fig. 1 that besides the overall decrease in transmission spectra in all wavelengths, there is a dramatic degradation in the visible region centered at a wavelength of 430 nm for both types of radiation. Moreover, these induced effects are very depend on the applied irradiation dose.

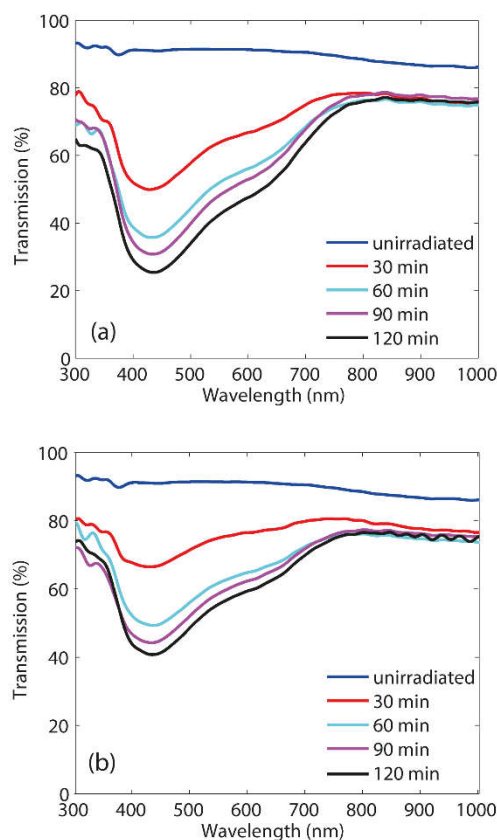


Figure 1 Optical transmission spectra of (a) e^- and (b) γ -ray beams irradiated samples with respect to total dose

We compared the obtained transmission spectra from irradiated samples to see the effect of the radiation type more clearly.

Fig. 2 shows measured transmission spectra of unirradiated and 2 hours irradiated glass samples with γ -ray and e^- beams.

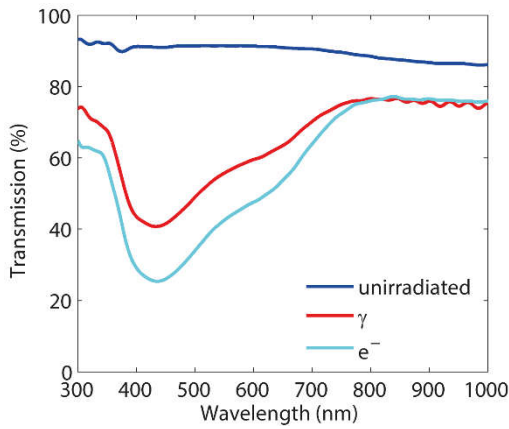


Figure 2 Optical transmission spectra of 2 hours irradiated glass samples with different radiation sources

Results show that absorption band in the VIS is very sensitive to irradiation type and applied dose. The change of refractive index of irradiated samples was also measured in order to relate relative decrease in transmission spectra with refractive index. The variation of the refractive index of the samples was measured at 589.3 nm wavelength (average of sodium D lines) via widely used Abbe refractometer by using proper index matching liquid. The refractive index value of the glass samples was measured as 1.5132 ± 0.0005 prior to irradiation. The variation of the refractive index of the samples were measured as 0.0020 for 2-hour e^- beam irradiated samples.

The absorption coefficient (μ) of glass was defined as follows. T_0 and T_1 are transmission values before and after irradiation in which ω is the thickness of the sample in Eq. 1.

$$\mu = \frac{1}{\omega} \ln \left(\frac{T_0}{T_1} \right) \quad (1)$$

We calculated the absorption spectra for all irradiated samples. μ is found to increase in our spectral range due to the irradiation. In order to quantify the wavelength dependence, Fig. 3 shows calculated values of μ at three different wavelengths and for different radiation types. Our results showed that the absorption was totally depend on the irradiation dose for both γ -ray and e^- -beams irradiation.

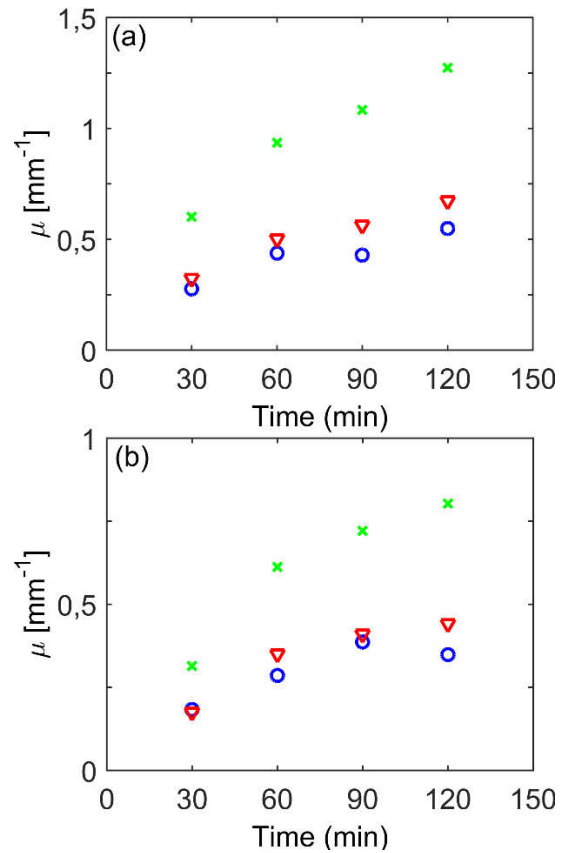
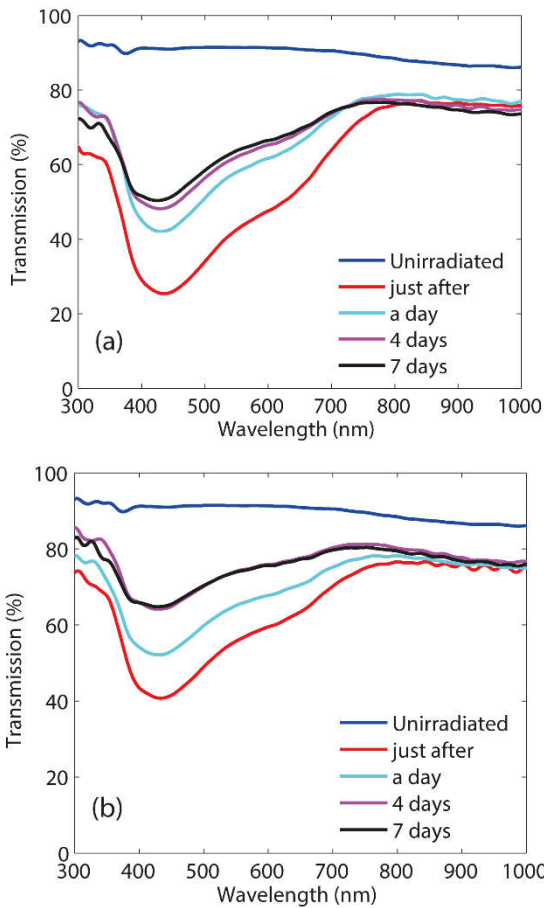


Figure 3 Calculated absorption values for (a) γ -ray and (b) e^- beams irradiation at three wavelengths.

This dependence was very large around 430 nm. Since the irradiation induced refractive index change [21], [22] effects the reflectivity of the glass samples, one should take into account the reflectivity change while calculating the absorption coefficient. However, it was found in [5], this was only effective in the range of 220-275 nm. Our results are in the spectral range of 300-1000 nm. Therefore, we disregard its effect on calculation of μ . We also measured % 0.2 change in the refractive index at 590 nm which is in agreement with [5].

We also analyzed the time dependence of induced effects on the glass samples. Throughout the experiments, irradiated samples were kept under daylight at room temperature. Transmission spectra of irradiated samples were 30 min, a day, 4 days and 7 days after the radiation sources were turned off. Fig. 4 shows obtained results from 2-hours irradiated samples. Since the irradiated samples were kept in ambient conditions, a very small increase in transmission spectra in VIS was acquired for both e^- and γ -ray beams irradiation cases even at room temperature.



Şekil 4 Time-dependent optical transmission measurements on 2 hours (a) e^- and (b) γ -ray beams irradiated glass samples

However, this recovery nearly stops and transmission spectra preserves itself after 4 days. On the other hand, transmission spectra obtained from irradiated samples kept in dark at room temperature did not show prominent increase even after a week. In order to quicken the recovery process we baked the irradiated samples for an hour at 100 °C, 125 °C and 150 °C. Obtained results are presented in Fig. 5.

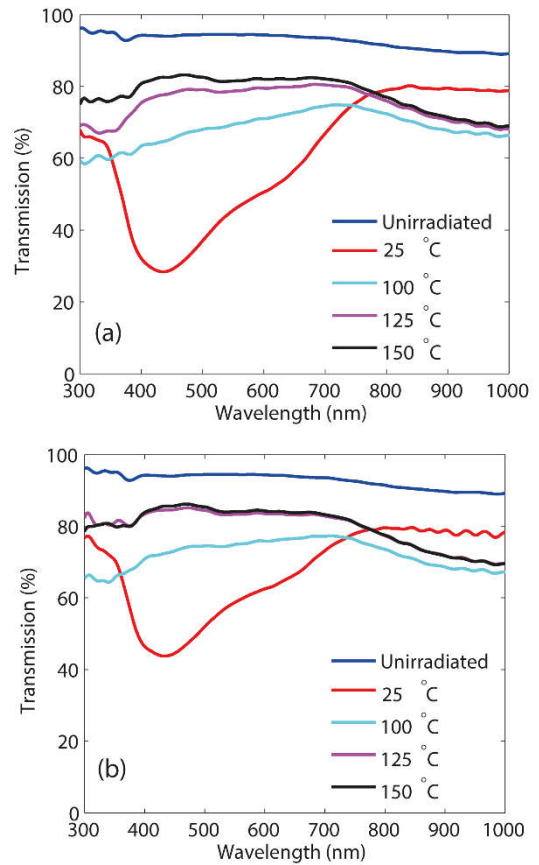


Figure 5 Effects of bleaching on the optical transmission spectra of 2 hours (a) e^- and (b) γ -ray beams irradiated glass samples.

After bleaching, the induced absorption dip around 430 nm was disappeared although the overall increase in absorption was observed. Moreover, the temperatures in our experiments are well below the glass melting point, bleaching allows the rearrangement of electrons in the states. This behavior was also observed by [5] in transmission spectra of γ -ray irradiated borosilicate glass samples.

4. CONCLUSION

Our results showed that regardless of types of irradiation same types of colour centers were produced in soda-lime glass samples. Strong absorption band around 430 nm was obtained with respect to total applied dose. Absorption coefficient of glass samples with respect to total dose and types of irradiation was calculated. These calculations clearly show that one should take into account the optical properties of glass samples exposed to irradiation. We have also conducted on time-dependent experiments immediately after the radiation source was turned off. We also found that irradiation induced effects change in time even at room temperature under daylight. The

transmission of irradiated glass samples approximate to that of unirradiated glass samples after a week. In order to quicken this recovery, we baked the irradiated samples at different temperatures for an hour. We found that this process is much efficient at higher temperatures.

ACKNOWLEDGMENTS

The authors thank NUBA (Akdeniz University Nuclear Research and Application Center) for irradiation facility. We also would like to thank Dr. Timur Sahin for useful discussions.

REFERENCES

- [1] A. Bishay, "Radiation induced color centers in multicomponent glasses," *Journal of Non-Crystalline Solids* vol.3 no.1, pp. 54-114, 1970.
- [2] S. M. J. Akhtar, M. Ashraf, S. H. Khan, "A study of neutron and gamma radiation effects on transmission of various types of glasses, optical coatings, cemented optics and fiber," *Optical Materials*, vol. 29, pp. 1595-1603, 2007.
- [3] F. H. ElBatal, M. A. Marzouk, A. M. Abdelghany, "Uv-visible and infrared absorption spectra of gamma irradiated V₂O₅-doped in sodium phosphate, lead phosphate, zinc phosphate glasses: A comparative study," *Journal of Non-Crystalline Solids*, vol. 357, no. 3, pp. 1027-1036, 2011.
- [4] A. Morono, P. Martin, A. Gusarov, E. R. Hodgson, "Radiation induced absorption and luminescence of selected alternative radiation resistant glasses," *Journal of Nuclear Materials*, vol. 386-388, pp. 1030-1033, 2009.
- [5] J. Du, J. Wu, L. Song, L. Zhao, "Reflectivity and absorption coefficient of a borosilicate glass during Co-60-gamma irradiation calculated from data measured by an integrating sphere," *Radiation Effects and Defects in Solids*, vol. 167, no. 1, pp. 37-48, 2012.
- [6] J. Du, J. Wu, L. Zhao, L. Song, "Color centers of a borosilicate glass induced by 10 MeV proton, 1.85 MeV electron and ⁶⁰Co-γ ray," *Radiation Physics and Chemistry*, vol. 86, pp. 59–63, 2013.
- [7] A. M. Abdelghany, H. A. ElBatal, F. M. EzzElDin, "Influence of CuO content on the structure of lithium fluoroborate glasses: Spectral and gamma irradiation studies," *Spectrochimica Acta Part A-Molecular and Biomolecular Spectroscopy*, vol. 149, pp. 788–792, 2015.
- [8] F. H. ElBatal, M. A. Ouis, A. M. Abdelghany, N. A. Ghoneim, "Structural and Optical Correlation of Gamma-Irradiated 3d Transition Metals-Doped Lithium Disilicate Glasses," *Silicon*, vol. 7, no. 4, pp. 409–417, 2015.
- [9] N. Baydogan, A. B. Tugrul, "Borosilicate glass for gamma irradiation fields," *Solid State Sciences*, vol. 14, no. 11-12, pp.1692–1697, 2012.
- [10] C. Bootjomchai, "Comparative studies between theoretical and experimental of elastic properties and irradiation effects of soda lime glasses doped with neodymium oxide," *Radiation Physics and Chemistry*, vol. 110, pp. 96–104, 2015.
- [11] S. Baccaro, A. Cemmi, I. Di Sarcina, F. Menchini, "Gamma Rays Effects on the Optical Properties of Cerium-Doped Glasses," *International Journal of Applied Glass Science*, vol. 6, no. 3, pp. 295–301, 2015.
- [12] R. Kaur, S. Singh, O. P. Pandey, "Influence of CdO and gamma irradiation on the infrared absorption spectra of borosilicate glass," *Journal of Molecular Structure*, vol. 1049, pp. 409–413, 2013.
- [13] T. V. Bocharova, D. S. Sysoev, V. A. Aseev, N. O. Tagil'tseva, "Radiation-induced color centers in phosphogermanate glass-like materials," *Glass Physics and Chemistry*, vol. 41, no. 4, pp. 378–384, 2015.
- [14] M. A. Marzouk, Y. M. Hamdy, H. A. ElBatal, F. M. E. ElDin, "Photoluminescence and spectroscopic dependence of fluorophosphate glasses on samarium ions concentration and the induced defects by gamma irradiation", *Journal of Luminescence*, vol. 166, pp. 295–303, 2015.

- [15] P. Yasaka, N. Pattanaboonmee, H. J. Kim, P. Limkitjaroenporn, J. Kaewkhao, "Gamma radiation shielding and optical properties measurements of zinc bismuth borate glasses," *Annals Of Nuclear Energy*, vol. 68, pp. 4-9, 2014.
- [16] C. Bootjomchai, J. Laopaiboon, C. Yenchai, R. Laopaiboon, "Gamma-ray shielding and structural properties of barium-bismuth-borosilicate glasses," *Radiation Physics and Chemistry*, vol. 81, no. 7, pp.785-790, 2012.
- [17] A. Saeed, R. M. El Shazly, Y. H. Elbashar, A. M. Abou El-azm, M. M. El-Okar, M. N. H. Comsan, A. M. Osman, A. M. Abdalmonem, A. R. El-Sersy, "Gamma ray attenuation in a developed borate glassy system," *Radiation Physics and Chemistry*, vol. 102, pp. 167-170, 2014.
- [18] P. Dandamudi, M. N. Kozicki, H. J. Barnaby, Y. Gonzalez-Velo, M. Mitkova, K. E. Holbert, M. Ailavajhala, W. Yu, "Sensors based on radiation-induced diffusion of silver in germanium selenide glasses," *IEEE Transactions on Nuclear Science*, vol. 60, no. 6, pp. 4257-4264, 2013.
- [19] I. Kabacelik, H. Kutaruk, S. Yaltkaya, R. Sahin, "Gamma irradiation induced effects on the TCO thin films," *Radiation Physics and Chemistry*, vol. 134, pp. 89-92, 2017.
- [20] I. Boztosun, H. Dapo, M. Karakoç, S.F. Özmen, Y. Çeçen, A. Çoban, T. Caner, E. Bayram, T.R. Saito, T. Akdoğan, V. Bozkurt, Y. Küçük, D. Kaya, M. N. Harakeh, "Photonuclear reactions with zinc: A case for clinical linacs," *The European Physical Journal Plus*, vol. 130, no. 9, pp. 185, 2015.
- [21] F. M. Ezz-Eldin, I. Kashif, H. A. El-Batal, "Some physical properties of gamma irradiated alkali-silicate glasses," *Radiation Physics and Chemistry*, vol. 44, no. (1-2), pp. 39-43, 1994.
- [22] A. Gusarov, D. Doyle, A. Hermanne, F. Berghmans, M. Fruit, G. Ulbrich, M. Blondel, "Refractive-index changes caused by proton radiation in silicate optical glasses," *Applied Optics*, vol. 41, no. 4, pp. 678-684, 2002.

	SAKARYA ÜNİVERSİTESİ FEN BİLİMLERİ ENSTİTÜSÜ DERGİSİ <i>SAKARYA UNIVERSITY JOURNAL OF SCIENCE</i>		
	e-ISSN: 2147-835X Dergi sayfası: http://dergipark.gov.tr/saufenbilder		
	<u>Geliş/Received</u> Sep 19, 2017 <u>Kabul/Accepted</u> Nov 28, 2017	<u>Doi</u> 10.16984/saufenbilder.338899	

Some New Equalities On The Intuitionistic Fuzzy Modal Operators

Mehmet Çitil^{*1}, Feride Tuğrul²

ABSTRACT

In this study, properties of the two modal operator (\Box , \Diamond) defined on intuitionistic fuzzy sets were investigated. Afterwards, some intuitionistic fuzzy operations (\rightarrow , $@$, \cup , \cap , $\$, \#, *$) were researched with modal operators (\Box , \Diamond). New equalities were obtained and proved.

Keywords: intuitionistic fuzzy sets, modal operators, operations.

* Sorumlu Yazar / Corresponding Author

¹ Kahramanmaraş Sütçü İmam Üniversitesi, Fen Edebiyat Fakültesi, Matematik Bölümü, Kahramanmaraş, citil@ksu.edu.tr

² Kahramanmaraş Sütçü İmam Üniversitesi, Fen Edebiyat Fakültesi, Matematik Bölümü, Kahramanmaraş, feridetugrul@gmail.com

1. INTRODUCTION

The notion of fuzzy logic was firstly defined by L.A.Zadeh in 1965. Then, intuitionistic fuzzy sets (shortly ifs) were defined by K.Atanassov in 1986. Intuitionistic fuzzy sets form a generalization of the notion of fuzzy set. In intuitionistic fuzzy set theory, sum of the membership function and the non-membership function is a value between 0 and 1. The intuitionistic fuzzy set theory is useful in various application areas, such as algebraic structures, robotics, control systems, agriculture areas, computer, irrigation, economy and various engineering fields. The knowledge and semantic representation of intuitionistic fuzzy set become more meaningful, resourceful and applicable since it include the membership degree, the non-membership degree and the hesitation margin.

The notion of Intuitionistic Fuzzy Operator (IFO) was defined firstly by K.Atanassov[3]. Several operators are defined in Intuitionistic Fuzzy Sets Theory.They are classified in three groups: modal, topological and level operators.K.Atanassov defined some first type modal operator (\boxplus, \boxtimes) on intuitionistic fuzzy sets [3]. \boxplus_α and \boxtimes_α operators were defined by K.Dencheva in 2004[5]. $\boxplus_{\alpha\beta}$ and $\boxtimes_{\alpha\beta}$ operators were defined by K.Atanassov in 2006[6]. $\boxplus_{\alpha\beta\gamma}$ and $\boxtimes_{\alpha\beta\gamma}$ operators which are expansion of $\boxplus_{\alpha\beta}$ and $\boxtimes_{\alpha\beta}$ operators respectively were defined K.Atanassov[7]. G.Cuvalcioglu was defined $E_{\alpha\beta}$ operator which is expansion of \boxplus_α and \boxtimes_α operators [8]. K.Atanassov produced that it created a diagram of first type modal operators in 2008. K.Atanassov defined $\square_{\alpha,\beta,\gamma,\delta,\varepsilon,\tau}$ operator in 2009 and he produced that this operator is most general form of operators in the diagram. $Z_{\alpha,\beta}^{\omega,\theta}$ operator was defined by G.Cuvalcioglu in 2010 [9]. This operator is expansion of $E_{\alpha\beta}$, $\boxplus_{\alpha\beta}$ and $\boxtimes_{\alpha\beta}$ operators. Thisoperator settled in the diagram and expanded on the diagram [9]. G.Cuvalcioglu defined $Z_{\alpha,\beta}^{\omega,\theta}$ operator which is expansion of $Z_{\alpha,\beta}^\omega$, $\boxplus_{\alpha\beta}$ and $\boxtimes_{\alpha\beta}$ operators in 2012 [10]. So, the diagram took its final state when this operator was defined. Some properties of first type modal operators were researched by many researchers[7][11][12].

Modal operators (\square, \diamond) defined over the set of all IFS's transform every IFS into a FS. They are similar to the operators 'necessity' and 'possibility' defined in some modal logics. The notion of modal operator (\square, \diamond) introduced on intuitionistic fuzzy sets were defined by K.Atanassov in 1986 [2].

The aim of this paper is to obtain new equalities by means of modal operators (\square, \diamond) and some intuitionistic fuzzy operations. These equalities make it easy application areas of operators. Shorter equalities have obtained using features of some intuitionistic fuzzy operations with modal operators. In this paper; for every IFS M, N in X , we get $M = \{\langle \mu_M(x), \nu_M(x) \rangle\}$ instead of $M = \{\langle x, \mu_M(x), \nu_M(x) \rangle | x \in X\}$ and $N = \{\langle \mu_N(x), \nu_N(x) \rangle\}$ instead of $N = \{\langle x, \mu_N(x), \nu_N(x) \rangle | x \in X\}$ for simplicity in proofs. Some basic definitions that we build on our work are given as follow.

2. PRELIMINARIES

Definition 1 [1] Let X be a nonempty set, a fuzzy set A drawn from X is defined as $A = \{\langle x, \mu_A(x) \rangle | x \in X\}$, where $\mu_A(x) : X \rightarrow [0,1]$ is the membership function of the fuzzy set A .

Definition 2 [2],[3] Let X be a nonempty set, an intuitionistic fuzzy set A in X is an object having the form

$$A = \{\langle x, \mu_A(x), \nu_A(x) \rangle | x \in X\},$$

where the function

$$\mu_A(x), \nu_A(x) : X \rightarrow [0,1]$$

define respectively, the degree of membership and degree of nonmembership of the element $x \in X$, to the set A , which is a subset of X , and for every element $x \in X$,

$$0 \leq \mu_A(x) + \nu_A(x) \leq 1.$$

Furthermore, we have

$$\pi_A(x) = 1 - \mu_A(x) - \nu_A(x)$$

called the intuitionistic fuzzy set index or hesitation on margin of x in A . $\pi_A(x)$ is degree of indeterminacy of $x \in X$ to the IFS A and $\pi_A(x) \in [0,1]$ i.e., $\pi_A : X \rightarrow [0,1]$

for every $x \in X$. $\pi_A(x)$ expresses the lack of knowledge of whether x belongs to IFS A or not.

Definition 3 [2],[3] Let X be a nonempty set for every IFS M, N in X . For every two IFS's M and N the following operations and relations are valid.

$$M = \{ \langle x, \mu_M(x), \nu_M(x) \rangle \mid x \in X \}$$

$$M^c = \{ \langle x, \nu_M(x), \mu_M(x) \rangle \mid x \in X \}$$

$$M @ N = \{ \langle x, \frac{\mu_M(x) + \mu_N(x)}{2}, \frac{\nu_M(x) + \nu_N(x)}{2} \rangle \mid x \in X \}$$

$$M \rightarrow N = \{ \langle x, \max(\nu_M(x), \mu_N(x)), \min(\mu_M(x), \nu_N(x)) \rangle \mid x \in X \}$$

$$M \cap N = \{ \langle x, \min(\mu_M(x), \mu_N(x)), \max(\nu_M(x), \nu_N(x)) \rangle \mid x \in X \}$$

$$M \cup N = \{ \langle x, \max(\mu_M(x), \mu_N(x)), \min(\nu_M(x), \nu_N(x)) \rangle \mid x \in X \}$$

$$M \oplus N = \{ \langle x, \mu_M(x) + \mu_N(x) - \mu_M(x) \cdot \mu_N(x), \nu_M(x) \cdot \nu_N(x) \rangle \mid x \in X \}$$

$$M \otimes N = \{ \langle x, \mu_M(x) \cdot \mu_N(x), \nu_M(x) + \nu_N(x) - \nu_M(x) \cdot \nu_N(x) \rangle \mid x \in X \}$$

$$M \$ N = \{ \langle x, \sqrt{\mu_M(x) \cdot \mu_N(x)}, \sqrt{\nu_M(x) \cdot \nu_N(x)} \rangle \mid x \in X \}$$

$$M \# N = \{ \langle x, \frac{2\mu_M(x) \cdot \mu_N(x)}{\mu_M(x) + \mu_N(x)}, \frac{2\nu_M(x) \cdot \nu_N(x)}{\nu_M(x) + \nu_N(x)} \rangle \mid x \in X \}$$

$$M * N = \{ \langle x, \frac{\mu_M(x) + \mu_N(x)}{2(\mu_M(x)\mu_N(x) + 1)}, \frac{\nu_M(x) + \nu_N(x)}{2(\nu_M(x)\nu_N(x) + 1)} \rangle \mid x \in X \}$$

Definition 4 [2],[3] Let X be a nonempty set, for every IFS M, N in X . \square and \diamond modal operators are defined as;

$$\square M = \{ \langle x, \mu_M(x) \rangle \mid x \in X \} = \{ \langle x, \mu_M(x), 1 - \mu_M(x) \rangle \mid x \in X \}$$

$$\diamond M = \{ \langle x, 1 - \nu_M(x) \rangle \mid x \in X \} = \{ \langle x, 1 - \nu_M(x), \nu_M(x) \rangle \mid x \in X \} [1]$$

$$(\square M)^c = \{ \langle x, 1 - \mu_M(x), \mu_M(x) \rangle \mid x \in X \}$$

$$(\diamond M)^c = \{ \langle x, \nu_M(x), 1 - \nu_M(x) \rangle \mid x \in X \}$$

Theorem 1 [2],[3] Let X be a nonempty set, for every IFS M, N in X . The following equalities are ensured.

- $\square \square M = \square M$
- $\square \diamond M = \diamond M$
- $\diamond \square M = \square M$
- $\diamond \diamond M = \diamond M$

Theorem 2 [2],[3] Let X be a nonempty set, for every IFS M, N in X . The following equality could be provided by means of definition of @ operation.

$$\square M @ \square N = \square (M @ N)$$

Theorem 3 [2],[3] Let X be a nonempty set, for every IFS M, N in X ;

$$\diamond M @ \diamond N = \diamond (M @ N)$$

3. MAIN RESULTS

In this section, new equalities were obtained and proved by means of some intuitionistic fuzzy operations (\rightarrow , $@$, \cup , \cap , $\$, \#, *$) and modal operators (\square , \diamond).

Theorem 4 [4] Let X be a nonempty set, for every IFS M, N in X ;

$$(\square M \oplus \square N) @ (\square M \otimes \square N) = \square M @ \square N$$

Theorem 5 [4] Let X be a nonempty set, for every IFS M, N in X ;

$$(\diamond M \oplus \diamond N) @ (\diamond M \otimes \diamond N) = \diamond M @ \diamond N$$

Theorem 6 [4] Let X be a nonempty set, for every IFS M, N in X ;

$$[(\square M @ \square N) \$ (\square M \# \square N)] = \square M \$ \square N$$

Theorem 7 [4] Let X be a nonempty set, for every IFS M, N in X ;

$$[(\diamond M @ \diamond N) \$ (\diamond M \# \diamond N)] = \diamond M \$ \diamond N$$

Theorem 8 [4] Let X be a nonempty set, for every IFS M, N in X ;

$$\square [(\diamond M @ \diamond N)^c] = [\diamond (M @ N)]^c$$

Theorem 9 [4] Let X be a nonempty set, for every IFS M, N in X ;

$$[(\square M \oplus \diamond N)^c @ ((\square M)^c \otimes \diamond N)] \cup (\square M)^c = (\square M)^c$$

Theorem 10 Let X be a nonempty set, for every IFS M, N in X . The following equality is holds for;

$$[(\diamond M \oplus \square N) @ ((\diamond M)^c \otimes \square N)] \cup (\diamond M) = (\diamond M)$$

Proof.

$$\begin{aligned} (\diamond M \oplus \square N) &= \{(1 - v_M(x) + \mu_N(x) - ((1 - v_M(x)\mu_N(x), v_M(x)(1 - \mu_N(x))))\} \\ &= \{(1 - v_M(x) + \mu_N(x) - \mu_N(x) + v_M(x)\mu_N(x), v_M(x) - v_M(x)\mu_N(x))\} \\ &= \{(1 - v_M(x) + v_M(x)\mu_N(x), v_M(x) - v_M(x)\mu_N(x))\} | x \in X\} \\ ((\diamond M)^c \otimes \square N) &= \{(v_M(x)\mu_N(x), 1 - \mu_N(x) + 1 - v_M(x) - ((1 - v_M(x))(1 - \mu_N(x))))\} \\ &= \{(v_M(x)\mu_N(x), 1 - \mu_N(x) + 1 - v_M(x) - 1 + v_M(x) + \mu_N(x) - v_M(x)\mu_N(x))\} \\ &= \{(v_M(x)\mu_N(x), 1 - v_M(x)\mu_N(x))\} \end{aligned}$$

$$\begin{aligned} [(\diamond M \oplus \square N) @ ((\diamond M)^c \otimes \square N)] &= \left\{ \left\langle \frac{1-v_M(x)+2v_M(x)\mu_N(x)}{2}, \frac{1+v_M(x)-2v_M(x)\mu_N(x)}{2} \right\rangle \right\} \\ [(\diamond M \oplus \square N) @ ((\diamond M)^c \otimes \square N)] \cup (\diamond M) &= \left\{ \left\langle \max\left(\frac{1-v_M(x)+2v_M(x)\mu_N(x)}{2}, 1 - v_M(x)\right), \right. \right. \\ &\quad \left. \min\left(\frac{1+v_M(x)-2v_M(x)\mu_N(x)}{2}, v_M(x)\right) \right\rangle \right\} \\ &= \{(1 - v_M(x), v_M(x))\} \\ &= \diamond M \end{aligned}$$

$$[(\diamond M \oplus \square N) @ ((\diamond M)^c \otimes \square N)] \cup (\diamond M) = (\diamond M)$$

Theorem 11 Let X be a nonempty set, for every IFS M, N in X . We get the following equality;

$$[(\diamond M \oplus \square N)^c @ ((\diamond M)^c \otimes \square N)] \cup (\diamond M)^c = (\diamond M)^c$$

Proof.

$$\begin{aligned} (\diamond M \oplus \square N) &= \{(1 - v_M(x) + \mu_N(x) - ((1 - v_M(x)\mu_N(x), v_M(x)(1 - \mu_N(x))))\} \\ &= \{(1 - v_M(x) + \mu_N(x) - \mu_N(x) + v_M(x)\mu_N(x), v_M(x) - v_M(x)\mu_N(x))\} \\ &= \{(1 - v_M(x) + v_M(x)\mu_N(x), v_M(x) - v_M(x)\mu_N(x))\} \\ (\diamond M \oplus \square N)^c &= \{(v_M(x) - v_M(x)\mu_N(x), 1 - v_M(x) + v_M(x)\mu_N(x))\} \end{aligned}$$

$$\begin{aligned} ((\diamond M)^c \otimes \square N) &= \{(v_M(x)\mu_N(x), \\ &\quad 1 - \mu_N(x) + 1 - v_M(x) - ((1 - v_M(x))(1 - \mu_N(x))))\} \\ &= \{(v_M(x)\mu_N(x), 1 - \mu_N(x) + 1 - v_M(x) - 1 + v_M(x) + \mu_N(x) - v_M(x)\mu_N(x))\} \\ &= \{(v_M(x)\mu_N(x), 1 - v_M(x)\mu_N(x))\} \end{aligned}$$

$$\begin{aligned} [(\diamond M \oplus \square N)^c @ ((\diamond M)^c \otimes \square N)] &= \left\{ \left\langle \frac{v_M(x)}{2}, 1 - \frac{v_M(x)}{2} \right\rangle \right\} \\ [(\diamond M \oplus \square N)^c @ ((\diamond M)^c \otimes \square N)] \cup (\diamond M)^c &= \left\{ \left\langle \max\left(v_M(x), \frac{v_M(x)}{2}\right), \min\left(1 - v_M(x), 1 - \frac{v_M(x)}{2}\right) \right\rangle \right\} \\ &= \{(v_M(x), 1 - v_M(x))\} \\ &= (\diamond M)^c \end{aligned}$$

$$[(\diamond M \oplus \square N)^c @ ((\diamond M)^c \otimes \square N)] \cup (\diamond M)^c = (\diamond M)^c$$

Theorem 12 Let X be a nonempty set, for every IFS M, N in X ;

$$[(\square M \otimes \diamond N)^c @ ((\square M)^c \oplus \diamond N)] \cap (\square M)^c = (\square M)^c$$

The above equality is obtained.

Proof.

$$\begin{aligned} (\square M \otimes \diamond N) &= \{(\mu_M(x)(1 - v_N(x)), 1 - \mu_M(x) + v_N(x) - (1 - \mu_M(x))v_N(x))\} \\ &= \{(\mu_M(x) - \mu_M(x)v_N(x), 1 - \mu_M(x) + v_N(x) - v_N(x) + \mu_M(x)v_N(x))\} \\ (\square M \otimes \diamond N)^c &= \{(1 - \mu_M(x) + \mu_M(x)v_N(x), \mu_M(x) - \mu_M(x)v_N(x))\} \\ ((\square M)^c \oplus \diamond N) &= \{(1 - \mu_M(x) + 1 - v_N(x) - (1 - \mu_M(x))(1 - v_N(x)), \mu_M(x)v_N(x))\} \\ &= \{(1 - \mu_M(x) + 1 - v_N(x) - 1 + \mu_M(x) + v_N(x) - \mu_M(x)v_N(x), \mu_M(x)v_N(x))\} \\ &= \{(1 - \mu_M(x)v_N(x), \mu_M(x)v_N(x))\} \end{aligned}$$

$$\begin{aligned} [(\square M \otimes \diamond N)^c @ ((\square M)^c \oplus \diamond N)] &= \left\{ \left\langle \frac{2-\mu_M(x)}{2}, \mu_M(x) \right\rangle \right\} \\ [(\square M \otimes \diamond N)^c @ ((\square M)^c \oplus \diamond N)] \cap (\square M)^c &= \left\{ \left\langle \min\left(\frac{2-\mu_M(x)}{2}, 1 - \mu_M(x)\right), \max(\mu_M(x), \mu_M(x)) \right\rangle \right\} \\ &= \{(1 - \mu_M(x), \mu_M(x))\} \\ &= (\square M)^c \\ [(\square M \otimes \diamond N)^c @ ((\square M)^c \oplus \diamond N)] \cap (\square M)^c &= (\square M)^c \end{aligned}$$

Theorem 13 Let X be a nonempty set, for every IFS M in X . We get;

$$(\square M \oplus \diamond M) @ (\square M \otimes \diamond M) = \square M @ \diamond M$$

Proof.

$$\begin{aligned} (\square M \oplus \diamond M) &= \{(\mu_M(x) + 1 - v_M(x) - (\mu_M(x)(1 - v_M(x))), (1 - \mu_M(x))v_M(x))\} \\ &= \{(\mu_M(x) + 1 - v_M(x) - \mu_M(x) + \mu_M(x)v_M(x), v_M(x) - \mu_M(x)v_M(x))\} \\ &= \{(1 - v_M(x) + \mu_M(x)v_M(x), v_M(x) - \mu_M(x)v_M(x))\} \end{aligned}$$

$$\begin{aligned} (\square M \otimes \diamond M) &= \{(\mu_M(x)(1 - v_M(x)), 1 - \mu_M(x) + v_M(x) - (v_M(x)(1 - \mu_M(x))))\} \\ &= \{(\mu_M(x) - \mu_M(x)v_M(x), 1 - \mu_M(x) + v_M(x) - v_M(x) + \mu_M(x)v_M(x))\} \\ &= \{(\mu_M(x) - \mu_M(x)v_M(x), 1 - \mu_M(x) + \mu_M(x)v_M(x))\} \end{aligned}$$

$$\begin{aligned} (\square M \oplus \diamond M) @ (\square M \otimes \diamond M) &= \left\{ \left\langle \frac{1 - v_M(x) + \mu_M(x)}{2}, \frac{1 + v_M(x) - \mu_M(x)}{2} \right\rangle \right\} \\ &= \square M @ \diamond M \end{aligned}$$

$$(\square M \oplus \diamond M) @ (\square M \otimes \diamond M) = \square M @ \diamond M$$

Theorem 14 Let X be a nonempty set, for every IFS M, N in X . We obtain the following equality;

$$(\square M \oplus \diamond N) @ (\square M \otimes \diamond N) = \square M @ \diamond N$$

Proof.

$$(\Box M \cup \Diamond N) = \{\{\max(\mu_M(x), 1 - v_N(x)), \min(1 - \mu_M(x), v_N(x))\}\}$$

$$(\Box M \cap \Diamond N) = \{\{\min(\mu_M(x), 1 - v_N(x)), \max(1 - \mu_M(x), v_N(x))\}\}$$

Proof.

The proof is similar to proof of the Theorem 13.

$$\begin{aligned} (\Box M \oplus \Diamond N) &= \{\{\mu_M(x) + 1 - v_N(x) - (\mu_M(x)(1 - v_N(x))), (1 - \mu_M(x))v_N(x)\}\} \\ &= \{\{\mu_M(x) + 1 - v_N(x) - \mu_M(x) + \mu_M(x)v_N(x), v_N(x) - \mu_M(x)v_N(x)\}\} \\ &= \{\{1 - v_N(x) + \mu_M(x)v_N(x), v_N(x) - \mu_M(x)v_N(x)\}\} \\ (\Box M \otimes \Diamond N) &= \{\{\mu_M(x)(1 - v_N(x)), 1 - \mu_M(x) + v_N(x) - (v_N(x)(1 - \mu_M(x)))\}\} \\ &= \{\{\mu_M(x) - \mu_M(x)v_N(x), 1 - \mu_M(x) + v_N(x) - v_N(x) + \mu_M(x)v_N(x)\}\} \\ &= \{\{\mu_M(x) - \mu_M(x)v_N(x), 1 - \mu_M(x) + \mu_M(x)v_N(x)\}\} \end{aligned}$$

$$\begin{aligned} (\Box M \oplus \Diamond N) @ (\Box M \otimes \Diamond N) &= \left\{ \left\{ \frac{1 - v_N(x) + \mu_M(x)}{2}, \frac{1 + v_N(x) - \mu_M(x)}{2} \right\} \right\} \\ &= \Box M @ \Diamond N \end{aligned}$$

$$(\Box M \oplus \Diamond N) @ (\Box M \otimes \Diamond N) = \Box M @ \Diamond N$$

Theorem 15 Let X be a nonempty set, for every IFS M in X ;

$$(\Box M \cup \Diamond M) @ (\Box M \cap \Diamond M) = \Box M @ \Diamond M$$

The above equality is holds for.

Proof.

$$(\Box M \cup \Diamond M) = \{\{\max(\mu_M(x), 1 - v_M(x)), \min(1 - \mu_M(x), v_M(x))\}\}$$

$$(\Box M \cap \Diamond M) = \{\{\min(\mu_M(x), 1 - v_M(x)), \max(1 - \mu_M(x), v_M(x))\}\}$$

$$\begin{aligned} (\Box M \cup \Diamond M) @ (\Box M \cap \Diamond M) &= \left\{ \left\{ \frac{\max(\mu_M(x), 1 - v_M(x)) + \min(\mu_M(x), 1 - v_M(x))}{2}, \right. \right. \\ &\quad \left. \left. \frac{\min(1 - \mu_M(x), v_M(x)) + \max(1 - \mu_M(x), v_M(x))}{2} \right\} \right\} \\ &= \left\{ \left\{ \frac{\mu_M(x) + 1 - v_M(x)}{2}, \frac{1 - \mu_M(x) + v_M(x)}{2} \right\} \right\} \\ &= \Box M @ \Diamond M \end{aligned}$$

$$(\Box M \cup \Diamond M) @ (\Box M \cap \Diamond M) = \Box M @ \Diamond M$$

Theorem 16 Let X be a nonempty set, for every IFS M, N in X ;

$$(\Box M \cup \Diamond N) @ (\Box M \cap \Diamond N) = \Box M @ \Diamond N$$

It is easily seen similar to Theorem 15.

Theorem 17 Let X be a nonempty set, for every IFS M in X . We get the following equality;

$$(\Box M @ \Diamond M) \$ (\Box M \# \Diamond M) = \Box M \$ \Diamond M$$

Proof.

$$(\Box M @ \Diamond M) = \left\{ \left\{ \frac{\mu_M(x) + 1 - v_M(x)}{2}, \frac{1 - \mu_M(x) + v_M(x)}{2} \right\} \right\}$$

$$(\Box M \# \Diamond M) = \left\{ \left\{ \frac{2\mu_M(x)(1 - v_M(x))}{\mu_M(x) + 1 - v_M(x)}, \frac{2(1 - \mu_M(x))v_M(x)}{1 - \mu_M(x) + v_M(x)} \right\} \right\}$$

$$\begin{aligned} (\Box M @ \Diamond M) \$ (\Box M \# \Diamond M) &= \left\{ \left\{ \frac{\mu_M(x) + 1 - v_M(x)}{2} \frac{2\mu_M(x)(1 - v_M(x))}{\mu_M(x) + 1 - v_M(x)}, \right. \right. \\ &\quad \left. \left. \frac{1 - \mu_M(x) + v_M(x)}{2} \frac{2(1 - \mu_M(x))v_M(x)}{1 - \mu_M(x) + v_M(x)} \right\} \right\} \\ &= \left\{ \left\{ \sqrt{\mu_M(x)(1 - v_M(x))}, \sqrt{(1 - \mu_M(x))v_M(x)} \right\} \right\} \\ &= \Box M \$ \Diamond M \end{aligned}$$

$$(\Box M @ \Diamond M) \$ (\Box M \# \Diamond M) = \Box M \$ \Diamond M$$

Theorem 18 Let X be a nonempty set, for every IFS M, N in X ;

$$(\Box M @ \Diamond N) \$ (\Box M \# \Diamond N) = \Box M \$ \Diamond N$$

It is easily seen similar to Theorem 17.

Proof.

$$(\Box M @ \Diamond N) = \left\{ \left\{ \frac{\mu_M(x) + 1 - v_N(x)}{2}, \frac{1 - \mu_M(x) + v_N(x)}{2} \right\} \right\}$$

$$(\Box M \# \Diamond N) = \left\{ \left\{ \frac{2\mu_M(x)(1 - v_N(x))}{\mu_M(x) + 1 - v_N(x)}, \frac{2(1 - \mu_M(x))v_N(x)}{1 - \mu_M(x) + v_N(x)} \right\} \right\}$$

$$\begin{aligned}(\Box M @ \Diamond N) \$ (\Box M \# \Diamond N) &= \left\{ \left\langle \frac{\mu_M(x) + 1 - v_N(x)}{2}, \frac{2\mu_M(x)(1 - v_N(x))}{\mu_M(x) + 1 - v_N(x)} \right\rangle, \right. \\ &\quad \left. \left\langle \frac{1 - \mu_M(x) + v_N(x)}{2}, \frac{2(1 - \mu_M(x))v_N(x)}{1 - \mu_M(x) + v_N(x)} \right\rangle \right\} \\ &= \left\{ \left\langle \sqrt{\mu_M(x)(1 - v_N(x))}, \sqrt{(1 - \mu_M(x))v_N(x)} \right\rangle \right\} \\ &= \Box M \$ \Diamond N \\ (\Box M @ \Diamond N) \$ (\Box M \# \Diamond N) &= \Box M \$ \Diamond N\end{aligned}$$

Theorem 19 Let X be a nonempty set, for every IFS M, N in X . The equality is obtained.

$$(\Box M \cup \Box N) * (\Box M \cap \Box N) = \Box M * \Box N$$

Proof.

$$\begin{aligned}(\Box M \cup \Box N) &= \left\{ \left\langle \max(\mu_M(x), \mu_N(x)), \min(1 - \mu_M(x), 1 - \mu_N(x)) \right\rangle \right\} \\ (\Box M \cap \Box N) &= \left\{ \left\langle \min(\mu_M(x), \mu_N(x)), \max(1 - \mu_M(x), 1 - \mu_N(x)) \right\rangle \right\}\end{aligned}$$

$$\begin{aligned}(\Box M \cup \Box N) * (\Box M \cap \Box N) &= \left\{ \left\langle \frac{\max(\mu_M(x), \mu_N(x)) + \min(\mu_M(x), \mu_N(x))}{2(\mu_M(x)\mu_N(x) + 1)}, \right. \right. \\ &\quad \left. \left. \frac{\min(1 - \mu_M(x), 1 - \mu_N(x)) + \max(1 - \mu_M(x), 1 - \mu_N(x))}{2((1 - \mu_M(x))(1 - \mu_N(x)) + 1)} \right\rangle \right\} \\ &= \left\{ \left\langle \frac{\mu_M(x) + \mu_N(x)}{2(\mu_M(x)\mu_N(x) + 1)}, \frac{1 - \mu_M(x) + 1 - \mu_N(x)}{2((1 - \mu_M(x))(1 - \mu_N(x)) + 1)} \right\rangle \right\} \\ &= \Box M * \Box N \\ (\Box M \cup \Box N) * (\Box M \cap \Box N) &= \Box M * \Box N\end{aligned}$$

Theorem 20 Let X be a nonempty set, for every IFS M, N in X . We get the following equalities;

$$\begin{aligned}(\Box M \cup \Box N) * (\Box M \cap \Box N) &= \Box M * \Box N \\ (\Box M * \Box N) @ (\Box M * \Box N) &= \Box M * \Box N \\ (\Box M * \Box N) \$ (\Box M * \Box N) &= \Box M * \Box N\end{aligned}$$

Conclusion 1

This conclusion is easy to see from Theorem 20.

$$\begin{aligned}(\Box M \cup \Box N) * (\Box M \cap \Box N) &= (\Box M * \Box N) @ (\Box M * \Box N) \\ &= (\Box M * \Box N) \$ (\Box M * \Box N) \\ &= \Box M * \Box N\end{aligned}$$

Theorem 21 Let X be a nonempty set, for every IFS M, N in X . We obtain;

$$(\Diamond M \cup \Diamond N) * (\Diamond M \cap \Diamond N) = \Diamond M * \Diamond N$$

Proof.

$$\begin{aligned}(\Diamond M \cup \Diamond N) &= \left\{ \left\langle \max(1 - v_M(x), 1 - v_N(x)), \min(v_M(x), v_N(x)) \right\rangle \right\} \\ (\Diamond M \cap \Diamond N) &= \left\{ \left\langle \min(1 - v_M(x), 1 - v_N(x)), \max(v_M(x), v_N(x)) \right\rangle \right\}\end{aligned}$$

$$\begin{aligned}(\Diamond M \cup \Diamond N) * (\Diamond M \cap \Diamond N) &= \left\{ \left\langle \frac{\max(1 - v_M(x), 1 - v_N(x)) + \min(1 - v_M(x), 1 - v_N(x))}{2((1 - v_M(x))(1 - v_N(x)) + 1)}, \right. \right. \\ &\quad \left. \left. \frac{\min(v_M(x), v_N(x))}{2(v_M(x)v_N(x) + 1)} \right\rangle \right\} \\ &= \left\{ \left\langle \frac{1 - v_M(x) + 1 - v_N(x)}{2((1 - v_M(x))(1 - v_N(x)) + 1)}, \frac{v_M(x) + v_N(x)}{2(v_M(x)v_N(x) + 1)} \right\rangle \right\} \\ &= \Diamond M * \Diamond N \\ (\Diamond M \cup \Diamond N) * (\Diamond M \cap \Diamond N) &= \Diamond M * \Diamond N\end{aligned}$$

Theorem 22 Let X be a nonempty set, for every IFS M, N in X . The following equalities are hold for.

$$\begin{aligned}(\Diamond M \cup \Diamond N) * (\Diamond M \cap \Diamond N) &= \Diamond M * \Diamond N \\ (\Diamond M * \Diamond N) \$ (\Diamond M * \Diamond N) &= \Diamond M * \Diamond N \\ (\Diamond M * \Diamond N) @ (\Diamond M * \Diamond N) &= \Diamond M * \Diamond N\end{aligned}$$

Conclusion 2

This conclusion is easy to see from Theorem 22.

$$\begin{aligned}(\Diamond M \cup \Diamond N) * (\Diamond M \cap \Diamond N) &= (\Diamond M * \Diamond N) \$ (\Diamond M * \Diamond N) \\ &= (\Diamond M * \Diamond N) @ (\Diamond M * \Diamond N) \\ &= \Diamond M * \Diamond N\end{aligned}$$

Theorem 23 Let X be a nonempty set, for every IFS M, N in X . We get;

$$[(\Diamond M \$ \Diamond N) \cup (\Diamond M \$ \Diamond N)^c] @ [(\Diamond M \$ \Diamond N) \cap (\Diamond M \$ \Diamond N)^c] = (\Diamond M \$ \Diamond N) @ (\Diamond M \$ \Diamond N)^c$$

Proof.

$$\begin{aligned}(\Diamond M \$ \Diamond N) &= \left\{ \left\langle \sqrt{(1 - v_M(x))(1 - v_N(x))}, \sqrt{v_M(x)v_N(x)} \right\rangle \right\} \\ (\Diamond M \$ \Diamond N)^c &= \left\{ \left\langle \sqrt{v_M(x)v_N(x)}, \sqrt{(1 - v_M(x))(1 - v_N(x))} \right\rangle \right\}\end{aligned}$$

$$\begin{aligned}[(\Diamond M \$ \Diamond N) \cup (\Diamond M \$ \Diamond N)^c] &= \left\{ \left\langle \max(\sqrt{(1 - v_M(x))(1 - v_N(x))}, \sqrt{v_M(x)v_N(x)}), \right. \right. \\ &\quad \left. \left. \min(\sqrt{(1 - v_M(x))(1 - v_N(x))}, \sqrt{v_M(x)v_N(x)}) \right\rangle \right\}\end{aligned}$$

$$\begin{aligned}[(\Diamond M \$ \Diamond N) \cap (\Diamond M \$ \Diamond N)^c] &= \left\{ \left\langle \min(\sqrt{(1 - v_M(x))(1 - v_N(x))}, \sqrt{v_M(x)v_N(x)}), \right. \right. \\ &\quad \left. \left. \max(\sqrt{(1 - v_M(x))(1 - v_N(x))}, \sqrt{v_M(x)v_N(x)}) \right\rangle \right\}\end{aligned}$$

$$\begin{aligned} & [(\diamond M \ \$ \ \diamond N) \cup (\diamond M \ \$ \ \diamond N)^c] @ [(\diamond M \ \$ \ \diamond N) \cap (\diamond M \ \$ \ \diamond N)^c] \\ &= \left\langle \left\langle \frac{\max(\sqrt{(1-\nu_M(x))(1-\nu_N(x))}, \sqrt{\nu_M(x)\nu_N(x)}) + \min(\sqrt{(1-\nu_M(x))(1-\nu_N(x))}, \sqrt{\nu_M(x)\nu_N(x)})}{2}, \right. \right. \\ & \quad \left. \left. \frac{\max(\sqrt{(1-\nu_M(x))(1-\nu_N(x))}, \sqrt{\nu_M(x)\nu_N(x)}) + \min(\sqrt{(1-\nu_M(x))(1-\nu_N(x))}, \sqrt{\nu_M(x)\nu_N(x)})}{2} \right\rangle \right\rangle \\ &= \left\langle \left\langle \frac{\sqrt{(1-\nu_M(x))(1-\nu_N(x))} + \sqrt{\nu_M(x)\nu_N(x)}}{2}, \frac{\sqrt{(1-\nu_M(x))(1-\nu_N(x))} + \sqrt{\nu_M(x)\nu_N(x)}}{2} \right\rangle \right\rangle \end{aligned}$$

Theorem 24 Let X be a nonempty set, for every IFS M, N in X . The equality is obtained;

$$[(\Box M \ \$ \ \Box N) \cup (\Box M \ \$ \ \Box N)^c] @ [(\Box M \ \$ \ \Box N) \cap (\Box M \ \$ \ \Box N)^c] = (\Box M \ \$ \ \Box N) @ (\Box M \ \$ \ \Box N)^c$$

Proof. The proof is similar to proof of the Theorem 23.

Theorem 25 Let X be a nonempty set, for every IFS M, N in X . We get the following equality;

$$[(\Box M \cup \Box N) \# (\Box M \cap \Box N)] \$ [(\Box M \cup \Box N) @ (\Box M \cap \Box N)] = (\Box M \ \$ \ \Box N)$$

Proof.

$$(\Box M \cup \Box N) = \left\langle \left\langle \max(\mu_M(x), \mu_N(x)), \min(1 - \mu_M(x), 1 - \mu_N(x)) \right\rangle \right\rangle$$

$$(\Box M \cap \Box N) = \left\langle \left\langle \min(\mu_M(x), \mu_N(x)), \max(1 - \mu_M(x), 1 - \mu_N(x)) \right\rangle \right\rangle$$

$$\begin{aligned} [(\Box M \cup \Box N) \# (\Box M \cap \Box N)] &= \left\langle \left\langle \frac{2 \max(\mu_M(x), \mu_N(x)) \min(\mu_M(x), \mu_N(x))}{\max(\mu_M(x), \mu_N(x)) + \min(\mu_M(x), \mu_N(x))}, \right. \right. \\ & \quad \left. \left. \frac{2 \max(1 - \mu_M(x), 1 - \mu_N(x)) \min(1 - \mu_M(x), 1 - \mu_N(x))}{\max(1 - \mu_M(x), 1 - \mu_N(x)) + \min(1 - \mu_M(x), 1 - \mu_N(x))} \right\rangle \right\rangle \\ &= \left\langle \left\langle \frac{2\mu_M(x)\mu_N(x)}{\mu_M(x) + \mu_N(x)}, \frac{2(1 - \mu_M(x))(1 - \mu_N(x))}{(1 - \mu_M(x)) + (1 - \mu_N(x))} \right\rangle \right\rangle \\ [(\Box M \cup \Box N) @ (\Box M \cap \Box N)] &= \left\langle \left\langle \frac{\max(\mu_M(x), \mu_N(x)) + \min(\mu_M(x), \mu_N(x))}{2}, \right. \right. \\ & \quad \left. \left. \frac{\max(1 - \mu_M(x), 1 - \mu_N(x)) + \min(1 - \mu_M(x), 1 - \mu_N(x))}{2} \right\rangle \right\rangle \\ &= \left\langle \left\langle \frac{\mu_M(x) + \mu_N(x)}{2}, \frac{(1 - \mu_M(x)) + (1 - \mu_N(x))}{2} \right\rangle \right\rangle \end{aligned}$$

$$[(\Box M \cup \Box N) \# (\Box M \cap \Box N)] \$ [(\Box M \cup \Box N) @ (\Box M \cap \Box N)] = \left\langle \left\langle \sqrt{\mu_M(x)\mu_N(x)}, \sqrt{(1 - \mu_M(x))(1 - \mu_N(x))} \right\rangle \right\rangle$$

$$= (\Box M \ \$ \ \Box N)$$

$$[(\Box M \cup \Box N) \# (\Box M \cap \Box N)] \$ [(\Box M \cup \Box N) @ (\Box M \cap \Box N)] = (\Box M \ \$ \ \Box N)$$

Theorem 26 Let X be a nonempty set, for every IFS M, N in X . The following equality is holds for;

$$[(\diamond M \cup \diamond N) \# (\diamond M \cap \diamond N)] \$ [(\diamond M \cup \diamond N) @ (\diamond M \cap \diamond N)] = (\diamond M \ \$ \ \diamond N)$$

Proof. The proof is similar to proof of the Theorem 25.

Theorem 27 Let X be a nonempty set, for every IFS M, N in X .

$$[(\Box M \oplus \Box N)^c \rightarrow (\Box M \ \$ \ \Box N)] \rightarrow [(\Box M \ \otimes \ \Box N) \rightarrow (\Box M \ \$ \ \Box N)^c] \cap [(\Box M \ \$ \ \Box N)] = \Box M \ \$ \ \Box N$$

The above equality is obtained.

Proof.

$$(\Box M \oplus \Box N)^c \rightarrow (\Box M \ \$ \ \Box N) = \left\langle \left\langle \mu_M(x) + \mu_N(x) - \mu_M(x)\mu_N(x), \sqrt{1 - \mu_M(x) - \mu_N(x) + \mu_M(x)\mu_N(x)} \right\rangle \right\rangle$$

$$[(\Box M \ \otimes \ \Box N) \rightarrow (\Box M \ \$ \ \Box N)^c]^c = \left\langle \left\langle \sqrt{\mu_M(x)\mu_N(x)}, 1 - \mu_M(x)\mu_N(x) \right\rangle \right\rangle$$

Theorem 28 Let X be a nonempty set, for every IFS M, N in X . We obtain the following equality;

$$[(\diamond M \oplus \diamond N)^c \rightarrow (\diamond M \ \$ \ \diamond N)] \rightarrow [(\diamond M \ \otimes \ \diamond N) \rightarrow (\diamond M \ \$ \ \diamond N)^c] \cap [(\diamond M \ \$ \ \diamond N)] = \diamond M \ \$ \ \diamond N$$

Proof. The proof is similar to proof of the Theorem 27.

4. CONCLUSION

In this paper, properties of modal operators defined on intuitionistic fuzzy sets have been investigated. Then, some intuitionistic fuzzy operations have been researched with modal operators. New equalities have been obtained. These equalities make it easy application areas of operators. Shorter equalities have been obtained using features of some intuitionistic fuzzy operations with modal operators. These equalities are more useful because they are shorter and more practical. These equalities could be made use of in many application areas of operators and these offer more practical solutions as they provide simplicity. Robotic, economy, control systems, computer and algebraic structures are some of these application areas.

REFERENCES

- [1] L.A.Zadeh , "Fuzzy Sets*", *Information and Control*, vol.8, pp. 338-353, 1965.

[2] K.T.Atanassov, “ Intuitionistic fuzzy sets”, *Fuzzy Sets and Systems* , vol.20, no.1, pp. 87-96, 1986.

[3] K.T.Atanassov, “ Intuitionistic Fuzzy Sets,Theory and Applications” , *Physica-Verlag Heidelberg*, Germany, pp. 319, 1999.

[4] E. Eker, F. Tuğrul and M. Çitil, “ New equalities on the intuitionistic fuzzy operators and operations” , *Notes on Intuitionistic Fuzzy Sets*, vol.21, no.4, pp. 124-128, 2015.

[5] K.Dencheva, “ Extension of intuitionistic fuzzy modal operators” *Proc.of the Second Int. IEEE Symp. Intelligent Systems*, vol.3, pp. 22-24, 2004.

[6] K.T. Atanassov , “ The most general form of one type of intuitionistic fuzzy modal operators” ,*Notes on Intuitionistic Fuzzy Sets*, vol.12, no.2, pp. 36-38, 2006.

[7] K.T. Atanassov, “ Some Properties of the operators from one type of intuitionistic fuzzy modal operators” , *Advanced Studies on Contemporary Mathematics*, vol.15, no.1, pp.13-20, 2007.

[8] G. Çuvalcıoğlu, “ Some Properties of $E_{\alpha,\beta}$ operator” , *Advanced Studies on Contemporary Mathematics*, vol. 14, no.2, pp. 305-310, 2007.

[9] G. Çuvalcıoğlu, “ Expand the modal operator diagram with $Z_{\alpha,\beta}^{\omega}$ ” , *Jangjeon Math. Soc.*, vol.13, no.3, pp. 403-412, 2010.

[10] G. Çuvalcıoğlu, “ On the Diagram of One Type Modal Operators on Intuitionistic Fuzzy Sets: Last Expanding with $Z_{\alpha,\beta}^{\omega,\theta}$ ” ,*Iranian J. of Fuzzy Systems*, vol.10, no.1, pp. 89-106, 2013.

[11] G. Çuvalcıoğlu and, S.Yılmaz, “ Some properties of OTMOs on IFSs” , *Advanced Studies in Contemporary Mathematics*, vol.20, no.4, pp. 621-628, 2010.

[12] B. Doycheva , “ Inequalities with intuitionistic fuzzy topological and Gökhan Çuvalcıoğlu’s operators” , *Notes on Intuitionistic Fuzzy Sets*, vol.14, no.1, pp. 20-22, 2008.

	SAKARYA ÜNİVERSİTESİ FEN BİLİMLERİ ENSTİTÜSÜ DERGİSİ <i>SAKARYA UNIVERSITY JOURNAL OF SCIENCE</i>		
	e-ISSN: 2147-835X Dergi sayfası: http://www.saujs.sakarya.edu.tr		
	<u>Gelis/Received</u> Sep 27, 2017 <u>Kabul/Accepted</u> Jan 12, 2018	<u>Doi</u> 10.16984/saufenbilder.340076	

Some Characterizations Of Surfaces Generated by Two Curves In $Heis_3$

Gülden ALTAY SUROĞLU*¹

ABSTRACT

In this paper, some characterizations of surfaces which are constructed by using the group operation in $Heis_3$ are given. Then, a new classification for minimal factorable surfaces in $Heis_3$ is obtained.

Keywords: Heisenberg group, Levi-Civita connection, mean curvature, Gaussian curvature.

$Heis_3$ de İki Eğri Tarafından Üretilen Yüzeylerin Bazı Karakterizasyonları

ÖZ

Bu makalede, 3- boyutlu Heisenberg grubunda, grup çarpımıyla elde edilen yüzeylerin bazı karakterizasyonları incelendi. Daha sonra, 3- boyutlu Heisenberg grubunda minimal factorable yüzeylerin yeni bir sınıflandırması elde edildi.

Anahtar Kelimeler: Heisenberg grup, Levi-Civita konneksiyonu, ortalama eğrilik, Gauss eğriliği .

* Corresponding Author

¹ Fırat University, Faculty of Science, Department of Mathematics, Elazığ-guldenaltay23@hotmail.com

1. INTRODUCTION

Much of the modern global theory of complete minimal surfaces in three dimensional Euclidean space has been affected by the work of Osserman during the 1960's. Recently, many of the global questions arose in this classical subject. These questions deal with analytic and conformal properties, the geometry and asymptotic behavior, and the topology and classification of the images of certain injective minimal immersions $\varphi: M \rightarrow E^3$ which are complete in the induced Riemannian metric, [1-6]. In [7], a Weierstrass representation formula for simply connected immersed minimal surfaces in Heisenberg group H^{2n+1} is studied.

A surface S in the Euclidean 3-space is denoted by

$$r(u, v) = \{x(u, v), y(u, v), z(u, v)\}.$$

A classification and some fundamental formulas is given for factorable surfaces which are parametrized as

$z = f(x)g(y)$ or $y = f(x)g(z)$ or $x = f(y)g(z)$, in the Euclidean space and in the Minkowski space, where f and g are smooth functions on some interval of \mathbb{R} , [8,9]. In [9], factorable surfaces in 3- dimensional Minkowski space is studied and some classification of such surfaces whose mean curvature and Gauss curvature satisfy certain conditions are given.

A factorable surface in $Heis_3$, which is given by a left invariant Riemannian metric, parametrized with group product for two curves. The purpose of this paper is to study and classify minimal surfaces and minimal factorable surfaces which are obtained with group operation in $Heis_3$.

2. PRELIMINARIES

The Heisenberg group $Heis_3$ is defined as \mathbb{R}^3 with the group operation

$$(x, y, z) * (x_1, y_1, z_1) = \left(x + x_1, y + y_1, z + z_1 + \frac{1}{2}(xy_1 - x_1y) \right). \quad (1)$$

The left invariant Riemannian metric given by

$$g = ds^2 = dx^2 + dy^2 + \left(dz + \frac{1}{2}(ydx - xdy) \right)^2. \quad (2)$$

The following vector fields form a left invariant orthonormal frame on $Heis_3$, which is given the left invariant Riemann metric g :

$$e_1 = \frac{\partial}{\partial x} - \frac{y}{2} \frac{\partial}{\partial z}, e_2 = \frac{\partial}{\partial y} + \frac{x}{2} \frac{\partial}{\partial z}, e_3 = \frac{\partial}{\partial z}. \quad (3)$$

These vector fields are dual to the coframe

$$w^1 = dx, w^2 = dy, w^3 = dz + \frac{y}{2} dx - \frac{x}{2} dy. \quad (4)$$

We obtain

$$2\nabla_{e_i} e_j = \begin{bmatrix} 0 & e_3 & -e_2 \\ -e_3 & 0 & e_1 \\ -e_2 & e_1 & 0 \end{bmatrix}, \quad (5)$$

also, we have the Heisenberg bracket relations.

$$[e_1, e_2] = e_3, [e_3, e_1] = [e_2, e_3] = 0. \quad (6)$$

Let $\varphi: M \rightarrow Heis_3$ be an orientable surface, isometrically immersed in $Heis_3$. Denote the Levi-Civita connections of M and $Heis_3$ by $\tilde{\nabla}$ and ∇ , respectively. Let X and Y denote vector fields tangent to M and let \mathbf{N} be a normal vector field. Then the Gauss and Weingarten formulas are given, respectively,

$$\begin{aligned} \nabla_X Y &= \tilde{\nabla}_X Y + h(X, Y)\mathbf{N}, \\ \nabla_X \mathbf{N} &= -AX, \end{aligned} \quad (7)$$

where h and A are the second fundamental form and the shape operator. It is well known that the second fundamental form h and the shape operator A are related by

$$h(X, Y) = g(AX, Y). \quad (8)$$

At each tangent plane $T_p M$, $\{\varphi_u, \varphi_v\}$ is a basis, where u, v are local coordinates on M . Denote by E, F, G the coefficients of the first fundamental form on M :

$$E = g(\varphi_u, \varphi_u), F = g(\varphi_u, \varphi_v), G = g(\varphi_v, \varphi_v). \quad (9)$$

Let $\{\varphi_u, \varphi_v\}$ form an arbitrary basis on the surface M . We know that A is a self-adjoint endomorphism with respect to the metric on M , that is, $g(A(u), v) = g(u, A(v))$, $u, v \in T_p M$. Also,

$$-g(\nabla_X \mathbf{N}, Y) = g(\nabla_X Y, \mathbf{N}). \quad (10)$$

At each tangent plane $T_p M$ it can be taken a basis $\{\varphi_u, \varphi_v\}$ and

$$A(\varphi_u) = -\nabla_{\varphi_u} \mathbf{N} = h_{11}\varphi_u + h_{12}\varphi_v, \quad (11)$$

$$A(\varphi_v) = -\nabla_{\varphi_v} \mathbf{N} = h_{21}\varphi_u + h_{22}\varphi_v.$$

So, the mean curvature of the surface is

$$H = \frac{Gh_{11} - Fh_{12} - Fh_{21} + Eh_{22}}{2(EG - F^2)}. \quad (12)$$

It is known that, minimal surface is obtain with $H = 0$. So, M is a minimal surface if and only if

$$Gh_{11} - Fh_{12} - Fh_{21} + Eh_{22} = 0. \quad (13)$$

The Gaussian curvature of the surface is

$$K = \frac{h_{11}h_{22} - h_{12}h_{21}}{(EG - F^2)}. \quad (14)$$

3. MINIMAL SURFACES IN $Heis_3$

In this section, a new type of surfaces which are defined by two curves in $Heis_3$ is obtained. Also, some characterizations of this surface is given.

Theorem 3.1. Let $\alpha(x) = (\alpha_1(x), \alpha_2(x), \alpha_3(x))$ and $\beta(y) = (\beta_1(y), \beta_2(y), \beta_3(y))$ be differentiable nongeodesic curves in $Heis_3$ which is endowed with left invariant Riemannian metric g . Then, with the group operation in the equality (2.1), there is a $\varphi(x, y) = \alpha(x) * \beta(y)$ surface in $(Heis_3, g)$. The mean curvature of the surface $\varphi(x, y)$ is

$$H = \frac{1}{\|n\|(EG - F^2)} \{ (\alpha_2'Q - P\beta_2') [G(\alpha_1'\alpha_1'' + \alpha_2'P) + E(\beta_2'\beta_1'' + \beta_2'Q) - F(\alpha_2'\beta_1'' + \beta_1'\alpha_1'')] + \frac{1}{2}(\alpha_2'Q + \beta_2'P + \beta_2'P + \alpha_2'Q) + (\alpha_1'Q - \beta_1'P) [G(\alpha_1'\alpha_2'' - \alpha_1'P) + E(\beta_2'\beta_2'' - \beta_1'Q) - F(\alpha_2'\beta_2'' + \beta_1'\alpha_2'')] - \frac{1}{2}(\beta_1'P + \alpha_1'Q + \alpha_1'Q + \beta_1'P)] + (\alpha_1'\beta_2' - \alpha_2'\beta_1') [G((\alpha_1'P_x + \alpha_2'P_y)(\alpha_1'\beta_2' - \alpha_2'\beta_1')) + E((\beta_1'Q_x + \beta_2'Q_y)(\alpha_1'\beta_2' - \alpha_2'\beta_1')) - F(\alpha_1'Q_x + \alpha_2'Q_y + \beta_1'P_x + \beta_2'P_y + \frac{1}{2}(\alpha_1'\beta_2' + \alpha_2'\beta_1' - \alpha_2'\beta_1' - \alpha_1'\beta_2'))] \}, \quad (15)$$

where

$$P = \frac{1}{2}(\alpha_1'(\alpha_2 + 2\beta_2) - \alpha_2'(\alpha_1 + 2\beta_1) + 2\alpha_3'), \quad (16)$$

$$Q = \frac{1}{2}(\beta_1'\beta_2 - \beta_2'\beta_1 + 2\beta_3'), \quad (17)$$

E , F and G the are coefficients of the first fundamental form.

Proof. From derivatives of the surface $\varphi(x, y) = \alpha(x) * \beta(y)$ depend to x and y , we have

$$\varphi_x(x, y) = \alpha_1'e_1 + \alpha_2'e_2 + \frac{1}{2}(\alpha_1'(\alpha_2 + 2\beta_2) - \alpha_2'(\alpha_1 + 2\beta_1) + 2\alpha_3')e_3, \quad (19)$$

$$\varphi_y(x, y) = \beta_1'e_1 + \beta_2'e_2 + \frac{1}{2}(\beta_1'\beta_2 - \beta_2'\beta_1 + 2\beta_3')e_3. \quad (20)$$

From equations (19) and (20), coefficients of the first fundamental form are

$$E = g(\varphi_x, \varphi_x) = \alpha_1'^2 + \alpha_2'^2 + P^2, \quad (21)$$

$$F = g(\varphi_x, \varphi_y) = \alpha_1'\beta_1' + \alpha_2'\beta_2' + PQ, \quad (22)$$

$$G = g(\varphi_y, \varphi_y) = \beta_1'^2 + \beta_2'^2 + Q^2, \quad (23)$$

On the other hand, if (5), (19) and (20) are thought together, Levi-Civita connections obtained as

$$\nabla_{\varphi_x} \varphi_x = (\alpha_1'\alpha_1'' + \alpha_2'P)e_1 + (\alpha_1'\alpha_2'' - \alpha_1'P)e_2 + (\alpha_1'P_x + \alpha_2'P_y)e_3, \quad (24)$$

$$\nabla_{\varphi_x} \varphi_y = (\alpha_2'\beta_1'' + \frac{1}{2}(\alpha_2'Q + \beta_2'P))e_1 + (\alpha_2'\beta_2'' - \frac{1}{2}(\beta_1'P + \alpha_1'Q))e_2 + (\alpha_1'Q_x + \alpha_2'Q_y + \frac{1}{2}(\alpha_1'\beta_2' - \alpha_2'\beta_1'))e_3, \quad (25)$$

$$\nabla_{\varphi_y} \varphi_x = (\beta_1'\alpha_1'' + \frac{1}{2}(\beta_2'P + \alpha_2'Q))e_1 + (\beta_1'\alpha_2'' - \frac{1}{2}(\alpha_1'Q + \beta_1'P))e_2 + (\beta_1'P_x + \beta_2'P_y + \frac{1}{2}(\alpha_2'\beta_1' - \alpha_1'\beta_2'))e_3, \quad (26)$$

$$\nabla_{\varphi_y} \varphi_y = (\beta_2'\beta_1'' + \beta_2'Q)e_1 + (\beta_2'\beta_2'' - \beta_1'Q)e_2 + (\beta_1'Q_x + \beta_2'Q_y)e_3. \quad (27)$$

The unit normal vector field of the surface $\varphi(x, y)$ is

$$N = \frac{1}{\|n\|} ((\alpha_2'Q - P\beta_2')e_1 - (\alpha_1'Q - \beta_1'P)e_2 + (\alpha_1'\beta_2' - \alpha_2'\beta_1')e_3) \quad (28)$$

where

$$\|n\| = \sqrt{(\alpha_2'Q - P\beta_2')^2 + (\alpha_1'Q - \beta_1'P)^2 + (\alpha_1'\beta_2' - \alpha_2'\beta_1')^2}.$$

From (24) - (28) coefficients of the second fundamental form are

$$\begin{aligned} h_{11} = & \frac{1}{\|n\|} [(\alpha_2'Q - P\beta_2')(\alpha_1'\alpha_1'' + \alpha_2'P) \\ & - (\alpha_1'Q - \beta_1'P)(\alpha_1'\alpha_2'' - \alpha_1'P) \\ & + (\alpha_1'\beta_2' - \alpha_2'\beta_1')(\alpha_1'P_x + \alpha_2'P_y)], \end{aligned} \quad (29)$$

$$\begin{aligned} h_{12} = & \frac{1}{\|n\|} [(\alpha_2'Q - P\beta_2')(\alpha_2'\beta_1'' + \frac{1}{2}(\alpha_2'Q + \beta_2'P) \\ & - (\alpha_1'Q - \beta_1'P)(\alpha_2'\beta_2'' - \frac{1}{2}(\beta_1'P + \alpha_1'Q)) \\ & + (\alpha_1'\beta_2' - \alpha_2'\beta_1')(\alpha_1'Q_x + \alpha_2'Q_y + \frac{1}{2}(\alpha_1'\beta_2' - \alpha_2'\beta_1'))], \end{aligned} \quad (30)$$

$$\begin{aligned} h_{21} = & \frac{1}{\|n\|} [(\alpha_2'Q - P\beta_2')(\beta_1'\alpha_1'' + \frac{1}{2}(\beta_2'P + \alpha_2'Q)) \\ & - (\alpha_1'Q - \beta_1'P)(\beta_1'\alpha_2'' - \frac{1}{2}(\alpha_1'Q + \beta_1'P)) \\ & + (\alpha_1'\beta_2' - \alpha_2'\beta_1')(\beta_1'P_x + \beta_2'P_y + \frac{1}{2}(\alpha_2'\beta_1' - \alpha_1'\beta_2'))], \end{aligned} \quad (31)$$

$$\begin{aligned} h_{22} = & \frac{1}{\|n\|} [(\alpha_2'Q - P\beta_2')(\beta_2'\beta_1'' + \beta_2'Q) \\ & - (\alpha_1'Q - \beta_1'P)(\beta_2'\beta_2'' - \beta_1'Q) \\ & + (\alpha_1'\beta_2' - \alpha_2'\beta_1')(\beta_1'Q_x + \beta_2'Q_y)]. \end{aligned} \quad (32)$$

Then, if (21)- (23), (29)- (32) are written in the equation (12), the mean curvature of the surface $\varphi(x, y)$ is (15).

Corollary 3.2. Let $\varphi(x, y)$ be a surface in $(Heis_3, g)$. If $\varphi(x, y)$ is a minimal surface, then

$$\begin{aligned} & (\alpha_2'Q - P\beta_2')[G(\alpha_1'\alpha_1'' + \alpha_2'P) \\ & + E(\beta_2'\beta_1'' + \beta_2'Q) - F(\alpha_2'\beta_1'' + \beta_1'\alpha_1''] \end{aligned}$$

$$\begin{aligned} & + \frac{1}{2}(\alpha_2'Q + \beta_2'P + \beta_2'P + \alpha_2'Q)] \\ & + (\alpha_1'Q - \beta_1'P)[G(\alpha_1'\alpha_2'' - \alpha_1'P) \\ & + E(\beta_2'\beta_2'' - \beta_1'Q) - F(\alpha_2'\beta_2'' + \beta_1'\alpha_2''] \\ & - \frac{1}{2}(\beta_1'P + \alpha_1'Q + \alpha_1'Q + \beta_1'P)] \\ & + (\alpha_1'\beta_2' - \alpha_2'\beta_1')[G((\alpha_1'P_x + \alpha_2'P_y)(\alpha_1'\beta_2' - \alpha_2'\beta_1')) \\ & + E((\beta_1'Q_x + \beta_2'Q_y)(\alpha_1'\beta_2' - \alpha_2'\beta_1')) \\ & - F(\alpha_1'Q_x + \alpha_2'Q_y + \beta_1'P_x + \beta_2'P_y \\ & + \frac{1}{2}(\alpha_1'\beta_2' + \alpha_2'\beta_1' - \alpha_2'\beta_1' - \alpha_1'\beta_2'))] = 0. \end{aligned} \quad (33)$$

4. FACTORABLE SURFACES IN $Heis_3$

In this section we deduce new types of factorable surfaces in $Heis_3$. Moreover we obtain some characterizations of these surfaces. Then, some comperations are given with tables for new types of factorable surfaces.

4.1 Surfaces of Type 1

Let α and β be curves in $Heis_3$, which are given by $\alpha(x) = (u_1(x), 0, c)$, $\beta(y) = (0, v_2(y), -c)$. The factorable surface $\varphi(x, y) = \alpha(x) * \beta(y)$ of type 1 is can be parmetrized as

$$\begin{aligned} \varphi(x, y) = & (u_1(x), 0, c) * (0, v_2(y), -c) \\ = & \left(u_1(x), v_2(y), \frac{1}{2}u_1(x)v_2(y) \right), \end{aligned} \quad (34)$$

where c is a nonzero constant.

Theorem 4.1. Let $\varphi(x, y)$ be factorable surface of type 1 in $Heis_3$ which is endowed Riemannian metric. $\varphi(x, y)$ is a minimal surface in $Heis_3$.

Proof. From (34), it can be easily obtain,

$$\varphi_x = u_1'(x)(e_1 + v_2e_3), \quad (35)$$

$$\varphi_y = v_2'(y)e_2. \quad (36)$$

An orthogonal vector at each point is

$$N = \frac{1}{\sqrt{1+v_2^2(y)}}(-v_2e_1 + e_3). \quad (37)$$

The coefficients of the first fundamental form are

$$E = g(\varphi_x, \varphi_x) = u_1'^2(x)(1+v_2^2), \quad (38)$$

$$F = g(\varphi_x, \varphi_x) = g(\varphi_y, \varphi_x) = 0, \quad (39)$$

$$G = g(\varphi_y, \varphi_y) = v_2'^2. \quad (40)$$

On the other hand, from (5),

$$\nabla_{\varphi_x} \varphi_x = u_1''(x)u_1'(x)e_1 - u_1'^2(x)v_2(y)e_2 + u_1''(x)u_1'(x)v_2(y)e_3, \quad (41)$$

$$\nabla_{\varphi_x} \varphi_y = \frac{1}{2}v_2'(y)u_1'(x)(v_2(y)e_1 + e_3), \quad (42)$$

$$\nabla_{\varphi_y} \varphi_x = \frac{1}{2}v_2'(y)u_1'(x)(v_2(y)e_1 + e_3), \quad (43)$$

$$\nabla_{\varphi_y} \varphi_y = v_2''(y)v_2'(y)e_2. \quad (44)$$

So, the coefficients of second fundamental form are

$$h_{11} = 0, \quad (45)$$

$$h_{12} = \frac{u_1'(x)v_2'(y)}{2\sqrt{1+v_2^2(y)}}(1-v_2^2(y)), \quad (46)$$

$$h_{21} = \frac{u_1'(x)v_2'(y)}{2\sqrt{1+v_2^2(y)}}(1-v_2^2(y)), \quad (47)$$

$$h_{22} = 0. \quad (48)$$

Then, from equations (45)- (48) and (12), we have the mean curvature of the surface φ is $H = 0$. So, the surface $\varphi(x, y)$ is a minimal surface.

Corollary 4.2. Let $\varphi(x, y)$ be factorable surface of type 1 $\varphi(x, y)$ in $Heis_3$ which is endowed Riemannian metric. The Gaussian curvature of $\varphi(x, y)$ is $K \leq 0$ for all points in $Heis_3$.

Proof. From equations (45)- (48) , we have

$$K = -\frac{(1-v_2^2(y))^2}{4(1+v_2^2(y))^2} \quad (49)$$

Example4.3. Let

$\varphi(x, y) = \left(\sin x, \cos y, \frac{1}{2} \sin x \cos y \right)$ is a factorable surface Type 1 in $(Heis_3, g)$. The mean curvature of $\varphi(x, y)$ is, $H = 0$. Then, $\varphi(x, y)$ is a minimal surface in $(Heis_3, g)$.

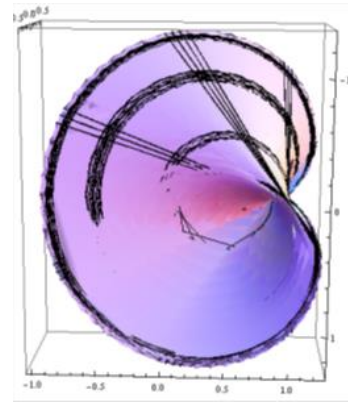


Figure 1. Minimal factorable surface Type1 in $(Heis_3, g)$.

4.2 Surfaces of Type 2

Let α and β be curves in $Heis_3$, which are given by $\alpha(x) = (0, u_2(x), d)$, $\beta(y) = (v_1(y), 0, -d)$. The factorable surface $M(\alpha, \beta) = \alpha(x) * \beta(y)$ of type 1 is can be parametrized as

$$\begin{aligned} \psi(x, y) &= (0, u_2(x), d) * (v_1(y), 0, -d) \\ &= \left(v_1(y), u_2(x), -\frac{1}{2} v_1(y)u_2(x) \right), \end{aligned} \quad (50)$$

where d is a nonzero constant.

Theorem 4.4. Let $\psi(x, y)$ is factorable surface of type 2 in the $Heis_3$. $\psi(x, y)$ is a minimal surface if and only if $v_1(y) = \text{constant}$.

Proof. The mean curvature of the surface ψ is can be obtain as

$$H = \frac{v_1'}{2(1+v_1^2(y))^{3/2}}. \quad (51)$$

So, if

$$v_1' = 0,$$

the surface $\psi(x, y)$ is a minimal surface.

Corollary 4.5 The Gaussian curvature of factorable surface of type 2 $\psi(x, y)$ in $Heis_3$ is

$$K = \frac{(v_1^2(y)+u_2^2(x))(1-v_1^2(y))}{4(1+v_1^2(y))^2}. \quad (52)$$

Example4.6. Let $a \in \mathbb{R}$,

$\psi(x, y) = \left(a, \cos x, \frac{1}{2} a \cos x \right)$ is a factorable

surface Type 2 in $(Heis_3, g)$. The mean curvature of $\psi(x, y)$ is $H = 0$. Then, $\phi(x, y)$ is a minimal surface in $(Heis_3, g)$.

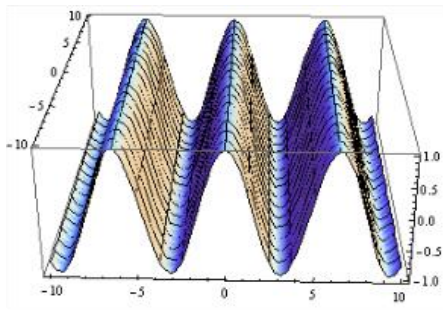


Figure 2. Minimal factorable surface Type2 in $(Heis_3, g)$.

REFERENCES

[1] E. Turhan, G. Altay, Maximal and Minimal Surfaces of Factorable Surfaces in $Heis_3$, *Int. J. Open Problems Compt. Math.*, vol. 3, no.2, pp. 200-212, 2010.
[2] J. Inoguchi, R. López, M. Munteanu, Minimal Translation Surfaces in the Heisenberg

group Nil_3 , *Geom Dedicata*, vol. 161, no. 1., pp. 221-231, 2012.

[3] M. P. Carmo, *Differential Geometry of Curves and Surfaces*, Boston, 1976.

[4] R. López, M. Munteanu, Minimal translation surfaces in Sol_3 , arxiv:1010.1085v1, 2010.

[5] Y. Yu, H. Liu, The factorable minimal surfaces, *Proceedings of The Eleventh International Workshop on Diff. Geom.* vol. 11, pp. 33-39, 2007.

[6] J. Oprea, *Differential Geometry and Its Applications*, New Jersey, 1997.

[7] E. Turhan, T. Körpınar, Minimal Immersion and Harmonic Maps in Heisenberg Group H^{2n+1} , *Int. J. Open Problems Compt. Math.*, vol. 3, no. 4, pp. 490-496, 2010.

[8] M. Bekkar, B. Senoussi, Factorable surfaces in the three-dimensional Euclidean and Lorentzian spaces satisfying $\Delta r_i = \lambda_i r_i$, *Journal of Geometry*, vol. 103, no. 1, pp. 17-29, 2012.

[9] H. Meng, H. Liu, Factorable Surfaces in 3- Minkowski Space, *Bull. Korean Math. Soc.*, vol. 46, no. 1, pp. 155-169, 2009.

	SAKARYA ÜNİVERSİTESİ FEN BİLİMLERİ ENSTİTÜSÜ DERGİSİ <i>SAKARYA UNIVERSITY JOURNAL OF SCIENCE</i>		
	e-ISSN: 2147-835X Dergi sayfası: http://www.saujs.sakarya.edu.tr		
	Received 19-06-2017 Accepted 13-01-2018	Doi 10.16984/saufenbilder.322378	

Meyer-Neldel Rule in Ac Conductivity of Cu Doped ZnO Thin Films

Nursel CAN^{*1}, Birsal CAN ÖMÜR¹, Ahmet ALTINDAL¹

ABSTRACT

Ac charge transport mechanisms have been comparatively investigated in ZnO thin films having different Cu dopant. A comparative study of the applicability of quantum mechanical tunnelling and correlated barrier hopping model to obtained ac electrical conductivity results has been performed. Comparing the temperature dependence of the frequency exponent shows that the correlated barrier hopping model best describes the experimental data on the ac conductivity in ZnO:Cu thin films. In order to gain an understanding of the applicability of Meyer-Neldel rule, the dependence of the thermal activation energy on Cu doping concentration in these films has also been studied. The obtained experimental results indicated that Meyer-Neldel rule can be successfully applied ac conductivity data for highly Cu doped films but not others which has been explained on the basis of distribution variations in density of states.

Keywords: Meyer-Neldel rule, ac charge transport mechanism, ZnO, thin film

1. INTRODUCTION

As an alternative to widely used indium tin oxide (ITO) film, zinc oxide (ZnO) films have attracted considerable interest as a transparent conducting electrode [1]. Because of its direct band gap of 3.37 eV [2] and large exciton binding energy of 6 meV [3], ZnO thin film has a great potential in various area including gas sensor [4], light emitting diodes and UV lasers [5] and surface acoustic wave devices [6]. Many recent investigations have indicated that the electrical properties of the ZnO films may be modified by doping with Al, In and Ga [7-10]. In spite of a large amount of work having been done on the effect of various impurities on the structural and morphological properties of ZnO films [11, 12],

the spread of activation energy in metal-oxide semiconductor is not fully understood. In general, the observed low temperature behaviour of the conductivity is attributed to the hopping of charge carrier over the barrier. However, no previous work has been performed on the applicability of Meyer-Neldel (MN) rule to the temperature dependence of ac conduction in ZnO thin film. It is well known that Cu doping leads to creation of donor states below the conduction band and the electrical behaviour of ZnO films dominated by the Cu doped dopant concentration. Hence, a study of ac conductivity and the applicability of MN rule in Cu doped ZnO thin film would be interesting. In the present work, the ac conduction properties of spray pyrolysed ZnO film with different Cu dopant concentration has been investigated in the frequency range 100 – 13×10⁶ Hz. The obtained

*Corresponding Author

¹Yildiz Technical University, Department of Physics, can@yildiz.edu.tr, bcan@yildiz.edu.tr, altindal@yildiz.edu.tr

conductivity data has been analyzed in the light of MN rule.

2. EXPERIMENTAL

Indium tin oxide (ITO) coated glasses were used as substrates to deposit Cu doped and pure zinc oxide films. Film deposition were carried out by spray pyrolysis technique from zinc acetate precursor. For the deposition of ZnO films, 0.5 g zinc acetate dihydrate was dissolved in appropriate amount of isopropyl alcohol containing monoethanolamine under stirring for 2 h at 60 °C. Copper chloride (CuCl₂) was used as dopant source. The concentration of the dopant was varied systematically between 0% and 6%. The resulting solution was sprayed onto the pre-heated ITO coated glass substrates at a constant temperature of 460 °C. A K type thermocouple was used to monitor the temperature of the substrate. Compressed nitrogen was used as the carrier gas. The structure of the ZnO:Cu films was investigated by X-ray diffraction (XRD) pattern. The XRD analysis was performed on a Rigaku XRD diffractometer using CuK α radiation (1.54059Å) as X-ray source. Impedance spectra of the samples were measured as function of temperature between 300 and 450 K and in the frequency range of 100 – 13 \times 10⁶ Hz by using a HP 4192 A impedance analyser. In order to avoid from ambient effect, impedance measurements were performed under 10⁻³ mbar. A schematic representation of the impedance measurement system is shown in Figure 1.

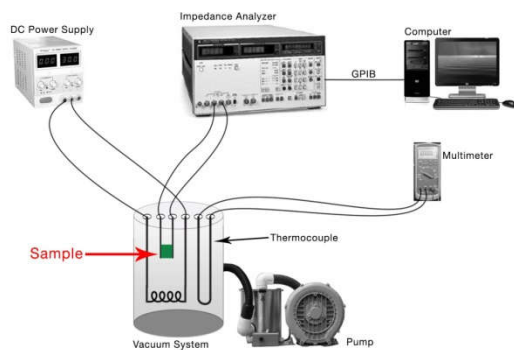


Figure 1. Schematic representation of the experimental set-up

3. RESULTS AND DISCUSSION

3.1. Structural analysis

In order to investigate the crystal structure and the phase composition the XRD pattern of ZnO and ZnO:Cu samples was recorded by using CuK α radiation as X-ray source. The recorded XRD patterns of pure zinc oxide and doped films with different copper concentrations is presented in Figure 2. The obtained XRD spectrum indicated the formation of hexagonal structure of ZnO. XRD analysis also showed that the (002) preferential orientation of all films is along crystal plane. The other peaks observed at 31.76°, 36.16°, 47.55°, and 56.61° are associated with (100), (101), (110), and (102) planes.

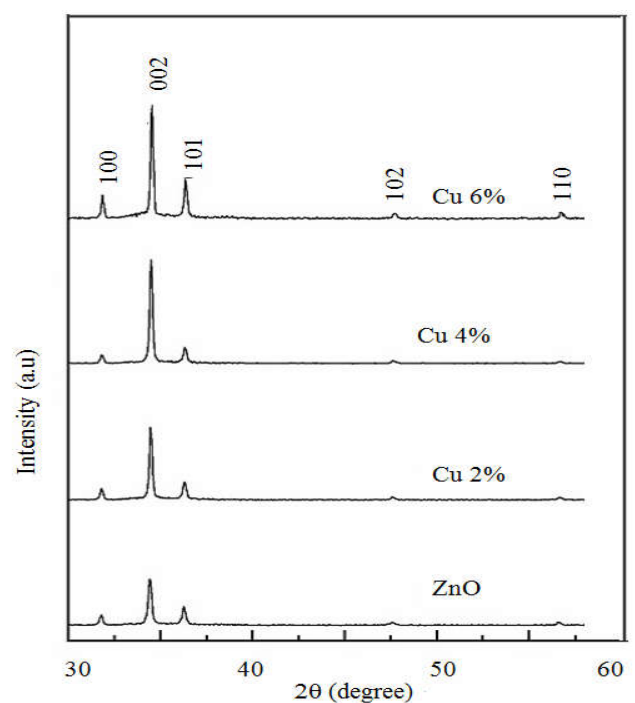


Figure 2. XRD patterns of spray pyrolysis deposited ZnO and Cu doped ZnO thin films

3.2. Ac conductivity studies

Figure 3 shows the room temperature ac conductivity variations with frequency for undoped and Cu doped ZnO films. Figure 3 shows that the room temperature conductivity of the ZnO films increase with the increase in Cu dopant concentration. The increase in conductivity with Cu dopant concentration can be attributed to the increase in carrier concentration in the doped ZnO films. A strong frequency dependence for all films investigated is clear. A review of the present literature suggests that for a large variety of materials, the expression for the ac conductivity can be written as

$$\sigma_{ac} = A\omega^m \quad (1)$$

where A is a constant, ω is the angular frequency of applied signals, m is an exponent. Although there is no unique interpretation for the observed frequency dependence of conductivity, it is known that this type of behaviour is characteristic of many metal-oxide semiconductors and molecular materials [13-16]. Quantum mechanical tunnelling (QMT) and correlated barrier hopping (CBH) models are widely used for evaluating the frequency dependence of the conductivity. In QMT model, a charge carrier motion between localized states near the Fermi level is assumed. According to the QMT model, the frequency dependence of the conductivity should obey Eq. (2).

$$\sigma_{ac}(\omega) = \frac{\pi}{3} q^2 kT (N_F)^2 \beta^{-5} \omega \left(\ln \left(\frac{v_0}{\omega} \right) \right)^4 \quad (2)$$

where q is the electronic charge, ω is the angular frequency, N_F is the density of localized states at Fermi level, β is the inverse localization length of wave function and v_0 is the characteristic phonon frequency. According to QMT model the exponent m should be temperature independent with a constant value around 0.8.

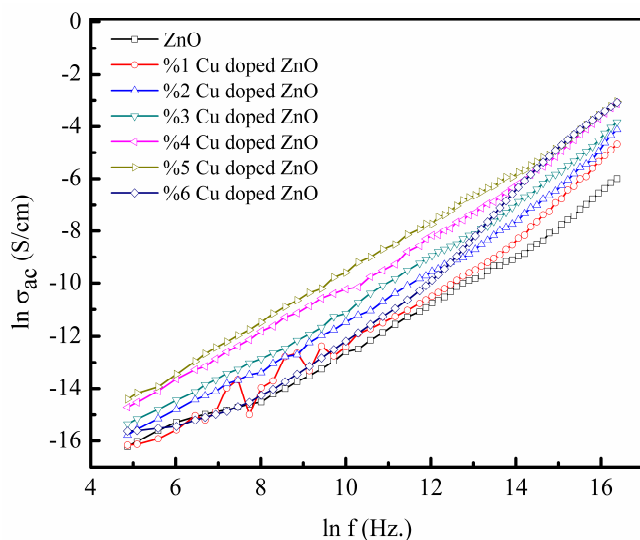


Figure 3. Variation of the conductivity with frequency for pure and Cu doped ZnO films

On the other hand, CBH model assumes that the charge transport take places via polaron hopping process over the potential barrier separating hoping centers. In CBH model, the frequency dependent is given by,

$$\sigma_{ac}(\omega) = \frac{\pi^2 N^2 \varepsilon}{24} \left(\frac{8q^2}{\varepsilon E_0} \right)^6 \frac{\omega^m}{\tau_0^\beta} \quad (3)$$

where E_0 is the optical band gap and ε is the dielectric constant of the material. CBH model

predicts a temperature dependent exponent m which is given by,

$$m = 1 - \frac{6kT}{E_0 + kT \ln(\omega\tau_0)} \quad (4)$$

In order to decide which mechanism is more appropriate for the observed frequency dependency, the values of the exponent m were derived from the slope of the curves showed in Figure 3. The variation of the m with temperature for all films investigated is depicted in Figure 4. As can be seen from the Figure 4, the exponent m decreases with increasing temperature. In the light of this finding it can be concluded that the QMT model is not appropriate to model ac conduction in pure and Cu doped ZnO films. The decreasing trend in exponent with increase in temperature confirms that ac conductivity in investigated films obeys the CBH model.

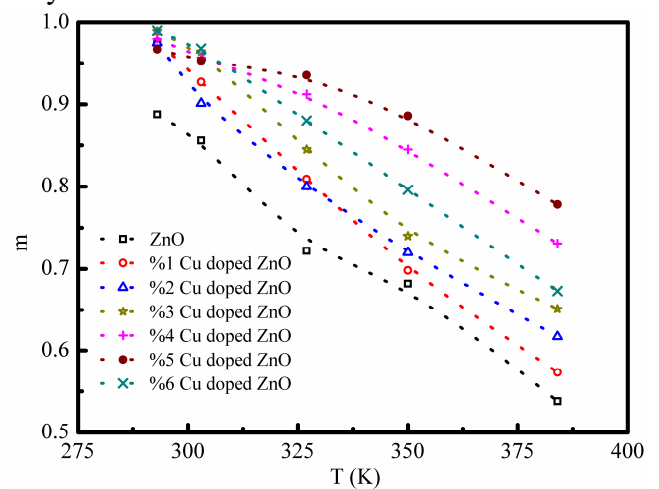


Figure 4. Temperature dependence of the exponent m for all films

3.3. Meyer-Neldel rule

In thermally activated processes, the dependence of electrical conductivity, $\sigma(T)$, on the temperature is given by

$$\sigma(T) = \sigma_0 \exp\left(-\frac{E_A}{kT}\right) \quad (5)$$

where σ_0 is pre-exponential factor, E_A is the thermal activation energy. In 1937, Meyer and Neldel [17] have discovered that thermal activation energy varies and it can be correlated to pre-exponential factor σ_0 as,

$$\sigma_0 = \sigma_{00} \exp\left(\frac{E_A}{kT_{MN}}\right) \quad (6)$$

where σ_{00} is a constant and T_{MN} is the characteristic Meyer-Neldel temperature. This type of relation has been observed in many thermally activated processes [18, 19] and known

as Meyer-Neldel relation. A combination of Eq. (5) and (6) gives,

$$\sigma(T) = \sigma_{00} \exp\left(\frac{E_A}{kT_{MN}}\right) \exp\left(-\frac{E_A}{kT}\right) \quad (7)$$

The applicability of the Meyer-Neldel rule to the measured ac conductivity data were checked by extracting the thermal activation energy. For this purpose, ac conductivity variations at various fixed frequencies were plotted in the Arrhenius form. As a representative result, the Arrhenius plots for the 4% Cu doped ZnO film at indicated fixed frequencies is presented in Figure 5. The variation of the ac conductivity with inverse temperature reveals that the charge transport occurs through an activated process which has single activation energy in the operating temperature range. The obtained results suggests that Eq.(5) can be used to represent the temperature dependence of the ac conductivity for samples investigated.

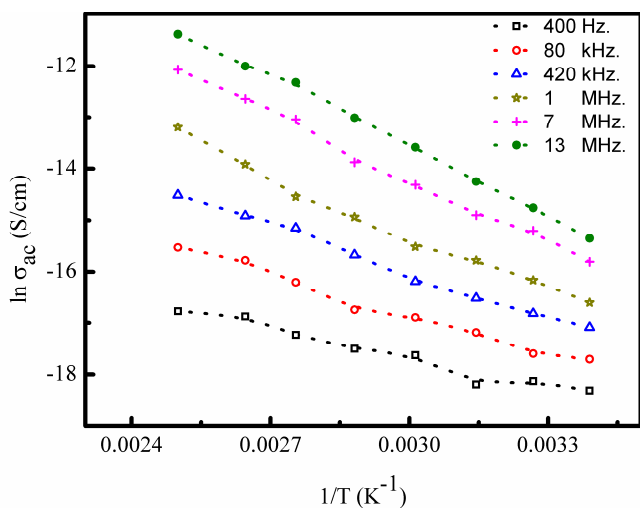


Figure 5. The temperature dependences of the measured ac conductivity at various frequencies for 4% Cu doped ZnO thin film

With the aid of Eq. (5), the value of the activation energy and pre-exponential factor derived from the slope and intercept of the $\ln \sigma_{ac}$ vs $1/T$ graphs. The variation of derived values of pre-exponential factor with thermal activation energy of the conductivity is shown in Figure 6. The linear relationship between the pre-exponential factor and ac thermal activation energy for the samples of 4%, 5% and 6% Cu doped ZnO films is clear. Deviation from linearity for other films is also clear.

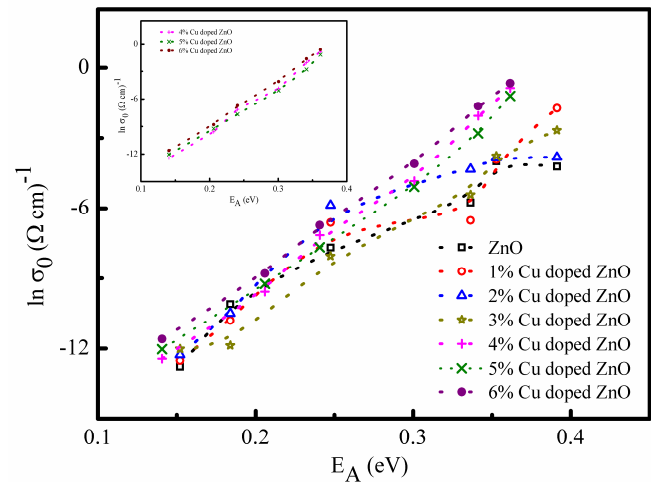


Figure 6. Variation of the pre-exponential factor with activation energy

A detailed literature survey indicates that various models have been investigated to explain Meyer-Neldel rule. A model which is developed by Fang [20], describes that the annealing time parameter obeys the Meyer-Neldel rule. Recently, Koga and Sestak [21] have discussed that a change of activation energy is thus compensated by the same change the logarithm of the pre-exponential factor due to the kinetic compensation effect. According to Roberts [22] and Cohen et al.[23] the origin of Meyer-Neldel rule in polycrystalline or amorphous semiconductors is due to long-range electrostatic random potential or exponential tailing of the majority band states. Another model which is proposed by Kemeny and Rosenberg [24] assumes that electrons and polarons tunnel through interatomic barriers from activation energy states. It should be mentioned here that the major drawback of the above mentioned models is that these models could not provide a universal explanation of MNR in any materials. These literature survey show definitely that a single general MNR equation for all material systems are not applicable to explain the observed MNR.

It can be concluded that the ac charge transport in ZnO films take place through thermally excited electrons. The applicability of MNR to the experimental ac conductivity data for highly Cu doped samples can be attributed to the exponential energy distribution of traps. The presence of any defects such as O vacancies and native defects with exponential energy distribution, which acts as trap centers for the charge carriers, may be responsible for the observed behaviour of ac conductivity in highly doped samples. It is also well known that, the distribution of the density of states may not be symmetrical with respect to the center of the band because of tailing of localized

REFERENCES

states at the band edges and the presence of defect states in the gap. Therefore, the main contribution to the experimentally obtained pre-exponential factor comes from the shift of Fermi level and temperature dependent shift of conduction and valance band edges [25]. When the Fermi level lies in conduction band tail or close to the minimum of density of states, a linear variation of pre-exponential factor with activation energy can be observed. On the other hand, if the Fermi level approaches the boundaries and the density of states spectrum is flat near the edge the linear relation between the pre-exponential factor and the thermal activation energy diminishes [26]. According to Kikuchi [27] another reason for the deviation from linearity in $\ln \sigma_0$ vs. E_A plots is the reduction in the minimum of density of state. In heavily doped samples, potential barrier formation does not occurs because of the large number of defect states. In this case, the Fermi level lies in the gap where the density of states does not vary much and charge transport is governed by the band tail transport. In weakly doped films, low values of free electron concentrations is expected. Because of low value of doping concentration an improvement in film microstructure is also expected which leads to delocalization of the tail states causing the Fermi level shift towards the band edge. Lower density of available free carriers and low value of defect density may cause a large increase in dangling bond density. In this case, the Fermi level lies in the plateau region of the density of states and this cause the observed deviation from linearity in $\ln \sigma_0$ vs. E_A plots.

4. CONCLUSION

The ac conduction mechanism Cu doped ZnO thin films were studied in a temperature range of 300 and 450 K and in the frequency range of 100 – 13×10^6 Hz. The measured ac conductivity data were discussed in terms of quantum mechanical tunnelling and correlated barrier hoping models. Analysis of the temperature dependence of the frequency exponent showed that, the ac conductivity data in pure and Cu doped ZnO films agrees fairly well with the predictions of the correlated barrier hopping model. A linear relation between the pre-exponential factor and thermally activation energy reveals that the Meyer-Neldel rule can be applied to highly Cu doped ZnO.

- [1] Y. S. Kim and W.P. Tai, "Electrical and optical properties of Al-doped ZnO thin films by sol-gel process", *Applied Surface Science*, vol. 253, pp. 4911–4916, 2007
- [2] J. Xu, J. Han, Y. Zhang, Y. Sun, and B. Xie, "Studies on alcohol sensing mechanism of ZnO based gas sensors", *Sensors Actuators B: Chemical*, vol. 132, pp. 334–339, 2008.
- [3] K. L. Chopra, S. Major, and D. K. Pandya, "Transparent conductors-a status review", *Thin Solid Films*, vol. 102, pp. 1–46, 1983.
- [4] Z. Yang, Y. Huang, G. Chen, Z. Guo, S. Cheng, and S. Huang, "Ethanol gas sensor based on Al-doped ZnO nanomaterial with many gas diffusing channels", *Sensors and Actuators B: Chemical*, vol. 140, pp. 549–556, 2009.
- [5] Y. Dai, Y. Zhang, Q. K. Li, and C.W. Nan, "Synthesis and optical properties of tetrapod-like zinc oxide nanorods", *Chemical Physics Letters*, vol. 358, pp. 83–86, 2002.
- [6] X. Y. Du, Y. Q. Fu, S. C. Tan, J. K. Lu, A. J. Flewitt, S. Maeng, S. H. Kim, Y. J. Choi, D. S. Lee, N. M. Park, J. Park, W. I. Milne, ZnO film for application in surface acoustic wave device, *Journal of Physics: Conference Series*, vol. 76, pp. 012035-012040, 2007.
- [7] F. Maldonado, A. Stashans, Al-doped ZnO: Electronic, electrical and structural properties, *Journal of Physics and Chemistry of Solids*, vol. 71, pp. 784–787, 2010.
- [8] H.-R. An, H.-J. Ahn, J.-W. Park, High-quality, conductive, and transparent Ga-doped ZnO films grown by atmospheric-pressure chemical-vapor deposition, *Ceramics International*, vol. 41, pp. 2253–2259, 2015.
- [9] Z. Q. Ma, W. G. Zhao, and Y. Wang, "Electrical properties of Na/Mg co-doped ZnO thin films", *Thin Solid Films*, vol. 515, pp. 8611–8614, 2007.
- [10] A. E. Jimenez-Gonzalez, J. A. Soto Ureuta, and R. Suarez-Parra, "Optical and electrical characteristics of aluminum-doped ZnO thin films prepared by solgel technique", *Journal*

- of Crystal Growth*, vol. 192, pp. 430–438, 1998.
- [11] U. Wahl, E. Rita, J. G. Correia, E. Alves, and J. P. Araujo, "Implantation site of rare earths in single-crystalline ZnO", *Applied Physics Letters*, vol. 82, pp. 1173–1175, 2003.
- [12] R. Kaur, A. V. Singh, and R. M. Mehra, "Structural, electrical and optical properties of sol-gel derived yttrium doped ZnO films", *Physica Status Solidi (a)*, vol. 202, pp. 1053–1059, 2005.
- [13] S. R. Elliott, "A theory of a.c. conduction in chalcogenide glasses", *Philosophical Magazine*, vol. 36, pp. 1291–1304, 1977.
- [14] S. R. Lukić-Petrović, F. Skuban, D. M. Petrović, and M. Slankamenac, "Effect of copper on DC and AC conductivities of (As₂Se₃)-(AsI₃) glassy semiconductors", *Journal of Non-Crystalline Solids*, vol. 356, pp. 2409–2413, 2010.
- [15] A. Altındal, Ş. Abdurrahmanoğlu, M. Bulut, and Ö. Bekaroğlu, "Charge transport mechanism in bis(double-decker lutetium(III) phthalocyanine) (Lu₂Pc₄) thin film", *Synthetic Metals*, vol. 150, pp. 181–187, 2005.
- [16] N. Kılınç, S. Öztürk, L. Arda, A. Altındal, and Z. Z. Öztürk, "Structural, electrical transport and NO₂ sensing properties of Y-doped ZnO thin films", *Journal of Alloys and Compounds*, vol. 536, pp. 138–144, 2012.
- [17] W. Meyer and H. Neldel, "Über die beziehungen zwischen der energiekonstanten e under der mengenkonstanten a in der leitwerts - temperaturformel bei oxydischen halbleitern", *Z. Techn. Phys B*, vol. 18, pp. 588–593, 1937.
- [18] J. W. Niemantsverdriet, K. Markert, and K. Wandelt, "The compensation effect and the manifestation of lateral interactions in thermal desorption spectroscopy", *Applied Surface Science*, vol. 31, pp. 211–219, 1988.
- [19] W. Bogusz, D. E. Kony, and F. Krok, "Application of the Meyer-Neldel rule to the electrical conductivity of Nasicon", *Materials Science and Engineering B*, vol. 15, pp. 169–172, 1992.
- [20] P. H. Fang, "A model of Meyer-Neldel rule", *Physics Letters A*, vol. 30, pp. 217–218, 1969.
- [21] N. Koga and J. Sestak, "Kinetic compensation effect as a mathematical consequence of the exponential rate constant", *Thermochimica Acta*, vol. 182, pp. 201–208, 1991.
- [22] G. G. Roberts, "Thermally assisted tunnelling and pseudointrinsic conduction: two mechanisms to explain the Meyer-Neldel rule", *Journal of Physics C: Solid State Physics*, vol. 4, pp. 167–176, 1971.
- [23] M. H. Cohen, E. N. Economou, and C. M. Soukoulis, "Electron transport in amorphous semiconductors", *Journal of Non-Crystalline Solids*, vol. 66, pp. 285–290, 1984.
- [24] G. Kemeny and G. B. Rosenberg, "Small Polarons in Organic and Biological Semiconductors", *The Journal of Chemical Physics*, vol. 53, pp. 3549–3551, 1970.
- [25] S. R. Elliott, *Physics of Amorphous Materials*, 2nd ed., Longman Group UK Limited, England, 1990.
- [26] J. Stuke, "Problems in the understanding of electronic properties of amorphous silicon", *Journal of Non-Crystalline Solids*, vol. 97–98, pp. 1–14, 1987.
- [27] M. Kikuchi, "The Meyer-Neldel rule and the statistical shift of the Fermi level in amorphous semiconductors", *Journal of Applied Physics*, vol. 64, pp. 4997–5001, 1988.

	SAKARYA ÜNİVERSİTESİ FEN BİLİMLERİ ENSTİTÜSÜ DERGİSİ <i>SAKARYA UNIVERSITY JOURNAL OF SCIENCE</i>		
	e-ISSN: 2147-835X Dergi sayfası: http://www.saujs.sakarya.edu.tr		
	<u>Received</u> 10-11-2018 <u>Accepted</u> 28-02-2018	<u>Doi</u> 10.16984/saufenbilder.377081	

Asymptotic Analysis of an Affine Transformation in the Supply of Missing Data

Hülya Kodal Sevindir*¹, Cüneyt Yazıcı², Süleyman Çetinkaya¹

ABSTRACT

Supply of missing data, also known as inpainting, is an important application of image processing. Wavelets are commonly used for inpainting algorithms. Shearlet transform which is an affine transformation is the improvement of the wavelet transform. An asymptotic analysis may help to evaluate the performance of an algorithm. In this article we compare the asymptotical analysis for wavelet and shearlet transforms in the case of inpainting where the missing data is shaped like a rectangle.

Keywords: Shearlet transform, wavelet transform, inpainting, asymptotic analysis

1. INTRODUCTION

Efficient representation of multidimensional data is an important issue which is an active research area [1-4]. Among these studies, Shearlet transform, introduced in 2006 by Guo et al., is a mathematical transform obtained as an extension of wavelets which is well-known as a good representation of one-dimensional data. [5,6] One of the most valuable properties of shearlets is that in order to control directional selectivity, it has the shearing parameter instead of the direction parameter in the curvelets. Due to this difference, shearlet transform can be represented by only one or a finite number of generator functions. That is why it presents optimal sparse representation for the multidimensional data. Besides, we can use shearlets for functions with finite support, and

because of this transformation, we can obtain fast/superfast and effective algorithms. [10-14]

Inpainting problem is an inverse problem which is mainly concerned with finding some missing data in a signal or image. Missing data issue is a common problem in real life, and inpainting has many application areas: removing scratches or unwanted overlaid texts and graphics from old photos, or in general any image, etc.

Some of the recent publications are as following: In [15], Häuser and Ma uses a shearlet based algorithm to recover missing data from seismic data. In [16], King et al. studied data separation and reconstruction by using clustered sparsity. In [17], King, Kutyniok, and Zhuang examined inpainting problem via clustered sparsity and showed an asymptotic analysis for the issue presented in [15]. In [18], King et al. considered the inpainting problem with missing data having

* Corresponding Author: hkodal@kocaeli.edu.tr

¹ Department of Mathematics, Faculty of Arts and Sciences, University of Kocaeli, Turkey

² Department of Mathematics Education, Faculty of Education, University of Kocaeli, Turkey

different shapes except for horizontally positioned rectangle shape; but they did not show an asymptotic analysis. In this article we consider the inpainting problem which has missing data in a horizontally positioned rectangle shape and presents an asymptotic analysis for wavelet and shearlet transforms for this particular case. [19]

In Section 2 we give brief information on the theory of wavelets and shearlets. In Section 3 we introduce basic definitions and theorems which will be used for asymptotic analysis along with reconstruction model. In Section 4 we do the asymptotic analysis of the shearlet transform used for the particular inpainting problem described in Section 3.

2. PRELIMINARIES

2.1. Wavelet Transform

For 2-D wavelets let $\gamma \in L^2(\mathbb{R}^2)$. Let the continuous affine systems of $L^2(\mathbb{R}^2)$ be defined as $\gamma_{N,s} = T_s D_N^{-1} \gamma = |\det N|^{\frac{1}{2}} \gamma(N(-s))$; $(N, s) \in F \times \mathbb{R}^2$. $GL_2(\mathbb{R})$ is the group of invertible matrices and let F be a subset of it. Here D_N is the dilation operator on $L^2(\mathbb{R}^2)$ determined by $D_N \gamma(t) = |\det N|^{-\frac{1}{2}} \gamma(N^{-1}t)$, $N \in GL_2(\mathbb{R})$. T_s is the translation operator on $L^2(\mathbb{R}^2)$, defined by $T_s \gamma(t) = \gamma(t - s)$, $s \in \mathbb{R}^2$. Any $g \in L^2(\mathbb{R}^2)$ can be recovered from its coefficients $(\langle g, \gamma_{N,s} \rangle)_{N,s}$. Therefore, one needs to discover requirements on γ . We explain a group structure like (N, s) . $(N', s') = (NN', s + Ns')$ to determine this. This group is said to be affine group on \mathbb{R}^2 . It is denoted by A_2 [20].

Theorem 2.1. Let l_m be a left Haar measure of A_2 and l_i be a left invariant Haar measure on $F \subset GL_2(\mathbb{R})$. Moreover, suppose that $\gamma \in L^2(\mathbb{R}^2)$ satisfies the admissibility condition $\int_F |\hat{\gamma}(N^T \delta)|^2 |\det N| l_i(N) = 1$. Then any function $g \in L^2(\mathbb{R}^2)$ can be recovered via the reproducing formula $g = \int_{A_2} \langle g, \gamma_{N,s} \rangle \gamma_{N,s} d\theta(N, s)$ explained weakly.

When the hypothesis of the above theorem are satisfied, $\gamma \in L^2(\mathbb{R}^2)$ is called a continuous wavelet. Thus, $L^2(\mathbb{R}^2) \ni g \rightarrow W_\gamma g(N, s) = \langle g, \gamma_{N,s} \rangle$ is defined to be the Continuous Wavelet Transform.

2.2. Shearlet Transform

Shearlets has arisen in late times by various powerful applications. [21-24] shows some of the

associated work. For produce waveforms with anisotropic support is required the scaling operator. Suppose that dilation operator like in wavelets. We will use the dilation operators D_{B_b} , $b > 0$, related to parabolic scaling matrices $B_b = \begin{pmatrix} b & 0 \\ 0 & \sqrt{b} \end{pmatrix}$. The orientations of the waveforms can be changed by an orthogonal transformation. We select the shearing operator D_{C_c} , $c \in \mathbb{R}$, where the shearing matrix C_c is given by $C_c = \begin{pmatrix} 1 & c \\ 0 & 1 \end{pmatrix}$ for orthogonal transformation. The shearing matrix uses variable c associated with the slopes. Lastly, T_s is used for the translation operator. Thus, continuous shearlet system $SH(\gamma)$ can be defined by combining these 3 operators for $\gamma \in L^2(\mathbb{R}^2)$: $SH(\gamma) = \{\gamma_{b,c,s} = T_s D_{B_b} D_{C_c} \gamma : b > 0, c \in \mathbb{R}, s \in \mathbb{R}^2\}$.

3. BASIC DEFINITIONS AND THEOREMS

In this section, we introduce some fundamental definitions and theorems which will be used later. Meyer wavelet function will be used for wavelet transformation. Auxilliary function $v \in C^\infty(\mathbb{R})$ which satisfies $v(\cdot) + v(1 - \cdot) = \mathbb{1}_{\mathbb{R}}(\cdot)$ to form Meyer wavelet function is defined as

$$v(x) = \begin{cases} 0, & x \leq 0 \\ x, & 0 < x < 1 \\ 1, & x \geq 1 \end{cases} \quad (1)$$

Indicator function $\mathbb{1}_{\mathbb{R}}(\cdot)$ is defined as $\mathbb{1}_A(x) = \begin{cases} 1, & x \in A \\ 0, & x \in A^c \end{cases}$. Meyer wavelet $\psi(\omega)$ is defined as

$$\psi(\omega) = \begin{cases} \frac{1}{\sqrt{2\pi}} \sin\left(\frac{\pi}{2} v\left(\frac{3|\omega|}{2\pi} - 1\right)\right) e^{j\omega/2}, & 2\pi/3 < |\omega| < 4\pi/3 \\ \frac{1}{\sqrt{2\pi}} \cos\left(\frac{\pi}{2} v\left(\frac{3|\omega|}{4\pi} - 1\right)\right) e^{j\omega/2}, & 4\pi/3 < |\omega| < 8\pi/3 \\ 0, & \text{otherwise} \end{cases} \quad (2)$$

Fourier transformation of 1-D Meyer wavelet function is then

$$W(\xi) = \begin{cases} e^{-\pi i \xi} \sin\left[\frac{\pi}{2} v(3|\xi| - 1)\right], & 1/3 \leq \xi \leq 2/3 \\ e^{-\pi i \xi} \cos\left[\frac{\pi}{2} v\left(\frac{3}{2}|\xi| - 1\right)\right], & 2/3 \leq \xi \leq 4/3 \\ 0, & \text{otherwise} \end{cases} \quad (3)$$

1-D Meyer scaling function is

$$\phi(\omega) = \begin{cases} \frac{1}{\sqrt{2\pi}}, & |\omega| < 2\pi/3 \\ \frac{1}{\sqrt{2\pi}} \cos\left(\frac{\pi}{2} v\left(\frac{3|\omega|}{2\pi} - 1\right)\right) e^{j\omega/2}, & 2\pi/3 < |\omega| < 4\pi/3 \\ 0, & \text{otherwise.} \end{cases} \quad (4)$$

Fourier transformation of 1-D Meyer scaling function is

$$\hat{\phi}(\xi) = \begin{cases} 1, & |\xi| \leq \frac{1}{3} \\ \cos\left[\frac{\pi}{2}v(3|\xi| - 1)\right], & \frac{1}{3} \leq |\xi| \leq \frac{2}{3} \\ 0, & \text{otherwise.} \end{cases} \quad (5)$$

Fourier transformation for $f \in L^1(\mathbb{R}^n)$ is $\mathcal{F}f := \hat{f} = \int_{\mathbb{R}^n} f(x)e^{-2\pi i \langle \cdot, x \rangle} dx$. Here, $\langle \cdot, \cdot \rangle$ stands for standard Euclidian inner product. Inverse Fourier transformation is defined as $\mathcal{F}^{-1}f := \check{f} = \int_{\mathbb{R}^n} f(\xi)e^{-2\pi i \langle \cdot, \xi \rangle} d\xi$. When W^h stands for wavelet function to investigate horizontal mask case, function $W^h \in C^\infty \cap L^2(\mathbb{R}^2)$ is defined as $W^h(\xi) = W(\xi_1)\hat{\phi}(\xi_2)$. Orthonormal Meyer wavelet system is defined as $\{\psi_\lambda\}: \lambda = (\iota, j, k), \iota \in \{h, v, d\}, j \in \mathbb{Z}, k \in \mathbb{Z}^2$ and function $\hat{\psi}_\lambda(\xi)$ is defined as $\hat{\psi}_\lambda(\xi) = 2^{-j}W^\iota(\xi/2^j)e^{-2\pi i k \xi/2^j}$, $\lambda = (\iota, j, k)$. Parabolic scaling matrix A_a^h and shear matrix S_s^h are defined as $A_a^h = \begin{pmatrix} a & 0 \\ 0 & \sqrt{a} \end{pmatrix}$ and $S_s^h = \begin{pmatrix} 1 & s \\ 0 & 1 \end{pmatrix}$. Shearlet function $\hat{\sigma}^h$ is defined as $\hat{\sigma}^h(\xi_1, \xi_2) = W(\xi_1)V\left(\frac{\xi_2}{\xi_1}\right)$. Function $V \in L^2(\mathbb{R})$ satisfies $\hat{V} \in C^\infty(\mathbb{R})$, $\text{supp } \hat{V} \subseteq [-1, 1]$ and $\sum_{k=-1}^1 |\hat{V}(\xi + \pi k)|^2 = 1, \xi \in [-1, 1]$. Notation $\hat{\sigma}_\eta$ is defined as $\hat{\sigma}_\eta = 2^{3j/4} \sigma^\iota(S_\iota^t A_{2^j}^\iota \cdot -k)$, $\eta = (\iota, j, k, \ell)$. Here, $\iota \in \{h, v\}, j \in \mathbb{Z}, k \in \mathbb{Z}^2, \ell \in \mathbb{Z}$. In this case shearlet system can be defined as $\{\phi(\cdot - k): k \in \mathbb{Z}^2\} \cup \{\sigma_\eta: \iota \in \{h, v\}, j \in \mathbb{Z}, j \geq 0, k \in \mathbb{Z}^2, \text{ and } \ell \in \mathbb{Z}, |\ell| \leq \lfloor 2^{j/2} \rfloor\}$. Here, $\lfloor x \rfloor$ stands for an integer larger than or equal to x .

3.1. Reconstruction Model

Modeling the reconstruction stage is highly important. To do so, let \mathcal{H} stand for Hilbert space, \mathcal{H}_M stand for the lost part and \mathcal{H}_K stand for the known part. Then we can write $\mathcal{H} = \mathcal{H}_M \oplus \mathcal{H}_K$. For a given signal $x^0 \in \mathcal{H}$, the unknown part of x^0 will be in the subspace \mathcal{H}_M and the known part of x^0 will be in the subspace \mathcal{H}_K . P_M and P_K show corresponding orthogonal projection transformations for these subspaces. In this case recovery problem is formulated as recovering x^0 from the known $P_K x^0$. To do so, iterative thresholding will be used. During inpainting applications, recovered image sequences $(f_j)_j$ will be obtained by $(f_j)_j = (P_{\mathcal{R}^2/\mathcal{M}_k} w\mathcal{L}_j)_j$. Thresholding determination stage is done as follows: For thresholding value β_j at level j , we consider the set $\mathcal{T}_j = \{i: |\langle f_j, \phi_i \rangle| \geq \beta_j\}$ and apply iterative thresholding. In this case, recovered image at level j is obtained as $L_j = \Phi \mathbb{1}_{\mathcal{T}_j} \Phi^* w\mathcal{L}_j$. Vectors $\Phi = \{\phi_i\}_{i \in I}$ in \mathcal{H} generates a Parseval frame for \mathcal{H} if for every $x \in \mathcal{H}$, $\sum_{i \in I} |\langle x, \phi_i \rangle|^2 = \|x\|^2$.

Definition 3.1. [17] If Φ is a Parseval frame and Λ is an index set of coefficients, then the concentration is defined on \mathcal{H}_M via $\kappa = \kappa(\Lambda, \mathcal{H}_M) = \sup_{f \in \mathcal{H}_M} \frac{\|\mathbb{1}_\Lambda \Phi^* f\|_1}{\|\Phi^* f\|_1}$.

Definition 3.2. [17] Let $\Phi_1 = \{\phi_{1i}\}_{i \in I}$ and $\Phi_2 = \{\phi_{2j}\}_{j \in J}$ be in \mathcal{H} . Let $\Lambda \subseteq I$. Then the cluster coherence $\mu_c(\Lambda, \Phi_1; \Phi_2)$ of Φ_1 and Φ_2 with respect to Λ can be defined by $\mu_c(\Lambda, \Phi_1; \Phi_2) = \max_{j \in J} \sum_{i \in \Lambda} |\langle \phi_{1i}, \phi_{2j} \rangle|$.

Lemma 3.1. [17] The relation between the concentration $\kappa(\Lambda, \mathcal{H}_M)$ and cluster coherence μ_c can be obtained like that $\kappa(\Lambda, \mathcal{H}_M) \leq \mu_c(\Lambda, P_M \Phi; P_M \Phi) = \mu_c(\Lambda, P_M \Phi; \Phi)$.

Lemma 3.2. [17] Let x^* and \mathcal{T} be computed by the horizontal mask algorithm when $\delta > 0$. Consider that x^0 is relatively sparse in Φ with respect to \mathcal{T} . Then $\|x^* - x^0\|_2 \leq c[\delta + \|\mathbb{1}_{\mathcal{T}} \Phi^* P_M x^0\|_1]$.

Let $w: \mathbb{R} \rightarrow [0, 1]$ be a smooth function having finite support in $[-\rho, \rho]$. Let L show the real image and $w\mathcal{L}$ show the recovered image. We can use the following relation to see the effect of $w\mathcal{L}$ on the recovery model: $\langle w\mathcal{L}, f \rangle = \int_{-\rho}^{\rho} w(x_2) f(0, x_2) dx_2$. Here, 2ρ corresponds to the height of the horizontal rectangle (See Figure 4.1). Fourier transformation of $w\mathcal{L}$ is defined as $\langle \widehat{w\mathcal{L}}, f \rangle = \langle w\mathcal{L}, \hat{f} \rangle = \int_{\mathbb{R}} w(\xi_2) \int_{\mathbb{R}} f(\xi_1, \xi_2) d\xi_2 d\xi_1$. Let \check{F}_j be the filter corresponding to 2-D Meyer wavelet function and shearlet function at level j . Fourier transformation of this filter is defined as $F_j = \sum_{\iota \in \{h, v, d\}} W^\iota(2^{-j}\xi)$. The filter of $w\mathcal{L}$ is denoted as $w\mathcal{L}_j$. Thus, we obtain $w\mathcal{L}_j = w\mathcal{L} * \check{F}_j = \int_{\mathbb{R}^2} w\mathcal{L}(\cdot - t) \check{F}_j(t) dt$. This equation corresponds to cross-correlation. The lemma below lets us to evaluate norm of $w\mathcal{L}_j$.

Lemma 3.3. [17] For any $c > 0$, $\|w\mathcal{L}_j\|_2 \geq c2^{j/2}$ is obtained as $j \rightarrow \infty$.

4. ASYMPTOTIC ANALYSIS OF HORIZONTAL MASK APPLICATION

To get precise error analysis, we first apply a mask function to an image so that some parts of the data is missing.

Let the function $\mathcal{M}_h(x_1, x_2) = \mathbb{1}_{\{|x_2| \leq h\}}$ be horizontal mask function with height $2h$. The mask function \mathcal{M}_h is shown in Figure 4.1.

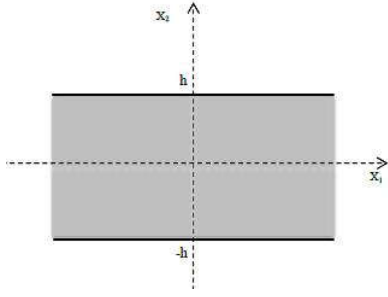


Figure 4.1 The image of horizontal mask function \mathcal{M}_h

Lemma 4.1. Fourier transformation $\widehat{\mathcal{M}}_h$ of the horizontal mask function \mathcal{M}_h can be written as $\widehat{\mathcal{M}}_h = 2h \text{sinc}(2h\xi_2) \delta(\xi_1)$.

Proof. The horizontal mask function \mathcal{M}_h can be described by the Heaviside function as $\mathcal{M}_h = H((x_1, x_2) + (0, h)) - H((x_1, x_2) - (0, h))$. From this equality, Fourier transformation $\widehat{\mathcal{M}}_h$ of the horizontal mask function \mathcal{M}_h can be written as explicitly

$$\begin{aligned} \widehat{\mathcal{M}}_h &= (e^{2\pi i h \xi_2} - e^{-2\pi i h \xi_2}) (2\pi i \xi_2)^{-1} \int_{-\infty}^{\infty} e^{-2\pi i x_1 \xi_1} dx_1 \\ &= 2 \sin(2\pi h \xi_2) / (2\pi \xi_2) \int_{-\infty}^{\infty} e^{-2\pi i x_1 \xi_1} dx_1 \\ &= 2h \text{sinc}(2h \xi_2) \int_{-\infty}^{\infty} e^{-2\pi i x_1 \xi_1} dx_1 \\ &= 2h \text{sinc}(2h \xi_2) \delta(\xi_1). \end{aligned} \quad (6)$$

We can represent the optimal δ -clustered sparsity by δ_j for filtered coefficients. Thresholding schemes will analyzed by $\delta_j = \sum_{\lambda \in \mathcal{T}_j^c} |\langle w\mathcal{L}_j, \Psi_\lambda \rangle|$ where the \mathcal{T}_j coefficients are obtained in the thresholding algorithm. The inpainting achieved on the filtered levels j will be denoted by L_j . Here, we will denote the real filtered image by $w\mathcal{L}_j$; that is, $w\mathcal{L} \star \check{F}_j$, where we will denote the original image by \mathcal{L} . Thus, the basic theorems will show that $\frac{\|L_j - w\mathcal{L}_j\|_2}{\|w\mathcal{L}_j\|_2} \rightarrow 0, j \rightarrow \infty$. Here, the asymptotic behavior of the gap h_j is important for these results.

Lemma 4.2. [17] For $j \rightarrow \infty$ and $h_j = o(2^{-j})$, thresholding values $\{\beta_j\}_j$ exist such that for $j \geq j_0$, $\{k: |k_1| \leq \rho 2^{j(1+n_1)}, |k_2| \leq \rho 2^{jn_1}\} \subseteq \mathcal{T}_j$ holds.

Lemma 4.3. [17] For $j \rightarrow \infty$ we obtain $\delta_j = \sum_{k \in \mathcal{T}_j^c} |\langle w\mathcal{L}_j, \Psi_\lambda \rangle| = o(\|w\mathcal{L}_j\|_2)$.

Lemma 4.4. For $j \rightarrow \infty$ and $h_j = o(2^{-j})$ we obtain $\sum_{k \in \mathcal{T}_j} |\langle \widehat{\mathcal{M}}_h w\mathcal{L}_j, \Psi_\lambda \rangle| = o(2^{j/2})$.

Proof. First let us evaluate the term $|\langle \mathcal{M}_{h_j} w\mathcal{L}_j, \Psi_\lambda \rangle|$. Let G_j be the inverse Fourier transformation of F_j . From the cross-correlation theorem and the property $G_j(x) = G_j(-x)$, we have $\langle \widehat{\mathcal{M}}_h \star \widehat{w\mathcal{L}}_j, \widehat{\Psi}_\lambda \rangle = \langle \mathcal{M}_h w\mathcal{L}_j, \Psi_\lambda \rangle$. Thus we obtain $\langle \mathcal{M}_h w\mathcal{L}_j, \Psi_\lambda \rangle = \langle \mathcal{M}_h G_j \star w\mathcal{L}, \Psi_\lambda \rangle = \langle \mathcal{M}_h w\mathcal{L}, G_j \star \Psi_\lambda \rangle = \langle \widehat{\mathcal{M}}_h \star \widehat{w\mathcal{L}}, F_j \widehat{\Psi}_\lambda \rangle$. For filter functions we get $\widehat{w\mathcal{L}}_j(\xi) = \widehat{w\mathcal{L}}(\xi) F_j(\xi) = \widehat{w\mathcal{L}}(\xi) F(\xi/2^j)$.

Function $\widehat{\Psi}_\lambda$ can be written as $\widehat{\Psi}_\lambda = 2^{-j} W^h(\xi/2^j) e^{-2\pi i \langle k, \xi/2^j \rangle}$. We then obtain

$$\begin{aligned} \langle \mathcal{M}_{h_j} w\mathcal{L}_j, \Psi_\lambda \rangle &= \langle \widehat{\mathcal{M}}_h \star \widehat{w\mathcal{L}}_j, \widehat{\Psi}_\lambda \rangle \\ &= 2h_j \int_{\mathbb{R}^2} \text{sinc}(2h_j \tau_2) \int_{\mathbb{R}^2} \widehat{w}(\xi_2) (\widehat{\Psi}_\lambda F_j)((0, \tau_2) \\ &\quad + (\xi_1, \xi_2)) d\xi d\tau_2 \\ &= 2h_j \int_{\mathbb{R}} \left[\widehat{w}(\xi_2) \int_{\mathbb{R}} \text{sinc}(2h_j \tau_2) F(\xi_1, (\xi_2 + \tau_2)/2^j) \right. \\ &\quad \times W^h(\xi_1, (\xi_2 + \tau_2)/2^j) e^{-2\pi i \langle k_2, (\xi_2 + \tau_2)/2^j \rangle} d\tau_2 d\xi_2 \\ &\quad \left. \times e^{-2\pi i \langle k_1, \xi_1 \rangle} d\xi_1 \right] \end{aligned} \quad (7)$$

From here, we get

$$\begin{aligned} \widehat{G}(\xi_1) &= \int_{\mathbb{R}} \widehat{w}(\xi_2) 2h_j \int_{\mathbb{R}} \text{sinc}(2h_j \tau_2) F(\xi_1, (\xi_2 + \tau_2)/2^j) \times \\ &\quad W^h(\xi_1, (\xi_2 + \tau_2)/2^j) e^{-2\pi i \langle k_2/2^j, (\xi_2 + \tau_2) \rangle} d\tau_2 d\xi_2 = \\ &= \int_{\mathbb{R}} \widehat{w}(\xi_2) \widehat{H}_{\xi_1}(\xi_2) e^{-2\pi i \langle k_2/2^j, \xi_2 \rangle} d\xi_2 \end{aligned} \quad (8)$$

and

$$\begin{aligned} \widehat{H}_{\xi_1}(\xi_2) &= 2h_j \int_{\mathbb{R}} \text{sinc}(2h_j \tau_2) F(\xi_1, (\xi_2 + \tau_2)/2^j) \\ &\quad \times W^h(\xi_1, (\xi_2 + \tau_2)/2^j) e^{-2\pi i \langle k_2, (\xi_2 + \tau_2)/2^j \rangle} d\tau_2. \end{aligned} \quad (9)$$

Finite support of function \widehat{G} will be the set $[1/2, 2]$. From this, we obtain $|\langle \mathcal{M}_{h_j} w\mathcal{L}_j, \Psi_\lambda \rangle| \leq c N_1 \|\widehat{G}\|_\infty \langle |k_1| \rangle^{-N_1}$. By Plancherel theorem and w having finite support, we obtain

$$\begin{aligned} \left| \int_{\mathbb{R}} \widehat{w}(\xi_2) \widehat{H}_{\xi_1}(\xi_2) e^{-2\pi i \langle k_2/2^j, \xi_2 \rangle} d\xi_2 \right| &= \left| (\widehat{w\mathcal{L}}_{\xi_1})^V \right| (-k_2/2^j) = \\ &= \left| (w \star H_{\xi_1})(-k_2/2^j) \right| = \left| \int w(-k_2/2^j - x) H_{\xi_1}(x) dx \right| \approx \\ &= c \left| \int_{-k_2/2^j - \rho}^{-k_2/2^j + \rho} H_{\xi_1}(x) dx \right| \end{aligned} \quad (10)$$

By using basic properties of Fourier transformation and cross-correlation theorem, we can write H_{ξ_1} as follows:

$$\begin{aligned} H_{\xi_1}(x) &= \left((2h_j \text{sinc}(2h_j \cdot)) e^{-2\pi i k_2/2^j} \right) \\ &\quad \star \left(F W^h(\xi_1, \cdot/2^j) \right)^V (-x) \end{aligned}$$

$$\begin{aligned}
 &= (2h_j \text{sinc}(2h_j \cdot) e^{-2\pi i k_2 / 2^j})^V (-x) \\
 &= ((FW^h)(\xi_1, \cdot / 2^j))^V (-x) \\
 &= \mathbb{1}_{[-h_j, h_j]}(-x - k_2 / 2^j) ((FW^h)(\xi_1, \cdot / 2^j))^V (-x) \quad (11)
 \end{aligned}$$

From here, when $h_j < \rho$, we obtain

$$\begin{aligned}
 & \left| \int_{-k_2/2^j-\rho}^{-k_2/2^j+\rho} H_{\xi_1}(x) dx \right| = \\
 & c \left| \int_{k_2/2^j-h_j}^{k_2/2^j+h_j} ((FW^h)(\xi_1, \cdot / 2^j))^V(x) dx \right| = \\
 & c \left| \int_{k_2-2^j h_j}^{k_2+2^j h_j} ((FW^h)(\xi_1, \cdot))^V(x) dx \right|. \quad (12)
 \end{aligned}$$

Thus by considering $|(FW^h)(\cdot)|^V(x) \leq c \langle |x| \rangle^{-N_2}$, we obtain

$$\|\hat{G}\|_{\infty} \leq c \langle \min\{|k_2 - 2^j h_j|, |k_2 + 2^j h_j|\} \rangle^{-N_2}. \quad (13)$$

Combining all these considerations, we obtain

$|\langle \mathcal{M}_{h_j} w \mathcal{L}_j, \Psi_{\lambda} \rangle| \leq c \langle |k_1| \rangle^{-N_1} \langle \min\{|k_2 - 2^j h_j|, |k_2 + 2^j h_j|\} \rangle^{-N_2}$. By using Lemma 4.2, as a result we obtain

$$\sum_{k \in \mathcal{T}_j} |\langle \mathcal{M}_{h_j} w \mathcal{L}_j, \Psi_{\lambda} \rangle| \leq c \sum_{k \in \mathcal{T}_j} \langle |k_1| \rangle^{-N_1} \langle \min\{|k_2 - 2^j h_j|, |k_2 + 2^j h_j|\} \rangle^{-N_2} \leq c \quad (14)$$

Expected convergence for normalized error ℓ_2 of reconstructed filter L_j can be obtained using iterative method via wavelet transformation by the following theorem.

Theorem 4.1. Consider 2-D Meyer orthonormal system Φ with the filter L_j for $h_j = o(2^{-j})$. Then $\frac{\|L_j - w \mathcal{L}_j\|_2}{\|w \mathcal{L}_j\|_2} \rightarrow 0, j \rightarrow \infty$ holds.

Proof. By letting $x^* = L_j$ and $x^0 = w \mathcal{L}_j$ in the Lemma 3.2, we obtain

$$\begin{aligned}
 \|L_j - w \mathcal{L}_j\|_2 &= \|\Phi \mathbb{1}_{\mathcal{T}^c} \Phi^* P_K w \mathcal{L}_j - \Phi \mathbb{1}_{\mathcal{T}} \Phi^* P_M w \mathcal{L}_j\|_2 = \\
 & \left\| \sum_{k \in \mathcal{T}_j^c} |\langle w \mathcal{L}_j, \Psi_{\lambda} \rangle| - \sum_{k \in \mathcal{T}_j} |\langle \mathcal{M}_{h_j} w \mathcal{L}_j, \Psi_{\lambda} \rangle| \right\|_2 \leq \\
 & \left\| \sum_{k \in \mathcal{T}_j^c} |\langle w \mathcal{L}_j, \Psi_{\lambda} \rangle| \right\|_2 + \left\| \sum_{k \in \mathcal{T}_j} |\langle \mathcal{M}_{h_j} w \mathcal{L}_j, \Psi_{\lambda} \rangle| \right\|_2 < \\
 & \underbrace{o(\|w \mathcal{L}_j\|_2)}_{\text{Lemma 4.3}} + \underbrace{c 2^{j/2}}_{\text{Lemma 4.4}} \quad (15)
 \end{aligned}$$

From Lemma 3.3, we obtain

$$\frac{\|L_j - w \mathcal{L}_j\|_2}{\|w \mathcal{L}_j\|_2} < \frac{o(\|w \mathcal{L}_j\|_2)}{\|w \mathcal{L}_j\|_2} + c_1 2^{-j/2} \rightarrow 0, j \rightarrow \infty \quad (16)$$

Similar to the wavelet transformation case above, expected convergence for normalized error ℓ_2 of

reconstructed filter L_j can be obtained by the following steps: We consider the set $\mathcal{T}_j := \{\eta = (i, j, \ell, k) : |\langle w \mathcal{L}_j, \sigma_{\eta} \rangle| \geq \beta_j\}$ of coefficients of thresholding values for $\beta_j > 0$.

Lemma 4.5. [17] For all $j \geq j_0$ and for some values j_0, v_1 and $v_2 < 1/4$, thresholding coefficients $\{\beta_j\}_j$ exist as follows: $\{(i, j, \ell, k) : |k_1| \leq \rho 2^{j(1+v_1)}, |k_2| \leq \rho 2^{jv_2}, \ell = 0; i = v\} \subseteq \mathcal{T}_j$. For $h_j = o(2^{-j/2})$ when $j \rightarrow \infty$.

Lemma 4.6. [17] When $j \rightarrow \infty$, we obtain $\sum_{\eta \in \mathcal{T}_j^c} |\langle w \mathcal{L}_j, \sigma_{\eta} \rangle| = o(2^{j/2})$

Lemma 4.7. When $j \rightarrow \infty$ for $h_j = o(2^{-j/2})$, we obtain $\sum_{\eta \in \mathcal{T}_j^c} |\langle \mathcal{M}_{h_j} w \mathcal{L}_j, \sigma_{\eta} \rangle| = o(2^{j/2}), j \rightarrow \infty$.

Proof. First, evaluation of $|\langle \mathcal{M}_{h_j} w \mathcal{L}_j, \sigma_{j, \ell, k}^i \rangle|$ is needed. Similar to the proof of Lemma 4.4, by using definitions of $\mathcal{M}_{h_j}, w \mathcal{L}_j, \sigma_{j, \ell, k}^i$, and cross-correlation theorem, we obtain

$$\begin{aligned}
 & \langle \mathcal{M}_{h_j} w \mathcal{L}_j, \sigma_{j, \ell, k}^i \rangle \\
 &= 2^{j/4} \int \int \hat{w}(\xi_2) 2h_j \int \text{sinc}(2h_j \tau_2) F\left(\xi_1, \frac{\xi_2}{2^j}\right) \\
 & \times W\left(\xi_1, \xi_2 / 2^j\right) V\left(\ell + 2^{-j/2} \frac{\tau_2 + \xi_2}{\xi_1}\right) \\
 & \times e^{-2\pi i b_2(\tau_2 + \xi_2)} d\tau_2 d\xi_2 \\
 & \times e^{-2\pi i(\xi_1, 2^j b_1)} d\xi_1 \quad (17)
 \end{aligned}$$

The function \hat{G} is defined as

$$\begin{aligned}
 \hat{G}(\xi_1) &= \int \hat{w}(\xi_2) 2h_j \int \text{sinc}(2h_j \tau_2) F\left(\xi_1, \frac{\xi_2}{2^j}\right) W\left(\xi_1, \xi_2 / 2^j\right) \\
 & V\left(\ell + 2^{-j/2} \frac{\tau_2 + \xi_2}{\xi_1}\right) \times e^{-2\pi i(b_2, \tau_2 + \xi_2)} d\tau_2 d\xi_2 \quad (18)
 \end{aligned}$$

This function has finite support on the set $[1/2, 2]$. From here, we obtain $|\langle \mathcal{M}_{h_j} w \mathcal{L}_j, \sigma_{j, \ell, k}^i \rangle| \leq c_{N_1} 2^{j/4} \|\hat{G}\|_{\infty} \langle |k_1| \rangle^{-N_1}$. The function \hat{H}_{ξ_1} is defined as

$$\begin{aligned}
 \hat{H}_{\xi_1}(\xi_2) &= 2h_j \int \text{sinc}(2h_j \tau_2) F\left(\xi_1, \xi_2 / 2^j\right) W\left(\xi_1, \xi_2 / 2^j\right) \\
 & V\left(\ell + 2^{-j/2} \frac{\tau_2 + \xi_2}{\xi_1}\right) \times e^{-2\pi i(b_2, \tau_2 + \xi_2)} d\tau_2 \quad (19)
 \end{aligned}$$

Let us investigate the norm $\|\hat{G}\|_{\infty}$:

$$\|\hat{G}\|_{\infty} = \left| \int \hat{w}(\xi_2) \hat{H}_{\xi_1}(\xi_2) e^{-2\pi i(b_2, \xi_2)} d\xi_2 \right| \quad (20)$$

By using Plancherel theorem and w having finite support, we obtain

$$\left| \int \widehat{w}(\xi_2) \widehat{H}_{\xi_1}(\xi_2) e^{-2\pi i \langle b_2, \xi_2 \rangle} d\xi_2 \right| = \left| (\widehat{w} \widehat{H}_{\xi_1})^V(-b_2) \right| \approx \frac{1}{c} \sum_{\eta \in \mathcal{T}_j} \left| \langle \mathcal{M}_{h_j} w \mathcal{L}_j, \sigma_\eta \rangle \right| \leq 2^{j/4} \sum_{\eta \in \mathcal{T}_j} \langle |k_1| \rangle^{-N_1} \langle \min \{ |k_2 - 2^{j/2} h_j|, |k_2 + 2^{j/2} h_j| \} \rangle^{-N_2} \leq 2^{j(1/4+v_2)} \quad (28)$$

From here, we obtain

$$H_{\xi_1}(x) = \left((2h_j \operatorname{sinc}(2h_j \cdot) e^{-2\pi i b_2}) \star \left(F(\xi_1, \cdot/2^j) W(\xi_1, \cdot/2^j) V(\ell + 2^{-j/2}(\cdot/\xi_1)) \right) \right)^V(-x) = (2h_j \operatorname{sinc}(2h_j \cdot) e^{-2\pi i b_2})^V(-x) \times \left(F(\xi_1, \cdot/2^j) W(\xi_1, \cdot/2^j) V(\ell + 2^{-j/2}(\cdot/\xi_1)) \right)^V(-x) = \mathbb{1}_{[-h_j, h_j]}(-x - b_2) \times \left(F(\xi_1, \cdot/2^j) W(\xi_1, \cdot/2^j) V(\ell + 2^{-j/2}(\cdot/\xi_1)) \right)^V(-x) \quad (22)$$

Thus when $h_j < \rho$, we obtain

$$\left| \int_{-b_2-\rho}^{-b_2+\rho} H_{\xi_1}(x) dx \right| = \left| \int_{b_2-h_j}^{b_2+h_j} \left(F(\xi_1, \cdot/2^j) W(\xi_1, \cdot/2^{j/2}) V(\ell + 2^{-j/2}(\cdot/\xi_1)) \right)^V(-x) dx \right| = \left| \int_{2^{j/2}(b_2-h_j)}^{2^{j/2}(b_2+h_j)} \left(F(\xi_1, \cdot/2^{j/2}) W(\xi_1, \cdot/2^{j/2}) \times V(\ell + (\cdot/\xi_1)) \right)^V(-x) dx \right| \quad (23)$$

and when $(k, \ell) \in \mathcal{T}_j$, we obtain

$$\left| \int_{-b_2-\rho}^{-b_2+\rho} H_{\xi_1}(x) dx \right| = \left| \int_{k_2-2^{j/2}h_j}^{k_2+2^{j/2}h_j} \left(F(\xi_1, \cdot/2^{j/2}) W(\xi_1, \cdot/2^{j/2}) \times V(\ell + (\cdot/\xi_1)) \right)^V(-x) dx \right| \quad (24)$$

From here considering the evaluation

$$\left| \left(F(\xi_1, \cdot/2^{j/2}) W(\xi_1, \cdot/2^{j/2}) V(\ell + (\cdot/\xi_1)) \right)^V(-x) \right| \leq c \langle |x| \rangle^{-N_2} \quad (25)$$

from previous calculations, we obtain

$$\|\widehat{G}\|_\infty \leq c \langle \min \{ |k_2 - 2^{j/2} h_j|, |k_2 + 2^{j/2} h_j| \} \rangle^{-N_2} \quad (26)$$

By combining all these evaluations, we obtain

$$\left| \langle \mathcal{M}_{h_j} w \mathcal{L}_j, \sigma_{j,\ell,k}^h \rangle \right| \leq c 2^{j/4} \langle |k_1| \rangle^{-N_1} \langle \min \{ |k_2 - 2^{j/2} h_j|, |k_2 + 2^{j/2} h_j| \} \rangle^{-N_2} \quad (27)$$

Thus finally when $v_2 < 1/4$ from Lemma 4.5, we obtain

As in the wavelet transformation case above, expected convergence for normalized error ℓ_2 of reconstructed filter L_j can be obtained using iterative method via shearlet transformation by the following theorem.

Theorem 4.2. Consider filter L_j for $h_j = o(2^{-j/2})$ with 2-D shearlet system Φ . Then

$$\frac{\|L_j - w \mathcal{L}_j\|_2}{\|w \mathcal{L}_j\|_2} \rightarrow 0, \quad j \rightarrow \infty \text{ holds.}$$

Proof. Similarly by letting $x^* = L_j$ and $x^0 = w \mathcal{L}_j$ in the Lemma 3.2, we obtain

$$\|L_j - w \mathcal{L}_j\|_2 = \|\Phi \mathbb{1}_{\mathcal{T}^c} \Phi^* P_K w \mathcal{L}_j - \Phi \mathbb{1}_{\mathcal{T}} \Phi^* P_M w \mathcal{L}_j\|_2 = \left\| \sum_{\eta \in \mathcal{T}^c} \langle w \mathcal{L}_j, \sigma_\eta \rangle - \sum_{\eta \in \mathcal{T}} \langle \mathcal{M}_{h_j} w \mathcal{L}_j, \sigma_\eta \rangle \right\|_2 \leq \left\| \sum_{\eta \in \mathcal{T}^c} \langle w \mathcal{L}_j, \sigma_\eta \rangle \right\|_2 + \left\| \sum_{\eta \in \mathcal{T}} \langle \mathcal{M}_{h_j} w \mathcal{L}_j, \sigma_\eta \rangle \right\|_2 < \underbrace{o(2^{j/2})}_{\text{Lemma 4.6}} + \underbrace{o(2^{j/2})}_{\text{Lemma 4.7}} \quad (29)$$

From Lemma 3.3, we obtain

$$\frac{\|L_j - w \mathcal{L}_j\|_2}{\|w \mathcal{L}_j\|_2} < \frac{o(2^{j/2})}{\|w \mathcal{L}_j\|_2} + \frac{o(2^{j/2})}{\|w \mathcal{L}_j\|_2} \rightarrow 0, \quad j \rightarrow \infty \quad (30)$$

Thus, we prove that the image can be reconstructed well asymptotically, when the height of the horizontal mask decays faster than $2^{-j/2}$.

5. CONCLUSION

In this paper, we show the asymptotic analysis of wavelet and shearlet transforms used for the inpainting where the missing data have a horizontal rectangle shape. As a conclusion, we found out that the shearlet transformation is more effective for the problem discussed than the wavelet transform. If the height of the horizontal mask decays faster than $2^{-j/2}$, we proved that the image can be reconstructed asymptotically.

REFERENCES

- [1] R. H., Bamberger and M. J. T., Smith, "A Filter Bank for the Directional Decomposition of Images: Theory and

- Design”, *IEEE Trans. Signal Process.*, 40, 882–893, 1992.
- [2] J. P., Antoine, P., Carrette, R., Murenzi and B., Piette, “Image Analysis with Two-dimensional Continuous Wavelet Transform”, *Signal Process.*, 31, 241–272, 1993.
- [3] E. J., Candès and D. L., Donoho, “New Tight Frames of Curvelets and Optimal Representations of Objects with Piecewise C^2 Singularities”, *Comm. Pure Appl. Math.*, 57, 219–266, 2002.
- [4] M. N., Do and M., Vetterli, “The Contourlet Transform: an Efficient Directional Multiresolution Image Representation”, *IEEE Trans. Image Process.*, 14, 2091–2106, 2005.
- [5] K., Guo, G., Kutyniok and D., Labate, “Sparse Multidimensional Representations Using Anisotropic Dilation and Shear Operators, Editors: G. Chen and M. J., Lai ” *Wavelets and Splines: Athens 2005*, Nashboro Press, Nashville, 189–201, 2006.
- [6] D., Labate, W. Q., Lim, G., Kutyniok, and G., Weiss, “Sparse Multidimensional Representation Using Shearlets”, in *Wavelets XI, Edited by M. Papadakis, A. F. Laine, and M. A. Unser, SPIE Proc.*, 5914, 254–262, 2005.
- [7] K., Guo, D., Labate, W. Q., Lim, G., Weiss and E., Wilson, “Wavelets with Composite Dilations”, *Electron. Res. Announc. Amer. Math. Soc.*, 10, 78–87, 2004.
- [8] K., Guo, D., Labate, W. Q., Lim, G., Weiss and E., Wilson, “The Theory of Wavelets with Composite Dilations, Editors: C. Heil”, *Harmonic Analysis and Applications*, Birkhauser, Boston, 231–250, 2006.
- [9] K., Guo, W.Q., Lim, D., Labate, G., Weiss and E., Wilson, “Wavelets with Composite Dilations and Their MRA Properties”, *Appl. Comput. Harmon. Anal.*, 20, 220–236, 2006.
- [10] G., Kutyniok and D., Ch., Labate, “Introduction to Shearlets”, *Shearlets: Multiscale Analysis for Multivariate Data*, Birkhäuser, Boston, 1–38, 2012.
- [11] www.shearlab.org
- [12] G. R., Easley, D., Labate and F., Colonna, “Shearlet-Based Total Variation for Denoising”, *IEEE Trans. Image Processing*, 18(2), 260–268, 2009.
- [13] Q., Guo, S., Yu, X., Chen, C., Liu and W., Wei, “Shearlet-based Image Denoising Using Bivariate Shrinkage with Intra-band and Opposite Orientation Dependencies”, *IEEE Conference Publications*, 1, 863–866, 2009.
- [14] G. R., Easley and D., Labate, “Image Processing Using Shearlets”, Editors: G., Kutyniok and D., Labate *Shearlets: Multiscale Analysis for Multivariate Data*, Birkhäuser, Boston, 283–325, 2012.
- [15] S., Häuser and J., Ma, “Seismic Data Reconstruction via Shearlet-Regularized Directional Inpainting”, http://www.mathematik.uni-kl.de/uploads/tx_sibibtex/seismic.pdf
- [16] E. J., King, G., Kutyniok and X., Zhuang, “Analysis of Data Separation and Recovery Problems Using Clustered Sparsity”, *SPIE Proceedings: Wavelets and Sparsity XIV*, 8138, 1-11, 2011.
- [17] E. J., King, G., Kutyniok and Zhuang X., “Analysis of Inpainting via Clustered Sparsity and Microlocal Analysis”, *J. Math. Imaging Vis.*, 48, 205–234, 2014.
- [18] E. J., King, G., Kutyniok and W.Q, Lim, “Image Inpainting: Theoretical Analysis and Comparison of Algorithms”, *SPIE Proceedings*, 8858, 1-11, 2013.
- [19] C., Yazıcı, “Shearlet Teorisi ve Medikal Verilere Uygulaması”, Kocaeli University, Unpublished Ph.D. Thesis for Mathematics Degree, 2015.
- [20] I., Daubechies, “Ten lectures on Wavelets”, *Society for Industrial and Applied Mathematics (SIAM)*, Philadelphia, 1992.

- [21] W. Q., Lim, “The Discrete Shearlet Transform: A New Directional Transform and Compactly Supported Shearlet Frames”, *Image Proc. IEEE Transactions on*, 19(5), 1166–1180, 2010.
- [22] K.,Guo and D., Labate, “Optimally Sparse Multidimensional Representation Using Shearlets”, *SIAM J. Math. Anal.*,39, 298–318, 2007.
- [23] G., Kutyniok and W. Q., Lim, “Image Separation Using Wavelets and Shearlets”, *Curves and Surfaces*, 6920, 416-430, 2012.
- [24] G., Kutyniok and D., Ch., Labate, “Introduction to Shearlets”, *Shearlets: Multiscale Analysis for Multivariate Data*, Birkhäuser, Boston, 1–38, 2012.

	SAKARYA UNIVERSITY JOURNAL OF SCIENCE		 SAKARYA UNIVERSITY
	e-ISSN: 2147-835X http://www.saujs.sakarya.edu.tr		
	<u>Received</u> 30-09-2017 <u>Accepted</u> 08-02-2018	<u>Doi</u> 10.16984/saufenbilder.340849	

The effect of rotation energies of H_2^+ molecule on the $Ne + H_2^+ \rightarrow NeH^+ + H$ reaction

Ezman KARABULUT¹

ABSTRACT

The noble gas atoms such as He, Ne and Ar have significantly electronic ionization values around liquid nitrogen temperature (at low temperature values). Because of this feature, the noble gases which are used for some gas detectors, and which is related certain chemical process occurring in the low temperature regions of atmosphere are encouraged to be researched. The chemical reactions subjected to these noble gas atoms have been believed to exhibit important behaviors at the same temperature values. The investigation of their quantum effects in particular energy range and the dependence on temperature of chemical reactions consisting of atom-diatom molecular systems include the subject of reaction dynamics. The title reaction has showed stable structure feature in the interaction region which is the nearest inter-atomic distance. For this reason, it causes to be examined of dynamic effects by depending on quantum states of initial hydrogen ion. The contributions of angular behaviors of hydrogen ion related to total angular momentum and the effects of these behaviors to reaction formations are examined via three dimensional quantum mechanical methods.

Key Words: Noble gas, Zero-point energy, Reaction probabilities, Angular momentum.

1. INTRODUCTION

In order to theoretically verify the scattering calculations in atom-two atom collisions, a realistic potential energy surface of the relevant system must be obtained. The presence of a deep potential well in the transition zone of the colinear collision state of the subject reaction makes it difficult to theoretically examine this reaction [1]. But, because of this transition feature of the reaction, the change in the internal energy of the hydrogen ion molecule in the reaction was explained to be more effective than the transition energy [2]. For Ar and Kr, which are the other noble gas atoms, it is very difficult to do dynamic

studies on them since they have non-adiabatic energy surfaces [3]. Coriolis Coupling (CC) and Centrifugal Sudden (CS) calculations were performed in the first dynamic study on the most realistic potential of $Ne + H_2^+$ reaction. This study was carried out for certain initial vibrational quantum states at the energy range of 0.5-1.5 eV. CC and CS results gave very different results for high total angular momentum values. It was also emphasized that the vibrational quantum state of the hydrogen ion molecule exhibits exothermic character of the reaction at vibrational states that are higher than $v = 1$ [4]. Then the analytical potential energy surface for the same reaction was

¹ Bitlis Eren University, Vocational School of Health Services-ezman.fizik@gmail.com

established and the vibrational states of the initial hydrogen ion in certain energies were discussed. However, since this potential energy surface is very similar to the previous energy surface, no dynamic calculations have been made on this potential [5]. By similar to previous work, CC calculations have been made in the range of 0-2.0 eV collision energy over certain vibrational states of hydrogen molecule ion and the resonance states in the obtained cross-sections were discussed. It was also compared with experimental and theoretical results in the literature. A real calculation was made for certain total angular momentum values and then the intermediate values were calculated by the appropriate interpolation method [6]. At the subsequent study, the differential cross sections were also examined again in certain collision energies, which were dependent on the initial vibrational states. It was also discussed the dependence of resonance structures on vibrational states [7]. Another study on the initial vibrational states has also made comparisons over the relevant cross sections of the previous potential energy surface in certain energies. In addition, the internal energy distributions of the product molecule were also evaluated using these energy and potentials, and both potentials exhibited similar behaviors at both high and low energies [8]. The final work on this reaction was the use of deuterium, the isotope of the hydrogen atom, to investigate isotope effects. This work CC and CS calculations were, total cross sections of $\text{Ne} + \text{H}_2^+$ and $\text{Ne} + \text{D}_2^+$ reactions were investigated by depending on initial vibrational states [9].

In the light of these works done, due to the transitional nature of the potential energy surface, it is emphasized that the initial molecular vibrational and rotational energy states significantly affect the result of the reaction. But, it was not calculated since the rotation energy distributions involve certain computational difficulties. The relevant reaction will be considered in the appropriate vibrational and energy range, and detailed investigations of the effects of different initial rotational energy states on reaction formation will clarify the uncertainties in the literature. At the same time, the effects that occur on the product conditions will be emphasized.

The remainder of work contains the theoretical information needed for the relevant calculations. Finally, the results obtained are interpreted.

2. THEORY

As the formation of free radicals occurs in a very short period of time, usually during femto-second (10^{-15} s), it is very difficult to experimentally measure the information required for the reaction. For this reason, it is very important that the theoretical studies in which solutions containing time in reaction dynamics are obtained. The time dependent Schrödinger equation is used to understand such movements.

$$i\hbar \frac{\partial}{\partial t} \psi(R, r, \theta, t) = \hat{H} \psi(R, r, \theta, t) \quad (1)$$

If the Hamiltonian operator is time independent, the solution of this equation is written as

$$\psi(R, r, \theta, t + \tau) = e^{-i\hat{H}\tau/\hbar} \psi(R, r, \theta, t) \quad (2)$$

This equation gives the relation between the function at time t and the function at time t + τ [10]

$$e^{-i\hat{H}\tau/\hbar} \psi = \left\{ 1 - (i\hat{H}\tau/\hbar) - \frac{1}{2!} (i\hat{H}\tau/\hbar)^2 - \frac{i}{3!} (i\hat{H}\tau/\hbar)^3 + \frac{1}{4!} (i\hat{H}\tau/\hbar)^4 \dots \right\} \psi \quad (3)$$

In the quantum mechanical study of reaction dynamics, the time dependent Schrödinger equation has to be solved for very large propagation times using very small time steps. The excess of the spread term required for convergence of this series leads to an increase in the processor time required at each time step. If the high-order terms in the expansion are neglected, this creates the error at each time step and increases the error amount by increasing the propagation time. Many methods have been developed to solve the time dependent Schrödinger equation until now [11-13]. By means of these developed techniques, many important problems of quantum mechanics such as inelastic scattering, reactive scattering and photo-dissociation can be investigated depending on the time [14]. The Reel-Wave Packet method, developed by Gray and Balint-Kurti, which has been widely used in recent years in solving the time dependent Schrödinger wave equation, allows only the use of the real part of the wave function [15]. The use of only the real part of the wave function reduces the size of the matrices encountered in numeric applications, besides it also severely reduces the propagation time. The above-mentioned equation 2 can be written in trigonometric form as

$$\psi(R, r, t + \tau) = \left\{ \cos\left[\frac{\hat{H}\tau}{\hbar}\right] - i \sin\left[\frac{\hat{H}\tau}{\hbar}\right] \right\} \psi(R, r, t) \quad (4)$$

Similarly, the wave function at t is also written in terms of the wave function at t - τ .

$$\psi(R, r, t - \tau) = \left\{ \cos\left[\frac{\hat{H}t}{\hbar}\right] + i \sin\left[\frac{\hat{H}t}{\hbar}\right] \right\} \psi(R, r, t) \quad (5)$$

If these two equations are collected to each other, in the form of

$$\psi(R, r, t + \tau) = -\psi(R, r, t - \tau) + 2\cos\left[\frac{\hat{H}\tau}{\hbar}\right]\psi(R, r, t) \quad (6)$$

is obtained. Since this recurrence relation does not contain a complex expression, the wave function $\psi(R, r, t + \tau)$ is a real function. However, because the equation contains trigonometric expression, it is difficult to use and the Hamiltonian operator to overcome this difficulty is written in form of

$$f(\hat{H}_s) = \frac{-\hbar}{\tau} \cos^{-1}(\hat{H}_s) \quad (7)$$

Thus, if the solution function is rearranged,

$$\psi(R, r, t + \tau) = -\psi(R, r, t - \tau) + 2\hat{H}_s\psi(R, r, t) \quad (8)$$

is obtained. In quantum space, the imaginary part of the wave function has no direct effect on the measurable values of the operators corresponding to the dynamic variables. For this reason, the virtual part of the wave function can be subtracted from the above equations. The real and imaginary parts of the wave function, respectively, are

$$q = R(\psi) \quad \text{and} \quad p = Im(\psi) \quad (9)$$

The spread of wave function in real terms is

$$q(R, r, t + \tau) = -q(R, r, t - \tau) + 2\hat{H}_sq(R, r, t) \quad (10)$$

When considered the destructive potential used to prevent reflection of the wave function from the coordinate interval ends, the spreading scheme is

$$q_{n+1} = \hat{A}(-\hat{A}q_{n-1} + 2\hat{H}_sq_n) \quad (11)$$

Where $n=1,2,\dots,N$ (iteration step). \hat{A} is the destructive potential. To start the recurrence relation, the first two values must be known and these values are

$$q_0 = R[\psi(R, r, t)] \quad \text{and} \\ q_1 = \hat{A}(\hat{H}_sq_0 - \sqrt{1 - \hat{H}_s^2}p_0) \quad (12)$$

Here \hat{H}_s can be scaled in form of $\hat{H}_s = a_s\hat{H} + b_s$. Where $a_s = 2/\Delta E$ and $b_s = -1 - a_sE_{min}$. Looking at Eq. 11, there is only one time effect of the Hamiltonian operator on the wave function. This provides a great advantage in terms of time to reach the desired quantum mechanical quantities [16, 17]. In this method is analyzed the components of the wave function that reach the asymptotic region of the product channel by passing through the strong interaction region of the potential energy surface. These components give information on reactive scattering. Since the wave components pass to the product channel, all scatter

information about the product quantum states can be calculated. In this method, an analysis line is selected in the asymptotic region of the product channel and at each time step the wave packet is analyzed on this analysis line and the time dependent coefficients are calculated.

$$C_{v_0j_0,K_0,vjK}^J(t) = \int q_{vj}(r, \theta) q_{v_0j_0,K_0,vjK}^J(R = R_\infty, r, \theta, t) dr d\theta \quad (13)$$

Fourier transformation of these coefficients gives the energy dependent amplitudes:

$$A_{v_0j_0,K_0,vjK}^J(E) = \frac{1}{2\pi} \int_0^\infty e^{iEt/\hbar} C_{v_0j_0,K_0,vjK}^J(t) dt \quad (14)$$

The energy-dependent amplitudes give the elements of the scattering matrix:

$$S_{v_0j_0K_0 \rightarrow vjK}^J(E) = \frac{-\hbar^2 a_s}{(1-E_s^2)^{1/2}} \left(\frac{k_f k_i}{\mu_{A-BC} \mu_{AB-C}} \right)^{1/2} e^{-ik_f R_\infty} \frac{2A_{v_0j_0,K_0,vjK}^J(E)}{g(-k_i)} \quad (15)$$

Where k_i and k_f , respectively, are the corresponding wave vector components in the reactant and product channels. μ_{A-BC} and μ_{AB-C} are the reduced masses in reactant and product channels. a_s is the energy scaling parameter in Chebychev polynomials. $g(-k_i)$ is the components of the initial wave packet with $-k_i\hbar$ momentum. The absolute square of scattering matrix depending on the final and initial quantum states of the reactants and products and the total energy gives the reaction probabilities.

$$P_{v_0j_0K_0 \rightarrow vjK}^J(E) = |S_{v_0j_0K_0 \rightarrow vjK}^J(E)|^2 \quad (16)$$

The sum of the reaction possibilities over all product rotation and vibrational states gives the total reaction probability. Total reaction probability at any energy value [18] is

$$P_{v_0j_0K_0}^{JK}(E) = \sum_v \sum_j P_{v_0j_0K_0 \rightarrow vjK}^J(E) \quad (17)$$

3.RESULTS AND DISCUSSION

We obtained the state to state dynamic calculations for the ground state ($1^2A'$) of the title reaction which was calculated using highly correlated complete active space self-consistent field and multi-reference configuration interaction wave function with a basis set of aug-cc-pV5Z. The subject reaction has a very deep energy floppy in the reaction transition zone and a very high (0.54 eV) endothermic energy. Because of these features, very large time spread in the Chebyshev iteration relationship and very high grid steps in

the movement of the reacting atoms are needed. Performing real calculations on such reactions is difficult due to both obtaining the relevant potential energy surface and excessive processor effort in the dynamic calculations. For this reason, especially in the high values of j , this difficulty is further increased. In this study, dynamic simulation was performed once the total angular momentum value was zero.

sum of all possible rotational charges of the product molecule.

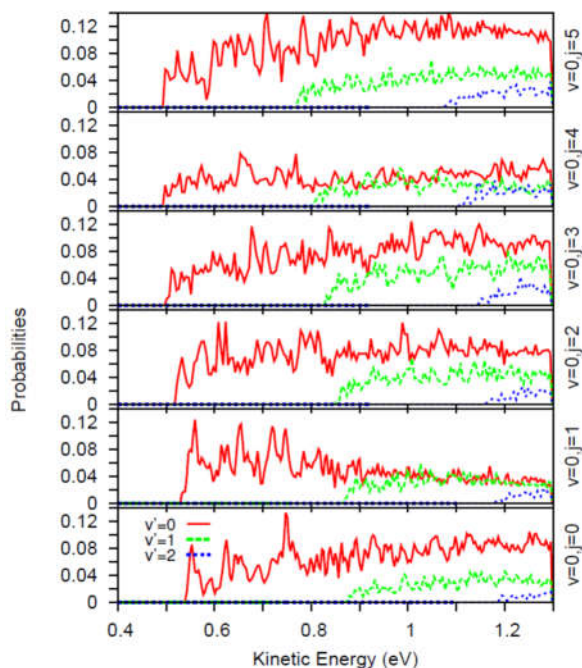


Figure1. The change of the vibrational quantum states of product molecule by depending on the rotational quantum states of the initial molecule.

Figure 1 shows the distributions of vibrational quantum states of the product molecule in certain rotational quantum states ($j=0-5$) of the reactant molecule. Because of the energy floppy at the transition state region in this reaction that occurs in a collinear manner (180°), reaching grid of wave packets requires a lot of propagation time. Due to these delays, fold reflections occur at the end of the grid and a resonant structure is observed throughout the relevant energy range. In the examined energy range, the product molecule contains only 3 vibrational quantum states. The changes in the vibrations of the product molecule shift to higher energies with increasing quantum numbers of vibrations, as expected. But, the highest contribution of dispersion is seen to be taken from the $v'=0$ vibrational quantum state. It is also seen that the reaction occurrences in this quantum state are fast in the threshold region. In this reaction, the changes on the rotation energies of the initial molecule are very prominent at the threshold. These distributions in the graph are the

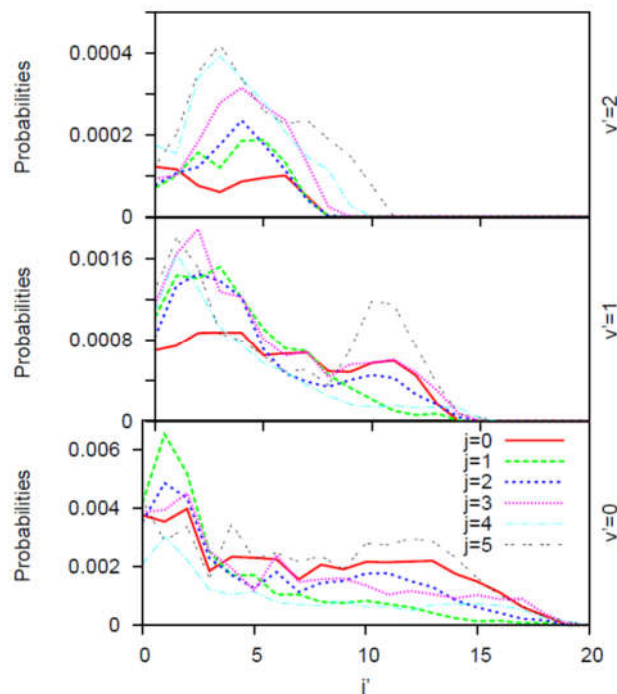


Figure2. The rotation and vibration distributions of product molecule by depending on the rotation quantum states of the initial molecule.

Figure 2 shows the relation of the average of all rotational quantum states of the product molecule to the states of vibration quantum states, in terms of the rotation quantum states of the initial molecule. In the case of $v'=0$ vibration quantum, it demonstrates that the contribution of the product rotation quantum state is much. However, a regular distribution of product rotation quantum states was not observed. It is seen that the highest contribution occurs again in the case of $v'=0$.

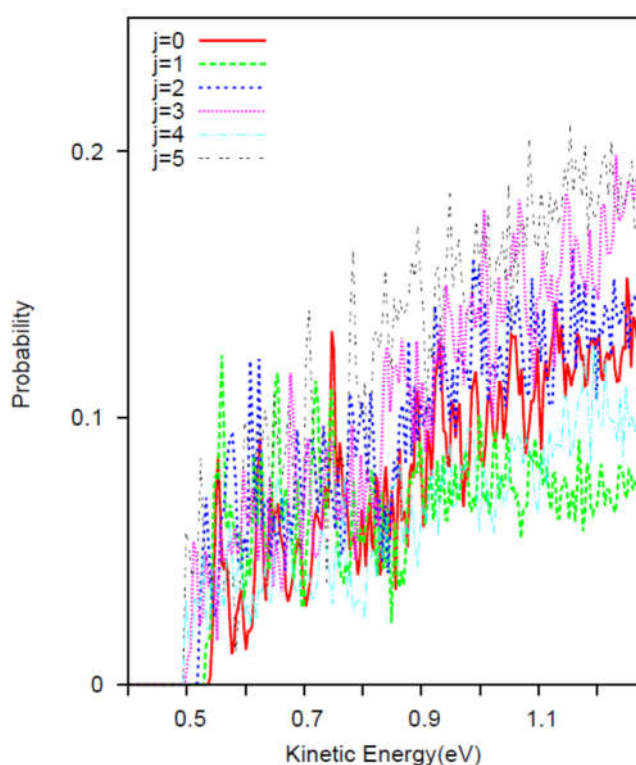


Figure3. The total reaction probabilities depending on the initial rotation quantum states.

Figure 3 shows the kinetic energy dependence of the total reaction probabilities collected over all product vibration and rotational energy quantum states. Because of the minimal energy pathway structure that promotes long distance interactions, vibration and rotation states have a more significant effect on the reaction, rather than the transition energy. Figure 3 showing that the rotational energies are effective and the previous works mentioned in the introduction part showing that the vibrational energies are effective are the best indicators of quantum effects of this reaction. As can be seen in Figure 3, the reaction probabilities depended on the rotation quantum state shows a significant irregularity in the examined energy range. This means that the transition energies are less effective than the rotational energies. The most important criterion for this situation is the barrier on minimum energy path of the system.

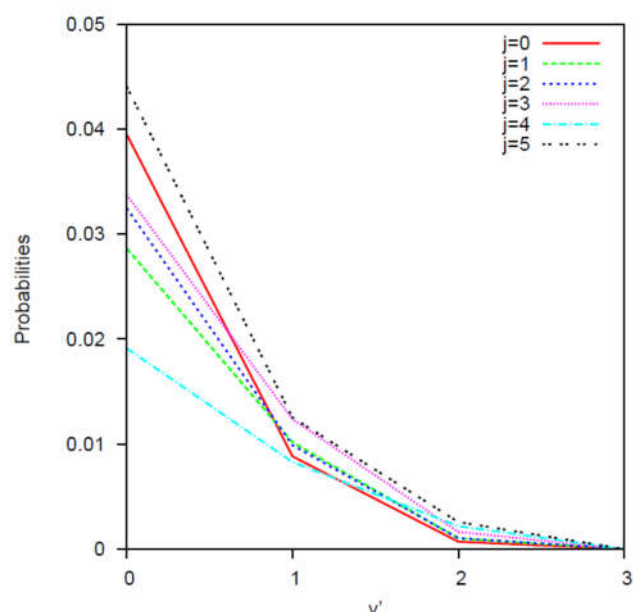


Figure4. The distribution of product vibrational quantum states by depending on the initial rotation quantum states.

Figure 4 shows the total reaction probability summed over all possible quantum states (vibration and rotation) of the product molecule for certain initial rotational energy quantum states. The product vibrational quantum state has a value up to the quantum state $v' = 2$ in the examined energy range. The increase of the vibrational quantum state of the product molecule has created an undesirable situation to form a new bond in the complex formation (i.e. to form the product molecule). The same case is also valid for the product rotation quantum states in Fig. 2. The increase in rotation and vibration energy of the product molecule supports to increase the related barrier. For this reason, to evaluate higher vibrational and rotational quantum states of the product molecule is possibly by thinking the system at higher transition energy range. Because the threshold energy value that is needed for the corresponding formation shifts towards the higher energy region.

CONCLUTIONS

Due to the endothermic nature of the reaction, the increase in the internal energy of the hydrogen ion shifts the necessary activation energy towards the lower energies, as expected. At the same time, any increase in the internal energy changes of the product molecule shifts the threshold energy generating the title reaction to higher energies. It was observed that the distributions of the vibrational quantum states were very distinct and regular and the rotational energy quantum states

were not in a certain regime when they were based on the same transition energy. It has been found that this state does not change depending on the quantum states of the product molecule. In this reaction, it is understood that the initial rotational quantum states do not reflect a distinctive feature in the energy range investigated.

ACKNOWLEDGEMENTS

The authors are grateful to Prof. G. G. Balint-Kurti for his guidance and to the Scientific and Technological Research Council of Turkey for TR-Grid facilities.

REFERENCES

- [1] Pendergast, P., Heck, J. M., Hayes, E. F., Jaquet, R., "Fit of The Potential Energy Surface for The Reaction $\text{Ne} + \text{H}_2^+ \rightarrow \text{NeH}^+ + \text{H}$ Using three Different Functional Forms," *Journal of Chemical Physics*, 98(6), 4543-4547, 1993.
- [2] Gonzalez, M., Blasco, R. M., Gimenez, X., Aguilar, A., "A Quasiclassical and Approximate Quantum Mechanical Study of the Intramolecular Isotope Effect in Proton Transfer Elementary Reactions: the $\text{Ne} + \text{HD}^+ \rightarrow \text{NeH}^+ (\text{NeD}^+) + \text{D} (\text{H})$ System at Low and Moderate Collision Energies (0.002-0.77 eV)," *Chemical Physics*, 209, 355-365, 1996.
- [3] Mayneris, J., Sierra, J. D., Gonzalez, M., "Time Dependent Quantum Dynamics Study of the $\text{Ne} + \text{H}_2^+ (v=0-4) \rightarrow \text{NeH}^+ + \text{H}$ Proton Transfer Reaction", *The Journal of Chemical Physics*, 128, 194307, 1-8, 2008.
- [4] Lv, S.-J., Zhang, P.-Y., Han, K.-L., He, G.-Z., "Exact Quantum Scattering Study of the $\text{Ne} + \text{H}_2^+$ Reaction on a New ab Initio Potential Energy Surface", *The Journal of Chemical Physics*, 132, 014303, 1-6, 2010.
- [5] Xiao, J., Yang, C.-L., Tong, X.-F., Wang, M.-S., Ma, X.-G., "Quasi-Classical Trajectory Study of the $\text{Ne} + \text{H}_2^+ \rightarrow \text{NeH}^+ + \text{H}$ Reaction Based on Global Potential energy Surface", *The Journal of Physical Chemistry A*, 115, 1486-1492, 2011.
- [6] Gamallo, P., Defazio, P., Gonzalez, M., "Time Dependent Quantum Dynamics Study of the $\text{Ne} + \text{H}_2^+ (v_0=0-4, j_0=1) \rightarrow \text{NeH}^+ + \text{H}$ Proton Transfer Reaction, Including the Coriolis Coupling. A System with Oscillatory Cross Sections", *The Journal of Physical Chemistry A*, 115, 11525-11530, 2011.
- [7] Gamallo, P., Larranaga, F. H., Gonzalez, M., "Resonances in the $\text{Ne} + \text{H}_2^+ \rightarrow \text{NeH}^+ + \text{H}$ Proton-Transfer Reaction", *The Journal of Physical Chemistry A*, 117, 5393-5400, 2013.
- [8] Gamallo, P., Martinez, R., Sierra, J. D., Gonzalez, M., "Understanding the Effect of Vibrational Excitation in Reaction Dynamics: The $\text{Ne} + \text{H}_2^+ (v_0=0-17, j_0=1) \rightarrow \text{NeH}^+ + \text{H}$, $\text{Ne} + \text{H}^+ + \text{H}$ Proton Transfer and Dissociation Cross Sections", *Phys. Chem. Chem. Phys.*, 16, 6641-6648, 2014.
- [9] Yao, C.-X., Zhang, P.-Y., "Time Dependent Wave-Packet Quantum Dynamics Study of the $\text{Ne} + \text{D}_2^+ (v_0=0-2, j_0=0) \rightarrow \text{NeD}^+ + \text{D}$ Reaction: Including the Coriolis Coupling", *The Journal of Physical Chemistry A*, 118, 5076-5082, 2014.
- [10] G. G. Balint-Kurti, R. N. Dixon, and C. C. Marston, "Grid Methods for solving the Schrödinger-equation and time-dependent quantum Dynamics of molecular photofragmentation and reactive scattering processes, *Int. Rev. Phys. Chem.* 11, 317-344, 1992.
- [11] A. Aşkar ve C. S. Çakmak, "Explicit Integration for the Time-Dependent Schrödinger Equation for Collision Problems" *J. Chem. Phys.* 68, 2794, 1978.
- [12] M. D. Feit, J. A. Fleck and A. Steiger, "Solution of the Schrödinger Equation for Collision Problems," *J. Chem. Phys.*, 68, 2794, 1978.
- [13] H. Tal-Ezer and R. Kosloff, "An Accurate and Efficient Scheme for Propagation of the time Dependent Schrödinger Equation," *J. Chem. Phys.* 81, 3967, 1984.
- [14] A. Lagana, A. Riganelli, "Reaction and Molecular Dynamics", Springer-Verlag Berlin Heidelberg, 74-87, 2000.
- [15] S. K. Gray, G. G. Balint-Kurti, "Quantum Dynamics with Real Wave Packets,

Including Application to three Dimensional $\text{D}+\text{H}_2$ Reactive Scattering," *Chem. Phys.*, 108, 950, 1998.

- [16] R. A. Sultanov, N. Balakrishnan, "Oxygen Chemistry in the Interstellar Medium: The Effect of Vibrational Excitation of H_2 in the $\text{O}(^3P)+\text{H}_2$ Reaction " *The Astrophysical Journal*, 629, 305-310, 2005.
- [17] X. Tang, C. Houchins, K. Lau, C. Y. Ng, R. A. Dressler, Y. Chiu, T. Chu, K. Han, "Time dependent wave packet Quantum Scattering Study of the Reaction $\text{He}+\text{HD}$," *Journal of Chem. Phys.*, 127, 164318, 2007.
- [18] F. Gogtas, "Time- Dependent Quantum Dynamics of Reactive Scattering $\text{Li}+\text{HF} \rightarrow \text{LiH}+\text{F}$," Ph. D. Thesis, University of Bristol, 195, 1995.

	SAKARYA ÜNİVERSİTESİ FEN BİLİMLERİ ENSTİTÜSÜ DERGİSİ <i>SAKARYA UNIVERSITY JOURNAL OF SCIENCE</i>		
	e-ISSN: 2147-835X Dergi sayfası: http://dergipark.gov.tr/saufenbilder		
	<u>Received</u> 27-07-2017 <u>Accepted</u> 21-02-2018	<u>Doi</u> 10.16984/saufenbilder.331231	

Conjugate Tangent Vectors, Asymptotic Directions, Euler Theorem and Dupin Indicatrix For k-Kinematic Surfaces

Yasemin Yıldırım^{*1}, Erhan Ata²

ABSTRACT

In this study, we define the k-kinematic surface M^g which is obtained from a surface M on Euclidean 3-space E^3 by applying rigid motion described by quaternions to points of M . Then we investigate and calculate for this surface some important concepts such as shape operator, asymptotic vectors, conjugate tangent vectors, Euler theorem and Dupin indicatrix which help to understand a surface differential geometrically well.

Keywords: Asymptotic direction, conjugate tangent vectors, Dupin indicatrix, Euler theorem.

1. INTRODUCTION

Surfaces have had application areas in many areas such as mathematics, kinematics, dynamics and engineering for many years and they have been in center of interest increasingly. Mathematicians have written many articles and books by investigating surfaces as Euclidean and non-Euclidean. For these studies, one can read [1-15]. Eisenhart defined parallel surfaces and their some properties in his book [3]. In [16], Ünlütürk and Özusağlam investigated the parallel surfaces in Minkowski 3-space. In [17], Tarakçı and Hacısalıhoğlu defined surfaces at a constant distance from edge of regression on a surface and gave some properties of such surfaces and then in [18-20] Sağlam and Kalkan investigated the other properties of this surface. Again Sağlam and Kalkan transported the surfaces at a constant

distance from edge of regression on a surface to Minkowski 3-space and obtained their properties which they have in Euclidean space.

Quaternions have many application areas in both theoretical and applied mathematics. The quaternions described firstly by Hamilton applied mechanics in 3-dimensional space [21]. The quaternions as a set correspond to \mathbb{R}^4 4-dimensional vector space on real numbers. The unit quaternions which are known as vensors provide a convenient mathematical description in rotations and directions in 3-dimension. They are simpler forming and numerically more stable and efficient than Euler angles and rotation matrices. The set of dual quaternions, invented by Clifford to describe space geometry in mathematics and mechanics, is a Clifford algebra which can be used for representation of rigid motions [22-24]. Motion of a point, line and objects has a great attraction in kinematics [25]. E. Study and Kotelnikov applied dual numbers and dual vectors

* Corresponding Author

¹ Dumlupınar Üniversitesi, yasemin.kemer@dpu.edu.tr

² Dumlupınar Üniversitesi, erhan.ata@dpu.edu.tr

to studies which they did in kinematics ([26], [27]). Homogeneous transformation is a point transformation. However, the line transformations in which transformed element is a line instead a point can be defined in 3-dimensional Cartesian space. Pottmann and Wallner studied on line transformations [28]. A screw is a 6-dimensional vector which is obtained from vectors such as power, torque, linear velocity and angular velocity emerged in rigid motion. When two lines are given it is easy to obtain one from another by screw motion [29]. Rigid motions include rotations, translations, reflections and combinations of these. Sometimes reflections are excluded in definition of rigid motion. The shape and dimension of any object remains same after the rigid motion. In kinematics, a suitable rigid motion represented by SE(3) is used for representing linear and angular changes. According to Charles theorem, every rigid motion can be expressed as a screw motion. A surface formed kinematically is a surface defined by a moving object envelope. This object can be a point, a line, a plane or any arbitrary figure. There are many applications of surfaces produced in many areas kinematically [30-35].

Selig and Husty took the dual quaternion which described a rigid motion and gave its effects on a point and a line in their study [36]. In [31-34] a computer-aided geometric design (CAGD) and surface design were combined. In these studies, they focused on the surfaces obtained by using point movements (substitution). The techniques for generating surfaces kinematically are more suitable in CAD/CAM, because these depend directly on the kinematic constraints of the bench and design requirements.

In this study, we define the kinematic surface by applying rigid motion expressed by dual quaternions as in [36] to points of a surface M in 3-dimensional Euclidean space E^3 and obtain a k-kinematic surface M^g by taking the rotation axis specially as the unit vector k . The k-kinematic surface M^g is a more general case of surfaces at a constant distance from edge of regression from a point on a surface and the parallel surfaces on which many studies have been done by mathematicians and differential geometers until now. In special cases one can obtain surfaces at a constant distance from edge of regression from a point on a surface and the parallel surfaces from the k-kinematic surfaces. Then, we calculate shape operator, asymptotic vectors, conjugate tangent vectors, Euler theorem and Dupin indicatrix,

which are well-known concepts in differential geometry, of the k-kinematic surface M^g and investigate the changes in these concepts under the rigid motion.

2. PRELIMINARIES

Let M be a surface of E^3 with the metric tensor \langle, \rangle . Let D be the Riemannian connection on E^3 and N be a unit normal C^∞ vector field on M . Then, for every $p \in M$ and $X \in T_p(M)$ we have $\langle N_p, N_p \rangle = 1$ and $\langle N_p, X \rangle = 0$. Let $S : T_p(M) \rightarrow T_p(M)$ be the shape operator defined by $S(X) = D_X N$. The Gaussian curvature $K(p)$ and mean curvature $H(p)$ of M at p are the determinant and the trace of S at $p \in M$, respectively. The eigenvalues of S are called the principal curvatures of M . If tangent of a curve is a principal vector at each of its points then this curve is a curvature line in M .

Definition 1. Let M and M^r be two surfaces in Euclidean space. Let \bar{N} be the unit normal vector field of M and $r \in \mathbb{R}$ be a constant. If there is a function

$$f : M \rightarrow M^r$$

$$p \rightarrow f(p) = p + r\bar{N}_p$$

between the surfaces M and M^r then M^r is called parallel surface of M and the function f is called the parallelization function between the surfaces M and M^r [37].

Definition 2. Let M be an Euclidean surface in E^3 and S be the shape operator of M . For $X_p \in T_p(M)$ if

$$\langle S(X_p), X_p \rangle = 0$$

then X_p is called an asymptotic direction of M at $p \in M$ [38].

Definition 3. Let M be an Euclidean surface in E^3 and S be the shape operator of M . For $X_p, Y_p \in T_p(M)$ if

$$\langle S(X_p), Y_p \rangle = 0$$

then X_p and Y_p are called conjugate tangent vectors of M at $p \in M$ [38].

Definition 4. Let M be an Euclidean surface in E^3 and S be the shape operator of M . For an umbilic point $p \in M$ the function

$$k_n : T_p(M) \rightarrow R$$

$$k_n(X_p) = \frac{1}{\|X_p\|^2} \langle S(X_p), X_p \rangle$$

is called the normal curvature function of M at p [37].

Definition 5. Let M be an Euclidean surface in E^3 and S be the shape operator of M . Then the Dupin indicatrix of $p \in M$ is

$$D_p = \{X_p \mid \langle S(X_p), X_p \rangle = \pm 1,$$

$$X_p \in T_p(M)\} \text{ [37].}$$

Definition 6. Let M and M^f be two surfaces in E^3 and N_p be a unit normal vector of M at a point $p \in M$. Let $T_p(M)$ be the tangent space at $p \in M$ and $\{X_p, Y_p\}$ be an orthonormal basis of $T_p(M)$. Let $Z_p = d_1X_p + d_2Y_p + d_3N_p$ be a unit vector where $d_1, d_2, d_3 \in \mathbb{R}$ are constant numbers such that $d_1^2 + d_2^2 + d_3^2 = 1$. If a function with the condition

$$f : M \rightarrow M^f, f(p) = p + rZ_p, r \text{ constant,}$$

M^f is called as the surface at a constant distance from edge of regression on M [17].

2.1. Quaternions

Let us firstly begin with Hamilton's quaternions and their connection with rotations. A rotation of angle θ , about a unit vector $v = (v_x, v_y, v_z)^T$ is represented by the quaternion,

$$r = \cos \frac{\theta}{2} + \sin \frac{\theta}{2} (v_x \mathbf{i} + v_y \mathbf{j} + v_z \mathbf{k}).$$

The conjugation

$$p' = rp\bar{r}$$

gives the action of such a quaternion on a point $p = x\mathbf{i} + y\mathbf{j} + z\mathbf{k}$ in space, where

$$\bar{r} = \cos \frac{\theta}{2} - \sin \frac{\theta}{2} (v_x \mathbf{i} + v_y \mathbf{j} + v_z \mathbf{k}).$$

The quaternions representing rotations satisfy $r\bar{r} = 1$ and also r and \bar{r} represent the same rotation. The set of unit quaternions, those satisfying $r\bar{r} = 1$, comprise the group $\text{Spin}(3)$, which is the double cover of the group of rotations $\text{SO}(3)$.

Let ε be the dual unit which satisfies the relation $\varepsilon^2 = 0$ and commutes with the quaternion units \mathbf{i}, \mathbf{j} and \mathbf{k} . For ordinary quaternions q_0 and q_1 ,

$$h = q_0 + \varepsilon q_1$$

indicates a general dual quaternion. A rigid transformation is represented by a dual quaternion

$$g = r + \frac{1}{2} \varepsilon tr,$$

where r is a quaternion representing a rotation as above and $t = t_x \mathbf{i} + t_y \mathbf{j} + t_z \mathbf{k}$ is a pure quaternion representing the translational part of the transformation [36].

Points in space are represented by dual quaternions of the form,

$$\hat{p} = 1 + \varepsilon p,$$

where p is a pure quaternion as above. The action of a rigid transformation on a point is given by,

$$\begin{aligned} \hat{p}' &= (r + \frac{1}{2} \varepsilon tr) \hat{p} (r + \frac{1}{2} \varepsilon \bar{r} t) \\ &= (r + \frac{1}{2} \varepsilon tr) (1 + \varepsilon p) (r + \frac{1}{2} \varepsilon \bar{r} t) \\ &= 1 + \varepsilon (rp\bar{r} + t). \end{aligned}$$

Note that, as with the pure rotations, g and $-g$ represent the same rigid transformation [36].

3. KINEMATIC SURFACES AND k-KINEMATIC SURFACES

Firstly, let us give the definition of the kinematic surface:

Definition 7. Let M and M^g be two surfaces in E^3 and $p \in M$. Let

$r = \cos \frac{\theta}{2} + \sin \frac{\theta}{2} (v_x \mathbf{i} + v_y \mathbf{j} + v_z \mathbf{k})$ be a rotation by

an angle of θ radian about the unit vector $\vec{v} = (v_x, v_y, v_z)$ and \vec{t} be the translational vector. If there is a function defined as

$$f : M \rightarrow M^g$$

$$p \rightarrow f(p) = rp\bar{r} + t$$

then the surface M^g is called a kinematic surface of the surface M .

Let the rotation axis be the unit vector k and the translational vector be any unit vector Z_p at a point $p \in M$. Then, we can obtain a new kinematic surface, let us call this surface as " k -kinematic surface".

Definition 8. Let M and M^g be two surfaces in E^3 and $p \in M$. Let $r = \cos \frac{\theta}{2} + \sin \frac{\theta}{2} k$ be a

rotation by an angle of θ radian about the unit vector k and \vec{Z}_p be the translational vector. If there is a function defined as

$$f(p) = \cos \theta p + \sin \theta \bar{k} \wedge p + (1 - \cos \theta) \langle \bar{k}, p \rangle \bar{k} + \lambda \bar{Z}_p$$

then M^g is called a k-kinematic surface of the surface M .

As an example, let us consider the half cylinder

$$M = \{\phi(u, v) \mid \phi(u, v) = (\cos u, \sin u, v), 0 \leq u \leq \pi/2, 0 \leq v \leq 2\}.$$

Let the rotation angle be $\pi/2$ and translational

vector be $\bar{Z} = \left(\frac{\sqrt{3}}{3}, \frac{\sqrt{3}}{3}, \frac{\sqrt{3}}{3}\right)$. Rotating every

point of M by $\pi/2$ angle over the \bar{k} and translating 6 unit along \bar{Z} gives the k-kinematic surface

$$M^g = \{\psi(u, v) \mid \psi(u, v) = (-\sin u + 2\sqrt{3}, \cos u + 2\sqrt{3}, v + 2\sqrt{3}) 0 \leq u \leq \pi/2, 0 \leq v \leq 2\}.$$

Image of a point $P = (0, 1, 2) \in M$ will be $P' = (-1 + 2\sqrt{3}, 2\sqrt{3}, 2 + 2\sqrt{3}) \in M^g$ (Figure 1).

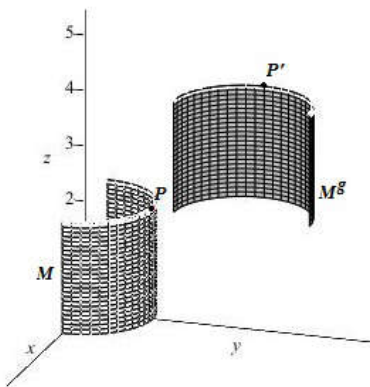


Figure 1. k-kinematic surface of an half cylinder

One can easily see that for $\forall X_p \in T_p M$

$$f_*(X_p) = \cos \theta X_p + \sin \theta \bar{k} \wedge X_p + (1 - \cos \theta) \langle \bar{k}, X_p \rangle \bar{k} + \lambda \bar{Z}_p,$$

so the tangent vectors on M can be transferred to the surface M^g by the transformation f_* .

Let (ϕ, U) be a parametrization of the surface M

. Then, one can write that

$$\phi: U \subset E^3 \rightarrow M (u, v) \rightarrow p = \phi(u, v).$$

It follows that $\{\phi_u, \phi_v\}_p$ is a basis of $T_p(M)$. Let N_p be a unit normal vector at $p \in M$ and $d_1, d_2, d_3 \in \mathbb{R}$ be constant real numbers. Then we can write that $\bar{Z}_p = d_1 \phi_u|_p + d_2 \phi_v|_p + d_3 N_p$. Since

$$M^g = \{f(p) \mid f(p) = \cos \theta p + \sin \theta \bar{k} \wedge p + (1 - \cos \theta) \langle \bar{k}, p \rangle \bar{k} + \lambda \bar{Z}_p\},$$

a parametric representation of the surface M^g is

$$\psi(u, v) = \cos \theta \phi(u, v) + \sin \theta \bar{k} \wedge \phi(u, v) + (1 - \cos \theta) \langle \bar{k}, \phi(u, v) \rangle \bar{k} + \lambda \bar{Z}_p$$

and

$$M^g = \{\psi(u, v) \mid \psi(u, v) = \cos \theta \phi(u, v) + \sin \theta \bar{k} \wedge \phi(u, v) + (1 - \cos \theta) \langle \bar{k}, \phi(u, v) \rangle \bar{k} + \lambda (d_1 \phi_u + d_2 \phi_v + d_3 N(u, v)), d_1, d_2, d_3, \lambda \text{ are constants}\}$$

or

$$M^g = \{\psi(u, v) \mid \psi(u, v) = \cos \theta \phi(u, v) + \sin \theta \bar{k} \wedge \phi(u, v) + (1 - \cos \theta) \langle \bar{k}, \phi(u, v) \rangle \bar{k} + \lambda_1 \phi_u + \lambda_2 \phi_v + \lambda_3 N(u, v), \lambda_1, \lambda_2, \lambda_3 \text{ are constants}\}.$$

where $\lambda_1 = \lambda d_1$, $\lambda_2 = \lambda d_2$ and $\lambda_3 = \lambda d_3$. Let us take ϕ_u and ϕ_v as the principal directions of the surface M . Let k_1 and k_2 be the associated principal curvatures, respectively. Then, we get $\psi_u = (\cos \theta + \lambda_3 k_1) \phi_u + \sin \theta \langle k, N \rangle \phi_v - (\lambda_1 k_1 + \sin \theta \langle k, \phi_v \rangle) N + (1 - \cos \theta) \langle k, \phi_u \rangle k$

$$- (\lambda_1 k_1 + \sin \theta \langle k, \phi_v \rangle) N + (1 - \cos \theta) \langle k, \phi_u \rangle k$$

and

$$\psi_v = -\sin \theta \langle k, N \rangle \phi_u + (\cos \theta + \lambda_3 k_2) \phi_v - (\lambda_2 k_2 - \sin \theta \langle k, \phi_u \rangle) N + (1 - \cos \theta) \langle k, \phi_v \rangle k.$$

Therefore, the unit normal vector field of the surface M^g can be calculated as

$$N^g = \frac{\psi_u \wedge \psi_v}{A}$$

where $A = \|\psi_u \wedge \psi_v\|$.

Theorem 1. Let the pair (M, M^g) be given in E^3 . Let $\{\phi_u, \phi_v\}$ be orthonormal and principle vector fields on M and k_1, k_2 be principle curvatures of M . Then the matrix of the shape operator S^g of M^g is

$$S^g = \frac{1}{A^2} \begin{bmatrix} \mu_1 & \mu_2 \\ \mu_3 & \mu_4 \end{bmatrix}$$

where

$$\begin{aligned} \mu_1 &= \left[\langle N^g, \psi_{uv} \rangle \langle \psi_u, \psi_v \rangle - \langle N^g, \psi_{uu} \rangle \langle \psi_v, \psi_v \rangle \right], \\ \mu_2 &= \left[\langle N^g, \psi_{uu} \rangle \langle \psi_u, \psi_v \rangle - \langle N^g, \psi_{uv} \rangle \langle \psi_u, \psi_u \rangle \right], \\ \mu_3 &= \left[\langle N^g, \psi_{vv} \rangle \langle \psi_u, \psi_v \rangle - \langle N^g, \psi_{uv} \rangle \langle \psi_v, \psi_v \rangle \right], \\ \mu_4 &= \left[\langle N^g, \psi_{uv} \rangle \langle \psi_u, \psi_v \rangle - \langle N^g, \psi_{uu} \rangle \langle \psi_u, \psi_u \rangle \right]. \end{aligned}$$

4. ASYMPTOTIC DIRECTIONS AND CONJUGATE TANGENT VECTORS FOR k-KINEMATIC SURFACES

Theorem 2. Let M^g be a k-kinematic surface of a surface M and $\{\phi_u, \phi_v\}$ be orthonormal and principle vector fields on M and k_1, k_2 be principle curvatures of M . Let $X_p \in T_p(M)$.

Then $f_*(X_p) \in T_{f(p)}(M^g)$ is an asymptotic direction of M^g if and only if

$$\mu_1^* x_1^2 + \mu_2^* x_1 x_2 + \mu_3^* x_2^2 = 0 \tag{1}$$

where

$$\begin{aligned} x_1 &= \langle X_p, \phi_u \rangle, & x_2 &= \langle X_p, \phi_v \rangle, \\ \mu_1^* &= \mu_1 \langle \psi_u, \psi_u \rangle + \mu_2 \langle \psi_u, \psi_v \rangle, \\ \mu_2^* &= \mu_1 \langle \psi_u, \psi_v \rangle + \mu_2 \langle \psi_v, \psi_v \rangle + \mu_3 \langle \psi_u, \psi_u \rangle + \mu_4 \langle \psi_u, \psi_v \rangle, \\ \mu_3^* &= \mu_3 \langle \psi_u, \psi_v \rangle + \mu_4 \langle \psi_v, \psi_v \rangle. \end{aligned}$$

Proof. Let $X_p \in T_p(M)$. Then, we can write that $X_p = x_1 \phi_u + x_2 \phi_v$, where $x_1 = \langle X_p, \phi_u \rangle$ and $x_2 = \langle X_p, \phi_v \rangle$. Besides, one can write that

$$\begin{aligned} f_*(X_p) &= x_1 f_*(\phi_u) + x_2 f_*(\phi_v) \\ &= x_1 \psi_u + x_2 \psi_v. \end{aligned} \tag{2}$$

On the other hand, calculating $S^g(f_*(X_p))$ gives

$$\begin{aligned} S^g(f_*(X_p)) &= x_1 S^g(f_*(\phi_u)) + x_2 S^g(f_*(\phi_v)) \\ &= (\mu_1 x_1 + \mu_3 x_2) \psi_u + (\mu_2 x_1 + \mu_4 x_2) \psi_v. \end{aligned} \tag{3}$$

Calculating inner product of (2) and (3) gives the result.

Theorem 3. Let M^g be a k-kinematic surface of a surface M and $\{\phi_u, \phi_v\}$ be orthonormal basis such that ϕ_u and ϕ_v are principle vector fields on M and k_1, k_2 be principle curvatures of M . Let θ_1 and θ_2 be the angles between the unit vector X_p and ϕ_u and ϕ_v , respectively. Then

$f_*(X_p) \in T_{f(p)}(M^g)$ is an asymptotic direction of M^g if and only if

$$\mu_1^* \cos^2 \theta_1 + \mu_2^* \cos \theta_1 \cos \theta_2 + \mu_3^* \cos^2 \theta_2 = 0. \tag{4}$$

Proof. Let θ_1 be the angle between X_p and ϕ_u and θ_2 be the angle between X_p and ϕ_v . Then we have

$$\cos \theta_1 = \langle X_p, \phi_u \rangle = x_1. \tag{5}$$

Similarly, we can obtain

$$\cos \theta_2 = \langle X_p, \phi_v \rangle = x_2. \tag{6}$$

Substituting (5) and (6) into (1) completes the proof.

Theorem 4. Let M^g be a k-kinematic surface of a surface M and $\{\phi_u, \phi_v\}$ be orthonormal basis such that ϕ_u and ϕ_v are principle vector fields on M . Then for $X_p, Y_p \in T_p(M)$, $f_*(X_p) \in T_{f(p)}(M^g)$ and $f_*(Y_p) \in T_{f(p)}(M^g)$ are conjugate tangent vectors if and only if

$$\mu_1^* x_1 y_1 + \mu_2^* x_1 y_2 + \mu_3^* x_2 y_1 + \mu_4^* x_2 y_2 = 0, \tag{7}$$

where

$$\begin{aligned} x_1 &= \langle X_p, \phi_u \rangle, & x_2 &= \langle X_p, \phi_v \rangle, \\ y_1 &= \langle Y_p, \phi_u \rangle, & y_2 &= \langle Y_p, \phi_v \rangle, \\ \mu_1^* &= \mu_1 \langle \psi_u, \psi_u \rangle + \mu_2 \langle \psi_u, \psi_v \rangle, \\ \mu_2^* &= \mu_1 \langle \psi_u, \psi_v \rangle + \mu_2 \langle \psi_v, \psi_v \rangle, \\ \mu_3^* &= \mu_3 \langle \psi_u, \psi_u \rangle + \mu_4 \langle \psi_u, \psi_v \rangle, \\ \mu_4^* &= \mu_3 \langle \psi_u, \psi_v \rangle + \mu_4 \langle \psi_v, \psi_v \rangle. \end{aligned}$$

Proof. Let $X_p, Y_p \in T_p(M)$. Then, since $\{\phi_u, \phi_v\}$ is an orthonormal basis on $T_p(M)$ we have $X_p = x_1 \phi_u + x_2 \phi_v$ and $Y_p = y_1 \phi_u + y_2 \phi_v$, where $x_1 = \langle X_p, \phi_u \rangle$, $x_2 = \langle X_p, \phi_v \rangle$, $y_1 = \langle Y_p, \phi_u \rangle$ and $y_2 = \langle Y_p, \phi_v \rangle$. It follows that

$$\begin{aligned} f_*(X_p) &= x_1 f_*(\phi_u) + x_2 f_*(\phi_v) \\ &= x_1 \psi_u + x_2 \psi_v \end{aligned}$$

and

$$\begin{aligned} f_*(Y_p) &= y_1 f_*(\phi_u) + y_2 f_*(\phi_v) \\ &= y_1 \psi_u + y_2 \psi_v. \end{aligned} \tag{8}$$

On the other hand, one can obtain that

$$\begin{aligned} S^g(f_*(X_p)) &= x_1 S^g(f_*(\phi_u)) + x_2 S^g(f_*(\phi_v)) \\ &= (\mu_1 x_1 + \mu_3 x_2) \psi_u + (\mu_2 x_1 + \mu_4 x_2) \psi_v \end{aligned} \tag{9}$$

Inner product of (8) and (9) gives

$$\begin{aligned} \langle S^g(f_*(X_p)), f_*(Y_p) \rangle &= \mu_1^* x_1 y_1 + \mu_2^* x_1 y_2 \\ &\quad + \mu_3^* x_2 y_1 + \mu_4^* x_2 y_2, \end{aligned}$$

where

$$\begin{aligned} x_1 &= \langle X_p, \phi_u \rangle, & x_2 &= \langle X_p, \phi_v \rangle, \\ y_1 &= \langle Y_p, \phi_u \rangle, & y_2 &= \langle Y_p, \phi_v \rangle, \\ \mu_1^* &= \mu_1 \langle \psi_u, \psi_u \rangle + \mu_2 \langle \psi_u, \psi_v \rangle, \\ \mu_2^* &= \mu_1 \langle \psi_u, \psi_v \rangle + \mu_2 \langle \psi_v, \psi_v \rangle, \end{aligned}$$

$$\mu_3^* = \mu_3 \langle \psi_u, \psi_u \rangle + \mu_4 \langle \psi_u, \psi_v \rangle,$$

$$\mu_4^* = \mu_3 \langle \psi_u, \psi_v \rangle + \mu_4 \langle \psi_v, \psi_v \rangle.$$

This completes the proof.

Theorem 5. Let M^g be a k-kinematic surface of a surface M and $\{\phi_u, \phi_v\}$ be orthonormal basis such that ϕ_u and ϕ_v are principle vector fields on M and k_1, k_2 be principle curvatures of M . Let θ_1, θ_2 be the angles between the unit vector X_p and ϕ_u, ϕ_v , respectively and α_1, α_2 be the angles between the unit vector Y_p and ϕ_u, ϕ_v , respectively. Then $f^*(X_p)$ and $f^*(Y_p)$ are conjugate tangent vectors if and only if

$$\mu_1^* \cos \theta_1 \cos \alpha_1 + \mu_2^* \cos \theta_1 \cos \alpha_2 + \mu_3^* \cos \theta_2 \cos \alpha_1 + \mu_4^* \cos \theta_2 \cos \alpha_2 = 0$$

Proof. Let θ_1 be the angle between X_p and ϕ_u and θ_2 be the angle between X_p and ϕ_v . Then we have

$$\cos \theta_1 = \langle X_p, \phi_u \rangle = x_1. \tag{10}$$

and

$$\cos \theta_2 = \langle X_p, \phi_v \rangle = x_2. \tag{11}$$

Similarly, let α_1 be the angle between Y_p and ϕ_u and α_2 be the angle between Y_p and ϕ_v . Then we get

$$\cos \theta_1 = \langle Y_p, \phi_u \rangle = y_1. \tag{12}$$

and

$$\cos \theta_2 = \langle Y_p, \phi_v \rangle = y_2. \tag{13}$$

Substituting (10), (11), (12) and (13) into (7) completes the proof.

5. EULER THEOREM AND DUPIN INDICATRIX FOR k-KINEMATIC SURFACES

Theorem 6. Let M^g be a k-kinematic surface of a surface M and $\{\phi_u, \phi_v\}$ be orthonormal basis such that ϕ_u and ϕ_v are principle vector fields on M and k_1, k_2 be principle curvatures of M . Let $X_p \in T_p(M)$ and $k_n^g(f^*(X_p))$ be the normal curvature of M^g in the direction $f^*(X_p)$. Then

$$k_n^g(f^*(X_p)) = \frac{\mu_1^* x_1^2 + \mu_2^* x_1 x_2 + \mu_3^* x_2^2}{\lambda_1^* x_1^2 + 2\lambda_2^* x_1 x_2 + \lambda_3^* x_2^2}, \tag{14}$$

where

$$x_1 = \langle X_p, \phi_u \rangle, \quad x_2 = \langle X_p, \phi_v \rangle,$$

$$\mu_1^* = \mu_1 \langle \psi_u, \psi_u \rangle + \mu_2 \langle \psi_u, \psi_v \rangle,$$

$$\mu_2^* = \mu_1 \langle \psi_u, \psi_v \rangle + \mu_2 \langle \psi_v, \psi_v \rangle + \mu_3 \langle \psi_u, \psi_u \rangle + \mu_4 \langle \psi_u, \psi_v \rangle,$$

$$\mu_3^* = \mu_3 \langle \psi_u, \psi_v \rangle + \mu_4 \langle \psi_v, \psi_v \rangle,$$

$$\lambda_1^* = \langle \psi_u, \psi_u \rangle, \quad \lambda_2^* = \langle \psi_u, \psi_v \rangle, \quad \lambda_3^* = \langle \psi_v, \psi_v \rangle.$$

Proof. Let $X_p \in T_p(M)$. Then, we have

$$X_p = x_1 \phi_u + x_2 \phi_v, \quad \text{where} \quad x_1 = \langle X_p, \phi_u \rangle,$$

$$x_2 = \langle X_p, \phi_v \rangle. \text{ It follows that}$$

$$f^*(X_p) = x_1 f^*(\phi_u) + x_2 f^*(\phi_v) = x_1 \psi_u + x_2 \psi_v$$

and

$$S^g(f^*(X_p)) = x_1 S^g(f^*(\phi_u)) + x_2 S^g(f^*(\phi_v)) = (\mu_1 x_1 + \mu_3 x_2) \psi_u + (\mu_2 x_1 + \mu_4 x_2) \psi_v.$$

By an easy calculation we get

$$\|f^*(X_p)\|^2 = x_1^2 \langle \psi_u, \psi_u \rangle + 2x_1 x_2 \langle \psi_u, \psi_v \rangle + x_2^2 \langle \psi_v, \psi_v \rangle = \lambda_1^* x_1^2 + 2\lambda_2^* x_1 x_2 + \lambda_3^* x_2^2$$

and

$$\begin{aligned} \langle S^g(f^*(X_p)), f^*(X_p) \rangle &= (\mu_1 \langle \psi_u, \psi_u \rangle + \mu_2 \langle \psi_u, \psi_v \rangle) x_1^2 \\ &\quad + (\mu_3 \langle \psi_u, \psi_v \rangle + \mu_4 \langle \psi_v, \psi_v \rangle) x_2^2 \\ &\quad + (\mu_1 \langle \psi_u, \psi_v \rangle + \mu_2 \langle \psi_v, \psi_v \rangle) x_1 x_2 \\ &\quad + \mu_3 \langle \psi_u, \psi_u \rangle + \mu_4 \langle \psi_u, \psi_v \rangle x_1 x_2 \\ &= \mu_1^* x_1^2 + \mu_2^* x_1 x_2 + \mu_3^* x_2^2. \end{aligned}$$

Therefore we obtain

$$k_n^g(f^*(X_p)) = \frac{\mu_1^* x_1^2 + \mu_2^* x_1 x_2 + \mu_3^* x_2^2}{\lambda_1^* x_1^2 + 2\lambda_2^* x_1 x_2 + \lambda_3^* x_2^2}.$$

Theorem 7. Let M^g be a k-kinematic surface of a surface M and $\{\phi_u, \phi_v\}$ be orthonormal basis such that ϕ_u and ϕ_v are principle vector fields on M and k_1, k_2 be principle curvatures of M . Let $X_p \in T_p(M)$ and $k_n^g(f^*(X_p))$ be the normal curvature of M^g in the direction $f^*(X_p)$. If we denote the angle between the unit vector X_p and ϕ_u by θ_1 and the angle between the unit vector X_p and ϕ_v by θ_2 then

$$k_n^g(f^*(X_p)) = \frac{\mu_1^* \cos^2 \theta_1 + \mu_2^* \cos \theta_1 \cos \theta_2 + \mu_3^* \cos^2 \theta_2}{\lambda_1^* \cos^2 \theta_1 + 2\lambda_2^* \cos \theta_1 \cos \theta_2 + \lambda_3^* \cos^2 \theta_2},$$

Proof. Substituting (5) and (6) into (14) gives the result.

Theorem 8. Let M^g be a k-kinematic surface of a surface M and $\{\phi_u, \phi_v\}$ be orthonormal basis such that ϕ_u and ϕ_v are principle vector fields on M and k_1, k_2 be principle curvatures of M . Then

$$D_{f^*(X_p)}^g = \{f^*(X_p) \in T_{f^*(X_p)}(M^g) \mid c_1^* x_1^2 + c_2^* x_1 x_2 + c_3^* x_2^2 = \pm 1\}, \tag{15}$$

where

$$f^*(X_p) = x_1\psi_u + x_2\psi_v,$$

$$c_1^* = \mu_1\langle\psi_u, \psi_u\rangle + \mu_2\langle\psi_u, \psi_v\rangle,$$

$$c_2^* = \mu_1\langle\psi_u, \psi_v\rangle + \mu_2\langle\psi_v, \psi_v\rangle + \mu_3\langle\psi_u, \psi_u\rangle + \mu_4\langle\psi_u, \psi_v\rangle,$$

$$c_3^* = \mu_3\langle\psi_u, \psi_v\rangle + \mu_4\langle\psi_v, \psi_v\rangle.$$

Proof. Let $f^*(X_p) \in T_{f(p)}(M^g)$. Then, since

$$D_{f(p)}^g = \{f^*(X_p) | \langle S^g(f^*(X_p)), f^*(X_p) \rangle = \pm 1\},$$

proof is clear.

Corollary 1. Let M^g be a k-kinematic surface of a surface M . Then the Dupin indicatrix of M^g at $f(p) \in M^g$ is

1. an ellipse if $c_2^2 - 4c_1c_3 < 0$,
2. a hyperbola if $c_2^2 - 4c_1c_3 > 0$,
3. a parabola if $c_2^2 - 4c_1c_3 = 0$.

REFERENCES

[1] A.C. Çöken, Ü. Çiftçi and C. Ekici, "On parallel timelike ruled surfaces with timelike rulings", *Kuwait Journal of Science and Engineering*, vol.35.1A, 21, 2008.

[2] T. Craig, "Note on Parallel Surfaces", *Journal für die reine und angewandte Mathematik*, vol. 94, pp. 162-170, 1883.

[3] L.P. Eisenhart, *A treatise on the differential geometry of curves and surfaces*, Ginn, 1909.

[4] S. Nizamoğlu, "Surfaces réglées parallèles", *Ege Üniv. Fen Fak. Derg.*, vol. 9, pp. 37-48, 1986.

[5] A. Grey, "Modern differential geometry of curves and surfaces", *Studies in Advanced Mathematics*, CRC Press, Ann Arbor, 1993.

[6] A.M. Patriciu, "On some 1,3H3-helicoidal surfaces and their parallel surfaces at a certain distance in 3-dimensional Minkowski space", *Annals of the University of Craiova-Mathematics and Computer Science Series*, vol. 37(4), pp. 93-98, 2010.

[7] W. Kühnel, "Differential Geometry", Student Mathematical Library, vol. 16. American Mathematical Society, Providence, 2002.

[8] R. Lopez, "Differential geometry of curves and surfaces in Lorentz-Minkowski space",

International Electronic Journal of Geometry, vol.7, pp.44-107, 2014.

[2] C. Ekici and A. C. Çöken, "The integral invariants of parallel timelike ruled surfaces", *Journal of Mathematical Analysis and Applications*, vol. 393(2), pp. 97-107, 2012.

[10] M. Çimdiker and C. Ekici "On the Spacelike Parallel Ruled Surfaces with Darboux Frame", *International Journal of Mathematical Combinatorics*, vol. 2, pp. 60-69, 2017.

[11] M. Dede and C. Ekici "On parallel ruled surfaces in Galilean space", *Kragujevac Journal of Mathematics*, vol. 40(1), pp. 47-59, 2016.

[12] Y. Ünlütürk and C. Ekici, "On Parallel Surfaces of Ruled Surfaces with Null Ruling in Minkowski 3-space", *International Mathematical Forum*, vol. 7(15), pp. 727-736, 2012.

[13] Ü. Z. Savcı, A. Görgülü and C. Ekici, "Parallel Surfaces of Ruled Weingarten Surfaces", *New Trends in Mathematical Sciences*, vol. 3(4), pp. 237-246, 2015.

[14] Y. Ünlütürk and C. Ekici, "Parallel Surfaces Satisfying the Properties of Ruled Surfaces in Minkowski 3 space", *Global Journal of Science Frontier Research: F Mathematics and Decision Sciences*, vol.14(1-F), pp. 79-95, 2014.

[15] Y. Ünlütürk, C. Ekici and E. Özusağlam, "Spacelike parallel ruled surfaces in Minkowski 3 space E_1^3 ", *Journal of Advanced Research in Pure Mathematics*, vol. 7(4), pp. 210-215, 2015.

[16] Y. Ünlütürk and E. Özusağlam, "On Parallel Surfaces In Minkowski 3-Space", *TWMS J. App. Eng. Math.*, vol. 3(2), pp. 214-222, 2013.

[17] Ö. Tarakçı and H.H. Hacısalihoğlu, "Surfaces At A Constant Distance From The Edge Of Regression On A Surface", *Applied Mathematics and Computation*, vol. 155, pp. 81-93, 2004.

[18] D. Sağlam and Ö. Boyacıoğlu Kalkan, "Surfaces At A Constant Distance From Edge Of Regression On A Surface In E_1^3 ", *Differential Geometry-Dynamical Systems*, vol. 12, pp. 187-200, 2010.

- [19] D. Sağlam and Ö. Boyacıoğlu Kalkan, "The Euler Theorem and Dupin Indicatrix For Surfaces At A Constant Distance From Edge Of Regression On A Surface In E_1^3 ," *Matematički Vesnik*, vol. 65(2), pp. 242-249, 2013.
- [20] D. Sağlam and Ö. Kalkan, "Conjugate tangent vectors and asymptotic directions for surfaces at a constant distance from edge of regression on a surface in E_1^3 ," *Konuralp Journal of Mathematics (KJM)*, vol. 2(1), pp. 24-35, 2014.
- [21] W.R. Hamilton, "On Quaternions; or on a new System of Imaginaries in Algebra" (letter to John T. Graves, dated October 17, 1843)." *Philos. Magazine*, vol.25, pp. 489-495, 1843.
- [22] W.K. Clifford, "Preliminary sketch of biquaternions", *Proc. London Math. Soc.*, pp. 381-395, 1871.
- [23] A.T. Yang, "Application of Quaternion Algebra and Dual Numbers to the Analysis of Spatial Mechanisms", Ph.D Thesis, Columbia University, 1963.
- [24] A.T. Yang and F. Freudenstein, "Application of a dual-number quaternion algebra to the analysis of spatial mechanisms", *ASME journal of Applied Mechanics*, vol. 86E(2), pp. 300-308, 1964.
- [25] E. Study, "Von den Bewegungen und Umlegungen", *Math. Ann.*, vol.39, pp.441-566, 1891.
- [26] E. Study, *Geometrie der Dynamen*, Leipzig, Germany, 1903.
- [27] A.P. Kotelnikov, *Vintovoe Schislenie i Nikotoriya Prilozheniya evo k Geometrie i Mechaniki*, Kazan, 1895.
- [28] H. Pottmann and J. Wallner, *Computational Line Geometry*, Springer Verlag, New York, 2001.
- [29] F.M. Dimentberg, *The Screw Calculus and Its Applications in Mechanics*, Moscow, 1965.
- [30] M. Hamann, "Line-symmetric motions with respect to reguli", *Mechanism and Machine Theory*, vol. 46 (7), pp. 960-974, 2011.
- [31] Q.J. Ge, "Kinematics-driven geometric modeling: A framework for simultaneous NC tool-path generation and sculpted surface design", in: *Proceedings of the 1996 IEEE International Conference on Robotics and Automation*, Minneapolis, MN, pp.1819-1824, 1996.
- [32] Q.J. Ge, D. Kang and M. Sirchia, "Kinematically generated dual tensor-product surfaces", in: *ASME Design Engineering Technical Conference*, 1998.
- [33] B. Jütler, M.G. Wagner, "Computer aided geometric design with spatial rational B-spline motions", *ASME J. Mech. Design*, vol. 119(2) pp. 193-201, 1996.
- [34] H. Pottmann, J. Wallner, "Contributions to motion based surface design", *Technical report Nr. 45, Institut fr Geometrie*, Technische Universitt Wien, 1997
- [35] K. Sprott, B. Ravani, "Kinematic generation of ruled surfaces", *Advances in Computational Mathematics*, vol. 17, pp. 115-133, 2002.
- [36] J.M. Selig, M. Husty, "Half-turns and line symmetric motions", *Mech. Mach. Theory*, vol. 46(2), pp. 156-167, 2011.
- [37] H.H. Hacısalihoğlu, *Diferensiyel Geometri*, İnönü Üniversitesi Fen-Edeb. Fakültesi Yayınları, Ankara, 1983.
- [38] A. Sabuncuoğlu, *Diferensiyel Geometri*, Nobel Yayıncılık, 2010.

	SAKARYA ÜNİVERSİTESİ FEN BİLİMLERİ ENSTİTÜSÜ DERGİSİ <i>SAKARYA UNIVERSITY JOURNAL OF SCIENCE</i>		
	e-ISSN: 2147-835X Dergi sayfası: http://www.saujs.sakarya.edu.tr		
	<u>Received</u> 10-08-2017 <u>Accepted</u> 26-02-2018	<u>Doi</u> 10.16984/saufenbilder.333927	

Comparison of Leaf Beetle (Coleoptera: Chrysomelidae) Diversity of Turkey and Neighboring Countries with Respect to Species Numbers and Endemicity

Ali Nafiz Ekiz*¹

ABSTRACT

According to number of leaf beetle species and subspecies, Turkey is the most diverse country by far among its neighbors with 916 reported taxa. The species numbers of neighboring countries are as follows: Bulgaria 603, Ukraine 582, Greece 507, Romania 495, Iran 479, Russia (only the southern European part included) 441, Azerbaijan 373, Armenia 294, Georgia 273, Syria 254, Cyprus (whole island) 136, Iraq 120 and Moldova 103. As to number of endemic taxa, Iran and Turkey keep ahead with 103 and 88 endemics respectively. The closest country is Greece with 32 endemics and Moldova contains no endemic taxa. However, when we calculate the rate of endemism, Iran is unmatched with an endemism ratio of 21.50%, followed by Iraq and Turkey having 10.00% and 9.61% endemism ratios respectively.

Keywords: Chrysomelidae, biodiversity, Turkey, number of species, endemism.

1. INTRODUCTION

A criterion, maybe the best one, for understanding and evaluating the biodiversity of a particular region, is to know the species numbers dwelling there. From this point of view, this study mainly aims to compare the leaf beetle diversity of Turkey and neighboring countries with respect to species numbers and the rate of endemism. The secondary aim of the study is to determine a possible correlation between the species numbers and the surface area of selected countries.

The leaf beetles (Chrysomelidae) constitute a diverse family with about 37,000 (possibly up to 50,000) described species arranged in 19 subfamilies and more than 2000 genera all over the world. Larvae and adults of Chrysomelidae live

and feed on leaves, flowers, stems or roots. Many members of the family are phytophagous and economically important pests or biological control agents of certain weeds [1,2,3].

Thanks to its location, Turkey has a quite rich biodiversity, so rich to be compared with continents. According to IUCN data [4], Europe has 12.500 plant species while 11.000 present only in Anatolia, and one third of these species are endemics. 1.500 vertebrate species (over 100 endemics) and more than 20.000 invertebrate species (about 4.000 endemics) are present in Turkey. Turkey is located in the middle of three biodiversity hotspots. These are Mediterranean basin, Caucasus and Irano-Anatolian hotspots. These hotspots make the area very important for biological biodiversity and conservation.

* Corresponding Author

¹ Uşak University, Faculty of Science and Arts, Department of Biology, Uşak, Turkey – nafiz.ekiz@usak.edu.tr

Turkey has many neighbors either by land or sea. The main purpose of this paper is to compare the leaf beetle diversity of these countries. Totally 14 countries are involved and compared: Turkey, Greece, Bulgaria, Romania, Moldova, Ukraine, Russia (South European part), Georgia, Armenia, Azerbaijan, Iran, Iraq, Syria and Cyprus Island.

2. MATERIAL AND METHODS

The neighboring countries of Turkey are selected according to contiguity either by land or sea. Totally 14 countries are included. Total number of leaf beetles (species and subspecies) reported from each country is determined by reviewing the relevant literature [5,6,7,8,9,10,11,12,13], as well as the number of endemics. The endemicity rates

of all countries are calculated and compared. The number of total taxa and endemics are then evaluated considering the total surface area (data taken from the website of FAO) of each country. Statistical analysis is performed via Excel 2010 software.

3. RESULTS AND DISCUSSION

Within these 14 countries, Turkey is the most diverse country with 916 leaf beetle taxa (including species and subspecies, and also including seed beetles, a subfamily of leaf beetles) [5,6,7,8,9,10,11]. The leaf beetle and seed beetle numbers of the neighbors are as in the Table 1 [5,12,13].

Table 1. The number of leaf beetle taxa of Turkey and neighboring countries

Countries	N. of leaf beetle taxa	Number of endemics	Endemism ratio (%)
Turkey	916	88	9.61
Bulgaria	603	10	1.66
Ukraine	582	6	1.03
Greece	507	32	6.31
Romania	495	17	3.43
Iran	479	103	21.50
Russia (S. Europe)	441	11	2.49
Azerbaijan	373	5	1.34
Armenia	294	12	4.08
Georgia	273	9	3.30
Syria	254	9	3.54
Cyprus Island	136	2	1.47
Iraq	120	12	10.00
Moldova	103	0	0

When we come to numbers of endemic leaf beetles (Table 1), Turkey still has a considerable number of endemics but here Iran has a spectacular number of endemic taxa [5,6,12]. Other prominent country is Greece [5]. Moldova has no endemics [5]. An interesting result is that, although it is an island, Cyprus has only two endemics [5]. This maybe shows a strong contact with the motherland Anatolia. When we look at the species numbers and endemic taxa numbers together, Iran and

Turkey stand out at first, but some important data about the endemism ratios must also be caught within the Table. When we look at the endemism ratios, Iran and Turkey are still prominent, but Iraq also has a high number of endemism ratio. Iraq has only 120 species and 10% of them are endemics. The actual number of taxa and endemism ratios of countries are given together in Figure 1. The three peaks that draw attention at first sight are Iran (21.50%), Iraq (10%) and Turkey (9.61%).

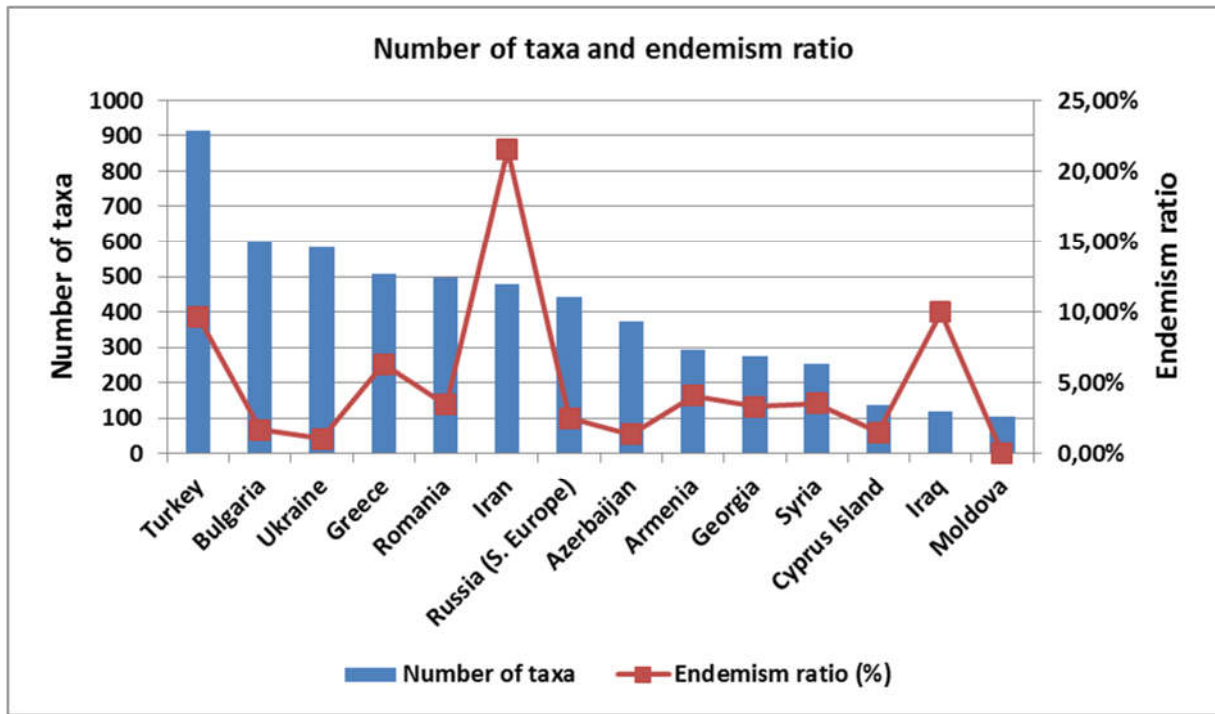


Figure 1. Number of taxa and endemism ratios (only the Southern European part of Russia is included)

One may expect more diverse habitat types in larger areas and thus more species numbers. The surface areas of the countries included in this study are taken from the web site of FAO [14]. The surface area of Russia is omitted from the analysis because only the Southern European part is involved in this study. Normally, there should be a correlation between the surface area and the number of species a country has. However, when we correlate these two variables, we see a weak

insignificant correlation ($r=0.41, p>0.05$) (Figure 2, left). The results belonging to Iran greatly deviates from the regression line. Iran is a very large country with diverse climatic factors and habitats but the reported leaf beetle diversity is not rich as expected. This is most likely a result of low number of field studies on leaf beetles. As to my knowledge, recently the faunistic works on leaf beetles are increasing and I believe that the numbers will increase also.

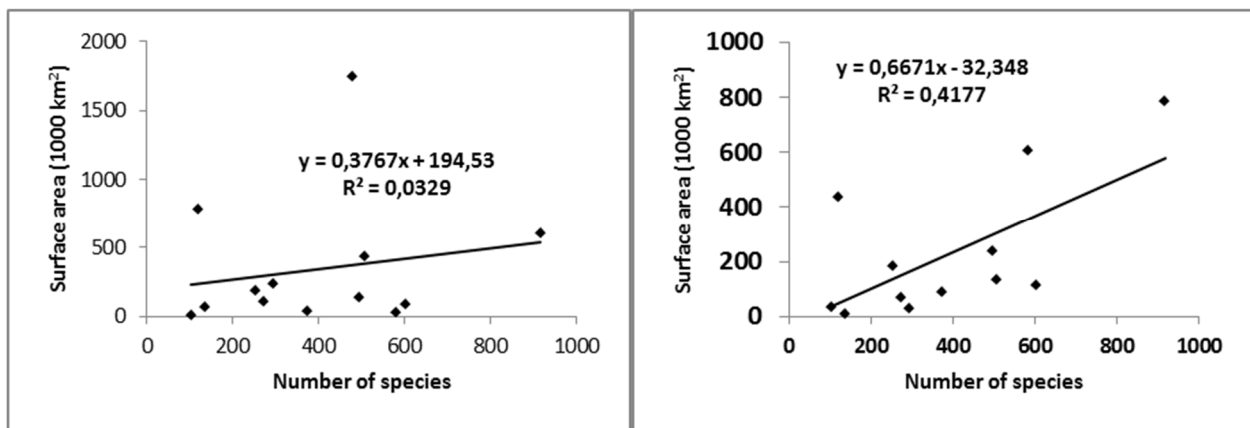


Figure 2. Correlation between the surface area and the number of taxa. (left, Iran is included; right, Iran is excluded)

When we exclude Iran from the data set (Figure 2, right), the correlation between the surface area and number of species increases and there is a modest positive correlation between these two variables ($r=0.65, p<0.05$).

ACKNOWLEDGEMENTS

This paper is presented as an oral presentation in SEAB-2016 (Symposium on Euroasian Biodiversity) held in Antalya, Turkey on 23-27 May 2016, and included in the abstract book.

REFERENCES

- [1] P. Jolivet, E. Petitpierre and T.H. Hasiao, "Biology of Chrysomelidae". Series entomologica, 42. Netherlands: Kluwer Academic Publishers, 606 pp. 1998.
- [2] R.G. Booth, M.L. Cox and R.B. Madge, "IIE guides to insects of importance to man. 3. Coleoptera". Cambridge: Cambridge University Press, 384 pp. 1990.
- [3] P. Jolivet and K.K.Verma, "Biology of leaf beetles". UK: Intercept Publishers, 332 pp. 2002.
- [4] <https://www.iucn.org/content/biodiversity-turkey>
- [5] I. Löbl, and A. Smetana, "Catalogue of Palaearctic Coleoptera: Chrysomeloidea, (Vol 6)". Stenstrup: Apollo Books, 924 pp, 2010.
- [5] A.N. Ekiz, İ. Şen, E.G. Aslan and A. Gök, "Checklist of leaf beetles (Coleoptera: Chrysomelidae) of Turkey, excluding Bruchinae", *Journal of Natural History*, 47:33-34, pp. 2213-2287, 2013.
- [7] E.G. Aslan, R. Beenen, F. Bayram and B. Aslan, "*Chloropterus versicolor* (Morawitz) in Turkey: Indigeneity Confirmed (Coleoptera: Chrysomelidae)". *J. Entomol. Res. Soc.*, 15(2), pp. 113-116, 2013.
- [8] İ. Şen and A. Gök, "A New Record of the Genus *Cassida* Linnaeus, 1758 from Turkey: *Cassida ferruginea* Goeze, 1777 (Coleoptera: Chrysomelidae)". *J. Entomol. Res. Soc.*, 15(1), pp. 69-72, 2013.
- [9] B. Aslan, F. Bayram and E.G. Aslan "First Record of the Flea Beetle *Psylliodes wrasei* Leonardi and Arnold (Chrysomelidae: Galerucinae: Alticini) in Turkey: A Promising Biological Control Agent for Hoary Cress, *Lepidium draba* L. (Brassicaceae)". *J. Entomol. Res. Soc.*, 16(2), pp. 111-115, 2014.
- [10] E.G. Aslan and K. Alkan, "The Alticini (Coleoptera: Chrysomelidae: Galerucinae) fauna of Davraz Mountain (Isparta): comments on host plant and altitude preferences with two new records for Turkish fauna". *Turk J Zool* 39, pp. 488-493, 2015.
- [11] J. Bezděk, "A Review of Palaearctic *Scelolyperus* (Coleoptera: Chrysomelidae: Galerucinae), with description of *S. perreus* sp. nov. from Turkey". *Annales Zoologici*, 65(1), pp. 21-39, 2015.
- [12] B. Gruev and V. Tomov, "A distributional atlas and catalogue of the leaf beetles of Bulgaria (Coleoptera: Chrysomelidae)". *Zoocartographica Balcanica* Vol. 3. Sofia-Moscow, Pensoft, pp.1-350, 2007.
- [13] M. Mirzaei, J. Nozari and V.H. Naveh, "Leaf Beetles (Coleoptera: Chrysomelidae) of Tehran, Alborz and Qazvin Provinces, Iran". *Acta Phytopathologica et Entomologica Hungarica*, 50(2), pp. 223-228, 2015.
- [14] <http://www.fao.org/faostat/en/#country>

	SAKARYA ÜNİVERSİTESİ FEN BİLİMLERİ ENSTİTÜSÜ DERGİSİ <i>SAKARYA UNIVERSITY JOURNAL OF SCIENCE</i>		
	e-ISSN: 2147-835X Dergi sayfası: http://www.saujs.sakarya.edu.tr		
	<u>Received</u> 06-12-2016 <u>Accepted</u> 26-02-2018	<u>Doi</u> 10.16984/saufenbilder.273829	

Synthesis of Nano Poly(2-thiophenecarboxaldehyde) and Characterization of Structure

Sezen SİVRİKAYA^{*1}, Aslıhan DALMAZ², Sefa DURMUŞ³

ABSTRACT

This article describes a chemical oxidative polymerization for the preparation of nano polymeric thiophene by using FeCl₃ as oxidant. 2-thiophenecarboxaldehyde (2-THCA) compound was used as a monomer at this polymerization process. The structure of synthesized nano polymeric thiophene was confirmed by scanning electron microscopy (SEM), fourier transform infrared spectroscopy (FTIR), thermogravimetric analysis (TGA), raman spectroscopy, and elemental analysis of C, H, O and S. SEM images showed that the poly(2-thiophenecarboxaldehyde) (PTHCA) was synthesized in nanoscale and had a homogeneous and smooth structure. The size of the synthesized nano particles was not more than 35 nm. Thermal analysis of nano polymeric thiophene showed that the polymer is thermally stable up to 450-460 °C. When elemental analysis results of PTHCA were examined, it was seen that the obtained data after the synthesis of nano polymeric thiophene and the theoretically determined data were agree with each other.

Keywords: 2-thiophenecarboxaldehyde, nano polymer, characterization

1. INTRODUCTION

Over the last few decades, extensive researches have been focused on the development of new functional organic materials for optics, electronics and other industrial applications. The most used organic materials for these applications were conductive polymers (ICPs) [1] such as polyaniline, polypyrrole (PPy) [2-4] and polythiophene (PTH) [5]. Among these polymers, polythiophene (PTH) has considerable attention due to the some characteristic properties such as high electrical [6] conductivity, environmental and thermal stability [7], oxidation and/or reduction levels, electrical and optical properties, high

energy density, easy and low cost synthesis or potential application in various fields such as electromagnetic interference (EMI), polymer rechargeable batteries, DNA detection, organic light emitting diodes (OLEDs), photovoltaic cells [8], electrical memory performance, separation membranes, sensors [9], biomedical fields and so on [10-20].

Two techniques for polymerization of thiophene have been reported in the literature. The first one is electrochemical polymerization and the second one is chemical oxidative polymerization [21]. In electrochemical polymerization some potential is applied through a solution of monomer. The

* Corresponding Author

¹ Department of Polymer Engineering, Faculty of Technology, Duzce University, TR-81620, Duzce, Turkey
sezensivrikaya@duzce.edu.tr

² Department of Composite Material Technologies, Graduate School Natural and Applied Sciences, Duzce University, TR-81620, Duzce, Turkey

³ Department of Chemistry, Faculty of Art and Science, Duzce University, TR-81620, Duzce, Turkey

chemical oxidants or cross-coupling catalysts are used in chemical polymerization process. The chemical method for the synthesis of polythiophenes offers two advantages when compared to electrochemical method, larger monomer selection and ability to synthesize polythiophenes nanoparticles using appropriate catalysts [22-25].

In the present work, we synthesized PTHCA by chemical polymerization method. In the polymerization process, FeCl_3 was used as an oxidant and 2-THCA was used as a monomer for the polymerization of thiophene. The synthesized nano polymeric thiophene was characterized by different techniques such as scanning electron microscope (SEM), fourier transform infrared spectroscopy (FTIR), thermogravimetric analysis (TGA), raman spectroscopy, and elemental analysis of C, H, O and S.

2. EXPERIMENTAL: MATERIAL AND METHODS

2.1. Material and Methods

2-thiophenecarboxaldehyde, anhydrous ferric(III) chloride, chloroform and methanol were all purchased from Merck KGaA, Darmstadt, Germany.

Fourier transform infrared (FTIR) spectra of the polythiophene were recorded by Perkin Elmer Spectrum FTIR in the range of $4000\text{--}400\text{ cm}^{-1}$ with ATR technique. Thermal properties of the PTHCA were investigated using thermogravimetric analyzer Shimadzu DTG-60H instruments. The thermogravimetric experiments were conducted under nitrogen atmosphere in a temperature range of $25\text{--}1200\text{ }^\circ\text{C}$ with a heating rate of $10\text{ }^\circ\text{C}/\text{min}$. The morphology of polythiophene was analyzed by using FEI Quanta FEG 250 scanning electron microscopy (SEM). Raman spectroscopic studies were carried out by a Renishaw Invia Raman Microscope. The polythiophene composition was determined by elemental analysis using Thermo Scientific Flash 2000 elemental analyzer.

2.2. Synthesis of poly 2-thiophene carboxaldehyde

4.7 mL of 0.05 mol of 2-THCA was mixed with 350 mL of chloroform in a two-necked round-bottom flask containing a magnetic stir bar. 0.15 mol of anhydrous FeCl_3 was dissolved in 150 mL chloroform. Anhydrous FeCl_3 solution was put in a dropping funnel and it was added drop by drop to the stirred thiophene solution. The polymerization was continued at room temperature for 24 hours. Dark brown precipitate was filtered and washed first with CHCl_3 and then washed with methanol several times to remove the oxidant. The consisted PTHCA powder was dried at $50\text{ }^\circ\text{C}$ for 24 h. The reaction for the synthesis of PTHCA was presented in Figure 1. Reaction mechanism was occurred (i); head-to-tail-head-to-tail (ii) head-to-head-head-to-tail (iii) head-to-tail-tail-to-tail and (iv) head-to-head-tail-to-tail as shown in the literature [24, 26]. Since the polymerization yield is about 20%, the soluble fraction is too weak to determine the average molecular weight and NMR analysis [24, 26-27].

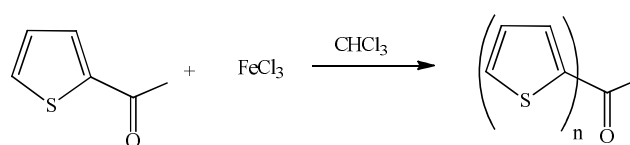


Figure 1. Synthesis of PTHCA

3. RESULTS

3.1. FTIR Spectroscopy Analysis

The chemical structures of PTHCA and 2-THCA were elucidated by FTIR spectroscopy and the spectra were demonstrated in Figure 2. The FTIR spectrum of THCA (Figure 2a) showed that a broad --OH stretching absorption band was between 3500 and 3100 cm^{-1} and the aliphatic C--H stretching band was between 2990 and 2850 cm^{-1} . As the --OH stretching band and the aliphatic C--H stretching band were aligned, they appeared as a broad band from 3089 to 2837 cm^{-1} in the spectrum. When the FTIR spectrum of PTHCA (Figure 2b) was examined, the major peaks observed at 1629 cm^{-1} and 1423 cm^{-1} assigned for C=C asymmetric and symmetric stretching vibration of thiophene ring. The other peaks at 1313 cm^{-1} , 1055 cm^{-1} and 1029 cm^{-1} were due to deformation of C-H bending and CH in-plane of vibrations. The peak at 891 cm^{-1} and at 661 cm^{-1} was assigned for C-S bending vibration and C-S-C ring deformation stretching of PTHCA,

respectively. These peaks proved that the polymerization process was successfully carried out and the PTHCA was synthesized.

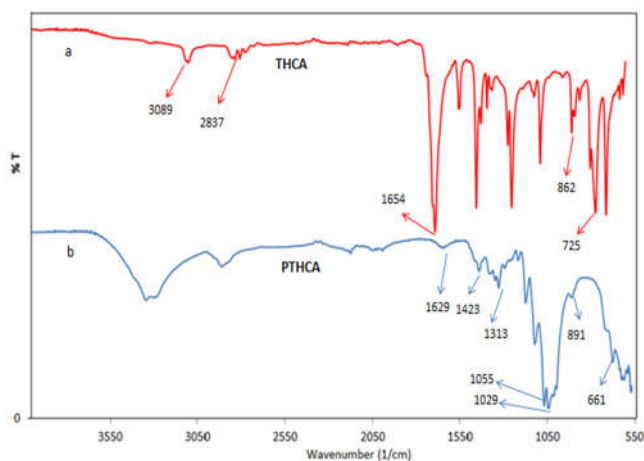


Figure 2. FTIR spectra of (a) 2-THCA and (b) PTHCA

3.2. Raman Spectroscopy Analysis

The Raman spectrum peak exhibited a peak at 1641 cm^{-1} showed dispersion with increasing polymer chain length [28]. The most significant peaks at 1584 cm^{-1} and 1462 cm^{-1} accredited with the C=C ring stretching of the PTHCA. The peak at about 1354 cm^{-1} was C–C ring stretching. The peaks at 1147 cm^{-1} and 1027 cm^{-1} assigned to the ring symmetric bending vibration and the in-plane C-H bending mode, respectively. The peak at 779 cm^{-1} was attributed to the ring deformation C–S–C. Raman spectrum of PTHCA was described in Figure 3.

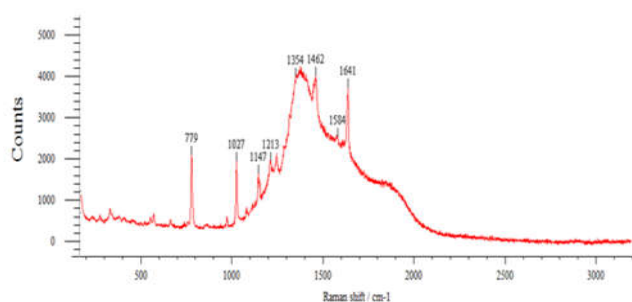


Figure 3. Raman spectrum of PTHCA

3.3. Scanning Electron Microscopy Analysis

The scanning electron microscope (SEM) in Figure 4 exhibited the surface morphology of PTHCA. These SEM images clearly indicated that the formed particles were uniform and homogeneous. Their dimensions were no more than 35 nm. This means that the synthesized PTHCA was nano-sized. Smooth surface of

polythiophene indicates that the synthesized PTHCA has a better conductivity than other rough polythiophene compounds [20].

3.4. Thermogravimetric analysis

As shown in Figure 5, TGA study of the PTHCA indicates that there were two weight loss areas and the initial decomposition occurred at about 50–150 °C due to the loss of solvent and water. The second weight loss started at 512 °C was due to thermal decomposition of polythiophene. The TGA curve showed that the first and second weight loss areas of the polythiophene were 12 and 78 wt %, respectively. The DTA curve showed as small exothermic peak at about 100 °C related with the loss of solvent and water from polythiophene and an exothermic peak at 600 °C conformed to thermal degradation of polythiophene. Thermal analysis of nano polymeric thiophene showed that the polymer is thermally stable up to 450-460 °C.

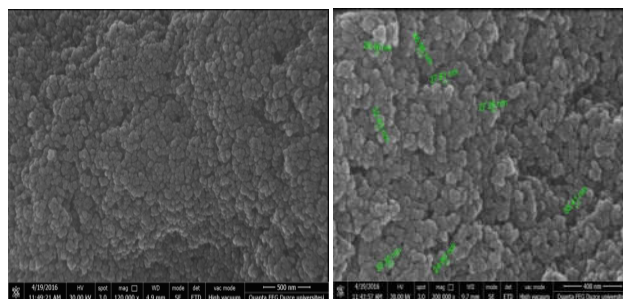


Figure 4. SEM images of PTHCA

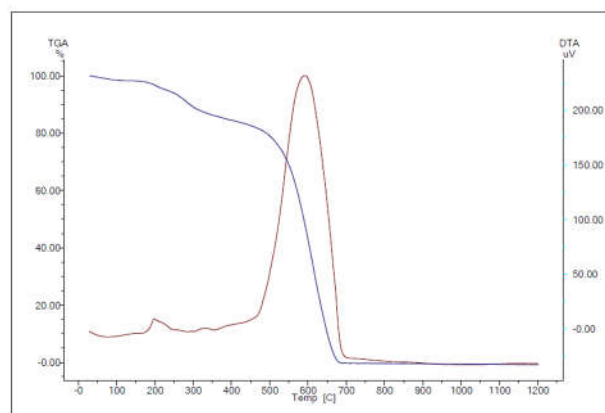


Figure 5. TGA and DTA spectra of PTHCA

3.5. Elemental analysis

Elemental analysis was performed to determine the elemental composition of the synthesized PTHCA. Theoretical and experimental results of PTHCA were presented at Table 1. The results

presented in Table 1 proved that the experimental data were compatible with theoretical ones for the synthesized polythiophene.

Table 1. Elemental analysis of polythiophene

PTHCA	Theoretical	Experimental
% C	57.11	54.48
% H	4.79	4.31
% S	25.41	27.02
% O	12.68	10.67

4. CONCLUSION

The nano polythiophene particles were successfully synthesized by chemical oxidative polymerization method. The structure of nano polythiophene was characterized by FTIR, TGA, Raman Spectroscopy and Elemental Analysis techniques. The surface morphology of nano poly(2-thiophenecarboxaldehyde) was also examined with SEM. The sizes of the synthesized nano particles were not more than 35 nm. The TGA studies showed that the PTHCA was thermally stable up to 512 °C.

Acknowledgments

This work was supported by the Duzce University Research Fund with Project Number 2014-05-03-259 and 2015-05-03-354.

REFERENCES

- [1] J. Huang, "Synthesis and applications of conducting polymer polyaniline nanofibers," *Pure and Applied Chemistry*, vol. 78, no. 1, pp. 15–27, 2006.
- [2] T. Sudwilai, J. J. Ng, C. Boonkrai, N. Israsena, S. Chuangchote, and P. Supaphol, "Polypyrrole-coated electrospun poly(lactic acid) fibrous scaffold: effects of coating on electrical conductivity and neural cell growth," *Journal of Biomaterials Science-Polymer Edition*, vol. 25, no. 12, pp. 1–13, 2014.
- [3] R. Garg, D. Kumar, and S. K. Chakarvarti, "Synthesis of microwires of polypyrrole via chemical polymerization using track etch membrane as template," *American Journal of Material Science Technology* vol. 3, no. 1, pp. 1–12, 2014.
- [4] X. Zhou, A. Yang, Z. Huang, G. Yin, X. Pu, and J. Jin, "Enhancement of neurite adhesion, alignment and elongation on conductive polypyrrole-poly(lactide acid) fibers with cell-derived extracellular matrix," *Colloids Surfaces B Biointerfaces*, vol. 149, pp. 217–225, 2017.
- [5] S. K. Moosvi, K. Majid, and T. Ara, "Study of thermal, electrical, and photocatalytic activity of iron complex doped polypyrrole and polythiophene nanocomposites," *Industrial Engineering Chemistry Research*, vol. 56, no. 15, pp. 4245–4257, 2017.
- [6] R. Kroon, D. Kiefer, D. Stegerer, L. Yu, M. Sommer, and C. Müller, "Polar side chains enhance processability, electrical conductivity, and thermal stability of a molecularly p-Doped polythiophene," *Advanced Materials*, vol. 29, no. 24, pp. 1–7 1700930, 2017.
- [7] B. X. Valderrama-Garca, E. Rodriguez-Alba, E. G. Morales-Espinoza, K. M. Chane-Ching, E. Rivera, S. Reed, and M. Resendiz, "Synthesis and characterization of novel polythiophenes containing pyrene chromophores: thermal, optical and electrochemical properties," *Molecules*, vol. 21, no. 2, pp.1-18, 2016.
- [8] H. Kim, D. Yeo, B. Won, S. Yu, and D. Jung, "Effects of bending radii on the characteristics of flexible organic solar cells investigated by impedance analysis," *Journal of Nanoscience and Nanotechnology*, vol. 16, no. 5, pp. 5384–5388, 2016.
- [9] C. Guo, P. Li, M. Pei, and G. Zhang, "A new polythiophene derivative-based fluorescent sensor for Co^{2+} , Cu^{2+} , Cd^{2+} , and its complex with Cu^{2+} for sensing homocysteine and glutathione," *Sensors Actuators, B-Chemical*, vol. 221, pp. 1223–1228, 2015.
- [10] S. Sakthivel and A. Boopathi, "Synthesis and preparation of polythiophene thin film by spin coating method," *J. Chemistry Chem. Sci.*, vol. 4, no. 3, pp. 150–155, 2014.
- [11] A. Acharya, R. Mishra, and G. S. Roy, "Characterization of CdSe/polythiophene nanocomposite by TGA/DTA, XRD, UV-VIS Spectroscopy, SEM-EDXA and FTIR," *Armenian Journal of Physics*, vol. 3, no. 3, pp. 195–202, 2010.
- [12] A. Gök, M. Omastová, and A. G. Yavuz,

- "Synthesis and characterization of polythiophenes prepared in the presence of surfactants," *Synthetic Metals*, vol. 157, no. 1, pp. 23–29, 2007.
- [13] B. Massoumi and M. Jaymand, "Conducting poly(vinyl chloride)-graft-polythiophene: synthesis, characterization, and materials properties," *Journal of Materials Science-Materials in Electronics*, vol. 27, no. 3, pp. 2267–2275, 2016.
- [14] S. Kumar, P. K. Dutta, and P. Sen, "Preparation and characterization of optical property of crosslinkable film of chitosan with 2-thiophenecarboxaldehyde," *Carbohydrate Polymers*, vol. 80, no. 2, pp. 564–570, 2010.
- [15] M. O. Ansari, M. M. Khan, S. A. Ansari, and M. H. Cho, "Polythiophene nanocomposites for photodegradation applications: Past, present and future," *Journal of Saudi Chemical Society*, vol. 19, no. 5, pp. 494–504, 2015.
- [16] T. A. Skotheim and J. R. Reynolds, *Handbook of Conducting Polymers: Conjugated Polymers Processing and Applications*, 2007.
- [17] H. A. Ho, A. Najari, and M. Leclerc, "Optical detection of DNA and proteins with cationic polythiophenes," *Accounts of Chemical Research*, vol. 41, no. 2, pp. 168–178, 2008.
- [18] J. K. Mwaura, X. Zhao, H. Jiang, K. S. Schanze, and J. R. Reynolds, "Spectral broadening in nanocrystalline TiO₂ solar cells based on poly(p-phenylene ethynylene) and polythiophene sensitizers," *Chemistry of Materials*, vol. 18, no. 26, pp. 6109–6111, 2006.
- [19] Y. Zou, W. Wu, G. Sang, Y. Yang, Y. Liu, and Y. Li, "Polythiophene derivative with phenothiazine-vinylene conjugated side chain: synthesis and its application in field-effect transistors," *Macromolecules*, vol. 40, no. 20, pp. 7231–7237, 2007.
- [20] R. Liu and Z. Liu, "Polythiophene: Synthesis in aqueous medium and controllable morphology," *Chinese Science Bulletin*, vol. 54, no. 12, pp. 2028–2032, 2009.
- [21] S. Murugavel and M. Malathi, "Morphological and electrical conductivity properties of unsubstituted polythiophene nanostructures prepared by surfactant-assisted chemical polymerization method," *International Journal of ChemTech Research*, vol. 9, no. 3, pp. 616–622, 2016.
- [22] R. J. Waltman, J. Bargon, and A. F. Diaz, "Electrochemical studies of some conducting polythiophene films," *The Journal of Physical Chemistry*, vol. 87, no. 8, pp. 1459–1463, 1983.
- [23] B. Sari, M. Talu, F. Yildirim, and E. Ku, "Synthesis and characterization of polyurethane/polythiophene conducting copolymer by electrochemical method," *Applied Surface Science*, vol. 205, pp. 27–38, 2003.
- [24] I. Ben Khalifa, S. Ayachi, B. Zaidi, M. Bouachrine, A. Mabrouk, and K. Alimi, "Correlation structure-properties of poly(3-methyl-thiophene) (P3MTh) synthesized using TiCl₄ as an oxidant," *Synthetic Metals*, vol. 162, no. 19–20, pp. 1724–1730, 2012.
- [25] M. Chahma, "Synthesis and characterization of poly(thiophene sulfides) prepared via chemically initiated oxidative polymerization methods," *Synthetic Metals*, vol. 155, no. 3, pp. 474–479, 2005.
- [26] J. M. Xu, H. S. O. Chan, S. C. Ng, and T. S. Chung, "Polymers synthesized from (3-alkylthio) thiophenes by the FeCl₃ oxidation method," *Synthetic Metals*, vol. 132, pp. 63–69, 2002.
- [27] C. Lopez-Mata, M. E. Nicho, H. Hu, G. Cadenas-Pliego, E. Garcia Hernandez, "Optical and morphological properties of chemically synthesized poly(3-octylthiophene) thin films," *Thin Solid Films*, vol. 490, no. 2, pp. 189–195, 2005.
- [28] E. Agosti, M. Rivola, V. Hernandez, M. Del Zoppo, and G. Zerbi, "Electronic and dynamical effects from the unusual features of the Raman spectra of oligo and polythiophenes," *Synthetic Metals*, vol. 100, no. 1, pp. 101–112, 1999.

	SAKARYA ÜNİVERSİTESİ FEN BİLİMLERİ ENSTİTÜSÜ DERGİSİ <i>SAKARYA UNIVERSITY JOURNAL OF SCIENCE</i>		
	e-ISSN: 2147-835X Dergi sayfası: http://www.saujs.sakarya.edu.tr		
	<u>Received</u> 10-10-2017 <u>Accepted</u> 11-03-2018	<u>Doi</u> 10.16984/saufenbilder.342571	

Numerical Solutions of the Gardner Equation via Trigonometric Quintic B-spline Collocation Method

Ozlem Ersoy Hepson*¹

ABSTRACT

The main purpose of this paper is to get the numerical solutions of the Gardner equation which are widely used in various disciplines. For this purpose, the time integration of the system is achieved by the classical Crank-Nicolson method owing to its large stability region. Space discretization is done by using the trigonometric quintic B-spline functions. Thus the Gardner equation turns into a penta diagonal matrix equation and the Thomas algorithm is applied owing to lower cost of computation when compared Gauss or Gauss-Jordan elimination methods.

Keywords: Gardner Equation, trigonometric quintic B-spline, collocation, wave generation, interaction of two solitary waves.

1. INTRODUCTION

The Gardner equation is a model for the description of weakly nonlinear dispersive waves in situations

$$u_t + \alpha uu_x + \beta u^2 u_x + \gamma u_{xxx} \quad (1.1)$$

where α , β and γ are constant parameters and $u^2 u_x$ is a dissipative term. Nonlinear ion-acoustic waves in plasmas have been studied for a long time. The Gardner equation governing these waves in plasmas with the negative ion concentration close to critical is used [1]. The equation can also describe internal waves with large amplitudes and weakly nonlinear dispersive waves [2]. An

analytical study deals with unsteady wave patterns occurring in the dispersive resolution of the upstream and downstream hydraulic jumps in the transcritical flows governed by the Gardner equation[3]. In [4], construction of conservative finite difference schemes is applied to the Gardner equation. The Restrictive Taylor Approximation is described to obtain numerical solution of Gardner equation in [5]. Extended tanh method was used to construct solitary and soliton solutions of Gardner equations by Bekir [6]. Projective Riccati equations used to generate some hyperbolic type solitary wave [7]. In [8], a new exact traveling wave solutions get by $(G'/G, 1/G)$ expansion approach. The mapping method is employed to carry out the integration of the equation [9]. Lie group and tan-cot methods are also effective

¹ ozersoy@ogu.edu.tr

methods to obtain the solutions of the Gardner equation [10]. A recent study also has dealt with the Gardner equation by solving it numerically using finite element method based on polynomial quintic B-splines[11].

Recently trigonometric B-splines have been adapted to construct numerical techniques for getting solutions of differential equations such as diffusion problems, Fisher equation and Burger equations in [12,13,14]. Quintic trigonometric B-spline functions are newly defined basis function that are different from polynomial [15,16], exponential [17,18] ones but in the family of trigonometric B-splines. Also trigonometric quintic B-spline collocation method was applied to solve coupled Burgers' equation system in [19].

In this paper, the numerical solutions of Gardner equation by the trigonometric quintic B-spline finite element method are searched. Fully-integration of Gardner equation is obtained by using Crank-Nicolson method and trigonometric quintic B-spline collocation method for the time and space discretization respectively. The efficiency of the proposed method together with the trigonometric quintic B-splines is observed on solutions of Gardner equation.

The initial condition

$$u(x, 0) = f(x) \tag{1.2}$$

and the zero Neumann boundary conditions

$$\begin{aligned} u_{xx}(a, t) = 0, u_{xx}(b, t) = 0, \\ u_{xxx}(a, t) = 0, u_{xxx}(b, t) = 0 \end{aligned} \tag{1.3}$$

at both end of the artificial $[a, b]$.

2. TRIGONOMETRIC QUINTIC B-SPLINE COLLOCATION METHOD

Consider a uniform partition of the problem domain $[x_0=a, x_N=b]$, with the grids $x_m, m=0, 1, \dots, N$ and $h=(b-a)/N$. The definition of the trigonometric quintic B-splines requires the support of ghost grids located out of the problem domain. Trigonometric quintic B-splines $T_m(x), m=-2, \dots, N+2$ are defined at the nodes x_m by [20]

$$T_m(x) = \frac{1}{h} \begin{cases} \rho^5(x_{m-2}) & , x_{m-2} \leq x < x_{m-1} \\ -\rho^4(x_{m-2})\rho(x_m) - \rho^3(x_{m-2})\rho(x_{m+1})\rho(x_{m-1}) & , x_{m-1} \leq x < x_m \\ -\rho^2(x_{m-2})\rho(x_{m+2})\rho^2(x_{m-1}) - \rho(x_{m-2})\rho(x_{m+3})\rho^3(x_{m-1}) \\ -\rho(x_{m+4})\rho^4(x_{m-1}) & , x_m \leq x < x_{m+1} \\ \rho^3(x_{m-2})\rho^2(x_{m+1}) + \rho^2(x_{m-2})\rho(x_{m+2})\rho(x_{m-1})\rho(x_{m+1}) \\ +\rho^2(x_{m-2})\rho^2(x_{m+2})\rho(x_m) + \rho(x_{m-2})\rho(x_{m+3})\rho^2(x_{m-1})\rho(x_{m+1}) + \\ \rho(x_{m-2})\rho(x_{m+3})\rho(x_{m-1})\rho(x_{m+2})\rho(x_m) + \rho(x_{m-2})\rho^2(x_{m+3})\rho^2(x_m) \\ +\rho(x_{m+4})\rho^3(x_{m-1})\rho(x_{m+1}) + \rho(x_{m+4})\rho^2(x_{m-1})\rho(x_{m+2})\rho(x_m) \\ +\rho(x_{m+4})\rho(x_{m-1})\rho(x_{m+3})\rho^2(x_m) + \rho^2(x_{m+4})\rho^3(x_m) & , x_{m+1} \leq x < x_{m+2} \\ -\rho^2(x_{m-2})\rho^3(x_{m+2}) - \rho(x_{m-2})\rho(x_{m+3})\rho(x_{m-1})\rho^2(x_{m+2}) \\ -\rho(x_{m-2})\rho^2(x_{m+3})\rho(x_m)\rho(x_{m+2}) - \rho(x_{m-2})\rho^3(x_{m+3})\rho(x_{m+1}) \\ -\rho(x_{m+4})\rho^2(x_{m-1})\rho^2(x_{m+2}) - \rho(x_{m+4})\rho(x_{m-1})\rho(x_{m+3})\rho(x_m)\rho(x_{m+2}) \\ -\rho(x_{m+4})\rho(x_{m-1})\rho^2(x_{m+3})\rho(x_{m+1}) - \rho^2(x_{m+4})\rho^2(x_m)\rho(x_{m+2}) - \\ \rho^2(x_{m+4})\rho(x_m)\rho(x_{m+3})\rho(x_{m+1}) - \rho^3(x_{m+4})\rho^2(x_{m+1}) & , x_{m+2} \leq x < x_{m+3} \\ \rho(x_{m-2})\rho^4(x_{m+3}) + \rho(x_{m+4})\rho(x_{m-1})\rho^3(x_{m+3}) + \rho^2(x_{m+4})\rho(x_m)\rho^2(x_{m+3}) \\ +\rho^3(x_{m+4})\rho(x_{m+1})\rho(x_{m+3}) + \rho^4(x_{m+4})\rho(x_{m+2}) & , x_{m+3} \leq x < x_{m+4} \\ -\rho^5(x_{m+4}) & , x_{m+3} \leq x < x_{m+4} \\ 0 & \text{otherwise} \end{cases}$$

where

$$\rho(x_{m+2}) = \sin((x - x_m)/2),$$

$$\theta = \sin(h/2)\sin(h)\sin(3h/2)\sin(2h)\sin(5h/2),$$

$$m = 0(1)N.$$

Let $U(x, t)$ be approximate solution to $u(x, t)$ defined as

$$U(x, t) = \sum_{m=-2}^{N+2} \delta_m(t) T_m(x)$$

Where δ_m are time dependent parameters that are determined from the collocation points $x_m, m=0, 1, \dots, N$ and the manipulations on initial and boundary data. Trigonometric quintic B-splines and its first four derivatives are continuous on element $[x_{m-2}, x_{m+4}]$. The functional and derivative values of $U(x, t)$ at a grid x_m is described in terms of time dependent parameters δ as

$$U(x_m) = a_1\delta_{m-1} + a_2\delta_m + a_3\delta_{m+1} + a_4\delta_{m+2} + a_5\delta_{m+3},$$

$$U'(x_m) = b_1\delta_{m-1} + b_2\delta_m - b_2\delta_{m+2} - b_1\delta_{m+3},$$

$$U''(x_m) = c_1\delta_{m-1} + c_2\delta_m + c_3\delta_{m+1} + c_4\delta_{m+2} + c_5\delta_{m+3},$$

$$U'''(x_m) = d_1\delta_{m-1} + d_2\delta_m - d_2\delta_{m+2} - d_1\delta_{m+3},$$

$$U''''(x_m) = e_1\delta_{m-1} + e_2\delta_m + e_3\delta_{m+1} + e_4\delta_{m+2} + e_5\delta_{m+3}$$

$$(2.1)$$

The coefficients of the time dependent parameters in (2.1) take the forms

$$a_1 = \sin^5(h/2)/\theta$$

$$a_2 = 2\sin^5(h/2)\cos(h/2) (16\cos^2(h/2)-3)/\theta$$

$$B = \begin{bmatrix} \psi_6 & \psi_7 & \psi_8 & \psi_9 & \psi_{10} & & & & & & \\ & \psi_6 & \psi_7 & \psi_8 & \psi_9 & \psi_{10} & & & & & \\ & & \ddots & \ddots & \ddots & \ddots & \ddots & & & & \\ & & & \psi_6 & \psi_7 & \psi_8 & \psi_9 & \psi_{10} & & & \end{bmatrix}$$

and

$$\psi_1 = (2/\Delta t + \alpha\lambda + 2\beta\kappa\lambda)a_1 + (\alpha\kappa + \beta\kappa)b_1 + \gamma d_1,$$

$$\psi_2 = (2/\Delta t + \alpha\lambda + 2\beta\kappa\lambda)a_2 + (\alpha\kappa + \beta\kappa^2)b_2 + \gamma d_2$$

$$\psi_3 = (2/\Delta t + \alpha\lambda + 2\beta\kappa\lambda)a_3,$$

$$\psi_4 = (2/\Delta t + \alpha\lambda + 2\beta\kappa\lambda)a_2 - (\alpha\kappa + \beta\kappa^2)b_2 - \gamma d_2$$

$$\psi_5 = (2/\Delta t + \alpha\lambda + 2\beta\kappa\lambda)a_1 - (\alpha\kappa + \beta\kappa^2)b_1 - \gamma d_1,$$

$$\psi_6 = (2/\Delta t + \beta\kappa^2\lambda)a_1 - \gamma d_1$$

$$\psi_7 = (2/\Delta t + \beta\kappa^2\lambda)a_2 - \gamma d_2,$$

$$\psi_8 = (2/\Delta t + \beta\kappa^2\lambda)a_3$$

$$\psi_9 = (2/\Delta t + \beta\kappa^2\lambda)a_2 + \gamma d_2,$$

$$\psi_{10} = (2/\Delta t + \beta\kappa^2\lambda)a_2 + \gamma d_1$$

The boundary conditions $U_{xx}(a,t)=0$, $U_{xx}(b,t)=0$, $U_{xxx}(a,t)=0$ and $U_{xxx}(b,t)=0$

are used to eliminate parameters $\delta_{-1}^{n+1}, \sigma_{-1}^{n+1}, \delta_{-0}^{n+1}, \sigma_{-0}^{n+1}, \delta_{N+2}^{n+1}, \sigma_{N+2}^{n+1}, \delta_{N+3}^{n+1}, \sigma_{N+3}^{n+1}$ from the system (2.5) so that we have a solvable $(2N+2) \times (2N+2)$ 5-banded matrix system. This system is solved with Matlab program using Thomas algorithm.

Time evolution of parameters δ_m^{n+1} and σ_m^{n+1} is computed once the initial parameters δ_m^0 and σ_m^0 are obtained via initial and boundary conditions as below:

$$U_{xx}(a,0) = c_1\delta_{-2}^0 + c_2\delta_{-1}^0 + c_3\delta_0^0 + c_2\delta_1^0 + c_1\delta_2^0 = 0,$$

$$U_{xxx}(a,0) = d_1\delta_{-2}^0 + d_2\delta_{-1}^0 - d_2\delta_1^0 - d_1\delta_2^0 = 0,$$

$$U(x,0) = a_1\delta_{m-1}^0 + a_2\delta_m^0 + a_3\delta_{m+1}^0 + a_2\delta_{m+2}^0 + a_1\delta_{m+3}^0 = U(x_m,0), m = 0(1)N-1,$$

$$U_{xx}(b,0) = c_1\delta_{N-1}^0 + c_2\delta_N^0 + c_3\delta_{N+1}^0 + c_2\delta_{N+2}^0 + c_1\delta_{N+3}^0 = 0,$$

$$U_{xxx}(b,0) = d_1\delta_{N-1}^0 + d_2\delta_N^0 - d_2\delta_{N+2}^0 - d_1\delta_{N+3}^0 = 0.$$

3. NUMERICAL EXAMPLES

In this section, we solve some analytical and non-analytical initial boundary value problems to validate the proposed method and present the

results. The accuracy of suggested method problem is shown by calculating the error norm

$$L_\infty = |u-U|_\infty = \max |u_m^n - U_m^n|$$

where u_m and U_m represent exact and numerical solutions at the n.th time level, respectively.

3.1. Kink type Wave Propagation

Use Kink type wave solution of the Gardner equation is [17]

$$u(x,t) = \frac{1}{10} - \frac{1}{10} \tanh\left(\frac{\sqrt{30}}{60}\left(x - \frac{1}{30}t\right)\right) \quad (3.1)$$

kink type wave travels to the right with the velocity $1/30$, Fig 1. The initial condition required to start the iteration of the time integration is determined by assuming $t=0$ in the analytical solution (3.1). We choose homogeneous Neumann conditions. We compute the numerical solutions using the selected values $\alpha=1$, $\beta=-5$ and $\mu=1$ with different values of time step size Δt . In our first computation, we take $\Delta t=0.1$ and $\Delta t=0.01$ while the number of partition N changes. The corresponding results are presented in Table 1. In our computation, we compute the maximum absolute errors at time level $t=12$ in the finite interval $[-80,80]$. The error distribution is plotted in Fig 2. The error is concentrated about the points where the wave height changes rapidly.

Table 1. Comparison of the max. Error norms at $t=12$

N	$\Delta t=0.1$	$\Delta t=0.01$
200	1.2361×10^{-3}	1.3288×10^{-3}
400	7.2063×10^{-5}	8.3593×10^{-5}
600	1.3221×10^{-5}	1.6551×10^{-5}
800	3.9570×10^{-6}	5.1655×10^{-6}

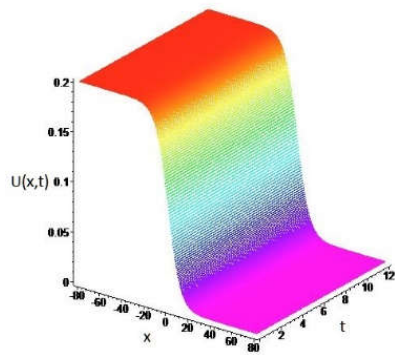


Fig. 1. Motion of the kink type wave at $t=12$, $N=200$

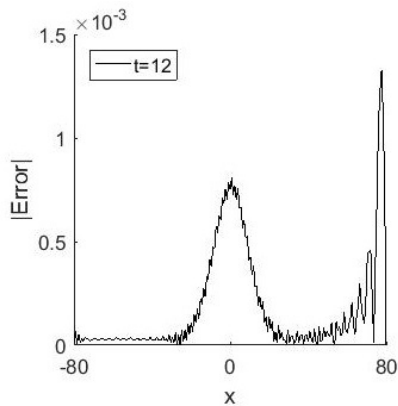


Fig. 2. The maximum error distributions at $t=12$, $N=200$

3.2. Generation of new wave

Generation of wave is studied for the Gardner's equation in the study [4]. In this section, same simulation is carried out for the perturbed Gardner's equation. Thus to the perturbed Gardner equation of the form

$$u_t + \alpha u u_x + \beta u^2 u_x + \mu u_{xxx} = \zeta \tag{3.2}$$

for $\zeta > 0$ can be useful to study the wave generation from an initial positive pulse. The decomposition of the balance among the nonlinear terms and the third order derivative is expected not to keep the shape or velocity as propagating. Thus, the initial condition is generated from the initial condition of the first problem sensitively as

$$u(x,t) = \frac{2}{3} \frac{5}{4 + \sqrt{14} \cosh\left(\frac{x}{3} - \frac{5}{3}\right)} \tag{3.3}$$

by perturbation the initial condition. We choose the parameters $\alpha=10$, $\beta=-3$ and $\mu=1$ in the Gardner equation (3.2). We run the proposed algorithms with the discretization parameters $N=400$ and $\Delta t=0.01$ in the artificial problem interval $[-40,60]$ up to the time $t=15$. Simulation of the wave generation is shown in Figs 3-6. Initial wave is split into three new solitary waves and further one has started to become solitary wave when time reach at $t=15$, seen in Fig. 6.

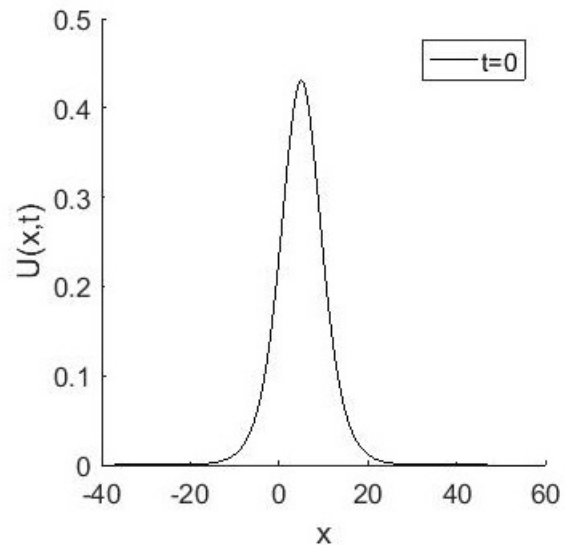


Fig. 3. Wave generation for initial data

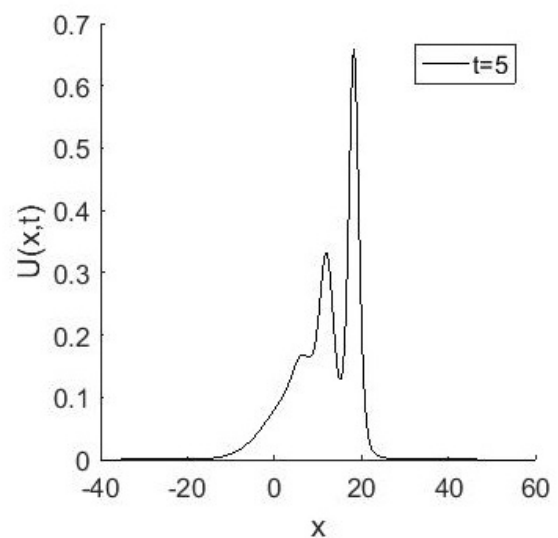


Fig. 4. Wave generation for $t=5$

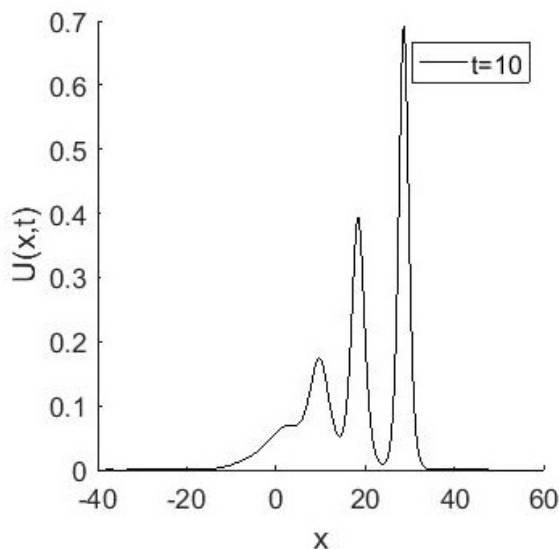


Fig. 5. Wave generation for $t=10$

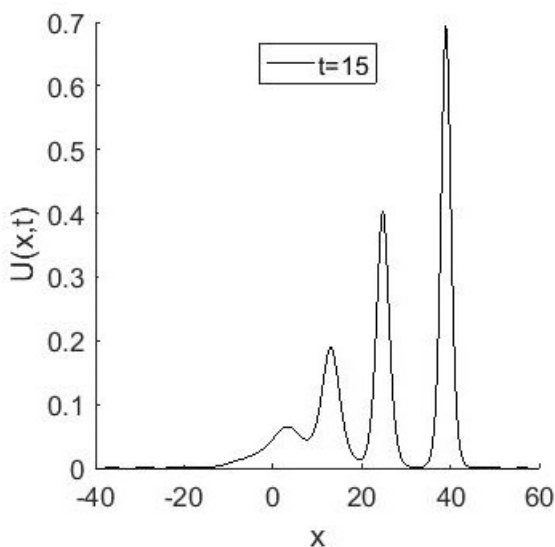


Fig. 6. Wave generation for $t=15$

3.3. Interaction of two solitary waves

The interaction of two positive bell shape solitaries are also studied in the paper [22] using the cosh hyperbolic type initial condition. The following exponential initial condition

$$u(x,0) = -\frac{1}{2} + 2 \frac{(e^{x-5} + 2e^{2x+5}) \left(1 - \frac{1}{9}e^{3x}\right) + \frac{1}{3}e^{3x}(e^{x-5} + 2e^{2x+5})}{(e^{x-5} + e^{2x+5})^2 + \left(1 - \frac{1}{9}e^{3x}\right)^2}$$

is also derived from the analytical solution given in [22]. This initial condition gives two well separated positive bell shaped solitaries of heights 1.49963 and 0.49999 positioned at $x=-2.5$ and $x=7.2$ respectively, at the beginning, Fig. 7. Both

solitaries propagate in the opposite directions along the horizontal axis as time goes. Continuation of simulation is depicted Fig. 8-11. We assume that $\alpha=6$, $\beta=6$ and $\mu=1$ in the Gardner equation (1.1). The designed routines are run up to the terminating time $t=5$ with the discretization parameters $N=600$ and $\Delta t=0.01$ in the finite problem interval $[-10,20]$.

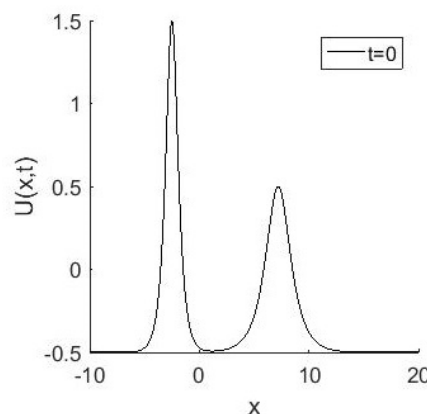


Fig. 7. Interaction of two positive bell shape solitaries for $t=0$

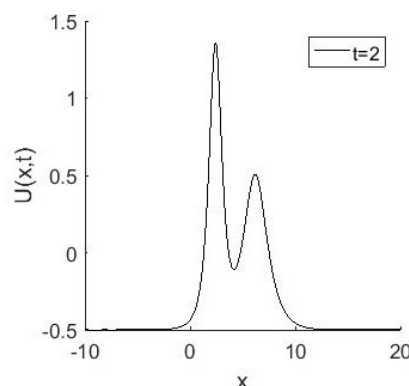


Fig. 8. Interaction of two positive bell shape solitaries for $t=2$

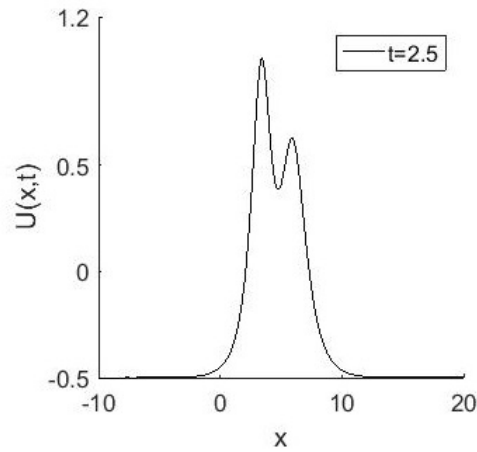


Fig. 9. Interaction of two positive bell shape solitaries for $t=2.5$

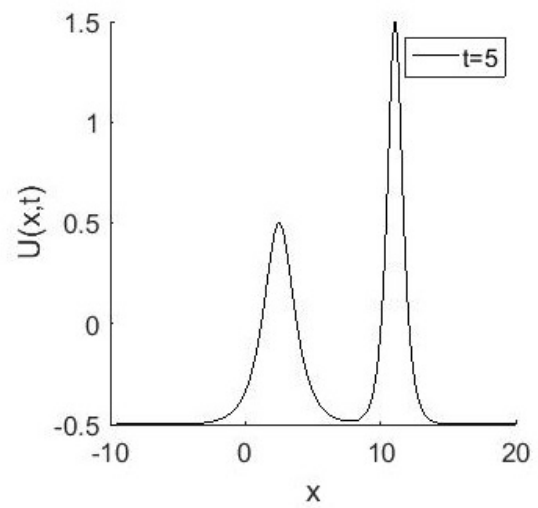


Fig. 11. Interaction of two positive bell shape solitaries for $t=5$

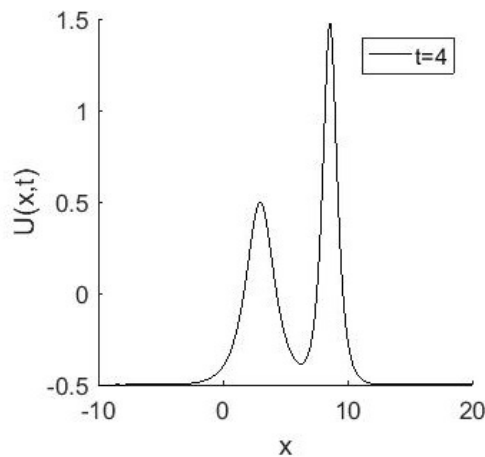


Fig. 10. Interaction of two positive bell shape solitaries for $t=4$

CONCLUSION

The collocation method based on trigonometric quintic B-spline functions is derived for the numerical solutions of some analytical and non-analytical problems for the Gardner equation. The errors between the numerical and the analytical solutions in case the existence of the analytical solutions for the first problem are measured. The perturbation of a single positive bell shaped solitary wave is derived to study wave generation for the Gardner equation successfully in the second problem. As a last test problem, interaction of two solitary waves are studied. The present method simulated the interaction successfully. As a conclusion, trigonometric quintic B-spline collocation method gives numerical solutions of the Gardner equation with high accuracy.

ACKNOWLEDGMENTS

This study was partially presented at International Conference on Mathematics and Engineering, Istanbul, Turkey, 2017.

REFERENCES

- [1] M. Ruderman, T. Talipova and E. Pelinovsky, "Dynamics of modulationally

unstable ion-acoustic wavepackets in plasmas with negative ions", *Journal of Plasma Physics*, vol. 74, no. 05, pp. 639-656, 2008.

[2] A. Kamchatnov, Y. Kuo, T. Lin, T. Horng, S. Gou, R. Clift, G. El and R. Grimshaw, "Undular bore theory for the Gardner equation", *Physical Review E*, vol. 86, no. 3, p. 036605, 2012.

[3] A. Kamchatnov, Y. Kuo, T. Lin, T. Horng, S. Gou, R. Clift, G. El and R. Grimshaw, "Transcritical flow of a stratified fluid over topography: analysis of the forced Gardner equation", *Journal of Fluid Mechanics*, vol. 736, pp. 495-531, 2013.

[4] H. Nishiyama and T. Noi, "Conservative difference schemes for the numerical solution of the Gardner equation", *Computational and Applied Mathematics*, vol. 35, no. 1, pp. 75-95, 2014.

[5] T. Rageh, G. Salem and F. El-Salam, "Restrictive Taylor Approximation for Gardner and KdV Equations", *Int. J. Adv. Appl. Math. and Mech*, vol. 1, no. 3, pp. 1-10, 2014.

[6] A. Bekir, "On traveling wave solutions to combined KdV–mKdV equation and modified Burgers–KdV equation", *Communications in Nonlinear Science and Numerical Simulation*, vol. 14, no. 4, pp. 1038-1042, 2009.

[7] Z. Fu, S. Liu and S. Liu, "New kinds of solutions to Gardner equation", *Chaos, Solitons & Fractals*, vol. 20, no. 2, pp. 301-309, 2004.

[8] E. Zayed and M. Abdelaziz, "The Two-Variable -Expansion Method for Solving the Nonlinear KdV–mKdV Equation", *Mathematical Problems in Engineering*, vol. 2012, pp. 1-14, 2012.

[9] E. Krishnan, H. Triki, M. Labidi and A. Biswas, "A study of shallow water waves with Gardner's equation", *Nonlinear Dynamics*, vol. 66, no. 4, pp. 497-507, 2011.

[10] A. Jawad, "New Exact Solutions of Nonlinear Partial Differential Equations using Tan-Cot Function Method", *ISSN 1923-8444 [Print] Studies in Mathematical Sciences*, vol. 5, no. 2, pp. 13-25, 2012.

[11] N. Yagmurlu, O. Tasbozan, Y. Ucar and A. Esen, "Numerical Solutions of the Combined KdV-

MKdV Equation by a Quintic B-spline Collocation Method", *Applied Mathematics & Information Sciences Letters*, vol. 4, no. 1, pp. 19-24, 2016.

[12] M. Abbas, A. Majid, A. Ismail and A. Rashid, "Numerical Method Using Cubic Trigonometric B-Spline Technique for Nonclassical Diffusion Problems", *Abstract and Applied Analysis*, vol. 2014, pp. 1-11, 2014.

[13] O. Ersoy Hepson and I. Dag, "The Numerical Approach to the Fisher's Equation via Trigonometric Cubic B-spline Collocation Method", *Communications in Numerical Analysis*, vol. 2017, no. 2, pp. 91-100, 2017.

[14] O. Ersoy Hepson, I. Dag and O. Kacmaz, "The Trigonometric Cubic B-spline Algorithm for Burgers' Equation", *International Journal of Nonlinear Science*, vol. 24, no. 2, pp. 120-128, 2017.

[15] A. Korkmaz and I. Dag, "Quartic and quintic B-spline methods for advection–diffusion equation", *Applied Mathematics and Computation*, vol. 274, pp. 208-219, 2016.

[16] A. Korkmaz and I. Dag, "Solitary wave simulations of Complex Modified Korteweg–de Vries Equation using differential quadrature method", *Computer Physics Communications*, vol. 180, no. 9, pp. 1516-1523, 2009.

[17] O. Ersoy, A. Korkmaz and I. Dag, "Exponential B-Splines for Numerical Solutions to Some Boussinesq Systems for Water Waves", *Mediterranean Journal of Mathematics*, vol. 13, no. 6, pp. 4975-4994, 2016.

[18] I. Dag and O. Ersoy, "The exponential cubic B-spline algorithm for Fisher equation", *Chaos, Solitons & Fractals*, vol. 86, pp. 101-106, 2016.

[19] A. Tok Onarcın and O. Ersoy Hepson, "Higher Order Trigonometric B-spline Algorithms to the Solution of Coupled Burgers' Equation", *AIP Conference Proceedings*, vol. 1926, 2018.

[20] P. Keskin, "Trigonometric B-spline solutions of the RLW equation", Eskisehir Osmangazi University Department of Mathematics & Computer, 2017.

- [21] S. Rubin and R. Graves, Cubic spline approximation for problems in fluid mechanics. Washington: NASA, United States, 1975, pp. 1-93.
- [22] A. Wazwaz, "Partial Differential Equations and Solitary Waves Theory", Nonlinear Physical Science, no. 1867-8440, p. 700, 2009.

	SAKARYA ÜNİVERSİTESİ FEN BİLİMLERİ ENSTİTÜSÜ DERGİSİ <i>SAKARYA UNIVERSITY JOURNAL OF SCIENCE</i>		
	e-ISSN: 2147-835X Dergi sayfası: http://www.saujs.sakarya.edu.tr		
	<u>Received</u> 02-10-2017 <u>Accepted</u> 15-01-2018	<u>Doi</u> 10.16984/saufenbilder.341372	

Investigation of Inhibition Effects of Honey, Pollen, Propolis and Royal Jelly Extracts on Thioredoxin Reductase Enzyme Activity

Gamze AKBULUT¹, Ebru AKKEMİK*^{1,2}

ABSTRACT

The thioredoxin reductase enzyme is an enzyme that prevents the mechanism of apoptosis from working and thus triggers the formation of cancer. Therefore, the inhibition of the thioredoxin reductase enzyme is thought to prevent or inhibit cancer. In this study, the effects of extracts of plateau honey, pine honey, chestnut honey, mad or wild honey, pollen, propolis and royal jelly on thioredoxin reductase enzyme activity were investigated. Enzyme activities were measured at constant substrate and different inhibitor concentrations to calculate IC₅₀ values. Total antioxidant activity were investigated in order to compare the extracts used in the inhibition study. The strongest inhibitory effect was seen in the pollen methanol extract (IC₅₀ = 2.44µg /mL)

Keywords: cancer, bee products, thioredoxin reductase

1. INTRODUCTION

In today's world, it is commonly recognized that cancer is one of the biggest global public health issues that we face. The high cost of drugs used in cancer treatment and the significant side effects of these drugs have been the driving force behind the search for new drugs, the results of which have led to many candidate drugs being synthesized. In order to evaluate the synthesized substances as medicines, these substances must undergo many long, demanding tests. Data from 2012 show that there were 14.1 million cancer cases worldwide. This number is expected to rise to 19.3 million by 2025 [1].

Thioredoxin reductase (TrxR; EC 1.6.4.5), which is a member of the Flavo Enzyme class and has a homodimeric structure, catalyzes the reduction of thioredoxin. Thioredoxin is known to be present in all organisms [2]. The TrxR/Trx system also plays a functional role in the construction of deoxyribonucleotides, where Trx protein acts as an electron provider [3], [4]. TrxR plays an important role in DNA synthesis, redox signaling, antioxidant defense, selenium metabolism and regulation of apoptosis [2]. Owing to these stated functions, thioredoxin reductase has become the focus of researchers. AIDS, cancer and autoimmune disease-related studies have shown that TrxR may be associated with many human diseases [4]. TrxR is the target enzyme in cancer research, particularly because of its relationship with apoptosis [3], [5], [6].

* Corresponding Author

¹ Faculty of Engineering and Architecture, Food Engineering, Siirt University, 56100, Siirt/ Turkey

² Science and Technology Research and Application Center, Siirt University 56100, Siirt, Turkey

Honey, pollen, propolis and royal jelly, all of which are recognized as major bee (*Apis mellifera*) products, have many phenolic compounds [7]. Throughout human history, bee products, in addition to serving as a source of food, have been used for therapeutic purposes, including the treatment of burns, gastrointestinal disorders, asthma, infected wounds, and skin ulcers [7-9]. The therapeutic effects of bee products continue to be investigated to this day. As a source of food, bee products have been reported to contain about 150–200 ppm compounds, such as polyphenols (phenolic acids, flavonoids, and their derivatives), terpenes, steroids, and amino acids [7], [8], [10], [11]. The content of these products depends on many factors, like plant type, climate and environmental conditions [11].

The main reason for the different colors, tastes and compositions of the honeys is that they are obtained from different botanical [11]. Four distinct types of honey (three floral type and one secretion type) were used in our study: plateau honey, a multiflora honey, which has a sharp taste and is very nutritious [12]; chestnut honey, which is made from the nectar or pollen of a chestnut flower and has a dark brown color and a bitter taste [13]; "mad" or "wild" honey, which it is known as locally, is obtained from *Rhododendron ponticum*, an endemic species that grows only in the Black Sea region (this honey contains grayanotoxins, which are polyhydroxylated cyclic diterpenes possessing structures, and it has been reported that excessive consumption of mad honey causes hypotension, bradycardia, and vertigo [14]; and pine honey, which is produced from the secretion of a bug known as the "Basra bug", or "*Marchalina hellenica*", instead of flower nectar [15].

Propolis is a resinous substance with a dark brown color and is produced to protect hives from bacterial/fungal infections from bees. In addition, propolis is used for cleaning and sealing the hives. Propolis has antibacterial, antiviral, antioxidant, anticancer, and anti-inflammatory activities [16], [17]. Pollen is the reproductive cells of plants. Bees consume pollen as part of their diet and use it to feed the larvae [15]. Royal jelly is a natural product produced by the main worker bees for the purpose of feeding the bee embryos. Royal jelly is a very rich product that includes protein, carbohydrates, various fatty acids (short chain) and mineral substances [18].

Bee products are known to have anticancer properties. However, the mechanism governing its

anticancer activities remains unclear. Taking into account the complex nature of cancer, in this study, we aimed to determine which of the bee products studied has better effectiveness on thioredoxin reductase enzyme activity and the impact of the products on cancer mechanisms.

2. MATERIALS AND METHODS

2.1. Chemicals and instruments

Analytical grade solvents (methanol, ethanol, and dimethyl sulfoxide (DMSO)), 5,5'-dithio-bis(2-nitrobenzoic acid) (DTNB), nicotinamide adenine dinucleotide zhosphate (NADPH), and other reagents were obtained from Sigma-Aldrich (Milan, Italy). Thioredoxin reductase recombinant from rat liver was also obtained from Sigma-Aldrich (Milan, Italy). Honeys, pollen, royal jelly and propolis were procured commercially on the Turkish market. In this study, Evolution 201 UV-Visible Spectrophotometer (Thermo Scientific) was used in kinetic study.

2.2. Samples and preparation of extracts

A modification of the procedure described by Şahin et al. was used to perform extractions [19]. Approximately 5 g of the samples were placed in 100 mL of solvent (methanol, ethanol, DMSO and water) medium. Each sample was then stirred at room temperature for 24 hours using a shaker. The suspension was centrifuged at 10,000g for 15 min. The resulting supernatant (methanol and ethanol) was concentrated in a rotary evaporator under reduced pressure. The other supernatant (DMSO and water) was concentrated in a lyophilizator (-52°C and 0,132 bar). The obtained residue was dissolved in a very small amount of the same solvent and held at 4°C until used.

2.1. Thioredoxin reductase catalytic activity and inhibition

The DTNB method was used to measure the activity of the thioredoxin reductase enzyme. This method catalyzes the reduction of disulfide bonds in DTNB by the NADPH-dependent thioredoxin reductase enzyme [20]. In a 1.0 ml reaction mix, the final concentrations were 20 mM potassium phosphate, 2 mM ethylene diamine tetra acetic acid, 0.02 mM b-nicotinamide adenine dinucleotide phosphate, reduced form, 0.02% (w/v) bovine serum albumin, 0.1% ethanol, 0.5

mM 5,5'-dithio-bis(2- nitrobenzoic acid) DTNB, and 0.15 unit thioredoxin reductase. Concentrations were immediately mixed by inversion, and the increase was recorded in a Spectrophotometer A412nm for approximately 3 minutes. One unit is based on the determination of TNB oxidation per minute. Enzyme activities were measured at constant substrate and different inhibitor concentrations to find IC₅₀ value. In preliminary experiments, DMSO, ethanol, and methanol were found to have no significant inhibition effect on ThxR. The tube not containing inhibitor was used as control and its activity was considered as 100%. Each experiment was repeated 3 times. Activity-% [Inhibitor] plots were drawn for inhibitors.

2.4. Determination of total phenolic content

The content of total polyphenols was estimated according to the Folin-Ciocalteu method using gallic acid as a reference standard [21]. Using a standard graph, total phenolic content was expressed as mg of gallic acid equivalents per g of extract.

3. RESULT

Solvents with different polarities (methanol, ethanol, DMSO and water) were used to determine the differences created by the solvent environment. In methanol, the solubility of plateau honey, chestnut honey, pine honey, mad honey, pollen, propolis and royal jelly were determined to be 0.2909, 0.3071, 0.4188, 0.3036, 0.1797, 0.3643 and 0.1084 g/ml, respectively (Table 1); in ethanol, the solubility of plateau honey, chestnut honey, pine honey, mad honey, pollen, propolis and royal jelly were found to be 0.0263, 0.0313, 0.1289, 0.0240, 0.0445, 0.4104 and 0.0065 g/ml, respectively (Table 1); and in DMSO, the solubility of plateau honey, chestnut honey, pine honey, pollen, and royal jelly were calculated as 0.4582, 0.4708, 0.4580, 0.2064, and 0.0881 g/ml, respectively (Table 1). DMSO (mad honey and propolis) was not studied because it could not be evaporated in the last stage of extraction. Finally, in water, the solubility of plateau honey, chestnut honey, pine honey, mad honey, pollen, propolis and royal jelly were found to be 0.3668, 0.3782, 0.3395, 0.3400, 0.2025, 0.0152 and 0.0109 g/ml, respectively (Table 1).

Table 1. Inhibitory effects of bee products extracts against TrxR and the solubility

Samples	Solvent	Concentration of extracted sample (g/mL)	ThxR	
			IC ₅₀ (mg/mL)	R ²
Mad Honey	Ethanol	0,1289	5,350	0.8917
	Methanol	0,4188	4,260	0.9560
	DMSO	-	-	-
	Water	0,3395	Not inh	Not inh
Plateau Honey	Ethanol	0,0263	0,862	0.9140
	Methanol	0,2909	2,500	0.9752
	DMSO	0,4582	4,030	0.9766
	Water	0,3668	0,191	0.9729
Pine Honey	Ethanol	0,0240	Not inh	Not inh
	Methanol	0,3036	Not inh	Not inh
	DMSO	0,4580	36,58	0.9010
	Water	0,3400	Not inh	Not inh
Chestnut Honey	Ethanol	0,0313	2,768	0.9249
	Methanol	0,3071	151,1	0.8862
	DMSO	0,4708	4,200	0.9731
	Water	0,3782	25,24	0.9448
Pollen	Ethanol	0,0445	0,056	0.8260
	Methanol	0,1797	0,024	0.9726
	DMSO	0,2064	2,14	0.9608
	Water	0,2025	*	*
Propolis	Ethanol	0,4104	0,400	0.9832
	Methanol	0,3643	0,068	0.8534
	DMSO	-	-	-
	Water	0,0152	*	*
Royal Jelly	Ethanol	0,0065	0,060	0.9134
	Methanol	0,1084	3,204	0.9496
	DMSO	0,0881	10,69	0.9382
	Water	0,0109	*	*

-The solvent could not be evaporated

*Could not be determined

Enzyme activities were measured at constant substrate and different inhibitor concentrations to find IC₅₀ value. The tube not containing inhibitor was used as control and its activity was considered as 100%. Activity-% [inhibitor] plots were drawn for inhibitors. According to the resulting plots, the IC₅₀ values for each plateau honey extract (water, ethanol, methanol and DMSO) were 0.191, 0.862, 2.500 and 4.030 mg/mL for TrxR, respectively (Table 1, Figure 1); the IC₅₀ values of each chestnut honey extract (water, ethanol, methanol and DMSO) were 25.24, 2.768, 151.1 and 4.200 mg/mL for TrxR, respectively (Table 1, Figure 1); the IC₅₀ values of each mad honey extract (ethanol and methanol) were 5.350 and 4.260 mg/mL for TrxR, respectively (Table 1, Figure 1); the IC₅₀ values of each pine honey extract (DMSO) were 36.58 mg/mL for TrxR (Table 1, Figure 1).

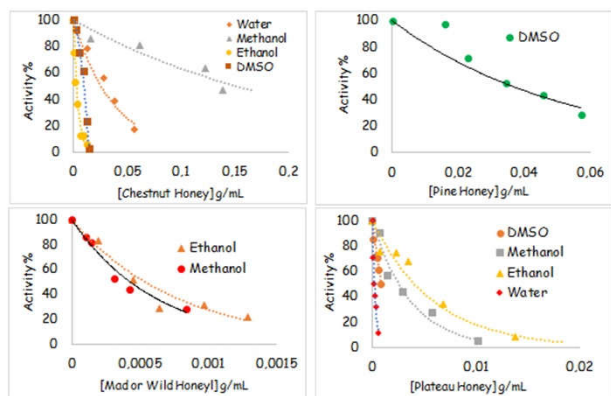


Figure 1. Inhibitory effects of honey extracts against TrxR

According to the resulting plots, the IC₅₀ values of each pollen extract (ethanol, methanol and DMSO) were 0.056, 0.024 and 2.14 mg/mL for TrxR, respectively (Table 1, Figure 2); the IC₅₀ values of each propolis extract (ethanol and methanol) were 0.400 and 0.068 mg/mL for TrxR, respectively (Table 1, Figure 2); and finally, the IC₅₀ values of each royal jelly extract (ethanol, methanol and DMSO) were 0.060, 3.204 and 10.69 mg/mL for TrxR, respectively (Table 1, Figure 2).

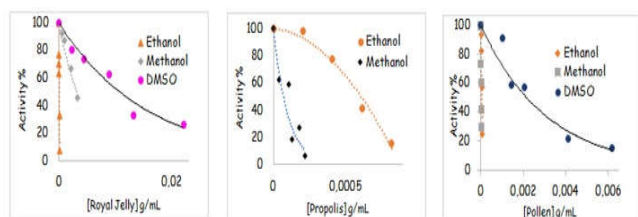


Figure 2. Inhibitory effects of bee products extracts against TrxR

In the investigation of different solvent extractions (methanol, ethanol, water, and DMSO) of plateau honey, chestnut honey, pine honey, pollen, royal jelly, and in the measurement of their total phenolic contents (Table 2), it was observed that for the honey samples, the total polyphenol content was between 28,067 and 116,91 mg GAE/g, whereas for the pollen (ethanol and DMSO) and royal jelly (ethanol, methanol and DMSO) the amounts were respectively between 471,567–1.151,0 GAE/g and between 0.060–10.69 GAE/g (Table 2). With the method that we applied, the total phenolic contents of pollen methanol and water extracts and all extracts of propolis were not able to be determined due to the occurrence of settling in the tube.

Table 2. Phenolic content of bee products

Samples	Solvent	Total polyphenol mg GAE/g sample
Mad Honey	Ethanol	31,733
	Methanol	54,733
	DMSO	-
Plateau Honey	Water	48,900
	Ethanol	28,067
	Methanol	68,733
Pine Honey	DMSO	84,400
	Water	53,233
	Ethanol	31,067
Chestnut Honey	Methanol	81,233
	DMSO	80,733
	Water	86,733
Pollen	Ethanol	30,733
	Methanol	85,900
	DMSO	116,91
Propolis	Water	87,233
	Ethanol	471,567
	Methanol	*
Royal Jelly	DMSO	1.151,0
	Water	*
	Ethanol	*
Royal Jelly	Methanol	*
	DMSO	-
	Water	*
Royal Jelly	Ethanol	48,233
	Methanol	81,567
	DMSO	113,40
Royal Jelly	Water	*

-The solvent could not be evaporated/
*Could not be determined

4. DISCUSSION

Studies have shown that the human TrxR system is associated with cancer cell proliferation and anti-apoptosis processes [2], [22]. The thioredoxin system regulates the redox state of Trx (thioredoxin) and the transfer of apoptosis signals. For example, reduced Trx binds apoptosis signaling kinase-1 (ASK1) and stops apoptosis. Oxide Trx, however, cannot do that [22], [23]. TrxR is a unique enzyme present in all living cells, yet in tumor cells, the TrxR level is 10 times greater than that seen in normal cells, indicating that the active thioredoxin system is effective in proliferating tumor cells. Therefore, this protein has been proposed as a target for cancer treatment. In a study conducted for this purpose, it was reported that the interaction of TrxR1 with electrophiles results in two important biological consequences, namely p53 conformational degradation and apoptosis induction [22], [24],

[25]. There are many cancer drugs that inhibit TrxR [3], and many new drug candidates are regularly being synthesized. In order to evaluate the synthesized substances as medicines, these substances must undergo many long, demanding tests. As a result, many researchers have turned to natural products. For this reason, we preferred to focus on bee products in our work.

Many studies have reported that propolis, pollen, royal jelly and honey contain a variety of phenolic acids and flavonoids, which have a wide range of biological effects, including antioxidant, antibacterial, anti-inflammatory, and anticancer activities [16], [18], [26], [27], [28]. As mentioned earlier, bee products have been shown to elicit anti-cancer activity, yet precisely how this is done is unclear. Our study has aimed to identify which of the bee products has the best inhibitory activity on TrxR and to offer insight into how bee products prevent cancer. When we look at Table 1, it can be seen that plateau honey with an IC₅₀ value of 0.191-4.030 mg/mL showed the best inhibition properties among all the honeys. In other words, multiflora honey has a better inhibitory effect on TrxR enzyme activity than uniflora honey. Looking again at Table 1, the floral honey can be seen to cause better inhibition than the secretion honey.

When examining the inhibition effects of pollen, propolis and royal jelly on thioredoxin reductase enzyme activities, pollen methanol extract was found to have the strongest inhibitory effect (Table 1). Overall, it was found that out of all the bee products, pollen, when included in the honey, had the strongest inhibitory effect. In terms of the total phenolic content (Table 1), pollen had the highest. We suspect that the inhibitory effect on the enzyme is high due to the phenolic content of its structure. With these conclusions we have determined that pollen, out of all the bee products, may be more effective on cancer and would be beneficial for cancer patients to use under the guidance of a doctor.

ACKNOWLEDGMENTS

This study was supported in part by the Scientific Research Projects Unit of Siirt University (2016-Siüfeb-07). The Study Was Presented as Abstract In The "International Dna Day And Genome Congress" In The Name of "The Investigation Of Inhibition Effects of Honey, Polen, Propolis and Royal Jelly Extracts on Thioredoxin Reductase Enzyme Activity" (April 24-28, 2017 Ahi Evran University, KIRŞEHİR / TURKEY, IDDGC17-OP-205

REFERENCES

- [1] Anonymous, "Yeni Dünya Kanser İstatistikleri Yayınlandı," 2017. [Online]. Available: <http://kanser.gov.tr/daire-faaliyetleri/kanser-istatistikleri/860-yeni-dunya-kanser-istatistikleri-yayinlandi.html>. [Accessed: 05-Aug-2017].
- [2] B. Tandogan and N. N. Ulusu, "Thioredoxin Reductase," *Hacettepe J. Biol. Chem.*, vol. 39, no. 1, pp. 87–92, 2011.
- [3] J. Lu, E.-H. Chew, and A. Holmgren, "Targeting thioredoxin reductase is a basis for cancer therapy by arsenic trioxide," *Proc. Natl. Acad. Sci.*, vol. 104, no. 30, pp. 12288–12293, Jul. 2007.
- [4] D. Mustacich and G. Powis, "Thioredoxin reductase.," *Biochem. J.*, vol. 346 Pt 1, pp. 1–8, Feb. 2000.
- [5] A. Jordan and P. Reichard, "Ribonucleotide reductases.," *Annu. Rev. Biochem.*, vol. 67, pp. 71–98, 1998.
- [6] M. Cox and D. L. Nelson, *Lehninger Principles of Biochemistry*, 5th ed. New York: W.H. Freeman and Company., 2008.
- [7] J. W. White, "Composition of Honey," in *Honey: A Comprehensive Survey*, E. Crane, Ed. London: Heinemann, 1975, pp. 157–206.
- [8] A. M. Gómez-Caravaca, M. Gómez-Romero, D. Arráez-Román, A. Segura-Carretero, and A. Fernández-Gutiérrez, "Advances in the analysis of phenolic compounds in products derived from bees," *J. Pharm. Biomed. Anal.*, vol. 41, no. 4, pp. 1220–1234, Jun. 2006.
- [9] M. Ahn, S. Kumazawa, Y. Usui, J. Nakamura, M. Matsuka, F. Zhu, and T. Nakayama, "Antioxidant Activity and Constituents of Propolis Collected in

- Various Areas of Korea," *J. Agric. Food Chem.*, vol. 52, no. 4, pp. 7286–7292, 2004.
- [10] M. Küçük, S. Kolaylı, Ş. Karaoğlu, E. Ulusoy, C. Baltacı, and F. Candan, "Biological activities and chemical composition of three honeys of different types from Anatolia," *Food Chem.*, vol. 100, no. 2, pp. 526–534, Jan. 2007.
- [11] F. Karadal and Y. Yildirim, "Balın Kalite Nitelikleri, Beslenme ve Sağlık Açısından Önemi," *Erciyes Üniv Vet Fak Derg YILDIRIM Erciyes Üniv Vet Fak Derg Derlemeler J Fac Vet Med Univ Erciyes*, vol. 9, no. 93, pp. 197–209, 2012.
- [12] Anonymous, "Bal Çeşitleri," 2017. [Online]. Available: <http://apiterapi.uzerine.com/index.jsp?objid=340>, [Accessed: 05-Aug-2017].
- [13] S. Kolaylı, Z. Can, O. Yildiz, H. Sahin, and S. A. Karaoglu, "A comparative study of the antihyaluronidase, antiurease, antioxidant, antimicrobial and physicochemical properties of different unifloral degrees of chestnut (*Castanea sativa* Mill.) honeys," *J. Enzyme Inhib. Med. Chem.*, vol. 6366, no. March 2017, pp. 1–9, 2016.
- [14] N. Sütlüpmar, A. Mat, and Y. Satganoglu, "Poisoning by toxic honey in Turkey," *Arch. Toxicol.*, vol. 67, no. 2, pp. 148–150, 1993.
- [15] O. Yilmaz, "Honey Bee Products in Turkey," *J. Anim. Sci. Adv.*, vol. 6, no. 10, p. 1779, 2016.
- [16] M. Marcucci, "Propolis: chemical composition, biological properties and therapeutic activity Mc Marcucci Propolis: chemical composition, biological properties and therapeutic activity," 1995.
- [17] Z. Selamoglu Talas, "Propolis reduces oxidative stress in l-NAME-induced hypertension rats," *Cell Biochem. Funct.*, vol. 32, no. 2, pp. 150–154, 2014.
- [18] T. Nagai and R. Inoue, "Preparation and the functional properties of water extract and alkaline extract of royal jelly," *Food Chem.*, vol. 84, no. 2, pp. 181–186, 2004.
- [19] H. Sahin, R. Aliyazicioglu, O. Yildiz, S. Kolaylı, a Innocenti, and C. T. Supuran, "Honey, polen, and propolis extracts show potent inhibitory activity against the zinc metalloenzyme carbonic anhydrase.," *J. Enzyme Inhib. Med. Chem.*, vol. 26, no. 3, pp. 440–444, 2011.
- [20] A. Holmgren, "Bovine thioredoxin system. Purification of thioredoxin reductase from calf liver and thymus and studies of its function in disulfide reduction.," *J. Biol. Chem.*, vol. 252, no. 13, pp. 4600–6, Jul. 1977.
- [21] F. Odabasoglu, A. Aslan, A. Cakir, H. Suleyman, Y. Karagoz, M. Halici, and Y. Bayir, "Comparison of antioxidant activity and phenolic content of three lichen species," *Phyther. Res.*, vol. 18, no. 11, pp. 938–941, Nov. 2004.
- [22] M. Saitoh, H. Nishitoh, M. Fujii, K. Takeda, K. Tobiume, Y. Sawada, M. Kawabata, K. Miyazono, and H. Ichijo, "Mammalian thioredoxin is a direct inhibitor of apoptosis signal-regulating kinase (ASK) 1," *EMBO J.*, vol. 17, no. 9, pp. 2596–2606, 1998.
- [23] J. Fang, J. Lu, and A. Holmgren, "Thioredoxin reductase is irreversibly modified by curcumin: a novel molecular mechanism for its anticancer activity.," *J. Biol. Chem.*, vol. 280, no. 26, pp. 25284–90, Jul. 2005.
- [24] P. B. Cassidy, K. Edes, C. C. Nelson, K. Parsawar, F. A. Fitzpatrick, and P. J. Moos, "Thioredoxin reductase is required for the inactivation of tumor suppressor p53 and for apoptosis induced by endogenous electrophiles," *Carcinogenesis*, vol. 27, no. 12, pp. 2538–2549, Aug. 2006.
- [25] K. Becker, S. Gromer, R. H. Schirmer, and S. Müller, "Thioredoxin reductase as a pathophysiological factor and drug target.," *Eur. J. Biochem.*, vol. 267, no. 20, pp. 6118–25, Oct. 2000.
- [26] M. Marcucci, F. Ferreres, C. García-Viguera, V. S. Bankova, S. L. De Castro, A. P. Dantas, P. H. Valente, and N. Paulino, "Phenolic compounds from Brazilian propolis with pharmacological activities.," *J. Ethnopharmacol.*, vol. 74, no. 2, pp. 105–12, Feb. 2001.
- [27] K. Pyrzynska and M. Biesaga, "Analysis of phenolic acids and flavonoids in honey," *TrAC Trends Anal. Chem.*, vol. 28, no. 7, pp. 893–902, Aug. 2009.
- [28] B. W. LeBlanc, O. K. Davis, S. Boue, A. DeLucca, and T. Deeby, "Antioxidant activity of Sonoran Desert bee pollen," *Food Chem.*, vol. 115, no. 4, pp. 1299–1305, Aug. 2009.

	SAKARYA ÜNİVERSİTESİ FEN BİLİMLERİ ENSTİTÜSÜ DERGİSİ <i>SAKARYA UNIVERSITY JOURNAL OF SCIENCE</i>		
	e-ISSN: 2147-835X Dergi sayfası: http://www.saujs.sakarya.edu.tr		
	<u>Received</u> 11-08-2017 <u>Accepted</u> 20-02-2018	<u>Doi</u> 10.16984/saufenbilder.334104	

Structural, Conformational and Spectroscopic Properties of C₁₆H₁₆BrNO₃ Schiff-Base Molecule: A Theoretical Investigation

Meryem Evecen*¹

ABSTRACT

Molecular geometry, vibrational frequencies and electronic properties (total energy, dipole moment, electronegativity, chemical hardness and softness) of the Schiff-bases compound C₁₆H₁₆BrNO₃ were investigated using DFT(B3LYP) method. Besides, the conformational analysis was made with respect to selected degrees of torsional freedom $\tau(C3C2C1N1)$ torsional. Molecular electrostatic potential, frontier molecular orbital energies and non linear optic analysis of molecule have been performed by using Gaussian 09W program. The non linear optic analysis indicates that this molecule can be evaluated as an attractive object for nonlinear optical material studies.

Keywords: Benzylidene, electronic properties, HOMO-LUMO, vibrational frequencies

1. INTRODUCTION

The Schiff-bases chemistry is very important due to their usage in anion sensors [1], thermochromism [2], photochromism [3], antifungal, antibacterial properties [4], antimicrobial activity [5], anticancer and antiinflammatory activities [6,7] and also in modern technologies. They may also both serve as reagents for stereo selective organic synthesis [8,9] and widely used as ligands in the formation of transition metal complexes[10]. In addition, they are used as non-linear optics compounds [11]. Therefore, a careful study of Schiff bases characteristics is important in their application successfully. Because of the structural characteristics of Schiff base products which contain electron donor and acceptor groups

connected through a conjugated chain, they will be the potential nonlinear optical (NLO) or electro-optical materials [12].

The important class of Schiff bases is benzylidene anilines. Generally, benzylidene anilines have been widely used in medicinal, biological chemistry and coordination and therefore their molecular and crystal structure have been of considerable interest by experimental and theoretical studies.

In [13], the IR spectra and X-ray crystallography of 4-bromo-*N*-(2,3,4-trimethoxybenzylidene) aniline (C₁₆H₁₆BrNO₃) was studied. In spite of widely usage of benzylidene anilines, the analysis of literature showed that no any computational study on BMBA molecule has been published yet. The objective of this study is to analyze the structural parameters, vibrational properties, frontier molecular orbital energies, conformational

* Corresponding Author

¹ Amasya University, Faculty of Arts and Sciences, Department of Physics, Amasya, e-mail: meryem.evecen@amasya.edu.tr

properties, natural atomic charges and NLO properties of the title molecule, 4-bromo-*N*-(2,3,4-trimethoxybenzylidene)aniline (BMBA), by density functional theory (DFT) technique in the B3LYP/6-311++G(d,p) level of theory and then compare our results with the available experimental work published before.

2. COMPUTATIONAL METHOD

For all the calculations on the BMBA, Gaussian 09 package was used [14] on the personal computer. Moreover, the X-ray coordinates in literature were utilised in order to obtain the initial guess of BMBA for modelling [13]. The structure optimization was done by density functional theory with the 6-311++G(d,p) basis set. The visual GaussView 5.0 [15] program was used in order to obtain the structural properties, electronic and vibrational spectra. The vibrational frequency signals were found real that confirm the optimized geometry and scaling factor of 0.96 was used for obtained frequencies [16].

3. RESULTS AND DISCUSSION

3.1. Geometry Optimization

The initial molecular geometry was directly taken from the X-ray diffraction experimental result without any constraints [13]. The crystal structure [13] and the theoretical geometric structure of BMBA molecule are shown in Fig. 1(a) and (b)-(e). BMBA's space group is $P\bar{1}$ and crystal structure is triclinic. These crystal structure parameters of the molecule are $a = 7.9103(3) \text{ \AA}$, $b = 9.9902(4) \text{ \AA}$, $c = 10.7821(3) \text{ \AA}$, $\alpha = 93.068(8)^\circ$, $\beta = 108.568(3)^\circ$, $\gamma = 109.679(3)^\circ$ and $V = 748.10(5) \text{ \AA}^3$ [13].

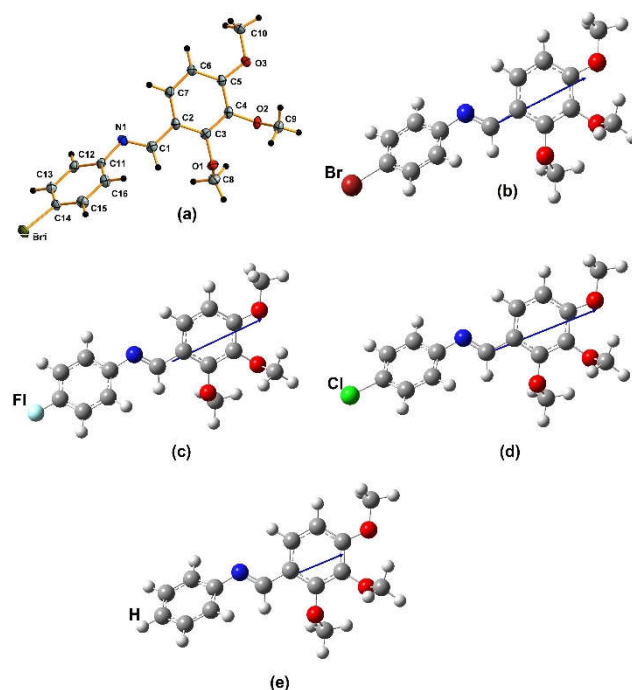


Figure 1. (a) The molecular structure of the BMBA molecule with atom-labeling scheme. Displacement ellipsoids are drawn at the 50% probability level [13]; (b) The theoretical geometric structure of BMBA; (c), (d) and (e) The theoretical geometric structure with F, Cl and H substituent, respectively

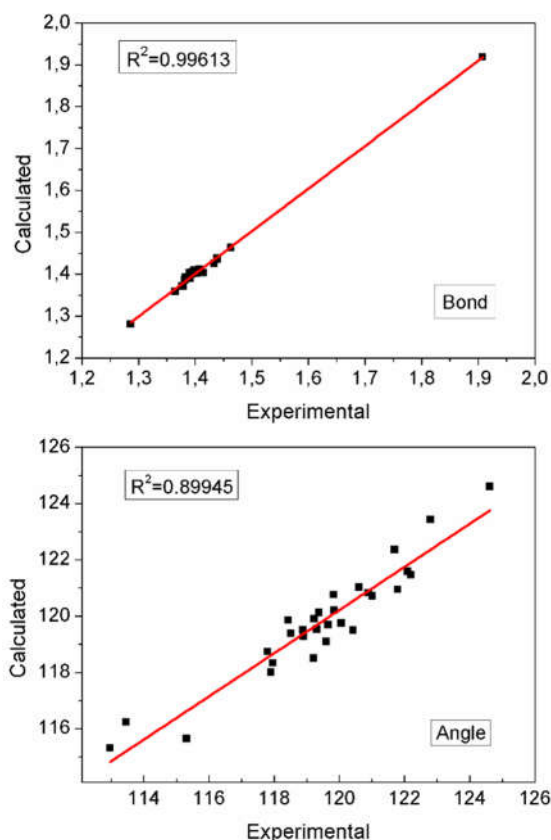


Figure 2. Comparison between calculated and experimental structural parameters of BMBA.

Optimized geometrical parameters (bond lengths, angles and dihedral angles) of the BMBA have been obtained using the B3LYP/6-311++G(d,p) method. The results can be visible in Table 1 and are compared with the experimental BMBA data [13]. The N1-C1 and N1-C11 bond lengths are found 1.281 and 1.403 Å, respectively. As found in similar experimental values, it conform to the value for a double and single bonds [13,17]. The two methoxy groups attached at C3 and C4 are twisted away from the benzene ring of C2-C7. These dihedral angles are corresponding C2C3O1C8, and C3C4O2C9 of 113.3° (103.6 (2)°), -105.21° (-88.7 (2)°) for theoretical (experimental) values, respectively. The last methoxy group attached at C5 is almost coplanar with the C2-C7 ring, as shown by the torsion angle C6C5O3C10 of -2.3° (-7.2 (3)°) for theoretical (experimental) value. When the experimental X-ray single crystal structure and optimized theoretical structure parameters of the BMBA are compared (see Fig. 2), conformational discrepancies are observed between them. To understand these discrepancies, torsion angles are compared; τ_1 (C3C2C1N1) [-159.3 (17)°] and τ_2 (C12C11N1C1) [-140.4 (18)°] for X-ray single crystal. These dihedral angles have been calculated at -178.2° and -143.7° for B3LYP, respectively. As a similar compounds containing different substituent from Group VIIA, were presented the crystal structure of C₁₆H₁₆XNO₃(X=Cl and F) [17,18].

F, Cl, Br and H atoms have the same number of electrons in the last shell. As expected, these elements have certain properties in common. In here, DFT calculations for the compounds containing the F, Cl and H in place of the Br atoms were done by the same method in order to analyze the substituent effects on the τ_1 and τ_2 torsion angles (Fig. 1). Firstly, from obtained optimized geometry we compared all structures energetically: $E_{Br} < E_{Cl} < E_F < E_H$. We see that bond length and angles agree with literature [13, 17-21]. Then, the τ_1 and τ_2 dihedral angles are calculated as -178.0° and -144.0° for Cl, -177.7° and -144.7° for F and -177.9° and -142.9 for H. These values are agree with similar molecules [19-21]. While the calculated values of the Br, Cl and H substituent torsion angles show no noticeable differences when compared to each other, the calculated F substituent torsion angle has a few difference from Br. As seen Table 1, we can say the molecular geometry of the investigated compound has been a little effected by the changes of substituent.

Table 1. Selected parameters for molecular structure of BMBA and substituent

Parameters	Exp.[13]	BMBA	^a CMBA/ ^b FMBA/ ^c MBA
Bond lengths (Å)			
Br1-C14	1.908	1.919	1.761/1.359/1.084
O1-C3	1.380	1.371	1.371/1.371/1.372
O1-C8	1.438	1.438	1.438/1.437/1.437
O2-C4	1.377	1.371	1.371/1.371/1.372
O2-C9	1.440	1.435	1.435/1.435/1.435
O3-C5	1.365	1.358	1.358/1.359/1.359
O3-C10	1.434	1.425	1.425/1.424/1.424
N1-C1	1.286	1.281	1.281/1.281/1.280
N1-C11	1.415	1.403	1.403/1.405/1.405
C1-C2	1.463	1.463	1.463/1.463/1.464
C2-C3	1.408	1.412	1.412/1.411/1.411
C2-C7	1.395	1.400	1.400/1.400/1.400
C3-C4	1.391	1.399	1.399/1.399/1.399
C4-C5	1.399	1.409	1.409/1.408/1.408
C5-C6	1.403	1.401	1.401/1.401/1.400
C6-C7	1.382	1.386	1.386/1.387/1.387
C12-C11	1.390	1.403	1.403/1.404/1.403
C16-C11	1.395	1.404	1.405/1.405/1.405
C13-C12	1.391	1.390	1.389/1.390/1.390
C14-C13	1.383	1.393	1.393/1.387/1.396
C15-C14	1.387	1.391	1.391/1.385/1.394
C16-C15	1.388	1.392	1.392/1.393/1.393
Bond angles (°)			
C8O1C3	113.46	116.23	116.21/116.17/116.12
C9O2C4	112.97	115.31	115.30/115.29/115.25
C10O3C5	117.80	118.73	118.73/118.70/118.67
C11N1C1	118.43	119.86	119.91/119.93/119.86
C2C1N1	121.70	122.36	122.32/122.28/122.25
C3C2C1	119.84	120.21	120.23/120.27/120.32
C7C2C1	122.20	121.46	121.45/121.44/121.41
C7C2C3	117.96	118.33	118.32/118.29/118.27
C2C3O1	119.60	119.09	119.11/119.13/119.18
C4C3O1	119.38	120.12	120.09/120.05/119.99
C4C3C2	121.01	120.72	120.73/120.75/120.76
C3C4O2	120.43	119.49	119.49/119.49/119.50
C5C4O2	119.83	120.76	120.75/120.75/120.74
C5C4C3	119.66	119.69	119.70/119.71/119.71
C4C5O3	115.31	115.65	115.65/115.66/115.67
C6C5O3	124.62	124.60	124.61/124.62/124.62
C6C5C4	120.06	119.75	119.74/119.72/119.71
C7C6C5	119.23	119.90	119.91/119.91/119.91
C6C7C2	122.09	121.59	121.60/121.61/121.62
C12C11 N1	117.91	118.00	117.95/117.80/117.93
C16C11N1	122.80	123.43	123.49/123.51/123.23
C16C11C12	119.21	118.50	118.49/118.63/118.79
C13C12C11	120.60	121.03	121.03/121.01/120.54
C14C13C12	118.90	119.27	119.30/118.65/120.38
C13C14Br1	119.31	119.53	119.53/118.93/120.30
C15C14Br1	118.89	119.51	119.54/118.94/120.26
C15C14C13	121.80	120.95	120.92/122.12/119.44
C16C15C14	118.52	119.38	119.41/118.77/120.48
C15C16C11	120.90	120.83	120.81/120.78/120.34
Dihedral angles (°)			
C2C3O1C8	103.6	113.3	113.1/112.9/112.6
C3C4O2C9	-88.7	-105.2	-105.1/-105.0/-104.7
C6C5O3C10	-7.2	-2.3	178.2/178.3/178.2
C2C1N1C11	-176.5	-176.8	-176.8/-176.9/-176.9

C12C11N1C1	-140.4	-143.7	-144.0/-144.7/-142.9
C3C2C1N1	-159.3	-178.2	-178.0/-177.7/-177.9

^aCMBA: 4-Chloro-*N*-(2,3,4-trimethoxybenzylidene)aniline

^bFMBA: 4-Fluoro-*N*-(2,3,4-trimethoxybenzylidene)aniline

^cMBA: *N*-(2,3,4-trimethoxybenzylidene)aniline

3.2. Conformational analysis

For defining the favored position of low energy structures computations were performed using B3LYP/6-311++G(d,p) as a function of the selected degrees of torsional freedom $\tau(\text{C3C2C1N1})$, which was varied from -180° to $+180^\circ$ in steps of 20° . The respective values of the selected degrees of torsional freedom, $\tau(\text{C3C2C1N1})$, is -159.3° in X-ray single crystal structure [13], but it is -178.2° in DFT optimized geometry. In Fig. 3, we have shown the molecular energy profiles (Hartree) with respect to rotations about the selected torsion angle (degree). It is seen from Fig. 3 that the low energy domains is located at -178.2° , optimized geometry. Also, it has two saddle point at -80° and 80° . Besides second favorable conformer is calculated at -40° torsional value as metastable structure.

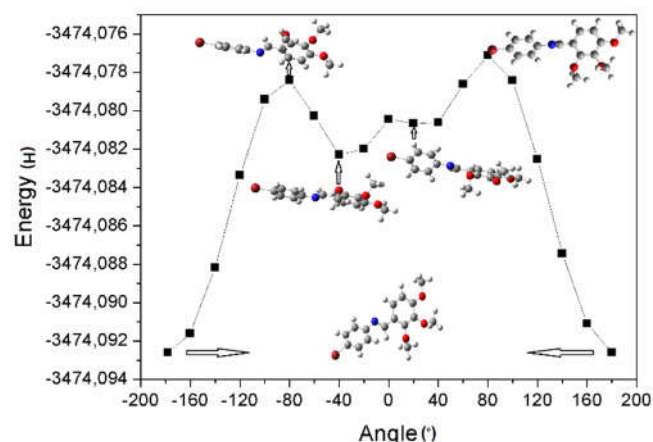


Figure 3. Potential energy surface scan using B3LYP/6-311++G(d,p) method for $\tau(\text{C3C2C1N1})$ dihedral angle of the title compound

3.3. Vibrational spectra

The BMBA molecule consists of 37 atoms, which undergo 105 normal modes of vibrations. The harmonic frequencies along with intensities were computed with the help of Gauss View program and were illustrated in Table 2. C-H aromatic and aliphatic experimental frequencies appeared between 2911 and 2998 cm^{-1} [13]. The characteristic region of vibrational stretchings are appeared between 3000 and 3100 cm^{-1} in general.

In this study, C-H (aromatic) frequencies are estimated at $3051\text{--}3083\text{ cm}^{-1}$. The -CH=N- (aliphatic) in-plane bending vibration is observed at 2942 cm^{-1} . This vibration is agreement with experimental over the range. The bending vibrations of C-H in plane/out of plane are located at $1000\text{--}1300/800\text{--}950\text{ cm}^{-1}$, respectively [22-25]. In here the C-H in plane (out of plane) bending vibrations are found in the range $1075\text{--}1463\text{ cm}^{-1}$ ($788\text{--}982\text{ cm}^{-1}$). Three methoxyl groups connected with the phenyl group, the C-O stretching vibrations associated with the ring are calculated at 1199 and 1260 cm^{-1} and below this value in the mixed modes. This mode was found at 1209 cm^{-1} in FT-IR spectrum by Joshi *et al.* [26]. The C-O in-plane bending is calculated at 752 cm^{-1} in the highly mixed modes.

In [13], C=C aromatic frequency is given at $1413\text{--}1594\text{ cm}^{-1}$. The vibrations of C=C and C-C stretchings are found in the region of $1390\text{--}1620\text{ cm}^{-1}$ [27] and $1280\text{--}1625\text{ cm}^{-1}$ [28]. In this study, C=C and C-C stretching vibrations are very prominent at $1242\text{--}1564\text{ cm}^{-1}$ and $1019\text{--}1463\text{ cm}^{-1}$ region. The vibration modes containing the ring CCC were also observed at $674\text{--}1037\text{ cm}^{-1}$ region in the FT-IR spectra. The task identification of C=N, C-N vibrations are very difficult because of the possibility mixing of several bands in these regions. In the literature, the C-N vibrational stretchings are found in between 1266 and 1382 cm^{-1} [29], 1120 and 1150 cm^{-1} [30], and 1200 and 1300 cm^{-1} [31]. In this work, these modes are labelled at 846 and 1186 cm^{-1} for BMBA. Schiff-bases proton transfer can be identified by using the characteristic region of $1700\text{--}1500\text{ cm}^{-1}$. C=N (azomethine) stretching vibration was appeared at 1606 and 1534 cm^{-1} . Hence it has been observed at 1615 cm^{-1} for experimental value [13]. In this study, the in-plane and out-of-plane bending vibrations of carbon-nitrogen group are assigned which are also supported by the literature [32]. The C-Br vibrations are often found over the $480\text{--}1290\text{ cm}^{-1}$ range since its vibration is easily affected by the adjacent atoms or groups [33,34]. In here, the medium bands at 1037 cm^{-1} is assigned to C-Br stretching vibration coupled with ring deformation. Additionally, for the compounds containing the Cl, F and H in place of the Br atoms frequencies were calculated and added in Table 2. C-Cl vibrations are in the region $480\text{--}1129\text{ cm}^{-1}$ for simple chlorine compounds [35,36]. The C-Cl stretching vibrations was observed at 1056 and 1096 cm^{-1} in FT-IR spectrum [37]. In this study, it

was observed at 1054 cm⁻¹. Normally, the C-F stretching vibrations appear in the region 1000-1300 cm⁻¹ for several fluoro-benzenes as very strong in the IR spectra [38]. As this region, the corresponding C-F stretching vibration is observed at 1171 and 1193 cm⁻¹. The other vibrational frequencies can be seen in Table 2. These BMBA and substituent (Cl/F/H) vibrations are also in agreement with each other.

Table 2. Vibrational wavenumbers of BMBA and substituents, in cm⁻¹, and assignments

Theoretical		Assignments ^a
BMBA	CMBA/FMBA/MBA	
3083	3083/3082/3082	v(C-H) _s R1
3071	3070/3071/3064	v(C-H) _s R2
3067	3067/3067/3066	v(C-H) _{as} R1
3058	3058/3060/3058	v(C-H) _{as} R2
3051	3051/3054/3052	v(C-H) _{as} R2
3013	3013/3013/3012	v(C-H ₃) _{as} M3
3011	3011/3010/3009	v(C-H ₃) _{as} M1
3005	3004/3004/3004	v(C-H ₃) _{as} M2
2976	2976/2975/2974	v(C-H ₃) _{as} M1
2967	2967/2967/2966	v(C-H ₃) _{as} M2
2952	2952/2951/2951	v(C-H ₃) _{as} M3
2942	2941/2940/2941	v(-CH=N-) _s
2900	2900/2899/2899	v(C-H ₃) _s M2
2898	2897/2897/2897	v(C-H ₃) _s M1
2892	2892/2892/2891	v(C-H ₃) _s M3
1606	1607/1608/1609	v(C=N) _s
1564	1566/1573/1570	v(C=C) _s +β(CCC) _R
1547	1550/1556/1554	v(C=C) _s +v(C=N) _s
1463	1464/1469/1464	γ(C-H) _R +v(C-O) _s +v(C-C)
1449	1450/1461/1455	γ(C-H) _{R1} +α(C-H ₃) _M
1444	1444/1450/1450	α(C-H ₃) _{M1}
1444	1444/1444/1444	α(C-H ₃) _{M2,M3}
1432	1433/1433/1433	α(C-H ₃) _{M3}
1430	1430/1430/1430	α(C-H ₃) _{M2}
1424	1424/1424/1424	α(C-H ₃) _{M1}
1411	1410/1410/1409	v(C=C) _s +ω(C-H ₃) _M
1384	1384/1385/1384	ω(C-H ₃) _M +γ(C-H)
1334	1334/1334/1334	γ(C-H)+v(C-C) _s
1273	1273/1274/1273	v(C=C) _s +γ(C-H)
1260	1260/1260/1260	v(C=C) _{R1} +γ(C-H)+v(C-O)
1252	1253/1258/1259	v(C=C) _{R2} +γ(C-H)+v(C-O)
1242	1241/1240/1239	v(C=C) _{R1} +γ(C-H)+v(C-C)
1199	1198/1199/1198	ω(C-H ₃) _M +v(C-O) _s
1186	1186/1193/1185	v(C-N) _s +v(C-F)
1174	1174/1171/1173	α(C-H) _{R1} +v(C-N)+v(C-F)
1152	1152/1152/1152	ω(C-H ₃) _{M1,M2}
1144	1142/1141/1143	α(C-H) _{R2}
1141	1141/1122/1140	α(C-H) _{R1}
1121	1121/1121/1121	δ(C-H ₃) _M
1075	1075/1075/1075	v(C-O) _s +α(C-H) _{R1}
1037	1054/ - / -	v(CBr(Cl)) _{as} +β(CCC)
1019	1019/1019/1019	v(CH ₃ -O) _{sM} +v(C-C) _s
992	992/992/993	v(CH ₃ -O) _{sM} +β(CCC)
982	984/985/979	δ(C-H)+β(CCC)
937	936/932/940	δ(C-H) _{R2}
931	931/930/931	δ(C-H) _{R1}

927	927/927/926	δ(C-H) _{R2} +v(CH ₃ -O-C) _{sM}
847	848/853/841	v(C-N) _s +β(CCC)
809	811/820/810	ω(C-H) _{R2}
788	788/788/788	ω(C-H) _{R1}
752	754/726/757	β(CCC)+β(COC)
690	700/697/678	τ(CCC) _{R2}
675	680/667/671	β(CCC) _R
646	647/647/647	τ(CCC) _{R1}
619	621/624/607	β(CCC) _{R2}
577	582/584/585	τ(CCC) _{R1} +β(CCC) _{R2}

^a v, stretching; α, scissoring; ω, wagging; γ, rocking; δ, twisting; β, bending(in plane); τ, torsion(out of plane); s, symmetric; as, asymmetric. Abbreviations: M1, methy(C13); M2, methy(C14); M3, methy(C15); M, M1M2M3; R1, C2-C7; R2, C11-C16 ring; R, R1 and R2.

3.4. Frontier molecular orbitals

According to the frontier orbital theory the reactivity of reactants is largely dependent on the energies of the frontier molecular orbitals (FMO) [39]. The investigation on the FMO energy levels of BMBA give us that the corresponding electronic transfers happened between the HOMO -1 and LUMO+1. The predicted frontier molecular orbital for BMBA is depicted in Fig. 4. Both the HOMO and the LUMO are mostly the π-antibonding type orbitals. The value of the energy separation between the HOMO and LUMO is 4.079 eV. From the Fig. 4, electrons in the HOMO-1, HOMO and LUMO are localized all over the molecule, whereas electrons in the LUMO+1 are mainly found on the C11-C16 benzene ring. It is clearly visible that the charge density in the isolated molecule is shifting from one portion of the molecule to the other. In case of LUMO the charge is mainly accumulated from the phenyl ring. In LUMO the charge is acquired by the same parts significantly.

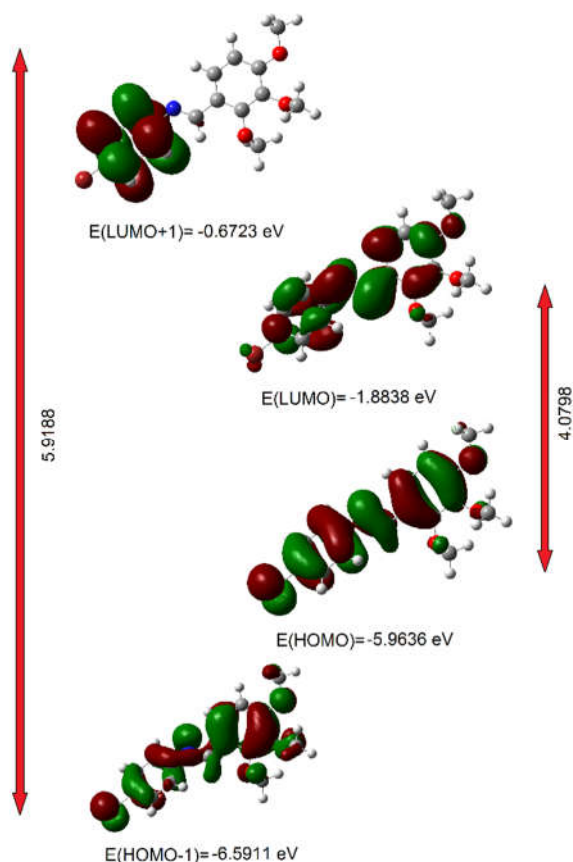


Figure 4. Molecular orbital surfaces and energy levels given in parantheses for the HOMO-1, HOMO, LUMO and LUMO+1 of BMBA

We have also calculated global hardness and global softness to investigate chemical reactivity and stability of BMBA. Also, considering the chemical hardness, large HOMO-LUMO gap (ΔE_{H-L}) means a hard molecule and small ΔE_{H-L} means a soft molecule. The global hardness is $\eta = (E_{LUMO} - E_{HOMO})/2$ and softness is $S = 1/2\eta$ [12], in which E_{LUMO} and E_{HOMO} are defined as LUMO and HOMO energies, respectively. η , S , E_{LUMO} , E_{HOMO} and ΔE_{H-L} for BMBA are calculated as 2.040 eV, 0.245 eV⁻¹, -1.883 eV, -5.963 eV and 4.079 eV, respectively.

3.5. Molecular electrostatic potential

Molecular electrostatic potential (MEP) regions having partially negative charge and defined as red-electron rich were connected to electrophilic reactivity. Moreover, MEP regions having partially positive charge and defined as the blue-electron deficient were connected to nucleophilic reactivity and it can be seen in Fig. 5. The total electron density extreme limits are -0.035 to +0.035 a.u.

The MEP clearly indicates regions having the negative potential were observed around the O1,

O2, O3, N and Br atoms. These negative values of $V(r)$ are -0.028, -0.035, -0.033 and -0.023 a.u. for O1, O2-O3, N and Br atoms, respectively. From these values, we can say that oxygen atoms of the BMBA molecule would be preferred sites for an electrophilic attack. Moreover, in MEP, positive regions are located on the C-H bonds between value of +0.028 with +0.015 a.u. Thus, these regions are indicated as favored sites for nucleophilic interaction where chemical bonding and molecule interact with one another can take place [22]. The MEP mapping is also very useful in understanding hydrogen bonding interactions [40].

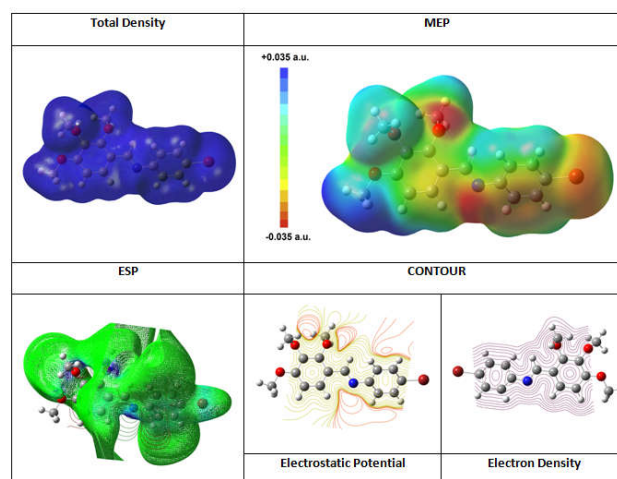


Figure 5. The total electron density mapped with electrostatic potential surface of BMBA

3.6. Nonlinear optics

NLO materials are utilised in applications including telecommunications, signal processing, optical interconnections, etc. The nonlinear optical property is associated with molecular nonlinear polarization [41].

The non-linear polarization (p) for a molecule, can be calculated as follows

$$p = \mu_0 + \alpha_{ij} E_j + \beta_{ijk} E_j E_k + \dots \quad (3.6.1)$$

where μ_0 , α_{ij} and β_{ijk} are the permanent dipole moment, the linear polarizability and the first hyperpolarizability tensor components, respectively. Using the x, y, z components, μ , α and β can be calculated as:

$$\mu = \sqrt{\mu_x^2 + \mu_y^2 + \mu_z^2} \quad (3.6.2)$$

$$\alpha = \frac{\alpha_{xx} + \alpha_{yy} + \alpha_{zz}}{3} \quad (3.6.3)$$

$$\beta = \sqrt{(\beta_{xxx} + \beta_{xyy} + \beta_{xzz})^2 + (\beta_{yyy} + \beta_{yzz} + \beta_{yxx})^2 + (\beta_{zzz} + \beta_{zxx} + \beta_{zyy})^2} \quad (3.6.4)$$

The electronic dipole moment μ_i ($i=x,y,z$), polarizability α_{ij} and the first hyperpolarizability β_{ijk} of BMBA obtained by DFT-B3LYP method and the 6-311++G(d,p) basis set are reported in Table 3. μ is calculated as 5.26 D. In here, the highest value for μ is found μ_x as 5.23 D for the molecule. The polarizability α , is calculated 39.73 Å³. The calculated value of β is 6.47×10^{-30} cm⁵/esu, which is grater than that of urea (β of urea is 0.77×10^{-30} cm⁵/esu obtained by B3LYP/6-311++G(d,p)). The first order hyperpolarizability of BMBA is nearly 8.40 times of urea. We conclude that BMBA is an attractive object for future studies of NLO material.

Table 3. The calculated μ , α and β components

Paramet.	Compounds			
	BMBA	CMBA	FMBA	MBA ^c
μ_x	5.23	5.14	4.76	2.90
μ_y	-0.53	-0.60	-0.64	-0.32
μ_z	-0.11	-0.09	-0.08	-0.10
μ (Debye)	5.26	5.18	4.80	2.92
α_{xx}	438.59	417.94	374.08	370.74
α_{xy}	-11.11	-11.48	-8.22	-9.70
α_{yy}	218.27	213.67	207.54	207.92
α_{xz}	-6.75	-5.75	-5.57	-4.61
α_{yz}	-10.48	-11.02	-11.28	-11.34
α_{zz}	148.30	143.23	136.82	138.95
α (Å ³)	39.73	38.23	35.45	35.41
β_{xxx}	-721.71	-628.32	-509.76	-1251.24
β_{xxy}	309.07	292.60	297.83	377.32
β_{xyy}	16.39	26.28	8.37	-30.62
β_{yyy}	-162.52	-174.48	-172.69	-159.47
β_{xxz}	97.46	69.33	70.02	20.18
β_{xyz}	-17.30	-3.41	15.53	-21.67
β_{yyz}	7.76	1.60	4.74	14.20
β_{zzz}	-27.24	-6.45	-2.37	-47.38
β_{yzz}	-31.11	-40.75	-35.90	-30.87
β_{zzz}	3.03	-4.04	5.79	0.78
β (cm ⁵ /esu)	6.47×10^{-30}	5.33×10^{-30}	4.47×10^{-30}	11.60×10^{-30}

For the investigation of the substituent effects on the NLO properties, μ , α and β were calculated for the molecules having the Cl, F and H instead of Br atom of BMBA (Table 3). From Table 3, one can easily assume that the calculated values of μ were a little affected by the substituents. These values of μ and α for the BMBA compound are bigger than those of substituent. Besides, the calculated values of β have minor differences from each other except for H substituent compound.

4. CONCLUSIONS

The equilibrium geometries, vibrational frequencies and vibrational assignments of the

BMBA molecule were determined and analyzed. These vibrational assignments along with the electronic transitions are important to understand the molecular. Optimized geometric structure and vibrational assignments show a good agreement with results obtained from experiments.

The mapping electron density give information about the shape, size and charge density distribution. Molecular electrostatic potential of BMBA indicates that the positive potential sites are around the hydrogen atoms while the negative potential sites are on oxygen atoms and phenyl rings. HOMO-LUMO made very clearly the involvement of charge transfer between the donor and acceptor groups. The NLO is identified as a featured attribute of BMBA which was inspected and authenticated via computed polarizability and hyperpolarizability. The calculated hyperpolarizability of BMBA is much higher than the standard NLO material urea.

ACKNOWLEDGMENTS

This research was assisted by The Amasya University Research Centre under the Projects Number of FMB-BAP 15-092.

REFERENCES

- [1] J. H. Choi, H. Y. Lee, A. D. Towns, "Dyeing properties of novel azo disperse dyes derived from phthalimide and color fastness on poly (lactic acid) fiber," *Fiber Polym.* Vol. 11, no. 2, pp. 199-204, 2010.
- [2] E. N. Shepelenko, A. V. Tsukanov, Y. V. Revinskii, A. D. Dubonosov, V. A. Bren, V. I. Minkin, "Benzoid-quinoid tautomerism of schiff bases and their structural analogs: LIII. Schiff bases derived from 5-hydroxy- and 5-hydroxy-6-nitro-2, 3-diphenyl-1-benzofuran-4-carbaldehydes," *Russ. J. Org. Chem.* vol. 43, no. 4, pp. 559-562, 2007.
- [3] E. Hadjoudis, A. Ronroyianni, K. Ambroziak, T. Dziembowska, I. M. Mavridis, "Photochromism and thermochromism of solid trans-N, N'-bis-(salicylidene)-1, 2-cyclohexanediamines and trans-N, N'-bis-(2-hydroxy-naphylidene)-1, 2-cyclohexanediamine," *J. Photochem. Photobiol. A* vol. 162, no. 2, pp. 521-530, 2004.

- [4] C. M. da Silva, D. L. da Silva, L. V. Modolo, R. B. Alves, M. de Resende, C. V. B. Martins, A. de Fatima, "Schiff bases: A short review of their antimicrobial activities," *J. Adv. Res.* Vol. 2, no. 1, pp. 1-8, 2011.
- [5] J. H. Choi, J. Y. Choi, H. Y. Lee, A. D. Towns, C. Yoon, "Novel azo dyes derived from phthalimide. Part 2: Dyeing properties and colour fastness on polyester fibres," *Coloration Technology*, vol. 124, no. 6, pp. 364-369, 2008.
- [6] R. Pignatello, A. Panico, P. Mazzane, M. R. Pinizzotto, A. Garozzo, P. M. Fumeri, "Schiff bases of N-hydroxy-N'-aminoguanidines as antiviral, antibacterial and anticancer agents," *European journal of medicinal chemistry*," vol. 29, no. 10, pp. 781-785, 1974.
- [7] D. R. Williams, "Metals, ligands, and cancer," *Chemical reviews*, vol. 72, no.3, pp. 203-213, 1972.
- [8] L. Sundararaman, R. Kandasamy, H. Stoeckli-Evans, V. Gopalsamy, "[4-Chlorophenyl] iminomethyl phenol," *Acta Crystallographica Section E: Structure Reports Online*, vol. 63, no. 12, pp. 4805-4805, 2007.
- [9] K. Srinivasan, R. Biravaganesh, R. Gandhimathi, P. Ramasamy, "Growth and characterization of NMBA (4-nitro-4'-methyl benzylidene aniline) single crystals," *Journal of crystal growth*, vol. 236, no. 1-3, pp. 381-392, 2002.
- [10] M. Aslantas, E. Kendi, N. Demir, A. E. Sabik, M. Tumer, M. Kertmen, "Synthesis, spectroscopic, structural characterization, electrochemical and antimicrobial activity studies of the Schiff base ligand and its transition metal complexes," *Spectrochimica Acta Part A: Molecular and Biomolecular Spectroscopy*, vol. 74, no. 3, pp. 617-624, 2009.
- [11] Y. Sun, Y. Wang, Z. Liu, C. Huang, C. Yu, "Structural, proton-transfer, thermodynamic and nonlinear optical studies of (E)-2-((2-hydroxyphenyl) iminiomethyl) phenolate," *Spectrochimica Acta Part A: Molecular and Biomolecular Spectroscopy*, vol. 96, pp. 42-50, 2012.
- [12] A. Subashini, R. Kumaravel, S. Leela, H. S. Evans, D. Sastikumar, K. Ramamurthi, "Synthesis, growth and characterization of 4-bromo-4' chloro benzylidene aniline—A third order non linear optical material," *Spectrochimica Acta Part A: Molecular and Biomolecular Spectroscopy*, vol. 78, no. 3, pp. 935-941, 2011.
- [13] K. Fejfarová, A. D. Khalaji, M. Dušek, "(E)-4-Bromo-N-(2, 3, 4-trimethoxybenzylidene) aniline," *Acta Crystallographica Section E: Structure Reports Online*, vol. 66, no. 8, pp. 2062-2062, 2010.
- [14] M. J. Frisch et al, Gaussian 09, Revision C. 01, Gaussian Inc., Wallingford CT, 2009.
- [15] R. Dennington, T. Keith, J. Millam, Semichem Inc, Shawnee Mission KS, GaussView, Version 5 (2009).
- [16] H. Tanak, A. A. Agar, O. Büyükgüngör, "Combined experimental and DFT computational studies on (E)-1-(5-nitrothiophen-2-yl)-N-[4-(trifluoromethyl) phenyl] methanimine," *Journal of Molecular Structure*, vol. 1048, pp. 41-50, 2013.
- [17] R. K. Balachandar, S. Kalainathan, S. M. Eappen, J. Podder, "4-Fluoro-N-[(E)-3, 4, 5-trimethoxybenzylidene] aniline," *Acta Crystallographica Section E: Structure Reports Online*, vol. 69, no. 8, pp. 1234-1234, 2013.
- [18] A. Dehno Khalaji, J. Asghari, K. Fejfarová, M. Dušek, "4-Chloro-N-(3, 4, 5-trimethoxybenzylidene) aniline," *Acta Crystallographica Section E: Structure Reports Online*, vol. 65, no. 2, pp. o253-o253, 2009.
- [19] D. Mahadevan, S. Periandy, M. Karabacak, S. Ramalingam, "FT-IR and FT-Raman, UV spectroscopic investigation of 1-bromo-3-fluorobenzene using DFT (B3LYP, B3PW91 and MPW91PW91) calculations," *Spectrochimica Acta Part A: Molecular and Biomolecular Spectroscopy*, vol. 82, no. 1, pp. 481-492, 2011.
- [20] S. Ramalingam, S. Periandy, B. Elanchezian, S. Mohan, "FT-IR and FT-Raman spectra and vibrational investigation of 4-chloro-2-fluoro toluene using ab initio HF and DFT (B3LYP/B3PW91) calculations," *Spectrochimica Acta Part A: Molecular and Biomolecular Spectroscopy*, vol. 78, no. 1, pp. 429-436, 2011.

- [21] H. Tanak, "Crystal structure, spectroscopy, and quantum chemical studies of (E)-2-[(2-Chlorophenyl) iminomethyl]-4-trifluoromethoxyphenol," *The Journal of Physical Chemistry A*, vol. 115, no. 47, pp. 13865-13876, 2011.
- [22] V. Krishnakumar, N. Prabavathi, "Simulation of IR and Raman spectral based on scaled DFT force fields: a case study of 2-amino 4-hydroxy 6-trifluoromethylpyrimidine, with emphasis on band assignment," *Spectrochimica Acta Part A: Molecular and Biomolecular Spectroscopy*, vol. 71, no. 2, pp. 449-457, 2008.
- [23] A. Altun, K. Gölcük, M. Kumru, "Structure and vibrational spectra of p-methylaniline: Hartree-Fock, MP2 and density functional theory studies," *Journal of Molecular Structure: THEOCHEM*, vol. 637, no. 1-3, pp. 155-169, 2003.
- [24] S. J. Singh, S. M. Pandey, "Vibrational-spectra of some fluoroaminotoluenes," *Indian Journal of Pure and Applied Physics*, vol. 12, no.4, pp. 300-302, 1974.
- [25] S. Muthu, E. Isac Paulraj, "Spectroscopic and molecular structure (monomeric and dimeric structure) investigation of 2-[(2-hydroxyphenyl) carbonyloxy] benzoic acid by DFT method: A combined experimental and theoretical study," *Journal of Molecular Structure*, vol. 1038, pp. 145-162, 2013.
- [26] B. D. Joshi, P. N. Chaudhary, "Molecular structure, MESP, homo-lumo and vibrational analysis of β -asarone using density functional theory," *Kathmandu Univ J Sci Eng Tech*, vol. 9, pp. 1-14, 2013.
- [27] M. Arivazhagan, V. Krishnakumar, R. John Xavier, G. Ilango, V. Balachandran, "FTIR, FT-Raman, scaled quantum chemical studies of the structure and vibrational spectra of 1, 5-dinitronaphthalene," *Spectrochimica Acta Part A: Molecular and Biomolecular Spectroscopy*, vol. 72, no. 5, pp. 941-946, 2009.
- [28] G. Varsanyi, *Vibrational Spectra of Benzene Derivatives*, Academic Press, New York, 1969.
- [29] U. Karunanithi, S. Arulmozhi, M. Dinesh Raja and J. Madhavan, "Growth and Characterization of Pure and Doped L-Phenylalanine Maleate Single Crystals," *Int. J. Eng. Res. Dev.*, vol. 3, no. 1, pp.51-55, 2012.
- [30] M. Irani, R. Ranjbar-Karimi, H. Izadi, "Synthesis and Pesticide Activity of some New Arylic and Pyridylic Oxime Ether Derivatives of Ionone," *Organic Chemistry Research*, vol. 2, no. 2, pp. 192-196, 2016.
- [31] J.B. Lambert, H.F. Shurvell, D.A. Lightner, R.G. Cooks, *Org. Struct. Spectrosc.*, Simon & Schuster/A Viacom Company, New Jersey, 1998.
- [32] B. Smith, *Infrared Spectra Interpretation. A Systematic Approach*, CRC Press, Washington, DC, 1999.
- [33] E. F. Mooney, "The infrared spectra of chloro-and bromobenzene derivatives—I: Anisoles and phenetoles," *Spectrochimica Acta*, vol. 19, no. 6, pp. 877-887, 1963.
- [34] E. F. Mooney, "The infra-red spectra of chloro-and bromobenzene derivatives—II. Nitrobenzenes," *Spectrochimica Acta*, vol. 20, no. 6, pp. 1021-1032, 1964.
- [35] K. Rastogi, M. A. Palafox, R. P. Tanwar, L. Mittal, "3, 5-Difluorobenzonitrile: ab initio calculations, FTIR and Raman spectra," *Spectrochimica Acta Part A: Molecular and Biomolecular Spectroscopy*, vol. 58, no. 9, pp. 1989-1997, 2002.
- [36] H. Tanak, M. Toy, "Molecular structure, spectroscopic and quantum chemical studies on 2'-chloro-4-dimethylamino azobenzene," *Journal of Molecular Structure*, vol. 1068, pp. 189-197, 2014.
- [37] M. Evecen, G. Duru, H. Tanak, A.A. Ağar, "Synthesis, crystal structure, spectral analysis and DFT computational studies on a novel isoindoline derivative," *Journal of Molecular Structure*, vol. 1118, pp. 1-9, 2016.
- [38] M. P. Kumpawat, A. Ojha, N. D. Patel, "Vibrational-spectra and normal coordinate analysis of some substituted anilines," *Canadian Journal of Spectroscopy*, vol. 25, no. 1, pp. 1-14, 1980.
- [39] I. Fleming, "Frontier Orbitals and Organic Chemical Reactions," Wiley, London, 1976.
- [40] N. Okulik, A. H. Jubert, "Theoretical analysis of the reactive sites of non-steroidal anti-inflammatory drugs," *Internet*

Electronic Journal of Molecular Design,
vol. 4, no. 1, pp. 17-30, 2005.

studies of 4-(1, 3-dioxoisindolin-2-yl)
antipyrine," *Journal of Molecular Structure*,
vol. 1030, pp. 113–124, 2012.

- [41] Z. Yu, G. Sun, Z. Liu, C. Yu, C. Huang, Y. Sun, "Synthesis, crystal structure, vibrational spectral and density functional

	SAKARYA ÜNİVERSİTESİ FEN BİLİMLERİ ENSTİTÜSÜ DERGİSİ SAKARYA UNIVERSITY JOURNAL OF SCIENCE		
	e-ISSN: 2147-835X Dergi sayfası: http://www.saujs.sakarya.edu.tr		
	<u>Received</u> 14-11-2017 <u>Accepted</u> 07-03-2018	<u>Doi</u> 10.16984/saufenbilder.352088	

A collocation method for solving boundary value problems of fractional order

Sertan Alkan^{*1}, Aydin Secer²

ABSTRACT

In this work, the Sinc-Collocation Method (SCM) is used to find the approximate solutions of the second-order fractional boundary value problems based on the conformable fractional derivative. For this purpose, a theorem is proved to represent the terms having fractional derivatives in terms of sinc basis functions. To show the effectiveness and accuracy of the method, some special problems are handled and the determined solutions are compared with the approximate solutions arising from using the other numerical methods as well as the exact solutions of the problems.

Keywords: Differential Equations with Fractional Order, Sinc-Collocation Method, Boundary Value Problems, Conformable Fractional Derivative.

1. INTRODUCTION

Fractional calculus is a subject of calculus that involves noninteger order differential and integral operators.

The background of fractional calculus dates back to the end of the 17th century. In 1695, half-order derivative was mentioned in a letter from L'Hopital to Leibniz [1]. Since then, fractional calculus developed mainly as a pure theoretical field for mathematicians. However, in the last few decades fractional calculus has fastinated the interest of many researchers in several areas [2-9]. Many mathematicians contributed to the development of fractional calculus, therefore many definitions for the fractional derivative are available. The most popular definitions are Riemann-Liouville and Caputo definition of fractional derivatives. Riemann-Liouville and

Caputo definitions of α order α^{th} derivative of function f is given as,

$$D_a^\alpha (f)(t) = \frac{1}{\Gamma(n-\alpha)} \frac{d^n}{dt^n} \int_a^t \frac{f(x)}{(t-x)^{\alpha-n+1}} dx$$

and

$$D_{*,a}^\alpha (f)(t) = \frac{1}{\Gamma(n-\alpha)} \int_a^t \frac{f^n(x)}{(t-x)^{\alpha-n+1}} dx$$

respectively, where $a \in [n-1, n), n = 1, 2, \dots$

In the last years, Khalil et al.[10] identified a new definition of fractional derivative called the conformable fractional derivative. In [11], Abdeljawad developed the definition of conformable fractional derivative and set basic concepts of this new fractional calculus. For a detailed overview of the conformable fractional derivative and applications, we refer the reader to [12-15] and references there in.

* Corresponding Author

¹ Iskenderun Technical University, Department of Computer Engineering, Iskenderun, Hatay - sertan.alkan@iste.edu.tr

² Yildiz Technical University, Department of Mathematical Engineering, Esenler, Istanbul - asecer@yildiz.edu.tr

In particular, in this paper SCM is illustrated to determine the approximate solutions of fractional order boundary value problems in the following form

$$\begin{cases} \mu_2(x)y''(x) + \mu_a(x)y^\alpha + \mu_1(x)y'(x) + \\ \mu_\beta(x)y^\beta(x) + \mu_0(x)y(x) = f(x) \\ y(a) = 0, y(b) = 0 \end{cases} \quad (1)$$

Here $y^{(\alpha)}$ and $y^{(\beta)}$ are the conformable fractional derivative for $1 < \alpha \leq 2$ and $0 < \beta \leq 1$.

Approximate solutions of the equation (1) based on Riemann-Liouville and Caputo derivatives has been studied in several articles with various numerical methods. For example, Variational Iteration Method [16], Adomian Decomposition Method [17], Homotopy Perturbation Method [18], Homotopy Analysis Method [19], Haar Wavelet Method [20] etc. In this paper, we investigate the sinc-collocation method (SCM) to obtain the approximate solution of the equation (1) based on the conformable fractional derivative.

In this paper, SCM is firstly applied to determine the solution of the FBVPs based on conformable fractional derivative. The solution function is expanded to a finite series regarding to the composite translated sinc functions and some unknown coefficients. These unknown coefficients are determined by this method. To show the sufficiency and reliability of the SCM, the method is applied some special FBVPs. Obtained numerical results are compared with the exact ones in addition to ones of other numerical methods. As a result of the comparison one can say that SCM is a strong and hopeful method for finding the approximate solutions of FBVPs.

The paper organized as follows. In section 2, we have illustrated some fundamental definitions and properties of fractional calculus and SCM. In section 3, we use SCM to determine an approximate solution of a general fractional differential equation and obtained results are stated as a new theorems. In section 4, by using tables and graphs some special problems are given to show the abilities of present method. Lastly, in section 5, The paper is ended with a conclusion.

2. PRELIMINARIES

In this section, some fundamental definitions and properties with regard to fractional calculus and

sinc basis functions are introduced. For more information, see [21-26].

Definition 1. Let $a \in (n, n + 1]$ and f be an $n -$ differentiable function at t , where $t > 0$ Then the conformable fractional derivative of f of order α is defined as

$$T_a(f)(t) = \lim_{\varepsilon \rightarrow 0} \frac{f^{([\alpha]-1)}(t+\varepsilon t^{([\alpha]-a)}) - f^{([\alpha]-1)}(t)}{\varepsilon} \quad (2)$$

where $[\alpha]$ is the smallest integer greater than or equal to α .

Remark 1. As a consequence of Definition1, one can easily show that

$$T_a(f)(t) = t^{([\alpha]-a)} f^{([\alpha]}(t)$$

where $a \in (n, n + 1]$ and f is $(n + 1)$ differentiable at $t > 0$.

Theorem 2. Let $a \in (n, n + 1]$ and $f; g$ be $\alpha -$ differentiable at a $t > 0$. Then

1. $T_a(af + bg) = aT_a(f) + bT_a(g)$, for all $a, b \in R$.
2. $T_a(t^p) = pt^{p-a}$, for all $p \in R$.
3. $T_a(\lambda) = 0$, for all constant functions $f(t) = \lambda$.
4. $T_a(fg) = fT_a(g) + gT_a(f)$.
5. $T_a\left(\frac{f}{g}\right) = \frac{gT_a(f) + fT_a(g)}{g^2}$.

Definition 2. The Sinc function is defined as

$$\text{sinc}(x) = \begin{cases} \frac{\sin \pi x}{\pi x}, & x \neq 0 \\ 1, & x = 0 \end{cases}, \quad x \in \mathbb{R}$$

Definition 3. The translated sinc function with space knots are given by:

$$S(k, h) = \text{sinc}\left(\frac{x - kh}{h}\right) = \begin{cases} \frac{\sin\left(\pi \frac{x - kh}{h}\right)}{\pi \frac{x - kh}{h}}, & x \neq kh \\ 1, & x = kh. \end{cases}$$

where $h > 0$ and $k = 0, \pm 1, \pm 2, \dots$

For constructing the approximation on (a, b) , the conformal map is identified with

$$\phi(z) = \ln\left(\frac{z - a}{b - z}\right)$$

Here, the basis function on (a, b) are determined from

$$S_k(z) = S(k, h)(z) \circ \phi(z) = \text{sinc}\left(\frac{\phi(z) - kh}{h}\right) \quad y_n^{(\beta)}(x) = \sum_{k=-M}^N c_k x^{1-\beta} \phi'(x) \frac{d}{d\phi} S_k(x) \quad (6)$$

The inverse map of $\omega = \phi(z)$ is

$$z = \phi^{-1}(\omega) = \frac{a + be^\omega}{1 + e^\omega}$$

the sinc grid points $z_k \in (a, b)$ will be denoted by x_k because they are real. For the evenly spaced knots $\{kh\}_{k=-\infty}^{\infty}$, the image corresponding to these knots is defined by

$$x_k = \phi^{-1}(kh) = \frac{a + be^{kh}}{1 + e^{\omega kh}}, k = 0, \pm 1, \pm 2, \dots$$

3. THE SINC-COLLOCATION METHOD

Let us consider an approximate solution for $y_n(x)$ in Eq.(1) of the form

$$y_n(x) = \sum_{k=-M}^N c_k S_k(x), n = M + N + 1 \quad (3)$$

Here, $S_k(x)$ is the composite function of $S(k, h)$ and $\phi(x)$. The unknown coefficients c_k in Eq.(3) are obtained with SCM using the following theorems.

Theorem 3. The first two derivatives of $y_n(x)$ are given with

$$\frac{d}{dx} y_n(x) = \sum_{k=-M}^N c_k \phi(x) \frac{d}{d\phi} S_k(x) \quad (4)$$

and

$$\begin{aligned} \frac{d^2}{dx^2} y_n(x) &= \sum_{k=-M}^N c_k \left(\phi''(x) \frac{d}{d\phi} S_k(x) \right. \\ &\left. + (\phi'(x))^2 \frac{d^2}{d\phi^2} S_k(x) \right) \end{aligned} \quad (5)$$

Theorem 4. The conformable fractional derivatives of order β and α of $y_n(x)$ for $1 < \alpha \leq 2$ and $0 < \beta \leq 1$ are given by

$$y_n^{(\alpha)}(x) = \sum_{k=-M}^N c_k x^{2-\alpha} \left(\phi''(x) \frac{d}{d\phi} S_k(x) + (\phi'(x))^2 \frac{d^2}{d\phi^2} S_k(x) \right) \quad (7)$$

respectively.

Proof. The conformable fractional derivative of order β of $y_n(x)$ in (3) is written as

$$y_n^{(\beta)}(x) = \sum_{k=-M}^N c_k S_k^{(\beta)}(x).$$

Here, according to Remark 1, we can write

$$S_k^{(\beta)}(x) = x^{1-\beta} S_k'(x).$$

Now, if we use Eq.(4), we obtain

$$y_n^{(\beta)}(x) = \sum_{k=-M}^N c_k x^{1-\beta} \phi'(x) \frac{d}{d\phi} S_k(x)$$

Similarly, we may write the conformable fractional derivative of order α of $y_n(x)$ in(3) as

$$y_n^{(\alpha)}(x) = \sum_{k=-M}^N c_k S_k^{(\alpha)}(x).$$

By using Remark 1, we have

$$S_k^{(\alpha)}(x) = x^{2-\alpha} S_k''(x).$$

Then by Eq.(5), we get the desired result

$$y_n^{(\alpha)}(x) = \sum_{k=-M}^N c_k x^{2-\alpha} \left(\phi''(x) \frac{d}{d\phi} S_k(x) + (\phi'(x))^2 \frac{d^2}{d\phi^2} S_k(x) \right)$$

After relocating each term of Eq.(1) with the approximation illustrated in Eq.(3)-(7) and producing the ending equation by $\{(1/\phi')^2\}$, we determine the system

$$\sum_{k=-M}^N \left[c_k \left\{ \sum_{i=0}^2 g_i(x) \frac{d^i}{d\phi^i} S_k \right\} \right] = \left(f(x) \left(\frac{1}{\phi'(x)} \right)^2 \right)$$

$$A = \sum_{i=0}^2 \frac{1}{h^i} D(g_i) I^{(i)}$$

$$B = D \left(\frac{f}{\phi'} \right) 1$$

where

$$g_0(x) = \mu_0(x) \left(\frac{1}{\phi'(x)} \right)^2$$

$$g_1(x) = \left[\left(\mu_1(x) + \mu_\beta(x)x^{1-\beta} \right) \left(\frac{1}{\phi'(x)} \right) - (\mu_2(x) + \mu_\alpha(x)x^{2-\alpha}) \left(\frac{1}{\phi'(x)} \right)' \right]$$

$$g_2(x) = \mu_2(x) + \mu_\alpha(x)x^{2-\alpha}$$

We know from [25] that

$$\delta_{jk}^{(0)} = \delta_{kj}^{(0)}, \quad \delta_{jk}^{(1)} = -\delta_{kj}^{(1)}, \quad \delta_{jk}^{(2)} = \delta_{kj}^{(2)}$$

After taking $x = x_j$, we find the next theorem.

Theorem 5. If the considered approximate solution of BVP (1) is Eq.(3), then the discrete sinc-collocation system for the determination of the unknown coefficients $\{c_k\}_{k=-M}^N$

$$\sum_{k=-M}^N \left[c_k \left\{ \sum_{i=0}^2 \frac{g_i(x_j)(-1)^i}{h^i} \delta_{jk}^{(i)} \right\} \right] = \left(f(x_j) \left(\frac{1}{\phi'(x_j)} \right)^2 \right); j = -M, \dots, N \quad (8)$$

Let us define some notations to rewrite the equation system we have obtained in the matrix form.

Let $D(y)$ be a diagonal matrix whose diagonal elements are $y(x_{-M}), y(x_{-M+1}), \dots, y(x_N)$ and all the other elements are zero and $I^{(i)}$ be the matrices formed by

$$I^{(i)} = \left[\delta_{jk}^{(i)} \right], i = 0, 1, 2$$

where $D, I^{(0)}, I^{(1)}$ and $I^{(2)}$ are $n \times n$ order matrices. For calculating the unknown coefficients c_k in (8), we can write this system using the previous notations in the matrix form

$$Ac = B \quad (9)$$

Here,

$$c = (c_{-M}, c_{-M+1}, \dots, c_N)^T$$

Now we have a linear system of with n equations given by (9). The unknown coefficients c_k can be determined by solving the system.

4. COMPUTATIONAL EXAMPLES

In this section, we consider three different problems being approximately solved in [20] based on Riemann-Liouville and Caputo fractional differential operator. The exact solutions of those three problems are known and will be investigated by using the present method with Mathematica10 software. In each example, we consider $h = \pi/\sqrt{N}$, $N = M$.

Example 1. [20] Let us consider the fractionally damped mechanical oscillator equation in the form of

$$y^{(\alpha)}(x) + \lambda y^{(\beta)}(x) + \nu y(x) = f(x), \quad 1 < \alpha \leq 2; \quad 0 < \beta \leq 1$$

with subject to $y(0) = 0, y(1) = 0$. Here, we take $\alpha = \frac{7}{4}, \beta = \frac{1}{2}, \lambda = 1, \nu = -\frac{1}{\sqrt{\pi}}$ and

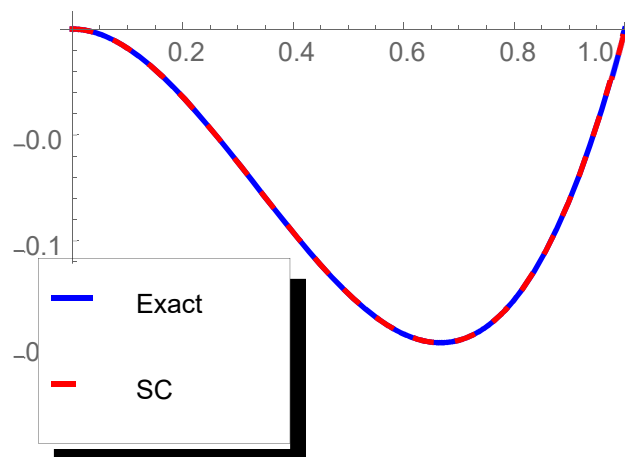
$$f(x) = -\frac{x^3}{\sqrt{\pi}} + 3x^{5/2} + \frac{x^2}{\sqrt{\pi}} - 2x^{3/2} - 6x^{5/4} - 2x^{1/4}.$$

$y(x) = x^2(x - 1)$ is the exact solution of the problem. The numerical results determined by SCM for this problem are illustrated in Table 1. Also, the comparison of the exact and approximate solutions for various values of N are given graphically in Figure 1.

Table 1: Absolute errors for various values of N for Example 1

x	$N=4$	$N=8$	$N=16$	$N=32$	$N=64$
0.1	2.996×10^{-5}	6.306×10^{-5}	1.656×10^{-5}	2.624×10^{-8}	3.376×10^{-10}
0.2	3.129×10^{-3}	4.556×10^{-4}	2.219×10^{-5}	3.620×10^{-7}	4.409×10^{-10}

0.3	5.175 $\times 10^{-3}$	6.260 $\times 10^{-4}$	8.078 $\times 10^{-6}$	3.999 $\times 10^{-7}$	2.295 $\times 10^{-10}$
0.4	5.196 $\times 10^{-3}$	8.101 $\times 10^{-4}$	4.094 $\times 10^{-5}$	3.222 $\times 10^{-7}$	4.657 $\times 10^{-11}$
0.5	1.571 $\times 10^{-4}$	4.189 $\times 10^{-5}$	1.689 $\times 10^{-6}$	1.502 $\times 10^{-8}$	1.442 $\times 10^{-11}$
0.6	5.082 $\times 10^{-3}$	8.232 $\times 10^{-4}$	4.039 $\times 10^{-5}$	3.091 $\times 10^{-7}$	5.855 $\times 10^{-11}$
0.7	6.423 $\times 10^{-3}$	5.832 $\times 10^{-4}$	8.029 $\times 10^{-6}$	3.721 $\times 10^{-7}$	2.390 $\times 10^{-10}$
0.8	3.144 $\times 10^{-3}$	3.412 $\times 10^{-4}$	1.944 $\times 10^{-5}$	3.309 $\times 10^{-7}$	4.018 $\times 10^{-10}$
0.9	1.188 $\times 10^{-3}$	6.109 $\times 10^{-5}$	1.349 $\times 10^{-5}$	2.124 $\times 10^{-8}$	2.862 $\times 10^{-10}$



(c) $N = 64$

Figure 1: Graphs of the exact and the approximate solutions for Example 1

Example 2. [20] Let us assume the fractional differential equation

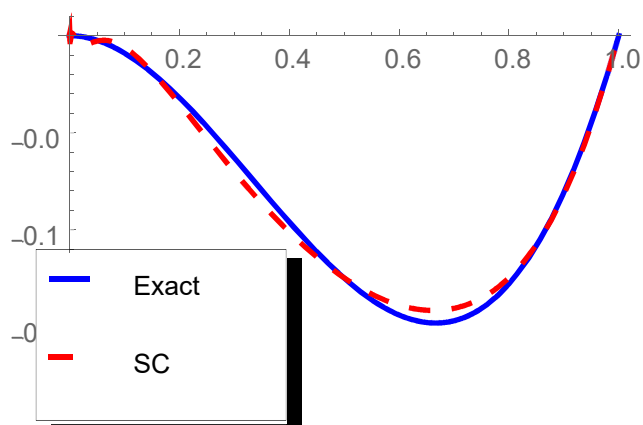
$$y^{(\alpha)}(x) = y^{(\beta)}(x) - e^{x-1} - 1, 1 < \alpha \leq 2; 0 < \beta \leq 1$$

with subject to $y(0) = 0, y(1) = 0$.

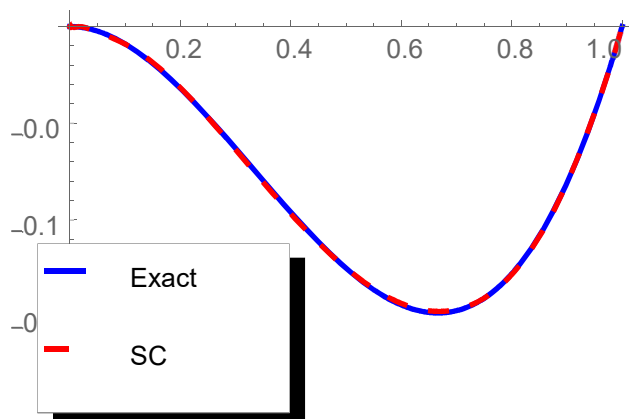
$y(x) = x(1 - e^{x-1})$ is the exact solution of the problem for $\alpha = 2$ and $\beta = 1$. In Table 2, the numerical results determined by SCM are compared with the results determined by using Haar wavelet (HWM) and Homotopy perturbation methods (HPM). In addition to presented results in Table 2, the graphs of approximate solutions for various values of α when $\beta = 1$ and $N = 64$ are given in Figure 2. We can easily see that when α approaches to 2, the approximation solutions of fractional order differential equation approach to the solutions of integer order differential equation via the graphs in Figure 2.

Table 2: Numerical comparisons for Example 2 when $N = 64, \alpha = 2$ and $\beta = 1$

x	Fourth order HPM [27]	HWM ($J = 10$)[20]	SCMM	Exact
0.1	0.05934820	0.05934300	0.05934303	0.05934303
0.2	0.11014318	0.11013418	0.11013420	0.11013421
0.3	0.15103441	0.15102438	0.15102440	0.15102441
0.4	0.18048329	0.18047531	0.18047534	0.18047535
0.5	0.19673826	0.19673463	0.19673467	0.19673467
0.6	0.19780653	0.19780792	0.19780797	0.19780797
0.7	0.18142196	0.18142718	0.18142724	0.18142725
0.8	0.14500893	0.14501532	0.14501539	0.14501540
0.9	0.08564186	0.08564623	0.08564632	0.08564632



(a) $N = 4$



(b) $N = 16$

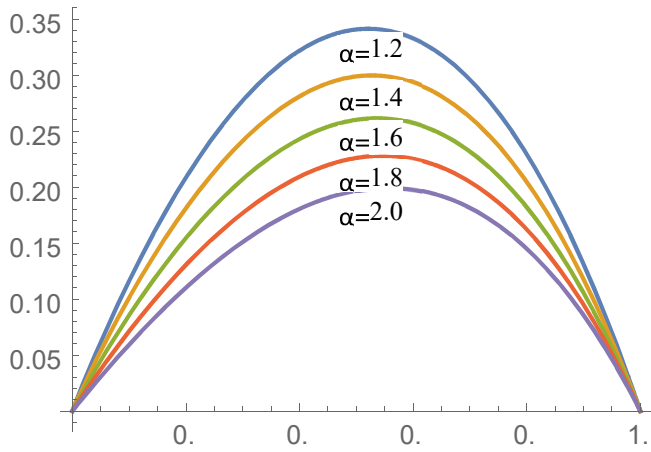


Figure 2: Graphs of the approximate solutions for various values of α for Example 2.

Example 3.[20] Finally, consider the Bagley-Torvik equation the following

$$ay''(x) + by^{(\alpha)}(x) + cy(x) = f(x), 1 < \alpha \leq 2$$

with subject to $y(0) = 0, y(1) = 0$

where $\alpha = \frac{3}{2}, a = 1, b = \frac{8}{17}, c = \frac{13}{51}$ and

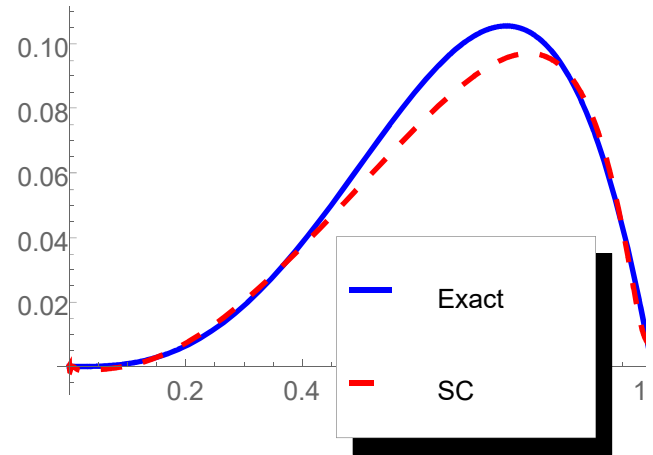
$$f(x) = \frac{1}{51}(360x + 144x^{1.5} - 612x^2 - 288x^{2.5} + 13x^3 - 13x^4).$$

The exact solution of this problem is $y(x) = x^3(1-x)$. The numerical solutions which are obtained by using SCM for this problem are presented in Table 3. In addition to presented results in Table 3, the graphs of the exact and approximate solutions for various values of N are given in Figure 3.

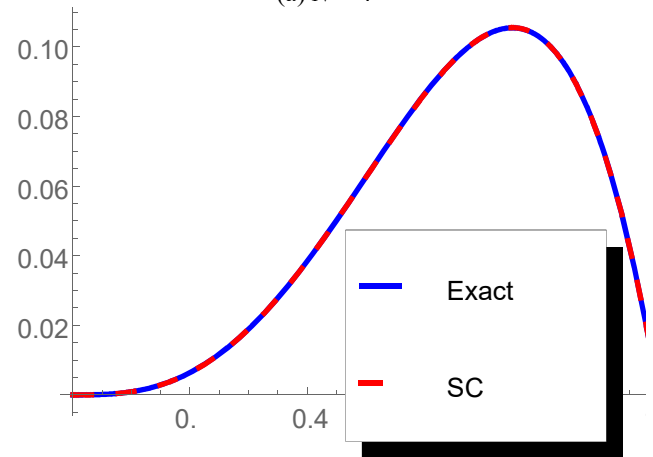
Table 3: Absolute errors for various values of N for Example 3

x	$N=4$	$N=8$	$N=16$	$N=32$	$N=64$
0.1	6.735×10^{-4}	2.391×10^{-4}	4.792×10^{-6}	8.709×10^{-8}	3.369×10^{-10}
0.2	8.435×10^{-4}	8.087×10^{-5}	1.427×10^{-5}	8.789×10^{-8}	1.422×10^{-10}
0.3	1.406×10^{-3}	3.240×10^{-4}	1.995×10^{-6}	1.728×10^{-7}	1.305×10^{-10}
0.4	1.161×10^{-3}	2.492×10^{-4}	2.353×10^{-5}	2.404×10^{-7}	6.230×10^{-11}
0.5	6.392×10^{-3}	5.979×10^{-4}	2.072×10^{-5}	1.768×10^{-7}	1.856×10^{-10}
0.6	1.148×10^{-2}	1.397×10^{-3}	5.836×10^{-5}	3.949×10^{-7}	1.661×10^{-10}
0.7	1.228×10^{-2}	9.068×10^{-4}	1.759×10^{-5}	6.010×10^{-7}	5.980×10^{-10}

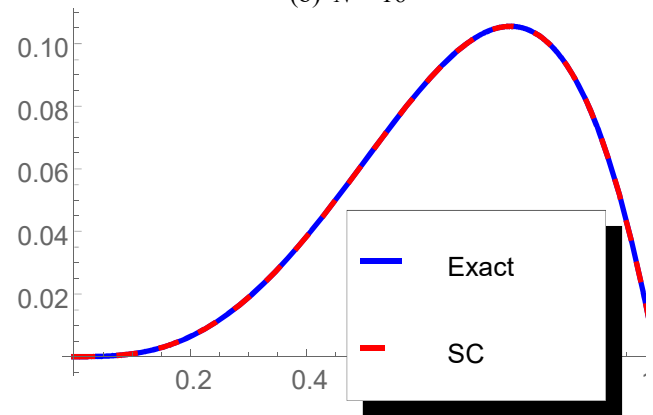
0.8	5.562×10^{-3}	6.948×10^{-4}	2.740×10^{-5}	7.810×10^{-7}	9.854×10^{-10}
0.9	3.363×10^{-3}	2.501×10^{-4}	3.491×10^{-5}	3.870×10^{-8}	9.605×10^{-10}



(a) $N = 4$



(b) $N = 16$



(c) $N = 64$

Figure 3: Graphs of exact and approximate solutions for Example 3

5. CONCLUSION

This study focused on the application of SCM to and the approximate solutions of a class of fractional order two-point boundary value

problems. The suggested method is applied to some particular examples to show the applicability and accuracy of the method for FBVPs. Numerical results obtained from the method are compared with the exact solutions and differences are presented in tables and graphical forms. Regarding the results displayed in tables and graphical forms, it can be concluded that SCM is a very effective and convenient method for obtaining the approximate solution of FBVPs.

REFERENCES

- [1] S.G. Samko, A.A. Kilbas, O.I. Marichev, "Fractional Integrals and Derivatives", *Gordon and Breach*, Yverdon, 1993.
- [2] K. Miller, B. Ross, "An introduction to the fractional calculus and fractional differential equations", New York, Wiley, 1993.
- [3] K. B. Oldham, J. Spanier, "The fractional calculus", *Academic Press*, New York and London, 1974.
- [4] I. Podlubny, "Fractional differential equations", *Academic Press*, San Diego, 1999.
- [5] R. Herrmann, "Fractional Calculus: An Introduction for Physicists", *World Scientific*, Singapore, 2014.
- [6] J. Sabatier, O. P. Agrawal, J. A. T. Machado, "Advances in Fractional Calculus: Theoretical Developments and Applications in Physics and Engineering", *Springer*, 2007.
- [7] S. Alkan, V. Hatipoglu, "Approximate solutions of Volterra-Fredholm integro-differential equations of fractional order", *Tbilisi Mathematical Journal*, Vol.10,no.2, pp. 1-13, 2017.
- [8] R. P. Meilanov, R. A. Magomedov, "Thermodynamics in Fractional Calculus", *Journal of Engineering Physics and Thermophysics*, Vol.87, no.6, pp.1521-1531, 2014.
- [9] V. F. Hatipoglu, S. Alkan, A. Secer, "An efficient scheme for solving a system of fractional differential equations with boundary conditions", *Advances in Difference Equations*, Vol. 2017.1, pp.204, 2017.
- [10] Khalil, R., Al Horani, M., Yousef, A. and Sababeh, M., "A new definition of fractional derivative", *J.Comput. Appl. Math.*, Vol. 264, pp.65-70, 2014.
- [11] Thabet Abdeljawad, "On the conformable fractional calculus", *Journal of Computational and Applied Mathematics*, Vol.279, pp.57-66,2015.
- [12] N. Benkhattou, S. Hassani, D.F.M. Torres, "A conformable fractional calculus on arbitrary time scales", *J. King Saud Univ.-Sci.*, Vol.28, no.1, pp.93-98, 2016.
- [13] W.S. Chung, "Fractional Newton mechanics with conformable fractional derivative", *J. Comput. Appl. Math.*, Vol.290, pp.150-158, 2015.
- [14] H. Batar, J. Losada, J.J. Nieto, W. Shammakh, "Three-point boundary value problems for conformable fractional differential equations", *J. Funct. Space*, Vol.6, 2015.
- [15] E. Hesameddini, E. Asadollahifard, "Numerical solution of multi-order fractional differential equations via the sinc collocation method", *Iranian Journal Of Numerical Analysis And Optimization*, Vol.5, no.1, pp.37-48, 2015.
- [16] G. Wu, E. W. M. Lee, "Fractional variational iteration method and its application", *Phys. Lett. A.*, Vol.374, pp.2506-2509, 2010.
- [17] V. Daftardar-Gejji, H. Jafari, "Solving a multi-order fractional differential equation using adomian decomposition", *Appl. Math. Comput.*, Vol.189, pp.541-548, 2007.
- [18] O. Abdulaziz, I. Hashim, S. Momani, "Solving systems of fractional differential equations by homotopy perturbation method", *Phys. Lett. A.*, Vol.372, pp.451-459, 2008.
- [19] I. Hashim, O. Abdulaziz, S. Momani, "Homotopy analysis method for fractional IVPs", *Commun. Nonlinear Sci. Numer. Simul.*, Vol.14, pp.674-684, 2009.
- [20] M. U. Rehman, R. A. Khan, "A numerical method for solving boundary value problems for fractional differential equations", *Appl. Math. Model.*, Vol. 36, no.3, pp.894-907, 2012.
- [21] F. Stenger, "Approximations via Whittaker's cardinal function", *J. Approx. Theory*, Vol.17, no.3, pp.222-240, 1976.

- [22] F. Stenger, "A sinc-Galerkin method of solution of boundary value problems", *Math. Comput.*, Vol.33, pp.85-109, 1979.
- [23] E. T. Whittaker, "On the functions which are represented by the expansions of the interpolation theory", *Proc. R. Soc. Edinb.*, Vol.35, pp.181-194, 1915.
- [24] J. M. Whittaker, "Interpolation Function Theory, Cambridge Tracts in Mathematics and Mathematical Physics", Cambridge University Press, London, 1935.

	SAKARYA ÜNİVERSİTESİ FEN BİLİMLERİ ENSTİTÜSÜ DERGİSİ SAKARYA UNIVERSITY JOURNAL OF SCIENCE		
	e-ISSN: 2147-835X Dergi sayfası: http://www.saujs.sakarya.edu.tr		
	Received 10-08-2017 Accepted 20-03-2018	Doi 10.16984/saufenbilder.333936	

Effects of different parameter estimators to error rate in discriminant analysis

Hayrinisa DEMİRCİ BİÇER*¹, Cenker BİÇER²

ABSTRACT

Discriminant analysis is defined as a statistical technique that classifies a unit whose properties are measured, into one of the known finite numbers of populations. In this classifying process, an error occurs when the unit is classified to different population from its own population. This error is called the error rate or the probability of incorrect classification. It is desirable to minimize this error. This study focuses on determining the parameter estimation method that provides the minimum error rate, when the parameters of Weibull populations are not known. Maximum likelihood (ML), moments (MOM) and least squares (LS) methods are chosen from among parameter estimation methods. By a conducted simulation study, it is investigated that the error rate how is affected by the ML, LS and MOM estimates.

Keywords: optimal classification, Weibull distribution, error rate, discriminant analysis

1. INTRODUCTION

Discriminant analysis is a statistical method that classifies a unit to the one of the known and finite number of groups (populations) based on the measurements of unit. In this study, the number of groups is chosen as two for ease of operations.

Let Π_1 and Π_2 be two different populations each having a distribution from the same parametric class and $\underline{X} = (X_1, X_2, \dots, X_p)'$ be a p -dimensional random vector. Also, let we denote the probability density function of the population Π_j ($j = 1, 2$) by $f_j(\underline{x}; \underline{\alpha}_j)$, where $\underline{\alpha}_j$ is the parameter vector of j th density.

Suppose that the measurements of the random vector \underline{X} are in the p -dimensional sample space R^p . In the problem of classification, this sample

space is divided into two regions such as B_1 and B_2 , in which $B_1 \cup B_2 = R^p$ and $B_1 \cap B_2 = \emptyset$. Hence, If the observation vector \underline{X}_0 is in the region B_j , the unit \underline{x}_0 of \underline{X}_0 is assigned to B_j .

In classifying process, an error occurs when the unit is classified to different population from its own population. That is, the observation actually belongs to Π_j but it can be classified to Π_i . For the determined regions B_1 and B_2 , the conditional probability of misclassifying of unit \underline{x}_0 from Π_j to Π_i is given by

$$P(\underline{x}_0 \text{ classify to } \Pi_i | \underline{x}_0 \in \Pi_j) = \int_{R_i} f_j(\underline{x}, \underline{\alpha}_j) d\underline{x} = p_{ij} \quad (1)$$

and the probability of misclassification of the observation \underline{x}_0 into Π_i is given by

$$P(\underline{x}_0 \text{ classify to } \Pi_i \text{ with error}) = q_j p_{ij} \quad (2)$$

* Corresponding Author

¹ Faculty of Arts and Sciences, Department of Statistics, Kırıkkale University, hdbicer@hotmail.com

² Faculty of Arts and Sciences, Department of Statistics, Kırıkkale University, cbicer@kku.edu.tr

Hence, the probability of total misclassification (TMC) for two groups is obtained as follows:

$$P(TMC) = \sum_{\substack{j=1 \\ i \neq j (j=1,2)}}^2 q_j P(\underline{x}_0 \text{ classify to } \Pi_i \text{ when } \underline{x}_0 \in \Pi_j) \quad (3)$$

[1],[2].

Under the assumption that the equal cost of misclassification for each group, the classification problem can be defined as the determination of regions B_1 and B_2 with a minimum TMC. In the literature, this classification rule is known as the optimal classification rule (OCR). When the parameter vectors $\underline{\alpha}_1$ and $\underline{\alpha}_2$ are known, the OCR is given by

$$\xi : \begin{cases} \underline{x}_0 \text{ classify to } \Pi_1, \text{ if } U = \frac{f(\underline{x}_0; \underline{\alpha}_1)}{f(\underline{x}_0; \underline{\alpha}_2)} > k \\ \underline{x}_0 \text{ classify to } \Pi_2, \text{ otherwise} \end{cases} \quad (4)$$

$$\text{where } k = \frac{q_2}{q_1}.$$

In many real-life problems, the values of parameter vectors $\underline{\alpha}_1$ and $\underline{\alpha}_2$ are unknown. However, they can be estimated by using samples from Π_1 and Π_2 with sizes of n_1 and n_2 , respectively. Let $\hat{\underline{\alpha}}_1$ and $\hat{\underline{\alpha}}_2$ be estimates of the parameter vectors $\underline{\alpha}_1$ and $\underline{\alpha}_2$, respectively. In this situation, the OCR based on the sample is given by

$$\hat{\xi} : \begin{cases} \underline{x}_0 \text{ classify to } \Pi_1, \text{ if } W = \frac{f(\underline{x}_0; \hat{\underline{\alpha}}_1)}{f(\underline{x}_0; \hat{\underline{\alpha}}_2)} > k \\ \underline{x}_0 \text{ classify to } \Pi_2, \text{ otherwise} \end{cases} \quad (5)$$

[3],[4].

2. ERROR RATES IN DISCRIMINANT ANALYSIS

In the literature, there are introduced several types of error rates associated with discriminant rules, such as optimal error rate, conditional actual error rate and expected actual error rate [2], [3], [5], [6],[7]. Let we assume that $\alpha_i(\xi)$, ($i = 1, 2$) is the probability of misclassification from Π_i and that the parameter vectors $\underline{\alpha}_1$ and $\underline{\alpha}_2$ are known. When the classification rule given by (4) is used, the rate of misclassification $\alpha_i(\xi)$ is defined as follows:

$$\alpha_1(\xi) = P(U \leq k | \underline{X} \in \Pi_1) \quad (6)$$

and

$$\alpha_2(\xi) = P(U > k | \underline{X} \in \Pi_2). \quad (7)$$

These two probabilities of misclassification are known as the optimal error rate. Since the Π_1 and Π_2 are randomly tagged, it is enough to calculate one of $\alpha_1(\xi)$ and $\alpha_2(\xi)$ to obtain the optimal error rate. Hence, for a unit \underline{X}_0 which is known to come from Π_1 , the probability of misclassification to Π_2 is given by

$$\alpha(\xi) = P(U \leq k). \quad (8)$$

The conditional actual error rate is defined (like in the optimal error rate) as follows, based on the classification rule given by (5), and it depends on parameter estimates

$$\alpha(\hat{\xi}) = P(W \leq k). \quad (9)$$

In the literature, $\alpha(\hat{\xi})$ is also known as the conditional error rate. By taking the expectation of (9), we can immediately write

$$E(\alpha(\hat{\xi})) = E(P(W \leq k)). \quad (10)$$

Equation (10) is known as expected actual error rate or unconditional error rate [2], [3], [5], [7], [8], [9].

When the parameters of populations are unknown, these error rates can be found by using the distribution of the sample discriminant function generated by the parameter estimates obtained from the samples. However, it is not always easy to obtain the distribution of the sample discriminant function. For this reason, there are many estimators for the error rates when the distribution of the sample discriminant function is unknown or cannot be obtained analytically.

In this study, the resubstitution estimator introduced by [10] is considered for the estimate of the error rate. From now on, resubstitution estimator will be indicated by $\hat{\alpha}^R$. The $\hat{\alpha}^R$ is calculated as follow. Assume that samples of sizes n_1 and n_2 from groups Π_1 and Π_2 , respectively, are taken. These $n_1 + n_2$ observations are reclassified by using the classification rule given by (5). Also, let α_{n_1} and α_{n_2} indicate the numbers

of the misclassified observations from Π_1 to Π_2 and Π_2 to Π_1 , respectively. Under these assumptions, $\hat{\alpha}^R$ is defined as follows

$$\hat{\alpha}^R = \frac{\alpha_{n_1} + \alpha_{n_2}}{n_1 + n_2}. \quad (11)$$

[8], [9],[10]

3. DISCRIMINANT ANALYSIS FOR WEIBULL POPULATIONS

In this section, some basic information about the Weibull distribution and the optimal classification rule for the Weibull distributed populations proposed by [8] and [9] are discussed.

The Weibull distribution (WE) is an important distribution family for analyzing the nonsymmetric and the positive valued data. The WE has got two parameters, a scale parameter $\beta > 0$ and a shape parameter $\theta > 0$. The probability density function (pdf) of WE with the parameters θ and β is

$$f_{WE}(x; \theta, \beta) = \theta \beta x^{\beta-1} e^{-\theta(x)^\beta}, x > 0 \quad (12)$$

and the corresponding cumulative distribution function (cdf) is

$$F_{WE}(x; \theta, \beta) = 1 - e^{-\theta(x)^\beta}, x > 0. \quad (13)$$

Also, the hazard function of WE is given by

$$h_{WE}(x; \theta, \beta) = \theta \beta^\theta x^{\theta-1} \quad (14)$$

The hazard function (or the failure rate) of this distribution is increasing when the parameter β is greater than 1, constant when β equal to 1 (the exponential case), and decreasing when β is less than 1. A detailed discussion on it has been provided by [11]. In the rest of this study, for brevity, the WE with parameters θ and β will be indicated as $WE(\theta, \beta)$. Suppose that X_1, X_2, \dots, X_n be a random sample from $WE(\theta, \beta)$. Several parameter estimators such as maximum likelihood, method of moment and least squares for the parameters of $WE(\theta, \beta)$ are given below.

The ML estimators of the parameters θ and β , say $\hat{\theta}_{ML}$ and $\hat{\beta}_{ML}$, respectively, are given by

$$\hat{\theta}_{ML} = \frac{n}{\sum_{i=1}^n X_i^{\hat{\beta}_{ML}}} \quad (15)$$

and

$$\hat{\beta}_{ML} = \left(\frac{\sum_{i=1}^n X_i^{\hat{\beta}_{ML}} \ln X_i}{\sum_{i=1}^n X_i^{\hat{\beta}_{ML}}} - \frac{1}{n} \sum_{i=1}^n \ln X_i \right)^{-1}. \quad (16)$$

The MOM estimators of the parameters θ and β , $\hat{\theta}_{MOM}$ and $\hat{\beta}_{MOM}$, respectively, are given by

$$\bar{X} - \left(\frac{1}{\hat{\theta}_{MOM}} \right)^{\frac{1}{\hat{\beta}_{MOM}}} \Gamma \left(1 + \frac{1}{\hat{\beta}_{MOM}} \right) = 0 \quad (17)$$

and

$$\sum \frac{X_i^2}{n} - \left(\frac{1}{\hat{\theta}_{MOM}} \right)^{\frac{2}{\hat{\beta}_{MOM}}} \Gamma \left(1 + \frac{2}{\hat{\beta}_{MOM}} \right) = 0 \quad (18)$$

Both ML and MOM estimators cannot be obtained analytically but estimates of the parameters can be numerically computed from nonlinear systems (15)-(16) and (17)-(18), respectively.

Finally, to obtain the LS estimators of parameters θ and β , say $\hat{\theta}_{LS}$ and $\hat{\beta}_{LS}$, respectively, first, the random sample X_1, X_2, \dots, X_n is sorted ascending order. On the other hand, By using the transformation $\eta = \theta^{1/\beta}$, the following equation can be easily written from (13).

$$\ln x_i = -\ln \eta + \frac{1}{\beta} \left(\ln \left(-\ln \left(1 - F(x_i) \right) \right) \right). \quad (19)$$

Hence, the following simple linear regression equation can be written by taking

$$Y_i = \ln x_i, \quad \beta_0 = -\ln \eta, \quad \beta_1 = \frac{1}{\beta} \quad \text{and}$$

$$X_i = \left(\ln \left(-\ln \left(1 - F(x_i) \right) \right) \right) \quad (20)$$

Considering the linear regression model given by (20), $\hat{\beta}_0$ and $\hat{\beta}_1$ can be easily estimated by using

$$\hat{\beta}_1 = \frac{n \sum_{i=1}^n X_i Y_i - \sum_{i=1}^n X_i \sum_{i=1}^n Y_i}{n \sum_{i=1}^n X_i^2 - \left(\sum_{i=1}^n X_i \right)^2} \quad (21)$$

and

$$\hat{\beta}_0 = \bar{y}_i - \hat{\beta}_1 \sum_{i=1}^n \frac{x_i}{n} \quad (22)$$

Therefore, LS estimates of the parameters are obtained as $\hat{\beta}_{LS} = \frac{1}{\hat{\beta}_1}$, $\hat{\eta} = e^{-\hat{\beta}_0}$ and $\hat{\theta}_{LS} = \hat{\eta}^{\hat{\beta}_{LS}}$

Where $F(x_i)$ is unknown but it can be estimated with formula $\frac{i}{n+1}$ or $\frac{i-0.3}{n+0.4}$, see [12].

Now, we consider the classification problem for the Weibull distributed populations.

Suppose that $X_{11}, X_{12}, \dots, X_{1n_1}$ and $X_{21}, X_{22}, \dots, X_{2n_2}$ are two independent random samples from Π_1 and Π_2 , respectively, in which Π_1 and Π_2 follow $WE(\theta_i, \beta_i)$ $i=1,2$. Then, under the assumptions equal classification cost and equal prior probability, the OCR is given by

$$R_{WE}(s): \begin{cases} \underline{x}_0 \text{ classify into } \Pi_1, \text{ if } x_0^{\hat{\beta}_1 - \hat{\beta}_2} e^{-[\hat{\theta}_1 x_0^{\hat{\beta}_1} - \hat{\theta}_2 x_0^{\hat{\beta}_2}]} > \frac{\hat{\beta}_2 \hat{\theta}_2}{\hat{\beta}_1 \hat{\theta}_1} \\ \underline{x}_0 \text{ classify into } \Pi_2, \text{ otherwise} \end{cases} \quad (23)$$

where $\hat{\beta}_1, \hat{\beta}_2, \hat{\theta}_1$ and $\hat{\theta}_2$ are estimates of the parameters $\beta_1, \beta_2, \theta_1$ and θ_2 , respectively. See [8] and [9] for further information on this OCR and its derivation.

In literature, unknown values of the parameters are generally estimated by using the maximum likelihood method, because of the fact that they are easy to obtain and to calculate. In this study, the classification problem for WE populations is considered in case of using the ML, the LS and the MOM estimators instead of unknown values of the parameters and it is investigated that the error rate how is affected by these estimates.

When the parameter values are unknown, the OCR is given by two cases ($\beta_1 = \beta_2 = \beta$) and ($\theta_1 = \theta_2 = \theta$).

Case 1: The OCR $R_{WE}(s)$ for the case of $\beta_1 = \beta_2 = \beta$ is

$$R_{WE}(s): \begin{cases} \underline{x}_0 \text{ classify into } \Pi_1, \text{ if } \bar{x}_1 < \bar{x}_2 \text{ and } \underline{x}_0 < c_1 \\ \underline{x}_0 \text{ classify into } \Pi_2, \text{ if } \bar{x}_1 < \bar{x}_2 \text{ and } \underline{x}_0 \geq c_1 \end{cases} \quad (24)$$

or

$$R_{WE}(s): \begin{cases} \underline{x}_0 \text{ classify into } \Pi_1, \text{ if } \bar{x}_1 \geq \bar{x}_2 \text{ and } \underline{x}_0 \geq c_1 \\ \underline{x}_0 \text{ classify into } \Pi_2, \text{ if } \bar{x}_1 \geq \bar{x}_2 \text{ and } \underline{x}_0 < c_1 \end{cases} \quad (25)$$

Where $c_1 = \left[\frac{\log \hat{\theta}_2 - \log \hat{\theta}_1}{\hat{\theta}_2 - \hat{\theta}_1} \right]^{1/\hat{\beta}}$ and

$$\hat{\beta} = (\hat{\beta}_1 + \hat{\beta}_2) / 2.$$

Case 2: The OCR $R_{WE}(s)$ for the case of $\theta_1 = \theta_2 = \theta$ is

$$R_{WE}(s): \begin{cases} \underline{x}_0 \text{ classify into } \Pi_1, \text{ if } \bar{x}_1 < \bar{x}_2 \text{ and } \underline{x}_0 < c_2 \\ \underline{x}_0 \text{ classify into } \Pi_2, \text{ if } \bar{x}_1 < \bar{x}_2 \text{ and } \underline{x}_0 \geq c_2 \end{cases} \quad (26)$$

or

$$R_{WE}(s): \begin{cases} \underline{x}_0 \text{ classify into } \Pi_1, \text{ if } \bar{x}_1 \geq \bar{x}_2 \text{ and } \underline{x}_0 \geq c_2 \\ \underline{x}_0 \text{ classify into } \Pi_2, \text{ if } \bar{x}_1 \geq \bar{x}_2 \text{ and } \underline{x}_0 < c_2 \end{cases} \quad (27)$$

Where $c_2 = (\log \hat{\beta}_2 - \log \hat{\beta}_1)$ and $\hat{\theta} = (\hat{\theta}_1 + \hat{\theta}_2) / 2$, see [9].

4. SIMULATION STUDY

In this section, some simulation studies are performed to comparatively present the error rate performance of OCR discussed in the previous section using the estimates of unknown parameters obtained by ML, LS and MOM. Two cases $\beta_1 = \beta_2 = \beta$ and $\theta_1 = \theta_2 = \theta$ given in the previous section are considered in the simulation studies. In the case 1, the parameter β was chosen as 0.5,1,3.6. When the estimates ML, LS and MOM used instead of unknown parameters, the error rates calculated for $n_1 = n_2 = 20,40,60$ and 100 and for $\theta_1 = 0.5,2$ and 4 and at different values of θ_2 . Simulated results based on 1000 Monte-Carlo simulations are tabulated in Table 1-3.

Table 1. Error rates for Case 1, $\beta = 0.5$

θ_1	θ_2	Method	n=20	n=40	n=60	n=100	θ_1	θ_2	Method	n=20	n=40	n=60	n=100	
0.5	1	ML	0.36320	0.36946	0.37047	0.37245	2	4	ML	0.36305	0.36915	0.37511	0.37198	
		LS	0.36500	0.37175	0.37198	0.37349			LS	0.36483	0.37084	0.37566	0.37279	
		MOM	0.42080	0.42529	0.42381	0.42377			MOM	0.38313	0.38455	0.38493	0.38011	
	2	ML	0.26035	0.25818	0.26142	0.26311		6	ML	0.30103	0.30259	0.30658	0.30715	
		LS	0.25998	0.25760	0.26128	0.26331			LS	0.30040	0.30321	0.30655	0.30694	
		MOM	0.35333	0.35549	0.36044	0.34680			MOM	0.34558	0.35696	0.36025	0.37241	
	4	ML	0.17035	0.17334	0.17376	0.17391		8	ML	0.25938	0.26268	0.26378	0.26411	
		LS	0.16895	0.17298	0.17358	0.17358			LS	0.25870	0.26218	0.26365	0.26390	
		MOM	0.29765	0.30720	0.30095	0.29920			MOM	0.29653	0.30425	0.31174	0.31169	
	8	ML	0.10683	0.10730	0.10981	0.11085		10	ML	0.22853	0.23454	0.23093	0.23106	
		LS	0.10720	0.10743	0.11033	0.11068			LS	0.22760	0.23404	0.23062	0.23112	
		MOM	0.28473	0.31843	0.30274	0.31232			MOM	0.24280	0.24449	0.23662	0.23260	
	10	ML	0.08933	0.09465	0.09358	0.09384		20	ML	0.14803	0.14704	0.15143	0.15050	
		LS	0.09070	0.09499	0.09374	0.09416			LS	0.14840	0.14709	0.15113	0.15064	
		MOM	0.25093	0.25784	0.24228	0.25135			MOM	0.14918	0.14814	0.15166	0.15087	
	12	ML	0.08023	0.08169	0.08122	0.08157		4	6	ML	0.40125	0.41518	0.41754	0.42201
		LS	0.08185	0.08229	0.08141	0.08196			LS	0.40590	0.41979	0.42076	0.42386	
		MOM	0.22253	0.23663	0.22443	0.22755			MOM	0.43178	0.44839	0.45113	0.45667	
	14	ML	0.06912	0.07256	0.07204	0.07157		8	ML	0.36078	0.37015	0.37089	0.37484	
		LS	0.07100	0.07310	0.07262	0.07192			LS	0.36493	0.37300	0.37190	0.37501	
		MOM	0.21878	0.23491	0.23272	0.22964			MOM	0.39268	0.40130	0.39933	0.40386	
	16	ML	0.06555	0.06529	0.06703	0.06699		10	ML	0.32708	0.32991	0.33304	0.33668	
		LS	0.06740	0.06630	0.06759	0.06734			LS	0.32765	0.33044	0.33357	0.33736	
		MOM	0.21845	0.23196	0.23379	0.23567			MOM	0.34678	0.34266	0.34213	0.34368	
20	ML	0.05430	0.05429	0.05360	0.05571	20	ML	0.22553	0.23076	0.23112	0.23212			
	LS	0.05695	0.05537	0.05463	0.05649		LS	0.22423	0.23061	0.23058	0.23190			
	MOM	0.22515	0.20900	0.22004	0.20418		MOM	0.23830	0.23734	0.23740	0.23713			

Table 2. Error rates for Case 1, $\beta = 1$

θ_1	θ_2	Method	n=20	n=40	n=60	n=100	θ_1	θ_2	Method	n=20	n=40	n=60	n=100	
0.5	1	ML	0.36005	0.36778	0.37417	0.37389	2	4	ML	0.36368	0.37061	0.37329	0.37384	
		LS	0.36325	0.37108	0.37557	0.37490			LS	0.36680	0.37130	0.37368	0.37469	
		MOM	0.36613	0.37186	0.37622	0.37557			MOM	0.36828	0.37506	0.37483	0.37542	
	2	ML	0.25610	0.26056	0.26231	0.26279		6	ML	0.30013	0.30330	0.30597	0.30515	
		LS	0.25685	0.26075	0.26241	0.26312			LS	0.30070	0.30419	0.30571	0.30495	
		MOM	0.25753	0.26185	0.26298	0.26310			MOM	0.30268	0.30519	0.30699	0.30547	
	4	ML	0.17598	0.17390	0.17540	0.17350		8	ML	0.25700	0.26073	0.26174	0.26410	
		LS	0.17515	0.17388	0.17525	0.17347			LS	0.25693	0.26010	0.26160	0.26412	
		MOM	0.17598	0.17388	0.17568	0.17355			MOM	0.25853	0.26105	0.26197	0.26398	
	8	ML	0.10955	0.11035	0.10886	0.10974		10	ML	0.22820	0.23034	0.23266	0.23206	
		LS	0.10963	0.11104	0.10903	0.11018			LS	0.22855	0.22971	0.23232	0.23179	
		MOM	0.10913	0.11040	0.10866	0.10982			MOM	0.22933	0.23034	0.23255	0.23208	
	10	ML	0.09225	0.09505	0.09379	0.09405		20	ML	0.14900	0.15179	0.15013	0.15078	
		LS	0.09368	0.09560	0.09435	0.09426			LS	0.14890	0.15188	0.15006	0.15069	
		MOM	0.09230	0.09500	0.09392	0.09417			MOM	0.19008	0.18458	0.17601	0.16585	
	12	ML	0.07840	0.08123	0.08131	0.08250		4	6	ML	0.40180	0.41466	0.42130	0.42241
		LS	0.07988	0.08171	0.08165	0.08322			LS	0.40753	0.41805	0.42492	0.42463	
		MOM	0.07915	0.08140	0.08134	0.08259			MOM	0.40610	0.41989	0.42572	0.42562	
	14	ML	0.06635	0.07264	0.07183	0.07349		8	ML	0.36188	0.36844	0.37336	0.37319	
		LS	0.06962	0.07414	0.07253	0.07380			LS	0.36455	0.36984	0.37485	0.37383	
		MOM	0.07190	0.07345	0.07233	0.07361			MOM	0.36488	0.37097	0.37531	0.37504	
	16	ML	0.06130	0.06594	0.06590	0.06602		10	ML	0.33110	0.33101	0.33573	0.33575	
		LS	0.06300	0.06736	0.06656	0.06631			LS	0.33180	0.33134	0.33597	0.33574	
		MOM	0.07020	0.07055	0.06697	0.06699			MOM	0.33450	0.33240	0.33782	0.33639	
20	ML	0.05155	0.05381	0.05645	0.05589	20	ML	0.22815	0.22843	0.23363	0.23316			
	LS	0.05395	0.05536	0.05726	0.05631		LS	0.22740	0.22830	0.23366	0.23301			
	MOM	0.09735	0.09934	0.09378	0.07454		MOM	0.25820	0.25749	0.25083	0.24563			

Table 3. Error rates for Case 1, $\beta = 3.6$

θ_1	θ_2	Method	n=20	n=40	n=60	n=100	θ_1	θ_2	Method	n=20	n=40	n=60	n=100	
0.5	1	ML	0.36265	0.36725	0.36924	0.37327	2	4	ML	0.36025	0.37093	0.36977	0.37434	
		LS	0.36460	0.36830	0.37106	0.37396			LS	0.36670	0.37279	0.37086	0.37489	
		MOM	0.36285	0.36664	0.36947	0.37263			MOM	0.36055	0.37011	0.36914	0.37421	
	2	ML	0.25948	0.26269	0.26338	0.26244		6	ML	0.29755	0.30448	0.30619	0.30640	
		LS	0.25773	0.26219	0.26316	0.26248			LS	0.29670	0.30470	0.30676	0.30638	
		MOM	0.25898	0.26249	0.26320	0.26245			MOM	0.29723	0.30449	0.30599	0.30624	
	4	ML	0.17435	0.17114	0.17331	0.17464		8	ML	0.25760	0.26056	0.26177	0.26046	
		LS	0.17390	0.17093	0.17316	0.17470			LS	0.25745	0.26099	0.26138	0.26066	
		MOM	0.17428	0.17090	0.17334	0.17467			MOM	0.25715	0.26061	0.26148	0.26045	
	8	ML	0.10598	0.10831	0.10924	0.10965		10	ML	0.23245	0.23229	0.22940	0.23156	
		LS	0.10658	0.10886	0.10928	0.10963			LS	0.23120	0.23168	0.22878	0.23183	
		MOM	0.10573	0.10845	0.10922	0.10963			MOM	0.23170	0.23220	0.22934	0.23162	
	10	ML	0.09033	0.09209	0.09384	0.09349		20	ML	0.14783	0.14993	0.15041	0.15033	
		LS	0.09118	0.09376	0.09422	0.09381			LS	0.14780	0.14964	0.15027	0.15027	
		MOM	0.09060	0.09234	0.09392	0.09355			MOM	0.14813	0.14973	0.15030	0.15031	
	12	ML	0.07740	0.08074	0.08270	0.08210		4	6	ML	0.40007	0.41291	0.41840	0.42318
		LS	0.07918	0.08119	0.08308	0.08218			LS	0.40540	0.41670	0.42074	0.42525	
		MOM	0.07798	0.08080	0.08284	0.08218			MOM	0.39850	0.41239	0.41765	0.42278	
	14	ML	0.06850	0.07198	0.07258	0.07365		8	ML	0.35970	0.36914	0.37276	0.37305	
		LS	0.07000	0.07185	0.07334	0.07416			LS	0.36328	0.37018	0.37411	0.37421	
		MOM	0.06897	0.07153	0.07265	0.07363			MOM	0.35933	0.36881	0.37265	0.37313	
	16	ML	0.06472	0.06595	0.06492	0.06576		10	ML	0.32913	0.33314	0.33415	0.33644	
		LS	0.06637	0.06676	0.06569	0.06643			LS	0.33013	0.33355	0.33423	0.33664	
		MOM	0.06477	0.06608	0.06501	0.06595			MOM	0.32923	0.33256	0.33428	0.33661	
	20	ML	0.05217	0.05373	0.05541	0.05561		20	ML	0.22788	0.22754	0.23349	0.23208	
		LS	0.05460	0.05484	0.05619	0.05633			LS	0.22755	0.22726	0.23326	0.23180	
		MOM	0.05292	0.05409	0.05539	0.05575			MOM	0.22773	0.22750	0.23345	0.23204	

In the case of 2, as similar to case of 1, $\theta_1 = \theta_2 = \theta$ was chosen as 0.5, 1 and 3.6. The error rates calculated for $n_1 = n_2 = 20, 40, 60$ and 100 and for

$\beta_1 = 0.5, 2$ and 4 and at different values of β_2 . Simulated results based on 1000 Monte-Carlo simulation are compatible with Table 4-6.

Table 4: Error rates for Case 2, $\theta = 0.5$

β_1	β_2	Method	n=20	n=40	n=60	n=100	β_1	β_2	Method	n=20	n=40	n=60	n=100	
.5	1	ML	0.31513	0.31666	0.32199	0.32292	2	4	ML	0.31083	0.32019	0.31993	0.32190	
		LS	0.31675	0.31841	0.32364	0.32337			LS	0.31463	0.32234	0.32118	0.32311	
		MOM	0.39233	0.39506	0.39439	0.38608			MOM	0.31093	0.32013	0.31922	0.32190	
	2	ML	0.18550	0.19228	0.19281	0.19339		6	ML	0.23550	0.23848	0.23616	0.24133	
		LS	0.18890	0.19359	0.19407	0.19438			LS	0.23828	0.24019	0.23733	0.24267	
		MOM	0.29990	0.30461	0.30807	0.31167			MOM	0.23555	0.23873	0.23630	0.24176	
	4	ML	0.10715	0.10979	0.11151	0.11100		8	ML	0.18575	0.19384	0.19351	0.19391	
		LS	0.10813	0.11171	0.11222	0.11188			LS	0.18883	0.19531	0.19485	0.19443	
		MOM	0.23680	0.25583	0.25870	0.26139			MOM	0.18708	0.19444	0.19407	0.19414	
	8	ML	0.05987	0.06340	0.06282	0.06326		10	ML	0.15595	0.15919	0.16153	0.16345	
		LS	0.06070	0.06451	0.06333	0.06369			LS	0.15920	0.16125	0.16229	0.16413	
		MOM	0.21680	0.23880	0.23730	0.22728			MOM	0.15785	0.16028	0.16175	0.16364	
	10	ML	0.04842	0.05128	0.05292	0.05245		20	ML	0.08695	0.09173	0.09400	0.09369	
		LS	0.04940	0.05174	0.05353	0.05295			LS	0.08905	0.09328	0.09457	0.09441	
		MOM	0.20930	0.21186	0.22623	0.21329			MOM	0.08890	0.09285	0.09445	0.09411	
	12	ML	0.04387	0.04274	0.04548	0.04560		4	6	ML	0.37785	0.38453	0.38832	0.38838
		LS	0.04405	0.04293	0.04565	0.04599			LS	0.38130	0.38810	0.38996	0.38929	
		MOM	0.20003	0.21520	0.22078	0.21472			MOM	0.37825	0.38534	0.38817	0.38851	
	14	ML	0.03997	0.04007	0.03954	0.03964		8	ML	0.31313	0.32059	0.32139	0.32177	
		LS	0.03980	0.04021	0.03986	0.04000			LS	0.31518	0.32129	0.32289	0.32197	
		MOM	0.21265	0.20933	0.21515	0.22244			MOM	0.31268	0.32045	0.32204	0.32210	
	16	ML	0.03160	0.03418	0.03475	0.03532		10	ML	0.26450	0.26965	0.27476	0.27513	
		LS	0.03172	0.03469	0.03498	0.03555			LS	0.26703	0.27171	0.27563	0.27616	
		MOM	0.19830	0.21331	0.20146	0.21852			MOM	0.26528	0.27066	0.27480	0.27551	
	20	ML	0.02762	0.02761	0.02878	0.02896		20	ML	0.15583	0.16078	0.16113	0.16313	
		LS	0.02755	0.02776	0.02866	0.02901			LS	0.15880	0.16226	0.16247	0.16364	
		MOM	0.19865	0.21020	0.19699	0.20729			MOM	0.15778	0.16199	0.16215	0.16336	

Table 5: Error rates for Case 2, $\theta = 1$

β_1	β_2	Method	n=20	n=40	n=60	n=100	β_1	β_2	Method	n=20	n=40	n=60	n=100	
0.5	1	ML	0.33605	0.33758	0.33938	0.34378	2	4	ML	0.33005	0.34254	0.34242	0.34378	
		LS	0.33670	0.33785	0.34132	0.34485			LS	0.33413	0.34441	0.34311	0.34439	
		MOM	0.34603	0.34434	0.34256	0.34618			MOM	0.32970	0.34265	0.34224	0.34387	
	2	ML	0.21085	0.21756	0.21621	0.21768		6	ML	0.25795	0.26440	0.26342	0.26367	
		LS	0.21423	0.21965	0.21770	0.21867			LS	0.26308	0.26628	0.26486	0.26422	
		MOM	0.22018	0.22448	0.22228	0.22176			MOM	0.25970	0.26508	0.26356	0.26354	
	4	ML	0.12478	0.12813	0.12917	0.12865		8	ML	0.20830	0.21391	0.21772	0.21792	
		LS	0.12815	0.13086	0.13028	0.12934			LS	0.21210	0.21608	0.21943	0.21869	
		MOM	0.13365	0.13524	0.13334	0.13231			MOM	0.21050	0.21485	0.21791	0.21794	
	8	ML	0.06920	0.07358	0.07423	0.07466		10	ML	0.17713	0.18346	0.18536	0.18555	
		LS	0.07060	0.07473	0.07513	0.07520			LS	0.18158	0.18645	0.18686	0.18670	
		MOM	0.07818	0.08306	0.08066	0.07829			MOM	0.18045	0.18485	0.18620	0.18615	
	10	ML	0.06072	0.06109	0.06316	0.06193		20	ML	0.10388	0.10846	0.10940	0.11031	
		LS	0.06260	0.06173	0.06377	0.06239			LS	0.10610	0.10990	0.11097	0.11132	
		MOM	0.07295	0.06740	0.06926	0.06672			MOM	0.10563	0.10950	0.11049	0.11084	
	12	ML	0.05105	0.05184	0.05362	0.05342		4	6	ML	0.38528	0.39671	0.40001	0.40371
		LS	0.05222	0.05307	0.05447	0.05378			LS	0.39148	0.39999	0.40104	0.40494	
		MOM	0.06105	0.06115	0.06015	0.05690			MOM	0.38645	0.39766	0.40016	0.40366	
	14	ML	0.04582	0.04671	0.04800	0.04750		8	ML	0.33335	0.34303	0.34218	0.34409	
		LS	0.04607	0.04728	0.04817	0.04799			LS	0.33610	0.34573	0.34337	0.34387	
		MOM	0.05945	0.05508	0.05232	0.05389			MOM	0.33463	0.34311	0.34219	0.34403	
	16	ML	0.03905	0.04020	0.04131	0.04211		10	ML	0.29163	0.29715	0.29779	0.29746	
		LS	0.03917	0.04074	0.04152	0.04250			LS	0.29583	0.29913	0.29910	0.29868	
		MOM	0.05130	0.04994	0.04881	0.04691			MOM	0.29420	0.29790	0.29881	0.29800	
20	ML	0.03315	0.03381	0.03487	0.03485	20	ML	0.17750	0.18320	0.18428	0.18764			
	LS	0.03320	0.03451	0.03526	0.03509		LS	0.18133	0.18593	0.18573	0.18846			
	MOM	0.04737	0.04594	0.04369	0.04018		MOM	0.18045	0.18540	0.18494	0.18818			

Table 6: Error rates for Case 2, $\theta = 3.6$

β_1	β_2	Method	n=20	n=40	n=60	n=100	β_1	β_2	Method	n=20	n=40	n=60	n=100	
0.5	1	ML	0.28888	0.29654	0.29532	0.29628	2	4	ML	0.28943	0.29419	0.29736	0.29617	
		LS	0.29298	0.30040	0.29825	0.29773			LS	0.29448	0.29774	0.30001	0.29773	
		MOM	0.29770	0.30234	0.29828	0.30007			MOM	0.29115	0.29469	0.29739	0.29653	
	2	ML	0.14678	0.15398	0.15441	0.15445		6	ML	0.20075	0.20168	0.20514	0.20497	
		LS	0.15083	0.15666	0.15619	0.15553			LS	0.20538	0.20439	0.20690	0.20635	
		MOM	0.15388	0.15676	0.15880	0.15661			MOM	0.20213	0.20271	0.20558	0.20541	
	4	ML	0.06970	0.07290	0.07157	0.07333		8	ML	0.15020	0.15273	0.15353	0.15521	
		LS	0.07060	0.07409	0.07232	0.07370			LS	0.15403	0.15541	0.15494	0.15612	
		MOM	0.08065	0.07700	0.07259	0.07403			MOM	0.15180	0.15320	0.15428	0.15534	
	8	ML	0.03302	0.03344	0.03411	0.03394		10	ML	0.11775	0.12011	0.12128	0.12082	
		LS	0.03320	0.03354	0.03446	0.03428			LS	0.12093	0.12244	0.12265	0.12159	
		MOM	0.03832	0.03730	0.03558	0.03559			MOM	0.11935	0.12163	0.12192	0.12121	
	10	ML	0.02590	0.02520	0.02585	0.02687		20	ML	0.05387	0.05690	0.05731	0.05698	
		LS	0.02550	0.02536	0.02598	0.02696			LS	0.05440	0.05735	0.05798	0.05757	
		MOM	0.03382	0.02917	0.02871	0.02676			MOM	0.05402	0.05726	0.05785	0.05735	
	12	ML	0.02075	0.02165	0.02196	0.02253		4	6	ML	0.36143	0.37055	0.37341	0.37540
		LS	0.02090	0.02140	0.02213	0.02269			LS	0.36865	0.37433	0.37653	0.37764	
		MOM	0.03152	0.02416	0.02437	0.02409			MOM	0.36328	0.37141	0.37488	0.37548	
	14	ML	0.01700	0.01824	0.01928	0.01996		8	ML	0.28970	0.29195	0.29794	0.29815	
		LS	0.01715	0.01837	0.01950	0.02000			LS	0.29498	0.29558	0.30023	0.29991	
		MOM	0.02615	0.02145	0.02233	0.01992			MOM	0.29280	0.29378	0.29913	0.29892	
	16	ML	0.01520	0.01655	0.01652	0.01643		10	ML	0.24300	0.24120	0.24231	0.24542	
		LS	0.01543	0.01679	0.01653	0.01640			LS	0.24760	0.24421	0.24452	0.24658	
		MOM	0.02425	0.01892	0.01952	0.01632			MOM	0.24565	0.24286	0.24346	0.24627	
20	ML	0.01225	0.01285	0.01309	0.01341	20	ML	0.11785	0.11869	0.12319	0.12211			
	LS	0.01233	0.01284	0.01298	0.01335		LS	0.12038	0.12074	0.12485	0.12281			
	MOM	0.01915	0.01581	0.01538	0.01478		MOM	0.11965	0.12014	0.12455	0.12266			

According to simulation results given by Tables 1-6, for both cases, we can say that the classification performance of the method increases when the unknown parameter values draw away from each other. Namely, the error rate decreases. In another saying, if one of the populations is overlapping the other, the error rate increases, otherwise, the error rate decreases. This is an expected case because the shapes of the pdfs of the overlapping

distributions are almost the same. This situation can be seen in Figures 1-2.

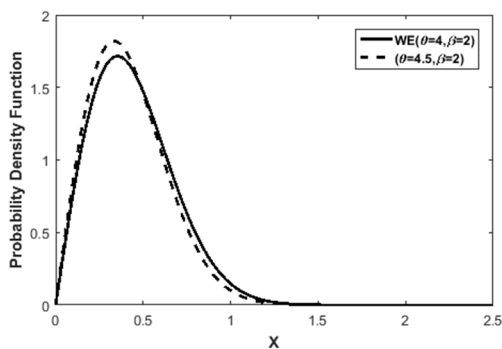


Figure 1. Overlapping distributions

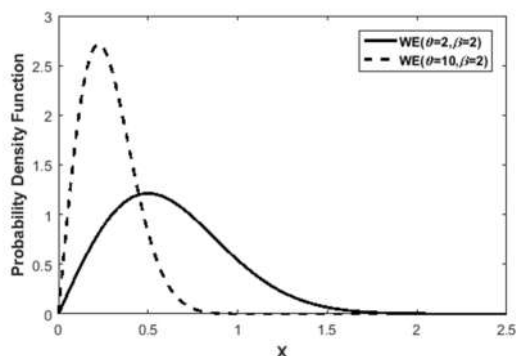


Figure 2. Non-overlapping distributions

However, even if the population parameters are close to each other, it can be said that the OCR works quite well. Furthermore, it can be seen from Tables 1-6 that the ML estimators provide the best classification performance in all cases. Besides, it is concluded from Table 1-6 that the LS estimators provide nearly same classification performance with the ML estimators. Since the LS estimators can be easily calculated for the Weibull parameters, their use instead of the unknown parameter values in the classification process may provide an advantage for researchers.

5. CONCLUSION

In this study, the problem of discriminant analysis for Weibull distributed populations is investigated considering the optimal classifier proposed by [8] and [9]. Also, when the values of the population parameters are unknown, a series of simulation studies are carried out with the aim to determine the parameter estimator which makes the error rate to be minimum. In accordance with this purpose, we employ the three estimators frequently used in the literature such as ML, LS, and MOM. In the numerical study, two basic cases are considered, such as $\beta_1 = \beta_2 = \beta$ and $\theta_1 = \theta_2 = \theta$. Each case is evaluated at different values of the parameters and at different sample sizes. The results of the numerical studies show that the OCR works well in all cases, even in the overlapping distributions.

The findings show that the minimum error rate for the OCR is obtained when the ML estimates are used instead of the unknown parameter values. Therefore, based on the simulation study results, to obtain the minimum error rate in the discriminant analysis between Weibull distributed populations, It can be said that the use of ML estimates is appropriate instead of the unknown values of the distribution parameters.

REFERENCES

- [1] P. A. Lachenburch, "Discriminant Analysis", *New York, Hafner*, 1975.
- [2] G. A. F. Seber, "Multivariate Observations", *New York, John Wiley & Sons. Inc*, 1984.
- [3] T. W. Anderson, "Introduction to Multivariate Statistical Analysis", *Wiley, New York*, 1984.
- [4] B. L. Welch, "Note on Discriminant Functions", *Biometrika*, 31, 218–220, 1939.
- [5] P. A. Lachenburch and R. Mickey, "Estimation of Error Rates in Discriminant Analysis", *Technometrics*, 10, 1–11, 1968.
- [6] S. M. Snapin, "An Evaluation of Smooted Error Rate Estimators in Discriminant Analysis", *Institute of Statistics Miemeo Series*, Chapel Hill, 1983.
- [7] M. Hills, "Allocation Rules and Their Error Rates", *J. Roy. Stat. Soc. B*, 28, 1-31, 1966.
- [8] H. D. Biçer, "Discriminant analysis in censored data: Weibull distribution case", *Doctoral dissertation, University of Ankara*, 2011.
- [9] H. D. Biçer, C. Atakan and C. Biçer, "İki parametrelili weibull dağılımına sahip kitlelerde diskriminant analizi", *NWSA Physical sciences*, 6(4), 124-133, 2011.
- [10] C. A. B. Smith, "Some Examples of Discrimination", *Annals of Eugenics*, 18, 272-282, 1978.
- [11] N. L. Johnson, S. Kotz and N. Balakrishnan, "Continuous univariate distributions", *New York, Wiley*, 1995.
- [12] M. Tiryakioğlu and D. Hudak, "Unbiased estimates of the Weibull parameters by the linear regression method", *Journal of Materials Science*, 43, 1914-1919, 2008.

	SAKARYA ÜNİVERSİTESİ FEN BİLİMLERİ ENSTİTÜSÜ DERGİSİ SAKARYA UNIVERSITY JOURNAL OF SCIENCE		
	e-ISSN: 2147-835X Dergi sayfası: http://dergipark.gov.tr/saufenbilder		
	Received 28-10-2017 Accepted 22-03-2018	Doi 10.16984/saufenbilder.347576	

Length-weight relationship and condition of *Arnoglossus kessleri* Schmidt, 1915 in Iskenderun Bay (Eastern Mediterranean, Turkey)

Sibel Alagöz Ergüden^{*1}, Ayhan Altun², Deniz Ergüden³

ABSTRACT

Length weight relationship (LWR) studies have an important role in estimating population biomass, determining growth rate and stock status of fishes. In this study a total of 133 scaldback, *Arnoglossus kessleri* Schmidt, 1915 were caught in Iskenderun Bay between September 2014 and May 2015 using a commercial bottom trawler. As a result, the estimates for b parameter of the LWR ranged between and 2.97, 2.68 and 2.74 for males, females and both sexes, respectively. Fulton's condition (KF) factor values also revealed significant variations ($p < 0.01$) for female (1.089) and male (1.100) specimens of *A. kessleri*. The 11.9 cm long male individual found in this study was the longest individual recorded for the Mediterranean Sea. No information currently exists on the length weight relationship of *A. kessleri* in the Mediterranean coast of Turkey. Therefore, this paper is an important contribution to the science and fisheries management applications for this species.

Keywords: *Arnoglossus kessleri*, Length-weight parameters, condition factor, Iskenderun Bay.

1. INTRODUCTION

The scaldback, *Arnoglossus kessleri* schmidt, 1915, is endemic to the mediterranean and black sea and distributed throughout the east mediterranean sea including aegean sea, the sea of Marmara and the Black Sea [1, 2], including the crimean peninsula and the sea of azov [3, 4].

Arnoglossus kessleri is a benthic species that can be found at depths ranging from 10 to 200 m on the upper part of the continental shelf. The species mainly feeds on small fishes and invertebrates [3]. Although *A. kessleri* is not commercially targeted

species, it is a bycatch product in fisheries and is usually discarded. Due to the lack of studies relating the species the conservation status of it has been declared as Data Deficient (DD) globally [5] and in the Mediterranean [6], and there have been no specific conservation measure in action up to date.

Length-weight relationship is an important aspect in fish and fisheries biology and very useful tool for the assessment of fish population dynamics and the management of fisheries [7]. Therefore; the relationship is often used to convert growth in length equations for prediction of weight-at-age and use in stock assessment models [8], to estimate

* Corresponding Author

¹ Çukurova University, Vocational School of İmamoğlu, İmamoğlu/Adana, Turkey - alagozs@cu.edu.tr

² İskenderun Technical University, Faculty of Marine Sciences and Technology, İskenderun/Hatay, Turkey - ayhan.altun@iste.edu.tr

³ İskenderun Technical University, Faculty of Marine Sciences and Technology, İskenderun/Hatay, Turkey - deniz.erguden@iste.edu.tr

biomass from the length-frequency distribution [9, 10] and to calculate the condition of the fish [11].

A number of studies on the length weight relationships of various populations of *A. kessleri* in Turkish Seas were reported previously [12-17]. Nevertheless, the sex ratio and the condition of the fish have not been included in previous studies.

No information currently exists on the length weight relationship of *A. kessleri* in the region covering eastern Mediterranean coast of Turkey. This study focused on the length and weight parameters of *A. kessleri* population from Iskenderun Bay in order to compare the population characteristics of this species with previous reports. Additionally, the condition and the sex ratio of the population have also been determined in order to contribute as much as possible for the growing data file of the species. Therefore, this paper is an important contribution to the science and fisheries management applications relating to *A. kessleri*.

2. MATERIALS AND METHODS

A total of 133 specimens of *A. kessleri* were collected via a commercial trawler at depths ranging from 30 m to 65 m in Iskenderun Bay (Figure 1) between September 2014 and May 2015. Length, weight and sex-ratio distributions were constructed separately. Total length (TL, cm) of specimens were measured to the nearest 0.1 cm. Total weight (W, g) was measured with a digital balance to an accuracy of 0.01 g. Sex was determined by macroscopic analysis of the gonads.

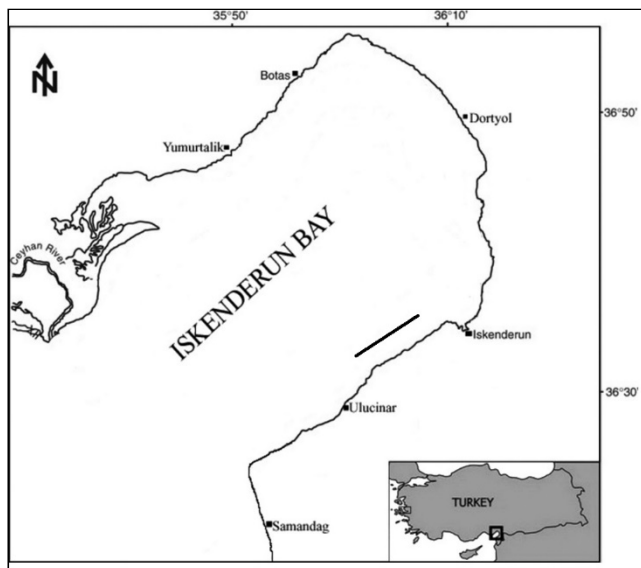


Figure 1. Sampling area of *Arnoglossus kessleri*

The growth relationship, isometric or allometric, between total length and total weight was calculated as $W = a \times TL^b$ using a plotted power function, where a is the power function coefficient (the regression intercept) and b is the exponent (the regression slope) [18]. The relationships were estimated by linear regression analyses based on natural logarithms: $\ln(W) = \ln(a) + b \ln(TL)$. The parameters a and b were calculated using least-squares regression as the coefficient of determination (r^2). An estimate of b equal to 3 is an indication of an isometric growth whereas a greater or lesser value is an indication of either positive or negative allometric growth, respectively.

Prior to the analyses, ln-ln plots of length and weight values were performed for visual inspection of outliers in accordance with Froese [19]. To verify if the results were significantly different from 3 the b values for each of male, female and total of the specimens were tested using a t-test at the 0.001 significance level.

Fulton's condition factor (KF) [20] was calculated using the equation: $KF = (W/L^3) \times 100$. Where: W = Total body weight (g), L = Total length (cm). The scaling factor of 100 was used to bring the KF close to unit.

3. RESULTS

Investigation of 133 specimens revealed that *A. kessleri* population inhabiting the waters of Iskenderun Bay was composed of 51.12% ($n=68$) female and 48.8% ($n=65$) male. Female to male sex ratio of the population was found as 1:0.95. Total length values of overall, female and male specimens ranged from 7.0-11.9 cm, 7.7-11.8 cm and 7.7-11.9 cm, respectively. Weight values for overall, female and male specimens were in the order of 5.32-19.4 g, 3.65-19.7 g and 3.65-19.7 g.

The growth was negative allometric for Iskenderun Bay population of *A. kessleri* and the b values ranged from 2.687 to 2.791 for all three groups: female, male and both sexes (Table 1). All regression values were found to be highly significant ($P < 0.001$) and the values of coefficient of determination (r^2) were greater than 0.95 for all groups. There was no significant difference between length of males and females. Males were slightly larger than females. Length-weight relationships for females, males and both sexes

were calculated as $W=0.00224TL^{2.687}$, ($R^2= 0.953$) (Figure 2), $W= 0.00177TL^{2.791}$ ($R^2= 0.960$) (Figure 3) and $W=0.00196TL^{2.745}$ ($R^2= 0.957$) (Figure 4).

Fulton’s condition (K) factor values also showed significant variations ($P<0.01$). Females were the best performers with a K factor of 1.089 and the values for males and both sexes were observed as 1.100 and 1.095, respectively. A geographic comparison concerning the length-weight relationship for the species was also made using the results reviewed from previous studies (Table 2).

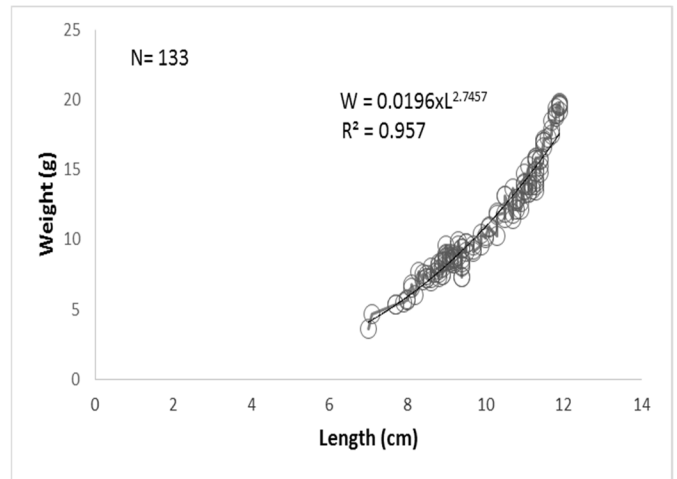


Figure 4. Length–weight relationships of *Arnoglossus kessleri* all specimens from Iskenderun Bay, Eastern Mediterranean coast of Turkey

Table 1. Descriptive statistics and estimated parameters of length-weight relationships for *Arnoglossus kessleri* from Iskenderun Bay (Eastern Mediterranean, Turkey).

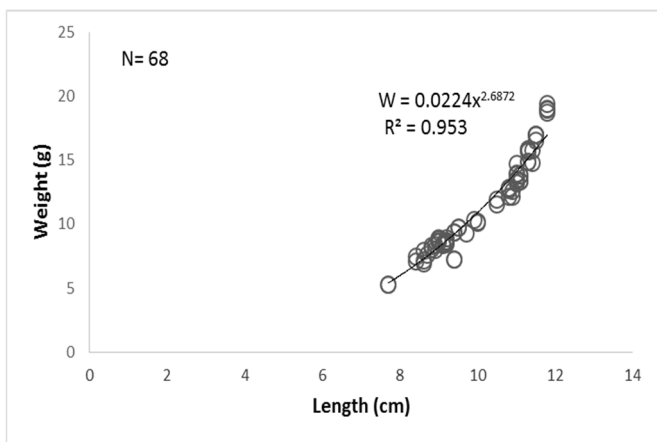


Figure 2. Length–weight relationships of *Arnoglossus kessleri* females from Iskenderun Bay, Eastern Mediterranean coast of Turkey

Table 2. Comparison of length-weight parameters for *A.*

Sex	n	TL (cm)		Parameters of the relationship				r^2
		L_{min}	W_{min}	a	95% C.I. of a	b	95% C.I. of b	
Female	68	7.7-	5.32-	0.022	0.0159-	2.68	2.540-	0.953
		11.8	19.4					
Male	65	7.0-	3.65-	0.017	0.0097-	2.79	2.648-	0.960
		11.9	19.7					
Both	133	7.0-	3.65-	0.019	0.0155-	2.74	2.645-	0.957
		11.9	19.7					

kessleri inhabiting the seas of Turkey.

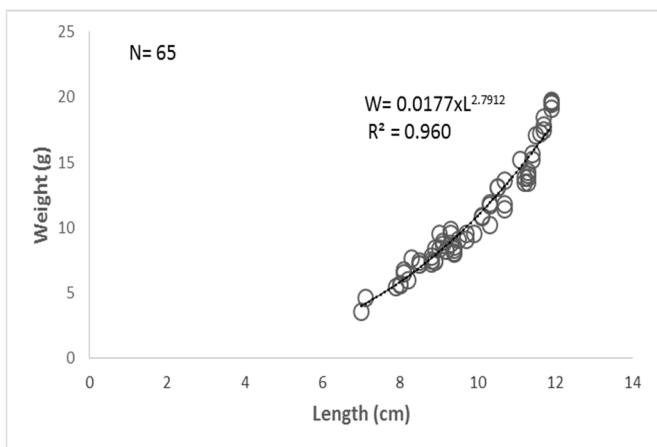


Figure 3. Length–weight relationships of *Arnoglossus kessleri* males from Iskenderun Bay, Eastern Mediterranean coast of Turkey

Reference	Locality	Country	Sex	n	Length Type	L _{min} -L _{max}	a	b	r ²
Türker Çakır et al. [23]	Northern Edremit Bay, north, Aegean Sea	Turkey	-	32	TL	5.2-8.9	0.00174	2.682	0.869
Bayhan et al. [12]	Izmir Bay, Aegean Sea	Turkey	-	76	TL	6.0-8.9	0.01790	2.601	0.878
İlkyaz et al. [14]	Izmir Bay, Turkey	-	-	7	TL	6.9-9.6	0.00185	2.740	0.960
Türker-Çakır et al. [13]	Edremit Bay, north, Aegean Sea	Turkey	-	32	TL	0.8-5.9	0.00004	3.124	0.944
Ak et al. (2009) [15]	Eastern Black Sea	Turkey	-	60	TL	4.3-9.8	0.02100	2.984	0.725
Ozen et al. [23]	Çanakkaile, Marmara Sea	Turkey	-	44	TL	2.9-9.8	0.00673	3.150	0.974
Keskin & Gaygusuz [16]	Erdek Bay, Marmara Sea	Turkey	-	24	TL	4.2-8.7	0.00410	3.474	0.968
Altın et al. [17]	Gökçeada Island, northern Aegean Sea	Turkey	-	393	TL	1.3-11.2	0.0050	3.292	0.933
This study	Iskenderun Bay (NE Mediterranean Sea)	Turkey	M	65	TL	7.0-11.9	0.0224	2.687	0.953
This study	Iskenderun Bay (NE Mediterranean Sea)	Turkey	F	68	TL	7.7-11.8	0.0177	2.791	0.960

4. DISCUSSION

The present data is the first set of data on maximum length and weight for *A. kessleri* in Mediterranean coast, Turkey. This study reveals that the length of males and females of *A. kessleri* did not differ significantly. However, the maximum length of males was slightly larger (11.9 cm) than that of the females (11.8 cm).

This study also reports the longest maximum total length of *A. kessleri* for entire Mediterranean Sea. Bauchot [21] reported that maximum total length of *A. kessleri* for males/unsexed as 10.0 cm in Mediterranean. However, Altın et al [17] found that maximum total length of *A. kessleri* from Gökçeada Island (northern Aegean Sea, Turkey) was 11.2 cm. The present study showed that the maximum total length of the species can extend to 11.9 cm for males and 11.8 for females. This study claims that the maximum total length of the species exceeds the values recorded in the FishBase so far.

The parameter b of length–weight relationships of *A. kessleri* from Iskenderun Bay was significantly different from 3 (P <0.05). The values of b for all groups were within the expected ranges of 2.5-3.5 [19].

Different growth patterns were reported for *A. kessleri* populations. Bayhan et al [12], İlkyaz et al [14] and Türker Çakır et al [22] reported negative allometry for *A. kessleri* from the Aegean coast (Izmir Bay and Edremit Bay), Turkey. Almost isometric growth has also been reported from eastern Black Sea [15]. On the contrary, Keskin and Gaygusuz [16], Altın et al [17] and Ozen et al [23] have reported that populations from the Sea of Marmara and Aegean Sea revealed positive allometric growths. Similar to results of Türker Çakır et al [13], Bayhan et al. [12] and İlkyaz et al. [14] a negative allometric growth was also observed in Iskenderun Bay. The value for all individuals was found as b=2.745.

The differences in the b-values may be attributed to seasonal changes in the water temperature and the maturity stage [24]. Besides different sampling area, age, sex and other factors, for example habitat, degree of stomach fullness, preservation techniques, etc., were not considered in this study.

In conclusion, the present study reports a new maximum total length for the native species, *A. kessleri* inhabiting Mediterranean Sea and provides some essential information on *A. kessleri* from Iskenderun Bay. The data on length and weight parameters are expected to be helpful in fisheries management in eastern Mediterranean, Turkey since the species has been declared as a data deficient species in the IUCN red list.

REFERENCES

- [1] N. Ünsal, and M. Oral, "Marmara Denizi'nde bulunan Bothidae (Dil balıkları) familyası türlerinin sistematığı ve dağılımları üzerine bir araştırma," *İstanbul Üniversitesi Su Ürünleri Fakültesi Su Ürünleri Dergisi*, vol. 7. no.1-2, pp. 65-76, 2003.
- [2] M. Bilecenoğlu, M. Kaya, B. Cihangir, and E. Çiçek, "An updated checklist of the marine fishes of Turkey," *Turkish Journal of Zoology*, vol. 38, no. 2014, pp. 901-929, 2014.
- [3] J. G. Nielsen, "Bothidae". in *Fishes of the North-eastern Atlantic and the Mediterranean*, P.J.P. Whitehead, M.L. Bauchot, J.C. Hureau, J. Nielsen and E. Tortonese (Eds.), France: UNESCO, Paris, pp. 1294-1298, 1986.

- [4] L. P. Salekhova, A. D. Gordina, and T. N. Klimova, "The ichthyofauna of coastal waters southwest of Crimea in 2003-2004," *Journal of Ichthyology*, vol. 47, no. 2, pp. 140-153, 2007.
- [5] IUCN, "The IUCN Red List of Threatened Species," [Online]. Available: <http://www.iucnredlist.org>, version/ (01/2017). [Accessed: 28-June-2017].
- [6] D. Abdul Malak, S. R. Livingstone, D. Pollard, B. A. Polidoro, A. Cuttelod, & et al., "Overview of the conservation status of the marine fishes of the Mediterranean Sea," Spain: Gland, Switzerland and Malaga, IUCN, pp. 61, 2011.
- [7] R. Froese, A. C. Tsikliras, and K. I. Stergiou, "Editorial note on weight-length relations of fishes," *Acta Ichthyologica et Piscatoria*, vol. 41 no. 4, pp. 261-263, 2011.
- [8] D. Pauly, "Fishbyte Section Editorial," *Naga, The ICLARM Quarterly*, vol. 16, no. 2-3, pp. 26-27, 1993.
- [9] J. Dulcic, and M. Kraljevic, "Weight-length relationship for 40 fish species in the eastern Adriatic (Croatian waters)," *Fisheries Research*, vol. 28, no. 3, pp. 243-251, 1996.
- [10] D. Erguden, C. Turan, and M. Gurlek, "Weight-length relationships for 20 lessepsian fish species caught by bottom trawl on the coast of Iskenderun Bay (NE Mediterranean Sea, Turkey)," *Journal of Applied Ichthyology*, vol. 25, no. 1, pp. 133-135, 2009.
- [11] G. Petrakis, and K. I. Stergiou, "Weight-length relationships for 33 fish species in Greek waters," *Fisheries Research*, vol. 21, no. 3-4, pp. 465-469, 1995.
- [12] B. Bayhan, T. M. Sever, and E. Taşkavak, "Length-weight relationships of seven flatfishes (Pisces: Pleuronectiformes) from Aegean Sea," *Turkish Journal of Fisheries and Aquatic Sciences*, vol. 8, pp. 377-379, 2008.
- [13] D. Türker Çakır, H. T. Koç, A. Basusta, and N. Basusta, "Length-weight relationships of 24 species from Edremit Bay, Aegean Sea," *e-Journal of New World Sciences Academy*, vol. 3, no. 1, pp. 47-51, 2008.
- [14] A. Ilkyaz, G. Metin, O. Soykan, and H. Kinacigil, Length-weight relationship of 62 fish species from the Central Aegean Sea, Turkey. *Journal of Applied Ichthyology*, vol. 24, no. 6, pp. 699-702, 2008.
- [15] O. Ak, S. Kutlu, and I. Aydin, "Length-weight relationship for 16 fish species from the Eastern Black Sea, Türkiye," *Turkish Journal of Fisheries Aquatic Sciences*, vol. 9, pp. 125-126, 2009.
- [16] Ç. Keskin, and Ö. Gaygusuz, "Length-weight relationships of fishes in shallow waters of Erdek Bay (Sea of Marmara, Turkey)," *IUFS Journal of Biology*, vol. 69, no. 2, pp. 87-94, 2010.
- [17] A. Altın, H. Ayyıldız, S. Kale, and C. Alver, "Length-weight relationships of forty-nine fish species from shallow waters of Gökçeada Island, northern Aegean Sea," *Turkish Journal of Zoology*, vol. 39, pp. 971-975, 2015.
- [18] W. E. Ricker, "Computation and interpretation of biological statistics of fish populations," *Bulletins of the Fisheries Research Board of Canada*, vol. 191, pp. 382, 1975.
- [19] R. Froese, "Cube law, condition factor and weight-length relationships: History, meta-analysis and recommendations," *Journal of Applied Ichthyology*, vol. 22, pp. 241-253, 2006.
- [20] R. S. Cone, "The need to reconsider the use of condition indices in fishery science," *Transactions of the American Fisheries Society*, vol. 118, pp. 510-514, 1989.
- [21] M. L. Bauchot, "Poissons osseux," in *Fiches FAO d'identification pour les besoins de la pêche. (rev. 1)*, W. Fischer, M.L. Bauchot and M. Schneider (Eds.), Méditerranée et mer Noire. Zone de pêche 37, Vol. II, Rome: Commission des Communautés Européennes and FAO, pp. 891-1421, 1987.
- [22] D. Türker Çakır, S. Akalın, A. Ünlüoğlu, B. Bayhan, and B. Hoşsucu, "The flatfish species in Edremit Bay and length-weight relationships for three of them *Citharus*

linguātula (Linnaeus, 1758), *Arnoglossus laterna* (Walbaum, 1792), *Arnoglossus kessleri* (Schmidt, 1915)," *E.U. Journal of Fisheries & Aquatic Sciences*, vol., 20 no, 3-4, pp. 529-536, 2003.

- [23] O. Ozen, H. Ayyildiz, A. Oztekin, and A. Altin, "Length-weight relationships of 17 less-studied fish species from Çanakkale, Marmara region of Turkey," *Journal of*

Applied Ichthyology, vol. 25, no. 2, pp. 238-239, 2009.

- [24] A. H. Weatherley, and H. S. Gill, "The Biology of Fish Growth," London: Academic Press, pp. 443, 1987.

	SAKARYA ÜNİVERSİTESİ FEN BİLİMLERİ ENSTİTÜSÜ DERGİSİ SAKARYA UNIVERSITY JOURNAL OF SCIENCE		
	e-ISSN: 2147-835X Dergi sayfası: http://www.saujs.sakarya.edu.tr		
	Received 12-02-2018 Accepted 21-03-2018	Doi 10.16984/saufenbilder.393479	

The First Indoor Radon Gas Measurement at Historical Places in Cappadocia, Nigde, Turkey

Vakkas Bozkurt*¹ and Sefa Ertürk¹

ABSTRACT

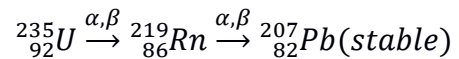
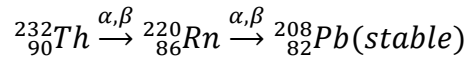
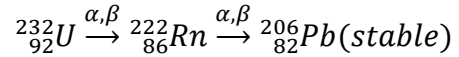
The aim of this study is to determine the concentration of Radon and its annual effective dose at the Nigde Museum and in a number of historical places namely the Sungur Bey, the Alaeddin, the Disari mosque and the Ak Medrese Culture House in Cappadocia, Nigde, Turkey. Nuclear track detector CR-39 were used to ascertain how much Radon concentration affects the people who are working in or visiting such places. Nuclear track detectors CR-39 were used for measurement for 132 days at the Nigde Museum, and for 63 days in the historical places. The exposed nuclear track detectors were then sent to the Sarayköy Nuclear Research and Training Center (SANAEM) to determine of Radon-222. The average Radon concentration results obtained for the Nigde Museum, the Sungur Bey, the Alaeddin, the Disari mosques and the Ak Medrese Culture House were 13.0 ± 2.94 Bq/m³, 31.67 ± 3.86 Bq/m³, 52.0 ± 5.72 Bq/m³, 42.67 ± 19.34 Bq/m³ and 31.0 ± 4.55 Bq/m³ respectively. The average effective dose of Radon was calculated for the Nigde Museum, the Sungur Bey, the Alaeddin, the Disari mosques and the Ak Medrese Culture House in Nigde and was found to be approximately 0.137 mSv/y, 0.062 mSv/y, 0.103 mSv/y, 0.084 mSv/y and 0.327 mSv/y respectively.

Keywords: Radon, environmental radioactivity, track detectors, diffusion chamber, CR-39

1. INTRODUCTION

The natural decay of radioactive substances in a series of heavy nuclei is known to result in the radioactive isotopes of lead. There are four natural radioactive series to be found in nature (Th-232, Np-237, U-238 and U-235).

The three that naturally occur in a radioactive decay chain existing in nature can be summarized as:



Rn-222, as part of the U-238 group, is the longest-lived isotope of Radon, with a half-life of approximately (3.825 days). Rn-222 can, therefore, represent a significant concentration in the atmosphere, a feature which invests an important role to Rn-222 for measuring radiation concentrations in nature. It must be stressed that Radon is one of the most dangerous radioactive elements in the environment in terms of radiation exposure: for instance, should Radon be inhaled into our lungs as we breathe in, it increases the risk of damage to the lung tissue; and is nowadays

* Corresponding Author

¹ Department of Physics, Faculty of Arts and Sciences, Nigde Omer Halisdemir University, 51100-vakkas.bozkurt@gmail.com

considered to be the second cause of lung cancer after cigarette smoking [1, 2, 3]. For this reason, Radon measurements play a critical role in monitoring human health and safety both in the home and workplace. Consequently, Radon is currently being widely measured throughout the world in natural environments as it can be a contributor to harmful health diseases [4].

Under normal temperature and atmospheric pressure, Radon is a colourless, invisible, tasteless and odourless gas that mixes with air in nature. Its atomic number is 86, its atomic weight is 222 g/mol and it has a neutron number of 136 in the nucleus. Radon gas results from the decay of the natural radioactive elements Uranium and Thorium. Uranium and Thorium-forming rock, present in the earth's crust, are found widely in soil, thus rendering it radioactive. Furthermore, Radon concentrations in soil are subject to many physical parameters such as soil structure, type of mineral, etc.

Radon gas measurements can be obtained by using active and passive measurement methods. The measurement of Radon using active-measurement techniques is performed in real time. In this technique, the concentration of Radon gas may be identified from an air sample to be determined by radiation counter; however, this not thought of as being preferable because Radon is greatly affected by external factors (humidity, pressure, air temperature, and so on). Consequently, the passive method is preferred for determining the average value of Radon concentration. By taking long-term measurements (daily, monthly, seasonal or annual), we can quantify the mean values of Radon concentrations over lengthy periods of time.

Radon is measured all over the world and limit for the Radon concentration for different countries are reported: USA-150 Bq/m³, Germany-250 Bq/m³, Australia-200 Bq/m³, China-200 Bq/m³, Denmark-400 Bq/m³, France-400 Bq/m³, India-150 Bq/m³, UK-200 Bq/m³, Ireland-200 Bq/m³, Sweden-200 Bq/m³, Canada-800 Bq/m³, Luxemburg-250 Bq/m³, Norway-200 Bq/m³, Russia-200 Bq/m³, Turkey-400 Bq/m³, EU-400 Bq/m³, ICRP-400 Bq/m³ and WHO-100 Bq/m³ [5].

Indoor Radon concentrations were also measured in different cities from Turkey. For example Radon concentration was measured in Sakarya as 40±5 Bq/m³ [6], in Adana as 37 Bq/m³ [7], in Ardahan as 53-736 Bq/m³, in Artvin as 21-321 Bq/m³ [8], in İzmir as 210 Bq/m³ [9], in Kilis,

Osmaniye, Antakya as 5-171, 6-209, 4-135 Bq/m³ respectively [10], and in Sivas as 56 Bq/m³ [5]. The arithmetic mean of the indoor Radon concentrations are reported as 81 Bq/m³ for Turkey of 81 provinces in Turkey [11] and the worldwide indoor Radon concentration was measured as 46 Bq/m³ [12].

The present study aimed to determine indoor Radon concentrations using CR-39 (a polycarbonate structure 500 micron thick) in diffusion chamber nuclear track detectors for selected areas where people are working or visiting, such as the Nigde Museum and certain selected historical places in Nigde, the Sungur Bey mosque (the mosque was constructed in 1335), the Alaeddin mosque (completed in 1223), the Disari (Celebi Husamettin) mosque (despite having no precise indication in the building, but it is supposed to have been built in the XVI century), and the Ak Medrese Culture House (finished in 1409). Nigde is a large town in the southern part of the Central Anatolian region of Turkey and is also part of Cappadocia, resulting in its attracting tourists to its historical sites. As well as these historical places, the Nigde Museum was chosen particularly in order to measure Radon concentrations from historical items within the museum and also to supervise the annual effective dose from these places.

2. MATERIALS AND METHODS

CR-39 plastic nuclear track detectors are widely used for Radon measurement in a natural environment and are favoured because of their availability, low-price, sensitivity and practical usage since they do not need any signal processing or power source during the measurement of radiation concentrations [13]. They prove to be one of the most useful nuclear track detectors for measuring indoor and outdoor Radon concentrations in any research areas. They also have high detection efficiency in identifying alpha particles emitted by Radon and its daughters.

CR-39 detectors were placed in the Nigde Museum for 132 days and at the Sungur Bey mosque, the Alaeddin mosque, the Disari (Celebi Husamettin) mosque and at the Ak Medrese Culture House) for 63 days, during which time the alpha particles produced from Rn-222 would leave tracks on the detectors. These tracks or images used in the analysis of traces of alpha on detectors under the Linux operating system employee

carries out a programme called the Radosys processing set [14]. The detectors counting traces of unwanted marks on the purified by a chemical etching process and within this process any real trace of alpha becomes observable. The counting process of alpha tracks was done through a film scanner and an image-processing program. All images were monitored and counted by the Radosys programme. The analysis of the tracks and the estimation of track density are automatically effected with the Radosys equipment. All Radon concentration measurements for CR-39 detectors which were bought from TAEK (Turkish Atomic Energy Agency) collected and sent to SANAEM at TAEK for analysis.

In this study, a total of 15 pieces of CR-39 detectors were placed at different places in Nigde: in the Nigde Museum (3) for 132 days, and in other selected historical places in Nigde, for 63 days: in the Sungur Bey mosque (3), in the Alaeddin mosque (3), in the Disari (Celebi Husamettin) mosque (3), and in the Ak Medrese Culture House (3 pieces of CR-39). Photographs of one-piece of the CR-39 detector placed in the Sungur Bey Mosque (a), the Alaeddin mosque (b), the Disari (Celebi Husamettin) mosque (c) and in the Ak Medrese Culture House (d) are shown in Figure 1.

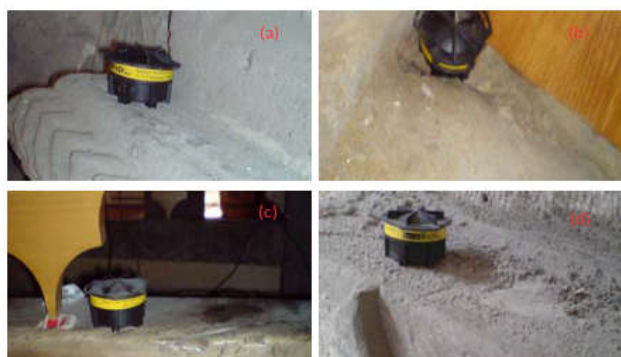


Figure 1. Photograph of located one-piece of a CR-39 detector cup in the Sungur Bey mosque (a), the Alaeddin mosque (b), the Disari (Celebi Husamettin) mosque (c) and in the Ak Medrese Culture House (d) here in Nigde.

3. RESULTS

In this study, we present the results of indoor Radon concentration in spring-summer season employing CR-39 detectors at the Nigde Museum as well as in the Sungur Bey, Alaeddin and Disari (Celebi Husamettin) mosques and in the Ak Medrese Culture House in Nigde; these can be seen in Table 1 shows the Radon concentration and

annual effective dose for each of these areas. Figure 2 shows average radon concentration of each location with standart deviation. The average Radon concentration measured in the Nigde Museum and at the Sungur Bey, the Alaeddin, the Disari (Celebi Husamettin) mosques and at the Ak Medrese Culture House in Nigde, were found to be 13.0 ± 2.94 Bq/m³, 31.67 ± 3.86 Bq/m³, 52.0 ± 5.72 Bq/m³, 42.67 ± 19.34 Bq/m³ and 31.0 ± 4.55 Bq/m³ respectively.

The arithmetic mean of indoor Radon concentrations values in these places ranged from 13.0 ± 2.94 Bq/m³ to 52.0 ± 5.72 Bq/m³, which is lower than the arithmetic mean of indoor Radon concentrations for Turkey (81 Bq/m³) [11] and obtained to be around for the world value as (46 Bq/m³) [12].

The annual average effective dose for indoor Radon is calculated using parameters introduced in the report by UNSCEAR [15]. From the measured Radon concentration, the annual effective dose of Radon was calculated with $E = C_{Rn} \times F \times t \times d$, equation.

E: Effective dose

C_{Rn} : The indoor Radon concentration (Bqm⁻³)

F: The equilibrium factor between Radon and its decay product equal to 0.4

t: The average indoor occupancy time for a person (y⁻¹)

d: The dose conversion factor for Radon exposure is 9 nSv (Bqhm⁻³)⁻¹

The Sungur Bey, the Alaeddin and the Disari (Celebi Husamettin) mosques are used daily by people at prayer times with an average occupancy-time for prayer being defined as 1.5 hours per day; this totals 548 hours per year. For the Ak Medrese Culture House and the Nigde Museum, daily activities have been found to total 8 hours, meaning that working or visiting time per year comes to 2920 hours. The average effective dose of Radon was calculated at the Nigde Museum, the Sungur Bey, the Alaeddin, the Disari (Celebi Husamettin) mosques and the Ak Medrese Culture House together with historical places in Nigde and found to be approximately 0.137 mSv/y, 0.062 mSv/y, 0.103 mSv/y, 0.084 mSv/y and 0.327 mSv/y respectively.

Table 1. The measured indoor Radon concentration and effective dose collected from the Nigde Museum and other historical places in Nigde.

Number of detectors and areas	Date of buildings	Height from floor	Radon concentration (Bq/m ³)	Annual effective dose (mSv/y)
1. Nigde Museum	1997	1.25 meter	10	0.105
2. Nigde Museum		1.20 meter	12	0.126
3. Nigde Museum		1.15 meter	17	0.179
1. Sungur Bey mosque	1335	2.80 meter	30	0.059
2. Sungur Bey mosque		3.70 meter	28	0.055
3. Sungur Bey mosque		4.0 meter	37	0.073
1. Alaeddin mosque	1223	1.80 meter	49	0.097
2. Alaeddin mosque		1.50 meter	47	0.093
3. Alaeddin mosque		1.70 meter	60	0.118
1. Disari mosque	XVI century	1.30 meter	70	0.138
2. Disari mosque		10 cm	30	0.059
3. Disari mosque		2.0 meter	28	0.055
1. Ak Medrese Culture House	1409	2.0 meter	30	0.315
2. Ak Medrese Culture House		2.0 meter	37	0.389
3. Ak Medrese Culture House		3.10 meter	26	0.273

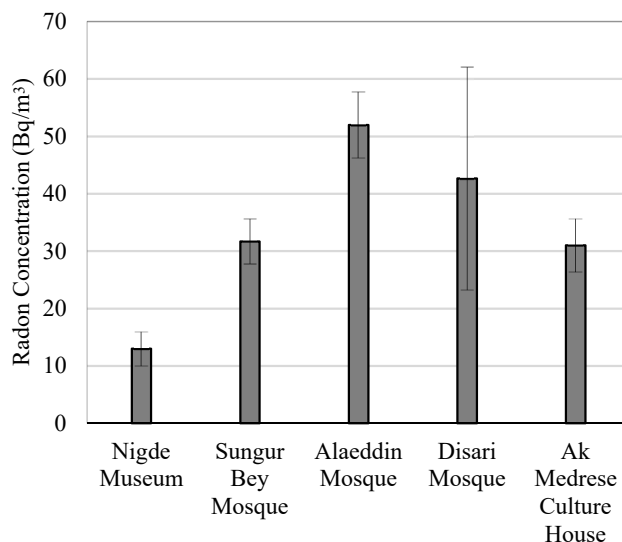


Figure 2. Average Radon concentration of each location.

4. CONCLUSION

The measurement of average Radon concentrations and its annual effective dose using CR-39 detectors at the Nigde Museum, the Sungur Bey mosque, the Alaeddin mosque, the Disari (Celebi Husametdin) mosque and at the Ak Medrese Culture House in Nigde, were shown to be lower than the limits recommended not only by the ICRP for indoor Radon concentrations, which is about 300 Bq/m³ (the annual mean concentration) and limit values for annual effective dose is about 10 mSv/y [16] but also by TAEK. For Turkey, the upper value for Radon concentration within dwellings is known to be 400 Bq/m³ and annual effective dose of 5 mSv [17].

In natural surroundings, there are many parameters involving the effect Radon levels for indoor dwellings such as temperature climate, heat conversion and ventilation equipment, etc.

The present measured Radon concentration and the annual effective dose both showed that no action needs to be taken at these places and measurements indicated that values are reasonably lower than the levels recommended by both ICRP and TAEK.

ACKNOWLEDGMENTS

We would like to thank Nigde University Research Fund for supporting this investigation and also the SANAEM laboratory for assistance with measurements.

REFERENCES

- [1] International commission on Radiological Protection (ICRP), *ICRP Publication 65, Annals of the ICRP*, vol. 23. Oxford: Pergamon Press, 1993.
- [2] Hileman B., "Indoor Air Pollution," *Environ. Sci. Technol*, vol. 17, no. 10, pp 469A, 1983.
- [3] Hopke P.K., Borak T.B., Doull J., et al., "Health Risks due to Radon in Drinking Water," *Environ. Sci. Technol*, vol. 34, no. 6, pp 921-926, 2000.
- [4] Matiullah, Fariha Malik and Muhammad Rafique, "Indoor Radon monitoring near an in situ leach mining site in D G Khan, Pakistan," *J. Radiol., Prot.*, 32(4), 427-437, 2012.
- [5] Metin Mihci, Aydin Buyuksarac, Attila Aydemir, Nilgun Celebi, "Indoor and outdoor Radon concentration measurement in Sivas, Turkey," *Journal of Environmental Radioactivity*, 101, 952-957, 2010.
- [6] Z. Zenginerler, F. Ertugral, H. Yakut, E. Tabar, N. Demirci and K. Gunermelikoglu, "Measurement of Seasonal Indoor Radon Concentration in Sakarya, Turkey," *Acta Physica Polonica A*, vol. 130, no. 1, 2016.
- [7] M. Degerlier and N. Celebi, "Indoor Radon concentration in Adana, Turkey," *Radiation Protection Dosimetry*, vol. 131, no. 2, 259-264, 2008.
- [8] B. Kucukomeroglu, Y.O. Yesilbag, A. Kurnaz, N. Celik, U. Cevik and N. Celebi, "Radiological Characterisation of Artvin and Ardahan provinces of Turkey," *Radiation Protection Dosimetry*, vol. 145, no. 4, 389-394, 2011.
- [9] Türkan Özbay and Özlem Karadeniz, "Indoor radon measurement in İzmir Province, Turkey" *International Journal of Environmental Analytical Chemistry*, vol. 96, no. 8, 752-762, 2016.
- [10] Bayram Can, Cumhuri Canbazoğlu, Nesil Albayrak, Nilgün Celebi, Mahmut Dogru, "Measurements of indoor radon concentration levels in Kilis, Osmaniye and Antakya, Turkey during spring season," *J. Radional Nucl. Chem.*, 292:1059-1063, 2012.
- [11] N. Celebi, B. Ataksor, H. Taskın and N. Albayrak Bingoldag, "Indoor Radon Measurements in Turkey Dwellings," *Radiation Protection Dosimetry*, vol.167, no. 4, 626-632, 2015.
- [12] UNSCEAR Report. United Nations scientific committee on the effects of atomic radiation sources, effects and risks of ionizing radiations, *New York: United Publication*, 2000.
- [13] Rehman Fazal-ur , Jamil K., Zakaullah M., AbuJarad, F., Mujahid, S.A., "Experimental and Monte Carlo simulation studies of an open cylindrical Radon monitoring device using CR-39 detector," *Journal of Environmental Radioactivity*, 65, 243-254, 2003.
- [14] Radosys User's Manual. Radosys Technical Specification, www.radosys.com, 2000.
- [15] UNSCEAR Sources and effects of ionizing radiation, *Report to General Assembly with Scientific Annexes*, 2000.
- [16] ICRP (International Commission on Radiological Protection) *ICRP Draft report for consultation*, ICRP ref 4829-9671-6554, 2011.
- [17] TAEK, *Radyasyon Güvenliği Yönetmeliği Sayı: 23999*, Madde 10 ve Madde 37 (24.03.2000).

	SAKARYA ÜNİVERSİTESİ FEN BİLİMLERİ ENSTİTÜSÜ DERGİSİ <i>SAKARYA UNIVERSITY JOURNAL OF SCIENCE</i>		
	e-ISSN: 2147-835X Dergi sayfası: http://www.saujs.sakarya.edu.tr		
	<u>Received</u> 16-02-2018 <u>Accepted</u> 26-03-2018	<u>Doi</u> 10.16984/saufenbilder.395615	

A Lyapunov Function For Logistic Equation On Time Scales

Veysel Fuat Hatipoğlu^{*1}

ABSTRACT

In this study we focus on the stability of dynamic logistic equation which is used in single species population dynamics. Here we have introduced a quadratic Lyapunov function for generalized dynamic logistic equation on time scales. By using proposed Lyapunov function, asymptotic stability conditions for the equilibrium solution of dynamic logistic equation have been investigated.

Keywords: Dynamic logistic equation, Lyapunov Function, Stability, Time Scales

1. INTRODUCTION

Logistic equation (or Verhulst equation) is often used to provide a model for single species population model. In the last century logistic equation has been applied to various branches of science such as ecology, medicine, physics and chemistry. For continuous case logistic equation is the differential equation

$$\frac{dx(t)}{dt} = rx(t) \left(1 - \frac{x(t)}{N}\right), t \geq 0, r > 0, \quad (1)$$

where $r > 0$ is the intrinsic growth rate, $x(t)$ is the population size at time t and $N > 0$ is the carrying capacity of the environment. For discrete case logistic equation is described by the difference equation

$$X_{t+1} = rX_t \left(1 - \frac{X_t}{N}\right), r > 0, \quad (2)$$

where $N > 0$ is the carrying capacity of the environment.

Unification and extension of continuous and discrete times is possible with time scales calculus. Therefore implementing equations (1) and (2) in a single equation is possible. In this manner logistic equation is considered on time scales by many authors [1] – [5]. Qualitative behavior of both continuous and discrete versions of logistic equation has been studied by several authors [6], [7]. However to the best of our knowledge, few articles are published on the asymptotic behavior of dynamic logistic equation on time scales. In [3] authors give the sufficient conditions for exponential asymptotic stability of a critical point of an almost linear dynamic equation and apply the findings to dynamic logistic equation. Their results show that the zero solution of dynamic logistic equation is unstable on any time scales and the solution of other equilibrium point $x = 1$ is exponentially stable depending on graininess function μ .

* Corresponding Author

¹ Muğla Sıtkı Koçman University, veysselfuat.hatipoglu@mu.edu.tr

2. PRELIMINARIES

A time scale \mathbb{T} is an arbitrary nonempty closed subset of \mathbb{R} . For $t \in \mathbb{T}$, forward jump operator $\sigma: \mathbb{T} \rightarrow \mathbb{T}$ is defined by

$$\sigma(t) := \inf\{s \in \mathbb{T} : s > t\}$$

The graininess function $\mu: \mathbb{T} \rightarrow [0, \infty)$ is defined by

$$\mu(t) = \sigma(t) - t.$$

The function $p: \mathbb{T} \rightarrow \mathbb{R}$ is said to be regressive provided $1 + \mu(t)p(t) \neq 0$ for all $t \in \mathbb{T}$. The set of all regressive rd-continuous functions $f: \mathbb{T} \rightarrow \mathbb{R}$ is denoted by \mathcal{R} . We refer to [1], [2] for detailed literature with the calculus of time scales. [2] gives the generalized logistic equation that is used in population dynamics as

$$y^\Delta = \frac{py(1-\frac{y}{N})}{1+\frac{\mu p}{N}y} \quad (3)$$

with $\frac{py}{N} \in \mathcal{R}$, where $N \neq 0$ is the carrying capacity of the population and $p \in \mathcal{R}$ is the growth rate. The solution of (3) is

$$y(t) = \frac{N}{\left(\frac{N}{y_0}-1\right)e_{\ominus p}(t,t_0)+1} \quad (4)$$

satisfying $y(t_0) = y_0$ where the function $\ominus p$ defined by $(\ominus p)(t) := \frac{p(t)}{1+\mu(t)p(t)}$ for all $t \in \mathbb{T}$.

Note that $y = 0$ and $y = N$ are the equilibrium solutions of (3). If we consider time scales as $\mathbb{T} = \mathbb{R}$ and $\mathbb{T} = \mathbb{Z}$ we see that (3) is identical with (1) and (2) respectively.

Definition of Lyapunov functions on time scales is as follows,

Definition 1. [8] A function $V(x): \mathbb{R}^n \rightarrow \mathbb{R}$, is called a time scale Lyapunov function for system (3) if

1. $V(x) \geq 0$ with equality if and only if $x = 0$, and
2. $V^\Delta(x(t)) \leq 0$.

In the next section we state the Lyapunov stability theorem on time scales and show the asymptotic stability of dynamic logistic equation on time scales.

3. STABILITY RESULTS

Following theorem gives the asymptotic stability conditions by using Lyapunov functions on time scales.

Theorem 2. [4] Given system (3) with equilibrium $x = 0$, if there exists an associated Lyapunov function $V(x)$, then $x = 0$ is Lyapunov stable. Furthermore, if $V^\Delta(x(t)) < 0$, then $x = 0$ is asymptotically stable.

Stability of the equilibria $y_1 = 0$ and $y_2 = N$ of equation (3) have been studied by Gard and Hoffacker [3] with $N = 1$. Authors showed that the equilibrium $y = 0$ of equation (3) is unstable on any time scale. In this section to show the Lyapunov stability of the equilibrium $y = N$ of logistic equation (3), we construct a Lyapunov function candidate in the form

$$V(t, y(t)) = (y - N)^2 \quad (5)$$

where N is the carrying capacity of the population. Letting $z = 1 - \frac{y}{N}$ we transform equation (3) to

$$z^\Delta = \frac{-pz(1-z)}{1+\mu p(1-z)} \quad (6)$$

where p is the growth rate with $p(1-z) \in \mathcal{R}$. Also Lyapunov function (5) transforms to

$$V(t, z(t)) = (Nz)^2. \quad (7)$$

We observe the stability of the zero solution $z_0 = 0$ of (6) (the $y_1 = N$ solution of logistic equation (3)). It is obvious that $V(t, z(t)) = (Nz)^2 \geq 0$. To verify $V(t, z(t))$ is a Lyapunov function for (6) we need to show $V^\Delta(t, z(t)) \leq 0$ for all $t \in \mathbb{T}$. Taking the Δ -derivative of (7),

$$V^\Delta(t, z(t)) = N^2(z + z^\sigma)z^\Delta.$$

Then we have,

$$V^\Delta(t, z(t)) = N^2(2z + \mu(t))z^\Delta. \quad (8)$$

Here we consider (8) in cases as $z < 0$, $0 < z < 1$, and $z = 0$.

Case 1. If $z < 0$ ($y > N$) then we have

$$p(t)z(t)(1 - z(t)) < 0 \quad (9)$$

and we have,

$$1 + \mu(t)p(t)(1 - z(t)) > 0. \quad (10)$$

Using the relations (9) and (10) in the equation (6), one can see that $z^\Delta > 0$ with $z < 0$ for all $t \in [t_0, \infty)_{\mathbb{T}}$. Therefore we can conclude that

$$V^\Delta(t, z(t)) = N^2(2z + \mu(t))z^\Delta < 0.$$

for any time scales satisfying $|z| > \frac{\mu(t)}{2}$.

Case 2. If $0 < z < 1$ ($0 < y < N$) we see that

$$p(t)z(t)(1 - z(t)) > 0 \tag{11}$$

and

$$1 + \mu(t)p(t)(1 - z(t)) > 0. \tag{10}$$

Writing (11) and (12) into (6) we obtain that $z^\Delta < 0$ for all $t \in [t_0, \infty)_{\mathbb{T}}$. Therefore since $\mu(t) \geq 0$ we have

$$V^\Delta(t, z(t)) = N^2(2z + \mu(t))z^\Delta < 0.$$

Hence (7) is a Lyapunov function for the equation (6) for the case $0 < z < 1$.

Case 3. When $z = 0$ ($y = N$), both $V(0,0) = 0$ and $V^\Delta(0,0) = 0$.

From the results of all cases equation (7) is a Lyapunov function for the dynamic logistic equation (6). Therefore by Theorem 1, $z = 0$ ($y = N$) solution of (6) is asymptotically Lyapunov stable for any time scale satisfying $|z| > \frac{\mu(t)}{2}$.

Asymptotically Lyapunov stability of the zero solution of dynamic logistic equation (6) indicates the asymptotically stability of the equilibrium solution $y = N$ of equation (3).

4. CONCLUSION

Population dynamics has been an important topic in ecology. Modeling and investigating the behavior of ecological phenomena have always been attractive for mathematicians. So this study is built on analyzing the Lyapunov stability of dynamic logistic equation on time scales. A Lyapunov function for dynamic logistic equation has been constructed. The study states that the equilibrium point $y = N$ namely carrying capacity of the population is asymptotically Lyapunov stable on time scales satisfying, $|z| > \frac{\mu(t)}{2}$. For future studies researchers might focus on the qualitative behavior of impulsive model of dynamic logistic equation.

REFERENCES

[1] M. Bohner and A. Peterson, *Dynamic Equations on Time Scales: An Introduction*

with Applications. Springer Science & Business Media, 2001.

- [2] M. Bohner and A. Peterson, *Advances in dynamic equations on time scales*. Springer Science & Business Media, 2002.
- [3] T. Gard and J. Hoffacker, "Asymptotic behavior of natural growth on time scales," *Dynamic Systems and Applications*, vol. 12, no. 1/2, pp. 131–148, 2003.
- [4] V. Lakshmikantham, S. Sivasundaram, and B. Kaymakçalan, *Dynamic systems on measure chains (Vol. 370)*. Springer Science & Business Media, 2013.
- [5] J. Zhang, M. Fan, and H. Zhu, "Periodic solution of single population models on time scales," *Mathematical and Computer Modelling*, vol. 52, no. 3, pp. 515–521, 2010.
- [6] P. Cull, "Stability of discrete one-dimensional population models," *Bulletin of Mathematical Biology*, vol. 50, no. 1, pp. 67–75, 1988.
- [7] M. W. Hirsch, S. Smale, and R. L. Devaney, *Differential equations, dynamical systems, and an introduction to chaos*. Academic press, 2012.
- [8] J. M. Davis, I. A. Gravagne, R. J. Marks, and A.A. Ramos, "Algebraic and dynamic Lyapunov equations on time scales." In Proc. IEEE 42nd Southeastern Symposium on System Theory (SSST), 2010, pp. 329–334.

	SAKARYA ÜNİVERSİTESİ FEN BİLİMLERİ ENSTİTÜSÜ DERGİSİ SAKARYA UNIVERSITY JOURNAL OF SCIENCE		
	e-ISSN: 2147-835X Dergi sayfası: http://www.saujs.sakarya.edu.tr		
	Received 11-01-2018 Accepted 26-03-2018	Doi 10.16984/saufenbilder.377423	

Evaluation of Two Stage Modified Ridge Estimator and Its Performance

Selma Toker^{*1}, Nimet Özbay²

ABSTRACT

Biased estimation methods are more desirable than two stage least squares estimation for simultaneous equations model suffering from the problem of multicollinearity. This problem can also be handled by using some prior information. Taking account of this knowledge, we recommend two stage modified ridge estimator in this article. The new estimator can also be evaluated as an alternative to the previously proposed two stage ridge estimator. A widespread performance criterion, mean square error, is taken into consideration to compare the two stage modified ridge, two stage ridge and two stage least squares estimators. A real life data analysis is investigated to support the theoretical results in practice. In addition, the intervals of the biasing parameter which provide the superiority of the two stage modified ridge estimator are determined with the help of figures. The researchers who deal with simultaneous systems with multicollinearity can opt for the two stage modified ridge estimator.

Keywords: modified ridge estimator, multicollinearity, simultaneous equations model, two stage least squares

1. INTRODUCTION

The matrix form of the simultaneous equations model is as follows

$$Y\Gamma + XB = U, \quad (1)$$

where $Y_{T \times M}$ and $X_{T \times K}$ are matrices of observations, $\Gamma_{M \times M}$ and $B_{K \times M}$ are the matrices of structural coefficients and $U_{T \times M}$ is the matrix of structural disturbances. The elements of X are nonstochastic and fixed with $\text{rank}(X) = K \leq T$ and the structural disturbances have zero mean and they are homoscedastic.

The model (1) can be written as

$$Y = X\Pi + V, \quad (2)$$

which is the reduced form. The reduced form coefficients are

$$\Pi = -B\Gamma^{-1} \quad (3)$$

and

$$V = U\Gamma^{-1}. \quad (4)$$

With the help of zero restrictions criterion the the equation below is the first equation of the system

$$y_1 = Y_1\gamma_1 + X_1\beta_1 + u_1. \quad (5)$$

There are $m_1 + 1$ included and $m_1^* = M - m_1 - 1$ excluded jointly dependent variables and K_1 included and $K_1^* = K - K_1$ excluded predetermined variables. $Y = [y_1 \ Y_1 \ Y_1^*]$ and $X = [X_1 \ X_1^*]$ are variables with the size of $T \times m_1$, $T \times m_1^*$, $T \times K_1$ and $T \times K_1^*$ corresponding to Y_1 , Y_1^* , X_1 and X_1^* . $\gamma_{.1} = [1 \ -\gamma_1 \ 0]'$ and $\beta_{.1} = [-\beta_1 \ 0]'$ are variables

* Corresponding Author

¹ Çukurova University, Department of Statistics, stoker@cu.edu.tr

² Çukurova University, Department of Statistics, nturker@cu.edu.tr

with the size of $m_1 \times 1$ and $K_1 \times 1$ corresponding to γ_1 and β_1 and u_1 is the first column of U .

The partition of the reduced form equation (2) can be arranged as follows

$$[y_1 \quad Y_1 \quad Y_1^*] = [X_1 \quad X_1^*] \begin{bmatrix} \pi_{11} & \Pi_{11} & \Pi_{11}^* \\ \pi_{21} & \Pi_{21} & \Pi_{21}^* \end{bmatrix} + [v_1 \quad V_1 \quad V_1^*], \quad (6)$$

where

$$y_1 = X\pi_1 + v_1 \quad (7)$$

and

$$Y_1 = X\Pi_1 + V_1. \quad (8)$$

In two preceding equations, $\pi_1 = [\pi_{11} \quad \pi_{21}]'$ and $\Pi_1 = [\Pi_{11} \quad \Pi_{21}]'$ are variables with the size of $K_1 \times 1$, $K_1^* \times 1$, $K_1 \times m_1$, $K_1^* \times m_1$, $T \times 1$ and $T \times m_1$ corresponding to π_{11} , π_{21} , Π_{11} , Π_{21} , v_1 and V_1 .

Considering only the first column of Γ , B and U in the reduced form coefficients (3) and (4), identifiability relationship between the structural parameters and the reduced form parameters for the first equation are obtained respectively as follows:

$$\pi_{11} = \Pi_{11}\gamma_1 + \beta_1, \quad (9)$$

$$\pi_{21} = \Pi_{21}\gamma_1 \quad (10)$$

and

$$v_1 = V_1\gamma_1 + u_1. \quad (11)$$

Reconsidering the first equation of the system (5),

$$y_1 = Z_1\delta_1 + u_1 \quad (12)$$

is obtained where

$$Z_1 = [Y_1 \quad X_1]_{T \times p_1}, \quad (13)$$

$$\delta_1 = [\gamma_1 \quad \beta_1]_{p_1 \times 1} \quad (14)$$

and $p_1 = m_1 + K_1$.

Thus, the structural equation (12) can be rewritten in the form of the following equation

$$y_1 = [X\Pi_1 \quad X_1] \begin{bmatrix} \gamma_1 \\ \beta_1 \end{bmatrix} + v_1 \quad (15)$$

by replacing the equations (8) and (11) so as to reach the final form of the equation (15):

$$y_1 = \bar{Z}_1\delta_1 + v_1, \quad (16)$$

where $\bar{Z}_1 = E(Z_1) = [X\Pi_1 \quad X_1]$, $E(v_1) = 0$ and $E(v_1v_1') = \sigma^2I$.

Two stage least squares (TSLS) estimation is commonly used for estimating the structural

parameters of the equation (16) depending on its ease of computation.

Explanatory endogenous variables are replaced by their instrumental variables which are ordinary least squares (OLS) estimates that are obtained by using the exogenous variables to apply the first stage of TSLS estimation. Then, for the second stage, OLS estimation is used again to obtain the regression coefficients.

TSLS estimator is defined as follows

$$\delta_1^{LS} = (\bar{Z}_1'\bar{Z}_1)^{-1}\bar{Z}_1'y_1. \quad (17)$$

Since \bar{Z}_1 is unknown,

$$\hat{\Pi}_1 = (X'X)^{-1}X'Y_1 \quad (18)$$

is used at the first stage to generate

$$\hat{\bar{Z}}_1 = [X\hat{\Pi}_1 \quad X_1]. \quad (19)$$

By doing so, the operational form of the TSLS estimator

$$\hat{\delta}_1^{LS} = (\hat{\bar{Z}}_1'\hat{\bar{Z}}_1)^{-1}\hat{\bar{Z}}_1'y_1 \quad (20)$$

is yielded.

In the presence of multicollinearity, TSLS does not give sensitive estimates anymore. So, alternative estimation methods to TSLS are required to deal with multicollinearity. In this context, the most popular estimator is ridge estimator (RE) of Hoerl and Kennard [1] which is recommended for estimating parameters in simultaneous equations model by Vinod and Ullah [2]. Two stage ridge regression yields estimates having smaller variance than the TSLS estimation.

When researchers confront with the problem of multicollinearity, biased estimation methods seem to be more attractive than the TSLS estimation. Such an alternative method is two stage RE which is given by Vinod and Ullah [2]. Ordinary and operational forms of the two stage RE are

$$\delta_1^{RE} = (\bar{Z}_1'\bar{Z}_1 + kI)^{-1}\bar{Z}_1'y_1 \quad (21)$$

and

$$\hat{\delta}_1^{RE} = (\hat{\bar{Z}}_1'\hat{\bar{Z}}_1 + kI)^{-1}\hat{\bar{Z}}_1'y_1, \quad (22)$$

where $k > 0$.

Sometimes additional prior information can be come across in simultaneous equations model and this can help to overcome the problem of multicollinearity, as well. By this consideration we define a new two stage estimator for the structural

coefficients based on the idea of modified ridge estimation of Swindel [3] subsequently.

In a summary, the organization of this article is as follows: Section 2 includes the new estimator for the simultaneous equations model; performance discussion of this new estimator is given in Section 3; Section 4 deals with the numerical example; Section 5 is for concluding remarks.

2. THE SUGGESTION OF NEW ESTIMATOR

There is a considerable interest in the existence of prior information. In this point of view, Swindel [3] offered a modified ridge estimator (MRE), which consists of a RE family, based on this information in linear regression model. By getting inspired from this idea, we propose two stage MRE based on prior information as

$$\delta_1(k, \delta_1^0) = (\bar{Z}'_1 \bar{Z}_1 + kI)^{-1} (\bar{Z}'_1 y_1 + k\delta_1^0), \quad (23)$$

where $k > 0$ and δ_1^0 is an arbitrary point in the parameter space which acts like the role of the origin.

Instead of this current form, to consider the prior information as a random variable seems more applicable as suggested by Swindel. Within this context, we replace δ_1^0 with δ_1^{RE} in equation (23) and two stage MRE is derived to be:

$$\delta_1^{MRE} = (\bar{Z}'_1 \bar{Z}_1 + kI)^{-1} (\bar{Z}'_1 y_1 + k\delta_1^{RE}), \quad (24)$$

where $k > 0$ and δ_1^{RE} is as in the equation (21). To simplify the expression (24), $\bar{Z}_1(k) = (\bar{Z}'_1 \bar{Z}_1 + kI)^{-1} \bar{Z}'_1 \bar{Z}_1$ is used so that

$$\delta_1^{MRE} = \bar{Z}_1(k) \delta_1^{LS} + (I - \bar{Z}_1(k)) \delta_1^{RE} \quad (25)$$

is obtained.

Let $\hat{\bar{Z}}_1(k) = (\hat{\bar{Z}}'_1 \hat{\bar{Z}}_1 + kI)^{-1} \hat{\bar{Z}}'_1 \hat{\bar{Z}}_1$, thus,

$$\hat{\delta}_1^{MRE} = \hat{\bar{Z}}_1(k) \hat{\delta}_1^{LS} + (I - \hat{\bar{Z}}_1(k)) \hat{\delta}_1^{RE} \quad (26)$$

is used in practice.

Notice that a convex combination of TSLS estimator and two stage RE reveals by suggesting the new estimator in the equation (25). This convex combination unifies the advantages of included estimators.

δ_1^{MRE} reduces to δ_1^{LS} as $k \rightarrow 0$ and δ_1^{RE} as $k \rightarrow \infty$. As k increases, δ_1^{MRE} follows a way through the parameter space from δ_1^{LS} to δ_1^{RE} . Therefore, we expect that the deficiencies that are arised from

multicollinearity with the use of TSLS estimator will be eliminated.

3. MSE PERFORMANCE OF THE NEW ESTIMATOR

The measure of the matrix mean square error (*MSE*) for any particular estimator $\bar{\delta}_1$ of δ_1 , is

$$MSE(\bar{\delta}_1) = V(\bar{\delta}_1) + Bias(\bar{\delta}_1)Bias(\bar{\delta}_1)', \quad (27)$$

where the first part is the variance function and the second part is the squared bias function.

The model (16) can be written in a canonical form as follows

$$y_1 = Z\alpha_1 + v_1, \quad (28)$$

where $Z = \bar{Z}_1 P$, $\alpha_1 = P' \delta_1$ and P is an orthogonal matrix such that $Z'Z = P' \bar{Z}'_1 \bar{Z}_1 P = \Lambda_1 = diag(\lambda_{11}, \dots, \lambda_{1p_1})$ where λ_{1i} are the eigenvalues of $\bar{Z}'_1 \bar{Z}_1$.

By using this canonical form, the TSLS estimator, the two stage RE and the two stage MRE can be written as

$$\alpha_1^{LS} = \Lambda_1^{-1} Z' y_1 = A_1 y_1, \quad (29)$$

$$\begin{aligned} \alpha_1^{RE} &= (\Lambda_1 + kI)^{-1} Z' y_1 \\ &= H_k Z' y_1 \\ &= A_2 y_1, \end{aligned} \quad (30)$$

and

$$\begin{aligned} \alpha_1^{MRE} &= (\Lambda_1 + kI)^{-1} (Z' y_1 + k\alpha_1^{RE}) \\ &= H_k \Lambda_1 \alpha_1^{LS} + k H_k \alpha_1^{RE} \\ &= (H_k + k H_k^2) Z' y_1 \\ &= A_3 y_1, \end{aligned} \quad (31)$$

where $H_k = (\Lambda_1 + kI)^{-1}$, $A_1 = \Lambda_1^{-1} Z'$, $A_2 = H_k Z'$ and $A_3 = (H_k + k H_k^2) Z'$.

The *MSEs* of the foregoing estimators are

$$MSE(\alpha_1^{LS}) = \sigma^2 \Lambda_1^{-1}, \quad (32)$$

$$\begin{aligned} MSE(\alpha_1^{RE}) &= \sigma^2 (I - k H_k) H_k \\ &\quad + k^2 H_k \alpha_1 \alpha_1' H_k', \end{aligned} \quad (33)$$

and

$$\begin{aligned} MSE(\alpha_1^{MRE}) &= \sigma^2 H_k (I - k H_k) (I + k H_k)^2 \\ &\quad + k^4 H_k^2 \alpha_1 \alpha_1' H_k^2. \end{aligned} \quad (34)$$

We refer the following lemmas that are to be used in theoretical comparisons.

Lemma 1. (Trenkler, [4]). Let $\bar{\delta}_1$ and $\bar{\delta}_2$ be two homogeneous linear estimators of δ_1 such that $D = V(\bar{\delta}_1) - V(\bar{\delta}_2) > 0$.

If $Bias(\bar{\delta}_2)'D^{-1}Bias(\bar{\delta}_2) < \sigma^2$ then $MSE(\bar{\delta}_1) - MSE(\bar{\delta}_2) > 0$.

Lemma 2. (Pliskin, [5]). A prior mean δ_1^0 is said to be good if $MSE(\delta_1^{RE}) - MSE(\delta_1(k, \delta_1^0))$ positive semidefinite for all positive values of k when both δ_1^{RE} and $\delta_1(k, \delta_1^0)$ are computed using the same value of k .

Firstly, we choose the superior one from two stage MRE and the TSLS estimator.

Theorem 1. Let k be fixed.

If $\alpha_1' H_k^2 (A_1 A_1' - A_3 A_3')^{-1} H_k^2 \alpha_1 < \frac{\sigma^2}{k^4}$ then $MSE(\alpha_1^{LS}) - MSE(\alpha_1^{MRE}) > 0$,

where $H_k = (\Lambda_1 + kI)^{-1}$, $A_1 = \Lambda_1^{-1} Z'$ and $A_3 = (H_k + kH_k^2) Z'$.

Proof:

$$\begin{aligned} V(\alpha_1^{LS}) - V(\alpha_1^{MRE}) &= \sigma^2 \Lambda_1^{-1} \\ &\quad - \sigma^2 H_k (I - kH_k) (I + kH_k)^2 \\ &= \sigma^2 k^2 H_k (H_k + \Lambda_1^{-1} + kH_k^2) H_k \\ &= \sigma^2 (A_1 A_1' - A_3 A_3'). \end{aligned}$$

Since $H_k + \Lambda_1^{-1} + kH_k^2 > 0$, $V(\alpha_1^{LS}) - V(\alpha_1^{MRE}) > 0$. From the Lemma 1 the proof is completed.

Secondly, we discuss the superiority of the two stage MRE to the two stage RE.

Theorem 2. Let k be fixed.

If $\alpha_1' H_k^2 (A_2 A_2' - A_3 A_3')^{-1} H_k^2 \alpha_1 < \frac{\sigma^2}{k^4}$ then $MSE(\alpha_1^{RE}) - MSE(\alpha_1^{MRE}) > 0$,

where $H_k = (\Lambda_1 + kI)^{-1}$, $A_2 = H_k Z'$ and $A_3 = (H_k + kH_k^2) Z'$.

Proof:

$$\begin{aligned} V(\alpha_1^{RE}) - V(\alpha_1^{MRE}) &= \sigma^2 (I - kH_k) H_k \\ &\quad - \sigma^2 H_k (I - kH_k) (I + kH_k)^2 \\ &= \sigma^2 H_k \Lambda_1 H_k (2kH_k + k^2 H_k^2) \\ &= \sigma^2 (A_2 A_2' - A_3 A_3'). \end{aligned}$$

$2kH_k + k^2 H_k^2 > 0$ thus $V(\alpha_1^{RE}) - V(\alpha_1^{MRE}) > 0$. From the Lemma 1 the proof is completed.

Through Theorem 1 and Theorem 2, we derive sufficient conditions for the superiority of the two stage MRE to the two stage RE and the TSLS estimator, as well. From the intuition behind Lemma 2 leads us to conclude that the prior mean δ_1^{RE} is a good information.

The current topic is to take account of the choice of the biasing parameter. Since the biasing parameter acts a prominent role in the performance of the mentioned estimators, the selection of this parameter is crucial. In this paper, we mainly determine the intervals of the biasing parameter with ridge trace so as to give the best results in the sense of mean square error for our new estimator. In addition, to estimate the biasing parameter we use some of the existing methods which are defined by Hoerl and Kennard [1], Hoerl et al. [6], Lawless and Wang [7] and Kibria [8]. These are defined to be as follows:

$$\hat{k}_{HK} = \frac{\hat{\sigma}^2}{\sum_{i=1}^{p_1} \hat{\alpha}_{1i}^2}, \quad (\text{Hoerl and Kennard, [1]}) \quad (35)$$

$$\hat{k}_{HKB} = \frac{p_1 \hat{\sigma}^2}{\sum_{i=1}^{p_1} \hat{\alpha}_{1i}^2}, \quad (\text{Hoerl et al., [6]}) \quad (36)$$

$$\hat{k}_{LW} = \frac{p_1 \hat{\sigma}^2}{\sum_{i=1}^{p_1} \lambda_{1i} \hat{\alpha}_{1i}^2}, \quad (\text{Lawless and Wang, [7]}) \quad (37)$$

$$\hat{k}_{AM} = \frac{1}{p_1} \sum_{i=1}^{p_1} \frac{\hat{\sigma}^2}{\hat{\alpha}_{1i}^2}, \quad (\text{Kibria, [8]}) \quad (38)$$

$$\hat{k}_{GM} = \frac{\hat{\sigma}^2}{(\prod_{i=1}^{p_1} \hat{\alpha}_{1i}^2)^{\frac{1}{p_1}}}, \quad (\text{Kibria, [8]}) \quad (39)$$

$$\hat{k}_M = \text{Median} \left\{ \frac{\hat{\sigma}^2}{\hat{\alpha}_{1i}^2} \right\}_{i=1}^{p_1}, \quad (\text{Kibria, [8]}) \quad (40)$$

where $\hat{\alpha}_{1i}$ and $\hat{\sigma}^2$ are the TSLS estimates of α_{1i} and σ^2 .

4. APPLICATION

We consider a constructed model given in Griffiths et. al [9] to illustrate the theoretical results. This aggregate econometric model of the U.S. economy is as follows

$$\text{Equation 1: } c_t = \gamma_{12} y_t + \beta_{11} + \beta_{12} c_{t-1} + e_{1t},$$

$$\text{Equation 2: } i_t = \gamma_{22} y_t + \beta_{21} + \beta_{22} i_t + e_{2t},$$

$$\text{Identity: } y_t = c_t + i_t + g_t,$$

where

c_t is private consumption expenditure in year t ,

i_t is private investment expenditure in year t ,

y_t is gross national expenditure in year t ,

g_t is government expenditure in year t ,
 r_t is a weighted average of interest rates in year t .

While c_t , i_t and y_t are used as endogenous variables, g_t and r_t are used as exogenous ones in this model.

The suggested data from Griffiths et al. [9] (p. 611) is used while doing the numerical example.

Since it is more convenient for application estimated scalar mean square error (mse) values are utilized. These estimated mse values for the foregoing estimators and estimates of the biasing parameter in canonical form are computed and shown in the Table 1.

and demonstrate the estimated mse performance of the estimators.

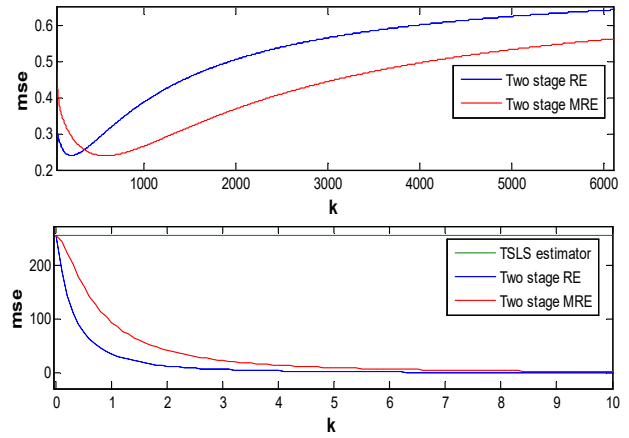


Figure 1. Estimated mse values for Equation 1

Table 1. Estimated mse values for the estimators

\hat{k}	$\widehat{mse}(\hat{\alpha}_1^{LS})$	$\widehat{mse}(\hat{\alpha}_1^{RE})$	$\widehat{mse}(\hat{\alpha}_1^{MRE})$
$\hat{k}_{LW} = 0.0030$	254.84	252.25	254.83
$\hat{k} = 1.5$	254.84	20.95	60.99
$\hat{k} = 3$	254.84	7.34	23.90
$\hat{k} = 5$	254.84	3.22	10.71
$\hat{k}_{HK} = 151.87$	254.84	0.24	0.32
$\hat{k} = 360$	254.84	0.25	0.25
$\hat{k}_{HKB} = 455.62$	254.84	0.27	0.24
$\hat{k}_M = 583.28$	254.84	0.30	0.23
$\hat{k} = 800$	254.84	0.34	0.24
$\hat{k}_{GM} = 1281.60$	254.84	0.42	0.29
$\hat{k} = 3000$	254.84	0.56	0.44
$\hat{k}_{AM} = 6052.86$	254.84	0.64	0.56
$\hat{k}_{LW} = 0.0039$	24.67	24.58	24.67
$\hat{k}_{HK} = 0.7219$	24.67	18.38	21.89
$\hat{k} = 1$	24.67	18.80	20.62
$\hat{k} = 1.5$	24.67	20.84	19.05
$\hat{k} = 2$	24.67	23.51	18.42
$\hat{k}_{HKB} = 2.16$	24.67	24.44	18.38
$\hat{k} = 3$	24.67	28.97	19.14
$\hat{k} = 4$	24.67	33.74	21.25
$\hat{k} = 5$	24.67	37.71	23.86
$\hat{k}_{GM} = 42.60$	24.67	65.40	59.51
$\hat{k}_M = 186.61$	24.67	70.40	68.84
$\hat{k}_{AM} = 252.76$	24.67	70.81	69.65

Figures 1-2 named as ridge trace are drawn to determine the intervals for the biasing parameter

Figure 1 is drawn in two parts corresponding to Equation 1. The first part below illustrates estimated mse behaviors of the TSLS estimator, two stage RE and the two stage MRE for the smaller values of the biasing parameter. In the meantime, the second part above is the plot for a wide range of k values. The two stage MRE outperforms the TSLS estimator and the two stage RE for the k values approximately greater than 360 whereas two stage RE is the best estimator for the smaller values of the biasing parameter. Based on the results obtained by means of ridge trace in Figure 1, for some chosen k values the estimated mse values are indicated in the Table 1. Besides, by using some existing methods in the previous section, estimated k values are computed for the Equation 1 and demonstrated in the Table 1. For example, for $\hat{k}_{LW} = 0.0030$ and $\hat{k}_{HK} = 151.87$ the two stage RE gives smaller estimated mse values than the TSLS estimator and the two stage MRE since these k values are rather small. On the other hand, the two stage MRE with $\hat{k}_{HKB} = 455.62$, $\hat{k}_M = 583.28$, $\hat{k}_{GM} = 1281.60$ and $\hat{k}_{AM} = 6052.86$ values is superior to the others. Thus, this result becomes compatible with the findings from the ridge trace.

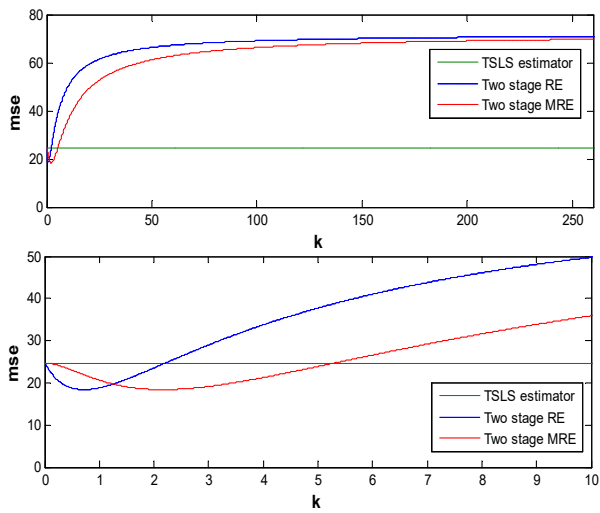


Figure 2. Estimated mse values for Equation 2

Similar to the Figure 1, Figure 2 is drawn in two parts to show estimated mse performances of the foregoing estimators, corresponding to Equation 2. The first part below is plotted for the smaller values of the biasing parameter while the second part above is the plotted for an extended range of k values. Till the magnitude of the k is nearly 1.5, the two stage RE is the best in comparison to the TSLS estimator and the two stage MRE. In the case that k lies between 1.5 and 5, the two stage MRE reaches its minimum in the sense of mse . When k is approximately greater than 5, the line for the two stage MRE is still below the line for two stage RE but it is above the line for the TSLS estimator. By this way, the Figure 2 plays a role in choosing some of the k values shown in the Table 1 for the Equation 2. In addition some computed k values for the existing estimation methods are also included in the Table 1. While $\hat{k}_{LW} = 0.0039$ and $\hat{k}_{HK} = 0.7219$, the two stage RE is preferable and this agrees with the ridge trace result obtained from Figure 2. Since $\hat{k}_{HKB} = 2.16$, the two stage MRE has the smallest estimated mse values at this point of estimate. As for $\hat{k}_{GM} = 42.60$, $\hat{k}_M = 186.61$ and $\hat{k}_{AM} = 252.76$, these estimation methods are useless for our new estimator since those are greater than 5.

5. CONCLUDING REMARKS

This article recommends the two stage MRE which is assigned to reduce the effect of multicollinearity in the simultaneous systems. This estimator is such a convex combined estimator that is resulted in unifying the advantages of the TSLS estimator and two stage RE. Taking two stage RE as prior information, the two stage MRE becomes

desirable with regard to dispelling multicollinearity. Within this framework, the new estimator is preferable to the two stage RE and the TSLS estimator.

We succeed in demonstrating the superiority of the two stage MRE over the two stage RE and the TSLS estimator with the help of theorems. The problem of choosing the biasing parameter of the two stage MRE is settled by the technique of ridge trace as well as some specific estimation methods.

The conclusion that two stage MRE outperforms the two stage RE and the TSLS estimator is drawn from data analysis based on the data set Griffiths [9]. Furthermore, graphical representation is accomplished to observe the estimated mse performances. By means of the graphs, it is observed that for greater values of the biasing parameter the two stage MRE is better than the two stage RE and the reverse is valid for smaller values of the biasing parameter. Likewise to the theoretical results, the numerical results are in favor of the two stage MRE.

ACKNOWLEDGMENTS

This paper is supported by Çukurova University Scientific Research Projects Unit Project Number: FBA-2018-9770.

REFERENCES

- [1] A. E. Hoerl and R. W. Kennard, "Ridge regression: biased estimation for nonorthogonal problems", *Technometrics*, vol. 12, no. 1, pp. 55-67, 1970.
- [2] H. D. Vinod and A. Ullah, "Recent advances in regression methods", Marcel Dekker, New York, Inc., 1981.
- [3] B. F. Swindel, "Good Ridge Estimators Based on Prior Information", *Communications in Statistics-Theory and Methods*, vol. A5, pp. 1065-1075, 1976.
- [4] G. Trenkler, "Generalized mean squared error comparisons of biased regression estimators", *Communications in Statistics-Theory and Methods*, vol. A9, no. 12, pp. 1247-1259, 1980.

- [5] J. L. Pliskin, "A ridge type estimator and good prior means", *Communications in Statistics-Theory and Methods*, vol. 16, no. 12, pp. 3429–3437, 1987.
- [6] A. E. Hoerl, R. W. Kennard and K. F. Baldwin, "Ridge regression: some simulations", *Communications in Statistics-Simulation and Computation*, vol. 4, pp. 105–123, 1975.
- [7] J. F. Lawless and P. A. Wang, "Simulation study of ridge and other regression estimators", *Communications in Statistics-Theory and Methods*, vol. 5, no. 4, pp. 307-323, 1976.
- [8] B. M. G. Kibria, "Performance of some new ridge regression estimators", *Communications in Statistics-Simulation and Computation*, vol. 32, no. pp. 419–435, 2003.
- [9] W. E Griffiths, R.C. Hill and G.G. Judge, "Learning and Practicing Econometrics", John Wiley&Sons Inc., New York, 1993.

	SAKARYA ÜNİVERSİTESİ FEN BİLİMLERİ ENSTİTÜSÜ DERGİSİ <i>SAKARYA UNIVERSITY JOURNAL OF SCIENCE</i>		
	e-ISSN: 2147-835X Dergi sayfası: http://dergipark.gov.tr/saufenbilder		
	<u>Received</u> 30-11-2017 <u>Accepted</u> 22-03-2018	<u>Doi</u> 10.16984/saufenbilder.359837	

The theoretical investigation of global reactivity descriptors, NLO behaviours and bioactivity scores of some norbornadiene derivatives

Serpil Eryılmaz*¹

ABSTRACT

In this study, global reactivity descriptors such as ionization potential, electron affinity, electronegativity, chemical hardness, softness and electrophilicity index of norbornadiene derivatives which include some halogen atoms and atom groups, have been investigated with DFT/BPV86/B3LYP/B3PW91 methods with 6-31G(d,p) basis set. To determine the non-linear optical behaviours of the structures; the total dipole moment, mean polarizability and first-order hyperpolarizability values have been examined at the same theoretical level. It has been found that thiol-bonded groups in comparison with others have a much better NLO material property. In addition, the potentials being drug-active compounds of the structures have been examined with Lipinski's rule of 5 and bioactivity scores. Thiol and hydroxyl-bonded groups have a good drug-likeness and bioactivity score relative to the others.

Keywords: Global reactivity descriptors, NLO, DFT, Lipinski's rule of 5, bioactivity score

1. INTRODUCTION

Quantum mechanically based approaches provide very effective results in the process of understanding the physical and chemical properties of molecular structures. Day by day developing software technology, along with the mathematical background foresee of these approaches provides positive contribution at the effects of the theoretical analyses. Density Functional Theory (DFT) is one of the quantum mechanical approaches that are quite successful in elucidating the electronic structures of substances and giving results which are consistent with experimental data at the same time [1-4].

Global reactivity descriptors such as ionization potential, electron affinity, electronegativity, chemical softness-hardness, chemical potential,

electrophilic index, are used to explain the reactivity and stability properties of over the entire molecular structure. In determining these identifiers in DFT-based calculations, the frontier molecular orbital energy values are considered as a starting point and some of them are obtained from derivative of the energy respect to electron density for the molecular structures [5-7].

The design of molecules exhibiting a non-linear optical behaviour is a current research topic in modern communication technology, optical data storage, transmission of optical signals, signal processing and in many optoelectronic applications areas [8-11]. The delocalization of π electrons that increased by conjugation, and the high polarization, are effective factors in displaying the non-linear optical character of molecular structures [12].

* Corresponding Author

¹Department of Physics, Faculty of Arts and Sciences, Amasya University, 05100, Amasya, Turkey, srplyilmaz@gmail.com

Norbornadiene which is used in the synthesis of complex polycyclic hydrocarbons is a significant organic compound. The structural properties of the compounds which is synthesized by 1,3-dipolar mono-domino cycloaddition reactions and having norbornadiene skeleton, isoxazole moiety, the aromatic groups were examined with spectroscopic and theoretical methods by our working group [13,14].

In the present paper, global reactivity descriptors and non-linear optical properties at the theoretical level have been examined of new derivatives obtained by connecting some atoms (-F, -Cl, -Br) and atom groups (-OH, -SH, -tert-Butyl) in *para*-position to the aromatic groups of the two compounds. Theoretical analyses were carried out with DFT method at 6-31G(d,p) basis set and three different functionals, such as BPV86, B3LYP, B3PW91 to examine the effects of functional selections on reactivity parameters and NLO behaviour of molecular structures.

Furthermore, the potential drug-active compound properties and some bioactivity scores have been examined as theoretical for the obtained derivatives.

2. COMPUTATIONAL DETAILS

The derivatives of compounds **1** and **2** having the norbornadiene skeleton have been obtained with halogens like fluorine, chlorine, bromine and also atomic groups such as hydroxyl, thiol, tert-butyl, and molecular structures are shown in Figure 1.

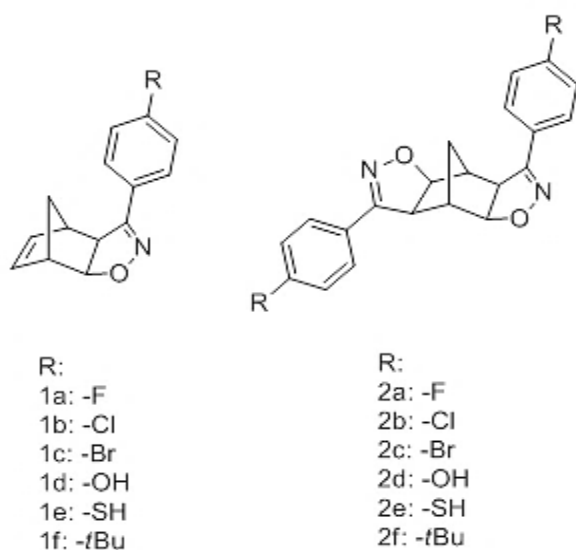


Figure 1. The chemical structures of the compound **1** and **2**

The geometric optimization of the obtained structures were realized with DFT using the BPV86, Burke and Perdew's 1986 functional with

correlation replaced by Vosko et al [15], B3LYP, Becke's Three-Parameter Hybrid Functional using the Lee, Yang and Parr correlation [16], and B3PW91, Becke's Three-Parameter Hybrid Method Functional with Perdew/Wang 91 [16-c,17] functionals with 6-31G(d,p) basis set in ground state. In this process, the theoretical analyses were carried out with Gaussian 09, Revision C.01 [18] electronic structure and GaussView 5.0.9 [19] graphical interface programmes. All theoretical analyses were performed on optimized structures. The optimized molecular geometries of compounds **1** and **2** are shown in Figure 2 and 3. In these figures a ... f are defined as (a)*p*-F, (b)*p*-Cl, (c)*p*-Br, (d)*p*-OH, (e)*p*-SH, (f)*p*-tert-Butyl.

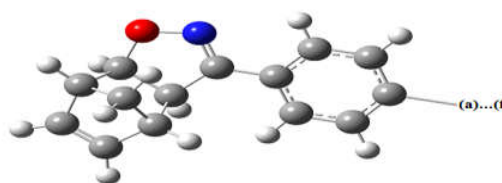


Figure 2. The optimized geometry of the compound **1**

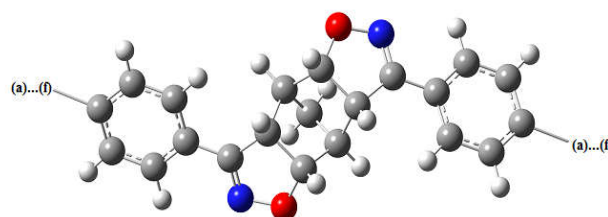


Figure 3. The optimized geometry of the compound **2**

The ionization potential (*I*) and electron affinity (*A*) according to Koopmans' Theory can be stated as [20],

$$I = -E_{\text{HOMO}} \text{ and } A = -E_{\text{LUMO}} \quad (1)$$

The electronegativity (χ), global chemical hardness (η) and electronic chemical potential (μ) are defined as [7,21];

$$\mu = \left(\frac{\partial E}{\partial N} \right)_{v(r)} = -\chi \quad (2)$$

$$\eta = \frac{1}{2} \left(\frac{\partial \mu}{\partial N} \right)_{v(\vec{r})} = \frac{1}{2} \left(\frac{\partial^2 E}{\partial N^2} \right)_{v(\vec{r})} \quad (3)$$

in here, *E*; is the energy, *N*; is the number of electrons, $v(\vec{r})$; is the external potential of the molecular system under consideration.

Also, these concepts are expressed using *I* and *A* values as follows, respectively [22-25];

$$\chi = (I+A)/2, \quad \eta = (I-A)/2, \quad \text{and } \mu = -(I+A)/2 \quad (4)$$

Global chemical softness (S) and electrophilicity index (ω) values are defined as follows [26-27];

$$S=1/2\eta \text{ and } \omega=\mu^2/2\eta \quad (5)$$

To have knowledge about NLO behaviours of the obtained structures were analysed total electric dipole moment, μ_{tot} , mean polarizability, $\langle\alpha\rangle$, total first-order hyperpolarizability, β_{tot} , values with the x,y,z components and can be computable with the following equations [28-30];

$$\mu_{tot} = (\mu_x^2 + \mu_y^2 + \mu_z^2)^{1/2} \quad (6)$$

$$\langle\alpha\rangle = \frac{(\alpha_{xx} + \alpha_{yy} + \alpha_{zz})}{3} \quad (7)$$

$$\beta_{tot} = [(\beta_{xxx} + \beta_{xyy} + \beta_{xzz})^2 + (\beta_{yyy} + \beta_{yzz} + \beta_{yxx})^2 + (\beta_{zzz} + \beta_{zxx} + \beta_{zyy})^2]^{1/2} \quad (8)$$

In order to determine the biological activity properties of the compounds, it has been investigated whether Lipinski's 5 rules [31,32] are provided for all the structures obtained. Also, a number of bioactivity scores such as GPCR ligand, ion channel modulator, nuclear receptor ligand, kinase inhibitor, protease inhibitor and enzyme inhibitor were examined at the theoretical level using Molinspiration Cheminformatics software [33-35].

3. RESULTS AND DISCUSSION

3.1. Global Reactivity Descriptors

The global reactivity descriptors such as ionization potential (I), electron affinity (A), electronegativity (χ), chemical hardness (η), chemical softness (S), chemical potential (μ) and electrophilicity index (ω) values were examined with DFT/BPV86/B3LYP/B3PW91/6-31G(d,p) level in gas phase to have information about the chemical stability of the compounds having norbornadiene skeleton. Reactivity parameters defined by the equations (1), (4), (5) and obtained results are given in Table 1.

When the ionization potential (I) values, which is the minimum energy required to remove an electron from the molecule in the gas phase [36] were examined; compounds **1d** and **2d** have a lower I value than the others with respect to used methods. As can be seen in Table 1, compounds **1c**

and **2b**, **2c** have a higher (A) value than others, according to electron affinity values which are the amount of energy that is increased when an electron has added the molecule [37]. According to these results, it can be said that hydroxyl-bonded groups with lower I values have better electron donating and the bromine and chlorine-bonded groups having a high A values have better electron accepting characteristics.

As regards the electronegativity values (χ) chlorine and bromine-bonded groups (**1b,c** and **2b,c**) can be said to have the character which attracts bond electrons more than the others. When the global chemical hardness-softness (η,S) values considered as a measure of the inhibition of intramolecular charge transfer were examined, it was observed that the structures **1e** and **2e** have lower chemical hardness, higher chemical softness value for both compounds. It can be considered that thiol-bonded groups with soft molecular structure are more reactive, they can give the easier electron to acceptor group and thus more likely to transfer of charge. The chemical potential (μ) and electrophilicity index (ω) indicate the tendency of structures to accept electrons. High chemical potential and electrophilicity index values are associated with a good electrophilic character [38]. For this reason, the chlorine and bromine-bonded structures have a better electrophilic character than the others.

Table 1. Global reactivity descriptors of the structures

Struc.	E_H (eV)	E_L (eV)	I (eV)	A (eV)	χ (eV)	η (eV)	S (eV ⁻¹)	μ (eV)	ω (eV)
BPV86									
1a	-5.09	-1.94	5.09	1.94	3.51	1.57	0.31	-3.51	3.93
1b	-5.21	-2.15	5.21	2.15	3.68	1.53	0.32	-3.68	4.43
1c	-5.21	-2.17	5.21	2.17	3.69	1.51	0.32	-3.69	4.48
1d	-4.78	-1.68	4.78	1.68	3.23	1.54	0.32	-3.23	3.38
1e	-4.91	-1.96	4.91	1.96	3.44	1.47	0.33	-3.44	4.01
1f	-4.96	-1.83	4.96	1.83	3.39	1.56	0.31	-3.39	3.68
2a	-5.14	-2.32	5.14	2.32	3.73	1.40	0.35	-3.73	4.95
2b	-5.34	-2.46	5.34	2.46	3.90	1.44	0.34	-3.90	5.29
2c	-5.33	-2.46	5.33	2.46	3.90	1.43	0.34	-3.93	5.31
2d	-4.82	-1.92	4.82	1.92	3.37	1.45	0.34	-3.37	3.92
2e	-5.00	-2.22	5.00	2.22	3.61	1.38	0.35	-3.61	4.70
2f	-5.01	-2.07	5.01	2.07	3.54	1.47	0.34	-3.54	4.27
B3LYP									
1a	-5.91	-1.12	5.91	1.12	3.51	2.39	0.20	-3.51	2.58

<i>1b</i>	-6.02	-1.34	6.02	1.34	3.68	2.33	0.21	-3.68	2.90
<i>1c</i>	-6.00	-1.35	6.00	1.35	3.67	2.32	0.21	-3.67	2.91
<i>1d</i>	-5.57	-0.85	5.57	0.85	3.21	2.35	0.21	-3.21	2.19
<i>1e</i>	-5.66	-1.16	5.66	1.16	3.41	2.25	0.22	-3.41	2.59
<i>1f</i>	-5.75	-1.00	5.75	1.00	3.37	2.37	0.21	-3.37	2.39
<i>2a</i>	-6.04	-1.40	6.04	1.40	3.72	2.32	0.21	-3.72	2.98
<i>2b</i>	-6.16	-1.63	6.16	1.63	3.90	2.26	0.22	-3.90	3.36
<i>2c</i>	-6.14	-1.64	6.14	1.64	3.89	2.25	0.22	-3.89	3.36
<i>2d</i>	-5.62	-1.08	5.62	1.08	3.35	2.27	0.22	-3.35	2.47
<i>2e</i>	-5.76	-1.40	5.76	1.40	3.58	2.18	0.22	-3.58	2.95
<i>2f</i>	-5.81	-1.21	5.81	1.21	3.51	2.29	0.21	-3.51	2.68

B3PW91

<i>1a</i>	-5.96	-1.16	5.96	1.16	3.56	2.40	0.20	-3.56	2.64
<i>1b</i>	-6.07	-1.40	6.07	1.40	3.73	2.33	0.21	-3.73	2.99
<i>1c</i>	-6.06	-1.42	6.06	1.42	3.74	2.31	0.21	-3.74	3.02
<i>1d</i>	-5.62	-0.90	5.62	0.90	3.26	2.35	0.21	-3.26	2.26
<i>1e</i>	-5.73	-1.22	5.73	1.22	3.47	2.25	0.22	-3.47	2.68
<i>1f</i>	-5.80	-1.05	5.80	1.05	3.43	2.37	0.21	-3.43	2.47
<i>2a</i>	-6.02	-1.5	6.02	1.56	3.79	2.23	0.22	-3.79	3.22
<i>2b</i>	-6.21	-1.71	6.21	1.71	3.96	2.25	0.22	-3.96	3.48
<i>2c</i>	-6.19	-1.72	6.19	1.72	3.95	2.23	0.22	-3.95	3.50
<i>2d</i>	-5.68	-1.15	5.68	1.15	3.41	2.26	0.22	-3.41	2.57
<i>2e</i>	-5.83	-1.48	5.83	1.48	3.65	2.17	0.23	-3.65	3.08
<i>2f</i>	-5.87	-1.29	5.87	1.29	3.58	2.28	0.21	-3.58	2.80

The variation of ionization potential (*I*), electron affinity (*A*), global chemical softness (*S*) and electrophilicity index (ω) values at different level for the structures are shown in Figure 1-8.

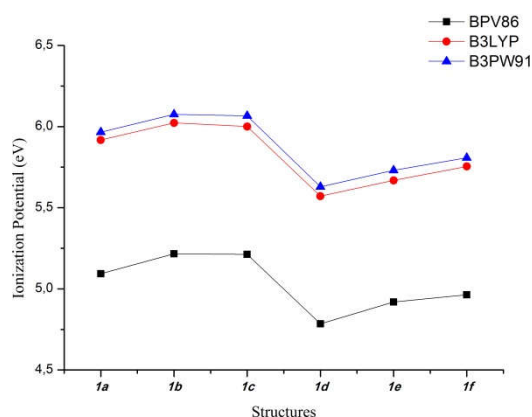


Figure 1. The variation of ionization potential for the compound 1

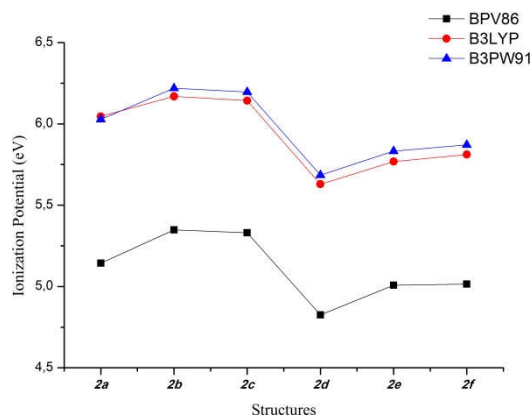


Figure 2. The variation of ionization potential for the compound 2

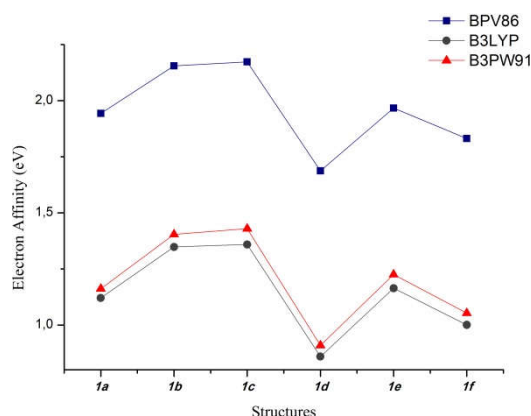


Figure 3. The variation of electron affinity for the compound 1

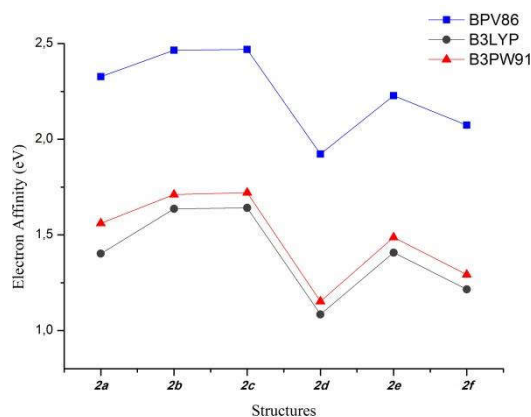


Figure 4. The variation of electron affinity for the compound 2

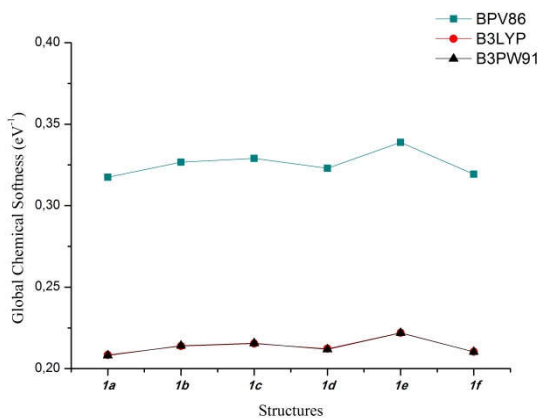


Figure 5. The variation of global chemical softness for the compound 1

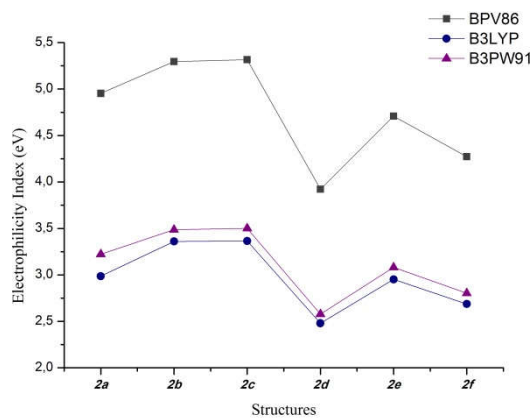


Figure 8. The variation of electrophilicity index for the compound 2

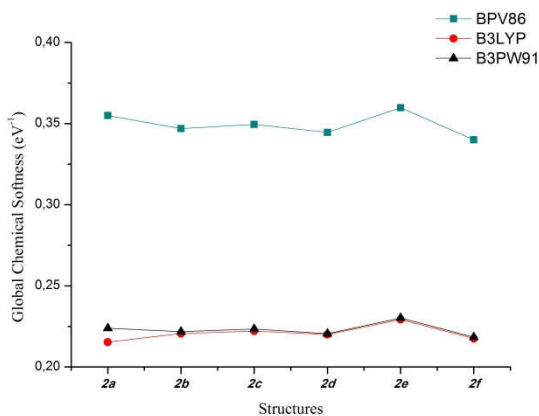


Figure 6. The variation of global chemical softness for the compound 2

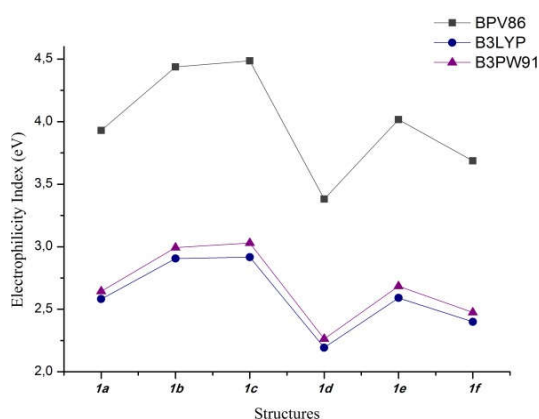


Figure 7. The variation of electrophilicity index for the compound 1

3.2. Non-Linear Optical (NLO) Behaviour

On behalf of determining the NLO behaviours of the derivatives of compounds 1 and 2, total electric dipole moment (μ_{tot}), mean polarizability ($\langle\alpha\rangle$), total first-order hyperpolarizability (β_{tot}) values were examined using the equations described with (6), (7), (8) at DFT/BPV86 B3LYP/B3PW91/6-31G(d, p) level.

The same parameters were examined for the urea molecule, which is considered as a threshold value in such analyses, to determine the possibility of being NLO materials of the obtained derivatives for the compounds 1 and 2. The calculated $\langle\alpha\rangle$, β_{tot} values for urea are, 4.0725×10^{-24} esu, 579.46×10^{-33} esu for the BPV86 functional, 3.8734×10^{-24} esu, 378.73×10^{-33} esu for the B3LYP functional, 3.8455×10^{-24} esu, 383.51×10^{-33} esu for the B3PW91 functional. When a comparison is made to β_{tot} values, it can be said that especially the thiol-bonded groups have a higher possibility of being NLO material. Namely, β_{tot} value is of the compound 1e, 14.46 times, compound 2e, 5.31 times for the BPV86, the compound 1e, 18.03 times, compound 2e, 6.39 times for the B3LYP, the compound 1e, 17.33 times, compound 2e, 6.61 times for the B3PW91 greater from the value of urea. The obtained results are tabulated in Table 2. In table, mean polarizability's unit was converted into esu (electrostatic unit), (1 a.u.= 0.1482×10^{-24} esu) and first-order hyperpolarizability's unit was converted into esu, (1 a.u.= 8.6393×10^{-33} esu) [39].

Table 2. The total dipole moment, mean polarizability and first-order hyperpolarizability values of the structures

Structures	μ_{tot} (Debye)	$\langle\alpha\rangle$ ($\times 10^{-24}$ esu)	β_{tot} ($\times 10^{-33}$ esu)
BPV86			
<i>1a</i>	3.1169	22.9014	1478.86
<i>1b</i>	3.1072	25.2135	721.93
<i>1c</i>	3.4026	26.5592	1101.86
<i>1d</i>	4.4131	23.9046	2670.14
<i>1e</i>	3.8795	26.9375	8381.64
<i>1f</i>	3.1638	30.7047	4164.08
<i>2a</i>	1.9502	37.1056	818.53
<i>2b</i>	2.1069	42.0626	1345.84
<i>2c</i>	2.0818	44.8897	1672.22
<i>2d</i>	0.2941	39.3484	1212.25
<i>2e</i>	0.9840	45.8642	3081.69
<i>2f</i>	1.5567	53.2837	207.24
B3LYP			
<i>1a</i>	3.2125	21.6641	884.37
<i>1b</i>	3.4698	23.8012	1006.99
<i>1c</i>	3.8182	25.0684	1285.78
<i>1d</i>	4.1198	22.5645	3063.83
<i>1e</i>	3.9902	25.3133	6831.49
<i>1f</i>	3.3436	29.0320	2231.58
<i>2a</i>	2.0290	34.7829	832.35
<i>2b</i>	2.1642	39.3022	1204.31
<i>2c</i>	2.1325	41.9448	1333.12
<i>2d</i>	0.3520	36.7529	1167.50
<i>2e</i>	1.0404	42.5736	2422.27
<i>2f</i>	1.7902	49.9637	492.51
B3PW91			
<i>1a</i>	3.2285	21.5051	878.85

<i>1b</i>	3.4801	23.7604	920.42
<i>1c</i>	3.4461	25.0298	1126.37
<i>1d</i>	4.5461	22.5209	2897.96
<i>1e</i>	4.1770	25.2955	6647.83
<i>1f</i>	3.3052	29.0074	2517.00
<i>2a</i>	2.0353	34.6991	924.64
<i>2b</i>	2.1741	39.2195	1193.24
<i>2c</i>	2.1506	41.8605	1350.64
<i>2d</i>	0.3112	36.6649	1477.00
<i>2e</i>	1.0138	42.5424	2538.06
<i>2f</i>	1.5845	49.9040	284.77

3.3. Lipinski's Rule of 5 and Bioactivity Scores

Lipinski's rule of 5, which is considered as a starting point in the design optimization process of small molecules having the potential to be drug-active compound, was studied for all structures. And, these rules are as follows [31,32];

- . Molecular mass less than 500 Dalton,
- . Less than 5 hydrogen bond donors,
- . Less than 10 hydrogen bond acceptors,
- . High lipophilicity (expressed as LogP) less than 5,
- . Molar refractivity should be between 40-130.

The results obtained for all structures are given in Table 3.

Table 3. The analysis "Lipinski's rule of 5" for the structures

Structures	MW	HBD	HBA	LogP	MR
<i>1a</i>	229	0	2	2.75	62.03
<i>1b</i>	225	0	2	2.92	66.81
<i>1c</i>	291	0	2	2.22	63.41
<i>1d</i>	227	1	3	2.31	63.74
<i>1e</i>	243	0	2	2.90	69.33
<i>1f</i>	267	0	2	3.90	80.77
<i>2a</i>	366	0	4	3.75	94.19
<i>2b</i>	358	0	4	4.09	103.75

2c	490	0	4	2.70	96.96
2d	362	2	6	2.88	97.61
2e	394	0	4	4.05	108.78
2f	442	0	4	6.06	131.68

MW: Molecular mass, **HBD:** Hydrogen bond donors, **HBA:** Hydrogen bond acceptors, **LogP:** Lipophilicity coefficient, **MR :** Molar refractivity.

According to these results; except for the fact that the *tert*-butyl derivative of the compound **2** (**2f**) has a slightly higher of the lipophilicity coefficient and the molar refractivity values, all the other structures are within the foreseen limits.

The activity scores of the GPCR ligand, ion channel modulator, nuclear receptor legend, kinase inhibitor, protease inhibitor, enzyme inhibitor were examined for all the structures.

The bioactivity scores of derivatives of the compound **1** and **2** were computed through Molinspiration software [33-35] accessed online and results are shown in Table 4.

Table 4. Bioactivity scores of the compound **1** and **2**

	GPCR	ICM	KI	NRL	PI	EI
1a	-0.34	-0.70	- 1.40	-0.41	- 0.81	- 0.41
1b	-0.36	-0.69	- 1.47	-0.47	- 0.83	- 0.44
1c	-0.50	-0.79	- 1.51	-0.61	- 0.94	- 0.49
1d	-0.11	-0.49	- 1.08	-0.08	- 0.50	- 0.26
1e	-0.37	-0.21	- 1.41	-0.44	- 0.84	- 0.04
1f	-0.42	-0.89	- 1.63	-0.64	- 0.67	- 0.33
2a	-0.02	-0.39	- 0.40	-0.07	- 0.13	- 0.17
2b	-0.03	-0.39	- 0.45	-0.11	- 0.15	- 0.19
2c	-0.12	-0.45	- 0.47	-0.20	- 0.21	- 0.23
2d	0.01	-0.27	- 0.35	0.01	- 0.09	- 0.12
2e	0.01	-0.34	- 0.39	0.04	- 0.10	- 0.11
2f	-0.07	-0.51	- 0.54	-0.22	- 0.04	- 0.12
Acivicin	-0.03	-0.03	- 1.17	-0.77	- 0.30	- 0.04

GPCR: GPCR ligand, **ICM:** ion channel modulator, **KI** :kinase inhibitör, **NRL:** nuclear receptor legend, **PI:** protease inhibitor, **EI:** enzyme inhibitör.

For organic molecules, if these bioactivity scores are >0 , they are active, $(-5.0-0.0)$ are moderately active, and <-5.0 are interpreted as inactive [40].

When the values of these parameters especially which are effective in cholesterol, heart, vascular diseases and cancer-derived diseases, were examined, it can be said that the derivatives of the compound **1** and **2** are moderately active. These parameters were also examined for the Acivicin molecule, which is used as an antitumor antibiotic and contains the isoxazole group, just like the compound **1** and **2** examined. According to the results obtained for bioinformatics purposes, hydroxyl- and thiol-bonded for compound **1**, hydroxyl-bonded groups for compound **2**, appear to be more likely drug-precursor compounds.

4. CONCLUSION

In this paper, the global reactivity properties of fluorine, chlorine, bromine, hydroxyl, thiol, *tert*-butyl-bonded derivatives of compounds having the norbornadiene skeleton were examined by the DFT/BPV86/B3LYP/B3PW91 methods with 6-31G(d,p) basis set. Chemical reactivity parameters such as ionization potential (I), electron affinity (A), electronegativity (χ), chemical hardness (η), chemical softness (S), chemical potential (μ) and electrophilicity index (ω) values were examined for all the structures. This analysis shows that the structures **1d** and **2d** have lower value of I , structures **1c** and **2b**, **2c** have higher value of A , more electronegativity of structures **1b**, **c** and **2b**, **c** structures, **1e**, **2e** have more soft molecule structure, structure **1b**, **c** and **2b**, **c** have more electrophilic character than the others. As can be seen in Figure 1-8, the B3LYP and B3PW91 functionals have given more similar results with respect to BPV86 functional. The parameters required to determine the non-linear optical behaviours of the structures were calculated at the theoretical level indicated. It has been observed that compounds **1e** and **2e**, i.e., thiol-bonded groups, have the potential to be a higher NLO material than others for every three functionals. In addition, the potentials of all the structures to be a drug-active compound was evaluated with the Lipinski's rule of 5 and some bioactivity scores. It can be said that the compounds have drug-likeness properties that they provide the five rules of Lipinski and exhibit moderate bioactive properties. As it is well known, molecular structures exhibiting high NLO behaviour, have

electron motions between donor-acceptor groups through the π -conjugated system. Aromatic-thiol-bonded structures with electron donor character having high first-order hyperpolarizability value and the smaller HOMO-LUMO gap ($\Delta E=4.50$ eV for 1e, $\Delta E=4.36$ eV for 2e) than others, with possible intramolecular charge transfer effect also given remarkable results in bioactivity scores values.

ACKNOWLEDGMENTS

This study was supported by Amasya University Scientific Research Foundation. Project Number: FMB-BAP 054/085.

REFERENCES

- [1] P. Hohenberg and W. Kohn. "Inhomogeneous electron gas." *Physical Review*, vol. 136, pp. B864-B871, 1964.
- [2] W. Kohn and L. J. Sham. "Self-Consistent Equations Including Exchange and Correlation Effects." *Physical Review*, vol. 140, pp. A1133-A1138, 1965.
- [3] R. G. Parr and W. Yang. "*Density-functional theory of atoms and molecules.*" Oxford Univ. Press, Oxford, UK, 1989.
- [4] W. Koch and M. C. Holthausen. "*A Chemist's Guide to Density Functional Theory.*" John Wiley & Sons, New York, 2001.
- [5] R. G. Parr and R. G. Pearson. "Absolute hardness: companion parameter to absolute electronegativity." *Journal of the American Chemical Society*, vol. 105, pp. 7512-7516, 1983.
- [6] P. Geerlings, F. De Proft and W. Langenaeker. "Conceptual Density Functional Theory." *Chemical Reviews*. vol. 103, pp. 1793-1873, 2003.
- [7] P. W. Ayers et al., "Fukui Function", in *Chemical Reactivity Theory, A Density Functional View*, P. K. Chattaraj Ed, New York, USA CRC Press, Taylor&Francis Group, 2009, pp. 255-265.
- [8] P. N. Prasad and D. J. Williams. "*Introduction to Nonlinear Optical Effects in Organic Molecules and Polymers*", New York, USA, Wiley, 1991, pp. 272-273.
- [9] J. Zyss and D. S. Chemla, "Quadratic Nonlinear Optics and Optimization of the Second Order Nonlinear, optical Response of Molecular Crystals", in *Nonlinear Optical Properties of Organic Molecules and Crystals*. D. S. Chemla and J. Zyss Eds., New York, USA, Academic Press, 1987. pp. 272-273
- [10] D. Sajan, D. H. Joe, V.S. Jayakumar and J. Zaleski. "Structural and Electronic Contributions to Hyperpolarizability in methyl p-hydroxy benzoate". *Journal of Molecular Structure*, vol.785, pp. 43-53, 2006.
- [11] H. P. Gümüş and Y. Atalay. "3-hidroksi-4-hidroksimiinometil-5-hidroksimetil-1, 2-dimetilpiridinyum iyodid molekülünün geometrik yapısının incelenmesi." *Sakarya Üniversitesi Fen Bilimleri Enstitüsü Dergisi*, vol. 21, no. 3, pp. 564-571, 2017.
- [12] Z. Zonghua, C. Debeng, W. Xiu and L. Deming. "Preparation and nonlinear optical properties of organic and polymeric materials." *Ferroelectrics*, vol.101, pp.141-142, 1990.
- [13] S. Eryılmaz, M. Gül, E. İnkaya, Ö. İdil and N. Özdemir. "Synthesis, crystal structure analysis, spectral characterization, quantum chemical calculations, antioxidant and antimicrobial activity of 3-(4-chlorophenyl)-3a, 4, 7, 7a-tetrahydro-4, 7-methanobenzo [d] isoxazole." *Journal of Molecular Structure*, vol. 1122, pp. 219-233, 2016.
- [14] K. Mesci, S. Eryılmaz, M. Gül and E. İnkaya. "The investigation of spectroscopic and theoretical methods of bisoxaoline derivative of norbornadiene." *Anadolu University of Sciences & Technology-A: Applied Sciences & Engineering*, vol. 17, no. 4, pp. 641-659, 2016.
- [15] S. H. Vosko, L. Wilk and M. Nusair. "Accurate spin-dependent electron liquid correlation energies for local spin density

- calculations: a critical analysis." *Canadian Journal of Physics*, vol. 58, no.8, pp. 1200-1211, 1980.
- [16] a) A. D. Becke. "Density-functional exchange-energy approximation with correct asymptotic behavior." *Journal of Chemical Physics*, vol. 38, pp. 3098-3100, 1988. b) A. D. Becke. "Density-Functional Thermochemistry. I. The Effect of the Exchange-Only Gradient Correction." *Journal of Chemical Physics*, vol. 96, pp. 2155-2160, 1992. c) A. D. Becke. "Density functional thermochemistry III. The role of exact exchange." *Journal of Chemical Physics*, vol. 98, pp. 5648-5652, 1993.
- [17] J. P. Perdew, K. Burke and Y. Wang. "Generalized gradient approximation for the exchange-correlation hole of a many-electron system." *Physical Review. B, Condensed Matter*, vol. 54, pp. 16533-16539, 1996.
- [18] M. J. Frisch, G. W. Trucks, H. B. Schlegel, G. E. Scuseria, M. A. Robb, J. R. Cheeseman, G. Scalmani, V. Barone, B. Mennucci, G. A. Petersson, H. Nakatsuji, M. Caricato, X. Li, H. P. Hratchian, A. F. Izmaylov, J. Bloino, G. Zheng, J. L. Sonnenberg, M. Hada, M. Ehara, K. Toyota, R. Fukuda, J. Hasegawa, M. Ishida, T. Nakajima, Y. Honda, O. Kitao, H. Nakai, T. Vreven, J. A. Montgomery, Jr., J. E. Peralta, F. Ogliaro, M. Bearpark, J. J. Heyd, E. Brothers, K. N. Kudin, V. N. Staroverov, R. Kobayashi, J. Normand, K. Raghavachari, A. Rendell, J. C. Burant, S. S. Iyengar, J. Tomasi, M. Cossi, N. Rega, J. M. Millam, M. Klene, J. E. Knox, J. B. Cross, V. Bakken, C. Adamo, J. Jaramillo, R. Gomperts, R. E. Stratmann, O. Yazyev, A. J. Austin, R. Cammi, C. Pomelli, J. W. Ochterski, R. L. Martin, K. Morokuma, V. G. Zakrzewski, G. A. Voth, P. Salvador, J. J. Dannenberg, S. Dapprich, A. D. Daniels, Ö. Farkas, J. B. Foresman, J. V. Ortiz, J. Cioslowski, and D. J. Fox, *Gaussian 09* (Gaussian, Inc., Wallingford CT, 2009).
- [19] GaussView, Version 5, R. Dennington, T. A. Keith and J. M. Millam, *Semichem Inc.*, Shawnee Mission, KS, 2009.
- [20] T. Koopmans. "Ordering of wave functions and eigenenergies to the individual electrons of an atom." *Physica*. vol.1, no.1, pp. 104-113, 1933.
- [21] R. G. Parr and R. G. Pearson. "Absolute hardness: companion parameter to absolute electronegativity." *Journal of the American Chemical Society*, vol.105, no.26, pp. 7512-7516, 1983.
- [22] R. S. Mulliken. "A new electron affinity scale; together with data on valence states and on valence ionization potentials and electron affinities." *The Journal of Chemical Physics*, vol. 2, no.11, pp. 782-793, 1934.
- [23] a) R. G. Pearson. "Hard and soft acids and bases." *Journal of the American Chemical Society*, vol. 85, no.22, pp. 3533-3539, 1963. b) R. G. Pearson. "Hard and soft acids and bases, HSAB, part 1: Fundamental principles." *Journal of Chemical Education*, vol. 45, no.9, p581, 1968. c) R. G. Pearson. "Maximum chemical and physical hardness." *Journal of Chemical Education*, vol. 76, no. 2, p267, 1999.
- [24] A. Vektariene, G. Vektaris and J. Svoboda. "A theoretical approach to the nucleophilic behavior of benzofused thieno [3, 2-b] furans using DFT and HF based reactivity descriptors." *Arkivoc: Online Journal of Organic Chemistry*, vol.vii, pp. 311-329, 2009.
- [25] R. G. Parr and R. G. Pearson. "Absolute hardness: companion parameter to absolute electronegativity." *Journal of the American Chemical Society*, vol. 105, no.26, pp. 7512-7516, 1983.
- [26] R. G. Pearson. "Absolute electronegativity and hardness correlated with molecular orbital theory." *Proceedings of the National Academy of Sciences*, vol. 83, no.22, pp. 8440-8441, 1986.
- [27] P. K. Chattaraj and D. R. Roy. "Update 1 of: Electrophilicity index." *Chemical Reviews*, vol. 107, no.9, pp PR46-PR74, 2007.
- [28] J. Hernández-Paredes, D. Glossman-Mitnik, A. Duarte-Moller and N. Flores-Holguín.

- “Theoretical calculations of molecular dipole moment, polarizability, and first hyperpolarizability of glycine–sodium nitrate.” *Journal of Molecular Structure: THEOCHEM*. vol. 905, no.1, pp. 76-80, 2009.
- [29] J. Prashanth, G. Ramesh, J. L. Naik, J. K. Ojha, B. V. Reddy and G. R. Rao. “Molecular Structure, Vibrational Analysis and First Order Hyperpolarizability of 4-Methyl-3-Nitrobenzoic Acid Using Density Functional Theory.” *Optics and Photonics Journal*. vol. 5, no. 03, p. 91, 2015.
- [30] a) D. A. Kleinman. “Nonlinear dielectric polarization in optical media.” *Physical Review*. vol. 126, no. 6, pp.1977-1979, 1962.
b) S. Ramalingam, M. Karabacak, S. Periandy, N. Puviarasan and D. Tanuja. “Spectroscopic (infrared, Raman, UV and NMR) analysis, Gaussian hybrid computational investigation (MEP maps/HOMO and LUMO) on cyclohexanone oxime.” *Spectrochimica Acta Part A: Molecular and Biomolecular Spectroscopy*. vol. 96, pp. 207-220, 2012.
- [31] C. A. Lipinski. “Lead-and drug-like compounds: the rule-of-five revolution.” *Drug Discovery Today: Technologies*. vol. 1, no.4, pp. 337-341, 2004.
- [32] B. Jayaram, T. Singh, G. Mukherjee, A. Mathur, S. Shekhar and V. Shekhar, "Sanjeevini: a freely accessible web-server for target directed lead molecule discovery", *BMC Bioinformatics*. vol. 13, S7, 2012.
- [33] P. Ertl, B. Rohde and P. Selzer. “Fast calculation of molecular polar surface area as a sum of fragment-based contributions and its application to the prediction of drug transport properties.” *Journal of Medicinal Chemistry*. vol. 43, pp. 3714-3717, 2000.
- [34] C. A. Lipinski, F. Lombardo, B. W. Dominy and P.J. Feeney. “Experimental and computational approaches to estimate solubility and permeability in drug discovery and development settings.” *Advanced Drug Delivery Reviews*. vol. 23, pp. 4-25, 1997.
- [35] D. F. Veber, S.R. Johnson, H.-Y. Cheng, B.R. Smith, K.W. Ward and K.D. Kopple. “Molecular properties that influence the oral bioavailability of drug candidates.” *Journal of Medicinal Chemistry*. vol.45, pp. 2615-2623, 2002.
- [36] C. G. Zhan, J. A. Nichols and D. A. Dixon, “Ionization potential, electron affinity, electronegativity, hardness, and electron excitation energy: molecular properties from density functional theory orbital energies.” *The Journal of Physical Chemistry A*. vol. 107, no. 20, pp. 4184-4195, 2003.
- [37] N. Günay, H. Pir and Y. Atalay.” L-asparaginyum pikrat molekülünün spektroskopik özelliklerinin teorik olarak incelenmesi.” *SAÜ Fen Edebiyat Dergisi*, vol.1, pp.15-32, 2011.
- [38] V. P. Gupta. *Principles and Applications of Quantum Chemistry*. Waltham, USA, Academic Press, 2015, pp. 430-431.
- [39] D. Pegu and N. B. Singh. “Quantum Chemical Calculations of Molecular Structure, Electronic, Thermodynamic and Non-linear optical properties of 2-amino-3-nitro-6-methyl pyridine.” *International Journal of Advanced Research*. vol. 1, no.9, 2013.
- [40] S. Singh, A. K. Gupta and A. Verma. “Molecular Properties and Bioactivity score of the Aloe vera antioxidant compounds – in order to lead finding” *Research Journal of Pharmaceutical, Biological and Chemical Sciences*. vol. 4, no.2, pp.876-81, 2013.

	SAKARYA ÜNİVERSİTESİ FEN BİLİMLERİ ENSTİTÜSÜ DERGİSİ <i>SAKARYA UNIVERSITY JOURNAL OF SCIENCE</i>		
	e-ISSN: 2147-835X Dergi sayfası: http://www.saujs.sakarya.edu.tr		
	<u>Received</u> 30-12-2017 <u>Accepted</u> 29-30-2018	<u>Doi</u> 10.16984/saufenbilder.373062	

Continuous Dependence For Benjamin-Bona-Mahony-Burger Equation

Zeynep Sümeyye Çelik^{*1}, Şevket Gür²

ABSTRACT

In this work, it is proved that the solutions of Benjamin-Bona-Mahony-Burger equation depends continuously on the coefficients.

Keywords: BBMB equation, continuous dependence.

1. INTRODUCTION

In this study, it is considered the following problem for the BBMB equation:

$$u_t - u_{xxt} - \alpha u_{xx} + \gamma u_x + f(u) = 0 \quad (1)$$

$$u(x, 0) = u_0(x), \quad x \in \Omega \quad (2)$$

$$u(x, t) = 0, \quad x \in \partial\Omega, \quad t > 0 \quad (3)$$

where $u(x, t)$ states the velocity of fluid, α is a positive number, γ is an arbitrary real number, $\Omega \subset \mathbb{R}^n$ is a bounded domain whose boundary $\partial\Omega$ and $f(u)$ is a C^2 -smooth nonlinear function which states

$$f(u)u \geq F(u) \geq 0 \quad (4)$$

$$|f(u) - f(v)| \leq K|u - v| \quad (5)$$

where $F(u) = \int_0^u f(s)ds$, K is a positive number, $f(u)$ provides Lipschitz inequality.

The models proposed for the mathematical expression of the basic laws of nature are often not

linear. Most of these models are based on nonlinear partial differential equations.

Pseudoparabolic problems emerge in the many areas of physics and mathematics such as consolidation of clay, long waves propagation with small amplitude, fluid flow of fissured rock and thermodynamics[1-5]. BBMB equation(1) is a special case of pseudoparabolic-type equations.

Continuous dependence on coefficients of solutions of partial differential equations is a kind of structural stability that reflects the influence of small changing on coefficient of the solutions of equations. In the recent years, many results of this type can be found in the literature[6-13].

In this paper the authors carried out on the continuous dependence of the coefficients on the BBMB equation solutions.

Throughout in paper, $\|\cdot\|$ and (\cdot, \cdot) state the norm and inner product $L^2(\Omega)$. $H_0^1(\Omega)$ is a Hilbert space.

* Corresponding Author

¹ Milli Eğitim Bakanlığı, Geyve Sinan Bey Mesleki ve Teknik Anadolu Lisesi, Geyve, Sakarya

² Sakarya Üniversitesi, Fen Edebiyat Fakültesi, Matematik Bölümü, Serdivan, Sakarya
zcelik370@gmail.com

2. A PRIORI ESTIMATE

In this chapter, it is got a priori estimate of (1)-(3).

Theorem 1. Let $u_0 \in H_0^1(\Omega)$. Under the assumption (4), if u is the solution of (1)-(3) problem, then the following estimate holds:

$$\|u_x\|^2 \leq D \quad (6)$$

where $D > 0$ which depending on the parameters of (1)-(3) problem.

Proof. If (1) is multiplied by u and integrated over Ω , then it is got

$$\frac{d}{dt} [E(t)] + \alpha \|u_x\|^2 + \int_{\Omega} uf(u)dx = 0 \quad (7)$$

where $E(t) = \frac{1}{2} \|u\|^2 + \frac{1}{2} \|u_x\|^2$. If (7) is integrated on the interval $(0, t)$ and from (4) it is got

$$\frac{1}{2} \|u\|^2 + \frac{1}{2} \|u_x\|^2 \leq E(0). \quad (8)$$

Hence (6) follow from (8).

3. CONTINUOUS DEPENDENCE ON PARAMETERS

In this chapter, it is proved that (1)-(3) problem solution is continuous dependence on the coefficient α and γ in $H_0^1(\Omega)$.

Now, it is supposed that u and v are respectively (9)-(10) problems solutions:

$$\begin{cases} u_t - u_{xxt} - \alpha_1 u_{xx} + \gamma u_x + f(u) = 0, \\ u(x, 0) = u_0(x), & x \in \Omega, \\ u(x, t) = 0, & x \in \partial\Omega, t > 0, \end{cases} \quad (9)$$

$$\begin{cases} v_t - v_{xxt} - \alpha_2 v_{xx} + \gamma v_x + f(v) = 0 \\ v(x, 0) = u_0(x), & x \in \Omega, \\ v(x, t) = 0 & x \in \partial\Omega, t > 0. \end{cases} \quad (10)$$

Let $u - v = w$ and $\alpha_1 - \alpha_2 = \alpha$. Then w is a solution of the problem

$$\begin{cases} w_t - w_{xxt} - \alpha w_{xx} - \alpha v_{xx} + \gamma w_x + f(u) - f(v) = 0, \\ w(x, 0) = 0, & x \in \Omega, \\ w(x, t) = 0, & x \in \partial\Omega, t > 0. \end{cases} \quad (11)$$

The following theorem states that (1)-(3) problem solution depends continuously on the coefficient α in $H_0^1(\Omega)$.

Theorem 2. Suppose that (5) holds. Let w be (11) problem solutions. Then w provides the inequality

$$\frac{1}{2} \|w\|^2 + \frac{1}{2} \|w_x\|^2 \leq \frac{D}{2} |\alpha_1 - \alpha_2|^2 e^{M_1 t} \quad (12)$$

where D and M_1 are positive constants.

Proof. If (11) is multiplied by w and integrated over Ω , it is got

$$\frac{d}{dt} \left[\frac{1}{2} \|w\|^2 + \frac{1}{2} \|w_x\|^2 \right] + \alpha_1 \|w_x\|^2 + \alpha (w_x, v_x) + \int_{\Omega} (f(u) - f(v))w dx = 0. \quad (13)$$

If (5) and Cauchy-Schwarz inequality are used in (13), it is got

$$\frac{d}{dt} \left[\frac{1}{2} \|w\|^2 + \frac{1}{2} \|w_x\|^2 \right] \leq |\alpha| \|w_x\| \|v_x\| + K \|w\|^2. \quad (14)$$

If arithmetic-geometric mean inequality is used in (14), it is had

$$\frac{d}{dt} E_1(t) \leq M_1 E_1(t) + \frac{|\alpha|^2}{2} \|v_x\|^2 \quad (15)$$

where $E_1(t) = \frac{1}{2} \|w\|^2 + \frac{1}{2} \|w_x\|^2$ and $M_1 = \max\{1, 2K\}$. If Gronwall inequality and (6) are used in (15), it is obtained

$$E_1(t) \leq \frac{D_1}{2} |\alpha|^2 e^{M_1 t}. \quad (16)$$

Hence the proof is completed.

Finally, it is proved that the (1)-(3) problem solution depends continuously on the coefficient γ .

Now, it is supposed that u and v are respectively (17)-(18) problems solutions:

$$\begin{cases} u_t - u_{xxt} - \alpha u_{xx} + \gamma_1 u_x + f(u) = 0, \\ u(x, 0) = u_0(x), & x \in \Omega, \\ u(x, t) = 0, & x \in \partial\Omega, t > 0, \end{cases} \quad (17)$$

$$\begin{cases} v_t - v_{xxt} - \alpha v_{xx} + \gamma_2 v_x + f(v) = 0, \\ v(x, 0) = u_0(x), & x \in \Omega, \\ v(x, t) = 0, & x \in \partial\Omega, t > 0. \end{cases} \quad (18)$$

Let $u - v = w$ and $\gamma_1 - \gamma_2 = \gamma$. Then w is a solution of the problem

$$\begin{cases} w_t - w_{xxt} - \alpha w_{xx} + \gamma_1 w_x + \gamma v_x + f(u) - f(v) = 0, \\ w(x, 0) = 0, & x \in \Omega, \\ w(x, t) = 0, & x \in \partial\Omega, t > 0. \end{cases} \quad (19)$$

The following theorem is the main result of this section.

Theorem 3. Suppose that (5) holds. Let w be (19) problem solution. Then w provides the inequality

$$\frac{1}{2} \|w\|^2 + \frac{1}{2} \|w_x\|^2 \leq \frac{D}{2} |\gamma_1 - \gamma_2|^2 e^{M_2 t} \quad (20)$$

where D and M_2 are positive constants.

Proof. If (19) is multiplied by w and integrated over Ω , we have

$$\frac{d}{dt} \left[\frac{1}{2} \|w\|^2 + \frac{1}{2} \|w_x\|^2 \right] + \alpha \|w_x\|^2 - \gamma(v, w_x) + \int_{\Omega} (f(u) - f(v)) w dx = 0. \quad (21)$$

If (5) and Cauchy-Schwarz inequality are used in (21), it is got

$$\frac{d}{dt} \left[\frac{1}{2} \|w\|^2 + \frac{1}{2} \|w_x\|^2 \right] \leq |\gamma| \|v\| \|w_x\| + K \|w\|^2. \quad (22)$$

If arithmetic-geometric mean inequality is used in (22), it is had

$$\frac{d}{dt} E_2(t) \leq M E_2(t) + \frac{|\gamma|^2}{2} \|v\|^2 \quad (23)$$

where $E_2(t) = \frac{1}{2} \|w\|^2 + \frac{1}{2} \|w_x\|^2$ and

$M_2 = \max\{1, 2K\}$. If Gronwall inequality and (6) are used in (23), it is obtained

$$E_2(t) \leq \frac{D}{2} |\gamma|^2 e^{M_2 t}. \quad (24)$$

Hence the proof is completed.

REFERENCES

- [1] Quarteroni, A.: Fourier spectral methods for pseudo-parabolic equations. *SIAM J. Numer. Anal.* 24(2), 323-335 (1987)
- [2] Karch, G.: Asymptotic behaviour of solutions to some pseudoparabolic equations. *Math. Methods Appl. Sci.* 20,271-289 (1997)
- [3] Kaikina, E.I., Naumkin, P.I., Shishmarev, I.A.: The Cauchy problem for an equation of Sobolev type with power non-linearity. *Izv. Math.* 69(1), 59-111 (2005)
- [4] Korpusov, M.O., Sveshnikov, A.G.: Blow-up of solutions of strongly nonlinear equations of pseudoparabolic type. *J. Math. Sci.* 148(1), 1-142 (2008)
- [5] Dubey, S.A.: Numerical solution for nonlocal Sobolev-type differential equations. *Electron. J. Differ. Equ. Conf.* 19, 75-83(2010)
- [6] Franchi, F., Straughan, B.: Continuous dependence and decay for the Forchheimer equations. *Proc. R. Soc. Lond. Ser. A* 459, 3195-3202 (2003)
- [7] Lin, C., Payne, L.E.: Continuous dependence of heatux on spatial geometry for the generalized Maxwell-Cattaneo system. *Z. Angew. Math. Phys.* 55, 575-591 (2004)
- [8] Celebi, A.O., Kalantarov, V.K., Ugurlu, D.: Continuous dependence for the convective Brinkman-Forchheimer equations *Appl. Anal.* 84 (9), 877-888 (2005)
- [9] Celebi, A.O., Kalantarov, V.K, Ugurlu, D.: On continuous dependence on coefficients of the Brinkman-Forchheimer equations. *Appl. Math. Lett.*, 19, 801-807 (2006)
- [10] Yaman, M., Gür, Ş.: Continuous dependence for the pseudoparabolic equation. *Boundary Value Problem*, Art. ID 872572 (2010)
- [11] Straughan, B.: Continuous dependence on the heat source in resonant porous penetrative convection. *Stud. Appl. Math.* 127, 302-314 (2011)
- [12] Yaman, M., Gür, Ş.: Continuous dependence for the damped nonlinear hyperbolic equation. *Math. Comput. Appl.* 16 (2), 437-442 (2011)
- [13] Li, Y., Lin, C.: Continuous dependence for the nonhomogeneous Brinkman-Forchheimer equations in a semi-infinte pipe. *Appl. Mathematics and Computation* 244, 201-208 (2014)

	SAKARYA ÜNİVERSİTESİ FEN BİLİMLERİ ENSTİTÜSÜ DERGİSİ <i>SAKARYA UNIVERSITY JOURNAL OF SCIENCE</i>		
	e-ISSN: 2147-835X Dergi sayfası: http://www.saujs.sakarya.edu.tr		
	<u>Received</u> 19-03-2018 <u>Accepted</u> 05-04-2018	<u>Doi</u> 10.16984/saufenbilder.407581	

Description of Maximally Dissipative Quasi-Differential Operators for First Order

Pembe Ipek Al*¹

ABSTRACT

In this work, the general form of maximally dissipative extensions of the minimal operator generated by first order linear symmetric quasi-differential expression in the weighted Hilbert space of vector-functions at right semi-infinite interval has been found. Later on, the geometry of spectrum of these extensions is investigated.

Keywords: deficiency indices, space of boundary values, dissipative operator, spectrum

1. INTRODUCTION

It is known that a linear closed densely defined operator $T: D(T) \subset H \rightarrow H$ in Hilbert space H is said to be dissipative if and only if

$$\text{Im}(Tx, x) \geq 0$$

for all $x \in D(T)$, i.e. in other words its numerical range is contained in the upper complex plane. Moreover, it is called maximally dissipative if it has no non-trivial dissipative extension [1]. Maximally dissipative operators play a very important role in mathematics and physics. Dissipative operators have many interesting applications in physics like hydrodynamic, laser and nuclear scattering theories.

Note that the study of abstract extension problems for operators on Hilbert spaces goes at least back to J.von Neumann [2] such that in [2] a full characterization of all selfadjoint extensions of a

given closed symmetric operator with equal defect indices was investigated.

The further investigations of M. I. Vishik and M. S. Birman devoted to characterization of all non-negative selfadjoint extensions of a positive closed symmetric operator (see [3]). And more general informations can be found in [3]. Class of dissipative operators is an important class of nonselfadjoint operators in the operator theory. Functional model theory of B. Sz.-Nagy and C. Foias [4] is a basic method for investigation the spectral properties of dissipative operators. Note that spectrum set of the dissipative operator lies in closed upper half-pane.

The maximal dissipative extensions and their spectral analysis of the minimal operator having equal deficiency indices generated by formally symmetric differential-operator expression in the Hilbert space of vector-functions defined in one finite or infinite interval case have been researched by V. I. Gorbachuk, M. I. Gorbachuk [1] and F. S.

* Pembe Ipek Al

¹ Karadeniz Technical University, Institute of Natural Sciences, 61080, Trabzon, Turkey, ipekpeembe@gmail.com

Rofe-Beketov, A. M. Kholkin [5] in terms of generalized boundary values.

In this work using the Calkin-Gorbachuk method representation of all maximally dissipative extensions of the minimal operator generated by first order linear symmetric quasi-differential expression with operator coefficient in the weighted Hilbert spaces of vector-functions defined in the right semi-infinite interval case is given (section 3). In section 4 the structure of spectrum of these type extensions is investigated.

2. STATEMENT OF THE PROBLEM

Let H be a separable Hilbert space and $a \in \mathbb{R}$. In addition assumed that $\alpha, w : (a, \infty) \rightarrow (0, \infty), \alpha, w \in C(a, \infty)$ and $\frac{w}{\alpha^2} \in L^1(a, \infty)$. In the weighted Hilbert space $L_w^2(H, (a, \infty))$ of vector-functions consider the following linear quasi-differential expression with operator coefficient for first order in form

$$l(u) = i \frac{\alpha(t)}{w(t)} (\alpha u)'(t) + Au(t),$$

where A is a linear bounded selfadjoint operator in H . And also the operator E will be indicated identify operator in corresponding spaces.

By a standard way the minimal L_0 corresponding to quasi-differential expression $l(\cdot)$ in $L_w^2(H, (a, \infty))$ can be defined (see [6]). The operator $L = (L_0)^*$ is called maximal operator corresponding to $l(\cdot)$ in $L_w^2(H, (a, \infty))$.

In this case it will be shown that the minimal operator is symmetric and it has non zero equal deficiency indices in $L_w^2(H, (a, \infty))$ (see section 3).

In this work, firstly the representation of all maximally dissipative extensions of the minimal operator L_0 in $L_w^2(H, (a, \infty))$ is investigated. Later on, structure of the spectrum of these extensions will be investigated.

3. DESCRIPTION OF MAXIMALLY DISSIPATIVE EXTENSIONS

In this section using the Calkin-Gorbachuk method will be investigated the general representation of all maximally dissipative extensions of the minimal operator L_0 in $L_w^2(H, (a, \infty))$.

Before of all prove the following proposition.

Lemma 3.1 If \tilde{L} is any maximally dissipative extension of the minimal operator L_0 in $L_w^2(H, (a, \infty))$, then for every function $u \in D(\tilde{L})$ exist the boundary values $(\alpha u)(a)$ and $(\alpha u)(\infty)$ in H .

Proof. In this case for any $u \in D(\tilde{L})$ we have

$$\begin{aligned} \tilde{L} u(t) &= i \frac{\alpha(t)}{w(t)} (\alpha u)'(t) + Au(t) \\ &\in L_w^2(H, (a, \infty)). \end{aligned}$$

From these relations it is implies that $\frac{\alpha}{w} (\alpha u)' \in L_w^2(H, (a, \infty))$.

Now before of all it will be shown that the integrals

$$\int_t^c (\alpha u)'(x) dx, \quad a \leq t < c$$

and

$$\int_c^t (\alpha u)'(x) dx, \quad a < c < t \leq \infty$$

exist. Indeed, the following expressions are implemented, respectively, for any $a \leq t < c$

$$\begin{aligned} \int_t^c |(\alpha u)'(x)| dx &= \int_t^c \left| \frac{\alpha}{w} (\alpha u)' \sqrt{w} \frac{\sqrt{w}}{\alpha} \right| (x) dx \\ &\leq \left(\int_t^c \left| \frac{\alpha}{w} (\alpha u)' \right|^2 (x) w(x) dx \right)^{1/2} \left(\int_t^c \frac{w(x)}{\alpha^2(x)} dx \right)^{1/2} \\ &\leq \left(\int_a^\infty \left| \frac{\alpha}{w} (\alpha u)' \right|^2 (x) w(x) dx \right)^{1/2} \left(\int_a^\infty \frac{w(x)}{\alpha^2(x)} dx \right)^{1/2} \\ &< \infty \end{aligned}$$

and for $a < c < t \leq \infty$

$$\int_c^t |(\alpha u)'(x)| dx = \int_c^t \left| \frac{\alpha}{w} (\alpha u)' \sqrt{w} \frac{\sqrt{w}}{\alpha} \right| (x) dx$$

$$\begin{aligned} &\leq \left(\int_c^t \left| \frac{\alpha}{w} (\alpha u)' \right|^2 (x) w(x) dx \right)^{1/2} \left(\int_c^t \frac{w(x)}{\alpha^2(x)} dx \right)^{1/2} \left| \int_c^t (\alpha u)'(x) dx - \int_c^\infty (\alpha u)'(x) dx \right| \\ &\leq \left(\int_a^\infty \left| \frac{\alpha}{w} (\alpha u)' \right|^2 (x) w(x) dx \right)^{1/2} \left(\int_a^\infty \frac{w(x)}{\alpha^2(x)} dx \right)^{1/2} \leq \int_t^\infty |(\alpha u)'(x)| dx \\ &< \infty. \end{aligned}$$

Then for $a \leq t < c$ from the following equality

$$(\alpha u)(c) - (\alpha u)(t) = \int_t^c (\alpha u)'(x) dx$$

and the relation

$$\begin{aligned} &\left| \int_t^c (\alpha u)'(x) dx - \int_a^c (\alpha u)'(x) dx \right| \\ &= \left| \int_a^t (\alpha u)'(x) dx \right| \\ &\leq \int_a^t |(\alpha u)'(x)| dx \\ &\leq \left(\int_a^t \left| \frac{\alpha}{w} (\alpha u)' \right|^2 (x) w(x) dx \right)^{1/2} \left(\int_a^t \frac{w(x)}{\alpha^2(x)} dx \right)^{1/2} \end{aligned}$$

$\rightarrow 0, t \rightarrow a + 0$

it is obtained that

$$\lim_{t \rightarrow a+0} \int_t^c (\alpha u)'(x) dx$$

exists. Then

$$\begin{aligned} \lim_{t \rightarrow a+0} (\alpha u)(t) &= (\alpha u)(c) \\ &+ \lim_{t \rightarrow a+0} \int_t^c (\alpha u)'(x) dx. \end{aligned}$$

In the similar way for $a < c < t \leq \infty$ from equality

$$(\alpha u)(t) - (\alpha u)(c) = \int_c^t (\alpha u)'(x) dx$$

and

$\rightarrow 0, t \rightarrow \infty$

we have existence of the following limit

$$\lim_{t \rightarrow \infty} \int_c^t (\alpha u)'(x) dx.$$

Consequently for any $c \in (a, \infty)$,

$$\begin{aligned} \lim_{t \rightarrow \infty} (\alpha u)(t) &= (\alpha u)(c) \\ &+ \lim_{t \rightarrow \infty} \int_c^t (\alpha u)'(x) dx. \end{aligned}$$

Hence the proof of theorem is completed.

Lemma 3.2 The deficiency indices of the minimal operator L_0 in $L_w^2(H, (a, \infty))$ are in form

$$(n_+(L_0), n_-(L_0)) = (\dim H, \dim H).$$

Proof. For the simplicity of calculations it will be taken $A = 0$. It is clear that the general solutions of differential equations

$$i \frac{\alpha(t)}{w(t)} (\alpha u_\pm)'(t) \pm i u_\pm(t) = 0, t > a$$

in $L_w^2(H, (a, \infty))$ are in form

$$\begin{aligned} u_\pm(t) &= \frac{1}{\alpha(t)} \exp\left(\mp \int_a^t \frac{w(s)}{\alpha^2(s)} ds\right) f, \\ &f \in H, t > a. \end{aligned}$$

From these representations we have

$$\begin{aligned} \|u_+\|_{L_w^2(H,(a,\infty))}^2 &= \int_a^\infty w(t) \|u_+(t)\|_H^2 dt \\ &= \int_a^\infty w(t) \left\| \frac{1}{\alpha(t)} \exp\left(-\int_a^t \frac{w(s)}{\alpha^2(s)} ds\right) f \right\|_H^2 dt \\ &= \int_a^\infty \frac{w(t)}{\alpha^2(t)} \exp\left(-2\int_a^t \frac{w(s)}{\alpha^2(s)} ds\right) dt \|f\|_H^2 \\ &= \int_a^\infty \exp\left(-2\int_a^t \frac{w(s)}{\alpha^2(s)} ds\right) d\left(\int_a^t \frac{w(s)}{\alpha^2(s)} ds\right) \|f\|_H^2 \\ &= \frac{1}{2} \left(1 - \exp\left(-2\int_a^\infty \frac{w(s)}{\alpha^2(s)} ds\right)\right) \|f\|_H^2 < \infty. \end{aligned}$$

Hence

$$n_+(L_0) = \dim \ker(L + iE) = \dim H.$$

On the other hand it is clear that

$$\begin{aligned} \|u_-\|_{L_w^2(H,(a,\infty))}^2 &= \int_a^\infty w(t) \|u_-(t)\|_H^2 dt \\ &= \int_a^\infty \frac{w(t)}{\alpha^2(t)} \exp\left(2\int_a^t \frac{w(s)}{\alpha^2(s)} ds\right) dt \|f\|_H^2 \\ &= \int_a^\infty \exp\left(2\int_a^t \frac{w(s)}{\alpha^2(s)} ds\right) d\left(\int_a^t \frac{w(s)}{\alpha^2(s)} ds\right) \|f\|_H^2 \\ &= \frac{1}{2} \left(\exp\left(2\int_a^\infty \frac{w(s)}{\alpha^2(s)} ds\right) - 1\right) \|f\|_H^2 < \infty. \end{aligned}$$

Then we obtain

$$n_-(L_0) = \dim \ker(L - iE) = \dim H.$$

This completes the proof.

Consequently, the minimal operator has a maximally dissipative extension (see [1]).

In order to describe these extensions we need to obtain the space of boundary values.

Definition 3.3 [1] Let \mathcal{H} be any Hilbert space and $S: D(S) \subset \mathcal{H} \rightarrow \mathcal{H}$ be a closed densely defined symmetric operator in the Hilbert space \mathcal{H} having equal finite or infinite deficiency indices. A triplet $(\mathbf{H}, \gamma_1, \gamma_2)$ where \mathbf{H} is a Hilbert space, γ_1 and γ_2 are linear mappings from $D(S^*)$ into \mathbf{H} , is called a space of boundary values for the operator S if for any $f, g \in D(S^*)$

$$\begin{aligned} (S^*f, g)_{\mathcal{H}} - (f, S^*g)_{\mathcal{H}} &= (\gamma_1(f), \gamma_2(g))_{\mathbf{H}} \\ &\quad - (\gamma_2(f), \gamma_1(g))_{\mathbf{H}} \end{aligned}$$

while for any $F_1, F_2 \in \mathbf{H}$, there exists an element $f \in D(S^*)$ such that $\gamma_1(f) = F_1$ and $\gamma_2(f) = F_2$.

Lemma 3.4 The triplet (H, γ_1, γ_2) ,

$$\gamma_1: D(L) \rightarrow H, \gamma_1(u) = \frac{1}{\sqrt{2}}((\alpha u)(\infty) - (\alpha u)(a))$$

$$\begin{aligned} \gamma_2: D(L) \rightarrow H, \gamma_2(u) &= \frac{1}{i\sqrt{2}}((\alpha u)(\infty) \\ &\quad + (\alpha u)(a)), u \in D(L) \end{aligned}$$

is a space of boundary values of the minimal operator L_0 in $L_w^2(H, (a, \infty))$.

Proof. For any $u, v \in D(L)$,

$$\begin{aligned} (Lu, v)_{L_w^2(H,(a,\infty))} - (u, Lv)_{L_w^2(H,(a,\infty))} &= \left(i \frac{\alpha}{w} (\alpha u)' + Au, v\right)_{L_w^2(H,(a,\infty))} \\ &\quad - \left(u, i \frac{\alpha}{w} (\alpha v)' + Av\right)_{L_w^2(H,(a,\infty))} \\ &= \left(i \frac{\alpha}{w} (\alpha u)', v\right)_{L_w^2(H,(a,\infty))} \\ &\quad - \left(u, i \frac{\alpha}{w} (\alpha v)'\right)_{L_w^2(H,(a,\infty))} \\ &= \int_a^\infty \left(i \frac{\alpha(t)}{w(t)} (\alpha u)'(t), v(t)\right)_H w(t) dt \\ &\quad - \int_a^\infty \left(u(t), i \frac{\alpha(t)}{w(t)} (\alpha v)'(t)\right)_H w(t) dt \\ &= i \left[\int_a^\infty ((\alpha u)'(t), (\alpha v)(t))_H dt \right. \\ &\quad \left. + \int_a^\infty ((\alpha u)(t), (\alpha v)'(t))_H dt \right] \end{aligned}$$

$$\begin{aligned}
 &= i \int_a^\infty ((\alpha u)(t), (\alpha v)(t))'_H dt \\
 &= i \left[((\alpha u)(\infty), (\alpha v)(\infty))_H \right. \\
 &\quad \left. - ((\alpha u)(a), (\alpha v)(a))_H \right] \\
 &= (\gamma_1(u), \gamma_2(v))_H - (\gamma_2(u), \gamma_1(v))_H.
 \end{aligned}$$

Now for any given element $f, g \in H$ find the function $u \in D(L)$ such that

$$\gamma_1(u) = \frac{1}{\sqrt{2}}((\alpha u)(\infty) - (\alpha u)(a)) = f$$

and

$$\gamma_2(u) = \frac{1}{i\sqrt{2}}((\alpha u)(\infty) + (\alpha u)(a)) = g.$$

From this it is obtained that

$$(\alpha u)(\infty) = (ig + f)/\sqrt{2}$$

and

$$(\alpha u)(a) = (ig - f)/\sqrt{2}.$$

If we choose the function $u(\cdot)$ in following form

$$\begin{aligned}
 u(t) &= \frac{1}{\alpha(t)}(1 - e^{a-t}) (ig + f)/\sqrt{2} \\
 &\quad + \frac{1}{\alpha(t)}e^{a-t} (ig - f)/\sqrt{2},
 \end{aligned}$$

then it is clear that $u \in D(L)$ and $\gamma_1(u) = f, \gamma_2(u) = g$.

Hence the lemma is proof.

By using the method in [1] it can be established the following result.

Theorem 3.5 If \tilde{L} is a maximally dissipative extension of the minimal operator L_0 in $L^2_w(H, (a, \infty))$, then it is generated by the differential-operator expression $l(\cdot)$ and boundary condition

$$(\alpha u)(a) = K(\alpha u)(\infty),$$

where $K: H \rightarrow H$ is contraction operator. Moreover, the contraction operator K in H is determined uniquely by the extension \tilde{L} , i.e. $\tilde{L} = L_K$ and vice versa.

Proof. It is known that each maximally dissipative extension \tilde{L} of the minimal operator L_0 is described by differential-operator expression $l(\cdot)$ with boundary condition

$$(V - E)\gamma_1(u) + i(V + E)\gamma_2(u) = 0,$$

where $V: H \rightarrow H$ is a contraction operator. Therefore from Lemma 3.4 we obtain that

$$\begin{aligned}
 &(V - E)((\alpha u)(\infty) - (\alpha u)(a)) \\
 &+ (V + E)((\alpha u)(\infty) + (\alpha u)(a)) = 0, \\
 &u \in D(\tilde{L}).
 \end{aligned}$$

From this it is implies that

$$(\alpha u)(a) = -V(\alpha u)(\infty).$$

Choosing $K = -V$ in last boundary condition we have

$$(\alpha u)(a) = K(\alpha u)(\infty).$$

4. THE SPECTRUM OF THE MAXIMALLY DISSIPATIVE EXTENSIONS

In this section the structure of the spectrum of the maximally dissipative extensions of the minimal operator L_0 in $L^2_w(H, (a, \infty))$ will be investigated.

Theorem 4.1 The spectrum of any maximally dissipative extension L_K is in the form

$$\begin{aligned}
 \sigma(L_K) &= \left\{ \lambda \in \mathbb{C}: \lambda = \left(\int_a^\infty \frac{w(s)}{\alpha^2(s)} ds \right)^{-1} \right. \\
 &\quad \times (i \ln|\mu|^{-1} + \arg \mu + 2n\pi) \\
 &\quad \left. \mu \in \sigma \left(K \exp \left(iA \int_a^\infty \frac{w(s)}{\alpha^2(s)} ds \right) \right), n \in \mathbb{Z} \right\}
 \end{aligned}$$

Proof. Consider the following problem to spectrum for the extension L_K , i.e.

$$\begin{aligned}
 L_K(u) &= \lambda u + f, f \in L^2_w(H, (a, \infty)), \\
 \lambda &\in \mathbb{C}, \lambda_i = \text{Im} \lambda \geq 0.
 \end{aligned}$$

Then we have

$$i \frac{\alpha(t)}{w(t)} (\alpha u)'(t) + Au(t) = \lambda u(t) + f(t), t > a,$$

$$(\alpha u)(a) = K(\alpha u)(\infty).$$

The general solution of the last differential equation, i.e.,

$$\begin{aligned}
 (\alpha u)'(t) &= i \frac{w(t)}{\alpha^2(t)} (A - \lambda E)(\alpha u)(t) \\
 &\quad - i \frac{w(t)}{\alpha(t)} f(t)
 \end{aligned}$$

is in form

$$u(t; \lambda) = \frac{1}{\alpha(t)} \exp\left(i(A - \lambda E) \int_a^t \frac{w(s)}{\alpha^2(s)} ds\right) f_\lambda + \frac{i}{\alpha(t)} \int_t^\infty \exp\left(i(A - \lambda E) \int_s^t \frac{w(\tau)}{\alpha^2(\tau)} d\tau\right) \times \frac{w(s)}{\alpha(s)} f(s) ds, f_\lambda \in H, t > a.$$

$$= \int_a^\infty \left\| \frac{i}{\alpha(t)} \int_t^\infty \exp\left(i(A - \lambda E) \int_s^t \frac{w(\tau)}{\alpha^2(\tau)} d\tau\right) \frac{w(s)}{\alpha(s)} f(s) ds \right\|_H^2 w(t) dt$$

In this case

$$\left\| \frac{1}{\alpha(t)} \exp\left(i(A - \lambda E) \int_a^t \frac{w(s)}{\alpha^2(s)} ds\right) f_\lambda \right\|_{L_w^2(H, (a, \infty))}^2$$

$$= \int_a^\infty \left\| \frac{1}{\alpha(t)} \exp\left(i(A - \lambda E) \int_a^t \frac{w(s)}{\alpha^2(s)} ds\right) f_\lambda \right\|_H^2 w(t) dt$$

$$= \int_a^\infty \frac{w(t)}{\alpha^2(t)} \exp\left(2\lambda_i \int_a^t \frac{w(s)}{\alpha^2(s)} ds\right) dt \|f_\lambda\|_H^2$$

$$= \int_a^\infty \exp\left(2\lambda_i \int_a^t \frac{w(s)}{\alpha^2(s)} ds\right) d\left(\int_a^t \frac{w(s)}{\alpha^2(s)} ds\right) \|f_\lambda\|_H^2$$

$$= \frac{1}{2\lambda_i} \left(\exp\left(2\lambda_i \int_a^\infty \frac{w(s)}{\alpha^2(s)} ds\right) - 1 \right) \|f_\lambda\|_H^2$$

< ∞

and

$$\left\| \frac{i}{\alpha(t)} \int_t^\infty \exp\left(i(A - \lambda E) \int_s^t \frac{w(\tau)}{\alpha^2(\tau)} d\tau\right) \frac{w(s)}{\alpha(s)} f(s) ds \right\|_{L_w^2(H, (a, \infty))}^2$$

$$\leq \int_a^\infty \frac{w(t)}{\alpha^2(t)} \left(\int_t^\infty \exp\left(\lambda_i \int_s^t \frac{w(\tau)}{\alpha^2(\tau)} d\tau\right) \times \frac{w(s)}{\alpha(s)} \|f(s)\|_H ds \right)^2 dt$$

$$\leq \int_a^\infty \frac{w(t)}{\alpha^2(t)} \left(\int_t^\infty \frac{\sqrt{w(s)}}{\alpha(s)} \exp\left(\lambda_i \int_s^t \frac{w(\tau)}{\alpha^2(\tau)} d\tau\right) \times \|\sqrt{w(s)} f(s)\|_H ds \right)^2 dt$$

$$\leq \int_a^\infty \frac{w(t)}{\alpha^2(t)} \left(\int_t^\infty \frac{w(s)}{\alpha^2(s)} \exp\left(2\lambda_i \int_s^t \frac{w(\tau)}{\alpha^2(\tau)} d\tau\right) ds \right) \times \left(\int_t^\infty w(s) \|f(s)\|_H^2 ds \right) dt$$

$$\leq \int_a^\infty \frac{w(t)}{\alpha^2(t)} \left(\int_a^\infty \frac{w(s)}{\alpha^2(s)} \exp\left(2\lambda_i \int_s^t \frac{w(\tau)}{\alpha^2(\tau)} d\tau\right) ds \right) dt \times \|f\|_{L_w^2(H, (a, \infty))}^2$$

$$= \frac{1}{2\lambda_i} \int_a^\infty \frac{w(t)}{\alpha^2(t)} \left(\exp\left(2\lambda_i \int_a^t \frac{w(\tau)}{\alpha^2(\tau)} d\tau\right) - \exp\left(-2\lambda_i \int_t^\infty \frac{w(\tau)}{\alpha^2(\tau)} d\tau\right) \right) dt \|f\|_{L_w^2(H, (a, \infty))}^2$$

$$= \frac{1}{4\lambda_i^2} \left(\exp\left(2\lambda_i \int_a^\infty \frac{w(\tau)}{\alpha^2(\tau)} d\tau\right) + \exp\left(-2\lambda_i \int_a^\infty \frac{w(\tau)}{\alpha^2(\tau)} d\tau\right) - 2 \right) \|f\|_{L_w^2(H, (a, \infty))}^2 < \infty.$$

Hence, for $\lambda \in \mathbb{C}, \lambda_i = \text{Im} \lambda \geq 0,$
 $u(\cdot, \lambda) \in L_w^2(H, (a, \infty)).$

From this and boundary condition we have

$$\begin{aligned} & \left(E - K \exp \left(i(A - \lambda E) \int_a^\infty \frac{w(s)}{\alpha^2(s)} ds \right) \right) f_\lambda \\ &= -i \int_a^\infty \exp \left(i(A - \lambda E) \int_s^a \frac{w(\tau)}{\alpha^2(\tau)} d\tau \right) \\ & \quad \times \frac{w(s)}{\alpha(s)} f(s) ds \end{aligned}$$

that is,

$$\begin{aligned} & \left(\exp \left(i\lambda \int_a^\infty \frac{w(s)}{\alpha^2(s)} ds \right) E \right. \\ & \left. - K \exp \left(iA \int_a^\infty \frac{w(s)}{\alpha^2(s)} ds \right) \right) f_\lambda \\ &= -i \exp \left(i\lambda \int_a^\infty \frac{w(s)}{\alpha^2(s)} ds \right) \\ & \quad \times \int_a^\infty \exp \left(i(A - \lambda E) \int_s^a \frac{w(\tau)}{\alpha^2(\tau)} d\tau \right) \frac{w(s)}{\alpha(s)} f(s) ds. \end{aligned}$$

Therefore in order to $\lambda \in \sigma(L_K)$ the necessary and sufficient condition is

$$\begin{aligned} & \exp \left(i\lambda \int_a^\infty \frac{w(s)}{\alpha^2(s)} ds \right) = \mu \\ & \in \sigma \left(K \exp \left(iA \int_a^\infty \frac{w(s)}{\alpha^2(s)} ds \right) \right). \end{aligned}$$

Consequently,

$$\lambda \int_a^\infty \frac{w(s)}{\alpha^2(s)} ds = i \ln |\mu|^{-1} + \arg \mu + 2n\pi, n \in \mathbb{Z}.$$

On the other hand since $\int_a^\infty \frac{w(s)}{\alpha^2(s)} ds > 0$, then

$$\lambda = \left(\int_a^\infty \frac{w(s)}{\alpha^2(s)} ds \right)^{-1} (i \ln |\mu|^{-1} + \arg \mu + 2n\pi),$$

$$\mu \in \sigma \left(K \exp \left(iA \int_a^\infty \frac{w(s)}{\alpha^2(s)} ds \right) \right), n \in \mathbb{Z}.$$

This completes proof of theorem.

Corollary 4.2 If L_K is any maximally dissipative extension of the minimal operator L_0 and

$$\sigma \left(K \exp \left(iA \int_a^\infty \frac{w(s)}{\alpha^2(s)} ds \right) \right) = \{0\},$$

then $\sigma(L_K) = \emptyset$.

Example 4.3 All maximally dissipative extensions L_r of the minimal operator L_0 generated by the following first order linear symmetric singular quasi-differential expression

$$l(u) = it^{\gamma-\tau} (t^\gamma u(t))' + au(t), \gamma, \tau, a \in \mathbb{R} \text{ and } \tau - 2\gamma + 1 > 0$$

in the Hilbert space $L_{r,\tau}^2(1, \infty)$ are described by the boundary condition

$$(t^\gamma u)(1) = r(t^\gamma u)(\infty),$$

where $r \in \mathbb{C}$ and $|r| \leq 1$.

Moreover, in case when $r \neq 0$ the spectrum of maximally dissipative extension L_r is in the form

$$\begin{aligned} \sigma(L_r) = (\tau - 2\gamma + 1) & \left(i \ln |r|^{-1} + \frac{a}{\tau - 2\gamma + 1} \right. \\ & \left. + 2n\pi \right), n \in \mathbb{Z}. \end{aligned}$$

Acknowledgment

The author would like to thank Professor Z. I. ISMAILOV (Karadeniz Technical University, Trabzon, Turkey) for his various comments and suggestions.

References

- [1] V. I. Gorbachuk and M. I. Gorbachuk, "Boundary value problems for operator differential equations," Kluwer, Dordrecht, 1999.
- [2] J. Von Neumann, "Allgemeine eigenwerttheorie hermitescher funktionaloperatoren," *Math. Ann.*, vol. 102, pp. 49-131, 1929.

- [3] C. Fischbacher, "On the Theory of Dissipative Extensions," PhD Thesis, University of Kent School of Mathematics, Statistic and Actuarial Science, Canterbury, 2017.
- [4] B. Sz.-Nagy and C. Foias, "Analyse harmonique des operateurs de L' espace de Hilbert," Masson, Paris and Akad Kiado, Budapest, 1997 (English transl, North-Holland, Amesterdam and Akad Kiado, Budapest: 1970).
- [5] F. S. Rofe-Beketov and A. M. Kholkin, "Spectral analysis of differential operators.," *World Scientific Monograph Series in Mathematics*, vol. 7, 2005.
- [6] L. Hörmander, "On the theory of general partial differential operators," *Acta Mathematica*, vol. 94, pp. 161-248, 1955.

	SAKARYA UNIVERSITY JOURNAL OF SCIENCE		 SAKARYA UNIVERSITY
	e-ISSN: 2147-835X http://www.saujs.sakarya.edu.tr		
	<u>Received</u> 26-01-2018 <u>Accepted</u> 10-04-2018	<u>Doi</u> 10.16984/saufenbilder.384592	

A numerical technique based on Lucas polynomials together with standard and Chebyshev-Lobatto collocation points for solving functional integro-differential equations involving variable delays

Sevin Gümgüm^{*1}, Nurcan Baykuş Savaşaneril², Ömür Kıvanç Kürkcü¹, Mehmet Sezer³

Abstract

In this paper, a new numerical matrix-collocation technique is considered to solve functional integro-differential equations involving variable delays under the initial conditions. This technique is based essentially on Lucas polynomials together with standard and Chebyshev-Lobatto collocation points. Some descriptive examples are performed to observe the practicability of the technique and the residual error analysis is employed to improve the obtained solutions. Also, the numerical results obtained by using these collocation points are compared in tables and figures.

Keywords: functional equations, matrix technique, collocation points, Lucas polynomials, Residual error analysis

1. INTRODUCTION

In this paper, we employ a new numerical technique based on Lucas polynomials to solve the following functional integro-differential equation with variable delays

$$\sum_{k=0}^m P_k(t) y^{(k)}(t) + \sum_{r=0}^{m_1} Q_r(t) y^{(r)}(\alpha_r t + \beta_r(t)) = g(t) + \sum_{j=0}^{m_2} \gamma_j \int_{u_j(t)}^{v_j(t)} K_j(t,s) y(\lambda_j s + \mu_j) ds \quad (1)$$

under the initial conditions

$$\sum_{k=0}^{m-1} a_{ik} y^{(k)}(a) = \varphi_i, \quad i = 0, 1, 2, \dots, m-1 \quad (2)$$

where $P_k(t)$, $Q_r(t)$, $\beta_r(t)$, $g(t)$, $K_j(t,s)$, $u_j(t)$ and $v_j(t)$ ($m_1 \leq m$, $u_j(t) < v_j(t)$) are analytic functions defined on $a \leq t, s \leq b$; α_r , γ_j , λ_j , μ_j , a_{ik} and φ_i are suitable constants.

Functional differential and integro-differential equations with variable delays in the form (1) are usually used in modelling of physical phenomena and play an important role in mathematics, viscoelasticity, oscillating magnetic field, heat conduction, electromagnetics, biology and etc. [1-22,28-31]. It is generally hard to find the analytic solution of them. So, the numerical techniques are required to obtain their approximate solution. For example, some integro-differential equations and

* Corresponding Author

¹ Izmir University of Economics, Department of Mathematics, Izmir, sevin.gumgum@ieu.edu.tr; omur.kivanc@ieu.edu.tr

² Dokuz Eylul University, Izmir Vocational School, Izmir, nurcan.savasaneril@deu.edu.tr

³ Manisa Celal Bayar University, Department of Mathematics, Manisa, mehmet.sezer@cbu.edu.tr

their other classes have been solved by using the numerical techniques such as homotopy perturbation [2], variational iteration [3]; Legendre [5], Taylor [6-9], Laguerre [10,11], Taylor-Lucas [12], Dickson [13-15], Chelyshkov [16], Lucas [17], Bessel [18], Bernoulli [19,20], Chebyshev [28,29] polynomial techniques and also, B-Splines [21], backward substitution [22], Sinc techniques [30].

In this paper, by considering the matrix technique based on collocation points, which have been used by Sezer and coworkers [5,6,8-19], we purpose a new numerical technique to find an approximate solution of the problem (1)-(2). The solution is of the form

$$y(t) \cong y_N(t) = \sum_{n=0}^N a_n L_n(t), \tag{3}$$

where $L_n(t)$ is the Lucas polynomials and $a_n, n=0,1,2,\dots,N$ are unknown coefficients [12].

2. SOME BASICS OF LUCAS POLYNOMIALS

The Lucas polynomials are defined as follows [23-26]:

$$L_{n+1}(t) = t L_n(t) + L_{n-1}(t), \quad n \geq 1$$

with $L_0(t) = 2$ and $L_1(t) = t$ or their explicit form is

$$L_n(t) = \sum_{k=0}^{\lfloor n/2 \rfloor} \frac{n}{n-k} \binom{n-k}{k} t^{n-2k}, \tag{4}$$

where $n \geq 1$ and $\lfloor x \rfloor$ is the largest integer smaller than or equal to x .

The Lucas polynomials have the generating function [26]

$$\sum_{n=0}^{\infty} L_n(t) z^n = \frac{1+z^2}{1-z^2-zt}.$$

The derivative of $L_n(t)$ is of the form [26]

$$L'_n(t) = \frac{n}{t^2+4} (tL_n(t) + 2L_{n-1}(t)).$$

The relation between Lucas and Fibonacci polynomials is [25]

$$(t^2+4)F_n(t) = L_{n+1}(t) + L_{n-1}(t),$$

where $F_n(t)$ is the Fibonacci polynomials. For more properties of the Lucas polynomials, one can refer to [23-26].

3. FUNDAMENTAL MATRIX RELATIONS

In this section, we constitute the matrix forms of the unknown function $y(t)$ defined by the form (3), the derivative $y^{(k)}(t)$, the functional term $y^{(r)}(\alpha_r t + \beta_r(t))$, the kernel function $K_j(t,s)$ and the functional term $y(\lambda_j s + \mu_j)$ in Eq. (1). These matrix forms will enable us to solve the functional integro-differential equation (1) under the initial conditions (2). We can first write the truncated Lucas series (3) in the matrix form, for $n=0,1,2,\dots,N$,

$$y(t) \cong y_N(t) = \mathbf{L}(t)\mathbf{A}, \tag{5}$$

where

$$\mathbf{L}(t) = [L_0(t) \quad L_1(t) \quad \dots \quad L_N(t)],$$

$$\mathbf{A} = [a_0 \quad a_1 \quad \dots \quad a_N]^T.$$

Then, by using the Lucas polynomials $L_n(t)$ given by (4), we write the matrix form $\mathbf{L}(t)$ as follows;

$$\mathbf{L}(t) = \mathbf{T}(t)\mathbf{M}^T \tag{6}$$

where

$$\mathbf{T}(t) = [t \quad t^2 \quad \dots \quad t^N],$$

if N is odd,

$$\mathbf{M} = \begin{bmatrix} 2 & 0 & 0 & \dots & 0 \\ 0 & \frac{1}{1} \binom{1}{0} & 0 & \dots & 0 \\ \frac{2}{1} \binom{1}{1} & 0 & \frac{2}{2} \binom{2}{0} & \dots & 0 \\ 0 & \frac{3}{2} \binom{2}{1} & 0 & \dots & 0 \\ \vdots & \vdots & \vdots & \ddots & \vdots \\ \frac{(n-1)}{\binom{n-1}{2}} \binom{n-1}{2} & 0 & \frac{n-1}{\binom{n+1}{2}} \binom{n+1}{2} & \dots & 0 \\ 0 & \frac{n}{\binom{n+1}{2}} \binom{n+1}{2} & 0 & \dots & \frac{n}{n} \binom{n}{0} \end{bmatrix}$$

if N is even,

$$M = \begin{bmatrix} 2 & 0 & 0 & \dots & 0 \\ 0 & \frac{1}{1} \binom{1}{0} & 0 & \dots & 0 \\ \frac{2}{1} \binom{1}{1} & 0 & \frac{2}{2} \binom{2}{0} & \dots & 0 \\ 0 & \frac{3}{2} \binom{2}{1} & 0 & \dots & 0 \\ \vdots & \vdots & \vdots & \ddots & \vdots \\ 0 & \frac{n-1}{\binom{n}{2}} \binom{\frac{n}{2}}{\frac{n-2}{2}} & 0 & \dots & 0 \\ \frac{n}{\binom{n}{2}} \binom{\frac{n}{2}}{\frac{n}{2}} & 0 & \frac{n}{\binom{n+2}{2}} \binom{\frac{n+2}{2}}{\frac{n-2}{2}} & \dots & \frac{n}{n} \binom{n}{0} \end{bmatrix}$$

For example, we obtain M^T with $N=4$ as follows:

$$M^T = \begin{bmatrix} 2 & 0 & 0 & 0 & 0 \\ 0 & 1 & 0 & 0 & 0 \\ 2 & 0 & 1 & 0 & 0 \\ 0 & 3 & 0 & 1 & 0 \\ 2 & 0 & 4 & 0 & 1 \end{bmatrix}$$

By the matrix relations (5) and (6), it follows that $y_N(t) = T(t)M^T A$. (7)

Besides, it is well known from [9] that the relation between $T(t)$ and its derivative $T^{(k)}(t)$ is of the form

$$T^{(k)}(t) = T(t)B^k, \quad (8)$$

where

$$B = \begin{bmatrix} 0 & 1 & 0 & \dots & 0 \\ 0 & 0 & 2 & \dots & 0 \\ \vdots & \vdots & \vdots & \ddots & \vdots \\ 0 & 0 & 0 & \dots & N \\ 0 & 0 & 0 & \dots & 0 \end{bmatrix} \text{ and } B^0 \text{ is a unit matrix.}$$

By using (7) and (8), we have the matrix relation

$$y_N^{(k)}(t) = T(t)B^k M^T A, \quad k = 0, 1, 2, \dots, m. \quad (9)$$

Putting $t \rightarrow \alpha_r t + \beta_r(t)$ into (9), we obtain the matrix relation

$$y_N^{(r)}(\alpha_r t + \beta_r(t)) = T(t)S^T(\alpha_r, \beta_r(t))B^k M^T A, \quad (10)$$

where

$$S(\alpha_r, \beta_r(t)) = \begin{bmatrix} \binom{0}{0}(\alpha_r)^0(\beta_r(t))^0 & 0 & 0 & \dots & 0 \\ \binom{1}{0}(\alpha_r)^0(\beta_r(t))^1 & \binom{1}{1}(\alpha_r)^1(\beta_r(t))^0 & 0 & \dots & 0 \\ \binom{2}{0}(\alpha_r)^0(\beta_r(t))^2 & \binom{2}{1}(\alpha_r)^1(\beta_r(t))^1 & \binom{2}{2}(\alpha_r)^2(\beta_r(t))^0 & \dots & 0 \\ \vdots & \vdots & \vdots & \ddots & \vdots \\ \binom{N}{0}(\alpha_r)^0(\beta_r(t))^N & \binom{N}{1}(\alpha_r)^1(\beta_r(t))^{N-1} & \binom{N}{2}(\alpha_r)^2(\beta_r(t))^{N-2} & \dots & \binom{N}{N}(\alpha_r)^N(\beta_r(t))^0 \end{bmatrix}$$

Note that the matrix $T(\alpha_r t + \beta_r(t))$ can be constituted as $T(\alpha_r t + \beta_r(t)) = T(t)S^T(\alpha_r, \beta_r(t))$. On the other hand, the matrix forms of $\gamma(\lambda_j s + \mu_j)$ and $K_j(t, s)$ can be written as

$$\gamma(\lambda_j s + \mu_j) = T(s)S^T(\lambda_j, \mu_j)M^T A \quad (11)$$

and by using the Taylor series expansion of $K_j(t, s)$ [8], we have

$$K_j(t, s) = T(t)K_j T^T(s), \quad K_j = [k_{pq}^j] \quad (12)$$

where

$$k_{pq}^j = \frac{1}{p!q!} \frac{\partial^{p+q} K_j(0, 0)}{\partial t^p \partial s^q}, \quad p, q = 0, 1, \dots, N, \\ j = 0, 1, \dots, m_2.$$

By means of the relations (11) and (12), we obtain the matrix form of the integral part of Eq. (1) as follows;

$$\int_{u_j(t)}^{v_j(t)} K_j(t, s) \gamma(\lambda_j s + \mu_j) ds = \int_{u_j(t)}^{v_j(t)} T(t)K_j T^T(s) T(s)S^T(\lambda_j, \mu_j)M^T A ds \\ = T(t)K_j C_j(t)S^T(\lambda_j, \mu_j)M^T A \quad (13)$$

where

$$C_j(t) = \int_{u_j(t)}^{v_j(t)} T^T(s)T(s)ds = [c_{mn}^j(t)]; \\ c_{mn}^j(t) = \frac{(v_j(t))^{m+n+1} - (u_j(t))^{m+n+1}}{m+n+1}, \quad m, n = 0, 1, \dots, N.$$

4. LUCAS MATRIX-COLLOCATION TECHNIQUE

In this section, we first constitute the following matrix equation corresponding to the functional integro-differential equation (1), by substituting the matrix relations (9), (10) and (13) into Eq. (1):

$$\left\{ \begin{array}{l} \sum_{k=0}^m P_k(t)T(t)B^k + \sum_{r=0}^{m_1} Q_r(t)T(t)S^T(\alpha_r, \beta_r(t))B^r \\ - \sum_{j=0}^{m_2} \gamma_j T(t)K_j C_j(t)S^T(\lambda_j, \mu_j) \end{array} \right\} M^T A = g(t). \quad (14)$$

On the other hand, the standard (SCP) and Chebyshev-Lobatto (CLCP) collocation points we will use in the matrix equation (14) are defined respectively by

$$t_i = a + \frac{b-a}{N}i \text{ and } t_i = \frac{a+b}{2} + \frac{a-b}{2} \cos\left(\frac{\pi i}{N}\right),$$

$$i = 0, 1, \dots, N.$$

where

$$P_k = \text{diag}[P_k(t_0) \ P_k(t_1) \ \dots \ P_k(t_N)],$$

$$Q_r = \text{diag}[Q_r(t_0) \ Q_r(t_1) \ \dots \ Q_r(t_N)],$$

$$T = \begin{bmatrix} T(t_0) \\ T(t_1) \\ \vdots \\ T(t_N) \end{bmatrix} = \begin{bmatrix} 1 & t_0 & \dots & t_0^N \\ 1 & t_1 & \dots & t_1^N \\ \vdots & \vdots & \ddots & \vdots \\ 1 & t_N & \dots & t_N^N \end{bmatrix}, \bar{T} = \begin{bmatrix} T(t_0) & 0 & \dots & 0 \\ 0 & T(t_1) & \dots & 0 \\ \vdots & \vdots & \ddots & \vdots \\ 0 & 0 & \dots & T(t_N) \end{bmatrix},$$

$$S_r = \begin{bmatrix} S^T(\alpha_r, \beta_r(t_0)) \\ S^T(\alpha_r, \beta_r(t_1)) \\ \vdots \\ S^T(\alpha_r, \beta_r(t_N)) \end{bmatrix}, \bar{C}_j = \begin{bmatrix} C_j(t_0) & 0 & \dots & 0 \\ 0 & C_j(t_1) & \dots & 0 \\ \vdots & \vdots & \ddots & \vdots \\ 0 & 0 & \dots & C_j(t_N) \end{bmatrix},$$

$$\bar{S}(\lambda_j, \mu_j) = \begin{bmatrix} S^T(\lambda_j, \mu_j) \\ S^T(\lambda_j, \mu_j) \\ \vdots \\ S^T(\lambda_j, \mu_j) \end{bmatrix},$$

$$\bar{K}_j = \text{diag}[K_j \ K_j \ \dots \ K_j], \mathbf{G} = [g(t_0) \ g(t_1) \ \dots \ g(t_N)]^T.$$

Besides, the fundamental matrix equation (14) can be expressed in the form

$$\mathbf{W}\mathbf{A} = \mathbf{G} \text{ or } [\mathbf{W}; \mathbf{G}], \tag{15}$$

where

$$\mathbf{W} = [w_{mn}], \ m, n = 0, 1, \dots, N.$$

Now, by the relation (9), we can obtain the condition matrix form for the initial conditions (2) as

$$\mathbf{U}_i \mathbf{A} = \varphi_i \text{ or } [\mathbf{U}_i; \varphi_i], \ i = 0, 1, \dots, m-1 \tag{16}$$

such that

$$\mathbf{U}_i = \sum_{k=0}^{m-1} a_{ik} \mathbf{T}(a) \mathbf{B}^k \mathbf{M}^T = [u_{i0} \ u_{i1} \ \dots \ u_{iN}].$$

Eventually, in order to find the Lucas polynomial solution of the problem (1)-(2), by replacing m row matrices (16) into any m rows of the form (15). Thus, we have the augmented matrix

$$[\mathbf{W}^*; \mathbf{G}^*] \text{ or } \mathbf{W}^* \mathbf{A} = \mathbf{G}^*, \tag{17}$$

where

$$[\mathbf{W}^*; \mathbf{G}^*] = \begin{bmatrix} w_{00} & w_{01} & \dots & w_{0N} & ; & g(t_0) \\ w_{10} & w_{11} & \dots & w_{1N} & ; & g(t_1) \\ \vdots & \vdots & \vdots & \vdots & ; & \vdots \\ w_{N-m,0} & w_{N-m,1} & \dots & w_{N-m,N} & ; & g(t_{N-m}) \\ u_{00} & u_{01} & \dots & u_{0N} & ; & \varphi_0 \\ u_{10} & u_{11} & \dots & u_{1N} & ; & \varphi_1 \\ \vdots & \vdots & \vdots & \vdots & ; & \vdots \\ u_{m-1,0} & u_{m-1,1} & \dots & u_{m-1,N} & ; & \varphi_{m-1} \end{bmatrix}.$$

In Eq. (17), if $\text{rank } \mathbf{W}^* = \text{rank} [\mathbf{W}^*; \mathbf{G}^*] = N+1$, then the coefficient matrix \mathbf{A} is uniquely determined and so the solution of the problem (1)-(2) is obtained as

$$y_N(t) = \mathbf{L}(t)\mathbf{A} \text{ or } y_N(t) = \mathbf{T}(t)\mathbf{M}^T \mathbf{A}.$$

5. RESIDUAL ERROR ANALYSIS

In this section, an error analysis dependent on residual function is implemented to improve the Lucas polynomial solutions. By using Eq. (1), we can obtain the residual function on $t \in [a, b]$ as

$$R_N(t) = \sum_{k=0}^m P_k(t) y^{(k)}(t) + \sum_{r=0}^{m_1} Q_r(t) y^{(r)}(\alpha_r t + \beta_r(t)) - \sum_{j=0}^{m_2} \gamma_j \int_{u_j(t)}^{v_j(t)} K_j(t, s) y(\lambda_j s + \mu_j) ds - g(t) \tag{18}$$

In recent years, the residual error analysis has been applied by some authors [5,11,13,14,16,17,19,22]. Furthermore, the reader can refer to [15,27,28] for converge analysis based on residual function; residual correction and its theory. Let us now construct the residual error analysis for the Lucas polynomials. The error function $e_N(x)$ is defined by

$$e_N(t) = y(t) - y_N(t), \tag{19}$$

By Eqs. (18) and (19), the error equation is of the form

$$L[e_N(t)] = L[y(t)] - L[y_N(t)] = -R_N(t), \tag{20}$$

subject to the initial conditions

$$\sum_{k=0}^{m-1} a_{ik} e_N^{(k)}(a) = 0, \ i = 0, 1, \dots, m-1.$$

By Eqs. (19) and (20), we constitute the error problem. We solve this problem by following the procedure given in Sections 3 and 4. Thus, we

obtain the estimated error function $e_{N,M}(t)$ (or called the solution of the error problem (19)-(20)), so

$$e_{N,M}(t) = \sum_{n=0}^M y_n^* L_n(t), \quad (M > N).$$

Here, the corrected Lucas polynomial solution is obtained as $y_{N,M}(t) = y_N(t) + e_{N,M}(t)$ and the corrected error function is obtained as

$$E_{N,M}(t) = y(t) - y_{N,M}(t).$$

6. NUMERICAL EXAMPLES

In this section, the practicability of the present technique are illustrated with the numerical results of some descriptive examples. Also, these results are discussed in tables and figures, by considering SCP and CLCP. A computer code written on Mathematica (on Pc with 2GB RAM and 2.80 GHz CPU) has been performed to obtain the precise results. In order to compare the numerical results, we also perform L_∞ error defined as follows [29]:

$$L_\infty = \max_{a \leq i \leq b} |y(t_i) - y_N(t_i)|,$$

where $y(t)$ is the exact solution.

6.1. Example 1:

Let us consider the second-order functional integro-differential equation with variable delays

$$y''(t) - y'(t) + 2y' \left(\frac{t}{2} - \sin t \right) - 2ty(t) = g(t) + \int_t^{t+1} 3t^2 s^2 y(s) ds$$

subject to the initial conditions $y(0)=0$ and $y'(0)=0$. Here, $0 \leq t \leq 2$, $P_0(t) = -2t$, $P_1(t) = -1$, $P_2(t) = 1$, $Q_1(t) = 2$, $\alpha_1 = 1/2$, $\beta_1(t) = -\sin t$, $\gamma_0 = 1$, $K_0(t, s) = 3t^2 s^2$, $u_0(t) = t$, $v_0(t) = e^{t+1}$, $\lambda_0 = 1$, $\mu_0 = 0$,

$$g(t) = 2 - t^2 \left(\frac{3e^{5t+5}}{5} + 2t - \frac{3t^5}{5} \right) - 4 \sin(t).$$

We approximate the exact solution $y(t)$, by taking the Lucas polynomial solution form:

$$y(t) \cong y_2(t) = \sum_{n=0}^2 a_n L_n(t), \quad 0 \leq t \leq 2$$

and the standard collocation points for $a=0, b=2$ and $N=2$ are computed as $\{x_0=0, x_1=1, x_2=2\}$.

The fundamental matrix equation of this problem becomes

$$\left(\sum_{k=0}^2 P_k T B^k + Q_1(\bar{T}) S^T(\alpha_1, \beta_1(t)) B^1 - \gamma_0 \bar{T}(K_0)(\bar{C}_0) \bar{S}(1,0) \right) M^T A = G$$

where

$$T = \begin{pmatrix} 1 & 0 & 0 \\ 1 & 1 & 1 \\ 1 & 2 & 4 \end{pmatrix}, \quad B = \begin{pmatrix} 0 & 1 & 0 \\ 0 & 0 & 2 \\ 0 & 0 & 0 \end{pmatrix}, \quad P_0 = \begin{pmatrix} 0 & 0 & 0 \\ 0 & -2 & 0 \\ 0 & 0 & -4 \end{pmatrix},$$

$$P_1 = \begin{pmatrix} -1 & 0 & 0 \\ 0 & -1 & 0 \\ 0 & 0 & -1 \end{pmatrix}, \quad P_2 = \begin{pmatrix} 1 & 0 & 0 \\ 0 & 1 & 0 \\ 0 & 0 & 1 \end{pmatrix},$$

$$\bar{T} = \begin{bmatrix} 1 & 0 & 0 & 0 & 0 & 0 & 0 & 0 & 0 \\ 0 & 0 & 0 & 1 & 1 & 1 & 0 & 0 & 0 \\ 0 & 0 & 0 & 0 & 0 & 0 & 1 & 2 & 4 \end{bmatrix},$$

$$Q_1 = \begin{pmatrix} 2 & 0 & 0 \\ 0 & 2 & 0 \\ 0 & 0 & 2 \end{pmatrix}, \quad M = \begin{pmatrix} 2 & 0 & 0 \\ 0 & 1 & 0 \\ 2 & 0 & 1 \end{pmatrix}, \quad G = \begin{bmatrix} 2 \\ -13218.6 \\ -7.85 \times 10^6 \end{bmatrix},$$

$$\bar{C}_0 = \begin{bmatrix} 2.71828 & 3.69453 & 6.69518 & 0 & 0 & 0 & 0 & 0 & 0 \\ 3.69453 & 6.69518 & 13.6495 & 0 & 0 & 0 & 0 & 0 & 0 \\ 6.69518 & 13.6495 & 29.6826 & 0 & 0 & 0 & 0 & 0 & 0 \\ 0 & 0 & 0 & 6.389056 & 26.7991 & 134.143 & 0 & 0 & 0 \\ 0 & 0 & 0 & 26.7991 & 134.143 & 744.989 & 0 & 0 & 0 \\ 0 & 0 & 0 & 134.143 & 744.989 & 4405.09 & 0 & 0 & 0 \\ 0 & 0 & 0 & 0 & 0 & 0 & 18.0855 & 199.714 & 2698.36 \\ 0 & 0 & 0 & 0 & 0 & 0 & 199.714 & 2698.36 & 40684.7 \\ 0 & 0 & 0 & 0 & 0 & 0 & 2698.36 & 40684.7 & 653797 \end{bmatrix}$$

$$S_1 = \begin{pmatrix} S^T(\alpha_1, \beta_1(0)) \\ S^T(\alpha_1, \beta_1(1)) \\ S^T(\alpha_1, \beta_1(2)) \end{pmatrix} = \begin{bmatrix} 1 & 0 & 0 \\ 0 & 1 & 0 \\ 0 & 0 & 1 \\ 1 & -\sin 1 & \sin^2(1) \\ 0 & 1 & -\sin 1 \\ 0 & 0 & 1 \\ 1 & -\sin 2 & \sin^2(2) \\ 0 & 1 & -\sin 2 \\ 0 & 0 & 1 \end{bmatrix}, \quad \bar{S}(1,0) = \begin{pmatrix} S^T(1,0) \\ S^T(1,0) \\ S^T(1,0) \end{pmatrix} = \begin{bmatrix} 1 & 0 & 0 \\ 0 & 1 & 0 \\ 0 & 0 & 1 \\ 1 & 0 & 0 \\ 0 & 1 & 0 \\ 0 & 0 & 1 \\ 1 & 0 & 0 \\ 0 & 1 & 0 \\ 0 & 0 & 1 \end{bmatrix}$$

and

$$\bar{K}_0 = \begin{bmatrix} 0 & 0 & 0 & 0 & 0 & 0 & 0 & 0 & 0 \\ 0 & 0 & 0 & 0 & 0 & 0 & 0 & 0 & 0 \\ 0 & 0 & 3 & 0 & 0 & 0 & 0 & 0 & 0 \\ 0 & 0 & 0 & 0 & 0 & 0 & 0 & 0 & 0 \\ 0 & 0 & 0 & 0 & 0 & 0 & 0 & 0 & 0 \\ 0 & 0 & 0 & 0 & 0 & 0 & 0 & 0 & 0 \\ 0 & 0 & 0 & 0 & 0 & 3 & 0 & 0 & 0 \\ 0 & 0 & 0 & 0 & 0 & 0 & 0 & 0 & 0 \\ 0 & 0 & 0 & 0 & 0 & 0 & 0 & 0 & 0 \\ 0 & 0 & 0 & 0 & 0 & 0 & 0 & 0 & 3 \end{bmatrix}.$$

Then, the augmented matrix is

$$[\mathbf{W}^* ; \mathbf{G}^*] = \begin{bmatrix} 0 & 1 & 2 & ; & 2 \\ 2 & 0 & 2 & ; & 0 \\ 0 & 1 & 0 & ; & 0 \end{bmatrix}$$

Solving this system, \mathbf{A} is obtained as $\mathbf{A} = [-1 \ 0 \ 1]^T$. By the relation (7), $y(t)$ is obtained as

$$y(t) = \mathbf{T}(t)\mathbf{M}^T\mathbf{A} = \begin{bmatrix} 1 & t & t^2 \end{bmatrix} \begin{bmatrix} 2 & 0 & 2 \\ 0 & 1 & 0 \\ 0 & 0 & 1 \end{bmatrix} \begin{bmatrix} -1 \\ 0 \\ 1 \end{bmatrix},$$

thus, the solution of the problem becomes

$$y(t) = t^2,$$

which is the exact solution.

6.2. Example 2:

Consider the second-order integro-differential equation with variable delays

$$t^2 y''(t) - 2y'(t+1) - ty\left(\frac{t}{2} - \frac{t^2}{2}\right) = g(t) - \int_{t^2}^t tsy\left(\frac{s}{2} + 1\right) ds$$

subject to $t \in [0, 1]$, and the initial conditions $y(0) = 1$ and $y'(0) = 0$. The exact solution of this problem is $y(t) = \cos(t)$. Here, $g(t)$ can be easily found. By using SCP, we obtain the following solutions for $N=4$ and 7 :

$$y_4(t) = 1 + 2.77556 \times 10^{-16}t - 0.520263t^2 + 0.0317765t^3 + 0.0259313t^4 \quad \text{and}$$

$$y_7(t) = 1 + 1.36176 \times 10^{-16}t - 0.499905t^2 - 0.000443857t^3 + 0.0422884t^4 - 0.000285t^5 - 0.00146t^6 + 0.000103t^7.$$

As seen from Figure 1, a fast approximation is provided, so the Lucas polynomial solutions coincide with the exact solution. Notice that the Lucas polynomial solutions obtained by using SCP are plotted in Figures 1-4. Also, in Table 1, the numerical results are obtained by using SCP and CLCP in our technique.

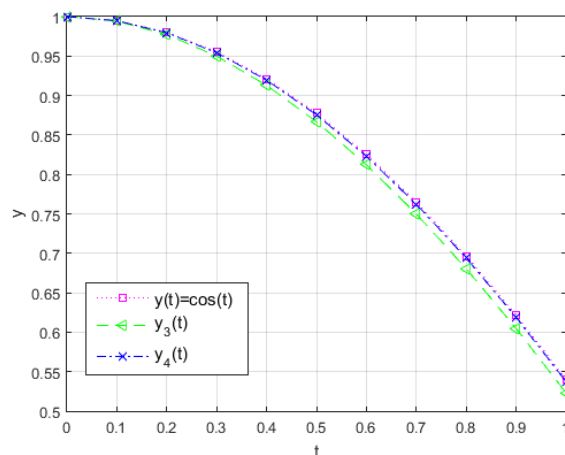


Figure 1. Comparison of the exact and Lucas polynomial solutions for Example 6.2.

Figure 2 and Table 1 show that the absolute errors decay, when N is increased and the residual error analysis is employed. In addition, when the interval of this problem is taken as the large interval $[0, 8]$, it is observed in Figure 3 that our solution $y_{20}(t)$ is in harmony with the exact solution. This consistency reflects on the phase plane of the solution $y_{20}(t)$ as seen in Figure 4.

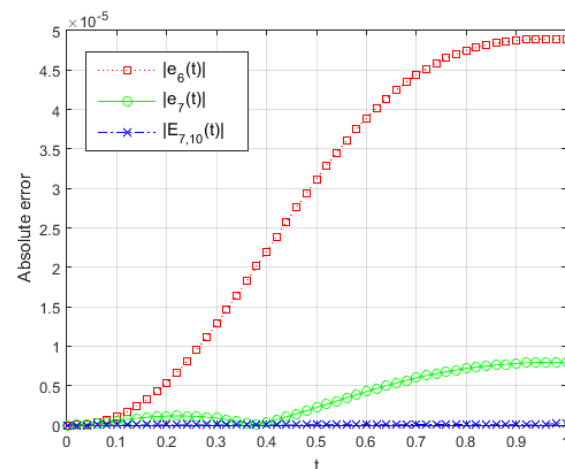


Figure 2. Behaviors of the absolute errors with respect to time t for Example 6.2.

Table 1. Comparison of the absolute errors and CPU time(s) (sec.) in terms of different collocation points for Example 6.2.

t_i	$ e_4(t_i) $;	$ e_4(t_i) $;	$ e_7(t_i) $;	$ e_7(t_i) $;
	SCP	CLCP	SCP	CLCP
0.0	$2.22e-16$	$2.22e-16$	0	0
0.2	$5.81e-04$	$5.28e-04$	$1.16e-06$	$1.04e-06$
0.4	$1.61e-03$	$1.44e-03$	$3.03e-07$	$1.43e-05$
0.6	$2.41e-03$	$2.13e-03$	$4.12e-06$	$3.10e-05$
0.8	$2.78e-03$	$2.43e-03$	$6.95e-06$	$4.02e-05$
1.0	$2.86e-03$	$2.48e-03$	$7.63e-06$	$4.18e-05$
Time(s)	$1.404 (N=4)$	$1.404 (N=4)$	$3.120 (N=7)$	$3.073 (N=7)$

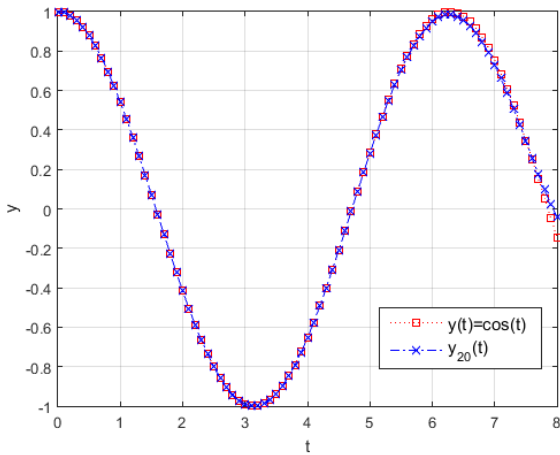


Figure 3. Oscillation of the exact and Lucas polynomial solution on large time interval [0,8] for Example 6.2.

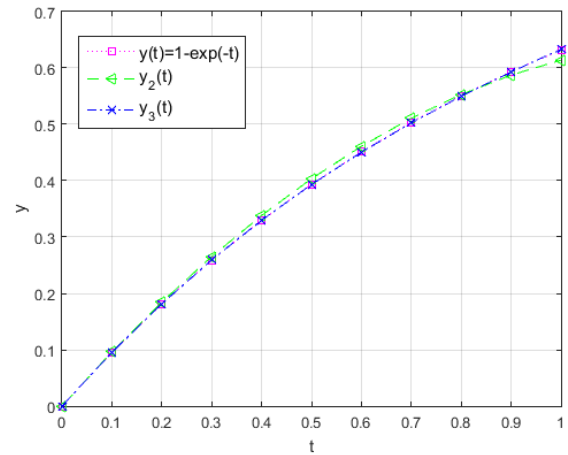


Figure 5. Comparison of the exact and Lucas polynomial solutions for Example 6.3.

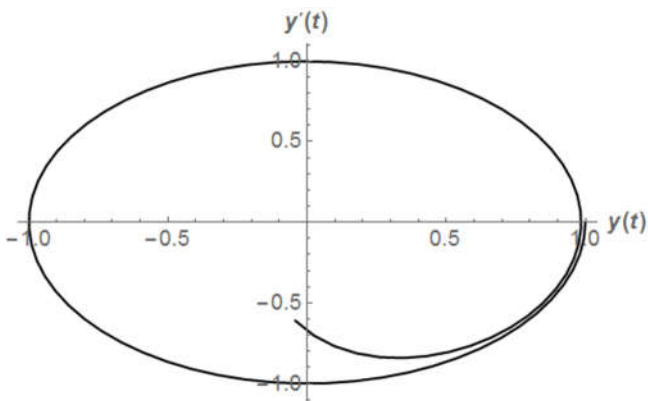


Figure 4. Consistency of the Lucas polynomial solution $y_{20}(t)$ in the phase plane for Example 6.2.

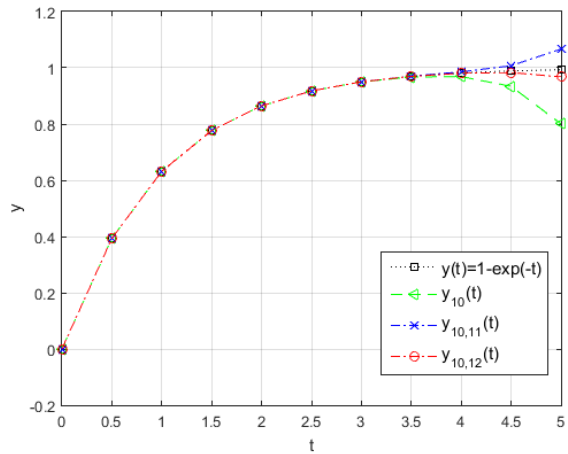


Figure 6. Comparison of the exact and Lucas polynomial solutions on large time interval [0,5] for Example 6.3.

6.3. Example 3:

Consider the first-order pantograph Volterra delay-integro-differential equation [30]

$$y'(t) - y\left(\frac{t}{2}\right) = 1 - \frac{3t}{2} + \int_0^t y(s) ds + \int_0^{t/2} y(s) ds$$

$$0 \leq t \leq 1,$$

subject to the initial condition $y(0) = 0$. Here, the exact solution of the problem is $y(t) = 1 - e^{-t}$. After solving this problem by employing $N=2-10$, $M=11, 12$; SCP and CLCP, we obtain the Lucas polynomial solutions. It is seen from Figure 5 that we approach speedily to the exact solution, when $N=2$ and 3. It is also worth specifying in Figure 6 that our solutions obtained on $[0,1]$ are consistent with the exact solution, even if these are on $[0,5]$. Notice that the Lucas polynomial solutions obtained by using CLCP are plotted in Figures 5 and 6.

By considering different collocation points, L_∞ errors are compared with the errors $\|E(h)\|_\infty$ of Sinc technique [30] in Table 2. As seen from Table 2, our error results are far better than those in the mentioned technique and CPU processes our computer program in a short time.

Table 2. Comparison of L_∞ errors and CPU time(s) (sec.) in terms of different N and collocation points for Example 6.3.

N, M	L_∞ error; SCP	L_∞ error; CLCP	$\ E(h)\ _\infty$ [30]	CPU time SCP	CPU time CLCP
2	$1.81e-02$	$1.81e-02$	-	0.3120	0.4056
3	$3.47e-03$	$1.10e-03$	-	0.4524	0.4836
4	$1.61e-04$	$6.27e-05$	-	0.5772	0.6084
5	$1.44e-05$	$1.61e-06$	$2.10e-03$	0.7644	0.8268
7	$3.48e-08$	$2.19e-09$	-	1.4040	1.2636
8	$1.18e-09$	$6.14e-11$	-	1.7472	1.5600
10	$1.55e-12$	$3.25e-14$	$1.26e-04$	2.9796	2.2152
10,11	$5.57e-14$	$6.61e-16$	-	n.a.	na.

6.4. Example 4:

Consider the first-order delay differential equation [31]

$$y'(t) - ty(t) - te^{3t^2/4}y\left(t - \left(\frac{t}{2}\right)\right) = 0, 0 \leq t \leq 2$$

subject to the initial condition $y(0) = 1$. Here, the exact solution of the problem is $y(t) = e^{t^2}$.

Dix [31] investigated the asymptotic behavior of solutions of the first-order differential equation with variable delays, using Lyapunov functionals. We solve this problem, implementing our technique with SCP and CLCP for $N=5-20$ and 50. CPU time is obtained (sec.) as 0.0312 ($N=5$) and 0.796 ($N=50$) for CLCP. Also, we obtain L_∞ error as $8.53e-014$ for CLCP and $N=50$. The Lucas polynomial solutions are plotted along with the exact solution in Figure 7.

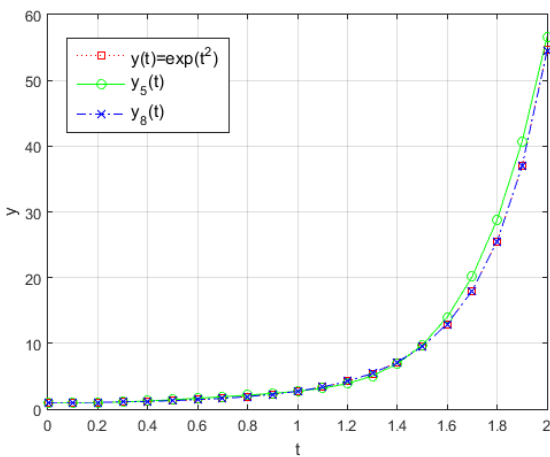


Figure 7. Comparison of the exact and Lucas polynomial solutions for Example 6.4.

Figure 8 shows that L_∞ errors decrease for different collocation points, as N is increased from 10 to 20. In addition, the numerical values of the exact, approximate solutions and L_∞ errors are compared in Table 3. It is clearly seen from Figure 8 and Table 3 that CLCP are more useful than SCP.

Table 3. Comparison of the exact, the approximate and the corrected approximate solutions and L_∞ errors in terms of different collocation points for Example 6.4.

t_i	Exact sol.	$y_{10}(t_i)$ SCP	$y_{10}(t_i)$ CLCP	$y_{10,13}(t_i)$ SCP	$y_{10,13}(t_i)$ CLCP
0.0	1	1	1	1	1
0.5	1.284	1.285	1.284	1.284	1.284
1.0	2.718	2.721	2.719	2.718	2.718
1.5	9.488	9.498	9.488	9.487	9.488
2.0	54.60	54.52	54.60	54.59	54.60
L_∞	-	$7.4e-02$	$9.1e-04$	$7.8e-03$	$4.3e-05$

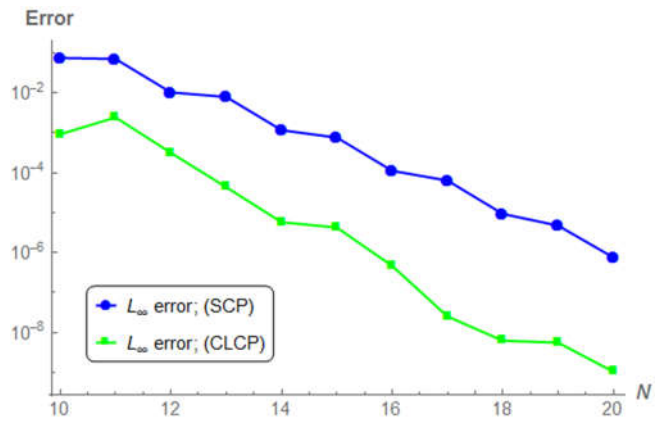


Figure 8. Logarithmic plot of L_∞ errors with SCP and CLCP with respect to N for Example 6.4.

7. CONCLUSION

A practical Lucas matrix-collocation technique has been employed to solve functional integro-differential equations with variable delays. In Figures 1-8 and Tables 1-3, the comparisons of the present results shows that the proposed technique is very applicable, consistent and fast (according to CPU time(s)). The accuracy increases, as N is increased. Our solutions have been improved via the efficient residual error analysis as seen in Figures 2, 6 and Tables 2, 3.

On the other hand, by investigating the obtained results, we can deduce that the use of CLCP in the present technique is more advantageous than the use of SCP. It would be suitable to apply the present technique to other tough problems. In addition, it is readily seen that the present technique has a simple procedure and is very easy for computer programming.

REFERENCES

- [1] V.V. Vlasov and R. Perez Ortiz, "Spectral Analysis of Integro-Differential Equations in Viscoelasticity and Thermal Physics", *Math. Notes*, vol. 98, no. 4, pp. 689–693, 2015.
- [2] M. Dehghan and F. Shakeri, "Solution of an integro-differential equation arising in oscillating magnetic field using He's homotopy perturbation method", *Prog. Electromagnet. Res. PIER*, vol. 78, pp. 361–376, 2008.
- [3] Y. Chu, F. You, J. M. Wassick, and A. Agarwal, "Integrated planning and scheduling under production uncertainties: Bi-level model formulation and hybrid solution method," *Computers and Chemical Engineering*, vol. 72, pp. 255–272, 2015.
- [4] F. S. Chan, V. Kumar, and M. Tiwari, "Optimizing the Performance of an Integrated Process Planning and Scheduling Problem: An AIS-FLC based Approach," *2006 IEEE Conference on Cybernetics and Intelligent Systems*, pp. 1–8, 2006.
- [5] W. Tan and B. Khoshnevis, "Integration of process planning and scheduling— a review," *Journal of Intelligent Manufacturing*, vol. 11, no. 1, pp. 51–63, 2000.
- [6] N. Kurt and M. Sezer, "Polynomial solution of high-order linear Fredholm integro-differential equations with constant coefficients," *J. Franklin Inst.*, vol. 345, pp. 839–850, 2008.
- [7] N. Kurt and M. Çevik, "Polynomial solution of the single degree of freedom system by Taylor matrix method," *Mech. Res. Commun.*, vol. 35, pp. 530–536, 2008.
- [8] N. Baykuş and M. Sezer, "Solution of High-Order Linear Fredholm Integro-Differential Equations with Piecewise Intervals," *Numer. Methods Partial Differ. Equ.*, vol. 27, pp. 1327–1339, 2011.
- [9] M. Sezer and A. Akyüz-Daşcıoğlu, "A Taylor method for numerical solution of generalized pantograph equations with linear functional argument," *J. Comput. Appl. Math.*, vol. 200, pp. 217–225, 2007.
- [10] N. Baykuş Savaşaneril and M. Sezer, "Laguerre Polynomial Solution of High-Order Linear Fredholm Integro-Differential Equations", *New Trends in Math. Sci.*, vol. 4, no. 2, 273–284, 2016.
- [11] B. Gürbüz, M. Sezer and C. Güler, "Laguerre collocation method for solving Fredholm-integro-differential equations with functional arguments," *J. Appl. Math.*, vol. 2014, Article ID: 682398, 12 pages, 2014.
- [12] N. Baykuş Savaşaneril and M. Sezer, "Hybrid Taylor–Lucas Collocation Method for Numerical Solution of High-Order Pantograph Type Delay Differential Equations with Variables Delays," *Appl. Math. Inf. Sci.*, vol. 11, no. 6, pp. 1795–1801, 2017.
- [13] Ö.K. Kürkcü, E. Aslan, and M. Sezer, "A numerical approach with error estimation to solve general integro-differential–difference equations using Dickson polynomials," *Appl. Math. Comput.*, vol. 276, pp. 324–339, 2016.
- [14] Ö.K. Kürkcü, E. Aslan, and M. Sezer, "A novel collocation method based on residual error analysis for solving integro-differential equations using hybrid Dickson and Taylor polynomials," *Sains Malays.*, vol. 46, pp. 335–347, 2017.
- [15] Ö.K. Kürkcü, E. Aslan, and M. Sezer, "A numerical method for solving some model problems arising in science and convergence analysis based on residual function," *Appl. Numer. Math.*, vol. 121, pp. 134–148, 2017.
- [16] C. Oğuz and M. Sezer, "Chelyshkov collocation method for a class of mixed functional integro-differential equations," *Appl. Math. Comput.*, vol. 259, pp. 943–954, 2015.
- [17] M. Çetin and M. Sezer, "C. Güler, Lucas polynomial approach for system of high-order linear differential equations and residual error estimation," *Math. Prob. Eng.*, vol. 2015, Article ID: 625984, 14 pages, 2015.
- [18] N. Şahin, Ş. Yüzbaşı, and M. Sezer, "A Bessel polynomial approach for solving general linear Fredholm integro-differential equations," *Int. J. Comput. Math.*, vol. 88, no. 14, pp. 3093–3111, 2011.
- [19] K. Erdem, S. Yalçınbaş, and M. Sezer, "A Bernoulli polynomial approach with residual correction for solving mixed linear Fredholm integro differential-difference equations," *J. Difference Equ. Appl.*, vol. 19, no. 10, pp. 1619–1631, 2013.

- [20] E. Tohidi, A.H. Bhrawy, and K. Erfani, "A collocation method based on Bernoulli operational matrix for numerical solution of generalized pantograph equation," *Appl. Math. Model.*, vol. 37, no. 6, pp. 4283–4294, 2013.
- [21] H-E.D. Gherjalar and H. Mohammodikia, "Numerical solution of functional integral and integro-differential equations by using B-Splines," *Appl. Math.*, vol. 3, pp. 1940–1944, 2012.
- [22] S. Yu. Reutskiy, "The backward substitution method for multipoint problems with linear Volterra-Fredholm integro-differential equations of the neutral type," *J. Comput. Appl. Math.*, vol. 296, pp. 724–738, 2016.
- [23] T. Koshy, "Fibonacci and Lucas Numbers with Applications," *Wiley*, New York, USA, 2001.
- [24] P. Filipponi and A.F. Horadam, "Second derivative sequences of Fibonacci and Lucas polynomials," *The Fibonacci Quarterly*, vol. 31, no. 3, pp. 194–204, 1993.
- [25] A. Constandache, A. Das, and F. Toppan, "Lucas polynomials and a standard Lax representation for the polytropic gas dynamics," *Lett. Math. Phys.*, vol. 60, no. 3, pp. 197–209, 2002.
- [26] E. W. Weisstein, "Lucas Polynomial, MathWorld: A Wolfram Web Resource," <http://mathworld.wolfram.com/LucasPolynomial.html>.
- [27] F.A. Oliveira, "Collocation and residual correction," *Numer. Math.*, vol. 36, pp. 27–31, 1980.
- [28] İ. Çelik, "Collocation method and residual correction using Chebyshev series," *Appl. Math. Comput.*, vol. 174, pp. 910–920, 2006.
- [29] M.A. Ramadan, K.R. Raslan, T.S.E. Danaf, and M.A.A.E. Salam, "An exponential Chebyshev second kind approximation for solving high-order ordinary differential equations in unbounded domains, with application to Dawson's integral," *J. Egyptian Math. Soc.*, vol. 25, pp. 197–205, 2017.
- [30] J. Zhao, Y. Cao, and Y. Xu, "Sinc numerical solution for pantograph Volterra delay-integro-differential equation," *Int. J. Comput. Math.*, vol. 94, no. 5, pp. 853–865, 2017.
- [31] J.G. Dix, "Asymptotic behavior of solutions to a first-order differential equation with variable delays," *Comput. Math. Appl.*, vol. 50, pp. 1791–1800, 2005.

	SAKARYA UNIVERSITY JOURNAL OF SCIENCE		 SAKARYA UNIVERSITY
	e-ISSN: 2147-835X http://www.saujs.sakarya.edu.tr		
	<u>Received</u> 07-12-2017 <u>Accepted</u> 17-04-2018	<u>Doi</u> 10.16984/saufenbilder.363843	

Cytogenetic Analysis of *Tegenaria elysii* (Araneae: Agelenidae)

Ümit KUMBIÇAK*¹

Abstract

There are 61 species of agelenid spiders in our country and the genus *Tegenaria* represents the widest group in terms of species number. In this study, it was aimed to investigate the cytogenetic properties of *Tegenaria elysii*. Chromosomes were obtained by making some modifications to the method of Pekár and Král (2001). Hypotonic, fixation and staining steps were applied to the gonads respectively. As a result, the number of diploid chromosomes and the sex chromosome system were found as $2n=42$, ♂ X_1X_20 /♀ $X_1X_1X_2X_2$. Total relative lengths of chromosomes decreased gradually from 6,83% to 3,31%. Sex chromosomes which positive heteropycnotics in the stage of meiosis. I have been detected to be isopycnic in the stage of meiosis II. 20 autosomal bivalent and two sex chromosomes were identified in which diplotene and diakinesis stages.

Keywords: Agelenidae, chromosome, karyotype

1. INTRODUCTION

Spiders are one of the largest animal group, and contain almost 47 000 species all around the world [1]. In our country, a total of 1117 spider species belonging to 52 families were determined [2]. Until now, although studies have been carried out in systematics, fauna and ecology, the cytogenetic investigations is scarce. The fact that tiny chromosome morphology, the presence of different sex chromosome systems and the requirement of modification in the method for each species limits the investigations on spider cytogenetics [3].

Spiders are divided into three subclasses namely Mesothelae, Mygalomorphae and Araneomorphae [4]. Among them, Agelenidae family is belonging

to the subclass Araneomorphae and easily distinguished from other families by its characteristics posterior spinneret which has two-segments and long, thin, tipped toward each other. *Tegenaria* Latreille 1804 differs from other genera by the number and position of gonadal teeth, the structure of the tibial and median apophyses, the shape of the conductor, the shape of the vulva only having a spiral duct, and the scleroid structure [5]. The araneomorph karyotypes are characterized by a predominance of acrocentric chromosomes, X_1X_20 sex chromosome system [6], relatively low diploid chromosome numbers (ranges from 10 to 49, [7]), and chiasmatic meiosis. Acrocentric/telocentric karyotypes of entelegynes with lower chromosome numbers could be derived from ancestral karyotypes by tandem fusions [8] or by cycles of centric fusions and subsequent pericentric inversions [7]. The latter hypothesis is

* Corresponding Author

¹ Nevşehir Hacı Bektaş Veli University, Faculty of Art and Sciences, Department of Molecular Biology and Genetics, Nevşehir, Turkey- umitkumbicak@nevsehir.edu.tr

supported by the fact that centric fusions are the most frequent source of chromosome polymorphism found in populations of entelegyne spiders [7, 9]. In this study, karyotype characteristics and meiotic behavior of *Tegenaria elysii* Brignoli, 1978 belonging to Agelenidae family, which is found in our country, were investigated for the first time.

2. EXPERIMENTAL

The male specimens of *Tegenaria elysii* were collected from Nevşehir, Kayseri and Kahramanmaraş between March to May in the year 2015 from different habitats and localities. The collection were made by hands or pitfall traps (Table 1). During the field study, no treatment was applied to the spiders, and each one was taken to falcon tubes and placed in the laboratory. Male gonads were used in obtaining chromosomes due to the lots of cells contained. Therefore, it was possible to determine various mitotic and meiotic stages from males. However, females were not used because of the low division frequency.

Table 1. Data of collection date, locality information and number of specimens used in this study

Collection Date	Number of species	Localities	
		Region	Coordinates
14.03.2015	2♂♂	Nevşehir, Acıgöl	38°32'24.58"N 34°32'51.72"E
11.04.2015	1♂	Kayseri, Pınarbaşı	38°42'47.93"N 36°22'49.75"E
19.04.2015	3♂♂	Kahramanmaraş, Göksun	38°00'42.27"N 36°28'15.80"E
23.05.2015	7♂♂	Kayseri, Pınarbaşı	38°42'45.51"N 36°23'26.84"E

The chromosome preparations were performed according to the method of [10] with some modifications. Alive male specimens were squeezed from the prosoma and separated from the opistosoma. Prosoma and pedipalps were kept in 70% ethanol for systematic diagnosis. The gonads were dissected out in physiological solution for invertebrates. Then three steps were used; hypotonic solution in 0.075 M KCl (for 15 min), twice fixation in methanol:glacial acetic acid (3:1 for 10 and 20 min); spreading in 60% glacial acetic

acid solution on heating plate that surface temperature 42 °C (for 20 min). The slides were air dried for overnight and stained with 5% Giemsa solution in Sorensen phosphate buffer (ph=6.8) for 50 min. Chromosome slides were investigated an BX53 microscope (Olympus) and well spread stages were photographed using DP26 digital camera with CellSens software (Olympus). The diploid chromosome number were determined by the mitotic metaphases or diplotene stages. Relative chromosome lengths (RCL) including standard deviations were calculated as a percentage of the total chromosome length of the diploid set by CellSens software. Classification of chromosome morphology was made by the protocol of (Table 2) [11].

Table 2. Determination of chromosome morphology according to the centromere position (C) and arm ratio (q/p)

Centromere position	Arm ratio (q/p)	Chromosome morphology
Median	1.00-1.70	Metacentric
Submedian	1.71-3.00	Submetacentric
Subterminal	3.01-7.00	Subtelocentric
Terminal	7.01-∞	Acrocentric

3. RESULTS

In this study, cytogenetic structure, diploid number, sex chromosome system and meiosis characteristics of *Tegenaria elysii* Brignoli, 1978 were determined for the first time.

1.1. Karyotype and sex chromosome system of *T. elysii*

The chromosome set of male *T. elysii* (2n=42, X₁X₂0) contained 42 chromosomes with telocentric morphology (Fig.1, 2).

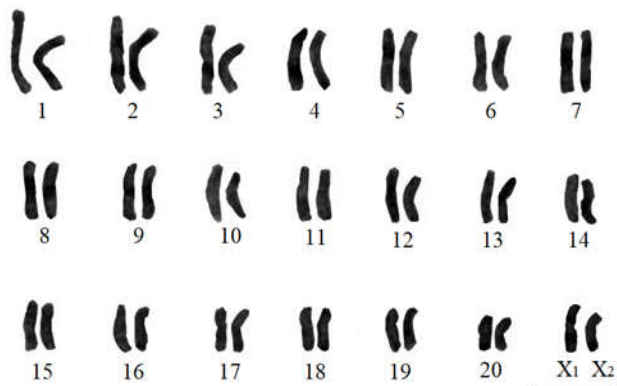


Fig.1. Karyotype of *T. elysii* based on spermatogonial metaphases (Scale=10 μ m)

Autosome pairs decreased gradually in size from 6,83% to 3,31% of total chromosome length (TCL). Relative length of X₁ and X₂ were 4,24% and 3,92% of TCL, respectively (Table 3). X₁ was longer than the 14th autosome pair and X₂ was longer than the 16th autosomal pair. X₁ and X₂ were in similar size.

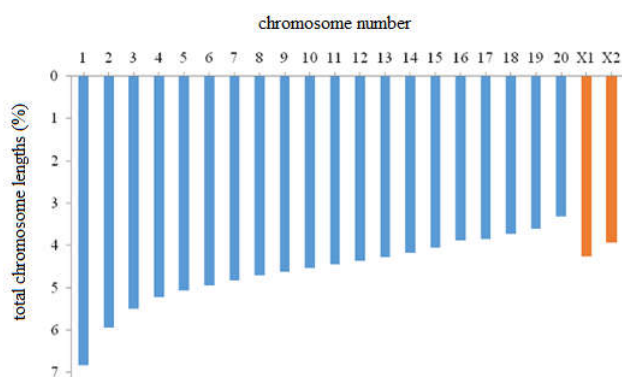


Fig. 2. Idiogram of *T. elysii* based on the haploid set of chromosomes

Table 3. Chromosome length measurements of *T. elysii*: short arm (p); long arm (q); relative lengths (p+q); arm ratio (q/p); TCL: total chromosome lengths (%); CM: chromosome morphology; T: telocentric ; \pm standart deviation)

	p μ m	q μ m	(p+q)	q/p	TCL (%)	CM
1	0	10,88 \pm 0,67	10,88 \pm 0,67	∞	6,83	T
2	0	9,46 \pm 0,4	9,46 \pm 0,4	∞	5,93	T
3	0	8,77 \pm 0,37	8,77 \pm 0,37	∞	5,5	T
4	0	8,32 \pm 0,36	8,32 \pm 0,36	∞	5,22	T
5	0	8,07 \pm 0,4	8,07 \pm 0,4	∞	5,06	T
6	0	7,87 \pm 0,43	7,87 \pm 0,43	∞	4,94	T
7	0	7,69 \pm 0,33	7,69 \pm 0,33	∞	4,82	T
8	0	7,51 \pm 0,35	7,51 \pm 0,35	∞	4,71	T
9	0	7,37 \pm 0,29	7,37 \pm 0,29	∞	4,62	T
10	0	7,22 \pm 0,32	7,22 \pm 0,32	∞	4,53	T
11	0	7,08 \pm 0,28	7,08 \pm 0,28	∞	4,44	T
12	0	6,97 \pm 0,25	6,97 \pm 0,25	∞	4,37	T
13	0	6,81 \pm 0,3	6,81 \pm 0,3	∞	4,27	T
14	0	6,66 \pm 0,28	6,66 \pm 0,28	∞	4,18	T
15	0	6,45 \pm 0,23	6,45 \pm 0,23	∞	4,05	T
16	0	6,19 \pm 0,42	6,19 \pm 0,42	∞	3,88	T
17	0	6,13 \pm 0,44	6,13 \pm 0,44	∞	3,85	T
18	0	5,93 \pm 0,5	5,93 \pm 0,5	∞	3,72	T
19	0	5,76 \pm 0,55	5,76 \pm 0,55	∞	3,61	T
20	0	5,27 \pm 0,62	5,27 \pm 0,62	∞	3,31	T
X ₁	0	6,76 \pm 0,35	6,76 \pm 0,35	∞	4,24	T
X ₂	0	6,25 \pm 0,39	6,25 \pm 0,39	∞	3,92	T

1.2. Meiotic characteristics of *T. elysii*

The sex chromosomes were stained positively heteropycnotic during the first substages of prophase I (i.e. leptotene, zygotene and pachytene) (Fig. 3.a). 20 autosomal bivalents and two univalent sex chromosomes were determined in diplotene, diakinesis and metaphase I. The bivalents had one chiasma (or sometimes two chiasmata) with terminal, interstitial and proximal type (Fig. 3.b). All chromosomes including sex chromosomes were "V" shaped in anaphase I and sex chromosomes were located on the periphery of nucleus (Fig. 3.c). During the second meiotic stages (i.e. prophase II, metaphase II and anaphase II), the sex chromosomes were isopycnotic but

were easily distinguished because of their earlier condensation (Fig. 3.d).

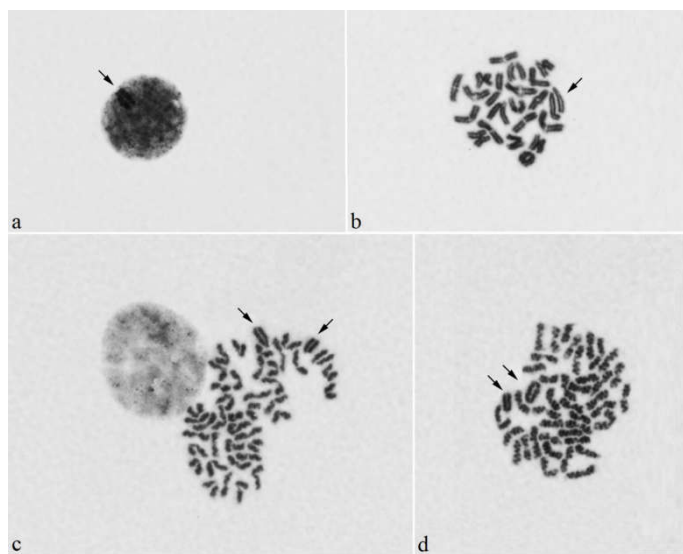


Fig. 3. Meiotic stages of male *T. elysii* a. Pachytene, b. Diplotene, c. Anaphase I, d. Prophase II (arrows indicate sex chromosomes) (Scale=10 μ m)

DISCUSSION

Upto now, 77 genera and 1272 species belonging to the family Agelenidae were determined [1]. 11 genera (i.e. *Agelena* Walckenaer, 1805; *Agelescape* Levy, 1996; *Allagelena* Zhang, Zhu ve Song, 2006; *Coelotes* Blackwall, 1841; *Eratigena* Bolzern, Burckhardt ve Hänggi, 2013; *Lycosoides* Lucas, 1846; *Maimuna* Lehtinen, 1967; *Pireneitega* Kishida, 1955; *Tegenaria* Latreille, 1804; *Textrix* Sundevall, 1833; *Urocoras* Ovtchinnikov, 1999) and 61 species are spread out in our country [2].

Cytogenetic studies on spiders are scarce due to the necessity for the spider to keep alive, specific applications for individuals, the low frequency of mitotic metaphases and tiny chromosome morphology. Despite all these difficulties, seven genera and 15 species belonging to the Agelenidae family were studied, previously. These species are listed as *Agelena auclandi* Burman; *Agelena gautami* Tikader, 1962; *Agelena labyrinthica* (Clerck, 1757); *Agelena limbata* Thorell, 1897; *Agelenopsis naevia* (Walckenaer, 1841); *Allagelena difficilis* (Fox, 1936); *Allagelena opulenta* (L. Koch, 1878); *Eratigena atrica* (C.L. Koch, 1843); *Pireneitega luctuosa* (L. Koch, 1878); *Tegeocoelotes corasides* (Bösenberg &

Strand, 1906); *Tegenaria campestris* (C.L. Koch, 1834); *Tegenaria domestica* (Clerck, 1757); *Tegenaria ferruginea* (Panzer, 1804); *Tegenaria parietina* (Fourcroy, 1785) ve *Tegenaria silvestris* L. Koch, 1872 [12]. According to these previously studies, the diploid chromosome number were determined between $2n\sigma=18$ (*E. atrica* [13]) and $2n\sigma=52$ (*A. naevia* [14]). However the most common diploid chromosome number is $2n\sigma=42-43$ in the family [12]. Although the family has a great diversity in the number of diploid chromosomes, the results obtained in our study were found to be consistent with family features.

The X_1X_20 sex chromosome system seen in most of the spiders is also characteristic for the agelenid spiders. It is known that this sex chromosome system is often encountered in spiders. It is assumed that the X_1X_20 system is generated from the X_0 system either by centric fission or by the duplication of the X chromosome. However, other sex chromosome systems that are rarely seen in the family are $X_1X_2X_30$ and $X_1X_2X_3X_4X_5Y$ [15]. The presence of the Y chromosome is explained by the disruption of a fragment from the large X chromosome [16]. In our study, the sex chromosome system of *T. elysii* was found to be compatible with other family members.

In primitive spider groups, chromosomal morphology is heterogeneous and has chromosomes of metacentric, submetacentric, acrocentric and telocentric type. However, modern spiders, including agelenid spiders, usually have a homogenous structure. Taxa usually have chromosomes of either acrocentric or telocentric type. Moreover, in the first meiotic division phases, the positive heteropycnotic structure of sex chromosomes, to be located on the nucleus surface, to move together, and the isopycnotic structure in the stage of second meiotic division, were also observed in other members of the family. In addition, at the stages of diplotene, diakinesis and metaphase I, the bivalents generally have one chiasma possesses a hypothesis, which leads to the idea that chromosome behavior is preserved in the family. In conclusion; these cytogenetic characters obtained for the Agelenidae family are not sufficient to distinguish the taxa alone and additional molecular based studies are needed.

ACKNOWLEDGMENTS

I am very grateful to Fahrettin Anıl Sırlıbaş and Serhat Bayrak for helps in collecting spiders and laboratory studies during preparing chromosome slides. This study was carried out in the Genetics Laboratory of Science and Art Faculty, Nevşehir Hacı Bektaş Veli University, Nevşehir, Turkey.

REFERENCES

- [1] Platnick N.I., "The World Spider Catalog (2018), Version 19.0", "American Museum of Natural History", <http://www.wsc.nmbe.ch/> 2018.
- [2] H. Demir and O. Seyyar, "Annotated checklist of the spiders of Turkey," *Munis Entomology & Zoology*, vol. 12, no. 2, pp. 433-469, 2017.
- [3] Ü. Kumbıçak, "Karyotype Analysis of *Gnaphosa lugubris* (Araneae:Gnaphosidae) by a Standard Giemsa Staining Method," *IAREC*, 2017.
- [4] Z. Kumbıçak, "Cytogenetic characterization of ten araneomorph spiders (Araneae): Karyotypes and meiotic features," *Biologia*, vol. 69, no. 5, pp. 644-650, 2014.
- [5] K. C. Karanfil, "Batı Karadeniz bölgesi huni örümcek faunası ve sistematığı (Araneae: Agelenidae)," *Kırıkkale Üniversitesi, Fen Bilimleri Enstitüsü, Biyoloji Anabilim Dalı Yüksek Lisans tezi*, 87 sf., 2015.
- [6] D. Araújo, D.M. Cella and A. D. Brescovit, "Cytogenetic analysis of the neotropical spider *Nephilengys cruentata* (Araneomorphae, Tetragnathidae): standard staining, NORs, C-bands and base-specific fluorochromes," *Brazilian Journal of Biology*, vol. 65, no. 2, pp. 193-202, 2005.
- [7] T. Kořínková and J. Král, "Karyotypes, sex chromosomes, and meiotic division in spiders," *In: Nenwing W (Ed) Spider Ecophysiology*, pp. 159–171, 2013.
- [8] S. Suzuki, "Cytological studies in spiders. III. Studies on the chromosomes of fifty-seven species of spiders belonging to seventeen families, with general considerations on chromosomal evolution," *Journal of science of the Hiroshima University, Series B. Division 1*, vol. 15, no. 2, pp. 23–136, 1954.
- [9] Z. Kumbıçak, E. Ekiz and S. Çiçekli, "Karyotypes of six spider species belonging to the families Gnaphosidae, Salticidae, Thomisidae, and Zodariidae (Araneae) from Turkey," *Comparative Cytogenetics*, vol. 8, no. 2, pp. 93-101, 2014.
- [10] S. Pekar and J. Král, "A Comparative Study of the Biology and Karyotypes of Two Central European Zodariid Spiders (Araneae, Zodariidae)," *Journal of Arachnology*, vol. 29, no. 3, pp. 345–353, 2001.
- [11] A. Levan, K. Feradga and A. A. Sandberg, "Nomenclature for centromeric position on chromosomes," *Hereditas*, vol. 52, pp. 201-220, 1964.
- [12] D. Araujo, M.C. Schneider, E. Paula-Neto and D.M. Cella, "The spider cytogenetic database", Available in, <http://www.arthropodacytogenetics.bio.br.spiderdatabase>, January, 2017.
- [13] J.B. Carnoy, "La cytotiérese chez les arthropodes," *La Cellule*, v. 1, p. 191-440, 1885.
- [14] L.B. Wallace, "The spermatogenesis of *Agalena naevia*," *Biological Bulletin*, v. 17, p. 120-161, 1909.
- [15] Ş. Civan, "Agelescape *levyi* Guseinov, Marusik & Koponen, 2005, *Tegenaria hasperi* Chyzer, 1897 ve *Tegenaria argaica* Nosek, 1905 (Araneae:Agelenidae) türlerinin sitogenetik özelliklerinin araştırılması," *Nevşehir Hacı Bektaş Veli University, Science Institute, Ms Thesis*, 74 pages, 2017.
- [16] D. Araujo, M. C. Schneider, E. P. Neto, and M. D. Cella, "Sex chromosomes and meiosis in spiders", A review, *chapter from the book meiosis – molecular mechanisms and cytogenetic diversity*, pp. 87-109, 2012.

	SAKARYA UNIVERSITY JOURNAL OF SCIENCE	
	e-ISSN: 2147-835X http://www.saujs.sakarya.edu.tr	
	<u>Received</u> 14-02-2018 <u>Accepted</u> 17-04-2018	<u>Doi</u> 10.16984/saufenbilder.395016

Biofilm Production and Antimicrobial Susceptibility Profiles of *Bacillus* spp. from Meats

Fatma Özdemir*¹, Seza Arslan¹

ABSTRACT

The genus *Bacillus* is frequently found in soil, water, and food. *Bacillus cereus* and *Bacillus anthracis* are the main pathogens causing foodborne diseases and serious infections in humans. A total of 52 *Bacillus* spp. from meat samples was tested for determination of biofilm production, antimicrobial resistance pattern, and beta-lactamase activity. The 24 (46.1%) *Bacillus* isolates were found to be for biofilm production. Of the 24 (46.1%) biofilm producer *Bacillus* isolates, 13 (25%), 6 (11.5%) and 5 (9.6%) were considered as strong, moderate and weak biofilm producer, respectively. The most common species for the production of biofilm was *Bacillus thuringiensis* (80%). Antimicrobial disk susceptibility tests of *Bacillus* spp. revealed high resistance to ampicillin (84.6%) followed by penicillin (75%), cefepime (34.6%), and cefoxitin (26.9%). A multidrug resistance to at least 3 or more antimicrobials was observed in the 25 isolates (48.1%). All *Bacillus* spp. were sensitive to vancomycin, gentamicin, amikacin, ciprofloxacin, and imipenem. The susceptibility rate to streptomycin, chloramphenicol, and trimethoprim-sulphamethoxazole was 94.2%. Among the isolates, the 6 (11.5%) isolates were found to be sensitive to all antimicrobial agents tested. Besides, only one isolate from meat was found to be positive for beta-lactamase test. The existence of biofilm production as a virulence factor and of multidrug resistance in bacteria isolated from food should not be underestimated in terms of food safety, public health, and economic concerns.

Keywords: *Bacillus* spp., biofilm production, antimicrobial resistance, beta-lactamase, meat

1. INTRODUCTION

The *Bacillus* genus are rod-shaped and endospore forming organisms that are widely distributed in the natural environment due to their many physiological properties such as endospore formation and nutritional versatility. Endospores readily survive and are being contaminants in environments and foods due to resistance to heat,

radiation, disinfectants, and desiccation. Therefore, the presence of *Bacillus* species such as *B. cereus*, *B. subtilis*, *B. licheniformis*, and *B. pumilus* in foods is inevitable and undesirable due to considered as foodborne pathogens and spoilage-associated species. The contamination of food with pathogenic and spoilage strains of *Bacillus* is a major concern for human health and food safety [1, 2]. Among the *Bacillus* species, mostly *B. cereus* and *B. anthracis* are known as the most frequent human pathogens which cause a wide range of infections including

*Corresponding Author

¹ Abant İzzet Baysal University, Faculty of Arts and Sciences, Department of Biology, Bolu/Turkey - ozkardes_f@ibu.edu.tr, arslan_s3@ibu.edu.tr

food poisoning, anthrax, bacteremia, pneumonia, endocarditis, meningitis, endophthalmitis, respiratory, and soft tissue infections [1, 3]. Many *Bacillus* species are able to produce a wide variety of enterotoxins, emetic toxins, extracellular enzymes, and biofilms which are considered as major contributing factors in the establishment of infections by these pathogenic bacteria [2].

Biofilms considered as a potential virulence factor by bacteria including *Bacillus* species are microbial communities embedded in an extracellular matrix consisted of polysaccharide [4, 5]. Most bacteria are able to form biofilms on abiotic surfaces in food processing facilities, thereby being a major source of food contamination. Besides, biofilms by pathogenic bacteria may easily attach to surfaces such as living tissues, indwelling medical devices and industrial or natural aquatic systems under suitable conditions. Therefore, biofilms play a significant role in the transmission of pathogens, microbial contamination and colonization that cause to infections [5, 6]. Moreover, biofilm producing bacteria can be responsible for development of some biomaterial-associated infections such as cystic fibrosis, native valve endocarditis, otitis media, periodontitis, and chronic prostatitis. However, bacteria within biofilms on medical devices as a cause of infection dramatically reduce antimicrobial susceptibility to antimicrobial agents [4, 7, 8]. In addition to the decrease in antibiotic susceptibility, the biofilm producing bacteria has an increased resistance to extreme temperatures, light, drying, cleaning agents [4].

Antimicrobial resistance has been increasing public health problem worldwide due to misuse or overuse of antimicrobial agents in aquaculture, agriculture, and human medicine [9, 10]. Resistant bacteria can be transmitted from food such as fish and ground beef to human. Infections caused by these resistant pathogens can be treated with difficulty. Although *Bacillus* species are an unusual source of human infection, they can cause mild to severe infections in immunocompromised individuals. Systemic antimicrobial therapy is usually required in the treatment of most serious *Bacillus* infections [1, 11]. Vancomycin, clindamycin, ciprofloxacin, and gentamicin can be used successfully in the treatment of most serious *Bacillus* infections [1].

Anthrax caused by *B. anthracis* generally is treatable with penicillin. Nevertheless, most strains of *B. anthracis* are resistant to many cephalosporins. Furthermore, a broad-spectrum beta-lactamase produced by *Bacillus* species inactivates the penicillins and cephalosporins thus make the organism resistant to penicillins and cephalosporins [2, 3].

Determination of biofilm production as an important virulence trait and screening antimicrobial resistance in bacteria from food are important for recognition of their pathogenic potential. Therefore, this study aims to determine the biofilm production, antimicrobial resistance profiles, and beta-lactamase activity of the *Bacillus* spp. isolated from meat samples.

2. MATERIALS AND METHODS

2.1. Bacterial isolates

A total of 52 *Bacillus* spp. comprising 24 *B. cereus*, 2 *B. anthracis*, 10 *B. thuringiensis*, 9 *B. subtilis*, 3 *B. licheniformis*, 2 *B. pumilus*, 1 *B. firmus*, and 1 *B. coagulans* from fish and ground beef were performed in this study. All isolates were grown in Brain Heart Infusion (BHI) broth (Merck, Darmstadt, Germany) at 37°C for 24 h.

2.2. Biofilm production

The adherence of *Bacillus* spp. was tested using a microtiter plate assay previously described by [12] with some modifications. Briefly, *Bacillus* isolates were grown in Tryptic Soy broth (TSB) (Merck) overnight at 37°C. The overnight culture was diluted with TSB in order to obtain optical density (OD) at approximately 1.5×10^8 CFU per mL. The 96 well flat bottom tissue culture plates were filled with 200 μ L of *Bacillus* culture in TSB. Negative control wells contained TSB only. The plates were incubated at 30°C for 48 h in a static condition. At the end of incubation, the contents of the plates were removed by inverting the plates, and then the wells were washed five times with sterile distilled water. The plates were air-dried for 45 min and each well was stained with 200 μ L of 1% crystal violet solution for 45 min. After staining, the plates were washed five times with sterile distilled water. For the quantitative analysis of biofilm formation, 200

μL of ethanol-acetone solution (4:1) was added to the wells. The OD of each well was measured at 570 nm using a microtiter plate reader (Thermo Electron Corporation Multiskan Spectrum, Vantaa, Finland). Isolates were classified into the four following categories based upon the absorbance: no biofilm producer ($\text{OD} \leq \text{ODc}$), and weak ($\text{ODc} < \text{OD} \leq 2\text{XODc}$), moderate ($2\text{XODc} < \text{OD} \leq 4\text{XODc}$), or strong ($\text{OD} > 4\text{XODc}$) biofilm producer [13], where ODc is the optical density measured for the negative control. Six replicate wells were performed for each experimental parameter and each data point was averaged from these six.

2.3. Antimicrobial susceptibility test

Bacillus spp. isolates from fish and ground beef were examined for evaluation of antimicrobial resistance patterns using the disk diffusion method according to the Clinical and Laboratory Standards Institute (CLSI) [14]. Twenty antimicrobial agents (Oxoid, Basingstoke, UK) were chosen according to their common use. They belonged to the following groups: penicillins (penicillin -10 units, ampicillin-10 μg), beta-lactams (amoxicillin-clavulanic acid - 30 μg , cephalothin - 30 μg , cefoxitin - 30 μg , ceftriaxone - 30 μg , cefepime - 30 μg), carbapenems (imipenem - 30 μg), glycopeptides (teicoplanin - 30 μg , vancomycin - 30 μg), aminoglycosides (gentamicin - 10 μg , streptomycin - 10 μg , amikacin - 30 μg), macrolides (erythromycin - 15 μg), tetracyclines (tetracycline - 30 μg), fluoroquinolones (ciprofloxacin - 5 μg), phenicols (chloramphenicol - 30 μg), miscellaneous (trimethoprim-sulfamethoxazole - 25 μg , clindamycin - 2 μg , rifampin - 5 μg). The turbidity of bacterial suspension was adjusted to 0.5 McFarland standard on Mueller Hinton broth (Merck). Then the suspensions were spread on Mueller Hinton agar (Merck) and the antibiotic disks were placed on the agar surface. The inhibition zone of each bacterium was measured after incubation on Mueller Hinton agar (37°C /18 h). The results were interpreted as susceptible, intermediate or resistant with respect to the CLSI [14] guideline for *Staphylococcus* spp.

2.4. Beta-lactamase activity

The production of beta lactamase was determined by the acidimetric strip method. This method was done as previously described [15]. Penicillin and bromocresol purple were dissolved in NaOH solution. A filter paper (Whatman No: 1) was placed in a Petri dish. A few drops of the solution were then added on to the filter paper until the filter strips was almost saturated. A loopfull of bacteria was kept in the center of the filter paper. The presence of purple color in the paper around the bacterial mass indicated positive reaction for beta-lactamase.

3. RESULTS

3.1. Biofilm production of *Bacillus* spp.

In the Table 1, the biofilm producing ability of the *Bacillus* spp. from meats is given. Of the 52 *Bacillus* spp. tested, the 24 (46.1%) isolates were considered as biofilm producers. The incidence of biofilm production in the *Bacillus* isolates from fish and ground beef was 45% and 50%, respectively. The biofilm producing isolates were categorized as strong (13 isolates), moderate (6 isolates), weak producers (5 isolates). The most common *Bacillus* species was *B. thuringiensis* (80%) regarded as biofilm producers. The biofilm production of the other *Bacillus* species was as follows: *B. licheniformis* 66.7%, *B. anthracis*, *B. thuringiensis* 50%, *B. pumilus* 50%, *B. subtilis* 33.3%, and *B. cereus* 12.5%. None of the *B. coagulans* and *B. firmus* was able to form biofilm. The distribution of the 24 biofilm producing *Bacillus* isolates from fish and ground beef and their antimicrobial resistance profiles and beta-lactamase activity is presented in Table 2. Most *Bacillus* isolates were resistant to ampicillin (95.5%) and penicillin (91.7%). A multidrug resistance was observed in 14 (58.3%) of the biofilm producing isolates to at least three or more antimicrobials. All of the 7 isolates from seawater fish were strong biofilm producer which had resistance to at least two antimicrobial agents. Moreover, *B. licheniformis* from seawater fish was resistant to eight antimicrobials. Only one isolate recognized as *B. cereus* from freshwater fish was sensitive to all antimicrobials tested.

Table 1. Biofilm production of *Bacillus* species by microtiter plate technique

<i>Bacillus</i> species	No.of isolates	Interpretation of biofilm			
		No adherence	Weak adherence	Moderate adherence	Strong adherence
<i>B. cereus</i>	24	16 ¹ (66.7%)	3 (12.5%)	3 (12.5%)	2 (8.3%)
<i>B. anthracis</i>	2	1 (50%)	-	1 (50%)	-
<i>B. thuringiensis</i>	10	2 (20%)	2 (20%)	1 (10%)	5 (50%)
<i>B. subtilis</i>	9	5 (55.6%)	-	1 (11.1%)	3 (33.3%)
<i>B. licheniformis</i>	3	1 (33.3%)	-	-	2 (66.7%)
<i>B. pumilus</i>	2	1 (50%)	-	-	1 (50%)
<i>B. coagulans</i>	1	1 (100%)	-	-	-
<i>B. firmus</i>	1	1 (100%)	-	-	-
Total	52	28 (53.9%)	5 (9.6%)	6 (11.5%)	13 (25%)

¹ Number of positive isolates

Table 2. The distribution of the 24 biofilm producing *Bacillus* isolates from fish and ground beef and their antimicrobial resistance profiles and beta-lactamase activity

Isolate	<i>Bacillus</i> spp.	Origin	Biofilm production	Antimicrobial resistance	Beta-lactamase
F1	<i>B. cereus</i>	Freshwater fish	Moderate	AMP, P, FEP	-
F2	<i>B. cereus</i>	Freshwater fish	Moderate	-	-
F3	<i>B. cereus</i>	Freshwater fish	Strong	AMP, P, FEP, DA	-
F4	<i>B. cereus</i>	Freshwater fish	Weak	AMP, P, TE	-
F5	<i>B. cereus</i>	Freshwater fish	Moderate	AMP, P, RD	-
F6	<i>B. cereus</i>	Freshwater fish	Weak	AMP, P, RD	-
F7	<i>B. thuringiensis</i>	Freshwater fish	Strong	AMP, P	-
F8	<i>B. thuringiensis</i>	Freshwater fish	Moderate	AMP	-
F9	<i>B. thuringiensis</i>	Freshwater fish	Strong	AMP, P, E	-
F10	<i>B. thuringiensis</i>	Freshwater fish	Weak	AMP, P	-
F11	<i>B. licheniformis</i>	Freshwater fish	Strong	AMP, P, AMC, DA	-
S1	<i>B. cereus</i>	Seawater fish	Strong	AMP, P	-
S2	<i>B. thuringiensis</i>	Seawater fish	Strong	AMP, P	-
S3	<i>B. thuringiensis</i>	Seawater fish	Strong	AMP, FEP	-
S4	<i>B. thuringiensis</i>	Seawater fish	Strong	AMP, P, TE	-
S5	<i>B. subtilis</i>	Seawater fish	Strong	AMP, P, AMC, DA	-
S6	<i>B. subtilis</i>	Seawater fish	Strong	AMP, P	-
S7	<i>B. licheniformis</i>	Seawater fish	Strong	AMP, P, FEP, FOX, S, E, TE, C	+
G1	<i>B. cereus</i>	Ground beef	Weak	AMP, P, FEP, FOX	-
G2	<i>B. anthracis</i>	Ground beef	Moderate	AMP, P	-
G3	<i>B. thuringiensis</i>	Ground beef	Weak	AMP, P, TE	-
G4	<i>B. subtilis</i>	Ground beef	Strong	AMP, P	-
G5	<i>B. subtilis</i>	Ground beef	Moderate	AMP, P, FEP, DA	-
G6	<i>B. pumilus</i>	Ground beef	Strong	AMP, P, FEP, FOX	-

Abbreviations of antimicrobial agents are listed in alphabetical order. AMC, amoxicillin-clavulanic acid; AMP, ampicillin; C, chloramphenicol; DA, clindamycin; E, erythromycin; FEP, cefepime; FOX, ceftiofur; P, penicillin; RD, rifampin; S, streptomycin; TE, tetracycline

3.2. Antimicrobial resistance profiles of *Bacillus* spp.

The antimicrobial susceptibility of 52 *Bacillus* spp. from fish and ground beef samples to various antimicrobial agents was examined. The antimicrobial resistance pattern of *Bacillus* spp. is given in Table 3. The most common resistance to ampicillin and penicillin G was detected in 84.6% and 75% of the *Bacillus* isolates, respectively. Among the cephalosporins tested, the isolates were resistant to cefepime (34.6%), followed by

cefoxitin (26.9%), cephalothin (13.5%), and ceftriaxone (13.5%).

Resistance to rifampin and clindamycin was 13.5%. Furthermore, all *Bacillus* spp. were sensitive to imipenem, vancomycin, amikacin, gentamicin, and ciprofloxacin. Multidrug resistance pattern was observed in 25 (48.1%) of the isolates to at least three or more antimicrobials (Table 4). Only six isolates had resistance to one antimicrobial. Resistance to two antimicrobials was also detected in 15 (28.8%) of the isolates.

Table 3. Antimicrobial resistance patterns of *Bacillus* spp. from meat

Antimicrobial Class	Antimicrobial agents	Conc. ¹ (µg/disk)	Number of isolates (%)		
			Resistant	Intermediate	Susceptible
Penicillins	Ampicillin	30	44 (84.6)	0 (0)	8 (15.4)
	Penicillin G	10	39 (75)	0 (0)	13 (25)
B-lactams	Amoxicillin-clavulanic acid	30	11 (21.2)	0 (0)	41 (78.8)
	Cefepime	30	18 (34.6)	3 (5.8)	31 (59.6)
Cephems	Cephalothin	30	7 (13.5)	2 (3.8)	43 (82.7)
	Ceftriaxone	30	7 (13.5)	15 (28.8)	30 (57.7)
	Cefoxitin	30	14 (26.9)	0 (0)	38 (73.1)
Carbapenems	Imipenem	10	0 (0)	0 (0)	52 (100)
Glycopeptides	Teicoplanin	30	1 (1.9)	1 (1.9)	50 (96.2)
	Vancomycin	30	0 (0)	0 (0)	52 (100)
Aminoglycosides	Amikacin	30	0 (0)	0 (0)	52 (100)
	Gentamicin	10	0 (0)	0 (0)	52 (100)
	Streptomycin	10	1 (1.9)	2 (3.9)	49 (94.2)
Macrolides	Erythromycin	15	2 (3.9)	8 (15.4)	42 (80.7)
Tetracyclines	Tetracycline	10	6 (11.5)	7 (13.5)	39 (75)
Fluoroquinolones	Ciprofloxacin	5	0 (0)	0 (0)	52 (100)
Lincosamides	Clindamycin	2	7 (13.5)	22 (42.3)	23 (44.2)
Folate pathway inhibitors	Trimethoprim/sulfamethoxazole	25	3 (5.8)	0 (0)	49 (94.2)
Phenicols	Chloramphenicol	30	1 (1.9)	2 (3.9)	49 (94.2)
Ansamycins	Rifampin	5	7 (13.5)	22 (42.3)	23 (44.2)

¹ Concentration of disk

Table 4. Multiple antimicrobial-resistant *Bacillus* spp. in meats

Antimicrobial resistance profiles	Number of antimicrobials	Number of resistant <i>Bacillus</i> spp. (%)
AMP, P, E	3	1 (1.9)
AMP, P, FEP	3	1 (1.9)
AMP, P, RD	3	1 (1.9)
AMP, P, TE	3	4 (7.6)
AMP, P, AMC, DA	4	2 (3.9)
AMP, P, AMC, RD	4	1 (1.9)
AMP, P, FEP, DA	4	2 (3.9)
AMP, P, FEP, FOX	4	2 (3.9)
AMP, P, FEP, FOX, DA	5	2 (3.9)
AMP, P, AMC, FEP, KF, CRO, FOX	7	2 (3.9)
AMP, P, AMC, KF, FOX, TEC, DA	7	1 (1.9)
AMP, P, AMC, FEP, CRO, FOX, SXT, RD	8	1 (1.9)
AMP, P, AMC, FEP, KF, CRO, FOX, RD	8	1 (1.9)
AMP, P, FEP, FOX, E, TE, C, S	8	1 (1.9)
AMP, P, AMC, FEP, KF, CRO, FOX, SXT, RD	9	2 (3.9)
AMP, P, AMC, FEP, KF, CRO, FOX, TE, RD	9	1 (1.9)
Total		25 (48.1)

Abbreviations of antimicrobial agents are listed in alphabetical order. AMC, amoxicillin-clavulanic acid; AMP, ampicillin; C, chloramphenicol; CRO, ceftriaxone; DA, clindamycin; E, erythromycin; FEP, cefepime; FOX, ceftiofloxacin; KF, cephalothin; P, penicillin; RD, rifampin; S, streptomycin; SXT, trimethoprim/sulfamethoxazole; TE, tetracycline; TEC, teicoplanin

3.3. Beta-lactamase production

In this study, only one isolate identified as *B. licheniformis* from seawater fish was found to be positive for beta-lactamase production (Table 2). Nevertheless, the 39 isolates were resistant to penicillin and none of them were positive for beta-lactamase.

4. DISCUSSION

Bacillus spp. as spore-forming bacteria are widely distributed in nature and isolated from the environment, food, animals, and humans. The resistance of spores to heat, radiation, disinfectants, and desiccation results in *Bacillus* species being frequent contaminants in foods. The pathogenic bacteria such as *B. cereus* and *B. anthracis* can be directly or indirectly transmitted through food to human and causes serious threat for public health and food safety [3].

Numerous studies have shown that *Bacillus* species known as the most common bacteria which

are capable of adhering and have a high tendency to form a biofilm on various surfaces in food industry, medical field, and water systems [4, 6, 16]. Biofilm production by *Bacillus* species from different sources using microtiter plate assay has been investigated [6, 16, 17]. The present data indicated that the biofilm production by microtiter assay was predominant in 8 (80%) of the *B. thuringiensis* isolates (Tables 1, 2). Of the 24 *B. cereus*, 8 (33.3%) were found to be positive for biofilm production in this study. Biofilm forming capability of *B. cereus* from a milk-processing dairy plant was documented [6]. In this study, among the *Bacillus* isolates, biofilm producers were commonly found in the ground beef isolates (50%), followed by the freshwater fish isolates (45.8%) and the seawater fish isolates (43.8%). In this study, among the biofilm producer *Bacillus* spp., the proportion of resistance to three or more antimicrobials was 58.3% while 35.7% in the non-biofilm producing isolates that it may be indication of a relationship between biofilm production and antimicrobial resistance. Indeed, *Bacillus* species in biofilms can generate highly resistant and

adhesive spores that will increase the resistance of the bacteria to antimicrobial agents or to disinfectants [4, 18]. The extensive use of antimicrobials in food animals and aquaculture for growth enhancement or treatment purposes has contributed to the emergence and development of antimicrobial resistance [3, 19]. Common antibiotic classes including penicillins, aminoglycosides, macrolides, quinolones, sulfonamides, and tetracyclines on the World Health Organization list are regularly used in agriculture and aquaculture [19]. Penicillin is the oldest and widely used in the treatment of *Bacillus* infections such as anthrax [1, 3]. Resistance among the *Bacillus* spp. was in particular seen to penicillin and cephalosporins [3]. Our results were in close agreement with previous studies reported a high resistance to penicillin and ampicillin in *Bacillus* spp. [20, 21, 22].

In this study, many of the isolates were susceptible to trimethoprim/sulfamethoxazole (94.2%), erythromycin (81%) and tetracycline (75%) that these antimicrobials have been used as alternative drugs for patients allergic to penicillin [1]. Furthermore, in a study conducted by Yim et al. [21], the results related to erythromycin, tetracycline, and trimethoprim/sulfamethoxazole were in agreement with our results. In our study susceptibility of the isolates to erythromycin and tetracycline was 80.7% and 75%, respectively. Similarly, Yim et al. [21] reported that isolates were susceptible to tetracycline (90.8%) and erythromycin (78.2%). Chaabouni et al. [22] also documented that susceptibility of isolates to tetracycline was 97% and to erythromycin 88%.

Chloramphenicol, clindamycin, tetracycline, and erythromycin have activity against *Bacillus* species [11]. On contrast, the isolates in our study were sensitive to clindamycin (44.2%), tetracycline (75%), erythromycin (80.7%), and chloramphenicol (94.2%). Compared to our results, Noor Uddin et al. [23] reported resistance to clindamycin (38.3%), chloramphenicol (30%) and erythromycin (16.7%) in *Bacillus* spp. from probiotic products used in aquaculture. A high level of resistance to chloramphenicol (61.5%) among *Bacillus* strains isolated from Mbuja was reported by Mohammadou et al. [24]. Infections associated with *Bacillus* have been treated

successfully by both vancomycin and clindamycin [3, 11] that this data agree with our results related resistance to vancomycin (100%) and clindamycin (86.5%). Besides, previous studies indicated that all *Bacillus* isolates were sensitive to vancomycin [20, 22, 24]. A study by Yim et al. [21] reported that vancomycin susceptibility rate was 86.2%. Noor Uddin et al. [23] reported that clindamycin resistance in the *Bacillus* strains from probiotic products used in aquaculture was 38.3% which were higher than our result (13.5%). Moreover, high levels of clindamycin resistance (65.5%) have been reported by Ikeda et al. [25] in *B. cereus* from blood stream infections. On the other hand, in this study, resistance to three or more antimicrobials was 48.1% in *Bacillus* spp. from meat when this rate was 20% in *Bacillus* spp. from probiotic products used in aquaculture reported by Noor Uddin et al. [23].

In conclusion, this study provides substantial information on the production of biofilms and antimicrobial resistance pattern in *Bacillus* spp. from fish and ground beef. The presence of biofilm producing bacteria and the emergence of antimicrobial resistant bacteria in certain fields including food, aquaculture, and medical may be considered as a major threat to public health and food safety.

REFERENCES

- [1] W. E. Farrar and A. C. Reboli, "The Genus *Bacillus*-Medical". In: Dworkin, M, Falkow S, Rosenberg E, Stackebrandt E, Schleifer KH. (Eds.), *The Prokaryotes*, vol.4. Springer, Minneapolis, pp. 609-630, 2006.
- [2] A. K. Bhunia, "Foodborne microbial pathogens: mechanisms and pathogenesis", Springer, New York, 2008.
- [3] N. A. Logan, A. R. Hoffmaster, S. V. Shadomy, K. E. Stauffer, "*Bacillus* and other aerobic endospore forming bacteria". In: Versalovic J, Carroll, KC, Funke G, Jorgensen JH, Landry, ML, Warnock DW. (Eds.), *Manual of Clinical Microbiology*, 10th edn, Vol. 1, Washington DC, American Society for Microbiology, pp. 381-402. 2011.

- [4] L. V. Poulsen, "Microbial biofilm in food processing", *Lebensmittel-Wissenschaft and Technologie*, vol. 32, pp. 321-326, 1999.
- [5] R. M. Donlan and J. W. Costerton, "Biofilms: survival mechanisms of clinically relevant microorganisms", *Clinical Microbiology Reviews*, vol. 15, pp. 167-193, 2002.
- [6] A. Cherif-Antar, B. Moussa Boudjema, N. Didouh, K. Medjahdi, B. Mayo, and A. B. Florez, "Diversity and biofilm-forming capability of bacteria recovered from stainless steel pipes of a milk-processing dairy plant", *Dairy Science and Technology*, vol. 96, pp. 27-38, 2016.
- [7] T. F. Mah and G. A. O'Toole, "Mechanisms of biofilm resistance to antimicrobial agents", *Trends in Microbiology*, vol. 9, pp. 34-39, 2001.
- [8] J. D. Brooks and S. H. Flint, "Biofilms in the food industry: problems and potential solutions", *International Journal of Food Science and Technology*, vol. 43 no. 12, pp. 2163-2176, 2008.
- [9] P. F. McDermott, S. Zhao, D. D. Wagner, S. Simjee, R. D. Walker, and D. G. White, "The food safety perspective of antibiotic resistance", *Animal Biotechnology*, 13:71-84. 2002.
- [10] J. Romero, C. G. Feijoó, and P. Navarrete, "Antibiotics in Aquaculture – Use, Abuse and Alternatives", *Health and Environment in Aquaculture*, 10.5772/28157, 2012.
- [11] C. U. Tuazon, H. W. Murray, C. Levy, M. N. Solny, J. A. Curtin, and J. N. Sheagren, "Serious infections from *Bacillus* sp.", *Journal of the American Medical Association*, 241:1137-1140, 1979.
- [12] D. Djordjevic, M. Wiedmann, and L. A. McLandsborough, "Microtiter plate assay for assessment of *Listeria monocytogenes* biofilm formation", *Applied and Environmental Microbiology*, vol. 68, pp. 2950-2958, 2002.
- [13] S. Stepanovic, D. Vukovic, I Dakic, B. Savic, and M. Svabic-Vlahovic, "A modified microtiter-plate test for quantification of staphylococcal biofilm formation", *Journal of Microbiological Methods*, vol.40, pp. 175-179, 2000.
- [14] Clinical and Laboratory Standards Institute. "Performance standards for antimicrobial disk susceptibility tests; approved standard-11th ed CLSI document M02-A1", vol. 32, no.1, *Clinical and Laboratory Standards Institute*, Wayne, PA, 2012.
- [15] T. R. Oberhofer and D. W. Towle, "Evaluation of the rapid penicillinase paper strip test for detection of beta-lactamase" *Journal of Clinical Microbiology*, vol.15, pp. 196-199, 1982.
- [16] R. Kuroki , K. Kawakami , L. Qin, C. Kaji, K. Watanabe, Y. Kimura, C. Ishiguro, S. Tanimura, Y. Tsuchiya, I. Hamaguchi, M. Sakakura, S. Sakabe S, K. Tsuji, M. Inoue, and H. Watanabe, "Nosocomial bacteremia caused by biofilm-forming *Bacillus cereus* and *Bacillus thuringiensis*", *Internal Medicine Journal*, vol. 48, pp. 791-796, 2009.
- [17] M. Morikawa, S. Kagihiro, M. Haruki, K. Takano, S. Branda, R. Kolter, and S. Kanaya, "Biofilm formation by a *Bacillus subtilis* strain that produces γ -polyglutamate", *Microbiology*, vol.152, pp. 2801-2807, 2006.
- [18] R. Majed, C. Faille, M. Kallassy, and M. Gohar, "*Bacillus cereus* biofilms-same only different", *Frontiers in Microbiology*, vol.7, 1054. doi: 10.3389/fmicb.2016.01054, 2016.
- [19] H. Y. Done, A. K. Venkatesan, and R. U. Halden, "Does the recent growth of aquaculture create antibiotic resistance threats different from those associated with land animal production in agriculture?", *Journal of the American Association of Pharmaceutical Scientists*, vol.17, no.3, pp. 513-24, 2015.
- [20] O. Kursun, A. Guner, and G. Ozmen, "Prevalence of *Bacillus cereus* in rabbit meat consumed in Burdur-Turkey, its enterotoxin producing ability and antibiotic

- susceptibility”, *Kafkas Universitesi Veteriner Fakültesi Dergisi*, vol. 17 (Suppl A): S31-S35, 2011.
- [21] J. H. Yim, K. Y. Kim, J. W. Chon, D. H. Kim, H. S. Kim, D. S. Choi, I. S. Choi, and K. H. Seo, “Incidence, antibiotic susceptibility, and toxin profiles of *Bacillus cereus* sensu lato isolated from Korean fermented soybean products”, *Journal of Food Science*, vol.80, no.6, M1266-67, 2015.
- [22] I. Chaabouni, I. Barkallah, C. Hamdi, A. Jouii, M. Saidi, J. Mahillon, and A. Cherif, “Metabolic capacities and toxigenic potential as key drivers of *Bacillus cereus* ubiquity and adaptation”, *Annals of Microbiology*, vol. 65, pp. 975-983, 2015.
- [23] G. M. Noor Uddin, M. H. Larsen, H. Christensen, F. M. Aarestrup, T. M. Phu, and A. Dalsgaard, “Identification and antimicrobial resistance of bacteria isolated from probiotic products used in shrimp culture”, *Plos One* vol. 10, no. 7, e0132338. <https://doi.org/10.1371/journal.pone.0132338>, 2015.
- [24] B. A. Mohammadou, G. Le Blay, C. M. Mbofung, and G. Barbier, “Antimicrobial activities, toxinogenic potential and sensitivity to antibiotics of *Bacillus* strains isolated from Mbaja, an Hibiscus sabdariffa fermented seeds from Cameroon”, *African Journal of Biotechnology*, vol.13, no. 35, pp. 3617-3627, 2014.
- [25] M. Ikeda, Y. Yagihara, K. Tatsuno, M. Okazaki, S. Okugawa, and K. Moriya, “Clinical characteristics and antimicrobial susceptibility of *Bacillus cereus* blood stream infection”, *Annals of Clinical Microbiology and Antimicrobials*, vol.14, 43, doi 10.1186/s12941-015-0104-2, 2015.

	SAKARYA UNIVERSITY JOURNAL OF SCIENCE		 SAKARYA UNIVERSITY
	e-ISSN: 2147-835X http://www.saujs.sakarya.edu.tr		
	<u>Received</u> 15-12-2017 <u>Accepted</u> 17-04-2018	<u>Doi</u> 10.16984/saufenbilder.366696	

Contributions to *Culicoides* Latreille, 1809 (Diptera: Ceratopogonidae) Fauna of Sinop Province

Fethi TURGUT*¹

Abstract

In recent years, Sinop Province has become an important touristic center of Black Sea Region in Turkey. Akliman is also one of the most visited touristic areas of Sinop. It is notable that aquatic and semi-aquatic habitats in Akliman and surrounding areas are suitable reproduction areas for *Culicoides* (Diptera: Ceratopogonidae). Biting female *Culicoides* midges irritate people and animals because they feed by blood sucking. Thus, the study aimed to determine the species of the genus in Akliman District of Sinop Province, which is little investigated. The present study was conducted in 2014 and 2015. The study area was divided into three stations. Specimens were collected using CDC miniature light trap and black fluorescent lamp light trap at these stations, which were kept inside bottles with 70% ethyl alcohol. *Culicoides* specimens were identified using stereomicroscope and light microscope. A total of 15 species of the *Culicoides* genus were identified in the study area. *Culicoides alazanicus*, *C. cataneii*, *C. gejelensis*, *C. griseidorsum*, *C. kibunensis*, *C. longipennis*, *C. obsoletus*, *C. picturatus* and *C. subfasciipennis* species are new records for Sinop. Male individuals belonging to *C. alazanicus* and *C. griseidorsum* in Turkey have been identified for the first time in this study.

Keywords: Sinop, Akliman, Diptera, Ceratopogonidae, *Culicoides*

1. INTRODUCTION

Midges of *Culicoides* Latreille, 1809 are small midges sized 1-3 mm [1]. *Culicoides* is the largest genus in the Ceratopogonidae family with around 1400 species [2]. They spend their larva and pupa stages in aquatic and semi-aquatic habitats. Particularly mud near water sources that is rich in organic matter is mostly preferred by these insects [3]. Adults are seen in Turkey between April and October [4, 5, 6]. They reach the highest population particularly in July and August [6]. Since the female *Culicoides* biting midges feed on blood, they are important in terms of health and veterinary medicine. Infestation is an important cause of irritation in many parts of the world [7]. Santiago-Alarcon et al. [8] found out that 13 of 20 *Culicoides* species detected in a study in a suburban forest in Germany fed on the blood of humans. Similarly, Santiago-Alarcon et al. [9] reported from a study in the urban forest that *Culicoides*

fed on birds, farm animals and mostly humans. Hadj-Henni et al. [10] suggested that humans, as well as horses, donkeys, cattle, cats and chickens are also sources of blood. Bites are painful in sensitive people and cause various allergic reactions to occur [4, 7, 11]. Additionally, they lead viruses, bacteria, protozoa and helminths to be transmitted to humans [7, 12, 13]. Particularly in farm animals, there are many diseases that arise from the role of *Culicoides* as a vector [4, 12, 14]. Although they are not a vector of dangerous disease in humans [15], Oropouche virus and nematodes causing mansonellosis are known to be transmitted to humans via *Culicoides* [12, 13].

Although there are many studies on *Culicoides* in Turkey, the number of faunistic studies in Black Sea Region is fewer compared to other regions, which remained under-researched. The first faunistic study in the Black Sea Region was carried out by Dik et al. [16]. A total of 13 species were reported from Amasya, Giresun, Ordu, Sinop and Samsun Provinces. Turgut

* Corresponding Author

¹ Sinop University, Vocational School of Health Services, Department of Medical Services and Techniques, Sinop, Turkey, fturgut@sinop.edu.tr

and Kılıç [17] detected a total of 36 species with two new records in Central Black Sea Region. Dik et al. [18] reported 35 species from Western Black Sea Region with two new records. As a result of these studies, the number of *Culicoides* species found in Turkey has been reached to 61 [18].

In recent years, Sinop Province has become one of the most important touristic centers of Black Sea Region. Akliman is one of the most famous tourist areas of Sinop. The district, which is also home to Hamsilos Nature Park, hosts many tourists in summer. Furthermore, Akliman and its surrounding areas present suitable areas for reproduction for *Culicoides* spp. because they contain both aquatic and semi-aquatic habitats. The present study aims to investigate the species of this genus which irritate people in Akliman District which has become an important touristic site of Sinop.

2. MATERIAL AND METHOD

This study was carried out in Akliman District of Sinop Province from May to November 2014 and from June to November 2015. Midges were collected from the study site every 10-15 days. The midges were caught using UV led and 6 V halogen bulb CDC miniature light traps as well as 18 W, 12 V black fluorescent lamp traps [17, 19]

Akliman is 12 km away from Sinop city center and on the coastline. This district, which is on the sea level, was investigated by separating into three stations, which are reported below (Figure 1).



Figure 1. Akliman District and sampling stations (figure from Goggle maps)

Station I (42°01'41.0"N 35°03'11.0"E): This is a paddy production area which is surrounded by agricultural areas. Additionally, Karasu Stream reaches the sea at this point. However, the flow rate of the stream at this point is slow, its connection with the sea is lost from time to time, and it is a dark green, turbid and stagnant water body.

Station II (42°02'28.3"N 35°02'26.7"E): Station II representing the area surrounding Sırakaraağaçlar Stream. Sırakaraağaçlar Stream is 3.2 km long and has two divisions. Its average depth is 1.5 m. While the part of the stream which flows into the sea is sandy, other parts are muddy and look like a swamp. At the end of spring and in summer, its connection with the sea is completely lost [20, 21]. Around this station, there are residential areas of Abalı Village as well as tourist accommodation facilities. Due to these residential areas and agricultural activities, waste water enters the Stream [21]. In summer, tourists stay at the accommodation facilities in this area.

Station III (42°03'14.7"N 35°02'20.4"E): Station III covers Hamsilos Nature Park. It is a location which is surrounded by a large forest with pine trees and low level of settlement. It contains reed fields formed by puddles. The area surrounding this station is one of the areas where tourists often visit in summer.

Light traps were placed into the station before sunset. CDC miniature trap caught specimens were collected using CDC miniature light trap until the morning while the trap with the black fluorescent lamp was kept in the field for 2-3 hours to collect specimens. Collected midges were kept inside 70% ethyl alcohol. Specimens of *Culicoides* genus were determined and identified using a stereomicroscope. Preparations of *Culicoides* specimens which could not be identified by using a stereomicroscope were made [22]. Preparations were investigated under the light microscope and identified.

Taxonomic measurements and terminology were in line with the study of Szadziewski [23]. Measurements are presented below:

Palpal ratio (PR): Calculated by dividing the length of third palpal segment by the length of its widest side.

Male Antenna Ratio (AR): Calculated by dividing the total length of four distal antenna segments by the total length of nine proximal segments.

Costal Ratio (CR): Calculated by dividing costal length by wing length. Costal length and wing length were measured from basal arculus.

Tarsal Ratio (TR): Calculated by dividing first tarsomere length (basitarsus) by second tarsomere length. While tarsomere length is calculated, its part in the joint is not included in the measurement.

3. RESULTS

In this study, 15 *Culicoides* species were identified in Akliman District of Sinop Province. 9 of these species are new records for Sinop Province.

Species review

Tribe: Culicoidini Kieffer, 1911

Genus: *Culicoides* Latreille, 1809

***Culicoides alazanicus* Dzhafarov, 1961**

Material examined: Station I: 21.VI.2014, ♂, 30.VII.2015, 5 ♀♀, 29.IX.2015, 4 ♀♀; Station II: 13.IX.2014, ♀, 25.IX.2014, ♀, 22.IX.2014, ♀, ♂, 02.VI.2015, ♀, 14.VII.2015, ♀, 3 ♂♂, 26.IX.2015, 3 ♀♀, ♂, 16.IX.2015, ♀, Station III: 22.VII.2015, ♀, 30.VII.2015, 2 ♀♀ (Table 1).

Male Description: Eyes bare. Flagellomeres 1-10 with long setae and flagellomeres 2-10 fused. Flagellomeres 1, 11, 12 and 13 with sensilla coeloconica. Flagellum length 705-737 μm (n=4). AR 0.88-0.94 (n=4). Third palpal segment length 43.3-52.1 μm (n=5), sensory pit

distinct. PR 0.31-0.35 (n=5) (Figure 2 c). Thorax dark brown. Legs light brown. Hind tibial comb with four spines. TR (I) 2-2.41, TR (II) 2.47-2.73, TR (III) 1.83-1.87 (n=6). Wing length 828-1034 μm (n=6). CR 0.52-0.54 (n=6) (Figure 2 a, b). Sternite IX with a deep and wide caudomedian excavation. Basal membrane of Sternite IX without spicules (Figure 2 d, e). Dorsal and ventral apodemes of gonocoxite thin and long. Dorsal apodeme of gonocoxite sclerotized (Figure 2 f). Apex of gonostylus like a beak. Tergite IX with long and outward apicolateral processes. Aedeagus arc wide, high and sclerotized. Basal arms of paramers sclerotized and curved with acute angle (Figure 2 d, e). Paramers inflated on the middle part, ends with tapering (Figure 2 g).

Distribution in Turkey: Bartın, Zonguldak [18]. New record for Sinop.

General distribution: Albania, Azerbaijan, Belgium, Bosnia and Herzegovina, Britain I., Corsica, Croatia, Czech Republic, Danish mainland, French mainland, Germany, Near East, Portuguese mainland, Slovakia, Spanish mainland [24, 25].

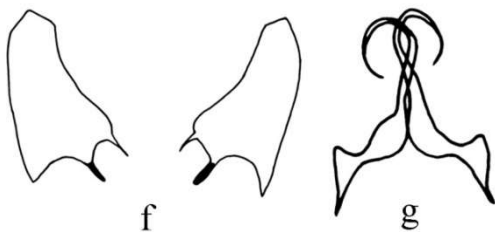
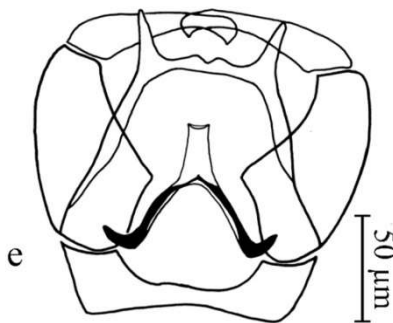
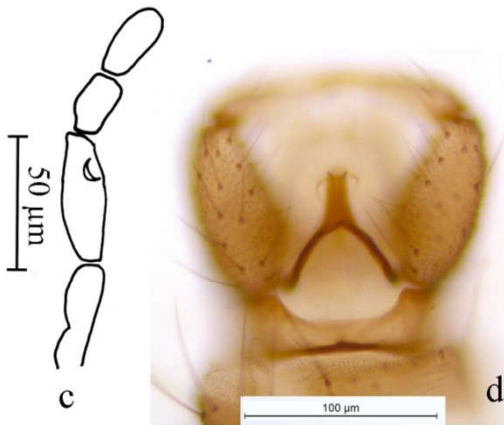
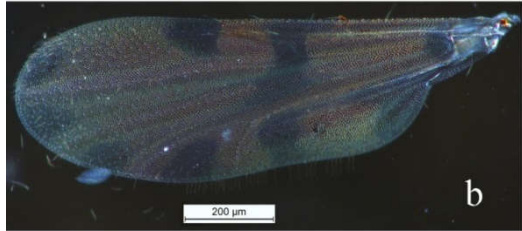
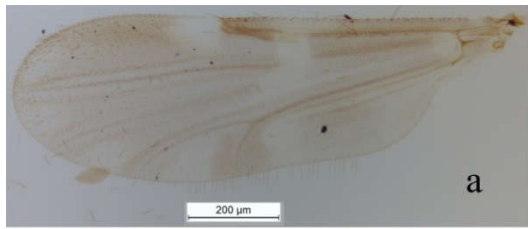


Figure 2. Male *Culicoides alazanicus* Dzhafarov, 1961. a) wing (bright field image), b) wing (dark field image), c) maxillary palp, d) and e) genitalia, f) dorsal and ventral apodemes of gonocoxite, g) parameres

Culicoides cataneii Clastrier, 1957

Material examined: Station II: 14.VII.2015, 2 ♀♀ (Table 1).

Distribution in Turkey: Adana [26], Ankara [4], Aydın [5, 27], Bursa [28], Çanakkale, Edirne, Tekirdağ [29], Elazığ [30], Hatay [31], Konya [3, 14], Kütahya [27], Samsun [17]. New record for Sinop.

General distribution: Albania, Algeria, Britain I., Channel Is., Corsica, Croatia, Cyprus, French mainland, Germany, Iran, Iraq, Israel, Italian mainland, Morocco, Portuguese mainland, Sardinia, Sicily, Spanish mainland, Switzerland, Turkmenistan, Ukraine, Vóreion Aiyáion (North Aegean Is.) [24, 25].

Culicoides circumscriptus Kieffer, 1918

Material examined: Station I: 27.VIII.2014, ♂, 30.VII.2015, ♀, 20.VIII.2015, 3 ♀♀, 28.VIII.2015, ♀, 29.IX.2015, 5 ♀♀, 4 ♂♂, 23.XI.2015, 5 ♀♀; Station II: 17.X.2014, ♀, Station III: 09.VI.2014, ♀ (Table 1).

Distribution in Turkey: Adana [26, 32], Amasya, Ordu, Samsun [16, 17], Ankara [4, 33], Antalya [26, 33, 34], Aydın [5, 27], Bartın, Bolu, Kastamonu, Zonguldak [18], Bursa [28], Çanakkale [29, 34], Çorum, Tokat [17], Edirne, İstanbul, Kırklareli, Tekirdağ [29], Denizli [27, 33], Elazığ [30], Giresun, Sinop [16], Hatay [19, 31, 32], İzmir [27, 32, 34], Konya [3, 14, 33, 35], Kütahya [27], Mersin [26], Muğla [27, 34], Niğde [36].

General distribution: Afro-tropical region, Albania, Azores Is., Belarus, Belgium, Bosnia and Herzegovina, Britain I., Bulgaria, Central European Russia, Corsica, Croatia, Cyprus, Czech Republic, Danish mainland, East Palaearctic, Estonia, French mainland, Germany, Ireland, Italian mainland, Lithuania, Near East, North Africa, North European Russia, Northern Ireland, Northwest European Russia, Norwegian mainland, Oriental region, Poland, Portuguese mainland, Romania, Sardinia, Sicily, Slovakia, Spanish mainland, Switzerland, Vóreion Aiyáion (North Aegean Is.) [24, 25].

Culicoides duddingstoni Kettle and Lawson, 1955

Material examined: Station I: 21.VI.2014, ♀, 22.VI.2015, ♀, 30.VII.2015, ♀, 28.VIII.2015, 2 ♀♀, 29.IX.2015, 3 ♀♀; Station II: 14.VII.2015, ♀, 26.VIII.2015, ♀, 20.X.2015, ♀; Station III: 22.VI.2015, 3 ♀♀, 30.VII.2015, 11 ♀♀ (Table 1).

Distribution in Turkey: Denizli, Kütahya [27], Konya [14], Samsun [17], Sinop [16].

General distribution: Britain I., Corsica, Czech Republic, Danish mainland, East Palaearctic, Estonia, Faroe Is., French mainland, Germany, Ireland, Near

East, Northern Ireland, Poland, Romania, Sardinia, Slovakia, Spanish mainland, Transcaucasus, Ukraine, Uzbekistan [24, 25].

***Culicoides festivipennis* Kieffer, 1914**

Material examined: Station I: 21.VI.2014, 3 ♀♀, ♂, 03.VII.2015, ♂, 30.VII.2015, 35 ♀♀, 2 ♂♂, 20.VIII.2015, 2 ♀♀, 29.IX.2015, 9 ♀♀; Station II: 13.VIII.2014, ♀, 25.VIII.2014, ♀, 02.X.2014, ♀, 17.X.2014, ♀, 02.VI.2015, 5 ♀♀, 14.VII.2015, 6 ♀♀, 13 ♂♂, 26.VIII.2015, 5 ♀♀, 4 ♂♂, 16.IX.2015, ♀, 05.XI.2015, ♀; Station III: 22.VII.2015, 3 ♀♀, 30.VII.2015, ♀ (Table 1).

Distribution in Turkey: Ankara [4], Antalya [33], Aydın [5], Bartın, Bolu, Düzce, Kastamonu, Zonguldak [18], Bursa [28], Çorum, Ordu, Samsun, Tokat [17], Diyarbakır [32], Edirne, Kırklareli [29], Elazığ [30], Hatay [31, 32], İzmir [27, 32], Konya [3, 14], Kütahya [27], Muğla [34], Niğde [36], Sinop [16].

General distribution: Albania, Austria, Belarus, Belgium, Bosnia and Herzegovina, Britain I., Central European Russia, Channel Is., Corsica, Croatia, Czech Republic, Danish mainland, East Palaearctic, Estonia, French mainland, Germany, Hungary, Ireland, Italian mainland, Lithuania, Luxembourg, Near East, North Africa, North European Russia, Northwest European Russia, Norwegian mainland, Poland, Portuguese mainland, Sardinia, Slovakia, Spanish mainland, Switzerland, The Netherlands [24, 25].

***Culicoides gejelensis* Dzhafarov, 1964**

Material examined: Station II: 13.VIII.2014, ♀, 25.VIII.2014, ♂, 14.VII.2015, 3 ♂♂, 16.IX.2015, ♀, 05.XI.2015, ♂, Station III: 30.VII.2015, ♀ (Table 1).

Distribution in Turkey: Amasya, Samsun [16, 17], Ankara [4], Antalya [26, 33], Aydın [5, 27], Bartın, Bolu, Düzce, Kastamonu, Zonguldak [18], Bursa [28], Çorum, Ordu, Tokat [17], Denizli [27], Edirne [29], Elazığ [30], Hatay [31], İzmir [27], Konya [3, 14], Kütahya [27], Mersin [26], Muğla [34], Niğde [36].
New record for Sinop.

General distribution: Albania, Algeria, Bosnia and Herzegovina, Corsica, Croatia, East Palaearctic, French mainland, Israel, Italian mainland, Near East, North Africa, Portuguese mainland, Sardinia, Sicily, Spanish mainland, Tajikistan, Transcaucasus, Turkmenistan, Ukraine, Uzbekistan, Vóreion Aiyáion (North Aegean Is.) [24, 25].

***Culicoides griseidorsum* Kieffer, 1918**

Material examined: Station I: 30.VII.2015, 4 ♀♀, 29.IX.2015, ♀; Station II: 28.V.2014, ♀, 14.VII.2015, ♂ (Table 1).

Male Description (n=1): Eyes bare. Flagellomeres 1-10 with long setae and flagellomeres 2-10 fused. Flagellomeres 1, 11 and 12 with sensilla coeloconica. Flagellum length 788 µm. AR 0.9. Third palpal segment with shallow sensory pit. Third palpal segment length 60 µm. PR 0.28. (Figure 3 c). Thorax dark brown. Scutellum and legs light brown, halteres pale. Hind tibial comb with four spines. TR (I) 2.04, TR (II) 2.34, TR (III) 1.95. Wing length 1200 µm. CR 0.53 (Figure 3 a, b). Sternite IX with a shallow and wide caudomedian excavation. Basal membrane of Sternite IX with small spicules (Figure 3 d, e). Dorsal apodeme of gonocoxite long and sclerotized. Ventral apodeme of gonocoxite short (Figure 3 f). Apex of gonostylus like a beak. Tergite IX with long and outward apicolateral processes. Aedeagus arc wide and high. Aedeagus apex looks like a triangle. Basal arms of paramers sclerotized and curved with acute angle (Figure 3 d, e). Paramers inflated on the middle part, ends with tapering (Figure 3 g).

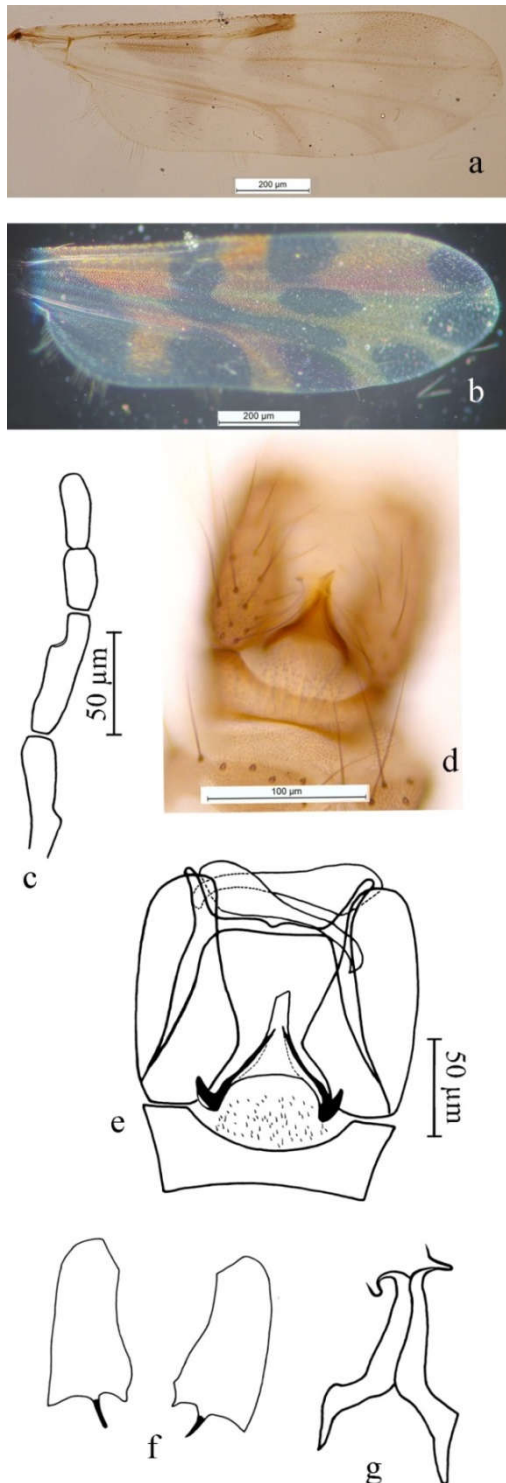


Figure 3. Male *Culicoides griseidorsum* Kieffer, 1918. a) wing (bright field image), b) wing (dark field image), c) maxillary palp, d) and e) genitalia, f) dorsal and ventral apodemes of gonocoxite, g) parameres

Distribution in Turkey: Samsun [17]. New record for Sinop.

General distribution: Britain I., Corsica, French mainland, Italian mainland, Poland, Spanish mainland, Near East, North Africa [24, 25].

***Culicoides kibunensis* Tokunaga, 1937**

Material examined: Station II: 14.VII.2015, ♀, 05.XI.2015, ♀ (Table 1).

Distribution in Turkey: Ankara [4], Bolu, Kastamonu, Zonguldak [18], Bursa [28], Denizli [27], Elazığ [30], Konya [3, 14], Ordu, Samsun, Tokat [17]. New record for Sinop.

General distribution: Albania, Andorra, Belarus, Belgium, Bosnia and Herzegovina, Britain I., Central European Russia, Channel Is., Corsica, Croatia, Czech Republic, Danish mainland, East Palaearctic, Estonia, French mainland, Germany, Hungary, Iran, Ireland, Israel, Italian mainland, Japan, Korea, Lithuania, Luxembourg, Near East, North Africa, North America, North China, North European Russia, Northern Ireland, Norwegian mainland, Poland, Portuguese mainland, Romania, Sardinia, Sicily, Slovakia, Slovenia, Spanish mainland, Switzerland, The Netherlands [24, 25].

***Culicoides longipennis* Khalaf, 1957**

Material examined: Station II: 11.IX.2014, ♂, 14.VII.2015, ♀, 26.VIII.2015, ♀ (Table 1).

Distribution in Turkey: Adana [26, 32], Amasya, Çorum, Ordu, Tokat [17], Ankara [4], Antalya [26, 33, 34], Aydın [5, 27, 33], Bartın, Bolu, Kastamonu, Zonguldak [18], Bursa [28], Denizli [27, 33], Edirne, İstanbul, Kırklareli [29], Elazığ [30], Hatay [19], İzmir [27, 32, 34], Konya [3, 14, 33], Kütahya [27], Mersin [26], Muğla [34], Niğde [36], Samsun [16, 17]. New record for Sinop.

General distribution: Algeria, Bosnia and Herzegovina, Corsica, Croatia, Cyprus, Dodekánisos (Dodecanese Is.), East Palaearctic, French mainland, Iran, Iraq, Israel, Italian mainland, Kazakhstan, Morocco, Near East, Portuguese mainland, Sardinia, Spanish mainland, Tajikistan, Transcaucasus, Turkmenistan, Ukraine, Uzbekistan, Vóreion Aiyáion (North Aegean Is.) [24, 25].

***Culicoides maritimus* Kieffer, 1924**

Material examined: Station II: 14.VII.2015, ♂, 16.IX.2015, ♀; Station III: 22.VII.2015, ♀ (Table 1).

Distribution in Turkey: Amasya, Tokat [17], Ankara, Antalya and Aydın [33], Bartın, Bolu, Zonguldak [18], Bursa [28], Denizli [27], Elazığ [30], Hatay and İzmir [32], Konya [3, 14, 33, 35], Niğde [36], Samsun [16, 17], Sinop [16].

General distribution: Albania, Algeria, Belgium, Britain I., Central European Russia, Corsica, Cyprus, Czech Republic, Danish mainland, East Palaearctic, French mainland, Germany, Hungary, Iran, Israel, Italian mainland, Kazakhstan, Morocco, Near East, Poland, Portuguese mainland, Romania, Sardinia, Sicily, Slovakia, Spanish mainland, The Netherlands, Transcaucasus, Tunisia, Turkmenistan, Ukraine, Uzbekistan, Vóreion Aiyáion (North Aegean Is.) [24, 25].

***Culicoides newsteadi* Austen, 1921**

Material examined: Station I: 22.VI.2015, ♀, 30.VII.2015, 20 ♀♀, ♂, 30.VII.2015, 2 ♀♀, ♂, 20.VIII.2015, 9 ♀♀, 2 ♂♂, 29.IX.2015, 3 ♀♀; Station II: 02.X.2014, ♀, 17.X.2014, 2 ♂♂, 14.VII.2015, 9 ♀♀, ♂, 26.VIII.2015, 19 ♀♀, 2 ♂♂, 16.IX.2015, 2 ♀♀, 05.XI.2015, ♂, 24.XI.2015, 3 ♀♀; Station III: 22.VII.2015, 2 ♀♀, 30.VII.2015, 48 ♀♀ (Table 1).

Distribution in Turkey: Ankara [4, 33], Antalya [26, 33], Amasya, Samsun [17], Aydın [5, 27, 33], Bartın, Bolu, Zonguldak [18], Çanakkale, Edirne, İstanbul, Kırklareli, Tekirdağ [29], Denizli [33], Elazığ [30], Konya [14, 33, 35], Sinop [16].

General distribution: Albania, Algeria, Austria, Azores Is., Balearic Is., Belgium, Britain I., Corsica, Cyprus, Danish mainland, Dodekánisos (Dodecanese Is.), East Palaearctic, Egypt, French mainland, Germany, Greek mainland, Hungary, Iran, Iraq, Ireland, Israel, Italian mainland, Latvia, Madeira Is., Morocco, Near East, Northern Ireland, Norwegian mainland, Portuguese mainland, Sardinia, Sicily, Slovakia, Spanish mainland, Switzerland, Tajikistan, The Netherlands, Transcaucasus, Turkmenistan, Ukraine, Vóreion Aiyáion (North Aegean Is.) [24, 25].

***Culicoides obsoletus* (Meigen, 1818)**

Material examined: Station II: 14.VII.2015, ♂ (Table 1).

Distribution in Turkey: Adana [26], Amasya, Samsun [16, 17], Ankara [4], Antalya [26, 33], Aydın [5, 27, 33], Bartın, Bolu, Düzce, Karabük, Kastamonu, Zonguldak [18], Bursa [28], Çanakkale [34], Çorum, Ordu, Tokat [17], Denizli [33], Edirne, İstanbul, Kırklareli, Tekirdağ [29], Elazığ [30], Giresun [16], Hatay [19], İzmir [32], Konya [14, 35], Kütahya [27], Mersin [26], Muğla [27]. New record for Sinop.

General distribution: Albania, Algeria, Andorra, Austria, Azores Is., Balearic Is., Belarus, Belgium, Bosnia and Herzegovina, Britain I., Canary Is., Central European Russia, Channel Is., Corsica, Croatia, Cyprus, Czech Republic, Danish mainland, East European Russia, East Palaearctic, Estonia, French

mainland, Germany, Hungary, Ireland, Italian mainland, Lithuania, Madeira Is., Morocco, Near East, North America, North European Russia, Northern Ireland, Northwest European Russia, Norwegian mainland, Poland, Portuguese mainland, Sardinia, Sicily, Slovakia, Spanish mainland, Switzerland, The Netherlands, Vóreion Aiyáion (North Aegean Is.) [24, 25].

***Culicoides picturatus* Kremer and Deduit, 1961**

Material examined: Station II: 14.VI.2015, ♀, ♂ (Table 1).

Distribution in Turkey: Amasya [16], Elazığ [30], Bartın, Bolu, Düzce, Kastamonu, Zonguldak [18], Hatay [31], Konya [14], Niğde [36], Tokat [17]. New record for Sinop.

General distribution: Britain I., Channel Is., Corsica, Danish mainland, French mainland, Israel, Italian mainland, Morocco, Near East, Portuguese mainland, Romania, Sardinia, Sicily, Spanish mainland [24, 25].

***Culicoides punctatus* (Meigen, 1804)**

Material examined: Station I: 30.VII.2015, 2 ♀♀, 20.VIII.2015, 2 ♀♀, 29.IX.2015, ♀; Station II: 26.VIII.2015, 4 ♀♀; Station III: 30.VII.2015, 2 ♀♀ (Table 1).

Distribution in Turkey: Amasya, Çorum, Ordu, Tokat [17], Ankara [4, 33], Antalya [26, 33], Aydın [33, 37], Bartın, Bolu, Düzce, Kastamonu, Zonguldak [18], Bursa [28], Çanakkale, Edirne, İstanbul, Kırklareli, Tekirdağ [29], Elazığ [30], İzmir [27], Konya [14, 33, 35], Kütahya [27], Niğde [36], Samsun [16, 17], Sinop [16].

General distribution: Afro-tropical region, Albania, Belarus, Belgium, Britain I., Central European Russia, Channel Is., Corsica, Cyprus, Czech Republic, Danish mainland, Dodekánisos (Dodecanese Is.), East Palaearctic, Estonia, Finland, French mainland, Germany, Hungary, Ireland, Italian mainland, Latvia, Lithuania, Luxembourg, Near East, North Africa, North European Russia, Northern Ireland, Northwest European Russia, Norwegian mainland, Poland, Portuguese mainland, Sardinia, Sicily, Slovakia, Spanish mainland, Switzerland, The Netherlands [24, 25].

***Culicoides subfasciipennis* Kieffer, 1919**

Material examined: Station I: 21.VI.2014, 2 ♀♀, ♂, 30.VII.2015, 3 ♀♀, 28.VIII.2015, 3 ♀♀; Station II: 14.VII.2015, 3 ♂♂; Station III: 30.VII.2015, ♀ (Table 1).

Distribution in Turkey: Antalya [33], Aydın, Denizli and Kütahya [27], Bartın, Bolu, Kastamonu,

Zonguldak [18], Çorum, Ordu, Samsun, Tokat [17], Elazığ [30], Konya [3, 14]. New record for Sinop.

General distribution: Algeria, Austria, Belarus, Belgium, Britain I., Central European Russia, Corsica, Czech Republic, Danish mainland, East European Russia, East Palaearctic, Estonia, French mainland, Germany, Hungary, Iran, Italian mainland, Lithuania, Mongolia, Morocco, Near East, North China, North European Russia, Poland, Portuguese mainland, Sardinia, Sicily, Slovakia, Spanish mainland, Switzerland, The Netherlands [24, 25].

Table 1. Male and female numbers of species according to stations

	Station I		Station II		Station III	
	♀	♂	♀	♂	♀	♂
<i>C. alazanicus</i>	9	1	9	5	3	-
<i>C. cataneii</i>	-	-	2	-	-	-
<i>C. circumscriptus</i>	15	5	1	-	1	-
<i>C. duddingstoni</i>	8	-	3	-	14	-
<i>C. festivipennis</i>	49	4	22	17	4	-
<i>C. gejjelensis</i>	-	-	2	5	1	-
<i>C. griseidorsum</i>	5	-	1	1	-	-
<i>C. kibunensis</i>	-	-	2	-	-	-
<i>C. longipennis</i>	-	-	2	1	-	-
<i>C. maritimus</i>	-	-	1	1	1	-
<i>C. newsteadi</i>	35	4	34	6	50	-
<i>C. obsoletus</i>	-	-	-	1	-	-
<i>C. picturatus</i>	-	-	1	1	-	-
<i>C. punctatus</i>	5	-	4	-	2	-
<i>C. subfasciipennis</i>	8	1	-	3	1	-

4. DISCUSSION

In this study, a total of 15 species of the *Culicoides* genus was determined in Aklıman District of Sinop Province.

Dik et al. [16], reported *C. circumscriptus*, *C. duddingstoni*, *C. festivipennis*, *C. maritimus*, *C. newsteadi* and *C. punctatus* from Sinop as a result of their study in Black Sea Region. In line with Dik et al.'s findings, all of the identified species were obtained in this study. In addition to these species, distribution of

C. alazanicus, *C. cataneii*, *C. gejjelensis*, *C. griseidorsum*, *C. kibunensis*, *C. longipennis*, *C. obsoletus*, *C. picturatus* and *C. subfasciipennis* species in Sinop was determined. With the recently registered species in Sinop, the number of species of the *Culicoides* fauna in Sinop reaches 15. Males of *C. alazanicus* and *C. griseidorsum* were firstly identified with this study in Turkey.

Dik et al. [16] reported two females *Culicoides* whose species they could not identify and they suggested that the specimens had characteristics of *Pictipennis* group. As a result of this study, no specimens of the specified characteristics could be determined.

C. alazanicus species was reported from Bartın and Zonguldak [18]. Detection of this species in Sinop shows its distribution along West Black Sea coastline. However, in spite of the sufficient number of field studies [18], the fact that the species has not been detected in Kastamonu is an interesting point. Further studies on the presence of the species in Kastamonu emerges.

C. griseidorsum species was detected in Turkey for the second time in Sinop after its first detection in Samsun [17]. Its male was detected for the first time in Turkey.

C. cataneii was detected in Turkey for the second time in Sinop following its first detection in Samsun Province of the Black Sea Region [17].

With the detection of *C. gejjelensis*, *C. longipennis*, *C. obsoletus* and *C. punctatus* species in Sinop, it was understood that these species were the most common species in Central and Western Black Sea Region. *C. obsoletus* was detected in all provinces of Central and Western Black Sea Region. *C. gejjelensis* and *C. punctatus* were reported from Karabük, while *C. longipennis* was reported from Central and Western Black Sea Region provinces other than Düzce and Karabük [17, 18]. With the detection of *C. picturatus* in Sinop, its distribution in Western Black Sea Region except Karabük can be noticed. When the data are assessed, these species are estimated to be distributed in Karabük and surrounding areas, and this can be verified as a result of the new studies.

When study areas are assessed on station basis, the highest number of species was caught in the Station II. In the Station II, all of the 15 reported species were detected. In the Station I, 8 species (*C. alazanicus*, *C. circumscriptus*, *C. duddingstoni*, *C. festivipennis*, *C. griseidorsum*, *C. newsteadi*, *C. punctatus* and *C. subfasciipennis*) were determined while in the Station III, 9 species (*C. alazanicus*, *C. circumscriptus*, *C. duddingstoni*, *C. festivipennis*, *C. gejjelensis*, *C. maritimus*, *C. newsteadi*, *C. punctatus* and *C.*

subfasciipennis) were identified. The fact that Station II is located close to residential areas, as well as the relatively higher human presence of this area and the presence of cattle barns are factors attracting *Culicoides* to the area. *C. cataneii*, *C. kibunensis*, *C. longipennis*, *C. obsoletus* and *C. picturatus* were only detected in the Station II. The fact that Station II all of the 15 species reported from the field studies in July 2015 were detected in the station. Particularly, the field study dated 14.VII.2015 is striking. 13 of 15 species were identified in this field study. Given that *Culicoides* reach its highest population density in July and August [6] is the most important reason for us to obtain this result.

Culicoides adults are generally reported to be seen in Turkey between April and October [6]. *Culicoides* is reported to be seen in Bursa between May and September [28], in Elazığ [30] and Konya [14] between April and October. Eren et al. [4] reported in their study in Ankara that they could not collect *Culicoides* specimens in April and after mid-October. Specimens were collected from Hatay [31] between April and October, from Niğde [36] between June and October and from Thrace Region [29] between August and October. In their study on the growth of larvae and pupae, which was carried out in Konya between April and November, Uslu and Dik [6] obtained adult midges between May and October. However, they could not obtain adult midges in November. In their study on reproduction areas of *Culicoides*, which was carried out in Konya during the whole year, Uslu and Dik [6] only could collect specimens were collected from between May and October. The findings from previous studies showed that adult *Culicoides* could only be seen in Turkey until the end of October. However, the collection of *Culicoides* specimens were collected from in November from Aklıman District is going to change this notion. In Sinop, *C. festivipennis*, *C. gejjelensis* and *C. kibunensis* were collected at the beginning of November, while *C. circumscriptus* and *C. newsteadi* were collected until the end of November. Therefore, it is prominent that these midges can survive until the end of November in provinces like Sinop where winter conditions are observed later than other areas.

Three nematodes (*Mansonella ozzardi*, *M. perstans*, *M. streptocerca*) causing mansonellosis and Oropouche virus are transmitted to humans by biting midges [12]. *Culicoides* species transmitting filarial nematodes and Oropouche virus don't have distribution in Turkey. These species are also not found in Sinop. Thus the most important harmful effect for people in this region is their attacks and discomfort caused by their biting.

Santiago-Alarcon et al. [8] reported *C. festivipennis*, *C. kibunensis* and *C. obsoletus* among the species fed by human blood. These three species are also found in Aklıman. Therefore it is highly probable that these species attack the people and suck blood in Aklıman District. Since Aklıman has highly suitable aquatic and semi-aquatic breeding habitats for *Culicoides*, it seems quite difficult to control the breeding sites of the biting midges. For this reason the solution in the fight against *Culicoides* may be the use of mosquito control methods in Aklıman.

As a result, findings from Aklıman District contribute to the *Culicoides* fauna of Black Sea Region and sheds light on new studies. Due to having different types of habitats, it is considered that the number of species collected in Sinop is expected to increase with the province-wide new faunistic studies.

REFERENCES

- [1] G. J. Venter, K. Labuschagne, S. N. Boikanyo, L. Morey, "The effect of high frequency sound on *Culicoides* numbers collected with suction light traps", *Journal of the South African Veterinary Association*, vol. 83, no. 1, pp. 35-40, 2012.
- [2] A. Borkent (2016). *World species of biting midges (Diptera: Ceratopogonidae)*. [Online]. Available: <http://www.inhs.illinois.edu/files/1114/2384/5200/CeratopogonidaeCatalog.pdf>
- [3] U. Uslu, B. Dik, "Description of breeding sites of *Culicoides* species (Diptera: Ceratopogonidae) in Turkey", *Parasite*, vol. 14, no. 2, pp. 173-177, 2007.
- [4] H. Eren, Ş. Yağcı, Ş. Dinçer, "Determination of *Culicoides* (Diptera: Ceratopogonidae) species in Ankara", *Ankara Üniversitesi Veteriner Fakültesi Dergisi*, vol. 42, pp. 179-182, 1995.
- [5] Ş. Yağcı, H. Eren, Ş. Dinçer, "Some of the species of Nematocera (Diptera) determined in Aydın area", *Türkiye Parazitoloji Dergisi*, vol. 23, no. 2, pp. 210-215, 1999.
- [6] U. Uslu, B. Dik, "Seasonal distribution of species *Culicoides* (Diptera: Ceratopogonidae) in Konya Province", *Veteriner Bilimleri Dergisi*, vol. 20, no.4, pp. 5-10, 2004.
- [7] Y. Braverman, R. Galun, "The medical and veterinary importance of the genus *Culicoides* (Diptera: Ceratopogonidae)", *Refuah Veterinarith*, vol. 30, no. 2, pp. 62-68, 1973.

- [8] D. Santiago-Alarcon, P. Havelka, H. M. Schaefer, G. Segelbacher, "Bloodmeal analysis reveals avian *Plasmodium* infections and broad host preferences of *Culicoides* (Diptera: Ceratopogonidae) vectors", *PLoS One*, vol 7, no.2: e31098, 2012.
- [9] D. Santiago-Alarcon, P. Havelka, E. Pineda, G. Segelbacher, H. M. Schaefer, "Urban forests as hubs for novel zoonosis: blood meal analysis, seasonal variation in *Culicoides* (Diptera: Ceratopogonidae) vectors, and avian haemosporidians", *Parasitology*, vol. 140, no. 14, 1799-1810, 2013.
- [10] L. Hadj-Henni, T. De Meulemeester, J. Depaquit, P. Noël, A. Germain, R. Helder, D. Augot, "Comparison of vertebrate cytochrome b and prepronociceptin for blood meal analyses in *Culicoides*", *Frontiers in Veterinary Science*, vol. 2, article 15, 2015.
- [11] D., Pekmezci, A. A. Sancak, O. Pınar, D. Çakıroğlu, S. Arslan, "Allergen determination in thoroughbred stallions via detecting serum specific IgE", *Kafkas Üniversitesi Veteriner Fakültesi Dergisi*, vol. 19, no. 6, 1045-1048, 2013.
- [12] G. R. Mullen, "Biting Midges (Ceratopogonidae)," in *Medical and Veterinary Entomology*, G. R. Mullen, L. Durden, Eds. USA, CA, San Diego: Academic Press, 2002, pp. 163-183.
- [13] S. Carpenter, M. H. Groschup, C. Garros, M. L. Felipe-Bauer, B. V. Purse, "*Culicoides* biting midges, arboviruses and public health in Europe", *Antiviral research*, vol. 100, no. 1, pp. 102-113, 2013.
- [14] B. Dik, T. Dinçer, "Studies on *Culicoides* (Diptera: Ceratopogonidae) species around Konya", *Doğa Türk Veterinerlik ve Hayvancılık Dergisi*, vol. 16, no. 2, pp. 199-215, 1992.
- [15] Y. H. Lin, M. T. Yu, T. W. Kuo, K. I. Lam, J. T. Yang, "Does *Culicoides* spp. (Diptera: Ceratopogonidae) not suck human blood in Riparian Habitat of a National Park", *Advances in Entomology*, vol. 5, pp. 93-98, 2017.
- [16] B. Dik, M. Kurt, İ. Aydın, "A study on *Culicoides* (Diptera: Ceratopogonidae) species in Black Sea Region in Turkey", *Bornova Veteriner Kontrol Araştırma Enstitüsü Dergisi*, vol. 30, no. 44, pp. 23-26, 2008.
- [17] F. Turgut, A. Y. Kılıç, "The Ceratopogonidae (Insecta: Diptera) fauna of the Central Black Sea Region in Turkey", *Turkish Journal of Zoology*, vol. 39, no. 6, pp. 1071-1089, 2015.
- [18] B. Dik, Ö. Kuçlu and R. Öztürk, "*Culicoides* Latreille, 1809 (Diptera: Ceratopogonidae) species in the Western Black Sea Region of Turkey, new records for the Turkish fauna", *Turkish Journal of Veterinary and Animal Sciences*, vol. 41, no. 2, pp. 228-237, 2017.
- [19] N. Tilki, B. Dik, "The effects of different light-sources on the capture of *Culicoides* species (Diptera: Ceratopogonidae)", *Türkiye Parazitoloji Dergisi*, vol. 27, no.2, pp. 144-147, 2003.
- [20] Z. Karşlı, O. Aral, "Population age, sex structure and growth of *Aphanius danfordii* (Boulenger, 1890) to Sırakaraağaçlar Stream, Turkey", *Journal of Animal and Veterinary Advances*, vol. 9, no. 10, pp. 1427-1431, 2010.
- [21] L. Bat, M. Akbulut, M. Çulha, M. Sezgin, "The macrobenthic fauna of Sırakaraağaçlar Stream flowing into the Black Sea at Aklıman, Sinop". *Journal of Black Sea/ Mediterranean Environment*, vol. 6, no. 1, 71-86, 2000.
- [22] W. Wirth, "The subgenus *Atrichopogon* (*Lophomyidium*) with a revision of the Nearctic species (Diptera: Ceratopogonidae)", *Insecta Mundi*, vol. 8, no. 1-2, pp. 17-36, 1994.
- [23] R. Szadziewski, "Biting midges (Diptera, Ceratopogonidae) from Baltic amber", *Polskie Pismo Entomologiczne*, vol. 57, pp. 3-283, 1988.
- [24] H. Remm, "Family Ceratopogonidae," in *Catalogue of Palaearctic Diptera, volume 3, Ceratopogonidae-Mycetophilidae*, A. Soos and L. Papp, Eds. Hungary, Budapest: Akademiai Kiado, 1988, pp.11-110.
- [25] R. Szadziewski, A. Borkent, P. Dominiak. (2017). *Fauna Europaea: Ceratopogonidae*. In: P. Beuk & T. Pape, *Fauna Europaea: Diptera Nematocera*. Fauna Europaea Version 2.6.2 [Online]. Available: URL <http://www.faunaeur.org>
- [26] B. Dik, "Determination of *Culicoides* Latreille, 1809 (Diptera: Ceratopogonidae) species in Adana, İçel and Antalya arounds", *Türk Veteriner Hekimliği Dergisi*, vol. 5, pp. 48-55, 1993.
- [27] B. Dik, "Determination of *Culicoides* species (Diptera: Ceratopogonidae) from Aegean Region", *Türkiye Parazitoloji Dergisi*, vol. 20, no. 1, pp. 131-137, 1996.

- [28] H., Eren, A. İnci, "Species of *Culicoides* (Diptera: Ceratopogonidae) determined in an area of Bursa (Gemlik)", *Türkiye Parazitoloji Dergisi*, vol. 26, no. 2, 199-200, 2002.
- [29] A. Deniz, T. Öncel, M. J. Patakakis, "Species composition of *Culicoides* Latreille, 1809 (Diptera: Ceratopogonidae) in Thrace Region of Turkey", *Kafkas Üniversitesi Veteriner Fakültesi Dergisi*, vol. 16, no. 6, pp. 1057-1060, 2010.
- [30] H. Yılmaz, N. Dumanlı, "Investigations on *Culicoides* (Diptera: Ceratopogonidae) species in Elazığ Province", *Fırat Üniversitesi Sağlık Bilimleri Dergisi*, vol. 11, no. 1, pp. 135-143, 1997.
- [31] B. Dik, M. Yaman, U. Uslu, "*Culicoides* species (Latreille, 1809) (Diptera: Ceratopogonidae) in Hatay Province", *Kafkas Üniversitesi Veteriner Fakültesi Dergisi*, vol. 16, no. Suppl. B, pp. 255-258, 2010.
- [32] S. Navai, "Biting-midges of the genus *Culicoides* (Diptera: Ceratopogonidae) from South-west Asia". Ph.D., College Park, University of Maryland, MD, USA, 1977
- [33] M. Jennings, J. Boorman, H. Ergün, "*Culicoides* from Western Turkey in relation to bluetongue disease of sheep and cattle", *Revue d'élevage et de médecine vétérinaire des pays tropicaux*, vol. 36, no. 1, pp. 67-70, 1983.
- [34] B. Dik, S. Yavru, U. Uslu, O. Yapıcı, E. Esin, "Determination of *Culicoides* species (Diptera: Ceratopogonidae) as suspect vectors of epizootic haemorrhagic disease and bluetongue viruses in southern and western Anatolia by RT-PCR", *Revue de Médecine Vétérinaire*, vol. 163, no.11, pp. 505-510, 2012.
- [35] B. Dik, R. Ergül, "Nocturnal flight activities of *Culicoides* (Diptera: Ceratopogonidae) species in Konya", *Türkiye Parazitoloji Dergisi*, vol. 30, no. 3, pp. 213-216, 2006.
- [36] B. Dik, M. Karatepe, B. Karatepe, Ş. Yağcı, "*Culicoides* Latr, 1809 (Diptera: Ceratopogonidae) species in the Niğde Province", *Türkiye Parazitoloji Dergisi*, vol. 30, no. 2, pp. 121-124, 2006.
- [37] M. Leclercq, "Contribution à l'étude des diptères suceurs de sang de Turquie". *Bulletin des Recherches Agronomiques de Gembloux*, vol. 1, pp. 455-457, 1966.

	SAKARYA UNIVERSITY JOURNAL OF SCIENCE		 SAKARYA UNIVERSITY
	e-ISSN: 2147-835X http://www.saujs.sakarya.edu.tr		
	<u>Received</u> 08-02-2018 <u>Accepted</u> 23-04-2018	<u>Doi</u> 10.16984/saufenbilder.392118	

Extraction of propionic acid by emulsion liquid membrane using trioctylamine in toluene

Aynur Manzak ^{*1}

Abstract

The extraction of carboxylic acids by emulsion liquid membranes has also attracted attention in biotechnology, due to the high selectivity for the desired product, high separation rate and lower costly. The emulsion type liquid membrane system consists of three phases (water/organic/water) in which the organic phase acts as a membrane between the aqueous internal phase and the aqueous external phase. The main parameters such as surfactant concentration, mixing speed, feed phase pH, carrier concentration, and feed phase concentration were investigated. In the optimum conditions, extraction efficiency was obtained 71% in 10 minutes using trioctylamine (5% w/w) as a carrier, Span 80 (4% w/w) as a surfactant, toluene (91% w/w) as a diluent, sodium carbonate (10% w/w) as a stripping solution, mixing speed 300 rpm and feed phase pH 2,5.

Keywords: propionic acid, trioctylamine, emulsion liquid membrane

1. INTRODUCTION

Most of the carboxylic acids that are being used in food and pharmaceutical industry are produced by fermentation with the improvement of the biotechnology. Separation of carboxylic acids from fermentation broth, reaction mixtures and waste solutions has gained importance recently. Despite being produced by fermentation, recovery of biomass product is not practical due to the impairing the biomasses and high cost recovery expenses.

Carboxylic acids in existing processes are removing the microorganisms from the fermentation foam and then precipitation of insoluble calcium salts. As this recycle technique is a complicated process, liquid-liquid extraction and liquid-membrane techniques are suggested as an alternative to traditional precipitation process. But liquid-liquid extraction has many

disadvantages due to the toxicity of the solvents and study with bacteria. This problem can be solved by using ultrafiltration [1,2], reverse osmosis [3,4], nano-filtration [5], membrane electro dialysis [6], emulsion liquid membrane [7,8], supported liquid membrane [9,10] as systems [11-14].

Emulsion Liquid Membrane (ELM) is a proper technique for the recovery of fermentation products. ELM is more efficient technique than liquid-liquid extraction, using solvent and solution with less values are its superiority. Extraction and stripping occur together on the large surfaces of liquid membranes prepared with the minimum amount of carrier in the ELM systems. Separation process of carboxylic acids with liquid membranes has attracted attention in biotechnology as it has provided high selectivity, separation speed and energy efficiency for the desired product. There are studies in which extraction of propionic acid

* Corresponding Author

¹Department of Chemistry, Sakarya University, Sakarya, Turkey, manzak@sakarya.edu.tr

was conducted by using reactive and liquid-liquid extraction systems [15-22].

Propionic acid that is produced by fermentation method, is a valuable chemical for agricultural applications and is being used protective compound in food and pharmaceutical industry.

ELM system consists of three phases; water/organic/water (W/O/W) that organic phase is moved as a membrane between internal aqueous phase and external aqueous phase. In this study, extraction of propionic acid was provided in aqueous solution.

2. EXPERIMENTAL

2.1. Materials

Propionic acid (Merck), surfactant Span 80 (Fluka), tertiary amine: trioctylamine (Merck), toluene and sodium carbonate (Sigma-Aldrich) were used in this study.

2.2. Preparation of membrane

(W/O) type emulsion was prepared mixing with surfactant Span 80 (sorbitan monooleate), carrier Alamine 300 (trioctylamine) and diluent (toluene) and stripping solution (Na_2CO_3) at 2000 rpm. (W/O/W) type emulsions were formed by adding mixture to feed solution. The mixing process was stopped at different periods and samples were taken from the aqueous phase. The acid concentration was measured by High Performance Liquid Chromatography (HPLC, Shimadzu LC-20AD and Hypersil C18 ODS Column).

The effects of surfactant concentration, mixing speed, carrier concentration, pH and concentration of feed solution parameters were investigated in this study. Two phases were occurred; feed phase and membrane phase at the end of the experiment. Emulsion was broken into its constituent using a high-voltage splitter with niobium electrodes.

3. RESULTS AND DISCUSSION

3.1. Effect of surfactant concentration

The surfactant was being used in order to increase the emulsion stability and decrease the surface tension in ELM processes. Span 80 (sorbitan monooleate) has been widely used in various

industrial applications. Surfactant concentration added to the membrane phase was changed between (3-5%). As it can be seen in Figure 1, surfactant addition has increased emulsion stability and extraction rate. Too little surfactant renders the membrane weak. 50% extraction efficiency was occurred in 10 minutes with 4% (w/w) concentration. The extraction efficiency was shown equation 1.

$$\eta = 1 - \frac{c}{c_0} \quad (1)$$

c : Actual concentration, c_0 : Initial concentration

Excess of surfactant increases the interface resistance and membrane viscosity and decreases the extraction.

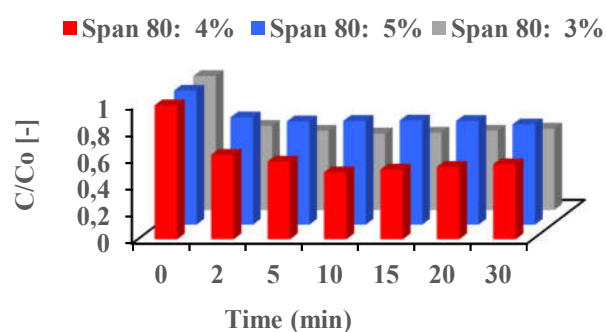


Figure 1. Effect of the surfactant concentration on the extraction rate (Diluent: Toluene, extractant: trioctylamine (5% w/w), feed phase concentration: propionic acid (10% w/v), feed phase pH: 2,5, stripping phase: Na_2CO_3 (10% w/v), mixing speed: 300 rpm)

3.2. Effect of mixing speed

Mixing speed is one of the parameters that affect the mass transfer rate in ELM processes. It affects the emulsion stability and diameter of emulsion drops. Mixing speed was changed 250, 300 and 500 rpm.

Increase on the mixing speed causes obtaining smaller emulsion drops and faster mass transfer speed. However unlimited increase causes a break of emulsion and decreases on the extraction that is effective parameter for propionic acid transport. The best appropriate mixing speed was found as 300 rpm.

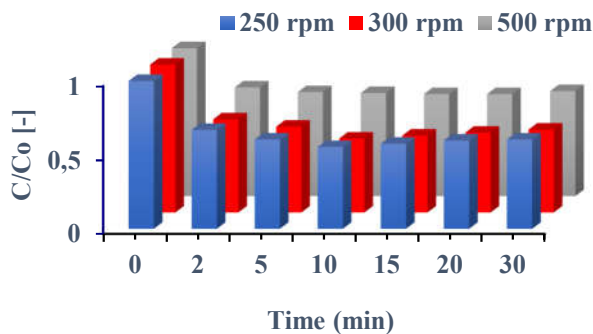


Figure 2. Effect of the mixing speed on the extraction rate (Diluent: Toluene, surfactant: Span 80 (4% w/w), extractant: trioctylamine (5% w/w), feed phase concentration: propionic acid (10% w/v), feed phase pH: 2,5, stripping phase: Na₂CO₃ (10% w/v))

3.3. Effect of feed solution pH

pH value of feed solution has an important role in ELM processes. Initial pH of the feed solution was differentiated between 1 and 4 in order to search the effect of pH on propionic acid extraction.

In order to change pH, HCl and NaOH were added to feed phase. The extraction rate decreased in Figure 3, when the HCl was added to feed phase. The competitive of HCl against the propionic acid has decreased the extraction of propionic acid. The best extraction efficiency was occurred in 10 minutes with pH: 2.5.

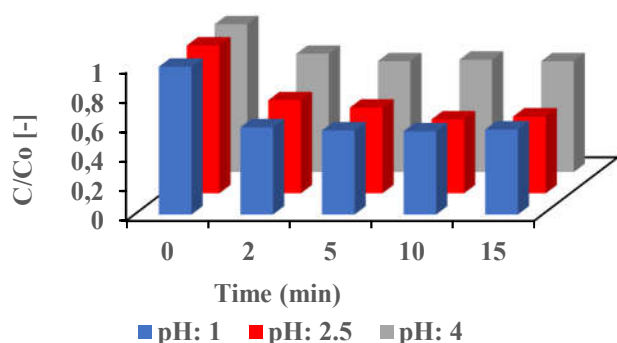


Figure 3. Effect of the feed solution pH on the extraction rate (Diluent: Toluene, surfactant: Span 80 (4% w/w), extractant: trioctylamine (5% w/w), feed phase concentration: propionic acid (10% w/v), stripping phase: Na₂CO₃ (10% w/v), mixing speed: 300 rpm)

3.4. Effect of extractant concentration

Tertiary amine (Alamine 300) that is used as carrier reacts with carboxylic acids. Extracted acid and extractant are possible easily recycled. This characteristic is being used in liquid membrane processes. Extracting ability of the extractants is identified by the formation of acid-amine complexes.

Characteristics of carriers are connected with the used solution as well as the basic characteristics of the molecule. During the solvent selection, immiscibility, volatility, viscosity and carbon number in the compound features with liquid solution are considered. Because of high dielectric constant and low viscosity, toluene was selected as solvent in propionic acid extraction in this study.

As it can be seen in the Figure 4, extraction of propionic acid has increased with the increase of the concentration of carrier agent.

Increase of carrier concentration more than (5% w/w) was caused deflection on stability of emulsion. Extraction efficiency was decreased.

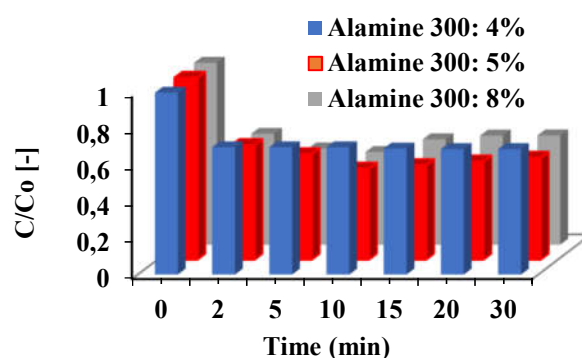


Figure 4. Effect of the extractant concentration on the extraction rate (Diluent: Toluene, surfactant: Span 80 (4% w/w), feed phase concentration: propionic acid (10% w/v), feed phase pH: 2,5, stripping phase: Na₂CO₃ (10% w/v), mixing speed: 300 rpm)

3.5. Effect of initial feed concentration

The different concentration of propionic acid in feed solutions was measured in the optimum conditions. Extraction has decreased with the increase of initial feed concentration, as it can be seen in the Figure 5.

The membrane was filled up with propionic acid complex and as there was no sufficient Na₂CO₃ in stripping agent, extraction was decreased. As the initial feed concentration was 10% (w/v), 50% acid was extracted. When the concentration was decreased to 1% (w/v), extraction efficiency was increased to 71% in 10 minutes.

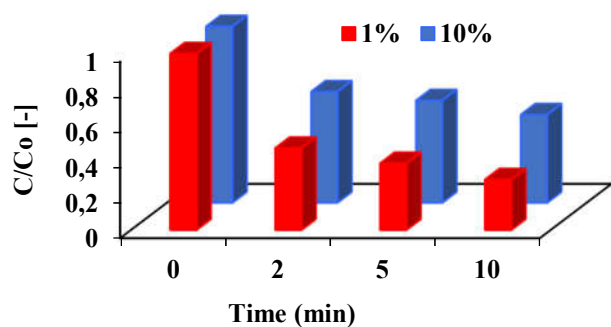


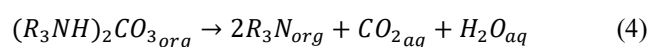
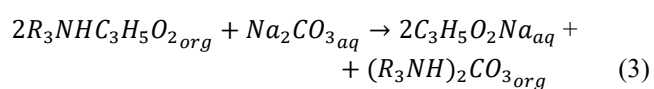
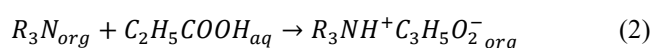
Figure 5. Effect of the feed solution concentration on the extraction rate (Optimum conditions: Diluent: Toluene (91% w/w), surfactant: Span 80 (4% w/w), extractant: trioctylamine (5% w/w), stripping phase: Na₂CO₃ (10% w/v), mixing speed: 300 rpm, feed phase pH: 2,5)

3.6. Transport mechanism of propionic acid

Alamine 300 contains R₃ basic nitrogen atom. It reacts with organic and inorganic acids in order to form amine based salt. Produced amine salts can create ion change reactions with other anions easily. Reaction with secondary and tertiary amines, ionized propionic acids have performed between the interfaces of aqueous and membrane phases.

The study in which sodium carbonate was used as stripping agent can be explained with the mechanisms below:

Formation of amine salt between interfaces of feed and membrane phases (2). Transfer of amine salt following stripping in interface of a membrane and internal phases (3). Deterioration of amine carbonate in the sub surfaces of membrane feed phases to carbon dioxide and transfer for the formation of amine (4).



4. CONCLUSIONS

In the extraction created with the mixture of a membrane and prepared by using carrier Alamine 300 in Toluene with the emulsion type liquid membrane process, 71% propionic acid extraction was occurred just in 10 minutes. The optimum conditions obtained from the experiments:

surfactant Span 80 (4% w/w), extractant Alamine 300 (5% w/w), diluent toluene (91% w/w), stripping phase Na₂CO₃ (10% w/w), mixing speed 300 rpm, feed phase pH 2,5.

REFERENCES

- [1] J.P.S.G. Crespo, M.J. Moura and M.J.T. Carrando, "Ultrafiltration membrane and cell recycle for continuous culture of *Propionibacterium*", *Journal of Membrane Science*, vol. 61, pp. 303-314, 1991.
- [2] A. Colombari, L. Roger and P. Boyaval, "Production of propionic acid from whey permeate by sequential fermentation, ultrafiltration and cell recycling", *Biotechnology and Bioengineering*, vol. 42, pp. 1091-1098, 1993.
- [3] L.R. Schlicher and M. Cheryan, "Reverse osmosis of lactic acid fermentation broth", *Journal of Chemical Technology and Biotechnology*, vol. 49, pp. 129-140, 1990.
- [4] B.R. Smith, R.D. MacBean and G.C. Cox, "Separation of lactic acid from lactose fermentation liquors by reverse osmosis", *Australian Journal of Dairy Technology*, vol. 32, pp. 23-26, 1977.
- [5] J.M.K. Timmer, H.C. Van der Horst and T. Robbertsen, "Transport of lactic acid through reverse osmosis and nanofiltration membranes", *Journal of Membrane Science*, vol. 85, pp. 205-216, 1993.
- [6] M. Hongo, Y. Nomura and M. Iwahara, "Novel method of lactic acid production by electro dialysis fermentation", *Applied and Environmental Microbiology*, vol. 52, pp. 314-319, 1986.
- [7] A. Manzak and O. Tutkun, "Extraction of citric acid through an emulsion liquid membrane containing Aliquat 336 as carrier", *Separation Science and Technology*, vol. 39, pp. 2497-2512, 2004.
- [8] N. Jusoh, N. Othman and N.A. Nasruddin, "Emulsion liquid membrane technology in organic acid purification", *Malaysian Journal of Analytical Sciences*, vol. 20, pp. 436-443, 2016.
- [9] L.-K. Ju and A. Verma, "Characteristics of lactic acid transport in supported liquid

- membranes,” *Separation Science and Technology*, vol. 29, pp. 2299-2315, 1994.
- [10] N.D. Patil, A.W. Patwardhan and A.V. Patwardhan, “Carboxylic acids separation using hollow fiber supported liquid membrane”, *Indian Journal of Chemical Technology*, vol. 24, pp. 30-31, 2017.
- [11] R. Wodzki and J. Nowaczyk, “Propionic and acetic acid pertraction through a multimembrane hybrid system containing TOPO or TBP”, *Separation and Purification Technology*, vol. 26, pp. 207-220, 2002.
- [12] A.M. Eyal and E. Bressler, “Industrial separation of carboxylic and amino acids by liquid membranes: Applicability, process considerations, and potential advantage”, *Biotechnology and Bioengineering*, vol. 41, pp. 287-295, 1993.
- [13] Y.H. Cho, H.D. Lee and H.B. Park, “Integrated membrane processes for separation and purification of organic acid from a biomass fermentation process”, *Industrial Engineering Chemistry Research*, vol. 51(30), pp. 10207–10219, 2012.
- [14] Q.Z. Li, X.L. Jiang, X.J. Feng, J.M. Wang, C. Sun, H.B. Zhang, M. Xian, and H.Z. Liu, “Recovery Processes of Organic Acids from Fermentation Broths in the Biomass-Based In the Biomass-Based Industry”, *Journal of Microbiology and Biotechnology*, vol. 26, pp. 1–8, 2016.
- [15] A. Keshav, K.L. Wasewar and S. Chand, “Extraction of propionic acid using different extractants (tri-n- butylphosphate, tri-n-octylamine and Aliquat 336)”, *Industrial Engineering Chemistry Research*, vol. 47, pp. 6192–6196, 2008a.
- [16] A. Keshav, K.L. Wasewar and S. Chand, “Equilibrium studies for extraction of propionic acid using tri-n- butyl phosphate in different solvents”, *Journal of Chemical Engineering Data*, vol. 53, no. 7, pp. 1424–1430, 2008b.
- [17] A. Keshav, K.L. Wasewar and S. Chand, “Equilibrium and kinetics of extraction of propionic acid using tri-n-octyl phosphineoxide”, *Chemical Engineering Technology*, vol. 31, no. 9, pp. 1290-1295, 2008c.
- [18] A. Keshav, K.L. Wasewar and S. Chand, “Reactive extraction of propionic acid with tri-n-octylamine in different diluents”, *Separation and Purification Technology*, vol. 63, pp. 179-183, 2008d.
- [19] A. Keshav, K.L. Wasewar and S. Chand, “Study of binary extractants and modifier – diluents systems for reactive extraction of propionic acid”, *Fluid Phase Equilibria*, vol. 275, pp. 21–26, 2008e.
- [20] A. Keshav, K.L. Wasewar and S. Chand, “Recovery of propionic acid by reactive extraction using tri-n- butyl phosphate in petroleum ether: equilibrium study”, *Chemical Biochemical Engineering Quarterly*, vol. 22, no. 4, pp. 433-437, 2008f.
- [21] A. Keshav, K.L. Wasewar and S. Chand, “Reactive extraction of propionic acid using Tri-n-octylamine, Tri-n-butyl phosphate and Aliquat 336 in sunflower oil as diluent”, *Journal of Chemical Technology and Biotechnology*, 2008g.
- [22] A. Keshav, K.L. Wasewar and S. Chand, “Recovery of propionic acid from aqueous stream by reactive extraction: Effect of diluents”, *Desalination*, vol. 244, pp. 12-23, 2009a.

	SAKARYA UNIVERSITY JOURNAL OF SCIENCE		 SAKARYA UNIVERSITY
	e-ISSN: 2147-835X http://www.saujs.sakarya.edu.tr		
	<u>Received</u> 19-03-2018 <u>Accepted</u> 17-04-2018	<u>Doi</u> 10.16984/saufenbilder.407781	

Catalytic Oxidation of 2-Mercaptoethanol by Cobalt(II)phthalocyanines Bearing Chalcone with Furan and Thiophene

Hüseyin KARACA¹

Abstract

Cobalt (II) phthalocyanines carrying on the four of the peripheral positions furan and thiophene as chalcones were synthesized. THF is used to investigate the catalytic oxidation of 2-mercaptoethanol. The synthesized phthalocyanines show catalytic activity on the oxidation of 2-mercaptoethanol. Cobalt (II) phthalocyanine derived by chalcone with furan has given catalytic specifications such as turnover number TON as 16.6, initial reaction rate as 0.293 $\mu\text{mol}/\text{sec}$ and the oxygen consumption as 10.06 $\mu\text{mol}/\text{min}$. The other cobalt (II) phthalocyanine derived by chalcone with thiophene has given catalytic specifications such as turnover number TON as 15.9, initial reaction rate as 0.213 $\mu\text{mol}/\text{sec}$ and the oxygen consumption as 9.88 $\mu\text{mol}/\text{min}$. So chalcone derived phthalocyanines can be used as catalyst is oxidation of mercaptan by air.

Keywords: Catalysis, 2-mercaptoethanol, oxidation, phthalocyanine

1. INTRODUCTION

Alkyl thiol compounds, known as mercaptans, are highly polluting compounds. The removal of thiol compounds is not only important in preventing environmental pollution. Furthermore, mercaptan compound poisons the catalysts those are added into the the petroleum products such as petrol and diesel for enhancing the performance. So the mercaptan oxidation process is used for the removal of thiols. The mercaptan oxidation is carried out by oxygen in the air and catalysts. This aerobic oxidation process of thiols is studied by using both homogeneous and heterogeneous catalysts [1-7].

Phthalocyanines (Pcs) have flexibility in structure. Adding some organic groups to peripheral or non peripheral positions and also changing the metal ion in the center of Pcs empowers the new properties. Metallophthalocyanines have active center like natural metalloenzymes. This similarity give the enzyme like activities to the phthalocyanines. Cobalt (II) ion in the center of phthalocyanine is giving the catalytic property to Pc. Cobalt (II) ion in the center of two

dimensional planar molecule can interact with both mercaptan and dissolved oxygen by the opposite sides but on the same line. The catalytic reaction occurs by this interaction [8-17]. Chalcone is an aromatic ketone that forms the center of many biological compounds. The aldol condensation reaction can be used to synthesis chalcones. This reaction is carried out between benzaldehyde and acetophenon while sodium hydroxide as catalyst. Chalcones are also intermediate step in the biosynthesis of flavonoids having biological activities. The electron transfer will take place between conjugated chalcone structures and phthalocyanine [18].

We have studied before catalytic oxidation of 2-mercaptoethanol by water soluble porphyrine complex and made this catalyst as heterogeneous by immobilizing on a polyester woven fabric as dye [8,9]. In this study the chalcone derived cobalt (II) phthalocyanines are used as catalyst for the oxidation of 2-mercaptoethanol. In our previous published research paper acetophenon derived chalcone group is used for derivatizing the phthalocyanine and used as catalyst for oxidation of 2-mercaptoethanol. In this study two chalcone groups these are 2-acetyl furan and

¹karaca@sakarya.edu.tr, Department of Chemistry, Sakarya University, 54050 Sakarya, Turkey

2-acetylthiophene are used to obtain chalcone by the reaction with 4-hydroxybenzaldehyde and then used in the synthesis of chalcone substituted metallophthalocyanine.

2. GENERAL REQUIREMENTS

2.1. General

The glassware used in this study is heated at 150 °C for 1h and cooled under inert nitrogen atmosphere then used in all experimental step. The fine chemicals used during the experimental section provided from commercial suppliers. A double walled glass reactor created and used for investigation of catalytic reaction. Dissolved oxygen in the reactor is measured by CYBERSCAN D300 oxygenmeter.

2.2. Synthesis of Catalysts

Figure 1 shows the synthetic route for Co(II)phthalocyanines, catalysts. The synthetic procedures are used as written in the literature and obtained compounds show same spectroscopic results [19-21].

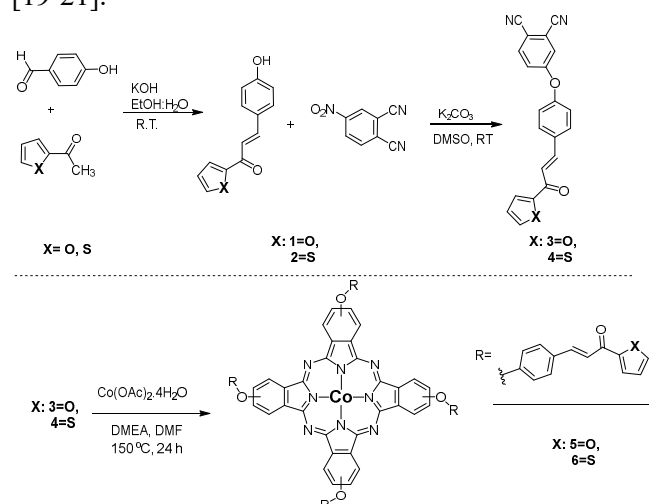


Figure 1. The synthetic route for Co(II)phthalocyanines, 5-6.

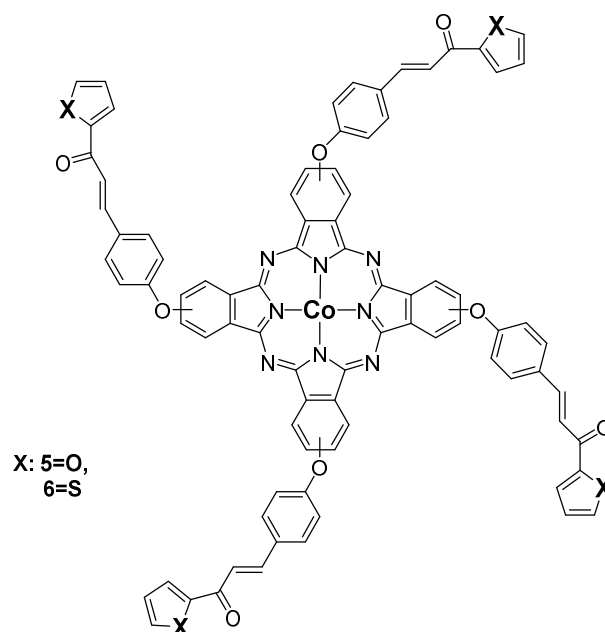


Figure 2. Co(II)Phthalocyanines

2.3. Catalytic oxidation of 2-mercaptoethanol

Catalytic oxidation of 2-mercaptoethanol was followed by measuring dissolved oxygen in the reactor in that the catalytic process was carried out by CyberScan DO 300. Both Co(II)phthalocyanines, 1 and 2, were weighed 0.152 μmol in 50 mL THF. Air is passed through into the solution by bubbling in the reactor in order to saturation of oxygen in the solution. 1 mL of 0.25 wt% aqueous sodium hydroxide solution was joined into the reaction vessel in order to make alkaline the solution. 7,3 μL (1.52 mmol) 2-mercaptoethanol was added by micropipette. The molar ratio of catalyst, Co(II)phthalocyanine, and substrate, 2-mercaptoethanol, was 1:10000. This ratio is very good ratio to measure catalytic effect. At the same time, recording of the measured dissolved oxygen was started. Because the oxygen consumption was started by catalytic oxidation of 2-mercaptoethanol. Then oxygen consumption was calculated depending on time.

The mercaptan/molecular oxygen ratio is 4/1 in all mercaptan oxidation method [2].



The rate of mercaptan oxidation was calculated by the decreasing of dissolved oxygen.

3. RESULTS AND DISCUSSION

The catalytic oxidation of 2-mercaptoethanol by Co(II)phthalocyanines is well known in the literature. The Co(II)phthalocyanines those are derived by chalcone and by thio chalcone group are synthesized by our group. Both of the metallophthalocyanines show

non-aggregation behaviour. This is very important for catalytic activity on oxidation of mercaptans. The opposite sides of metal center of Co(II)phthalocyanines can coordinate with substrate and oxygen. Because thio alcohol RSH is dissociated as RS⁻ anion and H⁺ in alkaline solution made by sodium hydroxide addition. The formed RS⁻ anion will coordinate to the metal center and O₂ on the other side of the metal center of Co(II)Pc. One electron is transferred from the thiolate to oxygen through the metal center of Co(II)Pc and so disulfide occurs. The catalytic reaction between 2-mercaptoethanol and oxygen is seen in equation (1). The ratio of thiol/catalyst is 10000 as catalytic concentration. After a small amount of NaOH solution was added into the mercaptan (RSH) solution, thiolate (RS⁻) anion will be produced and then Co(II)Pc will start to catalyse the oxidation of 2-mercaptoethanol

Both cobalt (II) phthalocyanines show very close results. Because both chalcones have very similar structure. The only difference between the structures are O and S atoms. The very big phthalocyanine skeleton and chalcone compounds have conjugated structures. So the effect of O and S atoms in the furan ring will be reduced.

Figure 3 shows the oxygen consumption in the reaction of catalytic oxidation of 2-mercaptoethanol by Co(II)Pc substituted by chalcone with furan as catalyst in THF.

The value that makes the first derivative of the equation zero gives the initial reaction rate, as 0.293 μmol/sec. Turnover number, TON, (mol oxygen per mol phthalocyanine), is calculated as 16.6. The oxygen consumption was calculated as 10.06 μmol/min.

Figure 4 shows the oxygen consumption in the reaction of catalytic oxidation of 2-mercaptoethanol by Co(II)Pc substituted by chalcone with thiophene as catalyst in THF.

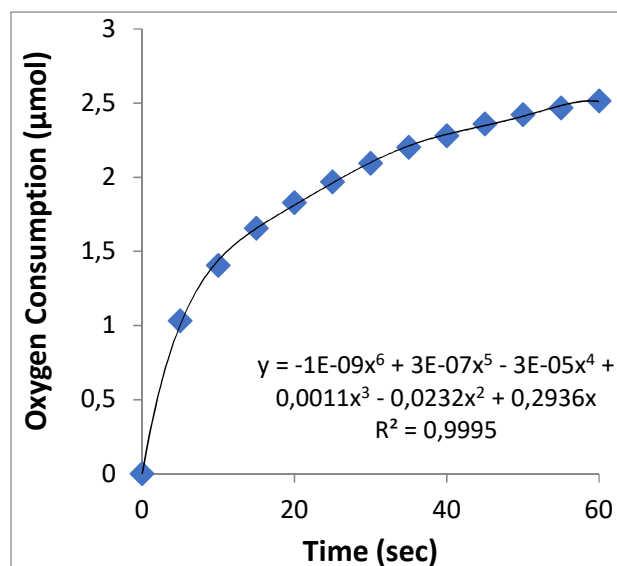


Figure 3. Oxygen consumption in the reaction of catalytic oxidation of 2-mercaptoethanol by Co(II)Pc substituted by chalcone with furan as catalyst in THF.

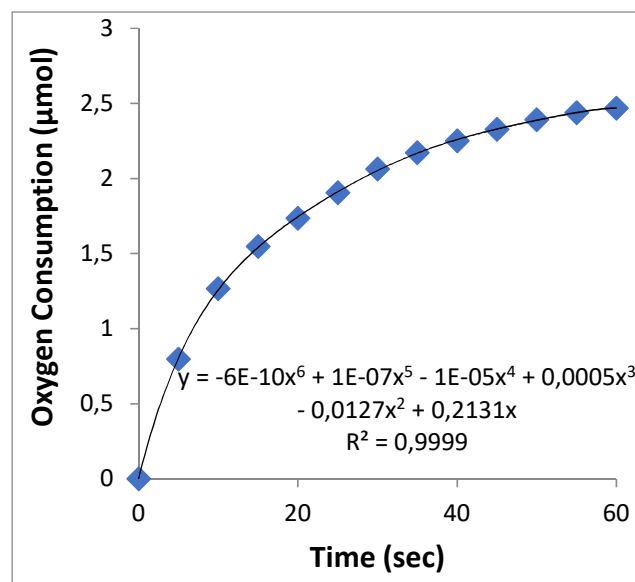


Figure 4. Oxygen consumption in the reaction of catalytic oxidation of 2-mercaptoethanol by Co(II)Pc substituted by chalcone with thiophene as catalyst in THF.

The value that makes the first derivative of the equation zero gives the initial reaction rate, as 0.213 μmol/sec. Turnover number, TON, (mol oxygen per mol phthalocyanine), is calculated as 15.9. The oxygen consumption was calculated as 9.88 μmol/min.

4. CONCLUSION

In conclusion, both Co(II) phthalocyanines which are substituted with chalcone with furan and thiophene have been synthesized and characterized. These phthalocyanines were synthesized by a synthetic route shown in figure 1. Both cobalt (II) phthalocyanines are nonaggregable and soluble in common organic solvents. THF is used to investigate the catalytic oxidation of 2-mercaptoethanol. The catalytic oxidation of 2-mercaptoethanol by cobalt (II) phthalocyanines is very much studied reaction. So the synthesized phthalocyanines show catalytic activity on the oxidation of 2-mercaptoethanol.

Cobalt (II) phthalocyanine derived by chalcone with furan has given catalytic specifications such as turnover number TON as 16.6, initial reaction rate as 0.293 $\mu\text{mol}/\text{sec}$ and the oxygen consumption as 10.06 $\mu\text{mol}/\text{min}$.

The other cobalt (II) phthalocyanine derived by chalcone with thiophene has given catalytic specifications such as turnover number, TON, as 15.9, initial reaction rate as 0.213 $\mu\text{mol}/\text{sec}$ and the oxygen consumption as 9.88 $\mu\text{mol}/\text{min}$.

So chalcone derived phthalocyanines can be used as catalyst in oxidation of mercaptan by air.

REFERENCES

- [1] S.M.S. Chauhan, A. Gulati, A. Sahay, and P.N.H. Nizar, "Autooxidation of alkyl mercaptans catalysed by cobalt(II)phthalocyanine tetrasodium sulphonate in reverse micelles" *J. of Molecular Catal. A: Chemical*, 105, pp. 159-165. 1996.
- [2] M. Kimura, Y. Yamaguchi, T. Koyama, K. Hanabusa, and H. Shirai, "Catalytic oxidation of 2-mercaptoethanol by cationic water-soluble phthalocyaninatocobalt (II) complexes" *J. of Porphyrins and Phthalocyanines*, 1, pp. 309, 1997.
- [3] J.H. Zagal, M.A. Gulppi, C. Depretz, and D. Levievre, "Synthesis and electrocatalytic properties of octaalkoxycobalt phthalocyanine for the oxidation of 2-mercaptoethanol" *J. of Porphyrins and Phthalocyanines*, 3, pp. 355-363, 1999.
- [4] D. Wöhrle, T. Buck, G. Schneider, G. Schulz-Ekloff, and H. Fischer, "Low molecular weight, polymeric and covalently bound Co(II)-phthalocyanines for the oxidation of mercaptanes" *J. Inorg. Organomet. Polym.*, 1, pp. 115-129, 1991.
- [5] G.R. Hodges, J.R. Smith, and J. Oakes, "Mechanism of Oxidation of Azo Dyes by a Sterically Hindered Anionic Oxoiron(IV) Porphyrin in Aqueous Solution" *J. Chem. Soc., Perkin Trans.*, 2, pp. 617-627, 1998.
- [6] G.R. Hodges, J.R. Smith, and J. Oakes, "The oxidation of azo dyes by peroxy acids and tert-butyl hydroperoxide in aqueous solution catalysed by iron(III) 5,10,15,20-tetra(2,6-dichloro-3-sulfonatophenyl) porphyrin: product studies and mechanism" *J. Chem. Soc., Perkin Trans.*, 2, pp. 1943-1952, 1999.
- [7] A. Filippova, A. Vashurin, S. Znoyko, I. Kuzmin, M. Razumov, A. Chernova, G. Shaposhnikov, O. Koifman. "Novel Co(II) phthalocyanines of extended periphery and their water-soluble derivatives. Synthesis, spectral properties and catalytic activity" *Journal of Molecular Structure*, 1149, 17-26, 2017.
- [8] H. Karaca, M. Teker, A. Gül. "Catalytic Oxidation of 2-Mercaptoethanol by a Water-Soluble Porphyrinatocobalt (II) Complex" *Chemistry Journal*, Vol. 06, Issue 01, pp. 55-58, 2016.
- [9] H. Karaca, N. Akçay, M. Teker. "Porphyrazine immobilization on polyester fabric and heterogeneous catalytic application on oxidation of 2-mercaptoethanol" *Fresenius Environmental Bulletin*, Volume 25 – No. 5, pp 1714-1718, 2016.
- [10] H. Karaca. "Redox chemistry, spectroelectrochemistry and catalytic activity of novel synthesized phthalocyanines bearing four schiff bases on the periphery" *Journal of Organometallic Chemistry*, 822, pp. 39-45, 2016.
- [11] J. Jeong, R.S. Kumar, N. Mergu, Y.-A. Son. "Photophysical, electrochemical, thermal and aggregation properties of new metal phthalocyanines" *Journal of Molecular Structure*, 1147, pp. 469-479, 2017.
- [12] A.R. Karimi, Z. Jafarzadeh, M. Sourini, A. Zendehtnam, A. Khodadadi, Z. Dalirnasab, M. Solimannejad, P. Zolgharnein. "Synthesis and computational studies of new metallo-phthalocyanines bearing dibenzoxanthenes and evaluation of their optical properties in solution and solid PMMA/ZnPc/Al nanocomposite

- films" *Turkish Journal of Chemistry*, 40, pp. 602-612, 2016.
- [13] A.R. Karimi, A. Khodadadi. "Synthesis and solution properties of new metal-free and metallo-phthalocyanines containing four bis(indol-3-yl)methane groups" *Tetrahedron Letters* 53,pp. 5223–5226, 2012.
- [14] A.A. Ramos, F.B. Nascimento, T.F.M. de Souza, A.T. Omori, T.M. Manieri, G. Cerchiaro and A.O. Ribeiro. "Photochemical and Photophysical Properties of Phthalocyanines Modified with Optically Active Alcohols" *Molecules*, 20, pp. 13575-13590, 2015.
- [15] A. Aktaş, İ. Acar, A. Koca, Z. Bıyıklıoğlu, H. Kantekin. "Synthesis, characterization, electrochemical and spectroelectrochemical properties of peripherally tetra-substituted metal-free and metallophthalocyanines" *Dyes and Pigments*, 99, pp. 613-619, 2013.
- [16] A.R. Karimi, F. Bagherian and M. Sourinia."Synthesis and characterization of 1,4-dihydropyridinesubstituted metallophthalocyanines " *Mendeleev Commun.*, 23, pp. 224–225, 2013.
- [17] F. Qiu, J. Liu, G. Cao, Y. Guan, Q. Shen, D. Yang & Q. Guo. "Synthesis, Thermo-Optic Properties, and Polymeric Thermo-Optic Switch Based on Novel Optically Active Polyurethane (Urea)" *Soft Material*, 11-3, pp. 233-243, 2013.
- [18] H. Karaca, B. Çayeğil, S. Sezer. "Synthesis characterization and metal sensing applications of novel chalcone substituted phthalocyanines" *Synthetic Metals*, 215, pp. 134–141, 2016.
- [19] E. Güzel, Ş. Çetin, A. Günsel, A. Bilgiçli, İ. Şişman, M.N. Yaraşır. "Comparative studies of photophysical and electrochemical properties of sulfur-containing substituted metal-free and metallophthalocyanines" *Research on Chemical Intermediates*, 44, 2, pp. 971-989. 2017.
- [20] P. Şen, D.K. Şimşek, S.Z. Yıldız. "Functional zinc(II) phthalocyanines bearing Schiff base complexes as oxidation catalysts for bleaching systems" *Appl. Organometal. Chem.*, 29, pp. 509–516, 2015.
- [21] S.Z. Yıldız, S. Çolak, M. Tuna. "Non-ionic peripherally substituted soluble phthalocyanines: Synthesis characterization and investigation of their solution properties" *Journal of Molecular Liquids*, 195, pp. 22–29, 2014.

	SAKARYA UNIVERSITY JOURNAL OF SCIENCE		 SAKARYA UNIVERSITY
	e-ISSN: 2147-835X http://www.saujs.sakarya.edu.tr		
	<u>Received</u> 07-11-2017 <u>Accepted</u> 25-04-2018	<u>Doi</u> 10.16984/saufenbilder.349758	

Annealing time effect on the optical properties of Zn(O,OH,S) films onto ZnO seed layer under un-vacuum ambient

Fatma Özütok*¹ and Emin Yakar²

Abstract

In this study, Zn (O,OH,S) films were synthesized onto ZnO seed layers by chemical bath deposition, which were annealed at 500 °C. The differences of structural, morphological and detailed optical properties of the films were investigated depending on the annealing time (between 30 min. and 90 min.). While samples of 30.min and 90 min. showed decomposed structures, sample of 60 min. showed different dimensions of nano-flower structures. Although all films had ZnO-hexagonal crystal structure, the most obvious ZnS-related peaks were observed in the sample of 90 min. Optical absorption edge was shifted at 362 nm from Uv-Vis spectroscopy. Although ZnO, Zn(OH)₂ vibration related peaks were so sharp, ZnS vibration peaks were so weak for all samples from FTIR. The PL intensities were differential depending on the annealing time but defect state-corresponding peaks were similar for each films.

Keywords: Zn(O,OH,S) film, ZnO seed layer, photoluminescence spectroscopy, FTIR, optical transparency

1. INTRODUCTION

Recently, Cu(In,Ga)(S,Se)₂ (CIGS)- solar cells are so active research topics that has been high efficiency values over 20 %, cost-cutting effects in the industrial production and an alternative material for traditional Si-solar cells [1,3]. (CIGS)- solar cells have a layer that called as ‘buffer layer’ which has a relatively critical precaution for reducing the interface recombinations, decreasing the mechanical tension stress between absorbent layer/TCO electrode and providing optimal band alignment throughout the junction. CdS film preferred as a buffer layer between i:ZnO window and CIGS absorbent is produced by frequently atomic layer deposition (ALD) or chemical bath deposition (CBD) [4,5]. In the buffer layer studies, cadmium-free alternative material necessity occurs due to CdS has high toxicity, the narrow band gap energy (~2.4 eV) and high interface recombinations between the absorber and window interface [6].

Zn-component materials (ZnO, ZnS and ZnSe etc.) and their mixing materials are preferred as cadmium free alternative materials which have minimum environmentally harmful components, low optical absorption values and abundant in nature [7]. Specific amount of hydroxyl groups and impurity containing Zn(O,OH,S) film are so attractive due to their prior and tuning properties compared to other Zn-constituent materials such as large band gap energy ($E_g \sim 2.6-3.8$ eV), reduce to photocurrent loss in the short-wavelength region, high optical transparency in the UV-Vis area (>75 %) and quantum efficiency enhancing in the blue wavelength region [8].

Much more studies have been reported in the literature about ZnO- and ZnS- films which have been produced by chemical bath, spin coating, ultrasonic spray pyrolysis, atomic layer deposition (ALD) or chemical vapor deposition (CVD) [9,11]. Among them, chemical bath deposition has beneficial properties such as simple set-up, short time of chemical reactions, non-expensive, non-vacuum ambient and producible even at low temperatures (<100 °C) [12]. On the other hand,

* Corresponding author

¹ Çanakkale Onsekiz Mart University, Science Faculty, Physics Department, fatmaozutok@comu.edu.tr

² Çanakkale Onsekiz Mart University, Engineering Faculty, Materials Science and Engineering Department

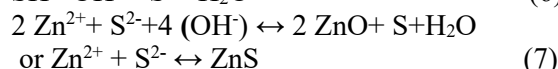
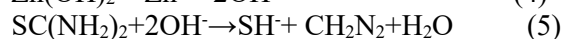
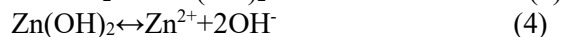
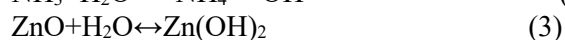
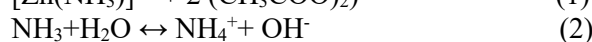
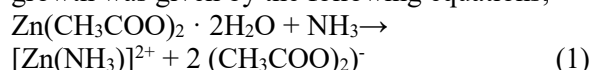
keeping under control of film growth and adherent/homogenous film production are necessary to increase buffer layer efficiency.

In this study, Zn(O,OH,S) films were synthesized onto ZnO seed layer by modified chemical bath deposition and annealing temperature was optimized at 500 °C. Using of ZnO seed layer can reduce the lattice mismatch between growing layer and substrate. Additionally, annealing time is a key parameter for improving the crystallinity and removing adsorbed impurities on the surface. Therefore, surface modification is ensured and adherent films are obtained. Structural and optical properties and surface morphology of Zn(O,OH,S) films were investigated depending on the three annealing times, 30 min., 60 min. and 90 min.

2. EXPERIMENTAL

Chemical bath deposition (CBD) technique was used for the synthesis of ZnO seed layer and Zn(O,OH,S) films. All reagents were of analytical grade and used without further purification. Amorphous glass cleaning procedure (ethanol, acetone and distilled water, respectively) was applied. ZnO seed layer preparation and ZnO film growth details were reported with modified chemical bath in our previous study [13]. In the 100 ml. distilled water including sulfide bath, 0.1 M thiourea and 0.1 M zinc-acetate dihydrate were used as S-source and Zn-source, respectively. This yellow-colored solution was mixed in an ultrasonic bath at 60±5 °C. ZnO seed layers were immersed into mixing solution while enough ammonia was dropped and optimum dipping time was determined as 4 minutes. After the film deposition, all films dried at room temperature and then annealed at 500 °C. Annealing times were chosen as 30 min., 60 min. and 90 min., respectively.

The possible chemical reactions of Zn(O,OH,S) film growth was given by the following equations;



In the Zn(O,OH,S) film growth process by CBD, Zn(OH)₂ layer and Zn(S, O) layer were presented and with removing the upper Zn(OH)₂ layer causes an improvement of buffer layer which investigated by Izaki [14]. Structural parameters of films were carried out by Rigaku SmartLab X-ray Diffractometer with CuK_α (1.5406 Å) radiation with powder method and step size was 0.0130 which was operated under 40 mA

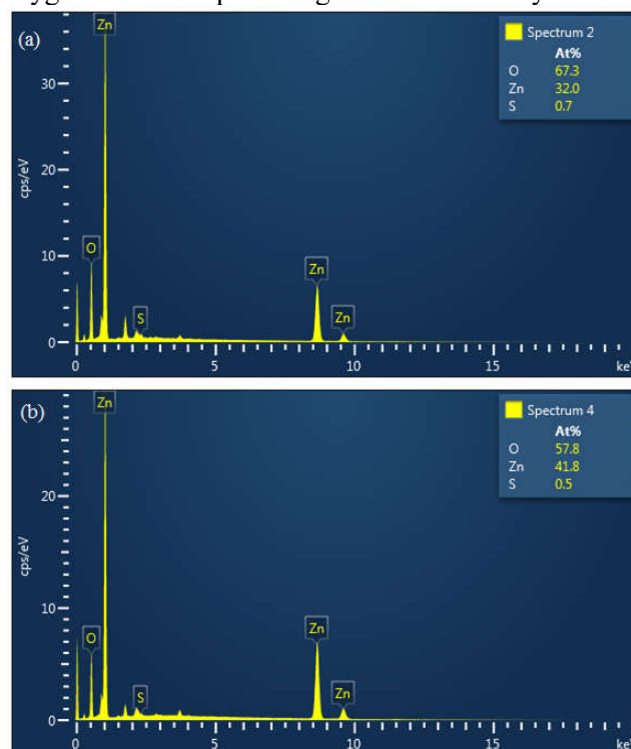
and 45 kV. Average crystalline sizes were estimated by Debye-Scherrer formulation which is given at below;

$$(D=0.94\lambda/\beta\cos\theta) \quad (8)$$

The surface morphologies and film composition of the samples were used by using JEOL JSM-7100 F SEM scanning electron microscopy and OXFORD Instruments X-Max EDX energy-dispersive x-ray spectroscopy, respectively which has been attached to each other. Optical properties (absorbance, transmittance, direct band gap energy) were investigated by Analytic Jena Uv-Vis spectroscopy which was recorded in the range of 300-900 nm. Direct band gap energies of the samples were calculated by Perrson model. At room temperature, photoluminescence intensities were measured by Quanta Master 400 Spectrofluorometer at 245 nm. excitation wavelength. FTIR (Fourier Transform Infrared Spectrum) measurements were performed on VERTEX 70 model spectrophotometer with an attenuated total reflectance (ATR) accessory between 400 and 4000 cm⁻¹ (Bruker, Germany).

3. RESULTS AND DISCUSSION

In Fig.1., EDX analysis showed that all samples had different percentage of zinc, sulfur and oxygen related elemental peaks as expected in the selected region on the film surface. No impurity elements were detected while much more Zn-elemental peaks were observed in 60 min.-annealing samples, much more S-elemental peaks were observed in 90-min.-annealing samples. Additionally, annealing time had no effect on the oxygen elemental percentage from EDX analysis.



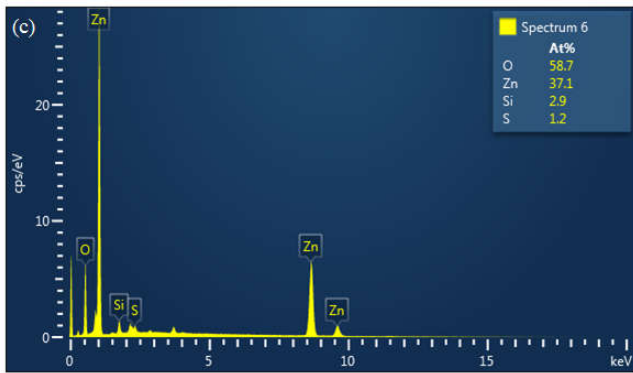


Fig.1. EDX analysis results of Zn(O,OH,S) films depending on the annealing time a)30 min. b) 60 min. and c)90 min.

The XRD profiles of samples were given in Fig.2. In the range of $2\theta=20^\circ-30^\circ$, a swelling was observed for all samples due to the amorphous glass substrate. The presence of (100), (002) and (101) peaks for all polycrystalline films represented ZnO-hexagonal crystal structure (JCPDS card no:36-1451), indicating that the presence of Zn(OH)₂ in the range of $2\theta=30^\circ-40^\circ$. As seen in Fig. 3., all films had different XRD intensities and full width at half maximum (FWHM) depending on the annealing time. There was no ZnS-related peak detected in 30 min.-and 60 min.-annealing samples. In spite of this, the most obvious ZnS-related peaks (JCPDS card no: 05-0566) were observed in sample of 90 min.-annealing which indicated that enough amount S-inclusion might create weak Zn(O,S) host matrix [15]. While 30 min.-annealing samples had (100) preferential orientation, 60 min. and 90 min.-annealing samples had (101) preferential orientation. However, (002) and (101) directions for 30 min.-annealing samples and (002) and (100) directions for 60 min.- and 90 min.-annealing samples might affect the orientation. Two suggestions were given in the literature about choosing both c- and a- axis orientation. One was suggested by Mathew et.al. that high boiling points solvents cause both of orientation and (002) direction was the most thermodynamically favorable growth [16]. Another was reviewed by Znaidi et.al. that surface energy of (100) orientation was higher than (002) orientation so it was observed that (100) orientation development [17]. Having the same preferential orientation samples 60 min.- and 90 min.- annealing samples showed that intensity increased with increasing FWHM and decreasing crystallinity and also the smallest grain sizes were obtained in 60 min. annealing samples.

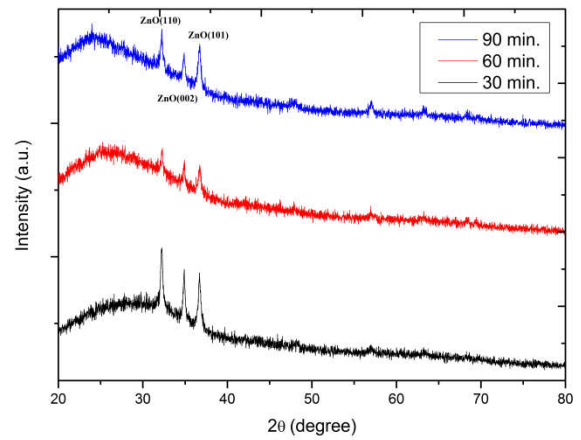


Fig.2. XRD patterns of Zn(O,OH,S) films depending on the annealing time

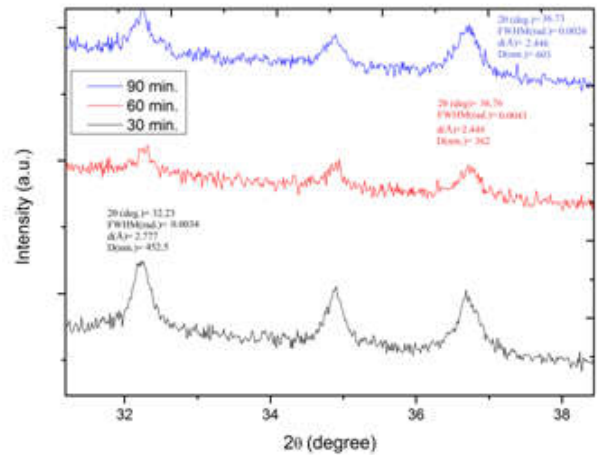


Fig.3. Structural parameters of Zn(O,OH,S) films depending on the preferential orientation under different annealing times

The SEM cross-section image as shown in Fig.4(a). There were two different layers of micrometer level thicknesses observed which indicating layer-by-layer and Zn(O,OH,S) film which was positioned on ZnO seed layer. On the other hand Fig. 4(b), Fig 4(c) and Fig.4(d) showed that surface morphology of samples were depending on the annealing time. Nano-flower like formations and much more homogeneous surface were observed in 60 min.-annealing samples. It indicated that Zn-rich ambient created nano-flower structures which were consistent with EDX results. McPeak explained that introducing Zn into the lattice increased the CIGS buffer layer efficiency[18]. Colloidal formations were detected in 30 min. and 90 min.-annealing samples, which indicated that heterogeneous precipitation might trigger density and compactness in the film growth.

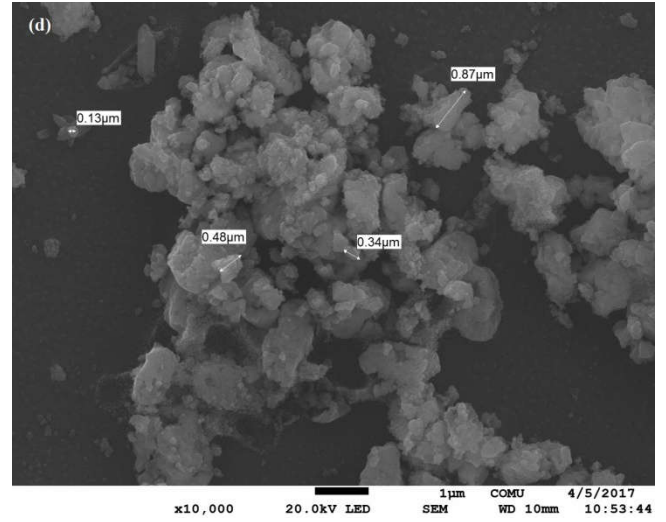
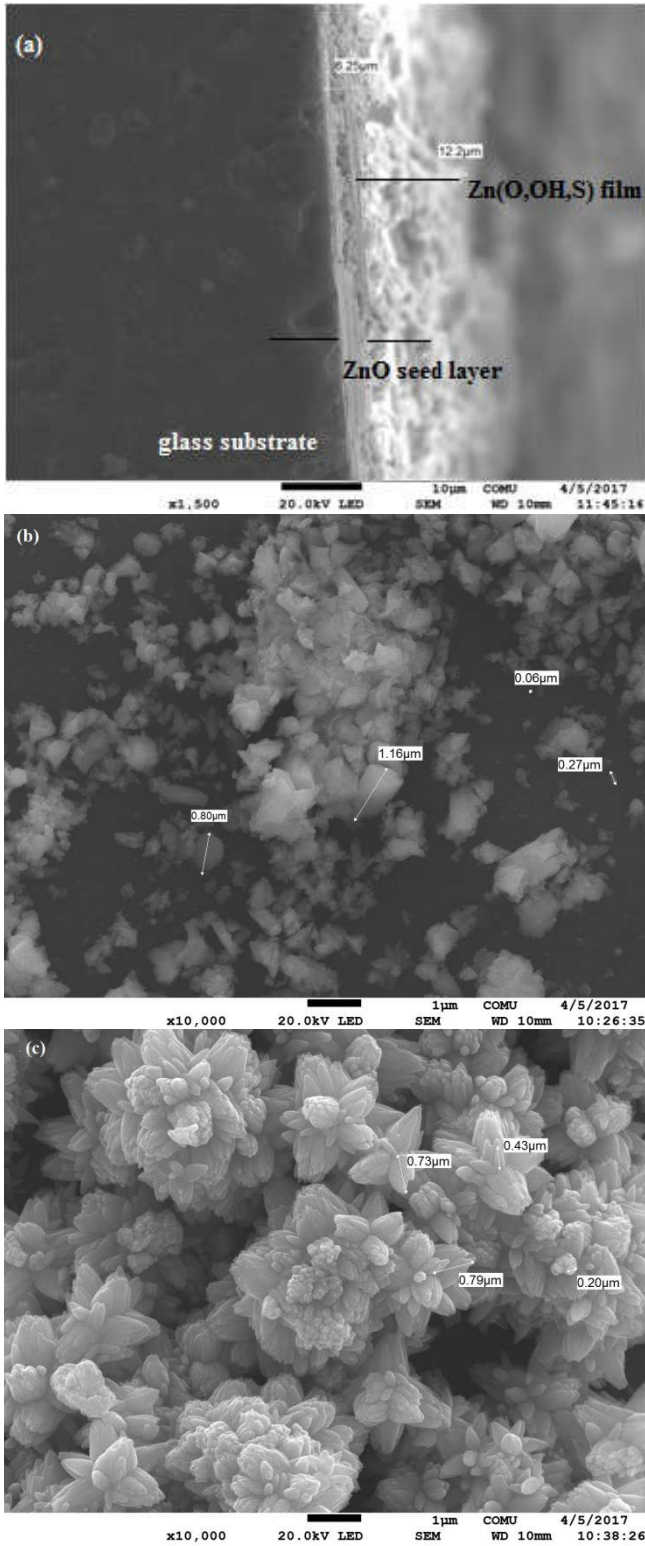


Fig.4.a)Cross section SEM image of Zn(O,OH,S) film and SEM images of Zn(O,OH,S) films for b) 30 min. c) 60 min. and d) 90 min. annealing time, respectively.

The transmission spectra of Zn(O,OH,S) films for different annealing times were shown in Fig.5. Optical absorption edge was almost coordinated at 362 nm. (3.42 eV) for all films. It was observed that red shift occurred compared to ZnO seed layer (370 nm.~3.35 eV) [ref 13] due to surface kinetic processes which may affect the homogeneous film growth.

It was determined that the average value of optical transmission increased with increasing of annealing time, compatible to similar studies which was attributed to the surface impurities decreased with increasing film surface temperature[19].

A lot of band gap measurement and evolution methods have been proposed in the literature (Tauc model [20], Viezbicke fitting model [21], Kubelka–Munk function with Tauc model [22] and Kim fitting model with BM effect [23] and etc.). Among them, the equation of Perrson model [24];

$$(\alpha h\nu)=A[h\nu-E_{g,ZnO}]^{1/2}+B[h\nu-E_{g,ZnO}+\Delta E_g(x)]^{1/2} \quad (9)$$

was so proper for Zn(O,OH,S) films in where $\Delta E_g(x)$ was a fit parameter ($x \sim 0.5$) which varies as a function of the (S/ S+O) ratio. Band gap values were changed between 2.9 ± 0.1 eV and 3.1 ± 0.1 eV range. This band gap variation phenomenon was investigated by different research groups. Hydroxyl groups may affect the band gap values but it has been still unclear which forms in film growth [25]. A study received by Mathew that the amorphous nature of ZnO decreased as the temperature increases so the band gap energies would decrease [16]. Additionally, optical band gap changes depending on O₂ vacancies and Zn interstitial sites which given by Abdallah [26].

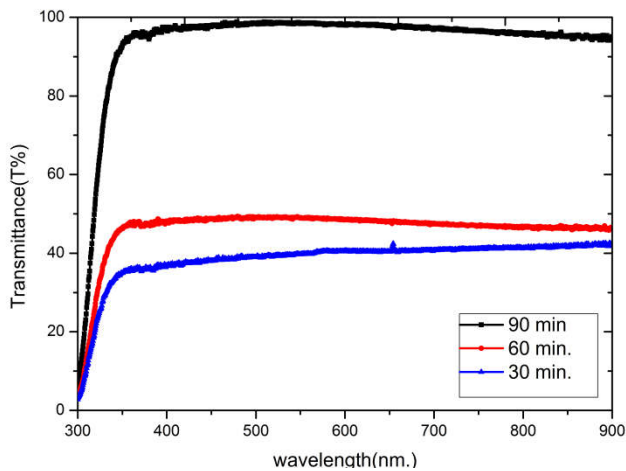


Fig.5. Optical transmittance spectrum of Zn(O,OH,S) films depending on the annealing time

FTIR spectrum gives a characteristic behavior about the vibration of atoms/molecules in the crystal structure. As can be seen in Fig. 6. hydroxyl (O-H) group stretching and bending vibrations were not observed at $3500-3900\text{ cm}^{-1}$ and $1400-1757\text{ cm}^{-1}$ respectively [27]. Very sharp peaks were determined at 410 cm^{-1} range, 765 cm^{-1} and 900 cm^{-1} which were assigned to Zn-O, OH-Zn-OH bending and M-O-M bonding vibrations [28,29,30]. Much more weak peaks were observed at 685 cm^{-1} and 2380 cm^{-1} which were attributed to Zn-S stretching and absorption of atmospheric CO_2 by a metallic cation, respectively [31,32]. These results show that proof of Zn(O,OH,S) films present onto ZnO seed layer.

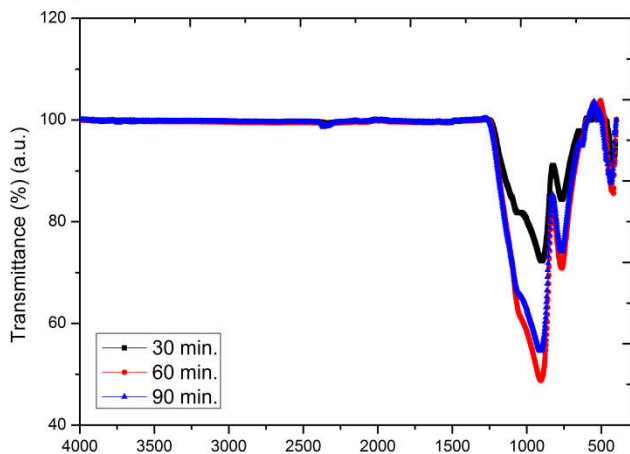


Fig.6. FTIR spectrum of Zn(O,OH,S) films depending on the annealing time

The photoluminescence (PL) spectra of Zn(O,OH,S) films were shown in Fig.7. in the range 300-650 nm. at room temperature. Detailed elemental vacancy investigation was realized by PL measurements. As the annealing time increased, the luminescence intensity decreased between in 300-420 nm. wavelength range which indicated that decreasing density of the defects, as explained by Lu [33]. The minimum PL intensity was observed for 60-min. annealing sample which originated from Zn-rich ambient. Additionally, the PL intensities were different whereas the peak positions (defect types) were similar

for all samples as expected. Blue emission [447 nm.(2.77 eV) and 467 nm(2.65 eV)] and green emission [488 nm.(2.54 eV) and 556 nm.(2.23 eV)] were observed which can be seen in Fig.7. Generally, a blue emission was centered at between 420-450 nm. and 440-480 nm. for ZnS and ZnO films, respectively [34,35]. This ZnO type-blue emission behaviour was consistent with XRD results. Blue emission that enhanced CIGS-solar cell performance which was attributed to radiation defects relevant to interface traps on grain boundary [36]. Very strong green emission (deep level emission) was observed at 2.54 eV which was attributed singly ionized oxygen vacancy site and its formation energy was lower than Zn_i interstitial site [37]. Another contribution to green emission came from very weak peak (2.23 eV) that would be indicating the presence of Zn(OH)_2 . The green emission arised from that holes can recombine with electrons in the conduction band and/or shallow donor states which have been trapped at oxygen vacancies.

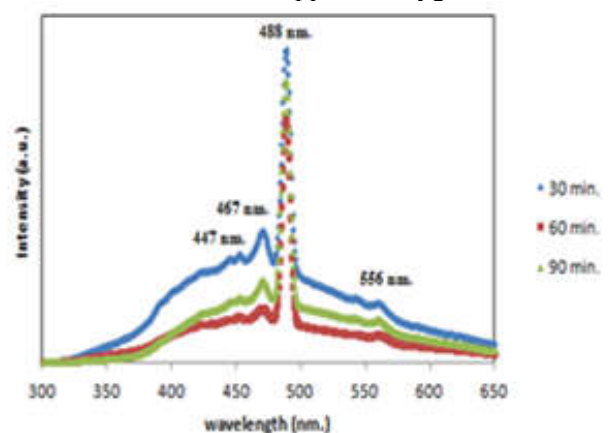


Fig.7. PL spectrum of Zn(O,OH,S) films depending on the annealing time ($\lambda_{exc.}=245\text{ nm.}$)

4. CONCLUSION

This study reported the influence annealing time on the surface morphology, crystallization, band gap energy and photoluminescence properties of chemical bath deposited Zn(O,OH,S) film onto ZnO seed layer. Annealing temperature was optimized at $500\text{ }^\circ\text{C}$ and annealing times varied as 30, 60 and 90 minutes. The XRD results show that all films have ZnO-hexagonal crystal structure with different preferential orientations. Nanoflower formations were observed in 60 min.-annealing samples with minimum PL intensities. Absorption edge was coordinated at 362 nm. for all films and optical transparency decreased with increasing annealing time. FTIR spectrum was an evidence about Zn(O,OH,S) film formation. In the literature, the intensity of near band emission was varying with temperature and the increase in the deep level PL peak can cause a decrease in the diffusion length from PL spectrums of Zn(O,OH,S) films. To summarize, annealing time severely affected on the

Zn(O,OH,S) film growth thereby structural and optical properties.

ACKNOWLEDGMENTS

This study is supported by Çanakkale Onsekiz Mart University Scientific Research Projects Coordination Unit. Project Number: FBA-2016-1051.

REFERENCES

- [1] M. Mezher, R. Garris, L. M. Mansfield, K. Horsley, L. Weinhardt, D. A. Duncan, M. Blum, S. G. Rosenberg, M. Bär, K. Ramanathan and C. Heske, "Electronic structure of the Zn(O,S)/Cu(In,Ga)Se₂ thin film solar cell interface", *Prog. Photovolt: Res. Appl.* Vol.24, No.8, pp.1142-1148, 2016.
- [2] R. Wuerz, A. Eicke, F. Kessler, S. Paetel, S. Efimenko, C. Schlege, "CIGS thin-film solar cells and modules on enamelled steel substrates", *Solar Energy Materials & Solar Cells* Vol.100, p.p.132-137, 2012.
- [3] Y.Tang, "Copper Indium Gallium Selenide Thin Film Solar Cells", *Nanostructured Solar Cells*, chapter 9, p.p.183-200, 2017.
- [4] H. H. Park, R. Heasley, R. G. Gordon, "Atomic layer deposition of Zn(O,S) thin films with tunable electrical properties by oxygen annealing", *APPLIED PHYSICS LETTERS* Vol.102, No.13, p.p.132110-132115, 2013.
- [5] C. Schwartz, D. Nordlund, T. Weng, D. Sokaras, L. Mansfield, A. S. Krishnapriyan, K. Ramanathan, K. E. Hurst, D. Prendergast, S. T. Christensen, "Electronic structure study of the CdS buffer layer in CIGS solar cells by X-ray absorption spectroscopy: Experiment and theory", *Solar Energy Materials & Solar Cells* Vol. 149, p.p.275-283, 2016.
- [6] T. Kobayashi, Z. J. Li Kao, T. Kato, H. Sugimoto, T. Nakada, "A comparative study of Cd- and Zn-compound buffer layers on Cu(In_{1-x}Ga_x)(S_ySe_{1-y})₂ thin film solar cells", *Prog. Photovolt: Res. Appl.* Vol.24, No.3, p.p.389-396, 2016.
- [7] B. T. Ahn, L. Larina, Ki H. Kim, S. Ji Ahn, "Development of new buffer layers for Cu(In,Ga)Se₂ solar cells", *Pure Appl. Chem.* Vol.80, No.10, p.p. 2091-2102, 2008.
- [8] C. Hubert, N. Naghavi, O. Roussel, A. Etcheberry, D. Hariskos, R. Menner, M. Powalla, O. Kerrec, D. Lincot, "The Zn(S,O,OH)/ZnMgO Buffer in Thin Film Cu(In,Ga)(S,Se)₂-Based Solar Cells Part I: Fast Chemical Bath Deposition of Zn(S,O,OH) Buffer Layers for Industrial Application on Co-evaporated Cu(In,Ga)Se₂ and Electrodeposited CuIn(S,Se)₂ Solar Cells", *Prog. Photovolt: Res. Appl.* Vol.17, No.7, p.p. 470-478, 2009.
- [9] E. Muchuweni, T.S. Sathiaraj, H. Nyakoty, "Synthesis and characterization of zinc oxide thin films for optoelectronic applications", *Heliyon*, Vol.3, No.4, p.p. 2405-2423, 2017.
- [10] C.H. Sun, P. Zhang, T.N. Zhang, X. Chen, Y.Y. Chen, Z.H. Ye, "ZnS thin films grown by atomic layer deposition on GaAs and HgCdTe substrates at very low temperature", *Infrared Physics & Technology*, Vol.85, p.p. 280-286, 2017.
- [11] F. U Hamelmann, "Thin film zinc oxide deposited by CVD and PVD", *Journal of Physics: Conference Series* Vol.764 p.012001, 2016.
- [12] P.B. Taunk, R. Das, D.P. Bisen, R.K. Tamrakar, Nootan Rathor, "Synthesis and optical properties of chemical bath deposited ZnO thin film", *Karbala International Journal of Modern Science* Vol.1, No.3, p.p. 159-165, 2017.
- [13] F. Özütok, S. Demiri, "Nanoflower-like ZnO Films Prepared by Modified Chemical Bath Deposition: Synthesis, Optical Properties and NO₂ Gas Sensing Mechanism", *Digest Journal of Nanomaterials and Biostructures* Vol.12, No.2, p.p. 309-317, 2017.
- [14] M. Izaki, S. Sugiyama, T. Okamoto, Y. Kusano, T. Maki, H. Komaki, H. Shibata and S. Niki, "Structure of chemically deposited Zn(S,O,OH) buffer layer and the effects on the performance of Cu(In,Ga)Se₂ solar cell", *Prog. Photovolt: Res. Appl.* Vol.24, No. 3, p.p. 397-404, 2016.
- [15] H. Ullah, A. Iqbal, M. Zakria and A. Mahmood, "Structural and spectroscopic analysis of wurtzite (ZnO)_{1-x}(Sb₂O₃)_x composite semiconductor", *Progress in Natural Science: Materials International* Vol.25, No.2, p.p. 131-136, 2015.
- [16] J. P. Mathew, G. Varghese and Jacob Mathew, "Effect of post-thermal annealing on the structural and optical properties of ZnO thin films prepared from a polymer precursor", Vol.21, No.7, p.p.078104-078112, 2012.
- [17] L. Znaidi, "Sol-gel-deposited ZnO thin films: A review", *Mat. Sci. Eng. B* Vol.174, No.1-3, p.p.18-30, 2010.
- [18] K. M. McPeak, B. Opanant, T. Shibata, D. Ko, M. A. Becker, S. Chattopadhyay, H. P. Bui, T. P. Beebe, Jr. Bruce A. Bunker, C. B. Murray and J. B. Baxter, "Microreactor Chemical Bath Deposition of Laterally Graded Cd_{1-x}Zn_xS Thin Films: A Route to High-Throughput

- Optimization for Photovoltaic Buffer Layers”, *Chem.of. Mat.*, Vol. 25, No.3, p.p.297-306, 2013.
- [19] V. Ghafouri, A. Ebrahimzad, M. Shariati, “The effect of annealing time and temperature on morphology and optical properties of ZnO nanostructures grown by a self-assembly method”, *Scientia Iranica F* Vol.20, No.3, p.p.1039–1048, 2013.
- [20] J. Tauc, R. Grigorovici, A. Vancu, “Optical properties and electronic structure of amorphous germanium”, *Phys. Status Solidi* Vol.15, No. 2, p.p.627–637, 1966.
- [21] B.D. Viezbicke, S. Patel, B.E. Davis and D.P. Birnie, “Evaluation of the Tauc method for optical absorption edge determination: ZnO thin films as a model system”, *Phys. Status Solidi B* Vol.252, No.8, p.p.1700- 1710, 2015.
- [22] S. Ebraheem, A. El-Saied, “Band Gap Determination from Diffuse Reflectance Measurements of Irradiated Lead Borate Glass System Doped with TiO₂ by Using Diffuse Reflectance Technique”, *Materials Sciences and Applications*, Vol.4, No. 5, p.p.324-329, 2013.
- [23] C. E. Kim, P. Moon, S. Kim, J. Myoung, H. W. Jang, J. Bang, I. Yun, “Effect of carrier concentration on optical bandgap shift in ZnO:Ga thin films”, *Thin Solid Films*, Vol.518, No. 22, p.p. 6304–6307, 2010.
- [24] C.Persson, “Strong Valence-Band Offset Bowing of ZnO_{1-x}S_x Enhances p-Type Nitrogen Doping of ZnO-like Alloys”, *PHYSICAL REVIEW LETTERS*, Vol.97, No. 14, p.p.146403-146407, 2006.
- [25] N.K. Allouche, T.B. Nasr, N.T.Kamouna and C. Guasch, “Synthesis and properties of chemical bath deposited ZnS multilayer films”, *Materials Chemistry and Physics* Vol.123, p.p.620-624, 2010.
- [26] B. Abdallah, A. K. Jazmatia, R. Refaai, “Oxygen Effect on Structural and Optical Properties of ZnO Thin Films Deposited by RF Magnetron Sputtering”, *Materials Research*, Vol.20, No.3, p.p. 607-612, 2017.
- [27] V. D. Mote, V. R. Huse, B. N. Dole, “Synthesis and Characterization of Cr Doped ZnO Nanocrystals”, *World Journal of Condensed Matter Physics*, Vol.2, p.p.208-211, 2012.
- [28] G. Janita Christobel, “Vibrational Spectroscopy of ZnO-ZnS Nanoparticles”, *International Journal of Science and Research*, Vol.5, No. 6, p.p. 2228-2230, 2016.
- [29] O. K. Srivastava, E. A. Secco, “Studies on metal hydroxy compounds: Infrared spectra of zinc derivatives ϵ -Zn(OH)₂, β -ZnOHCl, ZnOHF, Zn₅(OH)₈C₁₂, and Zn₆(OH)₈C₁₂·H₂O”, *CANADIAN JOURNAL OF CHEMISTRY*, Vol.45, p.p. 585-588, 1967.
- [30] W.B.White and R.Roy, “Infrared spectra-crystal structure correlations: comparison of simple polymorphic minerals”, *THE AMERICAN MINERALOGIST*, Vol. 49, p.p.1670-1688, 1964.
- [31] A. G. Rojas-Hernandez, K. J. Mendoza-Pena, E. Troyo-Vega, C. G. Perez-Hernandez, S. Munguia-Rodriguez, T. Mendivilreynoso, L. P. Ramirez-Rodriguez, R. Ochoa-Landin, M. E. Alvarez-Ramos, A. Deleon and S. J. Castillo, “ZnS nanoparticles synthesized through chemical aggregation using polyethyleneimine that works as both a stabilizer and a complexing agent”, *Chalcogenide Letters*, Vol. 14, No.1, p.p. 25-30, 2017.
- [32] A. Totterdill, T. Kovács, W. Feng, S Dhomse, C. J. Smith, J. C. Gómez-Martín, M. P. Chipperfield, P. M. Forster and J. M. C. Plane, “Atmospheric lifetimes, infrared absorption spectra, radiative forcings and global warming potentials of NF₃ and CF₃CF₂Cl (CFC-115)”, *Atmos. Chem. Phys.* Vol. 16, p.p.11451–11463, 2016.
- [33] L.Lu, M.Wong, “The Resistivity of Zinc Oxide Under Different Annealing Configurations and Its Impact on the Leakage Characteristics of Zinc Oxide Thin-Film Transistors”, *IEEE TRANSACTIONS ON ELECTRON DEVICES*, Vol.61, No. 4, p.p.1077-1084, 2014.
- [34] Z. Chen, X.X. Li, D. Guoping, Q. Yu, B. Li and X. Huang, “Luminescence properties of chlorine and oxygen co-doped ZnS nanoparticles synthesized by a solid-state reaction”, *Ceramics International*, Vol. 40, No.8, p.p.13151- 13157, 2014.
- [35] R. Jayakrishnan, K. Mohanachandran, R. Sreekumar, C.S. Kartha and K.P. Vijayakumar, “ZnO thin films with blue emission grown using chemical spray pyrolysis”, *Materials Science in Semiconductor Processing*, Vol.16, No.2, p.p.326-331, 2013.
- [36] P. A. Rodnyi and I. V. Khodyuk, “Optical and Luminescence Properties of Zinc Oxide”, *OPTICS AND SPECTROSCOPY* Vol.111, No. 5, p.p.776-785, 2011.
- [37] Y. Gong, T. Andelman, G. F. Neumark, S. O’Brien and I. L. Kuskovsky, “Origin of defect-related green emission from ZnO nanoparticles: effect of surface modification”, *Nanoscale Res Lett.*, Vol.2, p.p.297–302, 2007.

	SAKARYA ÜNİVERSİTESİ FEN BİLİMLERİ ENSTİTÜSÜ DERGİSİ <i>SAKARYA UNIVERSITY JOURNAL OF SCIENCE</i>		
	e-ISSN: 2147-835X		
	Dergi sayfası: http://dergipark.gov.tr/saufenbilder		
	<u>Received</u> 29-09-2017 <u>Accepted</u> 10-05-2018	<u>Doi</u> 10.16984/saufenbilder.340643	

Determination of the Effects of Mineral on Seed Yield by Different Statistic Methods in Bread Wheat (*Triticum aestivum* L.) under Drought Conditions

Murat Olgun, Okan Sezer, Metin Turan, Zekiye Budak Başçiftçi, Nazife Gözde Ayter Arpacıoğlu, Murat Ardiç^{*1}, Onur Koyuncu

ABSTRACT

The purpose of this study is to determine the effect of minerals (N, P, K, Ca, Mg, S, Fe, Mn, Zn and Cu) on yield components by different statistical methods and this will help to understand efficiency of them in breeding programs. This study was carried out in the location of Eskişehir Osmangazi University, Faculty of Agriculture, in 2014-15 arid cropping seasons. Success mainly depends on power of effectiveness parameters used and statistical methods could be safely used to reveal effectiveness of parameters in the breeding programs. Results of correlation, cluster, principal component and conditional formatting analyses revealed that with in the efficiency limits (between the lowest dose and toxicity level) integrative effects of minerals were determined. This means that behavior of minerals among genotypes are mainly similar. some minerals called **MEPG** (N, P, K, Ca, S and Zn) are mostly effective in growth, others called **MECA** (Mg, Fe, Mn and Cu) are mostly effective in photosynthesis, and 0,767 unit increase **MEGA** and 0,481 unit in **MECA** increases result in 1 unit increase in the grain yield. Harmankaya, Sultan, Müfitbey and Tosunbey were found as higher performance and stabile bread wheat genotypes. To determine the changes of the minerals in the genotypes, are important for definig their effect on yield as well as the yield components. Obtained data will make contributions to the success of breeding programs that will be done in the future.

Keywords: Bread wheat, genotypes, mineral, yield components, statistical analyze methods

1. INTRODUCTION

Bread wheat (*Triticum aestivum* L.) is one of the most produced crop and plays vital role in human nutrition, trade and industry in the world. Human population has been increasing more and more but increase in acreage and production of bread wheat haven't been meeting this. With these characteristics, wheat also appears to be far from meeting the growing need of humans for nutrition in the near future. Extensive adaptation capability

in different environments, resistance to pests and diseases make bread wheat popular in the world. Moreover, bread wheat is processed as source of starch, protein, minerals, vitamins etc. [11], [17], [45]. Meeting almost the need of 50% of carbohydrates, proteins and minerals in daily human nutrition, bread wheat occupy more than 50% of total food cereal production in the world [5], [44]. Like the other living organism, plants need certain minerals in enough level to act basic and important roles in physiological and biochemical processes. Studies reported that

* Corresponding Author

¹ Eskişehir Osmangazi Üniversitesi, Biyoloji Bölümü - mardic@ogu.edu.tr

effectiveness and necessity of minerals for plants closely depend upon availability of minerals in plants and soil plant growth stage, health of biochemical processes, effect of genotype x environment interaction, effect of stress environment [10], [22], [29], [30], [37], [41].

Plant growth effects the grain yield which is one of the important characters and so subject to many factors. Knowledge on genetic association between yield and yield components might develop the effectiveness of breeding programs with determining and using key criteria for selecting wheat genotypes. Basic purpose of wheat breeding programs is improve novel cultivars which have high winter resistance, high yielding ability and finally resistance to drought and diseases. These novel cultivars have high importance for breeding of the world. Some essential plant characteristics such as grain yield and seed weight per spike are known as important ingredients in bread wheat breeding programs [1], [16], [34], [40], [48]. As well as knowing the minerals that are effective in the plant and their mode of action in plants will be of benefit to the development of highly efficient genotypes [10], [29], [30], [41]. Determining the effect of plant characteristics on yield helps to create opportunity developing novel genotypes. Different statistical methods including correlation, principal component, cluster, factor and conditional formatting analyses could be used to assess plant characteristics in breeding programs [4], [35], [38], [46]. The purpose of this study is to determine the effect of minerals (N, P, K, Ca, Mg, S, Fe, Mn, Zn and Cu) on yield components by different statistical methods and this will help to understand efficiency of them in breeding programs.

2. MATERIALS AND METHODS

This study was carried out in the location of Eskişehir Osmangazi University, Faculty of Agriculture, in 2014-15 arid cropping seasons. Soil in the experimental area was loamy texture (39,4% sand, 40,2% silt and 20,4% clay); 0,38% CaCO₃, 228,5mmol kg⁻¹ P₂O₅, 307,44mmol kg⁻¹ K₂O, 6,18 pH, 2,13% organic matter and 2,13dS m⁻¹ electrical conductivity. Average, minimum and maximum temperatures, precipitations in 2014-15 and long term years in Eskişehir were given in Table 1. Precipitations in 2014-15 and long term years were 346,0 mm and 326,6 mm, respectively.

Maximum, minimum and average temperatures in 2014-15 and long term years were 25,3 and 23,8, -3,9 and -6,1, 10,2 and 8,9, respectively. Fifteen bread wheat genotypes (Alpu, Atay, Bezostaja, Harmankaya, Sönmez, Sultan, Müfitbey, Çetinel, İkizce, Nacibey, Es 26, Gerek, Tosunbey, Yıldırım and Palandöken 97) were used.

Table 1. Average, minimum and maximum temperatures, precipitations in 2014-15 and long term years in Eskişehir

Climatic Param.	Years	October	November	December	January	February	March	April	May	June	July	Tot./Av.
Max.Temp.	2014-15	29,2	21,6	17,5	18	20,9	22,2	23,0	30,3	32,0	37,9	25,3
	Long	18,4	1,5	15,7	13,6	18,5	20,6	26,1	30,2	36,7	37,5	23,8
Min.Temp.	2014-15	-0,5	-7,0	-8,0	-14,5	-17,0	-7,9	-3,8	0,2	8,7	10,5	-5,9
	Long	-7,2	-10,5	-7,2	-18,2	-11,3	-5,3	-5,3	-4,9	4,5	6,7	-6,1
Av.Temp.	2014-15	14,5	6,0	4,8	1,5	4,9	5,9	9,2	15,2	18,1	21,9	10,2
	Long	11,4	7,3	4,6	-3,6	-5,6	6,3	7,7	15,4	22,7	23,3	8,9
Tot. Rainf.	2014-15	9,0	29,5	65,1	36,0	42,8	32,6	23,9	20,7	79,0	7,4	346,0
	Long	25,5	29,8	45,9	38,2	32,5	33	35,4	43,1	29,3	13,9	326,6

*Data of regional meteorology station, Eskişehir. Long term years (1970-2015)

Fertilizers given were 60 kg N ha⁻¹ (half at sowing stage and half at tillering stage) and 60 kg ha⁻¹ P₂O₅ (once at sowing). Seeds were planted at the second week of September with 500 seed/ m² rate. Experimental design was randomized complete block design with three replications. Plot size was 6 m/1.2 m (7.2 m²). Grain yield, seed weight per spike (Ceylan 1994; Singhl et al. 2002), minerals as N, P, K, Ca, Mg, S, Fe, Mn, Zn and Cu [36] were evaluated. Samples for determining minerals were taken at tillering period, flowering period, maturity period and seed. The Kjeldahl method and a Vapodest 10 Rapid Kjeldahl Distillation Unit (Gerhardt, Konigs winter, Germany) were used to determine the total N content [13], [49]. The Ca, Mg, K, P, Fe, Cu, Mn, Zn contents in genotypes were determined by using an Inductively Coupled Plasma spectrometer (Perkin-Elmer, Optima 2100 DV, ICP/OES, Shelton, CT 06484-4794, USA [36]. Correlation principal components clusters, factor and conditional formatting analysis were used to determine the effect of minerals on wheat yield. Minitab 16, SPSS 16 and Excel 2016 software programs were used.

3. RESULTS

In the study, minimum, maximum, mean values of plant characters and minerals in bread wheat genotypes were given in Table 2. Correlation analysis is the way of evaluation of relationship between two variables. It is commonly used in breeding programs to assess relationships between plant characters. Once coefficient reaches to zero,

it means that two plant characters seem to be independent from each other.

Table 2. Minimum, maximum, mean values of plant characters and minerals in bread wheat genotypes

Variable	Mean	Minimum	Maximum	Variable	Mean	Minimum	Maximum
SeedYield	3,16±0,39	2,39	3,81	Mg	896,5±231,3	569,8	1311,6
SeedWe./Spike	1,77±0,14	1,57	2,060	S	846,8±229,5	517,8	1148,9
N	3,00±0,45	2,13	3,73	Fe	80,93±6,94	70,45	91,22
P	1855,3±290,8	1464,4	2345,7	Mn	37,62±5,43	26,77	46,54
K	14793±4254	10855	25513	Zn	40,43±11,69	25,02	60,29
Ca	1116,6±180,2	859,6	1472,4	Cu	50,17±6,37	39,47	59,00

If coefficient closes to 1/-1, it means that two characters are negatively/positively related to each other [38], [20]. Correlation analysis on plant characteristics in bread wheat was given in Table 3.

Table 3. Correlation analysis on plant characteristics in bread wheat

	Seed Yield	Seed We./Spike	N	P
Seed We./Spike	0,855**			
N	0,767**	0,718**		
P	0,831**	0,677**	0,749**	
K	0,846**	0,787**	0,799**	0,826**
Ca	0,588*	0,565*	0,635*	0,670**
Mg	0,864**	0,753**	0,801**	0,877**
S	0,825**	0,633*	0,829**	0,916**
Fe	0,835**	0,795**	0,577*	0,621*
Mn	0,482ns	0,408ns	0,289ns	0,309ns
Zn	0,626**	0,804**	0,825**	0,848**
Cu	0,511*	0,364ns	0,158ns	0,446ns
	K	Ca	Mg	S
Ca	0,763**			
Mg	0,877**	0,796**		
S	0,863**	0,727**	0,943**	
Fe	0,734**	0,420ns	0,724**	0,699**
Mn	0,127ns	0,173ns	0,593*	0,367ns
Zn	0,897**	0,580*	0,847**	0,877**
Cu	0,400ns	0,138ns	0,471ns	0,443ns
	Fe	Mn	Zn	
Mn	0,582*			
Zn	0,786**	0,240ns		
Cu	0,561*	0,588*	0,479ns	

Once relationship between Mn and seed yield was insignificant, significant relationship ($p < 0,05$) between Cu and seed yield was found. Cluster analysis is a hierarchical method, and the procedure forms its own set of closely related variables. In other words, the variables form groups according to the degree of closeness. In this method, the variables closest to each other are combined. The variables then join the same or different clusters according to their closeness [15], [27]. Cluster analysis in plant characteristics and bread wheat was given in Figure 1. Minerals have important roles in plants such as structural, enzymatic and osmotic processes [32]. Depending upon roles and efficiencies, concentrations of minerals expose changes, they increase and draw polynomial range during the developmental stage in plants [9]. Higher grain and biomass productions are directly related to amount and availability of minerals in soil [7].

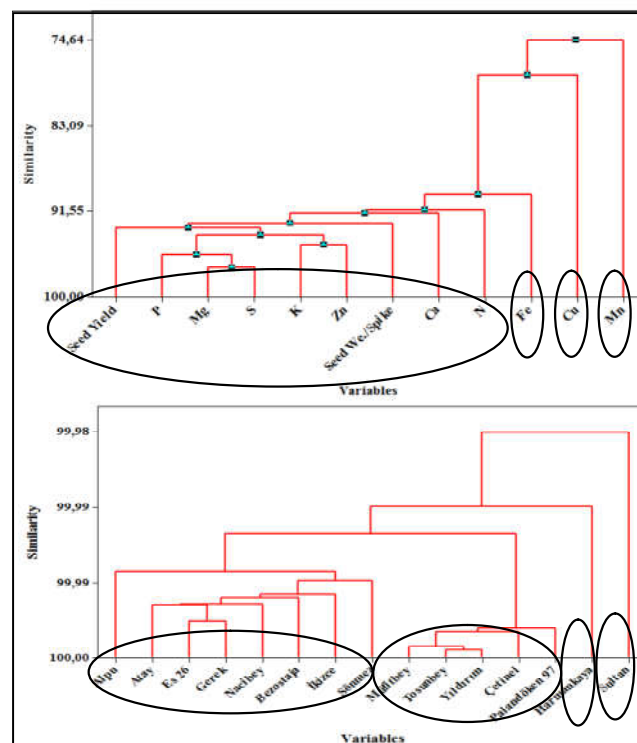


Figure 1. Cluster analysis in plant characteristics and bread wheat

Plant characteristics covered four groups; one big, three alone clusters. Fe, Cu and Mn occupied their separate groups; seed yield, P, Mg, S, K, Zn seed weight per spike, Ca and N joined big group. Besides, bread wheat genotypes were also divided into four clusters. Harmankaya and Sultan genotypes occupied separate groups. Alpu, Atay, Es 26, Gerek, Nacibey, Bezostaja, İkizce and Sönmez joined same group; Müfitbey, Tosunbey, Yıldırım, Çetinel and Palandöken 97 genotypes got into another group (Figure 1).

Nitrogen is the basic building block of the tissues in plants, and it is found in the structure of enzymes, organic and amino acids, nucleic acids, chlorophyll [3]. Phosphorus plays a role in the formation and storage of dry matter in generative development, such as flower, fruit and seed formation, in photosynthetic and metabolic events where energy transfer and storage events are required. phosphorus is found in the transfer and storage of energy in photosynthetic and metabolic events, flower, fruit and seed formation and development are found in the structure of various organic and amino acids [31]. Potassium plays a role in osmoregulation of the plant, in water intake, transport of metabolites and minerals, protein synthesis, regulation of stoma, cell division [33]. Calcium plant growth cell division is involved in many metabolic events such as ion uptake, and is involved in the formation of calmodulin, a Ca-linked protein in stress conditions, including

drought, and serves as a signal for stress proteins in stress conditions [8].

Principal component analysis (PCA) is a mathematical model to give information for multivariate data with lower variables. Besides, principal component analysis assist to reveal covariance properties of variables. It makes variables into smaller numbers in this form [2], [12], [24]. Principal component analysis on plant characteristics in bread wheat, and bi plot analysis of plant characteristics and bread wheat genotypes was given in Table 4 and Figure 2. The first and the second principal components (PC1 and PC2) explained 80,9% of total variability with variance 8,3368 (PC1-69,5%, variance 1,3697 and PC2-11,4%, variance 0,6903). PC1 having similar sign, represented seed yield, seed weight pers pike, N, P, K, Mg, S and Zn. Moreover, PC2 had Mn and Cu (Table 4). In biplot analysis (Figure 2), PC1 shows performance abilities of parameters, while PC2 denotes variations/stabilities of parameters. In this instance, inside of triangle assign better performance and stability in parameters.

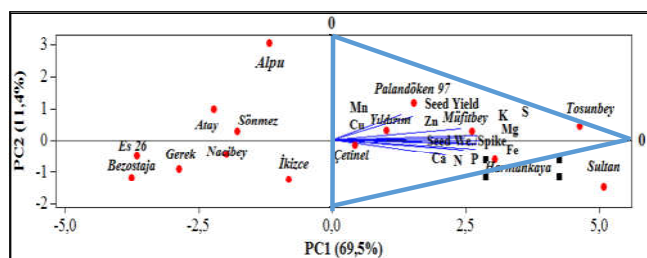


Figure 2. Biplot analysis of plant characteristics and bread wheat genotypes

Palandöken 97, Müfitbey, Yıldırim, Çetinel, Tosunbey and Harmanakaya genotypes seemed to be high performance and stabile genotypes. Furthermore, all minerals (N, P, K, Ca, Mg, S, Na, Fe, Mn, Zn and Cu), seed yield and seed weight per spike in all bread wheat genotypes were showed well performance and stability.

Table 4. Principal component analysis on plant characteristics in bread wheat

Eigenvalues of The Correlations						
	PC ₁	PC ₂	PC ₃	PC ₄	PC ₅	PC ₆
Eigenvalue	8,3368	1,3697	0,6903	0,6127	0,3932	0,2039
Proportion	0,695	0,114	0,058	0,051	0,033	0,017
Cumulative	0,695	0,809	0,866	0,917	0,950	0,967
	PC ₇	PC ₈	PC ₉	PC ₁₀	PC ₁₁	PC ₁₂
Eigenvalue	0,1812	0,1179	0,0498	0,0248	0,0125	0,0072
Proportion	0,015	0,010	0,004	0,002	0,001	0,001
Cumulative	0,982	0,992	0,996	0,998	0,999	1,000
Variable	PC ₁	PC ₂	PC ₃	PC ₄	PC ₅	PC ₆
SeedYield	0,325	0,101	-0,025	-0,176	-0,001	0,173
SeedWe./Spike	0,295	0,045	-0,042	-0,531	-0,299	0,492
N	0,293	-0,237	0,189	-0,224	0,467	0,050
P	0,312	-0,093	-0,024	0,278	0,275	0,333
K	0,321	-0,212	-0,233	0,021	-0,190	-0,036
Ca	0,253	-0,342	0,351	0,301	-0,625	-0,032
Mg	0,333	-0,022	0,203	0,187	-0,053	-0,081
S	0,324	-0,093	0,067	0,285	0,277	-0,341
Fe	0,259	0,297	-0,228	-0,338	-0,194	-0,662
Mn	0,154	0,600	0,660	-0,060	0,081	-0,009
Zn	0,322	-0,071	-0,292	-0,074	0,235	-0,037
Cu	0,179	0,565	-0,407	0,478	-0,108	0,222
Variable	PC ₇	PC ₈	PC ₉	PC ₁₀	PC ₁₁	PC ₁₂
SeedYield	0,370	0,656	0,007	-0,481	-0,152	-0,023
SeedWe./Spike	-0,039	-0,289	0,037	0,034	0,356	0,284
N	-0,522	0,280	-0,319	0,174	0,154	-0,213
P	0,583	-0,241	-0,260	0,350	-0,045	-0,199
K	-0,120	0,259	0,394	0,551	-0,416	0,217
Ca	-0,125	-0,044	-0,393	-0,162	-0,120	-0,036
Mg	-0,022	-0,081	0,638	-0,099	0,366	-0,495
S	0,085	-0,026	0,023	-0,139	0,332	0,686
Fe	0,187	-0,062	-0,278	0,177	0,110	-0,222
Mn	-0,048	-0,104	0,056	0,139	-0,344	0,127
Zn	-0,220	-0,494	0,050	-0,453	-0,490	-0,063
Cu	-0,356	0,123	-0,168	0,011	0,149	-0,02

Palandöken 97, Müfitbey, Yıldırim, Çetinel, Tosunbey and Harmanakaya genotypes seemed to be high performance and stabile genotypes. Furthermore, all minerals (N, P, K, Ca, Mg, S, Na, Fe, Mn, Zn and Cu), seed yield and seed weight per spike in all bread wheat genotypes were showed well performance and stability.

Magnesium is involved in metabolic events such as storage of photosynthetic energy, protein synthesis, nucleotide formation, and hydrolysis of many organic compounds [25], [33]. Sulfur influences product quality and product quality changes due to its various functions within the plant. It helps proteins, enzymes and vitamins function in plants. In plants, root hydraulic permeability, stoma openings and photosynthesis decrease in sulfur deficiency. Protein synthesis is reduced in sulfur deficiency. Chloroplast and chlorophyll synthesis decrease in sulfur deficiency [47]. Iron is the essential element of chlorophyll, which has vital importance in plant dry matter production, and functions in photosynthesis and associated enzymatic reactions in chlorophyll. Therefore, the development of young parts of the plant is closely related to the amount of Mg in dry matter production [28], [33]. Manganese is important for plant growth at a certain concentration. Trace element Mn plays a role in photosynthesis, respiration, enzyme activation and antioxydative metabolism [18], [39]. Zinc plays a role in the synthesis of carbohydrates, in structure of enzymes, in protein synthesis in membrane stability, photosynthesis and respiratory events, taking place in different metabolic events in plants [14], [42]. Copper is quite useful at a certain

concentration in plant development. Copper plays a role in protein synthesis by entering into the structure of certain enzymes. Cu, acting as a signal for certain hormones, plays a role in mitochondrial respiration in photosynthesis [50].

Analysis of conditional formatting in Excel is a way of revealing better variants. When two or more conditional formatting rules are applied to a cell range, these rules are evaluated according to the order of priority listed (from top to bottom) in the dialog box [4]. Conditional formatting of plant characteristics and bread wheat genotypes were given in Table 5. Clear information in plant characteristics and bread wheat genotypes could be observed.

Table 5. Conditional formatting of plant characteristics and bread wheat genotypes

	Seed Yield	Seed We./Spike	N	P	K	Ca	Mg	S	Fe	Mn	Zn	Cu	Mean
Alpu	3.2	1.8	2.4	1663.2	11556.4	859.6	805.6	650.9	84.3	46.5	33.6	59.0	1313.9
Atay	3.2	1.8	2.9	1510.2	10975.0	872.4	600.4	517.8	79.7	38.3	28.9	49.5	1223.3
Bezostaja	2.8	1.7	2.1	1503.1	12159.2	1111.3	569.8	527.3	76.7	26.8	25.0	42.7	1337.4
Harmankaya	3.7	1.9	3.6	2224.1	19942.2	1004.0	1005.4	1128.2	91.2	33.9	60.3	49.8	2129.0
Sönmez	2.9	1.6	2.6	1961.0	12527.8	984.6	758.6	833.2	71.3	32.5	36.3	58.9	1439.3
Sultan	3.8	2.0	3.7	2223.5	25513.4	1472.4	1311.6	1148.9	87.4	34.4	59.7	54.4	2659.6
Müfitbey	3.4	1.8	3.3	2145.4	18456.2	1352.8	1155.3	1116.6	85.7	43.5	42.1	54.6	2038.4
Cetinel	3.2	1.7	3.4	1712.3	14654.9	1198.3	946.0	975.7	81.5	40.6	41.5	48.7	1642.3
İkizece	3.1	1.7	3.1	2008.3	12547.7	1146.9	899.9	841.4	74.6	37.7	33.9	39.5	1469.5
Nacıbey	3.0	1.7	2.8	1687.6	11546.5	1104.9	821.5	746.9	73.2	38.8	27.6	42.5	1341.4
Es 26	2.4	1.6	2.6	1464.4	10854.7	992.4	582.4	574.4	75.9	31.9	31.7	48.5	1221.6
Gerek	2.7	1.7	2.9	1592.4	11346.3	1005.7	712.7	625.6	70.5	33.6	34.8	43.8	1289.4
Tosunbey	3.8	2.1	3.5	2345.7	18976.5	1398.3	1197.4	1108.4	89.5	44.6	58.4	56.2	2107.0
Yıldırım	3.2	1.9	3.1	1879.6	15642.3	1097.4	999.0	905.6	83.6	39.9	46.8	50.6	1729.4
Palandöken 97	3.3	1.8	3.0	1913.5	15196.5	1148.7	1082.7	1000.5	89.0	41.5	45.7	56.9	1715.3
Mean	3.2	1.8	3.0	1855.3	14793.0	1116.6	896.5	846.8	80.9	37.6	40.4	50.2	1643.8

Harmankaya, Sultan and Tosunbey in seed yield; Sultan and Tosunbey in seed weight per spike; Harmankaya, Sultan and Tosunbey in N and P; Sultan in K; Sultan and Tosunbey in Ca; Sultan, Müfitbey and Tosunbey in Mg; Harmankaya, Sultan, Müfitbey and Tosunbey in S and Fe; Alpu, Müfitbey and Tosunbey in Mn, Harmankaya, Sultan and Tosunbey in Zn, Alpu, Sönmez, Tosunbey and Palandöken 97 in Cu had the best performances. As a means of plant characteristics, Harmankaya, Sultan, Müfitbey and Tosunbey were similar and had the best performance. In means of genotypes, bread wheat genotypes in seed yield, N, Ca, Mg, S, Fe, Mn and Cu gave similarities (Table 5).

Factor analysis is a multivariate analysis technique that conceptually reduces to a smaller number of dimensions to facilitate the determination of relationships between variables known to be correlated. In other words, factor analysis facilitates the interpretation of the relationships between the concepts of the variables by revealing the factors belonging to the various variables related to each other. In other words, main aim in this technique is to allow summarize of covariance

structure on fewer dimensions in data collected [6], [19], [26]. Mineral concentrations in plant are formed by genotype x environment interactions. Mineral uptake and level are significantly related to plant health. Increase in mineral uptake by plants causes to increase dry matter and mineral content in plant and relatively more yield occurs [41], [43]. Minerals are generally known to be effective in plants such as biochemical events, photosynthesis, and growth, resistance to stress conditions, osmotic regulation; Minerals such as Mg, Cu, Fe, Mn play an important role mainly in photosynthetic events [33]. Inspired by this, the minerals were examined in two groups; MEPG: Minerals effective on plant growth (N, P, K, Ca, S and Zn) and MECA: Minerals effective on chlorophyll activity (Mg, Fe, Mn and Cu) in the present study. Descriptive factor analysis of plant characteristics and minerals were given in Table 6.

Table 6. Descriptive factor analysis of plant characteristics and minerals in bread wheat

Characters	Loadings	% of Variance explained	Suggested Factor Name
FACTOR I	5,860	56,396	MEPG: Minerals effective on plant growth
K	0,938		
S	0,897		
N	0,881		
Zn	0,875		
P	0,860		
Ca	0,825		
FACTOR II	1,353	24,067	MECA: Minerals effective on chlorophyll activity
Cu	0,845		
Mn	0,820		
Fe	0,620		
Mg	0,760		
Cumulative variance			80,163
*KMO Measure of Sampling Adequacy			0,70
FACTOR III	1,829	91,430	Seed Weight per Spike
Seed We./Spike	0,956		
Seed Yield	0,956		
Cumulative variance			91,430
*KMO Measure of Sampling Adequacy			0,50

Table 6 shows that two main factors are determined in parameters for 80,163% of total variability in the study. The first and the second factors accounted for 56,396% and 24,087%, respectively. The third factor covered 91,430% of total variability. The first factor gave 56,396% of total variability. The loading coefficients of the parameters are very close to each other, meaning that all parameters considered in **FACTOR I**, have almost equal effect on the total variance. So, all of

them created **MEPG** and they (N, P, K, Ca, S and Zn) are all recommended. In the same way, all parameters (Mg, Fe, Mn and Cu) occupied for **MECA** with 24,067% of total variability in **FACTOR II** and all were suggested. Seed yield and seed weight per spike in **FACTOR III** had same loading coefficient covering 91,430% of total variability. Suggested character was seed weight per spike (Table 6). Kaiser Meyer Olkin (**KMO**) test measures the fitness of the working volume for factor analysis. The value of **KMO** is set at 0.70, which is usually greater than 0.50 in scientific research, indicating that the working volume is sufficient. In addition, in **FACTOR III**, the loading coefficients of the seed yield and seed weight per spike were the same. Seed yield (**SY**) as dependent variable, **MEPG** and **MECA** as independent variables were taken, when preparing the hypothesis, **H₁** and **H₂**, given below, and the regression analysis was constructed on this (Figure 3).

MECA increases result in 1 unit increase in the grain yield.

Table 7. Multiple regression analysis in plant characteristics in bread wheat genotypes

Independent Variables	Standardized Regression Coefficients	t	P
MEPG	0,767	6,243	<0,0001
MECA	0,481	3,916	0,002
R ² : 0,905, F: 27,156** (df: 2,12)			
SY (SeedYield): 0,767 x MEPG (Minerals effective on plant growth) + 0,481 x MECA (Minerals effective on chlorophyll activity)			

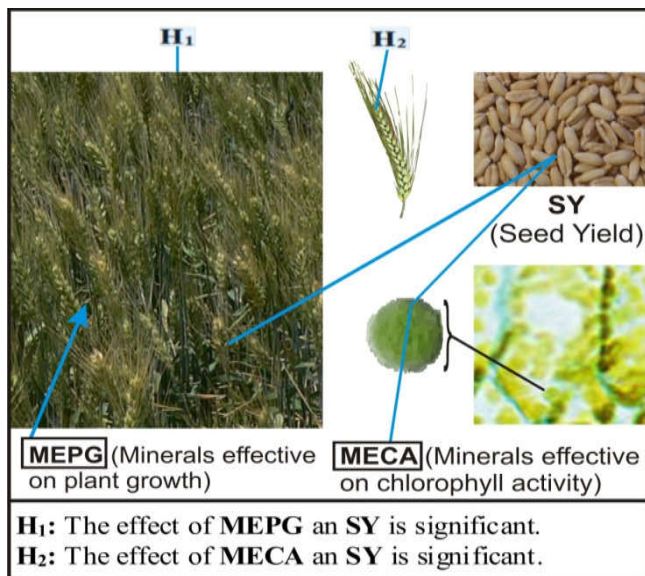


Figure 3. Hypothesis preparing diagram

Multiple regression analysis should cover some assumptions such as; linear Relationship between the dependent variable and the independent variables; normal distribution in variables; no high correlations among independent variables; similar variance of error terms in independent variables [21], [23]. Multiple regression analysis in plant characteristics was given in Table 7. In the analysis, **MEPG** and **MECA** as independent variables seed yield (**SY**) as dependent variable were taken into consideration. Table 7 assigns that the effect of variables in total was significant at 1%. Moreover, the individual effects of **MEPG** and **MECA** on seed yield (**SY**) were also found to be significant ($p < 0,01$). Formula explains that in 0,767 unit in increase **MEGA** and 0,481 unit in

DISCUSSION

Success mainly depends on the power of effectiveness parameters used and the statistical methods could be safely used to reveal effectiveness of parameters in the breeding programs. Results of correlation, cluster, principal component and conditional formatting analyses revealed that with in the efficiency limits (between the lowest dose and toxicity level) integrative effects of minerals were determined. This means that behavior of minerals among genotypes are mainly similar. As known, levels and trenchancies of minerals are generally under the influence of the genotype x environment interaction, but considerably under genotypic influence [1], [16], [40]. Minerals as nutrients and/or effective ingredients on enzymatic processes play vital role on biochemical processes of plant growth and development of seed, therefore on yield. Some minerals have mainly important in growth, resistance to stress conditions, osmotic regulation; some have mainly photosynthesis [22], [33]. Factor analysis revealed that while some minerals called MEPG (N, P, K, Ca, S and Zn) are mostly effective for growth, others called MECA (Mg, Fe, Mn and Cu) are mostly effective on photosynthesis, and 0,767 unit in increase MEGA and 0,481 unit in MECA increases result in 1 unit increase in the grain yield. Harmankaya, Sultan, Müfitbey and Tosunbey were found as higher performance and stabile bread wheat genotypes. Correlation principal components clusters, factor and conditional formatting analysis revealed that N, P, K, S, Mg, Zn and Fe are closely related to plant yield. Factor analysis revealed the effect of minerals on yield with a different approach by divides minerals into MEGA and MEPG. Factor analysis determined the real effect shapes of mineral on yield. To determine the changes of the minerals in the genotypes their effect on yield as well as the yield components will increase the success of breeding programs. Evaluating plants for minerals, distribution and effect of minerals on seed yield could make breeding objectives more successful.

REFERENCES

[1] E. Acevedo, A. P. Conesa, P. Monneveux and J. P. Srivastava, "Physiology-Breeding of Winter Ceceals for Stressed

- Mediterranean Environments" , INRA Editions, Versailles Cedex, France, 1989.
- [2] W. Anderson, "An Introduction to Multivariate Statistical Analysis" , 2nd edn., Wiley, New York, 1984.
- [3] J. I. Andriolo, L. Erpen, F. I. Cardoso, C. Cocco, G. S. Casagrande and D. I. Janisch, "Nitrogen Levels in the Cultivation of Strawberries in Soilless Culture" Horticultura Brasileira, vol. 29, 516–519, 2011.
- [4] Anonymous, "https://www.actx.edu/web/files/filecabinet/folder7/Excel" , 2007.
- [5] M Ashraf and P. J. C., "Harris Potential biochemical indicators of salinity tolerance in plants" , Plant Science, vol. 166, 3–16, 2004.
- [6] D. F. Austin and M. Lee, "Comparative mapping in F2:3 and F6:7 generations of quantitative trait loci for grain yield and yield components in maize" , Theor Appl Genet, vol. 92, no 7, 817–826, 1996.
- [7] D. J. Bonfil and U. Kafkafi, "Wild wheat adaptation in different soil ecosystems as expressed in the mineral concentration of the seeds" , Euphytica, vol. 114, 123–134, 2000.
- [8] J. H. F. Bothwell and C. K. Y. Ng "The evolution of Ca²⁺ signalling in photosynthetic eukaryotes" , New Phytol, vol. 166, 21–38, 2005.
- [9] F. Branca and M. Ferrari, "Impact of micronutrient deficiencies on growth: The stunting syndrome" , Annals of Nutrition and Metabolism, vol. 46, 8–17, 2002.
- [10] I. Çakmak, "Enrichment of cereal grains with zinc: agronomic or genetic biofortification?" , Plant and Soil, vol. 302, 1–17, 2008.
- [11] A. Ceylan, "Field Crop Production" , Aegean University Press, İzmir, 1994.
- [12] W. Dillon and M. Goldstein, "Multivariate Analysis: Methods and Applications" , Wiley, New York, 1984.
- [13] R. Doğan, "Determination of Grain Yield and Some Agronomic Characters of Bread Wheat (*Triticum aestivum* L.) Lines" , Journal of Agricultural Faculty of Uludağ University, vol. 16, no 2, 149–158, 2002.
- [14] A. A. El-Ghamery, M. A. El-Kholy and A. ElYouser, "Evaluation of cytological effects of Zn⁺² in relation to germination and root growth of *Nigella sativa* L. and

- Triticum aestivum* L.”, Mutation Research, vol. 537, 29–41, 2003.
- [15] S. E. Fienberg, “The Analysis of Cross-Classified Categorical Data” , The MIT Press, 1987.
- [16] L. F. Garcia del Moral, Y. Rharrabti, D. Villegas and C. Royo, “Evaluation of grain yield and its components in durum wheat under Mediterranean conditions: An ontogenic approach” , Agron J, vol. 95, no 2, 266–274, 2003.
- [17] İ. Genç, “Physiological and Morphological Basis in Cereals” , Çukurova Üniv Agric Fac Press, no 22, Ankara, 1977.
- [18] N. Gür, A. Topdemir, Ö. Munzuroğlu and D. Çobanoğlu, “The effect of heavy metal ions (Cu^{+2} , Pb^{+2} , Hg^{+2} , Cd^{+2}) on pollen germination and tube growth in *Clivia* sp.” , FU Journal of Science and Math, vol. 16, no 2, 177–182, 2004.
- [19] J. F. Hadr, R. E. Anderson, R. L. Tatham and W. C. Black, “Multivariate Data Analysis” , Prentice Hall, New Jersey, 1998.
- [20] J. Hiltbrunner, B. Streit and M. Liedgens, “Are graining densities an opportunity to increase grain yield of winter wheat in a living mulch of white clover?” , Field Crops Research, vol. 102, 163–171, 2007.
- [21] W. Hoyt, S. Leierer and M. Millington, “Analysis and interpretation of findings using multiple regression techniques” , Rehabilitation Counseling Bulletin, vol. 49, no 4, 223–233, 2006.
- [22] A. Hussain, H. Larsson, R. Kuktaite and E. Johansson, “Mineral Composition of Organically Grown Wheat Genotypes: Contribution to Daily Minerals Intake” , Int J Environ Res Public Health, vol. 7, no 9, 3442–3456, 2010.
- [23] J. Jaccard, V. Guilamo-Ramos, M. Johansson and A. Bouris, “Multiple regression analyses in clinical child and adolescent psychology” , Journal of Clinical Child and Adolescent Psychology, vol. 35, no 3, 456–479, 2006.
- [24] B. B. Jackson, “Multivariate Data Analysis An Introduction” , Illinois, Richard, D. Irwin, Inc., 2004.
- [25] M. Jezek, C. M. Geilfus, A. Bayer and K. H. Mühling, “Photosynthetic capacity, nutrient status and growth of maize (*Zea mays* L.) upon MgSO_4 leaf-application” , Front Plant Sci, vol. 5, 781, 2014.
- [26] R. A. Johnson and D. W. Wichern, “Applied Multivariate Statistical Analysis” , Prentice Hall, New Jersey, 2002.
- [27] K. Joreskog, “Factor Analysis by Least Squares and Maximum Likelihood Methods” , In: K. Enslein, A. Ralston ve H. Wilf, (eds) “Statistical Methods for Digital Computers” , Wiley, New York, 125–153, 1977.
- [28] C. Kaya and D. Higgs, “Improvements in the physiological and nutritional developments of tomato cultivars grown at high zinc by foliar application of phosphorus and iron” , Journal of Plant Nutrition, vol. 25, no 9, 1881–1894, 2002.
- [29] H. Kirchmann, L. Mattsson and J. Eriksson, “Trace element concentration in wheat grain: Results from the Swedish long-term soil fertility experiments and national monitoring program” , Environ Geochem Health, vol. 31, 561–571, 2009.
- [30] B. Kouakou, K. S. Alexis, D. Adjehi, D. K. Marcelin and G. Dago, “Biochemical changes occurring during germination and fermentation of millet and effect of technological processes on starch hydrolysis by the crude enzymatic extract of millet” , Journal of Applied Science Research, vol. 4, 1502–1510, 2008.
- [31] H. Lambers, M. D. Cramer, M. W. Shane, M. Wouterlood, P. Poot and E. J. Veneklass, “Structure and Functioning of Cluster Roots and Plant responses to Phosphate Deficiency” , Plant and Soil, vol. 248, 9–19, 2003.
- [32] H. W. Lopez, V. Krespine, A. Lemaire, C. Coudray, C. Feillet-Coudray, A. Messenger, C. Demigne and C. Remesy, “Wheat variety has a major influence on mineral bioavailability; Studies in rats” , Journal of Cereal Science, vol. 37, 257–266, 2003.
- [33] H. Marschner, “Mineral Nutrition of Higher Plants” , 2nd edn., London Academic Press, London, 1995.
- [34] M. C. Martinez-Ballesta, R. Dominguez-Perles, D. A. Moreno, B. Muries, C. Alcaraz-Lopez, E. Bastias, C. Garcia-Viguera and M. Carvajal, “Minerals in plant food: effect of agricultural practices and role in human health. A review” , Agronomy for Sustainable Development, vol. 30, 295–309, 2009.
- [35] D. L. Massart, B. G. M. Vandeginste, L. M. C. Buydens, S. de Jong, P. J. Lewi and J.

- Smeyers-Verbeke, "Straight line regression and calibration" , In: "Handbook of chemometrics and qualimetrics" , Amsterdam, The Netherlands, Elsevier, vol. A, 171–231, 1997.
- [36] D. Mertens, "AOAC official method 975.03" , In: W. Horwitz, and G. W. Latimer (eds), "Metal in Plants and Pet Foods. Official Methods of Analysis" , 18th edn., Maryland, USA, 3–4, 2005.
- [37] K. M. Murphy, K. G. Campbell, S. R. Lyon and S. S. Jones, "Evidence of varietal adaptation to organic farming systems" , *Field Crop Research*, vol. 102, 172–177, 2007.
- [38] K. Özdamar, "Statistical Data Analysis with Computer Programs" , 2nd edn., Eskişehir, Turkey, vol. I-II, 1999.
- [39] M. W. Paschke, A. Valdecantos and E. F. Redente, "Manganese toxicity thresholds for restoration grass species. *Environmental Pollution*" , vol. 135, 313–322, 2005.
- [40] D. C. Rasmusson, "A plant breeder's experience with ideotype breeding" , *Field Crop Res*, vol. 26, no 2, 191–200, 1991.
- [41] T. L. Roberts, "Nutrient best management practices: Western perspectives on global nutrient stewardship" , *Proceedings of the 19th World Congress of Soil Science: Soil solutions for a changing World*, 172–175, 2010.
- [42] G. R. Rout and P. Das, "Effect of metal toxicity on plant growth and metabolism: I. Zinc" , *Agronomie*, vol. 23, 3–11, 2003.
- [43] M. R. Schlemmer, D. D. Francis, J. F. Shanahan and J. S. Schepers, "Remotely measuring chlorophyll content in corn leaves with differing nitrogen levels and relative water content" , *Agronomy Journal*, vol. 97, no 1, 106–112, 2005.
- [44] U. B. Schulthess, J. Feil and S. C. Jutzi, "Yield independent variation in grain nitrogen and phosphorus concentration among Ethiopian wheat" , *Agronomy Journal*, vol. 89, no 3, 497–506, 2000.
- [45] P. R. Shewry, "Improving the protein content and composition of cereal grain" , *Journal of Cereal Science*, vol. 46, 239–250, 2007.
- [46] L. Slavkovic, B. Skrbic, N. Miljevic and A. Onjia, "Principal component analysis of trace elements in industrial soils" , *Environmental Chemistry Letters*, vol. 2, 105–108, 2004.
- [47] M. F. Soliman, S. F. Kostandi and M. L. Beusichem-Van, "Influence of sulphur and nitrogen fertilizer on the uptake of iron, manganese and zinc by corn plants grown in calcareous soil comm" , *Soil Sci Plant Anal*, vol. 23, 1289–1300, 1992.
- [48] A. J. Stewart, W. Chapman, G. I. Jenkins, I. Graham, T. Martin and A. Crozier, "The effect of nitrogen and phosphorus deficiency on flavonol accumulation in plant tissues" , *Plant Cell Enviroment*, vol. 24, 1189–1197, 2001.
- [49] B. Varga, Z. Svecnjak and A. Pospisi, "Grain yield and yield components of winter wheat grown in two management systems" , *Die Bodenkultur*, vol. 51, no 3, 145–150, 2002.
- [50] H. Wang, X. Q. Shan, B. Wen, S. Zhang and Z. J. Wang, "Responses of antioxidative enzymes to accumulation of copper in a copper hyperaccumulator of *Commoelina communis*" , *Archives of Environmental Contamination and Toxicology*, vol. 47, 185–192, 2004.

	SAKARYA UNIVERSITY JOURNAL OF SCIENCE		 SAKARYA UNIVERSITY
	e-ISSN: 2147-835X http://www.saujs.sakarya.edu.tr		
	<u>Received</u> 02-01-2018 <u>Accepted</u> 10-05-2018	<u>Doi</u> 10.16984/saufenbilder.373607	

Preparation and antibacterial activity of solvothermal synthesized ZnFe₂O₄/Ag-TiO₂ nanocomposite

Keziban Atacan^{*1}, Nuray Güy², Soner Çakar³

Abstract

In this study, ZnFe₂O₄ magnetic nanoparticles and ZnFe₂O₄/Ag-TiO₂ nanocomposite were synthesized solvothermally. The prepared materials were characterized using X-ray diffraction, Scanning electron microscopy, Fourier transform infrared spectroscopy and Vibrating sample magnetometer. In addition, the antibacterial performance of materials was evaluated against Gram-positive bacteria (*Staphylococcus aureus*) and Gram-negative bacteria (*Escherichia coli*). ZnFe₂O₄/Ag-TiO₂ nanocomposite was shown more powerful antibacterial efficiency against *Staphylococcus aureus* than *Escherichia coli*. Also, the inhibition diameter of 15±0.2 mm for ZnFe₂O₄/Ag-TiO₂ nanocomposite was measured since the antibacterial activity increased with nanocomposite formation.

Keywords: ZnFe₂O₄, TiO₂, silver nanoparticles, antibacterial activity

1. INTRODUCTION

Spinel ferrites have been extensively investigated in recent years in various fields, such as biomedical fields, optoelectronic devices, catalysis and drug loading materials owing to their physical, chemical and magnetic properties [1]. Furthermore, spinel ferrites have major features for many fields, including the elimination of contaminants from water and air, odor control, bacterial inactivation, water splitting for H₂ production, and many others [2]. Among various spinel ferrites, zinc ferrite (ZnFe₂O₄) magnetic nanoparticles (MNPs) have been widely used both drug delivery systems and other biomedical, biotechnology applications. ZnFe₂O₄ is synthesized by using various

techniques including sol-gel, coprecipitation and hydrothermal/solvothermal method and so on [3, 4]. Among them, the solvothermal synthesis is easy to control morphology of the products, so it is generally preferred [4, 5].

The substitution of spinel ferrite with a transition metal can increase the antibacterial property of ferrite nanoparticles (NPs) in biomedical applications. The spinel ferrite NPs have been required further study for biomedical application due to their biocompatibility and antibacterial properties [6, 7]. The modification of NPs with noble metals, such as Pt, Au, and Pd, has been accepted as one of the most efficient methods to improve the stability, biocompatibility and bacterial activity for biological applications [8]. Besides the other metal (Au, Ag, Cu, Pt, Pd, etc.)

*Corresponding Author: kezibanatacan@sakarya.edu.tr

¹Sakarya University, Biomedical, Magnetic and Semiconductor Materials Research Center (BIMAS-RC), 54187 Sakarya, Turkey

²Sakarya University, Science & Arts Faculty, Department of Chemistry, 54187 Sakarya, Turkey

³Bulent Ecevit University, Science and Technology Research and Application Center (ARTMER), 67100 Zonguldak, Turkey

NPs, the silver NPs (Ag NPs) have a lot of interest due to their low-cost and stability, large specific surface area and excellent antimicrobial activities [9]. Ag NPs have long been known to exert strong inhibitory and bactericidal effects. The Ag NPs with their unique chemical and physical properties are noted for an alternative for improving of new antibacterial materials due to their antimicrobial properties. The NPs get adhered to the bacterial membrane and also some of them pass through inside of the cell membrane. The bacterial membrane includes sulfur-containing proteins and so the Ag NPs are interacted with these proteins in the cell [10]. Furthermore, Ag NPs have widely used for various fields such as food, package and medicine due to having high surface area and physicochemical properties [11]. To the best of our knowledge, TiO₂ NPs have been found to be effective as antibacterial agent against both Gram-positive and Gram-negative bacteria. Verma et al. stated that TiO₂ NPs have their efficiency against the bacterial biofilm formed by *Enterobacter sp.* [12]. Chan et al. studied antibacterial activity of TiO₂ nanotubes against Gram-positive bacteria (*Bacillus atropheus*) as a function of annealing temperature [13].

Although some papers on antibacterial activities of TiO₂ and Ag-TiO₂ derivatives have been published, there have been no investigation on the antibacterial activity of ZnFe₂O₄/Ag-TiO₂ nanocomposite [14, 15]. The goal of this study is to investigate preparation, characterization and the antibacterial properties of ZnFe₂O₄/Ag-TiO₂ nanocomposite.

2. MATERIALS AND METHODS

2.1. Materials

All chemicals were of analytic grade and used as received without further purification. ZnCl₂ (>99%), FeCl₃.6H₂O (>99%), CH₃COONa.3H₂O (NaAc, >99%), NaOH (≥97%), NaBH₄ (≥96%), C₂H₅OH (>99.2%), Chromocult Coliform Agar and Baird Parker Agar were provided from Merck (Germany). Titanium isopropoxide (TTIP, 97%) was obtained from Sigma-Aldrich (USA). C₂H₆O₂ (99%, EG) and AgNO₃ were provided from Tekkim (Turkey).

2.2. Preparation of ZnFe₂O₄, TiO₂, Ag-TiO₂ and ZnFe₂O₄/Ag-TiO₂ nanocomposite

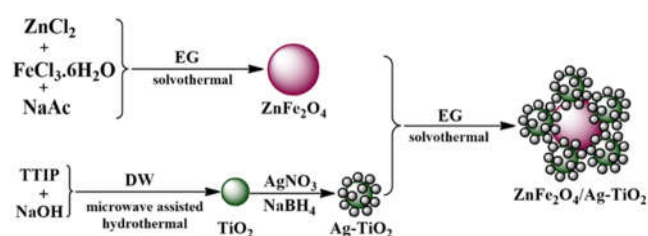
ZnFe₂O₄ magnetic NPs were synthesized through a solvothermal method with minor modifications [4, 16]. 0.34 g ZnCl₂ (1 mmol), 1.08 g FeCl₃.6H₂O (2 mmol) and 0.82 g of NaAc (4 mmol) were dissolved into 30 mL of EG under vigorous stirring for 1 h at room temperature. Then, the homogeneous solution was transferred into Teflon-coated autoclave (40 mL) and held at 180 °C for 18 h in furnace. The autoclave was cool. Finally, ZnFe₂O₄ MNPs were collected by a magnet and then they were washed with deionized water (DW) several times, washed with ethanol and dried at 70 °C for 24 h.

TiO₂ NPs were prepared by using microwave assisted hydrothermal method with some modification [17]. TTIP (5 mL) and 1 M NaOH (5 mL) were dissolved in DW (60 mL). After stirring intensively for 1 h at room temperature, the mixture was transferred into the Teflon-coated autoclave microwave assisted hydrothermal vessel and conducted microwave irradiation (CEM Mars5 model) with a controlled power of 380 W for 30 min at 100 °C. TiO₂ NPs were centrifuged at 5000 rpm for 15 min and washed with DW several times and ethanol. Then the obtained white powder was dried at 70 °C for 24 h.

For the doped Ag on TiO₂, 0.5 g of TiO₂ were dispersed in 40 mL of DW under ultrasonication for 30 min. After AgNO₃ was added to this reaction such that the gravimetric weight ratio of Ag to TiO₂ reaction was 5% [18], 0.0175 M (20 mL) NaBH₄ solution was added drop by drop to the mixture and stirred for 1 h. So, silver ions (Ag⁺) were reduced and clustered to metallic NPs (Ag) onto TiO₂ surface. The Ag-TiO₂ particles were centrifuged and washed twice with DW and ethanol. Then, the Ag-TiO₂ was dried at 70 °C for 24 h.

For the preparation of ZnFe₂O₄/Ag-TiO₂ nanocomposite, 0.035 g ZnFe₂O₄ MNPs and 0.07 g Ag-TiO₂ were dispersed into 30 mL of EG under vigorous stirring at room temperature for 30 min. Then, the mixture was transferred into Teflon-coated autoclave and heated at 180 °C for 4 h [19]. The autoclave was allowed to cool. ZnFe₂O₄/Ag-TiO₂ nanocomposite (mass ratio=2:1) was collected by a magnet. The separation, washing and drying process were carried out according to the same as ZnFe₂O₄ MNPs. Preparation of

ZnFe₂O₄/Ag-TiO₂ nanocomposite was shown in Scheme 1.



Scheme 1. Preparation of ZnFe₂O₄/Ag-TiO₂ nanocomposite

2.3. Test of antibacterial activity

The antibacterial activities of ZnFe₂O₄, TiO₂, Ag-TiO₂ and ZnFe₂O₄/Ag-TiO₂ were tested against the Gram-negative bacterium *Escherichia coli* (*E. coli*) and the Gram-positive bacterium *Staphylococcus aureus* (*S. aureus*). *E. coli* and *S. aureus* were grown aerobically at 37 °C overnight. 1 mL of fresh bacterial suspension was prepared from *E. coli* and *S. aureus* bacteria at room temperature using physiological saline solution and vortexed. After 0.1 mL aliquot of bacterial suspension was poured on sterile Petri dishes on the Chromocult Coliform Agar plate for *E. coli* and on the Baird Parker Agar plate for *S. aureus*. All samples were put in stated agar plate. Finally, petri dishes were incubated at 37 °C for 24 h in the dark [20]. After 24 h, all petri dishes were visually controlled for the presence of bacterial growth, and the zone of inhibition (ZOI) was measured. The test was performed in triplicate.

2.4. Characterizations of all samples

The prepared products were confirmed by XRD (PANalytical, Empyrean, Netherlands). FTIR spectra were recorded on Shimadzu UATR Two instrument (Japan). The morphologies of the samples were characterized using a Philips XL30 SFEG scanning electron microscope (SEM). Magnetic measurements were recorded at 300 K using vibration sample magnetometry (VSM Lake Shore-7407, USA).

3. RESULTS AND DISCUSSION

3.1. X-ray diffraction

Figure 1 shows the XRD patterns of ZnFe₂O₄, TiO₂, Ag-TiO₂ and ZnFe₂O₄/Ag-TiO₂. The XRD pattern of the pure ZnFe₂O₄ in Figure 1 can be perfectly assigned to the cubic phase of ZnFe₂O₄ (ICSD no. 98-009-1931). The diffraction peaks at $2\theta = 30.13^\circ$, 35.48° , 43.14° , 53.55° , 57.02° , and

62.67° were indexed to the (220), (311), (400), (422), (511) and (440) reflections of ZnFe₂O₄ with cubic spinel structure [19, 21]. The XRD spectra of TiO₂ indicated anatase phase formation (ICDS: 98-015-4601) due to (101) crystal plane [17]. As shown in Figure 1, the six diffractive peaks at 25.28° , 37.95° , 47.98° , 53.84° , 54.88° and 62.72° can be indexed to the (101), (004), (200), (105), (211), and (204) crystal planes of anatase TiO₂, respectively [8, 22]. The XRD pattern of Ag-TiO₂ shows the characteristic peaks corresponding to anatase TiO₂ phase. However, no diffraction peaks of Ag phase are observed, which confirms that the Ag particles are very small and dispersed on the TiO₂ support [14]. The invisibly diffraction peaks for Ag-TiO₂ at 37.88° and 44.50° reflect the crystallographic planes of (111) and (200) for the face-centered cubic of the silver crystal in Figure 1 [11]. At the XRD pattern of ZnFe₂O₄/Ag-TiO₂ nanocomposite, it can be seen that all added peaks are in good agreement with both ZnFe₂O₄ and Ag-TiO₂. In addition, no peaks related to other impurities are observed in the synthesized ZnFe₂O₄/Ag-TiO₂ nanocomposite, indicating that no chemical reaction between ZnFe₂O₄ and Ag-TiO₂ occurs.

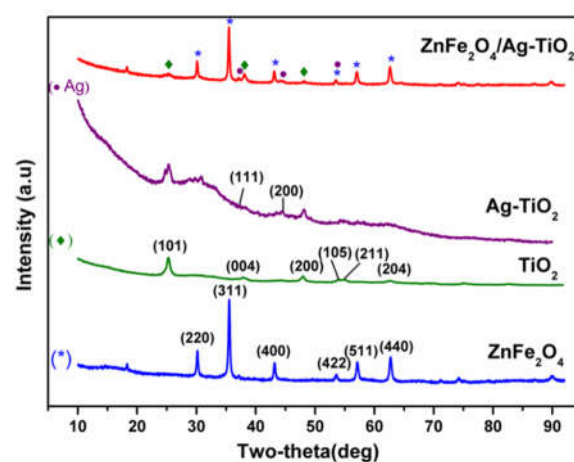


Figure 1. XRD patterns of ZnFe₂O₄, TiO₂, Ag-TiO₂ and ZnFe₂O₄/Ag-TiO₂

3.2. Fourier transform infrared spectroscopy

FTIR spectra of ZnFe₂O₄, TiO₂, Ag-TiO₂ and ZnFe₂O₄/Ag-TiO₂ indicated in Figure 2 in the range of 400–4000 cm⁻¹. From the FTIR spectrum of ZnFe₂O₄ MNPs, the strong and sharp absorption band appeared at 540 cm⁻¹ is in good agreement with vibration of Fe–O as typical band of spinel ferrite [23]. In addition, it can be found that the stretching vibration of Zn–O appears at 430 cm⁻¹, which corresponds to the M–O of the octahedron in the spinel structure [24]. According to Figure 2, a broad band below 1000 cm⁻¹ was monitored at

the spectra of both TiO_2 and Ag-TiO_2 , which can be assigned to the bending and stretching vibrations of Ti-O-Ti bonds [22]. In the FTIR of $\text{ZnFe}_2\text{O}_4/\text{Ag-TiO}_2$, most of the oxygen containing functional groups have been weakened during the solvothermal process [25]. However, the two characteristic absorption peaks of ZnFe_2O_4 exhibit slight shift in the curve of $\text{ZnFe}_2\text{O}_4/\text{Ag-TiO}_2$ nanocomposite (Figure 2), which also suggests that there are some interactions between ZnFe_2O_4 and Ag-TiO_2 in $\text{ZnFe}_2\text{O}_4/\text{Ag-TiO}_2$ nanocomposite.

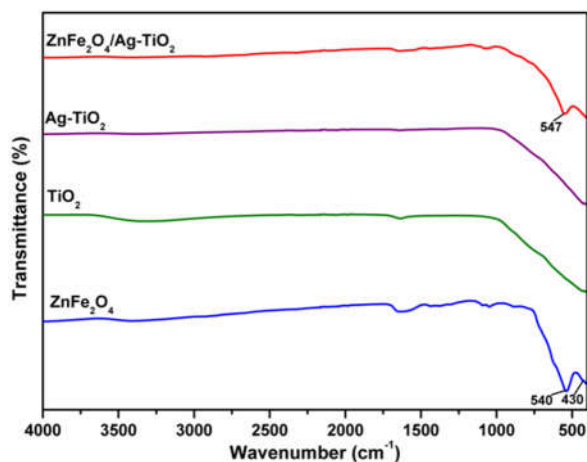


Figure 2. FTIR spectra of ZnFe_2O_4 , TiO_2 , Ag-TiO_2 and $\text{ZnFe}_2\text{O}_4/\text{Ag-TiO}_2$

3.3. Magnetic measurements

The magnetic properties of all samples were investigated by vibrating sample magnetometer (VSM) at room temperature, and the magnetic hysteresis loops are depicted in Figure 3. The saturation magnetization values of ZnFe_2O_4 MNPs is 12 emu/g. ZnFe_2O_4 MNPs are also superparamagnetic, as its magnetic hysteresis loop passed through the origin of the coordinate [19]. For TiO_2 and Ag-TiO_2 , the saturation magnetization values of 1.1 and 2.4 emu/g were obtained respectively. The $\text{ZnFe}_2\text{O}_4/\text{Ag-TiO}_2$ nanocomposite exhibits the saturation magnetization of 5.5 emu/g. The saturation magnetization of the magnetic composite decreases compared with that of ZnFe_2O_4 MNPs, which can be attributed to the less magnetic source.

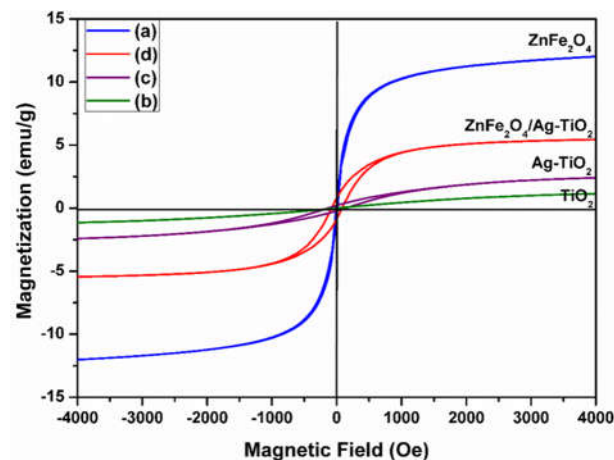


Figure 3. Magnetization hysteresis loops of ZnFe_2O_4 (a), TiO_2 (b), Ag-TiO_2 (c) and $\text{ZnFe}_2\text{O}_4/\text{Ag-TiO}_2$ (d)

3.4. Scanning Electron Microscopy

The morphology of all samples were investigated by scanning electron microscope, as shown in Figure 4. ZnFe_2O_4 MNPs are agglomerated NPs and their images show clustered structures and cauliflower-like shapes in Figure 4 (a). The TiO_2 shows very regular rough spherical morphology in Figure 4 (b). When silver NPs were doped, the size of TiO_2 decreased and no regular spherical particles was obtained in Figure 4 (c). The SEM image of the Ag-TiO_2 , confirmed that the Ag-TiO_2 distributed as reunite state and the aggregated particle [26]. As seen in Figure 4 (d), the agglomerated structure happens the scattered, which implies the $\text{ZnFe}_2\text{O}_4/\text{Ag-TiO}_2$ nanocomposite consisting of ZnFe_2O_4 and Ag-TiO_2 .

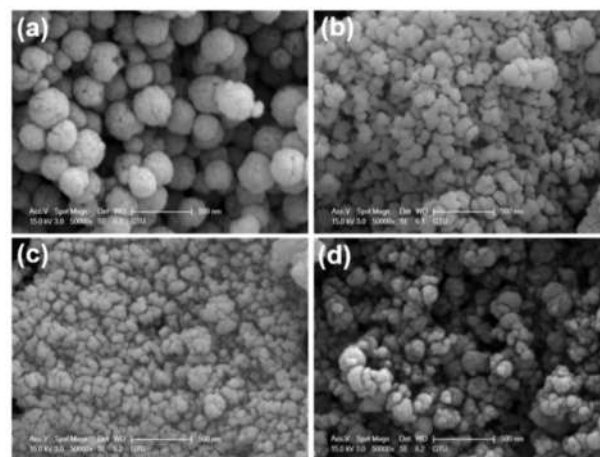


Figure 4. SEM images of ZnFe_2O_4 (a), TiO_2 (b), Ag-TiO_2 (c) and $\text{ZnFe}_2\text{O}_4/\text{Ag-TiO}_2$ (d)

3.5. Antibacterial activities of all samples

The antibacterial activities and the diameter for ZOI of the all samples against *S. Aureus* (gram-positive) and *E. coli* (gram-negative) were measured (Table 1). All samples showed stronger

antibacterial properties against *S. aureus* than *E. coli*. Gram-positive and gram-negative bacteria have differences in their membrane structure, the most distinctive of which is the thickness of the peptidoglycan layer. The peptidoglycan layer is a specific membrane feature of bacterial species. Therefore, the antibacterial effect of samples are associated with the peptidoglycan layer [27]. So, the maximum antibacterial activity was observed against *S. aureus* showing 15 mm but *E. coli* showed 12 mm (Table 1). It can be seen that, all materials have larger inhibition zone, indicating that the materials with antibacterial activities [28].

Zinc ferrite NPs can increase both their bioactivity and bactericidal efficiency owing to a large surface-to-volume ratio. As a result, the diameter of ZOI for ZnFe_2O_4 is 11 mm against *S. Aureus* but the diameter of ZOI for ZnFe_2O_4 is 8 mm against *E. coli* (Table 1). Sanpo et al. stated the antibacterial activity of transition zinc-substituted cobalt ferrite NPs ($\text{Co}_{0.5}\text{Zn}_{0.5}\text{Fe}_2\text{O}_4$) was assayed against *E. coli*. Then, they have confirmed that antibacterial activity is stronger against *E. coli* than nickel-substituted cobalt ferrite NPs ($\text{Co}_{0.5}\text{Ni}_{0.5}\text{Fe}_2\text{O}_4$) and manganese-substituted cobalt ferrite NPs ($\text{Co}_{0.5}\text{Mn}_{0.5}\text{Fe}_2\text{O}_4$) [7]. This could be based on the difference in chemical composition and surface roughness of the NPs. Also, Sanpo et al. reported that zinc-substituted cobalt ferrite nanopowders inhibit the growth of both *E. coli* and *S. aureus* [6].

TiO_2 displays good antimicrobial activity against *S. aureus* than *E. coli* (Table 1). In addition, the diameter of the ZOI for Ag-TiO_2 is larger than that of pure TiO_2 . Ag NPs decorated in nano TiO_2 are one of the methods that can improve antibacterial activity [29]. Ag NPs considerably decrease bacterial infections due to have high surface areas and so Ag NPs exhibit better antibacterial activities than the other nanoparticles. So, Ag NPs can reach more simply into the bacteria, causing mutilation on the respiration of bacteria and finally inducing to death of bacterial cell [20]. Reducing the particle size of the materials, the materials are more developed as biocompatibility and bacterial activity. Cao et al. synthesized Ag/TiO_2 and Ag/TiO_2 nanopowder by SEA method and they proved both of the antibacterial samples to be great inhibitory efficiency of mould growth in attacking and destructing bacterial cell membranes [14].

The $\text{ZnFe}_2\text{O}_4/\text{Ag-TiO}_2$ nanocomposite displays antibacterial activity against both *S. aureus* and *E. coli*, also the ZOI for $\text{ZnFe}_2\text{O}_4/\text{Ag-TiO}_2$ is larger

than that of ZnFe_2O_4 and Ag-TiO_2 (Table 1). Allafchian et al. synthesized $\text{NiFe}_2\text{O}_4/\text{PAMA}/\text{Ag-TiO}_2$ nanocomposite and they found that $\text{NiFe}_2\text{O}_4/\text{PAMA}/\text{Ag-TiO}_2$ nanocomposite showed a very good antibacterial activity against gram positive and negative bacteria [29]. Atacan et al. investigated antibacterial activities of $\text{Ag}/\text{CuFe}_2\text{O}_4$ and papain immobilized $\text{Ag}/\text{CuFe}_2\text{O}_4$ MNPs. They have found that papain immobilized $\text{Ag}/\text{CuFe}_2\text{O}_4$ MNPs show strong antibacterial efficiency [30]. This paper exhibits that after composing of nanocomposite, the antibacterial activity is significantly enhanced. The obtained results were conformed with the antibacterial properties and inhibition diameters when compared with other literatures.

Table 1. The diameters of zones of inhibition for all prepared samples in this study

Samples	ZOI (mm)	
	<i>S. Aureus</i>	<i>E. Coli</i>
ZnFe_2O_4	11±0.2	8±0.3
TiO_2	8±0.2	5±0.4
Ag-TiO_2	10±0.3	7±0.3
$\text{ZnFe}_2\text{O}_4/\text{Ag-TiO}_2$	15±0.2	12±0.3

4. CONCLUSIONS

In this study, we synthesized solvothermally $\text{ZnFe}_2\text{O}_4/\text{Ag-TiO}_2$ which exhibit antibacterial activity against *E. coli* and *S. aureus* bacteria. The main property of ZnFe_2O_4 MNPs can supply easier separation of NPs by using external magnetic field to avoid time consuming centrifugation in potential applications. By the way, the results indicated that all synthesized samples have stronger antibacterial activities against *S. aureus* than *E. coli* bacteria. But, the results indicated that the $\text{ZnFe}_2\text{O}_4/\text{Ag-TiO}_2$ nanocomposite have the most effective antibacterial property against *S. aureus* bacteria among all of the samples investigated in this study. The magnetic nanocomposite was proved to have both the good antibacterial activity of Ag-TiO_2 and the ZnFe_2O_4 MNPs. So, this work demonstrates that after composing of nanocomposite formation, antibacterial efficiency is obviously increased.

ACKNOWLEDGMENTS

We appreciate the financial support by the Scientific Research Projects Commission of Sakarya University (Project number: 2016-02-04-047).

REFERENCES

- [1] P. Guo, G. Zhang, J. Yu, H. Li, X.S. Zhao, "Controlled synthesis, magnetic and photocatalytic properties of hollow spheres and colloidal nanocrystal clusters of manganese ferrite," *Colloids and Surfaces A: Physicochemical and Engineering Aspects*, vol. 395, pp. 168–174, 2012.
- [2] G. Tong, F. Du, W. Wu, R. Wu, F. Liu, Y. Liang, "Enhanced reactive oxygen species (ROS) yields and antibacterial activity of spongy ZnO/ZnFe₂O₄ hybrid micro-hexahedra selectively synthesized through a versatile glucose-engineered co-precipitation/annealing process," *Journal of Materials Chemistry B*, vol. 1, pp. 2647–2657, 2013.
- [3] R. Liu, M. Lv, Q. Wang, H. Li, P. Guo, X.S. Zhao, "Solvothermal synthesis of size-tunable ZnFe₂O₄ colloidal nanocrystal assemblies and their electrocatalytic activity towards hydrogen peroxide," *Journal of Magnetism and Magnetic Materials*, vol. 424, pp. 155–160, 2017.
- [4] P. Guo, M. Lv, G. Han, C. Wen, Q. Wang, H. Li, X.S. Zhao, "Solvothermal synthesis of hierarchical colloidal nanocrystal assemblies of ZnFe₂O₄ and their application in water treatment," *Materials*, vol. 9, no. 806, pp. 1–10, 2016.
- [5] R. Ji, C. Cao, Z. Chen, H. Zhai, J. Bai, "Solvothermal synthesis of Co_xFe_{3-x}O₄ spheres and their microwave absorption properties," *Journal of Materials Chemistry C*, vol. 2, pp. 5944–5954, 2014.
- [6] N. Sanpo, C.C. Berndt, J. Wang, "Microstructural and antibacterial properties of zinc-substituted cobalt ferrite nanopowders synthesized by sol-gel methods," *Journal of Applied Physics*, vol. 112, pp. 1–7, 2012.
- [7] N. Sanpo, C. Wen, C.C. Berndt, J. Wang, "Antibacterial properties of spinel ferrite nanoparticles, in: Microbial Pathogens and Strategies for Combating Them," *Science, Technology and Education* (A. Méndez-Vilas, Ed.), pp. 239–250, 2013.
- [8] X. Hu, L. Xiao, X. Jian, W. Zhou, "Synthesis of mesoporous silica-embedded TiO₂ loaded with Ag nanoparticles for photocatalytic hydrogen evolution from water splitting," *Journal of Wuhan University of Technology- Materials Science Edition*, vol. 32, pp. 67–75, 2017.
- [9] Y. Chen, Y. Deng, Y. Pu, B. Tang, Y. Su, J. Tang, "One pot preparation of silver nanoparticles decorated TiO₂ mesoporous microspheres with enhanced antibacterial activity," *Materials Science and Engineering C*, vol. 65, pp. 27–32, 2016.
- [10] M. Rai, A. Yadav, A. Gade, "Silver nanoparticles as a new generation of antimicrobials," *Biotechnology Advances*, vol. 27, pp. 76–83, 2009.
- [11] S.W. Chook, C.H. Chia, S. Zakaria, M.K. Ayob, K.L. Chee, N.M. Huang, H.M. Neoh, H.N. Lim, R. Jamal, R. Rahman, "Antibacterial performance of Ag nanoparticles and AgGO nanocomposites prepared via rapid microwave-assisted synthesis method," *Nanoscale Research Letters*, vol. 7, pp. 1–7, 2012.
- [12] R. Verma, V.B. Chaudhary, L. Nain, A.K. Srivastava, "Antibacterial characteristics of TiO₂ nano-objects and their interaction with biofilm," *Materials Technology*, vol. 32, pp. 385–390, 2017.
- [13] C.M.N. Chan, A.M.C. Ng, M.K. Fung, H.S. Cheng, M.Y. Guo, A.B. Djurišić, F.C.C. Leung, W.K. Chan, "Antibacterial and photocatalytic activities of TiO₂ nanotubes," *Journal of Experimental Nanoscience*, vol. 8, pp. 859–867, 2013.
- [14] C. Cao, J. Huang, L. Li, C. Zhao, J. Yao, "Highly dispersed Ag/TiO₂ via adsorptive self-assembly for bactericidal application," *RSC Advances*, vol. 7, pp. 13347–13352, 2017.
- [15] J. Zhang, X. Liu, X. Suo, P. Li, B. Liu, H. Shi, "Facile synthesis of Ag/AgCl/TiO₂ plasmonic photocatalyst with efficiently antibacterial activity," *Materials Letters*, vol. 198, pp. 164–167, 2017.
- [16] W. Gu, Q. Xie, C. Qi, L. Zhao, D. Wu, "Phosphate removal using zinc ferrite synthesized through a facile solvothermal technique," *Powder Technology*, vol. 301, pp. 723–729, 2016.
- [17] S. Çakar, M. Özacar, "The effect of iron complexes of quercetin on dye-sensitized solar cell efficiency," *Journal of Photochemistry & Photobiology, A: Chemistry*, vol. 346, pp. 512–522, 2017.
- [18] N. Güy, M. Özacar, "The influence of noble metals on photocatalytic activity of ZnO for Congo red degradation," *International Journal of*

- Hydrogen Energy*, vol. 41, pp. 20100–20112, 2016.
- [19] X. Chen, Y. Dai, T. Liu, J. Guo, X. Wang, F. Li, "Magnetic core-shell carbon microspheres (CMSs)@ZnFe₂O₄/Ag₃PO₄ composite with enhanced photocatalytic activity and stability under visible light irradiation," *Journal of Molecular Catalysis A: Chemical*, vol. 409, pp. 198–206, 2015.
- [20] R. Liu, H. Ge, X. Wang, J. Luo, Z. Li, X. Liu, "Three-dimensional Ag-tannic acid-graphene as an antibacterial material," *New Journal of Chemistry*, vol. 40, pp. 6332–6339, 2016.
- [21] Z. Yang, Y. Wan, G. Xiong, D. Li, Q. Li, C. Ma, R. Guo, H. Luo, "Facile synthesis of ZnFe₂O₄/reduced graphene oxide nanohybrids for enhanced microwave absorption properties," *Materials Research Bulletin*, vol. 61, pp. 292–297, 2015.
- [22] L. Zhang, C. Ni, H. Jiu, C. Xie, J. Yan, G. Qi, "One-pot synthesis of Ag-TiO₂/reduced graphene oxide nanocomposite for high performance of adsorption and photocatalysis," *Ceramics International*, vol. 43, pp. 5450–5456, 2017.
- [23] R. Rahimi, M. Heidari-Golafzani, M. Rabbani, "Preparation and photocatalytic application of ZnFe₂O₄@ZnO core-shell nanostructures," *Superlattices and Microstructures*, vol. 85, pp. 497–503, 2015.
- [24] G. J. Rani, M. A. J. Rajan, "Reduced graphene oxide/ZnFe₂O₄ nanocomposite as an efficient catalyst for the photocatalytic degradation of methylene blue dye," *Research on Chemical Intermediates*, vol. 43, pp. 2669–2690, 2017.
- [25] J. Shen, G. Ma, J. Zhang, W. Quan, L. Li, "Facile fabrication of magnetic reduced graphene oxide-ZnFe₂O₄ composites with enhanced adsorption and photocatalytic activity," *Applied Surface Science*, vol. 359, pp. 455–468, 2015.
- [26] Y. Zhao, Z. Huang, W. Chang, C. Wei, X. Feng, L. Ma, X. Qi, Z. Li, "Microwave-assisted solvothermal synthesis of hierarchical TiO₂ microspheres for efficient electro-field-assisted-photocatalytic removal of tributyltin in tannery wastewater," *Chemosphere*, vol. 179, pp. 75–83, 2017.
- [27] J. S. Kim, E. Kuk, K. N. Yu, J. H. Kim, S. J. Park, H. J. Lee, S. H. Kim, Y. K. Park, Y. H. Park, C. Y. Hwang, Y. K. Kim, Y. S. Lee, D. H. Jeong, M. H. Cho, "Antimicrobial effects of silver nanoparticles," *Nanomedicine: Nanotechnology, Biology, and Medicine*, vol. 3, pp. 95–101, 2007.
- [28] Y. Z. Wang, Y. S. Wu, X. X. Xue, H. Yang, Z. H. Liu, "Microstructure and antibacterial activity of ions (Ce, Y, or B)-doped Zn-TiO₂: a comparative study," *Materials Technology*, vol. 32, pp. 310–320, 2017.
- [29] A. Allafchian, S. A. H. Jalali, H. Bahramian, H. Ahmadvand, "Preparation, characterization, and antibacterial activity of NiFe₂O₄/PAMA/Ag-TiO₂ nanocomposite," *Journal of Magnetism and Magnetic Materials*, vol. 404, pp. 14–20, 2016.
- [30] K. Atacan, M. Özacar, M. Özacar, "Investigation of antibacterial properties of novel papain immobilized on tannic acid modified Ag/CuFe₂O₄ magnetic nanoparticles," *International Journal of Biological Macromolecules*, vol. 109, pp. 720–731, 2018.

	SAKARYA UNIVERSITY JOURNAL OF SCIENCE		 SAKARYA UNIVERSITY
	e-ISSN: 2147-835X http://www.saujs.sakarya.edu.tr		
	<u>Received</u> 02-01-2018 <u>Accepted</u> 10-05-2018	<u>Doi</u> 10.16984/saufenbilder.373735	

Role of Ag and tannin modification on photocatalytic and antibacterial properties of ZnO nanoplates

Nuray Güy^{*1}, Soner Çakar², Keziban Atacan³

Abstract

In this study, photocatalytic and antibacterial activities of ZnO, Ag/ZnO, ZnO/tannin and Ag/ZnO/tannin synthesized by microwave-hydrothermal and borohydride reduction method have been investigated. The products were characterized by X-ray diffraction (XRD), field emission scanning electron microscopy (FESEM), energy dispersive spectroscopy (EDS), fourier transform infrared (FTIR) and UV-Vis diffuse reflectance/absorbance spectroscopy (DRS). Photocatalytic activities of products were explored for the degradation of malachite green (MG) dye in presence of UV light irradiation. When photocatalytic activities of them were compared, Ag/ZnO exhibited the highest photocatalytic activity. The photodegradation efficiency of 98.68% was recorded for Ag/ZnO after 30 min. The antibacterial activities of the prepared products were examined against *Escherichia coli* (*E. Coli*), *Staphylococcus aureus* (*S. aureus*) and *Candida* by the well diffusion method. The results showed more excellent antibacterial activity in Ag/ZnO/tannin compared to others.

Keywords: Antibacterial properties, photocatalyst, Ag/ZnO, tannin

1. INTRODUCTION

Nowadays, industrialization is increasing rapidly in developing countries. As well as the main advantages offered by industrialization, there are some handicaps caused by it. One of these handicaps is water pollution, which is caused by industrial dyestuff, negatively affecting ecosystem and human health. As a cationic dye Malachite

green (MG), is highly soluble in water and usually used in the textiles and paper industries. It is known that the use of MG damage to human and animal health, cause various types of cancer, affect respiratory and gastrointestinal systems [1,2]. Thus, appropriate method should be selected to treat wastewaters containing color pollutants such MG, before discharging to the environment [1,2]. Semiconductor photocatalysis, known as green technology, is seen as an effective method for removing toxic organic pollutants and pathogens

*Corresponding Author: nurayg@sakarya.edu.tr

¹Sakarya University, Science & Arts Faculty, Department of Chemistry, 54187 Sakarya, Turkey

²Bulent Ecevit University, Science and Technology Research and Application Center (ARTMER), 67100 Zonguldak, Turkey

³Sakarya University, Biomedical, Magnetic and Semiconductor Materials Research Center (BIMAS-RC), 54187 Sakarya, Turkey

in wastewater [3–5]. ZnO is an attractive and promising photocatalyst, which has a wide band gap of 3.37 eV, a high exciton binding energy of 60 meV, low cost, and an eco-friendly [6,7]. Furthermore, it is a bactericide and it inhibits both Gram-positive and Gram-negative bacteria [5,7,8].

The fast recombination ratio of photoinduced charge carriers has inhibited the activity of ZnO. So, doping of noble or transition metals, such as Ag, Au, Pt, Ni and Cu, onto ZnO can effectively enhance the photocatalytic efficiency of ZnO [5]. Among the noble metal doped ZnO photocatalysts, Ag/ZnO has drawn attention because of their abilities as effective separation of charge carriers and retardation of their recombination. The photogenerated electrons in the conduction band (CB) of ZnO can be migrated to Ag nanoparticles (NPs) because of the Schottky barrier at the Ag–ZnO interface. Thus, the Ag NPs facilitates the charge separation and enhancing the photocatalytic activity [9]. Besides, Ag NPs have unique antibacterial properties which facilitate the removal of pathogens from the water [3–5]. The modification of Ag NPs with ZnO is an efficient technique to generate antibacterial materials with advanced functional properties. The Gram-negative *Escherichia coli*, Gram-positive *Staphylococcus aureus* and fungi *Candida*, which usually are found as faecal contaminations in the hospital and municipal wastewaters, are the most studied microorganisms in the antibacterial applications [10,11].

Tannins, which are low cost and natural polymers, contain polyphenolic compounds of molecular weight changed between 500 and some thousands Daltons. In photocatalysis process, tannin can function as an electron trap and carrier to prolong lifetime of the electron-hole pairs. So, electron-hole recombination is effectively suppressed and the photocatalytic efficiency of the semiconductor is developed [12,13]. Antibacterial properties of tannins have been known for a long time [6,14]. The number and location of hydroxyl groups in this phenolic structure play an important role in their toxicity to microorganisms. As the number of hydroxyl groups increases, toxicity also increases. So, tannins inhibit growth of fungi, bacteria and viruses [15].

In this study, undoped ZnO, Ag/ZnO, ZnO/tannin and Ag/ZnO/tannin were synthesized by microwave-hydrothermal method. The prepared products were characterized by X-ray diffraction (XRD), field emission scanning electron

microscopy (FESEM) and UV–visible diffuse reflectance spectra (UV–Vis DRS). Although Ag/ZnO nanocomposites have been extensively studied in the literature, effect of tannin modification on photocatalytic and antibacterial features of ZnO was investigated in this work. The photocatalytic performance of the products for degradation of MG under UV light irradiation and their antibacterial activities against *Escherichia coli*, *Staphylococcus aureus* and *Candida* have been systematically evaluated.

2. MATERIALS AND METHODS

2.1. Materials

Zinc chloride (ZnCl₂, Merck), sodium hydroxide (NaOH, Merck), silver nitrate (AgNO₃, Carlo Erba), sodium borohydride (NaBH₄, Merck), and MG (commercial grade) Mueller-Hinton agar (Merck) and ethanol (Merck) and used without further purification. Commercial tannin extract, valonia, was obtained from MİRKİM Leather and Chemical Material, Gerede/Bolu-Turkey. All compounds except MG and tannin were of reagent grade.

2.2. Preparation of photocatalysts

Synthesis of ZnO: The ZnO nanoplates were synthesized by microwave-assisted hydrothermal method. ZnCl₂ (3.66 mmol, 0.5 g) was dissolved in 10 mL of distilled water then 10 mL of NaOH (20 mmol, 0.80 g) solution was dropped and stirred for 1 h. The reaction mixture was transferred into a Teflon autoclave and treated at 160 °C for 5 min under temperature-controlled mode in a microwave oven (CEM Mars 5) operating at 700 W and then cooled at room temperature. The products were centrifuged, washed with distilled water and absolute ethanol several times and finally, dried in an oven at 60 °C.

Synthesis of Ag/ZnO: Ag doped ZnO photocatalysts were prepared by borohydride reduction method. Required amount of the salt solution of the metal for doping was added to dispersed ZnO (1.23 mmol, 0.1 g) in 40 mL of water. The weight ratio of Ag to ZnO in this representative reaction was 5%. Then 20 mL of sodium borohydride (0.35 mmol, 0.013 g) solution as a reducing agent was dropped to the mixture and stirred for 1 h to reduce adsorbed metals ions to metallic NPs onto ZnO surface. The products were

washed distilled water and absolute ethanol several times, and then dried in an oven at 60 °C.

Synthesis of ZnO/tannin: 0.1 g tannin was dissolved into 40 mL of distilled water and ZnCl₂ (15.01 mmol, 2.0457 g) was added into the solution. Then, 20 mL of NaOH (80 mmol, 3.2 g) solution was dropped into the mixture and stirred for at 25 °C for 1 h. The resulting mixture was transferred into a Teflon autoclave and treated at 160 °C for 5 min under temperature-controlled mode in a microwave oven (CEM Mars 5) operating at 700 W and then cooled at room temperature. The product was washed distilled water and absolute ethanol several times, and then dried in an oven at 60 °C for 24 h.

Synthesis of Ag/ZnO/tannin: 0.1 g of ZnO/tannin was dispersed into 40 mL of distilled water. AgNO₃ solution was added to mixture such that the weight ratio of Ag to ZnO was 5%. Then 20 mL of sodium borohydride (0.35 mmol, 0.013 g) solution as a reducing agent was dropped to the mixture and stirred for 1 h at room temperature. The product was washed distilled water and absolute ethanol several times, and then dried in an oven at 60 °C for 24 h.

2.3. Characterization of photocatalysts

The prepared products were confirmed by powder X-ray diffraction (XRD, PANalytical Empyrean diffractometer with Cu K α ($\lambda=1.54 \text{ \AA}$) in the 2θ angles ranging from 10 to 90. The morphologies of ZnO, Ag/ZnO, ZnO/tannin and Ag/ZnO/tannin nanocomposites were characterized by using a field emission scanning electron microscopy (FESEM, FEI QUANTA FEG 450). The surface compositions of the samples were identified by energy dispersive spectroscopy (EDS). The UV–Vis absorption spectra of the MG solution and photocatalysts were determined by using a UV-Visible spectrophotometer (UV-Vis, Shimadzu UV-2600). The diffuse reflectance spectra of the products were analyzed by using a UV-Visible spectrophotometer fitted with a diffuse reflectance attachment. The band gap energies of the nanophotocatalysts were determined by the Kubelka–Munk function, $F(R)$ and by extrapolating the $[F(R)hv]^{1/2}$ versus photon energy (hv). Fourier Transform Infrared (FTIR) spectra of prepared photocatalysts were recorded by using a FTIR Spectrometer (Perkin Elmer FTIR Spectrum Two) in the range 400–4000 cm⁻¹ at room temperature.

2.4. Photocatalytic testing

Photocatalytic efficiencies of obtained products were examined by degradation of MG in an aqueous solution under a 100 W UV light (the strongest emission at 365 nm). For each experiment, 50 mg of photocatalyst was dispersed in 100 mL of 16 mg/L of the MG aqueous solution. Before illumination, the suspensions were stirred for 30 min in the dark to supply establishment of adsorption/desorption equilibrium of MG on surfaces of the photocatalysts in the aqueous solutions. 5 mL of the aliquots were sampled at predetermined time intervals, centrifuged and examined by recording variations in the absorption band (616 nm) in the UV–Vis spectra of MG. The percentage of degradation was determined by using the Eqs. (1) and (2) [16]:

$$\text{Degradation} = \frac{C_0 - C}{C_0} \times 100 \quad (1)$$

$$= \frac{A_0 - A}{A_0} \times 100 \quad (2)$$

where C_0 indicates the initial concentration after the equilibrium adsorption, C indicates the reaction concentration of MG, A_0 indicates the initial absorbance, and A indicates the changed absorbance of the MG at the characteristic absorption wavelength of 616 nm.

2.5. Antibacterial testing

The antibacterial activity of the all products were examined against Gram-negative bacteria *E. Coli*, Gram-positive bacteria *S. aureus* and fungi *Candida* by agar well diffusion method. In this study, Mueller-Hinton agar was used as a nutrient agar medium. This medium was poured into sterile Petri dishes and using sterile cottons wab, bacterial suspension was spread over the plates by spread plate method. All the products were placed on stated agar plate, followed by incubation at 37 °C for 24 h [17]. All the agar plates were visually examined for the existence of bacterial growth, and the diameter of inhibitory zones was measured in millimeter (mm).

3. RESULTS AND DISCUSSION

3.1. Characterization of photocatalysts

The phases of ZnO, Ag/ZnO, ZnO/tannin and Ag/ZnO/tannin were identified by XRD in Figure 1. As depicted in Figure 1(a), the peaks at 2θ

values of 31.7°, 34.4°, 36.2°, 47.5°, 56.6°, 62.9°, 66.4°, 68.0°, 69.1°, 72.6°, and 77.0°, indexed to (100), (002), (101), (102), (110), (103), (200), (112), (201), (004), and (202) planes of the ZnO crystal, respectively. Obviously, Ag/ZnO exhibits the usual wurtzite, just like original ZnO nanoplates, with similar peak intensities and shapes. However, the XRD patterns of Ag/ZnO illustrate diffraction peaks corresponding to the (111) and (200) facets of Ag (JCPDS cards file no.; ZnO:36-1451, Ag:04-0783), which has the face-centered cubic (fcc) structure [18]. Furthermore, similar peaks were observed in the ZnO/tannin and Ag/ZnO/tannin. But, the peak intensities only slightly decreased by modification tannin compared to the peaks of ZnO and Ag/ZnO. The average crystallite sizes of the samples were calculated by Scherrer equation ($D = 0.9\lambda/\beta \cos \theta$, where λ is the wavelength of the radiation, θ is the diffraction angle, and β is the corrected half width of the diffraction peak). It has been reported in the literature that ZnO powders exhibit the nature of crystals corresponding to the (100), (002) and (101) planes [19]. The average crystal sizes for samples are illustrated in Table 1. As can be seen from Table 1, Ag/ZnO has a larger crystal size than the others. Because the ionic radius of the Ag^+ (126 pm) ions substituted with the Zn^{2+} ions (74 pm) in ZnO crystal, is larger than that of Zn^{2+} ions. So it promotes the growth of the crystal size [18]. It is known that the crystal size influences the adsorption and the photocatalytic performance. However, our results, which are consistent with those of Zhong et al. [20] and Khataee et al. [21], showed that crystal sizes of samples caused no effect on the photocatalytic efficiency [18].

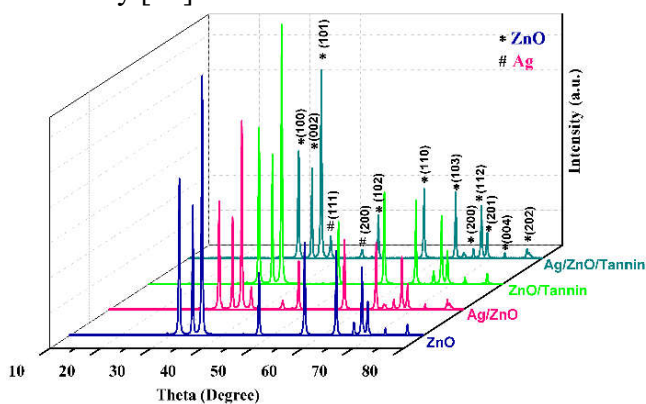


Figure 1. XRD patterns of ZnO and Ag/ZnO

Table 1. The crystal sizes of ZnO, Ag/ZnO, ZnO/tannin and Ag/ZnO/tannin

Compound	Structure	D _{average} (nm)
ZnO	Hexagonal	29.12

Ag/ZnO	Hexagonal	31.23
ZnO/tannin	Hexagonal	25.58
Ag/ZnO/tannin	Hexagonal	28.02

Morphology analysis of the ZnO, Ag/ZnO, ZnO/tannin and Ag/ZnO/tannin were investigated by FESEM and the images are shown in Figure 2. As can be observed in Figure 2(a), ZnO shows an irregular nanoplate like structure. Figure 2(b) shows a FESEM image of the Ag/ZnO. Ag doping does not change the plate structure of ZnO. Furthermore, from Figure 2(b), we can see dispersed small Ag NPs taking place on ZnO surface. The FESEM images of ZnO/tannin and Ag/ZnO/tannin are illustrated in Figure 2(c) and Figure 2(d), respectively. As can be seen, the surfaces ZnO and Ag/ZnO nanoplates are highly coated with the tannin molecules for ZnO/tannin and Ag/ZnO/tannin [22]. Table 2 illustrates EDS analysis results for the samples to confirm element compositions of them. The results for the Ag/ZnO show Ag, Zn and O elements while it does Zn and O elements for ZnO. Furthermore, the increase in the amount of O and presence of C is evidence of tannin in the ZnO/tannin and Ag/ZnO/tannin.

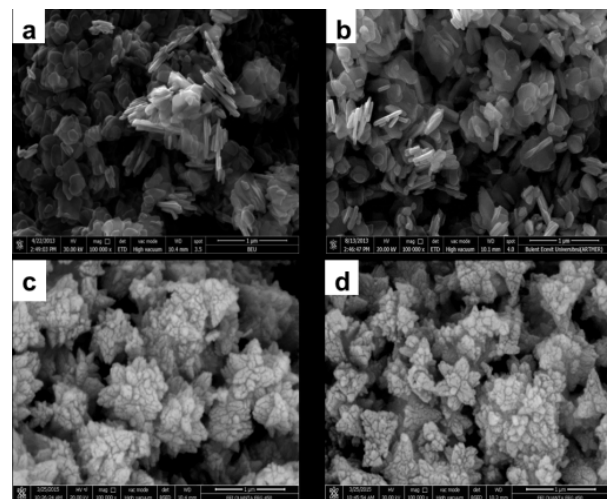


Figure 2. FESEM images of (a) ZnO, (b) Ag/ZnO, (c) ZnO/tannin and (d) Ag/ZnO/tannin

Table 2. The EDS analysis of ZnO, Ag/ZnO, ZnO/tannin and Ag/ZnO/tannin

Elements/ (at.%) (EDS)	ZnO	Ag/ZnO	ZnO/tannin	Ag/ZnO/ tannin
Zn	18.48	10.23	9.230	7.788
O	81.52	88.23	63.66	68.98
Ag	-	1.540	-	1.102
C	-	-	27.11	22.13
Total	100	100	100	100

The optical features of the prepared products were analyzed from the UV–Visible diffuse reflectance spectra and the results were illustrated in Figure 3. ZnO exhibits a sharp band at 377 nm, which corresponds to the ZnO nanoplates. Broad peak at 450 nm is observed in the reflectance spectra of the products representing the formation of Ag NPs. The diffuse reflectance is defined the Kubelka-Munk function by the equation $F(R) = (1-R)^2/2R$, where R is the diffuse reflectance of the sample. This spectra supplies the calculation of the band gap of the sample with the help of the Kubelka Munk theory [23]. As can be seen in Figure 4, the band gap energies are found to be 3.23 eV for ZnO and ZnO/tannin, and 3.22 eV for Ag/ZnO, and Ag/ZnO/tannin, corresponding to UV region of the electromagnetic spectrum. According the results, the band gap energies of the nano photocatalysts change slightly with doping Ag and tannin.

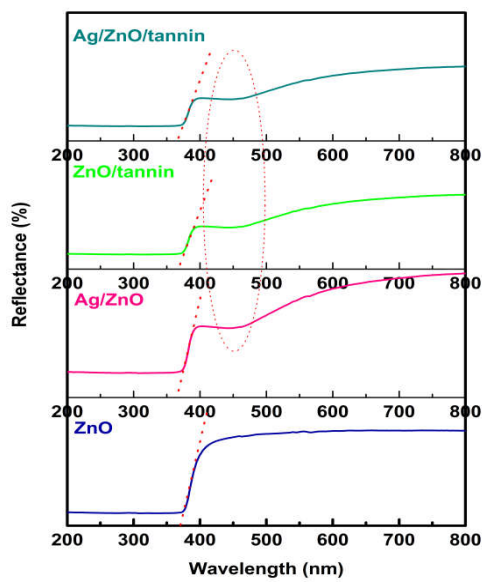


Figure 3. UV-Vis diffuse reflectance spectra of samples

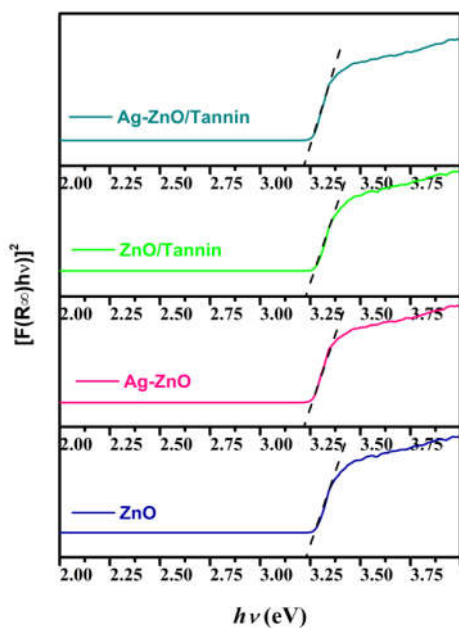


Figure 4. The plot of the transformed Kubelka–Munk function versus the gap energy of samples

To learn more information about the structures, FTIR spectra of ZnO, Ag/ZnO, ZnO/tannin and Ag/ZnO/tannin nanophotocatalysts were supplied and the spectra is shown in Figure 5. For the ZnO containing photocatalysts, the peak at 570 cm^{-1} is assigned to the stretching vibration of the Zn–O bond. In Figure 5(c)-(d), the C=C-C stretching vibration of aromatic ring can be seen in the $1560\text{--}1400\text{ cm}^{-1}$ region. The C-O stretching vibrations of hydrolysable tannins can be seen at 1200 cm^{-1} . At 800 cm^{-1} , C-H deformation peak has a weak intensity.

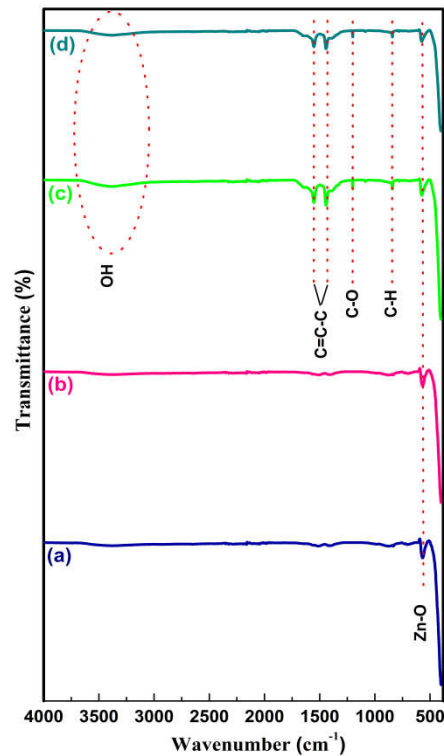


Figure 5. FTIR spectra of (a) ZnO, (b) Ag/ZnO (c) ZnO/tannin and (d) Ag/ZnO/tannin

3.2. Photocatalytic activity of materials

In this study, to investigate the photocatalytic efficiencies of the photocatalysts, we used MG which has the strong absorption at 616 nm. Figure 6 illustrates the time-dependent absorbance spectra of MG in the presence of ZnO, Ag/ZnO, ZnO/tannin and Ag/ZnO/tannin. As can be seen in Figure 6, MG degrades much faster in the presence of Ag/ZnO than in the presence of the other photocatalysts. Figure 7(a) exhibits the changes in the concentration of MG determined. As shown in Figure 7(a), photocatalytic activity was not observed in the absence of any catalyst under UV light. But, the degradation efficiencies for MG are about 95.8 and 98.7, 88.5, 90.7% for ZnO, Ag/ZnO, ZnO/tannin and Ag/ZnO/tannin

photocatalysts in the 30 min, respectively. Figure 7(b) illustrates the pseudo-first order kinetics of the MG photodegradation of the products. Pseudo-first order reaction kinetics is given by the following equation [19]:

$$\ln(C_t/C_0) = -kt \quad (3)$$

where k is the degradation rate constant and C_0 and C are the concentrations of dye, initial and at the reaction time t , respectively. The pseudo-first order rate constants of the ZnO, Ag/ZnO, ZnO/tannin and Ag/ZnO/tannin are shown in Table 3. According to the results, Ag/ZnO has the highest k value ($91.2 \times 10^{-6} \text{ min}^{-1}$) compared with others. It is claimed that the photocatalytic efficiency of the Ag/ZnO is ascribed to the presence of Ag on ZnO surface that effectively inhibits the recombination of charge carriers. Due to the SPR and synergistic effect of Ag NPs, the photoinduced electrons in the CB of ZnO flow to the surface of Ag NPs under UV light irradiation. As a result, Ag NPs serve as electron traps and retard electron-hole recombination [7,24]. However, the reason why the activities of ZnO/tannin and Ag/ZnO/tannin photocatalysts are lower than ZnO and Ag/ZnO respectively, can be explained by the tannin molecules covering the active surfaces of ZnO.

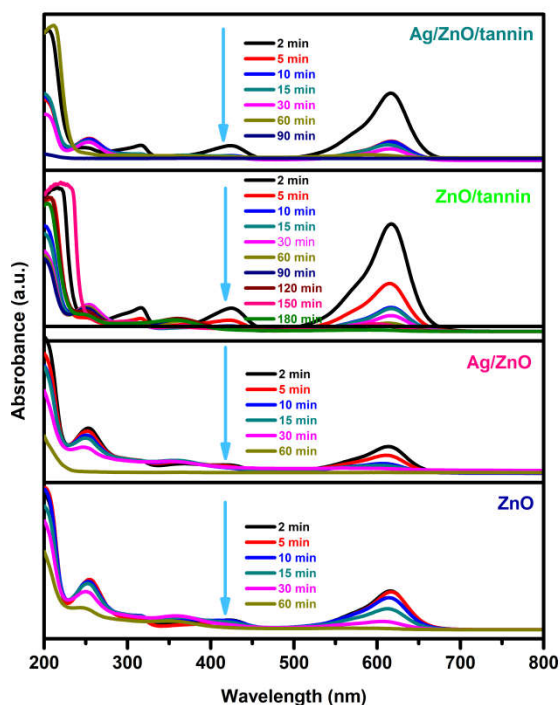


Figure 6. The absorption spectra of MG aqueous solution under UV light irradiation in the presence of samples

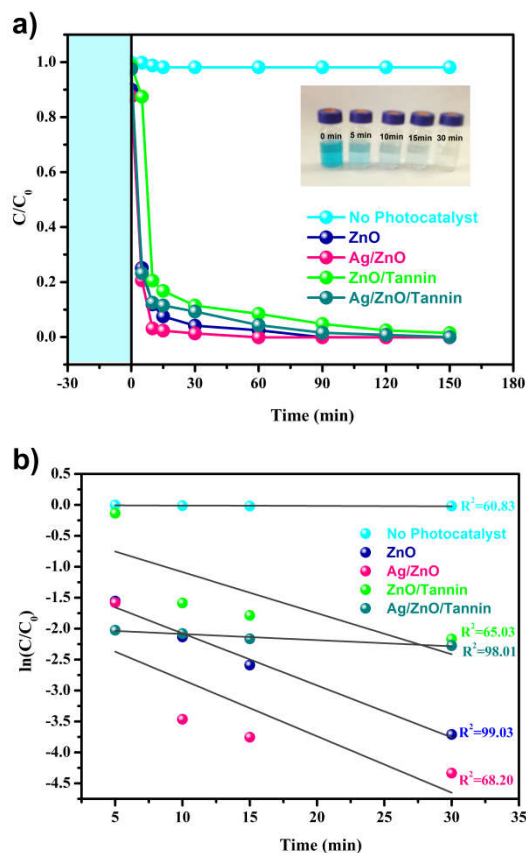


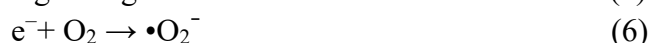
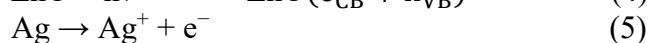
Figure 7. a) The photodegradation of MG in presence of various photocatalysts b) Pseudo-first order kinetics for MG dye

Table 3. Kinetics data of MG photodegradation in the presence of photocatalysts.

Samples	Rate constants, k (min^{-1})	Photodegradation ratios after 30 min irradiation (%)
ZnO	84.1×10^{-6}	95.85
Ag/ZnO	91.2×10^{-6}	98.68
ZnO/tannin	66.3×10^{-6}	88.54
Ag/ZnO/tannin	9.92×10^{-6}	90.72

3.3. Photocatalytic mechanism

The Ag/ZnO exhibits an enhancement in the photocatalytic activity under UV-light irradiation compared to the other photocatalysts. Ag NPs on the ZnO surface form a schottky barrier at the Ag-ZnO interface, they trap the electrons and prevent the return to the ZnO surface, and so it extends the lifetime of the charge carriers. The possible mechanism of the Ag/ZnO for degradation of MG can be proposed as follows [9,18]:



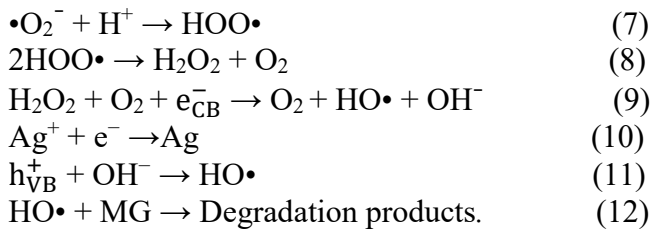


Figure 8 illustrates the schematic electron-hole separation in presence Ag-ZnO system under UV light. When ZnO is illuminated by UV light, an electron (e^-) in the VB can be excited to the CB, leaving a hole (h_{VB}^+) in the VB. The photogenerated electrons migrate from ZnO to the Ag to reach fermi energy level equilibration (E_f) because fermi level of Ag is lower than that of ZnO [3]. Then, electrons on the Ag react with adsorbed oxygen and form more super oxide radical anion ($\bullet\text{O}_2^-$), and simultaneously, VB holes of ZnO also produce hydroxyl ($\bullet\text{OH}$) radical by interaction with water. Consequently, these strong radicals are used for degradation MG [3,18,24].

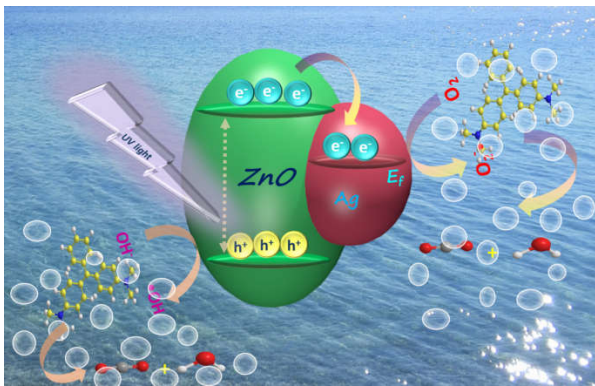


Figure 8. Schematic illustration of photocatalytic activation for MG using Ag/ZnO UV-light irradiation

3.4. Antibacterial activity of materials

Antimicrobial activities of the ZnO, Ag/ZnO, ZnO/tannin and Ag/ZnO/tannin were performed against *E. Coli*, *S. aureus* and *Candida*. Figure 9 illustrates the photographic images of the zone of inhibition for the products, and the diameters of the zones of inhibition are summarized in Table 3. When the diameters of the zones of inhibition (if present) for each product were compared, it was observed that Ag/ZnO/tannin nanocomposite were more effective against *E. Coli*, *S. aureus* and *Candida*. Because Ag NPs have high surface areas and unique physicochemical properties, they remarkably reduce bacterial infections [17]. Ag NPs may contact with more easily the bacterial cell membrane, causing structural changes and degradation and eventually, leading to bacterial cell death [25]. Furthermore, the diameter of the inhibition zone for Ag/ZnO is larger than that of

pure ZnO. The phenolic groups which tannin molecules contain, hinder bacterial growth and protease activity via harming its cell wall and cytoplasm, so the destruction of vegetative structure of bacteria is accelerated [15,25]. As a result, Ag/ZnO/tannin has better antimicrobial activity due to the synergistic effect of combining Ag, ZnO and tannin.

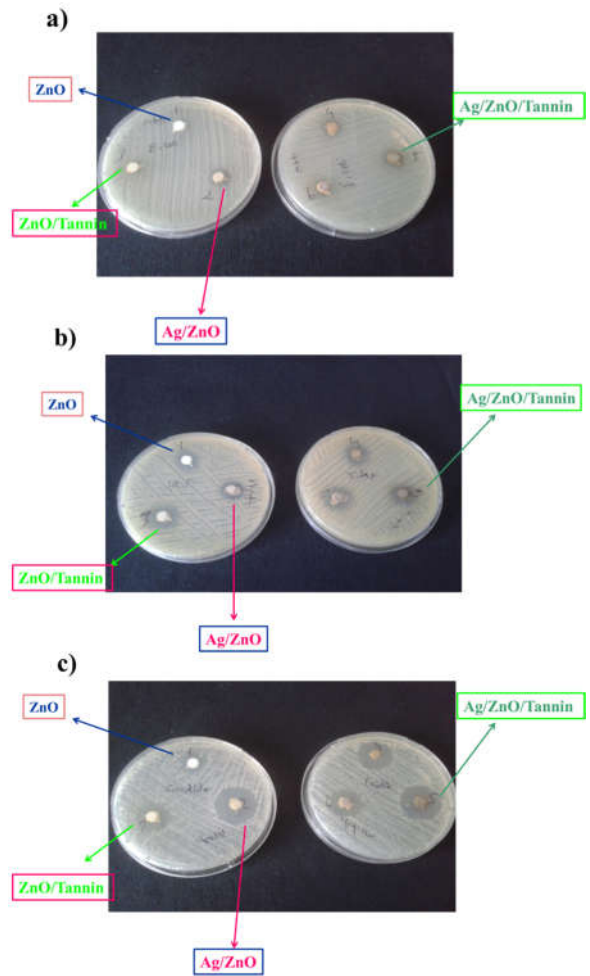


Figure 9. Inhibition zones of ZnO, Ag/ZnO, ZnO/tannin and Ag/ZnO/tannin against (a) *E. coli*, (b) *S. aureus* and (c) *Candida*.

Table 3. Antibacterial activities of ZnO, Ag/ZnO, ZnO/tannin and Ag/ZnO/tannin against pathogenic bacteria and fungal strains.

Type of NPs	Diameter of Inhibition Zone (mm)		
	Bacterial Strains		Fungal Strains
	E.Coli	S.Aureus	Candida
ZnO	0	9	12
Ag/ZnO	12	14	20
ZnO/tannin	10	11	18
Ag/ZnO/tannin	12	15	24

5. CONCLUSIONS

In summary, ZnO, Ag/ZnO, ZnO/tannin and Ag/ZnO/tannin were synthesized by microwave-hydrothermal method. These nanocomposites have potential applications in both photodegradation of MG and inhibition of bacteria and fungi. Ag/ZnO exhibits better photocatalytic efficiency for MG than other photocatalysts due to hindering electron hole pair recombination by Ag NPs and enhancing of the performance of Ag/ZnO by surface plasmon resonance of them. In the antibacterial tests, due to the strong interaction between metallic Ag, tannin and ZnO, Ag/ZnO/tannin exhibited enhanced and synergistic antibacterial activities for *E. coli*, *S. aureus* and *Candida*.

ACKNOWLEDGMENTS

We would like to thank Prof. Dr. Oğuz Karabay for his helping antibacterial studies in Faculty of Medicine at Sakarya University.

REFERENCES

- [1] M. Rahmani, M. Kaykhani, M. Sasani, "Application of Taguchi L16 design method for comparative study of ability of 3A zeolite in removal of Rhodamine B and Malachite green from environmental water samples", *Spectrochim. Acta Part A Mol. Biomol. Spectrosc.*, vol. 188, pp. 164–169, 2018.
- [2] X. Zhang, M. Wang, L. Lin, G. Xiao, Z. Tang, X. Zhu, "Synthesis of novel laccase-biotitania biocatalysts for malachite green decolorization", *J. Biosci. Bioeng.* In Press, 2018.
- [3] N.L. Gavade, A.N. Kadam, Y.B. Gaikwad, M.J. Dhanavade, K.M. Garadkar, "Decoration of biogenic AgNPs on template free ZnO nanorods for sunlight driven photocatalytic detoxification of dyes and inhibition of bacteria," *J. Mater. Sci. Mater. Electron*, vol. 27, pp. 11080–11091, 2016.
- [4] B. Pant, M. Park, H.Y. Kim, S.J. Park, "Ag-ZnO photocatalyst anchored on carbon nanofibers: Synthesis, characterization, and photocatalytic activities," *Synth. Met.*, vol. 220, pp. 533–537, 2016.
- [5] Z. Li, F. Zhang, A. Meng, C. Xie, J. Xing, "ZnO/Ag micro/nanospheres with enhanced photocatalytic and antibacterial properties synthesized by a novel continuous synthesis method," *RSC Adv.*, vol. 5, pp. 612–620, 2015.
- [6] R.T. Al-ani, N. Mohammed, V.M. Atheer, M.P. D, "Antibacterial Activity of Tannins Extracted from Some Medicinal Plants in vitro," *Department of Biochemistry, Medicine College, Al-Anbar University, Ramadi, IRAQ*, vol. 6, no. 1, pp. 8876-8882, 2008.
- [7] C. Karunakaran, V. Rajeswari, P. Gomathisankar, "Enhanced photocatalytic and antibacterial activities of sol-gel synthesized ZnO and Ag-ZnO," *Mater. Sci. Semicond. Process.*, vol. 14, pp. 133–138, 2011.
- [8] G. Nagaraju, Udayabhanu, Shivaraj, S.A. Prashanth, M. Shastri, K. V. Yathish, C. Anupama, D. Rangappa, "Electrochemical heavy metal detection, photocatalytic, photoluminescence, biodiesel production and antibacterial activities of Ag-ZnO nanomaterial," *Mater. Res. Bull.*, vol. 94, pp. 54–63, 2017.
- [9] W. Lu, G. Liu, S. Gao, S. Xing, J. Wang, "Tyrosine-assisted preparation of Ag/ZnO nanocomposites with enhanced photocatalytic performance and synergistic antibacterial activities," *Nanotechnology*, vol. 19, pp. 445711- 445721, 2008.
- [10] C. Piccirillo, R.A. Pinto, D.M. Tobaldi, R.C. Pullar, J.A. Labrincha, M.M.E. Pintado, P.M.L. Castro, "Light induced antibacterial activity and photocatalytic properties of Ag/Ag₃PO₄-based material of marine origin", *Journal Photochem. Photobiol. A Chem.*, vol. 296, pp. 40–47, 2015.
- [11] R. Van Grieken, J. Marugán, C. Pablos, L. Furones, A. López, "Comparison between the photocatalytic inactivation of Gram-positive *E. faecalis* and Gram-negative *E. coli* faecal contamination indicator microorganisms", *Applied Catal. B, Environ.*, vol. 100, pp. 212–220, 2010
- [12] X. Huang, Y. Wang, X. Liao, B. Shi, "Adsorptive recovery of Au³⁺ from aqueous solutions using bayberry tannin-immobilized mesoporous silica", *J. Hazard. Mater.*, vol. 183, pp. 793–798, 2010.
- [13] S. Ayhan, M. Özacar, "Competitive biosorption of Pb²⁺, Cu²⁺ and Zn²⁺ ions from aqueous solutions onto valonia tannin

- resin," *Journal of Hazardous Materials*, vol. 166, pp. 1488–1494, 2009.
- [14] K. Tomiyama, Y. Mukai, M. Saito, K. Watanabe, H. Kumada, T. Nihei, N. Hamada, T. Teranaka, "Antibacterial Action of a Condensed Tannin Extracted from Astringent Persimmon as a Component of Food Addictive Pancil PS-M on Oral Polymicrobial Biofilms," *Biomed Res. Int.*, vol. 2016, pp. 1-7, (2016).
- [15] S.M. Çolak, B.M. Yapici, A.N. Yapici, "Determination of antimicrobial activity of tannic acid in pickling process," *Rom. Biotechnol. Lett.*, vol. 15, pp. 5325–5330, 2010.
- [16] Y. Chang, J. Xu, Y. Zhang, S. Ma, L. Xin, L. Zhu, C. Xu, "Optical Properties and Photocatalytic Performances of Pd Modified ZnO Samples," *J. Phys. Chem. C*, vol. 113, pp. 18761–18767, 2009.
- [17] K. Atacan, M. Özacar, "Investigation of antibacterial properties of novel papain immobilized on tannic acid modified Ag/CuFe₂O₄ magnetic nanoparticles," *Int. J. Biol. Macromol.*, vol. 109, pp. 720–731, 2018.
- [18] N. Güy, M. Özacar, "The influence of noble metals on photocatalytic activity of ZnO for Congo red degradation," *Int. J. Hydrogen Energy*, vol. 41, pp. 20100–20112, 2016.
- [19] Şenay Şen Türkyılmaz, N. Güy, M. Özacar, "Photocatalytic efficiencies of Ni, Mn, Fe and Ag doped ZnO nanostructures synthesized by hydrothermal method: The synergistic/antagonistic effect between ZnO and metals," *J. Photochem. Photobiol. A Chem.*, vol. 341, pp. 39–50, 2017.
- [20] J.B. Zhong, J.Z. Li, X.Y. He, J. Zeng, Y. Lu, W. Hu, K. Lin, "Improved photocatalytic performance of Pd-doped ZnO", *Curr. Appl. Phys.*, vol. 12, pp. 998–1001, 2012.
- [21] A. Khataee, R. Darvishi, C. Soltani, Y. Hanifehpour, M. Safarpour, H.G. Ranjbar, S.W. Joo, "Synthesis and Characterization of Dysprosium-Doped ZnO Nanoparticles for Photocatalysis of a Textile Dye under Visible Light Irradiation", *Ind. Eng. Chem. Res.*, vol. 53, pp. 1924–1932, 2014.
- [22] S. Wu, P. Wang, Y. Cai, D. Liang, Y. Ye, Z. Tian, J. Liu, C. Liang, "Reduced graphene oxide anchored magnetic ZnFe₂O₄ nanoparticles with enhanced visible-light photocatalytic activity," *RSC Adv.*, vol. 5, pp. 9069–9074, 2015.
- [23] Z. Yang, Y. Wan, G. Xiong, D. Li, Q. Li, "Facile synthesis of ZnFe₂O₄/reduced graphene oxide nanohybrids for enhanced microwave absorption properties," *Mater. Res. Bull.*, vol. 61, pp. 292–297, 2015.
- [24] V. Vaiano, M. Matarangolo, J.J. Murcia, H. Rojas, J.A. Navio, M.C. Hidalgo, "Enhanced photocatalytic removal of phenol from aqueous solutions using ZnO modified with Ag," *Appl. Catal. B Environ.* vol. 225, pp. 197–206, 2018.
- [25] S.P. Adhikari, H.R. Pant, J.H. Kim, H.J. Kim, C.H. Park, C.S. Kim, "One pot synthesis and characterization of Ag-ZnO/g-C₃N₄ photocatalyst with improved photoactivity and antibacterial properties," *Colloids Surfaces A Physicochem. Eng. Asp.*, vol. 482, pp. 477–484, 2015.

	SAKARYA UNIVERSITY JOURNAL OF SCIENCE		 SAKARYA UNIVERSITY
	e-ISSN: 2147-835X http://www.saujs.sakarya.edu.tr		
	<u>Received</u> 22.01.2017 <u>Accepted</u> 10.05.2018	<u>Doi</u> 10.16984/saufenbilder.382220	

Fe/ZnO nanorod photoanode and pyrocatechol violet sensitizer based dye sensitized solar cells

Soner Cakar¹

Abstract

A ZnO and Fe/ZnO nanorods have been prepared and used in dye sensitized solar cells. The prepared ZnO and Fe/ZnO nanorods were characterized by XRD, SEM and SEM-EDS. Additionally, the pyrocatechol violet solutions with different pH values have been prepared, characterized and used in dye sensitized solar cells. The dyes which have different pH values were characterized via UV-Vis absorbance and cyclic voltammetry techniques. The Fe doping to ZnO nanorods increased the solar cell efficiency by 20-35%. The pyrocatechol violet dye can be binded to Fe atoms on the ZnO surface and the possible mechanism was discussed in detailed. The efficiency of best solar cell is obtained 1.39% with Fe/ZnO photoanode and pH 7.5 pyrocatechol violet dye solution.

Keywords: dye sensitized solar cells, Fe/ZnO nanorods, pyrocatechol violet, different pH.

1. INTRODUCTION

Dye sensitized solar cells (DDSCs) have been researched as one of the most promising methods for low cost power production [1]–[3]. DSSCs are composed of four main component; i) photoanode electrode, ii) sensitizers, iii) electrolyte and iv) counter electrode [4], [5]. The operation mechanism of these type solar cells is as following; the sunlight illuminates the sensitizers and it can excite the electron from HOMO to LUMO band of sensitizers. Then excited electrons are injected from sensitizer onto the semiconductor conductive band. Then, this electron moves to the counter electrode for back electron transfer. Meantime the electrolyte injects electron to HOMO band of sensitizers and this process has regenerated the electron. These processes are carried out simultaneously to provide an energy production by causing

continuous electron movement in the solar cell [6]–[8]. The sensitizers are the main component of the DSSCs and researchers are making a lot of effort to reach the higher cell efficiency values. These sensitizers are divided into three main groups as following: metal complex dyes, metal free organic dyes and natural dyes [9]. The ruthenium bipyridine complexes are the most stable ones and they are reported to have higher efficiencies (up to ~12%) [10]. Recently, the transition metal complex based flavonoid type were the first time used in DSSCs for our previous study [11], [12]. These type cell show lower conversion efficiency, but it can be lead nontoxic and non-containing precious metal. Furthermore, it can be related environmental friendly. Additionally, they can be racing the metal free organic dye for the solar cell efficiency. Therefore, they are promising alternative for metal free organic dye sensitized solar cells.

¹ Sakarya Üniversitesi, Kimya Bölümü, cakarsoner@gmail.com

TiO₂ has widely used photoanode materials for DSSCs due to chemical stability, higher electron mobility, etc [13]. With similar band gap, ZnO is potential alternative photoanode materials owing to its unique ionic mobility (115-155 cm² V⁻¹ s⁻¹) but the ZnO chemical stability is weaker than TiO₂ [11]. When the aqueous dye solution coated on ZnO surface, the ZnO can be dissolved to Zn²⁺ [4], [14]. This causes deformations on the surface of ZnO, thereby reducing the cell efficiency values.

Pyrocatechol violet has potential application for redox indicator as also known for fifty years. Recently it is applied for adsorption [15], supercapacitor [16] and sensor [17]. In this work the pyrocatechol violet is investigated for the first time as a sensitizer for solar cells. Pyrocatechol violet structure has been demonstrated in Fig 1. It includes -OH and sulfite anion, which enables the adsorption of ZnO surface and complexation of Fe atoms.

In this work we prepared Fe coated ZnO photoanode to protected ZnO photoanode. In our previous works, we have demonstrated that Fe-tannin complexes have improved the cell efficiency for dye sensitized solar cell [14], [18]. In order to form strong complexes with Fe in pyrocatechol violet dyes prepared, Fe atoms have been doped into ZnO semiconductor.

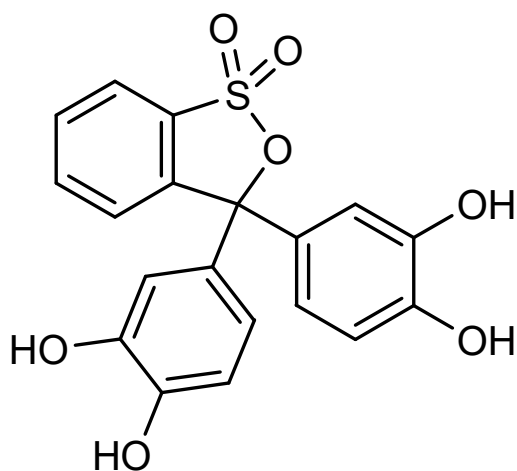


Figure 1. Pyrocatechol violet structure.

2. EXPERIMENTAL

2.1. Materials

Pyrocatechol violet (C₁₉H₁₄O₇S), iron (III) nitrate nonahydrate (Fe(NO₃)₃.9H₂O), zinc nitrate hexahydrate (Zn(NO₃)₂.6H₂O), potassium

hydroxide (KOH), fluorinated tin oxide glass (FTO glass, 7 Ω/sq.), ethyl cellulose, tetrabutylammonium cis-bis(isothiocyanato) bis(2,2'-bipyridyl-4,4'-dicarboxylato) ruthenium (II) (N719 dye), 2-propanol, 4-tert butylpyridine, were purchased from Sigma Aldrich. Iodine (I₂) was obtained from Riedel de Haen. Dihydrogen hexachloroplatinate (IV) hexahydrate (H₂PtCl₆.6H₂O) was obtained from Alfa Aesar. All materials were analytical grade and used as received without further treatment.

2.2. Synthesis procedure of Fe/ZnO

Fe/ZnO nanostructure were synthesized via hydrothermal procedure. The detailed synthesis procedure was described in the literature [4], [14]. The amount of 4.455 g Zn(NO₃)₂.6H₂O (15 mmol) and 0.217 g Fe(NO₃)₃.9H₂O (0.5 mmol) were dissolved 60 mL ultrapure water. This solution were vigorously stirred under magnetic stirrer at 30 min. After 1.3 g KOH (23 mmol) was added to this solution and vigorously stirred at 30 min. Then this solution was transferred into the microwave hydrothermal cup (Teflon like autoclave). The microwave radiation, temperature and time are 380W, 100°C and 1h, respectively. The mustard yellow product was centrifuged and washed with deionized water and ethanol three times. After then, The Fe/ZnO powder was dried at 60°C for 12h. For comparison, ZnO nanoparticles were synthesized using similar procedure.

2.3. Pyrocatechol violet preparation

3.863 g (10 mM) pyrocatechol violet (C₁₉H₁₄O₇S) was dissolved in 50 mL deionized water. The pH of these solutions is 0.5. In the literature, the color of pyrocatechol violet is significantly dependent on pH value. The color of neutral solution (pH 0.5) is red, the solution color is changed to yellow at pH range of 2-8, and the solution color returns red-violet at higher pH values than 8. However, the basic solutions of pyrocatechol violet are unstable and lose color very quickly. This probably due to the oxidation of pyrocatechol violet. The different pH values of pyrocatechol violet solution were prepared using 0.1 M NaOH and 0.1 M HCl. The samples with different pH values were coded as following; 0.5 PCV, 3.5 PCV, 5.5 PCV, 7.5 PCV, 9.5 PCV, 11.5 PCV.

2.4. Dye sensitized solar cell assembly

The photo anode films were coated on the FTO conductive glass via doctor blade technique. The viscous paste, which includes ZnO or Fe/ZnO nanorods and ethyl cellulose were prepared and coated on FTO glass. The prepared photo anodes were sintered at 450 °C for 30 min in the air. The ZnO or Fe/ZnO photo anodes were immersed in a water solution containing 10 mM dye sensitizers for 24 h in the dark. The counter electrode was prepared by spreading out a drop of 5 mM H₂PtCl₆.6H₂O solution on FTO glass and sintered at 450°C for 30 min. The electrolyte solution was a mixture of 0.05 M I₂, 0.1 M LiI and 0.5 M 4-tert-butylpyridine in acetonitrile. The photo anode and counter electrode were assembled in a typical sandwich shape and clipped together as an open cell. The internal space of these cells was filled with electrolyte solution.

2.5. Characterizations

The cyclic voltammetry (CV) measurements of pyrocatechol samples with different pH values were carried out on CHI 660C electrochemical workstation. The CV analysis were performed in a 0.1 M LiClO₄ solution in acetonitrile with a different scan rates by using traditional three electrode system (glassy carbon working electrode, platinum wire counter electrode and saturated calomel reference electrode). The photocurrent density-voltage curve (J-V) characteristics of the solar cells were measured by CHI 660C electrochemical workstation under 100 mWcm⁻² irradiation from a solar simulator (Xenon lamp, LCS-100, Oriol). The electrochemical impedance spectroscopy measurement (EIS) was carried out by CHI 660C electrochemical workstation in the frequency region from 0.1 Hz to 100 kHz.

3. RESULT AND DISCUSSION

3.1. Fe/ZnO characterizations

The x-ray diffraction pattern of the ZnO and Fe/ZnO nanorods are shown in Fig 2. The all diffraction peaks can be indexed in hexagonal wurtzite phase (ICDS: 98-005-7450) [4]. The peaks sharpness has demonstrate that the higher crystallinity of the ZnO phase. Because of the very small amount of doped Fe atoms was added the structure, the Fe atoms peaks was not observed in

the XRD structure. However, the Fe doped into ZnO structure has changed the lattice parameters slightly. The calculated lattice parameters are listed in Table 1. The six coordinated ionic radius of Zn²⁺ and Fe³⁺ is 0.740Å and 0.645Å, respectively [19]. The ionic radius of Fe³⁺ is lower than that of Zn²⁺ and this allows the doping process possible. Additionally, the crystalline sizes of the ZnO and Fe/ZnO samples were calculated by Debye-Scherrer equations. The detailed calculation parameters were described in previous works [14], [20].

Table 1. Lattice parameters of ZnO and Fe/ZnO nanorods.

Nanorods	Lattice Parameters		Volume (Å) ³	Space Group
	a (Å)	c (Å)		
ZnO	3.251	5.210	47.65	P 63/mmc
Fe/ZnO	3.252	5.212	47.79	P 63/mmc

The mean crystalline size values of ZnO and Fe/ZnO are 120.4 and 108.7 nm, respectively. Upon Fe doping to crystalline structure, the broadening of XRD peaks is slightly increased and this results demonstrate the decreasing crystalline size.

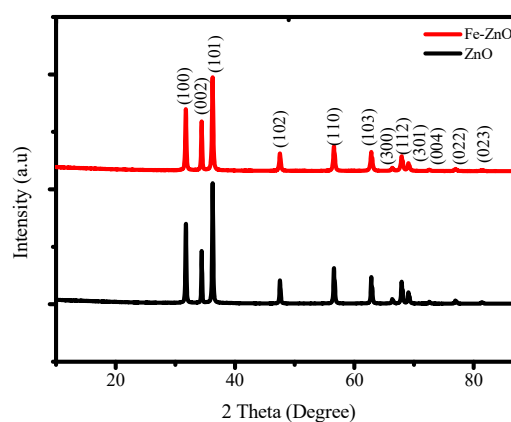


Figure 2. XRD patterns of ZnO and Fe/ZnO nanorods.

The ZnO nanorods prepared by hydrothermal methods are shown in Fig. 3A and Fe atoms doped to ZnO nanorods are shown in Fig 3B. The circles in Fig. 3B have shown the Fe atoms. The main goal of the study is to bind the Fe atoms physically to pyrocatechol violet structure. The possible binding mechanism of the Fe-pyrocatechol violet has shown in Fig 4. The -OH ion of pyrocatechol

violet can bind to the Fe atoms and this can improve the dye loading capacities and also increased the cell efficiency. The FE-SEM-EDS spectra of ZnO and Fe/ZnO samples are shown in Fig 4C and D, respectively. The EDS spectrum of Fe/ZnO nanorods has shown the presence of Fe atoms.

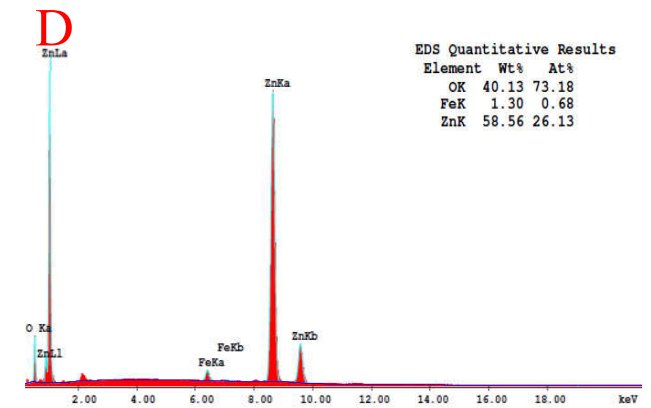
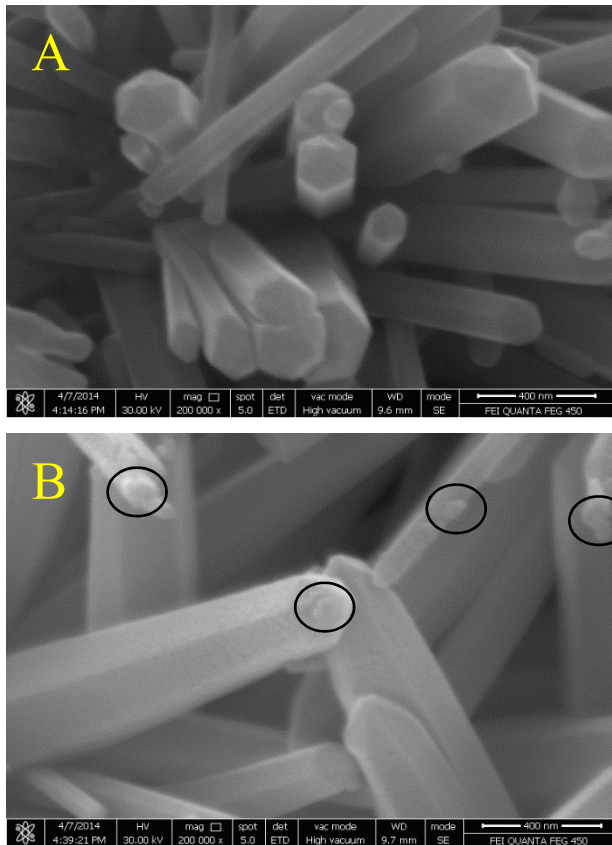


Figure 3. FE-SEM images of ZnO (A), Fe/ZnO (B) nanorods (The Fe structures were marked with a circle) and EDS spectra of ZnO (C), Fe-ZnO (C).

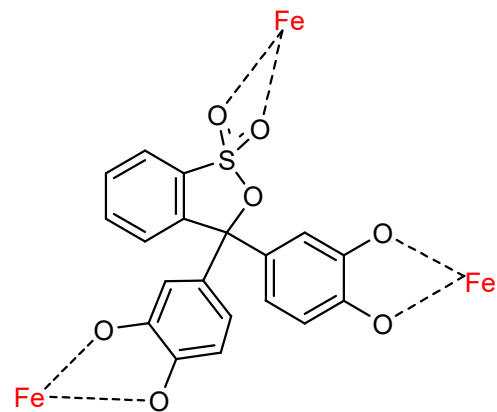
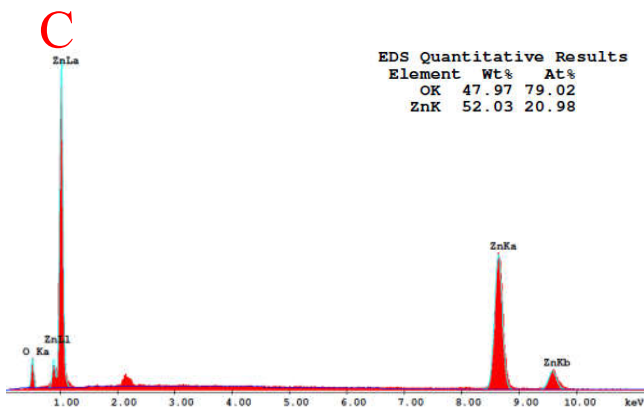


Figure 4. The possible complexation mechanism of Fe-pyrocatechol violet.



3.2. Pyrocatechol violet characterizations

The UV-Vis absorbance spectra of pyrocatechol violet different with pH values have shown in Fig 5. As can be seen in Fig. 5, the basic dye solution has also shown higher absorbance spectrum in the whole UV and VIS region compared to acidic solution. In the literature, the UV-Vis absorbance value is directly proportional to the cell efficiency values. When the dye has higher UV-Vis absorbance in the spectrum, the cell efficiency values of this type cell reach higher values. Because of this, it is predicted that the dye will have a higher cell efficiency, when it is found in the basic region. The UV-Vis absorption onset and calculated optical band gap values of these pyrocatechol violet dye solution with different pH values are summarized in Table 2.

The cyclic voltammetry of pyrocatechol violet with different pH values are shown in Fig 6. The oxidation and reduction potential of all prepared

pyrocatechol dyes with different pH values are listed in Table 2 and calculation details were reported previous works [4], [21], [22].

As can be seen in Table 2 and Fig 5, the oxidation value decreased with increasing pH values. This is probably due to the fact that the increasing pH value leads to the transformation of –OH group to the =O group. Likewise, the potential for reduction has been also affected. The increasing pH has changed the oxidation and reduction potential values. This also affects the electrochemical band gap values. The optical band gap values are slightly changed with pH alteration. The optical band gap values are very similar because the optical spectra has slightly changed with the pH alteration. For this reason, the electrochemical band gap value can be used more effectively.

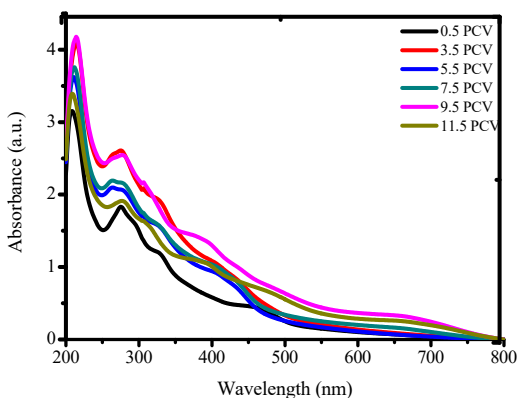


Figure 5. The UV-Vis spectra of Fe-pyrocatechol violet complex with different pH values.

Table 2. Electrochemical and optical properties of pyrocatechol violet with different pH values.

pH	UV-Vis		CV (V vs Ag/AgCl)		
	λ_{onset}	E_g^{OPT}	E_{OX}	E_{RED}	E_g^{EC}
0.5	718	1.72	-0.79	0.73	1.52
3.5	722	1.71	-0.63	0.68	1.31
5.5	725	1.70	-0.65	0.67	1.32
7.5	728	1.69	-0.44	0.58	1.02
9.5	741	1.67	-0.35	0.43	0.78
11.5	772	1.60	-0.28	0.37	0.65

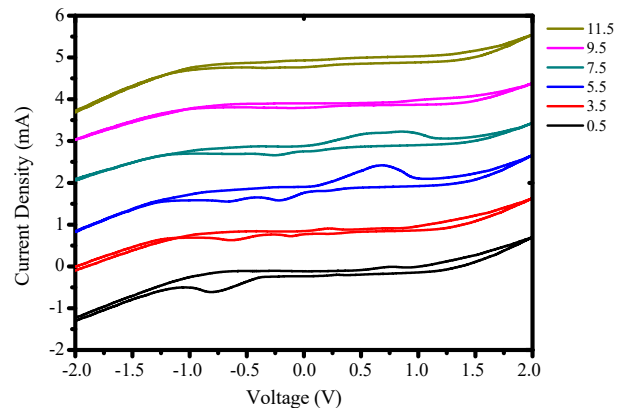


Figure 6. Cyclic voltammetry curves of pyrocatechol violet solution with different pH values.

3.3. Solar cell characterizations

The pyrocatechol violet dye based ZnO or Fe/ZnO solar cells with different pH values were investigated and current density-voltage (J-V) curves have been shown in Fig 7A and B and the photovoltaic parameters are listed in Table 3. The best solar cell is Fe/ZnO and pyrocatechol violet

Table 3. Photovoltaic parameters of ZnO and Fe/ZnO samples

	pH	Dye loading ($10^{-8}mol/cm^2$)	J_{sc} (mA/cm^2)	V_{oc} (V)	FF (%)	η (%)
ZnO	0.5	2.81	0.72	0.85	0.47	0.29
	3.5	3.11	0.86	0.84	0.48	0.35
	5.5	4.06	1.01	0.83	0.52	0.44
	7.5	4.25	2.13	0.85	0.53	0.96
	9.5	4.44	1.55	0.82	0.50	0.63
	11.5	3.28	0.62	0.84	0.44	0.23
Fe/ZnO	0.5	3.10	1.07	0.82	0.45	0.39
	3.5	3.29	1.28	0.83	0.44	0.47
	5.5	4.24	1.52	0.85	0.51	0.66
	7.5	4.86	3.19	0.84	0.52	1.39
	9.5	5.09	2.33	0.83	0.50	0.97
	11.5	3.71	0.93	0.85	0.47	0.37

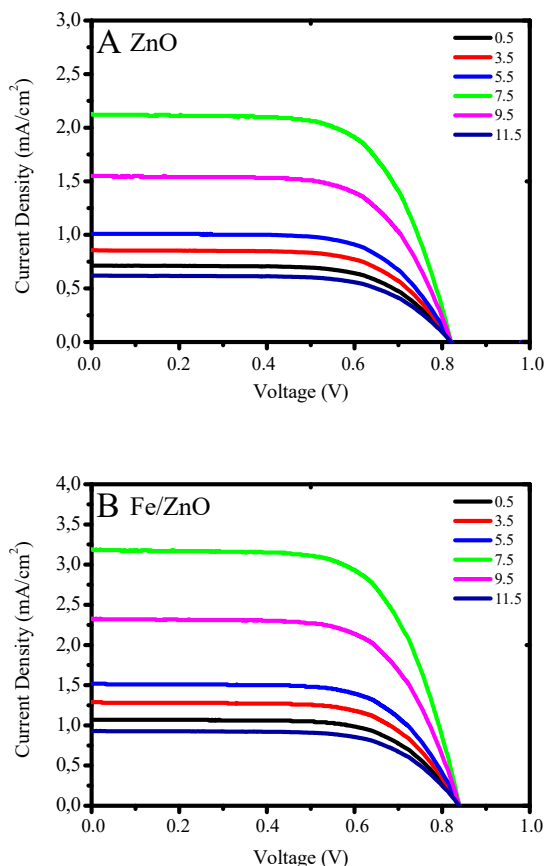


Figure 7. Current density-voltage curves of ZnO (A) and Fe/ZnO (B) samples.

solution at pH 7.5, and has a cell efficiency of 1.39 %. The solar cell efficiency values have increased after the Fe atoms addition to ZnO samples. Additionally, the solar cell efficiency values have slightly increased with the increasing pH values. However, in the basic condition (pH 9.5 and 11.5), the values have decreased. This is probably due to the fact that, in the basic condition, the dye molecules leak into solution, and in acidic condition, the ZnO or Fe/ZnO can dissolve into the solution. Due to these two shortcomings, the highest cell efficiency was observed under neutral conditions.

4. CONCLUSION

The ZnO and Fe/ZnO nanorod structures were synthesized by hydrothermal methods and characterized via XRD, FE-SEM and SEM-EDS. The pyrocatechol violet with different pH values were prepared and characterized by UV-Vis and CV technique. Then the dye sensitized solar cells was fabricated using ZnO or Fe/ZnO and pyrocatechol violet with different pH values dyes. The efficiency of best solar cell was found to be 1.39% with Fe/ZnO photoanode and pH 7.5

pyrocatechol violet dye solution. The Fe/ZnO nanorods has exhibit higher efficiencies than ZnO nanorods. These findings have confirmed that the doped Fe atoms can bind to pyrocatechol violet. The detailed complexation mechanism have been discussed. The Fe doping to ZnO nanorods have increased the dye sensitized solar cell efficiency values up to %20-35 for pyrocatechol violet with different pH dyes.

ACKNOWLEDGMENTS

This study is supported by Sakarya University Scientific Research Projects Coordination Unit. Project Number: 2016-50-02-009. I also would like to thank to Mr. Bekir Cakiroglu for his valuable contributions.

REFERENCES

A sample references list is given below;

- [1] A. Hagfeldt, G. Boschloo, L. Sun, L. Kloo, and H. Pettersson, "Dye-sensitized solar cells.," *Chem. Rev.*, vol. 110, pp. 6595–6663, 2010.
- [2] N. Kannan and D. Vakeesan, "Solar energy for future world: - A review," *Renew. Sustain. Energy Rev.*, vol. 62, pp. 1092–1105, 2016.
- [3] V. Sugathan, E. John, and K. Sudhakar, "Recent improvements in dye sensitized solar cells: A review," *Renew. Sustain. Energy Rev.*, vol. 52, pp. 54–64, 2015.
- [4] S. Çakar and M. Özacar, "Fe-querctin coupled different shaped ZnO rods based dye sensitized solar cell applications," *Sol. Energy*, vol. 155, pp. 233–245, 2017.
- [5] G. Calogero and G. Di Marco, "Red Sicilian orange and purple eggplant fruits as natural sensitizers for dye-sensitized solar cells," *Sol. Energy Mater. Sol. Cells*, vol. 92, no. 11, pp. 1341–1346, 2008.
- [6] G. Calogero, J.-H. Yum, A. Sinopoli, G. Di Marco, M. Grätzel, and M. K. Nazeeruddin, "Anthocyanins and betalains as light-harvesting pigments for dye-sensitized solar cells," *Sol. Energy*, vol. 86, no. 5, pp. 1563–1575, May 2012.
- [7] G. Calogero, A. Bartolotta, G. Di Marco, A. Di Carlo, and F. Bonaccorso, "Vegetable-based dye-sensitized solar cells," *Chem. Soc. Rev.*, vol. 44, no. 10, pp. 3244–3294,

- 2015.
- [8] J. Gong, J. Liang, and K. Sumathy, "Review on dye-sensitized solar cells (DSSCs): Fundamental concepts and novel materials," *Renew. Sustain. Energy Rev.*, vol. 16, no. 8, pp. 5848–5860, 2012.
- [9] M. R. Narayan, "Review : Dye sensitized solar cells based on natural photosensitizers," *Renew. Sustain. Energy Rev.*, vol. 16, no. 1, pp. 208–215, 2012.
- [10] J. Gong, K. Sumathy, Q. Qiao, and Z. Zhou, "Review on dye-sensitized solar cells (DSSCs): Advanced techniques and research trends," *Renew. Sustain. Energy Rev.*, vol. 68, no. December 2015, pp. 234–246, 2017.
- [11] R. Vittal and K.-C. Ho, "Zinc oxide based dye-sensitized solar cells: A review," *Renew. Sustain. Energy Rev.*, 2016.
- [12] H. Ejima, J. J. Richardson, and F. Caruso, "Metal-phenolic networks as a versatile platform to engineer nanomaterials and biointerfaces," *Nano Today*, vol. 12, pp. 136–148, 2016.
- [13] B. Roose, S. Pathak, and U. Steiner, "Doping of TiO₂ for sensitized solar cells," *Chem. Soc. Rev.*, vol. 44, no. 22, pp. 8326–8349, 2015.
- [14] S. Çakar and M. Özacar, "Fe–tannic acid complex dye as photo sensitizer for different morphological ZnO based DSSCs," *Spectrochim. Acta Part A Mol. Biomol. Spectrosc.*, vol. 163, pp. 79–88, 2016.
- [15] X. Wang, S. Bi, N. Gan, and Z. Wei, "Aluminum Speciation with Adsorptive Pyrocatechol Violet-Al(III) Complex by Derivative Adsorption Chronopotentiometry," *Electroanalysis*, vol. 13, no. 15, pp. 1279–1286, 2001.
- [16] Q. Wang, Y. F. Nie, X. Y. Chen, Z. H. Xiao, and Z. J. Zhang, "Use of pyrocatechol violet as an effective redox additive for highly promoting the supercapacitor performances," *J. Power Sources*, vol. 323, pp. 8–16, 2016.
- [17] S. Ayaz and Y. Dilgin, "Flow injection amperometric determination of hydrazine based on its electrocatalytic oxidation at pyrocatechol violet modified pencil graphite electrode," *Electrochim. Acta*, vol. 258, pp. 1086–1095, 2017.
- [18] S. Çakar, N. Güy, M. Özacar, and F. Fındık, "Investigation of Vegetable Tannins and Their Iron Complex Dyes for Dye Sensitized Solar Cell Applications," *Electrochim. Acta*, vol. 209, pp. 407–422, Aug. 2016.
- [19] R. D. Shannon, "Revised Effective Ionic Radii and Systematic Studies of Interatomic Distances in Halides and Chalcogenides," *Acta Crystallogr.*, vol. A32, pp. 751–767, 1976.
- [20] M. R. Parra and F. Z. Haque, "Aqueous chemical route synthesis and the effect of calcination temperature on the structural and optical properties of ZnO nanoparticles," *J. Mater. Res. Technol.*, vol. 3, no. 4, pp. 363–369, Oct. 2014.
- [21] J. Liu *et al.*, "New D- π -A system dye based on dithienosilole and carbazole: Synthesis, photo-electrochemical properties and dye-sensitized solar cell performance," *J. Photochem. Photobiol. A Chem.*, vol. 294, pp. 54–61, 2014.
- [22] M. Han, X. Zhang, X. Zhang, C. Liao, B. Zhu, and Q. Li, "Azo-coupled zinc phthalocyanines: Towards broad absorption and application in dye-sensitized solar cells," *Polyhedron*, vol. 85, pp. 864–873, 2015.

	SAKARYA UNIVERSITY JOURNAL OF SCIENCE		 SAKARYA UNIVERSITY
	e-ISSN: 2147-835X http://www.saujs.sakarya.edu.tr		
	<u>Received</u> 25-01-2018 <u>Accepted</u> 22-05-2018	<u>Doi</u> 10.16984/saufenbilder.383770	

Korovkin Theorem via Statistical e-Modular Convergence of Double Sequences

Sevda Yıldız*

Abstract

The main purpose of the present paper is to obtain an abstract version of the Korovkin type theorem via the concept of statistical e-convergence in modular spaces for double sequences of positive linear operators. After proving this theorem, we give an application showing that the new result is stronger than classical ones. Also, we study an extension to non-positive operators.

Keywords: Statistical e-modular convergence, double sequence, abstract Korovkin theorem

1. INTRODUCTION AND PRELIMINARIES

The Pringsheim convergence is well known convergence method for double sequences. Let \mathbb{N} denote the set of all natural numbers. A double sequence $x = (x_{i,j})$ is said to be convergent in Pringsheim's sense if, for every $\varepsilon > 0$, there exists $M = M(\varepsilon) \in \mathbb{N}$ such that $|x_{i,j} - Z| < \varepsilon$ whenever $i, j > M$. In this case the Pringsheim limit of x is denoted by $P\text{-}\lim x = Z$ and Z is called the Pringsheim limit of x (see [1]). In addition to the Pringsheim convergence, Boos et al. [2,3] introduced and investigated the following notion of e-convergence of double sequences, which is stronger method than Pringsheim's:

A double sequence $x = (x_{i,j})$ is e-convergent to a number L if

$$\forall \varepsilon > 0 \quad \exists j_0 \in \mathbb{N} \quad \forall j > j_0 \quad \exists i_j \in \mathbb{N} \\ \forall i \geq i_j : |x_{i,j} - Z| < \varepsilon.$$

Then, we write $e\text{-}\lim x_{i,j} = Z$. Recently, the statistical e-convergence has been introduced in [4] hereinbelow:

Let $B \subseteq \mathbb{N}$. Then the natural density of B is given by

$$\delta(B) := \lim_j \frac{1}{j} |\{k \leq j : k \in B\}|$$

provided that the limit on the right-hand side exists, where $|A|$ denotes the cardinality of the set A . Then a sequence $x = (x_{i,j})$ is called statistically e-convergent to the number Z if for every $\varepsilon > 0$,

$$\delta\left(\left\{j : \delta\left(\left\{i : |x_{i,j} - Z| \geq \varepsilon\right\}\right) = 0\right\}\right) = 1.$$

In that case, we write $st_e\text{-}\lim_{i,j} x_{i,j} = Z$. Clearly, if a double sequence $x = (x_{i,j})$ is e-convergent then it is statistically e-convergent, too. But, the converse of this implication may not be true. Namely, if the sequence statistically e-convergent then, it does not need to be e-convergent. Also, a double sequence which is statistically e-

* Sinop Üniversitesi Fen Bilimleri Enstitüsü/Matematik Anabilim Dalı, sevdaorhan@sinop.edu.tr

convergent need not to be statistical convergent (see also [4]).

Many researchers studied some versions of Korovkin type theorem by using different type of convergence methods after Bardaro and Mantellini's work[5] on modular spaces and they get interesting results [6-11]. In this paper, we study generalized version of the Korovkin type approximation theorem for the operators $T_{i,j}$, $i, j \in \mathbb{N}$, are acting on an abstract modular function space via statistical e-modular convergence. Then, we give an application showing that our result is stronger than classical ones. We also study an extension to non-positive operators.

Now we recall some well known notations and properties of modular spaces.

Assume that G be a locally compact Hausdorff topological space given via a uniform structure $U \subset 2^{G \times G}$ that generated the topology of G (see, [12]). Let B be the σ -algebra of all Borel subsets of G and $\mu: B \rightarrow \mathbb{R}$ is a positive σ -finite regular measure. Let the space of all real valued μ -measurable functions on G with identification up to sets of measure μ zero denoted by $L^0(G)$, $C_b(G)$ be the space of all continuous real valued and bounded functions on G and $C_c(G)$ be the subspace of $C_b(G)$ of all functions with compact support on G . In that case, a functional $\rho: L^0(G) \rightarrow [0, \infty]$ is a modular on $L^0(G)$ if the following conditions are provided:

- (i) $\rho(f) = 0$ iff $f = 0$ μ -almost everywhere on G ,
- (ii) $\rho(-f) = \rho(f)$ for every $f \in L^0(G)$,
- (iii) $\rho(\alpha f + \beta g) \leq \rho(f) + \rho(g)$ for every $f, g \in L^0(G)$ and for any $\alpha, \beta \geq 0$ with $\alpha + \beta = 1$.

If there is a constant $N \geq 1$ such that the inequality

$$\rho(\alpha f + \beta g) \leq N\alpha\rho(Nf) + N\beta\rho(Ng)$$

holds for every $f, g \in L^0(G)$, $\alpha, \beta \geq 0$ with $\alpha + \beta = 1$ then we say that a modular ρ is N -quasi convex. Note that if $N = 1$, then ρ is called

convex. Furthermore, if there exists a constant $N \geq 1$ such that

$$\rho(\alpha f) \leq N\alpha\rho(Nf)$$

holds for every $f \in L^0(G)$ and $\alpha \in (0, 1]$ then a modular ρ is called N -quasi semiconvex.

The modular space $L_\rho(G)$ with modular ρ , given by

$$L_\rho(G) := \left\{ f \in L^0(G) : \lim_{\lambda \rightarrow 0^+} \rho(\lambda f) = 0 \right\}$$

and the space of the finite elements of $L_\rho(G)$, given by

$$E_\rho(G) := \left\{ f \in L_\rho(G) : \rho(\lambda f) < \infty \text{ for all } \lambda > 0 \right\}$$

Also, note that if ρ is N -quasi semiconvex, then the space $\left\{ f \in L^0(G) : \rho(\lambda f) < \infty \text{ for some } \lambda > 0 \right\}$ coincides with $L_\rho(G)$.

We will need the following notions in this paper.

A modular ρ is monotone if $\rho(f) \leq \rho(g)$ for $|f| \leq |g|$. A modular ρ is called finite if $\chi_A \in L_\rho(G)$ whenever $A \in B$ with $\mu(A) < \infty$. A modular ρ is strongly finite if $\chi_A \in E_\rho(G)$ for all $A \in B$ such that $\mu(A) < \infty$ and a modular ρ is said to be absolutely continuous if there exists an $\alpha > 0$ such that: for every $f \in L^0(G)$ with $\rho(f) < \infty$, the following conditions hold:

- for each $\varepsilon > 0$ there exists a set $A \in B$ such that $\mu(A) < \infty$ and $\rho(\alpha f \chi_{G \setminus A}) \leq \varepsilon$,
- for every $\varepsilon > 0$ there is a $\delta > 0$ with $\rho(\alpha f \chi_B) \leq \varepsilon$ for every $B \in B$ with $\mu(B) < \delta$.

If a modular ρ is monotone and finite, then $C(G) \subset L_\rho(G)$. If ρ is monotone and strongly finite, then $C(G) \subset E_\rho(G)$. Also, if ρ is monotone, strongly finite and absolutely continuous, $C_c(G) = L_\rho(G)$ with regard to the modular convergence in the ordinary sense (for details and properties see also [13-15]).

Now we introduce the statistical e-modular and e-strong convergence of double sequences.

1.1 Definition: Let $(f_{i,j})$ be a double function sequence that its terms belong to $L_\rho(G)$. Then, $(f_{i,j})$ is said to be statistically e-modularly convergent to $f \in L_\rho(G)$ iff

$$st_e - \lim_{i,j} \rho(\lambda_0(f_{i,j} - f)) = 0$$

for some $\lambda_0 > 0$.

Also, $(f_{i,j})$ is statistically e-strongly convergent to f iff

$$st_e - \lim_{i,j} \rho(\lambda(f_{i,j} - f)) = 0$$

for every $\lambda > 0$.

We note that if there exists a constant $M > 0$ such that $\rho(2f) \leq M\rho(f)$ for every $f \in L^0(G)$ (see [16]) then it is said that the modular ρ satisfies a Δ_2 -condition. These two convergence methods are equivalent if and only if the modular satisfies the Δ_2 -condition.

Let us introduce the statistical e-superior limit and e-inferior limit of double sequences. For any real double sequence $x = (x_{i,j})$, the statistical e-superior limit of x is

$$st_e - \limsup_{i,j} x_{i,j} = \begin{cases} \sup B_x, & \text{if } B_x \neq \emptyset, \\ -\infty & \text{if } B_x = \emptyset, \end{cases}$$

where

$B_x := \{b \in \mathbb{R} : \delta(\{j : \delta(\{i : x_{i,j} > b\}) \neq 0\}) = 1\}$ and \emptyset denotes the empty set. Concordantly, in general, by $\delta(K) \neq 0$ we mean either $\delta(K) > 0$ or K fails to have the natural density. Similarly, the statistical inferior limit of x is

$$st_e - \liminf_{i,j} x_{i,j} = \begin{cases} \inf A_x, & \text{if } A_x \neq \emptyset, \\ \infty & \text{if } A_x = \emptyset, \end{cases}$$

where

$A_x := \{a \in \mathbb{R} : \delta(\{j : \delta(\{i : x_{i,j} < a\}) \neq 0\}) = 1\}$. For any real double sequence $x = (x_{i,j})$,

$$st_e - \liminf_{i,j} x_{i,j} \leq st_e - \limsup_{i,j} x_{i,j}$$

and also that, for any double sequence $x = (x_{i,j})$ satisfying

$$\delta(\{j : \delta(\{i : |x_{i,j}| > M\}) = 0\}) = 1$$

for some $M > 0$,

$$st_e - \lim_{i,j} x_{i,j} = Z$$

$$\text{iff } st_e - \liminf_{i,j} x_{i,j} = st_e - \limsup_{i,j} x_{i,j} = Z.$$

2. KOROVKIN TYPE APPROXIMATION VIA STATISTICAL E-CONVERGENCE

Here, we prove a Korovkin type approximation theorem with respect to an abstract finite set of test functions e_0, e_1, \dots, e_k via the statistical e-convergence.

Let $T = (T_{i,j})$ be a double sequence of positive linear operators from D into $L^0(G)$ with $C_b(G) \subset D \subset L^0(G)$. Let ρ be monotone and finite modular on $L^0(G)$. Suppose that the double sequence T , together with modular ρ , satisfies the following property:

there exists a subset $X_T \subset D \cap L_\rho(G)$ with $C_b(G) \subset X$ such that the inequality

$$st_e - \limsup_{i,j} \rho(\lambda T_{i,j} h) \leq R\rho(\lambda h) \tag{2.1}$$

holds for every $h \in X_T$, $\lambda > 0$ and for a positive constant R .

Set $e_0(v) \equiv 1$ for all $v \in G$, let e_r , $r = 1, 2, \dots, k$ and a_r , $r = 0, 1, 2, \dots, k$, be functions in $C_b(G)$. Put

$$P_u(v) = \sum_{r=0}^k a_r(u) e_r(v), \quad u, v \in G, \tag{2.2}$$

and suppose that $P_u(v)$, $u, v \in G$, satisfies the following properties:

(P.1) $P_u(u) = 0$, for all $u \in G$,

(P.2) for every neighbourhood $U \in \mathcal{U}$ there exists a positive number η with $P_u(v) \geq \eta$ whenever $u, v \in G, (u, v) \notin U$ (see for examples [17]).

Now, we can give our main theorem of this paper.

2.1.Theorem: Let ρ be a monotone, strongly finite, absolutely continuous and N -quasi semiconvex modular. Suppose that e_r and $a_r, r = 0, 1, 2, \dots, k$, satisfy properties (P.1) and (P.2).

Let $T = (T_{i,j})$ be a double sequence of positive linear operators from D into $L^0(G)$ satisfying (2.1). If

$$st_e - \lim_{i,j} \rho(\lambda(T_{i,j}e_r - e_r)) = 0 \tag{2.1.1}$$

for every $\lambda > 0, r = 0, 1, 2, \dots, k$ in $L_\rho(G)$, then for every $f \in D \cap L_\rho(G)$, with $f - C_b(G) \subset X_T$,

$$st_e - \lim_{i,j} \rho(\lambda_0(T_{i,j}f - f)) = 0 \tag{2.1.2}$$

for some $\lambda_0 > 0$ in $L_\rho(G)$.

Proof: We first claim that, for every $f \in C_c(G)$,

$$st_e - \lim_{i,j} \rho(\gamma(T_{i,j}f - f)) = 0 \tag{2.1.3}$$

for every $\gamma > 0$.

To see this assume that $f \in C_c(G)$. Then, since G is furnished with the uniformity \mathcal{U} , f is bounded and uniformly continuous on G . By the uniform continuity of f , choose $\varepsilon \in (0, 1]$, there is a set $U \in \mathcal{U}$ such that $|f(u) - f(v)| \leq \varepsilon$ whenever $u, v \in G, (u, v) \in U$.

For all $u, v \in G$ let $P_u(v)$ be as in (2.2), and $\eta > 0$ satisfy condition (P.2). Then for $u, v \in G,$

$$(u, v) \notin U, \text{ we have } |f(u) - f(v)| \leq \frac{2M}{\eta} P_u(v)$$

where $M := \sup |f(v)|$. Therefore, in any case we

get $|f(u) - f(v)| \leq \varepsilon + \frac{2M}{\eta} P_u(v)$ for all $u, v \in G,$

namely,

$$-\varepsilon - \frac{2M}{\eta} P_u(v) \leq f(u) - f(v) \leq \varepsilon + \frac{2M}{\eta} P_u(v) \tag{2.1.4}$$

Since $T_{i,j}$ is linear and positive, by applying it to (2.1.4) for every $i, j \in \mathbb{N}$ we have

$$\begin{aligned} & -\varepsilon T_{i,j}(e_0; u) - \frac{2M}{\eta} T_{i,j}(P_u; u) \\ & \leq f(u) T_{i,j}(e_0; u) - T_{i,j}(f; u) \\ & \leq \varepsilon T_{i,j}(e_0; u) + \frac{2M}{\eta} T_{i,j}(P_u; u) \end{aligned}$$

Hence

$$\begin{aligned} |T_{i,j}(f; u) - f(u)| & \leq |T_{i,j}(f; u) - f(u) T_{i,j}(e_0; u)| \\ & \quad + |f(u)| |T_{i,j}(e_0; u) - e_0(u)| \\ & \leq \varepsilon T_{i,j}(e_0; u) + \frac{2M}{\eta} T_{i,j}(P_u; u) \\ & \quad + M |T_{i,j}(e_0; u) - e_0(u)| \\ & \leq \varepsilon + (\varepsilon + M) |T_{i,j}(e_0; u) - e_0(u)| \\ & \quad + \frac{2M}{\eta} \sum_{r=0}^k a_r(u) |T_{i,j}(e_r; u) - e_r(u)| \end{aligned}$$

Let $\gamma > 0$. Now for each $r = 0, 1, 2, \dots, k$ and $u \in G$, choose $M_0 > 0$ such that $|a_r(u)| \leq M_0$ the last inequality gives that

$$\gamma |T_{i,j}(f; u) - f(u)| \leq \gamma \varepsilon + K \gamma \sum_{r=0}^k |T_{i,j}(e_r; u) - e_r(u)|$$

where $K := \varepsilon + M + \left(\frac{2M}{\eta}\right) M_0$. By applying the modular ρ to the above inequality and using the monotonicity of ρ , we get

$$\rho(\gamma(T_{i,j}f - f)) \leq \rho\left(\gamma \varepsilon + K \gamma \sum_{r=0}^k (T_{i,j}e_r - e_r)\right).$$

Thus, we can see that

$$\begin{aligned} \rho(\gamma(T_{i,j}f - f)) & \leq \rho((k+2)\gamma \varepsilon) \\ & \quad + \sum_{r=0}^k \rho((k+2)K\gamma(T_{i,j}e_r - e_r)). \end{aligned}$$

Because of ρ is strongly finite and N -quasi semiconvex, we get,

$$\begin{aligned} \rho(\gamma(T_{i,j}f - f)) & \leq N\varepsilon \rho((k+2)\gamma N) \\ & \quad + \sum_{r=0}^k \rho((k+2)K\gamma(T_{i,j}e_r - e_r)). \end{aligned} \tag{2.1.5}$$

For a given $\varepsilon^* > 0$, choose an $\varepsilon \in (0, 1]$ such that $N\varepsilon\rho((k+2)\gamma N) < \varepsilon^*$. Now we define the followings:

$$S_\gamma := \left\{ j : \delta \left(\left\{ i : \rho(\gamma(T_{i,j}f - f)) \geq \varepsilon^* \right\} \right) = 0 \right\}$$

$$S_{\gamma,r} := \left\{ j : \delta \left(\left\{ i : \rho \left((k+2)K\gamma(T_{i,j}e_r - e_r) \right) \geq \frac{\varepsilon^* - N\varepsilon\rho((k+2)\gamma N)}{k+1} \right\} \right) = 0 \right\},$$

where $r = 0, 1, 2, \dots, k$. Then, by hypothesis (2.1.1) we get $\delta(S_{\gamma,r}) = 1$, $r = 0, 1, 2, \dots, k$. If we take

$$S_{\gamma,k+1} = \bigcap_{r=0}^k S_{\gamma,r}, \text{ we have } \delta(S_{\gamma,k+1}) = 1. \text{ For each } j \in S_{\gamma,k+1} \text{ we define}$$

$$S_{\gamma,r}^j = \left\{ i : \rho \left((k+2)K\gamma(T_{i,j}e_r - e_r) \right) \geq \frac{\varepsilon^* - N\varepsilon\rho((k+2)\gamma N)}{k+1} \right\},$$

$r = 0, 1, 2, \dots, k$. From the inequality (2.1.5) for each $j \in S_{\gamma,k+1}$

$$\left\{ i : \rho(\gamma(T_{i,j}f - f)) \geq \varepsilon^* \right\} \subseteq \bigcup_{r=0}^k S_{\gamma,r}^j.$$

Hence $\delta(S_{\gamma,r}^j) = 0$, we obtain

$$\delta \left(\left\{ i : \rho(\gamma(T_{i,j}f - f)) \geq \varepsilon^* \right\} \right) = 0.$$

This implies that $S_{\gamma,k+1} \subseteq S_\gamma$. So, $\delta(S_\gamma) = 1$, which proves our claim (2.1.3). Now, let $f \in D \cap L_\rho(G)$ with $f - C_b(G) \subset X_T$. It is known from ([14], [18]) that there exists a sequence $(g_{k,l}) \subset C_c(G)$ such that $\rho(3\lambda_0^* f) < \infty$ and $P\text{-}\lim_{k,l} \rho(3\lambda_0^*(g_{k,l} - f)) = 0$ for some $\lambda_0^* > 0$. That is to say, for every $\varepsilon > 0$, there is a positive number $k_0 = k_0(\varepsilon)$ with

$$\rho(3\lambda_0^*(g_{k,l} - f)) < \varepsilon \text{ for every } k, l \geq k_0. \quad (2.1.6)$$

For all $i, j \in \mathbb{N}$, since the operators $T_{i,j}$ are linear and positive, we have

$$\begin{aligned} \lambda_0^* |T_{i,j}(f; u) - f(u)| &\leq \lambda_0^* |T_{i,j}(f - g_{k_0, k_0}; u)| \\ &\quad + \lambda_0^* |T_{i,j}(g_{k_0, k_0}; u) - g_{k_0, k_0}(u)| \\ &\quad + \lambda_0^* |g_{k_0, k_0}(u) - f(u)| \end{aligned}$$

holds for every $u \in G$. Now, applying modular ρ in the last inequality and using the monotonicity of ρ , we get

$$\begin{aligned} \rho(\lambda_0^*(T_{i,j}f - f)) &\leq \rho(3\lambda_0^*T_{i,j}(f - g_{k_0, k_0})) \\ &\quad + \rho(3\lambda_0^*(T_{i,j}g_{k_0, k_0} - g_{k_0, k_0})) \\ &\quad + \rho(3\lambda_0^*(g_{k_0, k_0} - f)). \end{aligned}$$

Hence, we have

$$\begin{aligned} \rho(\lambda_0^*(T_{i,j}f - f)) &\leq \varepsilon + \rho(3\lambda_0^*T_{i,j}(f - g_{k_0, k_0})) \\ &\quad + \rho(3\lambda_0^*(T_{i,j}g_{k_0, k_0} - g_{k_0, k_0})). \end{aligned}$$

By property (2.1) and also by using $g_{k_0, k_0} \in C_c(G)$ and $f - g_{k_0, k_0} \in X_T$, we obtain

$$\begin{aligned} st_e\text{-}\limsup_{i,j} \rho(\lambda_0^*(T_{i,j}f - f)) &\leq \varepsilon + R\rho(3\lambda_0^*(f - g_{k_0, k_0})) \\ &\quad + st_e\text{-}\limsup_{i,j} \rho(3\lambda_0^*(T_{i,j}g_{k_0, k_0} - g_{k_0, k_0})) \\ &\leq \varepsilon(1+R) + st_e\text{-}\limsup_{i,j} \rho(3\lambda_0^*(T_{i,j}g_{k_0, k_0} - g_{k_0, k_0})) \end{aligned}$$

also, by (2.1.3)

$$\begin{aligned} 0 &= st_e\text{-}\lim_{i,j} \rho(3\lambda_0^*(T_{i,j}g_{k_0, k_0} - g_{k_0, k_0})) \\ &= st_e\text{-}\limsup_{i,j} \rho(3\lambda_0^*(T_{i,j}g_{k_0, k_0} - g_{k_0, k_0})) \end{aligned}$$

which gives

$$0 \leq st_e\text{-}\limsup_{i,j} \rho(\lambda_0^*(T_{i,j}f - f)) \leq \varepsilon(1+R).$$

From arbitrariness of $\varepsilon > 0$, it follows that

$$st_e\text{-}\limsup_{i,j} \rho(\lambda_0^*(T_{i,j}f - f)) = 0.$$

Furthermore,

$$st_e\text{-}\lim_{i,j} \rho(\lambda_0^*(T_{i,j}f - f)) = 0,$$

this completes the proof.

2.2.Remark: In general, it is not possible to get statistical e-strong convergence unless the modular ρ satisfies the Δ_2 -condition in 2.1.Theorem.

If we take the e-limit instead of the statistical e-limit, then the condition (2.1) reduces to

$$e - \limsup_{i,j} \rho(\lambda T_{i,j} h) \leq R \rho(\lambda h) \tag{2.2.1}$$

for every $h \in X_T$, $\lambda > 0$ and for an absolute positive constant R . In that case, the following result immediately ensue from our 2.1.Theorem.

2.3.Corollary: Let ρ be a monotone, absolutely continuous, N -quasi semiconvex and strongly finite modular. Suppose that e_r and a_r , $r = 0, 1, 2, \dots, k$, satisfy properties (P.1) and (P.2). Let $T = (T_{i,j})$ be a double sequence of positive linear operators satisfying (2.2.1). If $(T_{i,j} e_r)$ is e-strongly convergent to e_r , $r = 0, 1, 2, \dots, k$, in $L_\rho(G)$ then $(T_{i,j} f)$ is e-modularly convergent to f in $L_\rho(G)$ where f is any function in $D \cap L_\rho(G)$ with $f - C_b(G) \subset X_T$. Now, we give an application showing that in general, our result is stronger.

2.4.Example: Let us consider $G = [0, 1]^2 = [0, 1] \times [0, 1] \subset \mathbb{R}^2$ and let $\varphi: [0, \infty) \rightarrow [0, \infty)$ is a continuous function with φ is convex, $\varphi(0) = 0$, $\varphi(x) > 0$ for any $x > 0$ and $\lim_{x \rightarrow \infty} \varphi(x) = \infty$. Then, the functional ρ^φ defined by

$$\rho^\varphi(f) := \int_0^1 \int_0^1 \varphi(|f(x, y)|) dx dy \text{ for } f \in L^0(G),$$

is a convex modular on $L^0(G)$ and

$$L^\varphi(G) := \{f \in L^0(G) : \rho^\varphi(\lambda f) < +\infty \text{ for some } \lambda > 0\}$$

is the Orlicz space generated by φ .

For every $(x, y) \in G$, let $e_0(x, y) = a_3(x, y) = 1$,
 $e_1(x, y) = x$, $e_2(x, y) = y$,
 $e_3(x, y) = a_0(x, y) = x^2 + y^2$, $a_1(x, y) = -2x$,
 $a_2(x, y) = -2y$.

For every $i, j \in \mathbb{N}$, $u_1, u_2 \in [0, 1]$, let $K_{i,j}(u_1, u_2) = (i+1)(j+1)u_1^i u_2^j$ and for $f \in C(G)$ and $x, y \in [0, 1]$ set

$$M_{i,j}(f; x, y) = \int_0^1 \int_0^1 K_{i,j}(u_1, u_2) f(u_1 x, u_2 y) du_1 du_2.$$

Then we get

$$\begin{aligned} & \int_0^1 \int_0^1 K_{i,j}(u_1, u_2) du_1 du_2 \\ &= (i+1) \left(\int_0^1 u_1^i du_1 \right) (j+1) \left(\int_0^1 u_2^j du_2 \right) = 1, \end{aligned}$$

and hence, $M_{i,j}(e_0; x, y) = e_0(x, y) = 1$. Also, we know from [19] that

$$|M_{i,j}(e_1; x, y) - e_1(x, y)| \leq \frac{1}{i+2},$$

$$|M_{i,j}(e_2; x, y) - e_2(x, y)| \leq \frac{1}{j+2},$$

$$|M_{i,j}(e_1^2; x, y) - e_1^2(x, y)| \leq \frac{2}{i+3},$$

$$|M_{i,j}(e_2^2; x, y) - e_2^2(x, y)| \leq \frac{2}{j+3},$$

and for each $i, j \geq 2$, $f \in L^\varphi(G)$ we get $\rho^\varphi(M_{i,j} f) \leq 32 \rho^\varphi(f)$. Now, we define the following double sequence of positive linear operators $T = (T_{i,j})$ on $L^\varphi(G)$ by using the operators $M = (M_{i,j})$:

$$T_{i,j}(f; x, y) = s_{i,j} M_{i,j}(f; x, y), \text{ for } f \in L^\varphi(G),$$

$x, y \in [0, 1]$ and $i, j \in \mathbb{N}$, where $(s_{i,j})$ is given by

$$s_{i,j} = \begin{cases} 2, & i \leq j, \\ 0, & i > j \text{ and } i \text{ is square,} \\ 1, & i > j \text{ and } i \text{ is not square.} \end{cases}$$

Observe now that $st_e - \lim_{i,j} s_{i,j} = 1$. However, $e - \lim_{i,j} s_{i,j}$, $P - \lim_{i,j} s_{i,j}$ and $st - \lim_{i,j} s_{i,j}$ do not exist. Then, it can be easily seen that, for every $h \in X_T = L^\varphi(G)$, $\lambda > 0$ and for positive constant R_0 that

$$st_e - \limsup_{i,j} \rho^\varphi(\lambda T_{i,j} h) \leq R_0 \rho^\varphi(\lambda h).$$

Now, observe that

$$T_{i,j}(e_0; x, y) - e_0(x, y) = s_{i,j} - 1,$$

$$T_{i,j}(e_1; x, y) - e_1(x, y) \leq \frac{2}{i+2} + (s_{i,j} - 1),$$

$$T_{i,j}(e_2; x, y) - e_2(x, y) \leq \frac{2}{j+2} + (s_{i,j} - 1),$$

$$T_{i,j}(e_3; x, y) - e_3(x, y) \leq 4\left(\frac{1}{i+3} + \frac{1}{j+3}\right) + 2(s_{i,j} - 1).$$

Hence, we can see, for any $\lambda > 0$, that

$$\begin{aligned} \rho^\varphi(\lambda(T_{i,j}e_0 - e_0)) &= \rho^\varphi(\lambda(s_{i,j} - 1)) \\ &= \int_0^1 \int_0^1 \varphi(|\lambda(s_{i,j} - 1)|) dx dy = \varphi(|\lambda(s_{i,j} - 1)|) \\ &= |s_{i,j} - 1| \varphi(\lambda) \end{aligned}$$

(2.4.1)

because of the definition of $(s_{i,j})$. Now, since

$$st_e - \lim_{i,j} (s_{i,j} - 1) = 0, \text{ we get}$$

$$st_e - \lim_{i,j} \rho^\varphi(\lambda(T_{i,j}e_0 - e_0)) = 0.$$

Also, we have

$$\begin{aligned} \rho^\varphi(\lambda(T_{i,j}e_1 - e_1)) &\leq \rho^\varphi\left(\lambda\left(\frac{2}{i+2} + (s_{i,j} - 1)\right)\right) \\ &\leq \rho^\varphi\left(\frac{\lambda}{i+2}\right) + \rho^\varphi(2\lambda(s_{i,j} - 1)) \\ &= \varphi\left(\frac{\lambda}{i+2}\right) + \varphi(|2\lambda(s_{i,j} - 1)|), \end{aligned}$$

which implies, for any $\lambda > 0$, that

$$\rho^\varphi(\lambda(T_{i,j}e_1 - e_1)) \leq \varphi\left(\frac{\lambda}{i+2}\right) + |s_{i,j} - 1| \varphi(2\lambda)$$

(2.4.2)

since φ is continuous, we have

$$e - \lim_{i,j} \varphi\left(\frac{\lambda}{i+2}\right) = \varphi\left(e - \lim_{i,j} \frac{\lambda}{i+2}\right) = \varphi(0) = 0,$$

also considering $st_e - \lim_{i,j} (s_{i,j} - 1) = 0$, from the inequality (2.4.2), we get

$$st_e - \lim_{i,j} \rho^\varphi(\lambda(T_{i,j}e_1 - e_1)) = 0.$$

Similarly, we can write that

$$st_e - \lim_{i,j} \rho^\varphi(\lambda(T_{i,j}e_2 - e_2)) = 0.$$

Finally, since

$$\begin{aligned} \rho^\varphi(\lambda(T_{i,j}e_3 - e_3)) &\leq \rho^\varphi\left(\lambda\left(4\left(\frac{1}{i+3} + \frac{1}{j+3}\right) + 2(s_{i,j} - 1)\right)\right) \\ &\leq \rho^\varphi\left(8\lambda\left(\frac{1}{i+3} + \frac{1}{j+3}\right)\right) + \rho^\varphi(4\lambda(s_{i,j} - 1)) \\ &= \varphi\left(8\lambda\left(\frac{1}{i+3} + \frac{1}{j+3}\right)\right) + \varphi(|4\lambda(s_{i,j} - 1)|), \end{aligned}$$

which yields

$$\begin{aligned} \rho^\varphi(\lambda(T_{i,j}e_3 - e_3)) &\leq \varphi\left(\frac{16\lambda}{i+3}\right) + \varphi\left(\frac{16\lambda}{j+3}\right) \\ &\quad + |s_{i,j} - 1| \varphi(4\lambda) \end{aligned}$$

(2.4.3)

then, since φ is continuous

$$e - \lim_{i,j} \varphi\left(\frac{16\lambda}{i+3}\right) = 0 \text{ and } e - \lim_{i,j} \varphi\left(\frac{16\lambda}{j+3}\right) = 0,$$

it follows from the inequality (2.4.3) that

$$st_e - \lim_{i,j} \rho^\varphi(\lambda(T_{i,j}e_3 - e_3)) = 0.$$

So, our new operator $T = (T_{i,j})$ satisfies all conditions of 2.1.Theorem and therefore we obtain

$$st_e - \lim_{i,j} \rho^\varphi(\lambda(T_{i,j}f - f)) = 0$$

for some $\lambda > 0$, for any $f \in L^\varphi(G)$. However, $(T_{i,j}e_0)$ is not e-modularly convergent. Thus $(T_{i,j})$ does not fulfil the 2.3.Corollary. Also, $(T_{i,j}e_0)$ is neither modularly convergent nor statistically modularly convergent. Hence, modular Korovkin theorem and statistical modular Korovkin theorem for double sequences do not satisfy.

3. AN EXTENSION TO NON-POSITIVE OPERATORS

In this section, we relax the positivity condition of linear operators in the Korovkin theorem. In ([17], [19]) there are some positive answers. Following this approach, we give some positive answers also

for statistical e-modular convergence and we prove a statistical e-modular Korovkin theorem.

Let $I \subset \mathbb{R}$ be a bounded interval, $C^2(I)$ (resp. $C_b^2(I)$) be the space of all functions defined on I , (resp. bounded and) continuous with their first and second derivatives,

$$C_+ := \{f \in C_b^2(I) : f \geq 0\},$$

$$C_+^2 := \{f \in C_b^2(I) : f'' \geq 0\}.$$

Let $e_r, r=1,2,\dots,k$ and $a_r, r=0,1,2,\dots,k$, be functions in $C_b^2(I)$, $P_u(v), u,v \in I$, be as in (2.1.4), and suppose that $P_u(v)$ satisfies the properties (P.1), (P.2) and

(P.3) there exists a positive real constant S_0 such that $P_u''(v) \geq S_0$ for all $u,v \in I$ (The second derivative is intended with respect to v).

Now, we prove the following Korovkin type approximation theorem for linear operators that not necessarily positive .

3.1.Theorem: Let ρ be as in 2.1.Theorem and $e_r, a_r, r=0,1,2,\dots,k$ and $P_u(v), u,v \in I$, satisfies the properties (P.1), (P.2) and (P.3). Assume that $T = (T_{i,j})$ be a double sequence of linear operators and $T_{i,j}(C_+ \cap C_+^2) \subset C_+$ for all $i,j \in \mathbb{N}$. If $T_{i,j}e_r$ is statistically e-strongly convergent to $e_r, r=0,1,2,\dots,k$, in $L_\rho(I)$ then $T_{i,j}f$ is statistically e-modularly convergent to f in $L_\rho(I)$ for every $f \in D \cap L_\rho(I)$ with $f - C_b(I) \subset X_T$.

Proof: Let $f \in C_b^2(I)$. Since f is uniformly continuous and bounded on I , given $\varepsilon > 0$ with $0 < \varepsilon \leq 1$, there exists a $\delta > 0$ such that $|f(u) - f(v)| \leq \varepsilon$ for all $u,v \in I, |u-v| \leq \delta$. Let $P_u(v), u,v \in I$, be as in (2.2) and let $\eta > 0$ be associated with δ , satisfying (P.2). As in 2.1.Theorem, for every $\beta \geq 1$ and $u,v \in I$, we have

$$-\varepsilon - \frac{2M}{\eta} P_u(v) \leq f(u) - f(v) \leq \varepsilon + \frac{2M}{\eta} P_u(v) \tag{3.1.1}$$

where $M := \sup_{v \in I} |f(v)|$. From (3.1.1) it follows that

$$h_{1,\beta}(v) := \varepsilon + \frac{2M\beta}{\eta} P_u(v) + f(v) - f(u) \geq 0, \tag{3.1.2}$$

$$h_{2,\beta}(v) := \varepsilon + \frac{2M\beta}{\eta} P_u(v) - f(v) + f(u) \geq 0. \tag{3.1.3}$$

Let H_0 satisfy (P3). For each $v \in I$, we get

$$h_{1,\beta}''(v) \geq \frac{2M\beta H_0}{\eta} + f''(v),$$

$$h_{2,\beta}''(v) \geq \frac{2M\beta H_0}{\eta} - f''(v).$$

Because of f'' is bounded on I , we can choose $\beta \geq 1$ in such a way that $h_{1,\beta}''(v) \geq 0, h_{2,\beta}''(v) \geq 0$ for each $v \in I$. Hence $h_{1,\beta}, h_{2,\beta} \in C_+ \cap C_+^2$ and then, by hypothesis

$$T_{i,j}(h_{\kappa,\beta}; u) \geq 0 \text{ for all } i,j \in \mathbb{N}, u \in I \text{ and } \kappa = 1,2. \tag{3.1.4}$$

From (3.1.2)-(3.1.4) and the linearity of $T_{i,j}$, we get

$$\begin{aligned} \varepsilon T_{i,j}(e_0; u) + \frac{2M\beta}{\eta} T_{i,j}(P_u; u) &+ T_{i,j}(f; u) - f(u) T_{i,j}(e_0; u) \geq 0, \\ \varepsilon T_{i,j}(e_0; u) + \frac{2M\beta}{\eta} T_{i,j}(P_u; u) &- T_{i,j}(f; u) + f(u) T_{i,j}(e_0; u) \geq 0, \end{aligned}$$

thus,

$$\begin{aligned} -\varepsilon T_{i,j}(e_0; u) - \frac{2M\beta}{\eta} T_{i,j}(P_u; u) &\leq f(u) T_{i,j}(e_0; u) - T_{i,j}(f; u) \\ &\leq \varepsilon T_{i,j}(e_0; u) + \frac{2M\beta}{\eta} T_{i,j}(P_u; u). \end{aligned}$$

Similarly as in the proof of 2.1.Theorem, using the modular ρ and for $i,j \in \mathbb{N}$, we have the assertion.

REFERENCES

[1] Pringsheim, "A. Zur theorie der zweifach unendlichen zahlenfolgen," *Math. Ann.*, vol. 53, pp. 289-321, 1900.

- [2] Boos, J., Leiger, T., Zeller, "K. Consistency theory for SM-methods," *Acta. Math. Hungar.*, vol. 76, pp. 83-116, 1997.
- [3] Boos, J. "Classical and modern methods in summability," *Oxford University Press Inc., New York*, 2000.
- [4] Sever, Y., Talo, Ö. "Statistical e-convergence of double sequences and its application to Korovkin type approximation theorem for functions of two variables," *Iranian Journal of Science and Technology, Transactions A: Science*, vol. 41, no. 3, pp. 851-857, 2017.
- [5] Bardaro, C. and Mantellini, I., "Korovkin's theorem in modular spaces," *Commentationes Math.*, vol. 47, pp. 239-253, 2007.
- [6] Bardaro, C., Boccuto, A., Demirci, K., Mantellini, I., Orhan, S., "Triangular A-statistical approximation by double sequences of positive linear operators," *Results Math.*, vol. 68, pp. 271-291, 2015.
- [7] Boccuto, A. and Dimitriou, X., "Korovkin-type theorems for abstract modular convergence," *Results in Mathematics*, vol. 69, pp. 477-495, 2016.
- [8] Demirci K., Orhan S., "Statistical relative approximation on modular spaces," *Results in Mathematics*, vol. 71, pp. 1167-1184, 2017.
- [9] Demirci, K., Kolay, B., "A-Statistical Relative Modular Convergence of Positive Linear Operators," *Positivity*, vol. 21, pp. 847-863, 2017.
- [10] Karakuş, S., Demirci, K., Duman, O., "Statistical approximation by positive linear operators on modular spaces," *Positivity*, vol. 14, pp. 321-334, 2010.
- [11] Yilmaz, B., Demirci, K., Orhan, S., "Relative Modular Convergence of Positive Linear Operators," *Positivity*, vol. 20, pp. 565-577, 2016.
- [12] Kuratowski K., "Topology," Volls I and II, *Academic Press, New York-London*, 1966/1968.
- [13] Kozłowski W. M., "Modular function spaces," *Pure Appl. Math.*, vol. 122, *Marcel Dekker, Inc., New York*, 1988.
- [14] Mantellini I., "Generalized sampling operators in modular spaces," *Commentationes Math.*, vol. 38, pp. 77-92, 1998.
- [15] Musielak J., "Nonlinear approximation in some modular function spaces" *I, Math. Japon.* vol. 38, pp. 83-90, 1993.
- [16] Musielak, J., "Orlicz spaces and modular spaces," *Lecture Notes in Mathematics*, vol. 1034 *Springer-Verlag, Berlin*, 1983.
- [17] Bardaro C., Boccuto A., Dimitriou X. and Mantellini I., "Abstract Korovkin type theorems in modular spaces and applications," *Cent. Eur. J. Math.*, vol. 11, no. 10, pp. 1774-1784, 2013.
- [18] Bardaro, C., Musielak, J., Vinti, G., "Nonlinear integral operators and applications," *de Gruyter Series in Nonlinear Analysis and Appl.* vol. 9 *Walter de Gruyter Publ., Berlin*, 2003.
- [19] Bardaro C., Boccuto A., Demirci K., Mantellini I., Orhan S. "Korovkin-type theorems for modular Ψ -A-statistical convergence," *J. Funct. Spaces.* Article ID 160401 vol. 2015, pp. 1-11, 2015.

	SAKARYA UNIVERSITY JOURNAL OF SCIENCE		 SAKARYA UNIVERSITY
	e-ISSN: 2147-835X http://www.saujs.sakarya.edu.tr		
	<u>Received</u> 09-02-2018 <u>Accepted</u> 05-06-2018	<u>Doi</u> 10.16984/saufenbilder.392656	

Burnout Levels of Academic Staff: An Investigation at a Public University in Turkey

Nilgün Özgül^{*1}, Esra Polat

Abstract

Burnout is an important problem in academic life. Burnout of academic staff affect the quality of education and the success of the students. Because, being burnout not only brings about insufficiencies and illnesses in individuals, but also damages the other staff and the foundation as a result of their underperformance, psychological destruction and resignation. The aim of this study is to identify the burnout levels of academic staff and to evaluate the relationship between some variables of burnout levels by using Proportional Odds Model differently from other burnout studies about academic staff. For this purpose, 150 academicians are selected with "Stratified Simple Sampling" method from one of the biggest Public Universities in Ankara in Turkey, then, the personal information form and Maslach Burnout Inventory (MBI) are implemented to them. This study is important for recognizing the problems of academic staff and contributing to their productivity and success in their work.

Keywords: Academicians, Burnout, Maslach Burnout Inventory, Proportional Odds Model (POM)

1. INTRODUCTION

The use of the term burnout began to appear with some regularity in the 1970s in the United States, especially among people working in the human services such as teaching, social services, medicine, mental health and law enforcement which include face to face and intensive relations [1]. The term burnout was first introduced by [2], who defined it as "to fail, to wear out, or become exhausted by making excessive demands on energy, strength, or resources". The concept of burnout was further popularized with development of the Maslach Burnout Inventory (MBI) which is the most widely used, well validated instrument for the assessment of burnout. According to the [3], burnout is a syndrome constructing of three dimensions (emotional exhaustion, depersonalization and a sense of low personal accomplishment) that is associated with decreased work that is measured with the MBI [3]. [3]

separated the consequences of stress into three dimensions of burnout: (1) Emotional exhaustion (EE). (2) Depersonalization (DP). (3) Personal accomplishment (PA). EE can be considered the core symptom of burnout. Maslach defined that EE appears first as a response to excessive work demands that drain individual's emotional resources. The individual begins to have negative and undesired attitudes towards the people he/she works with, which is defined as DP. Reduced Personal Accomplishment (RPA), the third and final construct of burnout, is believed to be result of continued depersonalization and manifests itself as a decline in one's feelings of competence and successful achievement [4, 5].

In sum, according to Maslach and Jackson's [3] model, depersonalization and decreased personal accomplishment as consequences of chronic emotional exhaustion. The final step of burnout, comes quitting the job. When not being able to cope with the consequences of burnout, the

* Corresponding Author

¹ Hacettepe University, Faculty of Science, Department of Statistics, nozgul@hacettepe.edu.tr

“victim” comes to the end of the road. To conclude, burnout may lead to many consequences including symptoms such as stress, physical and psychological illnesses, depression, fatigue, absence, low performance, lack of involvement and excitement for work, none of which can be underestimated [4]

Academic staff in universities are affected from hitches arising from burnout [6]. Since academic staff is in a relationship with a lot of students and also university members, they are potential candidates suffer from burnout [7, 8].

There are several burnout studies about academic staff in Turkey. [9] investigated the demographic factors that affect the burnout levels of 185 academic staff in faculty of Economics and Administrative Science of one public university. [10] determined the burnout of physicians and its relation to socio-demographic features in medical faculty of one university. [11] examined the relationship between demographic factors of university faculty with their burnout levels at one public university. [12] also determined the burnout situations of 108 academicians working in some public universities. [13] investigated the relationship between some demographic variables of burnout levels of academicians in one public university. [14] measured the burnout levels of academicians and determined the factors affecting burnout levels of 160 academicians working in accounting and finance sub-department in 78 public and foundation universities in Turkey. [15] also investigated the factors affecting job satisfaction, burnout levels and job satisfaction of the academicians of one university. [8] examined the burnout levels of 648 academicians working in the Universities of Turkey. [16] determined that there is a significant difference in burnout levels of the academic staff in terms of some technical demographic variables in public and foundation universities in Istanbul.

The purpose of this study is to identify the burnout levels of academic staff and to investigate the factors that affect burnout levels of academicians. None of above studies investigate the levels of burnout thoroughly. In this study, to investigate the levels of burnout, differently from other studies, Proportional Odds Model (POM) is used. The significance of this study is the first time of using POM in a Burnout study. For this target, 150

academicians, working in the biggest Public University in Ankara, are selected with “Stratified Simple Sampling” method, the personal information form and Maslach Burnout Inventory (MBI) are implemented. This study is important to recognize the problems of academic staff by examining one of the biggest and famous university of Turkey established in Ankara.

2. METHOD

For this study, factors which have effects on burnout levels of academic staff are investigated with Proportional Odds Models (POM). The POM is a member of the family of cumulative logit models. The aim of cumulative logit models are determining relationship between one categorical dependent variable and various independent variables. In cumulative logit models the natural logarithm of odds of ordinal dependent variable is stated as a linear function of the independent variables. Cumulative logit model is frequently-used method as it enables to ordinal variables to be modeled where the dependent variable has at least 3 categories with these categories ordinally arranged, i.e. survey analysis (whether a respondent is not satisfied, satisfied or very satisfied) or the educational level (elementary, high, university) [17, 18].

2.1. Cumulative Logit Models

Cumulative logit model is the most widely used model for ordinal data in terms of interpreting or applying. Similar to the other logit models, in order to obtain cumulative probabilities, odds ratios are computed in cumulative logit models. There are $j - 1$ ways to compare j categorized dependent variable Y . Eq.1 shows cumulative logits of dependent variable Y for

$(Y \leq 1, Y > 1; Y \leq 2, Y > 2; \dots; Y \leq J-1, Y > J-1)$ [18, 19].

$$\text{logit} P(Y \leq j) = \log \frac{P(Y \leq j)}{1 - P(Y \leq j)} \quad (1)$$

Similar to the other logit models, one category is chosen as the reference category (generally the last category) in cumulative logit model. This model uses cumulative probabilities upto a threshold, therefore making the whole range of ordinal categories binary at that threshold. $J-1$ cut-off

points are predicted by this way and the predictions give information for every successive category about cumulative probabilities. Probability of being in the chosen category or being in an upper category are considered together in cumulative probability [18, 20].

Cumulative logits across $j-1$ response option categories. For $j=3$, (here, $y= 1$ to 3) these cumulative logits can be used to make predictions for the $j-1=2$ cumulative probabilities, given the collection of explanatory variables [21]:

$$\begin{aligned} \text{logit}[P(y \leq 1)] &= \log \left[\frac{P(y=1)}{1-P(y=1)} \right] = \log \left[\frac{P(y=1)}{P(y=2)+P(y=3)} \right] = \alpha_1 - \beta'x \\ \text{logit}[P(y \leq 2)] &= \log \left[\frac{P(y=1)+P(y=2)}{1-P(y \leq 2)} \right] = \log \left[\frac{P(y=1)+P(y=2)}{P(y=3)} \right] = \alpha_2 - \beta'x \end{aligned} \quad (2)$$

2.2. The Proportional Odds Model (POM)

POM is defined by [22] for ordinal logistic regression. In case where the dependent variable is ordinal and parallel lines assumption holds, POMs are commonly used [23, 24]. Parallel lines assumption expresses that the dependent variable's categories are parallel to each other. In other words, the regression slopes do not differ significantly across levels of dependent variable, therefore parameter estimations do not differ for cut-off points.

Figure. 1 shows the parallelity for $j-1$ response categories ($j=3$) [18, 19, 21, 25].

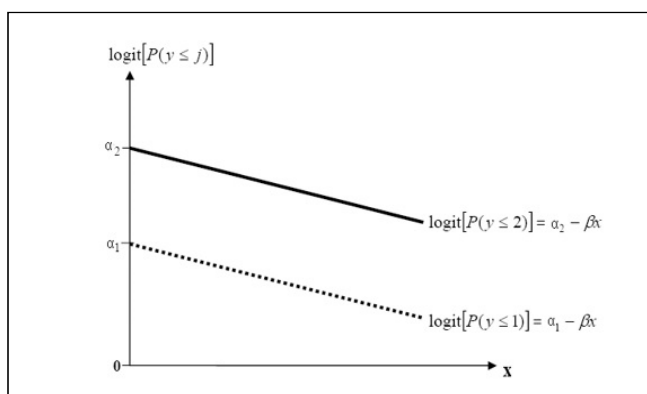


Figure 1. Parallelity for $j-1=2$ response categories

The POM is based on cumulative distribution function. POMs can be estimated as shown in Eq. 3 using cumulative probabilities [18].

$$P(Y \leq j) = \frac{\exp(\alpha_j - \beta'x)}{1 + \exp(\alpha_j - \beta'x)}, \quad j=1,2,\dots,J-1 \quad (3)$$

where α_j is the unknown parameter's estimator and index $j=1,2,\dots,j-1$ for $\alpha_1 \leq \alpha_2 \leq \dots \leq \alpha_{j-1}$. β is the regression parameter vector of x and shown as $\beta = (\beta_1, \dots, \beta_k)$. β_j is the increase in log-odds of falling into or above any category associated with a one-unit increase in x_j , holding all the other x -variables constant. The model can be transformed to linear by calculating natural logarithms of the odds ratios as shown in Eq. 4 [18, 26].

$$\text{logit}(\gamma_j) = \alpha_j - \beta'x \quad (4)$$

The odds ratio of the event $Y \leq j$ at $x_k + 1$ relative to the same event at x_k is,

$$\text{OR} = \frac{P(y \leq j/x_k + 1)}{1 - P(y \leq j/x_k + 1)} \div \frac{P(y \leq j/x_k)}{1 - P(y \leq j/x_k)} = \exp(-\beta_k) \quad (5)$$

3. APPLICATION AND RESULTS OF ANALYSIS

[27] has translated MBI, originally developed by [3], into Turkish and [28] investigated the validity and reliability of Burnout Inventor. In this study, the Turkish version of MBI was implemented to the responders. Since the Turkish language does not respond to 7-point degree scale, 5-point Likert type scale is used [27]. MBI utilized with 22 items having subscales for 3 dimensions: emotional exhaustion, depersonalization and personal accomplishment. High scores on emotional exhaustion and depersonalization and low scores on diminished personal accomplishment are signs of burnout. The items related Emotional

exhaustion are 1,2,3,6,8,13,14,16,20 (Scores: 27 or over High/ 17-26 Moderate/ 0-16 Low). The items related Depersonalization are 5, 10, 11, 15, 22 (Scores: 13 or over High/ 7-12 Moderate/ 0-6 High). The items related Personal accomplishment: are 4,7,9,12,17,18,19,21 (Scores: 0-31 High/ 32-38 Moderate/ 39 or over

Low). Using this 22-item tool, responders rate the frequency with which they experience various feelings or emotions on a 5-point Likert scale with response options ranging from "Never" to "Always". Independent variables which could have an effect on burnout levels can be seen on Table 1.

Table 1. Independent Variables and Levels

Independent Variable	Independent Variable Levels				
X1: Gender	1. Female	2. Male			
X2: Age Group	1. Under 27	2. Between 28-35	3. Between 36-43	4. Between 44-51	5. Over 52
X3: Marital Status	1. Single	2. Married			
X4: Having a child	1. Yes	2. No			
X5: Having own room at work	1. Yes	2. No			
X6: Satisfaction of colleagues	1. Yes	2. No			
X7: Average sleep time per day	1. Equal or less than 6 Hours	2. More than 6 hours			
X8: Exhaustion of the academic work	1. None	2. Low	3. Moderate	4. High	
X9: Economic Satisfaction	1. Very satisfied	2. Somewhat satisfied	3. Not very satisfied	4. Not at all satisfied	
X10: Spending time for social activities	1. Frequently	2. Sometimes	3. Rarely	4. Never	
X11: Spending time for Personal Need	1. Frequently	2. Sometimes	3. Rarely	4. Never	
X12: Levels of Technology Usage	1. Frequently	2. Sometimes	3. Rarely	4. Never	
X13: Household Size	1. Alone	2. Two	3. Three	4. Four	

First of all, validity of the POMs must be tested by likelihood ratio test. From Table 2 it is clear that all three models are fitted ($p=0.000 < 0,05$; $p=0.042 < 0.05$; $p=0.002 < 0.05$). After the test of models signficancy, parallel lines assumption is tested. The null hypothesis states that the location parameters (slope coefficients) are the same across response categories. For three models, the proportional odds assumption appears to have held because the significances of Chi-Square statistics

are $> .05$ ($p=0.446 > 0,05$; $p=0.776 > 0.05$; $p=0.975 > 0.05$).

Table 2. Model Fitting and Test of Parallel Lines for Three Levels of Burnout

Model	-2 Log Likelihood	df	Model Fitting (Sig.)	Test of Parallel Lines (Sig.)
Emotional Exhaustion	198.053	27	0.000	0.446
Depersonalization	247.010	27	0.042	0.776
Reduced Personal Accomplishment	176.774	27	0.002	0.975

Table 3. The Factors Affecting the Emotional Exhaustion Level of Academic Staff

Emotional Exhaustion Level	Variable	Coef. (β)	Odds Ratio (e^{β})	p value
Low category vs High and Moderate category	Threshold 1	0.243		0.971
Low and Moderate category vs High category	Threshold 2	5.068		0.445
Having own room at work	Yes No*	-1.476	0.023 (4.37**)	0.024
Satisfaction of colleagues	Yes No*	-1.713	0.180 (5.55**)	0.002
Exhaustion of the academic work	None	-2.694	0.068 (14.80**) 0.090 (11.07**)	0.049
	Low	-2.404		0.001
	Moderate High*	-0.680		0.206
Household Size	Alone	1.727	5.62	0.044
	Two	0.701		0.351
	Three	0.536		0.413
	Four*			

*Reference Categories

** The odds ratios under 1 are inverted to interpret the odds ratios rationally.

The results of POM for Emotional Exhaustion Level is given in Table 3. Having own room at work, satisfaction of colleagues, exhaustion of the academic work, household size are the variables that effect emotional exhaustion. The academic staff who are not having own room are 4.37 times more likely feel emotional exhaustion than who are having own room. The academic staff who are not satisfied with their colleagues are 5.55 times more likely feel emotional exhaustion than who are satisfied. The academic staff who feel high

exhaustion of the academic work are 14.80 times more likely feel emotional exhaustion than who never feel exhaustion of the academic work. The academic staff who feel high exhaustion of the academic work are 11.07 times more likely feel emotional exhaustion than who feel low exhaustion of the academic work. The academic staff who live alone are 5.62 times more likely feel emotional exhaustion than whose household size is four.

Table 4. The Factors Affecting the Depersonalization Level of Academic Staff

Depersonalization Level	Variable	Coef. (β)	Odds Ratio (e^{β})	p value
Low category vs High and Moderate category	Threshold 1	-8.433		0.070
Low and Moderate category vs High category	Threshold 2	-5.317		0.250
Average sleep time per day	Equal or Less than 6 Hours More than 6 Hours*	0.744	2.10	0.047
Exhaustion of the academic work	None	-4.163	0.015 (64.26**)	0.043
	Low	-0.583		0.363
	Moderate	-0.723		0.142
	High*			

*Reference Categories

** The odds ratios under 1 are inverted to interpret the odds ratios rationally.

The results of POM for Depersonalization Level is given in Table 4. Average sleep time per day and exhaustion of the academic work are the variables that effect depersonalization. The academic staff who sleep equal or less than 6

hours are 2.10 times more likely depersonalized than who sleep more than 6 hours. The academic staff who feel high exhaustion of the academic work are 64.26 times more likely depersonalized than who never feel exhaustion of the academic work.

Table 5. The Factors Affecting the Reduced Personal Accomplishment Level of Academic Staff

Reduced Personal Accomplishment Level	Variable	Coef. (β)	Odds Ratio (e^{β})	p value
Low category vs High and Moderate category	Threshold 1	-28.347		0.000
Low and Moderate category vs High category	Threshold 2	-23.487		0.000
Average sleep time per day	Equal or Less than 6 Hours More than 6 Hours*	0.968	2.63	0.046
Age groups	Under 27	1.408		0.251
	Between 28-35	2.344	10.42	0.033
	Between 36-43	2.119	8.32	0.050
	Between 44-51	2.886	17.92	0.012
	Over 52*			

*Reference Categories

The results of POMs for Reduced Personal Accomplishment Level is given in Table 5. Average sleep time per day and age are the variables that effect reduced personal accomplishment. Reduced in the personal accomplishment of academic staff who sleep equal or less than 6 hours is 2.63 times higher than those who sleep more than 6 hours. Reduced

in the personal accomplishment of academic staff who are between 28-35 years is 10.42 times higher than who are older than 52 years. Reduced in the personal accomplishment of academic staff who are between 36-43 years is 8.32 times higher than who are older than 52 years. Reduced in the personal accomplishment of academic staff who

are between 44-51 years is 17.92 times higher than who are older than 52 years.

4. CONCLUSION

The purpose of this study is to examine the academic staff's burnout level in terms of some variables. In this study, different from other studies both in Turkey and the other countries, POM method is used to find the levels of burnout and which variables are effective for the levels of burnout. Findings indicate that %6 of the academic staff is struggling with burnout. The variables that effect emotional exhaustion are having own room at work, satisfaction of colleagues, exhaustion of the academic work and household size. The results show that academicians feel emotional exhaustion if they do not have their own room at university, they do not get along with their colleagues and they live alone. Moreover, it is clear that there is so much pressure in academic life because of academic work load. The variables that effect depersonalization are average sleep time per day and exhaustion of the academic work. The results show that academicians are in tendency to be depersonalized because of academic work load and lack of sleep. The variables that effect reduced diminished personal accomplishment are average sleep time per day and age group. The results show that the academicians who are between 44-51 years old and suffer from sleeplessness have reduced personal accomplishment.

As a conclusion, in the light of the results of this study, it could be suggested to university administrators to supply better physical conditions and avoid work overload for academic staff, hence, education life quality improves and consequently both the academic staff and students are satisfied. it must be mentioned that burnout is an important topic that needs to be investigated further in academic life. In the future studies, researchers could extend burnout studies using POM to public and private universities in Turkey and make comparisons of burnout levels of academic staff among public and private universities.

REFERENCES

- [1] C. Maslach, W.B. Schaufeli, P.L. Michael. "Job Burnout.", *Annu. Rev. Psychol.*, vol. 52, pp. 397-422, 2001.
- [2] H.J. Freudenberger. "Staff Burn-Out." *Journal of Social Issues*, vol.30, number 1, pp. 159-165, 1974.
- [3] C. Maslach and S.E. Jackson. "The Measurement of Experienced Burnout." *Journal of Occupational Behavior*, vol. 2, pp. 99-113, 1981.
- [4] E.E. Demirel and T.P Cephe. "Looking into burnout levels among English language instructors." *Journal of Language and Linguistic Studies*, vol. 11, number 1, pp. 1-14, 2015
- [5] A. Hamidizadeh, K. Hasan and H. Fatemeh. "Is workaholism antecedent of Burn out?" *European Journal of Academic Essays*, vol. 1, number 8, pp.1-9, 2014.
- [6] J.R. Lackritz. "Exploring burnout among university faculty: incidence, performance, and demographic issues." *Teaching and Teacher Education*, vol. 20, pp. 713-729, 2014.
- [7] A.G. Blix, R.J. Cruise, B.N. Mitchell, G.G Blix. "Occupational stress among university teachers." *Educational Research*, vol. 36, number 2, pp. 157-169, 1994.
- [8] B. Toker. "Burnout Among University Academicians: An Empirical Study on The Universities of Turkey." *Doğuş Üniversitesi Dergisi*, vol. 12, number 1, pp.114-121, 2011.
- [9] G. Budak and O. Sürgevil. "Tükenmişlik ve tükenmişliği etkileyen örgütsel faktörlerin analizine ilişkin akademik personel üzerinde bir uygulama." *D.E.Ü. İ.İ.B.F. Dergisi*, vol. 20, number 2, pp. 95-108, 2005.
- [10] İ.Y. Aktuğ, A. Susur, S. Keskin, Y. Balcı, G. Seber. "Osmangazi Üniversitesi Tıp Fakültesi'nde çalışan hekimlerde tükenmişlik düzeyleri." *Osmangazi Tıp Dergisi*, vol. 28, number 2, pp. 91-101, 2006.
- [11] S. Tümkiye. "Faculty burnout in relation to work environment and humor as a coping strategy." *Educational Sciences: Theory &*

- Practice*, vol. 6, number 3, pp. 911-921, 2006.
- [12] H. Gürbüz, H. Tutar, N.Ö. Başpınar. "Burnout levels of executive lecturers: a comparative approach in three universities." *Sosyal Bilimler Dergisi*, vol. 18, pp. 65-85, 2007.
- [13] K. Ardiç and S. Polatçı. "Tükenmişlik Sendromu Akademisyenler Üzerinde Bir Uygulama (GOÜ Örneği)". *Gazi Üniversitesi İktisadi ve İdari Bilimler Fakültesi Dergisi*, vol. 10, number 2, pp. 69-96, 2008.
- [14] M. Eker and A. Anbar. "Work related factors that affect burnout among accounting and finance academicians." *İş-Güç, Endüstri İlişkileri ve İnsan Kaynakları Dergisi*, vol. 10, number 4, pp. 111-137, 2008.
- [15] C. Serinkan and A. Bardakçı. "Pamukkale Üniversitesi'ndeki akademik personelin iş tatminleri ve tükenmişlik düzeylerine ilişkin bir araştırma." *Sosyal Bilimler Dergisi*, vol. 21, pp. 115-132, 2009.
- [16] R. Demir, E. Türkmen, A. Doğan. "Examination of Burnout Level of Academics in Terms of Demographic Variables." *International Journal of Social Sciences and Education Research*, vol. 1, number 4, pp. 1194-1222, 2015.
- [17] D.W. Hosmer and S. Lemeshow. *Applied Logistic Regression*. Second Edition, Wiley Series in Probability and Statistics, 2000, pp. 375.
- [18] E. Arı and Z. Yıldız Z. "Parallel Lines Assumption in Ordinal Logistic Regression and Analysis Approaches." *International Interdisciplinary Journal of Scientific Research*, vol. 1, number 3, pp. 8-23, 2014.
- [19] D.G. Kleinbaum, and M. Klein. "Ordinal Logistic Regression," in *Logistic Regression*. D.G. Kleinbaum and M. Klein Eds., New York: Springer, 2010, pp.463-488.
- [20] A.A. O'Connell. "Logistic Regression Models for Ordinal Response Variables." *Quantitative Applications in the Social Sciences*, Sage Publications, pp. 105, 2006.
- [21] N. A. Barak. "An Application of Ordinal and Multinomial Logit Models." MS thesis, Hacettepe University Institute of Health Sciences in *Biostatistics*, Ankara, 2005.
- [22] P. McCullagh. "Regression Models for Ordinal Data." *Journal of the Royal Statistical Society, Series B (Methodological)*, vol. 42, no. 2, pp. 109-142, 1980.
- [23] R. Brant. "Assessing Proportionality in the Proportional Odds Model for Ordinal Logistic Regression." *Biometrics*, vol. 46, number 4, pp. 1171-1178, 1990.
- [24] R. Bender and U. Grouven. "Using Binary Logistic Regression Models for Ordinal Data with Non- Proportional Odds." *J. Clin Epidemiol* vol. 51, number 10, pp. 809-816, 1998.
- [25] A.S. Fullerton and J. Xu. "The proportional odds with partial proportionality constraints model for ordinal response variables." *Social science research*, vol. 41, number 1, pp. 182-198, 2012.
- [26] D.G. Kleinbaum and C.V. Ananth. "Regression Models for Ordinal Responses: Review of Methods and Applications." *International Journal of Epidemiology*, vol. 26, number 6, pp. 1323-1333, 1997.
- [27] C. Ergin. "Doktor ve hemşirelerde tükenmişlik ve Maslach Tükenmişlik Ölçeği'nin Uyarlanması," VII. Ulusal Psikoloji Kongresi Bilimsel Çalışmaları, Türk Psikologlar Derneği Yayınları, Ankara, 1992, pp. 143-154.
- [28] O. Çam. "Tükenmişlik Envanterinin geçerlik ve güvenilirliğinin araştırılması (Investigation of the validity and reliability of Burnout Inventory)," 7th National Psychology Congress Proceedings, Ankara, Turkey, 1992, pp. 155-160.

	SAKARYA UNIVERSITY JOURNAL OF SCIENCE		 SAKARYA UNIVERSITY
	e-ISSN: 2147-835X http://www.saujs.sakarya.edu.tr		
	<u>Received</u> 23-03-2018 <u>Accepted</u> 29-05-2018	<u>Doi</u> 10.16984/saufenbilder.409153	

Bisector Surfaces Through A Common Line Of Curvatures And Its Classifications

Muhammed Talat SARIAYDIN*¹

Abstract

In this paper, we study the Bisector surface, which defines the line of curvature on a surface play an importance role. Firstly, the Bisector surface constructed by a point and a space curve given in Euclidean 3-space. Then, it is investigated that the necessary and sufficient condition for directrix curve of this surface to satisfy line of curvature. After this, we classify the Bisector surfaces.

Keywords: Bisector surface, ruled surface, the line of curvature, rational surface.

1. INTRODUCTION

The bisector surface is obtained points which are equidistant from any two objects. The distance is measured orthogonal to both objects. For an object in the plane or space, the medial surface is also much the same related to the bisector surface. Therefore, the medial surface can be defined as the set of interior points of the object which have the minimum distance, [4,15]. Additionally, the computation of the bisector often not easy, [15]. Then, this surface is often used in scientific research from the past with geometric properties of two curve, a curve with a point, a curve with surface and two surface bisectors in Euclidean 3- space.

For example, Horvath proved that all bisectors are topological images of a plane of the embedding Euclidean 3-space in [6] and Elber studied a new

computational model for constructing a curve-surface and surface-surface bisectors in E^3 in [5].

Because Modern surface modeling systems contain the Ruled surface, this surface frequently used many areas such that simulation of the rigid body, design, production, motion analysis. For this reason, it has an important place in kinematical geometry and positional mechanisms in Euclidean 3-space. For instance, Brosius classified rank 2-vector bundles on a ruled surface and Onder and other authors viewed ruled surfaces Minkowski space, [2,11,14].

In this paper, we obtain a classification, which is the Bisector surface constructed by a point and a space curve given in Euclidean 3-space. Firstly, it is tersely summarized properties the basic concepts on surfaces. Then, we give general conditions to classify the Bisector surface. Finally, we give some

* Corresponding Author

¹ Selçuk University, Faculty of Science, Department of Mathematics, Konya-talatsariaydin@gmail.com

examples and showed them with the figure in E^3 .

$$\tau = \frac{(\alpha', \alpha'', \alpha''')}{\kappa^2}. \quad (9)$$

2. PRELIMINARIES

A ruled surface is a surface swept out by a straight line moving along a curve β . The various positions of the generating line are called the rulings of the surface. Such a surface thus always has a parametrization in ruled form

$$X(u, v) = \beta(u) + v\delta(u), \quad (1)$$

where we call β the base curve, δ the director curve. Alternatively, we may visualize δ as a vector field on β , [13].

The ruled surface (1) is developable iff

$$(\beta'(u), \delta(u), \delta'(u)) = 0. \quad (2)$$

Then, the developable surface is cylinder iff

$$m(u) \times m'(u) = 0, \quad (3)$$

where $\mathbf{T}(s)$ is a tangent vector of $\beta(u)$ and $m(u) = \delta(u) \times \mathbf{T}(s)$. The developable surface is a cone iff

$$w'(u) = 0, \quad (4)$$

where $w(u)$ is the line of striction of surface (1). The developable surface is a tangent surface iff, [12],

$$w'(u) \parallel m(u). \quad (5)$$

Denote by $\{\mathbf{T}, \mathbf{N}, \mathbf{B}\}$ the moving Frenet frame along the curve α in the space E^3 . For an arbitrary curve α with first and second curvature, κ and τ in the space E^3 , the following Frenet-Serret formulae is given

$$\mathbf{T}' = \kappa\mathbf{N}, \quad (6)$$

$$\mathbf{N}' = -\kappa\mathbf{T} + \tau\mathbf{B}, \quad (7)$$

$$\mathbf{B}' = -\tau\mathbf{N}. \quad (8)$$

Here, curvature functions are defined by $\kappa = \kappa(s) = \|\mathbf{T}'(s)\|$ and $\tau(s) = -\langle \mathbf{N}, \mathbf{B}' \rangle$. Torsion of the curve α is given by the aid of the mixed product, [14],

3. CLASSIFICATIONS OF THE BISECTOR SURFACES IN E^3

In this paper, our goal is to find the necessary and sufficient condition for the directrix curve of this surface to satisfy line of curvature. In [16], to construct the Bisector surface obtained a point and a space curve, they gave the parametric form of the surface as follows;

$$\mathbf{B}(s, t) = (\mathbf{b}_x(s, t), \mathbf{b}_y(s, t), \mathbf{b}_z(s, t)). \quad (10)$$

Here,

$$\begin{aligned} \mathbf{b}_x(s, t) &= \mathbf{h}_1(s) + t\mathbf{q}_x(s), \\ \mathbf{b}_y(s, t) &= \mathbf{h}_2(s) + t\mathbf{q}_y(s), \\ \mathbf{b}_z(s, t) &= \mathbf{h}_3(s) + t\mathbf{q}_z(s), \\ \mathbf{q}_i(s) &= t_i^c(s) \times (c_i(s) - p_i) \end{aligned} \quad (11)$$

and q_i is components of direction vector,

$$\mathbf{h}_1(s) = \frac{1}{\mathbf{J}(s)} \begin{vmatrix} d_1(s) & y'(s) & z'(s) \\ d_2(s) & y_n(s) & z_n(s) \\ m(s) & y_b(s) & z_b(s) \end{vmatrix}, \quad (12)$$

$$\mathbf{h}_2(s) = \frac{1}{\mathbf{J}(s)} \begin{vmatrix} x'(s) & d_1(s) & z'(s) \\ x_n(s) & d_2(s) & z_n(s) \\ x_b(s) & m(s) & z_b(s) \end{vmatrix}, \quad (13)$$

$$\mathbf{h}_3(s) = \frac{1}{\mathbf{J}(s)} \begin{vmatrix} x'(s) & y'(s) & d_1(s) \\ x_n(s) & y_n(s) & d_2(s) \\ x_b(s) & y_b(s) & m(s) \end{vmatrix}, \quad (14)$$

and

$$\mathbf{J}(s) = \begin{vmatrix} x'(s) & y'(s) & z'(s) \\ x_n(s) & y_n(s) & z_n(s) \\ x_b(s) & y_b(s) & z_b(s) \end{vmatrix}, \quad (15)$$

Firstly, we will show that it is the line of curvature of directrix curve of the Bisector surface and developable surface of the Bisector surface

Theorem 3.1. The directrix curve of the Bisector surface is a line of curvature if and only if

$$\theta = -\int_{s_0}^s \tau ds + \theta_0, \quad (16)$$

$$\frac{\mathbf{I}_2}{\sqrt{\mathbf{I}_2^2 + \mathbf{I}_3^2}} = \sin \theta, \quad \frac{\mathbf{I}_3}{\sqrt{\mathbf{I}_2^2 + \mathbf{I}_3^2}} = -\cos \theta. \quad (17)$$

Proof. Assume that the normal surface of $H(s)$ is

$$K(s, t) = H(s) + tL(s). \quad (18)$$

Here,

$$L(s) = \mathbf{n}(s)\cos\theta(s) + \mathbf{b}(s)\sin\theta(s) \quad (19)$$

and $\{\mathbf{t}(s), \mathbf{n}(s), \mathbf{b}(s)\}$ is the Frenet frame of directrix curve of Bisector. Because the surface $K(s, t)$ is a developable surface. we can easily write the following equation,

$$(H_s, L, L_s) = 0, \quad (20)$$

$$\Leftrightarrow (\mathbf{t}, \mathbf{n}\cos\theta + \mathbf{b}\sin\theta, (-\theta_s \sin\theta - \tau \sin\theta)\mathbf{n} + (\tau \cos\theta + \theta_s \cos\theta)\mathbf{b}) = 0 \quad (21)$$

$$\Leftrightarrow \theta_s + \tau = 0, \quad (22)$$

$$\Leftrightarrow \theta_s = -\tau \quad (23)$$

From the last equation above, we can easily write

$$\theta = -\int_{s_0}^s \tau ds + \theta_0. \quad (24)$$

On the other hand, suppose that curve $t_i^c(s) \times (c_i(s) - p_i)$ written by without loss of generality below form;

$$t_i^c(s) \times (c_i(s) - p_i) = \mathbf{I}_1(s)\mathbf{t}(s) + \mathbf{I}_2(s)\mathbf{n}(s) + \mathbf{I}_3(s)\mathbf{b}(s). \quad (25)$$

Here, $t_i^c(s) \times (c_i(s) - p_i)$ is a unit speed curve, $t_i^c(s) \times (c_i(s) - p_i) \neq 0$, and $\mathbf{I}_1^2 + \mathbf{I}_2^2 + \mathbf{I}_3^2 = 1$. Then, the corresponding Bisector surface is

$$B(s, t) = H(s) + t(t_i^c(s) \times (c_i(s) - p_i)), \quad (26)$$

$$\mathbf{I}_1^2 + \mathbf{I}_2^2 + \mathbf{I}_3^2 = 1, t_i^c(s) \times (c_i(s) - p_i) \neq 0. \quad (27)$$

Therefore, normal of the Bisector surface is

$$N(s, t_0) = \frac{-\mathbf{I}_3(s)\mathbf{n}(s) + \mathbf{I}_2(s)\mathbf{b}(s)}{\sqrt{\mathbf{I}_2^2 + \mathbf{I}_3^2}}. \quad (28)$$

Because the directrix curve is a line of curvature, normal of Bisector surface $B(s, t)$ and normal of

curve $H(s)$ are parallel to each other. Reconsidering these equations (19) and (28). We can be express as follows

$$\frac{\mathbf{I}_2}{\sqrt{\mathbf{I}_2^2 + \mathbf{I}_3^2}} = \sin \theta, \quad \frac{\mathbf{I}_3}{\sqrt{\mathbf{I}_2^2 + \mathbf{I}_3^2}} = -\cos \theta.$$

Then, the proof is complete.

Theorem 3.2. Assume that $B(s, t)$ is the developable Bisector surface with a common line of curvature. Bisector surface $B(s, t)$ is a cylinder if and only if $t_i^c(s) \times (c_i(s) - p_i)$ is a constant curve, and $a = 0$.

Proof. We suppose that the Bisector surface $B(s, t)$ is a developable surface. Then, it is easily seen that

$$\det\left(H_s(s), t_i^c(s) \times (c_i(s) - p_i), \frac{d}{ds} t_i^c(s) \times (c_i(s) - p_i)\right) = 0. \quad (29)$$

From the last equation above, $H_s(s)$, $t_i^c(s) \times (c_i(s) - p_i)$, $\frac{d}{ds} t_i^c(s) \times (c_i(s) - p_i)$ are linearly dependent. That is, we get

$$a(s)H(s) + b(s)(t_i^c(s) \times (c_i(s) - p_i)) + c(s)\left(\frac{d}{ds} t_i^c(s) \times (c_i(s) - p_i)\right) = 0, \quad (30)$$

If $a(s) = 0$, then

$$\left\langle t_i^c(s) \times (c_i(s) - p_i), \frac{d}{ds} t_i^c(s) \times (c_i(s) - p_i) \right\rangle = 0. \quad (31)$$

That is, $t_i^c(s) \times (c_i(s) - p_i)$ is a constant curve. Thus, the Bisector surface $B(s, t)$ is a cylinder.

Remark 3.3. We assume that $t_i^c(s)$ and $(c_i(s) - p_i)$ are linearly dependent. Because $c_i(s)$ is regular, and so $c_i(s)$ and $(c_i(s) - p_i)$ parallel to each other. Then, we can see that the point p_i is on tangent of curve $c_i(s)$ for all s . That is, we are obtain a degererate case.

Theorem 3.4. Assume that $B(s, t)$ is the developable Bisector surface with a common line of

curvature. Bisector surface $B(s, t)$ is a cone if and only if

$$a \neq 0, \quad (32)$$

$$\xi(s) = \mu_s(s). \quad (33)$$

Proof. We suppose that the coefficient of curve $H_s(s)$ in eq. (30) is not zero. That is, $a \neq 0$. Then we can write

$$H_s(s) = \xi(s)Q(s) + d(s)Q_s(s), \quad (34)$$

where

$$\xi(s) = -b/a, d(s) = -c/a. \quad (35)$$

On the other hand, we can write from eq. (26)

$$H(s) = \kappa(s) + \mu(s)Q(s). \quad (36)$$

Here, if

$$\mu(s) = \frac{\langle H(s), Q_s(s) \rangle}{\|Q_s(s)\|^2}, \quad (37)$$

then $\kappa(s)$ is a striction curve. Taking derivative eq. (36), it is easily seen that

$$\kappa(s) = (\xi(s) - \mu(s))Q(s). \quad (38)$$

From the last equation above, we assume that $\xi(s) = \mu(s)$. We get $\kappa_s(s) = 0$. That is $\kappa(s) = \kappa_0$. Rearranging eqs. (26) and (36), we get

$$B(s, t) = \kappa_0 + (\mu(s) + t)Q(s). \quad (39)$$

That is, the Bisector surface $B(s, t)$ is a cone.

Theorem 3.5. Assume that $B(s, t)$ is the developable Bisector surface with a common line of curvature. Bisector surface $B(s, t)$ is a tangential developable if and only if

$$a \neq 0, \quad (40)$$

$$\xi(s) \neq \mu_s(s). \quad (41)$$

Proof. The proof is clear that theorem 3.3.

Example 3.6. Let us consider a fixed point and a regular unit speed curve parametrized by s in E^3 by

$$b = (1, 1, 1), \quad (42)$$

$$a(s) = (\cos s, 0, \sin s). \quad (43)$$

One calculates tangent of this curve and the

direction vector, respectively, as the following

$$t_a(s) = (-\sin s, 0, \cos s), \quad (44)$$

$$P(s) = (\cos s, 1 - \cos s - \sin s, \sin s). \quad (45)$$

Then, the figure of the Bisector surface, $\pi/8 \leq s \leq \pi/2$ $1 \leq t \leq 5$, is



Figure 1. Bisector surface

Example 3.7. Let us consider a fixed point and a regular unit speed curve parametrized by s in E^3 by

$$w = (1, 0, 1), \quad (46)$$

$$q(s) = (0, \cos s, \sin s). \quad (47)$$

One calculate the direction vector, respectively, as the following

$$P(s) = (\sin s - 1, -\cos s, -\sin s). \quad (48)$$

Then, the figure of the Bisector surface is



Figure 2. Bisector Ruled surface

REFERENCES

- [1] V. Asil, T. Körpınar, and E. Turhan. "On inextensible flows of tangent developable of

- biharmonic B-Slant helices according to Bishop frames in the special 3-dimensional Kenmotsu manifold." *Boletim da Sociedade Paranaense de Matemática*, vol. 31, no. 1, pp. 89-97, 2013.
- [2] J. E. Brosius, "Rank 2-Vector Bundels on a Ruled Surface," *Math. Ann.*, vol. 256, pp. 155-168, 1983.
- [3] M. P. Do Carmo, "Differential Geometry of Curves and Surfaces, Englewood Cliffs," *Prentice Hall*, 1976.
- [4] G. Elber and K. Myung-Soo, "The Bisector Surface of Rational Space Curves," *ACM Transactions on Grap.*, vol. 17, pp. 32-49 1998.
- [5] G. Elber and M. S. Kim, "A Computational Model for Nonrational Bisector Surfaces: Curve-Surface and Surface-Surface Bisectors," *Geometric Modeling and Processing 2000. Theory and Applications*, pp. 364-372, 2000.
- [6] A. G. Horvath, "Bisectors in Minkowski 3-space," *Sci.Reseach J.Bolyai*, 2000.
- [7] T. Körpınar and E. Turhan, "Time-tangent surfaces around Biharmonic particles and its Lorentz transformations in Heisenberg spacetime." *International Journal of Theoretical Physics*, vol. 52, no. 12 pp. 4427-4438, 2013.
- [8] T. Körpınar, and E. Turhan, "Rectifying Developable Surface of Timelike Biharmonic Curve In The Lorentzian Heisenberg Group Heis." *TWMS Journal of Applied and Engineering Mathematics*, vol. 2, no. 1, pp. 101, 2012.
- [9] T. Körpınar, and E. Turhan, "New solution of differential equation for dual curvatures of dual spacelike biharmonic curves with timelike principal normal according to dual Bishop frames in the dual Lorentzian space." *Acta Universitatis Apulensis*, vol. 30, pp. 77-86, 2012.
- [10] T. Körpınar, and E. Turhan, "Parallel Surfaces to S-Tangent Surfaces of Biharmonic S-Curves according to Sabban Frame in Heisenberg Group Heis3." *Journal of Science and Arts* vol. 2, no. 20, pp. 229-236, 2012.
- [11] W. Kühnel, "Curves- Surfaces- Manifolds, Differential Geometry," *Amer. Math. Soc.*, 2003.
- [12] C. Li, R. Wang and C. Zhu, "An Approach For Designing a Developable Surface Through a Given Line of Curvature," *Comp. Aid. Des.*, vol. 45, pp. 621-627, 2013.
- [13] B. O'Neill, "Elementary Differential Geometry," New York, *Academic Press Inc.*, 1966.
- [14] M. Önder and H. H. Uğurlu, "Mannheim Offsets of the Timelike Ruled Surfaces with Spacelike Rulings in Dual Lorentzian Space," arXiv:0906.4660v3 [math.Dg]
- [15] M. Peternell, "Geometric Properties of Bisector Surfaces," *Graphical Models*, vol. 62 pp. 202-236, 2000.
- [16] M. T. Sariaydin and V. Asil, "On Bisector Surface in Minkowski Space," *Prespacetime*, vol. 8, no. 7, pp. 865-874, 2017.
- [17] Y. Ünlütürk and E. Ozusaglam, "On parallel surfaces in Minkowski 3-space." *TWMS Journal of Applied and Engineering Mathematics*, vol. 3, no. 2, pp. 214, 2013.
- [18] Y. Ünlütürk and C. Ekici, "Parallel Surfaces of Spacelike Ruled Weingarten Surfaces in." *New Trends in Mathematical Sciences*, vol. 1, no. 1, pp. 85-92, 2015.
- [19] Y. Ünlütürk, "On Timelike Parallel Ruled Surfaces With Spacelike Ruling." *Konuralp Journal of Mathematics (KJM)*, vol. 1, no. 1, 24-33, 2013.
- [20] Y. Ünlütürk, M. Cimdiker, and C. Ekici, "Characteristic properties of the parallel ruled surfaces with Darboux frame in Euclidean 3-space." *Communication in Mathematical Modeling and Applications*, vol. 1, no. 1, pp. 26-43, 2016.

	SAKARYA UNIVERSITY JOURNAL OF SCIENCE		 SAKARYA UNIVERSITY
	e-ISSN: 2147-835X http://www.saujs.sakarya.edu.tr		
	<u>Received</u> 27-03-2018 <u>Accepted</u> 29-05-2018	<u>Doi</u> 10.16984/saufenbilder.410044	

On Total Shear Curvature of Surfaces in E^{n+2}

Betül Bulca*¹ & Kadri Arslan¹

Abstract

In this study we consider the surfaces in E^{n+2} . First, we give preliminaries of second fundamental form and curvature properties of the surfaces. Further, we obtained some results related with the total shear curvature of the surfaces. Finally, we give an example of a surface in Euclidean 4-space E^4 with vanishing shear curvature.

Keywords: Shear tensor, Gaussian curvature, mean curvature, umbilical surface.

1. INTRODUCTION

The second fundamental tensor of a Riemannian submanifold plays an important role to characterize the total curvature and mean curvature of the submanifold. The shape operator of a submanifold is related with the second fundamental tensor. So, in order to characterize the umbilicity of the submanifolds we need to find the shape operator of the submanifold.

Recently, Cipriani at all. introduced the concept of total shear tensor and shear operator for a Riemannian submanifold [5].

For the case of surfaces in n-dimensional Euclidean spaces E^n , K. Enomoto defined a difference function F to characterize the umbilicity of the surfaces Euclidean spaces [7].

This paper is organized as follows: In section 2, we give some basic concepts of the second fundamental form and curvatures of the surfaces in E^n . In Section 3, we define the total shear curvature of a surface in (n+2)-dimensional Euclidean space E^{n+2} with respect to its total shear tensor. Further, we obtain some results of these surfaces. In the final section, we give an example

of generalized spherical surfaces in E^4 which have vanishing total shear curvature.

2. BASIC CONCEPTS

Consider a surface $M \subset E^{n+2}$ given with the parametrization $X(u, v)$. The coefficients of the first fundamental form of M are given by

$$g_{11} = \langle X_u, X_u \rangle, g_{12} = \langle X_u, X_v \rangle, g_{22} = \langle X_v, X_v \rangle \quad (2.1)$$

where $X_u, X_v \in T_p M$. For the local vector fields $X_1 = X_u, X_2 = X_v$ tangent to M , the equation of Gauss is defined by

$$\tilde{\nabla}_{X_i} X_j = \nabla_{X_i} X_j + h(X_i, X_j), \quad 1 \leq i, j \leq 2 \quad (2.2)$$

where ∇ and $\tilde{\nabla}$ are the covariant derivatives of M and E^{n+2} , respectively [4].

For any arbitrary orthonormal normal frame field $\{N_1, N_2, \dots, N_n\}$ of M , the Weingarten equation of M becomes

$$\tilde{\nabla}_{X_j} N_\alpha = -A_{N_\alpha} X_j + \nabla_{X_j}^\perp N_\alpha, \quad X_j \in \chi(M) \quad (2.3)$$

where ∇^\perp is the connection in the normal bundle. These two equations satisfy the following relations:

* Corresponding Author

¹ Uludağ University, Faculty of Arts and Science, Department of Mathematics, Bursa,
bbulca@uludag.edu.tr, arslan@uludag.edu.tr

$$\langle A_{N_\alpha} X_j, X_i \rangle = \langle h(X_i, X_j), N_\alpha \rangle = L_{ij}^\alpha, \quad (2.4)$$

$$1 \leq i, j \leq 2; 1 \leq \alpha \leq n.$$

From the equation (2.2) one can get the second fundamental form

$$h(X_i, X_j) = \sum_{\alpha=1}^n L_{ij}^\alpha N_\alpha, 1 \leq i, j \leq 2. \quad (2.5)$$

The shape operator matrix of the surface M with respect to N_α is given by (see, [2])

$$A_{N_\alpha} = \begin{pmatrix} \frac{L_{11}^\alpha}{g_{11}} & \frac{1}{\sqrt{g}} \left(L_{12}^\alpha - \frac{g_{12}}{g_{11}} L_{11}^\alpha \right) \\ \frac{1}{\sqrt{g}} \left(L_{12}^\alpha - \frac{g_{12}}{g_{11}} L_{11}^\alpha \right) & \frac{1}{g} \left(g_{11} L_{22}^\alpha - 2g_{12} L_{12}^\alpha + \frac{g_{12}^2}{g_{11}} L_{11}^\alpha \right) \end{pmatrix} \quad (2.6)$$

Then the Gaussian curvature K of the surface M is given by

$$K = \sum_{\alpha=1}^n \det(A_{N_\alpha}) = \frac{1}{g} \sum_{\alpha=1}^n (L_{11}^\alpha L_{22}^\alpha - (L_{12}^\alpha)^2), \quad (2.7)$$

where $g = g_{11}g_{22} - g_{12}^2$ is the Riemannian metric on M .

Further, the mean curvature vector of the surface M is given by

$$\begin{aligned} \vec{H} &= \frac{1}{2} \sum_{\alpha=1}^n \text{tr}(A_{N_\alpha}) N_\alpha \\ &= \frac{1}{2g} \sum_{\alpha=1}^n (L_{11}^\alpha g_{22} + L_{22}^\alpha g_{11} - 2L_{12}^\alpha g_{12}) N_\alpha. \end{aligned} \quad (2.8)$$

A point p is said to be *umbilical* with respect to N_α if A_{N_α} is proportional to the identity transformation of $T_p M$. Consequently, M is called *totally umbilical* if M is umbilical at every point of M [3].

3. THE TOTAL SHEAR CURVATURE OF THE SURFACES IN E^{n+2}

Let M be a smooth surface in $(n+2)$ -dimensional Euclidean space E^{n+2} . The second fundamental tensor ϕ on $T_p M$ is defined as follows; chose an orthonormal frame $\{N_1, N_2, \dots, N_n\}$ of $T_p^\perp M$ and for each α , $1 \leq \alpha \leq n$ define maps

$$\phi_\alpha : T_p M \times T_p M \rightarrow T_p^\perp M$$

$$\phi_\alpha(X_i) = A_{N_\alpha}(X_i) - \langle \vec{H}, N_\alpha \rangle X_i, i = 1, 2. \quad (3.1)$$

The second fundamental tensor ϕ is given by (see, [6])

$$\phi(X_i, X_j) = \sum_{\alpha=1}^n \langle \phi_\alpha(X_i), X_j \rangle N_\alpha. \quad (3.2)$$

Substituting (2.4), (2.5), (2.8) and (3.1) into (3.2) we obtain the following result.

Proposition 3.1. Let M be a local surface in E^{n+2} given with the regular patch $X(u, v)$. For the orthonormal frame $\{N_1, N_2, \dots, N_n\}$ of $T_p^\perp M$ the second fundamental tensor ϕ is

$$\phi(X_i, X_j) = \sum (L_{ij}^\alpha - g_{ij} H_\alpha) N_\alpha \quad (3.3)$$

where H_α is the α^{th} mean curvature of the surface M defined by

$$H_\alpha = \frac{1}{2g} (L_{11}^\alpha g_{22} + L_{22}^\alpha g_{11} - 2L_{12}^\alpha g_{12}). \quad (3.4)$$

Furthermore, the total shear tensor \tilde{h} is defined as:

$$\tilde{h}(X_i, X_j) = h(X_i, X_j) - g_{ij} \vec{H}, X_i, X_j \in \mathcal{X}(M) \quad (3.5)$$

where g is the induced metric and \vec{H} is the mean curvature vector of M . The shear operator associated to $N_\alpha \in \mathcal{X}^\perp(M)$ is defined by:

$$\tilde{A}_{N_\alpha} = A_{N_\alpha} - \text{tr} \tilde{A}_{N_\alpha} I \quad (3.6)$$

where I denotes the identity operator [5].

The total shear tensor and shear operators are obviously related by

$$\langle \tilde{A}_{N_\alpha} X_i, X_j \rangle = \langle \tilde{h}(X_i, X_j), N_\alpha \rangle; \quad (3.7)$$

$$\forall X_i, X_j \in \mathcal{X}(M), \forall N_\alpha \in \mathcal{X}^\perp(M).$$

Substituting (2.5) and (2.8) into (3.5) we get the following result.

Proposition 3.2. Let M be a smooth surface in $(n+2)$ -dimensional Euclidean space E^{n+2} . For the orthonormal frame $\{N_1, N_2, \dots, N_n\}$ of $T_p^\perp M$ the total shear tensor \tilde{h} is given by

$$\tilde{h}(X_i, X_j) = \sum_{\alpha=1}^n (L_{ij}^\alpha - g_{ij} H_\alpha) N_\alpha. \quad (3.8)$$

As a consequence of previous propositions we obtain the following result.

Corollary 3.3. Let M be a local surface in $(n+2)$ -dimensional Euclidean space E^{n+2} with the regular patch $X(u, v)$. For the orthonormal frame $\{N_1, N_2, \dots, N_n\}$ of $T_p^\perp M$ the total shear tensor \tilde{h} coincides with the second fundamental tensor ϕ , i.e.,

$$\phi(X_i, X_j) = \tilde{h}(X_i, X_j). \quad (3.9)$$

By the use of total shear tensor \tilde{h} defined in (3.5) it is possible to define total shear curvature \tilde{K} of M as follows;

Definition 3.4. Let M be a local surface in $(n+2)$ -dimensional Euclidean space E^{n+2} . The total shear curvature \tilde{K} of M at point p is defined by:

$$\tilde{K}(p) = \frac{1}{g} \sum_{\alpha=1}^n \left\{ \begin{array}{l} \langle \tilde{h}(X_u, X_u), \tilde{h}(X_v, X_v) \rangle \\ - \langle \tilde{h}(X_u, X_v), \tilde{h}(X_u, X_v) \rangle \end{array} \right\}. \quad (3.10)$$

The following result shows that the total shear curvature \tilde{K} is related with the Gaussian curvature K and the mean curvature $H = \|\tilde{H}\|$ of M .

Lemma 3.5. Let M be a local surface in $(n+2)$ -dimensional Euclidean space E^{n+2} with total shear curvature \tilde{K} . Then

$$\tilde{K} = K - H^2 \quad (3.11)$$

holds.

Proof. Let us assume that M be a smooth surface in E^{n+2} . Then, from (3.8) and (3.10) we have

$$\begin{aligned} \tilde{K} &= \frac{1}{g} \sum_{\alpha=1}^n (L_{11}^\alpha - g_{11}H_\alpha)(L_{22}^\alpha - g_{22}H_\alpha) - (L_{12}^\alpha - g_{12}H_\alpha)^2 \\ &= \frac{1}{g} \sum_{\alpha=1}^n (L_{11}^\alpha L_{22}^\alpha - (L_{12}^\alpha)^2) + \frac{1}{g} \sum_{\alpha=1}^n (g_{11}g_{22} - (g_{12})^2) H_\alpha^2 \\ &\quad - \frac{1}{g} \sum_{\alpha=1}^n (L_{11}^\alpha g_{22} + L_{22}^\alpha g_{11} - 2L_{12}^\alpha g_{12}) H_\alpha. \end{aligned}$$

Furthermore, by the use of (2.7) and (2.8) with (3.4) we get the result.

Remark. In [7] K. Enomoto defined a curvature function $F(p)$ on M by

$$F(p) = (H^2 - K)(p) \quad (3.12)$$

for $p \in M$. It is to see that, the total shear curvature \tilde{K} coincides with the Enomoto curvature function F , i.e. $\tilde{K}(p) = -F(p)$.

We obtain the following result;

Theorem 3.6. Let M be a local surface in $(n+2)$ -dimensional Euclidean space E^{n+2} . Then for every $p \in M$ the total shear curvature \tilde{K} is identically zero if and only if M is a totally umbilical surface in E^{n+2} .

Proof. Let $\{N_1, N_2, \dots, N_n\}$ be an orthonormal frame of $T_p^\perp M$. Using (2.7) and (2.8) the Enomoto curvature function becomes

$$F(p) = \|\tilde{H}^2(p) - K(p)\| = \frac{1}{4} \sum_{\alpha=1}^{n-2} \{ (tr(A_{N_\alpha}))^2 - 4\det(A_{N_\alpha}) \}$$

So, using elementary linear algebra, we can see that

$$(tr(A_{N_\alpha}))^2 - 4\det(A_{N_\alpha}) \geq 0,$$

and the equality holds if and only if A_{N_α} is proportional to the identity transformation [7]. This completes the proof of the theorem.

4. SPHERICAL SURFACES WITH VANISHING TOTAL SHEAR CURVATURE

Let M^2 be a local surface given with the regular patch (radius vector) $E^n \subset E^{n+1}$;

$$M^2 : X(u, v) = \varphi(u) + \lambda \cos\left(\frac{u}{c}\right) \rho(v) \quad (4.1)$$

where the vector function

$$\varphi(u) = (f_1(u), \dots, f_n(u); 0, \dots, 0)$$

given with

$$\|\varphi'(u)\|^2 = 1 - \frac{\lambda^2}{c^2} \sin^2\left(\frac{u}{c}\right)$$

and generates a generalized spherical curve with radius vector

$$\gamma(u) = \varphi(u) + \lambda \cos\left(\frac{u}{c}\right) e_{n+1} \quad (4.2)$$

and the vector function

$$\rho(v) = (0, \dots, 0; g_1(v), \dots, g_m(v))$$

given with $\|\rho(v)\| = 1$, $\|\rho'(v)\| = 1$. So, the surface M^2 is obtained by rotating the generalized spherical curve γ along the spherical curve ρ which is called generalized spherical surface in E^{n+m} .

For $n=2$ and $m=2$, the radius vector (4.2) satisfying the indicated properties described the generalized spherical surface given with the radius vector

$$X(u, v) = (f_1(u), f_2(u), \lambda \cos\left(\frac{u}{c}\right) \cos v, \lambda \cos\left(\frac{u}{c}\right) \sin v) \quad (4.3)$$

where

$$f_1(u) = \int \sqrt{1 - \frac{\lambda^2}{c^2} \sin^2\left(\frac{u}{c}\right)} \cos \alpha(u) du, \quad (4.4)$$

$$f_2(u) = \int \sqrt{1 - \frac{\lambda^2}{c^2} \sin^2\left(\frac{u}{c}\right)} \sin \alpha(u) du$$

are differentiable functions. This surface called a *generalized spherical surface* of first kind.

The tangent space of M^2 is spanned by the vector fields:

$$X_u = (f_1'(u), f_2'(u), -\frac{\lambda}{c} \sin\left(\frac{u}{c}\right) \cos v, -\frac{\lambda}{c} \sin\left(\frac{u}{c}\right) \sin v),$$

$$X_v = (0, 0, -\lambda \cos\left(\frac{u}{c}\right) \sin v, \lambda \cos\left(\frac{u}{c}\right) \cos v)$$

and hence the coefficients of the first fundamental form of M^2 are

$$g_{11} = 1, g_{12} = 0, g_{22} = \lambda^2 \cos^2\left(\frac{u}{c}\right). \quad (4.5)$$

We calculate the second partial derivatives of $X(u, v)$:

$$X_{uu} = (f_1''(u), f_2''(u), -\frac{\lambda}{c^2} \cos\left(\frac{u}{c}\right) \cos v, -\frac{\lambda}{c^2} \cos\left(\frac{u}{c}\right) \sin v),$$

$$X_{uv} = (0, 0, \frac{\lambda}{c} \sin\left(\frac{u}{c}\right) \sin v, -\frac{\lambda}{c} \sin\left(\frac{u}{c}\right) \cos v), \quad (4.6)$$

$$X_{vv} = (0, 0, -\lambda \cos\left(\frac{u}{c}\right) \cos v, -\lambda \cos\left(\frac{u}{c}\right) \sin v).$$

Let us consider the following orthonormal normal frame field of M^2 :

$$N_1 = \frac{1}{\kappa_\gamma} (f_1''(u), f_2''(u), -\frac{\lambda}{c^2} \cos\left(\frac{u}{c}\right) \cos v, -\frac{\lambda}{c^2} \cos\left(\frac{u}{c}\right) \sin v), \quad (4.7)$$

$$N_2 = \frac{1}{\kappa_\gamma} \left(-\frac{\lambda f_2'}{c^2} \cos\left(\frac{u}{c}\right) + \frac{\lambda f_2''}{c} \sin\left(\frac{u}{c}\right), -\frac{\lambda f_1''}{c} \sin\left(\frac{u}{c}\right) + \frac{\lambda f_1'}{c^2} \cos\left(\frac{u}{c}\right), (f_1' f_2'' - f_2' f_1'') \cos v, (f_1' f_2'' - f_2' f_1'') \sin v \right)$$

where

$$\kappa_\gamma = \sqrt{(f_1'')^2 + (f_2'')^2 + \frac{\lambda^2}{c^4} \cos^2\left(\frac{u}{c}\right)} \quad (4.8)$$

is the curvature of the profile curve γ .

Using (4.6) and (4.7) we can calculate L_{ij}^α as follows;

$$L_{11}^1 = \kappa_\gamma, L_{12}^1 = L_{21}^1 = L_{11}^2 = 0,$$

$$L_{22}^1 = \frac{\lambda^2 \cos^2\left(\frac{u}{c}\right)}{c^2 \kappa_\gamma}, \quad (4.9)$$

$$L_{22}^2 = -\frac{\lambda \cos\left(\frac{u}{c}\right) \kappa_1}{\kappa_\gamma}$$

where

$$\kappa_1 = f_1' f_2'' - f_2' f_1'' \quad (4.10)$$

is the curvature of the projection of the curve γ on the Oe_1e_2 - plane [1].

As a consequence of (2.7), (2.8), (4.9) and (3.11) it is easy to show that the total shear curvature \tilde{K} is identically zero if and only if

$$(g_{22} L_{11}^1 - L_{22}^1)^2 + (L_{22}^2)^2 = 0 \quad (4.11)$$

holds.

We get the following result.

Theorem 4.1. Let M^2 be a generalized spherical surface given the parametrization (4.1). If for every $p \in M$ the total shear curvature \tilde{K} is identically zero then

$$f_1(u) = \cos \alpha \int \cos\left(\frac{u}{c}\right) du, \quad (4.12)$$

$$f_2(u) = \sin \alpha \int \cos\left(\frac{u}{c}\right) du$$

holds, where $\alpha(u)$ is a constant function.

Proof. Suppose that the total shear curvature \tilde{K} of the generalized spherical surface surface M^2 vanishes identically, then by the use of (4.9) and (4.5) with (4.11) the following equalities hold:

$$\kappa_1(u) = 0 \text{ and } \kappa_\gamma = \frac{1}{c}. \quad (4.13)$$

Consequently, the equation (4.10) and (4.4), (4.13) imply that $\alpha(u)$ is a constant function.

Furthermore, the equation (4.8) and $\kappa_\gamma = \frac{1}{c}$ imply

that $\lambda = c$. Substituting these values into (4.4) we get the result.

Remark. Since $\kappa_1(u)=0$ then the spherical surface given with the parametrization (4.12) lies in 3-dimensional Euclidean space E^3 .

REFERENCES

- [1] B. Bayram, K. Arslan and B. Bulca, "Generalized Spherical Surfaces in E^4 ," *Honam Mathematical J.*, vol. 39, no. 3, pp. 363-377, 2017.
- [2] B. Bulca and K. Arslan, "Surfaces Given with the Monge Patch in E^4 ," *Journal of Mathematical Physics, Analysis, Geom.*, vol. 9, pp. 435-447, 2013.
- [3] B. Y. Chen, "Pseudo-umbilical surfaces with constant Gauss curvature," in *Proceedings of the Edinburgh Mathematical Society (Series 2)*, vol. 18, no. 2, pp. 143-148, 1972.
- [4] B. Y. Chen, *Geometry of Submanifolds*. Dekker, New York, 1973.
- [5] Cipriani, N., Senovilla, J.M.M. and Veken, J.V.D., "Umbilical Properties of Spacelike co-dimension two Submanifolds," *Results Math.*, vol. 72, no. 1-2, pp. 25-46, 2017.
- [6] M. Do Carmo, L. F. Cheung and W. Santos, "On the compactness of constant mean curvature hypersurfaces with finite total curvature," *Arch. Math.*, vol. 73, pp. 216-222, 1999.
- [7] K. Enomoto, "Umbilical Points on Surfaces in R^n ," *Nagoya Math. J.*, vol. 100, pp. 135-143, 1985.

	SAKARYA ÜNİVERSİTESİ FEN BİLİMLERİ ENSTİTÜSÜ DERGİSİ <i>SAKARYA UNIVERSITY JOURNAL OF SCIENCE</i>		
	e-ISSN: 2147-835X Dergi sayfası: http://dergipark.gov.tr/saufenbilder		
	<u>Received</u> 26-07-2017 <u>Accepted</u> 29-05-2018	<u>Doi</u> 10.16984/saufenbilder.331028	

On Inextensible Flows Developable Surfaces Associated Focal Curve According to Ribbon Frame

Mustafa Yeneroğlu

ABSTRACT

In this paper, we investigate inextensible flows of focal curves in Euclidean 3-space E^3 associated to developable surfaces to ribbon frame. We present some new generalizations for torsion and curvature of focal curves in E^3 associated to developable surfaces. Finally, in case of having a flow of developable surface is inextensible we prove that this surface is not minimal.

Keywords: Developable surface, inextensible flows, ribbon frame

1. INTRODUCTION

One of the major research field of the differential geometry is the analysis of space curves. For any unit speed curve, the focal curve is defined as the centres of the osculating spheres. According to Frenet frame $\{t(s), n(s), b(s)\}$ of unity speed curve $\gamma(s)$, the focal curve is given as follows,

$$C_{\psi}(s) = (\gamma + c_1 n + c_2 b)(s),$$

where the coefficients c_1, c_2 are smooth functions that are called focal curvatures of γ . There have been several studies related to the focal curve using this definition Vergas, Arslan, Korpınar concerned with this issue [1,2,3].

Any ribbon consists of two functions $p(s)$ and $\theta(s)$ are defined in interval $s \in [0, Z]$, where Z is considered as the ribbon's intrinsic length under construction. If $A(s)$ is defined as a unit vector field, then it must have an angle $\theta(s)$ to the ribbon's center curve. On the other hand, assuming $p(s)$ is a generating function, $A(s)$ is the direction field for the Darboux vector $\mathbf{W}(s)$ together with $p(s)$. An orthonormal triple $\{\mathbf{c}, \mathbf{v}, \mathbf{h}\}$ has the following differential system:

$$\mathbf{c}' = pA \times \mathbf{c}$$

$$\mathbf{v}' = pA \times \mathbf{v}$$

$$\mathbf{h}' = pA \times \mathbf{h}$$

This orthonormal triple defines a ribbon frame. According to this frame, the focal curve can be given as follows:

$$C_{\psi}(s) = (\gamma + c_1 \mathbf{v} + c_2 \mathbf{h})(s)$$

In CAGD, usage of splines on the construction of curve design is highly significant. Inextensible flows of curves preserve their shape connection thanks to their control polygon. Thus, formulation of algorithms for processing can be calculated. Kwon, Park and Chi examined inextensible flows of curves and developable surfaces [6]. Korpınar, Turhan and Altay gave inextensible flows of developable surfaces associated focal curve [3]. Recently, Bohr and Markvosen examined the ribbon frame [4]. Giomi and Mahadevan gave developable ribbons [7]. Also some authors have studied focal curves and flows in [8-14].

In this paper, we give inextensible flows of focal curves together with ribbon frame. We give some

new generalizations for torsion and curvature of focal curves associated with developable surfaces.

2. PRELIMINARIES

For the construction of ribbon and the center curve of the ribbon we need two smooth functions, $p(s)$ and $\theta(s)$. We also assume that they are defined in the interval $s \in [0, Z]$, where Z is the intrinsic length of the ribbon under construction. We also suppose that $\theta(s) \in [0, \pi] \forall s$ and $\sin(\theta(s)) > 0 \forall s$, throughout the paper. In this construction unit vector field $A(s)$ is significant since it is defined by having the angle $\theta(s)$ to the center curve of the ribbon and it is also a field tangent to the ribbon. In fact, $A(s)$ will generate the Darboux vector $\mathbf{W}(s)$ since it is a direction field together with the generating function $p(s)$ as a multiplying factor, i.e. $\mathbf{W}(s) = p(s)A(s)$, [4].

We assume that $\{\mathbf{c}(s), \mathbf{v}(s), \mathbf{h}(s)\}$ are unique orthonormal vectors such that they are solutions to the below system:

$$\begin{aligned} \mathbf{c}'(s) &= p(s)A(s) \times \mathbf{c}(s), \\ \mathbf{v}'(s) &= p(s)A(s) \times \mathbf{v}(s), \\ \mathbf{h}'(s) &= p(s)A(s) \times \mathbf{h}(s), \end{aligned} \tag{1}$$

where $A(s)$ is defined in terms of $\mathbf{h}(s)$ and $\mathbf{c}(s)$ as the following:

$$A(s) = \sin(\theta(s))\mathbf{h}(s) + \cos(\theta(s))\mathbf{c}(s). \tag{2}$$

For the purpose of uniqueness we also implement arbitrary initial conditions referring to a basis in \mathbb{R}^3 for given fixed coordinate system

$$\{\mathbf{c}(0), \mathbf{v}(0), \mathbf{h}(0)\} = \{(1,0,0), (0,1,0), (0,0,1)\}. \tag{3}$$

The above system is stated as follows explicitly:

$$\mathbf{c}'(s) = p(s) \sin(\theta(s))\mathbf{v}(s) \tag{4}$$

$$\begin{aligned} \mathbf{v}'(s) &= -p(s) \sin(\theta(s))\mathbf{c}(s) + p(s) \cos(\theta(s))\mathbf{h}(s) \\ \mathbf{h}'(s) &= -p(s) \cos(\theta(s))\mathbf{v}(s), \end{aligned} \tag{2}$$

where the dot notation denotes differentiation according to s . If we consider notation of compact matrix, then we have

$$\mathbf{R}'(s) = \mathbf{R}(s)\mathbf{\Xi}(s), \tag{5}$$

where $\mathbf{R}(s)$ is the orthogonal matrix so that it satisfies $2 \det(\mathbf{R}(s)) = 1$. Further, columns of the $\mathbf{R}(s)$ are the coordinate functions of $\{\mathbf{c}(s), \mathbf{v}(s), \mathbf{h}(s)\}$ respectively [4], where

$$\mathbf{\Xi}(s) = \begin{bmatrix} 0 & -p(s)\sin(\theta(s)) & 0 \\ p(s)\sin(\theta(s)) & 0 & -p(s)\cos(\theta(s)) \\ 0 & p(s)\cos(\theta(s)) & 0 \end{bmatrix}. \tag{6}$$

3 Focal Curve According to Ribbon Frame

In the case of focal curve is denoted by F_ψ^B , we have the following expression

$$F_\psi^R(s) = (\boldsymbol{\psi} + c_1\mathbf{v} + c_2\mathbf{h})(s), \tag{7}$$

where the coefficients c_1, c_2 are smooth functions of the curve $\boldsymbol{\psi}$. They are named as first and second focal curvatures of $\boldsymbol{\psi}$.

Lemma 1. Let $\boldsymbol{\psi} : I \rightarrow E^3$ be a unit speed curve and F_ψ^R its focal curve on E^3 . Then, the focal curvatures of F_ψ^R are

$$c_1 = \frac{1}{p(s)\sin\theta(s)} \tag{8}$$

$$c_2 = \frac{p'(s)\sin\theta(s) + \theta'(s)p(s)\cos\theta(s)}{p(s)^3\sin^2\theta(s)\cos\theta(s)} \tag{9}$$

Lemma 2. Let F_ψ^R be the focal curve of the unit speed curve $\boldsymbol{\psi} : I \rightarrow E^3$ on E^3 . If $p(s)$ is constant then, the focal curvatures of F_ψ^R are

$$c_1 = \frac{1}{p(s)\sin\theta(s)} \tag{10}$$

$$c_2 = \frac{\theta'(s)}{\sin^2\theta(s)} \tag{11}$$

Lemma 3. Let F_ψ^R be the focal curve of the unit speed curve $\boldsymbol{\psi} : I \rightarrow E^3$ on E^3 . If $\theta(s)$ is constant then, the focal curvatures of F_ψ^R are

$$c_1 = \frac{1}{p(s)\sin\theta(s)} \tag{12}$$

$$c_2 = \frac{p'(s)}{2p(s)^3 \sin 2\theta(s)} \quad (13)$$

4. Inextensible Flows of Developable Surfaces Associated with Focal Curve According to Ribbon Frame

A ruled surface in E^3 is defined by

$$\Omega_{(\psi, \delta)}(s, u) = \psi(s) + u\delta(s).$$

Here, we have following smooth maps $\Omega_{(\psi, \delta)} : I \times \mathbb{R} \rightarrow E^3$, $\psi : I \rightarrow E^3$, $\delta : I \rightarrow E^3 \setminus \{0\}$ where I is unit circle S^1 or an open interval. From the definition ψ and δ are called base and director curve.

Definition 4. Let assume that Gaussian curvature U vanishes everywhere on the surface then a smooth surface $\Omega_{(\psi, \delta)}$ is called a developable surface.

Definition 5. Let $\psi : I \rightarrow E^3$ be a unit speed curve. We define the developable surface as follows

$$\Omega_{(F_\psi^R, \psi)}(s, u) = F_\psi^R(s) + u\psi'(s), \quad (14)$$

where $F_\psi^R(s)$ is focal curve.

Definition 6. Let first fundamental form $\{E, F, G\}$ of a surface evolution satisfies following.

$$\frac{\partial E}{\partial t} = \frac{\partial F}{\partial t} = \frac{\partial G}{\partial t} = 0 \quad (15)$$

Then the surface evolution $\Omega(s, u, t)$ and its flow $\frac{\partial \Omega}{\partial t}$ are inextensible.

This definition says that the surface $\Omega(s, u, t)$ is the isometric image of the original surface $\Omega(s, u, t_0)$ which is determined for initial time t_0 . $\Omega(s, u, t)$ can be visualized as a waving flag for a developable surface. There is no any nontrivial inextensible evolution for a given rigid surface.

Definition 7. We can define one-parameter family of developable ruled surface as follows:

$$\Omega(s, u, t) = F_\psi^R(s, t) + u\psi'(s, t). \quad (16)$$

Theorem 8. Let we assume that Ω is developable surface associated to a focal curve in E^3 . If $\frac{\partial \Omega}{\partial t}$ is inextensible, then

$$\frac{\partial}{\partial t} [(upsin\theta)^2 + (c_1pcos\theta)^2] = 0 \quad (17)$$

Proof. Let $\Omega(s, u, t)$ be a one-parameter family of developable surface. Then, we say that Ω is inextensible.

$$\begin{aligned} \Omega_s &= c_1 p \cos \theta \mathbf{h} + up \sin \theta \mathbf{v}, \\ \Omega_u &= \mathbf{c}. \end{aligned}$$

Calculating first fundamental form gives rise to obtain following results.

$$\begin{aligned} E &= \langle \Omega_s, \Omega_s \rangle = u^2 (p \sin \theta)^2 + c_1^2 (p \cos \theta)^2, \\ F &= 0, \\ G &= 1. \end{aligned}$$

Considering above results, we have

$$\begin{aligned} \frac{\partial E}{\partial t} &= 0, \\ \frac{\partial F}{\partial t} &= 0, \\ \frac{\partial G}{\partial t} &= 0. \end{aligned}$$

If $\frac{\partial \Omega}{\partial t}$ is inextensible, then we have (17).

Theorem 9. Let the flow of the developable surface Ω which is associated to focal curve in E^3 , be inextensible then this surface is not minimal.

Proof. Assume that $\Omega(s, u, t) = F_\psi^R(s, t) + u\psi'(s, t)$ be a one-parameter family of developable ruled surface. Second fundamental form's component of developable surface are

$$\begin{aligned} h_{11} &= \sqrt{[\tan \theta]^2 + u^2 (p \sin \theta)^2}, \\ h_{12} &= -p \cos \theta, \\ h_{22} &= 0. \end{aligned}$$

We also have components of metric

$$\begin{aligned} g_{11} &= [\tan \theta]^2 + u^2 (p \sin \theta)^2, \\ g_{12} &= 0, \\ g_{22} &= 1. \end{aligned}$$

So, one-parameter family of developable ruled surface $\Omega(s, u, t) = F_{\psi}^R(s, t) + u\psi'(s, t)$ has the following mean curvature

$$H = g^{ij}h_{ij} = \frac{p \cos \theta}{\sqrt{[\tan \theta]^2 + u^2 (w \sin \theta)^2}}$$

Ω is a minimal ruled surface in E^3 if and only if $p \cos \theta = 0$.

REFERENCES

- [1]. P. Alegre, K. Arslan, A. Carriazo, C. Murathan and G. Öztürk, "Some Special Types of Developable Ruled Surface," *Hacettepe Journal of Mathematics and Statistics*, Vol. 39 No.3, pp. 319-325, 2010.
- [2]. R. Uribe-Vargas, "On vertices, focal curvatures and differential geometry of space curves," *Bull. Brazilian Math. Soc.* Vol. 36 No. 3, 285—307, 2005.
- [3]. T. Korpınar, E. Turhan and G. Altay, "Inextensible flows of developable surfaces associated focal curve of helices in Euclidean 3-space E^3 ", *Acta Universitatis Apulensis*, Vol. 29, pp. 235-240, 2012.
- [4]. J. Bohr and S. Markvorsen, "Ribbon Crystals", *Plos one*, Vol.8 (10) (2013).
- [5]. M. Yeneroglu, "New focal curves according to ribbon frame," *Prespacetime Journal*, Vol. 7 No. 5, 2016.
- [6]. D.Y. Kwon, F.C. Park and D.P. Chi, "Inextensible flows of curves and developable surfaces," *Applied Math. Letters*, Vol. 18 No. 10, 1156-1162, 2005.
- [7]. Giomi, L. Mahadevan, "Statistical mechanics of developable ribbons," *Phys. Rev. Lett.*, Vol. 104, 2010.
- [8]. D. E. Blair, "Contact Manifolds in Riemannian Geometry", *Lecture Notes in Mathematics*, Springer-Verlag 509, Berlin-New York, 1976.
- [9]. M.P. Carmo, "Differential Geometry of Curves and Surfaces", *Pearson Education*, 1976.
- [10]. T. Körpınar, "On the Fermi-Walker Derivative for Inextensible Flows", *Zeitschrift für Naturforschung A.*, Vol.70, No.7, pp.477-482, 2015.
- [11]. T. Körpınar, "A New Method for Inextensible Flows of Timelike Curves in Minkowski Space-Time E_1^4 ", *International Journal of Partial Differential Equations*, Vol. 2014, Article ID 517070, 7 pages
- [12]. T. Körpınar, "Bianchi Type-I Cosmological Models for Inextensible Flows of Biharmonic Particles by Using Curvature Tensor Field in Spacetime", *Int J Theor Phys*, Vol. 54, pp.1762-1770, 2015.
- [13]. T. Körpınar, S. Bas, "On Characterization Of B- Focal Curves In E^3 ", *Bol. Soc. Paran. Mat.*, Vol.31, No.1, pp. 175-178, 2013.
- [14]. V. Asil, T. Körpınar, "Dual focal curves of dual spacelike curves in the Dual Lorentzian $D13$ " *Palestine Journal of Mathematics* , Vol.2, No.1, pp.1-3, 2013.

	SAKARYA ÜNİVERSİTESİ FEN BİLİMLERİ ENSTİTÜSÜ DERGİSİ SAKARYA UNIVERSITY JOURNAL OF SCIENCE		
	e-ISSN: 2147-835X Dergi sayfası: http://www.saujs.sakarya.edu.tr		
	Received 02-11-2017 Accepted 21-05-2018	Doi 10.16984/saufenbilder.348912	

Approximation By Three-Dimensional q-Bernstein-Chlodowsky Polynomials

Nazmiye Gönül Bilgin¹, Merve ÇETİNKAYA

ABSTRACT

In the present paper we introduce positive linear three-dimensional Bernstein-Chlodowsky polynomials on a non-tetrahedron domain and we get their q-analogue. We obtain approximation properties for these positive linear operators and their generalizations in this work. The rate of convergence of these operators is calculated by means of the modulus of continuity.

Keywords: Bernstein-Chlodowsky Polynomials, q- Bernstein-Chlodowsky Polynomials, linear positive operators, modulus of continuity.

1. INTRODUCTION

In recent years, many generalizations of well-known linear positive operators, based on q-calculus were introduced and studied by several authors. In 1996, Philips by using the q-binomial coefficients and the q-binomial theorem introduced a generalization of the Bernstein operators called q-Bernstein Operators [1]. q-Bernstein-Chlodowsky polynomials defined by Karsli Gupta in the one-dimensional case [2]. Buyukyazici introduced the two-dimensional q-analogue of Bernstein-Chlodowsky polynomial in [3]. He give these polynomials on a domain $D_{ab} = [0, a] \times [0, b]$. In this paper we define three-dimensional Bernstein-Chlodowsky and q-Bernstein-Chlodowsky polynomials. Then we compute the rate of convergence of these operators by means of the modulus of continuity. The aim of this paper is to prove Korovkin type theorems and to give some examples of numerical solutions for the three-dimensional q- Bernstein-Chlodowsky polynomials.

Firstly, we give some notions about q-integers. Let $q > 0$. For each non-negative integer n , we define the q-integer $[n]_q$ as

$$[n]_q = \begin{cases} \frac{1 - q^n}{1 - q}, & \text{if } q \neq 1 \\ n, & \text{if } q = 1 \end{cases}$$

and the q-factorial $[n]_q!$ as

$$[n]_q! = \begin{cases} [n]_q [n-1]_q \cdots [1]_q, & n = 1, 2, \dots \\ 1, & n = 0 \end{cases}$$

For integers n and k , with $0 \leq k \leq n$, q-binomial coefficients are then defined as follow

$$\begin{bmatrix} n \\ k \end{bmatrix}_q = \frac{[n]_q!}{[k]_q! [n-k]_q!}$$

q-based Bernstein-Chlodowsky type polynomials for a function f of two variables as follows in [1].

Let (α_n) and (β_m) be increasing sequences of positive real numbers;

$$\lim_{n \rightarrow \infty} \alpha_n = \lim_{m \rightarrow \infty} \beta_m = \infty, \quad \lim_{n \rightarrow \infty} \frac{\alpha_n}{[n]_{q_n}} = 0 \text{ and}$$

¹ Zonguldak Bülent Ecevit University, Faculty of Sciences-Department of Mathematics, nazmiyegonulbilgin@hotmail.com

$$\lim_{m \rightarrow \infty} \frac{\beta_m}{[m]_{q_m}} = 0.$$

For any $\alpha_n > 0, \beta_m > 0$ where

$$(x, y) \in D_{\alpha_n \beta_n} = \{(x, y) : 0 \leq x \leq \alpha_n, 0 \leq y \leq \beta_m\}.$$

The two-dimensional q-Bernstein-Chlodowsky operators;

$$\begin{aligned} & \check{B}_{n,m}^{q_n, q_m}(f; x, y) \\ &= \sum_{k=0}^n \sum_{j=0}^m f\left(\frac{[k]_{q_n}}{[n]_{q_n}} \alpha_n, \frac{[j]_{q_m}}{[m]_{q_m}} \beta_m\right) \begin{bmatrix} n \\ k \end{bmatrix}_{q_n} \begin{bmatrix} m \\ j \end{bmatrix}_{q_m} \left(\frac{x}{\alpha_n}\right)^k \left(\frac{y}{\beta_m}\right)^j \\ & \times \prod_{s_1=0}^{n-k-1} \left(1 - q_n^{s_1} \frac{x}{\alpha_n}\right) \prod_{s_2=0}^{m-j-1} \left(1 - q_m^{s_2} \frac{y}{\beta_m}\right) \end{aligned}$$

$$\check{B}_n^{q_n}(f; x, y) = \sum_{k=0}^n f\left(\frac{[k]_{q_n}}{[n]_{q_n}} \alpha_n, y\right) \begin{bmatrix} n \\ k \end{bmatrix}_{q_n} \left(\frac{x}{\alpha_n}\right)^k$$

$$\times \prod_{s_1=0}^{n-k-1} \left(1 - q_n^{s_1} \frac{x}{\alpha_n}\right)$$

$$\begin{aligned} & \check{B}_m^{q_m}(f; x, y) \\ &= \sum_{j=0}^m f\left(x, \frac{[j]_{q_m}}{[m]_{q_m}} \beta_m\right) \begin{bmatrix} m \\ j \end{bmatrix}_{q_m} \left(\frac{y}{\beta_m}\right)^j \prod_{s_2=0}^{m-j-1} \left(1 - q_m^{s_2} \frac{y}{\beta_m}\right) \end{aligned}$$

Buyukyazici gave approximation properties these operators in [3].

Theorem 1.1. Let $e_{ij} : D_{ab} \rightarrow D_{ab}$,

$$e_{ij}(x, y) = x^i y^j, i, j = 0, 1, 2 \text{ and for any } (x, y) \in D_{ab};$$

$$\text{i. } \check{B}_{n,m}^{q_n, q_m}(e_{00}; x, y) = 1$$

$$\text{ii. } \check{B}_{n,m}^{q_n, q_m}(e_{10}; x, y) = x$$

$$\text{iii. } \check{B}_{n,m}^{q_n, q_m}(e_{01}; x, y) = y$$

$$\text{iv. } \check{B}_{n,m}^{q_n, q_m}(e_{20}; x, y) = x^2 + \frac{x(\alpha_n - x)}{[n]_{q_n}}$$

$$\text{v. } \check{B}_{n,m}^{q_n, q_m}(e_{02}; x, y) = y^2 + \frac{y(\beta_m - y)}{[m]_{q_m}}.$$

Theorem 1.2. Let $f \in C(D_{ab})$, for any sufficiently large fixed positive real a and b, ($a \leq \alpha_n, b \leq \beta_m$) then

$\check{B}_{n,m}^{q_n, q_m}(f; x, y)$ linear positive operators sequence satisfy next equalities.

$$\lim_{n, m \rightarrow \infty} \|\check{B}_{n,m}^{q_n, q_m}(e_{00}; x, y) - 1\|_{C(D_{ab})} = 0 \quad (1)$$

$$\lim_{n, m \rightarrow \infty} \|\check{B}_{n,m}^{q_n, q_m}(e_{10}; x, y) - x\|_{C(D_{ab})} = 0 \quad (2)$$

$$\lim_{n, m \rightarrow \infty} \|\check{B}_{n,m}^{q_n, q_m}(e_{01}; x, y) - y\|_{C(D_{ab})} = 0 \quad (3)$$

$$\lim_{n, m \rightarrow \infty} \|\check{B}_{n,m}^{q_n, q_m}(t^2 + \tau^2; x, y) - (x^2 + y^2)\|_{C(D_{ab})} = 0 \quad (4)$$

Using Korovkin type theorem we get

$$\lim_{n, m \rightarrow \infty} \|\check{B}_{n,m}^{q_n, q_m}(f; x, y) - f(x, y)\|_{C(D_{ab})} = 0 \quad (5)$$

2. CONSTRUCTION OF OPERATORS

Definition 2.1.

Let $\{b_n\}, \{c_m\}, \{d_r\}$ be increasing sequences of real numbers and let them satisfy the next properties. Let

$$\lim_{n \rightarrow \infty} b_n = \lim_{m \rightarrow \infty} c_m = \lim_{r \rightarrow \infty} d_r = \infty,$$

$$\lim_{n \rightarrow \infty} \left(\frac{b_n}{n}\right) = \lim_{m \rightarrow \infty} \left(\frac{c_m}{m}\right) = \lim_{r \rightarrow \infty} \left(\frac{d_r}{r}\right) = 0$$

and for $b_n, c_m, d_r > 0$;

$$\begin{aligned} \tilde{D}_3 := D_{b_n, c_m, d_r} = \{(x, y, z) : 0 \leq x \leq b_n, 0 \leq y \\ \leq c_m, 0 \leq z \leq d_r\} \end{aligned}$$

is defined.

We can introduce the Bernstein-Chlodowsky type polynomials for a function f of three variables same as [4], [5];

$$\begin{aligned} & B_{n,m,r}(f; x, y, z) \\ &= \sum_{k=0}^n \sum_{j=0}^m \sum_{l=0}^r f\left(\frac{k}{n} b_n, \frac{j}{m} c_m, \frac{l}{r} d_r\right) \binom{n}{k} \binom{m}{j} \binom{r}{l} \left(\frac{x}{b_n}\right)^k \\ & \times \left(1 - \frac{x}{b_n}\right)^{n-k} \binom{m}{j} \left(\frac{y}{c_m}\right)^j \\ & \times \left(1 - \frac{y}{c_m}\right)^{m-j} \binom{r}{l} \left(\frac{z}{d_r}\right)^l \left(1 - \frac{z}{d_r}\right)^{r-l} \end{aligned} \quad (6)$$

Lemma 2.1. Let $B_{n,m,r}(f; x, y, z)$ defined in (6) and $B_{n,m,r}(f; x, y, z), C_{\tilde{D}_3} \rightarrow C_{\tilde{D}_3}$ where

$$e_{i_1, i_2, i_3} = x^{i_1} y^{i_2} z^{i_3}, \quad i_1 + i_2 + i_3 \leq 2$$

for $i_1, i_2, i_3 \in \{0, 1, 2\}$. We have the following equalities:

$$\text{i. } B_{n,m,r}(e_{0,0,0}; x, y, z) = 1$$

$$\text{ii. } B_{n,m,r}(e_{1,0,0}; x, y, z) = x$$

$$\text{iii. } B_{n,m,r}(e_{0,1,0}; x, y, z) = y$$

$$\text{iv. } B_{n,m,r}(e_{0,0,1}; x, y, z) = z$$

$$\text{v. for } g(x, y, z) = e_{2,0,0}(x, y, z) + e_{0,2,0}(x, y, z) + e_{0,0,2}(x, y, z)$$

$$\begin{aligned} B_{n,m,r}(g; x, y, z) = x^2 + \frac{x(b_n - x)}{n} + y^2 + \frac{y(c_m - y)}{m} \\ + z^2 + \frac{z(d_r - z)}{r}. \end{aligned}$$

Proof.

$$\text{i) } B_{n,m,r}(e_{0,0,0}; x, y, z) = \sum_{k=0}^n \sum_{j=0}^m \sum_{l=0}^r \binom{n}{k} \binom{m}{j} \binom{r}{l} \left(\frac{x}{b_n}\right)^k$$

$$\begin{aligned}
 & x \left(1 - \frac{x}{b_n}\right)^{n-k} \binom{m}{j} \left(\frac{y}{c_m}\right)^j \left(1 - \frac{y}{c_m}\right)^{m-j} \\
 & x \binom{r}{l} \left(\frac{z}{d_r}\right)^l \left(1 - \frac{z}{d_r}\right)^{r-l} \\
 & = \sum_{k=0}^n \sum_{j=0}^m \binom{n}{k} \left(\frac{x}{b_n}\right)^k \left(1 - \frac{x}{b_n}\right)^{n-k} \binom{m}{j} \left(\frac{y}{c_m}\right)^j \left(1 - \frac{y}{c_m}\right)^{m-j} \\
 & x \sum_{l=0}^r \binom{r}{l} \left(\frac{z}{d_r}\right)^l \left(1 - \frac{z}{d_r}\right)^{r-l} \\
 & = \sum_{k=0}^n \binom{n}{k} \left(\frac{x}{b_n}\right)^k \left(1 - \frac{x}{b_n}\right)^{n-k} \sum_{j=0}^m \binom{m}{j} \left(\frac{y}{c_m}\right)^j \left(1 - \frac{y}{c_m}\right)^{m-j} \\
 & x \sum_{l=0}^r \binom{r}{l} \left(\frac{z}{d_r}\right)^l \left(1 - \frac{z}{d_r}\right)^{r-l} \\
 & = 1
 \end{aligned}$$

$$\begin{aligned}
 \text{ii) } B_{n,m,r}(e_{1,0,0}; x, y, z) & = \sum_{k=0}^n \sum_{j=0}^m \sum_{l=0}^r \frac{k}{n} b_n \binom{n}{k} \left(\frac{x}{b_n}\right)^k \\
 & x \left(1 - \frac{x}{b_n}\right)^{n-k} \binom{m}{j} \left(\frac{y}{c_m}\right)^j \left(1 - \frac{y}{c_m}\right)^{m-j} \\
 & x \binom{r}{l} \left(\frac{z}{d_r}\right)^l \left(1 - \frac{z}{d_r}\right)^{r-l} \\
 & = \sum_{k=0}^n \sum_{j=0}^m \frac{k}{n} b_n \binom{n}{k} \left(\frac{x}{b_n}\right)^k \left(1 - \frac{x}{b_n}\right)^{n-k} \binom{m}{j} \left(\frac{y}{c_m}\right)^j \\
 & x \left(1 - \frac{y}{c_m}\right)^{m-j} \sum_{l=0}^r \binom{r}{l} \left(\frac{z}{d_r}\right)^l \left(1 - \frac{z}{d_r}\right)^{r-l} \\
 & = \sum_{k=0}^n \sum_{j=0}^m \frac{k}{n} b_n \binom{n}{k} \left(\frac{x}{b_n}\right)^k \left(1 - \frac{x}{b_n}\right)^{n-k} \\
 & x \binom{m}{j} \left(\frac{y}{c_m}\right)^j \left(1 - \frac{y}{c_m}\right)^{m-j} \\
 & = \sum_{k=0}^n \frac{k}{n} b_n \binom{n}{k} \left(\frac{x}{b_n}\right)^k \left(1 - \frac{x}{b_n}\right)^{n-k} \\
 & x \sum_{j=0}^m \binom{m}{j} \left(\frac{y}{c_m}\right)^j \left(1 - \frac{y}{c_m}\right)^{m-j} \\
 & = \sum_{k=0}^n \frac{k}{n} b_n \binom{n}{k} \left(\frac{x}{b_n}\right)^k \left(1 - \frac{x}{b_n}\right)^{n-k} = B_n(e_1, x) = x
 \end{aligned}$$

$$\begin{aligned}
 \text{iii) } B_{n,m,r}(e_{0,1,0}; x, y, z) & = \sum_{k=0}^n \sum_{j=0}^m \sum_{l=0}^r \frac{j}{m} c_m \binom{n}{k} \left(\frac{x}{b_n}\right)^k \\
 & x \left(1 - \frac{x}{b_n}\right)^{n-k} \binom{m}{j} \left(\frac{y}{c_m}\right)^j \left(1 - \frac{y}{c_m}\right)^{m-j} \\
 & x \binom{r}{l} \left(\frac{z}{d_r}\right)^l \left(1 - \frac{z}{d_r}\right)^{r-l}
 \end{aligned}$$

$$\begin{aligned}
 & = \sum_{k=0}^n \sum_{j=0}^m \frac{j}{m} c_m \binom{n}{k} \left(\frac{x}{b_n}\right)^k \left(1 - \frac{x}{b_n}\right)^{n-k} \binom{m}{j} \left(\frac{y}{c_m}\right)^j \\
 & x \left(1 - \frac{y}{c_m}\right)^{m-j} \sum_{l=0}^r \binom{r}{l} \left(\frac{z}{d_r}\right)^l \left(1 - \frac{z}{d_r}\right)^{r-l} \\
 & = \sum_{k=0}^n \binom{n}{k} \left(\frac{x}{b_n}\right)^k \left(1 - \frac{x}{b_n}\right)^{n-k} \\
 & x \sum_{j=0}^m \frac{j}{m} c_m \binom{m}{j} \left(\frac{y}{c_m}\right)^j \left(1 - \frac{y}{c_m}\right)^{m-j} \\
 & = \sum_{k=0}^n \binom{n}{k} \left(\frac{x}{b_n}\right)^k \left(1 - \frac{x}{b_n}\right)^{n-k} B_m(e_{1,1}, y) \\
 & = y \sum_{k=0}^n \binom{n}{k} \left(\frac{x}{b_n}\right)^k \left(1 - \frac{x}{b_n}\right)^{n-k} = y
 \end{aligned}$$

$$\begin{aligned}
 \text{iv) } B_{n,m,r}(e_{0,0,1}; x, y, z) & = \sum_{k=0}^n \sum_{j=0}^m \sum_{l=0}^r \frac{l}{r} d_r \binom{n}{k} \left(\frac{x}{b_n}\right)^k \\
 & x \left(1 - \frac{x}{b_n}\right)^{n-k} \binom{m}{j} \left(\frac{y}{c_m}\right)^j \left(1 - \frac{y}{c_m}\right)^{m-j} \\
 & x \binom{r}{l} \left(\frac{z}{d_r}\right)^l \left(1 - \frac{z}{d_r}\right)^{r-l} \\
 & = \sum_{k=0}^n \sum_{j=0}^m \binom{n}{k} \left(\frac{x}{b_n}\right)^k \left(1 - \frac{x}{b_n}\right)^{n-k} \binom{m}{j} \left(\frac{y}{c_m}\right)^j \left(1 - \frac{y}{c_m}\right)^{m-j} \\
 & x \sum_{l=0}^r \frac{l}{r} d_r \binom{r}{l} \left(\frac{z}{d_r}\right)^l \left(1 - \frac{z}{d_r}\right)^{r-l} \\
 & = \sum_{k=0}^n \sum_{j=0}^m \binom{n}{k} \left(\frac{x}{b_n}\right)^k \left(1 - \frac{x}{b_n}\right)^{n-k} \\
 & x \binom{m}{j} \left(\frac{y}{c_m}\right)^j \left(1 - \frac{y}{c_m}\right)^{m-j} B_r(e_{1,1}, z) \\
 & = z \sum_{k=0}^n \binom{n}{k} \left(\frac{x}{b_n}\right)^k \left(1 - \frac{x}{b_n}\right)^{n-k} \\
 & x \sum_{j=0}^m \binom{m}{j} \left(\frac{y}{c_m}\right)^j \left(1 - \frac{y}{c_m}\right)^{m-j} \\
 & = z \sum_{k=0}^n \binom{n}{k} \left(\frac{x}{b_n}\right)^k \left(1 - \frac{x}{b_n}\right)^{n-k} = z
 \end{aligned}$$

v) for

$$\begin{aligned}
 g(x, y, z) & := e_{2,0,0}(x, y, z) + e_{0,2,0}(x, y, z) + e_{0,0,2}(x, y, z) \\
 B_{n,m,r}(g; x, y, z) & = x^2 + \frac{x(b_n - x)}{n} + y^2 + \frac{y(c_m - y)}{m} \\
 & \quad + z^2 + \frac{z(d_r - z)}{r}
 \end{aligned}$$

$$\begin{aligned}
 B_{n,m,r}(e_{2,0,0}; x, y, z) &= \sum_{k=0}^n \sum_{j=0}^m \sum_{l=0}^r \frac{k^2}{n^2} b_n^2 \binom{n}{k} \left(\frac{x}{b_n}\right)^k \\
 &\times \left(1 - \frac{x}{b_n}\right)^{n-k} \binom{m}{j} \left(\frac{y}{c_m}\right)^j \left(1 - \frac{y}{c_m}\right)^{m-j} \\
 &\times \binom{r}{l} \left(\frac{z}{d_r}\right)^l \left(1 - \frac{z}{d_r}\right)^{r-l} \\
 &= \sum_{k=0}^n \sum_{j=0}^m \frac{k^2}{n^2} b_n^2 \binom{n}{k} \left(\frac{x}{b_n}\right)^k \left(1 - \frac{x}{b_n}\right)^{n-k} \\
 &\times \binom{m}{j} \left(\frac{y}{c_m}\right)^j \left(1 - \frac{y}{c_m}\right)^{m-j} \\
 &\times \sum_{l=0}^r \binom{r}{l} \left(\frac{z}{d_r}\right)^l \left(1 - \frac{z}{d_r}\right)^{r-l} \\
 &= \sum_{k=0}^n \frac{k^2}{n^2} b_n^2 \binom{n}{k} \left(\frac{x}{b_n}\right)^k \left(1 - \frac{x}{b_n}\right)^{n-k} \\
 &\times \sum_{j=0}^m \binom{m}{j} \left(\frac{y}{c_m}\right)^j \left(1 - \frac{y}{c_m}\right)^{m-j} \\
 &= \sum_{k=0}^n \frac{k^2}{n^2} b_n^2 \binom{n}{k} \left(\frac{x}{b_n}\right)^k \left(1 - \frac{x}{b_n}\right)^{n-k} \\
 &= B_n(e_2, x) = x^2 + \frac{x(b_n - x)}{n}
 \end{aligned}$$

$$\begin{aligned}
 B_{n,m,r}(e_{0,2,0}; x, y, z) &= \sum_{k=0}^n \sum_{j=0}^m \sum_{l=0}^r \frac{j^2}{m^2} c_m^2 \binom{m}{j} \left(\frac{y}{c_m}\right)^k \\
 &\times \left(1 - \frac{x}{b_n}\right)^{n-k} \binom{m}{j} \left(\frac{y}{c_m}\right)^j \left(1 - \frac{y}{c_m}\right)^{m-j} \\
 &\times \binom{r}{l} \left(\frac{z}{d_r}\right)^l \left(1 - \frac{z}{d_r}\right)^{r-l} \\
 &= \sum_{k=0}^n \sum_{j=0}^m \frac{j^2}{m^2} c_m^2 \binom{m}{j} \left(\frac{y}{c_m}\right)^k \\
 &\times \left(1 - \frac{x}{b_n}\right)^{n-k} \binom{m}{j} \left(\frac{y}{c_m}\right)^j \left(1 - \frac{y}{c_m}\right)^{m-j} \\
 &\times \sum_{l=0}^r \binom{r}{l} \left(\frac{z}{d_r}\right)^l \left(1 - \frac{z}{d_r}\right)^{r-l} \\
 &= \sum_{k=0}^n \binom{n}{k} \left(\frac{x}{b_n}\right)^k \left(1 - \frac{x}{b_n}\right)^{n-k} \\
 &\times \sum_{j=0}^m \frac{j^2}{m^2} c_m^2 \binom{m}{j} \left(\frac{y}{c_m}\right)^j \left(1 - \frac{y}{c_m}\right)^{m-j} \\
 &= \sum_{k=0}^n \binom{n}{k} \left(\frac{x}{b_n}\right)^k \left(1 - \frac{x}{b_n}\right)^{n-k} B_m(e_2, y)
 \end{aligned}$$

$$\begin{aligned}
 &= \sum_{k=0}^n \binom{n}{k} \left(\frac{x}{b_n}\right)^k \left(1 - \frac{x}{b_n}\right)^{n-k} y^2 + \frac{y(c_m - y)}{m} \\
 &= y^2 + \frac{y(c_m - y)}{m}
 \end{aligned}$$

$$\begin{aligned}
 B_{n,m,r}(e_{0,0,2}; x, y, z) &= \sum_{k=0}^n \sum_{j=0}^m \sum_{l=0}^r \frac{l^2}{r^2} d_r^2 \binom{r}{l} \left(\frac{z}{d_r}\right)^k \\
 &\times \left(1 - \frac{x}{b_n}\right)^{n-k} \binom{m}{j} \left(\frac{y}{c_m}\right)^j \left(1 - \frac{y}{c_m}\right)^{m-j} \\
 &\times \binom{r}{l} \left(\frac{z}{d_r}\right)^l \left(1 - \frac{z}{d_r}\right)^{r-l} \\
 &= \sum_{k=0}^n \sum_{j=0}^m \binom{n}{k} \left(\frac{x}{b_n}\right)^k \left(1 - \frac{x}{b_n}\right)^{n-k} \\
 &\times \binom{m}{j} \left(\frac{y}{c_m}\right)^j \left(1 - \frac{y}{c_m}\right)^{m-j} \\
 &\times \sum_{l=0}^r \frac{l^2}{r^2} d_r^2 \binom{r}{l} \left(\frac{z}{d_r}\right)^l \left(1 - \frac{z}{d_r}\right)^{r-l} \\
 &= \sum_{k=0}^n \sum_{j=0}^m \binom{n}{k} \left(\frac{x}{b_n}\right)^k \left(1 - \frac{x}{b_n}\right)^{n-k} \\
 &\times \binom{m}{j} \left(\frac{y}{c_m}\right)^j \left(1 - \frac{y}{c_m}\right)^{m-j} B_r(e_2, z) \\
 &= \left(z^2 + \frac{z(d_r - z)}{r}\right) \sum_{k=0}^n \binom{n}{k} \left(\frac{x}{b_n}\right)^k \left(1 - \frac{x}{b_n}\right)^{n-k} \\
 &\times \sum_{j=0}^m \binom{m}{j} \left(\frac{y}{c_m}\right)^j \left(1 - \frac{y}{c_m}\right)^{m-j} \\
 &= \left(z^2 + \frac{z(d_r - z)}{r}\right) \sum_{k=0}^n \binom{n}{k} \left(\frac{x}{b_n}\right)^k \left(1 - \frac{x}{b_n}\right)^{n-k} \\
 &= z^2 + \frac{z(d_r - z)}{r}
 \end{aligned}$$

We get

$$\begin{aligned}
 B_{n,m,r}(g; x, y, z) &= x^2 + \frac{x(b_n - x)}{n} + y^2 \\
 &+ \frac{y(c_m - y)}{m} + z^2 + \frac{z(d_r - z)}{r}.
 \end{aligned}$$

Theorem 2.1 Let $f \in C(\tilde{D}_3)$, then for any sufficiently large fixed positive real numbers b, c and $(b < b_n, c < c_m, d < d_r)$ then we get

$$\lim_{n,m,r \rightarrow \infty} \max_{(x,y,z) \in \tilde{D}_3} |B_{n,m,r}(f; x, y, z) - f(x, y, z)| = 0.$$

Proof. Using Lemma 2.1

$$\|B_{n,m,r}(e_{0,0,0}; x, y, z) - e_{0,0,0}(x, y, z)\|_{C(\tilde{D}_3)} = 0$$

$$\begin{aligned} & \|B_{n,m,r}(e_{1,0,0}; x, y, z) - e_{1,0,0}(x, y, z)\|_{C(\bar{D}_3)} = 0 \\ & \|B_{n,m,r}(e_{0,1,0}; x, y, z) - e_{0,1,0}(x, y, z)\|_{C(\bar{D}_3)} = 0 \\ & \|B_{n,m,r}(e_{0,0,1}; x, y, z) - e_{0,0,1}(x, y, z)\|_{C(\bar{D}_3)} = 0 \\ & \|B_{n,m,r}((e_{2,0,0}; x, y, z) + (e_{0,2,0}; x, y, z) \\ & \quad + (e_{0,0,2}; x, y, z) \\ & \quad - (x^2 + y^2 + z^2))\|_{C(\bar{D}_3)} \\ & \leq b \frac{b_n}{n} + c \frac{c_m}{m} + d \frac{d_r}{r}. \end{aligned}$$

The proof is completed using

$$\lim_{n \rightarrow \infty} \frac{b_n}{n} = \lim_{m \rightarrow \infty} \frac{c_m}{m} = \lim_{r \rightarrow \infty} \frac{d_r}{r} = 0.$$

We can show the uniform approximation of the three dimensional Bernstein-Chlodowsky polynomials in next example.

Example 2.1. The convergence of

$B_{n,m,r}(f; x, y, z)$ to $f(x, y, z) = x^6 + y^6 + z^6 - \left(\frac{1}{6}\right)^{1/8}$, $b_n = \sqrt{n}$, $c_m = \sqrt{m}$, $d_r = \sqrt{r}$ is illustrated in Figure 2.1.

$n = m = r = 50$ (yellow), $n = m = r = 30$ (red), $n = m = r = 15$ (gray), $n = m = r = 10$ (magenta).

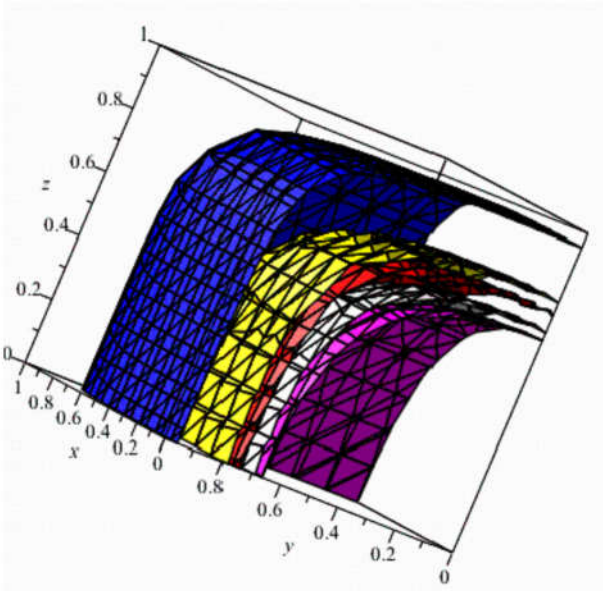


Figure 2.1. Approximation of $f(x, y, z) = x^6 + y^6 + z^6 - \left(\frac{1}{6}\right)^{1/8}$ (blue) by $B_{n,m,r}(f; x, y, z)$.

Definition 2.2.

Let $\{\alpha_n\}, \{\beta_m\}, \{\gamma_r\}$ be increasing sequences of positive real numbers and let them satisfy the following properties:

$$\lim_{n \rightarrow \infty} \alpha_n = \lim_{m \rightarrow \infty} \beta_m = \lim_{r \rightarrow \infty} \gamma_r = \infty$$

that the sequences

$$\lim_{n \rightarrow \infty} \frac{\alpha_n}{[n]_{q_n}} = \lim_{m \rightarrow \infty} \frac{\beta_m}{[m]_{q_m}} = \lim_{r \rightarrow \infty} \frac{\gamma_r}{[r]_{q_r}} = 0$$

where $q > 0$, $\{q_n\}$ is a sequences of real numbers such that $0 < q_n \leq 1$ for all n and $\lim_{n \rightarrow \infty} q_n = 1$.

For any $\alpha_n > 0, \beta_m > 0, \gamma_r > 0$ we denote by $D_{\bar{3}}$:

$$D_{\bar{3}} := D_{\alpha_n, \beta_m, \gamma_r} = \{(x, y, z) : 0 \leq x \leq \alpha_n, \\ 0 \leq y \leq \beta_m, \quad 0 \leq z \leq \gamma_r\}$$

We can define the q- Bernstein- Chlodowsky type polynomials for a function f of three variables as follows:

$$\begin{aligned} & \tilde{B}_{n,m,r}^{q_n, q_m, q_r}(f; x, y, z) \\ & = \sum_{k=0}^n \sum_{j=0}^m \sum_{l=0}^r f\left(\frac{[k]_{q_n}}{[n]_{q_n}} \alpha_n, \frac{[j]_{q_m}}{[m]_{q_m}} \beta_m, \frac{[l]_{q_r}}{[r]_{q_r}} \gamma_r\right) \end{aligned}$$

$$\begin{aligned} & \times \begin{bmatrix} n \\ k \end{bmatrix}_{q_n} \begin{bmatrix} m \\ j \end{bmatrix}_{q_m} \begin{bmatrix} r \\ l \end{bmatrix}_{q_r} \\ & \times \left(\frac{x}{\alpha_n}\right)^k \left(\frac{y}{\beta_m}\right)^j \left(\frac{z}{\gamma_r}\right)^l \prod_{s_1=0}^{n-k-1} \left(1 - q_n^{s_1} \frac{x}{\alpha_n}\right) \\ & \times \prod_{s_2=0}^{m-j-1} \left(1 - q_m^{s_2} \frac{y}{\beta_m}\right) \prod_{s_3=0}^{r-l-1} \left(1 - q_r^{s_3} \frac{z}{\gamma_r}\right) \end{aligned}$$

Remark 2.1. We use following notations next section.

$$\tilde{B}_n^{q_n}(f; x, y, z) = \sum_{k=0}^n f\left(\frac{[k]_{q_n}}{[n]_{q_n}} \alpha_n, y, z\right) \begin{bmatrix} n \\ k \end{bmatrix}_{q_n}$$

$$\times \left(\frac{x}{\alpha_n}\right)^k \prod_{s_1=0}^{n-k-1} \left(1 - q_n^{s_1} \frac{x}{\alpha_n}\right)$$

$$\tilde{B}_m^{q_m}(f; x, y, z) = \sum_{j=0}^m f\left(x, \frac{[j]_{q_m}}{[m]_{q_m}} \beta_m, z\right) \begin{bmatrix} m \\ j \end{bmatrix}_{q_m}$$

$$\times \left(\frac{y}{\beta_m}\right)^j \prod_{s_2=0}^{m-j-1} \left(1 - q_m^{s_2} \frac{y}{\beta_m}\right)$$

$$\tilde{B}_r^{q_r}(f; x, y, z) = \sum_{l=0}^r f\left(x, y, \frac{[l]_{q_r}}{[r]_{q_r}} \gamma_r\right) \begin{bmatrix} r \\ l \end{bmatrix}_{q_r}$$

$$x \left(\frac{z}{\gamma_r}\right)^l \prod_{s_3=0}^{r-l-1} \left(1 - q_r^{s_3} \frac{z}{\gamma_r}\right)$$

Lemma 2.2. Let $e_{i_1, i_2, i_3}: D_{\bar{3}} \rightarrow D_{\bar{3}}$,
 $e_{i_1, i_2, i_3}(x, y, z) = x^{i_1} y^{i_2} z^{i_3}$, $i_1, i_2, i_3 \in \{0, 1, 2\}$ for
 any $x, y, z \in D_{\bar{3}}$ then we get

- i. $\tilde{B}_{n,m,r}^{q_n, q_m, q_r}(e_{0,0,0}; x, y, z) = 1$
- ii. $\tilde{B}_{n,m,r}^{q_n, q_m, q_r}(e_{1,0,0}; x, y, z) = x$
- iii. $\tilde{B}_{n,m,r}^{q_n, q_m, q_r}(e_{0,1,0}; x, y, z) = y$
- iv. $\tilde{B}_{n,m,r}^{q_n, q_m, q_r}(e_{0,0,1}; x, y, z) = z$
- v. for $g(x, y, z) := e_{2,0,0}(x, y, z) + e_{0,2,0}(x, y, z) + e_{0,0,2}(x, y, z)$

$$\tilde{B}_{n,m,r}^{q_n, q_m, q_r}(g; x, y, z) = x^2 + \frac{x(\alpha_n - x)}{[n]_{q_n}} + y^2 + \frac{y(\beta_m - y)}{[m]_{q_m}} + z^2 + \frac{z(\gamma_r - z)}{[r]_{q_r}}$$

Proof: We calculate using definition of $\tilde{B}_{n,m,r}^{q_n, q_m, q_r}(f; x, y, z)$;

$$\begin{aligned} & i) \tilde{B}_{n,m,r}^{q_n, q_m, q_r}(e_{0,0,0}; x, y, z) \\ &= \sum_{k=0}^n \sum_{j=0}^m \sum_{l=0}^r [k]_{q_n} [j]_{q_m} [l]_{q_r} \left(\frac{x}{\alpha_n}\right)^k \left(\frac{y}{\beta_m}\right)^j \left(\frac{z}{\gamma_r}\right)^l \\ & \times \prod_{s_1=0}^{n-k-1} \left(1 - q_n^{s_1} \frac{x}{\alpha_n}\right) \prod_{s_2=0}^{m-j-1} \left(1 - q_m^{s_2} \frac{y}{\beta_m}\right) \\ & \times \prod_{s_3=0}^{r-l-1} \left(1 - q_r^{s_3} \frac{z}{\gamma_r}\right) \\ &= \left\{ \sum_{k=0}^n [k]_{q_n} \left(\frac{x}{\alpha_n}\right)^k \prod_{s_1=0}^{n-k-1} \left(1 - q_n^{s_1} \frac{x}{\alpha_n}\right) \right\} \\ & \times \left\{ \sum_{j=0}^m [j]_{q_m} \left(\frac{y}{\beta_m}\right)^j \prod_{s_2=0}^{m-j-1} \left(1 - q_m^{s_2} \frac{y}{\beta_m}\right) \right\} \\ & \times \left\{ \sum_{l=0}^r [l]_{q_r} \left(\frac{z}{\gamma_r}\right)^l \prod_{s_3=0}^{r-l-1} \left(1 - q_r^{s_3} \frac{z}{\gamma_r}\right) \right\} \\ &= \tilde{B}_n^{q_n}(e_0, x) \tilde{B}_m^{q_m}(e_0, y) \tilde{B}_r^{q_r}(e_0, z) = 1 \\ & ii) \tilde{B}_{n,m,r}^{q_n, q_m, q_r}(e_{1,0,0}; x, y, z) = \sum_{k=0}^n \sum_{j=0}^m \sum_{l=0}^r \frac{[k]_{q_n}}{[n]_{q_n}} \alpha_n [k]_{q_n} \\ & \times [j]_{q_m} [l]_{q_r} \left(\frac{x}{\alpha_n}\right)^k \left(\frac{y}{\beta_m}\right)^j \left(\frac{z}{\gamma_r}\right)^l \\ & \times \prod_{s_1=0}^{n-k-1} \left(1 - q_n^{s_1} \frac{x}{\alpha_n}\right) \prod_{s_2=0}^{m-j-1} \left(1 - q_m^{s_2} \frac{y}{\beta_m}\right) \end{aligned}$$

$$\begin{aligned} & \times \prod_{s_3=0}^{r-l-1} \left(1 - q_r^{s_3} \frac{z}{\gamma_r}\right) \\ &= \left\{ \sum_{k=0}^n \frac{[k]_{q_n}}{[n]_{q_n}} \alpha_n [k]_{q_n} \left(\frac{x}{\alpha_n}\right)^k \prod_{s_1=0}^{n-k-1} \left(1 - q_n^{s_1} \frac{x}{\alpha_n}\right) \right\} \\ & \times \left\{ \sum_{j=0}^m [j]_{q_m} \left(\frac{y}{\beta_m}\right)^j \prod_{s_2=0}^{m-j-1} \left(1 - q_m^{s_2} \frac{y}{\beta_m}\right) \right\} \\ & \times \left\{ \sum_{l=0}^r [l]_{q_r} \left(\frac{z}{\gamma_r}\right)^l \prod_{s_3=0}^{r-l-1} \left(1 - q_r^{s_3} \frac{z}{\gamma_r}\right) \right\} \\ &= \tilde{B}_n^{q_n}(e_1, x) \tilde{B}_m^{q_m}(e_0, y) \tilde{B}_r^{q_r}(e_0, z) = x \\ & iii) \tilde{B}_{n,m,r}^{q_n, q_m, q_r}(e_{0,1,0}; x, y, z) = \sum_{k=0}^n \sum_{j=0}^m \sum_{l=0}^r \frac{[j]_{q_m}}{[m]_{q_m}} \beta_m [k]_{q_n} \\ & \times [j]_{q_m} [l]_{q_r} \left(\frac{x}{\alpha_n}\right)^k \left(\frac{y}{\beta_m}\right)^j \left(\frac{z}{\gamma_r}\right)^l \end{aligned}$$

$$\begin{aligned} & \times \prod_{s_1=0}^{n-k-1} \left(1 - q_n^{s_1} \frac{x}{\alpha_n}\right) \prod_{s_2=0}^{m-j-1} \left(1 - q_m^{s_2} \frac{y}{\beta_m}\right) \\ & \times \prod_{s_3=0}^{r-l-1} \left(1 - q_r^{s_3} \frac{z}{\gamma_r}\right) \\ &= \left\{ \sum_{k=0}^n [k]_{q_n} \left(\frac{x}{\alpha_n}\right)^k \prod_{s_1=0}^{n-k-1} \left(1 - q_n^{s_1} \frac{x}{\alpha_n}\right) \right\} \\ & \times \left\{ \sum_{j=0}^m \frac{[j]_{q_m}}{[m]_{q_m}} \beta_m [j]_{q_m} \left(\frac{y}{\beta_m}\right)^j \prod_{s_2=0}^{m-j-1} \left(1 - q_m^{s_2} \frac{y}{\beta_m}\right) \right\} \\ & \times \left\{ \sum_{l=0}^r [l]_{q_r} \left(\frac{z}{\gamma_r}\right)^l \prod_{s_3=0}^{r-l-1} \left(1 - q_r^{s_3} \frac{z}{\gamma_r}\right) \right\} \\ &= \tilde{B}_n^{q_n}(e_0, x) \tilde{B}_m^{q_m}(e_1, y) \tilde{B}_r^{q_r}(e_0, z) = y \\ & iv) \tilde{B}_{n,m,r}^{q_n, q_m, q_r}(e_{0,0,1}; x, y, z) \\ &= \sum_{k=0}^n \sum_{j=0}^m \sum_{l=0}^r \frac{[l]_{q_r}}{[r]_{q_r}} \gamma_r [k]_{q_n} [j]_{q_m} [l]_{q_r} \left(\frac{x}{\alpha_n}\right)^k \left(\frac{y}{\beta_m}\right)^j \left(\frac{z}{\gamma_r}\right)^l \\ & \times \prod_{s_1=0}^{n-k-1} \left(1 - q_n^{s_1} \frac{x}{\alpha_n}\right) \prod_{s_2=0}^{m-j-1} \left(1 - q_m^{s_2} \frac{y}{\beta_m}\right) \\ & \times \prod_{s_3=0}^{r-l-1} \left(1 - q_r^{s_3} \frac{z}{\gamma_r}\right) \\ &= \left\{ \sum_{k=0}^n [k]_{q_n} \left(\frac{x}{\alpha_n}\right)^k \prod_{s_1=0}^{n-k-1} \left(1 - q_n^{s_1} \frac{x}{\alpha_n}\right) \right\} \end{aligned}$$

$$\begin{aligned}
 & \times \left\{ \sum_{j=0}^m [m]_{q_m} \left(\frac{y}{\beta_m}\right)^j \prod_{s_2=0}^{m-j-1} \left(1 - q_m^{s_2} \frac{y}{\beta_m}\right) \right\} \\
 & \times \left\{ \sum_{l=0}^r \frac{[l]_{q_r}}{[r]_{q_r}} \gamma_r [l]_{q_r} \left(\frac{z}{\gamma_r}\right)^l \prod_{s_3=0}^{r-l-1} \left(1 - q_r^{s_3} \frac{z}{\gamma_r}\right) \right\} \\
 & = z
 \end{aligned}$$

$$\begin{aligned}
 v) \tilde{B}_{n,m,r}^{q_n, q_m, q_r}(e_{2,0,0}; x, y, z) &= \sum_{k=0}^n \sum_{j=0}^m \sum_{l=0}^r \frac{[k]_{q_n}^2}{[n]_{q_n}^2} \alpha_n^2 [k]_{q_n} \\
 & \times [m]_{q_m} [l]_{q_r} \left(\frac{x}{\alpha_n}\right)^k \left(\frac{y}{\beta_m}\right)^j \left(\frac{z}{\gamma_r}\right)^l
 \end{aligned}$$

$$\begin{aligned}
 & \times \prod_{s_1=0}^{n-k-1} \left(1 - q_n^{s_1} \frac{x}{\alpha_n}\right) \prod_{s_2=0}^{m-j-1} \left(1 - q_m^{s_2} \frac{y}{\beta_m}\right) \\
 & \times \prod_{s_3=0}^{r-l-1} \left(1 - q_r^{s_3} \frac{z}{\gamma_r}\right) \\
 & = \left\{ \sum_{k=0}^n \frac{[k]_{q_n}^2}{[n]_{q_n}^2} \alpha_n^2 [k]_{q_n} \left(\frac{x}{\alpha_n}\right)^k \prod_{s_1=0}^{n-k-1} \left(1 - q_n^{s_1} \frac{x}{\alpha_n}\right) \right\}
 \end{aligned}$$

$$\begin{aligned}
 & \times \left\{ \sum_{j=0}^m [m]_{q_m} \left(\frac{y}{\beta_m}\right)^j \prod_{s_2=0}^{m-j-1} \left(1 - q_m^{s_2} \frac{y}{\beta_m}\right) \right\} \\
 & \times \left\{ \sum_{l=0}^r \frac{[l]_{q_r}}{[r]_{q_r}} \gamma_r [l]_{q_r} \left(\frac{z}{\gamma_r}\right)^l \prod_{s_3=0}^{r-l-1} \left(1 - q_r^{s_3} \frac{z}{\gamma_r}\right) \right\} \\
 & = \tilde{B}_n^{q_n}(e_2, x) \tilde{B}_m^{q_m}(e_0, y) \tilde{B}_r^{q_r}(e_0, z) \\
 & = x^2 + \frac{x(\alpha_n - x)}{[n]_{q_n}}
 \end{aligned}$$

$$\tilde{B}_{n,m,r}^{q_n, q_m, q_r}(e_{0,2,0}; x, y, z) = \sum_{k=0}^n \sum_{j=0}^m \sum_{l=0}^r \frac{[j]_{q_m}^2}{[m]_{q_m}^2} \beta_m^2 [k]_{q_n}$$

$$\times [m]_{q_m} [l]_{q_r} \left(\frac{x}{\alpha_n}\right)^k \left(\frac{y}{\beta_m}\right)^j \left(\frac{z}{\gamma_r}\right)^l$$

$$\times \prod_{s_1=0}^{n-k-1} \left(1 - q_n^{s_1} \frac{x}{\alpha_n}\right) \prod_{s_2=0}^{m-j-1} \left(1 - q_m^{s_2} \frac{y}{\beta_m}\right)$$

$$\times \prod_{s_3=0}^{r-l-1} \left(1 - q_r^{s_3} \frac{z}{\gamma_r}\right)$$

$$= \left\{ \sum_{k=0}^n [n]_{q_n} \left(\frac{x}{\alpha_n}\right)^k \prod_{s_1=0}^{n-k-1} \left(1 - q_n^{s_1} \frac{x}{\alpha_n}\right) \right\}$$

$$\times \left\{ \sum_{j=0}^m \frac{[j]_{q_m}^2}{[m]_{q_m}^2} \beta_m^2 [j]_{q_m} \left(\frac{y}{\beta_m}\right)^j \prod_{s_2=0}^{m-j-1} \left(1 - q_m^{s_2} \frac{y}{\beta_m}\right) \right\}$$

$$\times \left\{ \sum_{l=0}^r [l]_{q_r} \left(\frac{z}{\gamma_r}\right)^l \prod_{s_3=0}^{r-l-1} \left(1 - q_r^{s_3} \frac{z}{\gamma_r}\right) \right\}$$

$$\begin{aligned}
 & = \tilde{B}_n^{q_n}(e_0, x) \tilde{B}_m^{q_m}(e_2, y) \tilde{B}_r^{q_r}(e_0, z) \\
 & = y^2 + \frac{y(\beta_m - y)}{[m]_{q_m}}
 \end{aligned}$$

$$\tilde{B}_{n,m,r}^{q_n, q_m, q_r}(e_{0,0,2}; x, y, z) = \sum_{k=0}^n \sum_{j=0}^m \sum_{l=0}^r \frac{[l]_{q_r}^2}{[r]_{q_r}^2} \gamma_r^2$$

$$\times [k]_{q_n} [j]_{q_m} [l]_{q_r} \left(\frac{x}{\alpha_n}\right)^k \left(\frac{y}{\beta_m}\right)^j \left(\frac{z}{\gamma_r}\right)^l$$

$$\times \prod_{s_1=0}^{n-k-1} \left(1 - q_n^{s_1} \frac{x}{\alpha_n}\right) \prod_{s_2=0}^{m-j-1} \left(1 - q_m^{s_2} \frac{y}{\beta_m}\right)$$

$$\times \prod_{s_3=0}^{r-l-1} \left(1 - q_r^{s_3} \frac{z}{\gamma_r}\right)$$

$$= \left\{ \sum_{k=0}^n [n]_{q_n} \left(\frac{x}{\alpha_n}\right)^k \prod_{s_1=0}^{n-k-1} \left(1 - q_n^{s_1} \frac{x}{\alpha_n}\right) \right\}$$

$$\times \left\{ \sum_{j=0}^m [j]_{q_m} \left(\frac{y}{\beta_m}\right)^j \prod_{s_2=0}^{m-j-1} \left(1 - q_m^{s_2} \frac{y}{\beta_m}\right) \right\}$$

$$\times \left\{ \sum_{l=0}^r \frac{[l]_{q_r}^2}{[r]_{q_r}^2} \gamma_r^2 [l]_{q_r} \left(\frac{z}{\gamma_r}\right)^l \prod_{s_3=0}^{r-l-1} \left(1 - q_r^{s_3} \frac{z}{\gamma_r}\right) \right\}$$

$$= \tilde{B}_n^{q_n}(e_0, x) \tilde{B}_m^{q_m}(e_0, y) \tilde{B}_r^{q_r}(e_2, z)$$

$$= z^2 + \frac{z(\gamma_r - z)}{[r]_{q_r}}$$

and so

$$\tilde{B}_{n,m,r}^{q_n, q_m, q_r}(g; x, y, z) = x^2 + \frac{x(\alpha_n - x)}{[n]_{q_n}}$$

$$+ y^2 + \frac{y(\beta_m - y)}{[m]_{q_m}} + z^2 + \frac{z(\gamma_r - z)}{[r]_{q_r}}.$$

Theorem 2.2. Let $f \in C(D_{\mathbb{R}^3})$, then for any sufficiently large fixed positive real numbers a, b, c and $(a \leq \alpha_n, b \leq \beta_m, c \leq \gamma_r)$ then we get

$$\lim_{n,m,r \rightarrow \infty} \max_{(x,y,z) \in D_{\mathbb{R}^3}} |\tilde{B}_{n,m,r}^{q_n, q_m, q_r}(f; x, y, z) - f(x, y, z)| = 0.$$

Proof.

Using Lemma 2.2. for $e_{0,0,0}, e_{1,0,0}, e_{0,1,0}$;

$$\begin{aligned} & \|\tilde{B}_{n,m,r}^{q_n, q_m, q_r}(e_{i_1, i_2, i_3}; x, y, z) - e_{i_1, i_2, i_3}(x, y, z)\|_{C(D_{\mathbb{R}^3})} = 0 \\ & \|\tilde{B}_{n,m,r}^{q_n, q_m, q_r}(e_{2,0,0} + e_{0,2,0} + e_{0,0,2}; x, y, z) - x^2 + y^2 + z^2\|_{C(D_{\mathbb{R}^3})} \\ & \leq a \frac{\alpha_n}{[n]_{q_n}} + b \frac{\beta_m}{[m]_{q_m}} + c \frac{\gamma_r}{[r]_{q_r}}. \end{aligned}$$

From Volkov Theorem and $\{\alpha_n\}, \{\beta_m\}, \{\gamma_r\}$ this equations

$$\lim_{n,m,r \rightarrow \infty} \max_{(x,y,z) \in D_{\mathbb{R}^3}} |\tilde{B}_{n,m,r}^{q_n, q_m, q_r}(f; x, y, z) - f(x, y, z)| = 0.$$

That is completed the proof.

Example 2.2. The convergence of $\tilde{B}_{n,m,r}^{q_n, q_m, q_r}(f; x, y, z)$ to

$f(x, y, z) = (2x)^3(3y)^{1/8}z + 1, \alpha_n = \sqrt{n}, \beta_m = \sqrt[3]{m}, \gamma_r = \sqrt[4]{r} + 1, q = \frac{1}{6}$ is illustrated in Figure 2.2. $n = m = r = 2$ (yellow), $n = m = r = 5$ (magenta).

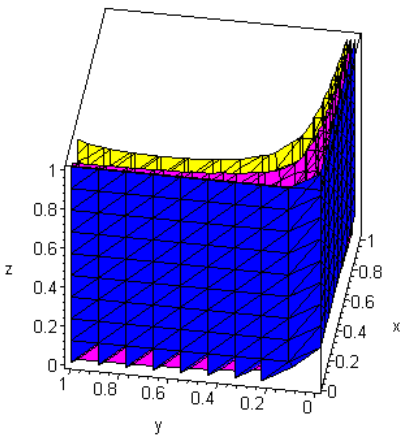


Figure 2.2 Approximation of $f(x, y, z) = (2x)^3 + (3y)^{1/8}z + 1$ (blue) by $\tilde{B}_{n,m,r}^{q_n, q_m, q_r}(f; x, y, z)$.

3. RATES OF CONVERGENCE

In this section we want to find the rate of convergence of the sequence of operators $\{B_{n,m,r}\}$ and $\{\tilde{B}_{n,m,r}^{q_n, q_m, q_r}\}$.

Let $f \in C(\tilde{D}_{\mathbb{R}^3})$ be a continuous function and δ_n, δ_m and δ_r a positive number sequence.

$w_1(f, \delta_n), w_2(f, \delta_m), w_3(f, \delta_r)$ are partial continuity modulus of the function $f(x, y, z)$.

It is also known that $\lim_{\delta_n \rightarrow 0} w_1(f, \delta_n) = \lim_{\delta_m \rightarrow 0} w_2(f, \delta_m) = \lim_{\delta_r \rightarrow 0} w_3(f, \delta_r) = 0$

Lemma 3.1. Let $x, y, z \in [0, A]$, then for any sufficiently large n and then we same as [5] get

$$|B_{n,m,r}(f; x, y, z) - f(x, y, z)| \leq 2A(w_1(f, \delta_n) + w_2(f, \delta_m) + w_3(f, \delta_r)).$$

Proof.

$$\begin{aligned} & |B_{n,m,r}(f; x, y, z) - f(x, y, z)| \\ & \leq \sum_{k=0}^n \sum_{j=0}^m \sum_{l=0}^r \left| f\left(\frac{k}{n}b_n, \frac{j}{m}c_m, \frac{l}{r}d_r\right) - f(x, y, z) \right| \binom{n}{k} \binom{m}{j} \binom{r}{l} \\ & \quad x \left(\frac{x}{b_n}\right)^k \left(1 - \frac{x}{b_n}\right)^{n-k} \left(\frac{y}{c_m}\right)^j \\ & \quad x \left(1 - \frac{y}{c_m}\right)^{m-j} \left(\frac{z}{d_r}\right)^l \left(1 - \frac{z}{d_r}\right)^{r-l} \\ & = \sum_{k=0}^n \sum_{j=0}^m \sum_{l=0}^r \left| f\left(\frac{k}{n}b_n, \frac{j}{m}c_m, z\right) - f\left(x, \frac{j}{m}c_m, z\right) \right| \\ & \quad x \binom{n}{k} \binom{m}{j} \binom{r}{l} \left(\frac{x}{b_n}\right)^k \left(1 - \frac{x}{b_n}\right)^{n-k} \\ & \quad x \left(\frac{y}{c_m}\right)^j \left(1 - \frac{y}{c_m}\right)^{m-j} \left(\frac{z}{d_r}\right)^l \left(1 - \frac{z}{d_r}\right)^{r-l} \\ & \quad + \sum_{k=0}^n \sum_{j=0}^m \sum_{l=0}^r \left| f\left(x, \frac{j}{m}c_m, z\right) - f(x, y, z) \right| \\ & \quad x \binom{n}{k} \binom{m}{j} \binom{r}{l} \left(\frac{x}{b_n}\right)^k \left(1 - \frac{x}{b_n}\right)^{n-k} \\ & \quad x \left(\frac{y}{c_m}\right)^j \left(1 - \frac{y}{c_m}\right)^{m-j} \left(\frac{z}{d_r}\right)^l \left(1 - \frac{z}{d_r}\right)^{r-l} \\ & = \sum_{k=0}^n \sum_{j=0}^m \sum_{l=0}^r \left| f\left(\frac{k}{n}b_n, \frac{j}{m}c_m, \frac{l}{r}d_r\right) - f\left(\frac{k}{n}b_n, \frac{j}{m}c_m, z\right) \right| \\ & \quad x \binom{n}{k} \binom{m}{j} \binom{r}{l} \left(\frac{x}{b_n}\right)^k \left(1 - \frac{x}{b_n}\right)^{n-k} \left(\frac{y}{c_m}\right)^j \\ & \quad x \left(1 - \frac{y}{c_m}\right)^{m-j} \left(\frac{z}{d_r}\right)^l \left(1 - \frac{z}{d_r}\right)^{r-l} \\ & \leq \sum_{k=0}^n \sum_{j=0}^m \sum_{l=0}^r w_1\left(f; \left|\frac{k}{n}b_n - x\right|\right) \\ & \quad x \binom{n}{k} \binom{m}{j} \binom{r}{l} \left(\frac{x}{b_n}\right)^k \left(1 - \frac{x}{b_n}\right)^{n-k} \end{aligned}$$

$$\begin{aligned}
 & x \left(\frac{y}{c_m}\right)^j \left(1 - \frac{y}{c_m}\right)^{m-j} \left(\frac{z}{d_r}\right)^l \left(1 - \frac{z}{d_r}\right)^{r-l} \\
 & + \sum_{k=0}^n \sum_{j=0}^m \sum_{l=0}^r w_2 \left(f; \left| \frac{j}{m} c_m - y \right| \right) \binom{n}{k} \binom{m}{j} \binom{r}{l} \\
 & x \left(\frac{x}{b_n}\right)^k \left(1 - \frac{x}{b_n}\right)^{n-k} \\
 & x \left(\frac{y}{c_m}\right)^j \left(1 - \frac{y}{c_m}\right)^{m-j} \left(\frac{z}{d_r}\right)^l \left(1 - \frac{z}{d_r}\right)^{r-l} \\
 & + \sum_{k=0}^n \sum_{j=0}^m \sum_{l=0}^r w_3 \left(f; \left| \frac{l}{r} d_r - z \right| \right) \\
 & x \binom{n}{k} \binom{m}{j} \binom{r}{l} \left(\frac{x}{b_n}\right)^k \left(1 - \frac{x}{b_n}\right)^{n-k} \\
 \\
 & x \left(\frac{y}{c_m}\right)^j \left(1 - \frac{y}{c_m}\right)^{m-j} \left(\frac{z}{d_r}\right)^l \left(1 - \frac{z}{d_r}\right)^{r-l} \\
 & = \psi_1(x, y, z) + \psi_2(x, y, z) + \psi_3(x, y, z) \\
 & \text{is found. If calculated all of them respectively;} \\
 & \psi_1(x, y, z) = \sum_{k=0}^n \sum_{j=0}^m \sum_{l=0}^r w_1 \left(f; \left| \frac{k}{n} b_n - x \right| \right) \\
 & x \binom{n}{k} \binom{m}{j} \binom{r}{l} \left(\frac{x}{b_n}\right)^k \left(1 - \frac{x}{b_n}\right)^{n-k} \\
 & x \left(\frac{y}{c_m}\right)^j \left(1 - \frac{y}{c_m}\right)^{m-j} \left(\frac{z}{d_r}\right)^l \left(1 - \frac{z}{d_r}\right)^{r-l} \\
 & = \sum_{k=0}^n w_1 \left(f; \left| \frac{k}{n} b_n - x \right| \right) \binom{n}{k} \left(\frac{x}{b_n}\right)^k \left(1 - \frac{x}{b_n}\right)^{n-k} \\
 & x \sum_{j=0}^m \binom{m}{j} \left(\frac{y}{c_m}\right)^j \left(1 - \frac{y}{c_m}\right)^{m-j} \\
 & x \sum_{l=0}^r \binom{r}{l} \left(\frac{z}{d_r}\right)^l \left(1 - \frac{z}{d_r}\right)^{r-l} \\
 & = \sum_{k=0}^n w_1 \left(f; \left| \frac{k}{n} b_n - x \right| \right) \binom{n}{k} \left(\frac{x}{b_n}\right)^k \left(1 - \frac{x}{b_n}\right)^{n-k} \\
 & x \sum_{j=0}^m \binom{m}{j} \left(\frac{y}{c_m}\right)^j \left(1 - \frac{y}{c_m}\right)^{m-j} \\
 & = \sum_{k=0}^n w_1 \left(f; \left| \frac{k}{n} b_n - x \right| \right) \binom{n}{k} \left(\frac{x}{b_n}\right)^k \left(1 - \frac{x}{b_n}\right)^{n-k}
 \end{aligned}$$

At this condition $x \in [0, A]$ and $A > 1$ if take $t = \frac{k}{n} b_n$ when

$|f(t) - f(x)| \leq w_1(f, \delta_n) \left(1 + \frac{|t-x|}{\delta_n}\right)$ obtain by using Cauchy-Schwarz inequality;

$$\begin{aligned}
 & \psi_1(x, y, z) \leq \\
 & w_1(f, \delta_n) \left\{ 1 + \frac{1}{\delta_n} \left[\sum_{k=0}^n \binom{k}{n} b_n - x \right]^2 \binom{n}{k} \left(\frac{x}{b_n}\right)^k \left(1 - \frac{x}{b_n}\right)^{n-k} \right\}^{1/2} \\
 & \leq w_1(f, \delta_n) \left\{ 1 + \frac{1}{\delta_n} \sqrt{A \frac{b_n}{n}} \right\}
 \end{aligned}$$

is found. By choosing $\delta_n = \sqrt{\frac{b_n}{n}}$;

$$\begin{aligned}
 & \psi_1(x, y, z) \leq w_1 \left(f, \sqrt{\frac{b_n}{n}}\right) \{1 + \sqrt{A}\} \\
 & \leq 2Aw_1 \left(f, \sqrt{\frac{b_n}{n}}\right).
 \end{aligned}$$

Similarly

$$\begin{aligned}
 & \psi_2(x, y, z) = \sum_{k=0}^n \sum_{j=0}^m \sum_{l=0}^r w_2 \left(f; \left| \frac{j}{m} c_m - y \right| \right) \\
 & x \binom{n}{k} \binom{m}{j} \binom{r}{l} \left(\frac{x}{b_n}\right)^k \left(1 - \frac{x}{b_n}\right)^{n-k} \\
 & x \left(\frac{y}{c_m}\right)^j \left(1 - \frac{y}{c_m}\right)^{m-j} \left(\frac{z}{d_r}\right)^l \left(1 - \frac{z}{d_r}\right)^{r-l} \\
 & = \sum_{k=0}^n \binom{n}{k} \left(\frac{x}{b_n}\right)^k \left(1 - \frac{x}{b_n}\right)^{n-k} \\
 & x \sum_{j=0}^m w_2 \left(f; \left| \frac{j}{m} c_m - y \right| \right) \binom{m}{j} \left(\frac{y}{c_m}\right)^j \left(1 - \frac{y}{c_m}\right)^{m-j} \\
 & x \sum_{l=0}^r \binom{r}{l} \left(\frac{z}{d_r}\right)^l \left(1 - \frac{z}{d_r}\right)^{r-l} \\
 & = \sum_{k=0}^n \binom{n}{k} \left(\frac{x}{b_n}\right)^k \left(1 - \frac{x}{b_n}\right)^{n-k} \\
 & x \sum_{j=0}^m w_2 \left(f; \left| \frac{j}{m} c_m - y \right| \right) \binom{m}{j} \left(\frac{y}{c_m}\right)^j \left(1 - \frac{y}{c_m}\right)^{m-j} \\
 & = \sum_{j=0}^m w_2 \left(f; \left| \frac{j}{m} c_m - y \right| \right) \binom{m}{j} \left(\frac{y}{c_m}\right)^j \left(1 - \frac{y}{c_m}\right)^{m-j}
 \end{aligned}$$

At this condition $y \in [0, A]$ and $A > 1$ if take $t = \frac{j}{m} c_m$ then for any sufficiently large n and when

$|f(t) - f(y)| \leq w_2(f, \delta_m) \left(1 + \frac{|t-y|}{\delta_m}\right)$ obtain by using Cauchy-Schwarz inequality;

$$\psi_2(x, y, z) \leq$$

$$w_2(f, \delta_m) \left\{ 1 + \frac{1}{\delta_m} \left[\sum_{j=0}^m \left(\frac{j}{m} c_m - y \right)^2 \binom{m}{j} \left(\frac{y}{c_m} \right)^j \left(1 - \frac{y}{c_m} \right)^{m-j} \right]^{1/2} \right\}$$

$$\leq w_2(f, \delta_m) \left\{ 1 + \frac{1}{\delta_m} \sqrt{A \frac{c_m}{m}} \right\}$$

founded. By choosing $\delta_m = \sqrt{\frac{c_m}{m}}$;

$$\psi_2(x, y, z) \leq w_2 \left(f, \sqrt{\frac{c_m}{m}} \right) \{1 + \sqrt{A}\}$$

$$\leq 2Aw_2 \left(f, \sqrt{\frac{c_m}{m}} \right)$$

is found. Finally

$$\psi_3(x, y, z) = \sum_{k=0}^n \sum_{j=0}^m \sum_{l=0}^r w_3 \left(f; \left| \frac{l}{r} d_r - z \right| \right)$$

$$\times \binom{n}{k} \binom{m}{j} \binom{r}{l} \left(\frac{x}{b_n} \right)^k \left(1 - \frac{x}{b_n} \right)^{n-k}$$

$$\times \left(\frac{y}{c_m} \right)^j \left(1 - \frac{y}{c_m} \right)^{m-j} \left(\frac{z}{d_r} \right)^l \left(1 - \frac{z}{d_r} \right)^{r-l}$$

$$= \sum_{k=0}^n \binom{n}{k} \left(\frac{x}{b_n} \right)^k \left(1 - \frac{x}{b_n} \right)^{n-k}$$

$$\times \sum_{j=0}^m \binom{m}{j} \left(\frac{y}{c_m} \right)^j \left(1 - \frac{y}{c_m} \right)^{m-j}$$

$$\times \sum_{l=0}^r w_3 \left(f; \left| \frac{l}{r} d_r - z \right| \right) \binom{r}{l} \left(\frac{z}{d_r} \right)^l \left(1 - \frac{z}{d_r} \right)^{r-l}$$

$$= \sum_{l=0}^r w_3 \left(f; \left| \frac{l}{r} d_r - z \right| \right) \binom{r}{l} \left(\frac{z}{d_r} \right)^l \left(1 - \frac{z}{d_r} \right)^{r-l}$$

At this conditions $z, t \in [0, A]$ ve $A > 1$ if take $t = \frac{l}{r} d_r$ when

$|f(t) - f(z)| \leq w_3(f, \delta_r) \left(1 + \frac{|t-z|}{\delta_r}\right)$ obtain by using Cauchy-Schwarz inequality;

$$\psi_3(x, y, z) \leq$$

$$w_3(f, \delta_r) \left\{ 1 + \frac{1}{\delta_r} \left[\sum_{l=0}^r \left(\frac{l}{r} d_r - z \right)^2 \binom{r}{l} \left(\frac{z}{d_r} \right)^l \left(1 - \frac{z}{d_r} \right)^{r-l} \right]^{1/2} \right\}$$

$$\leq w_3(f, \delta_r) \left\{ 1 + \frac{1}{\delta_r} \sqrt{A \frac{d_r}{r}} \right\}$$

founded. By choosing $\delta_r = \sqrt{\frac{d_r}{r}}$;

$$\psi_3(x, y, z) \leq w_3 \left(f, \sqrt{\frac{d_r}{r}} \right) \{1 + \sqrt{A}\}$$

$$\leq 2Aw_3 \left(f, \sqrt{\frac{d_r}{r}} \right)$$

is obtained.

$$\begin{aligned} |B_{n,m,r}(f; x, y, z) - f(x, y, z)| \\ \leq 2A(w_1(f, \delta_n) + w_2(f, \delta_m) \\ + w_3(f, \delta_r)) \end{aligned}$$

Then proof is completed.

Example 3.1. The error bound of the function $f(x, y, z) = \frac{x^2+y^2+z^2}{2+\exp(7)}$,

$$b_n = \sqrt{n}, c_m = \sqrt[3]{m}, d_r = \sqrt[4]{r} + 1.$$

Table 3.1. The error bound of

$$f(x, y, z) = \frac{x^2+y^2+z^2}{2+\exp(7)}.$$

n,m,r	Error bound for full modulus of continuity of function $f(x, y, z)$
10	0.0218237378
10 ²	0.0073671615
10 ³	0.0027753196
10 ⁴	0.0011048136
10 ⁵	0.0004521637
10 ⁶	0.0001876932
10 ⁷	0.0000784867
10 ⁸	0.0000329479
10 ⁹	0.0000138598

Using the q-modulus of continuity we get the rate of convergence following.

Lemma 3.2. For any $f \in D_{\mathfrak{z}}$, the following inequality hold.

$$a) \quad |\tilde{B}_{n,m,r}^{q_n, q_m, q_r}(f; x, y, z) - f(x, y, z)| \leq 3 \left[w_1 \left(f; \sqrt{\frac{a\alpha_n}{[n]_{q_n}}} \right) + w_2 \left(f; \sqrt{\frac{b\beta_m}{[m]_{q_m}}} \right) + \left(f; \sqrt{\frac{c\gamma_r}{[r]_{q_r}}} \right) \right]$$

$$b) \quad |\tilde{B}_{n,m,r}^{q_n, q_m, q_r}(f; x, y, z) - f(x, y, z)| \leq 3w \left(f; \sqrt{\frac{a\alpha_n}{[n]_{q_n}}} + \sqrt{\frac{b\beta_m}{[m]_{q_m}}} + \sqrt{\frac{c\gamma_r}{[r]_{q_r}}} \right)$$

Proof. Using next equality

$$\sum_{k=0}^n f \left(\frac{[k]_{q_n}}{[n]_{q_n}} \alpha_n \right) = \sum_{j=0}^m f \left(\frac{[j]_{q_m}}{[m]_{q_m}} \beta_m \right) = \sum_{l=0}^r f \left(\frac{[l]_{q_r}}{[r]_{q_r}} \gamma_r \right)$$

we estimate the difference between $\tilde{B}_{n,m,r}^{q_n, q_m, q_r}(f; x, y, z)$ and $f(x, y, z)$;

$$\begin{aligned} & \tilde{B}_{n,m,r}^{q_n, q_m, q_r}(f; x, y, z) - f(x, y, z) = \\ & \sum_{k=0}^n \sum_{j=0}^m \sum_{l=0}^r \left[f \left(\frac{[k]_{q_n}}{[n]_{q_n}} \alpha_n, \frac{[j]_{q_m}}{[m]_{q_m}} \beta_m, \frac{[l]_{q_r}}{[r]_{q_r}} \gamma_r \right) - f(x, y, z) \right] \\ & \times \begin{bmatrix} n \\ k \end{bmatrix}_{q_n} \begin{bmatrix} m \\ j \end{bmatrix}_{q_m} \begin{bmatrix} r \\ l \end{bmatrix}_{q_r} \left(\frac{x}{\alpha_n} \right)^k \left(\frac{y}{\beta_m} \right)^j \left(\frac{z}{\gamma_r} \right)^l \\ & \times \prod_{s_1=0}^{n-k-1} \left(1 - q_n^{s_1} \frac{x}{\alpha_n} \right) \prod_{s_2=0}^{m-j-1} \left(1 - q_m^{s_2} \frac{y}{\beta_m} \right) \\ & \times \prod_{s_3=0}^{r-l-1} \left(1 - q_r^{s_3} \frac{z}{\gamma_r} \right) \\ & = \sum_{k=0}^n \sum_{j=0}^m \sum_{l=0}^r \left[f \left(\frac{[k]_{q_n}}{[n]_{q_n}} \alpha_n, \frac{[j]_{q_m}}{[m]_{q_m}} \beta_m, \frac{[l]_{q_r}}{[r]_{q_r}} \gamma_r \right) \right. \\ & \quad \left. - f \left(\frac{[k]_{q_n}}{[n]_{q_n}} \alpha_n, y, z \right) + f \left(\frac{[k]_{q_n}}{[n]_{q_n}} \alpha_n, y, z \right) \right. \\ & \quad \left. - f(x, y, z) \right] \end{aligned}$$

$$\begin{aligned} & \times \begin{bmatrix} n \\ k \end{bmatrix}_{q_n} \begin{bmatrix} m \\ j \end{bmatrix}_{q_m} \begin{bmatrix} r \\ l \end{bmatrix}_{q_r} \left(\frac{x}{\alpha_n} \right)^k \left(\frac{y}{\beta_m} \right)^j \left(\frac{z}{\gamma_r} \right)^l \\ & \times \prod_{s_1=0}^{n-k-1} \left(1 - q_n^{s_1} \frac{x}{\alpha_n} \right) \prod_{s_2=0}^{m-j-1} \left(1 - q_m^{s_2} \frac{y}{\beta_m} \right) \\ & \times \prod_{s_3=0}^{r-l-1} \left(1 - q_r^{s_3} \frac{z}{\gamma_r} \right) \end{aligned}$$

then

$$|\tilde{B}_{n,m,r}^{q_n, q_m, q_r}(f; x, y, z) - f(x, y, z)| \leq$$

$$\begin{aligned} & \sum_{k=0}^n \sum_{j=0}^m \sum_{l=0}^r \left[f \left(\frac{[k]_{q_n}}{[n]_{q_n}} \alpha_n, \frac{[j]_{q_m}}{[m]_{q_m}} \beta_m, \frac{[l]_{q_r}}{[r]_{q_r}} \gamma_r \right) \right. \\ & \quad \left. - f \left(\frac{[k]_{q_n}}{[n]_{q_n}} \alpha_n, y, z \right) \right] \\ & \times \begin{bmatrix} n \\ k \end{bmatrix}_{q_n} \begin{bmatrix} m \\ j \end{bmatrix}_{q_m} \begin{bmatrix} r \\ l \end{bmatrix}_{q_r} \left(\frac{x}{\alpha_n} \right)^k \left(\frac{y}{\beta_m} \right)^j \left(\frac{z}{\gamma_r} \right)^l \\ & \times \prod_{s_1=0}^{n-k-1} \left(1 - q_n^{s_1} \frac{x}{\alpha_n} \right) \prod_{s_2=0}^{m-j-1} \left(1 - q_m^{s_2} \frac{y}{\beta_m} \right) \\ & \times \prod_{s_3=0}^{r-l-1} \left(1 - q_r^{s_3} \frac{z}{\gamma_r} \right) \\ & = \sum_{k=0}^n \sum_{j=0}^m \sum_{l=0}^r \left[f \left(\frac{[k]_{q_n}}{[n]_{q_n}} \alpha_n, y, z \right) - f(x, y, z) \right] \end{aligned}$$

$$\begin{aligned} & \times \begin{bmatrix} n \\ k \end{bmatrix}_{q_n} \begin{bmatrix} m \\ j \end{bmatrix}_{q_m} \begin{bmatrix} r \\ l \end{bmatrix}_{q_r} \left(\frac{x}{\alpha_n} \right)^k \left(\frac{y}{\beta_m} \right)^j \left(\frac{z}{\gamma_r} \right)^l \\ & \times \prod_{s_1=0}^{n-k-1} \left(1 - q_n^{s_1} \frac{x}{\alpha_n} \right) \prod_{s_2=0}^{m-j-1} \left(1 - q_m^{s_2} \frac{y}{\beta_m} \right) \\ & \times \prod_{s_3=0}^{r-l-1} \left(1 - q_r^{s_3} \frac{z}{\gamma_r} \right) \end{aligned}$$

$$\leq \sum_{k=0}^n \sum_{j=0}^m \sum_{l=0}^r w_2 \left(f; \left| \frac{[j]_{q_m}}{[m]_{q_m}} \beta_m - y \right| \right)$$

$$\begin{aligned} & \times \begin{bmatrix} n \\ k \end{bmatrix}_{q_n} \begin{bmatrix} m \\ j \end{bmatrix}_{q_m} \begin{bmatrix} r \\ l \end{bmatrix}_{q_r} \left(\frac{x}{\alpha_n} \right)^k \left(\frac{y}{\beta_m} \right)^j \left(\frac{z}{\gamma_r} \right)^l \\ & \times \prod_{s_1=0}^{n-k-1} \left(1 - q_n^{s_1} \frac{x}{\alpha_n} \right) \prod_{s_2=0}^{m-j-1} \left(1 - q_m^{s_2} \frac{y}{\beta_m} \right) \\ & \times \prod_{s_3=0}^{r-l-1} \left(1 - q_r^{s_3} \frac{z}{\gamma_r} \right) \end{aligned}$$

$$\leq \sum_{k=0}^n \sum_{j=0}^m \sum_{l=0}^r w_1 \left(f; \left| \frac{[k]_{q_n}}{[n]_{q_n}} \alpha_n - x \right| \right)$$

$$\begin{aligned} & \times \begin{bmatrix} n \\ k \end{bmatrix}_{q_n} \begin{bmatrix} m \\ j \end{bmatrix}_{q_m} \begin{bmatrix} r \\ l \end{bmatrix}_{q_r} \left(\frac{x}{\alpha_n} \right)^k \left(\frac{y}{\beta_m} \right)^j \left(\frac{z}{\gamma_r} \right)^l \\ & \times \prod_{s_1=0}^{n-k-1} \left(1 - q_n^{s_1} \frac{x}{\alpha_n} \right) \prod_{s_2=0}^{m-j-1} \left(1 - q_m^{s_2} \frac{y}{\beta_m} \right) \\ & \times \prod_{s_3=0}^{r-l-1} \left(1 - q_r^{s_3} \frac{z}{\gamma_r} \right) \end{aligned}$$

$$\leq \sum_{k=0}^n \sum_{j=0}^m \sum_{l=0}^r w_3 \left(f; \left| \frac{[l]_{q_r}}{[r]_{q_r}} \gamma_r - z \right| \right) \\
 \times \begin{bmatrix} n \\ k \end{bmatrix}_{q_n} \begin{bmatrix} m \\ j \end{bmatrix}_{q_m} \begin{bmatrix} r \\ l \end{bmatrix}_{q_r} \left(\frac{x}{\alpha_n} \right)^k \left(\frac{y}{\beta_m} \right)^j \left(\frac{z}{\gamma_r} \right)^l \\
 \times \prod_{s_1=0}^{n-k-1} \left(1 - q_n^{s_1} \frac{x}{\alpha_n} \right) \prod_{s_2=0}^{m-j-1} \left(1 - q_m^{s_2} \frac{y}{\beta_m} \right) \\
 \times \prod_{s_3=0}^{r-l-1} \left(1 - q_r^{s_3} \frac{z}{\gamma_r} \right) \\
 = \check{\psi}_2(x, y, z) + \check{\psi}_1(x, y, z) + \check{\psi}_3(x, y, z)$$

By using Lemma 2.2.(i) and properties continuity, we get

$$\check{\psi}_2(x, y, z) = \sum_{k=0}^n \sum_{j=0}^m \sum_{l=0}^r w_2 \left(f; \left| \frac{[j]_{q_m}}{[m]_{q_m}} \beta_m - y \right| \right) \\
 \times \begin{bmatrix} n \\ k \end{bmatrix}_{q_n} \begin{bmatrix} m \\ j \end{bmatrix}_{q_m} \begin{bmatrix} r \\ l \end{bmatrix}_{q_r} \left(\frac{x}{\alpha_n} \right)^k \left(\frac{y}{\beta_m} \right)^j \left(\frac{z}{\gamma_r} \right)^l \\
 \times \prod_{s_1=0}^{n-k-1} \left(1 - q_n^{s_1} \frac{x}{\alpha_n} \right) \prod_{s_2=0}^{m-j-1} \left(1 - q_m^{s_2} \frac{y}{\beta_m} \right) \\
 \times \prod_{s_3=0}^{r-l-1} \left(1 - q_r^{s_3} \frac{z}{\gamma_r} \right) \\
 = \sum_{j=0}^m w_2 \left(f; \left| \frac{[j]_{q_m}}{[m]_{q_m}} \beta_m - y \right| \right) \begin{bmatrix} m \\ j \end{bmatrix}_{q_m} \left(\frac{y}{\beta_m} \right)^j \\
 \times \prod_{s_2=0}^{m-j-1} \left(1 - q_m^{s_2} \frac{y}{\beta_m} \right) \\
 \leq w_2(f; \delta_m) \left\{ 1 + \frac{1}{\delta_m} \left[\sum_{j=0}^m \left(\frac{[j]_{q_m}}{[m]_{q_m}} \beta_m - y \right)^2 \begin{bmatrix} m \\ j \end{bmatrix}_{q_m} \left(\frac{y}{\beta_m} \right)^j \prod_{s_2=0}^{m-j-1} \left(1 - q_m^{s_2} \frac{y}{\beta_m} \right) \right]^{1/2} \right\}$$

Expending the squared term and making use of Lemma 2.2 (i), (iii) and (v) we have

$$\check{\psi}_2(x, y, z) \leq w_2(f; \delta_m) \left\{ 1 + \frac{1}{\delta_m} \sqrt{\frac{y(\beta_m - y)}{[m]_{q_m}}} \right\}$$

$$\leq w_2(f; \delta_m) \left\{ 1 + \frac{1}{\delta_m} \sqrt{\frac{b\beta_m}{[m]_{q_m}}} \right\}.$$

By choosing $\delta_m = \sqrt{\frac{b\beta_m}{[m]_{q_m}}}$ we get

$$\check{\psi}_2(x, y, z) \leq 3w_2 \left(f; \sqrt{\frac{b\beta_m}{[m]_{q_m}}} \right).$$

In the some way we have

$$\check{\psi}_1(x, y, z) \leq 3w_1 \left(f; \sqrt{\frac{a\alpha_n}{[n]_{q_n}}} \right) \text{ and}$$

$$\check{\psi}_3(x, y, z) \leq 3w_3 \left(f; \sqrt{\frac{c\gamma_r}{[r]_{q_r}}} \right). \text{ We define}$$

$A := \max\{a, b, c\}$ then we get

$$|B_{n,m,r}(f; x, y, z) - f(x, y, z)| \leq 3A(w_1(f, \delta_n) + w_2(f, \delta_m) + w_3(f, \delta_r)).$$

Example3.2. The error bound of the function $f(x, y, z) = \frac{xy+10-z}{10}$, $\alpha_n = \sqrt{n}$, $\beta_m = \sqrt[3]{m}$, $\gamma_r = \sqrt[4]{r} + 1$ and $q = 1$.

Table3.2. The error bound of $f(x, y, z) = \frac{xy+10-z}{10}$.

n, m, r	Error bound for q-modulus of continuity of function $f(x, y, z)$
10	0.7244296242
10 ²	0.2210754467
10 ³	0.0792069915
10 ⁴	0.0308396231
10 ⁵	0.0125035752
10 ⁶	0.0051698321
10 ⁷	0.0021582801

4. CONCLUSION

We give Bernstein-Chlodowsky and q generalized this operators so researchers can compare their approximation we have beter approach result for q-Bernstein-Chlodowsky operators means of modulus of continuity.

REFERENCES

- [1] G.M.Philips, "On Generalized Bernstein Polynomials", in *Numerical Analysis: D.F. Griffiths, G.A. Watson Eds, World Scientific Singapore, pp. 263-269, 1996.*
- [2] H. Karsli and V. Gupta, "Some Approximation Properties of q-Chlodowsky Operators",

Applied Mathematics and Computation, vol. 195, pp. 220–229, 2008.

Variables”, *Applied Mathematics and Computation* vol. 156, pp. 367–380, 2004.

[3] I. Buyukyazici, “One the Approximation Properties of Two-Dimensional q-Bernstein-Chlodowsky Polynomials”, *Mathematical Communications* vol. 14, no. 2, pp. 255-269, 2009.

[5] A.K. Gazanfer, “Weighted Approximation Of Continuous Functions Of Three Variables in a Tetrahedron With Variable Boundary By Bernstein-Chlodowsky Polynomials”, Ph. D. Thesis, Graduate School of Natural and Applied Sciences, Bulent Ecevit Univ., Zonguldak Turkey, 2015.

[4] I. Buyukyazici and E. Ibikli, “The Approximation Properties of Generalized Bernstein-Chlodowsky Polynomials of Two

	SAKARYA UNIVERSITY JOURNAL OF SCIENCE		 SAKARYA UNIVERSITY
	e-ISSN: 2147-835X http://www.saujs.sakarya.edu.tr		
	<u>Received</u> 02-03-2018 <u>Accepted</u> 14-06-2018	<u>Doi</u> 10.16984/saufenbilder.400272	

Geometric Kinematic Approach to Rigid Objects with Point Contact Based on A Local-Surface Frame

Vahide Bulut¹

Abstract

Controlling the relative motion between two contacting rigid bodies is necessary when manipulation and locomotion tasks are encountered in robotics. In this paper, we express the kinematics of spin-rolling motion of rigid objects with point contact based on the local-surface frame method. We give the relationship between the Darboux frame and local-surface frame, and also between the Frenet-Serret frame and local-surface frame. Additionally, we obtain velocity of the moving object according to the local-surface frame curvatures of the respective contact curve and geometric invariants. We can have proper information about trajectory planning if we take the formulations of moving object into consideration according to the local-surface frame.

Keywords: Frenet-Serret frame, Darboux frame, Local-Surface frame, kinematics, point contact.

1. INTRODUCTION

During the robot manipulation tasks, the robot arm needs to be able to control the contact motion, when it interacts with an object. If the robot grasps an object it may be necessary to roll or to slide the object in a specified manner [1]. The point contact motion can be defined as the combination of sliding, spin, and rolling motion.

Kinematics of point contact has been examined widely by researchers. Some of them studied on contact between planar rigid bodies (for example, [2, 3, 4, 5, 6]). Recently, some researchers have studied on the kinematics of 3D contact between two rigid bodies. Pars describes the configuration space as five-dimensional associated with the relative motion between two rigid bodies in point contact [7]. Cai and Roth study the kinematics of two contacting bodies in point contact according to spatial motion [8, 9].

They examined the relative motion between two rigid bodies with point contact by using local geometric properties of each rigid body [9]. However, they studied the spatial motion of the rigid bodies with line contact [10]. Montana derives the equations of contact from a geometric perspective [11]. Cui and Dai applies Darboux frame method to developing geometric kinematics of rigid objects with point contact [12].

This paper presents the local-surface frame method to express the kinematics of rigid bodies with point contact. Also, we show some relationships between the Darboux frame and local-surface frame, and the Frenet-Serret frame and local-surface frame. Moreover, we give the velocity equations with respect to local-surface frame curvatures of the respective contact curve and geometric invariants.

¹ Department of Mathematics, Ege University, Izmir, 35100, Turkey, vahidebulut@mail.ege.edu.tr

2. PRELIMINARIES

Let $\alpha(s)$ be a unit speed curve that satisfies $\|\alpha'(s)\| = 1$ in E^3 and the Frenet-Serret frame $\{\alpha; \mathbf{t}, \mathbf{N}, \mathbf{B}\}$ of this curve parametrized by arc length parameter s , is:

$$\begin{aligned} \alpha'(s) &= \mathbf{t} \\ \frac{\mathbf{t}'(s)}{\|\mathbf{t}'(s)\|} &= \mathbf{N}(s) \\ \mathbf{t}(s) \times \mathbf{N}(s) &= \mathbf{B}(s) \end{aligned} \tag{1}$$

where the vectors \mathbf{t} , \mathbf{N} , and \mathbf{B} are the unit tangent vector, unit principal normal vector, and unit binormal normal vector, and $\kappa = \kappa(s) = \|\mathbf{t}'(s)\|$ and $\tau = \tau(s) = \|\mathbf{B}'(s)\|$ are the curvature and torsion of the curve $\alpha(s)$ at s_0 , respectively. The Frenet vector and the unit Frenet vector of this curve can be defined as follows:

$$\mathbf{f} = \tau \mathbf{t} + \kappa \mathbf{B} \tag{2}$$

and

$$\mathbf{w} = \frac{\mathbf{f}}{\|\mathbf{f}\|} = \frac{\tau \mathbf{t} + \kappa \mathbf{B}}{\sqrt{\tau^2 + \kappa^2}}$$

Let $X(u, v)$ be a regular surface and the curve $\alpha(s)$, parametrized by arc length parameter s , be on the surface $X(u, v)$. Since the curve $\alpha(s)$ is also a space curve, the curve $\alpha(s)$ has the Frenet-Serret frame as mentioned above. The curve $\alpha(s)$ lies on the surface $X(u, v)$, and there exists another frame called as a Darboux frame $\{\mathbf{t}, \mathbf{g}, \mathbf{n}\}$ of the curve $\alpha(s)$ at s_0 , where \mathbf{t} is the unit tangent vector of the curve $\alpha(s)$, \mathbf{n} is the unit normal vector of the surface $X(u, v)$ and \mathbf{g} is a unit vector given by $\mathbf{g} = \mathbf{n} \times \mathbf{t}$. The derivative formulas of Darboux frame are given as follows:

$$\begin{bmatrix} \mathbf{t}' \\ \mathbf{g}' \\ \mathbf{n}' \end{bmatrix} = \begin{bmatrix} 0 & \kappa_g & \kappa_n \\ -\kappa_g & 0 & \tau_g \\ -\kappa_n & -\tau_g & 0 \end{bmatrix} \begin{bmatrix} \mathbf{t} \\ \mathbf{g} \\ \mathbf{n} \end{bmatrix}, \tag{3}$$

where, κ_g is the geodesic curvature, κ_n is the normal curvature, and τ_g is the geodesic torsion of the curve $\alpha(s)$. The Darboux vector and the unit Darboux vector of this curve are [13]:

$$\mathbf{d} = \tau_g \mathbf{t} + \kappa_n \mathbf{g} + \kappa_g \mathbf{n} \tag{4}$$

and

$$\mathbf{d}_0 = \frac{\mathbf{d}}{\|\mathbf{d}\|} = \frac{\tau_g \mathbf{t} + \kappa_n \mathbf{g} + \kappa_g \mathbf{n}}{\|\tau_g \mathbf{t} + \kappa_n \mathbf{g} + \kappa_g \mathbf{n}\|}.$$

Let the right-handed system, which we call as a Local-Surface frame, of the surface $X(u, v)$ be defined as $(\mathbf{t}_1, \mathbf{t}_2, \mathbf{n})$ which can then be given as

$$\begin{aligned} \mathbf{t}_1 &= \frac{X_u(u, v)}{\|X_u(u, v)\|} \\ \mathbf{t}_2 &= \frac{X_v(u, v)}{\|X_v(u, v)\|} \\ \mathbf{n} &= \frac{X_u(u, v) \times X_v(u, v)}{\|X_u(u, v) \times X_v(u, v)\|} \end{aligned} \tag{5}$$

where X_u and X_v are the partial derivatives of $X(u, v)$ with regard to parameters u and v [14]. In this paper, we suppose that Local-Surface frame $(\mathbf{t}_1, \mathbf{t}_2, \mathbf{n})$ of surface $X(u, v)$ is an orthonormal coordinate system.

3. EXAMINATION OF THE RELATIONSHIPS BETWEEN THREE FRAMES

Initially, we can express the relationships between the Frenet-Serret frame and Darboux frame. Let the angle between the unit vectors \mathbf{n} and \mathbf{N} be θ as shown in Figure (1). We can write the following equations:

$$\begin{aligned} \mathbf{n} &= \mathbf{N} \cos \theta + \mathbf{B} \sin \theta \\ \mathbf{g} &= \mathbf{N} \sin \theta - \mathbf{B} \cos \theta \end{aligned} \tag{6}$$

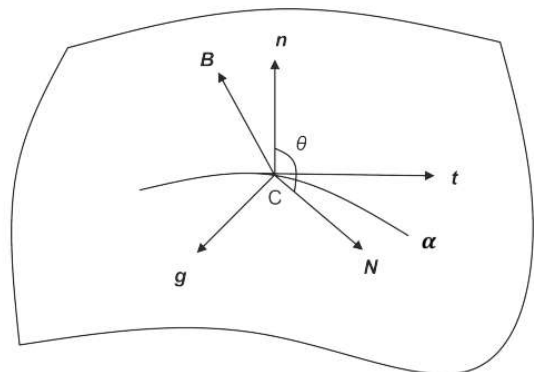


Figure 1: The relationship between the Darboux and Serret-Frenet frames of the curve α

On the other hand, let the parameter curves $X_u(u, v)$ and $X_v(u, v)$ be lines of curvature and the angle between the unit vectors t and t_1 be φ as shown in Figure (2).

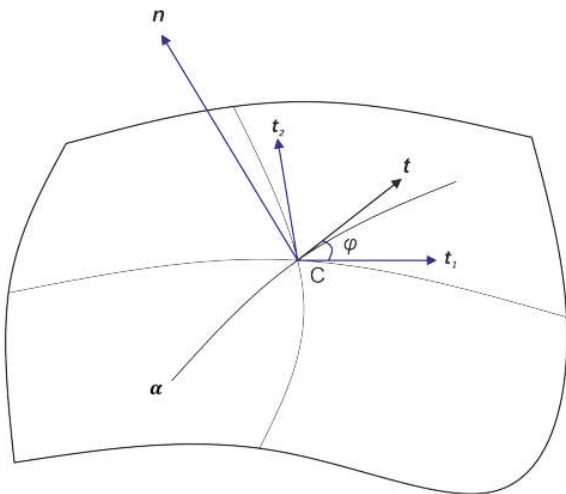


Figure 2: The relationship between the Darboux and Local-Surface frames of the curve α

Then, we can express the relationships below:

$$t = t_1 \cos \varphi + t_2 \sin \varphi$$

$$g = t_1 \sin \varphi - t_2 \cos \varphi \tag{7}$$

$$n = t_1 \times t_2$$

Using the equations (3) and (7), we can define the derivative formulas of Local-Surface frame as:

$$\begin{bmatrix} t_1' \\ t_2' \\ n' \end{bmatrix} = \begin{bmatrix} 0 & 0 & \rho_1 \\ 0 & 0 & \rho_2 \\ -\rho_1 & -\rho_2 & 0 \end{bmatrix} \begin{bmatrix} t_1 \\ t_2 \\ n \end{bmatrix}, \tag{8}$$

where $\rho_1 = \kappa_n \cos \varphi - \tau_g \sin \varphi$ and $\rho_2 = \kappa_n \sin \varphi + \tau_g \cos \varphi$. As known that we can write the Local-Surface frame vector with

$$l = l_{t1} + l_{t2} + l_n. \tag{9}$$

Therefore, we can write the Local-Surface frame vector using the equations (8) and (9) as follows:

$$l = \rho_2 t_1 - \rho_1 t_2. \tag{10}$$

Remark: We can write the following relations using the relationships $\rho_1 = \kappa_n \cos \varphi - \tau_g \sin \varphi$ and $\rho_2 = \kappa_n \sin \varphi + \tau_g \cos \varphi$:

- i. If $\kappa_n = 0$, then the curve α is asymptotic

curve, $\rho_1 = -\tau_g \sin \varphi$ and $\rho_2 = \tau_g \cos \varphi$.

- $\varphi = 0 \Rightarrow \rho_1 = 0$ and $\rho_2 = \tau_g$,
- $\varphi = \pi/2 \Rightarrow \rho_1 = -\tau_g$ and $\rho_2 = 0$.

- ii. If $\tau_g = 0$, then the curve α is line of curvature, $\rho_1 = \kappa_n \cos \varphi$ and $\rho_2 = \kappa_n \sin \varphi$.

- $\varphi = 0 \Rightarrow \rho_1 = \kappa_n$ and $\rho_2 = 0$,
- $\varphi = \pi/2 \Rightarrow \rho_1 = 0$ and $\rho_2 = \kappa_n$.

- iii. $\rho_1^2 + \rho_2^2 = \kappa_n^2 + \tau_g^2$.

- If $\tau_g = 0$, then the curve α is line of curvature, and $\kappa_n = \sqrt{\rho_1^2 + \rho_2^2}$,
- If $\kappa_n = 0$, then the curve α is asymptotic curve, and $\tau_g = \sqrt{\rho_1^2 + \rho_2^2}$.

- iv. $\kappa_n = \rho_1 \cos \varphi + \rho_2 \sin \varphi$,

$$\tau_g = -\rho_1 \sin \varphi + \rho_2 \cos \varphi, \text{ and } \kappa_g = -1.$$

Finally, we can examine the relationships between the Frenet-Serret frame and Local-Surface frame as follows:

$$\begin{bmatrix} t \\ N \\ B \end{bmatrix} = \begin{bmatrix} \frac{\cos \varphi}{D} & \frac{\sin \varphi}{D} & 0 \\ \frac{-\sin \varphi}{D} & \frac{\cos \varphi}{D} & \frac{\rho_1 \cos \varphi + \rho_2 \sin \varphi}{D} \\ \frac{\rho_1 \sin \varphi \cos \varphi + \rho_2 \sin^2 \varphi}{D} & \frac{-(\rho_1 \cos^2 \varphi + \rho_2 \sin \varphi \cos \varphi)}{D} & \frac{1}{D} \end{bmatrix} \begin{bmatrix} t_1 \\ t_2 \\ n \end{bmatrix}, \tag{11}$$

where, $D = \sqrt{(\rho_1 \cos \varphi + \rho_2 \sin \varphi)^2 + 1}$.

4. GEOMETRIC KINEMATIC EXAMINATIONS OF SPIN-ROLLING MOTION

Let the objects E and \bar{E} , and the surfaces S and \bar{S} which belong to these objects be given, and we suppose that they make spin-rolling motion without slipping at every moment. The curves α and $\bar{\alpha}$ are the contact trajectory curves on the surfaces S and \bar{S} of the objects E and \bar{E} , respectively. We suppose that the object E is a fixed and object E has spin-rolling motion relative to the object \bar{E} . Hence, the Local-Surface frames $\{E\}$ and $\{\bar{E}\}$ belong to the objects E and \bar{E} are fixed and moving Local-Surface frames, respectively. Let the contact point of the curves α and $\bar{\alpha}$ be C , and the moving and fixed Local-Surface frames attached to the contact point C be (t_1, t_2, n) and $(\bar{t}_1, \bar{t}_2, \bar{n})$, respectively. Since, the unit tangent vectors of the curves α and $\bar{\alpha}$ are same, i.e since

$$\frac{d\bar{c}}{d\bar{s}} = \mathbf{t}_C,$$

we can write the equation below.

$$\mathbf{t}_C = \mathbf{t}_1 \cos \varphi + \mathbf{t}_2 \sin \varphi \tag{12}$$

$$\mathbf{t}_C = \bar{\mathbf{t}}_1 \cos \bar{\varphi} + \bar{\mathbf{t}}_2 \sin \bar{\varphi}$$

Then, we can express the Local-Surface frame $(\bar{\mathbf{t}}_1, \bar{\mathbf{t}}_2, \bar{\mathbf{n}})$ as follows:

$$\begin{aligned} \bar{\mathbf{t}}_1 &= \mathbf{t}_1 \cos \phi + \mathbf{t}_2 \sin \phi \\ \bar{\mathbf{t}}_2 &= \mathbf{t}_1 \sin \phi - \mathbf{t}_2 \cos \phi \end{aligned} \tag{13}$$

$$\bar{\mathbf{n}} = \mathbf{n},$$

where ϕ is the angle between the vectors \mathbf{t}_1 and $\bar{\mathbf{t}}_1$. If we have $\phi = 0$, then it will be true that $\mathbf{t}_1 = \bar{\mathbf{t}}_1$, $\mathbf{t}_2 = \bar{\mathbf{t}}_2$, and $\mathbf{n} = \bar{\mathbf{n}}$. Also, these frames will always coincide because of the rolling constraints. Additionally, let s and \bar{s} be arc lengths of the curves α and $\bar{\alpha}$, and also let us take an arbitrary point \bar{P} be on the object E . We can write the position vector of the point \bar{P} of the object E according to the frame $\{\bar{E}\}$ as

$$\bar{\mathbf{p}} = \bar{\mathbf{c}} + \bar{\mu}_1 \bar{\mathbf{t}}_1 + \bar{\mu}_2 \bar{\mathbf{t}}_2 + \bar{\mu}_3 \bar{\mathbf{n}}. \tag{14}$$

Then if we take derivative of the equation (14) according to \bar{s} , we have:

$$\begin{aligned} \frac{d\bar{\mathbf{p}}}{d\bar{s}} &= \left(\cos \bar{\varphi} + \frac{d\bar{\mu}_1}{d\bar{s}} - \bar{\mu}_3 \bar{\rho}_1 \right) \bar{\mathbf{t}}_1 \\ &+ \left(\sin \bar{\varphi} + \frac{d\bar{\mu}_2}{d\bar{s}} - \bar{\mu}_3 \bar{\rho}_2 \right) \bar{\mathbf{t}}_2 \\ &+ \left(\frac{d\bar{\mu}_3}{d\bar{s}} + \bar{\mu}_1 \bar{\rho}_1 + \bar{\mu}_2 \bar{\rho}_2 \right) \bar{\mathbf{n}}, \end{aligned} \tag{15}$$

where $\bar{\rho}_1 = \bar{\kappa}_n \cos \bar{\varphi} - \bar{\tau}_g \sin \bar{\varphi}$ and $\bar{\rho}_2 = \bar{\kappa}_n \sin \bar{\varphi} + \bar{\tau}_g \cos \bar{\varphi}$. Since the point \bar{P} of the object \bar{E} is a fixed point, we can write the following relation.

$$\frac{d\bar{\mathbf{p}}}{d\bar{s}} = 0. \tag{16}$$

Using the equations (15) and (16) we get the equation below:

$$\frac{d\bar{\mu}_1}{d\bar{s}} = \bar{\mu}_3 \bar{\rho}_1 - \cos \bar{\varphi}$$

$$\frac{d\bar{\mu}_2}{d\bar{s}} = \bar{\mu}_3 \bar{\rho}_2 - \sin \bar{\varphi} \tag{17}$$

$$\frac{d\bar{\mu}_3}{d\bar{s}} = -\bar{\mu}_1 \bar{\rho}_1 - \bar{\mu}_2 \bar{\rho}_2.$$

On the other hand, the point \bar{P} can also be written according to frame $\{E\}$ as

$$\mathbf{p} = \mathbf{c} + \mu_1 \mathbf{t}_1 + \mu_2 \mathbf{t}_2 + \mu_3 \mathbf{n}. \tag{18}$$

Similarly, if we take derivative of the equation (18) according to s , it yields

$$\begin{aligned} \frac{d\mathbf{p}}{ds} &= \left(\cos \varphi + \frac{d\mu_1}{ds} - \mu_3 \rho_1 \right) \mathbf{t}_1 \\ &+ \left(\sin \varphi + \frac{d\mu_2}{ds} - \mu_3 \rho_2 \right) \mathbf{t}_2 \\ &+ \left(\frac{d\mu_3}{ds} + \mu_1 \rho_1 + \mu_2 \rho_2 \right) \mathbf{n}. \end{aligned} \tag{19}$$

During rolling motion, the velocities of the contact curves α and $\bar{\alpha}$ will be equal because of the rolling constraints. Hence, it will be true that $s = \bar{s}$. On the other hand, if the equation (13) is substituted into (15), then we have the following equation.

$$\begin{aligned} \frac{d\bar{\mathbf{p}}}{d\bar{s}} &= \left[\left(\cos \bar{\varphi} + \frac{d\bar{\mu}_1}{d\bar{s}} - \bar{\mu}_3 \bar{\rho}_1 \right) \cos \phi \right. \\ &- \left. \left(\sin \bar{\varphi} + \frac{d\bar{\mu}_2}{d\bar{s}} - \bar{\mu}_3 \bar{\rho}_2 \right) \sin \phi \right] \mathbf{t}_1 \\ &+ \left[\left(\cos \bar{\varphi} + \frac{d\bar{\mu}_1}{d\bar{s}} - \bar{\mu}_3 \bar{\rho}_1 \right) \sin \phi \right. \\ &+ \left. \left(\sin \bar{\varphi} + \frac{d\bar{\mu}_2}{d\bar{s}} - \bar{\mu}_3 \bar{\rho}_2 \right) \cos \phi \right] \mathbf{t}_2 \\ &+ \left(\frac{d\bar{\mu}_3}{d\bar{s}} + \bar{\mu}_1 \bar{\rho}_1 + \bar{\mu}_2 \bar{\rho}_2 \right) \mathbf{n} \end{aligned} \tag{20}$$

Using the relation in (16), we can obtain the same relationships in (17). Due to rolling constraints, the Local-Surface frames $\{E\}$ and $\{\bar{E}\}$ will coincide at any moment. Hence, it will be true that:

$$\mu_1 = \bar{\mu}_1, \quad \mu_2 = \bar{\mu}_2, \quad \text{and} \quad \mu_3 = \bar{\mu}_3. \tag{21}$$

and

$$\frac{d\mu_1}{ds} = \frac{d\bar{\mu}_1}{d\bar{s}}, \quad \frac{d\mu_2}{ds} = \frac{d\bar{\mu}_2}{d\bar{s}} \quad \text{and} \quad \frac{d\mu_3}{ds} = \frac{d\bar{\mu}_3}{d\bar{s}}. \quad (22)$$

From now on, we can use s instead of s and \bar{s} , and we can use μ_i instead of μ_i and $\bar{\mu}_i$ because of contact situation and coincidence. Therefore, substituting the equations (15) and (22) into (19) we have the following equation:

$$\begin{aligned} \frac{d\mathbf{p}}{ds} &= (\cos \varphi - \cos \bar{\varphi} + \mu_3 \rho_1^*) \mathbf{t}_1 \\ &+ (\sin \varphi - \sin \bar{\varphi} + \mu_3 \rho_2^*) \mathbf{t}_2 \\ &+ (-\mu_1 \rho_1^* - \mu_2 \rho_2^*) \mathbf{n}. \end{aligned} \quad (23)$$

where

$$\rho_1^* = \bar{\rho}_1 - \rho_1 \quad \text{and} \quad \rho_2^* = \bar{\rho}_2 - \rho_2. \quad (24)$$

5. LOCAL-SURFACE FRAME BASED VELOCITY OF THE SPIN-ROLLING MOTION

In this section, we find the Local-Surface frame based translational velocity of the object \bar{E} according to the fixed local-surface frame $\{E\}$ by using the equation (23) as

$$\begin{aligned} \mathbf{v}_p &= \frac{d\mathbf{p}}{ds} \frac{ds}{dt} = \vartheta (\cos \varphi - \cos \bar{\varphi} + \mu_3 \rho_1^*) \mathbf{t}_1 \\ &+ \vartheta (\sin \varphi - \sin \bar{\varphi} + \mu_3 \rho_2^*) \mathbf{t}_2 \\ &+ \vartheta (-\mu_1 \rho_1^* - \mu_2 \rho_2^*) \mathbf{n}, \end{aligned} \quad (25)$$

where, $\vartheta = ds/dt$ is the magnitude of the rolling velocity. Additionally, using the angular velocity

$$\boldsymbol{\omega} = \omega_1 \mathbf{t}_1 + \omega_2 \mathbf{t}_2 + \omega_3 \mathbf{n}, \quad (26)$$

we can determine the velocity of the point P according to the fixed local-surface frame $\{E\}$ with

$$\begin{aligned} \mathbf{v}_p &= \boldsymbol{\omega} \times \Gamma_{CP} = (-\mu_2 \omega_3 + \mu_3 \omega_2) \mathbf{t}_1 \\ &+ (\mu_1 \omega_3 - \mu_3 \omega_1) \mathbf{t}_2 \\ &+ (-\mu_1 \omega_2 + \mu_2 \omega_1) \mathbf{n}, \end{aligned} \quad (27)$$

where $\Gamma_{CP} = \mu_1 \mathbf{t}_1 + \mu_2 \mathbf{t}_2 + \mu_3 \mathbf{n}$. Due to coincidence we can write $\mathbf{t}_1 = \bar{\mathbf{t}}_1$ and $\mathbf{t}_2 = \bar{\mathbf{t}}_2$, and also $\varphi = \bar{\varphi}$. Hence, it is true that $\cos \varphi - \cos \bar{\varphi} = 0$ and $\sin \varphi - \sin \bar{\varphi} = 0$. Therefore, using the equations (25) and (27) we can express the equation below:

$$\omega_1 = -\vartheta \rho_2^*, \quad \omega_2 = -\vartheta \rho_1^*, \quad \text{and} \quad \omega_3 = 0. \quad (28)$$

Therefore, the angular velocity of object \bar{E} according to fixed local-surface frame $\{E\}$ can be written with the following equation:

$$\boldsymbol{\omega} = \vartheta (-\rho_2^* \mathbf{t}_1 + \rho_1^* \mathbf{t}_2). \quad (29)$$

6. CONCLUSION

In this paper, we gave the kinematics of spin-rolling motion of rigid objects with point contact with respect to the Local-Surface frame method. We studied on the relationships between the Darboux frame and Local-Surface frame, and also between the Frenet-Serret frame and Local-Surface frame. On the other hand, we found the velocity formulations of a moving object based on the Local-Surface frame curvatures of the contact curve and geometric invariants.

REFERENCES

- [1] D. L. Brock, "Enhancing the dexterity of a robot hand using controlled slip", *In In 1988 IEEE Conference on Robotics and Automation*, 1988.
- [2] J. S. Beggs, "Advanced Mechanism", *The Macmillan Company, New York*, 1966.
- [3] A. S. Hall, "Kinematics and Linkage Design", *Balt Publishers, West Lafayette, Indiana*, 1966.

[4] B. Paul, "Kinematics and Dynamics of Planar Machinery", *Prentice-Hall, Inc., Englewoods Cliffs, N.J.*, 1979.

[5] N. Rosenauer and A.H. Willis, "Kinematics of Mechanisms", Associated General Publications Pty Ltd, Sydney, Australia, 1953.

[6] E. T. Whittaker, "A Treatise on the Analytical Dynamics of Particles & Rigid Bodies", *Cambridge University Press*, 1988.

[7] L. A. Pars, "A Treatise on Analytical Dynamics". *Wiley, New York*, 1968.

[8] C. Cai and B. Roth, "On the planar motion of rigid bodies with point contact", *Mechanism and Machine Theory*, 21(6):453-466, 1986.

[9] C. Cai and B. Roth, "On the spatial motion of rigid bodies with point contact", *In In Proceedings of 1987 International Conference on Robotics and Automation*, 1987.

[10] C. Cai and B. Roth, "On the spatial motion of rigid bodies with line contact", *In In Proceedings of 1988 International Conference on Robotics and Automation*, 1988.

[11] D. J. Montana, "The kinematics of contact and grasp", *The International Journal of Robotics Research*, 7(3):17-32, 1988.

[12] L. Cui and J.S. Dai, "A darboux frame based formulation of spin-rolling motion of rigid objects with point contact", *In IEEE Transactions on Robotics* 26, 2010.

[13] B. O'Neill, "Elementary Differential Geometry", *Academic press Inc. New York*, 1966.

[14] A. W. Nutbourne and R. R. Martin, "Differential Geometry Applied to Curve and Surface Design", *1:Foundations, West Sussex, Chichester, UK; E.Horwood, NY,USA*, 1988.

	SAKARYA UNIVERSITY JOURNAL OF SCIENCE		 SAKARYA UNIVERSITY
	e-ISSN: 2147-835X http://www.saujs.sakarya.edu.tr		
	<u>Received</u> 15-01-2018 <u>Accepted</u> 10-05-2018	<u>Doi</u> 10.16984/saufenbilder.379170	

Theoretical calculations of LASO molecule by using DFT/B3LYP and DFT/HSEH1PBE levels: A detailed vibrational, NMR and NLO analysis

Hacer Gümüş¹

Abstract

L-arginine semi-oxalate (LASO) molecule [$C_6H_{15}N_4O_2^+ \cdot C_2HO_4^-$] was synthesized and its IR and 1H NMR and ^{13}C NMR spectroscopy were studied by P. Vasudevan et al. In this study, the geometric structure determination of LASO molecule was optimized to obtain its molecular geometric structure by using the Gaussian program. The theoretical harmonic vibrational wavenumbers of LASO molecule were also calculated. The calculated theoretical data were checked with the experimental data. The experimental and the theoretical data were seen compatible with each other. Further more; LASO molecule is studied by means of NMR spectra. Finally, the analysis of nonlinear optical (NLO) properties, molecular orbitals (MO), molecular surfaces and Mulliken, APT and NBO populations were viewed. All theoretical calculations have been fulfilled by employing the Density Functional Theory (DFT) at B3LYP/6-311++G(d,p) and HSEH1PBE/6-311++G(d,p) levels.

Keywords: LASO, IR, NMR, NLO and DFT.

1. INTRODUCTION

L-arginine complexes are made up of zwitterionic positively charged semi-oxalate ions and amino acid molecules. Firstly, different molecules are collected into separate variable sheets. The fundamental monad in the arginine sheet is a centrosymmetric dimer, while the semi-oxalate ions constitute hydrogen-bonded structure ring in their sheet. In the L-arginine complex each semi-oxalate ion is encircled by arginine molecules and L-arginine complex may be defined as a subsumption compound [2]. Molecular structure of LASO molecule have been examined by P. Vasudevan et al. [1] and its FT-IR and the NMR spectroscopy and the thermal analyses have been done experimentally. The experimentally defined molecular structure and the atom numbers have been shown in Figure 1.

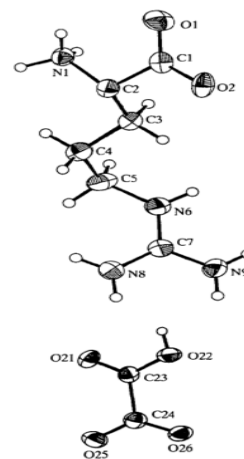


Figure 1. The asymmetric unit of LASO molecule, showing the atomic numbering scheme.

2. DETAILS OF THE COMPUTATION

The whole molecular structure calculations of LASO molecule at fundamental level performed by Gaussian program [3] and GaussView 5 software [4]. Calculated

¹ Kocaeli Üniversitesi, Dr. Öğrt. Üyesi Hacer GÜMÜŞ (hacerpir@gmail.com)

bond lengths and calculated bond angles, IR and NMR spectra, electric and electronic features, mulliken, APT and NBO populations and molecular surfaces for LASO molecule have been reached by using B3LYP [5,6] and HSEH1PBE [7-10] methods at 6-311++G(d,p) level [11]. Theoretical geometric structure of LASO which performed with B3LYP level has been displayed in Figure 2.

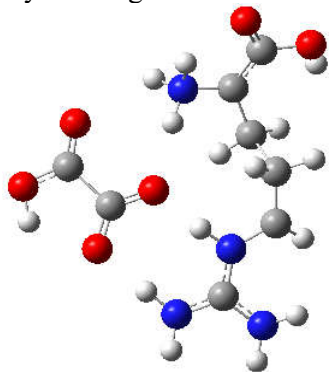


Figure 2. Optimized molecular structure of LASO.

3. CALCULATION RESULTS

3.1. Geometrical Parameters

LASO molecule $[C_6H_{15}N_4O_2^+.C_2HO_4^-]$ has P1 space group and triclinic crystal [2]. These results are taken from the data reported by Nagasuma R. Chandr et al. [2]. The calculated bond distances and the angles are listed in Table 1 together with the comparative experimental X-ray values [1]. As could easily be seen from the Table 1, C-C bond distances have been calculated in the range of 1.40786-1.60788 Å and 1.403-1.586 Å in the same methods, respectively. The C-C bond distances are experimentally determined to be 1.518 and 1.534 Å [1]. The C₁-O₁ and C₂-N₁ bond length are observed at 1.240 and 1.491 Å, respectively [1]. These bond distances were calculated as 1.238, 1.487 Å and 1.236, 1.473 Å at B3LYP and HSEH1PBE levels, respectively. O1-C1-O2 angle was found at 117.85° [1], and this angle has been calculated at 117.59950° and 117.909° using B3LYP and HSEHPBE levels, respectively. In Table 1, there exists great harmony between experimental and theoretically calculated parameters of the LASO molecule.

3.2. IR spectra analysis

P. Vasudevan et al. [1] have recently investigated the infrared spectra of the LASO molecule and have assigned the bands vibrations [1]. The experimental vibrational frequencies of LASO molecule have been reported [1], and the experimental values are listed in Table 2. The vibrational frequencies have been calculated. The theoretically calculated vibrational spectra for LASO molecule using HSEH1PBE and B3LYP levels, and the assignments have been given in Table 2.

Table 1. Geometrical parameters of the LASO.

	Exp[1]	Theoretical	
	X-Ray	B3LYP	HSEH1PBE
Bond lengths (Å)			
N1-C2	1.491	1.487	1.473
O1-C1	1.240	1.238	1.236
C2-O2	1.259	1.384	1.372
C2-C1	1.531	1.407	1.403
C3-C2	1.526	1.487	1.483
C3-C4	1.524	1.607	1.586
C5-C4	1.518	1.477	1.474
C5-N6	1.457	1.391	1.384
C7-N6	1.326	1.331	1.326
C7-N9	1.327	1.359	1.352
C7-N8	1.329	1.342	1.334
C13-O11	1.200	1.334	1.200
C14-O15	1.232	1.253	1.248
C13-O12	1.290	1.203	1.324
O16-C14	1.255	1.253	1.250
Bond angles (°)			
O1-C1-O2	117.85	117.59	117.90
N1-C2-C3	108.23	116.28	116.51
O1-C1-C2	125.94	124.17	123.84
O2-C1-C2	116.07	118.22	118.24
C4-C3-C2	113.58	114.50	114.24
C3-C2-C1	111.21	128.13	127.53
N6-C5-C4	113.82	116.89	116.29
C5-C4-C3	109.95	114.97	114.68
N6-C7-N9	118.40	119.40	119.24
C7-N6-C5	124.54	127.06	126.73
O12-C13-C14	114.11	112.57	112.32
O11-C13-C14	120.90	123.73	123.59
C13-C14- O16	116.05	115.16	114.94

Table 2. Harmonic vibrational wavenumbers (cm⁻¹) assignments for the LASO molecule.

Assignments	Exp[1]	Theoretical	
		B3LYP	HSEH1PBE
NH ₂ stretching	3384	3564	3471
NH ₃ stretching	3179	3260	3340
NH ₃ asymmetric stretching	3070	3212	3172
COO ⁻ asymmetric stretching	1647	1732	1697
N-H asymmetric bending	1502	1577	1534
COO ⁻ symmetric bending	1403	1427	1392
COO ⁻ vibrations	1233	1294	1256
CH ₂ wagging	1278	1281	1239
NH ₃ rocking	1172	1175	1146
C-N stretching	1032	1033	1006
COO ⁻ rocking	848	866	855
CH ₂ rocking	722	733	714

The whole calculated vibrational wavenumbers were scaled with a scaling agents of 0.9970 [12] and 0.9614 [13,14] at HSEH1PBE and B3LYP levels. The

calculated and the experimental infrared spectrum of the LASO molecule are displayed in Figure 3.

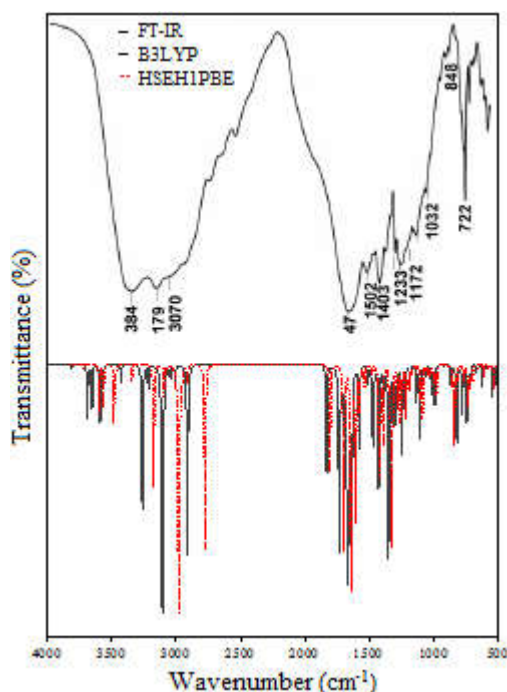


Figure 3. Infrared spectrum of the LASO molecule.

3.3. NMR spectra analyses

¹³C NMR and ¹H NMR were calculated within gage-including atomic orbital (GIAO) applying HSEH1PBE and B3LYP levels, and the obtained values were given in Table 3.

Table 3. The calculated and experimental ¹³C and ¹H isotropic NMR chemical shifts for the LASO.

	Exp.	Theoretical (GIAO)	
		B3LYP	HSEH1PBE
¹H			
H _{N7}	3.741	13.965	14.480
H _{N8}	3.729	11.030	11.622
H _{O1}	3.716	9.723	9.945
H _{N1}	3.155	8.427	8.657
H _{N1}	1.852	8.068	8.393
H _{C5}	1.840	4.903	4.985
H _{N1}	1.831	4.900	4.982
H _{O2}	1.819	3.965	4.015
H _{N9}	1.811	3.681	3.834
H _{N8}	1.799	3.576	3.716
H _{N9}	1.783	3.528	3.618
H _{C3}	1.603	2.794	2.885
H _{C4}	1.584	2.733	2.789
H _{C3}	1.571	2.361	2.430
¹³C			
C ₁	173.948	171.232	165.046
C ₁₃	166.353	169.831	164.025
C ₁₄	156.780	165.950	159.844
C ₆	153.450	148.222	142.661
C ₅	54.005	106.394	98.714
C ₂	40.449	69.214	59.162
C ₃	27.415	38.394	30.742
C ₄	23.849	37.203	29.830

The experimental and the calculated ¹H and ¹³C isotropic chemical shifts of the LASO molecule have been given in Table 3. The ¹³C chemical shift data for the whole calculations have the ranges ~171.232 from ~37.203 ppm at B3LYP method and ~165.046 from ~29.830 ppm at HSEH1PBE method, respectively. ¹H chemical shift data for the whole data have the ranges ~13.965 from ~2.231 ppm at B3LYP method and ~14.480 from ~2.343 ppm at HSEH1PBE method, respectively.

3.4. Electronic analysis

Highest occupied molecular orbital energy (HOMO) and lowest unoccupied molecular orbital energy (LUMO) are the types of molecular orbitals. HOMO-LUMO energies display that the charge transfer within the molecule. The HOMO is electron giving ability whereas the LUMO means electron accepting ability. HOMO-LUMO energies were calculated as -6.528 and -4.891 eV and the results were presented in Table 4.

Table 4. Electronic properties of LASO.

	B3LYP	HSEH1PBE
E _{LUMO}	-4.891 eV	-4.899 eV
E _{HOMO}	-6.528 eV	-6.530 eV
ΔE = E _{LUMO} - E _{HOMO}	1.636 eV	1.632 eV
I	6.528 eV	6.530 eV
A	4.892 eV	4.899 eV
χ	5.710 eV	5.714 eV
η	0.818 eV	0.816 eV
S	0.077 eV ⁻¹	0.077 eV ⁻¹
E _{TOTAL}	-984.53 a.u.	-983.53 a.u.

The gap among HOMO-LUMO energies characterizes chemically stability of a molecule [15] and this has been calculated as 1.636 eV at the B3LYP method. The calculated molecular orbital image was displayed in Figure 4. Negative-positive charges have been symbolized by green-red colors.

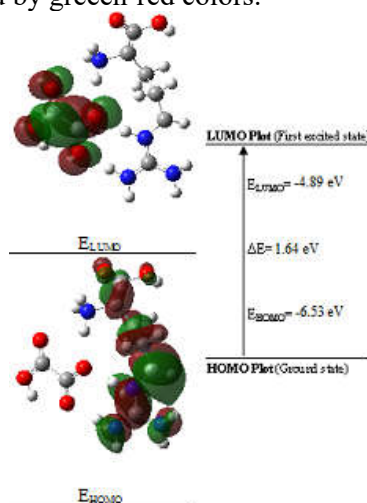


Figure 4. Molecular frontier orbital pictures of the LASO.

3.5. Electric analysis

Nonlinear optical properties of some organic matters have been researched in photonic materials recently [16]. Nonlinear optical properties are the crucial factors in quantum chemistry [17]. In this paper, we have presented the values of the total static dipole moment (μ), the mean polarizability ($\langle\alpha\rangle$), the anisotropy of the polarizability ($\Delta\alpha$) and the mean first-order hyperpolarizability ($\langle\beta\rangle$) as defined [18] in the following equations:

$$\mu = (\mu_x^2 + \mu_y^2 + \mu_z^2)^{1/2}$$

$$\langle\alpha\rangle = \left(\frac{\alpha_{xx} + \alpha_{yy} + \alpha_{zz}}{3} \right)$$

$$\Delta\alpha = \left(\frac{(\alpha_{xx} - \alpha_{yy})^2 + (\alpha_{yy} - \alpha_{zz})^2 + (\alpha_{zz} - \alpha_{xx})^2}{2} \right)^{1/2}$$

$$\langle\beta\rangle = (\beta_x^2 + \beta_y^2 + \beta_z^2)^{1/2}$$

where

$$\beta_x = \beta_{xxx} + \beta_{xyy} + \beta_{xzz}$$

$$\beta_y = \beta_{yyy} + \beta_{xxy} + \beta_{yzz}$$

$$\beta_z = \beta_{zzz} + \beta_{xxz} + \beta_{yyz}$$

Nonlinear optical (NLO) analysis has been performed by using the following procedure:

$$\mu = (\mu_x^2 + \mu_y^2 + \mu_z^2)^{1/2}$$

$$\mu = ((4.8)^2 + (3.6)^2 + (0.5)^2)^{1/2}$$

$$\mu = 6.02$$

$$\langle\alpha\rangle = \left(\frac{\alpha_{xx} + \alpha_{yy} + \alpha_{zz}}{3} \right)$$

$$\langle\alpha\rangle = \left(\frac{277.6 + 190.9 + 107.3}{3} \right)$$

$$\langle\alpha\rangle = 191.9 \text{ a.u.} = 28.10^{-24} \text{ esu}$$

$$\Delta\alpha = \left(\frac{(\alpha_{xx} - \alpha_{yy})^2 + (\alpha_{yy} - \alpha_{zz})^2 + (\alpha_{zz} - \alpha_{xx})^2}{2} \right)^{1/2}$$

$$\Delta\alpha = \left(\frac{(277.6 - 190.9)^2 + (190.9 - 107.3)^2 + (107.3 - 277.6)^2}{2} \right)^{1/2}$$

$$\Delta\alpha = 147.4 \text{ a.u.} = 22.10^{-24} \text{ esu}$$

$$\beta_x = \beta_{xxx} + \beta_{xyy} + \beta_{xzz} = 21640 - 7957 - 561 = 13122$$

$$\beta_y = \beta_{yyy} + \beta_{xxy} + \beta_{yzz} = 4945 + 13225 + 174 = 31292$$

$$\beta_z = \beta_{zzz} + \beta_{xxz} + \beta_{yyz} = -233 - 3288 + 811 = -2710$$

$$\langle\beta\rangle = (\beta_x^2 + \beta_y^2 + \beta_z^2)^{1/2}$$

$$\langle\beta\rangle = ((13122)^2 + (31292)^2 + (-2710)^2)^{1/2}$$

$$\langle\beta\rangle = 34040 \text{ a.u.} = 294082.10^{-33} \text{ esu}$$

The calculated values of LASO molecule at B3LYP/6-311++G(d,p) level were given in Table 6.

Table 4. Total static dipole moment (μ), the mean polarizability ($\langle\alpha\rangle$), the anisotropy of the polarizability ($\Delta\alpha$), the mean first-order hyperpolarizability ($\langle\beta\rangle$) LASO.

Property	B3LYP/6311++G(d,p)
μ_x	4.8 Debye
μ_y	3.6 Debye
μ_z	0.5 Debye
μ	6.02 Debye
α_{xx}	277.6 a.u.
α_{yy}	190.9 a.u.
α_{zz}	107.3 a.u.
$\langle\alpha\rangle$	191.9 a.u.
$\Delta\alpha$	147.4 a.u.
β_x	13122 a.u.
β_y	31292 a.u.
β_z	-2710 a.u.
$\langle\beta\rangle$	34040 a.u.

where dipole moment of 6.02 Debye, polarizability of 28.10^{-24} , anisotropy of the polarizability of 22.10^{-24} and first-order hyperpolarizability of 294082.10^{-33} have been calculated at B3LYP method for LASO molecule.

3.6. Electrostatic potential (ESP) and molecular electrostatic potential (MEP) analysis

MEPs are the technique of ESP map on iso-electron density surface. MEP has been founded commonly as a beneficial proportion to clarify hydrogen bonding. MEP is originated from it and at the same time views the dimension of the molecule, image as well as positive, negative and neutral electrostatic potential fields in terms of color classification [19]. Therotically calculated 3D MEP surfaces of LASO molecule have been performed from optimized molecular structure at B3LYP level. Polarization effect is clearly visible in

Figure

5.

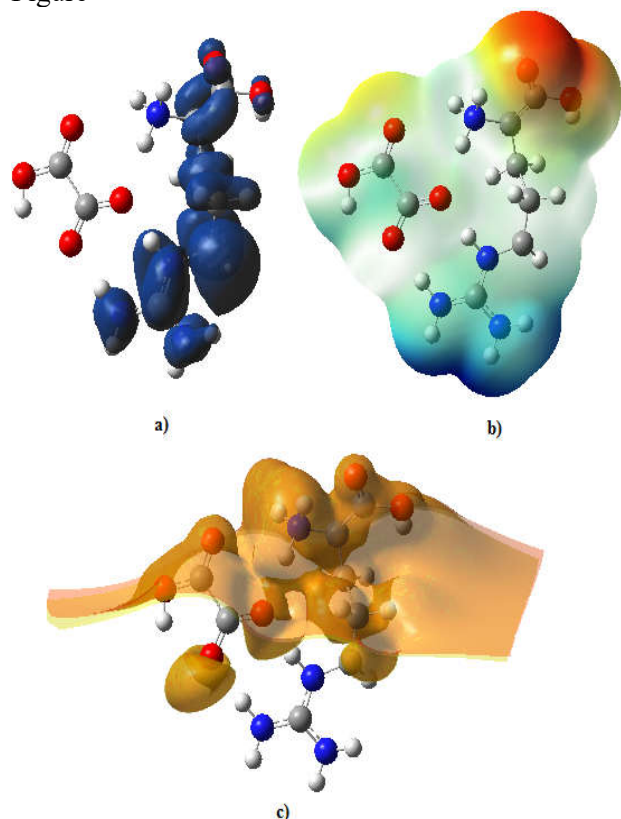


Figure 5. a) Spin density b) MEP and c) ESP pictures of LASO calculated at B3LYP level.

3.7. Mulliken, APT and NBO charge analysis

Between the orbital based definitions of atomic populations we put into utterances the famed Mulliken [20] population anatomy method and the density matrix based normal population anatomy [21-23]. The Mulliken charges analysis is one of the oldest and simplest method, with the electrons being divided up amongst the atoms according to the degree to which different atomic AO basis functions contribute to the overall wave function [24]. The Mulliken charge analysis of the LASO molecule has been calculated with HSEH1PBE and B3LYP methods of theory. Mulliken, APT and NBO atomic charge on each atom of the LASO have been presented in the graphical representation shown in Figure 6.

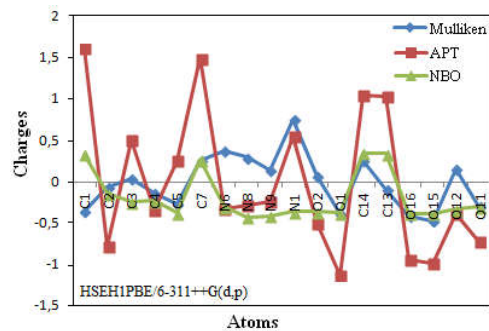
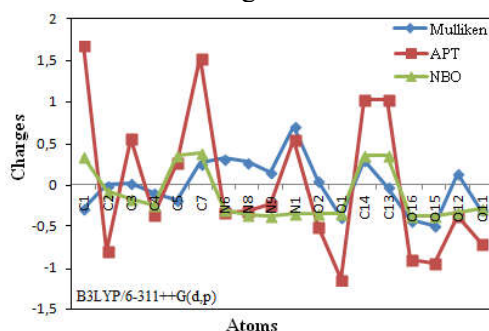


Figure 6. Charge analysis of LASO.

4. CONCLUSIONS

The geometry structure of the LASO molecule has been determined by HSEH1PBE and B3LYP methods. Calculated bond distances and angles compare well with the experimental data. Theoretical calculation of vibrational spectra and the harmonic vibration analysis have been performed and the vibration assignments have been checked with the experimental ones. The correlation factors between the theoretical (B3LYP/6-311++G(d,p)) and the experimental (that can be seen from the tables 1,2 and 3) ones for the LASO molecule have been found to be 0.9968, 0.9991 and 0.9493 respectively. Frontier MO, HOMO-LUMO energies were performed at B3LYP and HSEH1PBE levels. The LASO molecule exhibits strong effective intra- and intermolecular charge transfer and displays the first-hyperpolarizability of 294082.10^{-33} esu. The MEP plot clearly displays reactive parts, nucleophilic and electrophilic attack areas.

REFERENCES

- [1] P. Vasudevan S. Gokul Raj, S. Sankar, *Spectrochimica Acta Part A: Molecular and Biomolecular Spectroscopy*, vol. 106, pp. 210-215, 2013.1. 24, no. 6, pp. 51-63, 2013.
- [2] Nagasuma R. Chandra, Moses M. Prabu, Janani Venkatraman, S. Suresh and M. Vijaya, *Acta Cryst. B*, vol. 54, pp. 257-263, 1998.
- [3] M J Frisch et al. Gaussian 09, Revision D.01 (Wallingford, CT:Gaussian, Inc) 2009.
- [4] GaussView, Version 5, R Dennington, T Keith and J Millam (Shawnee Mission, KS: Semichem Inc) 2009.
- [5] A. D. Becke, *J Chem. Phys.*, vol. 98, pp. 5648, 1993.
- [6] C. Lee, W. Yang and R. G. Parr, *Phys. Rev. B*, vol. 37, pp.785, 1988.
- [7] J. Heyd and G. Scuseria, *J. Chem. Phys.* Vol. 121, pp. 1187, 2004.
- [8] J. Heyd and G. E. Scuseria *J. Chem. Phys.*, vol. 120, pp. 7274, 2004.

- [9] J. Heyd, J. E. Peralta, G. E. Scuseria and R. L. Martin, *J. Chem. Phys.*, vol. 123, pp. 174101, 2005.
- [10] J. Heyd, G. E. Scuseria and M. Ernzerhof, *J. Chem. Phys.*, vol. 124, pp. 219906, 2006.
- [11] M. J. Frisch, J. A. Pople and J. S. Binkley, *J. Chem. Phys.*, vol. 80, pp. 3265, 1984.
- [12] J. B. Foresman, E Frisch, *Exploring Chemistry with Electronic Structure Methods, Gaussian, Inc., Pittsburgh, PA, USA*, 1993.
- [13] A. Frish, A. B. Nielsen and A. J. Holder, *Gauss View User Manual, Gaussian Inc. Pittsburg, PA*, 2001.
- [14] W. H. James, E. G. Buchanan, C. W. Müller, J. C. Dean, D. Kosenkov, L. V. Slipchenko, L. Guo, A. G. Reidenbach, S. H. Gellman and T. S. Zwier, *J. Phys. Chem. A*, vol. 115, pp. 13783, 2011.
- [15] K. Fukui, *Science*, vol. 218, pp. 747, 1982.
- [16] A. Cornelis van Walree, Okke Franssen, W. Albert Marsman, C. Marinus Flipseb and W. Leonardus Jenneskens; *J. Chem. Soc., Perkin Trans. Vol. 2*, 1997.
- [17] D. Avci, A. Basoglu, Y. Atalay, *International Journal of Quantum Chemistry*, vol. 111, pp. 130-147, 2011.
- [18] G. Maroulis, *Static hyperpolarizability of the water dimer and the interaction hyperpolarizability of two water molecules*, *J. Chem. Phys.*, Vol. 113, No. 5, pp. 1813, 2000.
- [19] R. G. Pearson, *Proceeding of the National Academy of Sciences*, vol. 83, pp. 8440, 1986.
- [20] R. S. Mulliken, *J. Chem. Phys.*, vol. 23, pp. 1833, 1955.
- [21] A. E. Reed, R. B. Weinstock and F. Weinhold, *J. Chem. Phys.*, vol. 83, pp. 735, 1985.
- [22] A. E. Reed and F. Weinhold, *J. Chem. Phys.*, vol. 83, pp. 1736, 1985.
- [23] A. E. Reed, L. A. Curtiss and F. Weinhold, *Chem. Rev.*, vol. 88, pp. 899, 1988.
- [24] C. Cramer, *Essentials of Computational Chemistry: Theories and Models, Second Edition, John Wiley and Sons Ltd.*, 2004.

	SAKARYA UNIVERSITY JOURNAL OF SCIENCE		 SAKARYA UNIVERSITY
	e-ISSN: 2147-835X http://www.saujs.sakarya.edu.tr		
	<u>Received</u> 03-05-2018 <u>Accepted</u> 26-06-2018	<u>Doi</u> 10.16984/saufenbilder.420612	

Extending property on *EC*-Fully Submodules

Adnan TERCAN¹, Ramazan YAŞAR^{*2}

Abstract

There are several generalizations of *CS*-modules in literature. One of the generalization is based on fully invariant submodules. Recall that a module M is called *FI*-extending if every fully invariant submodule is essential in a direct summand. We call a module *EFI*-extending if every fully invariant submodule which contains essentially a cyclic submodule is essential in a direct summand. Initially we obtain basic properties in the general module setting. For example, a direct sum of *EFI*-extending modules is *EFI*-extending. Again, like the *FI*-extending property, the *EFI*-extending property is shown to carry over to matrix rings.

Keywords: fully invariant, *ec*-fully submodule, *FI*-extending, extending

1. INTRODUCTION

In recent years, the theory of extending modules and rings and their generalizations has come to play an important role in the theory of rings and modules. Recall that a module M is called an *extending* (or *CS*) module if every submodule of M is essential in a direct summand of M (see [4], [9] or [10]).

One of the extremely useful generalization of *CS* concept is *FI*-extending property (see [1] or [2]). Recall a module M is called *FI*-extending if every fully invariant submodule of M is essential in a direct summand. Following [3] and [5], by an *ec*-fully submodule N of a module M , we mean a fully invariant submodule N which contains essentially a cyclic submodule i.e., there exists an element x in N such that xR is essential in N .

In this paper, we are concerned with the study of modules M that every *ec*-fully submodule is essential in a direct summand of M . We call such a module as *EFI*-extending. Moreover, a ring R is

called right *EFI*-extending ring if R_R is an *EFI*-extending module. Clearly the notion of an *EFI*-extending module generalizes that of a *FI*-extending module by requiring that only every *ec*-fully submodule is essential in a direct summand rather than every fully invariant submodule.

In Section 2, we provide basic properties of *ec*-fully submodules. After defining *EFI*-extending modules, in Section 3 we prove basic results and properties of *EFI*-extending modules. It is shown that any direct sum of *EFI*-extending modules is *EFI*-extending and that the *EFI*-extending property of a ring R carries over to the full matrix ring $M_n(R)$, $n \geq 1$.

Throughout this paper, all rings are associative with unity and R denotes such a ring. All modules are unital right R -modules.

Recall that a submodule X of M is called *fully invariant* if for every $\alpha \in \text{End}_R(M)$, $\alpha(X) \subseteq X$. If M is an R -module and $A \subseteq M$, then we use $A \leq M$, $A \leq_e M$, $A \trianglelefteq M$, $A \trianglelefteq_{ec} M$, and $E(M)$ to denote that A is a submodule, essential submodule, fully

¹ Hacettepe University, Faculty of Science, Department of Mathematics, Beytepe, Ankara, Turkey

* Corresponding Author

² Hacettepe University, Faculty of Science, Department of Mathematics, Beytepe, Ankara, Turkey

invariant submodule, ec -fully submodule, and the injective hull of M , respectively.

Moreover $M_n(R)$ denotes the full ring of n -by- n matrices over R . For other terminology and notation, we refer to [2], [4], [7] and [10].

2. EC-FULLY SUBMODULES

Since ec -fully submodules are building bricks to the establishment of EFI -extending notion; first, we deal with this kind of submodules. To this end, we begin this section by recording some basic facts about them.

2.1. Lemma.

Let M be a module.

- (i) If $X \leq_{ec} Y$ and $Y \leq_{ec} M$ then $X \leq_{ec} M$.
- (ii) If $M = \bigoplus_{i \in \Lambda} X_i$ and $S \leq_{ec} M$, then $S = \bigoplus_{i \in \Lambda} \pi_i(S) = \bigoplus_{i \in \Lambda} (S \cap X_i)$, where π_i is the i^{th} -projection homomorphism of M .

Proof. The proof is routine.

The class of ec -fully submodules is properly contained in the class of fully invariant submodules. Next example provides a fully invariant submodule which is not ec -fully submodule. For details on this example, we refer to [8] or [10].

2.2. Example.

Let \mathbb{R} be the real field and S the polynomial ring $\mathbb{R}[x, y, z]$. Then the ring $R = S/S_s$, where $s = x^2 + y^2 + z^2 - 1$, is a commutative Noetherian domain. The free R -module $M = R \oplus R \oplus R$ contains an indecomposable submodule X_R of uniform dimension 2.

Now, let us build up the trivial extension of R with X_R i.e., let

$$T = \begin{bmatrix} R & X \\ 0 & R \end{bmatrix} = \left\{ \begin{bmatrix} r & x \\ 0 & r \end{bmatrix} : r \in R, x \in X \right\}.$$

Then $N = \begin{bmatrix} 0 & X \\ 0 & 0 \end{bmatrix} \leq T$ but N is not ec -fully submodule of T .

Proof. It is easy to check that R is a commutative Noetherian domain. Let $\phi: M \rightarrow R$ be the homomorphism defined by $\phi(a + Ss, b + Ss, c + Ss) = ax + by + cz + Ss$ for all $a, b, c \in S$. Clearly, ϕ is an epimorphism, and hence, its kernel X is a direct summand of M , i.e., $M = X \oplus X'$ for some submodule $X' \cong R$. Observe that R is uniform i.e., X' has uniform dimension 1 and hence X_R has uniform dimension 2.

Note that X is the R -module of regular sections of the tangent bundle of the 2-sphere S^2 . Furthermore, a celebrated result in differential geometry yields that X_R is an indecomposable module. Now the trivial extension of R with X_R i.e., $T = \begin{bmatrix} R & X \\ 0 & R \end{bmatrix}$ is a commutative ring and hence

$N = \begin{bmatrix} 0 & X \\ 0 & 0 \end{bmatrix}$ is a fully invariant submodule of T .

Assume that N contains essentially a cyclic submodule, say $\begin{bmatrix} 0 & x \\ 0 & 0 \end{bmatrix} T$, where $x \in X$. Thus xR is essential in X_R . It follows that xR has uniform dimension 2. However, this is impossible, because the mapping $\alpha: xR \rightarrow R$, defined by $\alpha(xr) = r$, where $r \in R$, is an R -isomorphism. Thus xR has uniform dimension 1. Therefore N does not contain essentially a cyclic submodule. Hence N is not ec -fully submodule of T .

Notice that the rank of free R -module M in the previous example can be replaced by any odd integer $n > 3$ (see [8]). There are more examples in this trend. We refer reader to look at [6] for the construction of this kind of examples. Following easy lemma shows that certain fully invariant submodules are ec -fully submodules.

2.3. Lemma.

Let M be a module which contains essentially a cyclic submodule. If K is a fully invariant direct summand of M , then K is an ec -fully submodule of M .

Proof. Suppose $Y = xR$ is an essential submodule of M , where $x \in M$. Let $\pi: M \rightarrow K$ be the canonical projection map. Then $xR \cap K = Y \cap K \leq \pi(Y) = \pi(x)R \leq K$. Since xR is essential in M then $xR \cap K$ is essential in K . It follows that $\pi(x)R$ is essential in K . Hence K is an ec -fully submodule of M .

It is natural to think of which modules (even rings) have the property that every *ec*-fully submodule is a direct summand. Next result provides a class of rings which satisfy the aforementioned property. First, recall the following module condition:

C_2 : If $X \leq M$ is isomorphic to a direct summand of M , then X is a direct summand of M (see [4] or [10]).

It is well-known that (von Neumann) regular rings satisfy the C_2 condition (see, for example [7]).

2.4. Proposition.

Let R be a (von Neumann) regular ring. Then an *ec*-fully submodule of R -module R is a direct summand.

Proof. Let I be an *ec*-fully submodule of R_R . Then there exists $x \in I$ such that xR is essential in I . By assumption, xR is a direct summand of R_R . Thus $R_R = xR \oplus L$ for some $L \leq R_R$. Now $xR \cap L$ is essential in $I \cap L$ which yields that $I \cap L = 0$. Therefore $R = xR \oplus L = I \oplus L$. It follows that $I \cong xR$. Since R_R has C_2 condition, I is a direct summand of R_R as required.

3. EFI-EXTENDING MODULES

In this section, we define and obtain basic properties of *EFI*-extending modules. Let us start by mentioning the definition of this new class of modules.

3.1. Definition

A module M is called *EFI*-extending if every *ec*-fully submodule of M is essential in a direct summand of M .

Obviously *FI*-extending modules (and hence extending modules) are *EFI*-extending modules. Moreover, (von Neumann) regular rings enjoy with the *EFI*-extending property. On the other hand, the ring of integers is an *EFI*-extending ring which is not regular. One might expect that whether *EFI*-extending property implies *FI*-extending or not? However, the following examples show that the class of *FI*-extending modules are properly contained in the class of *EFI*-extending modules.

3.2. Example

Let F be any field and let $F_i = F$, $i \in \Lambda$, where Λ is infinite. Define $R = \bigoplus_{i \in \Lambda} F_i + F1$, which is an F -subalgebra of $\prod_{i \in \Lambda} F_i$, where 1 is the identity of $\prod_{i \in \Lambda} F_i$. It is known that R is a regular (and hence *EFI*-extending ring by Proposition 2.4) ring which is not *FI*-extending (see [2, Ex. 2.3.32]).

3.3. Example [7, Ex. 7.54]

Let F be a field, and let $A = F \times F \times \dots$. So this ring is commutative. Now, let R be the subring of A consisting of sequences $(a_1, a_2, \dots) \in A$ that are eventually constant. For any $(a_1, a_2, \dots) \in R$, define $x = (x_1, x_2, \dots)$ by; $x_n = a_n^{-1}$ if $a_n \neq 0$, and $x_n = 0$ if $a_n = 0$. Then $x \in R$ and $a = axa$. Therefore, R is (von Neumann) regular. By Proposition 2.4, R is *EFI*-extending. Note that R is not a Baer ring. Hence R is not an *FI*-extending ring by [1, Theorem 4.7(iii)].

It is an open problem to determine if a direct summand of an *FI*-extending (or, also *EFI*-extending) module is always *FI*-extending (*EFI*-extending) (see [1]). The following result is in related with the *EFI*-extending version of the aforementioned problem.

3.4. Proposition

Let M be a module and $X \leq_{ec} M$. If M is *EFI*-extending, then X is *EFI*-extending.

Proof. Assume M is *EFI*-extending module. Let $S \leq_{ec} X$. By Lemma 2.1 (i), $S \leq_{ec} M$. Hence there exists a direct summand D of M such that $S \leq_e D$. Let $\pi: M \rightarrow D$ be the canonical projection endomorphism. Then $S = \pi(S) \leq \pi(X) \cap D = \pi(X)$. Hence $S \leq_e \pi(X)$ and $\pi(X)$ is a direct summand of X .

Next result deals with characterization of *EFI*-extending modules in terms of endomorphisms of injective hulls of the modules and complements of *ec*-fully submodules. To this end, the proof of the next theorem is based on the proof of the corresponding result for *FI*-extending modules (see [2, Proposition 2.3.2]).

3.5. Theorem

Let M be a module. Then the following are equivalent:

- (i) M is *EFI*-extending
- (ii) For $X \trianglelefteq_{ec} M$, there is $e^2 = e \in \text{End}(E(M))$ such that $X \leq_e eE(M)$ and $eM \leq M$.
- (iii) Each $X \trianglelefteq_{ec} M$ has a complement which is a direct summand.

Proof. (i) \Rightarrow (ii). Assume that $X \trianglelefteq_{ec} M$. Then there is $f^2 = f \in \text{End}(M)$ such that $X \leq_e fM$. Let $e: E(M) \rightarrow E(fM)$ be the canonical projection. Then we see that $X \leq_e eE(M)$ and $eM = fM \leq M$.

(ii) \Rightarrow (iii). Let $X \trianglelefteq_{ec} M$. Then there exists $e^2 = e \in \text{End}(E(M))$ such that $X \leq_e eE(M)$ and $eM \leq M$. Now, let us put $c = (1 - e)|_M$. Then $c^2 = c \in \text{End}(M)$. We show that cM is a complement of X . For this, first note that $cM \cap X = 0$ as $cM = (1 - e)M$. Say $K \leq M$ such that $cM = (1 - e)M \leq K$ and $K \cap X = 0$. From $M = (1 - e)M \oplus eM$, $K = (1 - e)M \oplus (K \cap eM)$ by the modular law. As $K \cap X = 0$ and $X \leq_e eE(M)$, $K \cap eE(M) = 0$ and so $K \cap eM = 0$. Thus, we get that $K = (1 - e)M$, then $K = cM$. Therefore cM is a complement of X .

(iii) \Rightarrow (i). Let $X \trianglelefteq_{ec} M$. There exists $g^2 = g \in \text{End}(M)$ so that gM is a complement of X . As $X \trianglelefteq_{ec} M$, $gX \leq X \cap gM = 0$. Hence $X = (1 - g)X$. To show that M is *EFI*-extending, we claim that $X \leq_e (1 - g)M$. For this, assume that $K \leq (1 - g)M$ such that $X \cap K = 0$. Then note that $gM \cap K = 0$. Take $gm + k = n \in (gM \oplus K) \cap X$ with $m \in M$, $k \in K$, and $n \in X$. Then $(1 - g)gm + (1 - g)k = (1 - g)n$, so $k = n \in X \cap K$ because $K \leq (1 - g)M$ and $X = (1 - g)X$. Now as $X \cap K = 0$, $k = n = 0$. Thus, $(gM \oplus K) \cap X = 0$. Since gM is a complement of X , $gM \oplus K = gM$ and so $K = 0$. Therefore, $X \leq_e (1 - g)M$. It follows that M is *EFI*-extending.

It is well-known that a direct sum of *FI*-extending modules is also *FI*-extending module. Now, we intend to have the corresponding result for *EFI*-extending modules.

3.6. Theorem

Let $M = \bigoplus_{i \in \Lambda} N_i$. If each N_i is an *EFI*-extending module, then M is an *EFI*-extending module.

Proof. Let $S \trianglelefteq_{ec} M$. By Lemma 2.1(ii), $S = \bigoplus_{i \in \Lambda} (S \cap N_i)$, and $S \cap N_i \trianglelefteq N_i$ for each $i \in \Lambda$. Assume S contains essentially the cyclic submodule xR , where $x \in S$. Let $\pi: S \rightarrow S \cap N_i$ be the projection map. Then $xR \cap (S \cap N_i) \leq \pi(xR) = \pi(x)R \leq S \cap N_i$. Since $xR \leq_e S$ then $xR \cap (S \cap N_i) \leq_e S \cap N_i$. It follows that $\pi(x)R \leq_e S \cap N_i$. Hence $S \cap N_i \trianglelefteq_{ec} N_i$ for each $i \in \Lambda$. As N_i is *EFI*-extending, there is a direct summand D_i of N_i with $S \cap N_i \leq_e D_i$ for every $i \in \Lambda$. Thus $S = \bigoplus_{i \in \Lambda} (S \cap N_i) \leq_e \bigoplus_{i \in \Lambda} D_i$. Since $\bigoplus_{i \in \Lambda} D_i$ is a direct summand of M we have that M is an *EFI*-extending module.

3.7. Corollary

If M is a direct sum of *FI*-extending (e.g., extending) modules, then M is *EFI*-extending.

Proof. Immediate by Theorem 3.6.

Applying Theorem 3.6 to Abelian groups (i.e., \mathbb{Z} -modules) we obtain the following corollary.

3.8. Corollary

Let M be a \mathbb{Z} -module. If M satisfies any of the following conditions, then M is an *EFI*-extending \mathbb{Z} -module.

- (i) M is finitely generated
- (ii) M is of bounded order (i.e., $nM = 0$ for some positive integer n)
- (iii) M is divisible.

Proof. (i) and (ii) M is a direct sum of uniform submodules. Then the result follows from Theorem 3.6.

(iii) M is extending and hence *FI*-extending. Thus M is *EFI*-extending.

Observe that an easy modification yields that the Corollary 3.8 above remains true when the ring of integers replaced with a Dedekind domain.

One more application of the Theorem 3.6 gives an affirmative answer for the direct summand

problem of *EFI*-extending Abelian groups which as follows.

3.9. Theorem

Let M be a direct sum of uniform \mathbb{Z} -modules. Then any direct summand of M is an *EFI*-extending module.

Proof. Let N be a direct summand of M . Then N is also a direct sum of uniform modules by [9, Theorem 4.45] (see, also [10]). Now, Theorem 3.6 gives that N is an *EFI*-extending module.

Our next objective is to carry over *EFI*-extending property to full matrix ring. First of all, we give an example of *EFI*-extending ring which shows that *EFI*-extending property is not left-right symmetric.

3.10. Example

Let $R = \begin{bmatrix} \mathbb{Z}_2 & \mathbb{Z}_2 \\ 0 & \mathbb{Z} \end{bmatrix}$. Then the ring R is right *EFI*-extending, but it is not left *EFI*-extending.

Proof. Note that R is right *FI*-extending by [2, Example 2.3.14]. Hence R is right *EFI*-extending ring. On the other hand, let $I = \begin{bmatrix} 0 & \mathbb{Z}_2 \\ 0 & 0 \end{bmatrix} \trianglelefteq_{ec} R$. It is easy to check that I is not essential in a direct summand of ${}_R R$. It follows that R is not left *EFI*-extending ring.

3.11. Theorem

Let R be a right *EFI*-extending ring. Then $M_n(R)$ is a right *EFI*-extending ring for all positive integer n .

Proof. Let $N \trianglelefteq_{ec} M_n(R)$. Then it is easy to see that $N = M_n(I)$ for some $I \trianglelefteq_{ec} R$. As R is right *EFI*-extending, there exists $e^2 = e \in R$ such that $I_R \leq_e eR_R$. This yields that as a right ideal of $M_n(R)$, N is essential in a direct $(eI)M_n(R)$ of $M_n(R)$, where I is the identity matrix of $M_n(R)$. Thus $M_n(R)$ is right *EFI*-extending, as required.

REFERENCES

- [1] Birkenmeier, G. F., Müller, B. J. and Rizvi S. T., "Modules in which every fully invariant submodule is Essential in a Direct Summand," *Communications in Algebra*, vol. 30, no.3, pp. 1395-1415, 2007.
- [2] Birkenmeier, G. F., Park, J. K. and Rizvi, S. T., *Extensions of rings and modules*, New York: Birkhäuser, 2013.
- [3] Celep, C. and Tercan A., "Modules whose ec-closed submodules are direct summand," *Taiwanese Journal of Mathematics*, vol.13, no.4, pp. 1247-1256, 2009.
- [4] Dung, N. V., Huynh, D. V., Smith, P. F., and Wisbauer, R., *Extending Modules*, Pitman Research Notes in Mathematics Series, 313, Longman, New York, 1994.
- [5] Kamal, M. A., and Elmnohy, O. A., "On P-extending modules," *Acta Math. Univ. Comeniana*, vol. 74, no. 2, pp. 279-286, 2005.
- [6] Kara, Y., Tercan, A. and Yaşar R., "*PI*-extending modules via nontrivial complex bundles and Abelian endomorphism rings," *Bulletin of the Iranian Mathematical Society*, vol. 43, no. 1, pp. 121-129, 2017.
- [7] Lam, T.Y., *Lectures on modules and rings*, vol. 189. Springer Science and Business Media, 2012.
- [8] Smith, P. F., and Tercan, A., "Direct summands of modules which satisfy (C-11)," *Algebra Colloquium*, vol. 11, pp. 231-237, 2004.
- [9] Smith, P. F., and Tercan, A., "Generalizations of CS-modules," *Communications in Algebra*, vol. 21, no.6, pp.1809-1847, 1993.
- [10] Tercan, A. and Yücel, C. C., *Module theory, extending modules and generalizations*, Basel: Birkhäuser, 2016.

	SAKARYA UNIVERSITY JOURNAL OF SCIENCE	
	e-ISSN: 2147-835X http://www.saujs.sakarya.edu.tr	
	<u>Received</u> 21-11-2017 <u>Accepted</u> 30-07-2018	<u>Doi</u> 10.16984/saufenbilder.356720

Screening of Xylanase and Glucose Isomerase Producing Bacteria Isolated from Hot Springs in Turkey

Dilsat Nigar Colak¹, Kadriye Inan Bektas, Muslum Tokgoz, Sabriye Canakci, Ali Osman Belduz

ABSTRACT

The aim of this study was screening of xylanase and glucose isomerase producing thermophilic bacteria isolated from some hot springs located in Aegean Region of Turkey. Total sixty eight thermophilic isolates (*Anoxybacillus*, *Brevibacillus*, *Geobacillus*, *Aneurinibacillus*, *Thermus*, *Paenibacillus* and *Proteobacter*) were collected previously from these fields and identified based on 16S rDNA gene sequences. Isolates were screened by plate assay for determining the xylanase and glucose isomerase production abilities separately in order to find new strains for industrial processes. After an incubation period of two days for xylanase and 5-6 days for glucose isomerase at 50-60 °C, positive isolates were determined. Enzyme producing isolates were confirmed by spectrophotometric measurements with crude enzyme extracts, birchwood xylan and glucose were used as substrates. Most of the isolates (fifty nine) were positive for xylan degradation while only sixteen of them were positive for glucose isomerase activity. Fourteen of the isolates showed both xylanase and glucose isomerase activity. None of the isolates belong to the genera *Paenibacillus*, *Aneurinibacillus*, and *Proteobacter* were glucose isomerase positive, although the glucose isomerase activity of *Geobacillus* isolates were notably high. Both xylanase and glucose isomerase activities were observed at 50-60 °C which is suitable for biotechnological applications.

Keywords: Birchwood xylan, Glucose isomerase, Thermophilic bacteria, Xylanase

1. INTRODUCTION

Microbial enzymes have widespread uses in industries because of their biocatalytic potential for a large number of reactions. Microbial enzymes show higher activity and stability than plant and animal enzymes at high temperatures. Microbial enzymes can also be cultured in large quantities in a short time by fermentation [1]. With the recent developments in biotechnology, important tools for the efficient development of new enzymes have provided. Thermophilic enzymes have especially been topics for much research because of their stability at high temperatures which allowing high substrate solubility, better mixing, more mass transfer rate, and less risk of contamination [2, 3]. These enzymes are not only more thermostable, but also

more resistant to extreme pH values, detergents, the other organic solvents and denaturing agents than their mesophilic counterparts what makes them extremely interesting for industrial processes [4, 5, 6]. The interest in microbial enzymes is increasing rapidly in recent years, the principle industrial sectors being in the food industries, starch processing, detergent, paper industry etc. We have focused on two of the industrial enzymes in this work that have great importance in food and paper industry; xylanases and glucose isomerases.

Xylan is considered as the second widely available polysaccharide in nature after cellulose [7]. It is located mainly in the secondary cell wall of annual plants and hardwoods and is thought to be form a linkage between lignin and other polysaccharides. The heterogeneous polysaccharide structure of xylan composed mostly of linear chains of D-xylose linked through β -1,4-glycosyl bonds [8, 9]. Because of its complexity and heterogeneity,

¹ Corresponding Author Giresun University, Derele Vocational School dilsat.nigar@giresun.edu.tr

several enzymes involved the complete degradation of xylan. Xylanases play a key role in this degradation [10]. Xylanase (E.C 3.2.1.8) degrades β -1,4- glycosidic linkages randomly, and produce xylose and xylo-oligosaccharides [11, 12, 13]. Xylanases have a great industrial importance, pulping and bleaching processes, food and feed industry, textile processes and waste treatment are the main applications of xylanase [14]. It is also used in preparation of xylooligosaccharides which are used as prebiotics and in combination with cellulase and pectinase for clarification of fruit juices [15]. Utilization of xylanase reduces the environmental pollution caused by chemicals. Microorganisms such as actinomycetes, fungi and bacteria are the main sources of xylanases [9]. Xylan producing microorganisms are widespread in the world and also reported in various extreme environments, such as thermal springs [16], marines [17], and Antarctic environments [18]. High temperatures are needed for most of the industrial applications that use xylanases, for this reason thermostable xylanases would be advantageous [19].

D-Glucose/xylose isomerase (D-xylose ketol isomerase; EC 5.3.1.5), commonly referred as glucose isomerase (GI), is one of the three highest tonnage value enzymes in industry, amylase and protease being the other two [20]. Glucose isomerases are used in industry to catalyze the reversible conversion of D-glucose to D-fructose on the first step of xylose metabolism in many microorganisms [21]. Interconversion of xylose to xylulose serves a nutritional requirement in saprophytic bacteria that living on decaying plant matter and also involves in the hemicellulose bioconversion for producing ethanol [20]. This isomerization reaction is important for the high fructose corn syrup (HFCS) production process from corn starch. HFCS is typically used as a sweetener in food industry. Until 1970s the main sweeteners of food industry was sucrose derived from sugar beet (40%) and sugarcane (60%). Glucose isomerase was firstly used in Japan for the production of HFCS and later in the United States and nowadays it becomes one of the most important industrial enzymes. High temperature and alkaline pH are needed in the enzyme process used in sweetener industry for conserving a higher concentration of fructose [22, 23]. The main sources of commercially available GI are mesophilic microorganisms that exhibit optimum activity at a pH range from 7.5 to 9.0 [24]. Isolating new thermophilic microorganisms that

are capable of producing GI with high level of activity and stability at elevated temperatures will be of great benefit in the industrial production of HFCS.

The aim of this study was to detect new thermotolerant/thermophilic bacterial strains with the capability of the production of thermostable xylanase and/or glucose isomerases for industrial applications. This paper would be helpful for paper and food industries since it will provide new xylanase and GI producing thermophilic microorganisms.

2. MATERIALS AND METHODS

2.1. Bacterial isolates and culture conditions

Water samples were collected from Karakoc, Kaynarca and Nebiler Hot Springs (Izmir), Alangullu and Camkoy Hot Springs (Aydin), and Geothermal field of Omerbeyli (Germencik/Aydin). All of 68 isolates derived from these samples were identified based on 16S rDNA sequences by Inan [25]. According to 16S rDNA sequence analysis, 26 of the isolates belong to the genus *Anoxybacillus*. 15 *Brevibacillus*, 13 *Geobacillus*, 7 *Thermus*, 4 *Aneurinibacillus*, 2 *Proteobacter* and 1 *Paenibacillus* isolates were also identified. All of the isolates were cultured in Luria Bertani (LB) medium with an optimum growing temperature of 50-60 °C.

2.2. Xylanase activity assay

2.2.1. Plate assay

Xylanase activity was determined by the method of Gessesse and Gashe [26]. Single colonies from fresh LB agar plates were patched onto xylan included plates (1% xylan, 0.2% yeast extract, 2% agar, 0.5% peptone, 0.05% NaCl, 0.05% MgSO₄, 0.015% CaCl₂ and pH 7.0) and incubated for 48 hours at 50-60 °C. After incubation period plates were flooded with 0.1% Congo red for 15 min and by washing two to three times with 1 M NaCl the dye was removed. Transparent zones around colonies represents the degradation of xylan.

2.2.2. Spectrophotometric measurements

Fresh cultures of each isolate (2 ml) were inoculated into xylanase specific medium (g/L: 10.0 g xylan, 5 g pepton, 2 g yeast extract, 0.5 g MgSO₄, 0.15 g CaCl₂ and 0.5 g NaCl, pH 7.5) for xylanase production. After centrifugation of 4500

x g for 5 min, supernatants were used as enzyme sources.

Dinitrosalicylic acid method was used for determining the xylanase activity by measuring the release of reducing sugars from Birchwood xylan [27]. 0.25 mL of enzyme sample was mixed with 0.75 ml of substrate (1% solubilised birchwood xylan) in phosphate buffer, pH 6.5 and incubated at optimum bacterial growing temperature for 20 min. 1.0 mL of dinitrosalicylic acid (DNS) solution was added to the samples and boiled for 5 min. The absorbance was measured at 540 nm. The reaction was terminated at zero time in the control tubes. Solubilised xylan was prepared by stirring birchwood xylan with 0.5 M Tris-HCl (pH 8.0) buffer for overnight at room temperature. After centrifugation supernatant was used as substrate.

2.3. Glucose isomerase activity assay

2.3.1. Plate assay

The method of Lee et al. [28] was used for determination of glucose isomerase activity. Bacterial isolates were incubated in agar plates supplemented with 1% xylose for overnight. Fructose (2%), MgSO₄ (5 mM), CoCl₂ (0.5 mM), glucose oxidase (20 U/ml), peroxidase (4 U/ml), and benzidine (0.4 mg/ml) in 100 mM MOPS (morpholinepropane sulfonic acid) buffer (pH 7.0) were mixed with top agar (0.7%) at 50°C and poured on the colonies. The plates were incubated for 5-6 days at 50-60°C. Positive samples showed a dark brown color around the colonies.

2.3.2. Spectrophotometric measurements

Bacterial cells were incubated in LB medium supplemented with 0.5% xylose and harvested at the late-logarithmic phase by centrifugation at 13,000 rpm for 5 min, resuspended with 25 mM phosphate buffer (0.2 mg lysozyme, 5 µg DNase and 0.1% Triton X-100, pH 7.0) and lysed by incubating in a shaker for 3-4 hours. After a centrifugation period of 15,000 rpm. for 30 min supernatants were collected for enzyme activity assays [29].

Cysteine-carbazole-sulfuric acid method was used for estimating the amount of fructose or xylulose formed after the enzyme reaction. Based on this method, glucose isomerase activity was measured by incubating a reaction mixture that contained 10 mM MgSO₄, 1 mM CoCl₂, 0.5 M glucose, and the enzyme in 100 mM MOPS buffer (pH 7.0) at 55°C

for 30 min. Incubation period followed by addition of 0.5 M perchloric acid for terminating the reaction. 1.5% cysteine hydrochloride and 0.12% carbazole added to the reaction mixture and mixed thoroughly, right after 70% sulfuric acid added, mixed and incubated at 60°C for 10 min. The absorbance was measured at 560 nm.

3. RESULTS AND DISCUSSION

In the present study, thermophilic isolates derived from different hot springs (formerly identified) were screened for xylanase and glucose isomerase activity.

3.1. Xylanase activity

Sixty eight isolates of bacteria were tested for xylanase production on xylan (1%) included agar plates for 2 days at 50-60 °C. Zone formation around the bacterial growth after addition of Congo red solution (0.1%) was identified for the xylanase positive isolates. Only nine of them were negative for xylanase activity based on plate assay. Five of the xylanase negative isolates belongs to the genus *Anoxybacillus*, three of them *Brevibacillus* and one of them belong to the genus *Geobacillus* (Table 1). Zone forming isolates were inoculated into xylan specific medium (10.0 g/L xylan) for xylanase production for further analyses. Dinitrosalicylic acid method [27] was used for spectrophotometric determination of xylanase activity. Spectrophotometric measurements at 540 nm with Birchwood xylan (1%) as substrate revealed that all 59 of the isolates were hydrolyse the xylan to xylo-oligosaccharide molecules. Especially *Anoxybacillus* TF15 and *Geobacillus* DF20, TF11, PDC9, PDC11, and TH2 exhibited a two fold activity than the other isolates with Birchwood xylan.

Xylanase producing bacterial strains were isolated from different kind of areas, such as Antarctic environments [18], marines [17], soda lakes [30] and thermal springs [16]. Microbial production of xylanases from bacteria, such as *Bacillus*, *Cellulomonas*, *Micrococcus*, *Staphylococcus*, *Paenibacillus*, have been reported [9, 31, 32, 33]. Because thermostability is a desired characteristic, thermostable xylanases have a great importance among industrial enzymes. An extreme thermophile *Rhodothermus marinus* producing xylanases active at 80 °C have been identified [34]. Some other thermostable xylanases for example *Bacillus spp.*, *Thermotoga sp.*, *Thermus*

sp., and *Streptomyces sp.* were also reported that active at 60-70 °C [35]. Xylanase producing thermophilic *Geobacillus* and *Anoxybacillus* strains were also reported [36, 37, 38, 39]. In this work, all of the *Thermus*, *Aneurinibacillus*, and *Proteobacter* isolates exhibited xylanase positive features. The only one *Paenibacillus* isolate included in this work was also degraded the xylan. Only a few of the *Anoxybacillus*, *Geobacillus* and *Brevibacillus* samples were negative for xylanase production.

3.2. Glucose Isomerase activity

Glucose isomerase activity was determined based on the method of Lee et al. [28]. All of the 68 thermophilic isolates were inoculated onto glucose isomerase specific plates. After an incubation period of 5-6 days, only 16 of the isolates have showed a dark brown color around colonies, which nine of them belongs to the genus *Geobacillus*, and the others include five *Anoxybacillus*, a *Brevibacillus* and a *Thermus* isolates (Table 1). Spectrophotometric measurements were carried out with cysteine-carbazole-sulfuric acid method for verifying the results. Among the sixteen isolates screened, five *Geobacillus* and an *Anoxybacillus* isolates showed maximum glucose isomerase activity. *Brevibacillus* and *Thermus* samples exhibited relatively poor activity.

Pseudomonas hydrophila was the first discovered microorganism that catalyse the isomerization of D-glucose to D-fructose [40], since then a large number of microbial species has been detected for glucose isomerase activity [41, 42]. *Lactobacillus* [43], *Streptomyces* [44], *Bacillus* [45, 46], *Arthrobacter* [47] are some of the glucose isomerase producing bacteria reported.

Paenibacillus, *Aneurinibacillus* and *Proteobacter* isolates used in this work did not exhibit glucose isomerase activity. There is also no evidence for *Aneurinibacillus* and *Proteobacter* genera about GI activity in literature, whereas D-xylose isomerase activity have been reported for *Paenibacillus sp.* strain by Moneke et al. [48]. Some of the isolates belong to the genera *Geobacillus*, *Anoxybacillus*, *Brevibacillus* and *Thermus* were positive for GI activity in our screening results. There is already some reports in literature about glucose isomerase activity of *Anoxybacillus* [49], *Geobacillus* [50], *Thermus* [51], and *Brevibacillus* [52] strains. Because of the industrial importance of Glucose isomerases, especially thermostable and acid-stable ones, further investigations are already under way.

Table 1. Production of xylanase and glucose isomerase by various bacterial isolates

Genus	Strain	Place (Hot Spring)	Glucose Isomerase	Xylanase
<i>Anoxybacillus</i>	PDF 1	Germencik/ Aydin	-	+
<i>Anoxybacillus</i>	PDF 2	Germencik/ Aydin	-	-
<i>Anoxybacillus</i>	PDF 3	Karakoc/Izmir	-	+
<i>Anoxybacillus</i>	PDF 15	Camkoy/ Aydin	-	+
<i>Anoxybacillus</i>	PDF 16	Camkoy/ Aydin	-	+
<i>Anoxybacillus</i>	PDF 18	Karakoc/Izmir	-	+
<i>Anoxybacillus</i>	PDF 21	Karakoc/Izmir	+	+
<i>Anoxybacillus</i>	PTF 26	Karakoc/Izmir	-	+
<i>Anoxybacillus</i>	PTF 37	Karakoc/Izmir	-	+
<i>Anoxybacillus</i>	PTF 38	Kaynarca/Izmir	-	+
<i>Anoxybacillus</i>	DF 1	Germencik/ Aydin	+	+
<i>Anoxybacillus</i>	DF 2	Germencik/ Aydin	-	+
<i>Anoxybacillus</i>	DF 3	Karakoc/Izmir	-	+
<i>Anoxybacillus</i>	DF 5	Kaynarca/Izmir	-	+
<i>Anoxybacillus</i>	DF 8	Kaynarca/Izmir	-	+
<i>Anoxybacillus</i>	DF 10	Kaynarca/Izmir	-	+
<i>Anoxybacillus</i>	DF 11	Kaynarca/Izmir	-	+
<i>Anoxybacillus</i>	DF 14	Alangullu/Aydin	-	-
<i>Anoxybacillus</i>	DF 15	Alangullu/Aydin	+	-
<i>Anoxybacillus</i>	DF 16	Alangullu/Aydin	-	+
<i>Anoxybacillus</i>	DF 17	Camkoy/ Aydin	-	+
<i>Anoxybacillus</i>	DF 18	Camkoy/ Aydin	-	+
<i>Anoxybacillus</i>	DF 19	Camkoy/ Aydin	-	-
<i>Anoxybacillus</i>	TF 15	Karakoc/Izmir	++	+
<i>Anoxybacillus</i>	TH 4	Nebiler/Izmir	-	-
<i>Anoxybacillus</i>	TH5	Camkoy/ Aydin	+	+
<i>Brevibacillus</i>	PDF 4	Camkoy/ Aydin	-	+
<i>Brevibacillus</i>	PDF 10	Camkoy/ Aydin	-	+

<i>Brevibacillus</i>	PDC 1	Germencik/ Aydin	-	+
<i>Brevibacillus</i>	PDC 2	Karakoc/Izmir	-	+
<i>Brevibacillus</i>	PDC 3	Alangullu/Aydin	-	+
<i>Brevibacillus</i>	PDC 4	Germencik/ Aydin	-	+
<i>Brevibacillus</i>	PDC 5	Nebiler/Izmir	+	+
<i>Brevibacillus</i>	PDC 6	Alangullu/Aydin	-	+
<i>Brevibacillus</i>	PDC 7	Kaynarca/Izmir	-	+
<i>Brevibacillus</i>	PDF 23	Germencik/ Aydin	-	-
<i>Brevibacillus</i>	PTF 25	Karakoc/Izmir	-	+
<i>Brevibacillus</i>	PTF 30	Karakoc/Izmir	-	-
<i>Brevibacillus</i>	PTF 33	Camkoy/ Aydin	-	+
<i>Brevibacillus</i>	PTF 40	Kaynarca/Izmir	-	+
<i>Brevibacillus</i>	PDF 41	Kaynarca/Izmir	-	-
<i>Paenibacillus</i>	PTF 34	Nebiler/Izmir	-	+
<i>Aneurinibacillus</i>	PDF 6	Alangullu/Aydin	-	+
<i>Aneurinibacillus</i>	PDF 13	Nebiler/Izmir	-	+
<i>Aneurinibacillus</i>	PDF 24	Nebiler/Izmir	-	+
<i>Aneurinibacillus</i>	PTF 32	Alangullu/Aydin	-	+
<i>Proteobacter</i>	PDF 20	Nebiler/Izmir	-	+
<i>Proteobacter</i>	PTF 31	Nebiler/Izmir	-	+
<i>Geobacillus</i>	DF 20	Germencik/ Aydin	++	+
<i>Geobacillus</i>	TF 11	Alangullu/Aydin	++	+
<i>Geobacillus</i>	TF 12	Karakoc/Izmir	+	+
<i>Geobacillus</i>	PDC 8	Kaynarca/Izmir	+	+
<i>Geobacillus</i>	PDC 9	Alangullu/Aydin	++	+
<i>Geobacillus</i>	PDC 10	Alangullu/Aydin	+	+
<i>Geobacillus</i>	PDC 11	Germencik/ Aydin	++	+
<i>Geobacillus</i>	PDC 12	Germencik/ Aydin	+	-
<i>Geobacillus</i>	PDC 13	Camkoy/ Aydin	-	+
<i>Geobacillus</i>	PDC 14	Karakoc/Izmir	-	+
<i>Geobacillus</i>	TH 2	Camkoy/ Aydin	++	+
<i>Geobacillus</i>	TH 3	Camkoy/ Aydin	-	+
<i>Geobacillus</i>	TH 6	Karakoc/Izmir	-	+
<i>Thermus</i>	TF 2	Germencik/ Aydin	-	+
<i>Thermus</i>	TF 3	Germencik/ Aydin	+	+
<i>Thermus</i>	TF 5	Nebiler/Izmir	-	+
<i>Thermus</i>	TF 6	Kaynarca/Izmir	-	+
<i>Thermus</i>	TF 7	Karakoc/Izmir	-	+
<i>Thermus</i>	TF 8	Kaynarca/Izmir	-	+
<i>Thermus</i>	TF 9	Germencik/ Aydin	-	+

4. CONCLUSIONS

In this study it is aimed to find out new thermophilic xylanase and/or glucose isomerase producing strains for industrial applications. For this purpose, formerly identified sixty eight thermophilic isolates collected from hot springs, located in the west side of Turkey, were screened for xylanase and glucose isomerase activity. Among sixty eight isolates, fifty nine of them exhibited xylanase activity which indicates that most of the bacteria derived from hot springs can degrade xylan. However only sixteen of the isolates showed glucose isomerase activity that is glucose degradation is not a common feature for these bacteria. Fourteen of the isolates were positive for both xylanase and glucose isomerase but further analyses should be done for determining that which substrate (xylan or glucose) is more preferable for these bacteria. The optimal enzyme activity of the isolates was

between 50-60 °C, which make them potential tools for industrial applications.

ACKNOWLEDGMENTS

This study was financially supported by Giresun University Research foundation (Project No: 140316-27).

REFERENCES

- [1] P. Anbu, S. C. Gopinath, A. C. Cihan, and B. P. Chaulagain, "Microbial enzymes and their applications in industries and medicine," *Biomed. Res. Int.*, pp. 1–3, 2015.
- [2] M. E. Bruins, A. E. M. Janssen, and R. M. Boom, "Thermostzymes and their applications," *Appl. Biochem. Biotechnol.* vol 90, pp.155-186, 2001.

- [3] J. Eichler, "Biotechnological uses of archaeal enzymes," *Biotechnol. Adv.* vol 19, pp. 261-278, 2001.
- [4] D. Covan, R. Daniel, and H. Morgan, "Thermophilic proteases: properties and applications," *Trends Biotechnol.* vol 3, pp. 68-72, 1985.
- [5] D. A. Covan, "Thermophilic proteins: stability and function in aqueous and organic solvents," *Comp. Biochem. Physiol., Part A: Mol. Integr. Physiol.* vol 118, pp.429-438, 1997.
- [6] A. Gupta, and S. K. Khare, "A protease stable in organic solvents from solvent tolerant strain *Pseudomonas aeruginosa*," *Bioresour. Technol.* vol 97, pp. 1788-1793, 2006.
- [7] T. Collins, C. Gerday, and G. Feller, "Xylanases, xylanase families and extremophilic xylanases," *FEMS Microbiol. Reviews.* vol 29, pp. 3-23, 2005.
- [8] N. Kulkarni, A. Shendye, and M. Rao, "Molecular and biotechnological aspects of xylanases," *FEMS Microbiology Reviews*, vol. 23, no 4, pp. 411-456, 1999.
- [9] Q. K. Beg, M. Kapoor, L. Mahajan, and G. Hoondal, "Microbial xylanases and their industrial applications: a review," *Applied Microbiology and Biotechnology.* vol 56, pp. 326-338, 2001.
- [10] A. Blanco, P. Diaz, J. Zueco, P. Parascandola, and F. I. J. Pastor, "A multidomain xylanase from a *Bacillus* sp. with a region homologous to thermostabilizing domains of thermophilic enzymes," *Microbiology*, vol 145, pp. 2163-2170, 1999.
- [11] C. Tachaapaikoon, K. L. Kyu, and K. Ratanakhanokchai, "Purification of xylanase from alkaliphilic *Bacillus* sp. K-8 by using corn husk column," *Process Biochemistry*, vol 12, pp. 2441-2445, 2006.
- [12] S. B. Chidi, B. Godana, I. Ncube, Van E. J. Rensburg, A. Cronshaw, and E. K. "Abotsi Production, purification and characterization of cellulase-free xylanase from *Aspergillus terreus* UL 4209," *African Journal of Biotechnology*, vol 7, no 21, pp. 3939-3948, 2008.
- [13] S. Ahmed, S. Riaz, and A. Jamil, "Molecular cloning of fungal xylanases: an overview," *Applied microbiology and biotechnology*, vol 84, no 1, pp. 19-35, 2009.
- [14] L. A. Van den Broek R. M. Lloyd, G. Beldman, J. C. Verdoes, B. V. McCleary, and A. G. Voragen, "Cloning and characterization of arabinoxylan arabinofuranohydrolase-d3 (Axhd3) from *Bifi-dobacterium adolescentis* DSM20083," *App. Microbiol. and Biotechnology.* vol 67, pp. 641-647, 2005.
- [15] D. Verma, A. Anand, and T. Satyanarayana, "Thermostable and alkalistable endoxylanase of the extremely thermophilic bacterium *Geobacillus thermodenitrificans* TSAA1: cloning, expression, characteristics and its applicability in generating xylooligosaccharides and fermentable sugars," *App. Biochemistry and Biotechnology*, vol 170, pp. 119-130, 2013.
- [16] K. Bouacem, et al. "Partial characterization of xylanase produced by *Caldicoprobacter algeriensis*, a new thermophilic anaerobic bacterium isolated from an Algerian hot spring," *Appl Biochem Biotechnol.* vol 174, pp. 1969-1981, 2014.
- [17] N. Annamalai, R. Thavasi, S. Jayalakshmi, and T. Balasubramanian, "Thermostable and alkaline tolerant xylanase production by *Bacillus subtilis* isolated from marine environment," *Indian J Biotechnol.* vol 8, pp. 291-297, 2009.
- [18] J. Bradner, M. Gillings, and K. Nevalainen, "Qualitative assessment of hydrolytic activities in Antarctic microfungi grown at different temperatures on solid media," *World J Microbiol Biotechnol.* vol 15, pp. 131-132, 1999.
- [19] B. Sonnleitner, and A. Fiechter, "Advantages of using thermophiles in biotechnological processes: expectations and reality," *Trends in Biotechnology*, no 1, pp. 74-80, 1983.
- [20] S. H. Bhosale, M. B. Rao, and V. V. Deshpande, "Molecular and industrial aspects of glucose isomerase," *Microbiol Rev.* vol 60, pp. 280-300, 1996.
- [21] M. G. Wovcha, D. L. Steuerwald, and K. E. Brooks, "Amplification of D-xylose and D-glucose isomerase activities in *Escherichia*

- coli by gene cloning," *Appl. Environ. Microbiol.* vol 45, pp. 1402–1404, 1983.
- [22] C. Bucke, In "Microbial Enzymes and Biotechnology" (Ed. W.M.Fogarty); *Applied Science Pub.*, London; pp. 93-129, 1983.
- [23] Y. B. Tewari, and R. N. Goldberg, "Thermodynamics of the conversion of aqueous glucose to fructose," *Appl. Biochem. Biotechnol.* vol 11, pp. 17–24, 1985.
- [24] F. H. Verhoff, G. Boguslawski, O. J. Lautero, S. T. Schlager, and Y. C. Jao, "Glucose isomerase," In "*H. Comprehensive biotechnology*;" Balanch, W., Drew, S., Wang, D.I.C, Pergamon Press, Oxford, pp. 837–859, 1985.
- [25] K. Inan, "İzmir ve Aydın illerindeki bazı kaplıçalardan izole edilen termofilik bakteri izolatlarının moleküler taksonomisi ve D1021 izolatının glukoz izomerazının karakterizasyonu," Doktora tezi. Karadeniz Teknik Üniversitesi, Fen Bilimleri Enstitüsü, Trabzon, 2011.
- [26] A. Gessesse, and B. A. Gashe, "Production of alkaline xylanase by an alkaliphilic *Bacillus* sp. Isolated from a soda lake," *Journal of applied Microbiology*, vol 83, pp. 402-406, 1997.
- [27] G. L. Miller, "Use of dinitrosalicylic acid reagent for determination of reducing sugars," *Anal Chem.* vol 31, pp. 426-428, 1959.
- [28] C. Lee, L. Bhatnagar, B. C. Saha, Y. E. Lee, M. Takagi, T. Imanaka, M. Bagdasarian, and J. G. Zeikus, "Cloning and Expression of the *Clostridium thermosulfurogenes* Glucose Isomerase Gene in *Escherichia coli* and *Bacillus subtilis*," *Appl. Environ. Microbiol.* vol 56, pp. 2638–2643, 1990.
- [29] Z. Dische, and E. A. Borenfreund, "New Spectrophotometric Method for the Detection and Determination of Ketosugars and Trioses," *J.Biol.Chem.* vol 192, pp. 583-587, 1951.
- [30] X. Huang, J. Lin, X. Ye, and G. Wang, "Molecular characterization of a thermophilic and salt-and alkaline-tolerant xylanase from *Planococcus* sp. SL4, a strain isolated from the sediment of a soda lake," *J Microbiol Biotechnol.* vol 25, pp. 662–671, 2015.
- [31] S. Subramanian, and P. Prema, "Cellulase-free xylanases from *Bacillus* and other micro-organisms," *FEMS Microbiol Lett.* vol 183, pp. 1–7, 2000.
- [32] S. Gupta, R. C. Kuhad, B. Bhushan, and G.S. Hoondal, "Improved xylanase production from a haloalkalophilic *Staphylococcus* sp. SG-13 using inexpensive agricultural residues," *World J Microbiol Biotechnol.* vol 17, pp. 5–8, 2001.
- [33] D. Chapla, H. Patel, D. Madamwar, and A. Shah, "Assessment of a thermostable xylanase from *Paenibacillus* sp. ASCD2 for application in prebleaching of eucalyptus kraft pulp," *Waste Biomass Valor.* vol 3, pp. 269–274, 2012.
- [34] L. Dahlberg, "Thermostable Xylanases from *Rhodothermus marinus*," Ph.D. dissertation, Biotechnology, Lund University, 1996.
- [35] H. Chakdar, M. Kumar, K. Pandiyan, A. Singh, K. Nanjappan, P. L. Kashyap, and A. K. Srivastava, "Bacterial xylanases: Biology to biotechnology," *Biotech.* vol 6, no 2, pp. 150, 2016.
- [36] D. Verma, and T. Satyanarayana, "Cloning, expression and applicability of thermo-alkali-stable xylanase of *Geobacillus thermoleovorans* in generating xylooligosaccharides from agro-residues," *Biores Technol.* vol 107, pp. 333–338, 2012.
- [37] A. Bhalla, K. M. Bischoff, and R. K. Sani, "Highly thermostable xylanase production from a thermophilic *Geobacillus* sp. strain WsUcF1 utilizing lignocellulosic biomass," *Front Bioeng Biotechnol.* vol 3, pp. 84, 2015.
- [38] M. Kacagan, S. Canakci, C. Sandalli, K. Inan, D. N. Colak, and A. O. Belduz, "Characterization of a xylanase from a thermophilic strain of *Anoxybacillus pushchinoensis* A8," *Biologia, Sec. Cellular and Molecular Biology*, vol 63, no 5, pp. 599-606, 2008.
- [39] J. T. Ellis, and T. S. Magnuson, "Thermostable and alkalistable xylanases produced by the thermophilic bacterium *Anoxybacillus flavithermus* TWX YL3," *ISRN Microbiol.* pp. 517-524, 2012.

- [40] R. O. Marshall, and E. R. Kooi, "Enzymatic conversion of D-glucose to Dfructose," *Sci.* vol 125, pp. 648–649, 1957.
- [41] S. A. Barker, and J. A. Shirley, "Glucose oxidase, Glucose dehydrogenase, Glucose isomerase, β -Galactosidase and Invertase," In *Microbial Enzymes and Bioconversion*, A. H. Rose (eds.). San Francisco, London New York, Toronto and Sydney: Academic Press. pp. 173-226, 1980.
- [42] I. V. Ulezlo, A. V. Ananychev, and A. M. Bezborodov, "Glucose isomerase (xylose ketol isomerase)," *Uspekhi Biologicheskoy Khimii* (Moscow), vol 27, pp. 136-163, 1986.
- [43] C. A. Kent, and A. N. Emery, "The preparation of an immobilised glucose isomerase. I. The production and selected properties of the partially purified enzyme from *Lactobacillus brevis*," *Journal of Appl. Chem. And Biotechn.* vol 23, no 9, pp. 689-703, 1973.
- [44] M. Weber, M. J. Foglietti, and F. Percheron, "Purification of alpha-amylase by affinity chromatography on cross-linked starch," *Biochimie*, vol 58, pp. 1299–1302, 1976.
- [45] J. Chauthaiwale, and M. Rao, "Production and purification of extracellular D-xylose isomerase from an alkaliphilic, thermophilic *Bacillus* sp." *Appl. Environ. Microbiol.* vol 60, pp. 4495–4499, 1994.
- [46] G. Boguslawski, and M. J. Rynski, "Novel strain of *Bacillus licheniformis* useful in production of glucose isomerase and method of screening *Bacillus* mutants for the ability to produce glucose isomerase in the absence of xylose," U.S. patent 4,355,103. 1982.
- [47] C. A. Smith, M. Rangarajan, and B. S. Hartley, "D-Xylose (D-glucose) isomerase from *Arthrobacter* strain NRRL B3728," *Biochem. J.* vol 277, pp. 255–261, 1991.
- [48] A. N. Moneke et al. "D-xylose isomerases from a newly isolated strain, *Paenibacillus* sp., and from *Alcaligenes ruhlandii*: isolation, characterization and immobilisation to solid supports," *Appl Micr B.* vol 50, no 5, pp. 552-557, 1998.
- [49] H. Karaoglu, D. Yanmis, F. A. Sal, A. Celik, S. Canakci, and A. O. Belduz, "Biochemical characterization of a novel glucose isomerase from *Anoxybacillus gonensis* G2 T that displays a high level of activity and thermal stability," *J Mol Catal B: Enzym*, vol 97, pp. 215–224, 2013.
- [50] L. Konak, Y. Kolcuoglu, E. Ozbek, A. Colak, and B. Ergenoglu, "Purification and characterization of an extremely stable glucose isomerase from *Geobacillus thermodenitrificans* Th2," *App. Biochem. and Microbiol.* vol 50: pp. 25-29, 2014.
- [51] K. Dekker, H. Yamagata, K. Sakaguchi, and S. Udaka, "Xylose (glucose) isomerase gene from the thermophile *Thermus thermophilus*: cloning, sequencing, and comparison with other thermostable xylose isomerases," *J Bacteriol.* vol 173, no 10, pp. 3078–3083, 1991.
- [52] K. Inan Bektas, A. Ozer, H. I. Guler, A. O Belduz, and S. Canakci, "*Brevibacillus gelatini* sp. nov., isolated from a hot spring," *Int. Journal of Systematic and Evolutionary Microbiology*, vol 66, pp. 712-718, 2016.

	SAKARYA UNIVERSITY JOURNAL OF SCIENCE		 SAKARYA UNIVERSITY
	e-ISSN: 2147-835X http://www.saujs.sakarya.edu.tr		
	<u>Received</u> 07-03-2018 <u>Accepted</u> 08-06-2018	<u>Doi</u> 10.16984/saufenbilder.402500	

Methylene Blue Adsorption and Preparation Silver Bound to Activated Carbon with Sol-Gel Methods

Esra Altıntığ*, Ömer Faruk Soydan

Abstract

This study examines the characterization and adsorption features of silver that was added to oxygen containing activated carbons using the sol-gel method. The surface area of the silver coated activated carbon (AC/Ag) Nano-composites, which were prepared using the sol-gel method, was measured with the Braunauer-Emmett-Teller surface area calculation method according to N₂ adsorption at 77 K. The microstructure and surface morphologies of the AC/Ag Nano-composite samples were examined with the use of Scanning Electron Microscope. Methylene Blue removal was performed with AC/Ag-1 with a highest surface area of 658.488 m²/g, and the Q_{max} value was calculated as 416.66 mg/g.

Keywords: Wild chestnut, silver, sol-gel, activated carbon, adsorption, desorption

1. INTRODUCTION

Environmental deterioration has recently been undergone with the advent of technology-oriented advancements. The soil and water pollutants may appear on the ground and deeper layers of earth due to the contributing factors such as rapid industrial expansion in association with growing population worldwide and even in domestic lands, and unawareness of chemicals used in agricultural and healthcare sectors. It should be remembered that the water pollution in particular has much catastrophic effects on our biologies especially when waste waters become non-clean or even uncleanable drinking waters. Keeping the vital elements secured from these beasts means lots of money and labor to have to be withdrawn from the productive economic actions and transferred into the protecting and cleaning issues of secondary importance. The adsorption method is one out of myriad ways of recovering from this natural disease, which is effective in cleaning air and

water from detrimental substances [1]. The material that has been for a long time used as adsorbent is the activated carbon (AC) preferable in this technique. This is currently produced from a substance mostly constituted by carbon atoms active in the soil pollutants. Production of clean water is made through distillation and purification of waste water using ACs. A carbon atom has an interior part and too much porous structure and however cannot be formulated or analyzed chemically [2]. Interestingly, there are three potential ways to get AC: (1) the chemical way, (2) the physical way, and (3) both in combination. Raw materials are carbonized and coal produced and heat-treated. The processing way is how the carbons in coal are physically activated at an optimum temperature through oxidization by gas [3]. Chemical operation can be performed using chemicals such as NaOH, ZnCl₂, H₃PO₄, and KOH together with carbonization [4]. The activated carbons produced in these ways are very popular in cleaning water by filtrating or distillating [5].

* Esra Altıntığ

Having both chemical and biochemical potentials, for example, silver-coated ACs are appropriate substances to have pure water [6]. Lately, various studies on silver nano materials (AgNPs) have been conducted in the fields of medicine, paint, textile etc. because of their special characteristics [7-9]. Photochemical synthesis [10], laser melting [11], wet chemical synthesis [12], sol gel [13] or any other methods are used for synthesis of AgNPs. This reaction is performed through Ag⁰ reduction and ligand usage along with both reduction and reservation of character solutions following decomposition (Ag⁺¹) in a proper solution by chemical synthesis.

The activated carbons that were produced through the sol-gel method in the previous study and in this study were coated with silver substances which were then characterized to analyze the features of the adsorption process.

2. MATERIALS AND METHODS

Materials

AgNO₃ (Merck), HNO₃ (Merck) (Trisodium citrate) Na₃Ct (Merck), Dimethylaminoethanol (DMAE) was used during the silver while binding the silver. Methylene Blue (MB). The obtained activated carbon samples were washed with ethanol (Merck). A Precisa XB 220A precision scale was used to measure the amounts in the experiments, while the mixing processes were handled with Wisestir MSH-20A and IKA RCT Classic magnetic mixers. All chemicals used are of analytical grade. Ultra-pure water produced by the Millipore Milli Q-system was used in these experiments.

Methods

Activated carbon which was produced and characteristics were determined previously was used in the study [14]. The activated carbons were first oxidized with 69% HNO₃. The obtained AC (1g) was impregnated in a 50 mL AgNO₃ solution and stirred for 1 hour at room temperature. The activated carbons coated with Ag⁺ ions were then filtered. A 50 mL trisodium citrate (Na₃Ct) solution was added into the AC/Ag⁺¹ composite. Then, a 1mL dimethyl ethanolamine (DMEA) solution was added drop wise into the mixture, and the reaction system was stirred for 3 hours at 90 °C. After the solid material was filtered and

washed with distilled water, it was dried in the oven for 12 hours at 70° C [8]. As a result, AC/Ag Nano-composite products were obtained. The preparation conditions of the AC/Ag Nano-composites are identified in Table 1.

Table 1. Preparation parameters of AC/Ag nano-composites

Sample	AgNO ₃ (g)	Na ₃ Ct (g)	DMEA (g)
AC/Ag-1	0.5	0.75	0.03
AC/Ag-2	1	1.5	0.06
AC/Ag-3	2	3	0.12
AC/Ag-4	4	4.5	0.18

Devices

Scanning Electron Microscope (SEM) images of the materials were taken with a Scanning Electron Microscope Jeol JSM-6060L. Fourier Transform Infrared Spectroscopy (FTIR) measurements were performed with SHIMADZU IR Prestige 21, and MB amounts were conducted with a UV HITACHI U-2900 Spectrophotometer. The Braunauer-Emmett-Teller (BET) surface area of the obtained products was handled in Bilecik Seyh Edebali University with a MICROMERITIC ASAP 2020. The BET surface area, and pore size were identified by using N₂ adsorption data with an analyzer (Gemini Model 2380).

The qualitative structure analysis of the samples was investigated between the positions with 2θ angles of 10-90° by using Rigaku model XRD instrument. An ICP-OES Spectro Arcos spectrometer (SPECTRO Analytical Instruments, Kleve, Germany) was used for determination of silver concentration. The operating parameters of the ICP-OES were set as recommended by the manufacturer.

Adsorption Work

Methylene Blue (MB) was chosen in this study due to its wide application and known strong adsorption onto solids. This value is mostly used for the determination of the surface area of pores over 15 Å. This shows the value of the adsorbed MB molecules in mg and identifies the adsorption capacity of bigger molecular structures of activated carbon [14]. MB stock solution was prepared by dissolving an accurate amount of MB

in distilled water to achieve a concentration of 1000 mg L⁻¹, and subsequently diluted to the required concentrations. The methylene blue adsorption was made using the mixture of 0.1 g AC and 100 mL MB solution blended at the concentration of 100 mg/L for one hour. For the measurement, the MB adsorption UV spectrometry of 664 nm was used. The below equation was used to calculate the MB quantity adsorped from the water solution.

$$qe = \frac{(Co - Ce)}{m} x V$$

Where Co and Ce are the initial and equilibrium MB concentration in mg/L respectively, m is the mass of adsorbent (g) and V is the volume of solution (L).

The removal (%) of MB was calculated using the following equation:

$$\text{Dye removal (\%)} = \frac{(Co - Ce)}{Co} x 100$$

All adsorption results were reported as the average values for three times experiments.

Desorption Work

AC/Ag covered samples were incinerated at 550 °C for 16 hours. The samples were then dissolved in 50 mL 10% HNO₃. After the samples were dissolved, the solution was washed and filtered with the blue filter paper. ICP-OES (Inductively coupled plasma - optical emission spectrometry) was the method to specify the silver ions (Ag quantities) present in each of the filtrated but dried sample solutions. Results were given in the table 2 and table 3.

3. SONUÇLAR VE TARTIŞMA (CONCLUSIONS AND DISCUSSION)

Properties of AC/Ag1-AC/Ag-4 nano composites

Characterization

The AC/Ag-1-AC/Ag-4 structures were characterized by their silver particle size. The dispersion and accidence of the nanoparticles have been characterized using FT-IR.

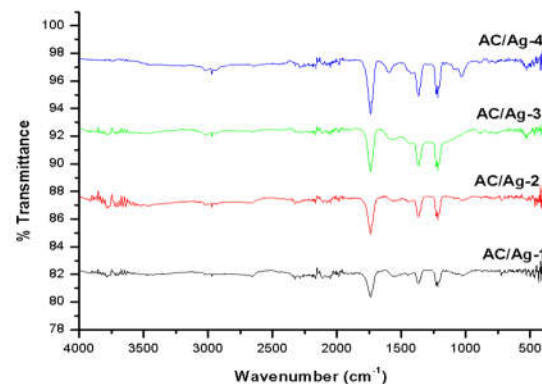


Figure 1. FTIR spectrums of AC/Ag-1-AC/Ag-4 nano composites

On FTIR spectrum the maximum level displayed vibration tension of C=O around 1739 cm⁻¹ and C-H at 2971 cm⁻¹ in AC/Ag-1 to AC/Ag-4 composites as presented in Fig. 1. The peak around 1739 cm⁻¹ showed C=O vibration tension. The adsorbent differences between 1366 and 1217 cm⁻¹ frequency were caused by C-H bond bendings and C-O bond tensions. The peak in 1029 cm⁻¹ refers to alcohol groups. Similar results are seen in the literature [14, 16].

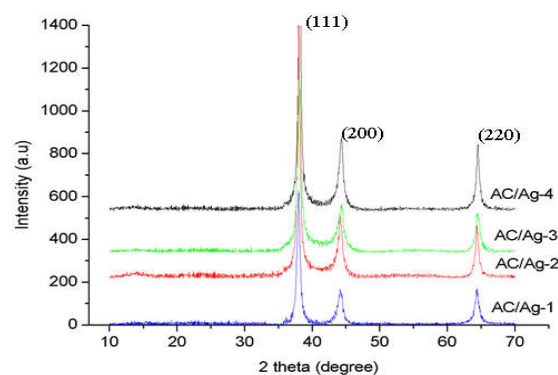


Figure 2. XRD patterns of AC/Ag-1-AC/Ag-4 nano composites

When the comparative XRD spectrums of AC/Ag-1-AC/Ag-4 in Figure 2 were examined, 2θ reflection peaks that support the existence of silver were showed at 38.039°, 44.180°, 64.360°. the index values were demonstrated silver level as (111), (200), (220) respectively [17]. The intensity was increased with the silver addition and activated carbons were passed to crystal structure from amorphous structure. It can be told metallic silver was existed in surface centered cubic structure. It was seen that XRD diffracted patterns that belong to AC/Ag mixtures; AgNO₃ in the environment was in the structure as impurity.

By means of their enormous surfaces, the activated carbons best fit to hold metal nanoparticles. To evaluate the influence of Ag particles on the microporous structures of AC, the specific surface area (SBET) and pore volume of AC/Ag-1-AC/Ag-4 were determined. The results are listed in Table 2.

Table 2. BET parameters of AC/Ag-1-Ag-4 Nano-composites

Proprieties	AC/Ag-1	AC/Ag-2	AC/Ag-3	AC/Ag-4
BET surface area ($m^2 g^{-1}$)	658.488	540.837	386.360	205.051
t-Plot Micropore Area ($m^2 g^{-1}$)	303.988	300.050	293.874	146.811
Average pore diameter (Å)	30.644	30.487	28.978	27.383
pore volume (cm^3/g)	0.091	0.0611	0.039	0.049
Silver content (wt%)	14.012	27.568	67.547	83.771

The silver ions coated on the activated carbon surface are reduced to metallic silver. [18]. As the amount of silver increases due to the direct trapping of silver particles in the pores, the BET surface area, total pore volume and average pore diameter of the AC/Ag nanoparticles decrease. A little amount of energy can help oxygen strongly attract silver toward itself because silver is extremely closer to the oxygen and the latter is superior to silver [19]. For this reason, the oxygen atoms can easily penetrate into the crystal cage and fill the octahedral void of silver which forms the nucleus for the silver crystals [20, 21].

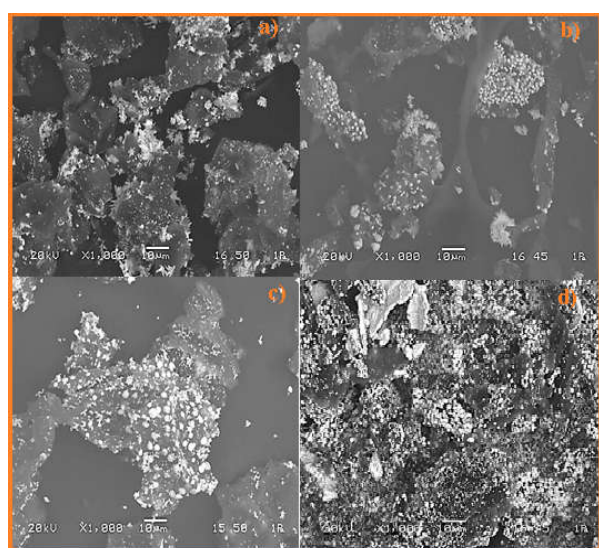


Figure 3. SEM image of AC/Ag-1 and Ag/AC-4 nanosamples

SEM images display the morphological data of surface area as well as type and size of particles, and EDX analysis of elements. On the activated carbons are covering more silver in quantities, and the silver nanoparticles exhibit the characteristic of homogenous distribution over the AC surface. However, as seen in Figure 3, silver amounts varied between 200 and 400 nanometers.

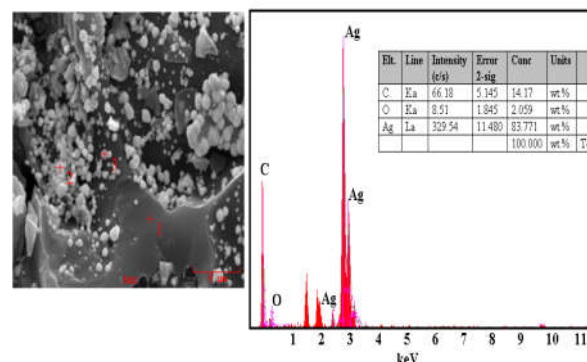


Figure 4.EDS analysis of the AC/Ag-4 sample

The result of the EDS analysis of the AC/Ag-4 sample is identified in Figure 4. For AC/Ag-4 sample, EDS analysis provides the recognition of the peak level of silver amount. The silver particles appear to be nanosized, in the range of <1.

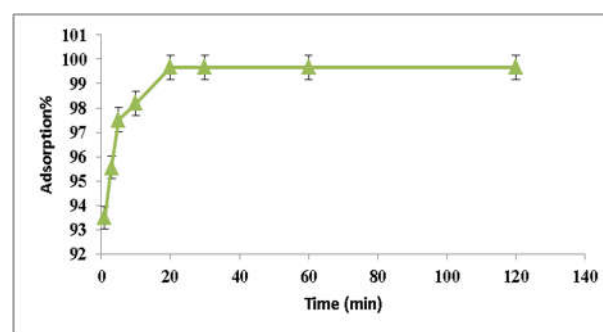


Figure 5. The effect of mixing time on adsorption of MB (MB concentration: 100 mg/L, temperature: 298 K).

The adsorption process was performed by keeping all variables constant and taking samples in determined periods. Maximum dyestuff adsorption was observed within 30 minutes after the experiment started. The contact time required to reach equilibrium was found to be 60 minutes.

Adsorption studies

0.02 g of adsorbent was dispersed in solution by the agitation of the solution at 600 rpm, at room temperature, and at optimum pH 7. Langmuir and Freundlich isotherms were used for the calculation

of the adsorption studies. The Langmuir adsorption isotherm is shown below:

$$\frac{1}{q} = KL/q_{max}\left(\frac{1}{C_e}\right) + 1/q_{max}$$

Q_{max} = maximum adsorption capacity (mg/g)

C_e = liquid phase dyestuff concentration balanced with adsorbent (mg/L)

KL = Langmuir adsorption constant (mg/L)

In the line graph, the vertical axis is of 1/q_e and the horizontal axis of 1/C_e, and the slope displays 1/q_{max} and K/q_{max} values when transferred [22].

The Freundlich adsorption isotherm is shown below:

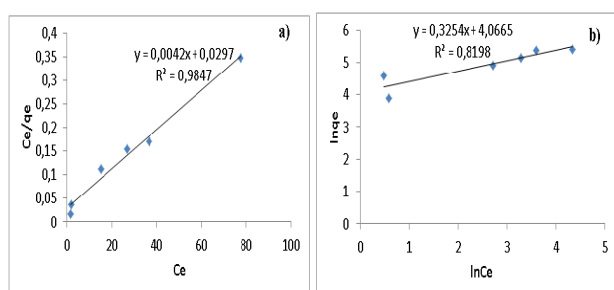


Figure. 6. AC/Ag-4 a) Langmuir and b) Freundlich Isotherms

Freundlich and Langmuir isotherm parameters were found when the experimental parameters at different concentrations were examined. It can be concluded from the studies that there is positive strong correlation between adsorption capacity and concentration amount. In the Freundlich isotherm equation, k represents the adsorption capacity, and n, a constant while in the Langmuir model Q_{max} is the adsorption capacity, and KL, a constant of energy need for adsorption. [24].

Table 3. Adsorption isotherms parameters of MB onto AC/Ag-4.

Sample	Langmuir Isotherms			Freundlich Isotherms		
	Q _{max} (mg g ⁻¹)	KL × 10 (L mg ⁻¹)	R ²	KF (mg g ⁻¹)	n	R ²
AC/Ag-4	416.66	0.028	0.87	1.091	1.517	0.97

The Table 3 shows that the AC/Ag-4 have highest adsorption capacity and shortest time to reach adsorption equilibrium compared with most of previous reports.

Table 4. Previous representative reports of adsorbents in application of MB removal.

Adsorbent	Amount of Adsorbent (g)	Initial (MB) concentration (mg/L)	Adsorption capacity (mg/g)	References
AgCl-NRs-AC	0.015	25	227.27	[25]
Ag NPs-AC	0.02	5	34.5	[26]
Ag/AC	0.2	500	240	[27]
Mn ₂ O ₃ /MCM-41	1	50	50	[28]
AgNP-CMSs	0.12	30	250	[29]
AC/Ag-4	0.2	100	416.66	This study

Desorption and recycling efficiency

Desorption studies were performed with water, 0.1 M HCl, 0.1 M NH₃ and 0.1 M NaOH. AC/Ag-4 (100 mg/100 mL) saturated with 100 mg/L of MB was placed in different desorption media and was constantly stirred on a rotatory shaker at 100 rpm for one hour. The adsorbent was separated and washed with distilled water.

93.4% of MB was desorbed in 60 min using HCl as a desorption medium (Figure 7.).

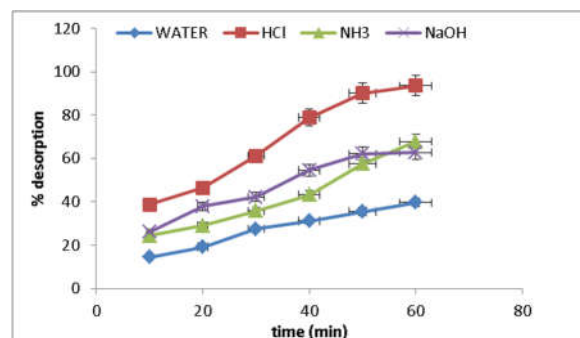


Figure. 7. Desorption studies of MB dye

In order to evaluate the possibility of regeneration and reuse of the AC/Ag-4 adsorbent, desorption experiments have been performed.

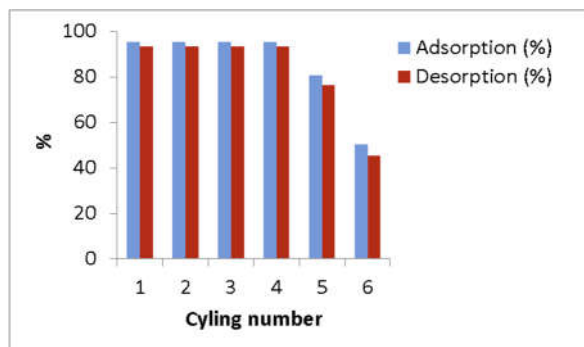


Figure 8. Recycling performance of the prepared AC/Ag-4 nanocomposites for MB removal (temperature: 298 K, adsorbent dosage: 0.1 g/100 mL), agitation: 120 rpm, contact time: 60 min, pH: 7).

Recycling efficiency of AC/Ag-4 was investigated for the removal of MB. After six cycles, the adsorption efficiency of AC/Ag-4 was reduced to 45% from 93.4% (Fig. 7). After every cycle, HCl was used as a desorption medium to remove adsorbed MB ions from the AC/Ag-4 surface.

SONUÇLAR (CONCLUSION)

In this study, the sol-gel method proved itself as an effective way to synthesize silver nanoparticles to cover the activate carbons. XRD, SEM and EDS were applied to characterize the adsorption process. The maximum level of AC/Ag-1 nano composites was determined as 416.66 mg/g by means of analyzing the adsorption. Langmuir and Freundlich techniques provided isotherms captured by observing various heat levels during MM adsorption. From the Langmuir model, higher levels of correlation coefficients in the adsorbents were an expected result because the surface was wider and homogenous. Therefore, AC-Ag composites can be preferable to remove dye thanks to the advantages of cost, efficiency and environment.

ACKNOWLEDGEMENT

This work was supported by the Sakarya University Scientific Research Foundation (Project Number: 2015-50-01-034). We thank Fatih Mehmet Kosar for language support and www.academicproofreading.com for proof reading.

REFERENCES

- [1] G. Mezohegyi, F.P. van der Zee, J. Font, A. Fortuny, A. Fabregat, "Towards advanced aqueous dye removal processes: a short review on the versatile role of activated carbon", *Journal of Environmental Management*, vol. 102, pp.148–164, 2012.
- [2] Y. Guo, A.D. Rockstraw, "Physical and chemical properties of carbons synthesized from xylan, cellulose and kraft lignin by H₃PO₄ activation", *Carbon*, vol. 44, pp. 1464-1475, 2006.
- [3] R.N. Khalili, M. Campbell, G. Sandi, J. Golas, "Production of Micro and Mesoporous Activated Carbon from Paper Mill Sludge", *Carbon*, vol. 38, pp.1905-1915, 2000.
- [4] H. Deng, L. Yang, G. Tao, J. Dai, "Preparation and characterization of activated carbon from cotton stalk by microwave assisted chemical activation-Application in methylene blue adsorption from aqueous solution", *Journal of Hazardous Materials*, vol. 166, pp.1514-1521, 2009.
- [5] T.H.Liou, S. Jung, "Characteristics of microporous/mesoporous carbons prepared from rice husk under base- and acid-treated conditions", *Journal of Hazardous Materials*, vol. 171, pp. 693–703, 2009.
- [6] W. Wang, K. Xiao, T. He, L. Zhu, "Synthesis and characterization of Ag nanoparticles decorated mesoporous sintered activated carbon with antibacterial and adsorptive properties", *Journal of Alloy Compounds*, vol. 647, pp. 1007-1012, 2015.
- [7] A.K. Karumuri, D.P. Oswal, H.A. Hostetler, S.M. Mukhopadhyay, "Silver nanoparticles attached to porous carbon substrates: robust materials for chemical-free water disinfection", *Materials Letters*, vol. 109, pp. 83–87, 2013.
- [8] L. Pei, J. Zhou, L. Zhang, "Preparation and properties of Ag-coated activated carbon nanocomposites for indoor air quality control", *Building and Environment*, vol. 63, pp. 108-113, 2013.

- [9] Z. Shi, H. Zhou, X. Qing, T. Dai, Y. Lu, "Facile fabrication and characterization of poly(tetrafluoroethylene)/polypyrrole/nano-silver composite membranes with conducting and antibacterial property", *Applied Surface Science*, vol. 258, pp. 6359–6365, 2012.
- [10] K. Mallick, M.J. Witcom, M.S. Scurrall, "Polymer stabilized silver nanoparticles: a photochemical synthesis route", *Journal of Materials Science*, vol. 39, pp. 4459–4463, 2009.
- [11] I. Lee, S.W. Han, K. Kim, "Simultaneous preparation of SERS-active metal colloids and plates by laser ablation", *Journal of Raman Spectroscopy*, vol. 32, pp. 947–952, 2001.
- [12] H. Bönemann, R. Richards, "Nanoscale metal particles—synthetic methods and potential applications", *European Journal of Inorganic Chemistry*, vol. 10, pp. 2455–2480, 2001.
- [13] S. Senthilkumar, K. Porkodi, R. Gomathi, A.G. Maheswari, N. Manonmani, "Sol gel derived silver doped nanocrystalline titania catalysed photodegradation of methylene blue from aqueous solution", *Dyes Pigments*, vol. 69, pp. 22–30, 2006.
- [14] E. Altıntığ, O.F. Soydan, "Activated carbon from wild chestnut shell upon chemical activation with phosphoric acid", *Oxidation Communication*, vol. 39 (I-II), pp. 808–816, 2016.
- [15] E. Daneshvar, A. Vazirzadeh, A. Niazi, M. Kousha, M. Naushad, A. Bhatnagar, "Desorption of Methylene blue dye from brown macroalgae: Effects of operating parameters, isotherm study and kinetic modeling", *Journal of Cleaner Production*, vol. 152, pp. 443–453, 2017.
- [16] M. Nasrollahzadeh, M. Atarod, B. Jaleh, M. Gandomirouzbahani, "In situ green synthesis of Ag nanoparticles on graphene oxide/TiO₂ nanocomposite and their catalytic activity for the reduction of 4-nitrophenol, Congo red and methylene blue", *Ceramics International*, vol. 42, pp. 8587–8596, 2016.
- [17] P.K. Khanna, R. Gokhale, V.V.V.S. Subbarao, A.K. Viswanath, B.K. Das, C.V.V. Satyanarayana, "PVA stabilized gold nanoparticles by use of unexplored albeit conventional reducing agent", *Materials Chemistry and Physics*, vol. 92 (1), pp. 229–233, 2005.
- [18] Y. Zhao, Z. Wang, X. Zhao, W. Li, S. Liu, "Antibacterial action of silver-doped activated carbon prepared by vacuum impregnation", *Applied Surface Science*, vol. 266, pp. 67–72, 2013.
- [19] H.Q. Tang, H.J. Feng, J.H. Zheng, J. Zhao, "A study on antibacterial properties of Ag⁺-implanted pyrolytic carbon", *Surface Coating Technology*, vol. 201, pp. 5633–5636, 2007.
- [20] O. Sawai, Y. Oshima, "Deposition of silver nanoparticles on activated carbon using supercritical water", *The Journal of Supercritical Fluids*, vol. 47, pp. 240–246, 2008.
- [21] E. Altıntığ, S. Kırkıl, "Preparation and properties of Ag-coated activated carbon nanocomposites produced from wild chestnut shell by ZnCl₂ activation", *Journal of the Taiwan Institute of Chemical Engineers*, vol. 63, pp. 180–188, 2016.
- [22] I. Langmuir, "The adsorption of gases on plane surfaces of glass, mica and platinum", *Journal of the American Chemical Society*, vol. 40, pp. 1361–1403, 1918.
- [23] H.M.F. Freundlich, "Over the adsorption in solution", *The Journal of Physical Chemistry*, vol. A57, pp. 358–471, 1906.
- [24] E. Bagda, "The feasibility of using Rosa canina galls as an effective new biosorbent for removal of methylene blue and crystal violet", *Desalination and Water Treatment*, vol. 43, pp. 63–75, 2012.
- [25] F. Nekouei, H. Kargarzadeh, S. Nekouei, F. Keshtpour, A.S.H. Makhlof, "Novel, facile, and fast technique for synthesis of AgCl nanorods loaded on activated carbon for removal of methylene blue dye", *Process Safety Environmental Protection*, vol. 103, pp. 212–226, 2016.
- [26] M. Ghaedi, S.H. Heidarpoor, S.N. Kokhdan, R. Sahraie, A. Daneshfar, B. Brazesh, "Comparison of silver and palladium nanoparticles loaded on activated carbon for efficient removal of Methylene blue: Kinetic

- and isotherm study of removal process”, *Powder Technology*, vol. 228, pp. 18–25, 2012.
- [27] T.Q. Tuan, N.V. Son, H.T.K. Dung, N.H. Luong, B.T. Thuy, N.T. Van Anh, N.D. Hoa, N.H. Hai, “Preparation and properties of silver nanoparticles loaded in activated carbon for biological and environmental applications”, *Journal of Hazardous Materials*, vol. 192, pp. 1321–1329, 2011.
- [28] B.Q. Han, F. Zhang, Z.P. Feng, S.Y. Liu, S.J. Deng, Y. Wang, “A designed $Mn_2O_3/MCM-41$ nanoporous composite for methylene blue and rhodamine B removal with high efficiency”, *Ceramics International*, vol. 40, pp. 8093–8101, 2014.
- [29] Q. Chen, Q. Wu, “Preparation of carbon microspheres decorated with silver nanoparticles and their ability to remove dyes from aqueous solution”, *Journal of Hazardous Materials*, vol. 283, pp. 193–201, 2015.

	SAKARYA UNIVERSITY JOURNAL OF SCIENCE		 SAKARYA UNIVERSITY
	e-ISSN: 2147-835X http://www.saujs.sakarya.edu.tr		
	Received 26-04-2018 Accepted 11-09-2018	Doi 10.16984/saufenbilder.418634	

A Clinical Trial Of The Evaluation Of Environmental Exposure In Yttrium 90 Radioembolization

Handan Tanyıldızı^{*1,2}, Iffet Cavdar², Muhammed Abuqebitah³, Mustafa Demir³

Abstract

The aim of this study is to measure the dose rate of two different forms of Y-90 microsphere used for radioembolization and to evaluate the results according to radiation safety regularities. 19 patients were enrolled in study (Age:61±1.5, F/M:12/7). As a result of the evaluation of the physicians, 7 patients were treated with TheraSphere and 12 patients were treated with SIR-Sphere. Dose rate measurements were taken at the stage of activity preparation, injection, radioactive wastes and discharge of patients using an electronic dosimeter (ED). The staff was exposed to dose rate of 1.3×10^{-4} $\mu\text{Sv}/\text{MBq.h}$ during activity preparation stage, 2.4×10^{-4} $\mu\text{Sv}/\text{MBq.h}$ in injection stage for Therapshere application. For SIR-spheres application, the staff was exposed to dose rate of 24.5×10^{-4} $\mu\text{Sv}/\text{MBq.h}$ during activity preparation stage, 10.1×10^{-4} $\mu\text{Sv}/\text{MBq.h}$ in injection stage. The average amount of dose received per operation was calculated 0.92 ± 0.48 μSv in TheraSphere and 3.22 ± 0.89 μSv in SIR-Spheres. For discharge of the patients, the average dose rate recorded from 1 m was found 4.0 ± 0.28 $\mu\text{Gy}/\text{h}$ for TheraSphere and 3.2 ± 0.15 $\mu\text{Gy}/\text{h}$ for SIR-Spheres. The dose rate of radioactive wastes measured from the surface of the container which contained the radioactive wastes generated after the application was 0.5 ± 0.1 $\mu\text{Sv}/\text{h}$ for TheraSphere and 1.1 ± 0.08 $\mu\text{Sv}/\text{h}$ for SIR-Spheres. It is emphasized that Y-90 Therasphere application provides radiation safety more than SIR-Spheres because of its closed system, even so both applications shows low dose rate around the patient and short-term storage of radioactive wastes after application would be sufficient.

Keywords: Exposure, radioembolization, yttrium 90, radiation protection.

1. INTRODUCTION

The use of microspheres filled with a beta-emitting radionuclide, typically Y-90, has only become clinically relevant since the middle-1980s [1]. The application of microspheres to the liver requires an interventional-technical procedure in the field of multidisciplinary as radiology and nuclear medicine departments and it is described in literature [2,3]. In a typical Y-90 microsphere

treatment, the aim is to deliver the maximum dose to tumor without causing toxic damage to the liver parenchyma [4]. In addition, the amount of Y-90 activity administered to the patient can be calculated with a patient specific dosimetry including several parameters such as volume of tumor and normal liver tissue, lung shunt fraction, tumor to liver count ratio, etc.

Y-90 filled microspheres are used in two different forms as glass in Therasphere and resin in SIR-Sphere. Although some production features

* Corresponding Author

¹Altınbaş University, Vocational School of Health Services, Medical Imaging Techniques Program, handan.tanyildizi@altinbas.edu.tr

²Istanbul University, Faculty of Science, Department of Physics.

³Istanbul University, Faculty of Medicine, Department of Nuclear Medicine.

are different, their basic physical properties are similar and they do the same physical interactions in the tissue. Y-90 has a physical half-life of 64.2 hours, and it decays to stable Zirconium 90. Y-90 emits pure high-energy beta rays (energy maximum, 2.27 MeV; mean, 0.9367 MeV) [5]. Irradiation from Y-90 microspheres is essentially confined to the liver because of 3.8 mm mean range and approximately 10-mm maximum range of β -particles in soft tissue [6]. However, the physical interactions that take place in the path length of the electrons within the tissue, leads to emit Bremsstrahlung radiation whose energy range from 20 to 500 keV [7].

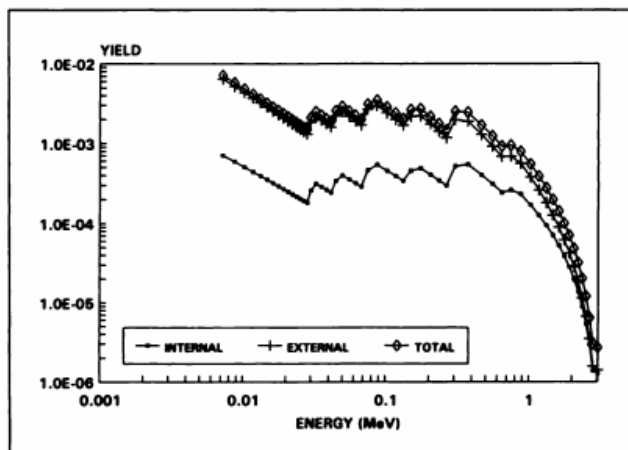


Figure 1. Bremsstrahlung spectrum of Y-90 microspheres formed along their range in the tissue [8].

Bremsstrahlung radiation is scattered at four different stages as Y-90 microsphere activity preparation, injection, patient and radioactive wastes. In all stages, medical staff who provide the care to the patient are exposed to the risk of Bremsstrahlung radiation. Therefore it is important to monitor dose rate measurements.

According to the recommendations based on Australian Radiation Protection and Nuclear Safety Agency (ARPANSA) and adopted by the Turkish Atomic Energy Authority (TAEK), the patients undergone radionuclide therapy discharged when the dose rate taken from 1 m far from patient between 25-40 μ Sv/h [9]. This condition was determined by the European Atomic Energy Community (EURATOM) as 20-40 μ Sv/h [10]. Radioactive wastes generated after injection should be placed in a plastic container labeled with a warning sign containing information about the type of radionuclide and the amount of activity. The plastic container's storage was carried out according to the recommendations published by International Atomic Energy Agency (IAEA) [11].

In this study, we aimed to measure the dose rate of Bremsstrahlung radiation released into the environment in two different forms of Y-90 microsphere therapy, to assess the results in terms of national and international radiation safety regularities and to evaluate the radiation protection conditions.

According to the measurement results, the radiation doses that health workers will be exposed per process will be calculated. It will also be tested whether the radiation protection rules applied during the process are sufficient.

2. MATERIAL AND METHODS

This study included 19 patients who applied to Cerrahpasa Medical Faculty/ Nuclear Medicine Department/ Radionuclide Therapy Service for Y-90 radioembolization and all radiation measurements that occur throughout the operation. All dose rate measurement was done in four different stages with using an electronic dosimeter (Polimaster PM1621 model, energy range 10keV-20MeV). ED is a suitable for detecting and monitoring radiation in the areas of nuclear facility. It gives instantaneous radiation exposure and very useful in non routine work in which radiation level vary considerably and may be quite hazardous e.g. Y-90 radioembolization. This detector is filled with gas. Radiation produced ionization in gas resulting positive and negative ions are produced inside the detector volume. Ions drift to the electrodes due to the applied voltage between electrodes. In an outer circuit the current is measured which is proportional to the number of ion pair produced per second.

2.1. Activity Preparation

The first measurement was taken from 0, 0.5 and 1 m from the activity vial isolated by lead shielding considered as a reference for the stage of Y-90 Theraspheres and SIR-Spheres activity preparation in hot lab. Total operation time was recorded for activity preparation.

2.2. Injection

The second measurement was taken over the liver after the injection in the interventional radiology department. Total operation time was recorded for injection.

2.3. Radioactive Wastes

The third measurement was taken from the plastic container surface (0 cm) containing radioactive waste generated after Y-90 application. The measurements were used to determine transport and storage conditions.

2.4. Discharge

Discharge of the patient means the return of the patient into the community and so the radiation dose level must be taken under control. According to the national and international regulations, the measurement was taken at a distance of 1 m from the patients to be discharging dose rate.

2.5. Annual Dose Calculation and Radiation Protection Instrumentation

The total body dose absorbed per application was calculated by multiplying the staff dose rate ($\mu\text{Sv/h}$) at the working distance with recorded and application time (h). The contribution rate of the dose absorbed per application to annual dose was determined.

The precautions taken during the application for radiation protection are detailed in Table 1.

3. RESULTS

The change in the dose rate of Y-90 activity during stage of preparation and injection across variable distances (cm) was shown in Tables 2 and 3 for Theraspheres and SIR-Spheres therapy.

In Therasphere, the dose rates irradiated from Bremsstrahlung radiation were quite low in the stage of preparation and injection. While the average amount of activity injected into the patient was 3596.4 ± 8.56 MBq. In this context, staff was exposed to 1.3×10^{-4} $\mu\text{Sv/MBq.h}$ in the stage of preparation and 2.4×10^{-4} $\mu\text{Sv/MBq.h}$ in the stage of injection.

In SIR-Spheres application, staff was exposed to 24.5×10^{-4} $\mu\text{Sv/MBq.h}$ in the stage of preparation and 10.1×10^{-4} $\mu\text{Sv/MBq.h}$ in the phase of injection. According to these results, the dose rates due to Bremsstrahlung radiation were found low in the phase of preparation and injection. Unlike the other measurements, it was seen that the measurement taken from 0 m was 24 $\mu\text{Sv/h}$ in the stage of preparation and 162 $\mu\text{Sv/h}$ in the stage of

injection in the application indicated by the number 9.

By considering the staff has worked during Y-90 activity loading from an average distance of 50 cm and with a total time of 0.5 h in the stage of preparation and injection, the average effective dose taken by staff per an application was calculated 0.92 ± 0.48 μSv for TheraSphere and 3.22 ± 0.89 μSv for SIR-Spheres.

The dose rate measurements recorded from radioactive wastes generated after application with TheraSpheres and SIR-Spheres application were given in Tables 4 and 5.

The mean dose rate measurement taken from the liver after Therasphere injection was found 19.75 ± 0.63 $\mu\text{Sv/h}$ and the mean dose rate 1 m from patients after 24 h at discharging time was 4 ± 0.28 $\mu\text{Sv/h}$. These dose rate measurements found to be lower than previously reported values [12]. The dose rate measured from the surface of the plastic container including collected radioactive waste in Therasphere therapy was found 0.5 ± 0.1 $\mu\text{Sv/h}$. In light of these results, it was observed that the dose rate measurements of radioactive waste were obtained below 1 $\mu\text{Sv/h}$.

The mean dose rate measurement taken from the liver after SIR-Spheres injection was 44.85 ± 0.95 $\mu\text{Sv/h}$ and the mean dose rate from 1 m to patients after 24 h at discharging was found 3.2 ± 0.15 $\mu\text{Sv/h}$. These dose rate measurements were found to be lower than previously reported values [12]. The dose rate measured from the surface of the plastic container including radioactive waste generated SIR-Spheres application was found 1.1 ± 0.08 $\mu\text{Sv/h}$.

Statistical analysis was performed with t-test (Student's t-test) to determine whether there was a difference in dose rate measurements recorded from the surface of the plastic container for Theraspheres and SIR-Spheres application. There was a significant difference between the measurements of radioactive wastes for Therasphere and SIR-Spheres (P: 0.001287).

4. DISCUSSION

Y-90 radioisotope in the treatment of primary and metastatic liver tumor is increasingly used due to its clinical suitability and encouraging results after treatment. It is also advantageous to be safer in sense of radiation protection, unlike in other Peptide Receptor Radionuclide Therapy (PRRT)

which has beta and high energy gamma rays such as Lu-177, I-131. In the field of radiation protection related to Y-90 are emphasized mainly the calibration procedures and the treatment method in the literature, on the other hand, the exposed doses to staff have been reported rarely [12-14]. Our results were found to be consistent with the work of Aubert et al. [13] which is about absorbed radiation dose of exposed to staff per application.

Y-90 microsphere treatment is performed approximately twice a week in our clinic, an average of 96 patients are treated per year. Considering the annual patient population, the dose contribution of Y-90 applications showed very low percentage to the annual permissible dose (0.44% for Therasphere and 1.5% for SIR-Spheres) for staff.

A comparative study was carried out by evaluating the environmental dose rate measurements between the Theraspheres and the SIR-Spheres. The environmental exposure level varied in both Y-90 applications in terms of our results, in the phase of preparation and injection, the environmental exposure resulting from SIR-Spheres application are higher than TheraSphere application. The reason for this difference is probably attributed to the open system of SIR-Spheres, therefore contamination probability had increased when the activity fraction was done in the laboratory.

External dose rate limits have not been yet established due to biodistribution of Y-90 and its pure beta emitting inside the body. According to the ICRP 2009 report, a limit was not shown because the Y-90 dose rate was too low [15]. On the other hand, in the study reported by R. Smart et al., the dose rate at 1 m distance from a patient given 4400 MBq Y-90 microsphere activity was found to be approximately 5 $\mu\text{Sv/h}$ [16].

It was observed that the average dose rates measured at 1 m distance from patients at discharging were below 4 $\mu\text{Sv/h}$ and the dose rates measured from radioactive wastes generated after the applications both Therasphere and SIR-Spheres were below 1 $\mu\text{Sv/h}$ as our results are compatible with the study reported by Cremonesi M. et al [17] and literature listed. Eventually, the environmental exposure doses originated from both SIR-Sphere and TheraSphere application are in compliance with the legislation.

In our study, it was enlightened that the staff was generally exposed to low doses, but when they performed an application with SIR-Spheres, they received about 3.5 times more dose than TheraSphere.

5. CONCLUSION

In SIR-Spheres applications, slightly higher levels of environmental exposure were observed due to contamination. Contamination can be summarized as misinterpreting the activity, spreading the activity while dividing the activity, and not releasing the wastes generated during the division process. Nonetheless, the staff of interventional radiology and nuclear medicine were exposed to low doses in both SIR-Spheres and Theraspheres applications. Further, radioactive wastes collected after SIR-Spheres application should be stored for 3 days -during this time the dose will be further reduced by half-time-, while that of Therasphere was not necessary to store before disposing.

Considering the instrumentation used in applications, it was found that using plexy material shielding to protect the environmental exposure providing more radiation protection against large-scaled beta particles as Y-90. It was also observed that the use of hot cell and lead aprons greatly reduce the absorbed dose from Bremsstrahlung.

REFERENCES

- [1].Dezarn Wa, Cessna Jt, Dewerd La, Feng W, Gates VI, Halama J, Et Al. "Recommendations Of The American Association Of Physicists In Medicine On Dosimetry, Imaging, And Quality Assurance Procedures For 90y Microsphere Brachytherapy In The Treatment Of Hepatic Malignancies", *Med Phys* 2011; 38(8):4824-45.
- [2].Ariel Im, Padula G, "Treatment Of Symptomatic Metastatic Cancer To The Liver From Primary Colon And Rectal Cancer By The Intra-Arterial Administration Of Chemotherapy And Radioactive Isotopes", *J Surg Oncol* 1978;10:327-336.
- [3].Ariel Im, Padula G, "Treatment Of Asymptomatic Metastatic Cancer To The Liver From Primary Colon And Rectal Cancer By The Intra-Arterial Administration Of Chemotherapy And

- Radioactive Isotopes”, *J Surg Oncol* 1982;20:151–156.
- [4]. Howells Cc, Stinauer Ma, Diot Q, Westerly Dc, Schefter Te, Kavanagh Bd, Et Al. “Normal Liver Tissue Density Dose Response In Patients Treated With Stereotactic Body Radiation Therapy For Liver Metastases”. *Int J Radiat Oncol Biol Phys* 2012;84(3):E441-6.
- [5]. Murthy R, Nunez R, Szklaruk J, Erwin W, Madoff Dc, Gupta S, Et Al. “Yttrium-90 Microsphere Therapy For Hepatic Malignancy: Devices, Indications, Technical Considerations And Potential Complications”, *Radiographics* 2005;25(1):S41-55.
- [6]. Gulec Sa, Mesoloras G, Stabin M. “Dosimetric Techniques In 90y-Microsphere Therapy Of Liver Cancer: The MIRD Equations For Dose Calculations”, *J Nucl Med* 2006;47(7):1209-11.
- [7]. Shen S, Denardo Gl, Yuan A, Denardo Da, Denardo Sj. “Planar Gamma Camera Imaging And Quantitation Of Yttrium-90 Bremsstrahlung”. *J Nucl Med* 1994;35(8):1381-9.
- [8]. Stabin Mg, Eckerman Kf, Ryman Jc, Williams Le. “Bremsstrahlung Radiation Dose In Yttrium-90 Therapy Applications”. *J Nucl Med* 1994;35:1377-1380.
- [9]. “Discharge Of Patients Undergoing Treatment With Radioactive Substances Radiation Protection Series Publication No. 4”, *Australian Radiation Protection And Nuclear Safety Agency (Arpansa)*, 2002
- [10]. https://Ec.Europa.Eu/Energy/Sites/Ener/Files/Documents/097_En.Pdf
- [11]. http://Www-Pub.Iaea.Org/Mtcd/Publications/Pdf/Pub1254_Web.Pdf
- [12]. Sarfaraz M, Kennedy As, Cao Zj, Sackett Gd, Yu Cx, Lodge Ma, Et Al. “Physical Aspects Of Yttrium-90 Microsphere Therapy For Nonresectable Hepatic Tumors”. *Med Phys* 2003;30:199–203.
- [13]. Aubert B, Guilabert N, Lamon A, Richard M. “Which Protection Against Radiation For New Protocols Of Internal Radiotherapy By Yttrium 90?” *Proceedings Of The 6th European Alara Network Workshop*. 2002; 34(7): 47–9.
- [14]. Tosi G. “Report On One Accident Occurred In A Nuclear Medicine Department In Italy”. *Proceedings Of The 6th European Alara Network Workshop*. 2002; 34(7): 225-244.
- [15]. ICRP Safety Reports Series No:63, Release Of Patients After Radionuclide Therapy. 2009; ISBN:978–92–0–108909–0, Issn 1020–6450.
- [16]. Edmonds J, Smart R, Laurent R, Butler P, Brooks P, Hoschir R, Et Al. “A Comparative Study Of The Safety And Efficacy Of Dysprosium-165 Hydroxide Macro-Aggregate And Yttrium-90 Silicate Colloid In Radiation Synovectomy —A Multicentre Double Blind Clinical Trial”, *Rheumatology* 1994; 33(10): 947-953.
- [17]. Cremonesi M, Ferrari M, Paganelli G, Rossi A, Chinol M, Bartolomei M, Et Al. “Radiation Protection In Radionuclide Therapies With (90) Y-Conjugates: Risks And Safety”. *Eur J Nucl Med Mol Imaging* 2006;33(11):1321-7.

APPENDICES

Table 1. Devices and instruments used for radiation protection in the different phases of therapy

Phases of therapy	Devices/instruments	Purpose
Hot Lab.	Hot cell	To shield Y-90 β - rays and bremsstrahlung
	Latex gloves	To avoid contamination
	Long tongs	To handle the Y-90 vial and reduce dose rate
	Polymethylmethacrylate cylindrical case	To shield Y-90 vials and syringes
	Lead aprons	To reduce the exposure to bremsstrahlung
	Electronic dosimeter	To monitor the dose rate outside the vial
Activity Administration	Infusion system	-
	Latex gloves	To avoid contamination
	Lead aprons	To reduce the exposure to bremsstrahlung
	Electronic dosimeter	To monitor the dose rate outside the vial and the radioactive waste
Patient hospitalisation	Lead aprons	To reduce the exposure to bremsstrahlung
	Electronic dosimeter	To monitor the spreading dose rate from patient at 1 meter

Table 2. Dose rate measurement in Y-90 Theraspheres therapy

Patient No	Activity (MBq)	Time (h)	Distance (cm)	Stage of Preparation (μ Sv/h)	Stage of Injection (μ Sv/h)
1	2397.6	0.5	0	11.7	4.2
			50	1.2	1.8
			100	0.7	0.9
2	4695.3	0.5	0	28.7	2.8
			50	1.5	2.5
			100	0.9	0.9
3	2997.0	0.5	0	1.8	3.8
			50	0.4	1.2
			100	0.2	0.4
4	3496.5	0.5	0	22	2
			50	1.5	1.3
			100	0.7	1
5	4095.9	0.5	0	24.4	3.8
			50	1.4	2.5
			100	0.3	0.7
6	2497.5	0.5	0	10	10
			50	1.5	4
			100	0.1	1.6
7	4995.0	0.5	0	6.7	4.1
			50	2.1	2.9
			100	0.4	0.6
Mean\pmSD.:	3596.4\pm8.56	0.5	0	15	4.4
			50	1.4	2.3
			100	0.47\pm0.10	0.87\pm0.13

Table 3. Dose rate measurement in Y-90 SIR-Spheres therapy

Patient No	Activity (MBq)	Time (h)	Distance (cm)	Phase of Preparation (μ Sv/h)	Phase of Injection (μ Sv/h)
1	1295	0.5	0	23	80
			50	7.8	4
			100	2.3	1.5
Continues...					
2	1554	0.5	0	45	27
			50	7.1	1
			100	2	0.6
3	1480	0.5	0	41	60
			50	5.6	4
			100	0.8	0.13
4	1295	0.5	0	21	16
			50	6.2	1
			100	1.7	0.8
5	1295	0.5	0	27	17
			50	8.2	1.4
			100	1.3	0.7
6	1665	0.5	0	31	72
			50	6.3	9
			100	2.4	2.1
7	1554	0.5	0	49	56
			50	6	7
			100	1.8	1.1
8	1665	0.5	0	35	31
			50	4.3	3.5
			100	1.4	0.9
9*	1480	0.5	0	24	162
			50	7.6	1.9
			100	2.6	0.6
10	1295	0.5	0	38	21.3
			50	18	5.6
			100	8	2.2
11	1480	0.5	0	28	34
			50	18	8.8
			100	6	2.7
12	1110	0.5	0	25	18.5
			50	9	3
			100	3	0.8
Mean\pmSD.:	1464.14\pm5.46	0.5	0	32.2	49.6
			50	8.7	4.2
			100	3.6\pm0.27	1.48\pm0.17

* Application that is thought to be contamination.

Table 4. Dose rate measurements which are taken from patients and their radioactive wastes in Y-90 Therasphere therapy

Patient No	Activity (MBq)	Discharge Measurement (μ Sv/h)	Dose rates taken	
			from liver after injection (μ Sv/h)	Dose rate of radioactive wastes (μ Sv/h)
1	2397.6	3.8	28	0.4
2	4695.3	2.7	14.4	0.28
3	2997.0	6.4	17	0.39
4	3496.5	5.2	18	0.28
5	4095.9	3.8	24	1.7
6	2497.5	3.9	20.1	0.23
7	4995.0	2.4	16.8	0.29
Mean\pmSD.	3596.4\pm8.56	4\pm0.28	19.75\pm0.63	0.5\pm0.1

Table 5. Dose rate measurements which are taken from patients and their radioactive wastes in Y-90 SIR-sphere therapy

Patient No	Activity (MBq)	Discharge Measurement (μ Sv/h)	Dose rates taken	
			from liver after injection (μ Sv/h)	Dose rate of radioactive wastes (μ Sv/h)
1	1295	4.6	58	1.1
2	1554	3.1	22.3	1.3
3	1480	2.6	20	1.5
4	1295	2.2	19	1.2
5	1295	3.7	32	1
6	1665	4.5	60	1.3
7	1554	3.7	55	1.1
8	1665	3.2	52	1.2
9	1480	2.8	37	0.9
10	1295	2.6	35	0.9
11	1480	2.9	42	1.2
12	1110	2.5	33	1
Mean:	1464.14\pm5.46	3.2\pm0.15	44.85\pm0.95	1.1\pm0.08

	SAKARYA UNIVERSITY JOURNAL OF SCIENCE		 SAKARYA UNIVERSITY
	e-ISSN: 2147-835X http://www.saujs.sakarya.edu.tr		
	<u>Received</u> 08-05-2018 <u>Accepted</u> 03-09-2018	<u>Doi</u> 10.16984/saufenbilder.422044	

Co-Mg ferrite nanocomposite as a humidity sensor device prepared by Co-Precipitation method

Tuğba Şaşmaz Kuru^{*1} and Volkan Eyüpoğlu²

Abstract

In the present study, the humidity sensing properties of Co-Mg nanocomposite prepared by chemically co-precipitated have been investigated by impedance analysis. The correlation between the impedance patterns and relative humidity have shown remarkable results for further investigation. Whereas, the humidity measurement capability of the sensor was high at low frequencies. Also, we identified that this ability was continuously diminished at higher frequencies. So, the hysteresis value for successive adsorption and desorption of the humidity on ferrite nanocomposite material was also determined as small and also the long time measurement stability was excellent. The response and the recovery times for nanocomposite materials were identified as 60 s and 300 s respectively. Finally, a direct relationship between the active electron and transport mechanism of the humidity onto the nanocomposite has been identified as an advanced investigation.

Keywords: Ferrite nanocomposite, Humidity sensor, Co-Precipitation method, Response and recovery time, Impedance.

1. INTRODUCTION

The sensors are the converters a physical response to another one like from pressure to electricity, from humidity to electricity, from light to electricity, etc. In today's world, we can come across lots of different sensors in a different field of the life from our homes to advanced technological devices. So, the novel exploration, development an also improvement of the materials which is used in the sensor production, have gained more attention among scientists and technologists for last three decades [1]. The sensor usage in our life is almost an obligation to run and control lots of machines and tools to increase their life quality and standards [2]. The humidity or moisture is a critical parameter for many industrial applications and daily life requirements especially in food, paper, wood, textile, electronic industries and etc. Moisture regulation and its control are

also a necessity for a lot of industrial production processes and moisture sense requiring devices like air conditioners and refrigerators as a simple sample [3]. In the light of these explanations, we can see that the humidity sensing and measurement can be applied to full range materials like polymer [4], crystal [5], thin film [6,7] and ceramic [8]. The higher impedance gap versus higher sensitivity [9], the stability in an extended period of time measurements [10], narrow hysteresis [11] properties of the sensors are sought as the essential requirements of the humidity sensor. The desired material, which should have lower response-recovery time interval, is another challenging issue of scientific studies [12]. In addition to these above, the economy of the sensor is another important factor to produce this material and so, it should be cheaper, durable, small size and constant resistivity towards ambient gases [13]. When we think about the mentioned

* Corresponding Author

¹ Vocational School of Health Services, Radiotherapy Program, Okan University, 34959, Istanbul Turkey

² Department of Chemistry, Çankırı Karatekin University, Uluayazi Campus, Çankırı, Turkey

properties of the humidity sensors, exploring the right material providing all features mentioned above is almost impossible. So, in much sensor-based research, scientists try to improve the optimization of the certain properties of the sensor materials.

In recent years, ferrite-based nanoparticles have been investigated as a newly discovered nanoparticle family [14]. Many experimental and theoretical studies have been conducted on this particle to illuminate their electrical, magnetic and structural properties and their applications in different fields [15-17]. However, their humidity sensing feature has not been already reviewed comprehensively and their humidity sensing capability and applicability in ambient weather conditions is considered as a remarkable topic in recent years [18]. The humidity sensor applicability tests of the materials can be performed by considering some physical analysis like impedance measurements [19,20], frequency shifting [21,22], capacitance [23,24] and current-resistance [25]. Therefore, phase quartz crystal microbalance, impedance, and two temperature [26] methods have been utilized in many different researches. However, lots of methods are still employed to control the relative humidity in different aspects to determine humidity with a humidifier or saturated salt solution [27,28].

In the current study, ferrite-based Co-Mg containing ferrite nanocomposite material was synthesized, and its applicability of humidity sensor was illuminated by impedance measurements giving the water by dropwise to the analysis environment. Thus, the conduction mechanism and the performance of nanocomposite material in sensor were clarified to verify the applicability of synthesized ferrite nanoparticles for the long-life humidity sensor.

2. EXPERIMENTAL

$\text{Co}(\text{NO}_3)_2 \cdot 6\text{H}_2\text{O}$, $\text{Mg}(\text{NO}_3)_2$, $\text{Fe}(\text{NO}_3)_3 \cdot 9\text{H}_2\text{O}$ and NaOH were purchased from (Merck, Germany, >99.0%) and directly used for the synthesis of $\text{Co}_{0.5}\text{Mg}_{0.5}\text{Fe}_2\text{O}_4$ based ferrite nanoparticle sample without further purifications. All aqueous solutions were prepared with deionized water (Milli-Q ultrapure water). Ferrite nanoparticle was synthesized according to the chemical co-

precipitation procedure [29]. All preparatory steps are shown in Fig. 1.

3. RESULTS AND DISCUSSIONS

The morphology and microstructures of the Co-Mg ferrite characterized by a scanning electron microscope (SEM, model JEOL—JSM 6060 LV) at an acceleration voltage of 20 kV. Fig. 1 shows SEM images of the sample. As seen from the figure, there is dewetting on the powder sample which also prevents us from commenting on grain size. However, some planar and spinel formations were observed. It means that such a structure is likely to make the adsorption process of water molecules easier because of the capillary pore and large surface area.

The energy dispersive X-ray (EDX) analysis result was also given in Fig. 2, to analyze the chemical composition of Co-Mg ferrite nanocomposite. All the peaks belong to the main elements of Fe, Co, O and Mg and there is no impurity. According to EDX results, the sample was successfully formed in the desired composition.

In the current study, the Fig. 3 represents the relationship between impedance frequency and humidity map of the ferrite nanoparticles. The figure apparently put forwards that the sample has extraordinary humidity map. According to the figure, it is noteworthy that the humidity value is obviously changed against tested frequency gap. The impedance value of the investigated sample was decreased in a constant humidity condition. The adsorbed water molecules on the sample have prevented the rotation against applied emd [30]. It is clear that the impedance values decreased exponentially in the frequency range between 20Hz-10kHz. For example, in 20 Hz test frequency, the impedance values were rapidly reduced from 4.44×10^7 ohm to 3.4×10^4 ohm. Especially at low frequencies, the rapid increase in the conductivity may be attributed to a result of the contribution to the conductivity of the water molecules. In that conditions, the conductivity occurs via surface conductivity mechanism. The rapid increase of the conductivity was related to the adsorbed water molecules from the sample surface [31]. It means that the sample absorbed more water molecules on its surface at low humidity and low-frequency conditions. We can

even say that this value is almost decreased linearly in higher frequency values greater than 10 kHz. As a remarkable result that impedance value is almost independent of the humidity at the frequency higher than 1 MHz. The decreasing impedance value with increasing relative humidity (RH) value can be explained by the adsorption mechanism of the water molecules. Also, there is an impedance dispersion at low frequencies, and it shows a shift towards higher frequencies with increasing ambient humidity values [32]. We can interpret that the investigated sample has a hydrophobic structure at a higher humidity than 70 % and up to 10^5 kHz frequency value that the

impedance value almost stable in this humidity and frequency interval [33].

The above results, which are logarithmically decreased, are well fitted to the Eq. 1.

$$Z = a \exp(-H/b) + c \quad (1)$$

Here, $R^2=0.99399$, a, b and c values are -184036 ohm, 876584220 and 7.5 ohm respectively.

The humidity measurement sensitivity of the investigated sample was calculated with Eq. 2

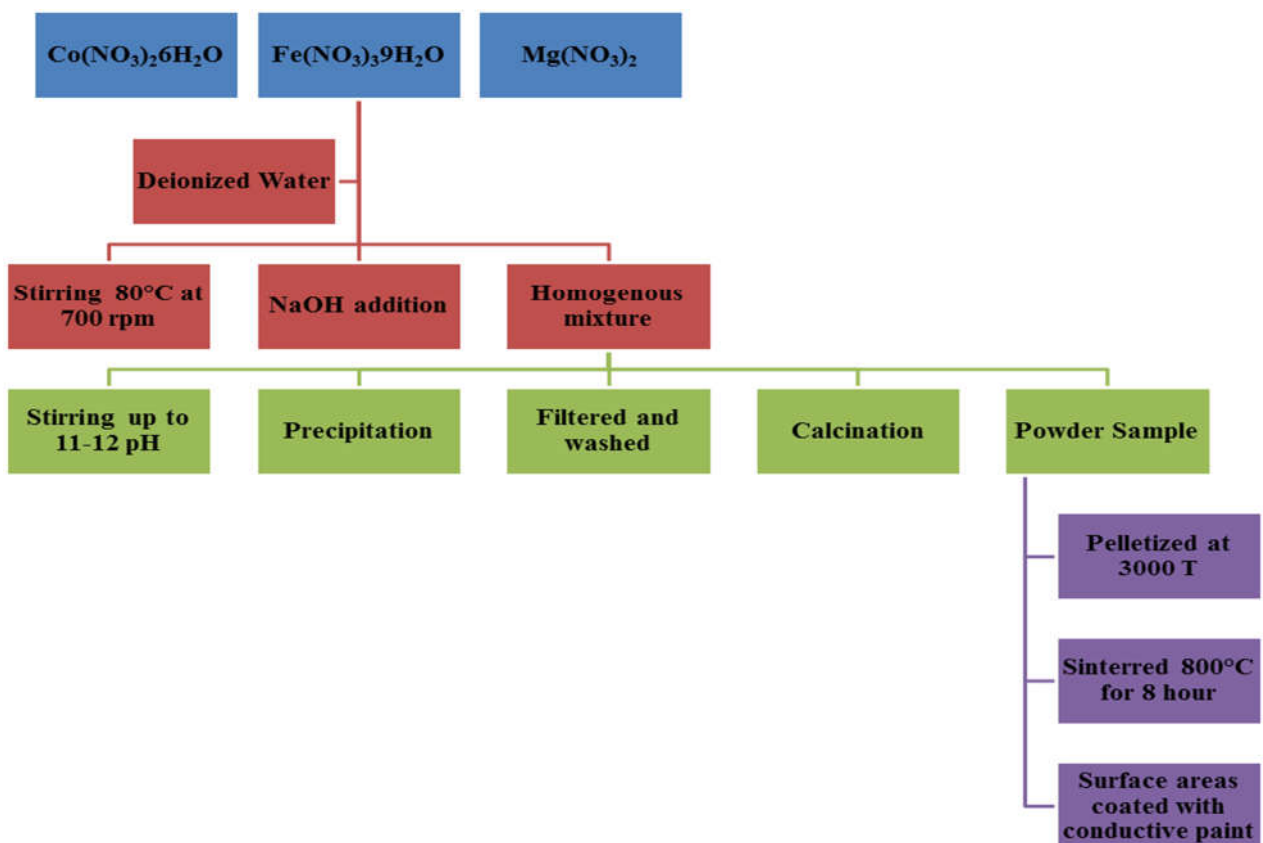


Figure 1. Preparation steps.

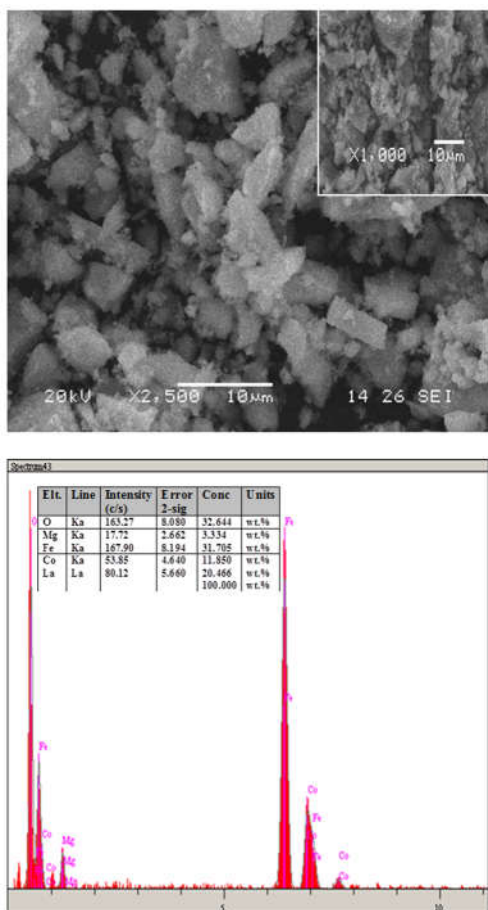


Figure 2. SEM micrographs at different magnitude and EDX analysis of Co-Mg ferrite nanoparticle

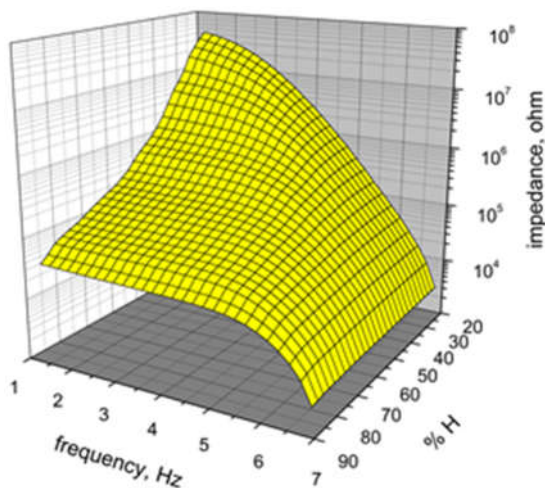


Figure 3. Humidity, impedance and frequency map of Co-Mg ferrite.

$$S\% = \left| \frac{Z_{measured} - Z_{20}}{Z_{20}} \right| \times 100 \quad (2)$$

In this equation, Z_{20} and $Z_{measured}$ values belong to the impedance values at 20% humidity and

measured [34]. The moisture measurement sensitivity versus ambient humidity for some different frequencies was given in Fig. 4. It can be clearly seen from the figure that the sensitivity is higher at low-frequency values. The sensitivity values lower than 1 kHz are more and more reliable, and their measurement accuracy for 40% RH increases up to 95% sensitivity. It is because of rapid changing of impedance with humidity at low frequencies. The sensitivity values increase with increasing ambient humidity. When the ambient humidity decreased below 40%, the sensitivity was also decreased rapidly. This situation is a result of slow changes in impedance values at the lower frequency region.

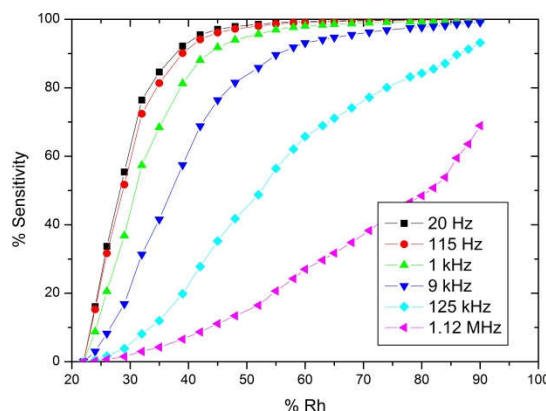


Figure 4. The sensitivity of the sensor device.

In the literature, impedance measurements were made for the definition of the answer of changing humidity in sensing materials. Hysteresis loop of humidity exhibits adsorption and desorption process of humidity sensors [35]. It is one of the critical parameters for the humidity sensor. Naturally, a hysteresis characteristic is used for testing a sensor's reliability [36]. Fig. 5. shows the hysteresis loops between adsorption and desorption processes that measured whole humidity range for seven % RH value, at 1 V, 10 kHz, and room temperature, and results given as a function of RH%. Co-Mg ferrite impedance decrease in a range of 22%-90% with increasing RH%. This figure demonstrates that the impedance values within desorption process nearly settle the amounts under the adsorption. This is the general feature of humidity sensors. As clearly seen from the figure Co-Mg ferrite exhibits a narrow hysteresis loop and this is one of the most desirable properties of humidity sensors for stability. Nevertheless, the sensing curves did not

overlap. Instead, a closed loop was noticed in the range of middle humidity.

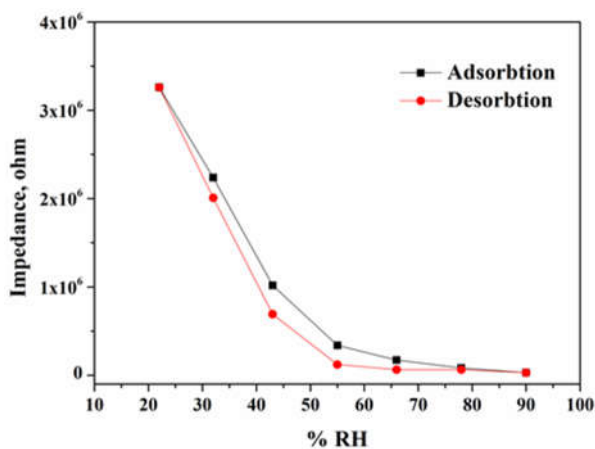


Figure 5. Humidity Hysteresis loop of the Co-Mg sample.

Response and recovery time is one of the key feature demonstrating the performance of the device. Fig. 5. shows response and recovery time of Co-Mg nanocomposite ferrite material. During the adsorption and desorption process, impedance measurements were made as a function of time, at 10 kHz and between 22% - 90% RH. As seen from the Fig. 6 that the response and the recovery curve is repeated. Response and recovery time is known as elapsed time of the total impedance change of the sample to the value reached in amounts corresponding to 90% during adsorption and desorption. According to this, the response time of the sample is 300 s while recovery time is 60 s. Thus, recovery time is shorter than response time. The reason for this is because adsorption is faster than desorption of the sample. The point to be noted here, in the laboratory conditions value of RH is 20%. It may be thought that these times will be shortened by lowering to smaller humidity values. Furthermore, as seen in the figure, the repeatability of the assay was confirmed.

In this study, Co-Mg ferrite measured different relative humidity. Fig. 7. demonstrates long-term stability at five different RH% levels. Impedance was measured every ten days for 60 days (first 10 days, it was measured more frequently). As seen, no significant changes have been observed in impedance at lower humidity. For all that, there is a small charge at 90% humidity. These results underline that Co-Mg ferrite has an excellent stability and it can be correctly applied to practical humidity sensors [37].

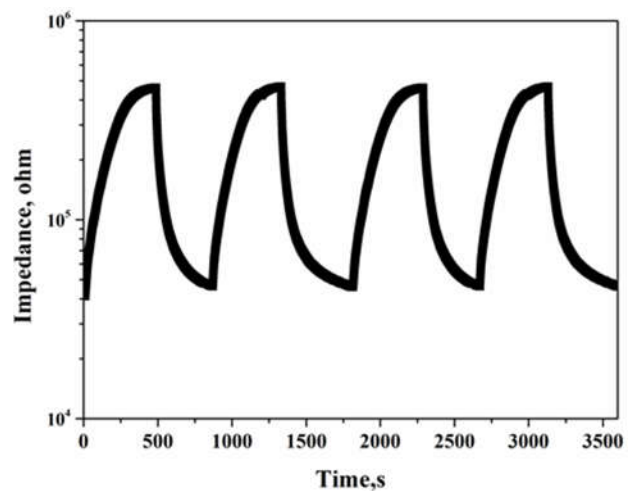


Figure 6. Response and recovery loops.

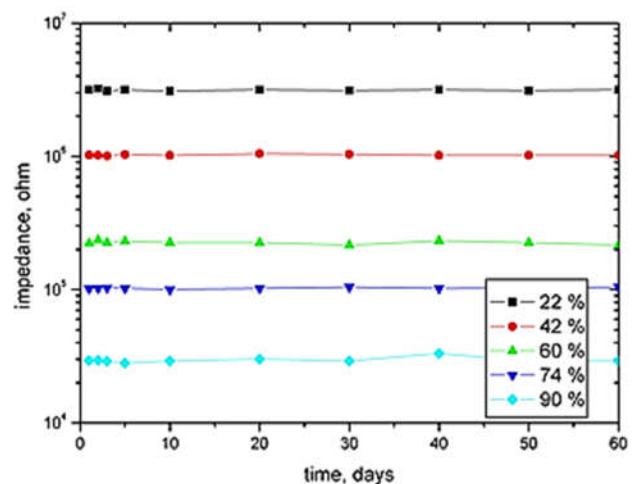


Figure 7. Long time stability of the sample at from humidities.

Nyquist's plots are necessary to introduce the sample conductivity mechanism. In Fig. 8. Nyquist plots of the sample being investigated are shown. These curves reveal one of the intrinsic features of impedance which belongs to sample [38]. A tail at low-frequency region represents the ionic case. However, as seen from all curves, tail, which is not the low-frequency side, has the meaning of appropriate electronic conductivity mechanisms. Undefined half circles at low humidities show that electronic conductivity mechanism is still active at much lower frequencies. Completed half loops are seen at 48% and higher humidity values. For these circuits, although electronic conductivity mechanism is completely active, this means a sign for possible ionic conductivity. The essence of the matter, the absence of ionic conductivity with increasing

humidity is a cause of non-increased conductivity. Semicircle suppressed by the low frequency indicates the Havriliak-Negami type relaxation mechanism. This situation defines the equivalent circuit formed by the parallel connected resistor-capacitor combination [39]. Equivalent circuits' resistance decreases from 5×10^7 ohm to 2.5×10^4 ohm, capacitor decreases from 18 pF to 3 pF while RH increase from 22% to 90%. This behavior of half loops means that same conductivity mechanism works for all RH values.

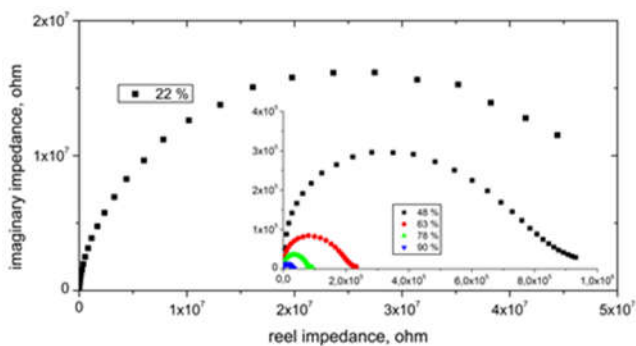


Figure 8. Co-Mg ferrites impedance measurement for Argand diagram.

4. CONCLUSION

Co-Mg ferrite nanoparticle prepared by chemical co-precipitation was studied as a humidity sensor material. Many features that are important for humidity sensors have been researched. Along with this investigation examined sample reveals excellent humidity, impedance and frequency map. According to this map, higher precision humidity measurements have demonstrated at the low-frequency region. According to design for a possible device, the low-frequency impedance-humidity fitting curve has been found to decrease logarithmically. Also, hysteresis curve, during adsorption and desorption, seems to be normal range. Although response and recovery times are a bit long, measurements covering a long time have shown, impedance remains stable for different humidity values. Finally, electronic conductivity mechanism has understood to be suitable for increasing relative humidity. According to these features, the investigated sample is interesting for humidity sensor application.

REFERENCES

- [1] Narsimha Parvatikar, Shilpa Jain, Syed Khasima, M. Revansiddappa, S.V. Bhoraskar, M.V.N. Ambika Prasad, Electrical and humidity sensing properties of polyaniline/WO₃ composites, *Sensors and Actuators B* 114 (2006) 599–603.
- [2] Pi-Guey Su, Lin-Nan Huang, Humidity sensors based on TiO₂ nanoparticles/polypyrrole composite thin films, *Sensors and Actuators B* 123 (2007) 501–507.
- [3] Enrico Traversa, Ceramic sensors for humidity detection: the state-of-the-art and future developments, *Sensors and Actuators B* 23 (1995) 135-156.
- [4] M.L. Singla, Sajeela Awasthi, Alok Srivastava, Humidity sensing; using polyaniline/Mn₃O₄ composite doped with organic/inorganic acids, *Sensors and Actuators B* 127 (2007) 580–585.
- [5] Jinjie Shi, Vincent K.S. Hsiao, Thomas R. Walker, Tony Jun Huang, Humidity sensing based on nanoporous polymeric photonic crystals, *Sensors and Actuators B* 129 (2008) 391–396.
- [6] Pi-Guey Su, Chao-Shen Wang, Novel flexible resistive-type humidity sensor, *Sensors and Actuators B* 123 (2007) 1071–1076.
- [7] Pi-Guey Su, Chao-Shen Wang, In situ synthesized composite thin films of MWCNTs/PMMA doped with KOH as a resistive humidity sensor, *Sensors and Actuators B* 124 (2007) 303–308.
- [8] B. Nait-Ali, C. Danglade, D.S. Smith, K. Haberkö, Effect of humidity on the thermal conductivity of porous zirconia ceramics, *Journal of the European Ceramic Society* 33 (2013) 2565–2571.
- [9] Hengchang Bi, Kuibo Yin, Xiao Xie, Jing Ji, Shu Wan, Litao Sun, Mauricio Terrones, Mildred S. Dresselhaus, Ultrahigh humidity sensitivity of graphene oxide, *Scientific Reports* | 3 : 2714.
- [10] Yong Zhang, Xuejun Zheng, Tong Zhang, Lunjun Gong, Shunhong Dai, Yiqiang Chen,

- Humidity sensing properties of the sensor based on Bi_{0.5}K_{0.5}TiO₃ powder, *Sensors and Actuators B* 147 (2010) 180–184.
- [11] Dewyani Patil, You-Kyong Seo, Young Kyu Hwang, Jong-San Chang, Pradip Patil, Humidity sensing properties of poly(o-anisidine)/WO₃ composites, *Sensors and Actuators B* 128 (2008) 374–382.
- [12] Yuan He, Tong Zhang, Wei Zheng, Rui Wang, Xiangwei Liu, Yan Xia, Jinwei Zhao, Humidity sensing properties of BaTiO₃ nanofiber prepared via electrospinning, *Sensors and Actuators B* 146 (2010) 98–102.
- [13] T. Islam, S. Ghosh, H. Saha, ANN-based signal conditioning and its hardware implementation of a nanostructured porous silicon relative humidity sensor, *Sensors and Actuators B* 120 (2006) 130–141.
- [14] Iulian Petrila, Florin Tudorache, Humidity sensor applicative material based on copper-zinc-tungsten spinel ferrite, *Materials Letters* 108 (2013) 129–133.
- [15] M. Abdullah Dar, Vivek Verma, S.P. Gairola, W.A. Siddiqui, Rakesh Kumar Singh, R.K. Kotnala, Low dielectric loss of Mg doped Ni–Cu–Zn nano-ferrites for power applications, *Applied Surface Science* 258 (2012) 5342–5347.
- [16] Kavita Verma, Ashwini Kumar, Dinesh Varshney, Effect of Zn and Mg doping on structural, dielectric and magnetic properties of tetragonal CuFe₂O₄, *Current Applied Physics* Volume 13, Issue 3, May 2013, Pages 467–473.
- [17] Huiqun Cao, Meifang Zhu, Yaogang Li, Jianhong Liu, Zhuo Ni, Zongyi Qin, A highly coercive carbon nanotube coated with Ni_{0.5}Zn_{0.5}Fe₂O₄ nanocrystals synthesized by chemical precipitation–hydrothermal process, *Journal of Solid State Chemistry* Volume 180, Issue 11, November 2007, Pages 3218–3223.
- [18] Jyoti Shah, Manju Arora, L.P. Purohit, R.K. Kotnala, Humidity response of Li-substituted magnesium ferrite, Significant increase in humidity sensing characteristics of praseodymium doped magnesium ferrite, *Sensors and Actuators A: Physical* Volume 167, Issue 2, June 2011, Pages 332–337.
- [19] Dipak Bauskar, B.B. Kale, Pradip Patil, Synthesis and humidity sensing properties of ZnSnO₃ cubic crystallites, *Sensors and Actuators B* 161 (2012) 396–400.
- [20] Vijay K. Tomer, Surender Duhan, A facile nanocasting synthesis of mesoporous Ag-doped SnO₂ nanostructures with enhanced humidity sensing performance, *Sensors and Actuators B* 223 (2016) 750–760.
- [21] Yongsheng Zhang, Ke Yu, Shixi Ouyang, Laiqiang Luo, Hongmei Hu, Qiuxiang Zhang, Ziqiang Zhu, Detection of humidity based on quartzcrystal microbalance coated with ZnO nanostructure films, *Physica B* 368 (2005) 94–99.
- [22] Xiaofeng Zhou, Jian Zhang, Tao Jiang, Xiaohua Wang, Ziqiang Zhu, Humidity detection by nanostructured ZnO: A wireless quartz crystal microbalance investigation, *Sensors and Actuators A* 135 (2007) 209–214.
- [23] Seema Agarwal, G.L. Sharma, Humidity sensing properties of (Ba, Sr) TiO₃ thin films grown by hydrothermal–electrochemical method, *Sensors and Actuators B* 85 (2002) 205–211.
- [24] M. Viviani, M.T. Buscaglia, V. Buscaglia, M. Leoni, P. Nanni, Barium perovskites as humidity sensing materials, *Journal of the European Ceramic Society* 21 (2001) 1981–1984.
- [25] Y.-S. Jo, Y. Lee, Y. Roh, Current–voltage characteristics of E- and poly-DNA, *Materials Science and Engineering C* 23 (2003) 841 – 846
- [26] Weon-Pil Tai, Jae-Hee Oh, Preparation and humidity sensing behaviors of nanocrystalline SnO₂ 2 yTiO bilayered films, *Thin Solid Films* 422 (2002) 220–224.
- [27] Qi Qi, Yingliang Feng, Tong Zhang, Xuejun Zheng, Geyu Lu, Influence of crystallographic structure on the humidity sensing properties of KCl-doped TiO₂

- nanofibers, *Sensors and Actuators B* 139 (2009) 611–617.
- [28] Xiangwei Liu, Rui Wang, Tong Zhang, Yuan He, Jinchun Tu, Xiaotian Li, Synthesis and characterization of mesoporous indium oxide for humidity-sensing applications, *Sensors and Actuators B* 150 (2010) 442–448.
- [29] Y. Köseoğlu, E. Şentürk, V. Eyüpoğlu, T. Şaşmaz Kuru, M. Hashim, S. S. Meena, Structural, Conductivity, and Dielectric Properties of $\text{Co}_{0.5}\text{Mg}_{0.5}\text{La}_{0.1}\text{Fe}_{1.9}\text{O}_4$ Ferrite Nanoparticles, *J Supercond Nov Magn*, 2016, Volume 29, Issue 11, pp 2813–2819.
- [30] T. Siciliano, M. Di Giulio, M. Tepore, E. Filippo, G. Micocci, A. Tepore, Tellurium sputtered thin films as NO_2 gas sensors, *Sensor and actuators B* 135, (2008) 255-261.
- [31] Qi Qi, Tong Zhang, Humidity sensing properties of KCl-doped Cu–Zn/CuO–ZnO nanoparticles *Sensors and Actuators B: Chemical* Volume 137, Issue 1, 28 March 2009, Pages 21–26.
- [32] Tuğba Şaşmaz Kuru, Mehmet Kuru, Sadık Bağcı, Structural, dielectric and humidity properties of Al-Ni-Zn ferrite prepared by co-precipitation method, *Journal of Alloys and Compounds* 753 (2018) 483-490.
- [33] Yang li, Chao Deng, Mujie Yang, A composite of quaternized and crosslinked poly(4-vinylpyridine) with processable polypyrrole for the construction of humidity sensors with improved sensing properties, *Synthetic Metals*, Volume 162, Issues 1–2, February 2012, Pages 205–211.
- [34] Wen Chuang Wang, Yong Tao Tian, Kun Li, Er Yang Lu, Dong Shang Gong, Xin Jian Li, Capacitive humidity-sensing properties of Zn_2SiO_4 film grown on silicon nanoporous pillar array, *Applied Surface Science*, Volume 273, 15 May 2013, Pages 372–376.
- [35] Mansoor Anbia, Seyyed Ebrahim Moosavi Fard, Humidity sensing properties of Ce-doped nanoporous ZnO thin film prepared by sol-gel method, *JOURNAL OF RARE EARTHS*, Vol. 30, No. 1, Jan. 2012, P. 38.
- [36] Wangchang Geng, Qing Yuan, Xingmao Jiang, Jinchun Tu, Libing Duan, Junwei Gu, Qiuyu Zhang, Humidity sensing mechanism of mesoporous MgO/KCl– SiO_2 composites analyzed by complex impedance spectra and bode diagrams, *Sensors and Actuators B: Chemical*, 174 (2012) 513-520.
- [37] T. Şaşmaz Kuru, E. Şentürk, Humidity sensing properties of ferrite based Al-Cd nanoparticles as a fast response sensor device, *Sensors and Actuators A* 249 (2016) 62–67.
- [38] Lijie Wang, Di Li, Rui Wang, Yuan He, Qi Qi, Yue Wang, Tong Zhang, Study on humidity sensing property based on Li-doped mesoporous silica MCM-41, *Sensors and Actuators B* 133 (2008) 622–627.
- [39] Qi Qi, Tong Zhang, Qingjiang Yu, Rui Wang, Yi Zeng, Li Liu, Haibin Yang, Properties of humidity sensing ZnO nanorods-base sensor fabricated by screen-printing, *Sensors and Actuators B* 133 (2008) 638–643.

	SAKARYA UNIVERSITY JOURNAL OF SCIENCE		 SAKARYA UNIVERSITY
	e-ISSN: 2147-835X http://www.saujs.sakarya.edu.tr		
	<u>Received</u> 30-05-2018 <u>Accepted</u> 04-08-2018	<u>Doi</u> 10.16984/saufenbilder.428697	

A Note On Convergence of Nonlinear General Type Two Dimensional Singular Integral Operators

Mine Menekşe Yılmaz^{*1}

Abstract

The object of this study is to present both the pointwise convergence and the rate of convergence of the nonlinear integral operators given by

$$V_{\zeta}(x, y; f) = \iint_{\Omega} K_{\zeta}(t, s, x, y; f(t, s)) ds dt, \quad (x, y) \in \Omega, \quad \zeta \in E$$

where $\Omega = \langle a, b \rangle \times \langle c, d \rangle$ is arbitrary bounded region in \mathbb{R}^2 or $\Omega = \mathbb{R}^2$, moreover, E is a set of nonnegative numbers, ζ_0 is an accumulation point of E , and the function f is Lebesgue-integrable function on Ω .

Keywords: Lebesgue point, nonlinear singular integral, Lipschitz condition, pointwise convergence.

1. INTRODUCTION

In [1], Musielak introduced a new type convergence problem using the nonlinear integral operators in the following form

$$T_{\omega}f(t) = \int_a^b K_{\omega}(s - t, f(s)) ds, \quad t \in \langle a, b \rangle \quad (1)$$

and by assuming the whose kernel K_{ω} satisfies the generalized Lipschitz condition.

By using this idea, Bardaro et al. ([1], [3]) and in [4], Karsli studied the special cases of equation (1) in some Lebesgue spaces. Also, in [5], Swiderski and Wachnicki gave the theorems on pointwise approximation of the operators of equation (1) in the class of integrable and periodic functions. For further informations on nonlinear integral

operators, we mention some of studies as [1]-[12]. Also, the several approximation properties of many new type integral operators have been studied and discussed by some authors, see [13]-[15].

In this note, first, we present the pointwise convergence, and in the sequel, we give the rate of convergence of general type nonlinear two dimensional singular integral operators of the following type:

$$V_{\zeta}(x, y; f) = \iint_{\Omega} K_{\zeta}(t, s, x, y; f(t, s)) ds dt,$$

$$(x, y) \in \Omega, \quad \zeta \in E \quad (2)$$

under various assumptions on $f(t, s)$ and $(K_{\zeta})_{\zeta \in E}$. By $L_1(\Omega)$, we denote the class of all functions $f(t, s)$ Lebesgue-integrable over the rectangle

^{*}Corresponding Author

¹menekse@gantep.edu.tr

$\Omega = \langle a, b \rangle \times \langle c, d \rangle$ or $\Omega = \mathbb{R}^2$ and E is a set of positive numbers and ζ_0 is an accumulation point of E .

First, we shall give the basic concepts which are used in this paper.

Definition 1.1. A point $(x_0, y_0) \in \Omega$ is a μ -generalized Lebesgue point of function $f \in L_1(\Omega)$ if

$$\lim_{(h,k) \rightarrow (0,0)} \frac{1}{\mu(h,k)} \int_0^h \int_0^k |f(x_0 \pm t, y_0 \pm s) - f((x_0, y_0))| ds dt = 0$$

where $0 < h \leq b - a$, $0 < k \leq d - c$ and $\mu(h, k) = \int_0^h \int_0^k \rho(t, s) ds dt$

is non-negative function provided $\rho(t, s)$ is nonnegative Lebesgue integrable function defined on $[0, b - a] \times [0, d - c]$ (see [16]).

We have created the following definition by taking advantage of the article [11] and [17].

Definition 1.2. If the family of functions $(K_\zeta)_{\zeta \in E}, K_\zeta: \mathbb{R}^2 \times \mathbb{R}^2 \times E \rightarrow \mathbb{R}$, holds the following condition and then we say that $(K_\zeta)_{\zeta \in E}$ belongs to class \mathcal{A} :

- a) $K_\zeta(t, s, x, y, 0) = 0$, for every $t, s, x, y \in \mathbb{R}$ and $\zeta \in E$.
- b) Let $T_\zeta: \mathbb{R}^2 \times \mathbb{R}^2 \times \Lambda \rightarrow \mathbb{R}_0^+$ be a function such that

$$|K_\zeta(t, s, x, y; u) - K_\zeta(t, s, x, y; v)| \leq T_\zeta(t, s; x, y)|u - v|,$$

for every $t, s, x, y \in \mathbb{R}$ and $\zeta \in E$. Moreover, for any fixed $(x, y) \in \Omega$, $T_\zeta(t, s, x, y)$ is integrable function of (t, s) .

- c) For every $u \in \mathbb{R}$ and any fixed $(x, y) \in \Omega$

$$\lim_{\zeta \rightarrow \zeta_0} \left| \iint_{\mathbb{R}^2} K_\zeta(t, s, x, y; u) ds dt - u \right| = 0$$

- d) For any fixed $(x, y) \in \Omega$ and for every $\delta > 0$

$$\lim_{\zeta \rightarrow \zeta_0} \left[\sup_{(t,s) \in \mathbb{R}^2 \setminus N_\delta(x,y)} T_\zeta(t, s; x, y) \right] = 0$$

where

$$N_\delta(x, y) = (x - \delta, x + \delta) \times (y - \delta, y + \delta).$$

- e) For any fixed $(x, y) \in \Omega$

$$\lim_{\zeta \rightarrow \zeta_0} \iint_{\mathbb{R}^2 \setminus N_\delta(x,y)} T_\zeta(t, s, x, y, u) ds dt = 0$$

- f) For every $\zeta \in E$

$$\|T_\zeta(\cdot)\|_{L_1(\mathbb{R}^2)} \leq M < \infty,$$

- g) For any fixed $x \in \langle a, b \rangle$, $T_\zeta(t, s; x, y)$ is non-increasing as a function of t on $\langle x - \delta, x \rangle$ and non-decreasing function on $[x, x + \delta)$, for each fixed $\lambda \in \Lambda$. Similarly, for any fixed $y \in \langle c, d \rangle$, $T_\zeta(t, s, x, y)$ is non-increasing as a function of s on $\langle y - \delta, y \rangle$ and non-decreasing function on $[y, y + \delta)$ for each fixed $\zeta \in E$.

Analogously, for any fixed $(x, y) \in \Omega$ and fixed $\zeta \in E$, $T_\lambda(t, s, x, y)$ is bimonotonically increasing with respect to (t, s) on both $\langle x, x + \delta \rangle \times \langle y, y + \delta \rangle$ and $\langle y - \delta, y \rangle \times \langle x - \delta, x \rangle$. Similarly, $T_\zeta(t, s; x, y)$ is bimonotonically increasing with respect to (t, s) on both $[x, x + \delta) \times \langle y - \delta, y \rangle$ and $\langle x - \delta, x \rangle \times [y, y + \delta)$.

2. POINTWISE CONVERGENCE

Now we shall prove the existence of the integral operators in equation (2) by the Theorem 2.1.

Theorem 2.1. If $f \in L_1(\Omega)$, then for every $\zeta \in E$, $V_\zeta \in L_1(\Omega)$ and $\|V_\zeta\|_{L_1(\Omega)} \leq M \|f\|_{L_1(\Omega)}$

Proof. We define a function

$$h(t, s) = \begin{cases} f(t, s), & (t, s) \in \Omega \\ 0, & (t, s) \in \mathbb{R} \setminus \Omega \end{cases} \quad (3)$$

Using Fubini's Theorem (see, e.g., [18]) and conditions (a), (b) and (f) of class \mathcal{A} we get the following inequalities:

$$\begin{aligned} & \|V_\zeta(x, y; f)\|_{L_1(\Omega)} \\ &= \left| \iint_{\Omega} K_\zeta(t, s, x, y; f(t, s)) ds dt \right| dy dx \\ &\leq \iint_{\Omega} \left(\int_{-\infty}^{\infty} \int_{-\infty}^{\infty} |h(t, s)| T_\zeta(t, s, x, y) ds dt \right) dy dx \\ &\leq \|f\|_{L_1(\Omega)} \|T_\zeta\|_{L_1(\mathbb{R}^2)}. \end{aligned}$$

The proof is completed for this case.

Now we assume that $\Omega = \mathbb{R}^2$. Following similar steps, as in the first case, we have

$$\|V_\zeta(x, y; f)\|_{L_1(\Omega)} \leq \|T_\zeta\|_{L_1(\mathbb{R}^2)} \|f\|_{L_1(\mathbb{R}^2)} \leq M \|f\|_{L_1(\mathbb{R}^2)}.$$

The proof is completed.

We shall show to pointwise convergence of the operator (2) at the μ -generalized Lebesgue point.

For $C > 0$, let P_C denote the set

$$\left\{ (x, y, \zeta) \in \mathbb{R}^2 \times E: \int_{x_0-\delta}^{x_0+\delta} \int_{y_0-\delta}^{y_0+\delta} \rho(|t-x_0|, |s-y_0|) \{T_\zeta(t, s; x_0, y_0) \times \dots\} dsdt < C \right\}$$

Theorem 2.2. Let (x_0, y_0) be a μ -generalized Lebesgue point of function $f \in L_1(\Omega)$ and functions K_ζ satisfies the assumptions listed in class \mathcal{A} , then for any $C > 0$ and $(x, y, \zeta) \in P_C$

$$\lim_{\zeta \rightarrow \zeta_0} V_\zeta(x_0, y_0; f) = f(x_0, y_0).$$

Proof. Suppose that $(x_0, y_0) \in \Omega$ is the μ -generalized Lebesgue point of function $f \in L_1(\Omega)$ and

$0 < x_0 - x < \frac{\delta}{2}$ and $0 < y_0 - y < \frac{\delta}{2}$ for all $\delta > 0$ satisfying

$$x_0 + \delta < b, x_0 - \delta > a,$$

$$y_0 + \delta < d, y_0 - \delta > c.$$

For the remaining cases, the proof follows a similar line. From Definition 1.1, for a given $\varepsilon > 0$ there exists a $\delta > 0$ such that for all h and k satisfying $0 < h, k \leq \delta$ the inequality:

$$\int_{x_0}^{x_0+h} \int_{y_0-k}^{y_0} |f(t, s) - f(x_0 - y_0)| dsdt < \varepsilon \mu(h, k)$$

holds.

By conditions (b) and (c) of class \mathcal{A} , and from equation (3) using the extention $g(t, s)$ of $f(t, s)$, we get the following inequality:

$$|V_\zeta(x_0, y_0; f) - f(x_0, y_0)| \leq \iint_{\Omega} |f(t, s) - f(x_0 - y_0)| T_\zeta(t, s; x_0, y_0) dsdt$$

$$+ |f(x_0, y_0)| \iint_{\mathbb{R}^2 \setminus \Omega} T_\zeta(t, s; x_0, y_0) dsdt + \left| \iint_{\mathbb{R}^2} K_\zeta(t, s; x_0, y_0; f(x_0, y_0)) dsdt - f(x_0, y_0) \right| = I_1 + I_2 + I_3.$$

The necessity of (e) and (c) of class \mathcal{A} provides the $I_2 \rightarrow 0$ and $I_3 \rightarrow 0$ as $\zeta \rightarrow \zeta_0$, respectively.

Splitting I_1 into two parts, we get the following:

$$I_1 = \iint_{\Omega \setminus N_\delta} |f(t, s) - f(x_0, y_0)| T_\zeta(t, s; x_0, y_0) dsdt + \iint_{N_\delta} |f(t, s) - f(x_0, y_0)| T_\zeta(t, s; x_0, y_0) dsdt = I_{11} + I_{12}$$

where $N_\delta = (x_0 - \delta, x_0 + \delta) \times (y_0 - \delta, y_0 + \delta)$ stands for the family of all neighborhoods of (x_0, y_0) in \mathbb{R}^2 .

For the integral I_{11} we may write the following

$$I_{11} = \iint_{\Omega \setminus N_\delta} |f(t, s) - f(x_0, y_0)| T_\zeta(t, s; x_0, y_0) dsdt \leq \left(\sup_{(t,s) \in \mathbb{R}^2 \setminus N_\delta(x,y)} T_\zeta(t, s; x_0, y_0) \right) \times (\|f\|_{L_1(\Omega)} + f(x_0, y_0) |b - a| |d - c|)$$

by condition (d), $I_{11} \rightarrow 0$ as ζ tends to ζ_0 .

Now, we focus on the integral I_{12} . It is easy to see that I_{12} can be written in the following form:

$$I_{12} = \left\{ \int_{x_0}^{x_0+\delta} \int_{y_0-\delta}^{y_0} + \int_{x_0-\delta}^{x_0} \int_{y_0-\delta}^{y_0} + \int_{x_0-\delta}^{x_0} \int_{y_0}^{y_0+\delta} + \int_{x_0}^{x_0+\delta} \int_{y_0}^{y_0+\delta} \right\} |f(t, s) - f(x_0, y_0)| L_\zeta(t, s; x_0, y_0) dsdt = I_{121} + I_{122} + I_{123} + I_{124}.$$

We shall prove $I_{12} \rightarrow 0$ as $\zeta \rightarrow \zeta_0$. It is enough to show that the integrals I_{121} , I_{122} , I_{123} and I_{124} tend to zero as $\zeta \rightarrow \zeta_0$ on P_C .

Let us define a new function as such:

$$G(t, s) := \int_{x_0}^t \int_s^{y_0} |f(u, v) - f(x_0, y_0)| dv du.$$

Then, for all t and s satisfying $t - x_0 \leq \delta$ and $y_0 - s \leq \delta$ we have

$$|G(t, s)| \leq \varepsilon \mu(t - x_0, y_0 - s) \tag{4}$$

The following equality holds for the integral I_{121} :

$$|I_{121}| = \left| \int_{x_0}^{x_0+\delta} \int_{y_0-\delta}^{y_0} |f(t, s) - f(x_0, y_0)| T_\zeta(t, s; x_0, y_0) ds dt \right|$$

$$= \left| (LS) \int_{x_0}^{x_0+\delta} \int_{y_0-\delta}^{y_0} T_\zeta(t, s; x_0, y_0) d_t d_s [-G(t, s)] \right|,$$

where (LS) means Lebesgue-Stieltjes integral.

Using the integration by parts (see [20]) to the Lebesgue-Stieltjes integral I_{121} , we have the following inequality:

$$|I_{121}| \leq \left| \int_{x_0}^{x_0+\delta} \int_{y_0-\delta}^{y_0} G(t, s) d_t d_s [T_\zeta(t, s; x_0, y_0)] \right|$$

$$+ \left| \int_{x_0}^{x_0+\delta} G(t, y_0 - \delta) d_t [T_\zeta(t, y_0 - \delta; x_0, y_0)] \right|$$

$$+ \int_{y_0-\delta}^{y_0} G(x_0 + \delta, s) d_s [T_\zeta(x_0 + \delta, s; x, y)]$$

$$+ |G(x_0 + \delta, y_0 - \delta) [T_\zeta(x_0 - \delta, y_0 - \delta; x, y)]|.$$

from equation (4), we have the following inequality:

$$I_{121} \leq \varepsilon \left\{ \int_{x_0}^{x_0+\delta} \int_{y_0-\delta}^{y_0} \mu(t - x_0, y_0 - s) d_t d_s [T_\zeta(t, s; x_0, y_0)] \right\}$$

$$+ \varepsilon \int_{x_0}^{x_0-\delta} \mu(t - x_0, \delta) |d_t [T_\zeta(t, y_0 - \delta; x_0, y_0)]|$$

$$+ \varepsilon \int_{y_0-\delta}^{y_0} \mu(\delta, y_0 - s) |d_s [T_\zeta(x_0 + \delta, s; x_0, y_0)]|$$

$$+ \varepsilon \mu(\delta, \delta) T_\zeta(x_0 + \delta, y_0 - \delta; x_0, y_0)$$

$$= i_1 + i_2 + i_3 + i_4.$$

Using the condition (g) and applying the integration by parts to each integral, the following inequality is obtained (for the rest of the operations see [19] and [20]).

$$|I_{121}| \leq \varepsilon \int_{x_0}^{x_0+\delta} \int_{y_0-\delta}^{y_0} T_\zeta(t, s; x_0, y_0) \rho(|t - x_0|, |s - y_0|) ds dt.$$

Computing the integrals I_{122} , I_{123} and I_{124} with the same method, and combining the obtained inequalities we have the following inequality

$$|I_{12}| \leq \varepsilon \int_{x_0-\delta}^{x_0+\delta} \int_{y_0-\delta}^{y_0+\delta} T_\zeta(t, s; x_0, y_0) \rho(|t - x_0|, |s - y_0|) ds dt$$

which in view of the definition of the set P_C tends to zero as $\zeta \rightarrow \zeta_0$.

Thus the proof of the theorem is completed.

Theorem 2.3. Let $(x_0, y_0) \in \mathbb{R}^2$ be a μ -generalized Lebesgue point of function $f \in L_1(\mathbb{R}^2)$ and function K_ζ satisfies the assumptions listed in class \mathcal{A} , then for any $C > 0$ and $(x, y, \zeta) \in P_C$

$$\lim_{\zeta \rightarrow \zeta_0} V_\zeta(x_0, y_0; f) = f(x_0, y_0).$$

Proof. The proof can be shown analogous to the proof of Theorem 2.2.

3. RATE OF CONVERGENCE

In this part, we establish the rate of pointwise convergence which we got in the Section 2.

Theorem 3.1. Suppose that the hypothesis of Theorem 2.2 is satisfied. Let

$$\Delta(\zeta, \delta, x_0, y_0) = \int_{x_0-\delta}^{x_0+\delta} \int_{y_0-\delta}^{y_0+\delta} T_\zeta(t, s; x_0, y_0) \rho(|t - x_0|, |s - y_0|) ds dt$$

for $0 < \delta < \delta_0$ and the following assumptions be satisfied:

- i. $\Delta(\zeta, \delta, x_0, y_0) \rightarrow 0$ as $\zeta \rightarrow \zeta_0$ for some $\delta > 0$.
- ii. For $(x_0, y_0) \in \Omega$

$$\iint_{\mathbb{R}^2 \setminus N_\delta} T_\zeta(t, s; x_0, y_0) ds dt = o(\Delta(\zeta, \delta, x_0, y_0))$$

as $\zeta \rightarrow \zeta_0$.

- iii. For $(x_0, y_0) \in \Omega$

$$\left| \iint_{\mathbb{R}^2} K_\zeta(t, s; x, y, u) ds dt - u \right| = o(\Delta(\zeta, \delta, x_0, y_0))$$

as $\zeta \rightarrow \zeta_0$

- iv. For $(x_0, y_0) \in \Omega$

$$\sup_{(t,s) \in \mathbb{R}^2 \setminus N_\delta} T_\zeta(t, s; x_0, y_0) = o(\Delta(\zeta, \delta, x_0, y_0))$$

$\delta > 0$, as $\zeta \rightarrow \zeta_0$.

Then, at each μ -generalized Lebesgue point of $f \in L_1(\Omega)$ and we have as $\zeta \rightarrow \zeta_0$.

$$|V_\zeta(x_0, y_0; f) - f(x_0, y_0)| = o(\Delta(\zeta, \delta, x_0, y_0)).$$

Proof. Omitted.

REFERENCES

[1] J. Musielak, "On some approximation problems in modular spaces", In: *Constructive Function Theory, Proceedings of International Conference Varna, 1-5 June, 1981*, Publication House of Bulgarian Academic of Sciences, Sofia, pp. 181-189, 1983.

[2] C. Bardaro, H. Karsli and G. Vinti, "On pointwise convergence of linear integral operators

with homogeneous kernels", *Integral Transforms and Special Functions*, 19(6), pp. 429–439, 2008.

[3] C. Bardaro, H. Karsli and G. Vinti, "Nonlinear integral operators with homogeneous kernels: pointwise approximation theorems", *Appl. Anal.*, Vol. 90, Nos. 3–4, pp. 463–47, 2011

[4] H. Karsli, "Convergence and rate of convergence by nonlinear singular integral operators on two parameters", *Appl. Anal.*, 85, pp.781-791, 2006.

[5] T. Swiderski and E. Wachnicki, "Nonlinear singular integrals depending on two parameters", *Comment. Math.*, 40, pp. 181-189, 2000.

[6] J. Musielak, "Approximation by nonlinear singular integral operators in generalized Orlicz spaces", *Comment. Math. Prace Mat.*, 31, pp. 79-88, 1991.

[7] C. Bardaro and G. Vinti, "Approximation by nonlinear integral operators in some modular function spaces, *Ann. Polon. Math.*, 63, pp.173-182, 1996.

[8] C. Bardaro, J. Musielak, and G. Vinti, "Nonlinear integral operators and applications", *De Gruyter Series in Nonlinear Analysis and Applications*, Vol. 9, Walter de Gruyter, Publ., Berlin-New York, 2003.

[9] C. Bardaro and I. Mantellini, "Pointwise convergence theorems for nonlinear Mellin convolution operators", *Int. J. Pure Appl. Math.*, 27(4), pp.431-447, 2006.

[10] C. Bardaro, G. Vinti and H. Karsli, "On pointwise convergence of linear integral operators with homogeneous kernels", *Integral Transform Sec. Funct.*, 19(6), pp. 429-439, 2008.

[11] H. Karsli, "On approximation properties of non-convolution type nonlinear operators", *Anal. Theory Appl.* 26 (2), pp.140-152, 2010.

[12] G. Uysal, M. Menekşe Yılmaz and E. Ibikli, "On pointwise convergence of bivariate nonlinear singular integral operators", *Kuwait Journal of Science*, 44(2):46-57, 2017.

- [13] L. N. Mishra, "On existence and behavior of solutions to some nonlinear integral equations with Applications", Ph.D. Thesis (2017), National Institute of Technology, Silchar 788 010, Assam, India.
- [14] V. N. Mishra, K. Khatri, L. N. Mishra, Deepmala; "Inverse result in simultaneous approximation by Baskakov-Durrmeyer-Stancu operators", *Journal of Inequalities and Applications*, 2013, 2013:586.doi:10.1186/1029-242X-2013-586.
- [15] A. Kumar, Vandana, "Some approximation properties of generalized integral type operators", *Tbilisi Mathematical Journal*, 11(1), pp. 99–116, 2018.
- [16] B. Rydzewska, "Approximation des fonctions de deux variables par des integrales singulieres doubles", *Fasc. Math.*, 8, pp. 35-45 (in French), 1974.
- [17] S. Esen Almali, "On approximation properties of certain multidimensional nonlinear integrals", *Journal of Nonlinear Sciences and Applications*, (9)5, pp. 3090-3097, 2016.
- [18] P. L. Butzer and R. J. Nessel, *Fourier Analysis and Approximation*, Academic Press, New York, London, 1971.
- [19] M. Menekşe Yılmaz, "A study on convergence of nonconvolution type double singular integral operators", *New Trends Math. Sci.*, 4 (4) pp. 67-78, 2016.
- [20] R. Taberski, "On double integrals and Fourier Series" *Ann. Polon. Math.* 15, pp. 97-115, 1964.

	SAKARYA UNIVERSITY JOURNAL OF SCIENCE		 SAKARYA UNIVERSITY
	e-ISSN: 2147-835X http://www.saujs.sakarya.edu.tr		
	<u>Received</u> 06-06-2018 <u>Accepted</u> 11-09-2018	<u>Doi</u> 10.16984/saufenbilder.431371	

The explanation of metallic nature of BBi(110) surface

Sadık BAĞCI*¹

Abstract

In this study, the structural, elastic and electronic properties for zinc-blende BBi have been investigated by using plane wave ab initio calculations within the density functional theory. The local density approximation was employed to take account of electronic exchange and correlation energies. The lattice constant and bulk modulus are in good agreement with previous theoretical results. The elastic constants are also calculated using the volume-conserving tetragonal and monoclinic strains. The electronic band structure and density of states of BBi are also presented and discussed in detail. Using our results for bulk properties of BBi, we have obtained the atomic relaxed geometry and electronic band structure of the (110) surface of BBi for the first time in the literature. We have also discussed total and partial electronic density of states for BBi(110) surface to explain metallic nature of this surface. At the end of our study, we have compared our surface electronic structure with other metallic (110) surfaces of AlBi, GaBi and InBi.

Keywords: Ab initio calculations, BBi(110) surface, Surface electronic structure, Surface electronic DOS

1. INTRODUCTION

In recent years, III-Bi compounds and their alloys have attracted the attention of the researchers because of their remarkable physical properties [1-13]. The first member of this series Boron Bismuth (BBi) has been reported in several theoretical studies [1-13] due to its interesting properties such as a small band gap, low ionicity, high mechanical strength and high melting point [14-18]. Although there are several theoretical works about physical properties of BBi, it has not been synthesized yet. In some of these theoretical works, the ground state phase of BBi is confirmed as zinc-blend (ZB) [4-6]. The ground state properties and also electronic and optical properties of BBi have been investigated by several theoretical research group in recent years [1-12]. Ferhat and Zaoui have reported negative band gap for BBi using full potential linearized augmented plane-wave (FLAPW) method [4]. On the other hand, Shouxin et al. have obtained indirect band gap for BBi by using generalized gradient approximation (GGA) [2]. In addition, Wang and Ye [7] have also attained similar result for energy band gap

of BBi using local density approximation (LDA). Otherwise, Madouri and Ferhat [6], Deligoz et al. [3] and B. G. Yalcin et al. [8,9] have calculated direct band gap for BBi compound using DFT. The dynamical properties of BBi are also presented by Deligoz et al. [3] and Belabbes et al. [13] in different studies.

In this study, the structural properties such as lattice parameter and bulk modulus of BBi have been calculated by using an ab initio pseudopotential method based on the density functional theory within the local density approximation. Using calculated lattice parameters, the cubic elastic constants, C_{11} , C_{12} and C_{44} , have been obtained under favour of volume-conserving tetragonal and monoclinic strains. The electronic band structure and density of states (DOS) of bulk BBi have been investigated and discussed in detail. All obtained bulk properties for BBi have been also compared with previous theoretical works. Although there are wide range of theoretical works related to bulk properties of BBi, its surface properties are totally paid no attention in the literature. However, the surface properties of a material play an important role to obtain the application areas in electronic and optical devices. Therefore, using

* Sadık Bağcı(sbagci@sakarya.edu.tr)

¹ Sakarya Üniversitesi Fen Edebiyat Fakültesi Fizik Bölümü Esentepe Kampüsü Serdivan / SAKARYA

bulk properties of BBi, we have obtained theoretical results of the relaxed atomic geometry of (110) surface of BBi, first time in the literature. The relaxed geometry of BBi(110) is similar with other III-V(110) surfaces: the cation-anion chain become tilted with the anions being raised. In addition to relaxed geometry of BBi(110), the surface electronic band structure and DOS have been also obtained and discussed. We have compared surface electronic states with projected bulk electronic spectrum to obtain surface electronic band structure of BBi(110) surface.

2. THEORY

The first principles calculations based on the density functional theory with the local density approximation have been performed by using the QUANTUM ESPRESSO package [19] in this study.

For the exchange and correlation effects were solved using local density approximation (LDA) [20,21]. The pseudopotentials for B and Bi are generated using a Troullier-Martin norm conserving scheme [22]. The 40 Ry cut off energy has been implemented to expand the electronic wave functions. We use ten special k points in the irreducible part of the Brillouin zone. We have used 15 atomic layers atomic slab and five atomic layers vacuum region to model a supercell geometry for the (110) surface of BBi. The Kohn-Sham equations have been used to achieve relaxation of atomic and electronic degrees of freedom [23]. For the relaxation of atomic geometry, all atoms were allowed to relax except the central plane of the atomic slab. The equilibrium positions of the atoms in the supercell geometry are ascertained by using the forces smaller than 0.1 mRy/au on the atoms. We have used nine special k points for surface calculations

The elastic constants for the ZB phase were extracted using the procedure discussed by Wang and Ye [7]. It is clearly known that three independent elastic constants namely C_{11} , C_{12} and C_{44} are used to describe elastic properties of a cubic crystal, basically. In this study we have used the volume-conserving tetragonal and monoclinic strains to calculate $C_{11}-C_{12}$ and C_{44} , respectively. After these calculations, the elastic constants of C_{11} and C_{12} have been obtained by using the relation $B=1/3(C_{11}+2C_{12})$. B is determined as bulk modulus in this relation.

3. RESULTS AND DISCUSSIONS

3.1. Structural and Electronic Properties of BBi

First of all, we have calculated total energy of the unit cell using different lattice parameters (a) to attain the

equilibrium lattice constant (a_0) of the zinc blende phase BBi. By means of this lattice parameter, the equilibrium bulk modulus (B) and its pressure derivative (B') have been also determined by Murnaghan equations [24]. Table 1 presents our calculated results for BBi, in comparison with available theoretical studies [1-4,9]. In this table, we have compared our obtained structural parameters with other previous theoretical studies. It can be seen from Table 1 that our results and previous studies are in good agreement to each other. We have also presented our calculated cubic elastic constants (C_{11} , C_{12} and C_{44}) and available previous theoretical values for BBi in this table. According to the our knowledge, BBi has never been synthesized, yet. Therefore, it is important to investigate the mechanical stability for zinc blende phase of BBi. It is clearly known that there are four requirements to determine mechanical stability in cubic crystal: $C_{11}>0$, $C_{44}>0$, $C_{11}-C_{12}>0$ and $C_{11}+2C_{12}>0$. It can be seen from Table 1 that, our obtained elastic constants obey these stability conditions similar with other previous theoretical results.

Table 1. Structural and elastic properties of BBi and their comparison with previous theoretical results.

Source (Method)	a (Å)	B (GPa)	B'	C_{11} (GPa)	C_{12} (GPa)	C_{44} (GPa)
This work (LDA)	5.365	87.70	4.09	122.16	70.47	85.97
Theory [1] (TBIP)	5.415	99.30	-	197.78	85.87	105.9
Theory [2] (GGA)	5.464	81.89	4.32	147.35	46.16	83.81
Theory [3] (LDA)	5.415	99.30	4.51	164.06	66.92	90.75
Theory [4] (LDA)	5.416	86.27	4.60	163.80	28.30	86.30
Theory [9] (GGA)	5.528	66.48	5.76	-	-	-

We have presented the calculated electronic band structure of BBi in Figure 1. The calculated overall band structures of BBi are similar with the obtained electronic band spectrum for the B-V compounds [25]. It can be seen from Fig. 1 that BBi has an indirect band gap with the valence band maximum locates at the Γ point and the conduction band minimum is along the Γ -

X direction close to the X point. The calculated band gap value of BBi is 0.56 eV.

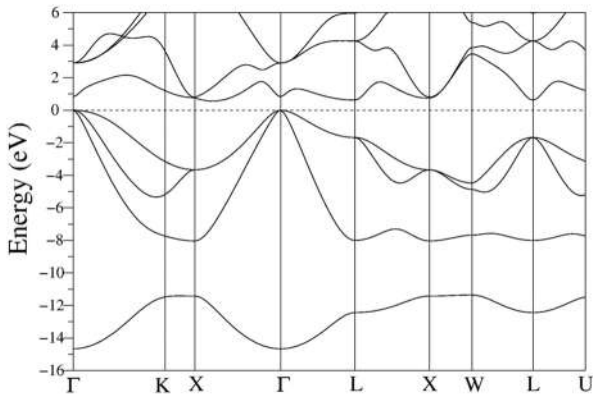


Figure 1. The electronic band structure for BBi.

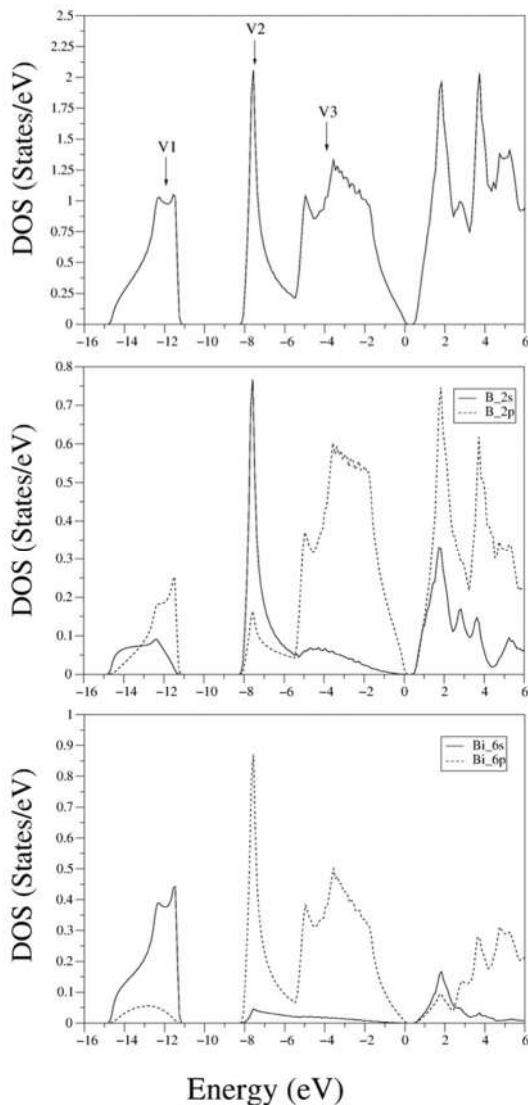


Figure 2. Total and partial density of states (DOS) for BBi.

The total and partial density of states (DOS) for BBi are presented in Figure 2, in order to explain all band characters, clearly. There are three distinct regions named V1, V2 and V3 in the total valence DOS. V1 is localized between -16 eV and -11 eV and consist of B-2s, B-2p and Bi-6s orbitals. V2 is the sharpest peak localized nearly -7 eV and the main contributions to this peak comes from the 6p bands of Bi atom and 2s bands of B atom. V3 is occurred by B and Bi p orbitals with the nearly same contributions. It can be seen from Fig. 2 that there is a strong p-p mixing in the V3 band which is mainly composed of Bi 6p hybridized with B 2p. For the conduction bands, main contribution to DOS comes from B 2p orbital hybridized with B 2s. As can be seen from Fig.2, there is also small contribution from Bi 6p orbital to DOS of conduction bands.

3.2. Structural and Electronic Properties of BBi(110) Surface

The clean cleaved (110) surface of zinc-blende materials retains the primitive (1×1) periodicity and the outermost layer of an ideal (110) surface contain equivalent cation and anion atoms. In our calculations, positions of the fourth layer atoms have been found to be very near the their classic bulk positions. Therefore, the relaxation of the (110) surface structure of BBi may be explained in terms of the tilt angles of the atomic chains in the three outermost layers. In Fig. 3, the schematic diagram of the relaxed top three layers of the BBi(110) surface and the key structural parameters have been presented. The relaxation of these surfaces is explained by the well known cation-anion chains become tilted with anions being raised, as displayed in Fig. 3.

Our computed surface structural parameters, defined in Fig. 3, are listed in Table 2 together with the previous theoretical results of other B-V(110) surfaces [25,26]. Our calculated surface bond length of top-layer atoms (2.285Å) is 2 % less than the calculated bulk bond length value of 2.323 Å. This shortening on the atomic bond length clearly indicates that interatomic bonding on BBi(110) surface is stronger than the corresponding bulk BBi bonding.

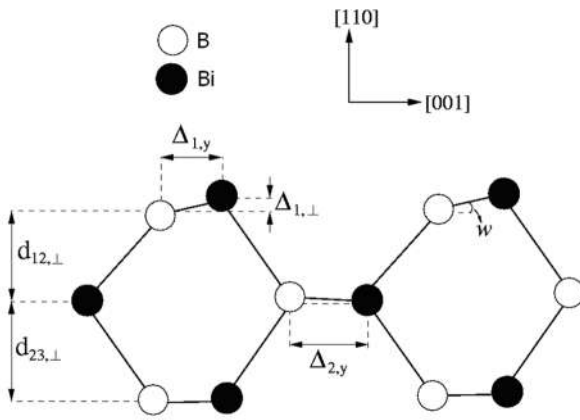


Figure 3. Schematic representation of the relaxed atomic positions indicating the key structural parameters for the cubic (110) surface of BBi.

The surface tilt angle of BBi(110) is found to be 27.4° . This means that the tilt angles of B-V(110) surfaces increases from BN(110) to BBi(110) as can be seen from Table 2. The another important surface structural parameter, the surface buckling $\Delta_{1,\perp}$ for BBi(110) is found to be 0.587 \AA which is convenient to raise from BN(110) towards BBi(110). Thus, these results are confirmed by Duke law says that $\Delta_{1,\perp}$ increase almost monotonically with the d_{sb} .

Table 2. Calculated structural parameters (in \AA) defined in Fig. 3 for BBi(110) surface and their comparison with other (110) surfaces of boron compounds.

BV(110) surface	$\Delta_{1,\perp}$	$\Delta_{1,y}$	$\Delta_{2,y}$	$d_{12,\perp}$	$d_{23,\perp}$	d_{sb}	ω
BBi(110)	0.58	1.131	1.337	1.30	1.72	2.28	27.4
)	7			6	2	5	$^\circ$
BSb(110)	0.54	1.102	1.421	1.28	1.67	2.22	26.5
o)[25]	9			4	4	4	$^\circ$
BAs(110)	0.48	0.99	1.161	1.177	1.52	2.00	26.1
o)[25]	5	2		4	7		$^\circ$
BP(110)	0.42	0.93	1.091	1.119	1.44	1.89	24.4
[25]	3	7		1	5		$^\circ$
BN(110)	0.21	0.66	0.87	1.12	1.30	1.44	17.9
) [26]	3	0	0	4	0	0	$^\circ$

The surface electronic band structure of BBi(110) is presented along the several symmetry directions of the surface Brillouin zone in Figure 4. In this figure, the solid curves are localized surface states for relaxed BBi(110) while the surface states in the fundamental gap shown as dotted curves are obtained from unrelaxed BBi(110) surface. It can be seen from Fig. 4 that the general pattern of surface electronic structure of BBi(110) is similar with other III-V(110) surfaces [25-28].

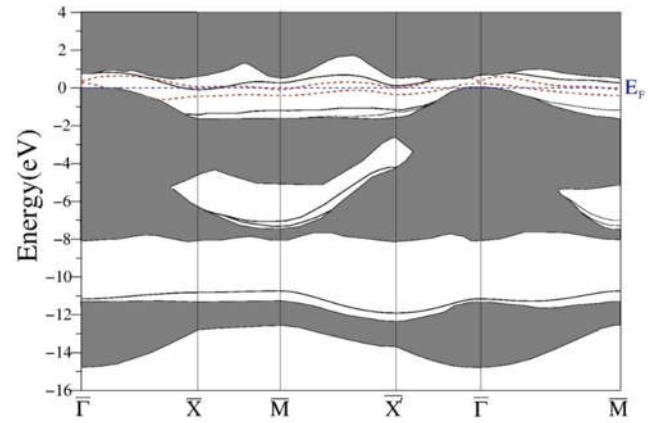


Figure 4. The electronic band structure of the BBi(110) surface. The projected bulk spectrum is shown by hatched regions. The localized surface states of the relaxed (solid curves) and unrelaxed (dotted red curves) BBi(110) surface. The Fermi level corresponds to 0 eV.

It is very important to note that BBi(110) surface is clearly metallic for both relaxed and unrelaxed structures with at least one surface state crossing the Fermi level, in contrast with bulk BBi is a narrow gap semiconductor. For the relaxed BBi(110) surface, there are five surface states in the gap regions between the projected bulk spectrum where the bulk states are not located in. Characters of these surface states are explained using electronic total and partial DOS shown in Figure 5. This figure presents total DOS for first three layer of BBi(110) and contribution of first, second and third layer atoms to total DOS, separately. The lowest surface state is derived from first and third layer Bi-6s orbitals, dominantly. Second layer Bi-6s and all three layer B-2p orbitals provide a small contribution to this surface state. There are two surface states in the stomach gap region. These surface states show strong dispersion along the $\bar{M} - \bar{X}'$ direction. These bands come from both Bi-6s and B-2s orbitals of all three layers. Other surface state with energy of -1 eV is nearly flat along the $\bar{X} - \bar{M} - \bar{X}'$ directions, and occurred by Bi-6p and B-2p orbitals with together. The highest surface state, in the fundamental gap between the valence band and the conduction band, are mainly due to all three layer B atoms.

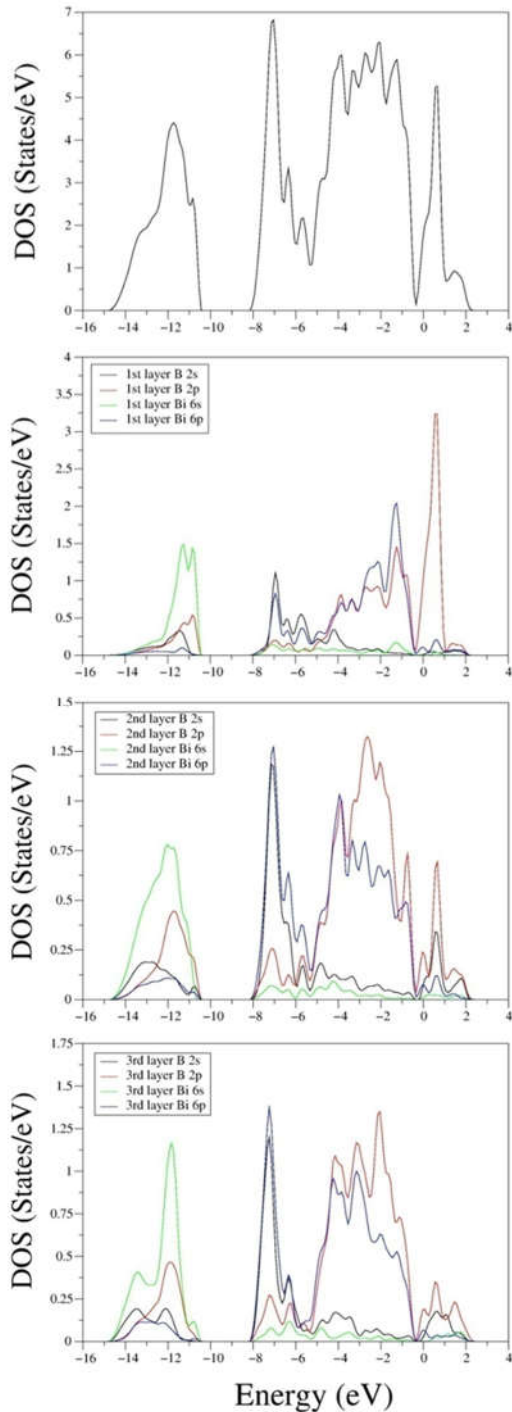


Figure 5. The total and partial density of states for first three layer of BBi(110) surface.

In addition, (110) surfaces of AlBi, GaBi and InBi are also metallic but only AlBi(110) has an insulator-metal transition with very narrow, nearly zero, energy band gap of bulk AlBi [29,30]. It is very interesting to note that BBi(110) surface shows more accurate transition from insulator to metal according to AlBi(110), because energy gap of bulk BBi clearly differ from zero. The first reason for insulator-metal transition for

BBi(110) is that the E_g value for surface become narrow according to corresponding bulk result of energy gap and this difference leads a transition when bulk value of energy gap is small enough. The second reason of this transition is binding characters of surface atoms are different from corresponding bulk ones.

4. CONCLUSION

In this study, the structural, elastic and electronic properties of zinc-blende BBi have been presented by applying local density approximation within the density functional theory. The structural parameters are in good agreement with previous theoretical results. The calculated elastic constants of BBi indicates that the zinc-blende phase of BBi is mechanically stable. The electronic band gap of BBi is also calculated as 0.56 eV. The structural and electronic properties of BBi(110) surface are obtained using our calculated bulk properties of BBi, The relaxed geometry of BBi(110) is similar with other III-V(110) surfaces: the cation-anion chain become tilted with the anions being raised. The tilt angle of BBi(110) is 27.4° very close to the corresponding tilt angles 26.1° for BAs(110) and 26.5° for BSb(110) surfaces. It is very important to note that BBi(110) surface is found to be metallic in contrast with bulk BBi is a narrow gap semiconductor. We have also presented total and partial electronic density of states for BBi(110) surface to explain metallic nature of this surface. At the end of our study, we have compared our surface electronic structure with other metallic (110) surfaces like AlBi, GaBi and InBi.

REFERENCES

- [1] S. Singh, M. Sarwan, Journal Of Optoelectronics and Advanced Materials 12 (2010) 2106.
- [2] S. Cui, W. Feng, H. Hu, Z. Feng, Y. Wang, Computational Materials Science 47 (2010) 968.
- [3] E. Deligöz, K. Colakoğlu, Y. O. Ciftci, H. Ozisik, Computational Materials Science 39 (2007) 533.
- [4] M. Ferhat, A. Zaoui, Physical Review B 73 (2006) 115107.
- [5] M. Ferhat, A. Zaoui, Appl. Phys. Lett. 88 (2006) 161902.
- [6] D. Madouri, M. Ferhat, Phys. Stat. Sol. (b) 242 (2005) 2856.
- [7] S. Q. Wang, H. Q. Ye, Phys. Stat. Sol. (b) 240 (2003) 45.
- [8] M. Ustundag, M. Aslan, B. G. Yalcin, Computational Materials Science 81 (2014) 471.

- [9] B. G. Yalcin, S. Bagci, M. Ustundag, M. Aslan, *Computational Materials Science* 98 (2015) 136.
- [10] S. Kaushik, D. Singh, G. Mishra, *Asian Journal of Chemistry* 24 (2012) 5655.
- [11] K. Amara, B. Soudini, D. Rached, A. Boudali, *Computational Materials Science* 44 (2008) 635.
- [12] B. G. Yalcin, M. Ustundag, M. Aslan, *Acta Physica Polonica A* 125 (2014) 574.
- [13] A. Belabbes, A. Zaoui, M. Ferhat, *J. Phys.: Condens. Matter* 20 (2008) 415221.
- [14] R. M. Wentzcovitch, K. J. Chang, M. L. Cohen, *Phys. Rev. B* 34 (1986) 1071.
- [15] A. Garcia, M. L. Cohen, *Phys. Rev. B* 47 (1993) 4215.
- [16] M. P. Surh, S. G. Louie, M. L. Cohen, *Phys. Rev. B* 43 (1991) 9126.
- [17] R. M. Wentzcovitch, M. L. Cohen, P. K. Lam, *Phys. Rev. B* 36 (1987) 6058.
- [18] O. A. Golikova, *Phys. Status Solidi A* 51 (1979) 11.
- [19] P. Giannozzi, S. Baroni, N. Bonini, M. Calandra, R. Car, C. Cavazzoni, et al., *J. Phys.: Condens. Matter* 21 (2009) 395502.
- [20] D. M. Ceperley and B. J. Alder, *Phys. Rev. Lett.* 45 (1980) 566.
- [21] J. P. Perdew and Y. Wang, *Phys. Rev. B* 45 (1992) 13244.
- [22] N. Troullier, J. L. Martins, *Phys. Rev. B* 43 (1991) 1993.
- [23] W. Kohn and L. J. Sham, *Phys. Rev.* 140 (1965) A1133.
- [24] F. D. Murnaghan, *Proc. Natl. Acad. Sci. USA* 50 (1944) 697.
- [25] S. Bağcı, S. Duman, H. M. Tütüncü and G. P. Srivastava, *Phys. Rev. B* 79 (2009) 125326.
- [26] S. Bağcı, S. Duman, H. M. Tütüncü and G. P. Srivastava, *G. Uğur, Diam. Relat. Mater.* (2006) 1161.
- [27] A. Umerski, G. P. Srivastava, *Phys. Rev. B* 51 (1995) 2334.
- [28] H. A. Badehian, H. Salehi, *Surf. Sci.* 628 (2014) 1.
- [29] W. Liu, W. T. Zheng, Q. Jiang, *Phys. Rev. B* 75 (2007) 235322.
- [30] S. Q. Wang, H. Q. Ye, *Phys. Rev. B* 66 (2002) 235111.

	SAKARYA UNIVERSITY JOURNAL OF SCIENCE		 SAKARYA UNIVERSITY
	e-ISSN: 2147-835X http://www.saujs.sakarya.edu.tr		
	<u>Received</u> 13-07-2018 <u>Accepted</u> 03-09-2018	<u>Doi</u> 10.16984/saufenbilder.443765	

Application of Monte Carlo Method for Gamma ray Attenuation Properties of Lead Zinc Borate Glasses

Urkiye AKAR TARIM¹, Orhan GÜRLER

Abstract

This work aims to introduce an useful computational model, based in Monte Carlo simulation, which can be used in practical application, and this paper presents values determined using a Monte Carlo algorithm for linear attenuation coefficient of lead zinc borate glasses with different percentages of PbO. The simulation results have been verified with predictions from the XCOM program in the studied energy region from 1 keV to 2000 keV and experimental results. Thus, this verification indicated that this research method can be followed to determine the interaction and attenuation of gamma rays with the several energies in different materials. Also, the values of mean free path and the half-value layer were calculated using the values of the linear attenuation coefficient. The dependence of these radiation shielding parameters on the energy of impinging gamma ray and the ratio of substances changes has been examined.

Keywords: Monte Carlo, gamma ray, attenuation, glass, shielding

1. INTRODUCTION

Monte Carlo method has for long been accepted as the most precise method for all the calculations that require the information of the probability distribution of responses of uncertain systems to uncertain inputs [1]. By the Monte Carlo technique, the works on particles' transport in materials can be performed successfully, with the knowledge of the elementary collision processes of particles. Monte Carlo method enables the simulation of particle transport processes with a physical reality. In these simulations, the traced particle is emitted according to distributions that describe the source. It travels in a path that determined by a probability distribution depending on the total interaction cross section and arrives to the site of a collision. According to the corresponding differential cross section, it scatters into another direction by an another energy. This

process is continued until the particle is absorbed in slowing down material or leaves the geometry under consideration. Interested physical quantities can be achieved by calculations that use the average over a set of Monte Carlo particle histories. The statistical uncertainties of the calculations using simulation outputs depend on the number of simulated particle histories [2].

Monte Carlo simulation is the most reliable way to predict the effects of a gamma ray beam. Because fast computers are available, many codes have been developed that allow a detailed simulation of the passage of radiation through matter and provide information about attenuation of it in matter [3]. Moreover, it is very flexible, there is virtually no limit to the analysis. It can generally be easily extended and developed as required [4].

The linear attenuation coefficient is one of the important characteristics that need to be studied and determined prior to using a material in radiation applications since the accurate

¹ uakar@uludag.edu.tr

attenuation coefficient values of materials are a very essential parameter in nuclear and radiation physics, radiation dosimetry, spectrometry, biological, medical, agricultural, environmental and industrial [5]. It qualifies the diffusion and penetration of gamma radiation in matter and represents the probability per unit path length of gamma radiation that the gamma ray will have an interaction with absorber atom. It is the basic parameter to acquire several other parameters related to dosimetry and shielding, such as mass-energy absorption coefficient, molecular, atomic and electronic cross-sections, effective atomic numbers, electron densities, half-value layer and tenth-value layer thickness for shielding effectiveness [6].

Monte Carlo technique that considered as a powerful and reliable computational tool, was used in many studies regarding the characterization of several shielding materials [7-12]. In the present work, a computer simulation program based on Monte Carlo method was written to be as virtual experimental system, instead of the real experimental system, concerning evaluation of attenuation properties for studied glass materials.

2. MATERIALS AND METHOD

In this paper, shielding properties of lead zinc borate glasses (ZnO-PbO-B₂O₃) have been investigated by Monte Carlo technique. Chemical compositions and densities of studied glass samples [13] are shown in Table 1. Increasing the lead oxide (PbO) content of glass sample causes the increase in glass density as it is clear from this table.

Table 1. Chemical compositions of the studied glass samples

Sample No	Compositions (wt %)			Density (g cm ⁻³)
	B ₂ O ₃	ZnO	PbO	
1	70	10	20	3.675
2	50	10	40	5.088
3	25	25	50	5.917
4	30	10	60	6.212
5	25	5	70	6.650

Simulations for determination of gamma ray shielding properties of the samples were performed for gamma ray energies of 80, 356, 662, 1173 and 1332 keV. Outcomes of the simulation code were used to calculate the values of linear

attenuation coefficient, half-value layer and mean free path, three of shielding properties, for the investigated samples. The equation below which is based on the Lambert-Beer law was used to calculate the linear attenuation coefficients (μ) of the samples.

$$\mu = \frac{1}{t_s} \ln \left(\frac{I_0}{I} \right) \quad (1)$$

where I_0 and I are the intensities of incident and transmitted gamma rays, respectively, and t_s is thickness of the attenuating sample. The transmitted gamma ray intensity was the outcome of the code. 1×10^7 gamma rays at points in the collimated beam were impinged on the glass sample and followed in this target. Tracking the gamma rays and attenuation of them in the target was detailed in our previous study [14]. In our algorithm, the free path length of each incident gamma ray is sampled according to an exponential distribution. Therefore, the cross sections of attenuating materials were derived from the XCOM program from NIST [15] and the relation given in Eq. (2) for fitting was written into the code for the calculation of cross sections (CS) for photoelectric effect and Compton scattering of glass samples for the energy range 10–2000 keV.

$$CS = \exp(a + bx + cx^2 + dx^3 + ex^4) \quad (2)$$

where x is the natural logarithm of the gamma ray energy and “a”, “b”, “c”, “d” and “e” are the parameters for fitting photoelectric effect and Compton scattering cross sections. These parameters are acquired separately for each of glass samples.

In algorithm, gamma rays that arrive the detector are counted and this value is defined as the transmitted intensity (I) of gamma rays. The slope of a linear fit of $\ln(I_0/I)$ versus thickness of sample target (see Fig. 1) is obtained and this value of slope is utilized in Eq. (1).

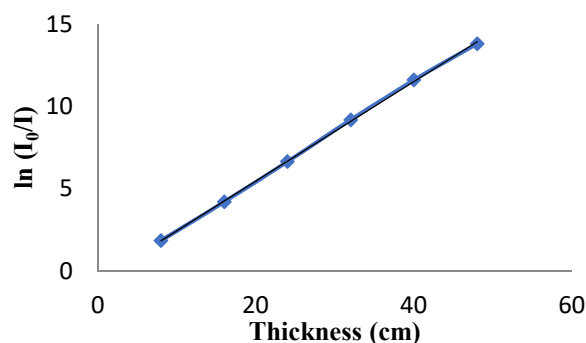


Figure 1. Plot of $\ln(I_0/I)$ versus attenuator material thickness (for Sample 3, %50 PbO, and 1332 keV gamma rays)

By using the linear attenuation coefficients achieved by the results from Monte Carlo simulations, half-value layer values were obtained for all samples by using the Eq. (3).

$$HVL = \frac{0.693}{\mu} \quad (3)$$

On the other hand, mean free path (MFP) values were calculated by the following relation that relates to linear attenuation coefficient:

$$MFP = \frac{1}{\mu} \quad (4)$$

3. RESULTS AND DISCUSSION

In this paper, we present a calculation method based on Monte Carlo algorithm to evaluate gamma ray attenuation properties of materials. Simulations were carried out using collimated beam of gamma rays with five different energies, 80, 356, 662, 1173 and 1332 keV.

The results for linear attenuation coefficient of glass samples obtained by simulation outputs have been successfully verified with experimental results [13] and theoretical ones [15]. The current calculated results and the published ones, experimental [13] and theoretical [15], are in good agreement as it is clear from Table 2. Small deviations observed between simulation results and literature values for all glass samples can be due to the experimental errors or utilization of fit function of cross-sections for glass samples in the written code.

Table 2. The linear attenuation coefficients of glass samples with different weight fraction of PbO at different gamma ray energies

Energy		Linear attenuation coefficients (cm ⁻¹)				
		Sample 1 (%20 PbO)	Sample 2 (%40 PbO)	Sample 3 (%50 PbO)	Sample 4 (%60 PbO)	Sample 5 (%70 PbO)
80 keV	Monte Carlo	2.0390	4.8298	7.1207	7.9735	9.4431
	Experiment	---	---	---	---	---
	XCOM	2.0830	4.7334	7.0176	8.0383	9.6492
356 keV	Monte Carlo	0.4587	0.8346	1.0377	1.1957	1.3793
	Experiment	---	---	---	---	---
	XCOM	0.4876	0.8516	1.0942	1.2551	1.4589
662 keV	Monte Carlo	0.2938	0.4375	0.5212	0.5531	0.6452
	Experiment	0.3072	0.4536	0.5399	0.5918	0.6582
	XCOM	0.2985	0.4426	0.5297	0.5762	0.6369
1173 keV	Monte Carlo	0.2097	0.2928	0.3336	0.3631	0.3912
	Experiment	0.2161	0.3082	0.3616	0.3850	0.4274
	XCOM	0.2127	0.2970	0.3449	0.3657	0.3939
1332 keV	Monte Carlo	0.1957	0.2732	0.3021	0.3379	0.3612
	Experiment	0.2049	0.2845	0.3283	0.3468	0.3787
	XCOM	0.1983	0.2754	0.3191	0.3374	0.3625

It is clear from Table 2 that the linear attenuation coefficient increases with the increasing density of the glass samples for both gamma ray energies.

Half-value layer (HVL) and mean free path (MFP) thicknesses of studied samples were calculated as being parameters for helping to quantify both the penetrating capability of gamma rays and the penetration through specified objects and plotted against the lead oxide content of them for the studied gamma ray energies in Figures 2 and 3. When HVL values are known, the penetration through other thicknesses can be easily determined.

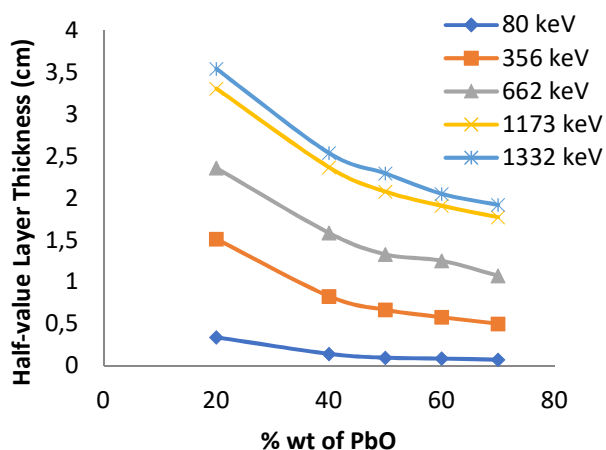


Figure 2. The half-value layer of glass samples versus lead oxide content for different gamma ray energies

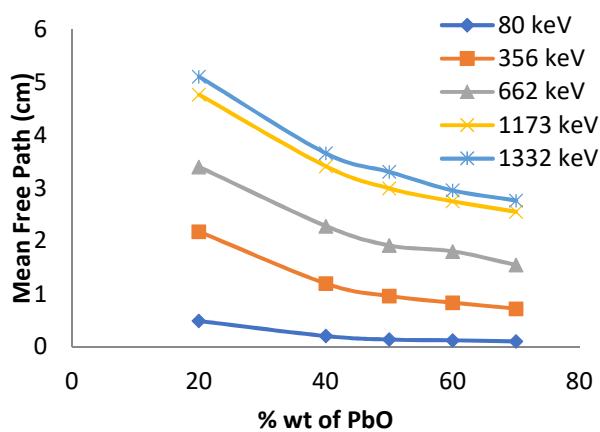


Figure 3. The mean free path of glass samples versus lead oxide content for different gamma ray energies

In Figures 2 and 3, both the half-value layer and the mean free path increase with the increase in the energy of gamma rays and decrease with increasing the lead oxide content, as an expected result.

All the calculations performed in the paper are required for the researchers who work with gamma radiation. Obtained quantities describe the shielding effectiveness of studied samples. Since

the choice of shielding material and determination of thickness of shielding material are dependent on incident gamma ray energy, we present each quantity depending on the energy.

4. CONCLUSIONS

The aim of this study has been to provide a computational tool that would perform calculations of important physical quantities for gamma ray attenuation. Designed program simulates gamma ray interactions in matter. Linear attenuation coefficient, HVL and MFP values for glasses with different composition and densities were calculated for energies of 80, 356, 662, 1173 and 1332 keV. It can be concluded from this work that the effect of gamma rays can be minimized by increasing material density, indirectly reducing the materials' HVL and TVL thickness. On the other hand, the values of linear attenuation coefficient (μ) decrease with increasing gamma ray energy but the mean free path and half-value layer increase with increase in the energy of gamma rays. Observed good agreement among Monte Carlo simulation, XCOM program and experimental data indicates that the algorithm may be employed to make calculations for characterization of several shielding materials.

Acknowledgement

Authors thank to Professor Emin N. Ozmutlu for his fit program and guidance.

References

- [1] J. E. Hurtado, and A. H. Barbat, "Monte Carlo Techniques in Computational Stochastic Mechanics," *Archives of Computational Methods in Engineering*, vol. 5, no. 1, pp. 3-30, 1998.
- [2] I. Kawrakow, "Accurate condensed history Monte Carlo simulation of electron transport. I. EGSnrc, the new EGS4 version," *Medical Physics*, vol. 27, no. 3, pp. 485-498, 2000.
- [3] F. Arqueros and G. D. Montesinos, "A simple algorithm for the transport of gamma rays in a medium," *American Journal of Physics*, vol. 71, no. 1, pp. 38-45, 2003.

- [4] Applied R&M Manual for Defence Systems Part D - Supporting Theory, Chapter 4:Monte-Carlo Simulation.
- [5] A. N. Mohammed, M. S. Karim, H. H. Daroysh, and L. Y. Abbas, "Monte Carlo assessment of gamma ray attenuation properties for MCP-96 alloy using transmission technique," *The Fifth Scientific Conference of the College of Science University of Kerbala*, pp. 95-104, 2017.
- [6] M. E. Medhat and V. P. Singh, "Geant4 Monte Carlo code application in photon interaction parameter of composite materials and comparison with XCOM and experimental data," *Indian Journal of Pure and Applied Physics*, vol. 54, pp. 137-143, 2016.
- [7] O. Ozyurt, N. Altinsoy, S. I. Karaaslan, A. Bora, B. Buyuk, and I. Erk, "Calculation of gamma ray attenuation coefficients of some granite samples using a Monte Carlo simulation code," *Radiation Physics and Chemistry*, vol. 144, pp. 271-275, 2018.
- [8] D. Han, W. Kim, S. Lee, H. Kim, and P. Romer, "Assessment of gamma radiation shielding properties of concretecontainers containing recycled coarse aggregates," *Construction and Building Materials*, vol. 163, no. 28, pp. 122-138, 2018.
- [9] R. Bagheri, S. P. Shirmardi, and R. Adeli, "Study on gamma-ray shielding characteristics of lead oxide, barite, and boron ores using MCNP-4C Monte Carlo code and experimental data," *Journal of Testing and Evaluation*, vol. 45, no. 6, 2259-2266, 2017.
- [10] L. F. Pirez and M. E. Medhat, "Different methods of mass attenuation coefficient evaluation: Influences in the measurement of some soil physical properties," *Applied Radiation and Isotopes*, vol. 111, pp. 66-74, 2016.
- [11] A. M. El-Khayatt, A. M. Ali, V. P. Singh, and N. M. Badiger, "Determination of mass attenuation coefficient of low-Z dosimetric materials," *Radiation Effects and Defects in Solids*, vol. 169, no. 12, pp. 1038-1044, 2014.
- [12] S. J. Stankovic, R. D. Ilic, K. Jankovic, D. Bojovic, and B. Loncar, "Gamma radiation absorption characteristics of concrete with components of different type materials," *Acta Physica Polonica A*, vol. 117, no. 5, pp. 812-816, 2010.
- [13] S. Y. El-Kameesy, S. A. El-Ghany, M. A. E. Azooz, and Y. A. A. El-Gammam, "Shielding properties of lead zinc borate glasses," *World Journal of Condensed Matter Physics*, vol. 3, pp. 198-202, 2013.
- [14] O. Gurler and U. Akar Tarim, "An investigation on determination of attenuation coefficients for gamma-rays by Monte Carlo method," *Journal of Radioanalytical and Nuclear Chemistry* vol. 293, pp. 397-401, 2012.
- [15] M. J. Berger, J. H. Hubbell, S. M. Seltzer, J. Chang, J. S. Coursey, R. Sukumar, D. S. Zucker, and K. Olsen, XCOM: photon cross sections database, NIST standard reference database 8 (XGAM), 2010.

	SAKARYA UNIVERSITY JOURNAL OF SCIENCE		 SAKARYA UNIVERSITY
	e-ISSN: 2147-835X http://www.saujs.sakarya.edu.tr		
	<u>Received</u> 19-07-2018 <u>Accepted</u> 05-09-2018	<u>Doi</u> 10.16984/saufenbilder.443551	

A Sequence Bounded Above by the Lucas Numbers

Engin Özkan¹ Ali Aydoğdu^{*2} Aykut Göçer¹

Abstract

In this work, we consider the sequence whose n^{th} term is the number of h -vectors of length n . The set of integer vectors $E(n)$ is introduced. For $n \geq 2$, the cardinality of $E(n)$ is the n^{th} Lucas number L_n is showed. The relation between the set of h -vectors $L(n)$ and the set of integer vectors $E(n)$ is given.

Keywords: Cardinality, h -vectors, Hilbert function, Lucas numbers

1. Introduction

Firstly, we give the well-known definitions of the Fibonacci and Lucas numbers. The Fibonacci numbers F_n are the terms of the sequence 1,1,2,3,5,8,13,21,34,55,89,... . Every Fibonacci number, except the first two, is the sum of the two previous Fibonacci numbers. The numbers F_n satisfy the second order linear recurrence relation.

$$F_n = F_{n-1} + F_{n-2}, \quad n = 2,3,4, \quad (1)$$

with initial values $F_0 = 0, F_1 = 1$.

The Lucas numbers L_n are defined

$$L_n = L_{n-1} + L_{n-2}, \quad n = 2,3,4, \dots \quad (2)$$

with initial conditions $L_0 = 2, L_1 = 1$. The first a few Lucas numbers are 2,1,3,4,7,11,18,29,47,76,...

Hilbert functions of graded rings are more convenient for many applications and are known to relate to many different subjects such as dimensions, multiplicity and Betti numbers (see: Bruns and Herzog, [1]). In [2], Enkoskoy and Stone introduced recursion formulas related to Hilbert functions. They showed the n^{th} term of

sequence, whose n^{th} term is the number of h -vectors of length n , is bounded above by the n^{th} Fibonacci number. Ozkan et al. [4] introduced the cardinality of the M -sequence of length n is bounded above by the n^{th} Lucas number.

The aim of this paper is to show the sequence defined by the number of h -vectors of length n is bounded above by the sequence of Lucas numbers. This paper is organized as follows. In Section 2 we give some concepts of h -vectors. Section 3 presents main results of this paper.

2. Materials and Methods

We first give some necessary background on Hilbert functions and h -vectors.

Let $R = k[x_1, x_2, \dots, x_n]$ be a polynomial ring over a field k with the standard grading. In particular, $\deg x_i = 1$ for $1 \leq i \leq n$. If I is a graded ideal, the quotient ring R/I is also graded and we denote by $(R/I)_t$ the k vector space of all degree t homogeneous elements of R/I . The Hilbert function $H_{R/I}: \mathbb{Z}_{\geq 0} \rightarrow \mathbb{Z}_{\geq 0}$ is defined to be the k vector space dimension of each graded

¹ Erzincan Binali Yıldırım University, Faculty of Arts and Sciences, Department of Mathematics, Erzincan, Turkey.

^{*} Corresponding Author

² Beykent University, Faculty of Arts and Sciences, Department of Mathematics, İstanbul, Turkey.

component, i.e. $H_{R/I}(t) := \dim_k(R/I)_t$. If the Krull dimension of the graded quotient ring is zero, there exists an $s \geq 0$ such that $H_{R/I}(s) \neq 0$ but $H_{R/I}(t) = 0$ for all $t > s$. In this case the h -vector of R/I is defined as

$$h(R/I) = (H_{R/I}(0), H_{R/I}(1), H_{R/I}(2), \dots, H_{R/I}(s)) \quad (3)$$

Thus the h -vector of R/I has finitely many non-zero entries. The length of R/I is the k vector space dimension of R/I , denoted $\lambda(R/I)$. In particular $\lambda(R/I) = \sum_{i=0}^s H_{R/I}(s)$. Throughout this paper we will refer to $\lambda(R/I)$ as the length of $h(R/I)$.

The sequence $\{l(n)\}_{n \geq 1}$ is defined by the number of h -vectors of length n . In particular, for $n \geq 1$ we define

$$L(n) = \{h = (h_0, h_1, \dots) \mid h \text{ is an } h\text{-vector and } \sum_i h_i = n\} \quad (4)$$

and set $l(n) = |L(n)|$.

Using Macaulay's Theorem, the authors of [2] constructed the h -vectors of length at most 7. The h -vectors of length at most 6 is given in Table 1. We write $t_0 t_1 \dots t_s$ for the h -vector (t_0, t_1, \dots, t_s) .

Table 1

λ	1	2	3	4	5	6
	1	11	111	1111	11111	111111
			12	121	1211	12111
				13	122	1221
					131	123
					14	1311
						132
						141
						15
Total	1	1	2	3	5	8

Definition 2.1. [3] For $n \geq 1$, the set of integer vectors $B(n)$ is defined recursively as follows:

1. $B(1) = \{(1)\}$,
2. $B(2) = \{(1,1)\}$,

3. For $n \geq 3$ define $B(n) := C(n) \cup D(n)$ where

$$C(n) := \{(1, t_1, \dots, t_s, 1) \mid (1, t_1, \dots, t_s) \in B(n-1)\}$$

$$D(n) := \{(1, t_1, \dots, t_s + 1) \mid (1, t_1, \dots, t_s) \in B(n-1), \text{ with } t_s - 1 > 1 \text{ or } s = 1\}.$$

Theorem 2.2. [3] The cardinality of $B(n)$ is the n^{th} Fibonacci number F_n .

Theorem 2.3. [2] For all $n \geq 1$, $L(n) \subseteq B(n)$. In particular the sequence of the cardinality of $L(n)$ is bounded above by the Fibonacci sequence.

Definition 2.4. For $n \geq 1$, the set of integer vectors $E(n)$ is defined recursively as follows:

1. $E(1) = \{(1)\}$,
2. $E(2) = \{(1,1,1), (1), (1,2)\}$,
3. For $n \geq 3$ define $E(n) := R(n) \cup S(n)$ where

$$R(n) := \{(1, t_1, \dots, t_s, 1) \mid (1, t_1, \dots, t_s) \in E(n-1)\},$$

$$S(n) := \{(1, t_1, \dots, t_s + 1) \mid (1, t_1, \dots, t_s) \in E(n-1), \text{ with } t_{s-1} > 1 \text{ or } s = 1\}.$$

We set $e(n) = |E(n)|$.

Remark 2.5. It is worth noticing that the sets $R(n)$ and $S(n)$ of Definition 2.4 form a set partition of $E(n)$.

The first few sets $E(n)$ are

$$E(1) = \{(1)\},$$

$$E(2) = \{(1,1,1), (1), (1,2)\},$$

$$E(3) = \{(1,1,1,1), (1,1), (1,2,1), (1,3)\},$$

$$E(4) = \{(1,1,1,1,1), (1,1,1), (1,2,1,1), (1,2,2), (1,3,1), (1,2), (1,4)\},$$

$$E(5) = \{(1,1,1,1,1,1), (1,1,1,1,1), (1,2,1,1,1),$$

$$(1,2,2,1), (1,3,1,1), (1,2,1), (1,4,1)$$

$$(1,2,3), (1,3,2), (1,3), (1,5)\}.$$

In Table 2, the integer vectors of length at most 6 and cardinality of integer sets is given. We write $t_0 t_1 \dots t_s$ for the h -vector (t_0, t_1, \dots, t_s) .

Table 2

n	1	2	3	4	5	6
	1	111	1111	11111	111111	1111111
		1	11	111	1111	11111
		12	121	1211	12111	121111
			13	122	1221	12211
				12	1311	1231
				14	121	1321
					141	1411
					123	1211
					132	131
					13	151
					15	1222
						124
						133
						142
						122
						14
						16
Total	1	3	4	7	11	18

3. Main Results

Theorem 3.1. The $e(n)$ is the n^{th} Lucas number L_n , for $n \geq 2$.

Proof. We shall prove by induction that, for all $n \geq 1$. When $n = 1$, the claim is true, since $e(1) = L_1 = 1$. Since $e(2) = L_2 = 3$, the claim is true for $n = 2$.

Suppose the claim is true for all $n = s$, that is $e(s) = L_s$. Then

$$e(s) + e(s - 1) = L_s + L_{s-1} = L_{s+1}. \tag{5}$$

Thus the claim holds for $n = s + 1$, that is $e(s + 1) = |E(s + 1)| = L_{s+1}$.

Theorem 3.2. For all $n \geq 2$, $L(n + 1) \subseteq E(n)$. In particular, the sequence $l(n + 1)$ is bounded from above by the Lucas sequence.

Proof. Note that $L(n)$ is the set of all integer vectors $(1, t_1, \dots, t_s)$ with $1 + t_1 + t_2 + \dots + t_s =$

$n + 1$ and the property that if $t_i = 1$ then $t_j = 1$ for all $j \geq i$. We will prove this by induction for all $n \geq 2$. For $n = 2$, the claim is true, since $L(3) \subseteq E(2)$:

$$L(3) = \{(1,1,1), (1,2)\} \quad \text{and} \quad E(2) = \{(1,1,1), (1), (1,2)\}.$$

When $n = 3$, the claim is true, since $L(4) \subseteq E(3)$:

$$L(4) = \{(1,1,1,1), (1,2,1), (1,3)\} \quad \text{and} \quad E(3) = \{(1,1,1,1), (1,1), (1,2,1), (1,3)\}.$$

Suppose $L(k + 1) \subseteq E(k)$, for $n = k$. We have to show that the claim is true for $n = k + 1$, that is, $L(k + 2) \subseteq E(k + 1)$.

Denote the number of element of a set A by $s(A)$. Then

$$L(k) \subseteq E(k - 1) \Rightarrow s(L(k)) \leq s(E(k - 1)),$$

$$L(k + 1) \subseteq E(k) \Rightarrow s(L(k + 1)) \leq s(E(k)),$$

Since $L(k) \cap L(k + 1) = \emptyset$, this also gives $s(L(k) \cup L(k + 1)) = s(L(k)) + s(L(k + 1))$.

Since $L(k) \subseteq E(k - 1)$ and $L(k + 1) \subseteq E(k)$, we set

$$L(k) \cup L(k + 1) \subseteq E(k - 1) \cup E(k). \tag{7}$$

Similarly, since $E(k - 1) \cap E(k) = \emptyset$, we get

$$s(E(k - 1) \cup E(k)) = s(E(k - 1)) + s(E(k)).$$

We then get from (7)

$$s(L(k)) + s(L(k + 1)) \leq s(E(k - 1)) + s(E(k)). \tag{8}$$

Hence

$$s(L(k)) + s(L(k + 1)) = s(L(k + 2)),$$

$$s(E(k - 1)) + s(E(k)) = s(E(k + 1)).$$

We know $s(L(k + 2)) \leq s(E(k + 1))$. Hence $L(k + 2) \subseteq E(k + 1)$.

Theorem 3.3. For all $n \geq 2$, we have the relation $E(n) \setminus L(n + 1) = L(n - 1)$.

Proof. We will prove this by induction for all $n \geq 2$. When $n = 2$, the claim is true, since $E(2) \setminus L(3) = L(1)$. For $n = 3$, the claim is true, since

$E(3) \setminus L(4) = L(2)$. Suppose that the claim is true for $n = s$, that is $E(s) \setminus L(s + 1) = L(s - 1)$.

We have to show that the claim is true for $n = s + 1$, that is, $E(s + 1) \setminus L(s + 2) = L(s)$.

The identity $E(s) \setminus L(s + 1) = L(s - 1)$ implies $E(s) = L(s - 1) \cup L(s + 1)$. From the last equality, it can be easily seen that

$$E(s + 1) \setminus L(s + 2) = L(s). \tag{9}$$

Example 3.4.

$$\begin{aligned} E(4) \setminus L(5) &= \{(1,1,1,1,1), (1,1,1), (1,2,1,1), \\ &\quad (1,2,2), (1,3,1), (1,2), (1,4)\} \setminus \{(1,1,1,1,1), \\ &\quad (1,2,1,1), (1,2,2), (1,3,1), (1,4)\} \\ &= \{(1,1,1), (1,2)\} = L(3) \end{aligned}$$

Corollary 3.5. For all $n \geq 2$, we have $|E(n)| - |B(n + 1)| = |B(n - 1)|$.

References

- [1] W. Bruns and J. Herzog, "Cohen-Macaulay Rings, in: Cambridge Studies in Advanced Mathematics, vol 39," Cambridge University Press, Cambridge, 1993.
- [2] T. Enkosky and B. Stone, "Sequence defined by h-vectors," Eprint arXiv:1308.4945.
- [3] T. Enkosky, B. Stone, "A sequence defined by M-sequences," *Discrete Mathematics*, vol. 333, pp. 35-38, 2014.
- [4] E. Ozkan, A. Geçer and İ. Altun, "A new sequence realizing Lucas numbers and the Lucas Bound," *Electronic Journal of Mathematical Analysis and Applications*, vol. 5, no. 1, 148-154, 2017.

	SAKARYA UNIVERSITY JOURNAL OF SCIENCE		 SAKARYA UNIVERSITY
	e-ISSN: 2147-835X http://www.saujs.sakarya.edu.tr		
	<u>Received</u> 19-07-2018 <u>Accepted</u> 16-08-2016	<u>Doi</u> 10.16984/saufenbilder.445147	

Asymptotically $\mathcal{J}_{\sigma\theta}$ -statistical equivalence of sequences of sets defined by a modulus functions

Nimet P. Akın¹, Erdinç Dündar^{*2}, Uğur ULUSU³

Abstract

We investigate the notions of strongly asymptotically $\mathcal{J}_{\sigma\theta}$ -equivalence, f -asymptotically $\mathcal{J}_{\sigma\theta}$ -equivalence, strongly f -asymptotically $\mathcal{J}_{\sigma\theta}$ -equivalence and asymptotically $\mathcal{J}_{\sigma\theta}$ -statistical equivalence for sequences of sets. Also, we investigate some relationships among these concepts.

Keywords: asymptotic equivalence, modulus function, \mathcal{J} -convergence, lacunary \mathcal{J} -Invariant equivalence

1. INTRODUCTION

Recently, concepts of statistical convergence and ideal convergence were studied and dealt with by several authors. Fast [1] and Schoenberg [2] independently introduced statistical convergence and this concept studied by many authors. Lacunary statistical convergence was defined by Fridy and Orhan [3] using the notion of lacunary sequence $\theta = \{k_r\}$. Kostyrko et al. [4] introduced and dealt with the idea of \mathcal{J} -convergence. \mathcal{J} -statistical convergence and \mathcal{J} -lacunary statistical convergence were introduced by Das et al. [5].

Several authors studied some convergence types of the notion of set sequences. Nuray and Rhoades [6] defined statistical convergence of set sequences. Lacunary statistical convergence of set sequences was introduced by Ulusu and Nuray [7] and they gave some examples and investigated some properties of this notion. \mathcal{J} -convergence of set sequences was studied by Kişi and Nuray [8]. On \mathcal{J} -lacunary statistical convergence of set sequences was studied by Ulusu and Dündar [9]. Also, after these important studies, the notions of statistical convergence, ideal convergence and \mathcal{J} -statistical

convergence of set sequences and some properties was studied and dealt with by several authors.

Several authors including Raimi [10], Schaefer [11], Mursaleen [12,13], Savaş [14,15], Mursaleen and Edely [16], Pancaroğlu and Nuray [17,18] and some authors have studied invariant convergent sequences. The notion of strong σ -convergence was defined by Savaş [16]. Savaş and Nuray [19] defined the ideas of σ -statistical convergence and lacunary σ -statistically convergence and gave some inclusion relations. Then, Pancaroğlu and Nuray [17] introduced the ideas of $\sigma\theta$ -summability and the space $[V_{\sigma\theta}]_q$. Recently, Ulusu and Nuray [20] defined the notions of $\sigma\theta$ -uniform density of subsets A of \mathbb{N} , $\mathcal{J}_{\sigma\theta}$ -convergence and investigated relationships between $\mathcal{J}_{\sigma\theta}$ -convergence and lacunary invariant convergence also $\mathcal{J}_{\sigma\theta}$ -convergence and $[V_{\sigma\theta}]_p$ -convergence.

Asymptotically equivalent and asymptotic regular matrices were presented by Marouf [21]. Patterson and Savaş [22,23] introduced asymptotically lacunary statistically equivalent sequences and also asymptotically $\sigma\theta$ -statistical equivalent sequences. Ulusu and Nuray [24] defined the ideas of some basic asymptotically equivalence for sequences of sets.

¹ Afyon Kocatepe University, Faculty of Education, Department of Mathematics and Science Education, Afyonkarahisar - npancaroglu@aku.edu.tr

* Corresponding Author

² Afyon Kocatepe University, Faculty of Science and Literature, Department of Mathematics, Afyonkarahisar - edundar@aku.edu.tr

³ Afyon Kocatepe University, Faculty of Science and Literature, Department of Mathematics, Afyonkarahisar - ulusu@aku.edu.tr

Pancaroglu et al. [25] studied asymptotically $\sigma\theta$ -statistical equivalent sequences of sets. Ulusu and Gülle [26] introduced asymptotically \mathcal{J}_σ -equivalence of sequences of sets.

Nakano [27] introduced modulus function. Maddox [28], Pehlivan and Fisher [29], Pancaroglu and Nuray [30,31] and several authors define some new concepts and give inclusion theorems using a modulus function f . Kumar and Sharma [32] studied \mathcal{J}_θ -equivalent sequences using a modulus function f . Kişi et al. [33] introduced f -asymptotically \mathcal{J}_θ -equivalent set sequences. P. Akin et al. [34] introduced f -asymptotically \mathcal{J} -invariant statistical equivalence of set sequences.

Now, we recall the basic concepts and some definitions and notations (See [18, 21, 24-26, 28, 29, 32, 33, 35-42]).

Two nonnegative sequences $u = (u_k)$ and $v = (v_k)$ are said to be asymptotically equivalent if

$$\lim_k \frac{u_k}{v_k} = 1$$

(denoted by $u \sim v$).

Throughout this study, we let (V, ρ) be a metric space and G, G_k and H_k ($k = 1, 2, \dots$) be non-empty closed subsets of V .

For any point $u \in V$ and any non-empty subset G of V , we define the distance from u to G by

$$d(u, G) = \inf_{g \in G} \rho(u, g).$$

Let $G_k, H_k \subseteq V$ such that $d(u, G_k) > 0$ and $d(u, H_k) > 0$, for each $u \in V$. The sequences $\{G_k\}$ and $\{H_k\}$ are asymptotically equivalent if for each $u \in V$,

$$\lim_k \frac{d(u, G_k)}{d(u, H_k)} = 1$$

(denoted by $G_k \sim H_k$).

Let $G_k, H_k \subseteq V$ such that $d(u, G_k) > 0$ and $d(u, H_k) > 0$, for each $u \in V$. The sequences $\{G_k\}$ and $\{H_k\}$ are asymptotically statistical equivalent of multiple K if for every $\varepsilon > 0$ and for each $u \in V$,

$$\lim_n \frac{1}{n} \left| \left\{ k \leq n : \left| \frac{d(u, G_k)}{d(u, H_k)} - K \right| \geq \varepsilon \right\} \right| = 0$$

(denoted by $G_k \stackrel{WS_L}{\sim} H_k$).

Let σ be a mapping of the positive integers into itself. A continuous linear functional φ on ℓ_∞ , the space of real bounded sequences, is said to be an invariant mean or a σ mean if and only if

1. $\phi(u) \geq 0$, when the sequence $u = (u_j)$ has $u_j \geq 0$ for all j ,
2. $\phi(i) = 1$, where $i = (1, 1, 1, \dots)$,
3. $\phi(u_{\sigma(j)}) = \phi(u)$ for all $u \in \ell_\infty$.

The mappings ϕ are assumed to be one-to-one and such that $\sigma^m(j) \neq j$ for all positive integers j and m , where $\sigma^m(j)$ denotes the m th iterate of the mapping σ at j . Thus ϕ extends the limit functional on c , the space of convergent sequences, in the sense that $\phi(u) = \lim u$ for all $u \in c$. If σ is a translation mappings that is $\sigma(j) = j + 1$, the σ mean is often called a Banach limit.

By a lacunary sequence we mean an increasing integer sequence $\theta = \{k_r\}$ such that $k_0 = 0$ and $h_r = k_r - k_{r-1} \rightarrow \infty$ as $r \rightarrow \infty$. Throughout the paper, we let $\theta = \{k_r\}$ be a lacunary sequence.

A sequence $\{G_k\}$ is Wijsman $\sigma\theta$ -statistically convergent to G if for every $\varepsilon > 0$ and for each $u \in V$,

$$\lim_{r \rightarrow \infty} \frac{1}{h_r} |\{k \in I_r : |d(u, G_{\sigma^k(m)}) - d(u, G)| \geq \varepsilon\}| = 0$$

uniformly in m . It is denoted by $G_k \rightarrow G$ ($[WS_{\sigma\theta}]$).

For non-empty closed subsets G_k, H_k of V define $d(u; G_k, H_k)$ as follows:

$$d(u; G_k, H_k) = \begin{cases} \frac{d(u, G_k)}{d(u, H_k)}, & u \notin G_k \cup H_k; \\ K, & u \in G_k \cup H_k. \end{cases}$$

The sequences $\{G_k\}$ and $\{H_k\}$ are Wijsman strongly asymptotically $\sigma\theta$ -equivalent of multiple K if for each $u \in V$,

$$\lim_{r \rightarrow \infty} \frac{1}{h_r} \sum_{k \in I_r} |d(u; G_{\sigma^k(m)}, H_{\sigma^k(m)}) - K| = 0$$

uniformly in m , (denoted by $G_k \stackrel{[WN]_{\sigma\theta}^K}{\sim} H_k$).

The sequences $\{G_k\}$ and $\{H_k\}$ are Wijsman asymptotically $\sigma\theta$ -statistical equivalent of multiple K if for each $u \in V$,

$$\lim_{r \rightarrow \infty} \frac{1}{h_r} \left| \left\{ k \in I_r : |d(u; G_{\sigma^k(m)}, H_{\sigma^k(m)}) - K| \geq \varepsilon \right\} \right| = 0$$

uniformly in m , (denoted by $G_k \stackrel{WS_{\sigma\theta}^K}{\sim} H_k$).

A family of sets $\mathcal{J} \subseteq 2^{\mathbb{N}}$ is called an ideal if and only if

- (i) $\emptyset \in \mathcal{J}$,
- (ii) For each $E, F \in \mathcal{J}$ we have $E \cup F \in \mathcal{J}$,
- (iii) For each $E \in \mathcal{J}$ and each $F \subseteq E$ we have $F \in \mathcal{J}$.

If $\mathbb{N} \notin \mathcal{I}$, \mathcal{I} is called non-trivial and if $\{n\} \in \mathcal{I}$ for each $n \in \mathbb{N}$, a non-trivial ideal is called admissible ideal. Throughout this study, we let \mathcal{I} be an admissible ideal.

Let $E \subseteq \mathbb{N}$ and

$$s_r = \min_n \{|E \cap \{\sigma^m(n) : m \in I_r\}|\}$$

and

$$S_r = \max_n \{|E \cap \{\sigma^m(n) : m \in I_r\}|\}.$$

If the limits

$$\underline{V}_\theta(E) = \lim_{r \rightarrow \infty} \frac{S_r}{h_r} \quad \text{and} \quad \overline{V}_\theta(E) = \lim_{r \rightarrow \infty} \frac{S_r}{h_r}$$

exist, then they are called a lower lacunary σ -uniform (lower $\sigma\theta$ -uniform) density and an upper lacunary σ -uniform (upper $\sigma\theta$ -uniform) density of the set E , respectively. If $\underline{V}_\theta(E) = \overline{V}_\theta(E)$, then

$$V_\theta(E) = \underline{V}_\theta(E) = \overline{V}_\theta(E)$$

is called the lacunary σ -uniform density or $\sigma\theta$ -uniform density of E .

Denoted by $\mathcal{J}_{\sigma\theta}$, we denote the class of all $E \subseteq \mathbb{N}$ with $V_\theta(A) = 0$.

A sequence $\{G_k\}$ is said to be Wijsman lacunary \mathcal{I} -invariant convergent or $\mathcal{J}_{\sigma\theta}^W$ -convergent to G if for every $\varepsilon > 0$ and for each $u \in V$, the set

$$A(\varepsilon, u) = \{k : |d(u, G_k) - d(u, G)| \geq \varepsilon\}$$

belongs to $\mathcal{J}_{\sigma\theta}$, that is, $V_\theta(A(\varepsilon, u)) = 0$. It is shown by $G_k \rightarrow G(\mathcal{J}_{\sigma\theta}^W)$.

A function $f: [0, \infty) \rightarrow [0, \infty)$ is called a modulus if

1. $f(u) = 0$ if and only if $u = 0$,
2. $f(u + v) \leq f(u) + f(v)$
3. f is increasing
4. f is continuous from the right at 0.

A modulus may be unbounded (for example $f(u) = q$, $0 < q < 1$) or bounded (for example $f(u) = \frac{u}{u+1}$).

Throughout this study, we let f be a modulus function.

The sequences $\{G_k\}$ and $\{H_k\}$ are said to be Wijsman f -asymptotically \mathcal{I} -equivalent of multiple K if for every $\varepsilon > 0$ and for each $u \in V$,

$$\{k \in \mathbb{N} : f(|d(u; G_k, H_k) - K|) \geq \varepsilon\} \in \mathcal{I}$$

(denoted by $G_k \overset{\mathcal{J}_W(f)}{\sim} H_k$).

The sequences $\{G_k\}$ and $\{H_k\}$ are said to be strongly Wijsman f -asymptotically \mathcal{J}_θ -equivalent of multiple K if for every $\varepsilon > 0$ and for each $u \in V$,

$$\left\{ r \in \mathbb{N} : \frac{1}{h_r} \sum_{k \in I_r} f(|d(u; G_k, H_k) - K|) \geq \varepsilon \right\} \in \mathcal{I}$$

(denoted by $G_k \overset{N_\theta^f(\mathcal{J}_W)}{\sim} H_k$).

The sequences $\{G_k\}$ and $\{H_k\}$ are said to be strongly Wijsman asymptotically \mathcal{J} -invariant equivalent of multiple K if for every $\varepsilon > 0$ and for each $u \in V$,

$$\left\{ n \in \mathbb{N} : \frac{1}{n} \sum_{k=1}^n |d(u; G_k, H_k) - K| \geq \varepsilon \right\} \in \mathcal{J}_\sigma$$

(denoted by $G_k \overset{[W_{\mathcal{J}_\sigma^K}]}{\sim} H_k$).

The sequences $\{G_k\}$ and $\{H_k\}$ are said to be Wijsman f -asymptotically \mathcal{J} -invariant equivalent of multiple K if for every $\varepsilon > 0$ and for each $u \in V$,

$$\{k \in \mathbb{N} : f(|d(u; G_k, H_k) - K|) \geq \varepsilon\} \in \mathcal{J}_\sigma$$

(denoted by $G_k \overset{W_{\mathcal{J}_\sigma^K(f)}}{\sim} H_k$).

The sequences $\{G_k\}$ and $\{H_k\}$ are said to be strongly f -asymptotically \mathcal{J} -invariant equivalent of multiple K if for every $\varepsilon > 0$ and for each $u \in V$,

$$\left\{ n \in \mathbb{N} : \frac{1}{n} \sum_{k=1}^n f(|d(u; G_k, H_k) - K|) \geq \varepsilon \right\} \in \mathcal{J}_\sigma$$

(denoted by $G_k \overset{[W_{\mathcal{J}_\sigma^K(f)}]}{\sim} H_k$).

The sequences $\{G_k\}$ and $\{H_k\}$ are said to be asymptotically \mathcal{J} -invariant statistical equivalent of multiple K if for every $\varepsilon > 0$, $\gamma > 0$ and for each $u \in V$,

$$\left\{ n \in \mathbb{N} : \frac{1}{n} |\{k \leq n : |d(u; G_k, H_k) - K| \geq \varepsilon\}| \geq \gamma \right\} \in \mathcal{J}_\sigma$$

(denoted by $G_k \overset{W_{\mathcal{J}_\sigma^K(S)}}{\sim} H_k$).

Lemma 1 [29] Let $0 < \delta < 1$. Then, for each $u \geq \delta$ we have $f(u) \leq 2f(1)\delta^{-1}u$.

2. MAIN RESULTS

Definition 2.1 The sequences $\{G_k\}$ and $\{H_k\}$ are said to be strongly Wijsman asymptotically $\mathcal{J}_{\sigma\theta}$ -equivalent of multiple K if for every $\varepsilon > 0$ and for each $u \in V$,

$$\left\{ r \in \mathbb{N} : \frac{1}{h_r} \sum_{k \in I_r} |d(u; G_k, H_k) - K| \geq \varepsilon \right\} \in \mathcal{J}_{\sigma\theta}$$

(denoted by $G_k \overset{[W_{j_{\sigma\theta}}^K]}{\sim} H_k$).

Definition 2.2 $\{G_k\}$ and $\{H_k\}$ are said to be Wijsman f -asymptotically $\mathcal{J}_{\sigma\theta}$ -equivalent of multiple K if for every $\varepsilon > 0$ and for each $u \in V$,

$$\{k \in \mathbb{N} : f(|d(u; G_k, H_k) - K|) \geq \varepsilon\} \in \mathcal{J}_{\sigma\theta}$$

(denoted by $G_k \overset{W_{j_{\sigma\theta}}^K(f)}{\sim} H_k$).

Definition 2.3 $\{G_k\}$ and $\{H_k\}$ are said to be strongly Wijsman f -asymptotically $\mathcal{J}_{\sigma\theta}$ -equivalent of multiple K if for every $\varepsilon > 0$ and for each $u \in V$,

$$\left\{ r \in \mathbb{N} : \frac{1}{h_r} \sum_{k \in I_r} f(|d(u; G_k, H_k) - K|) \geq \varepsilon \right\} \in \mathcal{J}_{\sigma\theta}$$

(denoted by $G_k \overset{[W_{j_{\sigma\theta}}^K(f)]}{\sim} H_k$).

Theorem 2.1 For each $u \in V$, we have

$$G_k \overset{[W_{j_{\sigma\theta}}^K]}{\sim} H_k \Rightarrow G_k \overset{[W_{j_{\sigma\theta}}^K(f)]}{\sim} H_k.$$

Proof. Let $G_k \overset{[W_{j_{\sigma\theta}}^K]}{\sim} H_k$ and $\varepsilon > 0$ be given. Select $0 < \delta < 1$ such that $f(i) < \varepsilon$ for $0 \leq i \leq \delta$. So, for each $u \in V$ and for $m = 1, 2, \dots$, we can write

$$\begin{aligned} \frac{1}{h_r} \sum_{k \in I_r} f(|d(u; G_{\sigma^k(m)}, H_{\sigma^k(m)}) - K|) &= \\ \frac{1}{h_r} \sum_{\substack{k \in I_r \\ |d(u; G_{\sigma^k(m)}, H_{\sigma^k(m)}) - K| \leq \delta}} f(|d(u; G_{\sigma^k(m)}, H_{\sigma^k(m)}) - K|) &+ \\ \frac{1}{h_r} \sum_{\substack{k \in I_r \\ |d(u; G_{\sigma^k(m)}, H_{\sigma^k(m)}) - K| > \delta}} f(|d(u; G_{\sigma^k(m)}, H_{\sigma^k(m)}) - K|) \end{aligned}$$

and so, by Lemma 1, we have

$$\begin{aligned} \frac{1}{h_r} \sum_{k \in I_r} f(|d(u; G_{\sigma^k(m)}, H_{\sigma^k(m)}) - K|) &< \\ < \varepsilon + \left(\frac{2f(1)}{\delta}\right) \frac{1}{h_r} \sum_{k \in I_r} |d(u; G_{\sigma^k(m)}, H_{\sigma^k(m)}) - K| \end{aligned}$$

uniformly in m . Thus, for every $\gamma > 0$ and for each $u \in V$,

$$\left\{ r \in \mathbb{N} : \frac{1}{h_r} \sum_{k \in I_r} f(|d(u; G_{\sigma^k(m)}, H_{\sigma^k(m)}) - K|) \geq \gamma \right\}$$

$$\subseteq \left\{ r \in \mathbb{N} : \frac{1}{h_r} \sum_{k \in I_r} |d(u; G_{\sigma^k(m)}, H_{\sigma^k(m)}) - K| \geq \frac{(\gamma - \varepsilon)\delta}{2f(1)} \right\}$$

uniformly in m .

Since $G_k \overset{[W_{j_{\sigma\theta}}^K]}{\sim} H_k$, the second set belongs to $\mathcal{J}_{\sigma\theta}$ and thus, the first set belongs to $\mathcal{J}_{\sigma\theta}$. This proves that

$$G_k \overset{[W_{j_{\sigma\theta}}^K(f)]}{\sim} H_k.$$

Theorem 2.2 If $\lim_{i \rightarrow \infty} \frac{f(i)}{i} = \alpha > 0$, then

$$G_k \overset{[W_{j_{\sigma\theta}}^K]}{\sim} H_k \Leftrightarrow G_k \overset{[W_{j_{\sigma\theta}}^K(f)]}{\sim} H_k.$$

Proof. If $\lim_{i \rightarrow \infty} \frac{f(i)}{i} = \alpha > 0$, then we have $f(i) \geq \alpha i$ for

all $i \geq 0$. Assume that $G_k \overset{[W_{j_{\sigma\theta}}^K(f)]}{\sim} H_k$. Since for $m = 1, 2, \dots$ and for each $u \in V$

$$\begin{aligned} \frac{1}{h_r} \sum_{k \in I_r} f(|d(u; G_{\sigma^k(m)}, H_{\sigma^k(m)}) - K|) &\geq \\ \geq \frac{1}{h_r} \sum_{k \in I_r} \alpha (|d(u; G_{\sigma^k(m)}, H_{\sigma^k(m)}) - K|) &= \\ = \alpha \left(\frac{1}{h_r} \sum_{k \in I_r} |d(u; G_{\sigma^k(m)}, H_{\sigma^k(m)}) - K| \right), \end{aligned}$$

it follows that for each $\varepsilon > 0$, we have

$$\begin{aligned} \left\{ r \in \mathbb{N} : \frac{1}{h_r} \sum_{k \in I_r} |d(u; G_{\sigma^k(m)}, H_{\sigma^k(m)}) - K| \geq \varepsilon \right\} &\subseteq \\ \subseteq \left\{ n \in \mathbb{N} : \frac{1}{h_r} \sum_{k \in I_r} f(|d(u; G_{\sigma^k(m)}, H_{\sigma^k(m)}) - K|) \geq \alpha \varepsilon \right\} \end{aligned}$$

uniformly in m . Since $G_k \overset{[W_{j_{\sigma\theta}}^K(f)]}{\sim} H_k$, it follows that second set belongs to $\mathcal{J}_{\sigma\theta}$. This proves that

$$G_k \overset{[W_{j_{\sigma\theta}}^K]}{\sim} H_k \Leftrightarrow G_k \overset{[W_{j_{\sigma\theta}}^K(f)]}{\sim} H_k.$$

Definition 2.4 We say that the sequences $\{G_k\}$ and $\{H_k\}$ are said to be Wijsman asymptotically lacunary \mathcal{J} -invariant statistical equivalent of multiple K , if for every $\varepsilon, \gamma > 0$ and for each $u \in V$

$$\left\{ r \in \mathbb{N} : \frac{1}{h_r} |\{k \in I_r : |d(u; G_k, H_k) - K| \geq \varepsilon\}| \geq \gamma \right\} \in \mathcal{J}_{\sigma\theta}$$

(denoted by $G_k \overset{W_{j_{\sigma\theta}}^K(S)}{\sim} H_k$).

Theorem 2.3 For each $u \in V$, we have

$$G_k \stackrel{[W_{j\sigma\theta}^K(f)]}{\sim} H_k \Rightarrow G_k \stackrel{W_{j\sigma\theta}^K(S)}{\sim} H_k.$$

ACKNOWLEDGEMENT

This study is supported by Afyon Kocatepe University Scientific Research Coordination Unit with the project number 18. KARİYER.76 conducted by Erdinç DÜNDAR.

REFERENCES

- [1] H. Fast, "Sur la convergence statistique," *Colloq. Math.*, vol. 2, pp. 241-244, 1951.
- [2] I. J. Schoenberg, "The integrability of certain functions and related summability methods," *Amer. Math. Monthly*, vol. 66, pp. 361-375, 1959.
- [3] J. A. Fridy, and C. Orhan, "Lacunary statistical convergence," *Pacific J. Math.*, vol. 160, no. 1, pp. 43-51, 1993.
- [4] P. Kostyrko, T. Šalát, and W. Wilczyński, "J-Convergence," *Real Anal. Exchange*, vol. 26, no. 2, pp. 669-686, 2000.
- [5] P. Das, E. Savaş and S. Kr. Ghosal, "On generalizations of certain summability methods using ideals," *Appl. Math. Lett.*, vol. 24, no. 9, pp. 1509-1514, 2011.
- [6] F. Nuray, and B. E. Rhoades, "Statistical convergence of sequences of sets," *Fasc. Math.*, vol. 49, pp. 87-99, 2012.
- [7] U. Ulusu, and F. Nuray, "Lacunary statistical convergence of sequence of sets," *Progress in Applied Mathematics*, vol. 4, no. 2, pp. 99-109, 2012.
- [8] Ö. Kişi, and F. Nuray, "A new convergence for sequences of sets," *Abstract and Applied Analysis*, Article ID 852796, 6 pages, 2013.
- [9] U. Ulusu, and E. Dündar, "J-Lacunary Statistical Convergence of Sequences of Sets," *Filomat*, vol. 28, no. 8, pp. 1567-1574, 2013.
- [10] R. A. Raimi, "Invariant means and invariant matrix methods of summability," *Duke Math. J.*, vol. 30, pp. 81-94, 1963.
- [11] P. Schaefer, "Infinite matrices and invariant means," *Proc. Amer. Math. Soc.*, vol. 36, pp. 104-110, 1972.
- [12] M. Mursaleen, "Invariant means and some matrix transformations," *Tamkang J. Math.*, vol. 10, no. 2, pp. 183-188, 1979.
- [13] M. Mursaleen, "Matrix transformation between some new sequence spaces," *Houston J. Math.*, vol. 9, no. 4, pp. 505-509, 1983.
- [14] E. Savaş, "Some sequence spaces involving invariant means," *Indian J. Math.*, vol. 31, pp. 1-8, 1989.

Proof. Assume that $G_k \stackrel{[W_{j\sigma\theta}^K(f)]}{\sim} H_k$ and $\varepsilon > 0$ be given. Since for each $u \in V$ and for $m = 1, 2, \dots$

$$\begin{aligned} \frac{1}{h_r} \sum_{k \in I_r} f(|d(u; G_{\sigma^k(m)}, H_{\sigma^k(m)}) - K|) &\geq \\ \frac{1}{h_r} \sum_{\substack{k \in I_r \\ |d(u; G_{\sigma^k(m)}, H_{\sigma^k(m)}) - K| \geq \varepsilon}} f(|d(u; G_{\sigma^k(m)}, H_{\sigma^k(m)}) - K|) & \\ \geq f(\varepsilon) \cdot \frac{1}{h_r} |\{k \in I_r : |d(u; G_{\sigma^k(m)}, H_{\sigma^k(m)}) - K| \geq \varepsilon\}|, & \end{aligned}$$

then for any $\gamma > 0$ and for each $u \in V$

$$\begin{aligned} \{r \in \mathbb{N} : \frac{1}{h_r} |\{k \in I_r : |d(u; G_{\sigma^k(m)}, H_{\sigma^k(m)}) - K| \geq \varepsilon\}| \geq \frac{\gamma}{f(\varepsilon)}\} & \\ \subseteq \left\{ r \in \mathbb{N} : \frac{1}{h_r} \sum_{k \in I_r} f(|d(u; G_{\sigma^k(m)}, H_{\sigma^k(m)}) - K|) \geq \gamma \right\} & \end{aligned}$$

uniformly in m . Since $G_k \stackrel{[W_{j\sigma\theta}^K(f)]}{\sim} H_k$, the last set belongs to $J_{\sigma\theta}$. So, the first set belongs to $J_{\sigma\theta}$ and $G_k \stackrel{W_{j\sigma\theta}^L(S)}{\sim} H_k$.

Theorem 2.4 If f is bounded, then for each $u \in V$

$$G_k \stackrel{[W_{j\sigma\theta}^K(f)]}{\sim} H_k \Leftrightarrow G_k \stackrel{W_{j\sigma\theta}^K(S)}{\sim} H_k.$$

Proof. Let f be bounded and $G_k \stackrel{W_{j\sigma\theta}^L(S)}{\sim} H_k$. Then, there exists a $M > 0$ such that $|f(a)| \leq M$ for all $a \geq 0$. Further using the fact, for $m = 1, 2, \dots$, we have

$$\begin{aligned} \frac{1}{h_r} \sum_{k \in I_r} f(|d(u; G_{\sigma^k(m)}, H_{\sigma^k(m)}) - K|) &= \\ \frac{1}{h_r} \sum_{\substack{k \in I_r \\ |d(u; G_{\sigma^k(m)}, H_{\sigma^k(m)}) - K| \geq \varepsilon}} f(|d(u; G_{\sigma^k(m)}, H_{\sigma^k(m)}) - K|) & \\ + \frac{1}{h_r} \sum_{\substack{k \in I_r \\ |d(u; G_{\sigma^k(m)}, H_{\sigma^k(m)}) - K| < \varepsilon}} f(|d(u; G_{\sigma^k(m)}, H_{\sigma^k(m)}) - K|) & \\ \leq \frac{M}{h_r} |\{k \in I_r : |d(u; G_{\sigma^k(m)}, H_{\sigma^k(m)}) - K| \geq \varepsilon\}| + f(\varepsilon) & \end{aligned}$$

uniformly in m . This proves that $G_k \stackrel{[W_{j\sigma\theta}^K(f)]}{\sim} H_k$.

- [15] E. Savaş, "Strong σ -convergent sequences," *Bull. Calcutta Math.*, vol. 81, pp. 295-300, 1989.
- [16] M. Mursaleen, and O. H. H. Edely, "On the invariant mean and statistical convergence," *Appl. Math. Lett.*, vol. 22, no. 11, pp. 1700-1704, 2009.
- [17] N. Pancaroğlu, and F. Nuray, "Statistical lacunary invariant summability," *Theoretical Mathematics and Applications*, vol. 3, no. 2, pp. 71-78, 2013.
- [18] N. Pancaroğlu, and F. Nuray, "On Invariant Statistically Convergence and Lacunary Invariant Statistically Convergence of Sequences of Sets," *Progress in Applied Mathematics*, vol. 5, no. 2, pp. 23-29, 2013.
- [19] E. Savaş, and F. Nuray, "On σ -statistically convergence and lacunary σ -statistically convergence," *Math. Slovaca*, vol. 43, no. 3, pp. 309-315, 1993.
- [20] U. Ulusu, and F. Nuray, "Lacunary \mathcal{J}_σ -convergence," (under review).
- [21] M. Marouf, "Asymptotic equivalence and summability," *Int. J. Math. Math. Sci.*, vol. 16, no. 4, pp. 755-762, 1993.
- [22] R. F. Patterson, and E. Savaş, "On asymptotically lacunary statistically equivalent sequences," *Thai J. Math.*, vol. 4, no. 2, pp. 267-272, 2006.
- [23] E. Savaş, and R. F. Patterson, " σ -asymptotically lacunary statistical equivalent sequences," *Central European Journal of Mathematics*, vol. 4, no. 4, pp. 648-655, 2006.
- [24] U. Ulusu, and F. Nuray, "On asymptotically lacunary statistical equivalent set sequences," *Journal of Mathematics*, Article ID 310438, 5 pages, 2013.
- [25] N. Pancaroğlu, F. Nuray, and E. Savaş, "On asymptotically lacunary invariant statistical equivalent set sequence," *AIP Conf. Proc.*, 1558:780, 2013.
- [26] U. Ulusu, and E. Güllü, "Asymptotically " \mathcal{J}_σ -equivalence of sequences of sets," (under review).
- [27] H. Nakano, "Concave modulars," *J. Math. Soc. Japan*, vol. 5, pp. 29-49, 1953.
- [28] I. J. Maddox, "Sequence spaces defined by a modulus," *Math. Proc. Camb. Phil. Soc.*, vol. 100, pp. 161-166, 1986.
- [29] S. Pehlivan, and B. Fisher, "Some sequences spaces defined by a modulus," *Mathematica Slovaca*, vol. 45, pp. 275-280, 1995.
- [30] N. Pancaroğlu, and F. Nuray, "Invariant Statistical Convergence of Sequences of Sets with respect to a Modulus Function," *Abstract and Applied Analysis*, Article ID 818020, 5 pages, 2014.
- [31] N. Pancaroğlu, and F. Nuray, "Lacunary Invariant Statistical Convergence of Sequences of Sets with respect to a Modulus Function," *Journal of Mathematics and System Science*, vol. 5, pp. 122-126, 2015.
- [32] V. Kumar, and A. Sharma, "Asymptotically lacunary equivalent sequences defined by ideals and modulus function," *Mathematical Sciences*, vol. 6, no. 23, 5 pages, 2012.
- [33] Ö. Kişi, H. Gümüş, and F. Nuray, " \mathcal{J} -Asymptotically lacunary equivalent set sequences defined by modulus function," *Acta Universitatis Apulensis*, vol. 41, pp. 141-151, 2015.
- [34] N. P. Akın, and E. Dünder, "Asymptotically \mathcal{J} -Invariant Statistical Equivalence of Sequences of Set Defined By A Modulus Function," (under review).
- [35] R. A. Wijsman, "Convergence of sequences of convex sets, cones and functions," *Bull. Amer. Math. Soc.*, vol. 70, pp. 186-188, 1964.
- [36] G. Beer, "On convergence of closed sets in a metric space and distance functions," *Bull. Aust. Math. Soc.*, vol. 31, pp. 421-432, 1985.
- [37] M. Baronti, and P. Papini, "Convergence of sequences of sets," *In Methods of Functional Analysis in Approximation Theory*, ISNM 76, Birkhäuser, Basel, pp. 133-155, 1986.
- [38] F. Nuray, H. Gök, and U. Ulusu, " \mathcal{J}_σ -convergence," *Math. Commun.*, vol. 16, pp. 531-538, 2011.
- [39] E. E. Kara, and M. İlkhani, "On some paranormed \mathcal{A} -ideal convergent sequence spaces defined by Orlicz function," *Asian J. Math. Comput. Research*, vol. 4, no. 4, pp. 183-194, 2015.
- [40] E. E. Kara, and M. İlkhani, "Lacunary \mathcal{J} -convergent and lacunary \mathcal{J} -bounded sequence spaces define by an Orlicz function," *Electron. J. Math. Anal. Appl.*, vol. 4, no. 2, pp. 87-94, 2016.
- [41] E. E. Kara, M. Dastan, and M. İlkhani, "On lacunary ideal convergence of some sequence," *New Trends in Mathematical Science*, vol. 5, no. 1, pp. 234-242, 2017.
- [42] U. Ulusu, and E. Dünder, "Asymptotically \mathcal{J} -Cesaro equivalence of sequences of sets," *Universal Journal of Mathematics and Applications*, vol. 1, no. 2, pp. 101-1015, 2018.

	SAKARYA UNIVERSITY JOURNAL OF SCIENCE		 SAKARYA UNIVERSITY
	e-ISSN: 2147-835X http://www.saujs.sakarya.edu.tr		
	<u>Received</u> 19-06-2018 <u>Accepted</u> 05-09-2018	<u>Doi</u> 10.16984/saufenbilder.434801	

AW(k)-type Salkowski Curves in the Euclidean 3-Space IE^3

İlim KİŞİ*

ABSTRACT

We deal with AW(k)-type ($k = 1, 2, \text{ and } 3$) Salkowski (anti-Salkowski) curves with constant $\kappa \neq 0$ ($\tau \neq 0$) in the Euclidean 3-space. We show that there is no AW(1)-type Salkowski curve and AW(1)-type anti-Salkowski curve in IE^3 . Also, we handle weak AW(2)-type and weak AW(3)-type Salkowski (anti-Salkowski) curves. Also, we show that there is no weak AW(2)-type Salkowski curve in IE^3 .

Keywords: AW(k)-type, Salkowski curve

1. INTRODUCTION

In study [1], AW(k)-type curves and submanifolds were defined by Arslan and West. Thereafter, many works related to this topic were handled by so many authors. In [2,3], the authors gave some features of the AW(k)-type curves in IE^m . In [4], the authors considered AW(k)-type ($k=1, 2, \text{ and } 3$) surfaces and curves. They gave some examples of surfaces and curves that satisfy AW(k)-type situations as well. In [5,6], the authors studied these types of curves with the parallel transport frame in Euclidean spaces IE^3 and IE^4 . In [7], Yoon studied these types of curves in the Lie group G . Also, the same author characterized AW(k)-type general helices in G .

The term "helix" is used in other sciences apart from mathematics because of its properties and applicability. Helices arise in DNA molecules, structures of proteins, and carbon nano tubes, and the like. [8,9]. Also, helices are used in fractal geometry, e.g. hyper helices [10]. Moreover, helices are used for the design of highways or kinematic motion simulations [11]. In the sense of

geometry, a helix is a kind of curve having a non-zero constant curvature and a non-zero constant torsion [12,13]. This curve is called as W-curve by F. Klein and S. Lie in [14].

A regular curve having constant Frenet curvature ratios is a ccr-curve [15]. In [16], authors give a characterization of these curves in IE^m . In that study, authors show that every W-curve is a ccr-curve. As is well-known, generalized helices in IE^3 are characterized by the fact that the quotient $\frac{\tau}{\kappa}$ is constant. It is in this sense that ccr-curves are generalization to IE^m of generalized helices in IE^3 .

Salkowski curves (anti-Salkowski curves), having constant curvature (having constant torsion), were introduced by Salkowski in 1909 in [17]. Thereafter, in [18,19], author studied non-lightlike Salkowski curves in IE_1^3 . In [20], the authors investigated Salkowski type Mannheim curves in IE^3 . In [21], the author characterized the

* Corresponding Author

Salkowski curve whose principal normal vector and a fixed line constitute a constant angle.

This article is arranged as follows: In section 2, some basic concepts of curves in IE^3 are given and the AW(k)-type curve concept is presented. In sections 3 and 4, AW(k)-type Salkowski curves and AW(k)-type anti-Salkowski curves are handled respectively.

2. BASIC CONCEPTS

Let $\gamma = \gamma(s) : I \rightarrow IE^3$ be a curve parametrized with the arc length function s in the Euclidean space IE^3 . If the derivatives $\gamma'(s), \gamma''(s)$, and $\gamma'''(s)$ of γ are linearly independent and $\gamma'(s), \gamma''(s), \gamma'''(s), \gamma^{(iv)}(s)$ are linearly dependent for all $s \in I$, then γ is a Frenet curve of osculating order 3. For each curve of osculating order 3, we can correlate an orthonormal 3-frame $\{T, N, B\}$ called as Frenet frame of the curve γ along γ ($\gamma'(s) = T(s)$) and functions $\kappa, \tau : I \rightarrow IR$ called as the Frenet curvatures of the curve γ . Then the famous Frenet frame formula of γ is given as follows:

$$\begin{bmatrix} T' \\ N' \\ B' \end{bmatrix} = \begin{bmatrix} 0 & \kappa & 0 \\ -\kappa & 0 & \tau \\ 0 & -\tau & 0 \end{bmatrix} \begin{bmatrix} T \\ N \\ B \end{bmatrix}$$

[22].

Now, we introduce AW(k)-type Frenet curves.

Proposition 2.1. Let γ be a Frenet curve of osculating order 3 in IE^3 . Thus, one can conclude:

$$\begin{aligned} \gamma'(s) &= T(s), \\ \gamma''(s) &= T'(s) = \kappa(s)N(s), \\ \gamma'''(s) &= -\kappa^2(s)T(s) + \kappa'(s)N(s) + \kappa(s)\tau(s)B(s), \\ \gamma^{(iv)}(s) &= -3\kappa(s)\kappa'(s)T(s) \\ &\quad + \{\kappa''(s) - \kappa^3(s) - \kappa(s)\tau^2(s)\}N(s) \\ &\quad + \{2\kappa'(s)\tau(s) + \kappa(s)\tau'(s)\}B(s). \end{aligned}$$

[2].

Notation 2.2. Let us write

$$\begin{aligned} N_1(s) &= \kappa(s)N(s), \\ N_2(s) &= \kappa'(s)N(s) + \kappa(s)\tau(s)B(s), \\ N_3(s) &= \{\kappa''(s) - \kappa^3(s) - \kappa(s)\tau^2(s)\}N(s) \\ &\quad + \{2\kappa'(s)\tau(s) + \kappa(s)\tau'(s)\}B(s). \end{aligned} \tag{1}$$

[2].

Definition 2.3. Frenet curves of osculating order 3 are

i) of type weak AW(2) if they enable

$$N_3(s) = \langle N_3(s), N_2^*(s) \rangle N_2^*(s), \tag{2}$$

ii) of type weak AW(3) if they enable

$$N_3(s) = \langle N_3(s), N_1^*(s) \rangle N_1^*(s), \tag{3}$$

where

$$\begin{aligned} N_1^*(s) &= \frac{N_1(s)}{\|N_1(s)\|} = N(s), \\ N_2^*(s) &= \frac{N_2(s) - \langle N_2(s), N_1^*(s) \rangle N_1^*(s)}{\|N_2(s) - \langle N_2(s), N_1^*(s) \rangle N_1^*(s)\|} = B(s) \end{aligned} \tag{4}$$

[2].

Definition 2.4. Frenet curves of osculating order 3 are

i) of type AW(1) if they enable

$$N_3(s) = 0, \tag{5}$$

ii) of type AW(2) if they enable

$$\|N_2(s)\|^2 N_3(s) = \langle N_3(s), N_2(s) \rangle N_2(s) \tag{6}$$

iii) of type AW(3) if they enable

$$\|N_1(s)\|^2 N_3(s) = \langle N_3(s), N_1(s) \rangle N_1(s) \tag{7}$$

[2].

3. AW(k)-TYPE SALKOWSKI CURVES IN IE^3

Here, we handle AW(k)-type Salkowski curves in IE^3 .

Let γ be a Salkowski curve parametrized with the arc length function, and $\{T, N, B\}$ be the Frenet frame of the curve in IE^3 . Since γ is a Salkowski curve, the curvature κ of the curve is a non-zero constant. Thus, the equations (1) become

$$\begin{aligned} N_1(s) &= \kappa N(s), \\ N_2(s) &= \kappa\tau(s)B(s), \\ N_3(s) &= \{-\kappa^3 - \kappa\tau^2(s)\}N(s) + \{\kappa\tau'(s)\}B(s). \end{aligned} \tag{8}$$

From Definition 2.3, we have the following theorems:

Theorem 3.1. There is no weak AW(2)-type Salkowski curve with constant $\kappa \neq 0$ in IE^3 .

Proof. Let γ be a Salkowski curve which is parametrized by the arc length function and given with constant $\kappa \neq 0$ in IE^3 . From the equations (2), (4) and (8), we get $-\kappa(\kappa^2 + \tau^2) = 0$, which is a contradiction. Thus, there is no weak AW(2)-type Salkowski curve with constant $\kappa \neq 0$ in IE^3 .

Theorem 3.2. Let γ be a Salkowski curve which is parametrized by the arc length function and given with constant $\kappa \neq 0$ in IE^3 . If γ is of type weak AW(3), γ is a W-curve.

Proof. Let γ be a unit speed Salkowski curve with constant $\kappa \neq 0$ and γ is of type weak AW(3) in IE^3 . From the equations (3), (4) and (8), we get $\kappa\tau' = 0$. Since $\kappa \neq 0$, $\tau' = 0$, i.e. τ is a constant. Hence, γ is a W-curve.

From Definition 2.4, we have the following theorems:

Theorem 3.3. There is no AW(1)-type Salkowski curve with constant $\kappa \neq 0$ in IE^3 .

Proof. Let γ be a Salkowski curve which is parametrized by the arc length function and given with constant $\kappa \neq 0$ in IE^3 . From the equations (5) and (8), we obtain $-\kappa(\kappa^2 + \tau^2) = 0$ and $\kappa\tau' = 0$. Since $\kappa \neq 0$, we get $\tau' = 0$, i.e. τ is a constant. Considering τ is a constant in $-\kappa(\kappa^2 + \tau^2) = 0$, we get a contradiction. Thus, there is no AW(1)-type Salkowski curve in IE^3 .

Theorem 3.4. Let γ be a Salkowski curve which is parametrized by the arc length function and given with constant $\kappa \neq 0$ in IE^3 . If γ is of type AW(2), then γ is a circle.

Proof. Let γ be a unit speed Salkowski curve with constant $\kappa \neq 0$ and γ is of type AW(2). Using the equations (6) and (8), we obtain $-\kappa^3\tau^2(\kappa^2 + \tau^2) = 0$. Since $\kappa \neq 0$, we get $\tau = 0$, which means that γ is a circle.

Theorem 3.5. Let γ be a Salkowski curve which is parametrized by the arc length function and given with constant $\kappa \neq 0$ in IE^3 . If γ is of type AW(3), then γ is a W-curve.

Proof. Let γ be a unit speed Salkowski curve with constant $\kappa \neq 0$ and γ is of type AW(3). Using the equations (7) and (8), we obtain $\kappa^3\tau' = 0$. Since $\kappa \neq 0$, we get $\tau' = 0$, i.e. τ is a constant. Thus, γ is a W-curve.

4. AW(k)-TYPE ANTI-SALKOWSKI CURVES IN IE^3

Here, we handle AW(k)-type anti-Salkowski curves in IE^3 .

Let γ be a unit speed anti-Salkowski curve, and $\{T, N, B\}$ be Frenet frame of the curve γ in IE^3 . Since γ is an anti-Salkowski curve with a non-zero constant torsion, the equations (1) become

$$\begin{aligned} N_1(s) &= \kappa(s)N(s), \\ N_2(s) &= \kappa'(s)N(s) + \kappa(s)\tau B(s), \\ N_3(s) &= \{\kappa''(s) - \kappa^3(s) - \kappa(s)\tau^2\}N(s) \\ &\quad + \{2\kappa'(s)\tau\}B(s). \end{aligned} \tag{9}$$

From Definition 2.3, we have Theorem 4.1 and Theorem 4.2:

Theorem 4.1. Let γ be an anti-Salkowski curve which is parametrized by the arc length function and given with constant $\tau \neq 0$ in IE^3 . If γ is of type weak AW(2), the differential equation

$$\kappa''(s) - \kappa^3(s) - \kappa(s)\tau^2 = 0$$

with the curvatures of γ holds.

Proof. Let γ be a unit speed anti-Salkowski curve with constant $\tau \neq 0$ and γ is of type weak AW(2) in IE^3 . From the equations (2), (4) and (9), we get the solution.

Theorem 4.2. Let γ be an anti-Salkowski curve which is parametrized by the arc length function and given with constant $\tau \neq 0$ in IE^3 . If γ is of type weak AW(3), γ is a W-curve.

Proof. Let γ be a unit speed anti-Salkowski curve with constant $\tau \neq 0$ and γ is of type weak AW(3) in IE^3 . From the equations (3), (4) and (9), we get $2\kappa'\tau = 0$. Since $\tau \neq 0$, $\kappa' = 0$, i.e. κ is a constant. Hence, γ is a W-curve.

From Definition 2.4, we have the following theorems:

Theorem 4.3. There is no AW(1)-type anti-Salkowski curve with constant $\tau \neq 0$ in IE^3 .

Proof. Let γ be an anti-Salkowski curve which is parametrized by the arc length function and given with constant $\tau \neq 0$ in IE^3 . From the equations (5) and (9), we obtain $\kappa'' - \kappa^3 - \kappa\tau^2 = 0$ and $2\kappa'\tau = 0$. Since $\tau \neq 0$, $\kappa' = 0$, i.e. κ is a constant. Considering κ is a constant in $\kappa'' - \kappa^3 - \kappa\tau^2 = 0$, we get a contradiction. Thus, there is no AW(1)-type anti-Salkowski curve with constant $\tau \neq 0$ in IE^3 .

Theorem 4.4. Let γ be an anti-Salkowski curve which is parametrized by the arc length function and given with constant $\tau \neq 0$ in IE^3 . If γ is of type AW(2), then the differential equation $2(\kappa'(s))^2 = \kappa''(s)\kappa(s) - \kappa^4(s) - \kappa^2(s)\tau^2 = 0$

with the curvatures of γ holds.

Proof. Let γ be a unit speed anti-Salkowski curve with constant $\tau \neq 0$ and γ is of type AW(2). Using the equations (6) and (9), we get

$$\|N_2\|^2 N_3 = ((\kappa')^2 + \kappa^2\tau^2) \begin{pmatrix} (\kappa'' - \kappa^3 - \kappa\tau^2)N \\ + 2\kappa'\tau B \end{pmatrix}$$

and

$$\langle N_3, N_2 \rangle N_2 = \kappa'(\kappa'' - \kappa^3 + \kappa\tau^2)(\kappa'N + \kappa\tau B).$$

From the definition of AW(2)-type, we get

$$((\kappa')^2 + \kappa^2\tau^2)(\kappa'' - \kappa^3 - \kappa\tau^2)$$

$$= (\kappa')^2(\kappa'' - \kappa^3 + \kappa\tau^2)$$

and

$$2\kappa'\tau((\kappa')^2 + \kappa^2\tau^2) = \kappa\kappa'\tau(\kappa'' - \kappa^3 + \kappa\tau^2),$$

which completes the proof.

Theorem 4.5. Let γ be an anti-Salkowski curve which is parametrized by the arc length function and given with constant $\tau \neq 0$ in IE^3 . If γ is of type AW(3), then γ is a W-curve.

Proof. Let γ be a unit speed anti-Salkowski curve with constant $\tau \neq 0$ and γ is of type AW(3). Using the equations (7) and (9), we obtain $2\kappa^2\kappa'\tau = 0$. Since $\kappa \neq 0$ and $\tau \neq 0$, we get $\kappa' = 0$, i.e. κ is a constant. Thus, γ is a W-curve.

REFERENCES

- [1] K. Arslan and A. West, "Product submanifolds with pointwise 3-planar normal sections," *Glasgow Math. J.*, vol.37, pp. 73-81, 1995.
- [2] K. Arslan and C. Özgür, "Curves and surfaces of AW(k) type," *Geometry and topology of Submanifolds IX, World Scientific*, 21-26, 1997.
- [3] C. Özgür and F. Gezgin, "On some curves of AW(k)-type," *Differential Geometry-Dynamical Systems*, vol. 7, pp. 74.80, 2005.
- [4] B. Kılıç and K. Arslan, "On curves and surfaces of AW(k)-type," *BAÜ Fen Bil. Enst. Dergisi*, vol. 6, no. 1, pp. 52-61, 2004.
- [5] I. Kişi, S. Büyükkütük, Deepmala, and G. Öztürk, "AW(k)-type curves according to parallel transport frame in Euclidean space IE^4 ," *Facta Universitatis, Series: Mathematics and Informatics*, vol. 31, no. 4, pp. 885-905, 2016.

- [6] I. Kişi and G. Öztürk, "AW(k)-type curves according to the Bishop frame," arXiv:1305.3381v1 [math.DG], 2013.
- [7] D. W. Yoon, "General helices of Aw(k)-type in the Lie group," *J. Appl. Math.*, pp.1-10, 2012.
- [8] N. Chouaieb, A. Goriely, and J.H. Maddocks, "Helices," *PANS*, 103, 9398.9403, 2006.
- [9] A. A. Lucas and P. Lambin, "Diffraction by DNA, carbon nanotubes and other helical nanostructures," *Rep. Prog. Phys.*, vol. 68, 1181.1249, 2005.
- [10] C. D. Toledo-Suarez, "On the arithmetic of fractal dimension using hyperhelices," *Chaos Solitons and Fractals*, vol. 39, pp. 342.349, 2009.
- [11] X. Yang, "High accuracy approximation of helices by quintic curve," *Comput. Aided Geometric Design*, vol. 20, pp. 303.317, 2003.
- [12] A. Gray, "Modern differential geometry of curves and surface," *CRS Press, Inc.*, 1993.
- [13] H. Gluck, "Higher curvatures of curves in Euclidean space," *Amer. Math. Monthly*, vol. 73, pp. 699-704, 1966.
- [14] F. Klein and S. Lie, "Über diejenigen ebenen kurven welche durch ein geschlossenes system von einfach unendlich vielen vertauschbaren lin-earen transformationen in sich übergehen," *Math. Ann.*, vol. 4, pp. 50-84, 1871.
- [15] J. Monterde, "Curves with constant curvature ratios," *Bulletin of Mexican Mathematic Society*, vol. 13, pp. 177-186, 2007.
- [16] G. Öztürk, K. Arslan, and H.H. Hacisalihoğlu, "A characterization of ccr-curves in \mathbb{R}^m ," *Proc. Estonian Acad. Sciences*, vol. 57, pp. 217-224, 2008.
- [17] E. Salkowski, "Zur transformation von raumkurven," *Math. Ann.*, vol. 66, pp. 517-557, 1909.
- [18] A.T. Ali, "Spacelike Salkowski and anti-Salkowski curves with spacelike principal normal in Minkowski 3-space," *Int. J. Open Problems Comp. Math.*, vol. 2, pp. 451.460, 2009.
- [19] A.T. Ali, "Timelike Salkowski and anti-Salkowski curves in Minkowski 3-space," *J. Adv. Res. Dyn. Cont. Syst.*, vol. 2, pp. 17.26, 2010.
- [20] F. Kaymaz and F. K. Aksoyak, "Some special curves and Mannheim curves in three dimensional Euclidean space," *Mathematical Sciences and applications E-Notes*, vol. 5, no. 1, pp. 34-39, 2017.
- [21] J. Monterde, "Salkowski curves revisited: A family of curves with constant curvature and non-constant torsion," *Computer Aided Geometric Design*, vol. 26, no. 3, pp. 271-278, 2009.
- [22] M. P. Do Carmo, "Differential geometry of curves and surfaces", *Prentice Hall, Englewood Cliffs, N. J.* 1976.

	SAKARYA UNIVERSITY JOURNAL OF SCIENCE		 SAKARYA UNIVERSITY
	e-ISSN: 2147-835X http://www.saujs.sakarya.edu.tr		
	<u>Received</u> 21-05-2018 <u>Accepted</u> 24-09-2018	<u>Doi</u> 10.16984/saufenbilder.425519	

Curves According to the Successor Frame in Euclidean 3-Space

Melek Masal *

Abstract

In the present study, the successor formulae of the successor curves defined by Menninger [1] are given. Then, by defining the successor planes, the geometric meanings of the successor curvatures are investigated and the relations across the components of the position vectors of successor curves are found. Furthermore, in this study, it is proven that lies in the 3rd.type successor plane, lies in the 1st type successor plane and by defining the involute-evolute S-pair, the distance between the corresponding points of these curves is found.

Keywords: Successor frame; Successor curves; Slant helix, Involute-evolute curves.

1. INTRODUCTION

The geometry of the curves may be surrounded by the topics on general helices, involute-evolute curves, Mannheim curves and Bertrand curves (see [2-10]). Such special curves are investigated and used to solve some real-world problems; such as problems of mechanical design or robotics by the help of well-known Frenet-Serret equations since the curves can be thought as the path of a moving particle in the Euclidean Space. After that, some researchers in the field aimed to determine another moving frame for a regular curve [11,12,13]. Menninger, for example, pioneered “Successor frame” using parallel vector fields [1].

In the original part of this study, the successor formulae of the successor curves in 3-dimensional Euclidean space E^3 are provided, and the successor curvatures of the successor curves in a geometrical treatment are described by specifying the i^{th} successor plane. Afterwards, by referring to the position vector of a successor curve as $\alpha = v_1T_1 + v_2N_1 + v_3B_1$, the relations between the components v_i are obtained. In the fourth

section, we define helix concerning the successor system and prove that T_1 -helix and B_1 -helix, respectively, lie in the 3rd type successor plane and the 1st type successor plane. We also see that there is no successor curve as N_1 -helix in E^3 . In the fifth section, we define the involute-evolute S-pair, and then, we find the distance between the corresponding points of these curves.

2. SUCCESSOR TRANSFORMATION OF FRENET APPARATUS

The Euclidean 3-space provided with the standard flat metric is given by

$$\langle, \rangle = dx_1^2 + dx_2^2 + dx_3^2$$

where $\{x_1, x_2, x_3\}$ is a rectangular coordinate system of E^3 . Recall that the norm of an arbitrary vector X is given by $\|X\| = \sqrt{\langle X, X \rangle}$. Let $\beta: I \subset \mathbb{R} \rightarrow E^3$ be an arbitrary curve in the Euclidean space E^3 . The curve β is stated to be a unit speed if the inner product

* Corresponding Author: Sakarya University, Faculty of Education, Mathematics and Science Education Department, 54300 Hendek, Sakarya, Turkiye, mmasal@sakarya.edu.tr

$\left\langle \frac{d\beta}{ds}, \frac{d\beta}{ds} \right\rangle = 1$ is satisfied. Throughout this paper, we will assume that all curves are unit speed curves. For any arbitrary unit speed curve, the Frenet-Serret Formulae are given by

$$\begin{aligned} T' &= \kappa N, \\ N' &= -\kappa T + \tau B, \\ B' &= -\tau N. \end{aligned} \quad (1)$$

Here T, N, B are completely determined by the curvature κ and torsion τ , as a function of parameter s , [4].

Definition 2.1

Let T be the unit tangent vector of the curve $\beta: \beta(s)$. A curve $\alpha: \alpha(s)$ that has T as the principal normal is called the successor curve of the curve β , and the frame $\{T_1, N_1, B_1\}$ is called the successor frame of the Frenet frame $\{T, N, B\}$ if $N_1 \equiv T$, [1].

Theorem 2.1

Every Frenet curve has a family of successor curves. Given a Frenet system $F = \{T, N, B, \kappa, \tau\}$, the totality of successor systems $F_1 = \{T_1, N_1, B_1, \kappa_1, \tau_1\}$ is as follows:

$$\begin{aligned} T_1 &= -\cos \varphi N + \sin \varphi B, \\ N_1 &= T, \\ B_1 &= \sin \varphi N + \cos \varphi B, \\ \kappa_1 &= \kappa \cos \varphi, \quad \tau_1 = \kappa \sin \varphi, \quad \varphi(s) = \varphi_0 + \int \tau(s) ds \end{aligned} \quad (2)$$

Depending on a parameter, φ_0 is a constant real number. The Darboux vector of the successor frame is $D_1 = \kappa B$, [1].

Remark 2.1

The inverse of the successor transformation may be denoted as predecessor transformation. Bilinski described it for the case, but it is not well-defined in general, [1].

3. SUCCESSOR CURVES

In this section, initially the successor formulae of the successor curves in 3-dimensional Euclidean space are given, and the successor curvatures of the successor curves are interpreted geometrically by describing the successor plane. Afterwards, by referring to the position vector of the successor curve as, the relations among the components are obtained.

Theorem 3.1

If α is the successor curve of the Frenet curve β is given with the Frenet system $\{T, N, B, \kappa, \tau\}$, and if $\{T_1, N_1, B_1, \kappa_1, \tau_1\}$ is the successor system of α in E^3 , then there exists the following formulae:

$$\begin{aligned} T_1' &= \kappa_1 N_1, \\ N_1' &= -\kappa_1 T_1 + \tau_1 B_1, \\ B_1' &= -\tau_1 N_1. \end{aligned}$$

Proof

Let α be the successor curve of the curve β given with the Frenet system $\{T, N, B, \kappa, \tau\}$ and let $\{T_1, N_1, B_1, \kappa_1, \tau_1\}$ be the successor system of α in E^3 . Then, if we differentiate each side of the Equation (2) with respect to s , the following is found:

$$\begin{aligned} T_1' &= \varphi' \sin \varphi N - \cos \varphi N' + \varphi' \cos \varphi B + \sin \varphi B', \\ N_1' &= T', \\ B_1' &= \varphi' \cos \varphi N + \sin \varphi N' - \varphi' \sin \varphi B + \cos \varphi B'. \end{aligned}$$

If the Frenet-Serret formulae, Equations (2), (3) and the Remark 2.1 are substituted in these last equations, then following equations are obtained:

$$\begin{aligned} T_1' &= \kappa_1 N_1, \\ N_1' &= -\kappa_1 T_1 + \tau_1 B_1, \\ B_1' &= -\tau_1 N_1. \end{aligned}$$

After that, the formulae, defined in Theorem 3.1, will be called as Successor Formulae.

Definition 3.1

Let α be the successor curve of the curve β given with the Frenet system $\{T, N, B, \kappa, \tau\}$ and let $\{T_1, N_1, B_1, \kappa_1, \tau_1\}$ be the successor system of α in E^3 . The subspace $Sp\{T_1, N_1\}$ is called the 1st type successor plane of α , the subspace $Sp\{T_1, B_1\}$ is called the 2nd type successor plane of α , and the subspace $Sp\{N_1, B_1\}$ is called the 3rd type successor plane of α .

Theorem 3.2

The Let α be the successor curve of the Frenet curve β in E^3 .

i) If α is a successor curve, then the successor approximation of the successor curve α can be obtained as;

$$\hat{\alpha}(s) = \alpha(0) + s(-\lambda_0 \kappa_{10})T_{10} + s(1 + \lambda_0')N_{10} + s(\lambda_0 \tau_{10})B_{10}.$$

ii) If $\kappa_1 = 0$, then the successor curve α lies in the 3rd type successor plane.

iii) If $\tau_1 = 0$, then the successor curve α lies in the 1st type successor plane.

Proof

Let α be the successor curve of the curve β given with the Frenet system $\{T, N, B, \kappa, \tau\}$ and let $\{T_1, N_1, B_1, \kappa_1, \tau_1\}$ be the successor system of α in E^3 . From the Definition 2.1, we can write, (Figure 3.1)

$$\alpha(s) = \beta(s) + \lambda(s)T(s)$$

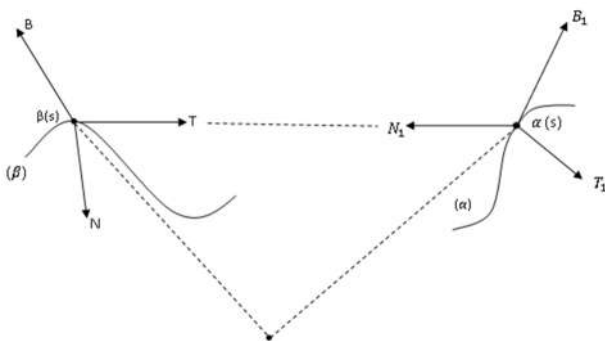


Figure 3.1

For Taylor expansion of the successor curve α in a neighborhood of s_0 , we can write

$$\alpha(s) \approx \alpha(0) + s\alpha'(0) + \frac{s^2}{2}\alpha''(0) + \frac{s^3}{6}\alpha'''(0) + \dots \quad (5)$$

where $s_0 = 0$. If successor system is called by $\{T_{10}, N_{10}, B_{10}, \kappa_{10}, \tau_{10}\}$ at the point $\alpha(0)$ and the Frenet system is called by $\{T_0, N_0, B_0, \kappa_0, \tau_0\}$ at the point $\beta(0)$, and if we differentiate each side of the Equation 4 with respect to s , following equations are obtained.

$$\alpha'(0) = (-\lambda_0 \kappa_{10})T_{10} + (1 + \lambda_0')N_{10} + (\lambda_0 \tau_{10})B_{10},$$

$$\alpha''(0) = \left((-2\lambda_0' - 1)\kappa_{10} - \lambda_0 \kappa_{10}' \right) T_{10} +$$

$$\left(\lambda_0'' - \lambda_0 (\kappa_{10}^2 + \tau_{10}^2) \right) N_{10} + \left((2\lambda_0' + 1)\tau_{10} + \lambda_0 \tau_{10}' \right) B_{10},$$

$$\alpha'''(0) = \left(\kappa_{10} (-3\lambda_0'' + \lambda_0 (\kappa_{10}^2 + \tau_{10}^2)) - (3\lambda_0' + 1)\kappa_{10}' - \lambda_0 \kappa_{10}'' \right) T_{10} +$$

$$+ \left((-3\lambda_0' - 1)(\kappa_{10}^2 + \tau_{10}^2) + \lambda_0''' - 3\lambda_0 (\kappa_{10} \kappa_{10}' + \tau_{10} \tau_{10}') \right) N_{10} +$$

$$+ \left(3\lambda_0''' \tau_{10} + (3\lambda_0' + 1)\tau_{10}' + \lambda_0 (\tau_{10} (\kappa_{10}^2 + \tau_{10}^2) + \tau_{10}'' \right) B_{10}.$$

If the above equations are put in the Equation (5), the following equation is found:

$$\alpha(s) \approx \alpha(0) +$$

$$+ (s(-\lambda_0 \kappa_{10}) + \frac{s^2}{2} \left((-2\lambda_0' - 1)\kappa_{10} - \lambda_0 \kappa_{10}' \right) +$$

$$\frac{s^3}{6} \left(\kappa_{10} (-3\lambda_0'' + \lambda_0 (\kappa_{10}^2 + \tau_{10}^2)) - (3\lambda_0' + 1)\kappa_{10}' - \lambda_0 \kappa_{10}'' \right) + \dots) T_{10}$$

$$+ (s(1 + \lambda_0') + \frac{s^2}{2} (\lambda_0'' - \lambda_0 (\kappa_{10}^2 + \tau_{10}^2)) +$$

$$\frac{s^3}{6} \left((-3\lambda_0' - 1)(\kappa_{10}^2 + \tau_{10}^2) + \lambda_0''' - 3\lambda_0 (\kappa_{10} \kappa_{10}' + \tau_{10} \tau_{10}') \right) + \dots) N_{10}$$

$$+ (s(\lambda_0 \tau_{10}) + \frac{s^2}{2} \left((2\lambda_0' + 1)\tau_{10} + \lambda_0 \tau_{10}' \right) +$$

$$\frac{s^3}{6} \left(3\lambda_0''' \tau_{10} + (3\lambda_0' + 1)\tau_{10}' + \lambda_0 (\tau_{10} (\kappa_{10}^2 + \tau_{10}^2) + \tau_{10}'' \right) + \dots) B_{10}$$

If s^2, s^3, s^4, \dots are omitted here, and the obtained piece is denoted by $\hat{\alpha}$, this is found

$$\hat{\alpha}(s) = \alpha(0) + s(-\lambda_0 \kappa_{10})T_{10} + s(1 + \lambda_0')N_{10} + s(\lambda_0 \tau_{10})B_{10} \quad (6)$$

This equation will be called as the successor approximation of the successor curve α .

As a result of Equation (6), if $\kappa_{10} = 0$, the curve lies in a plane spanning by $\{N_{10}, B_{10}\}$ and also if $\tau_{10} = 0$, the curve lies in a plane spanning by $\{T_{10}, N_{10}\}$. The geometric mean of κ_1 measures measures to an extent which the successor curve departs from a 3rd type successor plane whereas τ_1 measures to an extent which the successor curve departs from a 1st type successor plane.

Theorem 3.3

If $\alpha = v_1 T_1 + v_2 N_1 + v_3 B_1$ is the position vector of the successor curve α , then the coefficients $v_i = v_i(s)$ and $i = 1, 2, 3$ satisfy the following relations:

$$v_1' = \kappa_1 (v_2 - \lambda),$$

$$v_2' = 1 + \lambda' - v_1 \kappa_1 + v_3 \tau_1,$$

$$v_3' = -\tau_1 (v_2 - \lambda).$$

Where, the distance of the successor curve α to the Frenet curve β is λ .

Proof

Let $\alpha = v_1 T_1 + v_2 N_1 + v_3 B_1$ and $v_i = v_i(s)$ be the position vectors of the successor curve α . If we take the derivative of the position vector of the successor curve in view of the Theorem 3.1, the following can be obtained:

$$\alpha' = (v_1' - v_2 \kappa_1) T_1 + (v_1 \kappa_1 + v_2' - v_3 \tau_1) N_1 + (v_2 \tau_1 + v_3') B_1 \quad (7)$$

Furthermore, if equation 4 is differentiated, then the

$$\alpha' = (-\lambda\kappa_1)T_1 + (1 + \lambda')N_1 + (\lambda\tau_1)B_1 \quad (8)$$

equation where the distance of the successor curve α to the Frenet curve β is λ is obtained.

Thus, the Equations (7) and (8) give us

$$v_1' = \kappa_1(v_2 - \lambda),$$

$$v_2' = 1 + \lambda' - v_1\kappa_1 + v_3\tau_1,$$

$$v_3' = -\tau_1(v_2 - \lambda).$$

So, from the Definition 3.1, Theorem 3.2 and Theorem 3.3, we can reach the following result:

Corollary 3.1

Let $\alpha = v_1T_1 + v_2N_1 + v_3B_1$ be the position vector of the successor curve α , and the distance of the successor curve α to the Frenet curve β is λ .

i) If α is in the 1st type successor plane, then we get the following equation:

$$v_1' + v_2' = \kappa_1(v_2 - v_1) + \lambda' - \lambda\kappa_1 + 1$$

ii) If α is in the 2nd type successor plane, then we get the following equation:

$$\lambda'' = \lambda(\tau_1^2 - \kappa_1^2) + v_1\kappa_1' + v_3\tau_1'$$

iii) If α is in the 3rd type successor plane, then we get the following equation:

$$v_2' + v_3' = \tau_1(v_3 - v_2) + \lambda' + \lambda\tau_1 + 1$$

4. HELIX ACCORDING TO SUCCESSOR SYSTEM

In this section, the helix concerning the successor system is defined, and furthermore, T_1 -helix and B_1 -helix, respectively, lie in the 3rd type successor plane, and the 1st type successor plane is proven. It can also be observed that there is no successor curve as N_1 -helix in E^3 .

Definition 4.1

Let $\{T_1(s), N_1(s), B_1(s)\}$ be the successor system of a successor curve α . If T_1 at any point of the successor curve α makes a constant angle with a fixed line, then α is called T_1 -helix, and if N_1 at any point of the α makes a constant angle with a fixed line, then the α is called N_1 -helix, and if B_1 at any point of α makes a constant angle with a fixed line, then α is called B_1 -helix.

Theorem 4.1

If the successor curve α is a T_1 -helix, then

$$\frac{\kappa_1}{\tau_1} = \text{constant}$$

Proof

Assume that the successor curve α is a T_1 -helix. In this case, the following can be written by taking the definition into consideration:

$$\langle T_1, U \rangle = \cos \theta = \text{constant} \neq 0 \quad (9)$$

where U is a constant vector. If we differentiate the Equation (9) and consider Theorem 3.1, we get;

$$\langle \kappa_1 N_1, U \rangle = 0.$$

This shows $U = S_p \{T_1, B_1\}$. Therefore, the following can be written:

$$U = u_1 T_1 + u_2 B_1, \quad u_i = \text{constant}. \quad (10)$$

Taking derivative of the Equation (10), the Successor formulae give

$$u_1 \kappa_1 - u_2 \tau_1 = 0$$

Then, it is seen that

$$\frac{\kappa_1}{\tau_1} = \text{constant}$$

Theorem 4.2

There is no successor curve as N_1 -helix in E^3 .

Proof

Let the successor curve α be the N_1 -helix, assuming that there is a constant vector V which satisfies

$$\langle N_1, V \rangle = \cos \gamma = \text{constant} \quad (11)$$

Differentiating the Equation (11) and considering Theorem 3.1, the following is seen:

$$\langle -\kappa_1 T_1 + \tau_1 B_1, V \rangle = 0,$$

which means that $V = S_p \{N_1\}$. Then, it is seen that;

$$V = \nu N_1, \quad \nu = \text{constant} \quad (12)$$

If we differentiate the Equation (12), we get $\kappa_1 = 0$ and $\tau_1 = 0$. The curve α cannot be a N_1 -helix, due to the fact that κ_1 and τ_1 cannot vanish at the same time for any successor curve α .

Theorem 4.3

If the successor curve α is B_1 -helix, the $\frac{\kappa_1}{\tau_1} = \text{constant}$

Proof

Suppose that the successor curve α is -helix. Then, there is a constant vector W such as;

$$\langle B_1, W \rangle = \cos \psi = \text{constant} \quad (13)$$

From the equation presented above,

$$\langle \tau_1 N_1, W \rangle = 0 \quad (14)$$

is found. So, we can call

$$W = \omega_1 T_1 + \omega_2 B_1, \quad \omega_i = \text{constant}.$$

If we differentiate the Equation (14), we get

$$\omega_1 \kappa_1 - \omega_2 \tau_1 = 0$$

and

$$\frac{\kappa_1}{\tau_1} = \text{constant}$$

5. INVOLUTE-EVOLUTE CURVES ACCORDING TO THE SUCCESSOR SYSTEM

In this section the involute-evolute S-pair is defined, and the distance between the corresponding points of these curves are found.

Definition 5.1

Let $\{T_1, N_1, B_1, \kappa_1, \tau_1\}$ be the successor system of the successor curve α and let $\{T_1^*, N_1^*, B_1^*, \kappa_1^*, \tau_1^*\}$ be the successor system of the successor curve α^* . If $\langle N_1, N_1^* \rangle = 0$, then the curve pair (α, α^*) is called the involute-evolute successor pair or shortly involute-evolute S-pair according to the successor system.

Theorem 5.1

Let α be the successor curve of the Frenet curve β and α^* be the successor curve of the Frenet curve β^* . If (α, α^*) is the involute-evolute S-pair, then

$$\alpha^*(s) = \alpha(s) + (\lambda + s + c)N_1(s)$$

and

$$\lambda^* + s^* = c_1$$

Where c and c_1 are constants of integration.

Proof

Let α be the successor curve of the Frenet curve β and α^* be the successor curve of the Frenet curve β^* . If $\{T, N, B, \kappa, \tau\}$ and $\{T^*, N^*, B^*, \kappa^*, \tau^*\}$ are Frenet systems of the Frenet curves β and β^* respectively, and $\{T_1, N_1, B_1, \kappa_1, \tau_1\}$ and $\{T_1^*, N_1^*, B_1^*, \kappa_1^*, \tau_1^*\}$ are successor systems of the successor curves α and α^* respectively, then from the Definition 2.1, we can write;

$$\alpha(s) = \beta(s) + \lambda(s)T(s)$$

$$\alpha^*(s^*) = \beta^*(s^*) + \lambda^*(s^*)T^*(s^*) \quad (15)$$

If (α, α^*) is the involute-evolute S-pair, then from the Definition 5.1, the following can be written:

$$\alpha^*(s) = \alpha(s) + \lambda(s)N_1(s) \quad (16)$$

From Equations (15) and (16), we have;

$$\beta^*(s) + \lambda^*(s)T^*(s) = \beta(s) + \lambda(s)T(s) + a(s)N_1(s) \quad (17)$$

If we differentiate each side of the Equation (17) with respect to s and consider Theorem 3.1, the following is obtained:

$$\left\{ (-\lambda^* \kappa_1^*)T_1^* + (1 + \lambda^*)N_1^* + (\lambda^* \tau_1^*)B_1^* \right\} \frac{ds^*}{ds} = (-\kappa_1(\lambda + a))T_1 + (1 + \lambda' + a')N_1 + (\tau_1(\lambda + a))B_1$$

From the Definition 5.1, we get

$$1 + \lambda' + a' = 0, \quad 1 + \lambda^{*'} = 0$$

Thus,

$$\lambda^* = c_1 - s^*, \quad a = \lambda + s + c \quad (18)$$

Where c and c_1 are constants of integration.

If the Equation (18) is replaced by the Equation (16), then

$$\alpha^*(s) = \alpha(s) + (\lambda + s + c)N_1(s)$$

is obtained.

6. CONCLUSION

In this paper, the geometric meanings of the successor curvatures, the involute-evolute successor curves, the successor helices and some properties of these special curves have been introduced. This frame is new for the differential geometers; thus, we expect that it will broaden the horizon of the geometers in the field. We also hope that this new frame will attract geometers as the other special frames do (e.g. Sabban frame, Bishop frame, Darboux frame and so forth).

REFERENCES

- [1] Menninger, A. (2014) Characterization of the slant helix as successor curves of the general helix. *International Electronic Journal of Geometry*, 7(2):84-91.
- [2] Ali, A.T. (2011) Position vectors of general helices in Euclidean 3-space. *Bull. Math. Anal. Appl.* 3 (2): 198-205.

- [3] Bertrand, J. (1850) La theories de courbes a double courbure. *J. Math. Pures et Appl.* 15: 332-350.
- [4] Do Carmo, M.P. (1976) *Differential geometry of curves and surfaces*. Prentice Hall, Englewood Cliffs, New Jersey.
- [5] Fuchs, D. (2013) Evolutes and involutes of spatial curves. *Amer. Math. Monthly*, 120(3):217-231.
- [6] Izumiya, S. & Takeuchi, N. (2002) Generic properties of helices and Bertand curves. *J. Geom.*, 71(1): 97-109.
- [7] Liu, H. & Wang F., (2008) Mannheim partner curves in 3-space. *J. Geom.*, 88: 120-126.
- [8] Lucas, P. & Ortega-Yagues, J.A.,(2012) Bertrand curves in the three-dimensional sphere. *J. Geom. Phys.*, 62(9): 1903-1914.
- [9] Orbay, K. & Kasap, E. (2009) On Mannheim partner curves in . *Int. J. Phys. Sci.*, 4(5): 261-264.
- [10] Struik, D.J. (1988) *Lectures on classical differential geometry*. Dover, New-York.
- [11] Bektaş, Ö. & Yüce, S. (2013) Special involute-evolute partner D-curves in. *European Journal of Pure and Applied Mathematics*, 6(1):20-29.
- [12] Bükcü, B. & Karacan, M.K. (2009) The slant helices according to Bishop frame,. *World Academy of Science, Engineering and Technology*, 59:1039-1042.
- [13] Yılmaz, S. & Turgut, M. (2010) A new version of Bishop frame and application to spherical images. *J. Math. Anal. Appl.*, 371: 764-776.

	SAKARYA UNIVERSITY JOURNAL OF SCIENCE		 SAKARYA UNIVERSITY
	e-ISSN: 2147-835X http://www.saujs.sakarya.edu.tr		
	<u>Received</u> 23-07-2018	<u>Doi</u> 10.16984/saufenbilder.446955	
	<u>Accepted</u> 27-09-2018		

Rings and Modules Whose Socles are Relative Ejective

Nuray Eroğlu*¹

Abstract

Lifting homomorphism from modules to modules or even from certain submodule to the modules have been important both in ring and module theory. In this note we study rings and modules whose socles are relative ejective. Moreover we reduce our consideration to rings and modules with injective socles which provides the dual notion to PS -modules.

Keywords: Socle, M -injective module, radical of a module

1. INTRODUCTION

Throughout this paper all rings are associative with identity and all modules are unital right modules. Let R be a ring and let M be an R -module. Then the *radical* of M is defined by the intersection of all maximal submodules of M or M if M has no maximal submodule and denoted $RadM$. Recall that for a right R -module M the *singular submodule* is defined by

$$Z(M) = \{m \in M : mE = 0 \text{ for some essential right ideal } E \text{ of } R\}$$

and a module M is called *nonsingular* provided that $Z(M) = 0$ (see [2]). Note that W.K. Nicholson and J.F. Watters called a module M a *PS-module* if every simple submodule of M is projective, equivalently $SocM$ is projective (see [4]). To this end it is natural to think of rings with injective radical dual to PS -rings. In this case it is easy to see that the Jacobson radical of R is zero. Recently relative ejectivity was defined (see [1] and [8]). Let N, M be R -modules. Then N is called *M -ejective* if for each submodule K of M and each homomorphism $\varphi: K \rightarrow N$ there exist a homomorphism $\theta: M \rightarrow N$ and an essential submodule X of K such that $\theta|_X = \varphi|_X$ i.e.; $\theta(x) = \varphi(x)$ for all $x \in X$. It is clear that every

M -injective module is M -ejective. However, the converse is not true in general (see for example [1]).

In this paper we deal with modules and rings with M -ejective socles or injective socles. To this end, we obtain basic properties of EJS -modules and make sure that the class of EJS -modules is different from the class of weak CS -modules. For; unexplained terminology and notation we refer to [2], [3], [5]. So:

2. EJS -RINGS AND MODULES

Definition 1. Let M be an R -module. Then M is called an EJS (respectively INS)-module if $SocM$ is M -ejective (respectively injective). The ring R is said to be *right EJS (INS)-ring* whenever the right R -module R is an EJS (INS)-module.

Example 1. Let M be an R -module.

- i. If $SocM$ is injective or M -injective then M is an EJS -module.
- ii. If $SocM = 0$ then M is an EJS -module.

Observe that Example 1(ii) yields that in particular the rings of integers \mathbb{Z} and the polynomial ring $R[x]$ over a ring R are EJS -rings.

The following Lemma is the part of Corollary 2.5 in [1] which motivates our work.

Lemma 1. [1, Corollary 2.5] If $SocM$ is essential in M , then N is M -ejective if and only if for each

*Corresponding Author

¹ Tekirdag Namik Kemal University, Faculty of Arts and Sciences, Department of Mathematics, Tekirdag
neroglu@nku.edu.tr

homomorphism $\varphi: SocM \rightarrow N$ there exists a homomorphism $\theta: M \rightarrow N$ such that $\theta|_{SocM} = \varphi$. In other words, the diagram

$$\begin{array}{ccc} SocM & \xrightarrow{i} & M \\ \varphi \downarrow & \swarrow \theta & \\ N & & \end{array}$$

commutes where i denotes the inclusion mapping.

As the following example illustrates the condition $SocM$ is being essential in M is not superfluous in Lemma 1.

Example 2. Let p be any prime integer and let $M = (\mathbb{Z}/\mathbb{Z}p) \oplus \mathbb{Q}$ be the \mathbb{Z} -module. Then

- i. $SocM$ is not M -ejective.
- ii. Any $\varphi \in Hom_{\mathbb{Z}}(SocM, SocM)$ can be lifted to $\theta \in Hom_{\mathbb{Z}}(M, SocM)$.

Proof. First of all note that

$$SocM = \mathbb{Z}/\mathbb{Z}p \oplus 0 = N$$

is not essential in $M_{\mathbb{Z}}$.

i. Assume to the contrary and let $\pi: \mathbb{Z} \rightarrow N$ be the canonical epimorphism. Thus there exists a homomorphism $\theta: M \rightarrow N$ such that $\theta|_{\mathbb{Z}} = \pi$. In particular $\alpha = \theta|_{\mathbb{Q}}: \mathbb{Q} \rightarrow N$ lifts π i.e.; $\alpha|_{\mathbb{Z}} = \pi$.

$$\begin{array}{ccccc} 0 & \longrightarrow & \mathbb{Z} & \longrightarrow & \mathbb{Q} \\ & & \pi \downarrow & \swarrow \alpha & \\ & & \mathbb{Z}/\mathbb{Z}p & & \end{array}$$

Now $\alpha(1/p) = x + \mathbb{Z}p$ for some $x \in \mathbb{Z}$. Thus $p\alpha(1/p) = \alpha(1) = \pi(1) = 1 + \mathbb{Z}p$. It follows that $px + \mathbb{Z}p = 1 + \mathbb{Z}p$ and hence $1 \equiv 0 \pmod{p}$, a contradiction. Hence $SocM$ is not M -ejective.

ii. Let $\varphi: N \rightarrow N$ be any homomorphism. If $\varphi = 0$ then we have done. It follows that $\varphi = i$. Define $\pi: M \rightarrow N$ by $\pi(x + \mathbb{Z}p, y) = x + \mathbb{Z}p$. It is clear that $\pi|_N = i$. \square

Proposition 1. Assume $SocM$ is essential in M . Then M is an EJS -module if and only if M is semisimple.

Proof. (\Leftarrow) This part is clear.

(\Rightarrow) Suppose M is an EJS -module. Let $i: SocM \rightarrow SocM$ be the identity mapping. By Lemma 1, there exists a homomorphism $\theta: M \rightarrow SocM$ such that $\theta|_{SocM} = i$. Then $M = SocM + Ker\theta$. Let $x \in SocM \cap Ker\theta$. Thus

$$x = \theta(x) = 0.$$

Hence $M = SocM \oplus Ker\theta$. Since $SocM$ is essential in M , we obtain that

$$SocM = M$$

i.e.; M is semisimple. \square

Our next objective is to give an example which illustrates the former result. Incidentally, recall that a module M is called *weak CS* if every semisimple submodule is essential in a direct summand of M , see for example [7] or related references there in.

Example 3. Let p be prime number and A be \mathbb{Z} -module $(\mathbb{Z}/\mathbb{Z}p) \oplus (\mathbb{Z}/\mathbb{Z}p^3)$. Then A is a weak CS -module with essential socle which is not EJS -module.

Proof. It is clear that $SocA \leq_e A_{\mathbb{Z}}$. Now let us show that A is a weak CS -module. Note that A has uniform dimension 2. Let S be a semisimple submodule of A . If S is not simple, $S \leq_e A$. Suppose that S is simple. Then $S = (a + \mathbb{Z}p, p^2b + \mathbb{Z}p^3)\mathbb{Z}$ for some integers a, b such that $0 \leq a, b \leq p - 1$. If $a = 0$, then $S \leq_e L = 0 \oplus (\mathbb{Z}/\mathbb{Z}p^3)$. If $a \neq 0$, then $A = S \oplus L$. Thus, in any case, S is essential in a direct summand of A . Thus $A_{\mathbb{Z}}$ is a weak CS -module. Since $A_{\mathbb{Z}}$ is not semisimple, it is not EJS -module by Proposition 1. \square

One might expect that whether the EJS property implies weak CS condition or not? However there are several examples which eliminate this possibility. For example, let p be prime number and let $A = (\mathbb{Z}/\mathbb{Z}p) \oplus \mathbb{Z}$ be the \mathbb{Z} -module. Now, let us form the trivial extension of \mathbb{Z} with A i.e.;

$$R = \begin{bmatrix} \mathbb{Z} & A \\ 0 & \mathbb{Z} \end{bmatrix} = \left\{ \begin{bmatrix} n & (\bar{x}, y) \\ 0 & n \end{bmatrix} : n \in \mathbb{Z}, (\bar{x}, y) \in A \right\}.$$

Then $Soc(R_R) = \begin{bmatrix} 0 & \mathbb{Z}/\mathbb{Z}p \oplus 0 \\ 0 & 0 \end{bmatrix}$ which is not essential in R_R . It follows that R_R is not a weak CS -module. On the other hand, it is straightforward to see that R_R is an EJS -module.

Lemma 2. Let A be an Abelian group (i.e.; \mathbb{Z} -module). Then

- i. $RadA = \bigcap_{p \text{ prime}} pA$.
- ii. If A is torsion then $RadA = 0$ if and only if A is semisimple.

Proof. i. It is easy to check.

ii. (\Leftarrow) Clear.

(\Rightarrow) Let $A = \bigoplus_{p \text{ prime}} A_p$ where A_p is a torsion p -group. Let q be any prime such that $q \neq p$. Let $x \in A_p$. Then $p^n x = 0$ for some $n \geq 1$. Also $1 = sq + tp^n$ for some $s, t \in \mathbb{Z}$. It follows that $x =$

$sqx + tp^n x = q(sx) \in qA_p$. Therefore $A_p = qA_p$ for all primes $q \neq p$. Thus

$$\begin{aligned} \text{Rad}A_p &= \left(\bigcap_{q \text{ prime, } q \neq p} qA_p \right) \cap (pA_p) \\ &= A_p \cap pA_p = 0. \end{aligned}$$

It follows that $A_p \cong A_p/pA_p$ so A_p is semisimple and hence A is semisimple. \square

Combining Lemma 2(ii) together with Proposition 1, we have the next result.

Theorem 1. Let A be a torsion Abelian group. Then the following statements are equivalent.

- i. $\text{Rad}A = 0$.
- ii. A is semisimple.
- iii. A is an EJS -module.

Proof. (i) \Leftrightarrow (ii) By Lemma 2(ii).

(ii) \Leftrightarrow (iii) By Proposition 1. \square

Proposition 2. Let R be an EJS -ring. Then every projective simple right R -module is an EJS -module.

Proof. Suppose X is projective simple R -module. Then $X = xR$ for some $0 \neq x \in X$. Since $R/r(x) \cong X$ is projective simple where $r(x)$ is the right annihilator of x in R . Then $R = r(x) \oplus E$ for some $E \leq R$. Now

$$E \cong R/r(x)$$

is projective simple. Hence $E \leq \text{Soc}R$. Then $\text{Soc}R = E \oplus F$ for some right ideal F of R . Thus E is an EJS -module. Therefore

$$X \cong R/r(x) \cong E$$

is an EJS -module. \square

Now we focus on the case in which that $\text{Soc}M$ is an injective module. Recall that a module M is called an INS -module if $\text{Soc}M$ is injective. Also a ring R is called right INS -ring if R_R is an INS -module. We continue with the following easy Lemma.

Lemma 3. The class of INS -modules is closed under direct products, submodules and essential extensions.

Proof. It is straightforward to check. \square

Proposition 3. Let R be a ring. Then R is a right INS -ring if and only if R has a faithful right INS -module.

Proof. (\Rightarrow) Obvious.

(\Leftarrow) Suppose M is an INS -module. Then R_R embeds in $\prod M$. Thus $R \cong X \leq \prod M$. Since $\text{Soc}R \cong \text{Soc}X \leq \text{Soc}(\prod M)$, $\text{Soc}R$ is injective. \square

Theorem 2. Let R be a ring. Then R is an INS -ring if and only if the following conditions hold.

- i. $\text{Soc}R$ is finitely generated and projective.
- ii. Every projective simple right R -module is injective.

Proof. Assume that (i) and (ii) hold. $\text{Soc}R = U_1 \oplus U_2 \oplus \dots \oplus U_n$ where U_i 's are simple and projective. Thus $\text{Soc}R$ is injective.

Assume that R is an INS -ring. By hypothesis, $R = \text{Soc}R \oplus F$ for some right ideal F of R . Thus $\text{Soc}R$ is cyclic and projective. Now Proposition 2 completes the proof. \square

Theorem 3. Let R be a ring. Then $\text{Soc}R = eR$ for some $e^2 = e \in R$ if and only if $R = S \oplus T$ where S is semiprime Artinian ring and T is a ring with zero right socle.

Proof. Suppose $\text{Soc}R = eR$ where $e^2 = e \in R$. Thus $(1 - e)Re = 0$. Hence

$$R \cong \begin{bmatrix} eRe & eR(1 - e) \\ 0 & (1 - e)R(1 - e) \end{bmatrix} = \begin{bmatrix} S & M \\ 0 & T \end{bmatrix}.$$

Now $\text{Soc}R = \begin{bmatrix} S & M \\ 0 & 0 \end{bmatrix}$. Since

$$\begin{bmatrix} 0 & M \\ 0 & 0 \end{bmatrix} \leq R \text{ and } \begin{bmatrix} 0 & M \\ 0 & 0 \end{bmatrix} \leq \text{Soc}R,$$

$\begin{bmatrix} 0 & M \\ 0 & 0 \end{bmatrix} = fR$ for some $f^2 = f \in R$. It follows that $M = 0$. So [6] yields that $R \cong S \oplus T$ where S is semiprime Artinian and T has zero socle.

Conversely, let A be a right ideal of T and let $\varphi: A \rightarrow S$ be homomorphism. Now $\varphi(S) \leq S$ and $\varphi(A) = \varphi(A)S = \varphi(AS) \leq \varphi(A \cap S) = \varphi(0) = 0$. Hence $\varphi = 0$. Thus φ lifts to T . It follows that S is S -injective and T -injective. Therefore S is injective. \square

Corollary 1. If R is an INS -ring then $R \cong S \oplus T$ where S is a semiprime Artinian ring and T is a ring with zero right socle.

Proof. Immediate by Theorem 3. \square

Our next objective is to clarify when a nonsingular right R -module is an INS -module. To this end a nonsingular right R -module has a projective socle i.e.; it is a PS -module (see [4]).

Example 4. Let $M = \begin{bmatrix} K & K \\ 0 & K \end{bmatrix}$ and $R = \begin{bmatrix} K & K \\ 0 & K \end{bmatrix}$ where K is field. Then M is right nonsingular right R -module which is not an INS -module.

Proof. Suppose $\text{Soc}M = \begin{bmatrix} 0 & K \\ 0 & 0 \end{bmatrix}$ is injective. Define a homomorphism $\varphi: \begin{bmatrix} 0 & K \\ 0 & 0 \end{bmatrix} \rightarrow \begin{bmatrix} 0 & K \\ 0 & 0 \end{bmatrix}$ by $\varphi\left(\begin{bmatrix} 0 & x \\ 0 & 0 \end{bmatrix}\right) = \begin{bmatrix} 0 & x \\ 0 & 0 \end{bmatrix}$ for $x \in K$. Hence

$$\begin{bmatrix} 0 & 1 \\ 0 & 0 \end{bmatrix} = \varphi\left(\begin{bmatrix} 0 & 1 \\ 0 & 0 \end{bmatrix}\right) = \begin{bmatrix} 0 & y \\ 0 & 0 \end{bmatrix} \begin{bmatrix} 0 & 1 \\ 0 & 0 \end{bmatrix} = \begin{bmatrix} 0 & 0 \\ 0 & 0 \end{bmatrix}$$

for some $y \in K$. Which is a contradiction. It follows that $\text{Soc}M$ is not injective. However it is clear that M is nonsingular. \square

Corollary 2. Let R be commutative Noetherian ring and let M be a nonsingular R -module. Then M is an INS -module.

Proof. It is not difficult to see that any nonsingular simple R -module is injective. \square

Observe that Theorem 3 leads us to think of generalized triangular matrix EJS (INS)-rings. For, let R be ring as in Example 4. It can be seen easily that R is not EJS (and hence not INS)-ring (see [8]). Incidentally, we should mention that there are trivial extensions which are not EJS -rings (see [8]). Furthermore, it will be an essential search to investigate relationships between the class of EJS -modules and generalizations of extending modules.

REFERENCES

- [1] E. Akalan, G. F. Birkenmeier, and A. Tercan, "Goldie extending modules", *Comm. Algebra*, vol. 37, no. 2, pp. 663–683, 2009.
- [2] K. R. Goodearl, *Ring Theory*, New York: Marcel Dekker, 1976.
- [3] A. Harmancı and P. F. Smith, "Relative injectivity and modules classes", *Comm. Algebra*, vol. 20, no. 9, pp. 2471–2501, 1992.
- [4] W. K. Nicholson and J. F. Watters, "Rings with projective socle", *Proc. Amer. Math. Soc.*, vol. 102, no. 3, pp. 443–450, 1988.
- [5] D. W. Sharpe and P. Vámos, *Injective Modules*, Cambridge England: Cambridge University Press, 1972.
- [6] P. F. Smith "On the structure of certain PP-rings", *Math. Z.*, vol. 166, pp. 147–157, 1979.
- [7] P. F. Smith and A. Tercan "Generalizations of CS-modules", *Comm. Algebra*, vol. 21, no. 6, pp. 1809–1847, 1993.
- [8] A. Tercan and C. C. Yücel, *Module Theory, Extending Modules and Generalizations*, Bassel: Birkhäuser–Springer, 2016.

	SAKARYA ÜNİVERSİTESİ FEN BİLİMLERİ ENSTİTÜSÜ DERGİSİ <i>SAKARYA UNIVERSITY JOURNAL OF SCIENCE</i>		
	e-ISSN: 2147-835X Dergi sayfası: http://www.saujs.sakarya.edu.tr		
	<u>Received</u> 09-05-2018 <u>Accepted</u> 01-10-2018	<u>Doi</u> 10.16984/saufenbilder.422168	

Determining the Effect of Some Biasing Parameter Selection Methods for the Two Stage Ridge Regression Estimator

Nimet Özbay^{*1}, Selma Toker²

ABSTRACT

The use of biased estimation techniques is inevitable in connection with multicollinearity in simultaneous equations model. Two stage ridge estimator is a pioneer biased estimator which is used to recover the problems that are originated from the multicollinearity. The noteworthy issue regarding two stage ridge estimator is selection of its biasing parameter. Based on the works in the literature related to ridge estimator in a linear regression model, several methods on selection of the biasing parameter of the two stage ridge estimator are investigated in this paper. To demonstrate the best estimators of the biasing parameter, a Monte Carlo experiment is conducted. The utility of the proposed estimators of the biasing parameter for two stage ridge estimator is observed in terms of mean square error criterion.

Keywords: biasing parameter, multicollinearity, ridge estimator, two stage least squares

* Corresponding Author

¹ Çukurova University, Department of Statistics, nturker@cu.edu.tr

² Çukurova University, Department of Statistics, stoker@cu.edu.tr

1. INTRODUCTION

Let $Y_{T \times M}$ and $X_{T \times K}$ be matrices of observations, $\Gamma_{M \times M}$ and $B_{K \times M}$ be the matrices of structural coefficients and $U_{T \times M}$ be the matrix of structural disturbances. Then, simultaneous equations model is shown in the matrix form below:

$$Y\Gamma + XB = U \tag{1}$$

where the elements of X are nonstochastic and fixed with $rank(X) = K \leq T$ and the structural disturbances have zero mean and they are homoscedastic. The reduced form of the model (1) can be written as follows:

$$Y = X\Pi + V. \tag{2}$$

In equation (2)

$$\Pi = -B\Gamma^{-1} \tag{3}$$

and

$$V = U\Gamma^{-1} \tag{4}$$

are the reduced form coefficients.

$$y_1 = Y_1\gamma_1 + X_1\beta_1 + u_1 \tag{5}$$

is the first equation of the system which is derived according to zero restrictions criterion. For $m_1 + 1$ included and $m_1^* = M - m_1 - 1$ excluded jointly dependent variables and K_1 included and $K_1^* = K - K_1$ excluded predetermined variables, $Y = [y_1 \ Y_1 \ Y_1^*]$ and $X = [X_1 \ X_1^*]$ are assumed to be variables with the size of $T \times m_1$, $T \times m_1^*$, $T \times K_1$ and $T \times K_1^*$ corresponding to Y_1 , Y_1^* , X_1 and X_1^* . $\gamma_1 = [1 \ -\gamma_1 \ 0]'$ and $\beta_1 = [-\beta_1 \ 0]'$ are assumed to be variables with the size of $m_1 \times 1$ and $K_1 \times 1$ corresponding to γ_1 and β_1 and u_1 is the first column of U . $[y_1 \ Y_1 \ Y_1^*]' = [X_1 \ X_1^*] \begin{bmatrix} \pi_{11} & \Pi_{11} & \Pi_{11}^* \\ \pi_{21} & \Pi_{21} & \Pi_{21}^* \end{bmatrix} + [v_1 \ V_1 \ V_1^*]$,

is the partition of the reduced form equation (2) with the variables

$$y_1 = X\pi_1 + v_1$$

and

$$Y_1 = X\Pi_1 + V_1, \tag{6}$$

where $\pi_1 = [\pi_{11} \ \pi_{21}]'$ and $\Pi_1 = [\Pi_{11} \ \Pi_{21}]'$ are assumed to be variables having

the size of $K_1 \times 1$, $K_1^* \times 1$, $K_1 \times m_1$, $K_1^* \times m_1$, $T \times 1$ and $T \times m_1$ corresponding to π_{11} , π_{21} , Π_{11} , Π_{21} , v_1 and V_1 . Three subsequent equations show the identifiability relationship between the structural parameters and the reduced form parameters for the first equation:

$$\pi_{11} = \Pi_{11}\gamma_1 + \beta_1,$$

$$\pi_{21} = \Pi_{21}\gamma_1$$

and

$$v_1 = V_1\gamma_1 + u_1 \tag{7}$$

by taking account of only the first column of Γ , B and U in the reduced form coefficients (3) and (4).

With the notations

$$Z_1 = [Y_1 \ X_1]_{T \times p_1},$$

and

$$\delta_1 = [\gamma_1 \ \beta_1]_{p_1 \times 1}'$$

where $p_1 = m_1 + K_1$, the first equation of the system (5) is obtained as

$$y_1 = Z_1\delta_1 + u_1. \tag{8}$$

The structural equation (8) is formed as below by replacing the equations (6) and (7),

$$y_1 = [X\Pi_1 \ X_1] \begin{bmatrix} \gamma_1 \\ \beta_1 \end{bmatrix} + v_1. \tag{9}$$

Reconsidering the equation (9), the final form reveals as follows:

$$y_1 = \bar{Z}_1\delta_1 + v_1, \tag{10}$$

where $\bar{Z}_1 = E(Z_1) = [X\Pi_1 \ X_1]$, $E(v_1) = 0$ and $E(v_1v_1') = \sigma^2I$.

As a most common technique, two stage least squares (TSLS) estimation is applied to simultaneous equations model to estimate the structural parameters. The way for this purpose in the first stage is to replace explanatory endogenous variables by their instrumental variables which are ordinary least squares (OLS) estimates that are obtained by using the exogenous variables. Next for the second stage, the regression coefficients are estimated again by the OLS estimator. TSLS estimator is defined as follows

$$\delta_1^{LS} = (\bar{Z}_1'\bar{Z}_1)^{-1}\bar{Z}_1'y_1. \tag{11}$$

Since \bar{Z}_1 is unknown,

$$\hat{\Pi}_1 = (X'X)^{-1}X'Y_1$$

is used at the first stage to constitute

$$\hat{Z}_1 = [X\hat{\Pi}_1 \quad X_1].$$

By substituting this estimation of \bar{Z}_1 in the equation (11), the operational form of the TSLS estimator is derived as follows:

$$\hat{\delta}_1^{LS} = (\hat{Z}_1'\hat{Z}_1)^{-1}\hat{Z}_1'y_1.$$

Despite ease of computation of the TSLS estimator, running into multicollinearity in simultaneous equations model leads us to find alternative biased estimation methods to the TSLS estimation. Within this context, widely used estimator is ridge estimator (RE) (Hoerl and Kennard [1]) which is recommended for estimating parameters in simultaneous equations model by Vinod and Ullah [2]. Thus, two stage RE of Vinod and Ullah [2] plays a prominent role to eliminate the multicollinearity. Ordinary and operational forms of the two stage RE are

$$\delta_1^{RE} = (\bar{Z}_1'\bar{Z}_1 + kI)^{-1}\bar{Z}_1'y_1,$$

$$\hat{\delta}_1^{RE} = (\hat{Z}_1'\hat{Z}_1 + kI)^{-1}\hat{Z}_1'y_1,$$

where $k > 0$.

2. MATERIAL AND METHOD

The model (10) can be written in a canonical form as follows

$$y_1 = Z\alpha_1 + v_1,$$

where $Z = \bar{Z}_1P$, $\alpha_1 = P'\delta_1$ and P is an orthogonal matrix such that $Z'Z = P'\bar{Z}_1'\bar{Z}_1P = \Lambda_1 = \text{diag}(\lambda_{11}, \dots, \lambda_{1p_1})$ where λ_{1i} are the eigenvalues of $\bar{Z}_1'\bar{Z}_1$. By using this canonical form, the TSLS estimator can be written as

$$\alpha_1^{LS} = \Lambda_1^{-1}Z'y_1.$$

In practice, this estimator is used as follows

$$\hat{\alpha}_1^{LS} = \hat{\Lambda}_1^{-1}\hat{Z}'y_1,$$

where Λ_1 is substituted by $\hat{\Lambda}_1 = P'\hat{Z}'\hat{Z}P$ for the unknown Λ_1 and $\hat{Z} = \hat{Z}_1P$ is put in the place of Z .

Let us write the two stage RE in the canonical form as

$$\alpha_1^{RE} = (\Lambda_1 + kI)^{-1}Z'y_1.$$

This estimator is used practically as follows:

$$\hat{\alpha}_1^{RE} = (\hat{\Lambda}_1 + kI)^{-1}\hat{Z}'y_1.$$

As for comparing the performance of the estimators, the scalar mean square error (*mse*) is the most practical and efficient tool of measure. The *mse* of the TSLS estimator and the two stage RE are

$$mse(\alpha_1^{LS}) = \sigma^2 \sum_{i=1}^{p_1} \frac{1}{\lambda_{1i}},$$

$$mse(\alpha_1^{RE}) = \sigma^2 \sum_{i=1}^{p_1} \frac{\lambda_{1i}}{(\lambda_{1i} + k)^2} + k^2 \sum_{i=1}^{p_1} \frac{\alpha_{1i}^2}{(\lambda_{1i} + k)^2}, \quad (12)$$

where the first part of the equation (12) represents the function of variance while the second part shows the function of squared bias.

Two stage RE is preferable to the TSLS estimator with regard to more reliable calculations in the existence of multicollinearity. In the meantime, there is a difficulty in using the two stage RE depending on the selection of its biasing parameter. To eliminate this problem, we consider various methods which are also examined for linear regression model in the literature: Hoerl and Kennard [1], Hoerl et al. [3], Lawless and Wang [4], Hocking et al. [5], Kibria [6], Khalaf and Shukur [7], Alkhamisi et al. [8], Alkhamisi and Shukur [9], Muniz and Kibria [10] and Muniz et al. [11]. The aforementioned studies are broadly summarized in Mansson et al. [12], hence we follow this article to estimate the biasing parameter of the two stage RE.

We mainly investigate the estimators of the biasing parameter of the two stage RE below:

Hoerl and Kennard [1]:

$$\hat{k}_1 = \frac{\hat{\sigma}^2}{\hat{\alpha}_{1max}^2},$$

where $\hat{\sigma}^2$ is the unbiased estimator of σ^2 and $\hat{\alpha}_{1max}$ is the maximum element of $\hat{\alpha}_1$.

Hoerl et al. [3]:

$$\hat{k}_2 = \frac{p_1 \hat{\sigma}^2}{\sum_{i=1}^{p_1} \hat{\alpha}_{1i}^2}.$$

Lawless and Wang [4]:

$$\hat{k}_3 = \frac{p_1 \hat{\sigma}^2}{\sum_{i=1}^{p_1} \lambda_{1i} \hat{\alpha}_{1i}^2}.$$

Hocking et al. [5]:

$$\hat{k}_4 = \hat{\sigma}^2 \frac{\sum_{i=1}^{p_1} (\lambda_{1i} \hat{\alpha}_{1i})^2}{(\sum_{i=1}^{p_1} \lambda_{1i} \hat{\alpha}_{1i}^2)^2}.$$

Kibria [6]:

$$\hat{k}_5 = \frac{1}{p_1} \sum_{i=1}^{p_1} \frac{\hat{\sigma}^2}{\hat{\alpha}_{1i}^2}, \quad \hat{k}_6 = \frac{\hat{\sigma}^2}{(\prod_{i=1}^{p_1} \hat{\alpha}_{1i}^2)^{\frac{1}{p_1}}},$$

$$\hat{k}_7 = \text{Median} \left\{ \frac{\hat{\sigma}^2}{\hat{\alpha}_{1i}^2} \right\}.$$

Khalaf and Shukur [7]:

$$\hat{k}_8 = \frac{\lambda_{1max} \hat{\sigma}^2}{(T-p_1) \hat{\sigma}^2 + \lambda_{1max} \hat{\alpha}_{1max}^2},$$

where λ_{1max} is the maximum eigenvalue of $Z_1' Z_1$.

Alkhamisi et al. [8]:

$$\hat{k}_9 = \max \left(\frac{\lambda_{1i} \hat{\sigma}^2}{(T-p_1) \hat{\sigma}^2 + \lambda_{1i} \hat{\alpha}_{1i}^2} \right),$$

$$\hat{k}_{10} = \text{Median} \left(\frac{\lambda_{1i} \hat{\sigma}^2}{(T-p_1) \hat{\sigma}^2 + \lambda_{1i} \hat{\alpha}_{1i}^2} \right).$$

Muniz and Kibria [10]:

$$\hat{k}_{11} = \left(\prod_{i=1}^{p_1} \frac{\lambda_{1i} \hat{\sigma}^2}{(T-p_1) \hat{\sigma}^2 + \lambda_{1i} \hat{\alpha}_{1i}^2} \right)^{\frac{1}{p_1}},$$

$$\hat{k}_{12} = \max \left(\frac{1}{\sqrt{\hat{\sigma}^2 / \hat{\alpha}_{1i}^2}} \right),$$

$$\hat{k}_{13} = \left(\prod_{i=1}^{p_1} \frac{1}{\sqrt{\hat{\sigma}^2 / \hat{\alpha}_{1i}^2}} \right)^{\frac{1}{p_1}},$$

$$\left(\prod_{i=1}^{p_1} \sqrt{\hat{\sigma}^2 / \hat{\alpha}_{1i}^2} \right)^{\frac{1}{p_1}},$$

$$\hat{k}_{15} = \text{Median} \left(\frac{1}{\sqrt{\hat{\sigma}^2 / \hat{\alpha}_{1i}^2}} \right).$$

Muniz et al. [11]:

$$\hat{k}_{16} = \max \left(\frac{(T-p_1) \hat{\sigma}^2 + \lambda_{1max} \hat{\alpha}_{1i}^2}{\lambda_{1max} \hat{\sigma}^2} \right),$$

$$\hat{k}_{17} = \max \left(\frac{\lambda_{1max} \hat{\sigma}^2}{(T-p_1) \hat{\sigma}^2 + \lambda_{1max} \hat{\alpha}_{1i}^2} \right),$$

$$\hat{k}_{18} = \left(\prod_{i=1}^{p_1} \frac{(T-p_1) \hat{\sigma}^2 + \lambda_{1max} \hat{\alpha}_{1i}^2}{\lambda_{1max} \hat{\sigma}^2} \right)^{\frac{1}{p_1}},$$

$$\hat{k}_{19} = \left(\prod_{i=1}^{p_1} \frac{\lambda_{1max} \hat{\sigma}^2}{(T-p_1) \hat{\sigma}^2 + \lambda_{1max} \hat{\alpha}_{1i}^2} \right)^{\frac{1}{p_1}},$$

$$\hat{k}_{20} = \text{Median} \left(\frac{(T-p_1) \hat{\sigma}^2 + \lambda_{1max} \hat{\alpha}_{1i}^2}{\lambda_{1max} \hat{\sigma}^2} \right).$$

3. AN APPLICATION: A MONTE CARLO SIMULATION

A Monte Carlo simulation is a prominent way to demonstrate how the estimators of the biasing parameter effect the mastery of the two stage RE. These are the papers in which some Monte Carlo studies are handled in the simultaneous equations model: Wagner [13], Hendry [14], Park [15], Capps Jr and Grubbs [16], Johnston and Dinardo [17], Geweke [18], Agunbiade [19,20] and Agunbiade and Iyaniwura [21].

The structural form of the model built by Agunbiade and Iyaniwura [21] corresponding to three structural equations Equation 1, Equation 2 and Equation 3 is as follows:

$$y_{1t} = y_{3t} \gamma_{13} + x_{1t} \beta_{11} + x_{2t} \beta_{12} + u_{1t},$$

$$y_{2t} = y_{1t} \gamma_{21} + x_{1t} \beta_{21} + x_{3t} \beta_{23} + u_{2t},$$

$$y_{3t} = y_{2t} \gamma_{32} + x_{2t} \beta_{32} + x_{3t} \beta_{33} + u_{3t}.$$

Arbitrary model parameters for this structural model are also given as:

$$\gamma_{13} = 1.8, \beta_{11} = 0.2, \beta_{12} = 1.2,$$

$$\gamma_{21} = 1.5, \beta_{21} = 2.5, \beta_{23} = 2.1,$$

$$\gamma_{32} = 0.9, \beta_{32} = 0.4, \beta_{33} = 3.3.$$

Taking account of different levels of error variance (κ) and multicollinearity degree (ρ) with sample size $T = 60$ and using the root mean square error (*rmse*) criterion, the TSLS estimator and the two stage RE are compared empirically.

We generate predetermined variables having $N_3(0, \Sigma)$ where Σ is assumed to be as a correlation matrix with a given correlation ρ . Similarly, multivariate normal distribution is used to generate the error terms according to variance-covariance matrix below with the parameter κ :

$$\kappa \times \begin{bmatrix} 7.0 & 5.0 & 4.0 \\ 5.0 & 4.5 & 3.5 \\ 4.0 & 3.5 & 3.0 \end{bmatrix}.$$

Different choices of values that are used for the parameters are $\rho = 0.70, 0.80, 0.90, 0.99$ and $\kappa = 0.1, 1, 10, 100$. The experiment is repeated 10000 times by using MATLAB program. After the sample is generated, the estimated *rmse* is calculated by

$$\widehat{rmse}(\hat{\theta}) = \sqrt{\frac{1}{10000} \sum_{j=1}^{10000} (\hat{\theta}_j - \theta)' (\hat{\theta}_j - \theta)},$$

where θ is the parameter vector of a given structural equation, $\hat{\theta}$ is the estimator of this parameter vector and $\hat{\theta}_j$ is the estimation of the parameter vector in the *j*-th replication. The results are summarized in Tables 1-3 corresponding to Equation 1, Equation 2 and Equation 3 for the TSLS estimator and the two stage RE.

4. RESULTS AND DISCUSSION

According to Tables 1-3, to outperform the TSLS estimator is a general conclusion for the two stage RE with different estimations of the biasing parameter. At the same time, for the smallest value of the error variance ($\kappa = 0.1$) the superiority of the TSLS estimator may be observed. The point need to focus on is the noteworthy influence of the proposed estimators of the biasing parameter on efficiency of the two stage RE. By virtue of this simulation study, which estimator of the biasing parameter will be preferred is demonstrated. Thus, the difficulty in the selection of the biasing parameter of the two stage RE is dispelled. In consequence, $\hat{k}_3, \hat{k}_6, \hat{k}_{11}$ and \hat{k}_{20} seem to be the best performed biasing parameters for the efficiency of the two stage RE. In connection to the variation in the level of the error variance and multicollinearity, the estimation ability of the two stage RE changes through the recommended estimators of the biasing parameter. Increasing both the level of multicollinearity and the error variance has a positive effect on the estimated *rmse* values of the two stage RE.

Based on Tables 1-3, let us comment on the Equations 1-3 separately. Considering Table 1,

two stage RE with \hat{k}_3 gives the smallest estimated *rmse* values in general. However, we cannot reach a certain conclusion for a quite high level of multicollinearity. When the level of multicollinearity is lower the results are convincing for \hat{k}_{11} according to Table 2, in contrast \hat{k}_6 is preferable when the level of multicollinearity is higher. In Table 3, taking into consideration of the estimators of the biasing parameter, it is deduced that \hat{k}_3 and \hat{k}_{20} surpass their competitors. Moreover, Equation 1 yields the smallest estimated *rmse* values among all the equations.

5. CONCLUDING REMARKS

The usage of the two stage RE in order to estimate the exogenous variables of a structural equation compels us to concentrate on the selection of its biasing parameter. We clarify this problem in this article since there are not too many papers that are prone to this issue in the literature. We find out the best estimator of the biasing parameter within \hat{k}_1 to \hat{k}_{20} by a comprehensive application.

As for summarizing the outcomes of the Monte Carlo experiment, it is inferred that the level of the error variance and multicollinearity is an indicator which alters the estimated *rmse* values of the estimators. An increment in the magnitude of the error variance and multicollinearity results in an increment in the estimated *rmse* values of the two stage RE.

Generally, each estimator of the biasing parameter provides its own effect for two stage RE to be outperform the TSLS estimator. But, especially $\hat{k}_3, \hat{k}_6, \hat{k}_{11}$ and \hat{k}_{20} give the smallest estimated *rmse* values for two stage RE. As a result, we advise researchers, who confront with simultaneous equations model exposed to multicollinearity, that one of the proposed estimators of the biasing parameter for two stage RE can be preferred.

Table 1. Estimated *rmse* values of the estimators in Equation 1

Equation 1												
Two stage RE with different \hat{k} values												
ρ	κ	TOLS estimator	\hat{k}_1	\hat{k}_2	\hat{k}_3	\hat{k}_4	\hat{k}_5	\hat{k}_6	\hat{k}_7	\hat{k}_8	\hat{k}_9	\hat{k}_{10}
0.70	0.1	0.3190	0.4580	0.3667	0.1891	0.2881	0.4140	0.3920	0.4580	0.4306	0.2848	0.2155
	1	1.5333	1.2525	1.0873	0.5251	0.9142	1.1970	1.1533	1.2455	1.0176	0.8359	0.5426
	10	246.3471	1.8468	1.4123	1.1244	1.3533	1.7830	1.5962	1.8468	1.2808	1.2654	1.1284
	100	152.8417	2.1725	1.4335	2.0220	1.4356	2.1725	2.0964	1.4359	1.3220	1.3214	1.9960
0.80	0.1	0.3884	0.5853	0.4748	0.2271	0.3706	0.5381	0.5089	0.5853	0.5533	0.3657	0.2543
	1	26.8411	1.3493	1.2031	0.6179	1.0455	1.3046	1.2665	1.3326	1.1541	0.9734	0.6342
	10	202.8415	2.1717	1.4345	1.2748	1.3908	2.1701	2.0605	2.0590	1.3550	1.3468	1.2762
	100	2329.8874	2.1446	1.3877	2.6943	1.4420	2.0938	1.6165	1.4424	1.3586	1.3591	2.6750
0.90	0.1	0.5625	0.8613	0.7015	0.3113	0.5520	0.7928	0.7522	0.8613	0.8208	0.5442	0.3375
	1	35.1412	1.4507	1.3443	0.8101	1.2315	1.4235	1.3972	1.4238	1.3240	1.1792	0.8226
	10	278.8939	2.1251	1.4494	1.5941	1.4296	2.0455	1.6333	1.5294	1.4339	1.4376	1.5832
	100	302.7489	2.0248	1.3840	3.8961	1.4486	1.8450	1.4593	1.4492	1.3950	1.3967	4.0281
0.99	0.1	146.6652	1.4852	1.3721	0.8381	1.2544	1.4689	1.4375	1.4419	1.4684	1.2480	0.8501
	1	176.0489	1.6970	1.4860	1.7629	1.4938	1.5468	1.4857	1.4843	1.4859	1.4989	1.7470
	10	121.6339	1.5018	1.5609	3.3718	1.4687	1.4679	1.4773	1.4687	1.5120	1.5278	3.5032
	100	801.3517	1.7149	1.6326	4.0039	1.4572	1.5579	1.4094	1.4581	1.7184	1.4364	5.6537
Two stage RE with different \hat{k} continued values												
ρ	κ	TOLS estimator	\hat{k}_{11}	\hat{k}_{12}	\hat{k}_{13}	\hat{k}_{14}	\hat{k}_{15}	\hat{k}_{16}	\hat{k}_{17}	\hat{k}_{18}	\hat{k}_{19}	\hat{k}_{20}
0.70	0.1	0.3190	0.2188	0.2429	0.2256	0.3076	0.2198	0.2348	0.4452	0.2115	0.3738	0.2053
	1	1.5333	0.5601	0.5337	0.5297	0.7494	0.5284	0.5277	1.0176	0.5263	0.9550	0.5258
	10	246.3471	1.1352	1.1235	1.1230	1.2786	1.1229	1.1230	1.2809	1.1230	1.2757	1.1230
	100	152.8417	1.7921	2.2490	2.2591	1.3348	2.2523	2.2571	1.3220	2.2573	1.3214	2.2573
0.80	0.1	0.3884	0.2624	0.3062	0.2808	0.3973	0.2727	0.2943	0.5820	0.2598	0.4859	0.2512
	1	26.8411	0.6555	0.6299	0.6239	0.8959	0.6222	0.6215	1.1541	0.6194	1.0928	0.6188
	10	202.8415	1.2792	1.2743	1.2740	1.3894	1.2740	1.2741	1.3550	1.2740	1.3523	1.2740
	100	2329.8874	2.2707	3.2301	3.2668	1.3646	3.2576	3.2696	1.3586	3.2712	1.3596	3.2716
0.90	0.1	0.5625	0.3545	0.4502	0.4049	0.5957	0.3888	0.4301	0.8351	0.3676	0.7220	0.3506
	1	35.1412	0.8460	0.8279	0.8173	1.1429	0.8154	0.8154	1.3240	0.8120	1.2771	0.8111
	10	278.8939	1.5567	1.6015	1.6064	1.4348	1.6057	1.6060	1.4339	1.6064	1.4352	1.6065
	100	302.7489	3.1621	5.4807	5.7750	1.4358	5.7703	5.7953	1.3950	5.8239	1.4037	5.8323
0.99	0.1	146.6652	0.8783	1.1492	1.0159	1.3452	1.0104	1.1206	1.4684	0.9390	1.4123	0.9204
	1	176.0489	1.6890	1.6493	1.7123	1.4986	1.6923	1.7115	1.4859	1.7415	1.4900	1.7453
	10	121.6339	2.8040	2.6592	3.9992	1.6897	4.2288	3.7955	1.5120	4.9547	1.5683	5.2621
	100	801.3517	5.0154	5.2434	19.9796	1.5913	23.5878	9.0615	1.4335	23.7658	1.5182	26.7838

Table 2. Estimated *rmse* values of the estimators in Equation 2

Equation 2												
Two stage RE with different \hat{k} values												
ρ	κ	TOLS estimator	\hat{k}_1	\hat{k}_2	\hat{k}_3	\hat{k}_4	\hat{k}_5	\hat{k}_6	\hat{k}_7	\hat{k}_8	\hat{k}_9	\hat{k}_{10}
0.70	0.1	1.7328	2.4038	1.5714	1.0048	2.7424	2.4438	2.1268	2.4038	2.3885	2.7291	0.4568
	1	139.4882	3.2571	2.4577	4.8516	3.3082	3.2587	3.1719	3.2571	3.2423	3.2796	1.9585
	10	68.1909	3.4147	3.4153	4.7518	3.4141	3.4148	3.4150	3.4147	3.4340	3.4321	4.7233
	100	37.4451	3.3788	3.3808	4.0811	3.3853	3.3814	3.3811	3.3809	3.4435	3.4404	4.0905
0.80	0.1	35.1409	2.6655	1.8982	1.2808	2.9073	2.6926	2.4313	2.6655	2.6547	2.8968	0.5330
	1	308.9423	21.9702	9.8668	4.0395	3.3469	3.3096	3.3177	3.3079	21.9704	3.3261	3.4147
	10	161.9416	3.4166	3.4151	4.3654	3.4144	3.4139	3.4142	3.4143	3.4295	3.4332	4.3700
	100	218.0851	3.3761	3.3763	4.0589	3.3826	3.3779	3.3771	3.3791	3.4325	3.4260	4.0787
0.90	0.1	905.6709	2.9698	2.3482	2.0754	3.0989	2.9812	2.8107	2.9698	2.9644	3.0921	0.6846
	1	127.8484	3.5823	3.4065	7.5497	3.3907	3.3716	3.3572	3.3694	3.5856	3.3804	5.4459
	10	296.5322	3.4187	3.4131	3.9617	3.4124	3.4181	3.4120	3.4124	3.4358	3.4285	3.9695
	100	240.9072	3.3794	3.3714	4.1613	3.3788	3.3770	3.3728	3.3789	3.4209	3.4061	4.2422
0.99	0.1	169.8761	3.5599	3.3837	7.4558	3.3875	3.3623	3.3398	3.3587	3.5602	3.3859	5.2985
	1	248.7308	3.4291	3.4254	3.8590	3.4246	3.4233	3.4241	3.4246	3.4303	3.4257	3.8724
	10	215.3956	3.4913	3.4044	3.8136	3.4039	3.4383	3.4049	3.4039	3.4044	3.4050	4.0347
	100	579.4789	3.4869	3.3788	4.5570	3.3726	3.4221	3.3655	3.3726	3.3730	3.3741	5.5796

Table 2 continued

Equation 2												
Two stage RE with different \hat{k} continued values												
ρ	κ	TOLS estimator	\hat{k}_{11}	\hat{k}_{12}	\hat{k}_{13}	\hat{k}_{14}	\hat{k}_{15}	\hat{k}_{16}	\hat{k}_{17}	\hat{k}_{18}	\hat{k}_{19}	\hat{k}_{20}
0.70	0.1	1.7328	0.2842	2.3125	1.6939	1.9928	1.4974	2.6415	2.7291	1.5578	2.1062	1.1447
	1	139.4882	0.9873	3.1098	2.4657	3.0907	1.7203	3.1891	3.2796	1.8527	3.1568	1.5822
	10	68.1909	4.4597	4.8340	4.8432	3.5721	4.8446	4.8718	3.4321	4.8730	3.4350	4.8733
	100	37.4451	4.0466	4.1006	4.1007	3.6164	4.1007	4.1010	3.4404	4.1010	3.4419	4.1010
0.80	0.1	35.1409	0.3618	2.6305	2.1256	2.3385	1.9354	2.8751	2.8968	2.0274	2.4154	1.6033
	1	308.9423	4.2634	3.3318	3.3151	3.3168	3.3974	3.4251	3.3261	3.3075	3.3251	3.6322
	10	161.9416	4.2090	4.4047	4.4139	3.5265	4.4134	4.4249	3.4295	4.4259	3.4342	4.4260
	100	218.0851	4.0054	4.1000	4.1005	3.5938	4.1006	4.1013	3.4260	4.1013	3.4284	4.1014
0.90	0.1	905.6709	0.5167	2.9919	2.7126	2.7803	2.5743	3.1352	3.0921	2.6865	2.8019	2.3591
	1	127.8484	5.0335	3.6549	4.1843	3.4092	4.4624	3.6782	3.3804	5.1432	3.3577	6.1487
	10	296.5322	3.9140	3.9719	3.9755	3.4821	3.9745	3.9776	3.4242	3.9779	3.4290	3.9780
	100	240.9072	4.0185	4.3300	4.3359	3.5440	4.3372	4.3403	3.4052	4.3406	3.4103	4.3408
0.99	0.1	169.8761	4.8314	3.3739	3.3399	3.3398	3.3393	3.4056	3.3859	3.3402	3.3395	3.3477
	1	248.7308	3.7827	3.7012	3.7746	3.4360	3.7604	3.8136	3.4238	3.8515	3.4256	3.8510
	10	215.3956	3.6011	3.8614	4.1275	3.4119	4.0974	4.1603	3.4044	4.2188	3.4058	4.2308
	100	579.4789	4.2689	7.0720	8.2100	3.4409	8.2841	8.2728	3.3730	8.4380	3.3850	8.4737

Table 3. Estimated *rmse* values of the estimators in Equation 3

Equation 3												
Two stage RE with different \hat{k} values												
ρ	κ	TOLS estimator	\hat{k}_1	\hat{k}_2	\hat{k}_3	\hat{k}_4	\hat{k}_5	\hat{k}_6	\hat{k}_7	\hat{k}_8	\hat{k}_9	\hat{k}_{10}
0.70	0.1	0.8464	3.3219	1.4327	0.3946	2.9240	3.2077	2.7137	2.9301	3.2828	2.9008	1.1065
	1	134.3958	3.4250	2.9649	0.9547	3.3232	3.4096	3.3662	3.3242	3.3458	3.2766	1.3593
	10	5261.5765	3.3870	3.3368	1.7763	3.3714	3.3783	3.3663	3.3717	3.3090	3.2994	1.8970
	100	77.9728	3.3743	3.3721	2.7899	3.3658	3.3748	3.3735	3.3743	3.3102	3.3092	2.7982
0.80	0.1	1.7157	3.3436	1.7013	0.4664	3.0263	3.2606	2.8731	3.0297	3.3145	3.0067	1.0946
	1	514.3002	3.4434	3.0861	1.0880	3.3384	3.4425	3.3898	3.3389	3.3576	3.3034	1.4187
	10	272.4579	3.3834	3.3522	1.9536	3.3730	3.3762	3.3684	3.3731	3.3243	3.3175	2.0408
	100	83.0514	3.3805	3.3770	3.0741	3.3659	3.4314	3.4007	3.3805	3.3225	3.3214	3.0748
0.90	0.1	31.9403	3.3701	2.2007	0.6066	3.1702	3.3279	3.0975	3.1713	3.3534	3.1570	1.1274
	1	142.9223	3.3990	3.2329	1.3311	3.3585	3.3924	3.3703	3.3587	3.3706	3.3378	1.5675
	10	362.4192	3.3803	3.3686	2.2808	3.3752	3.3756	3.3728	3.3753	3.3422	3.3388	2.3211
	100	94.7380	3.3618	3.3660	3.6151	3.3662	3.3697	3.3676	3.3662	3.3331	3.3340	3.6302
0.99	0.1	166.4569	3.4011	3.2376	1.3090	3.3615	3.3952	3.3839	3.3615	3.3916	3.3594	1.5551
	1	65.6271	3.3860	3.3764	2.3546	3.3823	3.3824	3.3800	3.3823	3.3809	3.3773	2.3759
	10	225.4804	3.3666	3.3738	3.5326	3.3777	3.3762	3.3752	3.3777	3.3509	3.3603	3.6387
	100	252.5844	3.2694	3.3161	4.5658	3.3663	3.3664	3.3571	3.3663	3.2648	3.3430	5.3532
Two stage RE with different \hat{k} continued values												
ρ	κ	TOLS estimator	\hat{k}_{11}	\hat{k}_{12}	\hat{k}_{13}	\hat{k}_{14}	\hat{k}_{15}	\hat{k}_{16}	\hat{k}_{17}	\hat{k}_{18}	\hat{k}_{19}	\hat{k}_{20}
0.70	0.1	0.8464	1.0678	2.1807	1.1539	2.2325	1.0267	2.6362	3.2828	0.8628	2.6203	0.6755
	1	134.3958	1.6437	1.3952	0.9967	3.0480	1.0403	1.2012	3.3458	0.9593	3.1978	0.9411
	10	5261.5765	2.1444	1.7272	1.7031	3.0630	1.7010	1.6945	3.3090	1.6912	3.2798	1.6904
	100	77.9728	2.8800	2.7391	2.7389	3.2412	2.7389	2.7384	3.3107	2.7384	3.3100	2.7384
0.80	0.1	1.7157	1.1487	2.3837	1.3627	2.4544	1.2362	2.7747	3.3145	1.0306	2.7941	0.8249
	1	514.3002	1.7494	1.5706	1.0918	3.2532	1.1929	1.3490	3.3576	1.0933	3.2488	1.0738
	10	272.4579	2.2885	1.8988	1.8770	3.1254	1.8744	1.8656	3.3243	1.8628	3.3052	1.8620
	100	83.0514	3.0938	3.0620	3.0619	3.3017	3.0619	3.0618	3.3233	3.0618	3.3224	3.0618
0.90	0.1	31.9403	1.3151	2.7055	1.7665	2.8006	1.6603	2.9797	3.3534	1.3715	3.0418	1.1474
	1	142.9223	1.9512	1.8909	1.4428	3.1851	1.4791	1.6164	3.3706	1.3374	3.3098	1.3144
	10	362.4192	2.5452	2.2103	2.1950	3.2118	2.1926	2.1788	3.3422	2.1771	3.3345	2.1766
	100	94.7380	3.4682	3.7871	3.7885	3.2850	3.7882	3.7912	3.3348	3.7913	3.3340	3.7913
0.99	0.1	166.4569	2.0174	3.2507	2.6857	3.3476	2.9361	3.2938	3.3916	2.5141	3.3608	2.5367
	1	65.6271	2.7011	2.7847	2.6490	3.3236	2.6190	2.4656	3.3809	2.3484	3.3742	2.3243
	10	225.4804	3.3801	3.7603	3.8286	3.2855	3.8555	3.9546	3.3604	3.9657	3.3576	3.9702
	100	252.5844	4.3857	7.1006	9.1136	3.2635	9.4450	9.1312	3.3435	9.6483	3.3263	9.7321

ACKNOWLEDGMENTS

This paper is supported by Çukurova University Scientific Research Projects Unit Project Number: FBA-2018-9770.

REFERENCES

- [1] A. E. Hoerl and R. W. Kennard. "Ridge regression: biased estimation for non-orthogonal problems". *Technometrics*. vol. 12. no. 1. pp. 55-67. 1970.
- [2] H. D. Vinod and A. Ullah. "Recent advances in regression methods". Marcel Dekker. New York. Inc.. 1981.
- [3] A. E. Hoerl. R. W. Kennard and K. F. Baldwin. "Ridge regression: some simulations". *Communications in Statistics-Simulation and Computation*. vol. 4. pp. 105–123. 1975.
- [4] J. F. Lawless and P. A. Wang. "Simulation study of ridge and other regression estimators". *Communications in Statistics-Theory and Methods* . vol. 5. no. 4. pp. 307-323. 1976.
- [5] R. R. Hocking. F. M. Speed and M. J. Lynn. "A class of biased estimators in linear regression". *Technometrics*. vol. 18. no. 4. pp. 425-437. 1976.
- [6] B. M. G. Kibria. "Performance of some new ridge regression estimators". *Communications in Statistics-Simulation and Computation*. vol. 32. no. pp. 419–435. 2003.
- [7] G. Khalaf and G. Shukur. "Choosing ridge parameters for regression problems". *Communications in Statistics-Theory and Methods*. vol. 34. pp. 1177-1182. 2005.
- [8] M. Alkhamisi. G. Khalaf and G. Shukur. "Some modifications for choosing ridge parameters". *Communications in Statistics-Theory and Methods*. vol. 35. pp. 2005-2020. 2006.
- [9] M. Alkhamisi and G. Shukur. "Developing ridge parameters for SUR model". *Communications in Statistics-Theory and Methods*. vol. 37. no. 4. pp. 544-564. 2008.
- [10] G. Muniz and B. M. G. Kibria. "On some ridge regression estimators: an empirical comparisons". *Communications in Statistics-Simulation and Computation*. vol. 38. pp. 621-630. 2009.
- [11] G. Muniz. B. M. G. Kibria. G. Shukur and K. Mansson. "On developing ridge regression parameters: a graphical investigation". *SORT*. vol. 36. no. 2. pp. 115-138. 2012.
- [12] K. Mansson. G. Shukur and B. M. G Kibria. "A simulation study of some ridge regression estimators under different distributional assumptions". *Communications in Statistics-Simulation and Computation*. vol. 39. no. 8. pp. 1639-1670. 2010.
- [13] H. M. Wagner. "A monte carlo study of estimates of simultaneous linear structural equations". *Econometrica*. vol. 26. pp. 117-133. 1958.
- [14] D. F. Hendry. "The structure of simultaneous equation estimators". *Journal of Econometrics*. vol. 4. pp. 51-88. 1976.
- [15] S. B. Park. "Some sampling properties of minimum expected loss (MELO) estimates of structural coefficients". *Journal of Econometrics*. vol. 18. pp. 295–311. 1982.
- [16] O. Capps Jr and W. D. Grubbs. "A monte carlo study of collinearity in linear simultaneous equation models". *Journal of Statistical Computation and Simulation*. vol. 39. pp. 139-162. 1991.
- [17] J. Johnston and J. E. Dinardo. "Econometric methods". McGraw-Hill. New York. 1997.
- [18] J. Geweke. "Using simulation methods for bayesian econometric models: inference. development and communication". *Econometric Reviews*. vol. 18. no. 1. pp. 1-73. 1999.
- [19] D. A. Agunbiade. "A monte carlo approach to the estimation of a just identified simultaneous three-equations model with three multicollinear exogenous variables". Unpublished Ph.D. Thesis. University of Ibadan. 2007.
- [20] D. A. Agunbiade. "Effect of multicollinearity and the sensitivity of the estimation methods in simultaneous equation model". *Journal of Modern Mathematics and Statistics*. vol. 5. no. 1. pp. 9-12. 2011.
- [21] D. A. Agunbiade and J. O. Iyaniwura. "Estimation under multicollinearity: a comparative approach using monte carlo methods". *Journal of Mathematics and Statistics*. vol. 6 no. 2. pp. 183-192. 2010.

	SAKARYA UNIVERSITY JOURNAL OF SCIENCE		 SAKARYA UNIVERSITY
	e-ISSN: 2147-835X http://www.saujs.sakarya.edu.tr		
	<u>Received</u> 14-05-2018 <u>Accepted</u> 24-09-2018	<u>Doi</u> 10.16984/saufenbilder.423358	

Characterization of 3 fluoro-4-formylphenylboronic acid molecule with Density Functional Theory

Emine BABUR ŞAŞ^{*1}, Mustafa KURT²

Abstract

The geometric structure of 3-fluoro-4-fomylphenylboronic acid (3-4FPBA) molecule were investigated with DFT/B3LYP/6-311++G(d,p) level. The FT-IR and FT-Raman spectra were recorded for the title molecule. Theoretical wavenumber and Mulliken charges were also calculated by using the same method and compared theoretical wavenumber with experimental wavenumbers (FT-IR and FT-Raman) which have a good agreement. Furthermore, electronic structure properties of in the title molecule such as HOMO-LUMO and Molecular Electrostatic Potential (MEP) were investigated by TD-DFT method.

Keywords: 3-fluoro-4-fomylphenylboronic acid, 3-4FPBA, DFT, HOMO-LUMO.

1. INTRODUCTION

Boronic acids and their derivatives have an important place among the compounds due to their wide use. Boronic acids are naturally absent, but have been in the literature since 1860 [1]. Boronic acids and their derivatives have many applications in the field such as material science, analytical chemistry, medicine, biology, catalysis, organic synthesis and crystal engineering [2].

Biomedical applications of boronic acid-containing polymers and biological applications of specific dichlorophenylboronic acids have been investigated [3-5]. Half of the boronic acids are incorporated into nucleosides and amino acids as antiviral agents and anti-tumor [6]. In addition, derivatives of biologically important compounds have been synthesized as anti-metabolites for possible attack against cancer [7-9].

Phenylboronic acid is a compound that is soluble in most polar organic solvents. Phenylboronic acids are a versatile building block in organic synthesis. It is an important intermediate in the synthesis of active compounds in the pesticide and pharmaceutical industry [10]. Boronic acids, such as phenylboronic acid, are known to inhibit lipase (enzyme) acids [11]. This property of phenyl boronic acids has been used to

disrupt epithelial barrier function to enhance the absorption of topically applied active agents [12]. Boric acid and certain phenyl boronic acids are some beta-lactamase inhibitors. Phenyl boronic acids have been shown to be effective against beta-lactam antibiotic-resistant bacteria as a consequence of Porin mutation [13, 14].

The infrared spectrum of phenylboronic acid was obtained by Fanniran and Shurvell in 1968 [15]. Crystal structure was first described by Retting and Trotter in 1977 with the x-ray diffraction method [16]. In the literature, no studies have been found on the structural and vibrational spectroscopy of 3-4FPBA molecules.

In this study, molecular geometric parameters, vibrational modes, HOMO-LUMO, MEP and Mulliken charge quantum chemical DFT / B3LYP method and 6-311G ++ (d,p) basis set of 3-4FPBA molecules were obtained and interpreted.

2. EXPERIMENTAL DETAILS

The 3-4 FPBA molecule was 97% pure from Across Organics and powder samples were supplied. Molecular FT-IR and FT Raman spectra were recorded

* Corresponding Author Emine BABUR ŞAŞ Tel: +90 386 280 4748 e-mail address: baburemine@gmail.com

¹ Technical Sciences Vocational Schools, Ahi Evran University, Kırşehir, Turkey

² Department of Physics, Ahi Evran University, Kırşehir, Turkey

at 4000-400 cm^{-1} and 3500 -10 cm^{-1} regions. The FT-IR spectrum was obtained from a Perkin Elmer BX spectrometer using the KBr disc technique. The Dispersive Raman spectrum was also obtained using a Bruker RFS 100 / S FT-Raman instrument using a 1064 nm stimulated YAG laser.

3. COMPUTATIONAL DETAILS

All calculations in this study were performed with the Gaussian 09 program [17], DFT / B3LYP / 6-311G ++ (d,p) basis set [18,19]. By optimizing the molecule with this basis set, the molecular geometrical parameters, vibrational frequencies were calculated. In order to approximate the calculated vibration frequencies to the experimental vibration frequencies, these frequencies were multiplied by the scaling factor taken from certain references.

The molecular electrostatic potential surface (MEP) was demonstrated and evaluated in 2D and 3D dimensions, with a map showing the electron density of a molecule. The temperature capacity, entropy and enthalpy values were investigated for the different temperatures of the title molecule (100K-700K).

4. RESULTS

4.1. Geometric Optimization

The crystal structure of the working molecule is not present. Thus, the optimized molecule was compared to similar molecules [20, 21]. The 3-4FPBA molecule consists of a benzene ring, a group C = OH and a group B(OH)₂. First, the possible four conformation of the 3-4FPBA molecule was determined by the orientation of the group B(OH)₂ and was named C1, C2, C3 and C4. The determined conformations were divided into new conformations according to the orientation of the oxygen atom in the C = OH group, and these conformations were named C1A, C2A, C3A and C4A. The conformation with the lowest energy was determined by calculating the energies of eight determined conformation. All conformations of the molecule are shown in Figure 1 and the energy values of conformation are given in Table 1.

Table 1 Calculated energies and energy differences for eight possible conformers of 3-4FPBA.

Conformers	Energy (Hartree)	Energy Differences(Hartree)
C1A	-621.00362825	0.01477
C2A	-621.01429300	0.00411
C3A	-620.99751615	0.02089
C4A	-621.00863912	0.00976
C1	-621.01586806	0.00253
C2	-621.01840131	0.00000

C3	-621.01840132	0.00000
C4	-621.01256937	0.00583

The calculation results show that C3 conformation is the lowest energy conformation of the 3-4 FPBA molecule and the lowest energy structure is shown in Fig 1. All data calculated for the molecule were made using this conformation.

First, the C3 conformation is optimized and the source [20] of the single molecule is given in Table 2 together with experimental X-ray data and the like molecule [21] to compare the geometrical parameters (bond lengths and angles) of this conformation.

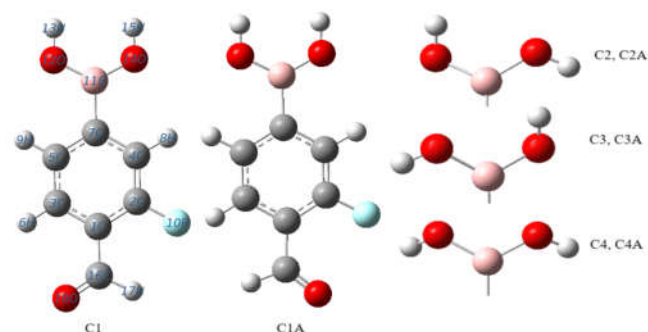


Figure 1. The possible conformation of the 3-4FPBA molecule

The bond lengths of the molecular boronic acid and the phenyl ring are compatible with each other as shown in Table 2. However, there are slight differences between the theoretical and experimental results. These differences can be attributed to the fact that theoretical calculations are made with the molecular gas and the experimental calculations are made with the solid state of the molecule.

The bond lengths indicated by the maximum deviation (deviation) of the 3-4FPBA molecule are the C-H bonds, which depend on the phenyl ring. The maximum deviation at the bond angles is seen at bond angle B12-O13-H16. The difference in these geometric parameters (bond angle and bond length) may be due to the intramolecular interaction of the fluorine atom and the boronic acid group attached to the phenyl ring.

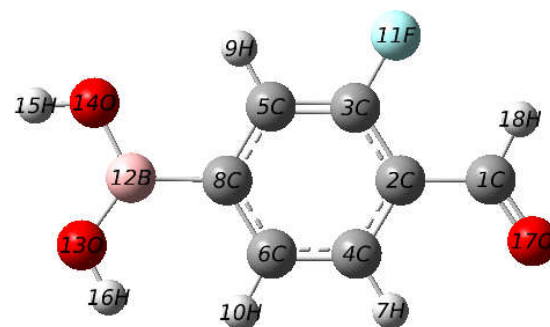


Figure 2. The lowest energy C3 conformation of the 3-4FPBA molecule

4.2. Vibration spectra

In the C3 conformation, 3-4FPBA molecules with C1 symmetry group have 18 atoms and 48 fundamental vibrations. Wavenumbers are calculated according to this conformation in the basis set of 6-311G ++(d,p) and are given in Table 3 by comparison with experimental values. For the calculated wave numbers to be fitted experimentally, the vibrational frequencies less than 1700 cm⁻¹ are multiplied by 0.983 and the larger vibrational frequencies are multiplied by the 0.958 scale factors [22]. Experimental FT-IR, dispersive Raman spectra and theoretical Infrared and Raman spectra for 3-4FPA molecules is shown at Fig 3.

Table 2 The some geometrical parameters optimized in 3-4FPBA

Bond Length	3-4FPBA	X-Ray [1]	3FPBA [2]
C1-C2	1.4774	-	-
C1-O17	1.2176	-	-
C1-H18	1.1017	-	-
C2-C3	1.3975	1.365	1.387
C2-C4	1.4034	1.375	1.393
C3-C5	1.3823	1.377	1.384
C3-F11	1.3576	1.377	1.357
C4-C6	1.3864	1.387	1.393
C4-H7	1.084	0.93	1.084
C5-C8	1.4028	1.406	1.404
C5-H9	1.0835	0.93	1.083
C6-C8	1.4076	1.398	1.404
C6-H10	1.0853	0.93	1.086
C8-B12	1.5768	1.562	1.569
B12-O13	1.3676	1.366	1.373
B12-O14	1.3659	1.343	1.366
O13-H16	0.9631	0.855	0.96
O14-H15	0.9659	0.851	0.963
Bond Angles			
C3-C2-C4	117.3	118.4	118.2
C2-C3-C5	122.8	123.9	122.6
C2-C3-F11	119.0	118.1	118.5
C5-C3-F11	118.3	118	118.9
C2-C4-C6	120.8	119.7	120.2
C2-C4-H7	118.4	120.2	119.6
C6-C4-H7	120.8	120.2	120.3
C3-C5-C8	119.8	118.6	119.6
C3-C5-H9	119.3	120.7	119.7
C8-C5-H9	120.9	120.7	120.7
C4-C6-C8	121.3	121.8	121.4
C4-C6-H10	118.1	119.1	118.1
C8-C6-H10	120.7	119.1	120.5
C5-C8-C6	118.2	117.6	118.1
C5-C8-B12	119.0	120.1	119.3
C6-C8-B12	122.8	122.1	122.6

C8-B12-O13	124.6	122.7	124.3
C8-B12-O14	117.5	119	118.3
O13-B12-O14	117.8	118.2	117.4
B12-O13-H16	116.6	124	115.1
B12-O14-H15	113.3	116	112.6

Table 3. Comparison of the calculated and experimental vibrational wavenumbers (cm⁻¹) of 3-4FPBA.

No.	Experimental wavenumbers		Theoretical wavenumbers			
	FT-IR	FT-Raman	Scaled	I _{IR}	S _{ra}	I _{ra}
1			33	6.23	0.23	0.00
2			71	2.59	1.44	0.01
3		121	129	8.86	0.71	0.00
4			137	16.93	4.38	0.01
5		166	189	6.93	7.71	0.01
6		211	202	4.20	2.09	0.00
7			273	0.45	1.99	0.00
8			289	8.76	6.80	0.01
9		333	330	3.65	2.29	0.00
10			418	29.44	3.42	0.00
11			441	39.55	0.31	0.00
12			451	277.70	0.93	0.02
13			498	51.74	1.11	0.02
14	502		506	25.68	1.12	0.02
15		524	534	17.61	15.30	0.27
16			581	44.37	1.52	0.02
17			602	7.10	1.27	0.02
18	671		673	58.18	42.94	0.45
19		686	677	70.72	3.54	0.04
20	723		724	38.12	2.67	0.02
21	803	804	798	53.08	28.12	0.20
22			827	29.64	0.65	0.00
23	890		896	49.48	17.16	0.09
24	906	906	906	17.72	0.30	0.00
25			965	50.42	0.45	0.00
26			970	244.73	1.46	0.01
27			1010	230.67	3.55	0.01
28			1011	1.03	6.04	0.02
29	1078		1080	117.58	48.01	0.16
30		113	1120	30.43	8.25	0.03
31			1187	115.40	143.41	0.38
32	1217	1223	1207	104.81	51.68	0.13
33		1267	1273	28.41	55.01	0.12
34			1299	121.57	25.07	0.05
35			1327	853.17	79.01	0.16
36	1341		1345	289.05	6.71	0.01
37	1410	1397	1406	346.22	2.37	0.00
38			1416	33.99	31.16	0.05
39	1495	1494	1502	129.63	25.08	0.04
40	1560		1562	58.80	20.99	0.03
41	1620	1621	1628	86.69	871.05	1.00
42	1674	1672	1655	571.52	453.11	0.46
43	2967	2883	2874	111.97	298.32	0.05
44			3038	26.61	177.12	0.02
45			3067	9.51	157.88	0.02
46	3219	3072	3072	1.87	296.56	0.04
47	3450		3631	99.84	310.14	0.02
48			3665	73.28	108.90	0.01

The O-H stretching vibration is observed in boronic acids, usually close to $3300\text{--}3200\text{ cm}^{-1}$. This band was found to be 3467 cm^{-1} in FT-IR for 2-fluorophenylboronic acid [24] at 3280 cm^{-1} in IR for the phenylboronic acid molecule [23], 3400 and 3332 cm^{-1} in FT-IR at 2,3-difluorophenylboronic acid molecule, and it was calculated to be 3685 and 3692 cm^{-1} [25]. It was calculated to be 3631 and 3665 cm^{-1} in 3-4FPBA molecules and at 3450 cm^{-1} in FT-IR.

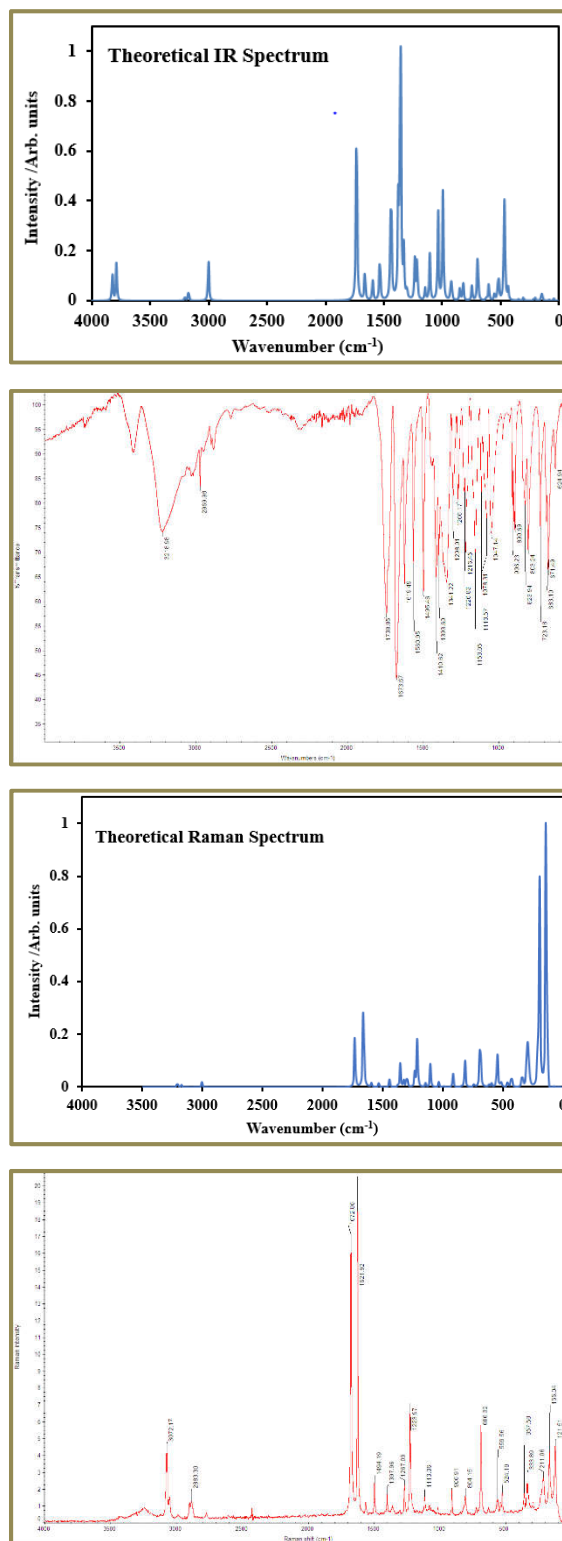
C-F stretching vibration is a mode in which the molecule is mixed with other modes. The C-F stretching vibration was generally observed as a strong band at $1000\text{--}1300\text{ cm}^{-1}$ in the IR spectrum [26, 27]. Narasimham et al. observed a C-F stretching vibration at 1250 cm^{-1} in the IR spectrum [28]. This vibration band was calculated as 1187 and 1207 cm^{-1} in the 3-4FPBA molecule and 1217 cm^{-1} in the FT-IR.

The B-O asymmetric stretching vibration was observed at 1350 cm^{-1} in the IR spectrum of the phenylboronic acid molecule [22], 1385 cm^{-1} in the FT-IR spectrum and 1370 cm^{-1} in the FT-Raman spectrum of the 2-fluorophenylboronic acid molecule [23]. Vargas and colleagues in the boron complexes deposited the band 1370 cm^{-1} as the B-O stretching vibration band [29]. A symmetric stretching vibration at 1327 cm^{-1} in the 3-4FPBA molecule was calculated. These modes are theoretically calculated at a range of $1400\text{--}1350\text{ cm}^{-1}$ [30-32].

The C-H stretching vibration in the phenyl ring is observed in the range of $3000\text{--}3100\text{ cm}^{-1}$, which is characteristic for these vibrations [29]. In this study, C-H stretching vibrations were calculated at $3038\text{--}3072\text{ cm}^{-1}$, and this vibration was observed at 3072 cm^{-1} in FT-Raman and 3219 cm^{-1} in FT-IR. These bands are 100% pure bands.

4.3. Frontier molecular orbital analysis

The HOMO-LUMO orbital energies and energy difference, called frontier molecule orbitals (FMO), were calculated using the TD-DFT method in the basis set of 6-311++G(d,p). The difference between the HOMO-LUMO energy values is an important parameter in determining the energy range, the electrical properties of the molecule.



energy required to pass from the most stable core state in the molecule to an excited state [33].

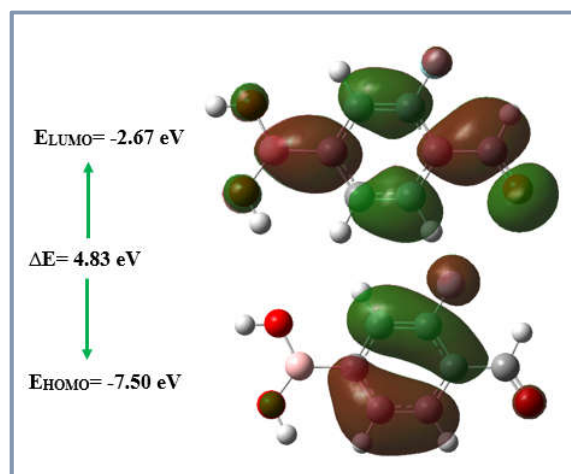


Figure 4. The frontier molecular orbitals of the 3-4FPBA for gas phase

The HOMO energy for the 3-4 FPBA molecule was calculated as -7.50 eV, the LUMO energy was -2.67 eV, the HOMO-LUMO energy difference was 4.83 eV, and it is given in Fig 4. In this graph, the red color is the positive phase and the green color is the negative phase. While the HOMO orbitals are concentrated in the ring, the LUMO orbitals are concentrated in the entire structure except hydrogen atoms.

Some parameters can be calculated using HOMO and LUMO energy values for a molecule. Chemical hardness, electronegativity and electrophilic index values in 3-4FPBA molecules were also calculated and given in Table 4. Intramolecular charge transfer of molecules with high chemical hardness values is low [34]

4. 4 Molecular Electrostatic Potential (MEP)

Molecular electrostatic potential (MEP) is a surface map showing the electron density of a molecule. A computational technique that is often used to determine effects such as nucleophilic reactions and electrophilic attack in a molecule. Reactants with a high tendency to give electrons when entering or exiting a reaction are called nucleophiles, while those with high tendency to take electrons are called electrofilms.

Nucleophilic and electrophilic reactions are displayed in different colors on the MEP surface map. The red color observed on this map has a negative potential, that is, blue and green colors showing electron-donating reactions show positive regions, that is, electron-withdrawing reactions. According to these results on the MEP surface map, the positive potential region (blue color) is around hydrogen and hydrogen atoms, while the negative potential region (red color) concentrates on electronegative atoms.

Table 4. The calculated energies values of 3-4FPBA

<i>Cisimetri</i>	Gas	DMSO	Ethanol
E_{total} (Hartree)	-474.5699	-474.5813	-474.4034
E_{HOMO} (eV)	-6.34	-6.45	-6.45
E_{LUMO} (eV)	-1.04	-1.25	-1.24
E_{HOMO-1} (eV)	-6.53	-6.62	-6.61
E_{LUMO+1} (eV)	-0.54	-0.62	-0.62
$E_{HOMO-1-LUMO+1}$ gap (eV)	5.99	6.00	6.00
$E_{HOMO-LUMO}$ gap (eV)	5.30	5.21	5.21
Chemical hardness (h)	2.65	2.60	2.61
Electronegativity (χ)	3.69	3.85	3.84
Chemical Potential (μ)	-3.69	-3.85	-3.84
Electrophilic index (ω)	2.57	2.85	2.83

These colors for the molecule -0.08751 a.u. (dark red) 0.08751 a.u. (dark blue) values and the electrostatic potential surface (MEP) of the molecule is given in Figure 5 as 3D surface. The highest positive potential in the molecule is around the hydrogen atom in the O-H group, with the most negative potential around the C = O double bond oxygen atom. In this case, the H atom contains a strong electron attractor and the O atom contains strong electron repulsion reactions.

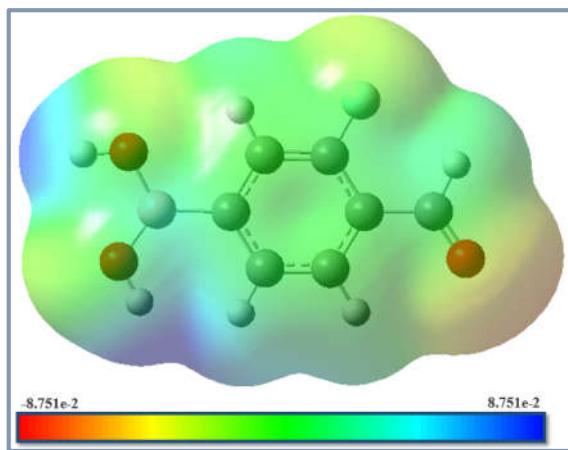


Figure 5. Molecular electrostatic potential (MEPs) 3D map for 3-4FPBA molecule

4.5. Mulliken atomic charges

Mulliken charge give a qualitative picture of a molecular population distribution [35]. However, this distribution does not fully reflect the electronegativities of each element. In some cases, an orbital can give a negative electron population, or an orbital can calculate more electrons than one. These depend strongly on the basis set used. Atomic charges are also used to define the molecular polarity of molecules [36]. The Mulliken charges distribution method is widely used despite some shortcomings. Mulliken charges experimental results are often used to make a qualitative set of estimates [37].

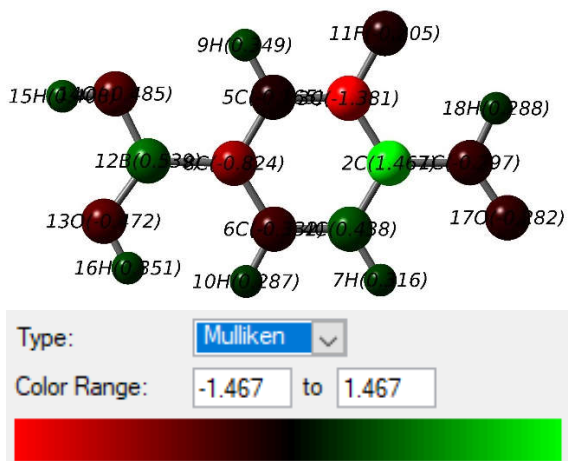


Figure 6. The Mulliken charge distribution for 3-4FPBA

The Mulliken atomic charges of the 3-4FPA molecule were calculated using the DFT/B3LYP method and the basis set of 6-311++G(d,p) and in given Fig. 6. The values of the Mulliken atomic charges of the molecule are compared in Table 5 with 3-FFPA and FBA it is given.

In all of the molecules that are compared, the atom of bromine leads to the redistribution of the electron density. The C2 atom in the phenyl ring of the 3-4 FPBA molecule has a more positive value than the 3-FFBA molecule. The C2 carbon atom's Mulliken charge is so high from other molecules that it can originate from the group of the formula linked to that atom (C = OH). In the 3-FFBA and 3-4FPBA molecules, the fluorine-bonded (C-F) C3 atom has the most negative charge in the ring. This is because the electronegativity due to the halogen group of the fluorine atom is a high atom.

Table 5. Mulliken atomic charges of the molecule FBA, 3-FFBA ve 3-4FPBA

Atom	FBA	3-FFBA	3-4FPBA
C1			-0.30
C2	-0.02	0.44	1.47
C3	-0.44	-0.86	-1.38
C4	-0.35	-0.44	0.44
C5	0.19	0.60	-0.16
C6	0.21	0.14	-0.33
H7	0.16	0.17	0.32
C8	-0.68	-0.75	-0.82
H9	0.20	0.23	0.35
H10	0.11	0.12	0.29
F11/H	0.16	-0.17	-0.21
B12	0.53	0.53	0.54
O13	-0.37	-0.37	-0.47
O14	-0.38	-0.37	-0.49
H15	0.29	0.29	0.41
H16	0.23	0.24	0.35
O17			-0.28
H18			0.29

5. DISCUSSION

In conclusion, conformation of 3-4 FPBA molecule was determined and geometric optimization was done for lowest energy conformation. After the optimization, the vibrational spectra of the molecules were investigated experimentally and theoretically and these values were compared. The electronic properties of the molecule (HOMO-LUMO and MEP) were then looked at, and the calculations revealed that the electrophilic and nucleophilic reactions took place around which atoms. Calculated and experimentally obtained values were compared and it was seen that the fit between them was good.

ACKNOWLEDGMENTS

This work was supported by Ahi Evran University Scientific Project Unit (BAP) with, Project No: TBY.A3.17.004.

REFERENCES

- [1] E. Frankland, B.F. Duppa, *Justus Liebigs Annalen der Chem* 115 (3) (1860) 319–322.
- [2] N.A. Petasis, *Aust. J. Chem.* 60 (2007) 795–798.
- [3] J.N. Cambre, B.S. Sumerlin, *Polymer* 52 (2011) 4631–4643.
- [4] M.R. Stabile, W.G. Lai, G. DeSantis, M. Gold, J.B. Jones, *Bioorg. Med. Chem. Lett.* 21 (1996) 2501–2506.
- [5] P.R. Westmark, B.D. Smith, *J. Pharm. Sci.* 85 (1996) 266–269.
- [6] X. Chen, G. Liang, D. Whitmire, J.P. Bowen, *J. Phys. Org. Chem.* 11 (1988), 378–386.
- [7] W. Tjarks, A.K.M. Anisuzzaman, L. Liu, S.H. Soloway, R.F. Barth, D.J. Perkins, D.M. Adams, *J. Med. Chem.* 35 (1992). 16228-11633.
- [8] Y. Yamamoto, *Pure Appl. Chem.* 63 (1991) 423–426.
- [9] F. Alam, A.H. Soloway, R.F. Barth, N. Mafune, D.M. Adam, W.H. Knoth, *J. Med. Chem.* 32 (1989) 2326–2330.
- [10] Meud, A., Erbes, M., Forstinker, K., US Patent No. 2002/0 161, p. 230, 2002.
- [11] Freeman, A., Segal, R., Dror, Y., US Patent No. 7.825.104, B2, 2010.
- [12] Thornfeldt C. R., Elias, P. M., Feingold, K. R., Holleran, W. M., US Patent No. 6,190,894, B1, 2001.
- [13] Weston, S., Shoichet, B., US Patent No. 6,075,014, A, 2000.
- [14] Shoichet, B., Weston, S., US Patent No. 6,184,363, B1, 2001.
- [15] Faniran, J. A., Shurvell, H. F., *Infrared spectra of phenylboronic acid (normal and deuterated) and diphenyl phenylboronate*, *Can. J. Chem.*, 46, 12, pp 2089-2095, 1968.
- [16] Rettig, S. J., Trotter, J., *Can. J. Chem.*, 55, 3071–3075, 1977.
- [17] M. J. Frisch, G.W. Trucks, H.B. Schlegel, G.E. Scuseria, M.A. Robb, J. R. Cross, J.B. Cheeseman, Gaussian 09, Revision A. 1 edn, Gaussian. Inc., Wallingford, CT, 2009.
- [18] P. Hohenberg, W. Kohn, "Inhomogeneous Electron Gas", *Physical Review*, vol. 136, pp. B864, 1964.
- [19] A.D. Becke, "Density-functional thermochemistry. III. The role of exact exchange", *Journal of Chemical Physics*, vol. 98, pp. 5648, 1993.
- [20] Y.M. Wu, C.C. Dong, S. Liu, H.-J. Zhu, Y.-Z. Wu, *Acta Cryst. E* 62 (2006) o4236–o4237.
- [21] 3 fluoro
- [22] Sundaraganesan, N., Ilakiamani, S., Salem, H., Wojciechowski, P.M., Michalska, D., *Spectrochim. Acta A* 61, 2995–3001, 2005.
- [23] Faniran, J. A., Shurvell, H. F., *Infrared spectra of phenylboronic acid (normal and deuterated) and diphenyl phenylboronate*, *Can. J. Chem.*, 46, 12, pp 2089-2095, 1968.
- [24] Erdogdu, Y., Güllüoğlu, M. T., Kurt, M., *J. Raman Spectrosc.* 40, 1615–1623, 2009.
- [25] Karabacak, M., Kose, E., Atac, A., Cipiloglu, M. A., Kurt, M., *Spectrochim. Acta Part A* 97, 892–908, 2012.
- [26] Eaton, V. J., Steele, D., *J. Mol. Spectrosc.* ,48, 446–458, 1973.
- [27] Pearce, R.A.R., Steele, D., Radcliffe, K.J., *J. Mol. Struct.* 15, 409–414, 1973.
- [28] Narasimham, N. A., El-Saban, M. Z., Rud-Nielson, J., *J. Chem. Phys.* 24, 420–433, 1956.
- [29] Silverstein, M., Basseler, G. C., Morill, C., *Spectrometric Identification of Organic Compounds*, Wiley: New York, 2001.
- [30] Kurt, M., Sertbakan, T. R., Özduran, M., Karabacak, M., *J. Mol. Struct.*, 921, 178–187, 2009.
- [31] Ayyappan, S., Sundaraganesan, N., Kurt, M., Sertbakan, T.R., Özduran, M., *J. Raman Spectrosc.* 41, 1379–1387, 2010.
- [32] Kurt, M., *J. Mol. Struct.* 874, 159–169, 2000
- [33] M. Arivazhagan, D. Anitha Rexalin, "FT-IR, FT-Raman, NMR studies and ab initio-HF, DFT-B3LYP vibrational analysis of 4-chloro-2-fluoroaniline", *Spectrochimica Acta A*, vol. 96, pp. 668–676, 2012.
- [34] Pearson, R., *Absolute electronegativity and hardness: applications to organic chemistry*, *J. Org.Chem.*, 54, 1423-1430, 1989.
- [35] Gruber, C., Buss, V., *Quantum-mechanically calculated properties for the development of quantitative structure-activity relationships (QSAR'S), pKA-values of phenols and aromatic and aliphatic carboxylic acids*, *Chemosphere*, 19, 1595–1609, 1989.
- [36] Karelson, M., Lobanov, V.S., *Quantum-chemical descriptors in QSAR/QSPR studies*. *Chemical Reviews*, 96, 1027-1043, 1996.
- [37] Hohenberg, P., Kohn, W., *Inhomogeneous Electron Gas*, *Physics Review*, 136 (3B), 864, 1964.

	SAKARYA ÜNİVERSİTESİ FEN BİLİMLERİ ENSTİTÜSÜ DERGİSİ <i>SAKARYA UNIVERSITY JOURNAL OF SCIENCE</i>		
	e-ISSN: 2147-835X Dergi sayfası: http://www.saujs.sakarya.edu.tr		
	<u>Received</u> 14-08-2018 <u>Accepted</u> 17-09-2018	<u>Doi</u> 10.16984/saufenbilder.453343	

Some remarks on completeness and compactness in G-metric spaces

Merve İlkan*¹, Emrah Evren Kara²

ABSTRACT

Complete metric spaces have great importance in functional analysis and its applications. The purpose of this paper is to introduce and study on some types of completeness in generalized metric spaces by the aid of Bourbaki Cauchy and cofinally Bourbaki-Cauchy sequences which are belonging to the class bigger than the class of Cauchy sequences. Moreover, by transporting some topological concepts to generalized metric spaces, the relations between these concepts and these new types of completeness properties are given.

Keywords: generalized metric spaces, compactness, completeness

1. INTRODUCTION

In mathematics and applied sciences, metric spaces play a central role. So several generalizations of the notion of a metric space have been proposed by many authors. Also, complete metric spaces have great importance to prove fundamental results in functional analysis which have many fascinating applications. For instance, Baire category theorem which is obtained when investigating the behavior of continuous functions is a very useful property to lighten the structure of complete metric spaces. Some applications of this theorem reveal various significant properties of complete metric spaces. Furthermore, Banach fixed point theorem is an important tool in the theory of complete metric spaces. By virtue of a great deal of applications in areas such as variational and linear inequalities, optimization and approximation theory, the progress of fixed point theory in metric spaces has drawn great interest. A large list of references can be found in the papers [1, 2, 3, 4, 6, 9, 10, 11, 12, 13, 14, 16] related to the fixed point results in generalized metric spaces. Many authors introduce

some new concepts between compactness and completeness in metric spaces and they give a number of new characterizations of these properties. For example, Beer [5] give some characterizations of cofinally complete metric spaces which implies that every cofinally Cauchy sequence has a convergent subsequence. More recently, Garrido and Merono [7] define Bourbaki-Cauchy sequences and cofinally Bourbaki-Cauchy sequences in metric spaces and they introduce two new types of completeness by using these new classes of generalized Cauchy sequences. Hence, these new concepts of completeness become properties stronger than the usual completeness. In [15], the authors define a new structure called as generalized metric or briefly G-metric and carry many concepts from metric spaces to the G-metric spaces. A generalized metric is a real valued function G defined on $X \times X \times X$ for a non-empty set X satisfying the following conditions.

$$(G1) \quad G(x, y, z) = 0 \text{ if } x = y = z,$$

$$(G2) \quad G(x, x, y) > 0 \text{ for all } x, y \in X \text{ with } x \neq y,$$

$$(G3) \quad G(x, x, y) \leq G(x, y, z) \text{ for all } x, y, z \in X \text{ with } z \neq y,$$

* Corresponding Author

¹ Department of Mathematics, Düzce University, Düzce, Turkey E-mail address: merveilkan@gmail.com

² Department of Mathematics, Düzce University, Düzce, Turkey E-mail address: karaevren@gmail.com

(G4) $G(x, y, z) = G(x, z, y) = G(y, z, x) = \dots$
(symmetry in all three variables),

(G5) $G(x, y, z) \leq G(x, a, a) + G(a, y, z)$ for all
 $x, y, z, a \in X$ (rectangle inequality).

The pair (X, G) is called a G -metric space. By G ,
one can construct a metric on X as follows:

$$d_G(x, y) = G(x, y, y) + G(x, x, y)$$

for all $x, y \in X$. Also, the inequality

$$G(x, y, y) \leq 2G(y, x, x)$$

holds for every $x, y \in X$.

The G -open ball (resp., G -closed ball) with centred
 $x \in X$ and radius ε is defined as $S_G(x, \varepsilon) = \{y \in X : G(x, y, y) < \varepsilon\}$
(resp., $S_G[x, \varepsilon] = \{y \in X : G(x, y, y) \leq \varepsilon\}$). The collection of all G -open
balls in X generates a topology $\tau(G)$ on X and this
topology is called G -metric topology. The sets of
 $\tau(G)$ are called as G -open. In a G -metric space, a
sequence (x_n) is said to be G -convergent to $x \in X$,
if $G(x_n, x_n, x) \rightarrow 0$ or equivalently
 $G(x_n, x, x) \rightarrow 0$ as $n \rightarrow \infty$. A sequence (x_n) is
said to be G -Cauchy if $G(x_n, x_m, x_l) \rightarrow 0$ as
 $n, m, l \rightarrow \infty$ or equivalently $G(x_n, x_m, x_m) \rightarrow 0$
as $n, m \rightarrow \infty$. If every G -Cauchy sequence in a G -
metric space is G -convergent, then the space is
called as G -complete. A subset S in a G -metric
space X is G -totally bounded if for every $\varepsilon > 0$
there exist finitely many elements x_1, x_2, \dots, x_n in
 X such that

$$S \subset \bigcup_{i=1}^n S_G(x_i, \varepsilon).$$

A G -metric space is said to be G -compact if the
space is a compact topological space with respect
to the G -metric topology, that is every G -open
cover of X has a finite subcover or equivalently
every sequence in the space has a G -convergent
subsequence. Further, a G -metric space is G -
compact if and only if it is G -complete and G -
totally bounded. For more concepts and some
characteristic properties of G -metric spaces, one
can see [8].

This paper is devoted to introduce and study on
some new properties in generalized metric spaces
which are stronger than completeness but weaker
than compactness. For this purpose, we define
some new classes of generalized Cauchy
sequences. Also, we transport some concepts in
metric spaces to generalized metric spaces and

give the relations between these concepts with new
properties.

2. MAIN RESULTS

For $m \in \mathbb{N}$, $S_G^m(x, \delta)$ consists of points y in X
such that there exists $a_1, a_2, \dots, a_{m-1} \in X$
satisfying $G(x, a_1, a_1) < \delta, G(a_1, a_2, a_2) < \delta,$
 $\dots, G(a_{m-1}, y, y) < \delta$. The open δ -enlargement
of a subset S in a G -metric space is defined as

$$S^\delta = \bigcup_{x \in S} S_G(x, \delta).$$

Hence, it can be easily seen that $S_G^m(x, \delta) =$
 $(S_G^{m-1}(x, \delta))^\delta$.

In a G -metric space, we call a subset as G -closed if
its complement is in $\tau(G)$. As in a usual metric
space, a set S is G -closed if and only if $x \in S$
whenever (x_n) is a sequence in S which is
 G -convergent to x . Also G -closed subsets of a
 G -compact set is G -compact.

By the G -neighborhood of a point x , we mean any
set U in $\tau(G)$ containing x . $G - Cl(S)$ stands for
the G -closure of S which consists of points x in X
such that every G -neighborhood of x and S has a
nonempty intersection.

Lemma 2.1. Let (X, G) be a G -metric space. Then
for all $x \in X, \varepsilon > 0$ and $m \in \mathbb{N}$ we have (1)
 $S_G^m(x, \varepsilon) \subseteq S_G(x, m\varepsilon),$

$$(2) S_G^m(x, \varepsilon/3) \subseteq S_{d_G}^m(x, \varepsilon) \subseteq S_G^m(x, \varepsilon).$$

Proof.

(1) Let $y \in S_G^m(x, \varepsilon)$. Then there exist
 $z_1, z_2, \dots, z_{m-1} \in X$ such that $G(x, z_1, z_1) < \varepsilon,$
 $G(z_1, z_2, z_2) < \varepsilon, \dots, G(z_{m-1}, y, y) < \varepsilon$. From
(G5), we obtain

$$\begin{aligned} G(x, y, y) &\leq G(x, z_1, z_1) + G(z_1, y, y) \\ &\leq G(x, z_1, z_1) + G(z_1, z_2, z_2) + G(z_2, y, y) \\ &\quad \vdots \\ &\leq G(x, z_1, z_1) + G(z_1, z_2, z_2) + \dots \\ &\quad + G(z_{m-1}, y, y) \\ &< \varepsilon + \varepsilon + \dots + \varepsilon = m\varepsilon \end{aligned}$$

which implies $y \in S_G(x, m\varepsilon)$.

(2) Choose $y \in S_G^m\left(x, \frac{\varepsilon}{3}\right)$. For $i = 0, \dots, m - 1$
we have $z_{i+1} \in S_G\left(z_i, \frac{\varepsilon}{3}\right)$, where $z_0 =$

$x, z_1, \dots, z_m = y \in X$. From the definition of the metric d_G with (G4) and (G5), we obtain

$$\begin{aligned} d_G(z_i, z_{i+1}) &= G(z_i, z_{i+1}, z_{i+1}) + G(z_i, z_i, z_{i+1}) \\ &\leq G(z_i, z_{i+1}, z_{i+1}) \\ &\quad + G(z_i, z_{i+1}, z_{i+1}) \\ &\quad + G(z_{i+1}, z_i, z_{i+1}) \\ &= G(z_i, z_{i+1}, z_{i+1}) \\ &\quad + G(z_i, z_{i+1}, z_{i+1}) \\ &\quad + G(z_i, z_{i+1}, z_{i+1}) \\ &< \varepsilon/3 + \varepsilon/3 + \varepsilon/3 = \varepsilon \end{aligned}$$

for $i = 0, \dots, m - 1$. This proves the first part of the inclusion in (2). The second part can be easily seen in a similar way.

A set S in a G -metric space (X, G) is called as G -Bourbaki bounded if for every $\varepsilon > 0$ there exist a finite number of elements x_1, x_2, \dots, x_n in X and $m \in \mathbb{N}$ such that

$$S \subset \bigcup_{i=1}^n S_G^m(x_i, \varepsilon).$$

A sequence (x_n) in (X, G) is said to be G -cofinally Cauchy if for every $\varepsilon > 0$ there exists an infinite subset \mathbb{N}_ε of \mathbb{N} such that for every $i, j, k \in \mathbb{N}_\varepsilon$, $G(x_i, x_j, x_k) < \varepsilon$. It is called as G -Bourbaki-Cauchy if for every $\varepsilon > 0$ there exist $m \in \mathbb{N}$ and $n_0 \in \mathbb{N}$ such that for every $n \geq n_0$, $c \in S_G^m(x, \varepsilon)$ ($x \in X$) and G -cofinally Bourbaki-Cauchy if for every $\varepsilon > 0$ there exist an infinite subset \mathbb{N}_ε of \mathbb{N} and $m \in \mathbb{N}$ such that for every $n \in \mathbb{N}_\varepsilon$, $x_n \in S_G^m(x, \varepsilon)$ ($x \in X$). We have the following corollaries whose proof follow from (2) in Lemma 2.1.

Corollary 2.2. Let (X, G) be a G -metric space and S be a subset of X . The following statements are equivalent.

- (1) S is G -Bourbaki bounded.
- (2) S is Bourbaki bounded with respect to the metric d_G .

Corollary 2.3. Let (X, G) be a G -metric space. The following statements are equivalent.

- (1) The sequence (x_n) is G -cofinally Cauchy.
- (2) The sequence (x_n) is a cofinally Cauchy sequence with respect to the metric d_G .

Corollary 2.4. Let (X, G) be a G -metric space. The following statements are equivalent.

- (1) The sequence (x_n) is G -Bourbaki-Cauchy.

- (2) The sequence (x_n) is a Bourbaki-Cauchy sequence with respect to the metric d_G .

Corollary 2.5. Let (X, G) be a G -metric space. The following statements are equivalent.

- (1) The sequence (x_n) is G -cofinally Bourbaki-Cauchy.
- (2) The sequence (x_n) is a cofinally Bourbaki-Cauchy sequence with respect to the metric d_G .

Theorem 2.6. Let (X, G) be a G -metric space and S be a subset of X . Then the following statements are equivalent:

- (1) S is G -Bourbaki bounded.
- (2) Any countable subset of S is G -Bourbaki bounded in X .
- (3) Any sequence in S has a G -Bourbaki-Cauchy subsequence in X .
- (4) Any sequence in S is G -cofinally Bourbaki-Cauchy in X .

Proof. If S is G -Bourbaki bounded, then every subset of S is G -Bourbaki bounded in X . Also, if a sequence has a G -Bourbaki-Cauchy subsequence, then the sequence itself is G -cofinally Bourbaki-Cauchy. Hence it is sufficient to show that the statements (2) \Rightarrow (3) and (4) \Rightarrow (1) hold.

(2) \Rightarrow (3) Let (x_n) be a sequence in S . Then, the set $\{x_n : n \in \mathbb{N}\}$ is G -Bourbaki bounded from the second statement. Hence for $\varepsilon_0 = 1$ there exist $m_1 \in \mathbb{N}$ and $z_1^1, \dots, z_{l_1}^1 \in X$ such that

$$\{x_n : n \in \mathbb{N}\} \subset \bigcup_{i=1}^{l_1} S_G^{m_1}(z_i^1, 1).$$

At least one of the G -open balls in this union, say $S_G^{m_1}(z_{i_1}^1, 1)$, contains infinitely many terms of the sequence (x_n) and so there is a subsequence (x_n^1) of the sequence (x_n) in $S_G^{m_1}(z_{i_1}^1, 1)$. For $\varepsilon_0 = 1/2$ there exist $m_2 \in \mathbb{N}$ and $z_1^2, \dots, z_{l_2}^2 \in X$ such that

$$\{x_n^1 : n \in \mathbb{N}\} \subset \bigcup_{i=1}^{l_2} S_G^{m_2}(z_i^2, 1/2)$$

since the set $\{x_n^1 : n \in \mathbb{N}\}$ is also G -Bourbaki bounded. Similarly, we say $S_G^{m_2}(z_{i_2}^2, 1/2)$ contains infinitely many terms of the sequence (x_n^1) and so there is a subsequence (x_n^2) of the sequence (x_n^1) in $S_G^{m_2}(z_{i_2}^2, 1/2)$. Given any $\varepsilon > 0$, there exists

$k_0 \in \mathbb{N}$ such that $\frac{1}{k_0} < \varepsilon$. By continuing the above process for $\varepsilon_0 = \frac{1}{k_0}$, we obtain

$$\{x_n^{k_0-1} : n \in \mathbb{N}\} \subset \bigcup_{i=1}^{l_{k_0}} S_G^{m_{k_0}} \left(z_i^{k_0}, \frac{1}{k_0} \right),$$

where $m_{k_0} \in \mathbb{N}$ and $z_1^{k_0}, \dots, z_{l_{k_0}}^{k_0} \in X$ and there is a subsequence $(x_n^{k_0})$ of the sequence $(x_n^{k_0-1})$ in $S_G^{m_{k_0}}(z_{i_{k_0}}^{k_0}, 1/k_0)$. Hence for all $n \geq k_0$ we have $x_n^n \in S_G^{m_{k_0}}(z_{i_{k_0}}^{k_0}, \varepsilon)$ which means that the diagonal subsequence (x_n^n) is a G -Bourbaki-Cauchy subsequence of (x_n) in X .

(4) \Rightarrow (1) Now, let every sequence in S be G -cofinally Bourbaki-Cauchy and suppose that S is not G -Bourbaki bounded in X . Then, there is an $\varepsilon_0 > 0$ such that for any finite subset $\{z_1, \dots, z_l\}$ of X and for all $m \in \mathbb{N}$, the union of G -open balls $S_G^m(z_1, \varepsilon_0), \dots, S_G^m(z_l, \varepsilon_0)$ do not cover S . Construct a sequence (x_n) in X such that for every $m \in \mathbb{N}$ and fixed $x_0 \in X$, $x_m \in S \setminus \bigcup_{i=0}^{m-1} S_G^m(x_i, \varepsilon_0)$, where $i = 0, \dots, m-1$. By our assumption, this sequence is G -cofinally Bourbaki-Cauchy and therefore there exist $m_0 \in \mathbb{N}$ and an infinite subset $\mathbb{N}_{\varepsilon_0}$ of \mathbb{N} such that for every $n \in \mathbb{N}_{\varepsilon_0}$, we have $x_n \in S_G^{m_0}(z_0, \varepsilon_0/2)$ ($z_0 \in X$). Choose $n_0 \in \mathbb{N}_{\varepsilon_0}$. Hence we obtain $x_n \in S_G^{2m_0}(x_{n_0}, \varepsilon_0)$ for all $n \in \mathbb{N}_{\varepsilon_0}$ which contradicts the construction of the sequence (x_n) .

A G -metric space (X, G) is said to be G -cofinally complete, G -Bourbaki complete or G -cofinally Bourbaki complete if every G -cofinally Cauchy, G -Bourbaki-Cauchy or G -cofinally Bourbaki-Cauchy sequence, respectively has a G -convergent subsequence in the space.

A subset in (X, G) is said to be G -relatively compact if G -closure of that subset is G -compact. (X, G) is said to be G -uniformly locally compact if there is a $\delta > 0$ such that for every $x \in X$ the set $G\text{-Cl}(S_G(x, \delta))$ is G -compact. Also, we call a subset in (X, G) as G -locally compact, G -locally totally bounded or G -locally Bourbaki bounded if each element in this set has a G -compact, G -totally bounded or G -Bourbaki bounded neighborhood, respectively.

Since every sequence in a compact G -metric space has a G -convergent subsequence, this space is also

G -Bourbaki complete. Further, a compact G -metric space is G -totally bounded and therefore it is G -Bourbaki bounded. On the contrary, if a G -metric space G -Bourbaki bounded and G -Bourbaki complete, then any sequence in this space has a G -Bourbaki-Cauchy subsequence from the preceding theorem and this subsequence has a G -convergent subsequence. Hence, this space is G -compact. Moreover, G -cofinally Bourbaki completeness is a stronger property than G -Bourbaki completeness since the class of G -cofinally Bourbaki Cauchy sequences is bigger than the class of G -Bourbaki-Cauchy sequences. Hence, we obtain the following results.

Theorem 2.7. A G -metric space is G -Bourbaki bounded and G -Bourbaki complete if and only if it is G -compact.

Theorem 2.8. A G -metric space is G -Bourbaki bounded and G -cofinally Bourbaki complete if and only if it is G -compact.

In the following theorem, a different characterization of G -Bourbaki completeness is given by G -relatively compactness of G -Bourbaki bounded subsets. Firstly, we prove a lemma which will be useful.

Lemma 2.9. The G -closure of a G -Bourbaki bounded subset in a G -metric space (X, G) is G -Bourbaki bounded.

Proof. Let S be a G -Bourbaki bounded subset in X and $\varepsilon > 0$. Then, we find some $m \in \mathbb{N}$ and $z_1, \dots, z_l \in X$ such that

$$S \subset \bigcup_{i=1}^l S_G^m(z_i, \varepsilon/2).$$

Take $x \in G\text{-Cl}(S)$. Then, we have $G(x, y, y) < \varepsilon/2$, where y belongs to $S_G^m(z_{i_0}, \varepsilon/2)$ for some $i_0 \in \{1, \dots, l\}$. Hence, we can choose some points $a_1, \dots, a_{m-1} \in X$ satisfying $G(z_{i_0}, a_1, a_1) < \varepsilon$, $G(a_1, a_2, 2) < \varepsilon, \dots, G(a_{m-1}, y, y) < \varepsilon$. Put $a_m = y$. Hence we obtain that $x \in S_G^{m+1}(z_{i_0}, \varepsilon)$. Thus, the inclusion

$$G\text{-Cl}(S) \subset S_G^{m+1}(z_{i_0}, \varepsilon)$$

holds and therefore $G\text{-Cl}(S)$ is G -Bourbaki bounded.

Theorem 2.10. A G -metric space (X, G) is G -Bourbaki complete if and only if every G -

Bourbaki bounded subset in X is G -relatively compact.

Proof. Let X be G -Bourbaki complete and S be a G -Bourbaki bounded subset in X . Take any sequence (x_n) in $G\text{-Cl}(S)$. Since $G\text{-Cl}(S)$ is also G -Bourbaki bounded, from Theorem 2.6, (x_n) has a G -Bourbaki-Cauchy subsequence. By G -Bourbaki completeness of X , it follows that this subsequence has a G -convergent subsequence. Since $G\text{-Cl}(S)$ is G -closed, we conclude that $G\text{-Cl}(S)$ is G -compact.

For the converse, let (x_n) be a G -Bourbaki Cauchy sequence in X and $S = \{x_n : n \in \mathbb{N}\}$. Then every sequence in S has a G -Bourbaki Cauchy subsequence and so from Theorem 2.6, S is G -Bourbaki bounded. By hypothesis, $G\text{-Cl}(S)$ is G -compact. Hence (x_n) has a G -convergent subsequence. This implies that X is G -Bourbaki complete.

It is clear that G -compactness implies G -Bourbaki completeness and G -cofinally Bourbaki completeness. Moreover, we will prove that the property of G -uniform local compactness is stronger than these two types of G -completeness. To show that, we give the following lemma.

Lemma 2.11. Let (X, G) be a G -uniformly locally compact space. If S is a G -compact subset in X , then $G\text{-Cl}(S^{\delta/2})$ is G -compact for some $\delta > 0$.

Proof. Let X be G -uniformly locally compact space. Then there is a $\delta > 0$ such that for every $x \in X$ the set $G\text{-Cl}(S_G(x, \delta))$ is G -compact. Now, let S be a G -compact subset in X . The G -open cover $\{S_G(y, \delta/2) : y \in S\}$ of S has a finite G -subcover $\{S_G(y_i, \delta/2) : y_i \in S, i = 1, \dots, l\}$, that is

$$S \subset \bigcup_{i=1}^l S_G(y_i, \delta/2). \quad (1)$$

Now, suppose that $z \notin (S_G(y_i, \delta/2))^{\delta/2}$ for $i = 1, \dots, l$. Then for every $x \in S_G(y_i, \delta/2)$ ($i = 1, \dots, l$), we have $z \notin S_G(x, \delta/2)$. From inclusion (1), we obtain $z \notin \bigcup \{S_G(x, \frac{\delta}{2}) : x \in S\}$ and this implies that

$$S^{\delta/2} \subset \bigcup_{i=1}^l (S_G(y_i, \delta/2))^{\delta/2}. \quad (2)$$

Choose $z \in (S_G(y_i, \delta/2))^{\delta/2}$ for some $i = 1, \dots, l$. Then there exists $x \in S_G(y_i, \delta/2)$ such that $z \in S_G(x, \delta/2)$. Thus, by using rectangle inequality, we have

$$G(y_i, z, z) \leq G(y_i, x, x) + G(x, z, z) < \delta,$$

that is $z \in S_G(y_i, \delta)$ and so $z \in G\text{-Cl}(S_G(y_i, \delta))$.

Hence, we write

$$\bigcup_{i=1}^l (S_G(y_i, \delta/2))^{\delta/2} \subset \bigcup_{i=1}^l G\text{-Cl}(S_G(y_i, \delta)). \quad (3)$$

By combining inclusions (2) and (3), we obtain

$$G\text{-Cl}\left(S^{\frac{\delta}{2}}\right) \subset \bigcup_{i=1}^l G\text{-Cl}(S_G(y_i, \delta)). \quad (4)$$

It is clear that the set in the right side of inclusion (4) is G -compact since it is the finite union of G -compact sets. We conclude that $G\text{-Cl}(S^{\delta/2})$ is G -compact since it is G -closed subset of a G -compact set.

Theorem 2.12. Let (X, G) be a G -metric space. If X is G -uniformly locally compact, then it is G -cofinally Bourbaki complete.

Proof. By hypothesis, there exists $\delta > 0$ such that the set $G\text{-Cl}(S_G(x, \delta/2))$ is G -compact for all $x \in X$ and hence we obtain from Lemma 2.11 that $G\text{-Cl}[(G\text{-Cl}(S_G(x, \frac{\delta}{2})))^{\delta/2}]$ is G -compact. The inclusion

$$G\text{-Cl}[(S_G(x, \frac{\delta}{2}))^{\delta/2}] \subset G\text{-Cl}[(G\text{-Cl}(S_G(x, \frac{\delta}{2})))^{\delta/2}]$$

implies that $G\text{-Cl}[(S_G(x, \frac{\delta}{2}))^{\delta/2}] = G\text{-Cl}(S_G^2(x, \delta/2))$ is G -compact.

Again, from Lemma 2.11, the set $G\text{-Cl}[(G\text{-Cl}(S_G^2(x, \frac{\delta}{2})))^{\delta/2}]$ is G -compact and from the inclusion

$$G\text{-Cl}[(S_G^2(x, \frac{\delta}{2}))^{\delta/2}] \subset G\text{-Cl}[(G\text{-Cl}(S_G^2(x, \delta/2)))^{\delta/2}]$$

we have that $G\text{-Cl}[(S_G^2(x, \frac{\delta}{2}))^{\frac{\delta}{2}}] = G\text{-Cl}(S_G^3(x, \frac{\delta}{2}))$ is G -compact.

Continuing this process, we observe that $G\text{-Cl}(S_G^m(x, \frac{\delta}{2}))$ is G -compact for all $m \in \mathbb{N}$.

Now, let (x_n) be a cofinally Bourbaki-Cauchy sequence in X . Then, we find $m \in \mathbb{N}$ and a subset $\mathbb{N}_{\delta/2} = \{n_1 < n_2 < \dots\} \subset \mathbb{N}$ such that $x_n \in S_G^m(x, \delta/2)$ for all $n \in \mathbb{N}_{\delta/2}$ and some $x \in X$. Hence, (x_{n_k}) is a sequence in $G - \text{Cl}(S_G^m(x, \delta/2))$ which is G -compact and so it has G -convergent subsequence. Thus, we conclude that X is G -cofinally Bourbaki complete.

Now, we have two lemmas to give some equivalent conditions for G -uniformly locally compactness of a generalized metric space.

Lemma 2.13. Let (X, G) be a G -metric space.

- (1) If X is G -locally totally bounded and G -cofinally complete, then it is G -locally compact.
- (2) If X is G -locally Bourbaki bounded and G -cofinally Bourbaki complete, then it is G -locally compact.

Proof. Let $x \in X$ and B be a G -totally bounded (G -Bourbaki bounded) neighborhood of x . Choose a G -closed ball $S_G[x, \varepsilon]$ contained in B . Since every subset of G -totally bounded (G -Bourbaki bounded) set is G -totally bounded (G -Bourbaki bounded), the G -closed ball $S_G[x, \varepsilon]$ is also G -totally bounded (G -Bourbaki bounded). Take a G -cofinally Cauchy (G -cofinally Bourbaki-Cauchy) sequence in $S_G[x, \varepsilon]$. By G -cofinally completeness (G -cofinally Bourbaki completeness) of X , we say that this sequence has a G -convergent subsequence and by G -closedness of $S_G[x, \varepsilon]$, we conclude that $S_G[x, \varepsilon]$ is G -cofinally complete (G -cofinally Bourbaki complete) and so G -complete. Hence we obtain a G -compact neighborhood of x which means X is G -locally compact.

Lemma 2.14. Let (X, G) be G -locally compact and (x_n) be a sequence in X such that $G - \text{Cl}(S_G(x_n, 1/n))$ is not G -compact for all $n \in \mathbb{N}$. Then (x_n) has no G -convergent subsequence.

Proof. Suppose that there is a G -compact neighborhood of every point in X . Take a sequence (x_n) in X such that $G - \text{Cl}(S_G(x_n, 1/n))$ is not G -compact for all $n \in \mathbb{N}$. We assume that the subsequence (x_{n_k}) is G -convergent to x . By hypothesis, x has a G -compact neighborhood B . Let $\varepsilon > 0$ such that $S_G(x, \varepsilon) \subset B$. We have for some $k_0 \in \mathbb{N}$ that $\frac{1}{k_0} < \frac{\varepsilon}{2}$. Also there exists $k_\varepsilon \in \mathbb{N}$

such that $G(x_{n_k}, x_{n_k}, x) < \varepsilon/2$ for all $k \geq k_\varepsilon$. Put $k' = \max\{k_0, k_\varepsilon\}$. We choose y from $S_G(x_{n_{k'}}, 1/n_{k'})$. Then by using rectangle inequality, we obtain

$$G(x, y, y) \leq G(x, x_{n_{k'}}, x_{n_{k'}}) + G(x_{n_{k'}}, y, y) < \varepsilon$$

and so we have $y \in S_G(x, \varepsilon)$ which yields the inclusion

$$G - \text{Cl}(S_G(x_{n_{k'}}, 1/n_{k'})) \subset S_G(x, \varepsilon) \subset B.$$

Since G -closed subset of a G -compact set is G -compact $G - \text{Cl}(S_G(x_{n_{k'}}, 1/n_{k'}))$ is G -compact which is a contradiction. Hence the sequence (x_n) constructed in the above way has no G -convergent subsequence.

Theorem 2.15. Let (X, G) be a G -metric space. Then the following statements are equivalent:

- (1) X is G -locally totally bounded and G -cofinally complete.
- (2) X is G -locally Bourbaki bounded and G -cofinally Bourbaki complete.
- (3) X is G -uniformly locally compact.

Proof. Firstly, let X be G -locally totally bounded and G -cofinally complete space. From Lemma 2.13, X is G -locally compact. Now, we assume that X is not G -uniformly locally compact. Then there is a point x_n in X such that $G - \text{Cl}(S_G(x_n, 1/n))$ is not G -compact for every $n \in \mathbb{N}$. Hence from Lemma 2.14, we say that the sequence (x_n) has no G -convergent subsequence. We can choose a sequence (w_k^n) in $G - \text{Cl}(S_G(x_n, 1/n))$ for each $n \in \mathbb{N}$ such that it has no G -convergent subsequence. Let $\mathbb{N} = \bigcup_{n=1}^{\infty} K_n$, where K_n is infinite subset of \mathbb{N} and $K_i \cap K_j = \emptyset$ for distinct $i, j \in \mathbb{N}$. Construct a sequence (θ_k) in the way that $\theta_k = w_k^n$ if $k \in K_n$. Given any $\varepsilon > 0$ there exists $n_\varepsilon \in \mathbb{N}$ such that $\frac{1}{n_\varepsilon} < \frac{\varepsilon}{9}$. Since $w_k^{n_\varepsilon} \in G - \text{Cl}(S_G(x_{n_\varepsilon}, 1/n_\varepsilon))$ for all $k \in \mathbb{N}$, we have

$$\begin{aligned} G(w_k^{n_\varepsilon}, x_{n_\varepsilon}, x_{n_\varepsilon}) &\leq G(w_k^{n_\varepsilon}, z, z) + G(z, x_{n_\varepsilon}, x_{n_\varepsilon}) \\ &\leq G(w_k^{n_\varepsilon}, z, z) + 2G(x_{n_\varepsilon}, z, z) \\ &< \frac{3}{n_\varepsilon} \end{aligned}$$

for some $z \in S_G(w_k^{n_\varepsilon}, 1/n_\varepsilon) \cap S_G(x_{n_\varepsilon}, 1/n_\varepsilon)$. Then for $i, j, k \in K_{n_\varepsilon}$, the inequality

$$\begin{aligned}
 G(\theta_i, \theta_j, \theta_k) &= G(w_i^{n_\varepsilon}, w_j^{n_\varepsilon}, w_k^{n_\varepsilon}) \\
 &\leq G(w_i^{n_\varepsilon}, x_{n_\varepsilon}, x_{n_\varepsilon}) \\
 &\quad + G(x_{n_\varepsilon}, w_j^{n_\varepsilon}, w_k^{n_\varepsilon}) \\
 &\leq G(w_i^{n_\varepsilon}, x_{n_\varepsilon}, x_{n_\varepsilon}) \\
 &\quad + G(w_j^{n_\varepsilon}, x_{n_\varepsilon}, x_{n_\varepsilon}) \\
 &\quad + G(x_{n_\varepsilon}, x_{n_\varepsilon}, w_k^{n_\varepsilon}) \\
 &< \frac{3}{n_\varepsilon} + \frac{3}{n_\varepsilon} + \frac{3}{n_\varepsilon} < \varepsilon
 \end{aligned}$$

holds which means that (θ_k) is G -cofinally Cauchy sequence in X . However it has no G -convergent subsequence which contradicts the fact that X is G -cofinally complete. Thus, X must be G -uniformly locally compact. Secondly, let X be G -uniformly locally compact space. Then we have that $S_G(x, \delta)$ is G -Bourbaki bounded neighborhood of x owing to the fact that δ is a positive real number such that $G - \text{Cl}(S_G(x, \delta))$ is G -compact and so it is G -Bourbaki bounded for every $x \in X$. Hence, it follows that G -uniformly locally compactness of X implies both G -locally Bourbaki boundedness of X and G -cofinally Bourbaki completeness of X which is proved in Theorem 2.12. Lastly, let X be G -locally Bourbaki bounded and G -cofinally Bourbaki complete space. Again, from Lemma 2.13, X is G -locally compact. Then every point in X has a G -compact neighborhood and thus G -totally bounded neighborhood which means X is G -locally totally bounded. Moreover, as we mention before that G -cofinally Bourbaki completeness implies G -cofinally completeness. Consequently, if X is G -locally Bourbaki bounded and G -cofinally Bourbaki complete, then it is G -locally totally bounded and G -cofinally complete.

REFERENCES

- [1] M. Abbas, T. Nazir and D. Doric, "Common fixed point of mappings satisfying (E.A) property in generalized metric spaces," *Applied Mathematics and Computation*, vol.218, pp. 7665-7670, 2012.
- [2] M. Abbas, T. Nazir and P. Vetro, "Common fixed point results for three maps in G-metric spaces", *Filomat*, vol.25, no.4, pp.1-17, 2011.
- [3] M. Abbas and B. E. Rhoades, "Common fixed point results for noncommuting mappings without continuity in generalized metric spaces," *Applied Mathematics and Computation*, vol.215, pp.262-269, 2009.
- [4] T. V. An, N. V. Dung and V. T. L. Hang, "A new approach to fixed point theorems on G-metric spaces," *Topology and its Applications*, vol.160, no.12, pp.1486-1493, 2013.
- [5] G. Beer, "Between compactness and completeness," *Topology and its Applications*, vol.155, no.6, pp.503-514, 2008.
- [6] B. S. Choudhury, and P. Maity, "Coupled fixed point results in generalized metric spaces," *Mathematical and Computer Modelling*, vol.54, pp.73-79, 2011.
- [7] M. I. Garrido, and A. S. Merono, "New types of completeness in metric spaces," *Annales Academiæ Scientiarum Fennicæ Mathematica*, vol.39, pp.733-758, 2014.
- [8] M. İlkhān and E.E. Kara, "Uniform continuity and Cauchy continuity in G-metric spaces," *Journal of Inequalities and Special Functions*, vol.8, no.3, pp.59-68, 2017.
- [9] A. Kaewcharoen, "Common fixed point theorems for contractive mappings satisfying Φ -maps in G-metric spaces," *Banach Journal of Mathematical Analysis*, vol.6, no.1, pp.101-111, 2012.
- [10] S. A. Mohiuddine and A. Alotaibi, "Some results on a triplet fixed point for nonlinear contractions in partially ordered G-metric spaces," *Fixed Point Theory and Applications*, vol.2012, no.179, 12 pages, 2012.
- [11] F. Moradlou, P. Salimi, and P. Vetro, "Some new extensions of Edelstein-Suzuki-type fixed point theorem to G-metric and G-cone metric spaces," *Acta Mathematica Scientia*, vol.33, no.4, pp.1049- 1058, 2013.
- [12] Z. Mustafa, F. Awawdeh, and W. Shatanawi, "Fixed Point Theorem for Expansive Mappings in G-Metric Spaces," *International Journal of Contemporary Mathematical Sciences*, vol.5, no.50, pp.2463-2472, 2010.
- [13] Z. Mustafa, H. Aydi and E. Karapınar, "On common fixed points in G-metric spaces using (E.A) property," *Computers & Mathematics with Applications*, vol.64, pp.1944-1956, 2012.

[14] Z. Mustafa, M. Khandagji, and W. Shatanawi, "Fixed point results on complete G-metric spaces," *Studia Scientiarum Mathematicarum Hungarica*, vol.48, no.3, pp.304-319, 2011.

[15] Z. Mustafa, and B. Sims, "A new approach to generalized metric spaces," *Journal of Nonlinear*

and Convex Analysis, vol.7, no.2, pp.289-297, 2006.

[16] M. Öztürk and M. Başarır, "On some common fixed point theorems with φ -maps on G-cone metric spaces," *Bulletin of Mathematical Analysis and Applications*, vol.3, no.1, pp.121-133, 2011.

	SAKARYA UNIVERSITY JOURNAL OF SCIENCE		 SAKARYA UNIVERSITY
	e-ISSN: 2147-835X http://www.saujs.sakarya.edu.tr		
	<u>Received</u> 20-04-2018 <u>Accepted</u> 15-10-2018	<u>Doi</u> 10.16984/saufenbilder.417384	

Investigation of Magnetic Properties of Spin 5/2 Ising Chain by Using Transfer Matrix Method

Mehmet Gökhan Şensoy^{*1}, Mehmet Batı²

Abstract

A magnetic property of the one dimensional spin 5/2 Ising model under the magnetic field has been investigated by means of transfer matrix method. Thermodynamic response functions are also obtained for varying values of temperature (in K) and scaling magnetic field. Entropy and heat capacity of the system were calculated by benefiting from the temperature dependencies of Helmholtz free energy. We observed that the heat capacity tends to shift to the relatively higher temperature regions as the strength of the magnetic field is increased, and these findings are consistent with previous results for the low spin values in one dimensional Ising systems.

Keywords: Magnetic properties, Ising chain, Transfer matrix method, Low dimensional systems

1. INTRODUCTION

Recent years, the thermodynamic properties of magnetic materials have been studied in many experimental and theoretical studies because of their potentials in nanotechnology industry [1-3]. These materials can be produced in the laboratory and their magnetic properties can be experimentally measured to use in industrial applications such as storage devices, industrial magnets and sensors [1-3].

The size of the nanomaterial affects significantly the magnetic properties in small-scale applications. Many theoretical models such as mean field theory [4], effective field theory [5], Monte Carlo simulation method [6], Green's function formalism [7] and transfer matrix method [8] have been used to investigate the unique properties of these materials in one-dimensional (1D) and two-dimensional (2D) systems. Ising model [9], can be used to describe the material

properties such as phase transition and temperature dependent magnetization.

Recent works are mainly focused on exactly solvable spin 1/2 and spin 1 systems based on Monte Carlo and Ising models [10, 11]. This kind of spin chain compounds shows a 1D ferromagnetic behavior modeled by spin chains [12]. In many theoretical studies on the thermodynamic properties, the spin 1/2 Ising system is used for the 1D chain structures.

The exact solution for the 1D Ising systems under external magnetic field was reported in previous work by Kassan-Ogly [13] including nearest neighbor and next-nearest neighbor interactions. The temperature behavior of the spin-correlation function in 1D spin 1 Ising model has been still studied in many theoretical works [11, 14]. Using only spin 1/2 and 1 is too idealized in theoretical studies, and this cannot represent the magnetic materials used in industrial applications such as permanent magnet. Therefore, the studies are expanded to higher spin systems greater than spin

* Corresponding Author (mehmet.sensoy@erdogan.edu.tr)

¹ Recep Tayyip Erdogan University, Department of Physics, 53100, Rize, Turkey, mehmet.sensoy@erdogan.edu.tr

² Recep Tayyip Erdogan University, Department of Physics, 53100, Rize, Turkey, mehmet.bati@erdogan.edu.tr

1. It is well known that the analysis of spin systems becomes difficult for the higher spin values.

The investigation of higher-order spin systems has been theoretically studied many decades ago by Anderson [15] and Kittel [16]. Then, in many experimental studies, the higher-order spin couplings have been observed in some magnetic compounds such as MnO and NiO [17]. The magnetic properties of this kind of complex systems were originally introduced by Iwashita et al. [18]. To understand the spin interactions for magnetic materials, the investigation of higher-order spin system such as 1D spin 2 or 5/2 systems becomes important. For instance, the disordered $\text{Fe}_{(1-q)}\text{Al}_q$ alloys show higher-order spin values, spin 2 and spin 5/2, for Fe^{+2} and Fe^{+3} , respectively [19], and these spin 5/2 systems have been modeled by using different theoretical methods [20-22].

In this work, we study the spin 5/2 in 1D chain system by using Ising model with transfer matrix method (TMM). This model is successfully applied to investigate numerically the magnetic properties of 1D system due to the hardness of exactly solving the higher-order spin systems.

2. MODEL AND METHOD

The Hamiltonian for the 1D spin 5/2 Ising model with the presence of an external field is given by

$$\mathcal{H} = -J \sum_{\langle ij \rangle} \sigma_i \sigma_j - H \sum_i \sigma_i \quad (1)$$

where J denotes the exchange coupling of ferromagnetic type ($J > 0$), $\langle ij \rangle$ represents nearest neighbor interaction and the field H is units of energy. σ spin values can be taken as

$$\sigma = \pm \frac{5}{2}, \pm \frac{3}{2}, \pm \frac{1}{2} \quad (2)$$

The partition function constructed by using periodic boundary conditions is given as

$$Z = \sum_{\{\sigma_i\}} e^{-\beta \mathcal{H}(\{\sigma_i\})} = \sum_{\{\sigma_i\}} e^{\beta J \sum_i (\sigma_i \sigma_{i+1} + \beta H (\frac{\sigma_i + \sigma_{i+1}}{2}))} \quad (3)$$

Here $\beta = 1/k_B T$, k_B is the Boltzmann constant. We have used the transfer matrix method (TMM) [23, 24] to perform the statistical analysis of the

considered system. The matrix elements of transfer matrix can be defined by

$$\langle \sigma_i | TM | \sigma_{i+1} \rangle = \exp \left\{ \beta \left[J \sigma_i \sigma_{i+1} + \frac{1}{2} H (\sigma_i + \sigma_{i+1}) \right] \right\} \quad (4)$$

Transfer matrix of the 1D spin 5/2-system is given as

$$TM \equiv \begin{pmatrix} e^{\frac{25}{4}\beta J + \frac{5}{2}\beta h} & e^{\frac{15}{4}\beta J + 2\beta h} & e^{\frac{5}{4}\beta J + \frac{3}{2}\beta h} & e^{\frac{5}{4}\beta J + \beta h} & e^{\frac{15}{4}\beta J + \frac{1}{2}\beta h} & e^{\frac{25}{4}\beta J + \beta h} \\ e^{\frac{15}{4}\beta J + 2\beta h} & e^{\frac{9}{4}\beta J + \frac{3}{2}\beta h} & e^{\frac{3}{4}\beta J + \beta h} & e^{-\frac{3}{4}\beta J + \frac{1}{2}\beta h} & e^{-\frac{9}{4}\beta J + \beta h} & e^{-\frac{15}{4}\beta J - \frac{1}{2}\beta h} \\ e^{\frac{5}{4}\beta J + \frac{3}{2}\beta h} & e^{\frac{3}{4}\beta J + \beta h} & e^{\frac{1}{4}\beta J + \frac{1}{2}\beta h} & e^{-\frac{1}{4}\beta J} & e^{-\frac{3}{4}\beta J - \frac{1}{2}\beta h} & e^{-\frac{5}{4}\beta J - \frac{3}{2}\beta h} \\ e^{-\frac{5}{4}\beta J + \beta h} & e^{-\frac{3}{4}\beta J + \frac{1}{2}\beta h} & e^{-\frac{1}{4}\beta J} & e^{\frac{1}{4}\beta J - \frac{1}{2}\beta h} & e^{\frac{3}{4}\beta J - \beta h} & e^{\frac{5}{4}\beta J - \frac{3}{2}\beta h} \\ e^{-\frac{15}{4}\beta J + \frac{1}{2}\beta h} & e^{-\frac{9}{4}\beta J} & e^{-\frac{3}{4}\beta J - \frac{1}{2}\beta h} & e^{-\frac{3}{4}\beta J - \beta h} & e^{\frac{3}{4}\beta J - \frac{1}{2}\beta h} & e^{\frac{15}{4}\beta J - 2\beta h} \\ e^{-\frac{25}{4}\beta J} & e^{-\frac{15}{4}\beta J - \frac{1}{2}\beta h} & e^{-\frac{5}{4}\beta J - \beta h} & e^{-\frac{5}{4}\beta J - \frac{3}{2}\beta h} & e^{\frac{5}{4}\beta J - \frac{1}{2}\beta h} & e^{\frac{25}{4}\beta J - 5\beta h} \end{pmatrix} \quad (5)$$

where we use the dimensionless parameters for numerical simplicity.

We scale our parameter with J so $\tilde{J} = \frac{J}{J} = 1.0$, where $h = H/J$ scaling field parameter and $\tilde{\beta} = J/k_B T$ scaling inverse thermodynamic temperature.

Since the matrix is identical for $(\sigma_1 \sigma_2)$, $(\sigma_2 \sigma_3)$ and so on, the partition function is then given by $Z = \sum_{\{\sigma_i\}} (TM)^N = \text{Tr} (TM)^N = \sum_{i=1}^6 \lambda_i^N$ (6)

while $N \gg 1$ the Helmholtz free energy is $F = -k_B T \ln(\lambda^>)$ where $\lambda^>$ is the biggest eigenvalues of TM in equation (5). We can construct thermodynamic expressions as internal energy E equation (7), ferromagnetic order parameter (magnetization) m equation (8), the magnetic susceptibility χ equation (9), entropy S equation (10) and the specific heat C equation (11) by using Helmholtz free energy F .

$$E = - \left(\frac{\partial \ln(\lambda^>)}{\partial \beta} \right)_h \quad (7)$$

$$m = - \left(\frac{\partial F}{\partial h} \right)_T \quad (8)$$

$$\chi = - \left(\frac{\partial^2 F}{\partial h^2} \right)_T = \left(\frac{\partial m}{\partial h} \right)_T \quad (9)$$

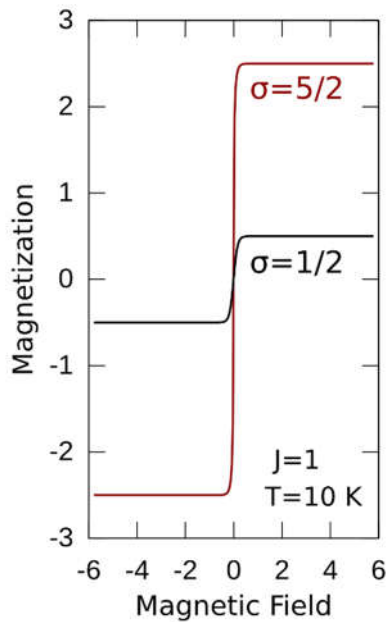
$$S = - \left(\frac{\partial F}{\partial T} \right)_h \quad (10)$$

$$C = -T \left(\frac{\partial^2 F}{\partial T^2} \right)_h = T \left(\frac{\partial S}{\partial T} \right)_h \quad (11)$$

3. RESULTS

We studied the magnetic properties of 1D spin 5/2 system by using the transfer matrix method. In 1D Ising model ($N \gg 1$) the phase transition to the ferromagnetic behavior happens at the critical temperature 0. Free energy is clearly analytic for finite temperature, and there can not be seen any phase transition at any finite temperature ($T > 0$). Thus in the linear-chain Ising model, spontaneous magnetization is not possible.

We have performed the magnetization behavior as a function of applied magnetic field to understand the differences between the low spin order and higher order spin systems, see Figure 1. It is easy to say that the maximum magnetization value for the spin 1/2 system is 0.5, while the maximum magnetization value for the spin 5/2 system is 2.5 as we expected.



The magnetizations were calculated at $T = 5, 100$ and 300 K as functions of reduced magnetic field. The magnetization (m) behavior at lower ($T=5, 100$ K) and higher temperatures ($T=300$ K), and the magnetization as a function of dimensionless magnetic field (h) and temperature are given in Figure 2.

The magnetization for any value of h at absolute zero is equal to the saturation value $5/2$, which implies ferromagnetic order in considering system. This means that phase transition occurs at $T=0$,

and no phase transition occurs at any finite temperature. At low temperature the spins align easily but contrary at high temperature to align the spins a strong magnetic field should be applied. We observed that the magnetization behavior with the change of magnetic field becomes more smooth and wider with the increase of the temperature, see Figure 2 a). When the temperature is close the critical temperature, the response of magnetization to the field becomes sharper. The magnetization becomes a step

function at $T=0$ K ($\beta \rightarrow \infty$). In 1-D system the critical temperature is 0 K, and the linear response of magnetization for a small magnetic field infinitely sharp. The changes in temperature determine how sharply magnetization saturates with the change of applied magnetic field. Results show that the saturation at low temperature requires a small magnetic field, but at higher temperature values it requires a higher magnetic field.

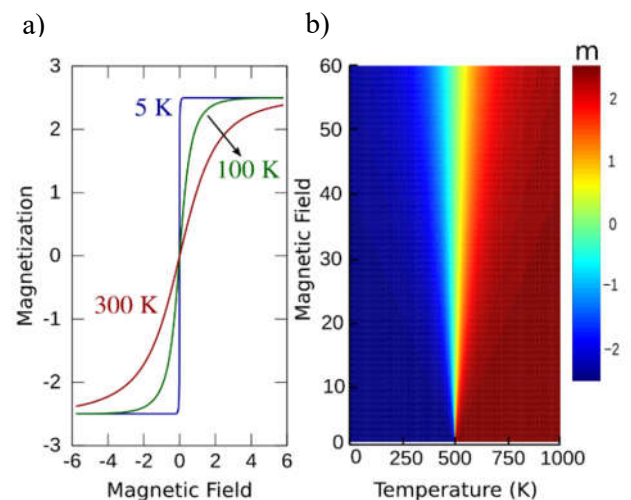


Figure 2. a) Magnetization behavior of 1D spin 5/2 system as a function of dimensionless magnetic field (h) for spin 1/2 and 5/2 at 10 K. The exchange coupling parameter (J) is 1.

It is worth mentioning that the magnetization responds extremely sensitive to the applied magnetic field in the limit of the low temperature values.

We have also observed that the magnetization can be controlled by tuning the energy (E) and entropy (S). The energy favors the largest possible value of

m which is aligned with the applied field. Therefore, the equilibrium m value can be minimized by the Helmholtz free energy (F), see Figure 3.

The equilibrium value of m is that minimizes F . In Figure 3, we see that only one minimum for all different temperature values and the free energy is minimum at $m = 0$. This supports the reason of being only one phase for the considering system. The ferromagnetic system can either have $+5/2$ or $-5/2$ values and thus, the F would choose only one favorite value.

The changes in entropy and internal energy of considered system with respect to temperature for different magnetic field ($h = 0.1, 1.0$ and 2.5) are given in Figure 4.

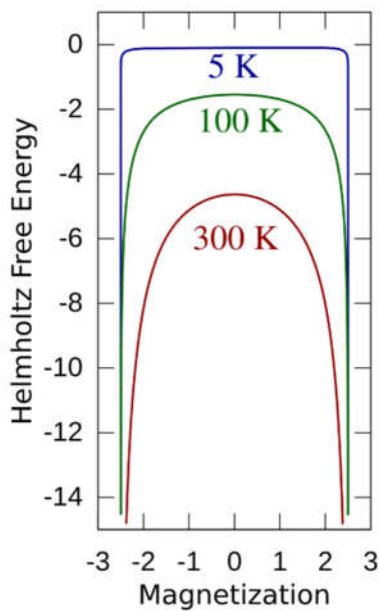


Figure 3. Helmholtz free energy as a function of magnetization at $T=5, 100$ and 300 K.

Results show that the higher h values ($h=2.5$) at critical temperature give rise to higher internal energy, and the internal energy converges to the zero at higher temperature values. At low T and h , the entropy becomes constant rapidly, while the energy becomes constant at higher temperatures for higher h values, see Figure 4 a).

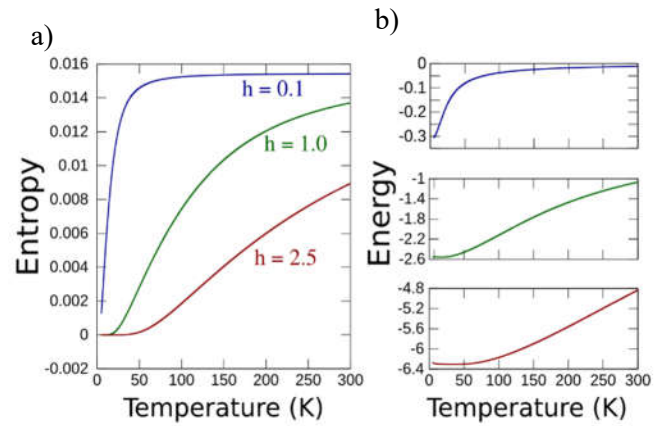


Figure 4. a) Entropy and b) Energy as a function of temperature for $h=0.1, 1.0$ and 2.5 .

In the limit of $T \rightarrow 0$ entropy goes to zero $S \rightarrow 0$. An ideal Ising chain would certainly obtain all its entropy of ordering above 0 K. To increase the temperature of the system, one needs to apply heat and adding heat to the system increases its entropy. As the field increases, more thermal energy is required to achieve saturation values of entropy (see Figure 4).

The magnetic susceptibility (χ) of the system is calculated by the derivative of magnetization. The magnetic field dependence of the susceptibility is reported in Figure 5 in the case of $T=5, 100$ and 300 K. The susceptibility peaks show that the maximum of χ is larger for low temperature value. The critical point is $h=0$ and diverges as $T \rightarrow 0$.

However, it is important to note that the singularity is not of the power law type instead it is exponential [22].

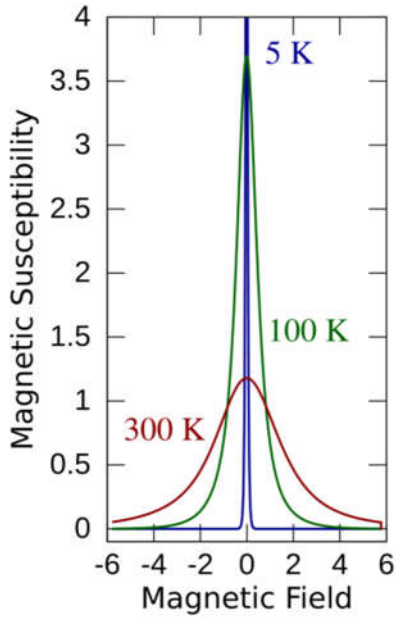


Figure 5. Magnetic susceptibility as a function of magnetic field at 5, 100 and 300 K.

We know how much energy changes with increasing of the temperature from the specific heat (C). The specific heat is a smooth function of temperature (finite at all temperatures) and vanishing at zero temperature. As expected there is no critical point at a finite temperature which corresponds to the singular behavior of specific heat. Specific heat values at $T=15$, 102 and 246 K are presented with the maximum for $h=0.1$, 1.0 and 2.5, respectively in Figure 6. If the magnetic field is increased, the peak of the specific heat at constant volume is shifted to higher temperature region as seen in Figure 6.

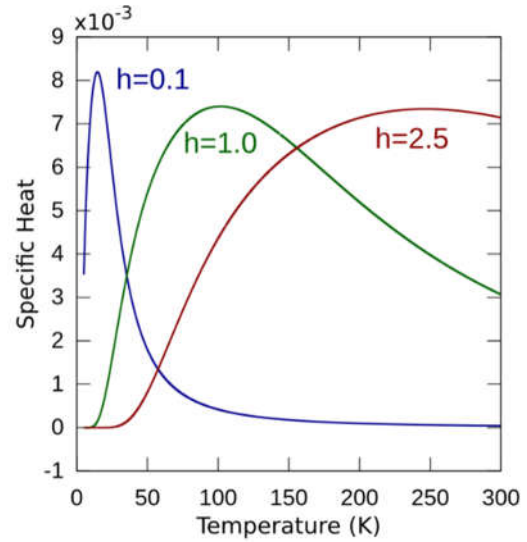


Figure 6. Specific heat as a function of temperature for $h=0.1$, 1.0 and 2.5.

4. CONCLUSION

Equilibrium properties of one dimensional spin 5/2 Ising system under magnetic field were studied by using transfer matrix method. Thermodynamic response functions are obtained for varying values of temperature and scaled magnetic field. We obtained the internal energy and specific heat as a function of temperature. Our numerical results show that heat capacity tends to shift to the relatively higher temperature regions as the magnetic field is increased and the curves are a broad maximum for higher magnetic field values. We have presented the graph in a magnetization-free energy (m-F) plane for different temperature values. Because of Helmholtz free energy has only one minimum, there is one phase for the considering system. Our results are conceptually consistent with the previous results for the lower spin systems in one dimensional Ising chain.

5. REFERENCES

- [1] Kodama, R. H., "Magnetic nanoparticles," *Journal of Magnetism and Magnetic Materials*, vol. 200, pp. 359-372, 1999.
- [2] Zeng, H, Li, J., Liu, J.P, Wang, Z. L., and Sun, S., "Exchange-coupled nanocomposite magnets by nanoparticle self-assembly,"

- Nature, vol. 420, pp. 395-398, 2002.
- [3] Kodama, R. H., Berkowitz, A. E., McNiff, E. J. and Foner, J. S., "Surface Spin Disorder in NiFe₂O₄ Nanoparticles," *Physical Review Letters*, vol. 774, pp. 394-397, 1996.
- [4] V. S. Leite and W. Figueiredo, "Spin-glass surface disorder on the magnetic behaviour of antiferromagnetic small particles," *Physica A: Statistical Mechanics and its Applications*, vol. 350, pp. 379-392, 2005.
- [5] Sarli, N. and Keskin, M., "Two distinct magnetic susceptibility peaks and magnetic reversal events in a cylindrical core/shell spin-1 Ising nanowire," *Solid State Communications*, vol. 152, pp. 354-359, 2012.
- [6] Eglesias, O, Battle, X, and Labarta, A., "Microscopic origin of exchange bias in core/shell nanoparticles," *Physical Review B*, vol. 72, pp. 212401, 2005.
- [7] Garanin, D. A. and Kachkachi, H., "Surface Contribution to the Anisotropy of Magnetic Nanoparticles," *Physical Review Letters*, vol. 90, pp. 65504, 2003.
- [8] Pathria, R. K. and Beale, P.D., "Statistical Mechanics", Third Edition, Academic Press, 2011.
- [9] Ising, E., "Beitrag zur Theorie des Ferromagnetismus", *Zeitschrift für Physik*, vol. 31, pp. 253 1925.
- [10] Vatansever, Z.D., Vatansever, E., "Thermal and magnetic phase transition properties of a binary alloy spherical nanoparticle: A Monte Carlo simulation study," *Journal of Magnetism and Magnetic Materials*, vol. 432, pp. 239-244, 2017.
- [11] Vatansever, Z.D., Vatansever, E., "Finite temperature magnetic phase transition features of the quenched disordered binary alloy cylindrical nanowire," *Journal of Alloys and Compounds* vol. 701, pp. 288-294, 2017.
- [12] Ovchinnikov, A.S., Bostrem, I.G., Sinitsyn, V.E., Boyarchenkov, A.S., Baranov, N.V., Inoue, K., "Low-energy excitations and thermodynamical properties of the quantum (5/2, 1/2, 1/2) ferrimagnetic chain," *Journal of Physics: Condensed Matter*, vol. 14, no. 34, pp. 8067-8078, 2002.
- [13] Kassin-Ogly, F.A., "One-dimensional ising model with next-nearest-neighbour interaction in magnetic field," *Phase Transitions*, vol. 14, pp. 353-365, 2001.
- [14] Proshkin, A. I., Ponomareva, T. Yu., Menshikh, I. A., Zarubin, A. V. and Kassin-Ogly, F. A., "Correlation function of one-dimensional s = 1 Ising model," *Physics of Metals and Metallography*, vol. 118, no. 10, pp. 929-934, 2017.
- [15] Anderson, P. W., "New Approach to the Theory of Superexchange Interactions," *Physical Review B*, vol. 115, pp. 2, 1959.
- [16] Kittel, C., "Model of Exchange-Inversion Magnetization," *Physical Review B*, vol. 120, pp. 335, 1960.
- [17] Rodbell, D. S. and Owen, J., "Sublattice Magnetization and Lattice Distortions in MnO and NiO," *Journal of Applied Physics*, vol. 35, pp. 1002-1003, 1964.
- [18] Iwashita, T. and Uryu, N., "Higher Order Spin Coupling in Complex Compounds," *Journal of the Physical Society of Japan*, vol.36, pp. 48-54, 1974.
- [19] Koebler, U., English, J., Hupe, O. and Hesse, J., "Effective spin quantum numbers in iron, cobalt and nickel," *Physica B: Condensed Matter*, vol. 339, pp. 156-163, 2003.
- [20] Kaneyoshi, T., Jascur, M., "Contribution to the Theory of the spin 5/2 Blume-Capel Model" *Physica Status Solidi (b)* vol. 175, pp. 225-236, 1993.
- [21] Saber, M., Tucker, J.W., "Phase Diagram and Magnetization Moments of the Spin-5/2 Diluted Ising Ferromagnet in a Transverse Field", *Physica Status Solidi (b)* vol. 189, pp. 229-238, 1995.
- [22] Song, W.J., Yang, C.Z. , "FRG-DPIR study of spin-5/2 Ising model with a random transverse field," *Solid State Com.*, vol. 92 pp. 361-364, 1994.
- [23] Kramers, H. A. and Wannier, G. H., "Statistics of the Two-Dimensional Ferromagnet. Part I," *Physical Review*, vol. 60, pp. 252-262, 1941.
- [24] Kramers, H. A. and Wannier, G. H., "Statistics of the Two-Dimensional Ferromagnet. Part II," *Physical Review*, vol. 60, pp. 263-276, 1941.

	SAKARYA UNIVERSITY JOURNAL OF SCIENCE		 SAKARYA UNIVERSITY
	e-ISSN: 2147-835X http://www.saujs.sakarya.edu.tr		
	<u>Received</u> 09-02-2018 <u>Accepted</u> 24-10-2018	<u>Doi</u> 10.16984/saufenbilder.392685	

On the Butterflies of Savur District (Mardin Province, Southeastern Turkey)Erdem Seven^{*1} Cihan Yıldız²**Abstract**

In this study, butterfly species collected from Savur district of Mardin Province in 2016 and 2017, are presented. A total of 35 species are given in the Papilionidae (2), Pieridae (11), Satyridae (8), Argynnididae (4), Lycaenidae (5) and Hesperidae (5) families from the research area that has not been studied previously on the butterflies. Original reference, synonyms, examined materials and distributions of each species are added. However, 6 species: *Euchloe ausonia* (Hübner, [1804]), *Pieris brassicae* (Linnaeus, 1758) (Pieridae), *Melitaea phoebe* (Goeze, 1779) (Argynnididae), *Plebejus zephyrinus* (Christoph, 1884) (Lycaenidae), *Carcharodus lavatherae* (Esper, [1783]) and *Eogenes alcides* Herrich-Schäffer, [1852] (Hesperidae) are the first record for Mardin Province.

Keywords: Fauna, Butterfly, Savur, Mardin**1. INTRODUCTION**

In Turkey, 5577 Lepidoptera species are known and, among them 412 species belong to the Rhopalocera (Butterfly) group [1]. When compared to other nearby areas in Turkey, it is seen that studies on the Lepidoptera fauna of Mardin Province is not adequate and comprehensive researches have not been undertaken. In the 19th century, collected samples of Lepidoptera species from Mardin Province by Armenian collectors were generally described by O. Staudinger and most of them were stored in various Natural History Museums in Germany.

In 1995, Hesselbarth et al., [2], were given Turkey's butterfly fauna and they also included some species captured from Mardin Province, on their extensive studies in 3 volumes. Otherwise,

Kemal and Koçak [3] were presented first exhaustive study on the synonymic list of 81 butterflies species in 2006 and afterwards, Kemal et al., [4] were listed totally 274 Lepidopteran species from Mardin Province. Furthermore, the last current list of 83 butterfly species were given by Koçak and Kemal [5] again, in their paper on Mardin's Lepidoptera species. Also, Kocak and Kemal was published a revised synonymous and distributional list of butterfly and moth species showing distribution in Turkey in 2018. But, there is no study on the butterfly fauna of Savur district so far. Therefore, presented research results will contribute to the Lepidoptera fauna of Savur district and Mardin Province.

In addition to these papers, studies carried out in the nearby areas: Seven [6, 7], Özkol [8], Hardy [9], Koçak and Kemal [10], Akın [11], Kemal and

* Corresponding Author

¹ Batman University, School of Tourism and Hotel Management, 72060, Batman² Tepe Dicle Middle School, Bismil, 21500, Diyarbakır

Aydın [12, 13] and Tshikolovets et al. [14] were also evaluated.

2. MATERIAL AND METHOD

547 samples were collected from Savur district of Mardin Province between April 2016 and April-July 2017. The materials, which were packed and taken to the storage boxes, were caught with the aid of insect nets. Researches were conducted in 6 localities (Figure 1). For each locality, habitat type, altitude, collecting date and coordinate informations are as follows:

1. Savur: Sparse oak field, 840 m, 12.04.2016, 37°33'20"N 40°54'33"E.
2. Kırdirek: Steppe area, 740 m, 27.05.2017, 37°40'24"N 40°44'26"E.
3. Hisarkaya 12 km SW: Moorland area, 750 m, 14-15.05.2017, 37°38'03"N 40°53'39"E.
4. Savur road 15 km NE: Arable field and steppe area, 900 m, 20-27.04.2017, 37°33'10"N 40°56'03"E.
5. Şenocak road 4 km E: Steppe area with sparse oaks, 800 m, 13.06.2017, 37°38'17"N 40°41'35"E.
6. Çınarönü road 3 km NW: Moorland area, 1000 m, 02-03.07.2017, 37°35'52"N 40°40'38"E.

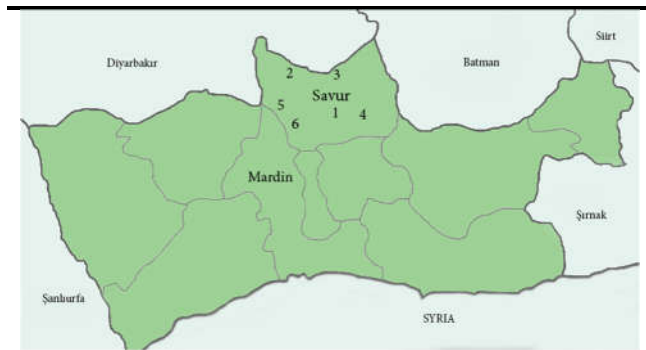


Figure 1. Studied locations in Savur district

Afterwards, the samples, which were stretched by being softened, were diagnosed according to Hesselbarth et al. [2]. Species that have been systematically identified are protected in Batman University, Faculty of Science and Arts, Biology Laboratory.

For each species original reference, synonyms, examined materials and distributions are presented. In regulating the distribution areas of the species, paper of Koçak and Kemal [1] was used. International country codes have been utilized to indicate the distribution of the species in the world and following spread of the species in Turkey are given with the plate code of the provinces.

Abbreviations used herein:

For the distribution of the species in the World: **AF** Afghanistan, **AL** Albania, **AM** Armenia, **AU** Australia, **AT** Austria, **AZ** Azerbaijan, **BE** Belgium, **BF** Burkina-Faso, **BG** Bulgaria, **BH** Bahrain, **B-H** Bosnia-Herzegovina, **BI** Baluchistan, **BJ** Benin, **BY** Byelorussia, **BW** Botswana, **BZ** Belize, **CA** Canada, **CF** Central African Republic, **CG** Congo, **CH** Switzerland, **CI** Ivory Coast, **CM** Cameroon, **CN** China, **CY** Cyprus, **CZ** Czech Republic, **DE** Deutschland, **DJ** Djibuti, **DK** Denmark, **DZ** Algeria, **EE** Estonia, **EG** Egypt, **EH** Western Sahara, **ER** Eritrea, **ES** Spain, **ET** Ethiopia, **FI** Finland, **FR** France, **GA** Gabon, **GB** United Kingdom, **GG** Georgia, **GH** Ghana, **GM** Gambia, **GN** Guinea, **GO** Equatorial Guinea, **GW** Guinea-Bissau, **GR** Greece, **HU** Hungary, **HV** Croatia, **IE** Ireland, **IL** Israel, **IN** India, **IQ** Iraq, **IR** Iran, **IS** Iceland, **IT** Italy, **JO** Jordan, **JP** Japan, **KE** Kenya, **KG** Kazakhstan, **KK** Kyrgyzstan, **KM** Comoro Islands, **KP** North Korea, **KR** South Korea, **KW** Kuwait, **LB** Lebanon, **LT** Lithuania, **LR** Liberia, **LS** Lesotho, **LU** Luxemburg, **LV** Latvia, **LY** Libya, **MA** Morocco, **MD** Moldova, **MG** Madagascar, **ML** Mali, **MK** Makedonia, **MN** Mongolia, **MT** Malta, **MR** Mauretania, **MW** Malawi, **MX** Mexico, **MZ** Mozambik, **NA** Namibia, **NE** Niger, **NG** Nigeria, **NL** Netherlands, **NO** Norway, **NP** Nepal, **OM** Oman, **PH** Philippine Islands, **PK** Pakistan, **PL** Poland, **PT** Portugal, **QA** Qatar, **RO** Romania, **RU** Russia Federation, **RW** Rwanda, **SA** Saudi Arabia, **SC** Seychelles, **SD** Sudan, **SE** Sweden, **SI** Sikkim, **SK** Slovakia, **SL** Sierra Leone, **SN** Senegal, **SO** Somalia, **SS** Slovenia, **ST** Sao Tome & Principe Islands, **SY** Syria, **SZ** Swaziland, **TD** Chad, **TG** Togo, **TH** Thailand, **TJ** Tajikistan, **TM** Turkmenistan, **TN** Tunisia, **TR** Turkey, **T-S** Tian Shan Mountains, **TW** Taiwan, **TZ** Tanzania, **UA** Ukraine, **UG** Uganda, **US** United States of America, **UZ** Uzbekistan, **VI** Virgin Islands, **VN** Viet Nam, **YE** Yemen, **YU** Yugoslavia, **ZA**

Republic of South Africa, **ZM** Zambia, **ZR** Zaire, **ZW** Zimbabwe.

And for the distribution of the species in Turkey: **01** Adana, **02** Adıyaman, **03** Afyon, **04** Ağrı, **05** Amasya, **06** Ankara, **07** Antalya, **08** Artvin, **09** Aydın, **10** Balıkesir, **11** Bilecik, **12** Bingöl, **13** Bitlis, **14** Bolu, **15** Burdur, **16** Bursa, **17** Çanakkale, **18** Çankırı, **19** Çorum, **20** Denizli, **21** Diyarbakır, **22** Edirne, **23** Elazığ, **24** Erzincan, **25** Erzurum, **26** Eskişehir, **27** Gaziantep, **28** Giresun, **29** Gümüşhane, **30** Hakkâri, **31** Hatay, **32** Isparta, **33** İçel, **34** İstanbul, **35** İzmir, **36** Kars, **37** Kastamonu, **38** Kayseri, **39** Kırklareli, **40** Kırşehir, **41** Kocaeli, **42** Konya, **43** Kütahya, **44** Malatya, **45** Manisa, **46** Kahramanmaraş, **47** Mardin, **48** Muğla, **49** Muş, **50** Nevşehir, **51** Niğde, **52** Ordu, **53** Rize, **54** Sakarya, **55** Samsun, **56** Siirt, **57** Sinop, **58** Sivas, **59** Tekirdağ, **60** Tokat, **61** Trabzon, **62** Tunceli, **63** Şanlıurfa, **64** Uşak, **65** Van, **66** Yozgat, **67** Zonguldak, **68** Aksaray, **69** Bayburt, **70** Karaman, **71** Kırıkkale, **72** Batman, **73** Şırnak, **74** Bartın, **75** Ardahan, **76** Iğdır, **77** Yalova, **78** Karabük, **79** Kilis, **80** Osmaniye, **81** Düzce.

3. RESULTS

In this study, a total of 35 butterfly species are presented within the families in alphabetical order as follows:

Papilionidae

Archon apollinaris (Staudinger, [1892])

Original reference: *Doritis apollinus* var. *apollinaris* Staudinger, [1892], Dt. ent. Z., Iris 4: 225. Syntypes: [Türkei]: nordöstlichen Kleinasien: Goman Otti, 1500 m. **Synonym(s):** *apollinaris* Staudinger, [1892]; *pallidior* Spuler, 1892; *#mardina* Stichel, 1907. **Examined materials:** 3♂ 1♀ Savur, 840 m, 12.04.2016. **Distribution in the world:** IR IQ TR. **Distribution in Turkey:** 13 21 23 24 30 47 49 56 62 65 73.

Zerynthia deyrollei (Oberthür, 1869)

Original reference: *Thais deyrollei* Oberthür, 1869, Pet. Nouv. Ent. (2): 7. Syntypes: [Turquie]: Alpes-Pontiques [Gümüşhane]. **Synonym(s):** *deyrollei* Oberthür, 1869; *eisneri* Bernardi, 1970; *lycaoniae* Eisner & Wagener, 1974; *#flavomaculata* Verity, 1905; *#ochracea* Verity, 1905; *#obscurior* Verity, 1905; *#subflava* Schultz,

1908; *#deflexa* Schultz, 1908; *#charis* Schultz, 1908; *#separata* Sheljuzhko, 1927. **Examined materials:** 7♂ 2♀ Savur road 15 km NE, 900 m, 27.04.2017. **Distribution in the world:** IL IQ IR JO LB TR. **Distribution in Turkey:** 01 02 03 05 06 07 12 13 14 15 18 19 21 23 24 25 26 27 28 29 30 31 32 33 37 38 42 43 44 46 47 49 50 51 56 58 60 62 63 64 65 66 68 70 71 73 80.

Pieridae

Anthocharis cardamines (Linnaeus, 1758)

Original reference: *Papilio cardamines* Linnaeus, 1758, Syst. Nat. (Edn.10)1: 468. Type: [Europe]. **Synonym(s):** *cardamines* Linnaeus, 1758; *hesperides* Newman, 1894; *britannica* Verity, 1908; *meridionalis* Verity, 1908 nec Lederer, 1852; *montivaga* Turati & Verity, 1911. **Examined materials:** 8♂ 4♀ Savur road 15 km NE, 900 m, 27.04.2017. **Distribution in the world:** AL AM AT BE BG B-H BY CH CN CY CZ DE DK EE ES FI FR GB GR HU HV IE IL IQ IR IT KG KK LB LT LU LV MK NL NO PL PT RO RU SE SK SS SY TM TR T-S UA VI YU. **Distribution in Turkey:** 01 03 04 05 06 07 08 09 10 13 14 15 16 17 18 20 21 23 24 25 27 28 29 30 31 32 33 34 35 36 37 39 41 42 43 44 45 46 47 48 51 52 53 55 56 58 60 61 62 65 66 70 71 73 74 75 76 78.

Anthocharis grueneri Herrich-Schäffer, [1851]

Original reference: *Anthocharis grueneri* Herrich-Schäffer, [1851], Syst. Bearb. Schmett. Eur. 6: 20 ibid. I: pl. 115, figs. 551- 554 [uninominal]. Syntypes: ? Creta [Kleinasien]. **Synonym(s):** *grueneri* Herrich-Schäffer, [1851]; *#diluta* Röber, 1907; *eros* Röber, 1907. **Examined materials:** 4♂ 2♀ Savur road 15 km NE, 900 m, 20.04.2017. **Distribution in the world:** AM AZ BG GG GR IL IQ IR LB MK SY TR. **Distribution in Turkey:** 01 02 03 04 05 06 07 12 13 21 24 25 27 29 30 31 32 33 35 36 38 42 43 44 45 46 47 50 51 56 58 60 62 65 66 70 71 73 76.

Aporia crataegi (Linnaeus, 1758)

Original reference: *Papilio crataegi* Linnaeus, 1758, Syst. Nat. (Edn. 10) 1: 467. Type: [Europe]. **Synonym(s):** *crataegi* Linnaeus, 1758; *nigronervosus* Retzius, 1783; *minör* Verity, 1907; *basanius* Fruhstorfer, 1910; *crataegiaugusta* Verity, 1937. **Examined materials:** 6♂ 2♀ Kirdirek, 740 m, 27.05.2017. **Distribution in the world:** AF AL AM AT AZ BE BG B-H BY CH CN CY CZ DE DK DZ EE ES FI FR GG GR HU

HV IL IQ IR IT JP KG KK KP LB LT LU LV JO
MA MK MN NL NO PT RO RU SE SK SS SY TJ
TM TR UA VI T-S TN. **Distribution in Turkey:**
01 02 03 04 05 06 07 08 09 10 11 12 13 14 15 16
17 18 19 20 21 22 23 24 25 26 27 29 30 31 32 33
34 35 36 37 38 39 40 41 42 43 44 46 47 48 49 50
51 53 54 55 56 58 60 61 62 63 65 66 69 70 71 72
73 74 75 76 78 80 81.

Colias crocea (Fourcroy, 1785)

Original reference: *Papilio croceus* Fourcroy, 1785, Entomologia Parisiensis: 250. Type: [France]: Paris. **Synonym(s):** *crocea* Fourcroy, 1785; *pyrenaica* Groum-Grshimailo, 1893. **Examined materials:** 2♂ Savur, 840 m, 12.04.2016; 6♂ 1♀ Kirdirek, 740 m, 27.05.2017; 5♂ Şenocak road 4 km E, 800 m, 13.06.2017; 5♂ Çınarönü road 3 km NW, 1000 m, 02.07.2017. **Distribution in the world:** AL AM AT AZ BE BG B-H BY CH CY CZ DE DK DZ EG ES FI FR GB GG GR HV IQ IR IT KG LB LT LU LY LV MA MK MT NL NO PL PT RO RU SA SD SE SK SS SY TR TN UA VI YU TD. **Distribution in Turkey:** 01 02 03 04 05 06 07 08 09 10 11 12 13 14 15 16 17 18 19 20 21 22 23 24 25 26 27 28 29 30 31 32 33 34 35 36 37 38 39 40 41 42 43 44 45 46 47 48 49 50 51 52 53 54 55 56 57 58 59 60 61 62 63 65 66 68 69 70 71 72 73 74 75 76 77 78 79 80 81.

Euchloe ausonia (Hübner, [1804])

Original reference: *Papilio ausonia* Hübner, [1804], Samml. eur. Schmett. 1: pl.113, figs. 582-583; 64-65. Syntypes: Italien. **Synonym(s):** *ausonia* Hübner, [1804]; *marchandae* Geyer, [1832]. **Examined materials:** 3♂ 2♀ Savur road 15 km NE, 900 m, 20.04.2017. **Distribution in the world:** AF AL AM AZ BE BG B-H BY CH CN CY DZ FR GG GR HV IL IQ IR IT JO KG LB LY MA MK RO RU SS SY TM TR TN T-S UA YU. **Distribution in Turkey:** 01 02 03 04 05 06 07 09 10 13 14 15 16 17 18 19 20 21 22 23 24 25 26 27 28 29 30 31 32 33 34 35 36 37 38 39 40 41 42 43 44 45 46 48 50 51 54 56 58 60 62 63 65 66 68 70 71 73 74 76 77 78 80.

Pieris ergane (Geyer, [1828])

Original reference: *Papilio ergane* Geyer, [1828], [in] Hübner, Samml. eur. Schmett. 1: Taf. 184 figs. 904- 907. Syntypes: [Crotia]: Ragusa. **Synonym(s):** *ergane* Geyer, [1828]; *narcaea* Freyer, [1828]. **Examined materials:** 13♂ 4♀ Şenocak road 4 km E, 800 m, 13.06.2017. **Distribution in the world:** AL AM AT AZ BG B-

H ES FR GG GR HU HV IQ IR IT LB MK RO SS
TR YU. **Distribution in Turkey:** 01 02 03 04 05
06 07 08 12 13 14 15 16 18 21 23 24 25 26 28 29
30 31 32 33 36 38 42 43 44 46 47 49 50 51 52 56
58 60 62 63 65 66 69 71 73 74 76.

Pieris mannii (Mayer, 1851)

Original reference: *Pont. mannii* Mayer, 1851, Stettin ent. Ztg. 12:151. Type: [Croatia]: Spaloto. **Synonym(s):** *mannii* Mayer, 1851; *manni* Verity, 1908; *alpigena* Verity, 1911; *roberti* Eitschberger & Steiniger, 1973. **Examined materials:** 2♂ 2♀ Şenocak road 4 km E, 800 m, 13.06.2017; 2♂ 5♀ Çınarönü road 3 km NW, 1000 m, 02.07.2017. **Distribution in the world:** AL AT BG B-H CH CZ ES FR GR HU HV IT IR MA MK RU SK SS TR UA YU. **Distribution in Turkey:** 01 02 03 06 07 08 10 11 13 14 17 18 21 23 24 25 26 28 29 30 31 32 33 34 35 36 37 38 39 42 43 44 45 46 47 48 49 50 51 53 56 61 62 65 67 69 73 74 75 76 78 80.

Pieris pseudorapae Verity, 1908

Original reference: *Pieris napi* var. *pseudorapae* Verity, [1908], Rhopalocera palaeartica: 144, pl. 32, 33, figs. Lectotype: [Lebanon]: Beyrouth (Bowden & Riley, 1967). **Synonym(s):** *pseudorapae* Verity, 1908. **Examined materials:** 3♂ Savur, 840 m, 12.04.2016; 9♂ 5♀ Kirdirek, 740 m, 27.05.2017; 11♂ 3♀ Şenocak road 4 km E, 800 m, 13.06.2017. **Distribution in the world:** AM AZ BG B-H GG GR HV IQ JO LB MD MK RO RU SY TR UA YU. **Distribution in Turkey:** 01 03 04 05 06 07 08 10 11 12 13 14 16 17 18 20 21 22 23 24 25 26 27 28 29 30 31 32 33 34 35 36 37 38 39 41 42 43 44 45 46 47 48 49 50 51 52 53 54 56 58 59 60 61 62 63 65 66 67 68 71 73 74 75 76 77 78 80 81.

Pieris rapae (Linnaeus, 1758)

Original reference: *Papilio rapae* Linnaeus, 1758, Syst. Nat. (Edn.10) 1: 468. Type: [Sweden (Verity, 1947)]. **Synonym(s):** *rapae* Linnaeus, 1758; *nelo* Bergsträßer, 1780; *metra* Stephens, 1827; *alpica* Rossi, 1929. **Examined materials:** 12♂ 6♀ Kirdirek, 740 m, 27.05.2017; 3♀ Hisarkaya 12 km SW, 750 m, 14.05.2017; 7♂ 3♀ Şenocak road 4 km E, 800 m, 13.06.2017; 2♂ 4♀ Çınarönü road 3 km NW, 1000 m, 02.07.2017. **Distribution in the world:** AF AL AM AU AT AZ BE BG BH B-H BY CH CN CY CZ DE DK DZ EE ES FI FR GB GG GR HU HV IE IN IQ IR IS IT JO JP KG KK KW LT LU LV MA MK MN MT MX NL NO OM PK PL PT QA RO RU SA SE SK SS SY TJ TM TN TR T-S TW UA US UZ

VI VN YU. **Distribution in Turkey:** 01 02 03 04 05 06 07 08 09 10 11 12 13 14 15 16 17 18 19 20 21 22 23 24 25 26 27 28 29 30 31 32 33 34 35 36 37 38 39 40 41 42 43 44 45 46 47 48 49 50 51 52 53 54 55 56 58 59 60 61 62 63 64 65 66 68 69 70 71 73 74 75 76 77 78 79 80.

Pieris brassicae (Linnaeus, 1758)

Original reference: *Papilio brassicae* Linnaeus, 1758, Syst. Nat. (Edn. 10) 1: 468. Type: [Europe].
Synonym(s): *brassicae* Linnaeus, 1758; *chariclea* Stephens, 1827; *#venata* Verity, 1908; *cyniphia* Turati, 1924. **Examined materials:** 5♂ 2♀ Kirdirek, 740 m, 27.05.2017. **Distribution in the world:** AF AL AT BE BG B-H BY CH CN CZ DE DK DZ EE ER ES FI FR GB GR HU HV IE IL IN IQ IR IS IT JO KG KK LB LT LU LV LY MA MK MT NL NO NP PK PL PT RO RU SK SY TM TR UA UZ TN T-S TH. **Distribution in Turkey:** 01 02 03 04 05 06 07 08 09 10 12 13 14 15 16 17 20 21 22 23 24 25 26 27 29 30 31 32 33 34 35 36 37 38 39 41 42 43 44 45 46 48 49 50 51 52 53 54 55 56 58 60 61 63 65 66 70 71 73 74 75 76 77 78 80 81.

Pontia edusa (Fabricius, 1777)

Original reference: *Papilio edusa* Fabricius, 1777, Genera Insectorum: 255. Type: [Deutschland]: Chilonii. **Synonym(s):** *edusa* Fabricius, 1777; *bellidice* Ochseneimer, 1808; *persica* Bienert, 1869; *#nitida* Verity, [1908]. **Examined materials:** 6♂ 4♀ Çınarönü road 3 km NW, 1000 m, 02.07.2017. **Distribution in the world:** BG CN CY DE GG GR IQ IR IT KG KK MK RU SY TJ TM TR T-S UZ YU. **Distribution in Turkey:** 01 02 03 04 05 06 07 08 09 10 11 12 13 14 15 16 17 18 19 20 21 22 23 24 25 26 27 28 29 30 31 32 33 34 35 36 38 39 40 41 42 43 44 46 47 48 49 50 51 52 53 54 55 56 58 59 60 61 62 63 65 66 67 68 69 70 71 73 74 75 76 77 78 79 80 81.

Satyridae

Coenonympha pamphilus (Linnaeus, 1758)

Original reference: *Papilio pamphilus* Linnaeus, 1758, Syst. Nat. (Edn. 10) 1: 472. Type: Suecia. **Synonym(s):** *pamphilus* Linnaeus, 1758; *menalcas* Poda, 1761; *nephele* Hufnagel, 1766; *marginata* Heyne, 1894; *orantia* Fruhstorfer, 1908; *scota* Verity, 1911; *infrarasa* Verity, 1926; *julduşica* Verity, 1926; *asiaemontium* Verity, 1926; *euxina* Verity, 1926; *posteuxina* Verity, 1926; *londonii* Verity, 1926; *neollyllus* De Lattin, 1950. **Examined materials:** 9♂ 3♀ Hisarkaya 12

km SW, 750 m, 15.05.2017; 4♀ Savur road 15 km NE, 900 m, 27.04.2017; 7♂ 1♀ Şenocak road 4 km E, 800 m, 13.06.2017; 12♂ 2♀ Çınarönü road 3 km NW, 1000 m, 03.07.2017. **Distribution in the world:** AL AM AT AZ BE BG B-H BY CH CN CZ DE DK DZ EE ES FI FR GB GG GR HU HV IE IQ IR IT KG KK LB LT LU LV MA MK MT NL NO PL RO RU SE SK TM TN TR T-S VI UZ YU. **Distribution in Turkey:** 01 03 04 05 06 07 08 09 10 11 12 13 14 16 17 18 19 20 21 22 23 24 25 26 27 28 29 30 32 33 34 35 36 37 38 39 40 41 42 43 44 45 46 47 48 49 50 51 52 53 54 55 56 57 58 59 60 61 62 65 66 67 68 69 70 71 72 73 74 75 76 77 78 80 81.

Coenonympha saadi (Kollar, [1849])

Original reference: *Satyrus saadi* Kollar, [1849], Denkschr. Akad. Wiss. Wien 1850: 11. Type: [Iran]: Farsistan, Schiraz (NHMW). **Synonym(s):** *saadi* Kollar, [1849]; *iphias* Eversmann, 1851. **Examined materials:** 27♂ 9♀ Kirdirek, 740 m, 27.05.2017. **Distribution in the world:** AM IR TR IQ. **Distribution in Turkey:** 02 12 13 21 23 25 27 30 44 46 47 56 58 62 63 65 72 73 76.

Hyponephele lycaon (Rottemburg, 1775)

Original reference: *Papilio lycaon* Rottemburg, 1775, Naturforscher 6: 17. Type: Deutschland: Brandenburg. **Synonym(s):** *lycaon* Rottemburg, 1775; *#lycaon* Kuhn, 1774; *eudora* Esper, 1778; *janirula* Esper, 1800; *rufomaculata* Korb, 2005. **Examined materials:** 7♂ Şenocak road 4 km E, 800 m, 13.06.2017; 13♂ 5♀ Çınarönü road 3 km NW, 1000 m, 02.07.2017. **Distribution in the world:** AL AT BG BY CH CN CZ DE EE ES FI FR GR HU IL IT IQ IR KG LB LT LV PL PT RO RU SK SY TR T-S UA VI YU. **Distribution in Turkey:** 01 02 03 04 07 08 09 11 12 13 14 15 16 20 21 23 24 25 26 27 29 30 32 33 35 36 38 42 43 44 46 47 48 49 50 51 56 60 62 63 65 70 73 75 76 78.

Kirinia roxelana (Cramer, [1777])

Original reference: *Papilio roxelana* Cramer, [1777], Uitl. Kapellen 2:101, pl.161, figs. C-F. Syntypes: [Türkei]: Constantinopel [=Istanbul], Smyrna [=Izmir]. **Synonym(s):** *roxelana* Cramer, [1777]; *#anatolica* Koçak, 1989. **Examined materials:** 3♂ 4♀ Kirdirek, 740 m, 27.05.2017; 5♂ 1♀ Şenocak road 4 km E, 800 m, 13.06.2017; 7♂ Çınarönü road 3 km NW, 1000 m, 02.07.2017. **Distribution in the world:** AL BG CY GR RO RU SY LB IQ IR TR UA YU. **Distribution in Turkey:** 01 02 03 05 06 07 08 09 10 11 13 14 15

16 17 19 20 21 22 23 25 26 27 29 30 31 32 33 34
35 38 39 42 43 44 45 46 47 48 49 51 55 56 58 59
60 62 65 66 71 72 73 78 80.

Lasiommata megera (Linnaeus, 1767)

Original reference: *Papilio megera* Linnaeus, 1767, Syst. Nat. (Edn. 12) 1(2): 771, nr. 142.
Synonym(s): *megera* Linnaeus, 1767; *caledonia* Verity, 1911; *alticola* Verity, 1911; *pseudoadrasta* Stauder, 1922; *infrapallens* Verity, 1922; *ocellator* Verity, 1923; *pallidedepulverata* Verity, 1923. **Examined materials:** 7♂ 2♀ Kırtdirek, 740 m, 27.05.2017; 3♀ Şenocak road 4 km E, 800 m, 13.06.2017. **Distribution in the world:** AL AT BE BG B-H BY CH CY CZ DE DK DZ EE ES FI FR GB GR HU HV IE IL IQ IR IT JO LB LT LU LV MA MK MT NL NO PL PT RO RU SE SK SS SY TM TN TR UA VI YU. **Distribution in Turkey:** 01 02 05 06 07 08 09 10 11 12 13 14 15 16 17 20 21 22 23 24 25 26 27 28 30 31 33 34 35 36 37 38 39 40 41 42 43 44 45 46 47 48 49 50 51 52 55 56 57 58 59 60 62 63 65 66 67 70 71 72 73 74 75 76 77 80.

Maniola telmessia (Zeller, 1847)

Original reference: *Hipparchia telmessia* Zeller, 1847, Isis 1847: 4. Syntypes 2*4+: [Türkei]: Makri [Fethiye]: [Greece]: Rhodus. Lectotype*: Marmaris (designated by Olivier, 1993) (in BMHN). **Synonym(s):** *telmessia* Zeller, 1847; *pallescens* Butler, 1868; *kurdistana* Heyne, 1894; *oreas* Le Cerf, 1912; *maniolides* Le Cerf, 1912; *ornata* Turati & Fiori, 1930; *marenigrans* Verity, 1938; *pelekasii* Kattulas & Koutsaftikis, 1978. **Examined materials:** 11♂ 6♀ Kırtdirek, 740 m, 27.05.2017. **Distribution in the world:** GR IL IQ IR JO LB SY TR. **Distribution in Turkey:** 01 02 03 07 09 10 12 13 15 17 20 21 23 27 30 31 32 33 35 42 44 45 46 47 48 51 56 62 63 65 70 72 73 80.

Melanargia grumi Standfuss, 1892

Original reference: *Melanargia grumi* Standfuss, 1892, [in] Romanoff, Mém. Lépid. 6: 661-664, pl.15 figs. 2a-c. Syntypes: [Türkei]: Mardin. **Synonym(s):** *grumi* Standfuss, 1892. **Examined materials:** 4♂ Kırtdirek, 740 m, 27.05.2017; 8♂ 7♀ Şenocak road 4 km E, 800 m, 13.06.2017; 9♂ 5♀ Çınarönü road 3 km NW, 1000 m, 02.07.2017. **Distribution in the world:** IQ TR IR. **Distribution in Turkey:** 02 13 21 23 30 47 56 63 72 73.

Pararge aegeria (Linnaeus, 1758)

Original reference: *Papilio aegeria* Linnaeus, 1758, Syst. Nat. (Edn.10) 1: 473. Syntypes: Europa, Mauritania. **Synonym(s):** *aegeria* Linnaeus, 1758; *meone* Cramer, 1782; *egeria* Ochsenheimer, 1807; *sardoa* Verity, 1908. **Examined materials:** 7♂ 1♀ Hisarkaya 12 km SW, 750 m, 14-15.05.2017; 3♂ 1♀ Şenocak road 4 km E, 800 m, 13.06.2017; 6♂ 2♀ Çınarönü road 3 km NW, 1000 m, 02.07.2017. **Distribution in the world:** AL AM AT AZ BE BG BY CH CY CZ DE DK DZ EE ES FI FR GB GG GR HU IE IQ IR IT LB LT LU LV MA MT NL NO PL PT RO RU SE SK SY TN TR UA VI YU. **Distribution in Turkey:** 01 05 06 07 08 09 11 13 14 15 16 17 18 20 21 25 26 27 28 29 30 31 32 33 34 35 38 39 41 42 44 46 47 48 52 53 55 56 58 60 61 65 67 73 74 75 77 80 81.

Argynnidæ

Argynnis pandora ([Denis & Schiffermüller], 1775)

Original reference: *Papilio pandora* [Denis & Schiffermüller], 1775, Ankündigung syst. Werkes Schmett. Wienergegend: 176. Type: Austria: Vienna district. **Synonym(s):** *pandora* [Denis & Schiffermüller], 1775; *maja* Cramer, 1775 nec Fabricius, 1775; *cynara* Fabricius, 1777; *cyrnea* Schwerda, 1926; *transcaucasica* Moucha, 1967; *deserticola* Gross & Ebert, 1975. **Examined materials:** 7♂ 2♀ Kırtdirek, 740 m, 27.05.2017; 11♂ 3♀ Şenocak road 4 km E, 800 m, 13.06.2017; 5♂ Çınarönü road 3 km NW, 1000 m, 03.07.2017. **Distribution in the world:** AF AL AM AT AZ BG B-H BY CH CN CY CZ DZ DE EE ES FR GG GR HU HV IQ IR IT KK LB MA MK PK PL PT RO RU SK SS SY TJ TM TN TR T-S UA UZ VI YU. **Distribution in Turkey:** 01 02 03 04 05 06 07 08 09 10 11 12 13 14 15 16 17 18 20 21 22 23 24 25 26 27 29 30 31 32 33 34 35 36 37 38 39 40 42 43 44 46 47 48 49 50 51 52 53 55 56 58 60 61 62 63 65 66 67 69 70 71 72 73 74 76 77 78 80 81.

Melitaea phoebe (Goeze, 1779)

Original reference: *Papilio phoebe* Goeze, 1779, Ent. Beyträge 3(1) 365. **Synonym(s):** #*phoebe* [Denis & Schiffermüller], 1775; *phoebe* Goeze, 1779; *paedotropos* Bergsträßer, [1780]; *tremulae* Piller & Mitterpacher, 1783. **Examined materials:** 3♂ Savur road 15 km NE, 900 m, 27.04.2017. **Distribution in the world:** AL AM AT AZ BE BG B-H BY CH CN CZ DE EE ES FR GG GR HU HV IT IR KG LT LU LV MK MN PL PT RO RU SK SS TR UA VI YU. **Distribution in**

Turkey: 01 04 05 06 08 10 11 13 14 16 17 22 23
24 25 26 27 30 31 33 34 36 39 41 42 44 46 50 51
55 58 59 60 61 62 65 66 69 71 73 75 77 78 80.

Melitaea arduinna (Fabricius, 1787)

Original reference: *Papilio arduinna* Fabricius, 1787, Mant. Ins. 2: 60, nr.577. Type: [Russia]: Russia australiori. **Synonym(s):** *arduinna* Fabricius, 1787; *rhodopensis* Freyer, [1836]; *uralensis* Eversmann, 1844; *evanescens* Staudinger, 1886; *#fulminans* Staudinger, 1886; *kocaki* Wagener & Gross, 1976. **Examined materials:** 3♂ 2♀ Savur road 15 km NE, 900 m, 27.04.2017. **Distribution in the world:** AF BG CN GR IQ JO KG KK MK RO RU TJ TR T-S UA UZ. **Distribution in Turkey:** 01 02 05 07 10 13 21 24 25 27 30 31 32 36 39 42 43 44 46 47 49 56 65 72 73 80.

Vanessa cardui (Linnaeus, 1758)

Original reference: *Papilio cardui* Linnaeus, 1758, Syst. Nat. (Edn. 10) 1: 475. Syntypes: Europa, Africa [Sweden (Verity, 1950)]. **Synonym(s):** *cardui* Linnaeus, 1758; *carduelis* Cramer, 1775; *elymi* Rambur, 1829; *kershawi* McCoy, 1868; *pallida* Schoyen, 1881; *japonica* Stichel, 1908; *universa* Verity, 1919; *takesakiana* Kato, 1925; *jacksoni* Clark, 1927. **Examined materials:** 4♂ Hisarkaya 12 km SW, 750 m, 14.05.2017; 3♂ 1♀ Şenocak road 4 km E, 800 m, 13.06.2017. **Distribution in the world:** AF AL AM AO AZ AT BE BF BG BH B-H BI BJ BW BY BZ CF CG CH CI CM CN CY CZ DE DK DJ DZ EE EG EH ER ET ES FI FR GA GB GG GH GM GN GO GR GW HU HV IE IL IN IQ IR IS IT JO KE KG KM JP KK KP KR KW LB LR LS LT LU LV LY MA MD MG MK ML MN MR MT MW MX MZ NA NE NG NL NO NP PH PK PL PT QA RO RU RW SA SC SD SE SL SI SK SN SO ST SS SY SZ TJ TD TG TM TN TR T-S TZ UA UG US UZ YE YU ZA ZM ZR ZW. **Distribution in Turkey:** 01 02 03 04 05 06 07 08 09 10 11 12 13 14 15 16 17 18 19 20 21 22 23 24 25 26 27 28 29 30 31 32 33 34 35 36 37 38 39 40 41 42 43 44 45 46 47 48 49 50 51 52 53 54 55 56 57 58 59 60 61 62 63 65 66 67 68 69 70 71 72 73 74 75 76 78 80 81.

Lycaenidae

Glaucopsyche alexis (Poda, 1761)

Original reference: *Papilio alexis* Poda, 1761, Insecta Musei Graecensis.: 77. Type: [Austria]: Steiermark. **Synonym(s):** *alexis* Poda, 1761;

damaetas [Denis & Schiffermüller, 1775; *#sublugens* Strand, 1909; *#insulicola* Turati & Fiori, 1930; *mironi* Coutsis, 1976. **Examined materials:** 3♂ 5♀ Savur road 15 km NE, 900 m, 20.04.2017. **Distribution in the world:** AF AL AM AT AZ BE BG BY CH CZ DE DK DZ EE ES FI FR GG GR HU IL IR IQ IT KG LT LB LU LV MK NO PL PT RO RU SE SK TM TN TR UA VI YU. **Distribution in Turkey:** 01 02 03 04 05 06 07 08 09 11 12 13 14 15 16 17 18 19 20 21 23 24 25 26 27 28 29 30 31 32 33 34 35 36 37 38 39 41 42 43 44 45 46 47 48 49 50 51 52 56 58 60 61 62 65 66 68 69 70 71 73 74 76 80.

Lycaena phlaeas (Linnaeus, 1761)

Original reference: *Papilio phlaeas* Linnaeus, 1761, Fauna Suecica (2) : 285. Type: Sweden, Westermannia. **Synonym(s):** *phlaeas* Linnaeus, 1761; *virgaureae* Fourcroy, 1785 nec Linn., 1758; *eleus* Fabricius, 1798; *aestivus* Zeller, 1850; *schmidtii* Gerhard, 1853. **Examined materials:** 7♂ 1♀ Şenocak road 4 km E, 800 m, 13.06.2017. **Distribution in the world:** AF AL AM AT AZ BE BG BI BY CA CH CN CY CZ DE DK DZ EE ES ET FI FR GB GG GR HU IE IL IN IQ IR IT JO JP KG KK LB LT LU LY LV MA MK MN MT NL NO PK PL PT RO RU SA SK SY TM TR UA UG US VI YE YU TN ZR. **Distribution in Turkey:** 01 02 03 04 05 06 07 08 09 10 11 12 13 14 15 16 17 18 20 21 22 23 24 25 26 27 28 29 30 31 32 33 34 35 36 37 38 39 41 42 44 45 46 47 48 49 50 51 52 53 54 55 56 58 59 60 61 62 63 65 66 68 69 71 72 73 74 76 78 80 81.

Plebejus zephyrinus (Christoph, 1884)

Original reference: *Lycaena zephyrus* var. *zephyrinus* Christoph, 1884, [in] Romanoff, Mem. Lépid. 1:102. Syntypes: [Turkmenistan]: Ashkhabad. **Synonym(s):** *zephyrinus* Christoph, 1884. **Examined materials:** 8♂ Çınarönü road 3 km NW, 1000 m, 02.07.2017. **Distribution in the world:** TR AZ GG IQ IR KG TM RU UZ. **Distribution in Turkey:** 13 30 56 65 72 73 76.

Polyommatus agestis ([Denis & Schiffermüller], 1775)

Original reference: *Papilio agestis* [Denis & Schiffermüller], 1775 Ankündigung syst. Werkes Schmett., Wienergegend: 184. Type: [Austria]: Vienna district. **Synonym(s):** *medon* Hufnagel, 1766 nec Linn., 1763; *alexis* Rottemburg, 1775 nec Poda, 1761; *agestis* [Denis & Schiffermüller], 1775; *astrarche* Bergsträßer, [1779]. **Examined**

materials: 4♂ 2♀ Kirdirek, 740 m, 27.05.2017; 2♂ 4♀ Savur road 15 km NE, 900 m, 27.04.2017.
Distribution in the world: AF AL AM AT AZ BE BG B-H BY CH CN CY CZ DE DK FR GB GG GR ES HU HV IL IN IQ IR IT JO KG KK LB LT LU MK MT NL PK PL RO RU SE SK SS SY TM TR T-S UA VI YU. **Distribution in Turkey:** 01 02 03 04 05 06 07 08 09 10 11 12 13 14 15 16 17 18 19 20 21 22 23 24 25 26 27 29 30 31 32 33 34 35 36 37 38 39 40 41 42 44 45 46 47 48 49 50 51 54 55 56 58 60 61 62 63 65 66 68 69 70 71 72 73 75 76 78 81.

Polyommatus icarus (Rottemburg, 1775)

Original reference: *Papilio icarus* Rottemburg, 1775, Naturforscher 6: 21. Type: Saxonia.
Synonym(s): *argus* Poda, 1761 nec Linn., 1758; *alexis* Scopoli, 1763 nec Pda, 1761; *thetis* Esper, 1777 nec Dru., 1773; *icarus* Rottemburg, 1775; *pampholyge* Bergsträßer, 1779; *candybus* Bergsträßer, 1779; *candiope* Bergsträßer, 1779; *candaon* Bergsträßer, 1779; *oceanus* Bergsträßer, 1779; *fusciolus* Fourcroy, 1785; *icarinus* Scriba, 1795; *pusillus* Gerhard, 1851; *neglectus* Stradomsky & Arzanov, 1999. **Examined materials:** 8♂ 4♀ Kirdirek, 740 m, 27.05.2017; 4♂ 1♀ Hisarkaya 12 km SW, 750 m, 14.05.2017.
Distribution in the world: AF AL AZ AT BE BG B-H BI BY CH CN CY CZ DE DK DZ EE ES FI FR GB GR HU HV IE IL IQ IR IT JO KG KK LB LT LU LV LY MA MK MN MT NL NO PK PL PT RO RU SE SK SS SY TJ TM TN TR T-S UA UZ VI YU. **Distribution in Turkey:** 01 02 03 04 05 06 07 08 09 10 11 12 13 14 15 16 17 18 19 20 21 22 23 24 25 26 27 28 29 30 31 32 33 34 35 36 37 38 39 40 41 42 43 44 45 46 47 48 49 50 51 52 53 54 55 56 57 58 59 60 61 62 63 64 65 66 67 68 69 70 71 72 73 75 76 78 80 81.

Hesperiidae

Carcharodus lavatherae (Esper, [1783])

Original reference: *Papilio lavatherae* Esper, [1783], Die Schmett. 1(2) : 148-149, pl. 82 fig. 4. Syntypes: Frankreich Schweis. **Synonym(s):** *lavatherae* Esper, [1783]; *australior* Verity, 1919; *pyrenaicus* Ricard, 1948. **Examined materials:** 5♂ 1♀ Hisarkaya 12 km SW, 750 m, 14.05.2017; 2♂ Çınarönü road 3 km NW, 1000 m, 02.07.2017.
Distribution in the world: AL AT BG B-H BY CH DE DZ ES FR GR HU HV IT IR MA MK RO RU SK SS TR TN UA VI YU. **Distribution in Turkey:** 01 03 04 05 06 07 08 12 13 14 17 18 19 21 23 24 25 29 30 32 33 36 37 38 39 40 41 42 44

46 49 50 51 56 58 60 62 65 66 68 70 72 73 74 75 76 78.

Carcharodus alceae (Esper, [1780])

Original reference: *Papilio alceae* Esper, [1780], Die Schmett. 1 (2): 4, pl. 51, fig. 1. Type: Süddeutschland: Erlangen. **Synonym(s):** *alceae* Esper, [1780]; *malvae* Hufnagel, 1766 nec Linn., 1758; *malvarum* Hoffmannsegg, 1804; *magnaustralis* Verity, 1924; *corsicus* Picard, 1948. **Examined materials:** 4♂ 1♀ Çınarönü road 3 km NW, 1000 m, 02-03.07.2017. **Distribution in the world:** AF AL AM AT AZ BE BG B-H BY CH CN CY CZ DE DZ ES FR GG GR HU HV IL IN IQ IR IT KG LB LU MA MK NL PK PL PT RO RU SK SS TM TN TR UA VI YE YU. **Distribution in Turkey:** 01 02 03 04 05 06 07 08 09 10 12 13 15 16 17 20 21 23 24 25 26 27 29 30 31 32 33 34 35 36 38 39 41 42 43 44 45 46 47 48 49 50 51 53 56 58 60 62 63 65 66 67 70 71 72 73 74 75 76 78 79 80.

Eogenes alcides Herrich-Schäffer, [1852]

Original reference: *Hesperia alcides* Herrich-Schäffer, [1852], Syst. Bearb. Schmett. Eur. 6: 38; ibidem 1: pl. 7, figs. 41-42. Syntypes: [Turkei]: Amasia. **Synonym(s):** *alcides* Herrich-Schäffer, [1852]. **Examined materials:** 3♂ Şenocak road 4 km E, 800 m, 13.06.2017. **Distribution in the world:** AM AZ BI CN GG KG IR IQ PK TM TR T-S. **Distribution in Turkey:** 05 08 20 23 24 25 30 35 36 42 50 56 60 62 63 65 66 72 73.

Thymelicus lineolus (Ochsenheimer, 1808)

Original reference: *Papilio lineola* Ochsenheimer, 1808, Schmett. Eur. 1 (2) : 230-231. Type: Germania. **Synonym(s):** *lineolus* Ochsenheimer, 1808; *virgula* Hübner, 1813 nec Retz., 1783; *ludoviciae* Mabilie, 1883; *pallida* Tutt, 1896; *clara* Tutt, 1905; *hemmingi* Romei, 1927; *melissus* Zerny, 1932; *fornax* Hemming, 1934. **Examined materials:** 9♂ 4♀ Kirdirek, 740 m, 27.05.2017; 12♂ 5♀ Hisarkaya 12 km SW, 750 m, 14.05.2017. **Distribution in the world:** AF AL AT AZ BG B-H BL BY CH CN CZ DE DK DZ EE ES FI FR GB GG GR HU HV IL IR IT JO KG KK LB LT LU LV MA MK NL NO PL PT RO RU SE SK SS TM TN TR T-S UA US VI YU. **Distribution in Turkey:** 01 02 03 04 05 06 07 08 10 12 13 14 15 16 18 19 20 21 22 23 24 25 26 27 29 30 31 32 33 34 36 38 39 40 42 43 44 46 47 48 49 50 51 56 58 60 62 63 65 66 69 70 71 73 74 75 76 78 80.

Thymelicus sylvestris (Poda, 1761)

Original reference: *Papilio sylvestris* Poda, 1761, Insecta Musei Graecensis: 79. Type: [Austria]: Graz. **Synonym(s):** *sylvestris* Poda, 1761; *flava* Brünnich, 1763; *linea* Müller, 1764; *thaumas* Hufnagel, 1766; *divaricatus* Fourcroy, 1785; *venula* Hübner, [1813]; *obscura* Verity, 1905. **Examined materials:** 6♂ 3♀ Kirdirek, 740 m, 27.05.2017; 7♂ 2♀ Hisarkaya 12 km SW, 750 m, 14.05.2017; 4♂ 3♀ Şenocak road 4 km E, 800 m, 13.06.2017. **Distribution in the world:** AL AM AT AZ BE BG BY CH CZ DE DK DZ EE ES FR GB GG GR HU IR IT IQ JO LB LT LU LV MA MK NL PL PT RO RU SK SY TR UA VI YU. **Distribution in Turkey:** 01 02 03 04 05 06 07 08 10 11 12 13 14 15 16 17 18 19 20 21 22 23 24 25 26 27 28 29 30 31 32 33 34 35 36 37 38 39 40 42 43 44 45 46 47 48 49 50 51 56 58 60 61 62 63 64 65 66 67 69 70 71 72 73 74 75 76 78 81.

4. DISCUSSION AND CONCLUSION

According to the results of the research, 35 species are presented within the Papilionidae, Pieridae, Satyridae, Argynnidae, Lycaenidae and Hesperidae families from Savur district, whose butterfly fauna is unknown until now. This paper is intended to contribute to the fauna of the area by conducted random field studies between April and July. Moreover, the results show that research region is comprised approximately 42 % of the species, when compared to the total number of butterfly species in the province of Mardin [5]. In addition, 6 species: *Euchloe ausonia* (Hübner, [1804]), *Pieris brassicae* (Linnaeus, 1758) (Pieridae), *Melitaea phoebe* (Goeze, 1779) (Argynnidae), *Plebejus zephyrinus* (Christoph, 1884) (Lycaenidae), *Carcharodus lavatherae* (Esper, [1783]) and *Eogenes alcides* Herrich-Schäffer, [1852] (Hesperidae) are recorded as new to Mardin Province.

It is expected that the number of samples will increase with the future researches, when habitat and land conditions are evaluated and compared to other nearby districts [6, 8, 11, 13] and areas [7, 9, 10, 12, 14]. In this respect, it is thought that entomological researches should be more supported and increased in the region.

REFERENCES

- [1] A.Ö. Koçak, M. Kemal, "A synonymous and distributional list of the species of the Lepidoptera of Turkey." *Cent. ent. Stud., Memoirs* 8: 1–487, 2018.
- [2] G. Hesselbarth, H.v. Oorschot, S. Wagener, "Die Tagfalter der Türkei unter Berücksichtigung der angrenzenden Länder," *Selbstverlag S. Wagener, Bocholt*. Bde. 1 & 2, 1354s. Bd.3, 847s, 1995.
- [3] M. Kemal, A.Ö. Koçak, "List of the Butterflies of Mardin Province (South East Turkey) (Lepidoptera, Papilionoidea, Hesperioidea)" *Cent. ent. Stud., Misc. Pap.* 96, 1–7, 2006.
- [4] M. Kemal, A.Ö. Koçak, K. Akın, "List of the Lepidoptera of Mardin Province (South East Turkey) with some faunistical remarks" *Cesa News* 16, 1–11, 2008.
- [5] A.Ö. Koçak, M. Kemal, "List of the Lepidoptera of Mardin Province (SE Turkey)," *Cesa News* 103, 27–37, 2015.
- [6] E. Seven, "Studies on the fauna and ecology of Papilionoidea and Hesperioidea (Lepidoptera) in Şirvan district (Siirt Prov., SE Turkey)." *Priamus (Supplement)*, (in Turkish) 20: 1–118, 2010.
- [7] E. Seven, "New Records for the Lepidoptera Fauna of Batman Province." *International Ecology Adnan Aldemir Symposium*, 16-19 May, Kars, 36–37, 2016.
- [8] H. Özkol, "Studies on the fauna and ecology of Papilionoidea and Hesperioidea of Gevaş District (Van)." *Cent. Ent. Stud., Priamus Suppl.* (in Turkish) 5: 1–55, 2007.
- [9] P.B. Hardy, "Butterflies in Jordan, Syria and Lebanon." *Entomologists Record*, 107: 107–116, 1995.
- [10] A.Ö. Koçak, M. Kemal, "Synonymical and distributional list of the species of Şırnak province (South East Turkey) (Lepidoptera)." *Centre for Entomological Studies Ankara*, 127:1–8, 2007.
- [11] K. Akın, "Ceylanpınar (Şanlıurfa) Papilionoidea ve Hesperioidea (Lepidoptera) faunası ve ekolojisi üzerine araştırmalar." *Yüksek lisans tezi*, Van Yüzüncü Yıl Üniversitesi, Van. 1–93, 2008.

- [12] M. Kemal, M. Aydın, "List of the Lepidoptera of Diyarbakır Province (East Turkey)." *Cesa News* 15: 1–6, 2008a.
- [13] M. Kemal, M. Aydın, "Spring Aspects of the diurnal *Lepidoptera* of Kulp District with new faunal records (Diyarbakır Province, East Turkey)." *Cesa News* 14: 1–12, 2008b.
- [14] V. Tshikolovets, A. Naderi, W. Eckweiler, "The Butterflies of Iran and Iraq." *Tshikolovets Publications*, Pardubice, 1–440, 2014.

	SAKARYA UNIVERSITY JOURNAL OF SCIENCE		 SAKARYA UNIVERSITY
	e-ISSN: 2147-835X http://www.saujs.sakarya.edu.tr		
	<u>Received</u> 05-11-2018 <u>Accepted</u> 12-11-2018	<u>Doi</u> 10.16984/saufenbilder.479060	

3×3 Dimensional Special Matrices Associated with Fibonacci and Lucas Numbers

Sinan Karakaya, Halim Özdemir*, Tuğba Petik

ABSTRACT

In the study, it has been developed a method for deriving special matrices of 3×3 dimensions, whose powers are related to Fibonacci and Lucas numbers, and some special matrices have been found via the method developed.

Keywords: Fibonacci numbers, Lucas numbers, Matrices

1. INTRODUCTION

Fibonacci numbers and the golden ratio have attracted the attention of many mathematicians, physicists, philosophers, painters, architects and musicians since ancient times. The golden ratio, which is related to Fibonacci numbers, is encountered in many art works. The most known of them is the ratio which is seen in the table Mona Lisa of Leonardo Da Vinci. Again, it is possible to see the golden ratio in Egyptian pyramids. Also, it is known that the ratio sequence of numbers obtained by dividing each number in the Fibonacci sequence by previous number in the sequence converges to the golden ratio. Fibonacci numbers and golden ratio are seen in many places in nature [see, e.g., 1,2].

There are also special number sequences other than Fibonacci number sequence. One of them is the Lucas numbers sequence. Fibonacci numbers, Lucas numbers and golden ratio have been involved in many mathematical studies for many years [see, e.g., 3-8].

Fibonacci and Lucas numbers are also correlated with matrices. It is known that some properties of Fibonacci and Lucas numbers can be proved by using matrices [see, e.g., 1,2].

This study has two-stages: First, an approach to the derivation of 3×3 dimensional matrix whose powers are related to Fibonacci and Lucas numbers is presented. Then, based on this approach, some special 3×3 dimensional matrices are obtained and some related identities are given.

2. PRELIMINARIES

In this section, some basic concepts and properties, which will be used in the study, related to Fibonacci and Lucas numbers sequences, are given.

Definition 2.1. Fibonacci sequence $\{F_n\}$ is defined by $F_n = F_{n-1} + F_{n-2}$ for all integers $n \geq 2$ with initial conditions $F_0 = 0$ and $F_1 = 1$ [1].

* Corresponding Author

Halim Özdemir, Fen Edebiyat Fakültesi, Matematik Bölümü, Sakarya – hozdemir@sakarya.edu.tr

Bu çalışma Saü-Fibonacci Q -Tipi Matrisler ve İlişkili Kombinasyonel Özellikler-2018-2-7-51 projesi tarafından desteklenmiştir.

Definition 2.2. Lucas sequence $\{L_n\}$ is defined by $L_n = L_{n-1} + L_{n-2}$ for all integers $n \geq 2$ with initial conditions $L_0 = 2$ and $L_1 = 1$ [1].

Definition 2.3. The special number $\alpha = \frac{1+\sqrt{5}}{2}$ is called as golden ratio [1].

The number α is the positive root of the equation $x^2 - x - 1 = 0$. The negative root of this equation is the number $\beta = \frac{1-\sqrt{5}}{2}$ [1].

Some of the properties related to Fibonacci numbers, Lucas numbers and golden ratio are as follows:

Theorem 2.4. (Binet Formula) For all non-negative integer n , the identity $F_n = \frac{\alpha^n - \beta^n}{\alpha - \beta}$ holds [1].

It can be derived Fibonacci sequence with negative subscripts from the Fibonacci sequence considering the fact that every term is the sum of the two terms preceding it:

$$\begin{aligned} F_{-1} &= F_1 - F_0 = 1 - 0 = 1, \\ F_{-2} &= F_0 - F_{-1} = 0 - 1 = -1, \\ F_{-3} &= F_{-1} - F_{-2} = 1 - (-1) = 2, \\ F_{-4} &= F_{-2} - F_{-3} = -1 - 2 = -3, \end{aligned}$$

and so on.

Similarly, it can be derived Lucas sequence with negative subscripts from Lucas sequence:

$$\begin{aligned} L_{-1} &= L_1 - L_0 = 1 - 2 = -1, \\ L_{-2} &= L_0 - L_{-1} = 2 - (-1) = 3, \\ L_{-3} &= L_{-1} - L_{-2} = -1 - 3 = -4, \\ L_{-4} &= L_{-2} - L_{-3} = 3 - (-4) = 7, \end{aligned}$$

and continue like this.

Theorem 2.5. The identities $F_{-n} = (-1)^{n+1} F_n$ and $L_{-n} = (-1)^n L_n$ hold for all integers $n \geq 1$ [1].

Theorem 2.6. The identity $L_n = F_{n-1} + F_{n+1}$ holds for all integers $n \geq 1$ [1].

Theorem 2.7. The equalities $\alpha^n = F_n \alpha + F_{n-1}$ and $\beta^n = F_n \beta + F_{n-1}$ hold for all integers $n \geq 0$ [1].

3. SOME SPECIAL MATRICES

In this section, as indicated in the Introduction section, by giving an approach for derivating 3×3 dimensional matrices associated with Fibonacci and Lucas numbers, based on this approach, special matrices are obtained.

Suppose that $S = \begin{pmatrix} a & b & c \\ d & e & f \\ g & h & i \end{pmatrix}$ is any 3×3 matrix

such that the eigenvalues of it are $\alpha = \frac{1+\sqrt{5}}{2}$,

$\beta = \frac{1-\sqrt{5}}{2}$, and $\gamma = 0$, and all the entries of it are integers. Represent the eigenvectors corresponding the eigenvalues α , β , and γ ,

respectively as $\mathbf{x} = \begin{pmatrix} x_1 \\ x_2 \\ x_3 \end{pmatrix}$, $\mathbf{y} = \begin{pmatrix} y_1 \\ y_2 \\ y_3 \end{pmatrix}$, and $\mathbf{z} = \begin{pmatrix} z_1 \\ z_2 \\ z_3 \end{pmatrix}$

For the eigenvalue-eigenvector pairs (α, \mathbf{x}) , (β, \mathbf{y}) , and (γ, \mathbf{z}) , respectively, it is obtained the linear equations systems

$$\begin{aligned} ax_1 + bx_2 + cx_3 &= \alpha x_1 \\ dx_1 + ex_2 + fx_3 &= \alpha x_2, \\ gx_1 + hx_2 + ix_3 &= \alpha x_3 \end{aligned} \tag{3.1}$$

$$\begin{aligned} ay_1 + by_2 + cy_3 &= \beta y_1 \\ dy_1 + ey_2 + fy_3 &= \beta y_2, \\ gy_1 + hy_2 + iy_3 &= \beta y_3 \end{aligned} \tag{3.2}$$

and

$$\begin{aligned} az_1 + bz_2 + cz_3 &= 0 \\ dz_1 + ez_2 + fz_3 &= 0. \\ gz_1 + hz_2 + iz_3 &= 0 \end{aligned} \quad (3.3)$$

The matrix S is diagonalizable since it has different eigenvalues. In this case, without loss of the generality, it can be written $S = P\Lambda P^{-1}$, where

$$\Lambda = \begin{pmatrix} \alpha & 0 & 0 \\ 0 & \beta & 0 \\ 0 & 0 & 0 \end{pmatrix}$$

and P is a nonsingular matrix. From this, we get $S^n = P\Lambda^n P^{-1}$ for all integers $n \geq 1$. Considering Theorem 2.7, it is obtained

$$\begin{aligned} S^n &= P \begin{pmatrix} \alpha^n & 0 & 0 \\ 0 & \beta^n & 0 \\ 0 & 0 & 0 \end{pmatrix} P^{-1} \\ &= P \begin{pmatrix} F_n \alpha + F_{n-1} & 0 & 0 \\ 0 & F_n \beta + F_{n-1} & 0 \\ 0 & 0 & 0 \end{pmatrix} P^{-1} \\ &= P(F_n \Lambda + F_{n-1} I - F_{n-1} \begin{pmatrix} 0 & 0 & 0 \\ 0 & 0 & 0 \\ 0 & 0 & 1 \end{pmatrix}) P^{-1} \\ &= F_n (P\Lambda P^{-1}) + F_{n-1} (PIP^{-1}) - F_{n-1} (P \begin{pmatrix} 0 & 0 & 0 \\ 0 & 0 & 0 \\ 0 & 0 & 1 \end{pmatrix} P^{-1}), \end{aligned}$$

that is,

$$S^n = F_n S + F_{n-1} I - F_{n-1} (P \begin{pmatrix} 0 & 0 & 0 \\ 0 & 0 & 0 \\ 0 & 0 & 1 \end{pmatrix} P^{-1}). \quad (3.4)$$

Thus, it is seen that the power of the matrix S is associated with Fibonacci numbers.

Now, if we write

$$D = P \begin{pmatrix} 0 & 0 & 0 \\ 0 & 0 & 0 \\ 0 & 0 & 1 \end{pmatrix} P^{-1},$$

then we get

$$S^n = F_n S + F_{n-1} (I - D). \quad (3.5)$$

Since

$$D = \begin{pmatrix} 0 & 0 & z_1 \\ 0 & 0 & z_2 \\ 0 & 0 & z_3 \end{pmatrix} P^{-1}$$

and

$$P^{-1} = \frac{1}{|P|} \begin{pmatrix} y_2 z_3 - z_2 y_3 & z_1 y_3 - y_1 z_3 & y_1 z_2 - z_1 y_2 \\ z_2 x_3 - x_2 z_3 & x_1 z_3 - z_1 x_3 & z_1 x_2 - x_1 z_2 \\ x_2 y_3 - y_2 x_3 & y_1 x_3 - x_1 y_3 & x_1 y_2 - y_1 x_2 \end{pmatrix},$$

it is obtained

$$D = \frac{1}{|P|} \begin{pmatrix} z_1(x_2 y_3 - y_2 x_3) & z_1(y_1 x_3 - x_1 y_3) & z_1(x_1 y_2 - y_1 x_2) \\ z_2(x_2 y_3 - y_2 x_3) & z_2(y_1 x_3 - x_1 y_3) & z_2(x_1 y_2 - y_1 x_2) \\ z_3(x_2 y_3 - y_2 x_3) & z_3(y_1 x_3 - x_1 y_3) & z_3(x_1 y_2 - y_1 x_2) \end{pmatrix}. \quad (3.6)$$

A writing of the determinant of the matrix P is

$$|P| = z_1(x_2 y_3 - y_2 x_3) + z_2(y_1 x_3 - x_1 y_3) + z_3(x_1 y_2 - y_1 x_2).$$

Hence, it can be provided that the entries of the matrix D are also integers with the appropriate choices of the terms $(x_2 y_3 - y_2 x_3)$, $(y_1 x_3 - x_1 y_3)$, and $(x_1 y_2 - y_1 x_2)$.

Now, it is given some special matrices S which occur for the special cases of the eigenvectors \mathbf{x} , \mathbf{y} , and \mathbf{z} and some identities associated with these.

If it is chosen

$$\mathbf{x}_1 = \begin{pmatrix} x_1 \\ x_2 \\ x_3 \end{pmatrix} = \begin{pmatrix} \alpha \\ \beta \\ -1 \end{pmatrix}, \quad \mathbf{y}_1 = \begin{pmatrix} y_1 \\ y_2 \\ y_3 \end{pmatrix} = \begin{pmatrix} \beta \\ \alpha \\ -1 \end{pmatrix},$$

then, it is necessary to hold the systems (3.1), (3.2), and (3.3) for being these vectors are eigenvectors associated with the eigenvalues α , β , and γ , respectively, of the matrix S . From these, the following equations must be hold:

$$\begin{cases} a+b-2c=3 \\ a-b=1 \end{cases}, \quad (3.7)$$

$$\begin{cases} d+e-2f=-2 \\ e-d=0 \end{cases}, \quad (3.8)$$

and

$$\begin{cases} g+h-2i=-1 \\ g-h=-1 \end{cases}. \quad (3.9)$$

Now, let us consider the different choices of the vector \mathbf{z} .

For example, if it is chosen as $z_1 = k$, $z_2 = -k$, and $z_3 = k$ where $k \in \mathbb{Z} \setminus \{0\}$ is arbitrary, then the matrix D in (3.6) is obtained as

$$D = \begin{pmatrix} 1 & 1 & 1 \\ -1 & -1 & -1 \\ 1 & 1 & 1 \end{pmatrix},$$

and also, the equation (3.3) turns to the system

$$\begin{cases} a-b+c=0 \\ d-e+f=0 \\ g-h+i=0 \end{cases}. \quad (3.10)$$

From the solutions of the equations systems (3.7), (3.8), (3.9), and (3.10), we get

$$S = \begin{pmatrix} 1 & 0 & -1 \\ -1 & -1 & 0 \\ 0 & 1 & 1 \end{pmatrix}. \quad (3.11)$$

If we use the equality (3.5) for the matrix S in (3.11), then we obtain

$$\begin{aligned} S^n &= F_n S + F_{n-1} (I - D) \\ &= \begin{pmatrix} F_n & -F_{n-1} & -F_n - F_{n-1} \\ -F_n + F_{n-1} & -F_n + 2F_{n-1} & F_{n-1} \\ -F_{n-1} & F_n - F_{n-1} & F_n \end{pmatrix} \\ &= \begin{pmatrix} F_n & -F_{n-1} & -F_{n+1} \\ -F_{n-2} & F_{n-3} & F_{n-1} \\ -F_{n-1} & F_{n-2} & F_n \end{pmatrix} \end{aligned}$$

for all integers $n \geq 1$. Thus, we have been proved the following theorem:

Theorem 3.1. If $S = \begin{pmatrix} 1 & 0 & -1 \\ -1 & -1 & 0 \\ 0 & 1 & 1 \end{pmatrix}$, then,

$$S^n = \begin{pmatrix} F_n & -F_{n-1} & -F_{n+1} \\ -F_{n-2} & F_{n-3} & F_{n-1} \\ -F_{n-1} & F_{n-2} & F_n \end{pmatrix} \quad \text{for all integers } n \geq 1.$$

Since one of the eigenvalue of the matrix S is zero, the matrix S is singular. So, the result obtained is valid for only all integers $n \geq 1$.

Taking different choices of the eigenvectors \mathbf{x} , \mathbf{y} , and \mathbf{z} , and progressing similarly to the above, it can be given different matrices S and related results. Now, it is presented, without proof, some of these kind of results, for clarification.

For the choice of $(\alpha, \begin{pmatrix} \beta \\ -1 \end{pmatrix})$, $(\beta, \begin{pmatrix} \alpha \\ -1 \end{pmatrix})$, and

$$(0, \begin{pmatrix} k \\ k \\ -k \end{pmatrix}):$$

Theorem 3.2. $S = \begin{pmatrix} -1 & -2 & -3 \\ 1 & 1 & 2 \\ 0 & 1 & 1 \end{pmatrix}$ and

$$S^n = \begin{pmatrix} -F_n & -F_{n+2} & -L_{n+1} \\ F_{n-2} & F_n & L_{n-1} \\ F_{n-1} & F_{n+1} & L_n \end{pmatrix} \quad \text{for all integers } n \geq 1.$$

For the choice of $(\alpha, \begin{pmatrix} \beta \\ -1 \end{pmatrix})$, $(\beta, \begin{pmatrix} \alpha \\ -1 \end{pmatrix})$, and

$$(0, \begin{pmatrix} -k \\ k \\ k \end{pmatrix}):$$

Theorem 3.3 $S = \begin{pmatrix} 3 & 2 & 1 \\ -1 & -1 & 0 \\ -2 & -1 & -1 \end{pmatrix}$ and For the choice of $(\alpha, \begin{pmatrix} \alpha \\ -\beta \\ 1 \end{pmatrix})$, $(\beta, \begin{pmatrix} \beta \\ -\alpha \\ 1 \end{pmatrix})$, and

$$S^n = \begin{pmatrix} F_{n+3} & F_{n+2} & F_{n+1} \\ -F_{n+1} & -F_n & -F_{n-1} \\ -F_{n+2} & -F_{n+1} & -F_n \end{pmatrix} \text{ for all integers } n \geq 1. \quad (0, \begin{pmatrix} k \\ -k \\ k \end{pmatrix}):$$

For the choice of $(\alpha, \begin{pmatrix} \alpha \\ -\beta \\ 1 \end{pmatrix})$, $(\beta, \begin{pmatrix} \beta \\ -\alpha \\ 1 \end{pmatrix})$, and

$$(0, \begin{pmatrix} k \\ k \\ k \end{pmatrix}):$$

Theorem 3.6. $S = \begin{pmatrix} -1 & 2 & 3 \\ -1 & 1 & 2 \\ 0 & 1 & 1 \end{pmatrix}$ and

$$S^n = \begin{pmatrix} -F_n & F_{n+2} & L_{n+1} \\ -F_{n-2} & F_n & L_{n-1} \\ -F_{n-1} & F_{n+1} & L_n \end{pmatrix} \text{ for all integers } n \geq 1.$$

Theorem 3.4. $S = \begin{pmatrix} 3 & -2 & -1 \\ 1 & -1 & 0 \\ 2 & -1 & -1 \end{pmatrix}$ and

$$S^n = \begin{pmatrix} F_{n+3} & -F_{n+2} & -F_{n+1} \\ F_{n+1} & -F_n & -F_{n-1} \\ F_{n+2} & -F_{n+1} & -F_n \end{pmatrix} \text{ for all integers } n \geq 1.$$

For the choice of $(\alpha, \begin{pmatrix} \alpha \\ -\beta \\ 1 \end{pmatrix})$, $(\beta, \begin{pmatrix} \beta \\ -\alpha \\ 1 \end{pmatrix})$, and

$$(0, \begin{pmatrix} k \\ k \\ -k \end{pmatrix}):$$

For the choice of $(\alpha, \begin{pmatrix} -\alpha \\ \beta \\ 1 \end{pmatrix})$, $(\beta, \begin{pmatrix} -\beta \\ \alpha \\ 1 \end{pmatrix})$, and

$$(0, \begin{pmatrix} k \\ k \\ k \end{pmatrix}):$$

Theorem 3.7. $S = \begin{pmatrix} 1 & 0 & -1 \\ 1 & -1 & 0 \\ 0 & -1 & 1 \end{pmatrix}$ and

$$S^n = \begin{pmatrix} F_n & F_{n-1} & -F_{n+1} \\ F_{n-2} & F_{n-3} & -F_{n-1} \\ -F_{n-1} & -F_{n-2} & F_n \end{pmatrix} \text{ for all integers } n \geq 1.$$

Theorem 3.5. $S = \begin{pmatrix} 1 & 0 & 1 \\ 1 & -1 & 0 \\ 0 & 1 & 1 \end{pmatrix}$ and

$$S^n = \begin{pmatrix} F_n & F_{n-1} & F_{n+1} \\ F_{n-2} & F_{n-3} & F_{n-1} \\ F_{n-1} & F_{n-2} & F_n \end{pmatrix} \text{ for all integers } n \geq 1.$$

For the choice $(\alpha, \begin{pmatrix} -\alpha \\ \beta \\ 1 \end{pmatrix})$, $(\beta, \begin{pmatrix} -\beta \\ \alpha \\ 1 \end{pmatrix})$, and

$$(0, \begin{pmatrix} k \\ k \\ -k \end{pmatrix}):$$

Theorem 3.8. $S = \begin{pmatrix} 3 & -2 & 1 \\ 1 & -1 & 0 \\ -2 & 1 & -1 \end{pmatrix}$ and

$$S^n = \begin{pmatrix} F_{n+3} & -F_{n+2} & F_{n+1} \\ F_{n+1} & -F_n & F_{n-1} \\ -F_{n+2} & F_{n+1} & -F_n \end{pmatrix} \text{ for all integers } n \geq 1.$$

For the choice $(\alpha, \begin{pmatrix} -\alpha \\ \beta \\ 1 \end{pmatrix})$, $(\beta, \begin{pmatrix} -\beta \\ \alpha \\ 1 \end{pmatrix})$, and

$$(0, \begin{pmatrix} -k \\ k \\ k \end{pmatrix}) :$$

Theorem 3.9. $S = \begin{pmatrix} -1 & 2 & -3 \\ -1 & 1 & -2 \\ 0 & -1 & 1 \end{pmatrix}$ and

$$S^n = \begin{pmatrix} -F_n & F_{n+2} & -L_{n+1} \\ -F_{n-2} & F_n & -L_{n-1} \\ F_{n-1} & -F_{n+1} & L_n \end{pmatrix} \text{ for all integers } n \geq 1.$$

Note that Teorem 2.6 has been used in Teorem 3.2, Teorem 3.6, and Teorem 3.9.

Based on the approach given here, it is seen that it can be written any finite dimensional matrix and

related results. Although the approach is simple, we believe that it is important in terms of its role and useful in the study related to these subjects.

REFERENCES

- [1] T. Koshy, Fibonacci and Lucas Numbers with Applications, Wiley Interscience, 2001.
- [2] R. C. Johnson, Fibonacci Numbers and Matrices, Durham University, 2009, <http://maths.dur.ac.uk/~dma0rcj/PED/b.pdf>.
- [3] S. Vajda, Fibonacci and Lucas Numbers and the Golden Section: Theory and Applications, Ellis Horwood Limited Publ., 9-62, 1989.
- [4] B. Demirtürk, Fibonacci and Lucas Sums with Matrix Method, International Mathematical Forum, 5(3), 99-107, 2010.
- [5] R. A. Dunlop, The Golden Ratio and Fibonacci Numbers, World Scientific Publishing, 35-62, 1997.
- [6] A. M. Meinke, Fibonacci Numbers and Associated Matrices, Thesis Submitted to Kent States University, 2011.
- [7] T. Mekonnen, On The Fibonnacci Numbers, Thesis Submitted to Addis Ababa University, 2013.
- [8] R. Keskin, B. Demirtürk, Some new Fibonacci and Lucas identities by matrix methods. Internat. J. Math. Ed. Sci. Tech. 41, 3, 379-387, 2010.

	SAKARYA UNIVERSITY JOURNAL OF SCIENCE		 SAKARYA UNIVERSITY
	e-ISSN: 2147-835X http://www.saujs.sakarya.edu.tr		
	Received 15-10-2018 Accepted 12-11-2018	Doi 10.16984/saufenbilder.470493	

Summability factors between the absolute Cesàro methods

G. Canan Hazar Güleç*

Abstract

If $\sum \varepsilon_n x_n$ is summable by the method Y whenever $\sum x_n$ is summable by the method X , then we say that the factor $\varepsilon = (\varepsilon_n)$ is of type (X, Y) and denote by (X, Y) . In this study we characterize the sets $(|C, \alpha|_k, |C, -1|)$, $k > 1$ and $(|C, -1|, |C, \alpha|_k)$, $k \geq 1$ for $\alpha > -1$. Also, in the special case, we give some inclusion relations between methods, which completes some open problems in literature.

Keywords: Sequence spaces, Absolute Cesàro summability, Summability Factors.

1. INTRODUCTION

Let $\sum x_n$ be an infinite series with partial sum (s_n) , and by (σ_n^α) and (u_n^α) we denote the n -th Cesàro means of order α with $\alpha > -1$ of the sequences (s_n) and (nx_n) , respectively, i.e.,

$$\sigma_n^\alpha = \frac{1}{A_n^\alpha} \sum_{v=0}^n A_{n-v}^{\alpha-1} s_v$$

and

$$u_n^\alpha = \frac{1}{A_n^\alpha} \sum_{v=1}^n A_{n-v}^{\alpha-1} v x_v \quad (1.1)$$

where $A_0^\alpha = 1$, $A_n^\alpha = \binom{\alpha+n}{n}$, $A_{-n}^\alpha = 0$, $n \geq 1$. The series $\sum x_n$ is said to be summable $|C, \alpha|_k$, $k \geq 1$, if (see [4])

$$\sum_{n=1}^{\infty} n^{k-1} |\sigma_n^\alpha - \sigma_{n-1}^\alpha|^k < \infty. \quad (1.2)$$

On the other hand, by the well known identity $u_n^\alpha = n(\sigma_n^\alpha - \sigma_{n-1}^\alpha)$ [8], the condition (1.2) can be stated by

$$\sum_{n=1}^{\infty} \frac{1}{n} |u_n^\alpha|^k < \infty.$$

Note that the definition of Flett [4] doesn't include the case $\alpha = -1$, although the Cesàro summability (C, α)

is studied usually for range $\alpha \geq -1$ (see [5]). Hence, Thorpe [22] gave the separate definition for $\alpha = -1$ as follows. If the series to sequence transformation

$$T_n = \sum_{v=0}^{n-1} x_v + (n+1)x_n \quad (1.3)$$

tends to a finite number s as n tends to infinity, then the series $\sum x_n$ is summable by Cesàro summability $(C, -1)$ to the number s [22].

Also, by the definition of Sarigöl [16] and Thorpe [22], the series $\sum x_n$ is said to be summable $|C, -1|_k$, $k \geq 1$, if (see [6])

$$\sum_{n=1}^{\infty} n^{k-1} |T_n - T_{n-1}|^k < \infty.$$

In this context the series spaces $|C_\alpha|_k$, $k \geq 1$, have been defined as the set of all series summable by the absolute Cesàro summability method $|C, \alpha|_k$ in [14] and [6] for $\alpha > -1$ and $\alpha = -1$, respectively.

If $\sum \varepsilon_n x_n$ is summable by the method Y whenever $\sum x_n$ is summable by the method X , then the sequence $\varepsilon = (\varepsilon_n)$ is said to be a summability factor of type (X, Y) and we write it by $\varepsilon \in (X, Y)$. In the special case if it is taken as $\varepsilon = 1$, then $1 \in (X, Y)$ leads to the comparisons of these methods, where $1 = (1, 1, \dots)$ i.e., $X \subset Y$.

* Corresponding Author

Such types of factors were investigated in detail by several authors [1-3, 10-13, 15, 17-21], and recently some well known results in [10-13, 15] have been extended by Sarıgöl [15] and Sarıgöl & Hazar [7].

In this study, we deal with the problem of absolute Cesàro summability factors. More precisely, we characterize the sets $(|C, \alpha|_k, |C, -1|)$, $k > 1$ and $(|C, -1|, |C, \alpha|_k)$, $k \geq 1$ for $\alpha > -1$. So we give the inclusion relations between these methods, which completes some open problems in literature.

2. MAIN RESULTS

In this section we characterize the sets $(|C, \alpha|_k, |C, -1|)$, $k > 1$ and $(|C, -1|, |C, \alpha|_k)$, $k \geq 1$ for $\alpha > -1$. Thus, in the special case, we give the inclusion relations between methods.

Now, we require the following lemmas for our investigations.

Throughout this paper, k^* denote the conjugate of $k > 1$, i.e., $1/k + 1/k^* = 1$, and $1/k^* = 0$ for $k = 1$.

Lemma 2.1. Let $1 < k < \infty$. Then, $A(x) \in \ell$ whenever $x \in \ell_k$ if and only if

$$\sum_{v=0}^{\infty} \left(\sum_{n=0}^{\infty} |a_{nv}| \right)^{k^*} < \infty$$

where $\ell_k = \{x = (x_v) : \sum |x_v|^k < \infty\}$ [15].

Lemma 2.2. Let $1 \leq k < \infty$. Then, $A(x) \in \ell_k$ whenever $x \in \ell$ if and only if

$$\sup_v \sum_{n=0}^{\infty} |a_{nv}|^k < \infty,$$

[9].

We begin with the characterization of the set $(|C, \alpha|_k, |C, -1|)$ for $k > 1$ and $\alpha > -1$.

Theorem 2.3. Let $k > 1$ and $\alpha > -1$. Then, $\varepsilon \in (|C, \alpha|_k, |C, -1|)$ if and only if

$$\sum_{r=1}^{\infty} \left(\sum_{n=r}^{\infty} \left| \left(\frac{(n+1)\varepsilon_n A_{n-r}^{-\alpha-1}}{n} - \varepsilon_{n-1} A_{n-1-r}^{-\alpha-1} \right) r^{1/k} A_r^\alpha \right| \right)^{k^*} < \infty. \quad (2.1)$$

Proof. Let define u_n^α and T_n by (1.1) and

$$T_n = \sum_{v=0}^{n-1} \varepsilon_v x_v + (n+1)\varepsilon_n x_n$$

respectively. Using the definitions of u_n^α and T_n , we define the sequences $y = (y_n)$ and $\tilde{y} = (\tilde{y}_n)$ by

$$y_n = \frac{u_n^\alpha}{n^{1/k}} = \frac{1}{n^{1/k} A_n^\alpha} \sum_{v=1}^n A_{n-v}^{\alpha-1} v x_v, n \geq 1$$

and $y_0 = x_0$ (2.2)

and

$$\tilde{y}_n = T_n - T_{n-1} = (n+1)\varepsilon_n x_n - (n-1)\varepsilon_{n-1} x_{n-1},$$

$n \geq 1$ and $\tilde{y}_0 = \varepsilon_0 x_0$ (2.3)

respectively. Then, $\varepsilon \in (|C, \alpha|_k, |C, -1|)$ iff $\tilde{y} \in \ell$ whenever $y \in \ell_k$. By inversion of (2.2), we write for $n \geq 1$

$$x_n = \frac{1}{n} \sum_{v=1}^n A_{n-v}^{-\alpha-1} v^{1/k} A_v^\alpha y_v \quad (2.4)$$

Hence, by (2.4) we get for $n \geq 1$

$$\begin{aligned} \tilde{y}_n &= (n+1)\varepsilon_n x_n - (n-1)\varepsilon_{n-1} x_{n-1} \\ &= (n+1)\varepsilon_n \frac{1}{n} \sum_{r=1}^n A_{n-r}^{-\alpha-1} r^{1/k} A_r^\alpha y_r \\ &\quad - (n-1)\varepsilon_{n-1} \frac{1}{n-1} \sum_{r=1}^{n-1} A_{n-1-r}^{-\alpha-1} r^{1/k} A_r^\alpha y_r \\ &= \sum_{r=1}^n \left(\frac{(n+1)\varepsilon_n A_{n-r}^{-\alpha-1}}{n} - \varepsilon_{n-1} A_{n-1-r}^{-\alpha-1} \right) r^{1/k} A_r^\alpha y_r \\ &= \sum_{r=1}^n c_{nr} y_r \end{aligned}$$

where

$$c_{nr} = \begin{cases} \left(\frac{(n+1)\varepsilon_n A_{n-r}^{-\alpha-1}}{n} - \varepsilon_{n-1} A_{n-1-r}^{-\alpha-1} \right) r^{1/k} A_r^\alpha, & 1 \leq r \leq n \\ 0, & r > n. \end{cases}$$

So $\tilde{y} \in \ell$ whenever $y \in \ell_k$ if and only if

$$\sum_{r=1}^{\infty} \left(\sum_{n=r}^{\infty} |c_{nr}| \right)^{k^*} < \infty,$$

by Lemma 2.1 or, equivalently, (2.1) holds. Thus the proof is completed.

Since $1 \in (|C, \alpha|_k, |C, -1|)$ leads us to a comparison of summability fields of methods $|C, \alpha|_k$ and $|C, -1|$, where $1 = (1, 1, \dots)$, that is $|C, \alpha|_k \subset |C, -1|$, taking $\varepsilon_n = 1$ for all $n \geq 1$ in Theorem 2.3 we get the following result.

Corollary 2.4. If $k > 1$ and $\alpha > -1$, then, $|C, \alpha|_k \subset |C, -1|$ if and only if

$$\sum_{r=1}^{\infty} \left(\sum_{n=r}^{\infty} \left| \left(\frac{(n+1)A_{n-r}^{\alpha-1}}{n} - A_{n-1-r}^{\alpha-1} \right) r^{1/k} A_r^{\alpha} \right| \right)^{k^*} < \infty.$$

Theorem 2.5. Let $k \geq 1$ and $\alpha > -1$. Then the necessary and sufficient condition for $\varepsilon \in (|C, -1|, |C, \alpha|_k)$, is

$$\sup_r \sum_{n=r}^{\infty} \left| \frac{r}{n^{1/k} A_n^{\alpha}} \sum_{v=r}^n \frac{A_{n-v}^{\alpha-1} \varepsilon_v}{v+1} \right|^k < \infty. \quad (2.5)$$

Proof. As in proof of Theorem 2.3, we define sequences $y = (y_n)$ and $\tilde{y} = (\tilde{y}_n)$ by

$$y_n = \frac{1}{n^{1/k} A_n^{\alpha}} \sum_{v=1}^n A_{n-v}^{\alpha-1} v \varepsilon_v x_v, n \geq 1$$

and $y_0 = \varepsilon_0 x_0$

and

$$\tilde{y}_n = (n+1)x_n - (n-1)x_{n-1}, n \geq 1 \text{ and}$$

$$\tilde{y}_0 = x_0 \quad (2.6)$$

respectively.

Then, $\varepsilon \in (|C, -1|, |C, \alpha|_k)$ if and only if $y \in \ell_k$ whenever $\tilde{y} \in \ell$. On the other hand, from (2.6) we write

$$x_n = \frac{1}{n(n+1)} \sum_{v=1}^n v \tilde{y}_v, n \geq 1 \text{ and } x_0 = \tilde{y}_0 \quad (2.7)$$

Hence, by (2.7) we get for $n \geq 1$

$$\begin{aligned} y_n &= \frac{1}{n^{1/k} A_n^{\alpha}} \sum_{v=1}^n A_{n-v}^{\alpha-1} v \varepsilon_v x_v \\ &= \frac{1}{n^{1/k} A_n^{\alpha}} \sum_{v=1}^n A_{n-v}^{\alpha-1} v \varepsilon_v \frac{1}{v(v+1)} \sum_{r=1}^v r \tilde{y}_r \\ &= \frac{1}{n^{1/k} A_n^{\alpha}} \sum_{r=1}^n r \left(\sum_{v=r}^n \frac{A_{n-v}^{\alpha-1} \varepsilon_v}{v+1} \right) \tilde{y}_r = \sum_{r=1}^n c_{nr} \tilde{y}_r \end{aligned}$$

where

$$c_{nr} = \begin{cases} \frac{r}{n^{1/k} A_n^{\alpha}} \sum_{v=r}^n \frac{A_{n-v}^{\alpha-1} \varepsilon_v}{v+1}, & 1 \leq r \leq n \\ 0, & r > n. \end{cases}$$

Then, $y \in \ell_k$ whenever $\tilde{y} \in \ell$ if and only if

$$\sup_r \sum_{n=r}^{\infty} \left| \frac{r}{n^{1/k} A_n^{\alpha}} \sum_{v=r}^n \frac{A_{n-v}^{\alpha-1} \varepsilon_v}{v+1} \right|^k < \infty$$

by Lemma 2.2, which is the same as the condition (2.5). This completes the proof.

Since $1 \in (|C, -1|, |C, \alpha|_k)$ leads us to a comparison of summability fields of methods $|C, \alpha|_k$ and $|C, -1|$, where $1 = (1, 1, \dots)$, that is $|C, -1| \subset |C, \alpha|_k$, taking $\varepsilon_n = 1$ for all $n \geq 1$ in Theorem 2.5 we get the following result.

Corollary 2.6. If $k \geq 1$ and $\alpha > -1$, then, $|C, -1| \subset |C, \alpha|_k$ if and only if

$$\sup_r \sum_{n=r}^{\infty} \left| \frac{r}{n^{1/k} A_n^{\alpha}} \sum_{v=r}^n \frac{A_{n-v}^{\alpha-1}}{v+1} \right|^k < \infty.$$

REFERENCES

- [1] H. Bor, "Some equivalence theorems on absolute summability methods," Acta Math. Hung., vol. 149, pp.208-214, 2016.
- [2] H. Bor and B. Thorpe, "On some absolute summability methods," Analysis 7, vol.2, pp.145-152, 1987.
- [3] H. Bor, "On two summability methods," Math. Proc. Cambridge Philos Soc., vol. 98, 147-149, 1985.
- [4] T.M. Flett, "On an extension of absolute summability and some theorems of Littlewood and Paley," Proc. London Math. Soc., vol. 7, pp. 113-141, 1957.
- [5] G.H. Hardy, Divergent Series, Oxford, 1949.
- [6] G.C. Hazar and M.A. Sarigöl, "Compact and Matrix Operators on the Space $|C, -1|_k$," J. Comput. Anal. Appl., vol.25, no.6, pp. 1014-1024, 2018.
- [7] G.C. Hazar, and M.A. Sarigöl, "On factor relations between weighted and Nörlund means," Tamkang J. Math. (in press).
- [8] E. Kogbetliantz, "Sur lesseries absolument sommables par la methods des moyannes arithmetiques," Bull. des Sci. Math. , vol. 49, pp.234-256, 1925.
- [9] I.J. Maddox, "Elements of functinal analysis, Cambridge University Press," London, New York, 1970.
- [10] S.M. Mazhar, "On the absolute summability factors of infinite series," Tohoku Math. J., vol.23, pp.433-451, 1971.
- [11] M.R. Mehdi, "Summability factors for generalized absolute summability I," Proc. London Math. Soc., vol.3., no.10, pp.180-199, 1960.
- [12] R.N. Mohapatra, "On absolute Riesz summability factors," J. Indian Math. Soc., vol.32, pp.113-129, 1968.

- [13] C. Orhan and M.A. Sarigöl, "On absolute weighted mean summability," Rocky Mount. J. Math., vol.23, pp.1091-1097, 1993.
- [14] M. A. Sarigöl, "Spaces of series Summable by absolute Cesàro and Matrix Operators ," Comm. Math. Appl. , vol.7, no.1, pp.11-22, 2016.
- [15] M.A. Sarigöl, "Extension of Mazhar's theorem on summability factors," Kuwait J. Sci., vol.42, no.3, pp.28-35, 2015.
- [16] M.A. Sarigöl, "On the local properties of factored Fourier series," Appl. Math. Comp., vol.216, pp.3386-3390, 2010.
- [17] M.A. Sarigöl, and H. Bor, "Characterization of absolute summability factors," J. Math. Anal. Appl., vol. 195, pp.537-545, 1995.
- [18] M.A. Sarigöl, "On two absolute Riesz summability factors of infinite series," Proc. Amer. Math. Soc. , vol.118, pp.485-488, 1993.
- [19] M.A. Sarigöl, "A note on summability," Studia Sci. Math. Hungar., vol.28, pp.395-400, 1993.
- [20] W.T. Sulaiman, "On summability factors of infinite series," Proc. Amer. Math. Soc., vol.115, pp.313-317, 1992.
- [21] W.T. Sulaiman, "On some absolute summability factors of Infinite Series," Gen. Math. Notes, vol.2, no.2, pp.7-13, 2011.
- [22] B. Thorpe, "Matrix transformations of Cesàro summable Series," Acta Math. Hung., vol. 48(3-4), pp.255-265, 1986.

	SAKARYA UNIVERSITY JOURNAL OF SCIENCE		 SAKARYA UNIVERSITY
	e-ISSN: 2147-835X http://www.saujs.sakarya.edu.tr		
	Received 26-09-2018 Accepted 14-11-2018	Doi 10.16984/saufenbilder.463978	

Pseudo-mirror nuclei in the mass regions $A \sim 170$ and $A \sim 200$

Bahadır Saygı¹

Abstract

The concept of pseudo-mirror nuclei is based on the $N_{\pi}N_{\nu}$ scheme introduced as an extension of the N_pN_n scheme. The $N_{\pi}N_{\nu}$ scheme tells us that if two nuclei from different mass region have equal number of integrated n-p interaction than the experimental observables $E(2^+)$, $E(4^+)/E(2^+)$ and $B(E2; 2^+ \rightarrow 0^+)$ are expected to be almost equal, therefore equal number of n-p interaction build similar level schemes up to certain spin quantum numbers. Pseudo-mirror nuclei have been introduced for the first time in the mass regions $A \sim 100$ and $A \sim 130$ for Mo, Zr, Nd and Ce nuclei. Later, a systematic work carried out over a broad region of Segre chart showed that not only the excitation energies but also related $B(E2)$ values of excited states in pseudo-mirror nuclei (PMN) are in good agreement. In the present work, we present new pseudo-mirror nuclei in the mass region $A \sim 170$ and $A \sim 200$ for the first time.

Keywords: Pseudo-mirror nuclei, n-p interaction, $N_{\pi}N_{\nu}$ Scheme

1. INTRODUCTION

Atomic nucleus is a many-body problem in applied quantum mechanics since its discovery in 1911 by Ernest Rutherford [1] while firing alpha particles on gold sheets in the University of Manchester. The discovery itself is an emergent phenomenon. It is quite interesting that nobody has assumed the existence until its discovery [2]. Soon later, the attention from many scientists drawn on nuclei it has been understood that its structure is quite complex. However, searching symmetries make this complexity rather simple over time. Heisenberg introduced the isospin concept which indicates neutron and protons are only different states of a nucleon [3]. Since then mirror nuclei have been a unique laboratory in order to investigate the behavior of different state of nucleon named proton and neutron under the

strong nuclear interaction [4,5]. Later, valence mirror and pseudo-mirror nuclei (PMN) have been introduced to understand the underlying structure of isospin symmetry [6-10]. Pseudo-mirror nuclei have been introduced by Moscrop et al [10] over Mo, Zr, Ce and Nd based on the $N_{\pi}N_{\nu}$ product, where $N_{\pi} = p_{p(h)}/2$ i.e. half the number of valence protons (or holes) and $N_{\nu} = n_{p(h)}/2$ is half the number of valence neutrons (or holes) from the nearest closed shell by considering the subshell closure. The $N_{\pi}N_{\nu}$ scheme is based on the N_pN_n scheme introduced by Casten [11], where the latter is a measure of n-p interaction which build the collectivity and deformation in nuclei beyond a major shell. Recent studies on the $B(E2)$ values of excited states in PMN over a broad region of Segre chart revealed that the nuclei having equal $N_{\pi}N_{\nu}$ quantity show similar nuclear structural behavior [12,13]. Figure 1 shows ^{108}Ru - ^{124}Ba pseudo-mirror nuclei both having $N_{\pi}N_{\nu} = 21$. It is quite surprising that these two nuclei from different mass regions exhibit similar

¹* Ege University, Science Faculty, Physics Department, Izmir, Turkey – bahadir.saygi@ege.edu.tr

level schemes based on their valence proton – neutron interactions. ^{100}Zr - ^{164}Hf , ^{136}Sm - ^{160}Yb , ^{102}Zr - ^{130}Nd , ^{136}Sm - ^{160}Yb and ^{168}Hf - ^{160}Er nuclei are some of the examples for PMN introduced by Moscrop et.al [10] and Saygı [12,13].

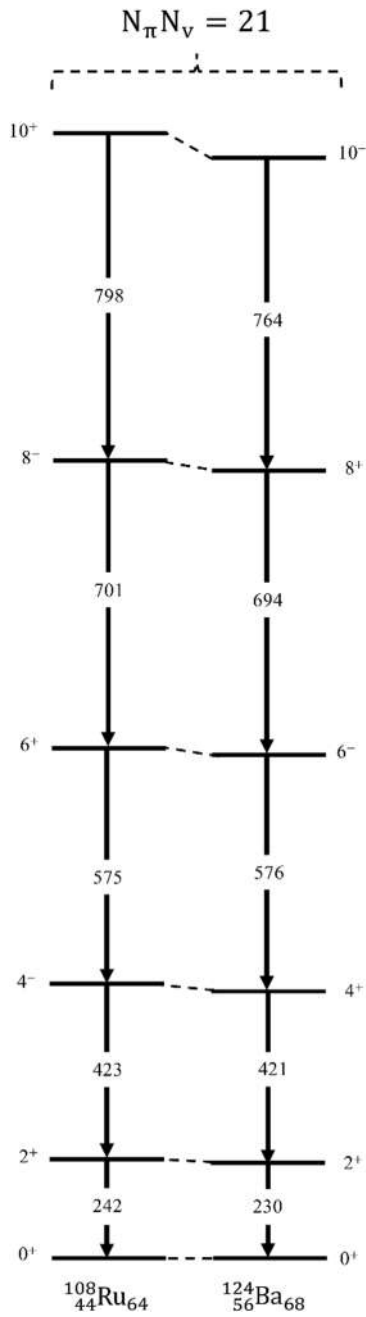


Figure 1: Excitation energies in ^{108}Ru - ^{124}Ba level schemes with $N_\pi N_\nu = 21$. Level schemes adopted from [14,15].

In the present work, we are going to introduce new PMN from the mass region $A \sim 170$ and $A \sim 200$. The mass region $A \sim 200$ have not been investigated yet from the point view of PMN so far. Figure 2 shows the level schemes of ^{164}Os

($6p_h$ - $6n_p$) - ^{208}Ra ($6p_p$ - $6n_h$), ^{166}Os ($6p_h$ - $8n_p$)- ^{206}Ra ($6p_p$ - $8n_h$) and ^{174}Pt ($4p_h$ - $14n_p$) - ^{198}Rn ($4p_p$ - $14n_h$) nuclei, where the $p_{p(h)}$ and $n_{p(h)}$ are the quantities which represent the number of valence proton particle (hole) and neutron particle (hole) from the nearest closed proton and neutron shells. The key point in the PMN is the exchange of particle and hole numbers from one of the pairs to the other.

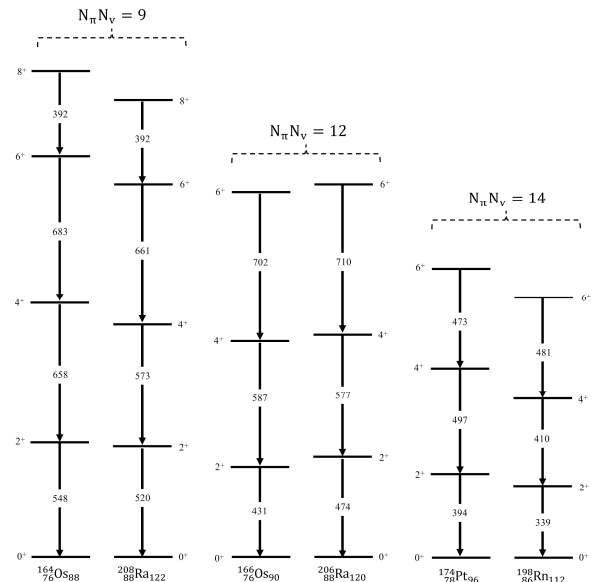


Figure 2: Excitation energies in ^{164}Os [16]- ^{208}Ra [17] with $N_\pi N_\nu = 9$, ^{166}Os [16]- ^{206}Ra [18] with $N_\pi N_\nu = 12$ and ^{174}Pt [19]- ^{198}Rn [20] with $N_\pi N_\nu = 14$.

The nuclei presented in the present manuscript follow general trend in the description of pseudo-mirror nuclei. The energies of excited 2^+ state in ^{164}Os - ^{208}Ra , ^{166}Os - ^{206}Ra and ^{174}Pt - ^{198}Rn are almost degenerate. The second quantity which is employed quite often to determine the pseudo-mirror nuclei is the ratio of $E(4^+)/E(2^+)$. The $E(4^+)/E(2^+)$ is 2.20 for the ^{164}Os and 2.10 for ^{208}Ra with $N_\pi N_\nu = 9$. The $E(4^+)/E(2^+)$ is 2.36 for the ^{166}Os and 2.21 for ^{206}Ra with $N_\pi N_\nu = 12$. The $E(4^+)/E(2^+)$ is 2.26 for the ^{174}Pt and 2.20 for ^{198}Rn with $N_\pi N_\nu = 14$. The difference of 0.1 between the $E(4^+)/E(2^+)$ values in the PMN pairs are in the range of the systematics result proceeded by Saygı [12]. The $E(4^+)/E(2^+)$ quantity is a good value which indicates the structural features of the nuclei of interest. Therefore, these nuclei are meeting the essential criteria to be accepted pseudo-mirror nuclei in the framework of the $N_\pi N_\nu$ scheme introduced by Moscrop et.al [10]. The last and the most important criteria to define

a couple of nuclei having equal $N_{\pi}N_{\nu}$ quantity is the reduced transition probabilities of the related excited states in the pseudo-mirror nuclei. However, the required data are not available while the present manuscript is being written. Therefore, we are strongly suggesting the measurement of reduced transition probabilities of excited states in these nuclei. None of the theories provided in Raman [21] systematic work predicts a relation between calculated $B(E2)$ values for the nuclei presented in here. Nonetheless, the $|\beta_2|$ deformations calculated by Möller [22] for ^{164}Os - ^{208}Ra with $N_{\pi}N_{\nu} = 9$ in agreement where the values are 0.129 and 0.125, respectively. The theoretical $|\beta_2|$ values for ^{166}Os - ^{206}Ra and ^{174}Pt - ^{198}Rn differ. The reason for this is possible the nuclei of interest in this manuscript have not been considered within the pseudo-mirror nuclei concept. Quadrupole-quadrupole interaction is assumed to establish nuclear structure beyond the closed shells, however, it seems integrated neutron-proton interaction dominates the quadrupole-quadrupole interaction when the number of valence nucleons either particles or holes [23-27]. Therefore, to explain the pseudo-mirror nuclei phenomena one should take account the neutron-proton interaction.

In summary, we have introduced the new pseudo-mirror nuclei ^{164}Os - ^{208}Ra with $N_{\pi}N_{\nu} = 9$, ^{166}Os - ^{206}Ra with $N_{\pi}N_{\nu} = 12$ and ^{174}Pt - ^{198}Rn with $N_{\pi}N_{\nu} = 14$ in the mass regions $A \sim 170$ and $A \sim 200$ for the first time. The available data do not let us to examine the reduced transition probabilities of the nuclei of interest in the present manuscript. However, the $E(4^+)/E(2^+)$ ratio still let us to describe the nuclei in the framework geometric collective model limits. Theoretical values have been investigated provided by Raman and Möller. We suggest that a model should consider the integrated proton-neutron interaction to interpret the structure of pseudo-mirror nuclei.

REFERENCES

- [1] E. Rutherford, "LXXIX. The scattering of α and β particles by matter and the structure of the atom," *Philosophical Magazine Series 6*, vol. 21, no. 125, pp. 669-688, 1911.
- [2] P.W. Anderson, "More is different," *Science*, vol. 177, no. 4047, pp. 393, 1972.
- [3] W. Heisenberg, "Über den Bau der Atomkerne. I," *Zeitschrift für Physik A Hadrons and Nuclei*, vol. 77, pp. 1, 1932.
- [4] J. Ekman et.al, "The $A = 51$ mirror nuclei ^{51}Fe and ^{51}Mn ," *The European Journal of Physics A*, vol. 9, pp. 13-17, 2000.
- [5] D. Tonev et.al, "Transition rates and nuclear structure changes in mirror nuclei ^{47}Cr and ^{47}V ," *Physical Review C*, vol. 65, pp. 034314, 2002.
- [6] R. Wirowski et.al, "Valence mirror nuclei," *Journal of Physics G: Nuclear Physics*, vol. 14, pp. L195, 1988.
- [7] R.F. Casten et.al, "Simplified shell model calculations for valence mirror nuclei," *Nuclear Physics A*, vol. 514, pp. 252, 1990.
- [8] J. Yan et.al, "Proton-neutron symmetry in valence mirror nuclei," *Physical Review C*, vol. 42, pp. 743, 1990.
- [9] M. Schimmer et.al, "The valence mirror nuclei ^{114}Sn and ^{146}Gd ," *Nuclear Physics A*, vol. 569, pp. 458, 1994.
- [10] R. Moscrop et.al, "Pseudo-mirror nuclei with $A=100$ and $A=130$," *Journal of Physics G: Nuclear Physics*, vol. 14, pp. L189, 1989.
- [11] R.F. Casten, "NpNn systematics in heavy nuclei," *Nuclear Physics A*, vol. 443, pp. 1, 1985.
- [12] B. Saygı, "Investigation of the $B(E2)$ systematics in pseudo-mirror nuclei," *Journal of Physics G: Nuclear and Particle Physics*, vol. 45, pp. 095104, 2018.
- [13] B. Saygı, "Symmetrical level schemes of the even-even $Sm_{A \approx 130}$ and $Yb_{A \approx 160}$ nuclei up to 10^+ in the yrast bands," *Nuclear Physics A*, vol. 980, pp. 15 -20, 2018.
- [14] J. Blachot, "Nuclear Data Sheets for $A = 108^*$," *Nuclear Data Sheets*, vol. 90, pp. 135, 2000.
- [15] J. Katakura and Z.D. Wu, "Nuclear Data Sheets for $A = 124^*$," *Nuclear Data Sheets*, vol. 109, pp. 1655, 2008.
- [16] S.L. King et.al, "First observation of excited states in the neutron deficient nuclei ^{164}Os and ^{166}Os ," *Physical Review C*, vol. 62, pp. 067301, 2000.
- [17] J.J. Ressler et.al, "Isomeric decay of ^{208}Ra ," *Physical Review C*, vol. 71, pp. 014302, 2005.
- [18] J.F.C. Cocks et.al, "Gamma-ray spectroscopy of neutron-deficient Ra

- isotopes," *Journal of Physics G: Nuclear Physics*, vol. 25, pp. 839, 1999.
- [19] G.D. Dracoulis et.al, "Shape coexistence from the structure of the yrast band in ^{174}Pt ," *Physical Review C*, vol. 44, pp. R1246, 1991.
- [20] R.B.E. Taylor et.al, "Gamma decay of excited states in ^{198}Rn identified using correlated radioactive decay," *Physical Review C*, vol. 59, pp. 673, 1999.
- [21] S. Raman et.al, "Transition probability from the ground to the first-excited 2^+ state of even-even nuclides," *Atomic Data and Nuclear Data Tables*, vol. 78, pp. 1, 2001.
- [22] P. Möller et.al, "Nuclear ground-state masses and deformations: FRDM (2012)," *Atomic Data and Nuclear Data Tables*, vol. 109-110, pp. 1, 2016.
- [23] A. De-Shalit and M. Goldhaber, "Mixed configurations in nuclei," *Physical Review*, vol. 92, pp. 1211, 1953.
- [24] I. Talmi, "Effective interactions and coupling schemes in nuclei," *Reviews of Modern Physics*, vol. 34, pp. 704, 1962.
- [25] P. Federman and S. Pittel, "Towards a unified microscopic description of nuclear deformation," *Physics Letter B*, vol. 69, pp. 385, 1977.
- [26] P. Federman and S. Pittel, "Unified shell-model description of nuclear deformation," *Physical Review C*, vol. 20, pp. 820, 1979.
- [27] J. Dobaczewski, W. Nazarawich, J. Skalski ve T. Werner, "Nuclear deformation: A proton-neutron effect?," *Physical Review Letter*, vol. 60, pp. 2254, 1988.

	SAKARYA UNIVERSITY JOURNAL OF SCIENCE		 SAKARYA UNIVERSITY
	e-ISSN: 2147-835X http://www.saujs.sakarya.edu.tr		
	<u>Received</u> 29-08-2018 <u>Accepted</u> 09-11-2018	<u>Doi</u> 10.16984/saufenbilder.455890	

Normal Stress Analysis In An Infinite Elastic Body With A Locally Curved Carbon Nanotube

Kadriye Şimşek Alan

ABSTRACT

In this paper, the results of normal stress values in unidirectional fibrous composite with locally curved carbon nanotube (CNT) were obtained as much as the second approximation and the obtained results were analyzed. The boundary form perturbation method is used to solve the problem. This investigation is made within the framework of a piecewise homogeneous body model by using the three-dimensional geometrically nonlinear exact equations of elasticity theory. The concentration of carbon nanotubes in the composite is assumed to be low and the interaction between them is neglected. Numerous results are obtained for the normal stress distribution and the effect of the problem parameters on this stress distribution is analyzed.

Keywords: Carbon Nanotube, stress distribution, geometric nonlinearity, locally curved

1. INTRODUCTION

One of the most important factors determining the stress state in fiber composite materials is the curvature of the fibers, [1,5,6,9,10]. For this reason, Akbarov and Guz [2] focused on the stress state in unidirectional composite. The investigation in [2] is made within the framework of a piecewise homogeneous body model, by using the exact three-dimensional equations of elasticity theory. But the unidirectional fibrous composites are traditional materials. Nowadays, nanotechnology is used in the world and the importance of nano materials is increasing day by day. For this reason researchers have concentrated their work on this field. One of these studies Alan and Akbarov [3] studied the normal stresses state in the nanocomposite with a locally curved covered nanofibers. In [4], a method was given for the investigation of the stress distribution in the nanocomposites with unidirectional locally

curved and hollow nanofiber. Coban and Kösker [8] was

considered the stress distribution in the infinite elastic body containing a single locally curved carbon nanotube (CNT). However, results for the first approximation were obtained only. Increasing the number of approaches is crucial in order to increase the sensitivity of the results.

In this study, a mathematical formulation was developed to determine the normal stress distribution of the infinite elastic body containing a single local curved carbon nanotube (CNT) as much as up to the second approximation on the Carbon nanotube and matrix interface. The problem is solved using the boundary form perturbation method. In addition, an Algorithm is designed to solve the related problem. We obtained the numerous numerical results on the normal stress distribution on the surface between the CNT and matrix. The influence of the problem parameters on this distribution were analyzed.

The investigation is made in the framework of the three-dimensional geometrically nonlinear exact equations of elasticity theory. The model " an infinite body containing a single CNT " regards the case where the concentration of carbon nanotubes in the composite is assumed to be low, and the interaction between the carbon nanotubes is neglected.

We acknowledge that the statements of some results of normal stress distribution in an infinite elastic body with a locally curved carbon nanotube in this paper were presented at 2nd International Conference of Mathematical Sciences (ICMS 2018) [11].

2. FORMULATION OF THE PROBLEM

Infinite elastic body with local curved carbon nanotube is given as in figure 1 .

In this work, the cross section of the carbon nanotube normal to its axial line is described two circles of constant radius R_1 and R_2 along the entire length and the body is compressed or stretched of the uniformly distributed normal forces with intensity p acting along Ox_3 axis direction. With the middle line of the carbon nanotube , we associate Lagrangian rectilinear $Ox_1x_2x_3$ and cylindrical $Or\theta z$ system of coordinates (Figure 1). The carbon nanotube and matrix materials are homogeneous, isotropic and linear elastic.

The equation of the carbon nanotube middle line is given as follows:

$$x_1 = F(x_3) = \varepsilon \delta(x_3), x_2 = 0 ;$$

$$x_1 = A \exp\left(-\left(\frac{x_3}{L}\right)^2\right) \cos\left(m \frac{x_3}{L}\right)$$

$$= \varepsilon L \exp\left(-\left(\frac{x_3}{L}\right)^2\right) \cos\left(m \frac{x_3}{L}\right) = \varepsilon \delta(x_3)$$

$$\varepsilon = \frac{A}{L} \tag{1}$$

Where A and L geometrical parameter were shown in Figure 1. We assume that A is smaller than L , we describe a small parameter $\varepsilon = \frac{A}{L}$

($0 \leq \varepsilon < 1$). The function δ_n^j is the local curving form of the carbon nanotube . Assume that on the contact surface between the carbon nanotube and matrix material is denoted by S . Then S satisfies the following equations.

$$r(\theta, t_3) = \frac{\varepsilon \delta(t_3) (1 + \varepsilon^2 (\delta'(t_3))^2) \cos \theta}{1 + \varepsilon^2 (\delta'(t_3))^2 \cos^2 \theta} +$$

$$\left\{ \frac{\varepsilon^2 (\delta(t_3))^2 (1 + \varepsilon^2 (\delta'(t_3))^2)^2 \cos \theta}{(1 + \varepsilon^2 (\delta'(t_3))^2 \cos^2 \theta)^2} + R^2 - (\varepsilon^2 (\delta(t_3))^2 (1 + \varepsilon^2 (\delta'(t_3))^2)) \right\}^{\frac{1}{2}}$$

$$z(\theta, t_3) = t_3 - \varepsilon \delta'(t_3) (r(\theta, t_3) - \varepsilon \delta(t_3)), \delta'(t_3) = \frac{d\delta(t_3)}{dt_3}$$

$$t_3 \in (-\infty, +\infty) \tag{2}$$

We determine the components of the normal vector on the contact surface as follows.

$$n_r = r(\theta, t_3) \frac{\partial z(\theta, t_3)}{\partial t_3} [A(\theta, z)]^{-1},$$

$$n_\theta = \left[\frac{\partial z(\theta, t_3)}{\partial \theta} \frac{\partial r(\theta, t_3)}{\partial t_3} - \frac{\partial r(\theta, t_3)}{\partial \theta} \frac{\partial z(\theta, t_3)}{\partial t_3} \right] [A(\theta, z)]^{-1}$$

$$n_z = -r(\theta, t_3) \frac{\partial r(\theta, t_3)}{\partial t_3} [A(\theta, t_3)]^{-1}$$

where

$$[A(\theta, t_3)] = \left[\left(r(\theta, t_3) \frac{\partial z(\theta, t_3)}{\partial t_3} \right)^2 + \left(\frac{\partial z(\theta, t_3)}{\partial \theta} \frac{\partial r(\theta, t_3)}{\partial t_3} - \frac{\partial r(\theta, t_3)}{\partial \theta} \frac{\partial z(\theta, t_3)}{\partial t_3} \right)^2 + \left(r(\theta, t_3) \frac{\partial r(\theta, t_3)}{\partial t_3} \right)^2 \right]^{1/2} \tag{3}$$

The Carbon nanotube and matrix material values are defined by superscripts (2) and (1), respectively.

Under this situation which has no motion, the following field equations must be satisfied for the carbon nanotube and matrix,

The equilibrium equations :

$$\nabla_i \left[\sigma^{(k)in} (g_n^j + \nabla_n u^{(kj)}) \right] = 0, \quad k=1,2 \tag{4}$$

The strain-displacement relations:

$$2\varepsilon_{jm}^{(k)} = \nabla_j u_m^{(k)} + \nabla_m u_j^{(k)} + \nabla_j u^{(k)n} \nabla_m u_n^{(k)}, \tag{5}$$

The constitutive equations (Hooke's Law):

$$\sigma_{(in)}^{(k)} = \lambda^{(k)} e^{(k)} \delta_i^n + 2\mu^{(k)} \varepsilon_{(in)}^{(k)},$$

$$e^{(k)} = \varepsilon_{(11)}^{(k)} + \varepsilon_{(22)}^{(k)} + \varepsilon_{(33)}^{(k)} \tag{6}$$

Where λ and μ the material constants.

We use the conventional notation is used In Eqs.(4) , (5) and (6) , and $\sigma^{(k)}$ and $\varepsilon_{jm}^{(k)}$ denote the physical components of the stress tensors and the strain tensors, respectively.

For detailed explanations and formulations on these notations, we refer to Akbarov and Guz [1]

Also, perfect contact conditions are defined at the interfaces S :

$$\sigma^{(1)in} \left(\mathbf{g}_n^j + \nabla_n \mathbf{u}^{(1)j} \right) \Big|_{S_1} \mathbf{n}_j = 0$$

$$\sigma^{(1)in} \left(\mathbf{g}_n^j + \nabla_n \mathbf{u}^{(1)j} \right) \Big|_{S_2} \mathbf{n}_j = \sigma^{(2)in} \left(\mathbf{g}_n^j + \nabla_n \mathbf{u}^{(2)j} \right) \Big|_{S_2} \mathbf{n}_j$$

$$, \quad \mathbf{u}^{(1)j} \Big|_{S_2} = \mathbf{u}^{(2)j} \Big|_{S_2}$$

(7)

The conditions are in given eq. (8)

$$\sigma_{zz}^{(1)} \xrightarrow{r \rightarrow \infty} p, \quad \sigma_{ij}^{(1)} \xrightarrow{r \rightarrow \infty} 0 \quad (ij) \neq zz, \quad (8)$$

where n_j are the covariant components of the unit normal vector to the surfaces S.

In this way, the mathematical formulation of the problem is completed with the solution of the equations systems (4), (5) and (6) within the contact condition (7).

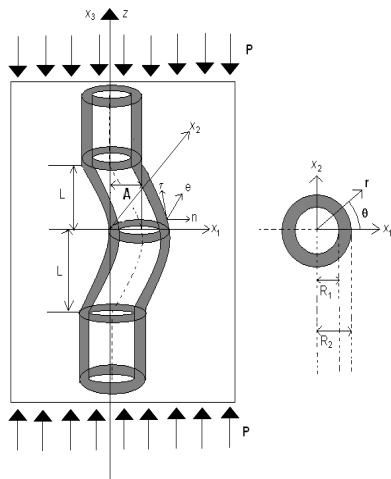


Figure 1: The geometry of a Locally Curved Carbon Nanotube and its cross section

3. SOLUTION OF THE PROBLEM

We solve our problem by using the boundary form perturbation method given in Akbarov and Guz [1]. According to this method, we can write the sought values in the series form in the small parameter ϵ :

$$\sigma_{rr}^{(k)} = \sum_{i=0}^{\infty} \epsilon^i \sigma_{rr}^{(k),i}, \dots, \epsilon_{rr}^{(k)} = \sum_{i=0}^{\infty} \epsilon^i \epsilon_{rr}^{(k),i}, \dots,$$

$$\mathbf{u}_r^{(k)} = \sum_{i=0}^{\infty} \epsilon^i \mathbf{u}_r^{(k),i} \quad (9)$$

The quantities r, z, n_r, n_θ and n_z are also given in series forms:

$$r = R + \sum_{i=1}^{\infty} \epsilon^i a_{ri}(\theta, t_3),$$

$$z = t_3 + \sum_{i=1}^{\infty} \epsilon^i a_{zi}(\theta, t_3),$$

$$n_r = 1 + \sum_{i=1}^{\infty} \epsilon^i b_{ri}(\theta, t_3), \quad n_\theta = \sum_{i=1}^{\infty} \epsilon^i b_{\theta i}(\theta, t_3),$$

$$n_z = \sum_{i=1}^{\infty} \epsilon^i b_{zi}(\theta, t_3) \quad , \quad t_3 \in (-\infty, \infty) \quad (10)$$

by using some routine operations, we can calculate the coefficients of the ϵ^k in (10) , for whose details see Akbarov Guz [1].

Substituting the power series (9) into Eq.(5), it can be obtain sets of equations for each approximation . Using relations (10) we expand the values of each approximation (9) in series 3*form in the vicinity (R, θ, t_3) . If we substitute these last expressions in boundary conditions and use expressions in equation (10), we obtain boundary conditions for each approximation after some mathematical transformations. For the zeroth and first approximations see Alan [4].

Now we will discuss the second approximation. We can write the mechanical and the geometrical relations for this approximation.

$$\sigma_{(in)}^{(k),2} = \lambda^{(k)} e^{(k),2} \delta_i^n + 2\mu^{(k)} \epsilon_{(in)}^{(k),2},$$

$$e^{(k),2} = \epsilon_{(11)}^{(k),2} + \epsilon_{(22)}^{(k),2} + \epsilon_{(33)}^{(k),2}$$

$$\epsilon_{rr}^{(k),2} = \frac{\partial u_r^{(k),2}}{\partial r},$$

$$\epsilon_{\theta\theta}^{(k),2} = \frac{\partial u_\theta^{(k),2}}{r \partial \theta} + \frac{u_r^{(k),2}}{r}, \quad \epsilon_{zz}^{(k),2} = \frac{\partial u_z^{(k),2}}{\partial z} \quad (11)$$

$$\epsilon_{r\theta}^{(k),2} = \frac{1}{2} \left(\frac{\partial u_r^{(k),2}}{r \partial \theta} + \frac{\partial u_\theta^{(k),2}}{\partial r} - \frac{u_\theta^{(k),2}}{r} \right),$$

$$\epsilon_{\theta z}^{(k),2} = \frac{1}{2} \left(\frac{\partial u_\theta^{(k),2}}{\partial z} + \frac{\partial u_z^{(k),2}}{r \partial \theta} \right)$$

$$\epsilon_{zr}^{(k),2} = \frac{1}{2} \left(\frac{\partial u_z^{(k),2}}{\partial r} + \frac{\partial u_r^{(k),2}}{\partial z} \right)$$

By using Akbarov and Guz [1], the contact conditions can be written for the second approximation.

$$\left(\sigma_{rr}^{(1),2} - \sigma_{rr}^{(2),2} \right) \Big|_{(R_1, \theta, t_3)} = -f_1 \left(\frac{\partial \sigma_{rr}^{(1),1}}{\partial r} - \frac{\partial \sigma_{rr}^{(2),1}}{\partial r} \right) - \gamma_z \left(\sigma_{rz}^{(1),1} - \sigma_{rz}^{(2),1} \right)$$

$$\left(\sigma_{r\theta}^{(1),2} - \sigma_{r\theta}^{(2),2} \right) \Big|_{(R_1, \theta, t_3)} = -f_1 \left(\frac{\partial \sigma_{r\theta}^{(1),1}}{\partial r} - \frac{\partial \sigma_{r\theta}^{(2),1}}{\partial r} \right)$$

$$- \phi_1 \left(\frac{\partial \sigma_{r\theta}^{(1),1}}{\partial z} - \frac{\partial \sigma_{r\theta}^{(2),1}}{\partial z} \right) - \gamma_\theta \left(\sigma_{\theta\theta}^{(1),1} - \sigma_{\theta\theta}^{(2),1} \right)$$

$$\begin{aligned}
 (\sigma_{zr}^{(1),2} - \sigma_{zr}^{(2),2}) \Big|_{(R_1, \theta, t_3)} &= -f_1 \left(\frac{\partial \sigma_{zr}^{(1),1}}{\partial r} - \frac{\partial \sigma_{zr}^{(2),1}}{\partial r} \right) \\
 -\varphi_1 \left(\frac{\partial \sigma_{zr}^{(1),1}}{\partial z} - \frac{\partial \sigma_{zr}^{(2),1}}{\partial z} \right) &- \gamma_r (\sigma_{zr}^{(1),1} - \sigma_{zr}^{(2),1}) \\
 -\gamma_\theta (\sigma_{z\theta}^{(1),1} - \sigma_{z\theta}^{(2),1}) &- \gamma_z (\sigma_{zz}^{(1),1} - \sigma_{zz}^{(2),1}) - \gamma_\theta (\sigma_{zz}^{(1),1} - \sigma_{zz}^{(2),1}) \\
 (u_r^{(1),2} - u_r^{(2),2}) \Big|_{(R_1, \theta, t_3)} &= -f_1 \left(\frac{\partial u_r^{(1),1}}{\partial r} - \frac{\partial u_r^{(2),1}}{\partial r} \right) \\
 &- \varphi_1 \left(\frac{\partial u_r^{(1),1}}{\partial z} - \frac{\partial u_r^{(2),1}}{\partial z} \right) \\
 (u_r^{(1),2} - u_r^{(2),2}) \Big|_{(R_1, \theta, t_3)} &= -f_1 \left(\frac{\partial u_\theta^{(1),1}}{\partial r} - \frac{\partial u_\theta^{(2),1}}{\partial r} \right) \\
 &- \varphi_1 \left(\frac{\partial u_\theta^{(1),1}}{\partial z} - \frac{\partial u_\theta^{(2),1}}{\partial z} \right) \\
 (u_z^{(1),2} - u_z^{(2),2}) \Big|_{(R_1, \theta, t_3)} &= -f_1 \left(\frac{\partial u_z^{(1),1}}{\partial r} - \frac{\partial u_z^{(2),1}}{\partial r} \right) \\
 &- \varphi_1 \left(\frac{\partial u_z^{(1),1}}{\partial z} - \frac{\partial u_z^{(2),1}}{\partial z} \right) \quad (12)
 \end{aligned}$$

$$\begin{aligned}
 (\sigma_{rr}^{(2),2}) \Big|_{(R_2, \theta, t_3)} &= f_1 \left(\frac{\partial \sigma_{rr}^{(2),1}}{\partial r} \right) + \gamma_z \sigma_{rz}^{(2),1} \\
 (\sigma_{r\theta}^{(2),2}) \Big|_{(R_2, \theta, t_3)} &= -f_1 \left(\frac{\partial \sigma_{r\theta}^{(2),1}}{\partial r} \right) + \varphi_1 \left(\frac{\partial \sigma_{r\theta}^{(2),1}}{\partial z} \right) \\
 &+ \gamma_\theta \sigma_{\theta\theta}^{(2),1} \\
 (\sigma_{zr}^{(2),2}) \Big|_{(R_2, \theta, t_3)} &= f_1 \left(\frac{\partial \sigma_{zr}^{(2),1}}{\partial r} \right) + \varphi_1 \left(\frac{\partial \sigma_{zr}^{(2),1}}{\partial z} \right) \\
 &+ \gamma_r (\sigma_{zr}^{(2),1}) + \gamma_\theta (\sigma_{z\theta}^{(2),1}) + \gamma_z \sigma_{zz}^{(2),1} + \gamma_\theta \sigma_{zz}^{(2),1}
 \end{aligned}$$

We used in Eq.(12) the following notation.

$$\begin{aligned}
 f_1 &= \delta(t_3) \cos \theta, \\
 \varphi_1 &= -R \frac{d\delta(t_3)}{dt_3} \cos \theta, \\
 \gamma_r &= \left(\frac{\delta(t_3)}{R} - \frac{d^2\delta(t_3)}{dt_3^2} R \right) \cos \theta, \\
 \gamma_\theta &= \frac{\delta(t_3)}{R} \sin \theta, \quad \gamma_z = -\frac{d\delta(t_3)}{dt_3} \cos \theta,
 \end{aligned} \quad (13)$$

$$\delta(t_3) = \exp\left(\frac{-x_3}{L}\right)^2 \cos\left(m \frac{-x_3}{L}\right)$$

Similar contact conditions can be given for subsequent approximation.

By using the method in [1] we can define governing equations for the second

approximation as follows. We use the physical components of the tensors and vectors in this equation.

$$\begin{aligned}
 \frac{\partial \sigma_{rr}^{(k),2}}{\partial r} + \frac{1}{r} \frac{\partial \sigma_{r\theta}^{(k),2}}{\partial \theta} + \frac{\partial \sigma_{rz}^{(k),2}}{\partial z} + \frac{1}{r} (\sigma_{rr}^{(k),2} - \sigma_{\theta\theta}^{(k),2}) + \sigma_{zz}^{(k),0} \frac{\partial^2 u_r^{(k),2}}{\partial z^2} &= 0, \\
 \frac{\partial \sigma_{r\theta}^{(k),2}}{\partial r} + \frac{1}{r} \frac{\partial \sigma_{\theta\theta}^{(k),2}}{\partial \theta} + \frac{\partial \sigma_{\theta z}^{(k),2}}{\partial z} + \frac{2}{r} \sigma_{r\theta}^{(k),2} + \sigma_{zz}^{(k),0} \frac{\partial^2 u_\theta^{(k),2}}{\partial z^2} &= 0 \quad (14) \\
 \frac{\partial \sigma_{rz}^{(k),2}}{\partial r} + \frac{1}{r} \frac{\partial \sigma_{\theta z}^{(k),2}}{\partial \theta} + \frac{\partial \sigma_{zz}^{(k),2}}{\partial z} + \frac{1}{r} \sigma_{rz}^{(k),2} + \sigma_{zz}^{(k),0} \frac{\partial^2 u_z^{(k),2}}{\partial z^2} &= 0,
 \end{aligned}$$

These equations coincide with the 3-dimensional linearized elasticity equations.

If we apply the following exponential Fourier transform with respect to z to the contact conditions in Eq. (12) and if we substitute the expressions for the first approximation in eq. (12), we obtain the Fourier transformed states of the contact conditions that include single or double integral on the right side.

$$\bar{\sigma}_{rr} = \int_{-\infty}^{+\infty} \sigma_{rr} e^{-isz} ds \quad (15)$$

To solve the contact conditions in equation (12), we apply the above Fourier transformation to the following equations (16) and (17).

$$\begin{aligned}
 u_r^{(m),n} &= \frac{1}{r} \frac{\partial}{\partial \theta} \psi^{(m),n} - \frac{\partial^2}{\partial r \partial z} \chi^{(m),n}; \\
 u_\theta^{(m),n} &= -\frac{\partial}{\partial r} \psi^{(m),n} - \frac{1}{r} \frac{\partial^2}{\partial \theta \partial z} \chi^{(m),n}; \\
 \Delta_1^{(m)} &= \frac{\partial^2}{\partial r^2} + \frac{1}{r} \frac{\partial}{\partial r} + \frac{1}{r^2} \frac{\partial^2}{\partial \theta^2}
 \end{aligned} \quad (16)$$

$$u_z^{(m),n} = (\lambda^{(m)} + \mu^{(m)})^{-1} \left((\lambda^{(m)} + 2\mu^{(m)}) \Delta_1^{(m)} + (\mu^{(m)} + \sigma_{zz}^{(m),0}) \frac{\partial^2}{\partial z^2} \right) \chi^{(m),n}$$

The functions of $\psi^{(m),q}$, $\chi^{(m),q}$ satisfy the following equations:

$$\begin{aligned}
 \left(\Delta_1^{(m)} + (\xi_1^{(m)})^2 \frac{\partial^2}{\partial z^2} \right) \psi^{(m),q} &= 0; \\
 \left(\Delta_1^{(m)} + (\xi_2^{(m)})^2 \frac{\partial^2}{\partial z^2} \right) \left(\Delta_1^{(m)} + (\xi_3^{(m)})^2 \frac{\partial^2}{\partial z^2} \right) \chi^{(m),q} &= 0
 \end{aligned} \quad (17)$$

Where, $\xi_i^{(m)}$ (m=1,2; i=1,2,3) are given in the following equations:

$$\zeta_1^{(m)} = \sqrt{\frac{\mu^{(m)} + \sigma_{zz}^{(m),0}}{\mu^{(m)}}},$$

$$\zeta_2^{(m)} = \sqrt{\frac{\mu^{(m)} + \sigma_{zz}^{(m),0}}{\mu^{(m)}}},$$

$$\zeta_3^{(m)} = \sqrt{\frac{\lambda^{(m)} + 2\mu^{(m)} + \sigma_{zz}^{(m),0}}{\lambda^{(m)} + 2\mu^{(m)}}}$$

After this employing, we obtain the following equations

$$\psi^{-(1),1} = \bar{A}_1^{(1)}(s)K_1(\xi_1^{(1)}s\frac{r}{L})\sin\theta,$$

$$\chi^{-(1),1} = i \left[\begin{array}{l} \bar{A}_2^{(1)}(s)K_1(\xi_2^{(1)}s\frac{r}{L}) + \\ \bar{A}_3^{(1)}(s)K_1(\xi_3^{(1)}s\frac{r}{L}) \end{array} \right] \cos\theta \quad (18)$$

$$\psi^{-(2),1} = \left[\bar{A}_{11}^{(2)}(s)I_1(\xi_1^{(2)}s\frac{r}{L}) + \bar{A}_{12}^{(2)}(s)K_1(\xi_1^{(2)}s\frac{r}{L}) \right] \sin\theta,$$

$$\chi^{-(2),1} = i \left[\begin{array}{l} \bar{A}_{21}^{(2)}(s)I_1(\xi_2^{(2)}s\frac{r}{L}) + \bar{A}_{22}^{(2)}(s)K_1(\xi_2^{(2)}s\frac{r}{L}) + \\ \bar{A}_{31}^{(2)}(s)I_1(\xi_3^{(2)}s\frac{r}{L}) + \bar{A}_{32}^{(2)}(s)K_1(\xi_3^{(2)}s\frac{r}{L}) \end{array} \right] \cos\theta$$

$$\psi^{-(1),2} = \bar{A}_{12}^{(1)}(s_1)K_2(\xi_1^{(1)}s_1\frac{r}{L})\sin 2\theta,$$

$$\chi^{-(1),2} = i \left[\bar{A}_{20}^{(1)}(s_1)K_0(\xi_2^{(1)}s_1\frac{r}{L}) + \bar{A}_{30}^{(1)}(s_1)K_0(\xi_3^{(1)}s_1\frac{r}{L}) + \right. \\ \left. \bar{A}_{22}^{(1)}(s_1)K_2(\xi_2^{(1)}s_1\frac{r}{L}) + \bar{A}_{32}^{(1)}(s_1)K_2(\xi_3^{(1)}s_1\frac{r}{L}) \right] \cos 2\theta$$

$$\psi^{-(2),2} = \left[\begin{array}{l} \bar{A}_{12}^{(2)}(s_1)I_2(\xi_1^{(2)}s_1\frac{r}{L}) + \\ \bar{B}_{12}^{(2)}(s_1)K_2(\xi_1^{(2)}s_1\frac{r}{L}) \end{array} \right] \sin 2\theta$$

$$\chi^{-(2),2} = i \left\{ \bar{A}_{20}^{(2)}(s_1)I_0(\xi_2^{(2)}s_1\frac{r}{L}) + \bar{B}_{20}^{(2)}(s_1)K_0(\xi_2^{(2)}s_1\frac{r}{L}) + \right. \\ \left. \bar{A}_{30}^{(2)}(s_1)I_1(\xi_3^{(2)}s_1\frac{r}{L}) + \bar{B}_{30}^{(2)}(s_1)K_1(\xi_3^{(2)}s_1\frac{r}{L}) + \right. \\ \left. \left[\bar{A}_{22}^{(2)}(s_1)I_2(\xi_2^{(2)}s_1\frac{r}{L}) + \bar{B}_{22}^{(2)}(s_1)K_2(\xi_2^{(2)}s_1\frac{r}{L}) + \right. \right. \\ \left. \left. \bar{A}_{32}^{(2)}(s_1)I_2(\xi_3^{(2)}s_1\frac{r}{L}) + \bar{B}_{32}^{(2)}(s_1)K_2(\xi_3^{(2)}s_1\frac{r}{L}) \right] \cos 2\theta \right\}$$

where $I_n(x)$ are Bessel functions of a purely imaginary argument and $K_n(x)$ are the Macdonald functions. Moreover, we used the Fourier transform parameters s and s_1 in (18) and (19) respectively. Employing the

Functions (18) and (19) in boundary-value problems of the related approximations, we obtain the systems of the linear equations. If we solve this systems of the linear equations, substituting the solution of the this equation systems into the quantities of the stresses, we determine the expressions of $\bar{\sigma}_{rr}^{(1),1}, \dots, \bar{\sigma}_{zz}^{(2),1}$. If we apply the following inverse transform for the stresses, we find the real stress values.

$$\sigma_{rr}^{(1),1} = \frac{1}{2\pi} \int_{-\infty}^{+\infty} \bar{\sigma}_{rr}^{(1),1} e^{isz} ds \quad (20)$$

Thus, the boundary value problem related to the second approximation was solved

4. NUMERICAL RESULT AND DISCUSSION

In the numerical investigation, the improved integral (20) are calculated by using the Gauss integration algorithm. In order to calculate this improper integrals, we replaced this improper integrals by the corresponding definite integrals. Hereafter, we divide the interval of these improper integrals into certain number of short intervals.

To determine the number of these intervals, we use the numerical convergence of the integral values i.e. we use the relation

$$\int_0^{+\infty} (.)ds \cong \int_0^{S^*} (.)ds = \sum_{i=0}^N \int_{S_i}^{S_{i+1}} (.)ds, \quad S_0 = 0.$$

This process resulted in calculation of triple integral. In these calculating, we used the approximation

$$\int_0^{\infty} \int_0^{\infty} \int_0^{\infty} (.)dsdzds_1 \cong \int_0^{S_*^{(1)}} \int_0^{Z_*} \int_0^{S_*^{(2)}} (.)dsdzds_1 \quad (21)$$

$$(19) \sum_{i=0}^{N_1} \sum_{j=0}^{N_2} \sum_{k=0}^{N_3} \int_{S_i^{(1)}}^{S_{i+1}^{(1)}} \int_{Z_j}^{Z_{j+1}^*} \int_{S_k^{(2)}}^{S_{k+1}^{(2)}} (.)dsdzds_1$$

Where $S_0^{(1)} = S_0 = S_0^{(2)} = 0$ and the values of N_1, N_2, N_3 and $S_*^{(1)}, Z_*, S_*^{(2)}$ were determined from convergence criterion. In addition, $S_{N_1}^{(1)} = S_*^{(1)}, Z_{N_2} = Z_*, S_{N_3}^{(2)} = S_*^{(2)}$.

$$\int_{S_i^{(1)}}^{S_{i+1}^{(1)}} \int_{Z_j}^{Z_{j+1}^*} \int_{S_k^{(2)}}^{S_{k+1}^{(2)}} (.)dsdzds_1$$

$$\int_{S_i^{(1)}}^{S_{i+1}^{(1)}} \int_0^{Z_{j+1}^*} \int_{S_k^{(2)}}^{S_{k+1}^{(2)}} (.)dsdzds_1$$

We used the Gauss integration algorithm for the calculation of triple integrals. To perform all

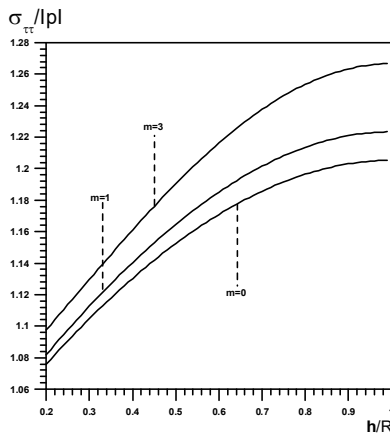
these operations, we wrote a computer program in Fortran 77 .

The numerical results related to the normal stress are analyzed on the intersection surfaces between the CNT and matrix . Due to symmetry, we are only examine the distribution of these stresses for $x_3 \geq 0$ (and) $0 \leq \theta \leq \pi$ (Figure 1). If $\varepsilon = 0$ (i.e. if the curving is absent), the stresses $\sigma_{\tau\tau}$ coincide with σ_{zz} .

We assume that α used in all figures and table is smaller than its critical values corresponding to microbuckling of the fiber in the matrix in [5]. It is assumed that $v^{(1)} = v^{(2)} = 0.3$, $\varepsilon = 0.07$, $\theta = 0$ and $\kappa = R_2/L$, $bk = h/R$. $\alpha = p/E^{(1)}$ shows the effect of geometrical non-linearity on the normal stresses values .

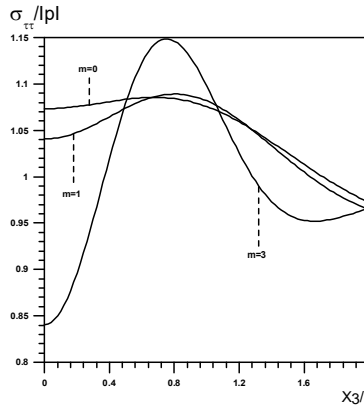
The relationship between $\sigma_{\tau\tau}/|p|$ and h/R is showed in Figure 2 . In this graph, $m=0, 1, 3$ at $\chi_3/L = 1.0$, $\kappa = 0.3$, $\alpha = 0.00005$ and $E^{(2)}/E^{(1)}=500$.

The same figure shows also the effect of the parameter m on the normal stresses values. From the graphs, it is seen that the maximal values of normal stresses increase monotonically with m . The results obtained when we increase the carbon nanotube thickness are the same in the case of the single local curved nanofiber in the infinite body at the same parameter values.



4*Figure 2: The relationship between the $\sigma_{\tau\tau}/p$ and h/R for $E^{(2)}/E^{(1)}=500$, $\varepsilon = 0.07$, $\kappa = 0.25$, $m = 0, m = 1$ and $m = 3$

Figure 3 shows the relationships between $\sigma_{\tau\tau}/|p|$ and x_3/L for $h/R=0.5$, $\kappa = 0.3$ and $E^{(2)}/E^{(1)}=400$. Likewise, the effect of the parameter m on the distribution of normal stresses can be seen. From Figure 3, we can say that absolute maximal values of normal stresses are monotonically increasing with m .



5*Figure 3: The relationship between the $\sigma_{\tau\tau}/p$ and x_3/L for $E^{(2)}/E^{(1)}=400$, $\varepsilon = 0.07$, $\kappa = 0.25$, $m = 0, m = 1$ and $m = 3$

Table 1 shows the effect of various values of $E^{(2)}/E^{(1)}$, m and α on $\sigma_{\tau\tau}/|p|$ normal stress values.

In this table, $\sigma_{\tau\tau}/|p|$ normal stress values are calculated for $m = 0, 1$ and 3 respectively. In this case the values of $\sigma_{\tau\tau}/|p|$ are calculated under $\kappa = 0.3$, $\chi_3/L = 1.0$ for $m = 0, 1$ and 3 respectively. From this table it is seen that the absolute maximal values of $\sigma_{\tau\tau}/|p|$ normal stresses increase monotonically with m .

Table 1: The values of σ_{rr}/p obtained for various α and $E^{(2)}/E^{(1)}$

m	$\frac{E^{(2)}}{E^{(1)}}$	A · N	$\alpha = \frac{p}{E^{(1)}}$							
			Tension				compression			
			0.0005	0.005	0.05	0.03	-0.0005	-0.005	-0.01	-0.015
0	300	1	1.0551	1.0559	1.0554	1.0566	-1.0550	-1.0537	-1.0517	-1.0488
		2	1.2328	1.2337	1.2308	1.0671	-1.2328	-1.2312	-1.0654	-1.0632
	500	1	1.0312	1.0359	1.0488	1.0466	-1.0311	-1.0248	-1.0160	-1.0035
		2	1.2309	1.0236	1.2486	1.0573	-1.2308	-1.2234	-1.0310	-1.0195
	1000	1	0.9897	1.0029	1.0403	1.0327	-0.9894	-0.9706	-0.9422	-0.8966
		2	1.2198	1.2348	1.2742	1.0438	-1.2195	-1.1980	-0.9589	-0.9149
1	300	1	1.1593	1.1571	1.1380	1.1460	-1.1593	-1.1613	-1.1631	-1.1644
		2	1.2996	1.2967	1.2715	1.1555	-1.2997	-1.3025	-1.1758	-1.1778
	500	1	1.1419	1.1428	1.1340	1.1394	-1.1419	-1.1399	-1.1361	-1.1295
		2	1.3017	1.3019	1.2871	1.1493	-1.3016	-1.3002	-1.1501	-1.1445
	1000	1	1.1093	1.1172	1.1281	1.1293	-1.1091	-1.0968	-1.0767	-1.0424
		2	1.2955	1.3031	1.3084	1.1395	-1.2953	-1.2829	-1.0923	-1.0595
3	300	1	1.4986	1.4866	1.4070	1.4370	-1.4989	-1.5118	-1.5260	-1.5413
		2	1.4940	1.4822	1.4044	1.4487	-1.4942	-1.5069	-1.5376	-1.5528
	500	1	1.5052	1.4932	1.4120	1.4428	-1.5055	-1.5836	-1.5320	-1.5465
		2	1.5042	1.4924	1.4126	1.4544	-1.5044	-1.5171	-1.5433	-1.5565
	1000	1	1.5064	1.4954	1.4154	1.4468	-1.5066	-1.5177	-1.5282	-1.5374
		2	1.5104	1.4995	1.4204	1.4578	-1.5106	-1.5216	-1.5392	-1.5477

In this work, a method was developed to study the normal stress distribution in an infinite elastic body with a locally curved carbon nanotube. In order to examine the normal stress distribution, the mathematical formulation of the relevant boundary value problem is given.

In this case, we assume that the concentration of an infinite elastic body containing a single locally curved carbon nanotube is low. We neglect the interaction between the carbon 6*nanotubes. For the investigation, we used the three-dimensional geometrically nonlinear exact equations of the theory of elasticity in the piecewise homogeneous model. We have developed a method that obtains normal stress values as much as up to the second approximation on the interface the carbon nanotube and matrix material. The numerical results were presented for a single locally curved and carbon nanotube. As a result of this research, the following were obtained :

- (i) When the radius of hollow approach to 0 as a limit , The normal stresses values in the carbon nanotube are the same as to the locally curved nanofiber in an

nanocomposite material in same parameter values.

- (ii) The absolute maximal values of the normal stresses $\sigma_{rr}/|p|$ increase monotonically with m.

The numerical results obtained agree with well-known mechanical consideration and, in some particular cases, coincide with known results.

Acknowledgements

The author acknowledges that the statements of some results in this paper were presented at the 2nd International Conference of Mathematical Sciences, ICMS 2018, Maltepe University, Istanbul, Turkey, and will be appeared in the American Institute of Physics Conference Proceedings of the 2nd International Conference of Mathematical Sciences, ICMS 2018, Maltepe University, Istanbul, Turkey ([11]).

REFERENCES

[1] S.D. Akbarov, A.N. Guz, "Mechanics of Curved Composites", *Kluwer Academic Publishers*, Dordrecht, The Netherlands, pp: 464, 2000.

- [2] S.D. Akbarov, A.N. Guz, "Method of Solving Problems in the Mechanics of Fiber Composites With Curved Structures", *Soviet Applied Mechanics*, pp. 777-785, 1985.
- [3] K.S. Alan, S.D. Akbarov, "Stress Analyses in an Infinite Elastic Body with a Locally Curved Covered Nanofiber" *Mechanics of Composite Materials*. Vol.47 no. 3, pp. 343–358. 2011.
- [4] K.S. Alan, "Normal Stresses in an Infinite Elastic Body with a Locally Curved and Hollow Nanofiber" *CMC-Computers Materials & Continua*, vol. 44, no.1, pp.1-21, 2014.
- [5] A.N. Guz, "Failure mechanics of composite materials in compression" – Kiev: Naukova Dumka, Russia ,–630 p. 1990.
- [6] A.N. Guz , "On one two-level model in the mesomechanics of compression fracture of Cracked Composites", *Int. Appl. Mech.* Vol.39 no.3, pp.274-285, 2003.
- [7] A.N. Guz, "Fundamentals of the Three-Dimensional Theory of Stability of Deformable Bodies", Springer. Newyork, NY. 1999.
- [8] F. Coban, R. Kosker, "On The Stress Distribution In An Elastic Body With A Locally Curved Carbon Nanotube", *3rd International Symposium On Innovative Technologies In Engineering And Science, Valencia, SPAIN*, pp.2299-2307, 2015.
- [9] A. Kelly , "Composite Materials: impediments do wider use and some suggestions to overcome these", *In Proceeding Book (ECCM-8)*, Napoles-Italy, Vol.I, pp.15-18, (3-6 June) 1998.
- [10] Yu.M. Tarnopolsky, I.G. Jigun, V.A. Polyakov, "Spatially-reinforced composite materials", *Handbook*, Mashinostroyenia, Moscow, Russia . 1987.
- [11] K.S. Alan, "Investigation of the Normal Stress In An Infinite Elastic Body With A Locally Curved Carbon Nanotube", *2nd International Conference of Mathematical Sciences (ICMS 2018)*, 31 July-6 August 2018, Istanbul, Turkey.

	SAKARYA UNIVERSITY JOURNAL OF SCIENCE		 SAKARYA UNIVERSITY
	e-ISSN: 2147-835X http://www.saujs.sakarya.edu.tr		
	<u>Received</u> 07-08-2018 <u>Accepted</u> 30-10-2018	<u>Doi</u> 10.16984/saufenbilder.451646	

Timelike Factorable Surfaces in Minkowski Space-Time

Sezgin Büyükkütük*

ABSTRACT

In this study, we discuss timelike factorable surfaces in Minkowski 4 – space IE_1^4 . We calculate Gaussian and mean curvatures of these surfaces and classify timelike flat and minimal factorable surfaces in Minkowski space-time.

Keywords: factorable surface, timelike surface, Minkowski 4 – space

1. INTRODUCTION

The Minkowski space defined by Lorentzian inner product is the mathematical structure in which Einstein's special relativity theory is the most appropriately represented. Since the inner product is not always positively defined, curves and surfaces vary in this space. Spacelike vectors, curves and surfaces show similarity to the Euclidean space structure.

In n – dimensional semi-Euclidean space, the Lorentzian inner product with t – index is defined by

$$g(X, Y) = -\sum_{i=1}^t x_i y_i + \sum_{j=t+1}^n x_j y_j \quad (1)$$

where $X = (x_1, \dots, x_n)$ and $Y = (y_1, \dots, y_n)$ [1]. The semi-Euclidean space defined by this metric is denoted by IE_t^n . Especially, for 4 – dimensional case with index $t = 1$, the semi-Euclidean space IE_1^4 is called Minkowski space-time. In this case, the Lorentzian metric (1) is expressed in the form of

$$g(X, Y) = -x_1 y_1 + x_2 y_2 + x_3 y_3 + x_4 y_4. \quad (2)$$

Any arbitrary vector $X = (x_1, \dots, x_4)$ is called timelike, null or spacelike if the Lorentzian inner product g is negative definite, zero or positive definite, respectively. Then, the length of the vector $X \in IE_1^4$ is calculated by

$$\|X\| = \sqrt{|g(X, X)|} \quad (3)$$

where $X = (x_1, \dots, x_4) \in IE_1^4$.

Let S be a surface in four-dimensional Minkowski space IE_1^4 . Then, the surface is called timelike if the induced metric g on S is a metric with index 1. Minkowski 4 – space can be written by the direct sum of the tangent space and the normal space of S at each point p :

$$IE_1^4 = T_p S \oplus T_p^\perp S \quad (4)$$

Represented by $\tilde{\nabla}$ and ∇ is the Levi-Civita connections on IE_1^4 and S , respectively. Let X_1 and X_2 indicate the tangent vector fields and let ξ indicates the normal vector field on S . Then, Gauss and Weingarten formulas are given by the followings:

$$\begin{aligned} \tilde{\nabla}_{X_1} X_2 &= \nabla_{X_1} X_2 + h(X_1, X_2), \\ \tilde{\nabla}_{X_1} \xi &= -A_\xi X_1 + D_{X_1} \xi, \end{aligned} \quad (5)$$

where h , D and A_ξ are the second fundamental tensor, the normal connection and the shape operator with regard to ξ , respectively [2].

Let S be a timelike surface in IE_1^4 given by the parameterization $F(u, v)$, $(u, v) \in U$ ($U \in IE^2$) and

* Corresponding Author: Department of Mathematics, Kocaeli University, Kocaeli, Turkey, sezginbuyukkutuk@gmail.com

$T_p S = \text{span}\{F_u, F_v\}$ is the tangent space at any point $p = F(u, v)$. In the chart (u, v) the coefficients of the first fundamental form of S are given by

$$E = g(F_u, F_u), \quad F = g(F_u, F_v), \quad G = g(F_v, F_v). \quad (6)$$

We suppose that $g(F_u, F_u) < 0$, $g(F_v, F_v) > 0$. Thus,

$$E < 0, \quad F > 0 \quad \text{and for the later use we set } W = \sqrt{F^2 - EG}$$

. We choose an orthonormal frame field $\{\xi_1, \xi_2\}$ of the normal bundle, i.e., $g(\xi_1, \xi_1) = 1$, $g(\xi_2, \xi_2) = 1$.

Therefore, we give the following derivative formulas:

$$\begin{aligned} \tilde{\nabla}_{F_u} F_u &= F_{uu} = -\Gamma_{11}^1 F_u + \Gamma_{11}^2 F_v + c_{11}^1 \xi_1 + c_{11}^2 \xi_2, \\ \tilde{\nabla}_{F_u} F_v &= F_{uv} = -\Gamma_{12}^1 F_u + \Gamma_{12}^2 F_v + c_{12}^1 \xi_1 + c_{12}^2 \xi_2, \\ \tilde{\nabla}_{F_v} F_v &= F_{vv} = -\Gamma_{22}^1 F_u + \Gamma_{22}^2 F_v + c_{22}^1 \xi_1 + c_{22}^2 \xi_2, \end{aligned} \quad (7)$$

where Γ_{ij}^k are the Christoffel's symbols and the functions c_{ij}^k , $i, j, k = 1, 2$ are given by

$$\begin{aligned} c_{11}^1 &= g(F_{uu}, \xi_1), & c_{11}^2 &= g(F_{uu}, \xi_2), \\ c_{12}^1 &= g(F_{uv}, \xi_1), & c_{12}^2 &= g(F_{uv}, \xi_2), \\ c_{22}^1 &= g(F_{vv}, \xi_1), & c_{22}^2 &= g(F_{vv}, \xi_2). \end{aligned} \quad (8)$$

The second fundamental form of the timelike surface $S : F(u, v)$ is expressed as follows:

$$\begin{aligned} h(F_u, F_u) &= c_{11}^1 \xi_1 + c_{11}^2 \xi_2, \\ h(F_u, F_v) &= c_{12}^1 \xi_1 + c_{12}^2 \xi_2, \\ h(F_v, F_v) &= c_{22}^1 \xi_1 + c_{22}^2 \xi_2, \end{aligned} \quad (9)$$

where F_u and F_v are tangent vectors.

By the use of Gram-Schmidt orthonormalization method, we can obtain the orthonormal tangent vectors as:

$$\begin{aligned} X_1 &= \frac{F_u}{\sqrt{|E|}}, \\ X_2 &= \frac{\sqrt{|E|}}{W} \left(F_v - \frac{F}{E} F_u \right). \end{aligned} \quad (10)$$

Hence, with the help of the orthonormal tangent vectors, the second fundamental form can be written as

$$\begin{aligned} h(X_1, X_1) &= h_{11}^1 \xi_1 + h_{11}^2 \xi_2, \\ h(X_1, X_2) &= h_{12}^1 \xi_1 + h_{12}^2 \xi_2, \\ h(X_2, X_2) &= h_{22}^1 \xi_1 + h_{22}^2 \xi_2 \end{aligned} \quad (11)$$

where the functions h_{ij}^k , $i, j, k = 1, 2$ are given by

$$\begin{aligned} h_{11}^k &= -\frac{c_{11}^k}{E}, \\ h_{12}^k &= \frac{E c_{12}^k - F c_{11}^k}{EW}, \\ h_{22}^k &= -\frac{E^2 c_{22}^k - 2E F c_{12}^k + F^2 c_{11}^k}{EW^2}. \end{aligned} \quad (12)$$

These coefficients are entries of shape operator matrices. Gaussian curvature of a timelike surface $S : F(u, v)$ by using the second fundamental form coefficients is defined by

$$K = \sum_{k=1}^2 h_{11}^k h_{22}^k - (h_{12}^k)^2, \quad (13)$$

(see, [3]).

The mean curvature vector field can be calculated by

$$\begin{aligned} H &= \frac{1}{2} \text{tr} h. \quad \text{Therefore, if } S \text{ is a timelike surface, then} \\ \text{the mean curvature vector field is} \\ H &= \frac{1}{2} (-h(X_1, X_1) + h(X_2, X_2)), \end{aligned} \quad (14)$$

where $\{X_1, X_2\}$ is a local orthonormal frame of the tangent bundle such that $g(X_1, X_1) = -1$, $g(X_2, X_2) = 1$ [2].

Any surface is said to be flat (minimal), if its Gaussian curvature (mean curvature vector) vanishes [4].

Factorable surfaces (also known homothetical surfaces) in IE^3 can be parameterized, locally, as $F(u, v) = (u, v, f(u)g(v))$, where f and g are smooth functions [5, 6]. Some authors have considered factorable surfaces in Euclidean space and in semi-Euclidean spaces [6, 7, 8, 9, 10, 11, 12]. In [5], Van de Woestyne proved that the only minimal factorable non-degenerate surfaces in L^3 are planes and helicoids.

In [13, 14], the authors gave the surface parametrization as

$$F(u, v) = (u, v, z(u, v), w(u, v)) \quad (15)$$

and called it Monge patch in IE^4 . Furthermore, in [14], the authors characterized this surface and gave some examples. Also, some surfaces and curves in four dimensional spaces can be found in [15, 16, 17, 18, 19, 20, 21, 22, 23, 24, 25, 26, 27, 28].

In the present study, we consider timelike factorable surfaces in Minkowski 4-space. We characterize

such surfaces in terms of their Gaussian curvature and mean curvatures and give the conditions for such surfaces to become flat and minimal.

2. TIMELIKE FACTORABLE SURFACES IN \mathbb{IE}_1^4

Definition 1: Let $S \subset \mathbb{IE}_1^4$ be a surface in 4-dimensional Minkowski space. If in (15), we take

$$z = f_1(u)g_1(v), \quad w = f_2(u)g_2(v),$$

where f_1, f_2, g_1, g_2 are differentiable functions in \mathbb{IE}_1^4 , then we can define a surface parameterization (Monge patch) which is called factorable surface in Minkowski 4-space.

Therefore, the parameterization of the factorable surface can be written as

$$F(u, v) = (u, v, f_1(u)g_1(v), f_2(u)g_2(v)). \quad (16)$$

Let S be a timelike factorable surface given by the parameterization (16) in \mathbb{IE}_1^4 . Then, the tangent space of the surface is spanned by the vector fields

$$\begin{aligned} F_u &= \frac{\partial F(u, v)}{\partial u} = (1, 0, f_1'(u)g_1(v), f_2'(u)g_2(v)), \\ F_v &= \frac{\partial F(u, v)}{\partial v} = (0, 1, f_1(u)g_1'(v), f_2(u)g_2'(v)). \end{aligned} \quad (17)$$

The first fundamental form coefficients are obtained as

$$\begin{aligned} E &= g(F_u, F_u) = -1 + (f_1'g_1)^2 + (f_2'g_2)^2, \\ F &= g(F_u, F_v) = f_1'f_1g_1'g_1 + f_2'f_2g_2'g_2, \end{aligned} \quad (18)$$

$$G = g(F_v, F_v) = 1 + (f_1g_1')^2 + (f_2g_2')^2.$$

Here, we suppose $E < 0$, namely the surface S is timelike, and so $EG - F^2 < 0$.

The second derivatives of $F(u, v)$ are

$$\begin{aligned} F_{uu} &= (0, 0, f_1''(u)g_1(v), f_2''(u)g_2(v)), \\ F_{uv} &= (0, 0, f_1'(u)g_1'(v), f_2'(u)g_2'(v)), \\ F_{vv} &= (0, 0, f_1(u)g_1''(v), f_2(u)g_2''(v)). \end{aligned} \quad (19)$$

Normal space of the timelike surface S is spanned by the orthonormal vector fields

$$\begin{aligned} \xi_1 &= \frac{1}{\sqrt{A}} (f_1'g_1, -f_1g_1', 1, 0), \\ \xi_2 &= \frac{1}{\sqrt{AD}} \begin{pmatrix} Af_2'g_2 - Bf_1'g_1, \\ Bf_1g_1' - Af_2g_2', -B, A \end{pmatrix}, \end{aligned} \quad (20)$$

where

$$\begin{aligned} A &= 1 - (f_1'g_1)^2 + (f_1g_1')^2, \\ B &= -f_1'f_2'g_1g_2 + f_1f_2g_1'g_2', \\ C &= 1 - (f_2'g_2)^2 + (f_2g_2')^2, \\ D &= AC - B^2. \end{aligned} \quad (21)$$

Since S is timelike surface in \mathbb{IE}_1^4 with respect to chosen orthonormal frame, A and D are positive definite. By the use of the equations (8), (19), and (20), we calculate the second fundamental form coefficients

$$\begin{aligned} c_{11}^1 &= \frac{f_1''g_1}{\sqrt{A}}, \quad c_{22}^1 = \frac{f_1g_1''}{\sqrt{A}}, \\ c_{12}^1 &= \frac{f_1'g_1'}{\sqrt{A}}, \quad c_{12}^2 = \frac{Af_2'g_2' - Bf_1'g_1'}{\sqrt{AD}}, \\ c_{11}^2 &= \frac{Af_2''g_2 - Bf_1''g_1}{\sqrt{AD}}, \\ c_{22}^2 &= \frac{Af_2g_2'' - Bf_1g_1''}{\sqrt{AD}}. \end{aligned} \quad (22)$$

With the help of (12) and (22), the shape operator matrices are

$$\begin{bmatrix} h_{11}^1 & h_{12}^1 \\ h_{12}^1 & h_{22}^1 \end{bmatrix}, \quad \begin{bmatrix} h_{11}^2 & h_{12}^2 \\ h_{12}^2 & h_{22}^2 \end{bmatrix},$$

where the functions h_{ij}^k are given by

$$\begin{aligned} h_{11}^1 &= \frac{-f_1''g_1}{E\sqrt{A}}, \quad h_{12}^1 = \frac{f_1'g_1'E - f_1''g_1F}{EW\sqrt{A}}, \\ h_{22}^1 &= -\frac{f_1g_1''E^2 - 2f_1'g_1'EF + f_1''g_1F^2}{EW^2\sqrt{A}}, \\ h_{11}^2 &= -\frac{Af_2''g_2 - Bf_1''g_1}{E\sqrt{AD}}, \end{aligned} \quad (23)$$

$$h_{12}^2 = \frac{\left(f_2' g_2' A - f_1' g_1' B \right) E - \left(f_2'' g_2 A - f_1'' g_1 B \right) F}{EW \sqrt{AD}},$$

$$h_{22}^2 = - \frac{\left(\begin{array}{l} \left(f_2 g_2'' A - f_1 g_1'' B \right) E^2 \\ - 2 \left(f_2' g_2' A - f_1' g_1' B \right) EF \\ + \left(f_2'' g_2 A - f_1'' g_1 B \right) F^2 \end{array} \right)}{EW^2 \sqrt{AD}}.$$

2.1. Timelike flat factorable surfaces

Theorem 1. Let S be a timelike factorable surface with the parametrization (16) in IE_1^4 . Then, its Gaussian curvature is given by

$$K = \frac{\left(\begin{array}{l} \left(f_1'' f_1 g_1'' g_1 - f_1'^2 g_1'^2 \right) C \\ - \left(\begin{array}{l} f_1'' f_2 g_1 g_2'' \\ + f_1 f_2'' g_1'' g_2 - 2 f_1' f_2' g_1' g_2' \end{array} \right) B \\ + \left(f_2'' f_2 g_2'' g_2 - f_2'^2 g_2'^2 \right) A \end{array} \right)}{DW^2}. \quad (24)$$

Proof. By the use of the equations (13) and (23), we obtain the desired result.

Theorem 2. Let S be a timelike factorable surface with the parameterization (16) in IE_1^4 . If S is given by one of the following parameterizations, then it is a flat surface:

- (1) $F(u, v) = (u, v, a_1 g_1(v), a_2 g_2(v)),$
- (2) $F(u, v) = (u, v, b_1 f_1(u), b_2 f_2(u)),$
- (3) $F(u, v) = (u, v, a_1 g_1(v), a_2 f_2(u)),$
- (4) $F(u, v) = (u, v, b_1 f_1(u), b_2 g_2(v)),$
- (5) $F(u, v) = \left(u, v, a_1 b_1, \exp(a_2 u + b_2) \exp(a_3 v + b_3) \right),$
- (6) $F(u, v) = \left(u, v, a_1 b_1, (a_2 u + b_2)^{\frac{1}{1-\lambda}} (a_3 v + b_3)^{\frac{\lambda}{\lambda-1}} \right),$

$$(7) F(u, v) = \left(u, v, \exp(a_1 u + b_1) \exp(a_2 v + b_2), \exp(a_3 u + b_3) \exp(a_3 \frac{a_1}{a_j} v + b_4) \right),$$

$$(8) F(u, v) = (u, v, f_1(u) \cos v, f_1(u) \sin v),$$

the function $f_1(u)$ satisfies

$$u = \pm \int \sqrt{\frac{a_1 f_1^2(u) + 1}{f_1^2(u) + 1}} df_1(u)$$

where $i, j = 1, 2, i \neq j$ and $a_k, b_k, k = 1, \dots, 4$ are real constants.

Proof. Let S be a timelike factorable surface given with the parameterization (16) in IE_1^4 . If $f_1'(u) = 0, f_2'(u) = 0$ or $g_1'(v) = 0, g_2'(v) = 0$ or $f_1'(u) = 0, g_2'(v) = 0$ ($f_2'(u) = 0, g_1'(v) = 0$),

then we obtain the cases (1), (2), (3) and (4).

If $f_1'(u) = 0, g_1'(v) = 0$, then we have

$$f_2'' f_2 g_2'' g_2 - f_2'^2 g_2'^2 = 0. \quad (25)$$

Let $p(u) = \frac{df_2}{du}$ and $q(v) = \frac{dg_2}{dv}$. By the use of (25), we can write

$$f_2(u) p(u) \frac{dp}{df_2} g_2(v) q(v) \frac{dq}{dg_2} - (p(u) q(v))^2 = 0, \quad (26)$$

If $p(u) \neq 0, q(v) \neq 0$, from (26), we get

$$f_2(u) \frac{dp}{df_2} g_2(v) \frac{dq}{dg_2} = p(u) q(v).$$

Then we have differential equation

$$\frac{f_2(u) \frac{dp}{df_2}}{p(u)} = \frac{q(v)}{g_2(v) \frac{dq}{dg_2}} = \lambda, \quad (27)$$

where λ is constant.

(1) If $\lambda = 1$, from (27) we have

$$\begin{aligned} f_2(u) &= \exp(a_2 u + b_2), \\ g_2(v) &= \exp(a_3 v + b_3), \end{aligned} \quad (28)$$

which gives the case (5).

(2) If $\lambda \neq 1$, from (27) we have

$$f_2(u) = (a_2 u + b_2)^{\frac{1}{1-\lambda}}, \quad (29)$$

$$g_2(v) = (a_3 v + b_3)^{\frac{\lambda}{\lambda-1}},$$

which gives the case (6).

Further, we assume $f_i'' f_i g_i'' - f_i' g_i'^2 = 0$ holds for $i = 1$ and $i = 2$. Then we get

$$f_1(u) = \exp(a_1 u + b_1), \quad g_1(v) = \exp(a_2 v + b_2), \quad (30)$$

$$f_2(u) = \exp(a_3 u + b_3), \quad g_2(v) = \exp(a_4 v + b_4),$$

Substituting these functions into $B = 0$ and $f_1'' f_2 g_1 g_2'' + f_1 f_2'' g_1'' g_2 - 2f_1' f_2' g_1' g_2' = 0$, we

have $a_4 = \frac{a_3 a_i}{a_j}$, $i, j = 1, 2$ ($i \neq j$) which vanish

Gaussian curvature of the surface. Thus, we obtain the case (7).

Also, if $f_1(u) = f_2(u)$ and $g_1(v) = \cos v$, $g_2(v) = \sin v$, then we get

$$-f_1''(u)f_1(u)(f_1'(u)^2 + 1) + (f_1'(u))^2((f_1'(u))^2 - 1) = 0$$

which gives the case (8).

Example 1. The surface with the parameterization

$$F(u, v) = \left(\begin{array}{l} u, v, \exp(2u + 3) \exp(3v + 4), \\ \exp(u + 1) \exp\left(\frac{2}{3}v + 2\right) \end{array} \right) \quad (31)$$

is timelike flat factorable surface in IE_1^4 and one can plot its projection to 3-dimensional space with the help of the maple command

$$\text{plot3d}([u + v, z, w], u = a..b, v = c..d). \quad (32)$$

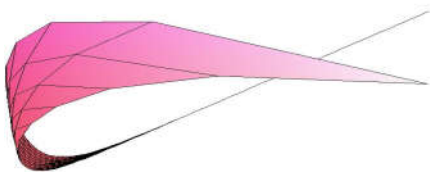


Figure 1 Projection of timelike flat factorable surface given by (31)

2.2. Timelike minimal factorable surfaces

Theorem 2. Let S be a timelike factorable surface with the parameterization (16) in IE_1^4 . Then its mean curvature vector is given by

$$\bar{H} = -\frac{f_1'' g_1 G + f_1 g_1'' E - 2f_1' g_1' F}{2\sqrt{AW^2}} \xi_1 - \frac{\left(\begin{array}{l} A(f_2'' g_2 G + f_2 g_2'' E - 2f_2' g_2' F) \\ -B(f_1'' g_1 G + f_1 g_1'' E - 2f_1' g_1' F) \end{array} \right)}{2\sqrt{ADW^2}} \xi_2. \quad (33)$$

Proof. By the use of the equations (11), (14) and (23), we obtain the desired result.

Theorem 3. Let S be a timelike factorable surface with the parameterization (16) in IE_1^4 . Then S is a minimal surface if and only if

$$f_i'' g_i G + f_i g_i'' E - 2f_i' g_i' F = 0, \quad i=1,2 \quad (34)$$

Proof. Let S be a factorable surface in IE_1^4 . Since we can write the mean curvature vector as $H = -H_1 \xi_1 - H_2 \xi_2$, for a minimal surface $H_1 = 0, H_2 = 0$. With reference to the previous theorem, we get (34). The converse statement is trivial.

Theorem 4. Let S be a timelike factorable surface with the parametrization (16) in IE_1^4 . If S is given by one of the following parameterizations, then it is minimal:

$$(1) F(u, v) = (u, v, (a_1 u + a_2) b_1, (a_3 u + a_4) b_2),$$

$$(2) F(u, v) = (u, v, a_1 (b_1 v + b_2), a_2 (b_3 v + b_4)),$$

$$(3) F(u, v) = (u, v, (a_1 u + a_2) b_1, a_3 (b_3 v + b_4)),$$

$$(4) F(u, v) = \left(\begin{array}{l} u, v, a_1 b_1, \\ (u + a_2) \frac{-1 - \exp(b_2 v + b_3)}{-1 + \exp(b_2 v + b_3)} \end{array} \right),$$

$$(5) F(u, v) = (u, v, a_1 b_1, \tan(a_2 u + a_3)(v + b_2)),$$

$$(6) F(u, v) = \left(\begin{array}{l} u, v, \\ \frac{-1 - a_1^2 + \exp(\pm 2a_1(a_1 u + a_2))}{2a_1 \exp(\pm 2a_1(a_1 u + a_2))} \cos v, \\ \frac{-1 - a_1^2 + \exp(\pm 2a_1(a_1 u + a_2))}{2a_1 \exp(\pm 2a_1(a_1 u + a_2))} \sin v \end{array} \right),$$

$$(7) F(u, v) = \left(\begin{array}{l} u, v, (u + a_1) \frac{-1 - \exp(b_1 v + b_2)}{-1 + \exp(b_1 v + b_2)}, \\ (u + a_1) \frac{-1 - \exp(b_1 v + b_2)}{-1 + \exp(b_1 v + b_2)} \end{array} \right),$$

$$(8) F(u, v) = \left(\begin{array}{l} u, v, \tan(a_1 u + a_2)(v + b_1), \\ \tan(a_1 u + a_2)(v + b_1) \end{array} \right),$$

$$(9) F(u, v) = (u, v, a_1 b_1, f_2(u)g_2(v)),$$

$$(10) F(u, v) = (u, v, f_1(u)g_1(v), f_1(u)g_1(v)),$$

the functions $f_i(u), g_i(v), i = 1, 2$ satisfy the equations

$$u = \int \frac{df_i(u)}{\sqrt{2m \ln f_i(u) + a_1}}, v = \int \frac{dg_i(v)}{\sqrt{a_2 g_i^4(v) - \frac{n}{2}}},$$

$$u = \int \frac{df_i(u)}{\sqrt{a_1 f_i^4(u) - \frac{m}{2}}}, v = \int \frac{dg_i(v)}{\sqrt{2n \ln g_i(v) + a_2}},$$

$$u = \int \frac{df_i(u)}{\sqrt{a_1 f_i^{2(1+c)}(u) - a_2}}, v = \int \frac{dg_i(v)}{\sqrt{a_3 g_i^{2(1-c)}(v) - a_4}},$$

where $c, m, n, a_k, b_k, k = 1, \dots, 4$ are real constants and $c \neq 1$.

Proof. Let S be a timelike factorable surface with the parameterization (16) in IE_1^4 . By the use of (34) with (18), we get,

$$\begin{aligned} & f_i'' g_i \left(1 + f_1'^2 g_1'^2 + f_2'^2 g_2'^2 \right) \\ & + f_i g_i'' \left(-1 + f_1'^2 g_1'^2 + f_2'^2 g_2'^2 \right) \\ & - 2f_i' g_i' \left(f_1' f_1 g_1' g_1 + f_2' f_2 g_2' g_2 \right) = 0, \quad i = 1, 2. \end{aligned} \quad (35)$$

If $g_1'(v) = 0, g_2'(v) = 0$ or $f_1'(u) = 0, f_2'(u) = 0$, we obtain the cases (1) and (2), respectively.

If $f_i'(u) = 0, g_j'(v) = 0, i, j = 1, 2, i \neq j$, then

$$f_1'' g_1 \left(1 + f_1'^2 g_1'^2 + f_2'^2 g_2'^2 \right) = 0, \quad (36)$$

$$f_2 g_2'' \left(-1 + f_1'^2 g_1'^2 + f_2'^2 g_2'^2 \right) = 0. \quad (37)$$

Since $E < 0$ and $G > 0$, then we get $f_1''(u) = 0, g_1'(v) = 0$ and $g_2''(v) = 0, f_2'(u) = 0$ which congruent the case (3).

If $f_1'(u) = 0, g_1'(v) = 0$, from the equality (35) for $i=2$, we get

$$\begin{aligned} & \frac{f_2''(u)}{f_2(u)} - \frac{g_2''(v)}{g_2(v)} \\ & + \left(f_2''(u) f_2(u) - f_2'^2(u) \right) g_2'^2(v) \\ & + \left(g_2''(v) g_2(v) - g_2'^2(v) \right) f_2'^2(u) = 0 \end{aligned} \quad (38)$$

If $f_2''(u) = 0$ or $g_2''(v) = 0$ in (38), we obtain the cases (4) and (5).

If $f_2''(u) g_2''(v) \neq 0$ in (38), differentiating (38) with respect to u and v , we have

$$\frac{\left(f_2''(u) f_2(u) \right)' - \left(-f_2'^2(u) \right)'}{\left(f_2'^2(u) \right)'} = - \frac{\left(g_2''(v) g_2(v) \right)' - \left(-g_2'^2(v) \right)'}{\left(g_2'^2(v) \right)'} = c \quad (39)$$

Thus, we can write

$$\begin{aligned} & f_2''(u) f_2(u) - (1+c) f_2'^2(u) = m, \\ & g_2''(v) g_2(v) - (1-c) g_2'^2(v) = n. \end{aligned} \quad (40)$$

If $c = 1, c = -1$, and $c \neq \pm 1$, then from the solution of (39), we obtain the case (9).

If $f_1(u) = f_2(u)$ and $g_1(v) = \cos v, g_2(v) = \sin v$, then we get

$$f_i''(u)(1 + f_i'^2(u)) - f_i(u)\left(-1 + f_i'^2(u)\right) = 0.$$

By the solution of this differential equation we obtain the case (6).

If $f_1(u) = f_2(u)$, $g_1(v) = g_2(v)$ in (35), then for $i = 1$ or $i = 2$, we find

$$\begin{aligned} & \frac{f_i''(u)}{f_i(u)} - \frac{g_i''(v)}{g_i(v)} \\ & + \left(f_i''(u)f_i(u) - f_i'^2(u) \right) 2g_i'^2(u) \\ & + \left(g_i''(v)g_i(v) - g_i'^2(v) \right) 2f_i'^2(u) = 0. \end{aligned} \quad (41)$$

If $f_i''(u) = 0$ or $g_i''(v) = 0$ in (40), we obtain the cases (7) and (8). Also, if $f_i''(u)g_i''(v) \neq 0$, we obtain the case (10), which completes the proof.

REFERENCES

- [1] B.Y. Chen and J. Van der Veken, "Marginally trapped surfaces in Lorentzian space forms with positive relative nullity," *Class. Quantum Grav.*, vol. 24, pp. 551–563, 2007.
- [2] G. Ganchev, "Timelike surfaces with zero mean curvature in Minkowski 4 – space," *Israel J. of Math.*, vol. 196, pp. 413–433, 2013.
- [3] B. Bektaş, U. Dursun, "Timelike rotational surface of elliptic, hyperbolic and parabolic types in Minkowski space IE_1^4 with pointwise 1 – type Gauss map," *Filomat*, vol. 29, no. 3, pp. 381–392, 2015.
- [4] B. Y. Chen, "Geometry of Submanifolds," *Marcel Dekker*, New York, 1973.
- [5] I. Van de Woestyne, "A new characterization of helicoids," *Geometry and Topology of Submanifolds V.*, World Sci. Publ. River Edge, NJ, 1993.
- [6] I. Van de Woestyne, "Minimal homothetical hypersurfaces of a semi-Euclidean space," *Results Math*, vol. 27, no. 3, pp. 333–342, 1995.
- [7] R. Lopez, M. Moruz, "Translation and homothetical surfaces in Euclidean spaces with constant curvature," *J. Korean Math. Soc.*, vol. 52, no. 3, pp. 523–535, 2015.
- [8] H. Meng, H. Liu, "Factorable surfaces in 3 – Minkowski space," *Bull. Korean Math. Soc.*, vol. 46, no. 1, pp. 155–169, 2009.
- [9] Y. Yu, H. Liu, "The factorable minimal surfaces," *Proceedings of The Eleventh International Workshop on Diff. Geom.*, vol. 11, pp. 33–39, 2007.
- [10] S. Büyükkütük, "A characterization of factorable surfaces," *PhD Thesis*, Kocaeli University, Kocaeli, Turkey, 2018.
- [11] S. Büyükkütük, G. Öztürk, "A characterization of factorable surfaces in Euclidean 4-space IE^4 ," *Koc. J. Sci. Eng.*, vol. 1, no. 1, pp. 15–20, 2018.
- [12] S. Büyükkütük, G. Öztürk, "Spacelike factorable surfaces in four-dimensional Minkowski space," *Bulletin of Mathematical Analysis and Applications*, vol. 9, no. 4, pp. 12–20, 2017.
- [13] Y. A. Aminov, "Surfaces in IE^4 with a Gaussian curvature coinciding with a Gaussian torsion up to sign," *Mathematical Notes*, vol. 56, pp. 5–6, 1994.
- [14] B. Bulca, K. Arslan, "Surfaces given with the Monge patch in IE^4 ," *Journal of Mathematical Physics, Analysis, Geometry*, vol. 9, no. 4, pp. 435–447, 2013.
- [15] K. Arslan, B. K. Bayram, B. Bulca, G. Öztürk, "Generalized rotational surfaces in IE^4 ," *Results in Mathematics*, vol. 61, no. 3-4, pp. 315–327, 2012.
- [16] K. Arslan, B. K. Bayram, B. Bulca, Y.H. Kim, C. Murathan, G. Öztürk, "Rotational embeddings in IE^4 with pointwise 1-type Gauss map," *Turk J. Math.*, vol. 35, pp. 493–499, 2011.
- [17] K. Arslan, B. Bulca, B. K. Bayram, Y. H. Kim, C. Murathan, G. Öztürk, "Tensor product surfaces with pointwise 1-type Gauss map," *Bull. Korean Math. Soc.*, vol. 48, no. 3, pp. 601–609, 2011.
- [18] K. Arslan, B. K. Bayram, B. Bulca, Y.H. Kim, C. Murathan, G. Öztürk, "Vranceanu surface in IE^4 with pointwise 1-type Gauss map," *Indian J. Pure Appl. Math.*, vol. 42, no. 1, pp. 41–51, 2011.
- [19] E. İyigün, K. Arslan, G. Öztürk, "A characterization of Chen surfaces in IE^4 ," *Bull. Malays. Math. Soc.*, vol. 31, no. 2, pp. 209–215, 2008.
- [20] İ. Kişi, G. Öztürk, "A new approach to canal surface with parallel transport frame," *International Journal of Geometric Methods in Modern Physics.*, vol. 14, no. 2, 2017.
- [21] G. Öztürk, İ. Kişi, S. Büyükkütük "Constant ratio quaternionic curves in Euclidean spaces," *Advances in Applied Clifford Algebras*, vol. 27, no. 2, pp. 1659–1673, 2017.

- [22] İ. Kişi, S. Büyükkütük, Deepmala, G. Öztürk, "AW(k)-type curves according to parallel transport frame in Euclidean space IE^4 ," *Facta Universitatis, Series: Mathematics and Informatics.*, vol. 31, no. 4, pp. 885-905, 2016.
- [23] K. Arslan, B. K. Bayram, B. Bulca, G. Öztürk, "On translation surfaces in 4-dimensional Euclidean space," *Acta et Commentationes Universitatis Tartuensis de Mathematica*, vol. 20, no. 2, pp. 123-133, 2016.
- [24] B. Bulca, K. Arslan, B. Bayram, G. Öztürk, "Spherical product surface in IE^4 ," *Analele Stiintifice ale Universtatii Ovidius Constanta.*, vol. 20, no. 1, pp. 41-54, 2012.
- [25] B. Bayram, B. Bulca, K. Arslan, G. Öztürk, "Superconformal ruled surfaces in IE^4 ," *Mathematical Communications.*, vol. 14, pp. 235-244, 2009.
- [26] B. Bulca, K. Arslan, B. Bayram, G. Öztürk, "Canal surfaces in 4-dimensional Euclidean space," *An International Journal of Optimization and Control Theories & Applications.*, vol. 7, no. 1, pp. 83-89, 2017.
- [27] G. Öztürk, S. Gürpınar, K. Arslan, "A new characterization of curves in Euclidean 4-space IE^4 ," *Buletinul Academici de Ştiinte a Republicii Moldova Matematica*, vol. 83, no. 1, pp. 39-50, 2017.
- [28] G. Öztürk, B. Bulca, B. K. Bayram, K. Arslan, "Meridean surfaces of Weingarten type in 4-dimensional Euclidean space IE^4 ," *Konuralp Journal of Mathematicss.*, vol. 4, no. 1, pp. 239-245, 2016.

	SAKARYA UNIVERSITY JOURNAL OF SCIENCE		 SAKARYA UNIVERSITY
	e-ISSN: 2147-835X http://www.saujs.sakarya.edu.tr		
	<u>Received</u> 08-06-2018 <u>Accepted</u> 05-11-2018	<u>Doi</u> 10.16984/saufenbilder.431977	

Incorporation of Cadmium into Hexagonal Boron Nitride by Solid State Reaction

Erhan Budak

Abstract

In this study, cadmium-hexagonal boron nitride (Cd-h-BN) was synthesized according to the O'Connor method with varying amounts of cadmium(II) nitrate. The structural characterizations were performed with FTIR, XRD, and SEM techniques while the cadmium contents in Cd-h-BN were determined by AAS. XRD results shown that an increase in interlayer distance of h-BN, and nano-scale products were observed at 1050°C. The lattice constants were calculated by Scherrer equation, and the results were very close to the original h-BN. Although different amounts of $\text{Cd}(\text{NO}_3)_2 \cdot 5\text{H}_2\text{O}$ were added in the starting mixtures, the cadmium contents of Cd-h-BN samples showed no significant difference, and few amounts of cadmium was intercalated to h-BN. In addition, increasing cadmium amount caused minor grain growth of h-BN samples.

Keywords: Hexagonal boron nitride; Metal intercalation; O'Connor Method; Nanocrystalline materials.

1. INTRODUCTION

Graphite-like hexagonal boron nitride (h-BN) is a typical layered substance which of planar hexagonal networks stacked with van der Waals forces to form three-dimensional structure. There are many techniques for h-BN synthesis, but the O'Connor method [1] was used to produce h-BN in the because of its easiness. According to this method in our previous study [2], it was claimed that a positive effect of transition metals was observed on the h-BN synthesis at relatively low temperatures. Moreover, an electronic interaction was occurred among the transition metal and h-BN layers ($d-\pi$ interaction) which influenced the interlayer distance. In addition to the electronic effects, the size of transition metal also affected the interlayer distance, i.e., a second-row transition metal, silver had a larger size than all the other metals studied in the previous work [2] resulting in a greater interlayer distance.

In present work, cadmium was chosen as model element to investigate the effects of second row transition metals on the structure of metal intercalated h-BN. Thus, the cadmium contents of the h-BN were measured to examine relationship between grain size and metal amount.

2. EXPERIMENTAL

According to O'Connor method [1], h-BN sample was synthesized in the presence of cadmium salt. Boron oxide (4 g) was mixed with urea (2 g) and varying amount of cadmium (II) nitrate pentahydrate (0.08, 0.16, 0.32, and 0.64 g). In precursor formation step, the powder mixture was pre-heated at 200°C for 2 hours in furnace, and then the precursor was ground in a mortar. Main heating process was performed at 1050°C for 2 hours in a cylinder furnace under ammonia (flow rate 120 mL / min). The raw h-BN was leached in hot 10% HCl then washed with methanol, and

dried at 100°C. The solutions for AAS were prepared according to Tereshkova [3] from obtained gray-white powder.

Type of chemical bonds were detected by Shimadzu 8400 FTIR, and XRD examinations were performed by the Rigaku DMAX 2000/PC. h-BN surface was monitored by Zeiss Evo 50, and the amounts of cadmium were calculated by using Perkin Elmer Analyst 100 model AAS.

3. RESULTS AND DISCUSSION

There are some studies [4-6] in the literature for h-BN stretching vibrations by IR spectroscopy. Two distinguishing bands (**Fig. 1**) were detected at ~1380 and ~780 cm⁻¹ and labeled as BN in-plane and out-of-plane vibrations respectively[4,6,7]. The broad absorption band near ~3200, and ~3400 cm⁻¹ were identified as the -NH, and -OH, stretching vibrations, respectively when the boron oxide and urea systems were used [2,8-11].

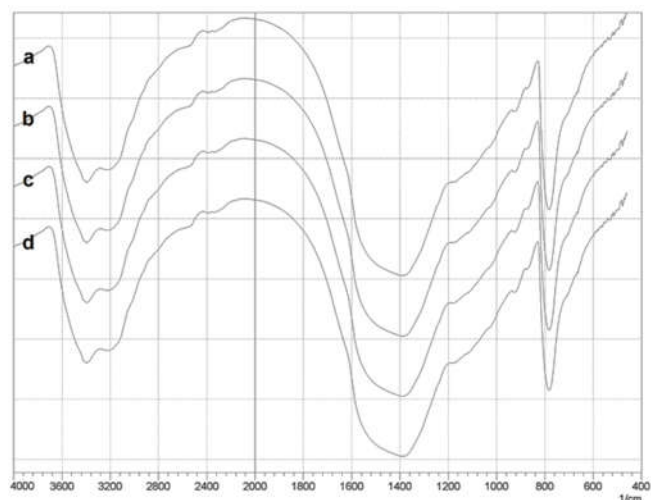


Fig. 1. FTIR spectrum of nano-crystalline h-BN compounds. The weight of Cd(NO₃)₂ amount in starting mixture a) 0.08 g, b) 0.16 g, c) 0.32 g, and d) 0.64 g.

The main peaks of h-BN (**Fig. 2**) (002, 10X, 004, 110, and 112) were observed (10X: Not separated 100 and 101 peaks of h-BN) in XRD patterns. Recent studies [6,12,13] have already pinpointed that the inseparable 100 and 101 peaks indicate formation of the nano-crystalline h-BN. Both NH₃ and metal salts lowers the synthesis temperature of h-BN; the metal salts pretend as catalytic agent [10,12,14] while NH₃ acts as the nitriding agent [4,15,16].

The enlargement in XRD peaks also illustrated that the grain sizes of h-BN were in nano-scale [12,13,17]. Average grain size of samples was

found 5 nm using Scherrer equation. Also, the lattice parameters and interlayer distance were estimated and presented in **Table 1**.

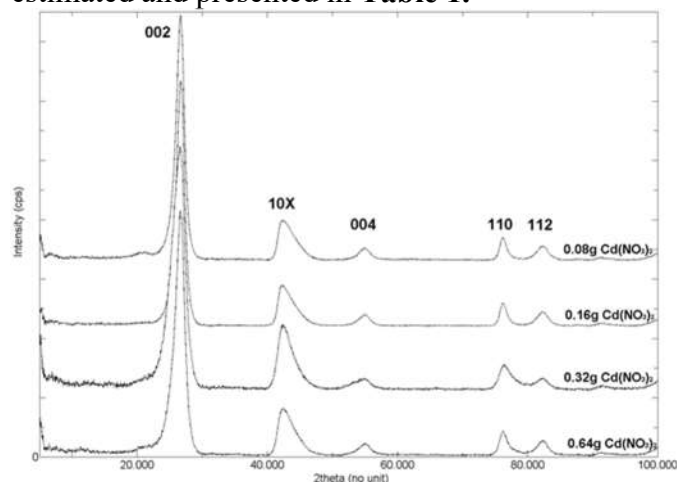


Fig. 2. XRD patterns of nano-crystalline h-BN samples.

Table 1. Computed lattice parameters of samples, and cadmium amount in the precursor and samples.

Cd in the precursor (%)	Lattice parameters	Cd in the Cd-h-BN (% w/w)
0.49	a (Å)	2.496
	c (Å)	6.686
	d (Å)	3.343
0.97	a (Å)	2.490
	c (Å)	6.722
	d (Å)	3.361
1.94	a (Å)	2.496
	c (Å)	6.678
	d (Å)	3.339
3.89	a (Å)	2.496
	c (Å)	6.688
	d (Å)	3.344

In our previous study [2], we claimed that the interlayer spacing was affected by the size of the metal atoms and their electron configuration. In addition, it was found that silver containing sample had a greater interlayer spacing. In present study, interlayer distance of samples was also found larger than 3.3281 Å.

The morphological examination was performed by means of using SEM images (**Fig. 3 and 4**) indicated nearly homogenously grained h-BN particles with flaky and irregular shapes as reported before [18].

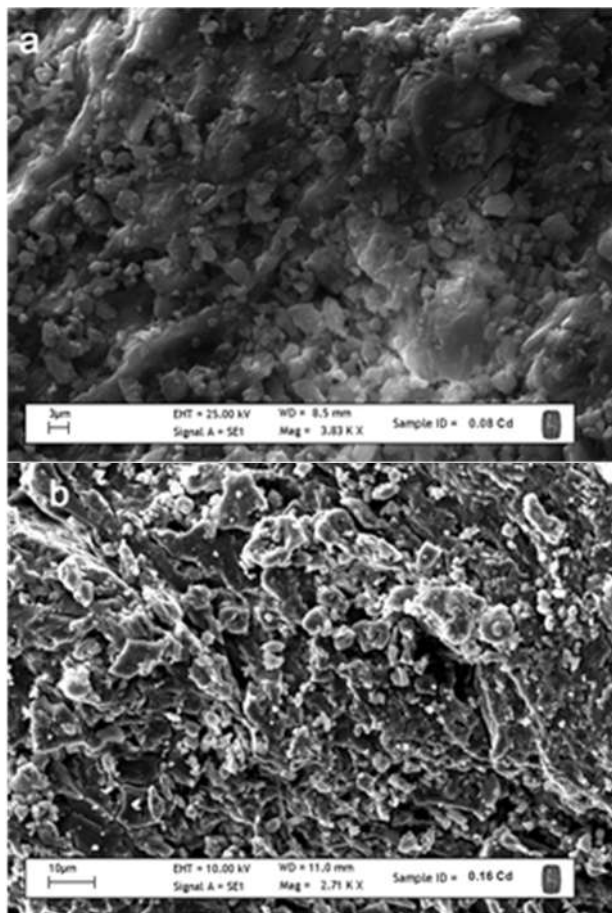


Fig. 3 SEM images of the samples. The sample was prepared with 0.08 g (a), and with 0.16 g (b) Cd (NO₃)₂.

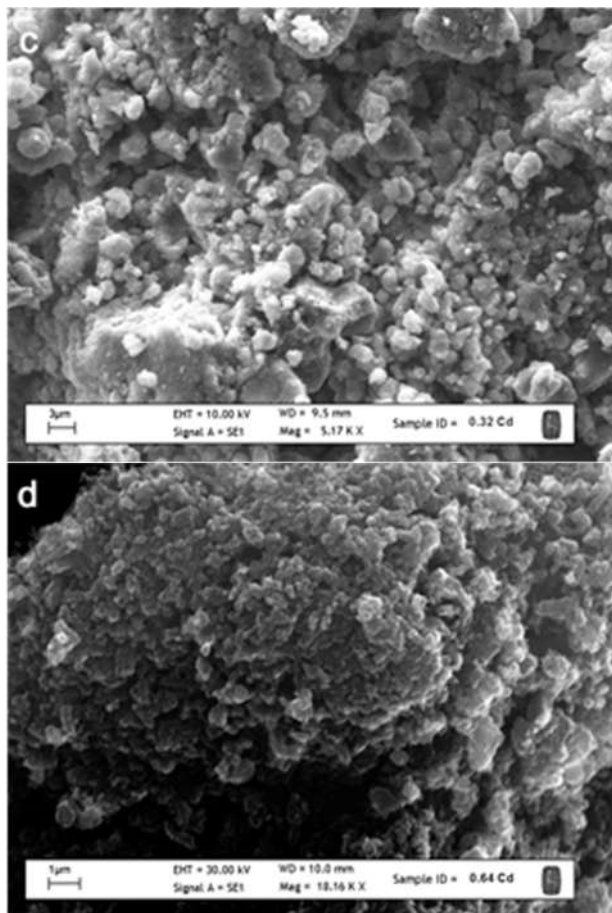


Fig.4 SEM images of the samples. The sample was prepared with 0.32 g (a), and with 0.64 g (b) Cd(NO₃)₂.

The cadmium amounts in the obtained samples were determined by AAS. Although different amounts of cadmium(II) nitrate pentahydrate were added in the starting mixtures, the cadmium contents of Cd-h-BN samples showed no significant difference (**Table 1**). Furthermore, using the values in **Table 1**, the ratio of B₃N₃ units to cadmium atoms was calculated as 5000:1 on molar basis. This ratio points out that few amounts of cadmium was intercalated to h-BN by modified O'Connor method. Shuvaev [19] proposed that transition metal can be located in pores and / or cracks of h-BN.

4. CONCLUSION

In summary, nano-sized h-BN were synthesized with varying amounts of cadmium (II) nitrate at 1050°C. It was found that the lattice parameters are very close to original h-BN. Traditional production of h-BN requires ≥1500°C in industrial scale. Reducing the temperature to 1000°C result with turbostratic (amorphous) structure. Usage of both ammonia and cadmium salt lower the formation temperature of h-BN. In addition, the electronic interaction among the transition metal and h-BN layers (d-π interaction) influenced the interlayer spacing of h-BN. In current study, according to AAS results, the cadmium contents of Cd-h-BN samples showed no significant difference, and the ratio of B₃N₃ units to cadmium atoms was calculated as 5000:1 on molar basis. This ratio indicates that few amounts of cadmium located in pores and / or cracks of h-BN.

5. REFERENCES

- [1] T. E. O'Connor, "Synthesis of Boron Nitride," *J. Am. Chem. Soc.*, vol. 84, no. 9, pp. 1753–1754, May 1962.
- [2] E. Budak and Ç. Bozkurt, "The effect of transition metals on the structure of h-BN intercalation compounds," *J. Solid State Chem.*, vol. 177, no. 4–5, 2004.
- [3] J. W. Tereshko, "Determination of Boron in Boron Nitride, Boronated Graphite Rods, Titanium Borides, and Zirconium Borides Using Tiron of EDTA as the Masking Agent," *Anal. Chem.*, vol. 35, no. 2, pp. 157–158, Feb. 1963.
- [4] M. Hubáček, T. Sato, and T. Ishii, "A coexistence of boron nitride and boric

- oxide," *J. Solid State Chem.*, vol. 109, no. 2, pp. 384–390, 1994.
- [5] J.-Q. Hu *et al.*, "Synthesis and Characterization of Nanocrystalline Boron Nitride," *J. Solid State Chem.*, vol. 148, no. 2, pp. 325–328, 1999.
- [6] L. Chen, Y. Gu, Z. Li, Y. Qian, Z. Yang, and J. Ma, "Low-temperature synthesis and benzene-thermal growth of nanocrystalline boron nitride," *J. Cryst. Growth*, vol. 273, no. 3–4, pp. 646–650, 2005.
- [7] L. Chen *et al.*, "A low-temperature route to nanocrystalline boron nitride whiskers and flakes," *Mater. Lett.*, vol. 58, no. 27–28, pp. 3634–3636, 2004.
- [8] M. Hubáček and M. Ueki, "Chemical reactions in hexagonal boron nitride system," *J. Solid State Chem.*, vol. 123, no. 2, pp. 215–222, 1996.
- [9] P. Dibandjo, L. Bois, F. Chassagneux, and P. Miele, "Thermal stability of mesoporous boron nitride templated with a cationic surfactant," *J. Eur. Ceram. Soc.*, vol. 27, no. 1, pp. 313–317, 2007.
- [10] M. Zheng, Y. Gu, Z. Xu, and Y. Liu, "Synthesis and characterization of boron nitride nanoropes," *Mater. Lett.*, vol. 61, no. 8–9, pp. 1943–1945, 2007.
- [11] S. Yuan *et al.*, "Fluffy-like boron nitride spheres synthesized by epitaxial growth," *Mater. Chem. Phys.*, vol. 112, no. 3, pp. 912–915, 2008.
- [12] L. Shi, Y. Gu, L. Chen, Z. Yang, J. Ma, and Y. Qian, "Formation of nanocrystalline BN with a simple chemical route," *Mater. Lett.*, vol. 58, no. 26, pp. 3301–3303, 2004.
- [13] E. Budak and Ç. Bozkurt, "Synthesis of hexagonal boron nitride with the presence of representative metals," *Phys. B Condens. Matter*, vol. 405, no. 22, 2010.
- [14] G. W. Zhou, Z. Zhang, Z. G. Bai, and D. P. Yu, "Catalyst effects on formation of boron nitride nano-tubules synthesized by laser ablation," *Solid State Commun.*, vol. 109, no. 8, pp. 555–559, 1999.
- [15] T. E. Warner and D. J. Fray, "Nitriding of iron boride to hexagonal boron nitride," *J. Mater. Sci.*, vol. 35, no. 21, pp. 5341–5345, 2000.
- [16] S. Kurooka, T. Ikeda, K. Kohama, T. Tanaka, and A. Tanaka, "Formation and characterization of BN films with Ti added," *Surf. Coatings Technol.*, vol. 166, no. 2–3, pp. 111–116, 2003.
- [17] L. Shi, Y. Gu, L. Chen, Y. Qian, Z. Yang, and J. Ma, "Synthesis and morphology control of nanocrystalline boron nitride," *J. Solid State Chem.*, vol. 177, no. 3, pp. 721–724, 2004.
- [18] J. C. S. Wu, Z. A. Lin, J. W. Pan, and M. H. Rei, "A novel boron nitride supported Pt catalyst for VOC incineration," *Appl. Catal. A Gen.*, vol. 219, no. 1–2, pp. 117–124, 2001.
- [19] A. T. Shuvaev *et al.*, "Graphite intercalation compounds with 3D-transition metals: Graphite-metal interaction," *Phys. B Condens. Matter*, vol. 158, no. 1–3, pp. 539–542, Jun. 1989.

ACKNOWLEDGEMENTS

I would like to thank Prof. Dr. Çetin BOZKURT for his guidance for the past twenty years and Dr. Ercan Selçuk ÜNLÜ for improving the earlier version of the manuscript language.